OCS Study
BOEM 2024-012

Deepwater Atlantic Habitats II: Continued Atlantic Research and Exploration in Deepwater Ecosystems with Focus on Coral, Canyon, and Seep Communities

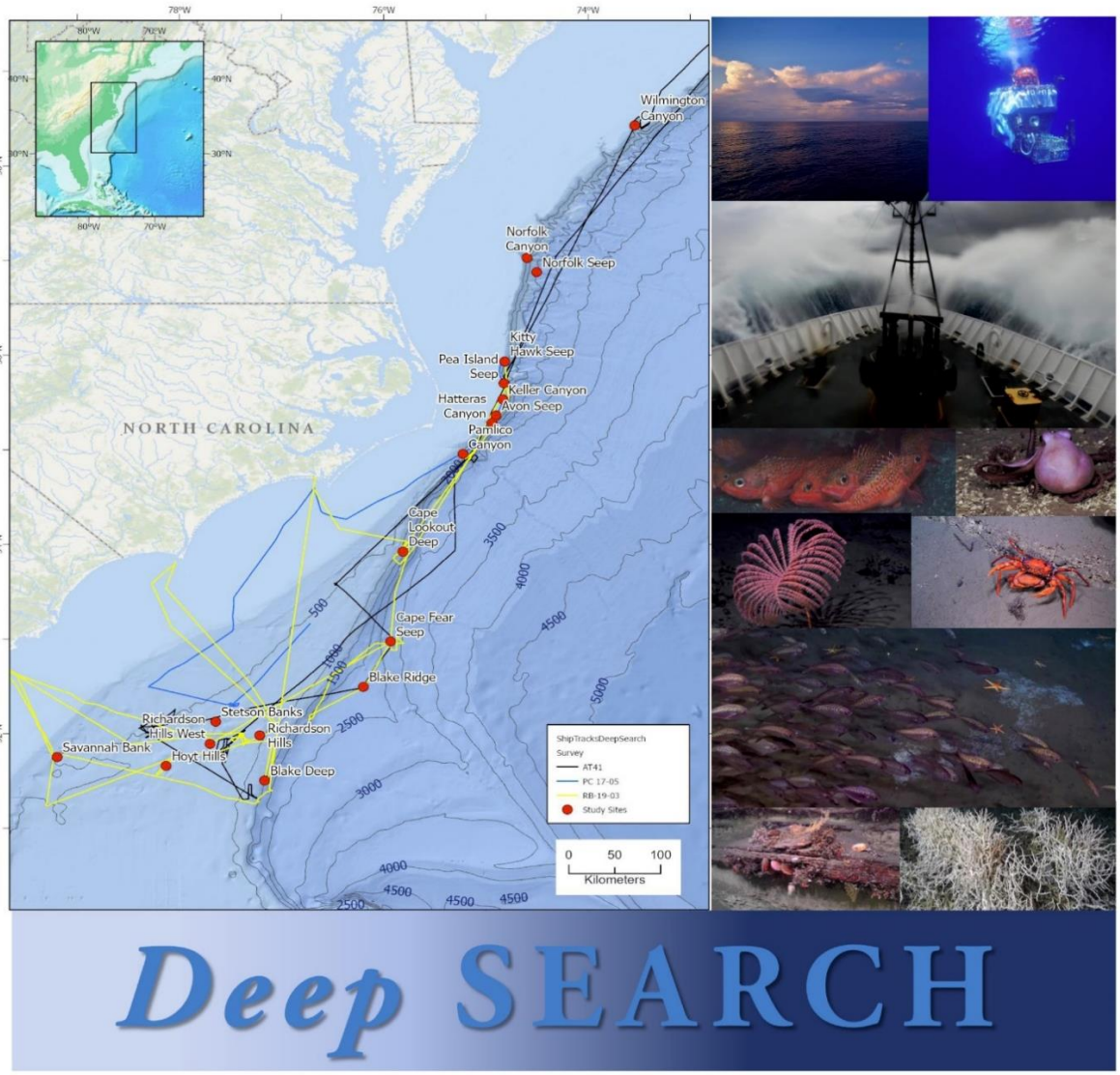

U.S. Department of the Interior
Bureau of Ocean Energy Management
Office of Environmental Programs
Sterling, VA

BOEM
Bureau of Ocean Energy Management

AUTHENTICATED
U.S. GOVERNMENT
INFORMATION
GPO

OCS Study
BOEM 2024-012

Deepwater Atlantic Habitats II: Continued Atlantic Research and Exploration in Deepwater Ecosystems with Focus on Coral, Canyon, and Seep Communities

March 2024

Authors:

Laura Anthony
Aaron Aunins
Sabrina Beckmann
Bernie B. Bernard **
Nicole Blank
Jill Bourque
Randi Bowman
Sandra Brooke **
James M Brooks **
Jane Carrick
Jason Chaytor **
Hannah Choi
Hee Jin Chung
Erik E. Cordes **
Emily Davenport **
Andrew Davies **
Danielle DeLeo
Amanda Demopoulos **
Abigail Engleman
Ryan Gasboro
Carlos Gomez
Andrea Gori
Adam Hallaj
Kimberly Hunter
Ivan Hürzeler **
Samantha Joye **
Christina Kellogg **
Jay Lunden **
Zachary Marinelli
Jennifer McClain-Counts
Catherine McFadden
Tara McIver
Furu Mienis **
Jennifer Miksis-Olds **
Cheryl Morrison **
Martha Nizinski
Nancy Prouty **
Andrea Quattrini **
Alexandra Roads
Diana Sahy
Emma Saso
John Schiff
Makiri Sei
Heather Shull
Anthony Sogluizzo
Tracey Sutton **
Joe Warren
Alexis Weinnig
Dylan Wilford
Gary A. Wolff **
Guang-Chao Zhuang

** Principal Investigator

Prepared under – Contract M17PC00009
By
TDI-Brooks International, Inc.
14391 S Dowling Rd
College Station TX 77845

U.S. Department of the Interior
Bureau of Ocean Energy Management
Office of Environmental Programs
Sterling, VA

BOEM
Bureau of Ocean Energy Management

DISCLAIMER

This study was funded, in part, by the US Department of the Interior, National Oceanographic Partnership Program (NOPP) involving the Bureau of Ocean Energy Management (BOEM), the National Oceanic and Atmospheric Administration (NOAA) Office of Ocean Exploration and Research (OER), and the US Geological Survey (USGS), under Contract Number M17PC00009. This report has been technically reviewed by BOEM, and it has been approved for publication. The views and conclusions contained in this document are those of the authors and should not be interpreted as representing the opinions or policies of BOEM, nor does mention of trade names or commercial products constitute endorsement or recommendation for use.

REPORT AVAILABILITY

Download a PDF file of this report at https://espis.boem.gov/Final%20Reports/BOEM_2024-012.pdf. To search other studies completed by BOEM's Environmental Studies Program, visit https://www.boem.gov/environment/environmental-studies/environmental-studies-information/.

CITATION

Cordes E, Demopoulos A, Bernard B, Brooke S, Brooks J, Joye S, Miksis-Olds J, Quattrini A, Sutton T, Wolff G (TDI-Brooks International, Inc., College Station, TX), et al. 2024. Deepwater Atlantic habitats II: continued Atlantic research and exploration in deepwater ecosystems with focus on coral, canyon, and seep communities. Final report. Sterling (VA): U.S. Dept. of the Interior, Bureau of Ocean Energy Management. 642 p. Report No.: OCS Study BOEM 2024-012.

Acknowledgements

BOEM would like to express deep appreciation for and recognize the significant contributions of individuals and organizations to the success of this study. Without their collective help, this project would not have happened.

- The National Oceanographic Partnership Program, which sponsored this multi-agency study; facilitated agency partnering, competitive proposal advertising, and meeting space logistics; and provided recommendations for proposal peer reviewers.
- The internal project reviewers: Charles Fisher, Larry Mayer, and Jon Moore.
- The capable Officers and crews of all the research vessels that went to sea: *Pisces*, *Atlantis II*, *Ronald Brown*, *Nancy Foster*, *and Brooks McCall*; as well as the expert crews of the deep submergence facilities used for this study: the HOV *Alvin*, ROV *Jason II*, and the AUV *Sentry*.
- Gregory Boland (retired from BOEM in 2018), the initial Contracting Officer's Representative and Chair of the Technical Evaluation Committee including representatives from BOEM, National Oceanic and Atmospheric Administration (NOAA), and U.S. Geological Survey (USGS). He conceived the original study design including the study objectives, general study locations and habitat types that included submarine canyons, seeps, and cold-water coral habitats.
- NOAA Ocean Exploration's Caitlin Adams, who helped organize the use of these ships and submersibles and directly participated in multiple cruises. She also coordinated public outreach information via the NOAA Ocean Exploration web site.
- Bureau of Safety and Environmental Enforcement (BSEE) Contracting Officer Paige Shin, who originated and expertly dealt with the complexities of this multi-agency partnership, which included novel and substantial contributions from NOAA Ocean Exploration and USGS.
- USGS Ecosystems Mission Area, a partner providing resources and funding to USGS scientists (A. Demopoulos, C. Morrison, C. Kellogg, J. Chaytor, and N. Prouty) through the USGS Environments Program, currently known as the Land Management Research Program.
- M. Khalil and L. Ball (USGS) for support throughout this project.

Current BOEM personnel:

- Michael Rasser, who served as the Contracting Officer Representative (COR) after Greg Boland retired. He managed the contract, participated in research cruises, and oversaw review and acceptance of all deliverables, including the final report. He also reviewed the original statement of work and served on the technical proposal evaluation committee.
- Mark Mueller, who served as the final Environmental Studies Program Representative, helping to oversee and administer the latter stages of the study and participating in the final research cruise on NOAA Ship *Nancy Foster*. He also assisted Greg Boland in initial study design and set up, including helping with writing the study profile and advocating for funding, helping define mission needs and study objectives, and serving on the Technical Proposal Evaluation Committee.
- Kate Segarra, who participated in a research cruise and assisted with the collection and processing of samples at sea.
- BOEM subject matter experts—including Tom Kilpatrick, Jennifer Le, Shane Guan, and Stephanie Sharuga—who reviewed the final report and provided substantial comments that improved the report.

Contents

List of Tables ..... **v**

List of Figures ..... **viii**

List of Abbreviations and Acronyms ..... **xvi**

1 Introduction **1**

1.1 Executive Summary 1

1.2 Context and Purpose 2

1.2.1 Regional Seabed Setting and Features 2

1.2.2 Hydrocarbon Seep Ecosystems 4

1.2.3 Submarine-Canyon Ecosystems 6

1.2.4 Deep-Sea Coral Ecosystems 8

1.3 Objectives and Hypotheses 10

1.3.1 Objectives 10

1.3.2 Hypotheses to be Tested 11

2 Field Acquisition **22**

2.1 Site Selection 22

2.1.1 Seep Sites 22

2.1.2 Canyon Sites 23

2.1.3 Coral Sites 24

2.2 Expeditions (Cruises) 26

2.2.1 First Expedition, NOAA Ship *Pisces* with AUV *Sentry* 29

2.2.2 Second Expedition, RV *Atlantis* with DSV *Alvin* 29

2.2.3 Third Expedition, RV *Brooks McCall* 32

2.2.4 Fourth Expedition, NOAA Ship *Ron Brown* with ROV *Jason* 32

2.2.5 Fifth Expedition, NOAA Ship *Nancy Foster* 32

2.3 Sites Visited with Submersibles 33

2.3.1 Seep Sites 33

2.3.2 Canyon Sites 37

2.3.3 Coral Sites 38

3 Physical Setting **44**

3.1 Oceanographic Setting 44

3.1.1 Physical Oceanography 44

3.1.2 Chemical Oceanography 49

3.1.3 Temporal Changes in Oceanographic Parameters 51

3.2 Geologic Setting 62

3.2.1 Historical Geology 62

3.2.2 Geomorphology 66

3.2.3 Methods 70

3.2.4 Results 77

3.3 Biogeochemistry and Microbiology 126

3.3.1 Water-Column Methods 126

3.3.2 Water-Column Results 129
3.3.3 Methods 139
3.3.4 Sediment Results 142
3.3.5 Microbial Community Assessment Methods 152
3.3.6 Microbial Community Assessment Results 153
4 Community Ecology 157
4.1 Community Structure 159
4.1.1 Methods 159
4.1.2 Results 167
4.1.3 Discussion 221
4.2 Fish Communities 229
4.2.1 Introduction 229
4.2.2 Methods 230
4.2.3 Results and Discussion 234
4.3 Octocoral Community Phylogenetics 252
4.3.1 Introduction 252
4.3.2 Methods 254
4.3.3 Results and Discussion 256
4.4 Trophic Ecology 272
4.4.1 Background 272
4.4.2 Methods 274
4.4.3 Results 275
4.4.4 Discussion 316
4.4.5 Conclusions 319
4.5 Remote Sensing of Deep-Sea Habitats 321
4.5.1 Soundscape Ecology 321
4.5.2 Methods 321
4.5.3 Results 325
4.5.4 Discussion 328
4.6 Environmental DNA Analysis of Deep-Sea Habitats 328
4.6.1 Introduction 328
4.6.2 Methods 329
4.6.3 Results 337
4.6.4 Discussion 352
5 Biology of Coral and Seep Fauna 355
5.1 Organismal Physiology 355
5.1.1 Introduction and Context 355
5.1.2 Methods 356
5.1.3 Results 358
5.1.4 Discussion 362
5.2 Coral Symbiosis and Microbiome 364
5.2.1 Methods 365

5.2.2 Results 367
5.2.3 Conclusions 373
5.3 Scleractinian Growth Rate 374
5.3.1 Methods 374
5.3.2 Results 377
5.3.3 Conclusions 381
5.4 Coral Size Distributions 382
5.4.1 Introduction 382
5.4.2 Methods 382
5.4.3 Results 383
5.4.4 Conclusions 383
5.5 Coral Reproductive Biology 386
5.5.1 Introduction 386
5.5.2 Methods 387
5.5.3 Results 389
5.5.4 Conclusions 402
5.6 Seep Mussel Reproductive Biology 405
5.6.1 Introduction 405
5.6.2 Methods 406
5.6.3 Results 406
5.6.4 Conclusions 409
5.7 Population Connectivity 409
5.7.1 Introduction 409
5.7.2 Bathymodiolinae 412
5.7.3 Corals 426
5.7.4 Plumarella spp. 433
5.7.5 Paramuricea spp. 436
5.7.6 Other Invertebrates 439
5.7.7 Conclusions 443
6 Prediction Modeling 445
6.1 *Lophelia pertusa* Mounds as Suitable Habitats 445
6.1.1 Methods 447
6.1.2 Results 448
6.2 Predicting *L. pertusa* Habitat Suitability 455
6.2.1 Methods 456
6.2.2 Results 458
6.2.3 Discussion 462
6.3 Seeps Occurrence Predictions 464
6.3.1 Methods 464
6.3.2 Results and Discussion 465
7 Synthesis of Study Results 468
7.1 Major Findings of This Study 468

7.1.1 Habitat Characterization 468
7.1.2 Community Ecology 469
7.1.3 Biology of Coral and Seep Fauna 470
7.1.4 Improved Prediction of Occurrence 471
7.2 Conclusions and Recommendations for Management 471
8 Deep SEARCH Outreach 476
8.1 Individual PI Contributions 476
8.1.1 Cheryl Morrison – USGS 476
8.1.2 Jennifer Miksis-Olds 476
8.1.3 Tracey Sutton 476
8.1.4 Samantha Joye 476
8.1.5 Erik Cordes 477
8.1.6 Andrea Quattrini 477
8.1.7 Ivan Hurzeler 477
8.2 Outreach Through NOAA Platforms 478
8.3 Outreach Through Press Releases 478
8.3.1 General Press 478
8.3.2 Press Specifically Regarding the Aug/Sep 2018 *Atlantis* Expedition 478
8.4 Outreach Through BOEM Platforms 480
9 References 482
10 Bibliography 538
Appendix A. Data Management with Links to All Data Repositories 542
Appendix B. Publications and Conference Presentations 597

List of Tables

Table 2-1. Expeditions associated with the Deep SEARCH project 27
Table 3-1. Six-month summary of Richardson Hills ALBEX Lander 53
Table 3-2. Authigenic carbonate XRD analysis 84
Table 3-3. Major element geochemistry by WDXRF 85
Table 3-4. ICP-OES-MS Major and trace elements analysis results 85
Table 3-5. XRD analysis results from selected sediment samples 88
Table 3-6. ICP-OES-MS Major and trace elements analysis results 89
Table 3-7. Composition of selected authigenic carbonates from seep areas. 95
Table 3-8. Clumped isotope (Δ_{47}) values of selected authigenic carbonates from seep areas 96
Table 3-9. Authigenic carbonate AMS ^{14}C calibrated radiocarbon ages 98
Table 3-10. Calibrated AMS ^{14}C radiocarbon ages of foraminifera and coral fragments 98
Table 3-11. Summary of measured U-Th concentrations 100
Table 3-12. XRD-derived mineralogy of selected canyon rocks 106
Table 3-13. ICP-OES-MS geochemical analyses of rocks from Blake Escarpment/Blake Deep and Pamlico Canyon 110
Table 3-14. XRD-derived mineralogy of phosphorite pavement 119
Table 3-15. ICP-OES-MS analyses of phosphorite pavement samples 121
Table 3-16. Deep SEARCH water-column biogeochemistry sample collections 126
Table 3-17. Deep SEARCH sediment biogeochemistry sample collections 126
Table 3-18. Detailed summary of pelagic sample collections 127
Table 3-19. Summary of sediment collections 139
Table 3-20. Authigenic carbonate samples analyzed for microbial community via DNA marker genes 153
Table 4-1. Summary of dives conducted during the AT41 and RB19 expeditions 160
Table 4-2. Habitat codes used for benthic habitat characterization 161
Table 4-3. Field Expeditions on Research Vessels 163
Table 4-4. PCR primers and protocols used to amplify target loci in non-octocoral specimens 165
Table 4-5. List of morphospecies observed 173
Table 4-6. ANOVA results on terms included in the dbRDA model for all habitats 186
Table 4-7. ANOVA results on terms included in the dbRDA model for Lophelia habitats 187
Table 4-8. DISTLM of environmental and terrain variables using data from AT41 and RB1903 dives 193
Table 4-9. DISTLM of environmental and terrain variables using a subset of RB1903 dives 194
Table 4-10. Community collection matrix 196
Table 4-11. DISTLM of environmental variables with coral-adjacent sediment communities 202
Table 4-12. DISTLM of environmental variables for seep sediment communities 210
Table 4-13. DISTLM of environmental variables with canyon sediment communities 215
Table 4-14. DISTLM of environmental variables with canyon hard-substrate communities 220

Table 4-15. Summary of submersible and ROV dives analyzed for demersal fish surveys 231
Table 4-16. Traits examined in functional diversity analyses 233
Table 4-17. Fishes collected and identified during ADEON pelagic sampling 235
Table 4-18. Fishes collected and identified during 2019 *Nancy Foster* sampling 239
Table 4-19. Summary of dives octocoral collections during AT41 and RB19 expeditions 254
Table 4-20. PCR primers and protocols used to amplify target loci in collected specimens (Cnidaria) ... 255
Table 4-21. Mean $\delta^{13}C$ and $\delta^{15}N$ for fauna, POM, and sediment collected from coral sites 277
Table 4-22. Mean $\delta^{13}C$ and $\delta^{15}N$ for fauna, POM, and sediment collected from seeps 287
Table 4-23. Values of δ34S and percent sulfur for a subset of fauna collected at seeps 291
Table 4-24. Values of $\delta^{13}C$ and $\delta^{15}N$ for fauna, POM and sediment collected at canyons 294
Table 4-25. Mean values of $\delta^{13}C$ and $\delta^{15}N$ for fauna collected with trawls 299
Table 4-26. Mean values of $\delta^{13}C$ and $\delta^{15}N$ for fishes collected across multiple sites 307
Table 4-27. Long-term dataset information and data collection parameters 324
Table 4-28. Metadata for dives where bottom water was collected for eDNA extraction 330
Table 4-29. Gene regions and associated metabarcoding primer pairs utilized 335
Table 4-30. Read pairs retained for analysis at the *cox1* and 18S metabarcoding marker 338
Table 4-31. ASVs counted in each metabarcoding set after denoising with dada2. 339
Table 4-32. ASVs identified as differentially abundant at the 18S marker through ANCOM 345
Table 4-33. ASV's contributing up to 70% if the variation between habitats at the 18S marker 345
Table 4-34. ASVs identified as differentially abundant through ANCOMs at the *cox1* marker 347
Table 4-35. ASV's contributing up to 70% if the variation between habitats at the cox1 marker 347
Table 5-1. Average of the different physical and chemical parameters measured 357
Table 5-2. Average respiration, excretion, and feeding rates, and oxygen to nitrogen ratio 359
Table 5-3. One-way ANOVA table of dependent variables results between two temperatures 360
Table 5-4. Semi-soft nutrient agars tested for bacterial isolation from *L. pertusa* 366
Table 5-5. Coral samples processed for microbiome characterization 369
Table 5-6. Coral samples processed for microarray analysis 373
Table 5-7. Metrics for deployed fragments derived from models using Autodesk Netfab 380
Table 5-8. Metrics of size measurements for three species of scleractinians from five research cruises in the study region in 2018 and 2019 383
Table 5-9. Number of coral samples processed for gametogenetic analysis from August 2018 cruise ... 388
Table 5-10. Number of coral samples processed for gametogenetic analysis from April 2019 cruise 388
Table 5-11. Average feret diameter of female oocytes from corals 390
Table 5-12. Gametogenic stages of male spermatocysts from corals 390
Table 5-13.Summary of gamete stages from *Bathymodiolus heckerae* from Blake Ridge Seep 407
Table 5-14. Bathymodiolin mussel samples collected 413
Table 5-15. Overall summary statistics for Bathymodiolin mussels across loci 418

Table 5-16. Pairwise Fst values for *G. childressi* 419
Table 5-17. Kinship associations and log-likelihood ratios among *G. childressi* individuals 420
Table 5-18. Inferred (posterior mean) migration rates from the BayesAss analysis 421
Table 5-19. Estimated inbreeding coefficients (Fis) at each site with standard error 421
Table 5-20. Pairwise Fst values for *B. heckerae* collected from Blake Ridge Seep 423
Table 5-21. Kinship associations and associated LLR among *B. heckerae* 423
Table 5-22. Overall population statistics for the Bathymodiolin mussels 424
Table 5-23. Overall statistics for *Lophelia pertusa* 430
Table 5-24. Overall population-level statistics for the *L. pertusa* sample sites 430
Table 5-25. Pairwise Fst values and corresponding p-values for *Plumarella* spp. 435
Table 6-1. Summary of variables included in habitat suitability models 448
Table A-1. Data available through OSF 542

List of Figures

Figure 1-1. Coral-formed bioherms 3
Figure 1-2. *Bathymodiolus heckerae* mussels in seep community 6
Figure 1-3. Some canyon invertebrates and fishes 7
Figure 1-4. Various coral assemblages from canyon sites visited 8
Figure 1-5. Bioherms capped with live deep-sea coral 9
Figure 2-1. Ship track map during operations for the three submersible cruises 28
Figure 2-2. *Alvin* dive locations during the second cruise 30
Figure 2-3. Locations of CTD casts and core acquired during the second cruise 31
Figure 2-4. Locations of sites visited during the fifth cruise 33
Figure 2-5. Rock faces with oddly shaped tubular concretions cemented in place 36
Figure 3-1. ALBEX-02 lander at Richardson Hills Reef area 45
Figure 3-2. Aggregated T-S plots with O_2 45
Figure 3-3. Individual temperature and salinity profiles with water depth 46
Figure 3-4. Individual T-S plots of CTD profiles 47
Figure 3-5. Variability in T-S in relation to presence or absence of the Gulf Stream 47
Figure 3-6. Meandering of the Gulf Stream near Richardson Reef 48
Figure 3-7. Aragonite saturation profiles over the Richardson Reef Complex 51
Figure 3-8. Time-series plots for ALBEX lander instruments 54
Figure 3-9. Current cloud of North and East velocity components of current speed 55
Figure 3-10. Hourly Rate of Change for environmental parameters from ALBEX 56
Figure 3-11. Two-month time series of low-frequency peak SPLs (dB re 1 mPa^2) 58
Figure 3-12. Daily time series of 10th, 50th (median), and 90th acoustic percentiles 58
Figure 3-13. SPD plots 59
Figure 3-14. Major geologic and tectonic basin features of Deep SEARCH study area 63
Figure 3-15. Different positions of the Suwannee and Gulf Stream currents over time 65
Figure 3-16. Schematic diagrams of the antecedent geology of the Deep SEARCH study area 66
Figure 3-17. Bathymetry and geomorphologic features of canyon systems 68
Figure 3-18. Bottom character type of the northern Blake Plateau 72
Figure 3-19. Sub-crop morphologic map of the central and northern Blake Plateau 73
Figure 3-20. Pea Island North bathymetry and water-column anomalies 78
Figure 3-21. Pea Island South bathymetry and water-column anomalies 79
Figure 3-22. Kitty Hawk seep bathymetry and column anomalies 80
Figure 3-23. Blake Ridge Seep bathymetry and water-column anomalies (1-m resolution) 81
Figure 3-24. Cape Fear Seep bathymetry and water-column anomalies (1-m resolution) 82
Figure 3-25. Thin section photomicrographs (all cross polarized) of authigenic carbonate samples 83

Figure 3-26. Stable carbon vs. oxygen isotopes 93
Figure 3-27. Clumped Isotopes 94
Figure 3-28. Grain size and $CaCO_3$/BOM of north ACS canyon cores 102
Figure 3-29. Grain size and $CaCO_3$/BOM Keller and Hatteras canyon cores 103
Figure 3-30. Pamlico Canyon map 104
Figure 3-31. Subsurface stratigraphy through which the Pamlico Canyon cuts 107
Figure 3-32. Photomicrographs of carbonate-rich canyon lithologies 108
Figure 3-33. Monocore and push core grain size and calcium carbonate A & B 112
Figure 3-34. Monocore and push core grain size and calcium carbonate C, D, and E 113
Figure 3-35. Regional map of the northern Blake Plateau and adjacent areas 114
Figure 3-36. Mound features identified in 25-m resolution bathymetry data 116
Figure 3-37. Multibeam bathymetry sub-bottom profiles across prominent coral mounds 117
Figure 3-38. Photomicrographs of phosphorite and ferromanganese crusts. 118
Figure 3-39. Grain size distribution and average $CaCO_3$ content of surficial samples 124
Figure 3-40. Cape Lookout (Deep) bank and multichannel seismic-reflection profile 125
Figure 3-41. Pelagic PO4 & DIN profiles from Pea Island Seep sites, expedition AT41 130
Figure 3-42. Pelagic NH_4 & NO_3 profiles from Pea Island Seep sites, expedition AT41 131
Figure 3-43. Pelagic DOC, DON, & DOP profiles from Pea Island Seep sites, expedition AT41 131
Figure 3-44. Pelagic CH_4 concentration and CH_4 oxidation rate profiles 132
Figure 3-45. Pelagic PO4 & DIN profiles from canyon and offshore sites 134
Figure 3-46. Pelagic NH4 & NO3 profiles from canyon and offshore sites 135
Figure 3-47. Pelagic DOC, DON, and DOP profiles from canyon and offshore sites 135
Figure 3-48. Pelagic CH_4 concentrations and CH_4 oxidation rates 136
Figure 3-49. Pelagic PO4 & DIN from deepwater coral sites 137
Figure 3-50. Pelagic NH4 & NO3 profiles from deepwater coral sites 138
Figure 3-51. Pelagic DOC, DON, and DOP profiles from deepwater coral sites 138
Figure 3-52. Pelagic CH_4 concentration and CH_4 oxidation rate from deepwater coral sites 139
Figure 3-53. Dissolved inorganic N and P from sediments associated with *Beggiatoa* 143
Figure 3-54. Sulfate and methane profiles from sediments associated with *Beggiatoa* 144
Figure 3-55. Rates of AOM vs. [CH4] in sediments associated with *Beggiatoa* 145
Figure 3-56. Dissolved hydrogen sulfide and Eh in sediments from deepwater sites 146
Figure 3-57. Dissolved sulfate and methane in sediments from deepwater sites 146
Figure 3-58. Rates of AOM vs. SR in sediments associated with *Beggiatoa* 147
Figure 3-59. Rates of AOM vs. [CH4] in sediments from deepwater sites 148
Figure 3-60. Rates of AOM vs. SR in shallow sediments from deepwater sites 148
Figure 3-61. Dissolved inorganic N and P in sediments from sites with clear SMTZs 149
Figure 3-62. Dissolved hydrogen sulfide and Eh in sediments from sites with clear SMTZs 150

Figure 3-63. Dissolved sulfate, DIC and methane in sediments from sites with clear SMTZs 150
Figure 3-64. Rates of AOM vs. [CH4] in sediments from sites with clear SMTZs 151
Figure 3-65. Rates of AOM vs. SR in sediments from sites with clear SMTZs 151
Figure 3-66. Bacterial and archaeal community composition in the authigenic carbonates 154
Figure 3-67. Results of multidimensional scaling (MDS) analysis 155
Figure 3-68. Results of RDA, relationship with phyla 155
Figure 3-69. Results of RDA, relationship with geochemicals 156
Figure 4-1. Examples of habitat types characterized during video analysis at seep sites 162
Figure 4-2. Collection locations for Deep SEARCH sites sampled during nine cruises 164
Figure 4-3. Habitat classifications—*Alvin* dives A4962, A4963, A4964, and A 4965 168
Figure 4-4. Habitat classifications—*Alvin* dives A4968, A4969; *Jason* dives J1128, J1129 169
Figure 4-5. Habitat classifications—*Jason* dives J1130, J1131, J1135, and J1138 170
Figure 4-6. Habitat classification for seep sites 171
Figure 4-7. Species-accumulation curves for the different sites and habitat types 172
Figure 4-8. Boxplots of species richness, Shannon Diversity, and Pielou's evenness 178
Figure 4-9. Shannon Diversity and Species Richness overlain on the dive tracks 179
Figure 4-10. Shannon Diversity and Species Richness in each ecosystem type vs. depth 180
Figure 4-11. Depth distributions of the most abundant morphospecies 181
Figure 4-12. nMDS ordination showing dissimilarities of canyon, *L. pertusa*, and coral communities 182
Figure 4-13. nMDS ordination showing dissimilarities within *L. pertusa* reef communities 183
Figure 4-14. nMDS ordination showing dissimilarities between canyon communities 183
Figure 4-15. nMDS ordination showing dissimilarities between non-Lophelia communities 184
Figure 4-16. dbRDA model showing Bray-Curtis megafaunal community dissimilarities 185
Figure 4-17. dbRDA model showing Bray-Curtis Lophelia community dissimilarities 186
Figure 4-18. Habitat classification of coral communities at seep sites 188
Figure 4-19. Community composition of fauna documented at each site 189
Figure 4-20. Species-accumulation curves for megafauna observed at seep sites 190
Figure 4-21. A) Non-metric multidimensional scaling (nMDS) plot using Sorensen's Index 191
Figure 4-22. dbRDA of Sorensen's Index of absence-presence data from observed megafauna 192
Figure 4-23. One-way ANOVA with density at coral sites 195
Figure 4-24. Pairwise Raup-Crick Dissimilarity vs. the pairwise difference in sample depth 198
Figure 4-25. Mean macrofaunal density in coral-adjacent sediment sites 198
Figure 4-26. Mean Shannon Diversity (H') in coral-adjacent sediment sites 199
Figure 4-27. Mean taxa evenness (J') in coral-adjacent sediment sites 200
Figure 4-28. Non-metric multidimensional scaling (nMDS) of coral-adjacent infauna in cores 200
Figure 4-29. Taxonomic composition of dominant macrofauna in coral-adjacent sediments 201
Figure 4-30. Bray-Curtis similarities of abundance data from coral-adjacent push cores 203

Figure 4-31. Mean macrofaunal density at seep and non-seep habitats and sites 204
Figure 4-32. Mean Shannon Diversity at seep and non-seep habitats and sites 205
Figure 4-33. Mean taxa evenness (J') at seep sites 206
Figure 4-34. Non-metric multidimensional scaling (nMDS) of seep-habitat infauna 207
Figure 4-35. CLUSTER analysis of seep sediment communities with SIMPROF groupings indicated 208
Figure 4-36. Taxonomic composition of dominant macrofauna at seep habitats 209
Figure 4-37. Bray-Curtis similarities of abundance data from seep-habitat push cores 210
Figure 4-38. Macrofaunal density of canyon habitats with depth 211
Figure 4-39. Shannon Diversity of canyon habitats with depth and rarefaction of communities 212
Figure 4-40. Taxa evenness (J') of canyon habitats with depth 213
Figure 4-41. Non-metric multidimensional scaling (nMDS) of canyon habitat sediment infauna 213
Figure 4-42. Taxonomic composition of dominant macrofauna at canyon habitats 214
Figure 4-43. dbRDA from the DISTLM analysis 215
Figure 4-44. Macrofaunal density of canyon hard-substrate habitats with depth 216
Figure 4-45. Shannon Diversity of canyon hard-substrate habitats with depth 217
Figure 4-46. Evenness of canyon hard-substrate habitats with depth 217
Figure 4-47. Non-metric multidimensional scaling (nMDS) of canyon hard-substrate infauna 218
Figure 4-48. Taxonomic composition of dominant macrofauna at canyon hard-substrate habitats 219
Figure 4-49. Carbon and nitrogen compositions vs. depth at hard-substrate habitats 221
Figure 4-50. DSL association with bottom topography at Pamlico Canyon 234
Figure 4-51. In situ frame grabs of fish species representing new records for the study areas 241
Figure 4-52. In situ frame grabs of fish species representing range extensions for the study areas 241
Figure 4-53. Species-accumulation curves by habitat 242
Figure 4-54. Non-metric multidimensional scaling ordination plot of fishes by habitat type 243
Figure 4-55. Non-metric multidimensional scaling ordination plot of fishes by region 243
Figure 4-56. Non-metric multidimensional scaling ordination plot of fish habitat type with depth 244
Figure 4-57. Non-metric multidimensional scaling ordination plot of region with depth 245
Figure 4-58. dbRDA ordination plot of habitat and region 246
Figure 4-59. dbRDA ordination plot of depth 246
Figure 4-60. dbRDA ordination plot of temperature 247
Figure 4-61. dbRDA ordination plot of species 247
Figure 4-62. Functional diversity estimates of fish assemblages across depth and habitat 249
Figure 4-63. Functional richness estimates of fish assemblages across depth and habitat 250
Figure 4-64. Functional dispersion estimates of fish assemblages across depth and habitat 250
Figure 4-65. Functional evenness estimates of fish assemblages across depth and habitat 251
Figure 4-66. Functional divergence estimates of fish assemblages across depth and habitat 251

Figure 4-67. Species-accumulation curve of octocoral sampling In the North Atlantic off the US eastern seaboard with 95% confidence intervals 256
Figure 4-68. Species richness and FI of phylogenetic diversity across 11 sites 257
Figure 4-69. FI of PD based on (a) depth (b) habitat type, and (c) SIMPROF group 258
Figure 4-70. Community composition of each site mapped onto a mutS + 28S phylogeny 259
Figure 4-71. Maximum likelihood phylogeny of the MutS barcode rooted at the midpoint 261
Figure 4-72. Maximum likelihood phylogeny of the 28S barcode rooted at the midpoint 262
Figure 4-73. Maximum likelihood phylogeny of the multilocus (MutS + 28S) barcode 264
Figure 4-74. CLUSTER analysis of 11 dive sites 265
Figure 4-75. Histogram of habitat type permutations from one-way ANOSIM analysis 266
Figure 4-76. Histogram of depth range permutations from one-way ANOSIM analysis 266
Figure 4-77. Multidimensional scaling ordination of samples coded to habitat type 267
Figure 4-78. Histogram of habitat-type permutations 267
Figure 4-79. Histogram of depth range permutations 268
Figure 4-80. Multidimensional scaling ordination of site depth 269
Figure 4-81. Multidimensional scaling ordination of average temperature 270
Figure 4-82. Multidimensional scaling ordination of region 271
Figure 4-83. Collection locations for sites sampled during nine cruises from 2016–2019 273
Figure 4-84. Average δ^{13}C and δ^{15}N of fauna, producers, and sediment at coral locations 276
Figure 4-85. Average δ^{13}C and δ^{15}N of fauna, POM, and sediment collected at seeps 286
Figure 4-86. Average isotope values for of a subset of fauna, plotting δ^{34}S vs. δ^{13}C and vs. δ^{15}N 290
Figure 4-87. Average δ^{13}C and δ^{15}N of fauna, POM and sediment from canyons 293
Figure 4-88. Average δ^{13}C and δ^{15}N values of corals from canyon and coral habitats 297
Figure 4-89. Average δ^{13}C and δ^{15}N values of midwater fauna from coral, seep, and canyon sites 298
Figure 4-90. Mean stable isotope values for fish families by species/taxa 306
Figure 4-91. Average δ^{13}C and δ^{15}N values vs. depth for midwater trawl fishes 309
Figure 4-92. Locations of the midwater trawls at Richardson Reef Complex 310
Figure 4-93. Average δ^{13}C and δ^{15}N values of fauna and POM collected from Richardson Reef 311
Figure 4-94. Average δ^{13}C and δ^{15}N values with 95% CI ellipses for each feeding group 311
Figure 4-95. Locations of the midwater trawls at Blake Ridge Seep 312
Figure 4-96. Mean δ^{13}C and δ^{15}N values of fauna, POM, and sediment from Blake Ridge 313
Figure 4-97. Average δ^{13}C and δ^{15}N values with 95% CI for each feeding group from Blake Ridge 313
Figure 4-98. Locations of the midwater trawls at Pamlico Canyon 314
Figure 4-99. Average δ^{13}C and δ^{15}N values of fauna, POM and Pamlico Canyon sediment 315
Figure 4-100. Average δ^{13}C and δ^{15}N values with 95% CI for each feeding group at Pamlico Canyon 316
Figure 4-101. Mean δ^{13}C and δ^{15}N of fishes at family level and species level 320
Figure 4-102. Title and abstract of Wilford et al (2021) 322

Figure 4-103. Site locations, depths, and bathymetry for Soundscape Code locations 323
Figure 4-104. Bottom habitat images for each of the five soundscape code locations 323
Figure 4-105. One-month soundscape codes for deep/shallow, coral/sandy bottom sites 326
Figure 4-106. Map of the dive sites from cruise RB1903 where bottom water was collected 331
Figure 4-107. Mounting and orientation of the Niskin bottles on *Jason* for collections 332
Figure 4-108. Laboratory setup for water filtration of 10 L seawater from Niskin bottles 333
Figure 4-109. Rarefaction curves of all field collected samples in the cox1 (A) and 18S (B) metabarcoding datasets 340
Figure 4-110. Shannon entropy and Pielou's evenness at 18S marker rarefied to 106,124 reads 341
Figure 4-111.Shannon entropy and Pielou's evenness at *cox1* marker rarefied to 72,933 reads 342
Figure 4-112. Principal coordinate plot based upon a Bray-Curtis dissimilarity matrix, *cox1* 343
Figure 4-113. Principal coordinate plot based upon a Bray-Curtis dissimilarity matrix, 18S 343
Figure 4-114. Relative abundance of the top 20 taxa in the 18S dataset 348
Figure 4-115. Relative abundance of the top 20 taxa in the *cox1* dataset 350
Figure 4-116. Relative abundance of Annelida, Mollusca, Cnidaria, and Arthropoda 351
Figure 5-1. Respiration rates for *Lophelia pertusa* exposed to the different temperatures 359
Figure 5-2. Excretion rates for *Lophelia pertusa* exposed to two different temperatures 361
Figure 5-3. O:N for *Lophelia pertusa* 361
Figure 5-4. Decrease in nauplii over time in the different temperature treatments 362
Figure 5-5. Method comparison observed ASVs for each coral by genus 368
Figure 5-6. Method comparison observed ASVs for each coral by genera 368
Figure 5-7. Bacterial community composition at the class level for four corals 370
Figure 5-8. PCoA for four deep-sea coral microbiome samples 371
Figure 5-9. Relative abundance of *Endozoicomonas* sequence variants 372
Figure 5-10. Schematic of workflow for creating models of coral fragments 376
Figure 5-11. Survival of coral fragments deployed August 2018–April 2019 378
Figure 5-12. Images of coral fragments after recovery and removal of tissue 379
Figure 5-13. Images of stained coral skeleton from a recovered fragment of *Lophelia pertusa* 381
Figure 5-14. Size-frequency distribution of coral colony heights for three species of scleractinians 384
Figure 5-15. Graphs showing relationship between depth and colony height 385
Figure 5-16. *Desmophyllum dianthus* thin section slides 391
Figure 5-17. *Desmophyllum dianthus* oocyte size-frequency distribution for April 2019 samples 391
Figure 5-18. *Enallopsammia profunda* oocyte size-frequency distribution for August 2018 and April 2019 samples 392
Figure 5-19. *Enallopsammia profunda* thin section slides 393
Figure 5-20. *Lophelia pertusa* oocyte size-frequency distribution for August 2018 samples 394
Figure 5-21. *Lophelia pertusa* thin section slides 394
Figure 5-22. *Madrepora oculata* oocyte size-frequency distribution for April 2019 samples 395

Figure 5-23. *Madrepora oculata* thin section slides 396
Figure 5-24. *Solenosmilia variabilis* oocyte size-frequency distribution for August 2018 and April 2019 samples 397
Figure 5-25. *Solenosmilia variabilis* thin section slides 397
Figure 5-26. *Acanthogorgia spissa* oocyte size-frequency distribution for August 2018 and April 2019 samples 398
Figure 5-27. *Acanthogorgia spissa* thin section slides 399
Figure 5-28. *Plumarella sp.* oocyte size-frequency distribution for April 2019 samples 400
Figure 5-29. *Plumarella sp.*: thin section slides 400
Figure 5-30. *Pseudodrifa nigra* oocyte size-frequency distribution for April 2019 samples 401
Figure 5-31. *Pseudodrifa nigra* thin section slides 401
Figure 5-32. *Swiftia casta* oocyte size-frequency distribution for April 2019 samples 402
Figure 5-33. *Swiftia casta* thin section slides 402
Figure 5-34. *Bathymodiolus heckerae* size-frequency distribution of samples collected in August 2018 and April 2019 from Blake Ridge Seep 407
Figure 5-35. *Bathymodiolus heckerae* oocyte size-frequency distribution for August 2018 and April 2019 samples 408
Figure 5-36. *Bathymodiolus heckerae* thin section slides 408
Figure 5-37. Map of study area marked with deep-sea sites used for population genomics 411
Figure 5-38. PCA plot representing genetic differentiation among *G. childressi* samples 419
Figure 5-39. Average probability of membership graph for *G. childressi* 420
Figure 5-40. PCA plot representing genetic differentiation among *B. heckerae* samples 422
Figure 5-41. Manhattan plot and score plot for *G. childressi* by site 424
Figure 5-42. REViGO treemap produced by the REVIGO server 425
Figure 5-43. PCA plot of genetic differentiation 430
Figure 5-44. Pairwise Fst values for *L. pertusa* individuals 431
Figure 5-45. Structure results (K=4, 5, 6) for *Lophelia pertusa* across nine sites 432
Figure 5-46. Structure and phylogenetic analyses for *Plumarelia* spp. 434
Figure 5-47. Structure results (K=4) for *Plumarella* spp. across the six sites 435
Figure 5-48. Pairwise transformed Fst values for *Plumarella* spp. 435
Figure 5-49. Phylogeny (IQ-TREE) of *Paramuricea* throughout the N. Atlantic Ocean 437
Figure 5-50. Membership of probability graphs from a Structure analysis of *Paramuricea* spp. 438
Figure 5-51. Phylogeny and membership of probability graphs of ophiuroid brittle stars 440
Figure 5-52. Phylogeny and membership of probability graph of sea cucumbers 441
Figure 5-53. Phylogeny (IQ-TREE) of *C. heheva* based on an alignment of COI data (652 bp) 442
Figure 6-1. Results of the early *Lophelia pertusa* predictive habitat models 446
Figure 6-2. Presence points for *L. pertusa*, Octocorallia, and Antipatharia 449
Figure 6-3. Taxon-environment relationships and Kernel density plots by taxon 450

Figure 6-4. RF variable response curves, evaluation and importance for *L. pertusa* 451
Figure 6-5. Ensemble-mean habitat suitability predictions for *L. pertusa* throughout the Blake Plateau . 452
Figure 6-6. RF variable response curves, evaluation, and importance for Octocorallia 453
Figure 6-7. Ensemble-mean habitat suitability predictions for Octocorallia throughout the Blake Plateau 454
Figure 6-8. Ensemble-mean habitat suitability predictions for Antipatharia throughout the Blake Plateau 455
Figure 6-9. Projected climatic suitability index (CSI) of *Lophelia pertusa* habitat 459
Figure 6-10. Change in climatic suitability (ΔCSI) maps for the SEUS margin 460
Figure 6-11. Change in climatic suitability index (ΔCSI) 460
Figure 6-12. (A) Predicted vs. Observed Results of RF regression (B) Changes in the distribution of predicted abundances (= % cover) of *Lophelia pertusa* in each scenario at the 2100 timepoint 461
Figure 6-13. Climate velocity based off regional ocean model data 462
Figure 6-14. Mean and SD of the Habitat Suitability Index in the study area 466
Figure 6-15. Seep model diagnostics 466
Figure 6-16. Terrain response curves from RF model runs 467
Figure 7-1. Deep SEARCH area showing BOEM wind leases 473

List of Abbreviations and Acronyms

ACI	acoustic complexity index
ACS	Albemarle canyon system
ADCP	Acoustic Doppler Current Profiler
ADEON	Atlantic Deep Sea Ecosystem Observatory Network
AMS	Accelerator Mass Spectrometry
ANCOM	Analysis of Composition of Microbiomes
ANOSIM	analysis of similarities
ANOVA	analysis of variance
AOM	anaerobic oxidation of methane
ASV	amplicon sequence variants
AUV	autonomous underwater vehicle
BCS	Baltimore Canyon Seep
BLE	Blake Escarpment
BMCC	*Brooks McCall* cruise
BOEM	Bureau of Ocean Energy Management
BOM	bulk organic matter
BP	benthic/pelagic
BPI	bathymetric profile index
BRS	Blake Ridge Seep
BS	benthic/suspension
COS	Center for Open Science
CSI	climatic suitability index
CTAB	cetyltrimethylammonium bromide
CTD	conductivity-temperature-depth
CWC	cold-water coral
CWR	cold-water coral reef
DCCC	deep coral/canyon/cold-seep
DIN	dissolved inorganic nitrogen
DIP	dissolved inorganic phosphate
DISTLM	distance-based linear modeling
DNA	deoxyribonucleic acid
DOC	dissolved organic carbon
DON	dissolved organic nitrogen
DOP	dissolved organic phosphorus
DSL	deep-scattering layer
DSV	Deep Submergence Vehicle
DW	dry weight
EFH	essential fish habitat
EHS	emergent hard substrate
FI	Faith’s Index
FLS	Florida Straits

FS	full siblings
GAM	General Additive Model
GBM	Gradient Boosting Machines
GBR	Great Barrier Reef
GLM	Generalized Linear Models
GOM	Gulf of Mexico
HA	half avuncular
HAPC	Habitat Area of Particular Concern
HOV	human occupied vehicle
HSD	Honestly Significant Difference
HTS	high-throughput sequencing
ICP-OES-MS	Inductively Coupled Plasma-Optical Emission Spectroscopy-Mass Spectroscopy
LCA	least common ancestor
LE	linear extension
LLR	log-likelihood ratio
LOI	loss on ignition
LVO	late vitellogenic oocytes
MAB	Mid-Atlantic Bight
MaxEnt	Maximum Entropy
MDS	multidimensional scaling
MOTU	molecular operational taxonomic unit
NC	Norfolk Canyon
NCBI	National Center for Biotechnology Information
NCEI	National Centers for Environmental Information
NCS	Norfolk Canyon Seep
NEUS	northeast US
NIOZ	Netherlands Royal Institute of Oceanography
NMNH	National Museum of Natural History
NOAA	National Oceanic and Atmospheric Administration
NOMEC	National Ocean Mapping, Exploration, and Characterization
OCS	outer continental shelf
OER	Ocean Exploration and Research
OSF	Open Science Framework
PCA	principal components analysis
PCoA	principal coordinates analysis
PCR	polymerase chain reaction
PDB	Pee Dee Belemnite
PERMANOVA	permutational analysis of variance
PO	parent-offspring
PMF	probability mass function
POM	particulate organic matter
RAD	restriction-site associated DNA
RAD-seq	restriction-site associated DNA sequencing

RDA	Redundancy Analysis
RF	Random Forest
RH	Richardson Hills
RNA	ribonucleic acid
ROC	receiver-operating characteristic
ROV	remotely operated vehicle
RV	Research Vessel
RW	Richardson West
SAV	Savannah Deep
SB	Savannah Banks
SD	standard deviation
SEAFLEAS	SEAfloor FLuid Expulsion Anomalies
SEARCH	Sea Exploration and Research of Coral/Canyon/Seep Habitats
SEUS	southeast US
SFC	structure-forming cnidarians
SIMPER	similarity of percentages
SIMPROF	similarity profile analysis
SMTZ	sulfate-methane transition zone
SNP	single nucleotide polymorphism
SPD	spectral probability density
SPL	sound pressure level
SR	sulfate reduction
SRB	sulfate-reducing bacteria
SSP	Shared Socioeconomic Pathway
TC	total carbon
TDN	total dissolved nitrogen
TDP	total dissolved phosphorus
TSS	true-skill statistic
UGA	University of Georgia
VO	vitellogenic oocytes
VPDB	Vienna Pee Dee Belemnite
WDXRF	Wavelength Dispersive X-ray Fluorescence
WIL	Wilmington
XRD	X-Ray Diffraction
YBP	years before present
YESL	yeast extract sodium lactate

1 Introduction

Chapter Authors: Erik E. Cordes, Amanda Demopoulos

1.1 Executive Summary

This document represents the final report for Contract M17PC00009, issued by the US Department of the Interior, Bureau of Ocean Energy Management (BOEM), titled "*Deepwater Atlantic Habitats II: Continued Atlantic Research and Exploration in Deepwater Ecosystems with Focus on Coral, Canyon, and Seep Communities*." This report is the final deliverable of BOEM Contract M17PC00009, conducted in partnership with the US Geological Survey (USGS). This project effort is now called **Deep SEARCH.** The study is a five-year, collaborative scientific research program focused on the outer continental shelf (OCS) between Virginia and Georgia. We surveyed that region's deep-sea coral, cold-seep, and canyon communities as habitats of focus. Our overarching goal was to improve understanding of the functional role of these three habitat types in order to advance scientific knowledge and inform future management decisions. The intended application of the new science was to develop better predictive capacities for the community types encountered.

Here, we present our site selection process; results from five directly supported cruises; detailed site descriptions of the geological, physical, chemical, and biological conditions encountered; and the results from six additional cruises conducted through our collaborations with the Atlantic Deep Sea Ecosystem Observatory Network (ADEON) project and the National Oceanic and Atmospheric Administration (NOAA) Office of Ocean Exploration and Research (OER). The research results, analyses, and findings include the oceanographic, geological, and geochemical setting of canyons, seeps, and coral environments; deep-sea soundscapes; community structure and trophic function from microbes to fishes; population connectivity; life history of selected species; habitat suitability modeling deep-sea corals and seeps; and our educational outreach to the public.

This study revealed some important findings. Among the most compelling are the following:

- Within the three major habitat types studied, some sites exhibited remarkable characteristics. The newly named Richardson Reef Complex is now understood to be one of the largest cold-water coral reef (CWR) complexes in the world.

- The seeps along the continental shelf edge, visited here for the first time, are remarkable for their extremely high rates of methane release and oxidation. Their chemistry fuels biological productivity that appears to also subsidize local pelagic communities.

- Pamlico Canyon is home to a very high diversity coral assemblage, has high overall diversity of infauna, and exhibits some of the highest densities of sediment infauna observed at this depth.

- We see numerous lines of evidence throughout our data assemblage of high connectivity among all habitat and community types. For example, we see interactions between the diel vertical-migrating midwater community and the benthic zone of the Richardson Reef Complex, as well as those of midwater organisms with the walls of the canyons and shallow seeps.

- The unique oceanographic conditions in the region have a corresponding influence on the various communities. The Gulf Stream cuts through the center of the study area, causing vertical mixing in its core down to 1,000 m, thus promoting a rapid translation of food to depth and nutrients to the surface and bringing elevated trophic and genetic connectivity of the components of the ecosystem. These currents are highly variable at the seabed, (apparently) inducing a high degree of adaptive resilience of the deep-sea corals of the region in response to rapidly changing environmental conditions.

Through this study, we have filled major data gaps for poorly known deepwater ecosystems, aiding the refinement of regional management strategies. Our improved understanding of the habitats and communities in offshore areas of the Atlantic Large Marine Ecosystem augments the capacity to predict the distribution of sensitive areas concerning the potential development of energy and marine minerals managed by the Bureau of Ocean Energy Management.

1.2 Context and Purpose

The deep ocean (> 200-m water depth) is magnificent in scale, yet our understanding of deep-sea faunal biogeography is constrained by scarce observations skewed towards several select groups. Patterns of biogeography and species diversity are dictated by gene flow and hinge upon a complex web of organism biology, evolutionary processes, and oceanographic and environmental variables. The mid-Atlantic slope between Virginia and Georgia encompasses a variety of habitats that exhibit similarities to canyon, coral, and seep communities in the greater Atlantic.

It is essential that marine management professionals are provided with ecosystem-based baseline information before they implement actions in a specific region, whether it be for conservation or other programs such as renewable energy, marine minerals, or hydrocarbon extraction. In addition to the necessary geophysical, geochemical, and geological survey information, ecosystem-based baseline information typically includes species identification, biodiversity assessments, ecology, food-web dynamics, and the evaluation of genetic connectivity between surrounding areas and related species. This is especially pertinent for ecosystems found on the continental slopes to deep-sea (> 200 m water depth) where ecosystem-level assessments have been historically difficult to perform due to the higher costs and technical challenges of working in deep water. With ongoing advances in offshore and onshore technologies, scientists are beginning to access deep-sea ecosystems to acquire, analyze, synthesize, and archive ecosystem-based baseline information.

Though poorly understood, deepwater ecosystems along the US continental margin support rich, enhanced biodiversity and sensitive biological communities. The preservation of this biodiversity is critical to the function and sustainability of these systems. They provide numerous ecosystem services, including the direct provisioning of food, genetic resources, and nutrient regeneration that support an array of life forms including humans (Thurber et al. 2014). Loss of deepwater biodiversity may lead to long-term, damaging effects to vast areas of the seafloor, its overlying water column, and ultimately to the health of the ocean. Thus, an ongoing flow of better information is needed to better understand deepwater ecosystem functions, including quantitative and robust information on faunal and habitat distributions, processes that shape population patterns and community structure, and the linkages between physical, chemical, and biological processes. These interdisciplinary and interconnected data sets are required for predicting organism and ecosystem-level responses to various anthropogenic impacts and for understanding the magnitude of different impact types on sensitive communities.

This project has started to fill in the data gaps that have hindered our understanding of deepwater ecosystems, including the offshore areas of the Atlantic Large Marine Ecosystem. The predictive habitat models developed through this work provide insight into the distribution of sensitive areas managed by the BOEM, aiding its mission to protect this marine environment concurrent with development of offshore energy and minerals.

1.2.1 Regional Seabed Setting and Features

The continental margin along the US East Coast is a topographically and environmentally complex region, composed of heterogeneous features, including cold seeps, submarine canyons, and hardbottom habitats, such as lithoherms capped with corals and coral-formed bioherms (**Figure 1-1**). These three

major seabed features and their associated environmental conditions influence the distribution and abundance of organisms, including many of commercial importance, while typically increasing local and regional biodiversity.

Such hardbottom habitats also play an important role in the evolution and diversity of deep-sea fauna. They facilitate the dispersal and maintenance of species, serving as dispersal "stepping-stones" and epicenters of reproductive isolation and speciation, as well as serving as refugia for various deep-sea populations. The Mid-Atlantic Planning Area encompasses a large water depth range (200–2,600 m), providing valuable context to examine the role that habitat and other environmental conditions play in shaping deep-sea benthic communities.

Figure 1-1. Coral-formed bioherms

The Gulf Stream is a dominant oceanographic feature in the study region, forming an important part of the Atlantic Meridional Overturning Circulation. The Gulf Stream is a major agent of poleward heat transport and one of the dominant currents in the North Atlantic Ocean. From the Florida Straits (FLS), there called the Florida Current, the Gulf Stream flows towards the Blake Plateau, continuously picking up speed due to the inflow of water via the Bahamas Channel and the Antilles Current (Meinen et al. 2019). The path of the Gulf Stream mainly follows the upper slope but is deflected seaward at the Charleston Bump. Presence of the Gulf Stream results in very strong northward oriented surface currents (~1.7 m s^{-1}) that decrease in speed with depth. The Gulf Stream is 50–100 km wide, extends to 700 m water depth at the Blake Plateau, and reaches 1,000 m near Cape Hatteras (Heiderich and Todd 2020). Even though current speeds decrease with water depth, strong lee waves have been found near the seafloor (Todd 2017). The Gulf Stream transitions from an attached Western Boundary current to a meandering free jet offshore near Cape Hatteras, flowing into a northeastern direction (Matsumoto et al. 2003; Andres et al. 2020). The northward flow of the Gulf Stream is balanced by strong equatorward flow along the upper slope (Seim and Edwards 2019).

Water transported within the Gulf Stream is characterized by physical and geochemical properties that can have a major influence on the functioning of deep-sea ecosystems. Antarctic Intermediate Water (AAIW) is transported northwards, joining the Gulf Stream in the FLS (Heiderich and Todd 2020). AAIW is characterized by fresh, low-oxygen, and high-nutrient waters. The AAIW signature slowly

disappears when the Gulf Stream is moving northwards due to mixing with other water masses. The other major near-bottom water mass present on the Blake Plateau is the southward-flowing upper Labrador Sea Water (uLSW), which joins the Gulf Stream near Cape Hatteras and is saltier than AAIW but more oxygenated (Heiderich and Todd 2020; Tsuchiya 1989).

The coastal current system is characterized by cool and fresh Mid-Atlantic Bight (MAB) waters that flow equatorward, while warm saltier waters flow poleward from the South Atlantic Bight. Both water masses converge near Cape Hatteras which is the end point of MAB circulation (with salinities < 34.5), where due to shoaling and narrowing of the shelf, water is exported to the deep ocean, which mainly occurs during spring and summer when equatorward flow in the region is strongest (Todd et al. 2019).

Primary productivity is strongly influenced by the interaction of Gulf Stream and adjacent shelf waters. During meandering of the Gulf Stream, eddies can shed off on both sides of the jet. Cyclonic cold core eddies break off when the meander is in an offshore position. These eddies move north at the same speed as the Gulf Stream and uplifting of the density structure of the front can result in the upward movement of nutrients and subsequent enhanced phytoplankton and bacterioplankton growth (Lee et al. 1991; Leterme et al. 2008). Small-scale blooms driven by such processes may enhance the food supply to deeper waters thereby influencing the food supply to deep-sea benthic communities. However, long-term deployments of moored observatories in the region of these eddies only showed one near-bed peak in fluorescence in March in the Cape Lookout area, related to the spring bloom (Mienis et al. 2014).

Deep-sea CWRs and seep community ecosystems often harbor abundant and diverse faunal communities, forming hotspots of biodiversity and playing an important role in biogeochemical cycling. So far very limited detailed knowledge is available on their distribution along the Southeast US (SEUS) margin, but also not much is known about the environmental conditions that influence these often-vulnerable ecosystems. More information on the environmental conditions is not only essential to better understand the functioning of the ecosystem, but also vital for ecosystem protection and sustainability plans in response to current and future leasing of the OCS for our energy and other resource needs.

1.2.2 Hydrocarbon Seep Ecosystems

Hydrocarbon seepage enhances habitat and environmental heterogeneity on continental margins across the globe (Cordes et al. 2010a, Levin and Sibuet 2012). The flow of seep fluids rich in methane and sulfide provides the required energy sources fueling microbial chemosynthesis and methanotrophy, and the dominant megafauna at these sites are dependent on endosymbionts for nutrition (Kochevar et al. 1992). These include *Bathymodiolus* sp. And *Gigantidas* sp. Mussels, *Lamellibrachia* sp. And *Escarpia* sp. Tubeworms, and vesicomyid clams (Cordes et al. 2009). These chemosynthetic species serve as foundation species by creating habitat and modifying both the physical and chemical environment, thereby promoting the colonization of other fauna that are often endemic to or dependent upon chemosynthetic habitats (Carney 1994, Bergquist et al. 2003, Cordes et al. 2005). Endemic seep taxa have developed specific adaptations that allow them to persist in environments that are characterized by high toxicity due to high concentrations of hydrogen sulfide and hydrocarbons along with resulting low dissolved oxygen concentrations (Tunnicliffe et al. 1998, Fisher et al. 2000, Hourdez et al. 2002).

These extreme living conditions associated with the seeps are ameliorated over time (Cordes et al. 2003) and the habitat structure provided by the foundation species, as well as authigenic carbonate, attracts background (non-endemic) fauna (Bergquist et al. 2003, Cordes et al. 2005), some of which are commercially important species (Baker et al. 2010). The presence of non-endemic fauna may be due to the availability of primary production within chemosynthetic habitats and/or the presence of three-dimensional structure provided by seep habitats, serving as predation refugia or breeding sites (Fisher 1993, MacAvoy et al. 2002, Gilhooly et al. 2007, Cordes et al. 2009). Studies to date, primarily coming from the oil-rich seeps of the Gulf of Mexico (GOM), have shown that non-endemic fauna can derive a

portion or all of their nutrition from chemosynthetic sources (MacAvoy et al. 2002, 2008, Cordes et al. 2010b, Demopoulos et al. 2010). This includes cold-water corals (CWCs) such as the octocoral *Callogorgia delta* in the GOM.

Recent investigations on the northeast US (NEUS) continental margin documented approximately 570 gas plumes emanating from the seafloor (Skarke et al. 2014), yet only a few dozen of these sites have been visually explored. In this region, hydrocarbon seeps occur on promontories overlooking canyon heads, ridges within canyons, and on the open upper to middle slope (Skarke et al. 2014, Quattrini et al. 2015, McVeigh et al. 2018, Turner et al. 2020). Methane seeps also occur south along the Cape Fear and Blake Ridge Diapirs (Van Dover et al. 2003; Brothers et al. 2013). Seafloor gas hydrate has been documented previously within the gas-hydrate stability zone along the Blake Ridge at 2,000 m depth (Van Dover et al. 2003) and at two seeps off New England (Skarke et al. 2014, Quattrini et al. 2015). In these settings, gas bubbles emitted from the seafloor saturate the waters beneath small overhangs with methane, promoting the formation of porous gas-hydrate flakes around the bubbles, which then combine to form a gas-hydrate mass (Skarke et al. 2014, Quattrini et al. 2015).

From the limited surveys previously conducted, *Gigantidas childressi* and *Bathymodiolus heckerae* mussels (**Figure 1-2**) appear to dominate the seep communities in this region. Given that these mussels rely on their endosymbionts for nutrition, their distribution is primarily constrained by the presence of methane and/or sulfide (Demopoulos et al. 2019, Vokhshoori et al. 2021). The seep communities of the region vary greatly with depth (Turner et al. 2020; Cleland et al. 2021), as is the case throughout the Atlantic Equatorial Belt (Cordes et al. 2007), therefore, temperature is probably an additional determinant of distribution, as it is for many other marine species. Seep mussels are found over a wide range of depths in this MAB region (Van Dover et al 2003, Coykendall et al. 2019), from the shallow "Bodie" Seep (~400 m) to the deep Blake Ridge Diapir (2,165 m); however, many of the recently discovered gas plumes are much shallower (Skarke et al. 2014) and warmer (Church et al. 1984) than the Bodie Seep. Numerous seep-endemic invertebrates such as *Alvinocaris* sp, and *Chiridota heheva*, as well as non-endemic fauna including commercially important species such as red crabs, have been observed at seep sites (Turner et al. 2020). The current project has further elucidated the genetic connectivity and energy exchange among these geographically isolated ecosystems.

Figure 1-2. *Bathymodiolus heckerae* mussels in seep community

1.2.3 Submarine-Canyon Ecosystems

Submarine canyons are common features that incise continental margins worldwide, connecting shallow shelves to deep abyssal plains (Shepard and Dill 1966, De Leo et al. 2010, Harris and Whiteway 2011). These features serve as major conduits for the downslope transport of particulate nutrients, lithogenic material, and organic matter (Keller et al, 1973, Bennett et al. 1985, Valentine 1987, Vetter and Dayton 1999, Oliveira et al. 2007, Puig et al. 2003, De Leo et al. 2010, Prouty et al. 2017), upwelling of nutrients, and sinks for macrophytic debris, organic-rich sediments, and particle-bound pollutants (Harrold et al. 1998, Vetter and Dayton 1999, Canals et al. 2006, Gibbs et al. 2020). The complex topography of submarine canyons leads to accelerated currents and dense water cascades (Keller et al. 1973, Shepard et al. 1979) that remove sediments and expose hardbottom features such as steep walls, pavements, and rocky debris. The high levels of habitat heterogeneity observed in canyons (Fernandez-Arcaya et al. 2017) has led to the hypothesis that canyons support higher biodiversity and biomass as compared to areas on the adjacent continental slope (Griggs et al. 1969, Rowe 1971, Vetter and Dayton 1998, de Leo et al. 2010); however, this hypothesis has rarely been systematically tested (Fernandez-Arcaya et al 2017).

Submarine canyons are thought to be among the most productive habitats in the deep sea (De Leo et al. 2010); their complex characteristics can enhance both pelagic and benthic biomass, as well as biodiversity of benthic fauna (Rowe et al. 1982, Schlacher et al. 2007, Vetter et al. 2010). Elevated food, strong currents, and exposed hard substrates concentrate suspension-feeding organisms such as corals and sponges, as well as mobile invertebrates and fishes, some of which are commercially important (Quattrini et al. 2015, Miller et al 2015, **Figure 1-**). Increased food availability may allow organisms to allocate more energy to reproduction and thus enhance overall reproductive success. High concentrations of breeding individuals with high reproductive output can broadcast larvae from canyons to surrounding areas that serve as sinks for these larvae (Snelgrove and Smith 2002; Rex et al. 2005; Vetter et al. 2010).

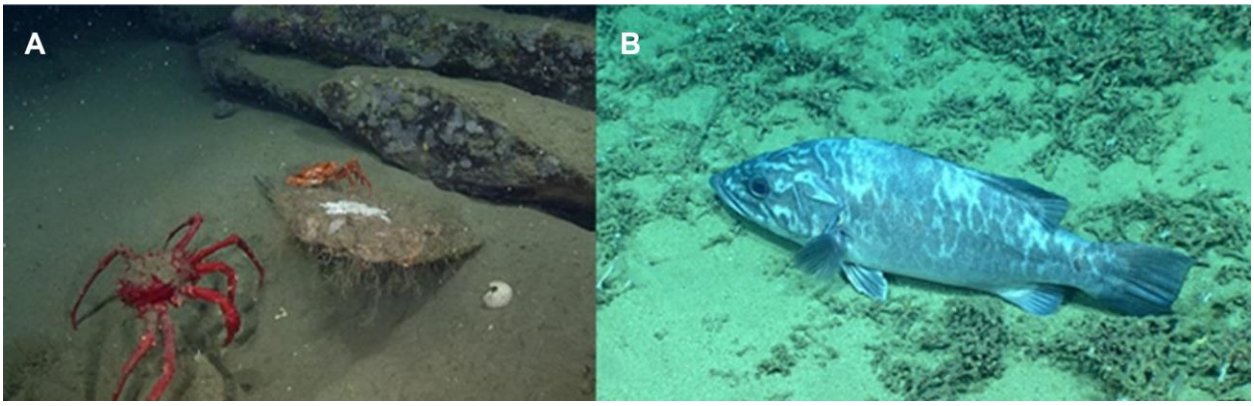

Figure 1-3. Some canyon invertebrates and fishes
(A) King crab *Neoithodes agassizi* and a small orange squat lobster. (B) The wreckfish *Polyprion americanus.*

Forty shelf-breaching canyons and hundreds of minor slope-sourced canyons exist along the northeast US continental margin (Obelcz et al. 2014, De Leo and Ross 2019). In the Mid-Atlantic Planning Area, shelf-breaching and slope-sourced canyons both occur offshore as far south as Cape Lookout, NC. Sessile invertebrate and fish assemblages in the shelf-incising Baltimore and Norfolk Canyons are perhaps the most thoroughly investigated, with past efforts by Barbara Hecker in the 1980s using towed camera systems and submersibles, and recent efforts by the Atlantic Canyons I program using remotely operated vehicles (ROVs) and otter trawls to survey benthic ecosystems in these canyons (Ross et al. 2015, Brooke et al. 2017). Similar fish assemblages have been found at comparable depths in Norfolk and Baltimore canyons, but differed among macrohabitats due apparently to vertical walls vs. sedimented slopes within each canyon (Ross et al. 2015). Differences among habitat types, depth ranges and environmental conditions were also apparent in the coral assemblages (12 species total) within each canyon (**Figure 1**-), with many species exhibiting patchy distributions (Brooke et al. 2017).

We observed more than 30 morphotypes of sponges in Baltimore and Norfolk Canyons. Our observations indicate that biodiversity and ecological assessments of sponge communities in canyon environments and other deepwater habitat features in the region are poorly understood. Sponges (and their symbionts) may play important, yet underappreciated roles, in nutrient cycling and carbon sequestration in the deep sea (Kahn et al. 2015).

To the north of Baltimore and Norfolk Canyons, Quattrini et al. (2015) surveyed benthic communities in canyons off New England. They reported variation in benthic assemblages between seafloor features, including open-slope, cold-seep, and canyon habitats. Differences in the abundance of the most common fish, crustacean, and coral species demonstrated that enhanced abundances in canyons occurs only for specific species. This study noted that, for future surveys to more thoroughly examine species distributions and abundances, they should incorporate sampling designs that include a replicated suite of habitats and depths, and should collect salient environmental data across different features. The current study was aimed at gathering more extensive quantitative surveys within the canyons specific to the Mid-Atlantic Planning Area.

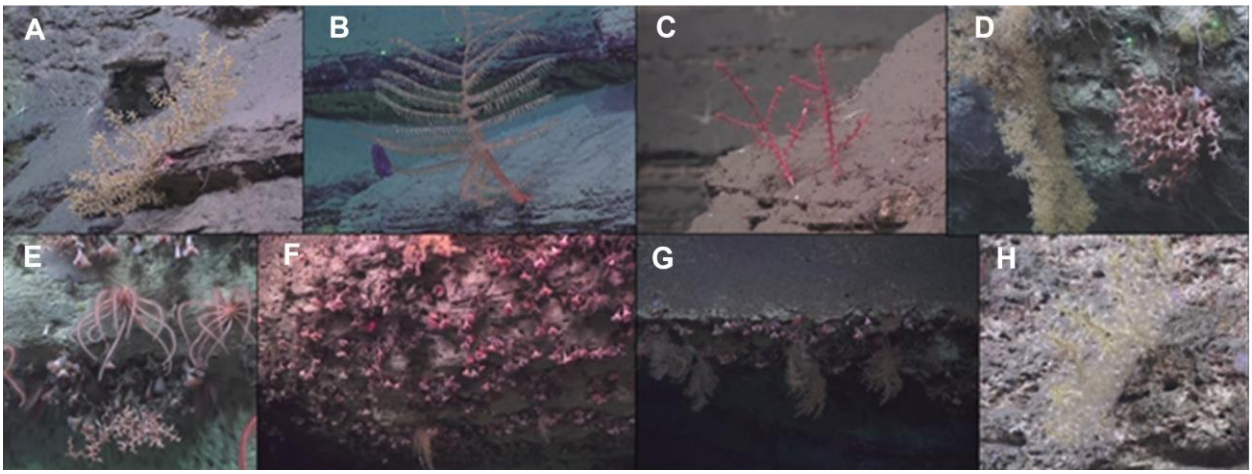

Figure 1-4. Various coral assemblages from canyon sites visited
(A) *Acanthogorgia*, sp., (B) *Bathypathes alternata*, (C) *Swiftia cf. pallida*, (D) *Acanthogorgia* sp. And *Solenosmilia variabils*, I Brisingid sea stars and *Solenosmilia variabilis*, (F) *Desmophyllum dianthus*, (G) Octocorals and *Desmophyllum dianthus*, and (H) *Acanthogorgia* sp.

1.2.4 Deep-Sea Coral Ecosystems

Deep-sea corals including scleractinians (stony corals), stylasterid hydrocorals (lace corals), antipatharians (black corals), and octocorals (soft corals, sea fans, sea pens), contribute materially to habitat complexity in the deep sea (Cordes et al. 2010a). When related to coral species, the term "deep sea" refers to aphotic waters greater than 200 m depth. However, because of the presence of many of these coral species in cold waters shallower than 200 m, we will use the term cold-water corals, or CWCs.

Corals predominantly recruit to, and colonize, hardbottom features. Such features include those present in submarine canyons, authigenic carbonates, and lithoherms (*sensu* Neumann et al. 1977). In submarine canyons, dense aggregations of corals have been observed on canyon walls (Huvenne et al. 2011, Johnson et al. 2013), which may enable them to access sufficient food delivered via currents (Huvenne et al. 2011, Brooke et al. 2017). In the mid-Atlantic region, massive reef frameworks are primarily formed by *Lophelia pertusa* along with other scleractinian (stony) corals and octocorals. These species form bioherms capped with live coral (**Figure 1-5**) that can rise 80–100 m above the surrounding seafloor (Partyka et al. 2007).

Key habitat requirements of CWCs include hard substrate, consistent and sufficient food availability and quality, and appropriate temperature regimes (Duineveld et al. 2012, Davies et al. 2008, Tittensor et al. 2009, Mienis et al. 2012, Georgian et al. 2015). Further studies have found that the saturation states of aragonite and calcite in the oceans can control coral growth by increasing the energetic cost of calcification (Guinotte et al. 2006, Lunden et al. 2013, Georgian et al. 2016).

By synthesizing available data on coral occurrences along with available data on their associated environment, coral habitat distribution models can be optimized along regional (Davies et al. 2008) and local (Georgian et al. 2014) scales. However, these models require ground truthing, as coral communities are not always present even when conditions appear conducive to their occurrence (Georgian et al. 2014). Coral absence within certain hardbottom environments may be a function of larval dispersal and population connectivity, the haphazard nature of recruitment, and/or high rates of mortality in early settlement stages (Doughty et al. 2014). The relative importance and frequency of these factors, particularly biotic factors, are currently unknown in CWC community assembly and distribution.

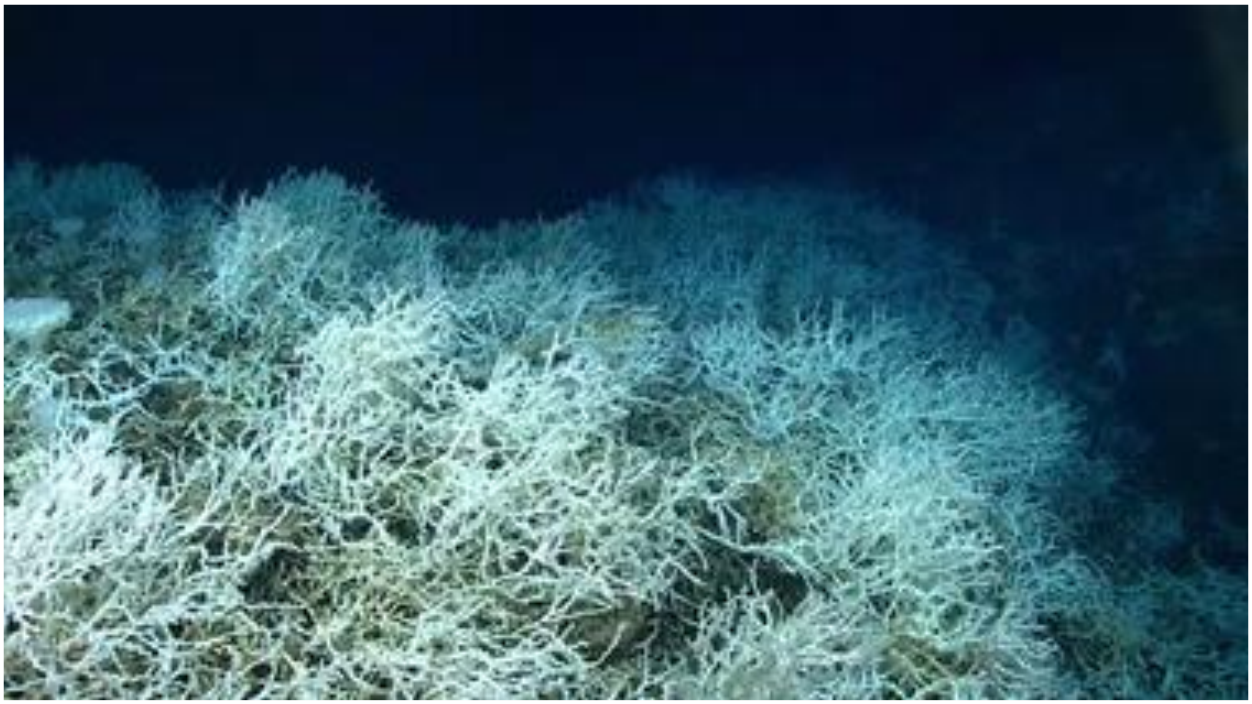

Figure 1-5. Bioherms capped with live deep-sea coral

Understanding how populations are structured across spatial scales and environmental gradients in the deep sea is essential for effective long-term protection of deep-sea ecosystems from negative anthropogenic impacts. Documenting the degree of genetic connectivity among populations of deep-sea foundation species, as well as their symbionts, can provide clues into realized dispersal of larvae, particularly when coupled with reproductive data and oceanographic models. It is likely that organisms within similar taxonomic and trophic groups, and with similar reproductive strategies such as broadcast spawning or asexual reproduction, will use the same exogenous factors (such as food) as reproductive cues and therefore have similar timing of their gametogenic cycles. Environmental cycles are attenuated or absent in the deep sea, and there is strong evidence that seasonal reproduction is driven by the influx of particulate organic carbon from surface phytoplankton blooms (Tyler et al. 1993, Witte 1996). Understanding reproductive strategy and timing of spawning in deep-sea corals and other benthic invertebrates can be used to refine dispersal models and inform studies intending to measure connectivity and community resilience.

Coral habitats are generally considered biodiversity hotspots (Marchese 2015, Cordes et al. 2016a), supporting diverse communities of invertebrates and fishes, some of which are facultative or obligate associates (Buhl-Mortensen and Mortensen 2005, Mosher and Watling 2009). Due to the cyclical growth pattern of reef-forming CWCs, *Lophelia pertusa* reef frameworks can be thousands to millions of years old, and they create a more complex and diverse localized setting with their calcium carbonate skeleton, which increases overall biodiversity in the region (Jensen and Frederiksen 1992, Mortensen and Fosså 2006, Cordes et al. 2008, Buhl-Mortensen et al. 2010).

The increased habitat heterogeneity created by *L. pertusa* reefs form niches that are occupied by many fishes and invertebrates, depending on the preference for various abiotic factors such as food sources, current speed, and protective covering (Etnoyer and Warrenchuk 2007, Buhl-Mortensen et al. 2010, Ross et al. 2010). Ophiuroid associates have been shown to improve the overall health and resilience of their symbiotic corals by removing sediments and epifauna (Girard et al 2016). CWCs also serve as food resources for certain seastars and sea urchins (Mah 2015) and as egg-laying substrate and nursery habitats for some fishes (Busby et al. 2006, Etnoyer and Warrenchuk 2007, Quattrini et al. 2009, Ross et al. 2015).

For fish species in particular, diversity is three times higher on *L. pertusa r*eefs compared to the surrounding soft bottoms (UK Biodiversity Group 2000). In the study area examined here, fish communities associated with *L. pertusa* reefs are quite different from those on other habitats (Ross and Quattrini 2007). Coral diversity in particular explains some of the variance in fish communities among deep-sea habitats in the western North Atlantic (Quattrini et al. 2015). The current project has helped reveal the connections between coral diversity and seafloor habitat structure, fish abundance, community structure, and functional diversity.

An increasing number of studies investigating how animals use information from their environmental soundscape for communication, orientation, and navigation have been conducted as a direct result of declining costs associated with collecting and analyzing passive acoustic monitoring data (Slabbekoorn and Bouton 2008, Pijanowski et al. 2011, Simpson et al. 2005, Stanley et al. 2012). An important new area of research is that of adapting habitat quality and biodiversity indicators developed for terrestrial applications to marine habitats and soundscapes (Denes et al. 2014, Parks et al. 2014, Staaterman et al. 2014).

Coral reef systems, in particular, have proven useful natural laboratories for the application of passive acoustic data to measure biodiversity. Research in the US Virgin Islands has shown that diel trends in low-frequency sound production correlate with shallow-coral reef species assemblages (Kaplan et al. 2015), while reef fishes respond more strongly to the higher-frequency components (> 570 Hz) of the reef soundscape (Simpson et al. 2008). While these studies reveal the potential value of acoustic metrics for monitoring and assessing biodiversity of reef habitats, soundscapes in CWC habitats have not previously been characterized. Development of soundscape-derived indicators for CWC habitats in this project provides useful metrics for monitoring these remote environments, with far-reaching implications including providing an integrated view of their oceanographic and ecological properties.

1.3 Objectives and Hypotheses

The overarching goal for this project was to enhance our ability to predict the location of seafloor communities within the study area that are particularly sensitive to natural and anthropogenic disturbances. In general, sites selected for further study would exhibit one or more of the following: bubble plumes acoustically imaged in the water column, evidence of distinctive topographic features on the seafloor, anomalies in the multibeam backscatter data, or seismic profiles indicative of hardbottom or hydrocarbon seepage. The general study area also encompasses a variety of different habitat types, including canyons, hardbottoms, CWC mounds, methane seeps, and soft sediments.

1.3.1 Objectives

Within the overarching goal, the study focused on four objectives, each designed to enable this predictive capacity. These objectives were:

1. Explore and characterize the biological communities of the study area. Data were to be gathered to describe communities from microbial to megafaunal, connected to their association with the three different focal habitat types. In addition, soundscapes were to be generated on CWC reef environments to explore the relationship between habitat type and acoustic bioindicators. Species identifications were to be determined by a combination of molecular and morphological methods in collaboration with our network of taxonomic colleagues. These planned investigations represented an interdisciplinary effort that encompassed subject matter experts within the group of contracted scientists as well as those represented by USGS collaborators. Their planned interactions were intended to generate and provide a comprehensive picture of community structure, function, and habitat association.

2. Examine the sensitivity to natural and anthropogenic disturbance of habitat-structuring fauna and associated communities. This objective was to be addressed using a combination of laboratory and field experiments, information on age structure and population dynamics of key species, the rarity of species and assemblages, and the genetic connectivity of dominant species. The application of acoustic bioindicators and acoustic similarity/dissimilarity indices was intended to provide novel metrics for quantitative comparisons of the impact of different levels of disturbance between locations.

3. Describe the oceanographic, geological, and geochemical conditions associated with each habitat type. We planned these characterizations to include time-series measurements of water-column temperature, salinity, dissolved oxygen, turbidity, and fluorometry, along with sediment biogeochemistry, and water-column and pore-fluid methane concentrations. These were to be evaluated using direct measurements, in situ samplers, and bubble-plume data from multibeam surveys, supporting pH and carbonate chemistry measurements, supporting nutrients and organics determinations, physical oceanography measurements (with ADEON and European collaborators), and geomorphology assessments (with USGS). In particular, the project plan intended to provide detailed and previously lacking biogeochemical information of coral, canyon, and seep habitats in the study area.

4. Model the distribution of habitats and fauna with respect to environmental conditions. After achievement of the above objectives, interpretation of the geological (geomorphology and habitat type) and biological (species and community distributions) data in the context of the acquired environmental data was intended as a **Synthesis of Study Results** chapter of this report. This information was to be incorporated into a quantitative, ensemble modeling framework at the ecosystem scale, to achieve a robust predictive capacity for the distribution and sustainability of target communities within the study area.

1.3.2 Hypotheses to be Tested

In order to achieve these four objectives, we developed and planned to test a series of specific hypotheses intended to generate focused questions that guided our field acquisition and laboratory analyses. Below is a complete list of the hypotheses from the proposal preceding project execution, a brief summary of the findings from project execution, and the location in this report of the full accounting of each finding. We have synthesized the results generated by testing these specific hypotheses to achieve our overarching goal: a robust predictive capacity for identifying the distribution of sensitive habitats using remotely sensed data in the study area.

Exploration Hypothesis 1. *Previously undescribed community types will be discovered in the study area over the course of this project*.

Findings: The discovery of the previously undescribed Richardson Reef Complex in an area thought to contain isolated coral mounds during the 2018 field campaign was the most important of several such discoveries. The higher resolution of the bathymetry gathered over the Blake Plateau also revealed the presence of numerous isolated CWC mounds over an extensive area of the central plateau that was previously thought to be largely devoid of coral structures. In addition, the 200–400 m depth seep communities that include vestimentiferan tubeworms in the northern part of the study area were undescribed prior to this study and appeared different from the communities at the deeper seeps in the community analysis.

Relevant Report Sections: **2.3 Sites Visited During this Study, 4.1 Community Structure**

Exploration Hypothesis 2. *New species, cryptic species, and range extensions of fauna from canyon, deep-coral, and cold-seep communities are present in the study area and will be discovered over the course of this study*.

Findings: We discovered numerous species, cryptic species, and range extensions in this study. We observed a total of 8 fish species in the North Atlantic for the first time, and 17 other fish species outside of their previously reported range. The totals for new species and range extensions of invertebrates are more difficult to tally, as taxonomic work in these groups often takes years. However, *Diodora tanneri*—collected at 709 m depth during dive J2-1129 at the Richardson Reef Complex—represents the first observation of this limpet species in *L. pertusa* habitats and represents a depth extension.

Relevant Report Sections: **4.1 Community Structure, 4.2 Fish Communities, 4.3 Community** *Phylogenetics*

Occurrence Hypothesis 1: *The occurrence of coral communities is directly related to seafloor topography, oceanographic parameters, and the availability of hard-substrate habitats in the study area.*

Findings: Corals of a variety of taxa were present throughout the study region in almost all benthic habitat types. It was in the synthesis of the abundance and distribution data with the environmental data where we truly tested this hypothesis. For the *L. pertusa* mounds, the elevation above the local seascape, as indicated by the bathymetric position index (BPI), was the best predictor of the presence of live, framework-forming corals. This was followed by temperature, dissolved oxygen concentration (DO), and 12culatount of carbon exported from the surface. For octocorals, BPI and slope were the best predictors, followed again by temperature, DO, and export carbon. The distribution of black corals (Order Antipatharia) was best predicted by a combination of slope and BPI.

Relevant Report Sections: **2. Site Summaries, 6.2 Improved Prediction of Occurrence**.

Occurrence Hypothesis 2: *The ability to predict the occurrence of coral communities will be improved by including oceanographic data in our models of coral distribution.*

Findings: The terrain variables are found to be the most important predictors of coral occurrence, but the oceanographic variables contribute greatly to the *L. pertusa* model. Since these models all tend to overpredict suitable habitat, the added layer of complexity of including the oceanographic parameters helps to constrain the models, but the best predictors remain the terrain variables. These predictions change, however, as the oceanographic variables, specifically temperature and pH, are altered according to projections of future climate onto the regional seafloor. In this projected version of the models, the deeper sites, including the Richardson Reef Complex, are important refugia of coral distribution as changing ocean temperature and pH is translated from the surface to depth.

Relevant Report Sections: **6.2 Improved Prediction of Occurrence**.

Occurrence Hypothesis 3: *The presence of coral and mussel species is primarily controlled by their ability to disperse to the site.*

Findings: Because there is apparently ample suitable habitat in the region as indicated by the synthesis of the mapping, oceanographic, and organismal distribution results into our predictive habitat model, a corollary hypothesis is that the coral and mussel larvae simply cannot travel to, and successfully recruit, in all of the suitable habitats available. The genetic connectivity studies address this hypothesis, but with different results among the taxa examined. For the mussel species, the simple conclusion is that there is ample gene flow among existing populations to consider them one large population throughout the study region. For the corals, the answer is more complicated. *L. pertusa* shows one population in the Northeast Canyons, one in Norfolk Canyon, and one on the Blake Plateau. However, the higher-resolution population genomic analyses presented in this study indicate previously undetected structure within the Blake Plateau sites, including elevated inbreeding at the Richardson site. In the octocoral *Plumarella* sp.

there was ample gene flow found throughout the region, while in the other octocoral, *Paramuricea* sp., we found four distinct species at four different sites/depths. Therefore, it is likely that species-specific dispersal capability has a role to play in the realized distribution of coral species in the study area.

Relevant Report Sections: **5.5 Population Connectivity**

Occurrence Hypothesis 4: *Acoustic imaging of bubble plumes and seafloor geology are reliable indicators of the presence of cold-seep communities.*

Findings: The abundant water-column anomalies in the multibeam bathymetry data acquired prior to and during this study were indeed good indicators of ongoing seepage. When we visited seafloor seep locations at Pea Island and Chincoteague, Blake Ridge, and Cape Fear, bubble plumes were visible, and we located seep fauna. These communities were primarily bathymodiolin mussels, but our observations also included the first documented vestimentiferan tubeworm along the Atlantic coast, this at Pea Island.

Relevant Report Sections: **2.3 Sites Visited During This Study, 3.2 Geology**

Distribution Hypothesis 1: *The distribution of coral species in the study area is controlled by temperature tolerance.*

Findings: Temperature was one of the controlling factors in determining coral distribution in the predictive habitat model synthesis. However, we directly tested this in the laboratory experiments with *L. pertusa* conducted at Temple University. In these experiments, we simulated in the laboratory the rapid shifts in temperature that we measured on the seafloor near the Richardson Reef Complex. A temporary "heat wave," wherein we increased temperature from 8 to 14°C over the span of 24 hours and then returned, induced an increase in respiration and excretion and a decrease in feeding rate, suggesting a substantial metabolic stress. Although this particular coral population appeared to be highly resilient to these types of stresses, each of these events incurs a metabolic cost and could lead to increased mortality.

Relevant Report Sections: **5.1 *Lophelia pertusa* Physiology, 6.2 Improved Prediction of Occurrence**

Distribution Hypothesis 2: *The distribution of scleractinian coral communities in the study region is further refined by the aragonite saturation state.*

Findings: Although the current distribution of the live corals on the *L. pertusa* mounds were primarily controlled by terrain variables, when we projected the climate projection models into the future, pH was second in importance only to temperature for controlling live *L. pertusa* distribution. So, while this hypothesis is largely rejected for the current distribution, aragonite saturation state will be an important controlling factor with the commonly predicted coming changes in ocean chemistry.

Relevant Report Sections: **6.2 Improved Prediction of Occurrence**

Distribution Hypothesis 3: *The distribution of Bathymodiolin mussels is controlled by methane concentration and methane flux.*

Findings: In general, we know this hypothesis to be validated because the mussels that we observed and sampled in this study contained methanotrophic symbionts. They are also largely reliant on methane-derived carbon as their nutritional source, as revealed by their stable isotope ratios. However, the sites with the highest methane flux and methane oxidation rates were at the shallower Pea Island and Kitty Hawk Seeps, where the mussels were not present. At the Cape Fear and Blake Ridge Seep sites where mussels were present, there were very high concentrations of sulfide detected, and the *Bathymodiolus heckerae* mussels present there have sulfide-oxidizing as well as methanotrophic symbionts, so it may be that sulfide, rather than methane, is the more important energy source for this species.

Relevant Report Sections: **2.3 Sites Visited During This Study, 3.3 Biogeochemistry and Microbial Ecology, 4.1 Community Structure**

Distribution Hypothesis 4: *The limits of seep mussel distribution are driven by thermal tolerance.*

Findings: At the broadest level of spatial distribution, mussels were present at the deeper Blake Ridge and Cape Fear Seep sites, but were not recorded from the shallower Pea Island and Kitty Hawk sites. It is likely that temperature tolerance controls their bathymetric distribution, but we did not explicitly test this hypothesis and there are other potential explanatory variables that cannot be ruled out, including those related to larval dispersal and biological interactions such as predation and competition.

Relevant Report Sections: **4.1 Community Structure, 5.5 Population Connectivity**.

Distribution Hypothesis 5: *The distribution of coral-associated communities is controlled by the interactions among a variety of environmental variables*.

Findings: Coral-associated communities included demersal fishes, benthic megafauna, and coral-associated macrofauna, all of which exhibited somewhat different controls on their distribution and community composition, although depth was the most important factor in nearly all analyses. For demersal fishes, temperature was also an important factor. Temperature is directly related to depth but also represents a specific variable, whereas depth conglomerates numerous related variables. For the other megafauna, pH and export carbon (also related to depth) were important factors, with the BPI explaining much of the remaining variance in *L. pertusa* -associated community structure.

Relevant Report Sections: **4.1 Community Structure, 4.2 Fish Communities**

Community Hypothesis 1: *The canyon communities will show higher similarity to the canyons to the north than communities to the south.*

Findings: In video surveys of the canyon communities, there was some overlap with the coral and seep communities, but the majority of the community space in the ordination was solely occupied by canyon axis transects. For demersal fishes, the assemblage was highly similar to the fishes of the mid-Atlantic canyons, with the community ordination grouping these two habitat types together. There were a number of species shared with hardbottom communities in the region, and lower degrees of similarity with the coral-associated fish assemblage of the SEUS. The other megafauna observed in the canyon video transects were very similar to those from previous studies, including observations in Pamlico Canyon of all of the coral species from the Baltimore and Norfolk Canyons to the north. The infauna communities in the canyons sampled here were also similar to those from the canyons to the north, although a degree of dissimilarity was associated with the break at Cape Hatteras.

Relevant Report Sections: **4.1 Community Structure, 4.2 Fish Communities**

Community Hypothesis 2: *The abundance of hard- and soft-substrate fauna and pelagic nekton are all enhanced in canyons compared to nearby slope habitats at similar depths.*

Findings: The active acoustic data from the canyons showed dense aggregations of water-column taxa over the edges of the canyons, as opposed to the low density of the acoustic signal in the areas between canyons. In the video transects, the mean megafaunal abundance per 1-minute video segment at Pamlico Canyon was 25.82 vs. 2.89 at Cape Lookout Deep, which occurs at the same depth. However, this was largely driven by high abundances of *Acesta* sp. present on overhangs in the step-like environment of Pamlico Canyon that provided an unsedimented refuge for this species and others such as *D. dianthus*. If this species is removed from the counts, the mean megafaunal abundances per segment at Pamlico Canyon are still elevated above those at Cape Lookout Deep; respectively 4 and 2.89 individuals per

1-minute of video. There were also higher densities of infauna within the canyons than there were in nearby non-canyon sediments. However, the highest infaunal densities recorded in this study, and indeed in any comparable study that we could find in the literature, were from the bacterial mats of the Pea Island and Kitty Hawk Seeps, which occur in between canyons.

Relevant Report Sections: **4.1 Community Structure, 4.2 Fish Communities**

Community Hypothesis 3: *Demersal fish assemblages will vary among habitat types (coral vs. canyon vs. seep), but the degree of specialty will decline with depth and latitude.*

Findings: Demersal fish assemblages varied among habitats, with habitats such as seeps and canyons containing functionally diverse, abundant, and species-rich communities of different composition as compared to hardbottoms and coral reefs. Communities became more similar below 2,000 m, and had lower functional diversity, regardless of habitat type. Communities of demersal fishes were highly similar among seep, hardbottom and soft-sediment habitats. The degree of specificity, however, did not decline with increasing latitude, as distinct differences could be seen among habitats in the MAB.

Relevant Report Sections: **4.2 Fish Communities**

Community Hypothesis 4: *Enhanced megafaunal biomass and diversity over deep-reef and canyon communities is subsidized by impingement with the deep-scattering layer.*

Findings: Validation of this hypothesis was among the most clear and important of all of the results of Deep SEARCH. We frequently observed the deep-scattering layer (DSL) interacting with the canyon and coral habitats, in particular over Pamlico Canyon and Richardson Reef Complex. At all Deep SEARCH sites where we conduct15culate15ticstic water-column sensing, we detected a DSL of enhanced fish/shrimp abundance at mesopelagic (300–500 m) depth. The exact depth range of the DSL varied by location, but at all locations where bottom topography intercepted these depths, intensities of backscattering signal strength, a proxy for DSL organismal abundance, increased, likely due to compaction of organisms into a smaller space than that available in deeper water. Sampling over the reefs revealed late juveniles of reef-associated taxa were major components of the pelagic assemblage, indicating clear ties between the benthic and pelagic ecosystems. When coupled with ROV observations of demersal fishes known to consume pelagic food resources at the same sites, we concluded that benthopelagic coupling at deep-reef and canyon habitats is an integral component of the ecology of these megafaunal assemblages.

Relevant Report Sections: **4.2 Fish Communities**

Community Hypothesis 5: *Invertebrates associated with octocorals include specific associations where a given symbiont is only found on one host species.*

Findings: In the SEUS region, we collected few octocorals that had conspicuous associates, and thus few associates were collected. However, of the associated symbionts collected in the region, there were a few species unique to their coral hosts. For example, we collected *Ophiocre15culatepus* only from a *Metallogorgia melanotrichos* as seen in other studies, and we collected an unidentified anemone only from *Plumarella* sp. We found other invertebrate symbionts on more than one coral species but, at least in this region, they occurred only on species of the same genus. The ophiuroid genus *Asteroschema* was unique to *Paramuricea* sp. Both *A. clavigerum* and an unidentified species of *Asteroschema* was collected from *Paramuricea aff. biscaya* whereas we collected an unidentified *Asteroschema* on both *P. aff. biscaya* and *P. biscaya*.

Relevant Report Sections: **4.1 Community Structure**

Community Hypothesis 6: *Soundscapes accurately characterize the existing diversity of coral habitats.*

Findings: We collected a complete set of acoustic data at the Richardson Reef Complex, and these appeared generally indicative of overall biodiversity when we compared them to similar data sets collected on shallow reefs. Specifically, the kurtosis, periodicity, and uniformity categories were found to indirectly relate to differences in ecosystem diversity in terms of sound producers. There was a higher diversity in the soundscape at the highly diverse Great Barrier Reef (GBR) site, and a lower diversity of the soundscape at the lower-diversity deepwater reefs. Within the Deep SEARCH study area, a multivariate analysis of benthic megafaunal community structure at the locations of the soundscape indices could potentially reveal how mean and/or variability in soundscape metrics at a site are related to presence, abundance, and/or functional diversity of component species. In other words, communities rich in motile scavengers perhaps emit sound differently than those rich in sessile taxa. However, megafaunal data were only available at the Richardson Hills site from the present study, therefore these initial analyses would require additional data collection to tease out spatiotemporal differences in community structure between sites based on passive acoustics.

Relevant Report Sections: **4.6 Soundscapes**

Community Hypothesis 7: *The communities associated with deep-coral habitat in the southern part of the study area will be more similar to those of the east and west Florida slope and northern GOM than the NE Atlantic.*

Findings: At the broadest level, the Blake Plateau shares the presence of large *L. pertusa* mounds with the west Florida slope and the NE Atlantic. There are coral mounds in the northern GOM, but they are less extensive than these other sites. The communities on the coral mounds share similarities among all of these areas, but the majority of the shared species (for those fauna that could be identified to the species level) are among the Blake Plateau, Florida slope, and GOM. In particular, the octocoral assemblages were more similar to those in the GOM and on the west Florida slope compared to the NE Atlantic. The only possible exception to this is in the sponge assemblage, but this may reflect the increased level of effort in the identification of sponges in the NE Atlantic as opposed to the GOM.

Relevant Report Sections: **4.1 Community Structure, 4.2 Fish Communities, 4.3 Community Phylogenetics**.

Community Hypothesis 8: *The communities associated with the cold seeps in the study area will be more similar to the GOM seeps than with those of the Barbados Accretionary Prism or Gulf of Guinea seeps.*

Findings: The communities associated with the seeps in this region fell into two distinct categories: the shallow, intercanyon seeps and the deeper, mussel-dominated seeps. The shallow seeps were not similar to any other communities that have been sampled in the larger Equatorial Atlantic Belt region (extending from the GOM to West Africa and inclusive of the Blake Plateau and Caribbean seeps). The Blake Ridge and Cape Fear Seep communities were very similar to one another, and even with the increased amount of data from this study, truly stand out from the rest of the seep communities in the region, most dramatically in the absence of any vestimentiferan tubeworms.

Relevant Report Sections: **4.1 Community Structure, 4.2 Fish Communities, 4.3 Community Phylogenetics.**

Community Hypothesis 9: *Among all habitats sampled, phylogenetic and functional community similarity will be explained by: 1. Habitat type, 2. Depth, and 3. Distance.*

Findings: Functional and phylogenetic diversity were both mostly explained by habitat type and depth. Functional diversity of fishes was distinctly different among habitats, with cold seeps and canyons harboring some of the most functional diversity. We saw this pattern, however, mostly at depths greater than 2,000 m. Overall, functional diversity decreased with increasing depth, regardless of habitat type. Phylogenetic diversity of octocorals was also largely driven by depth and habitat type. Communities at depths shallower than 2,000 m contained the highest phylogenetic diversity, likely attributed to the diversity of habitats and suitable areas for growth and recruitment of corals in the region. Overall, seeps contained low phylogenetic diversity of corals, with just a few coral species inhabiting authigenic carbonates in seep areas. We discerned no pattern between functional and phylogenetic diversity with geographic distance.

Relevant Report Sections: **4.3 Community Phylogenetics**.

Connectivity Hypothesis 1: *Trophic structure within seep communities will be fueled by chemosynthetic productivity while L. pertusa-associated food webs will be supported by photosynthetic products and efficient nutrient recycling.*

Findings: In general, benthic communities present at seep sites showed clear reliance on chemosynthetic productivity, whereas representative taxa from coral sites largely depended on photosynthetically derived organic matter. At both seep and coral sites, the particulate organic matter (POM) ranged from -29.8‰ to -20.0‰ $\delta^{13}C$ and -0.1‰ to 10.9‰ $\delta^{15}N$, with the majority of POM clearly within the range of photosynthetic productivity. An interesting exception were the POM values at the surface within the Gulf Stream over Richardson Reef Complex, which ranged from -26.0‰ to -20.8‰ $\delta^{13}C$ and -0.1‰ to 3.1‰ $\delta^{15}N$. The base of the food web at the seep sites, however, was represented by the primary producer symbiotic fauna of bathymodiolin mussels (muscle $\delta^{13}C$ range, -57.5 to -37.8 ‰) where they were present at the Blake Ridge, and there the bottom water POM was slightly depleted in ^{13}C (-27.9‰) compared to the surface (-22.7‰).

Relevant Report Sections: **4.4 Trophic Ecology**

Connectivity Hypothesis 2: *Seep fauna will show less reliance on seep productivity at shallow sites, in older mussel beds, and at sites of low fluid flux.*

Findings: This is a hypothesis consisting of three variables that we did not anticipate being as confounded as they were found to be in reality. There was a distinct correlation between depth and the $\delta^{13}C$ values of the benthic fauna at all trophic levels, with deeper fauna having more depleted ^{13}C ratios. The shallow seeps, which did not have mussel beds, appeared less reliant on chemosynthetic productivity, with the tubeworm, *Escarpia* sp., serving as the notable exception. However, the shallow seep sites were also the sites of the highest rates of fluid flux and methane oxidation rates, which may partially explain the high infaunal densities at the shallow seeps as compared to the deeper sites. In other words, while stable carbon isotope ratios indicated limited trophic provision of seep-derived carbon at shallow seeps, high infaunal community densities hinted at some key reliance on seep production fueling the sediment communities.

Relevant Report Sections: **3.3 Biogeochemistry and Microbial Ecology, 4.1 Community Structure, 4.4 Trophic Ecology**

Connectivity Hypothesis 3: *Trophic connectivity between seep habitats and the other communities in the region will be realized through grazing on free-living bacteria and transport by mobile predators.*

Findings: We generated ample anecdotal but little empirical evidence to support this hypothesis. At the shallow seeps, there were numerous, direct observations of midwater and demersal fishes and squid interacting with the seep communities. However, the large, mobile predators for which there are isotopic data indicated little input from methane-derived carbon, with some of the most ^{13}C enriched values measured from the seastars and other predators at the Pea Island and Kitty Hawk Seeps. In contrast, most of the mobile fauna at the deeper Blake Ridge site, including the brittlestar *Ophioctenella acies* and sea cucumber *Chiridota heheva* as well as galatheid crabs, unidentified decapod shrimps, and deposit feeding echinoid urchins and gastropods including typical seep associates, all reflected incorporation of chemosynthetic production. Whereas there was some evidence for isotopically light carbon traveling through the food web at the deep Blake Ridge Seep site and through the sponges at the Pea Island site, most of the other fauna collected at the shallower seeps primarily reflected background, photosynthetic productivity and detritivory.

Relevant Report Sections**: 2.3 Sites Visited During This Study, 4.1 Community Structure, 4.4 Trophic Ecology**

Connectivity Hypothesis 4: *Trophic connectivity will occur between pelagic and benthic species through benthic-pelagic coupling.*

Findings: Connectivity between the benthos and the pelagic fauna was most directly evidenced by direct observation during the human-operated vehicle (HOV) or ROV surveys and the active acoustic profiles obtained over the coral and canyon sites. The video of the fishes and squid utilizing the intercanyon seep habitats and the acoustic evidence for the impingement of the DSL on the benthic structures of the canyons and coral mounds were among the highlights. In addition, the presence of juvenile benthic fishes in the midwater trawls supports a link between the pelagic and benthic zones, given that these pelagic juveniles will eventually recruit to the benthos. The direct comparisons of stable isotope values from the benthic and pelagic communities overlying the Richardson Reef Complex indicated trophic enrichment in nitrogen from pelagic fauna to the benthos, indicating that the pelagic fauna were either acting as a trophic subsidy for the benthos or as independent and distinct food sources. However, the benthic-suspension feeders and pelagic fauna collected by midwater trawl had overlapping isotopic niches, which could potentially indicate a shared energy resource. There was much greater separation between the pelagic food web and the seep food web, indicating little transfer of seep-derived carbon from the seafloor seeps at 2,150 m to the midwater communities that were well above the seafloor in 200 and 500 m of water.

Relevant Report Sections: **2.3 Sites Visited During This Study, 4.2 Fish Communities, 4.4 Trophic Ecology**

Connectivity Hypothesis 5: *Populations will show a greater degree of genetic connectivity within depth ranges than across depth ranges*.

Findings: This hypothesis could only truly be examined in the populations of *L. pertusa* because there were not enough populations of mussel species in different depth ranges and the *Plumarella* sp. populations showed complete admixture. The populations within the Blake Plateau showed little genetic differentiation, although it should be noted that there was one haplotype present at the Richardson site that was not captured at the other sites. This could be due to isolated recruitment events from unknown source populations, potentially due to the increased depth at this site, or simply due to the absence of this rare haplotype in our samples from the other sites.

Relevant Report Sections: **5.5 Population Connectivity**.

Connectivity Hypothesis 6: *Populations will show a break in genetic connectivity north and south of Cape Hatteras, NC.*

Findings: The *L. pertusa* populations showed elevated connectivity among the sites of the Blake Plateau, but lower connectivity with the populations north of Cape Hatteras in Norfolk Canyon and Pea Island, despite the relatively small distance between these sites. This could not be tested in the other species for which we have population-level genetic data, but it should be noted that this hypothesis holds true at the community level for a variety of taxa, as discussed earlier.

Relevant Report Sections: **5.5 Population Connectivity**.

Connectivity Hypothesis 7: *Rates and directions of gene flow within species will correspond with predominant current directions*.

Findings: Connectivity of *Gigantidas childresssi* follows the predominant current directions in the region. We postulated genetic exchange to flow from the shallower, more northerly Baltimore Canyon Seep to the deeper, more southerly Norfolk Canyon Seep. This pattern matches the predominant current in the region as the Labrador Current moves southerly towards Cape Hatteras. Sample sizes were too small in all octocorals to determine rates and directions of gene flow. However, *Plumarella* sp. in the SEUS region exhibited panmixia, and all sites in which we collected *Plumarella* sp. were bathed by the Gulf Stream.

Relevant Report Sections: **5.5 Population Connectivity**.

Biology Hypothesis 1: *Coral-growth and recruitment rates are slower in deeper, and more variable environments*.

Findings: There were no conclusive results of the coral-growth analyses so this hypothesis could not be tested directly.

Relevant Report Sections: **5.3 Age and Growth Studies**

Biology Hypothesis 2. *Timing of seasonal reproduction in benthic invertebrates can be predicted from the timing of surface productivity blooms.*

Findings: There was a mixture of seasonal and continuous reproduction in the corals examined, so the reproductive timing could not be predicted for all of the species included in this part of the study. However, for those with periodic reproduction, including *Desmophyllum dianthus, Lophelia pertusa*, and *Solenosmilia variabilis* and possibly in *Plumarella* sp. and *Pseudodrifa nigra*, the onset of gametogenesis appears to be in the spring near our April sampling date, with spawning in the fall after our August sampling date.

Relevant Report Sections: *5.4 Reproductive Biology*

Biology Hypothesis 3: *Seep mussel condition index increases with methane flux*.

Findings: We collected samples from mussel beds at Blake Ridge Seep to test this hypothesis, but a freezer failure at Florida State University prevented accurate data from being obtained.

Biology Hypothesis 4: *Recruitment dynamics of seep mussels are positively correlated with methane flux.*

Findings: Size frequencies of mussels were only available from the mussel pot collections, and these do not directly address the question of recruitment dynamics. However, the data we have indicate a few very

large individuals with a clear recruitment pulse at smaller size classes (below 10 cm). This may indicate occasional, sporadic recruitment events with relatively low adult survivorship at large sizes.

Relevant Report Sections: **4.1 Community Structure**

Biology Hypothesis 5: *Fauna from highly variable environments show increased resilience to environmental disturbance.*

Findings: The Richardson site exhibited extreme variability in oceanographic conditions with temperature changing 6–8°C over a 24-hour period. Our experimental results showed that the *L. pertusa* colonies collected from the Richardson site were resilient to these types of changes, with all of the colonies surviving simulated shifts in temperature, but that this came with a metabolic cost.

Relevant Report Sections: **3.1 Oceanography, 5.1 *Lophelia pertusa* physiology**

Microbial Hypothesis 1: *Microbial abundance and activity (sulfate reduction (SR) and methane oxidation rates) will be highest and will occur over a broader spatial area in areas of active methane seepage*.

Findings: Methane oxidation rate was generally correlated to methane flux, with the highest rates of methane oxidation measured in the water column over and in the sediments at the Pea Island site, which was also the site of highest methane flux. SR was also elevated in Pea Island sediments.

Relevant Report Sections: **3.3 Biogeochemistry and Microbial Ecology**

Microbial Hypothesis 2: *Sediment SR rates will be explained by a combination of depth, sediment organic carbon content, and magnitude of gas or fluid seepage*.

Findings: SR rate was highest where there was a clear sulfate-methane transition zone (SMTZ), as we observed in the sediments beneath bacterial mats at Blake Ridge, Cape Fear, and Pea Island.

Relevant Report Sections: **3.3 Biogeochemistry and Microbial Ecology**

Microbial Hypothesis 3: *The composition of sulfate-reducing bacteria (SRBs) and methane-oxidizing microorganisms (MOMs) will change with depth and will be distinct from the microbial communities found at other gassy cold seeps such as in the GOM*.

Findings: The primary determinant of community similarity in the microbial communities was the location of their collection. We only obtained diversity data from Pea Island, Kitty Hawk, and Blake Ridge seeps, so it is difficult to evaluate whether depth or location with local geochemical conditions was more important, although the variance in community structure at the Blake Ridge site was comparable to the variance captured at the other two sites combined. Within a site, the composition of the microbial community at the seep primarily changed with the carbonate and detrital carbon content of the samples.

Relevant Report Sections: **3.3 Biogeochemistry and Microbial Ecology**

Microbial Hypothesis 4: *Distinct microbial communities exist at seep, coral, and soft-sediment habitats in and out of canyons.*

Findings: We did not directly test this hypothesis, as the microbial ecology studies focused on the seep sites. However, one of the most interesting findings was that there were relatively high methane oxidation rates in the shallow (< 300 m) waters overlying the Richardson Reef Complex. These were higher than any site where we measured the rate, except for the Pea Island site. This may be related to nutrient limitation in the mixed layer of the Gulf Stream, and further investigation may be warranted.

Relevant Report Sections: **3.3 Biogeochemistry and Microbial Ecology**

Microbial Hypothesis 5: *The functional potential of microbial communities, as evidenced from metatranscriptomic data, will vary between coral, mussel symbionts, bottom water, and soft-sediment samples.*

Findings: Numerous issues with molecular work throughout this study, from delays due to closure of labs and facilities during COVID and poor quality of preserved ribonucleic acid (RNA) samples resulted in a lack of data to fully address this hypothesis.

Relevant Report Sections: **3.3 Biogeochemistry and Microbial Ecology, 5.2 Coral Symbiosis and Microbiome**.

2 Field Acquisition

2.1 Site Selection

Section Authors: Erik E. Cordes, Amanda Demopoulos, Jason Chaytor, Andrea Quattrini, Cheryl Morrison, Sandra Brooke

The study region straddles the BOEM South Atlantic and Mid-Atlantic Planning Areas. The area of interest to BOEM lies between Norfolk Canyon (~37.5ºN) and the Georgia-Florida border (~30ºN), from 50 miles offshore out to the edge of the US exclusive economic zone. Within that study area are three general habitat types: seeps, canyons, and deep-sea corals. In some places these habitats co-occur and overlap. Below is a brief description of the sites that we picked for our acquisition surveys.

2.1.1 Seep Sites

Until the 1980s, the only confirmed seeps with dense biological communities along the US Atlantic margin were those on the Blake Ridge and Cape Fear diapirs off North Carolina. We also suspected a seep at a site on the upper continental slope near Baltimore Canyon (Hecker et al. 1983). Since those days, seep habitats within Baltimore Canyon and near Norfolk Canyon ("Norfolk Seep") have been discovered, and many more are suspected. Between the Norfolk Seep and the Blake Ridge Diapir, there are over 100 known gas venting sites, from 50 m to 2,650 m water depth, discovered during USGS and NOAA Ship *Okeanos Explorer* cruises over the last few years (Morrison 2019). The Cape Fear Seep is one of those. Some of these expulsion locations comprised clusters of seeps, and less common are individual sites. Only a few had been visually surveyed before our surveys. We selected as our seep sites Norfolk Seep, the Cape Fear Seep, and the Blake Ridge Seep.

Norfolk Seep was discovered in 2013 and is the most extensive of the known methane seeps in the North Atlantic (Prouty et al. 2016, Demopoulos et al. 2019). The seepage area is approximately 120 km off the coast of Virginia, just south of Norfolk Canyon in approximately 1,600 m depth and comprises two separate ridges, each about 1 km in length. Both ridges are almost completely covered in dense populations of bathymodiolin chemosynthetic mussels, with endemic seep associates such as the seep cucumber (*Chiridota heheva*) and alvinocarid shrimp. Unlike other deep seeps in the region, there were no siboglinid tubeworms or vesicomyid clams observed at this seep. The presence of large boulders of authigenic carbonate, methane hydrate, and streams of gas bubbles indicate the existence of long-term active seepage.

The Cape Fear Seep is the location of a persistent bubble plume observed in the multibeam surveys of the *Okeanos Explorer*, and three areas inhabited by clams and bacterial mats were detected by *Sentry* photographs (Brothers et al. 2013). Unlike other seeps in the region, methane-seep mussels had not been observed prior to this study.

The Blake Ridge Seep is the best-known seep site off of the East Coast. The Blake Ridge Diapir was the subject of extensive geological surveys as part of the Ocean Drilling Program (Paull et al 1996, 2000). Gas hydrates and extensive methane seepage have been documented from this site (Brothers et al. 2013). Chemosynthetic communities were initially described from visual surveys and collections (Van Dover et al. 2003), and included seep mussels (*Bathymodiolus heckerae*) and vesicomyid clams (*Vesicomya venustus*) at depths of 2,155 m. More recent autonomous underwater vehicle (AUV) surveys expanded the known extent of chemosynthetic communities at Blake Ridge to four discrete areas (Brothers et al 2013).

2.1.2 Canyon Sites

Previous research has highlighted the resources associated with submarine canyons along the western Atlantic margin (Quattrini et al. 2015, Ross et al. 2015, Brooke et al. 2017). These have primarily focused on the area between Virginia and New England, with one expedition further south off North Carolina. There are three named canyons off the coast of North Carolina; Keller, Hatteras and Pamlico, the former is unexplored, but the Hatteras Canyon complex has been the focus of some geological and biological studies. We chose Norfolk, Keller, Hatteras, and Pamlico as our canyon sites.

The head of Norfolk Canyon is approximately 90 km offshore from the mouth of Chesapeake Bay, Virginia, and is a long shelf-incised canyon that begins in 200 m of water on the shelf and ends on the abyssal plane deeper than 3,000 m. The walls of Norfolk Canyon have extensive areas of exposed hard substrate, which provide habitat for dense communities of sessile benthic fauna such as corals and sponges. These communities have been documented from 400 to 1,300 m depth to support diverse assemblages of other invertebrates. Norfolk Canyon was relatively unexplored, although there were records of several coral species, including the structure-forming scleractinian, *Desmophyllum pertusum*. Commercial fishery species such as red crab, hake and monkfish have been observed on the sediment of the canyon slopes. Norfolk Canyon is part of the Deep-Sea Coral Protected Area, implemented in 2015 through the Mid-Atlantic Fishery Management Council. It also lies within an area of frequent Naval activity, which made visiting the site logistically difficult.

Keller Canyon is the only one of the target canyons that incises the shelf, but much less so than those further north. The funneling effect of the shelf-incised canyons creates strong currents that remove sediment and allow development of hard-substrate benthic communities. Without accelerated currents, sediments cover all but the steepest slopes. Several multibeam surveys have collected data as single transit swaths across Keller Canyon, but the most comprehensive surveys to date were by the *Okeanos Explorer* (National Centers for Environmental Information [NCEI] Survey ID EX1106) and the Research Vessel (RV) *Henson* (NCEI Survey ID: HEN04-3), which together covered the canyon head to the abyssal plain and have revealed the rugged habitat along the head of Keller Canyon and adjacent shelf-slope break. Prior visual surveys with AUV *Sentry* revealed some octocorals and anemones, but low abundance/occurrence overall. Multibeam surveys by NOAA-USGS in 2011 revealed more than 50 areas of diffuse gas venting near Keller Canyon, in depths ranging from 53 to 930 m depth.

Hatteras Canyon and the adjacent slope were the subject of earlier surveys of benthic megafauna using research submersibles (Rowe and Menzies 1969, Rowe 1971). Their observations were of mostly soft-sediment fauna, primarily sea pens, large holothurians, asteroids, quill worms, and cerianthid anemones. They recorded differences in species composition between canyon and slope, which were attributed to higher sedimentation levels in the canyon that excluded many common slope invertebrates. None of the historical records noted any scleractinians or gorgonian octocorals, but more recent exploration of Hatteras Canyon (NOAA-OER) using the AUV *Sentry* observed octocorals on one of the steep canyon walls. Multibeam surveys by NOAA-USGS in 2012 revealed perhaps 12 areas of diffuse gas venting near Hatteras Canyon, in depths ranging from 183 to 374 m depth (Morrison 2019).

Pamlico Canyon only minimally impacts the shelf break and is located approximately 20 miles off the North Carolina Outer Banks. The axis of the canyon on the continental slope is approximately 15 nautical miles long from 400 m to over 3,000 m depth, but then extends onto the seafloor for over 100 miles to deeper than 5,000 m. It has been mapped and was first explored visually on an AUV *Sentry* cruise in 2016, which revealed octocorals attached to the canyon walls (Nizinski 2016). Bubble plumes have not been previously observed in the vicinity of this canyon. From these data, Pamlico seemed to be the best site in terms of abundance and diversity of corals, other inverts, and fishes, and was therefore one of the highest priority canyon sites for this study.

2.1.3 Coral Sites

The narrow continental shelf off Cape Hatteras gradually widens to the south, particularly off South Carolina and Georgia, then becomes narrow again off the coast of Florida. Between the continental shelf and slope in this region is a vast horizontal platform called the Blake Plateau (Dillon and Popenoe 1988). This feature is 228,000 km^2, has an average depth of 850 m, and is one of the most rugged areas of the southeastern US seabed. Hundreds of hardbottom features, ranging from low-relief ledges to massive conical peaks, contribute to the rugged topography. Hardbottom habitat includes areas of rocky outcrops and ledges, and large numbers of mounds, many of which are bioherms formed by the *L. pertusa* and *Enallopsammia profunda* at depths from 600 to 800 m. Most of the platform is carbonate in origin, but fields of manganese oxide nodules and slabs of phosphoritic rock have also been observed. Some of these areas have been the focus of substantial research effort, whereas others have barely been explored. We identified this as a rich area of potential study sites, and in a different biogeographic province and oceanographic regime from the northern part of the study area. Most sites we selected for our study lie within Coral Habitat Areas of Particular Concern (HAPC), established in 2009 by the South Atlantic Fishery Management Council. We selected Cape Lookout, Cape Fear, Stetson Banks, Savannah Banks, and the Blake Deep as our study sites.

Cape Lookout is located on the Blake Plateau in relatively shallow (320–550 m) water, and the series of topographic features that make up this site are the most northerly known *L. pertusa* bioherms on the US Atlantic Coast. There are perhaps 10 large and several small features at this location, with elevations up to 80 m and variable slopes. Multibeam bathymetry surveys have covered the full known extent of the mounds (NCEI Survey ID: NF-07-02-MPA and NF-08-01-MPA, and additional surveys by the *RV Pelagia* in 2010). The site is relatively well studied, with habitat and community data collected using submersible and ROV surveys (Ross 2006, Partyka et al, 2007, Ross and Nizinski 2007, Ross and Quattrini 2007, 2009, Quattrini et al. 2012), and detailed analysis of physical and geological conditions (Mienis et al. 2014). Physical oceanographic data indicate that this site is exposed to extreme environmental conditions of highly variable water temperature and strong currents. Community data show extensive colonies of *Desmophyllum pertusum* concentrated on the tops and current-facing aspects of the mounds, but with highly variable percentages (5–75%) of live coral. Other species of coral commonly found south, were notably lacking (Partyka et al 2007), but coral-associated invertebrates and fishes were abundant and diverse (Partyka et al 2007). Because of the existing information at this site, it was not the highest priority for our program.

The Cape Fear site comprises a single large (0.7 km^2) coral bioherm, in similar depths (360–500 m) to the Cape Lookout mounds. The mound is very steep, extremely rugged and rises 100 m above the seafloor. The mound comprises living and dead coral and is surrounded by areas of dead coral rubble. Localized high abundances of orange cup corals and anemones have been observed on the dead coral matrix, but large octocorals and other structure-forming scleractinians were absent. Multibeam bathymetry (NCEI Survey ID: NF-07-02-MPA) was available for this site and there are several publications that document the geology and biology of this feature (Ross 2006, Partyka et al. 2007, Ross and Nizinski 2007, Quattrini et al. 2012). As with Cape Lookout, this is one of the better-known sites in the proposed study region, and therefore was of lower priority.

Stetson Banks is a large area of rugged and varied habitat on the eastern Blake Plateau located off of South Carolina at depths of 550–850 m. It was first surveyed in the 1950s, and extensive coral communities were subsequently discovered during dredging, drop camera and submersible surveys (Stetson et al. 1962, Milliman et al. 1967, Pratt 1968, Ross and Nizinski 2007, Partyka et al. 2007). Stetson et al. (1962) estimated that more than 200 mounds, up to 150 m tall covered an area of 6,000 km^2. Although this expanse of coral habitat was discovered several decades ago, it remained relatively unexplored prior to our study. In addition to the 'hundreds of coral mounds' described by Stetson (1961), this area also contains complex ledges and slopes composed of consolidated rubble that has been undercut

by currents. Previously observed sessile invertebrate fauna is much more diverse at this location than at the North Carolina bioherms. In addition to the structure-forming stony corals (*Desmophyllum pertusum* and *Enallopsammia profunda*), several species of cup corals (*Bathypsammia* sp, *Caryophyllia* sp.), Antipatharians (*Leiopathes* sp., *Bathypathes* sp.) and Octocorals (*Plumarella pourtalesii*, *Acanella* sp., *Keratoisis flexibilis*, Plexauridae) have also been documented in the Stetson Banks region (Partyka et al. 2007). Sponges are also very abundant, with 18 different taxa observed by Reed et al. (2006). In addition to the older geological surveys, modern multibeam bathymetry is also available for portions of this region (NCEI Survey ID: PAT0503, EX1403, and the most recent *Okeanos Explorer* cruise EX1805). There were sufficient existing data to generate predictive habitat models for the area; and these predictions were first surveyed during a 2018 *Atlantis*/*Alvin* cruise.

Savannah Banks (475–600 m) is part of the Blake Plateau north of the large Charleston Bump feature that deflects the Gulf Stream and is intensively scoured by currents, exposing hard substrate (Popenoe and Manheim 2001). This large, complex site contains extensive hardbottom habitats that range in relief from flat to near vertical scarps and lithoherms, which can rise up to 100 m off the seafloor (Reed et al. 2006). This region comprises layers of hard limestone rock and soft mudstone, which is susceptible to erosion. The differential erosion of these two rock types has created a series of terraces and steep walls with overhanging ledges. Sessile benthic fauna, consisting of stony corals (*D. pertusum*, *Madrepo25culateata*), dense sponge communities (*Phakellia* spp., *Geodia* sp., Pachastrellidae and Hexactinellidae), octocorals (Isididae, Primnoidae), black corals (*Antipathes* spp.) and hydrocorals, were abundant on the limestone, but not the less stable mudstone. We observed broken phosphorite pavement at this site, but it was colonized by a sparse and different sessile community from the limestone substrate. Benthic communities were often dense in this area but composed of small colonies. Corals found in this area include the stony corals *D. pertusum* and *Enallopsammia profunda* (as individual colonies rather than the large contiguous thickets observed in other locations) as well as *25culateata*. Octocorals (*Keratoisis* sp., *Paramuricea* sp., *Swiftia* sp., *Eunicella modesta*), Antipatharians (*Leiopathes* sp.) and hydrocorals (*Stylaster* sp.) were also observed (Partyka et al. 2007, Reed et al 2006). The precious coral genus *Corallium* was also reported from this site (Partyka et al. 2007). This area was notable for the large numbers of wreckfish (*Polyprion americanus*) observed on the high-relief rocky bottom during 2001 surveys (Sedberry 2001), although these were not observed by Reed et al. (2006). Existing multibeam data for this site included NCEI Survey ID: PAT0503, EX1203. EW9702, RC2503, and EX1805. Due to the relatively large number of previous dives in this area, and the generally low cover of live coral in the mounds, this area was of lower priority for the study.

The Blake Deep is on the eastern edge of the Blake Plateau where it descends to the abyssal plain further offshore. It was mapped and first explored by the recent *Okeanos Explorer* cruise (EX1805 and 1806). There was a relatively high density of corals at this site, including the framework-forming *Solenosmilia variabilis*. This habitat type was a high priority for the NOAA Deep Sea Coral Research and Technology program (NOAA 2018) and was therefore a relatively high priority for our study. In recent years, the *Okeanos Explorer* (EX1203, 1403, 1805) has added a large amount of additional bathymetry for this region from the Florida Platform to the south of the study area, through to the Stetson Banks. This mapping effort revealed the presence of large numbers of mounds extending nearly 200 miles through this area. Previous observations, mostly from the Johnson Sea-Link, along with a few dives on EX1806 verified that these mounds (at least those that have been observed) are CWC mounds. This was a high priority area for our project, but it partially lies outside of the study area and was logistically difficult due to the frequent use of ports in the northern end of the study area.

2.2 Expeditions (Cruises)

Section Authors: Amanda Demopoulos, Erik E. Cordes

The Deep SEARCH project involved exploration and research of the Mid-Atlantic Planning Area seep, canyon, and coral habitats. The program was originally scheduled to have three primary research expeditions. However, because of numerous issues with weather, personnel emergencies onboard the ships, and technical difficulties, we planned six cruises, and five dedicated cruises were actually conducted. Deep SEARCH personnel also assisted with the planning and execution of three more cruises on the NOAA Ship *Okeanos Explorer,* which added exploratory and complementary mapping and video data to this project, and on three additional cruises through the ADEON project, on which many of our pelagic trawling and acoustics tasks were accomplished. In addition to those of the five dedicated Deep SEARCH cruises, events of these six supporting expeditions are summarized in this report where relevant. In total, Deep SEARCH personnel thus participated in 11 different research expeditions to the study area over the course of the project, including three concurrent cruises in the fall of 2019. The five Deep SEARCH dedicated cruises were as follows:

1) The first dedicated Deep SEARCH cruise was aboard the NOAA Ship *Pisces* and using the AUV *Sentry* in September 2017. This cruise was heavily impacted by weather but acquired some multibeam data and accomplished three *Sentry* dives in the study area.
2) The second dedicated cruise was originally scheduled for the NOAA ship *Nancy Foster*, but it was cancelled due to the need for some unexpected repairs because of an accident as the ship was coming out of shipyard. We split that cruise mission into three components: multibeam mapping, submersible sampling, and over-the-side sampling plus lander deployments. We completed the multibeam mapping portion of the project on the NOAA Ship *Okeanos Explorer* cruise in May-June 2018 through a collaborative effort with NOAA-OER. The second dedicated cruise of the project was aboard the RV *Atlantis* and used the Deep Submergence Vehicle (DSV) *Alvin* in August 2018. It was primarily supported through this project, but time at sea was augmented with support from the NOAA Deep-Sea Coral Research and Technology Program.
3) The third dedicated cruise was aboard the RV *Brooks McCall* in October 2018 and focused on lander deployments and over-the-side sampling.
4) The fourth dedicated cruise was aboard NOAA's RV *Ron Brown* and used the ROV *Jason II*. The expedition was conducted in April 2019 and was highly successful in accomplishing much of the sampling work described in this report.
5) The fifth dedicated cruise was a midwater trawling and lander expedition aboard the *Nancy Foster* in October 2019.

These five cruises are designated in Table 2-1 with an asterix within the context of the timeline of all Deep SEARCH related expeditions. Full field reports on each of the expeditions are included in the Appendices.

Table 2-1. Expeditions associated with the Deep SEARCH project

Year	Date(s)	Expedition and Vessel	Notes
2017	9/10–9/29	***Pisces* with *Sentry***	Impacted by three different hurricanes
2018	3/26–4/25	***(Nancy Foster)***	Cancelled after emergency repairs were necessary just before the cruise
2018	5/30–7/1	***Okeanos Explorer* with *D2***	Collaboration—mapping of Blake Plateau and ROV operations led by Cheryl Morrison
2018	6/6–6/25	***Endeavor***	Collaboration—ADEON cruise
2018	8/19–9/2	***Atlantis* with *Alvin***	-
2018	9/27–10/8	***Brooks McCall***	Lander deployments, over-the-side sampling
2018	10/1–10/24	***Okeanos Explorer***	Collaboration—mapping of Blake Plateau
2018	10/31–11/16	***Endeavor***	Collaboration—ADEON cruise
2019	4/9–4/30	***Ron Brown* with *Jason***	-
2019	10/5–11/21	***Okeanos Explorer* with *D2***	Collaboration—mapping leg plus ROV operations co-led by Alexis Weinnig
2019	10/22–10/30	***Nancy Foster***	Lander recovery, over-the-side sampling
2019	10/22–11/6	***Armstrong***	collaboration—ADEON cruise

Three of these five project-dedicated cruises included the deployment and operation of a submersible. The first cruise deployed the AUV *Sentry*, the second cruise deployed the DSV *Alvin*, and the fourth cruise deployed the ROV *Jason*. The three different submersibles gave us survey and acquisition opportunities that were distinct to the different capabilities of AUVs, DSVs, and ROVs. The ship's track during submersible operations for each of these three cruises is shown in **Figure 2-1**.

Following this map is a cruise summary for each of the five dedicated research expeditions of the Deep SEARCH project.

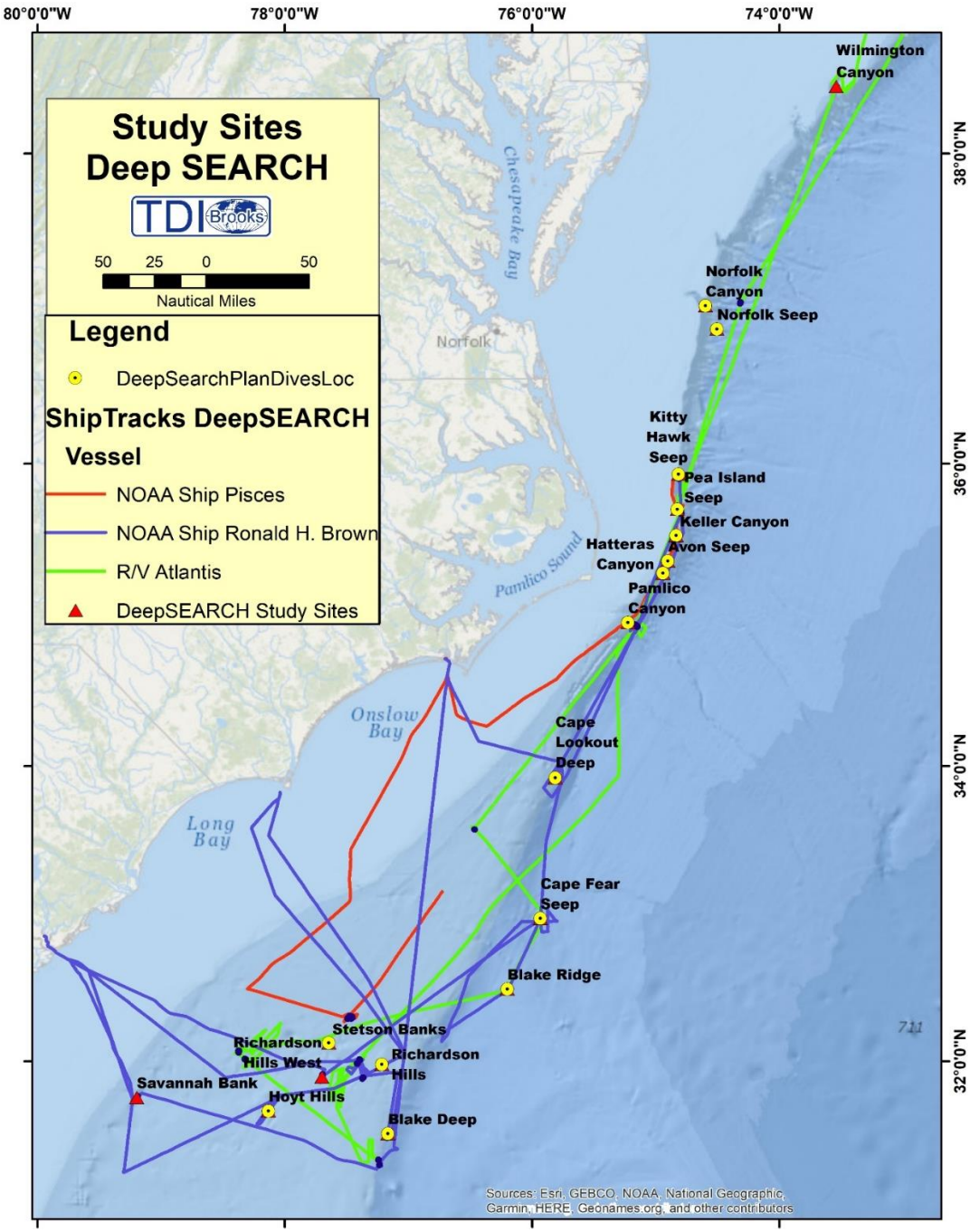

Figure 2-1. Ship track map during operations for the three submersible cruises

2.2.1 First Expedition, NOAA Ship *Pisces* with AUV *Sentry*

We used the NOAA Ship *Pisces* to conduct our first dedicated research expedition (cruise # PC1705) in the mid- and south Atlantic Ocean from 12 through 17 September 2017. This expedition focused on exploring the seafloor for seeps, corals, and canyons at selected survey sites. During this expedition, the *Pisces* mapped 44.7 km of seafloor. Using the AUV *Sentry*, we mapped an additional 8 km^2 of seafloor. These efforts helped to fill in the gaps in available seabed map information, some of which dated back to the 1800s.

Despite three hurricanes during this expedition, we were able to complete three *Sentry* dives. Two of these dives surveyed previously unverified seeps located offshore of North Carolina, and the third dive surveyed a potential coral habitat located offshore South Carolina. We confirmed several seeps by such ground truthing, imaged several seep habitats, and collected corresponding sub-bottom and backscatter data to provide context for these seep environments. In addition to bathymetry data, the ship and *Sentry* collected water-column acoustic data. Additional data collected by *Sentry* included sidescan, conductivity-temperature-depth (CTD), DO, redox, turbidity, and photographic. We collected water-column and sediment samples using the ship's CTD rosette and monocorer to help us better understand the environment in and around the surveyed sites.

2.2.2 Second Expedition, RV *Atlantis* with DSV *Alvin*

We conducted our second expedition onboard RV *Atlantis* using the DSV *Alvin* (cruise # AT41) from 19 August through 01 September 2018. This was the first submersible sampling cruise of the project. The cruise mobilized and demobilized in Woods Hole, MA. We employed *Alvin* to explore new sites, make a variety of deployments and collections, and conduct a variety of studies at two seep sites, three canyons, and four deep-sea coral sites **(Figure 2-2**). This effort included 11 *Alvin* dives used to explore new sites for the occurrence of CWC reefs; make collections of a variety of stony corals and octocorals corals for genetic and physiological studies; make collections of communities associated with seeps, canyons, and corals for ecological studies; collect quantitative digital imagery for characterization of sites and ecological communities; collect spatially explicit near-bottom physical oceanographic data; deploy live corals for growth experiments, and collect push cores for community and associated geochemical analyses. In addition to launching and recovering *Alvin*, we conducted several CTD casts with monocorers, as well as one multicorer deployment (**Figure 2-3**). We also acquired multibeam bathymetric data to augment previously acquired data from the *Okeanos Explorer*.

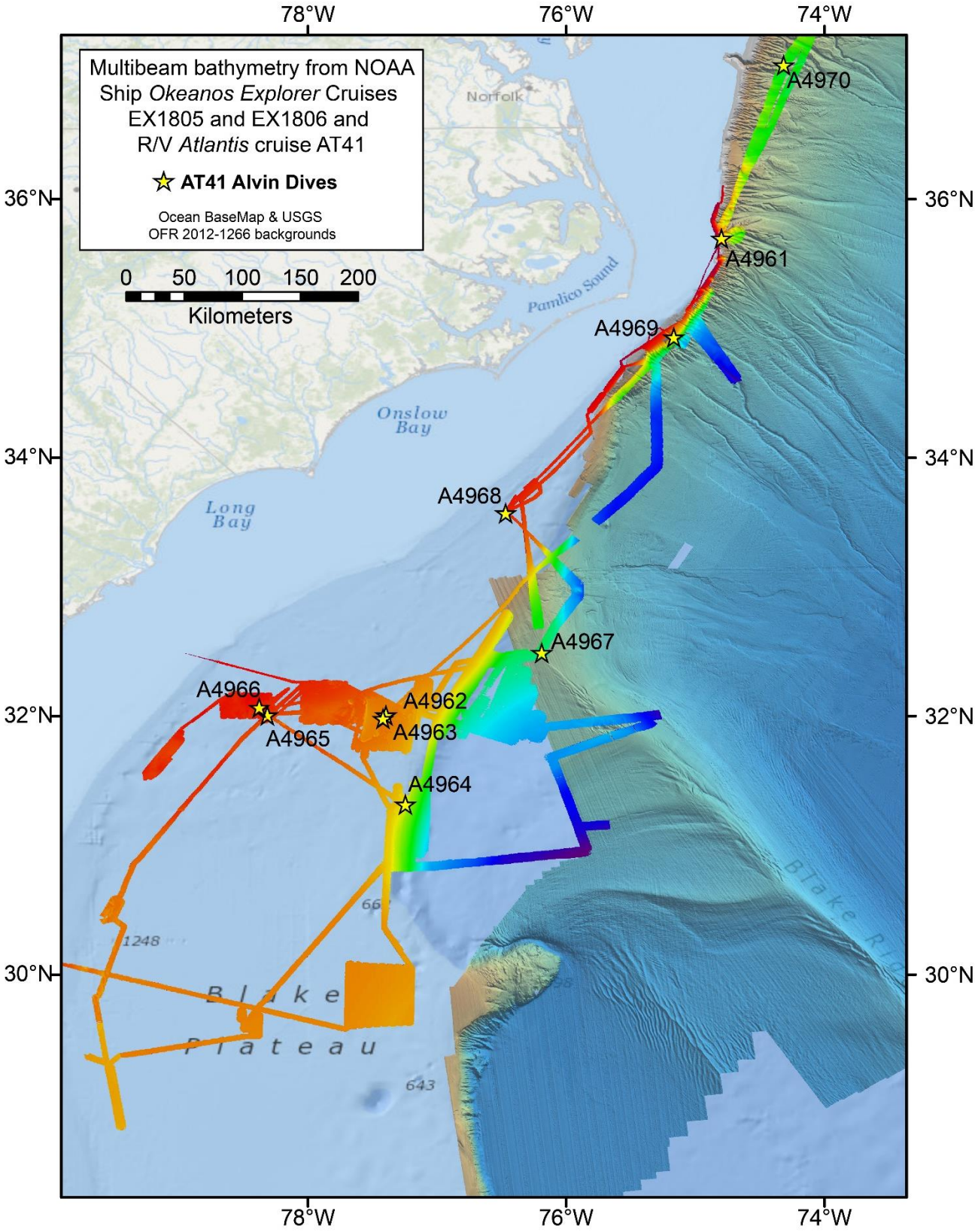

Figure 2-2. *Alvin* dive locations during the second cruise

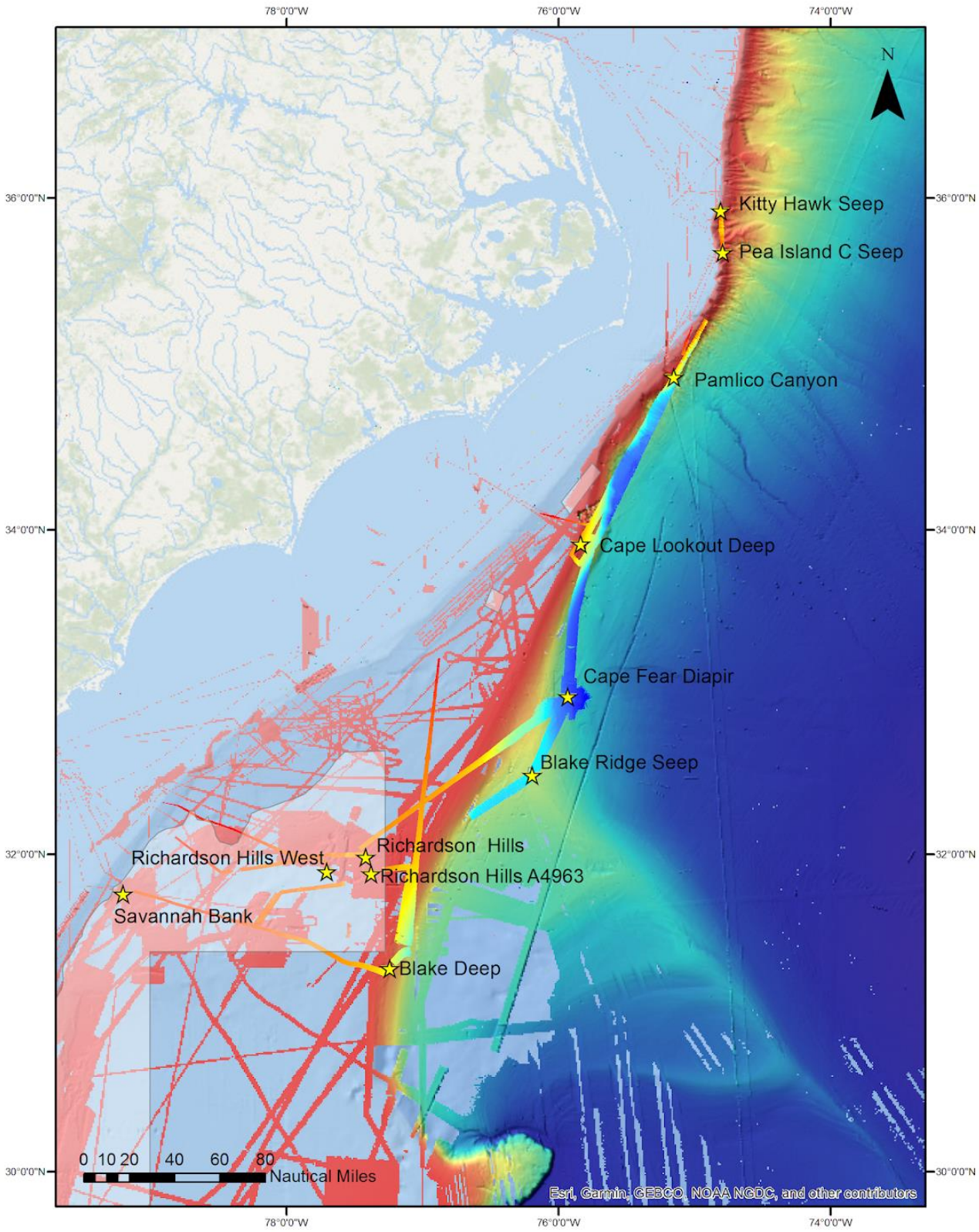

Figure 2-3. Locations of CTD casts and core acquired during the second cruise

2.2.3 Third Expedition, RV *Brooks McCall*

This expedition using RV *Brooks McCall* was conducted from 27 September through 08 October 2018. It was the third research cruise for the Deep SEARCH project. The primary goals for this mission were to conduct midwater trawling targeting the DSL, deploy two landers (one short and one long term), conduct CTD casts, and collect sediment samples using a monocorer, piston corer, and megacorer at pre-selected and permitted locations. We accomplished the following tasks: three piston cores acquired, six CTD casts (without monocore) acquired, and two long-term landers deployed.

2.2.4 Fourth Expedition, NOAA Ship *Ron Brown* with ROV *Jason*

Our fourth research cruise mobilized and demobilized in Charleston, SC and was conducted from 04 through 30 April 2019. One mid-cruise personnel transfer took place on 16 April. This cruise employed the ROV *Jason* to explore new sites, make a variety of deployments and collections, and conduct a variety of studies at four seep sites, one canyon site, and four deep-sea coral sites. We also deployed (April 11), recovered (13 April), and redeployed (15 April) a benthic lander at Richardson Reef Complex. The lander had a variety of instruments, including passive acoustic hydrophone, Acoustic Doppler Current Profiler (ADCP), baited camera, several sensors (CT, fluorescence, turbidity, DO), and sediment trap.

This cruise included 11 ROV dives and a mid-cruise personnel transfer. We used *Jason II* to explore 10 new sites for the occurrence of deepwater coral reefs; make collections of corals and seep fauna, including associates, for genetic and physiological studies; make collections of communities associated CWC and seeps for ecological studies; collect quantitative digital imagery for characterization of sites and communities; collect spatially explicit physical near-bottom oceanographic data; collect coral-growth experiments deployed via *Alvin* in 2018; and collect push cores for ecological and geochemical analyses. In addition to launching and recovering *Jason II*, several CTD casts with monocores, as well as one multicore deployment, were conducted.

2.2.5 Fifth Expedition, NOAA Ship *Nancy Foster*

The fifth Deep SEARCH expedition occurred on the NOAA ship *Nancy Foster* from 22 through 30 October 2019. The primary tasks of this cruise included recovering the benthic lander at Richardson Reef Complex that we had deployed on the third expedition. In addition, several midwater trawls were targeted and accomplished within the DSL. We conducted CTD casts to collect full water-column oceanographic data as well as discrete water samples for seawater chemistry, eDNA, and microbial diversity analysis. In addition, we collected monocore samples for community and geochemical analyses. Sites visited are shown in **Figure 2-4**.

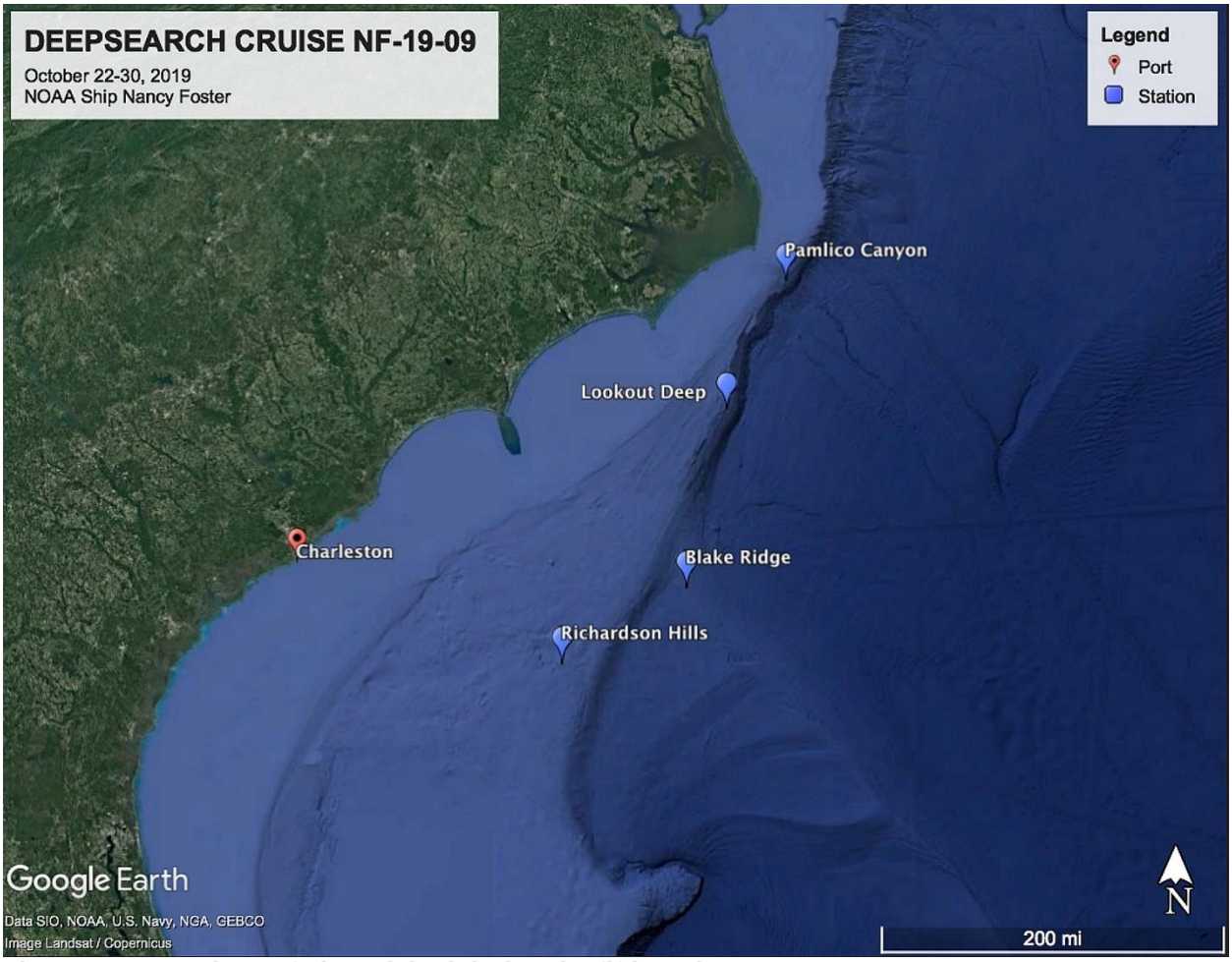

Figure 2-4. Locations of sites visited during the fifth cruise

2.3 Sites Visited with Submersibles

Section Authors: Amanda Demopoulos, Erik E. Cordes

2.3.1 Seep Sites

2.3.1.1 Kitty Hawk (*Sentry* and *Jason*)

Two dives, using AUV *Sentry* (dive 454) and ROV *Jason (*dive J2-1134), were conducted at Kitty Hawk at water depths ranging from 213 to 467 m.

***Sentry*-454 Dive**: *Sentry* dive 454 initially conducted multibeam soundings from 60 m above the seafloor over target seep locations based on acoustic anomalies detected previously through shipboard multibeam mapping efforts. There were areas throughout the survey that had low Eh and high turbidity, indicative of active venting from seeps. The seafloor was primarily composed of soft sediments, with carbonate boulders occurring infrequently throughout the AUV *Sentry* dive track. Shallow depressions and small "holes" were visible in the sediment in all surveyed areas and were spatially correlated on the bathymetry, sidescan and sub-bottom profiler datasets. The sub-bottom profiler records from the photo surveys contained scattered water-column anomalies that generally correlated well with previously identified seeps; however, anomalies unrelated to previous seep locations were also present.

Down-looking imagery collected by AUV *Sentry* revealed zoanthids and anemones attached to some of the rocks. We encountered a few bacterial mats and bubbles were imaged in a few locations. Notable animals we observed included horseshoe crabs, large lobsters, squid, and several fish species, such as scorpaenids, flatfishes, hakes, and macrourids. Other crustaceans included *Cancer* and *Chaceon* spp., cf. *Bathynectes* sp., cf. *Eumunida* sp., shrimp, and some type of lithodid crab. Quill worms (Onuphidae: cf. *Hyalinoecia*) were found in high abundances on the sediment surface. We observed human debris, including rope, fishing line, an unidentifiable metal frame, an anchor-shaped object, and other plastic material. We observed unusual track marks in several images throughout the dive.

***Jason* J2-1134 Dive**: As during the *Sentry* dive, active bubbling, microbial mats, soft sediments, and authigenic carbonate were observed throughout the J2-1134 dive. Siboglinid tubeworms were also observed and sampled in areas associated with the authigenic carbonate, including a large carbonate formation. The dive also encountered abundant quill worms and a scorpaenid fish on the seafloor (466.8 m). Other fish observed included a snipe eel, a paralepidid (cf. barracudina), eelpouts, and black-bellied rosefish. Other animals included lithodid or spider crabs, flounders, and many squat lobsters. Throughout the dive, we observed a few siboglinid tubeworms on rocky substrate. We also found some areas with active bubbling at 360 m and there collected high-quality imagery and push cores. We collected additional cores within mat environments at 334 m. As we transited to shallower depths, we also saw some large megafauna, including hammerhead sharks, conger(?) eels, a large manta ray, sea robin, flounder and lobsters. Though we were searching for live clams, none were found, but we did see more debris, and collected a plastic spoon at 220 m. Toward the end of the dive, there appeared a series of linear ridge features on the sonar, perhaps indicating low-profile bed forms.

2.3.1.2 Pea Island (*Sentry, Alvin, and Jason*)

The Pea Island seeps were grouped into two general locations, one to the north and one to the south, based on acoustic anomalies detected previously through shipboard multibeam mapping efforts. Water depths ranged from 168 to 574 m.

***Sentry*-455 Dive**: Initial surveys at the site by *Sentry* indicated areas of low Eh and high turbidity, likely due to localized resuspension of particles caused by active venting from seeps. The seafloor was primarily composed of soft sediments, with carbonate boulders occurring infrequently, but more often than during Dive 454 at Kitty Hawk, throughout the photo surveys. We observed large bacterial mats, as well as bubbles throughout the survey that may have been of sufficient size to correspond with the bright-patches that we saw in the sidescan sonar data. We observed evidence of seeps on all data sources, including the sidescan sonar, sub-bottom profiler and bathymetric water-column records, and in the photos. During the photo transects, the sub-bottom profiler was able to penetrate several 10s of meters into the sub-seafloor and imaged horizontal and tilted sediment layers adjacent to the smaller canyon walls. “Bright spots” (areas of intense, chaotic acoustic return) in the shallow subsurface were often found associated with seep and other anomalies in the water column.

We observed similar fauna on this dive as those encountered at the Kitty Hawk Seeps (Dive 454). Anemones were found attached to some of the rocks. Notable animals observed included a scalloped hammerhead shark (*Sphyrna lewini*), a catshark, large lobsters, squid, and several fish species (scorpaenids, flatfishes, hakes, macrourids). Most of the fishes were associated with carbonate rocks. Other crustaceans included *Cancer* sp. and *Chaceon* spp. and shrimp. Quill worms (Onuphidae: cf. *Hyalinoecia*) were found in high abundances on the sediment surface. We also observed human debris, including a glass bottle, fishing line, and other plastic.

***Alvin*-4961 Dive**: After the *Sentry* AUV had confirmed the presence of seeps at Pea Island, the *Alvin* dive targeted these seep areas. There was a squad of squid surrounding the sub during the entire dive. The dive explored two main seep areas, and these appeared to be very active with large bacterial mats and visible

bubble plumes in places. There was some outcropping carbonate at one site, quill worms in one of the bacterial mats, and *Chaceon* sp. crabs scattered throughout. We acquired a series of push cores in mats and in a control area to characterize the benthic infaunal communities and associated biogeochemical environment.

***Jason*-1133 Dive**: The overall dive plan was to investigate seep targets in the southern cluster (Pea Island C) where we had high-resolution *Sentry* imagery of seep carbonate, mats, and dense groups of fishes, but had not visited during the *Alvin*-4961 dive. During *Jason* descent, we observed high concentrations of POM and midwater fishes. During the dive, we saw bubbles as well as multiple pits and mounds on the sediment surface. We collected sediment cores within microbial mats. Gas bubbles were released during the coring (330 m). When collecting a rock sample, a siboglinid tubeworm appeared after we broke off a piece of rock from a larger carbonate sample; both were collected. This was the first tubeworm that we had observed in the US Atlantic seeps to date. Much like during the *Alvin*-4961 dive, high densities of squid were present, along with long-fined hake, and anemones. We collected a few more rock samples throughout the dive. There was a moderate current coming from the north that occasionally resuspended sediment and reduced visibility. We commonly observed patchy, moderately sized bacterial mats, along with large discrete authigenic carbonate mounds. These were densely colonized by *Actinoschyphia* sp., zoanthids and anemones. On one occasion we observed a colony of *L. pertusa* (at 11.5ºC and 280 m) and we collected a sample. Several *Eumunida picta* were associated with the coral colony. We saw no other seep-endemic megafauna, but otherwise this site appeared to be highly productive, as evidenced by the large number of fishes (jacks, blackbelly rosefish, *Lymonema* sp., cusk-eel fish, and eels) and crabs. Collections of 16 push cores (in active seep site with bubbles and off-seep) and four water samples (one in bubbles and three next to bacterial mats) were accomplished in addition to the collection of a coral sample.

2.3.1.3 Cape Fear (*Jason*)

***Jason*-1137 Dive**: We observed moderate to heavy marine snow, and the seafloor was composed of fine sediment with visibly abundant bioturbation and brittle stars. Bottom currents were fairly swift at 0.9 kt to the south, and areas of sediment scour were present. We observed small colonies of cf. *Anthomastus* sp., so we collected one early in the dive. We observed extensive bacterial mats, as well as abundant holothurians and euplectellid sponges, throughout the dive. During the dive, we saw several bamboo coral colonies and a few samples were collected. Other organisms encountered included *Chrysogorgia* sp., gastropods, *Umbellula* sp., ophiuroids, and holothurian trails, plus patches of dead sargassum. Other corals included cf. *Paragorgia* sp. Toward the end of the dive along the upper slope at 2,570 m, we observed some burrow/rock mud formations. and collected some rocks for characterization. The rock faces were composed of oddly shaped tubular concretions, cemented in place (**Figure 2-5**).

Figure 2-5. Rock faces with oddly shaped tubular concretions cemented in place

The material appeared very clayey and broke away easily when probed with the manipulator. The slope was primarily sedimented and interspersed with rocky outcrop features. During the latter part of the dive, we observed several large xenophyophores on the sediment surface. The seafloor features were similar in composition to seamounts to the north, with patches of exposed rock and xenophyophores present on the sediment. Toward the end of the dive, we collected a few more push cores in "background" sediments and Niskin bottle water samples, along with some *Chrysogorgia* sp. colonies on a rocky feature. None of the areas surveyed had dense coral cover, nor were they very seepy.

2.3.1.4 Blake Ridge (*Alvin* and *Jason*)

***Alvin*-4967 Dive:** There is a rather large depression, crater-like feature at the center of this site and was the target for this dive. There was abundant authigenic carbonate around the perimeter, but we observed little bacterial mat. We sampled the mussel bed using a mussel pot along with a set of push cores. The dive encountered high densities of live mussels (*Bathymodiolus heckerae*), both large and small size classes. There were no *Gigantidas childressi* observed or collected. There were also numerous lucinid clams and heart urchins burrowing through the reduced sediments. Mussels were observed in small and large clusters, as well as concentrated in long lines, apparently arranged over linear faults overlying the diapir. Some of the mussels had bacterial mats on the shells, which may indicate the presence of sulfide in the water column at this location. We also observed many large empty mussel shells. We obtained a mussel pot and a set of cores here.

***Jason*-1136 Dive**: The overall dive plan targeted an area of Blake Seep that had been dived on before, where we could target community collections of mussels and possibly clams, collect sediment cores within mats and adjacent to mussel beds, slurp bacterial mats, sample carbonates and water, and image hydrate. Within the first hour of the dive, we came upon a familiar scene of bucket lid markers (#3) and Bob Carney's (Louisiana State University) previously deployed bucket of rabbit food and oyster shells (tubeworm settlement substrate). His name was still clearly visible on the outside of the bucket. In addition, we saw some heavily corroded *Alvin* drop weights. Carney's experiment was planted in the middle of an extensive mussel bed (*B. heckerae*) containing mussels of various lengths (Ruppel 2003). Mussel pot collections targeted three different mussel patch sizes: small, medium, and large. These quantitative collections included communities found within different sized patches, and associated holothurians (cf. *Chirodota*). These scoops of mussels proved to be very tricky, due to the varying mussel sizes, but we successfully collected from several different patches. We saw a multitude of dead clam shells, and while no large live clams were seen on the seafloor, several small lucinid clams were present

within the mussel collections. We also collected push cores in mat environments, along with some urchins. Fishes we observed included a *Bathysaurus* sp. and an *Antimora* sp. with a parasite attached. During the dive, we also explored and imaged a large hydrate mound, with cave-like features where two *Gaidropsarus* sp. fish were hanging out. Many of the rocks we saw were either too big or not pliable/breakable, but we were able to collect one rock. We found a black coral attached to a mussel shell and we collected it (2,165 m). We collected water samples above a dense mussel bed and adjacent to the large hydrate mound. Several of the mussels were coated in white, fluffy material, not exactly like filamentous mat, but similar to what has been observed at the mussel beds to the north (Norfolk seeps). During the last part of the dive, we encountered a few octopuses in and around the mussels.

2.3.2 Canyon Sites

2.3.2.1 Norfolk (*Alvin*)

***Alvin*-4970 Dive**: *Alvin* landed in the flat, central part of the canyon and transited towards the wall at the edge of the canyon, flying over primarily soft sediment. At a few points we saw what appeared to be munitions debris. There was a small rise and some scattered boulders at the bottom of the wall, but overall, the substrate was primarily composed of soft sediment. Towards the top of the wall, there was a small field of *Acanella* sp. bamboo corals. Further up, there were groups of sea pens of different shapes and sizes, including short, long and slender forms, some of each were collected into the biobox and quivers.

2.3.2.2 Keller and Hatteras (*Pisces*)

We visited Keller and Hatteras using *Pisces*. We acquired **CTD data and collected core samples**. These water and sediment samples were collected using the ship's CTD rosette and monocorer to help us better understand the environment in and around the features that we explored. These deployments enabled ground truthing of the seeps detected at the head of Keller Canyon, where we collected one monocore sediment sample. While at Hatteras Canyon, we conducted three CTD casts with monocore sediment collections within the thalweg. Based on these limited data, the heads of these canyons were primarily composed of silt and sand grained sediments, with increased proportion of clay as depth increased within the canyon channel proper.

2.3.2.3 Pamlico (*Alvin* and *Jason*)

***Alvin*-4969 Dive**: *Alvin* arrived on bottom away from the side of the canyon wall where there was little observable current. There were a few boulders here. We acquired a set of push cores in the local soft sediment. *Alvin* then transited toward the "dog tail" of the canyon, where we saw a series of short ledges and steep walls while climbing up into the tail. We observed extensive soft sediments adjacent to the walls. The canyon axis did not appear to be very active. The canyon wall appeared to be composed of mudstone with occasional ledges and overhangs. Most of the corals present, including *Desmophyllum* sp. and *Solenosmilia* sp. along with *Acanthogorgia* sp. and *Paramuricea* sp, and *Acesta* sp. clams occurred on the underside of overhangs. There were small piles of dead coral rubble and a few larger live antipatharian colonies occasionally accumulated on the ledges. Currents increased appreciably at the top of the wall but were still not as high as experienced during the shallow dives on this mission. Near the top of the wall, at approximately 1,100 m, there was a large *Paragorgia* sp., and we took a subsample.

***Jason*-1132 Dive**: The bottom type at the base of the canyon (at 1,800 m) was heavily sedimented with a steep slope. We observed various *Acesta* sp. shells. We collected sediment cores at several locations throughout the dives, on sedimented ledges. We collected rock samples and *Acanthogorgia* sp. at 1,700 m. There were a series of rock steps and ledges, mainly populated by sea stars and ophiuroids. We observed a multitude of Brisingid sea stars and small underhang communities, including the corals

Solenosmilia sp, *Desmophyllum* sp., and some colonies of *Acanthogorgia* sp. The overall dive plan intended and accomplished a survey track laterally along the northern steep canyon wall in a northwest direction. We observed dense coral comm unities under the terrace overhangs. These communities were dominated by *Solenosmilia variabilis*, *Desmophyllum dianthus* and *Acanthogorgia* sp. We also commonly observed the fileshell *Acesta* sp. among the corals. We moved upslope to explore a different depth range (1,300–1,350 m) but, despite abundant exposed hard substrate at these depths, the habitat was almost devoid of megafauna. The bathymetry contours tended to spread further apart as we moved WNW up-canyon, so we decided to move back downslope to the steeper walls. Due to the extended length of the dive, we were able to make our way through most of the planned waypoints, covering space over a large vertical and lateral gradient, as well as distinct changes in the seafloor geological morphology.

2.3.2.4 Wilmington (*Alvin*)

***Alvin*-4960 Dive:** Unfortunately, when *Alvin* reached the bottom around 700 m, it encountered 3.5 kt currents and near-zero visibility. The pilot fought this for a while, but we observed a hazardous fishing line and had little control of the vehicle in these harsh conditions. *Alvin* came up to about 600 m depth but there was no change in conditions. Given the presence of fishing line in the area, the relative lack of control of the vehicle, and the low visibility, we decided to call the dive and recover the submersible.

2.3.3 Coral Sites

2.3.3.1 Blake Deep (*Alvin* and *Jason*)

***Alvin*-4964 Dive**: *Alvin* reached the seafloor in an area of small boulders with corals attached, surrounded by sandy sediments and occasional patches of coral rubble (primarily *Solenosmilia* sp.). At first, the landscape was dominated mainly by large bamboo coral colonies and a variety of other octocorals and antipatharians. We took a few coral fragments and cores, and then *Alvin* headed for the first defined waypoint (WPT). It then turned to approach the wall, but the coral cover declined a bit near the base of the wall. The rubble here was primarily *Madrepora* sp. The submersible started up the wall, in low coral abundance at first, but increasing towards the top. We collected from colonies of *Madrepora* sp., *Enallopsamia* sp., and *Solenosmilia* sp. along with a variety of octocorals and a large dead bamboo coral skeleton.

***Jason*-1131 Dive**: On this second dive at Blake Deep, we observed several coral species, including bamboo corals and anthipatharians. The substrate was primarily composed of hardbottom with thin sediment veneer, making push coring impossible. We saw octocorals and black corals attached to the occasional rock outcrops. The slope up was not very steep and was very sedimented. Highly sedimented rocks and interesting geology with sediment/rock shelves all the way up the ridge. At the top of the ridge (1,314 m) was a 0.5–1-m thick rock overhang with *Desmophyllum* sp., *Anthomastus* sp., black corals, anemones, and bamboo corals. At 1,311 m there was a sedimented area below the ridge where we took four push cores. The ROV came around the “nose” of the ridge at WPT 3 and while the community did not change much, there were bigger boulders, and extensive soft sediments. Continuing along the dive track, there were sparse corals on small sedimented rocks on a not very steep slope. We collected *Solenosmilia* sp., *Hemicorallium* sp., *Iridogorgia* sp., black coral, yellow plexaurids with *Astroschema* sp., dead bamboo coral skeleton, *Metallogorgia* sp., *Desmophyllum* sp., *Chrysogorgia* sp., *Lethothela* sp., *Swiftia* sp., and push cores. The corals encountered in the latter part of the dive were similar to those found at the start, including yellow plexaurids, stony corals (*Solenosmilia* sp.), and an unknown bamboo coral. We collected high-resolution imagery of a rock with large vase sponges, bamboo, *Solenosmilia* sp., *Chrysogorgia* sp., and *Desmophyllum* sp. We also observed a few different types of seapens. At the top of the feature, we observed a fish with several parasites, plus a few more plexaurids. We collected some of these and a *Chrysogorgia* sp. before coming off bottom.

2.3.3.2 Richardson Hills/Complex/West/Ridge (*Jason*)

***Jason*-1128 Dive**: On the descent of this ROV dive, we crossed a clear thermocline at approximately 750 m, far deeper than normal, but similar to the water-column profile over the other *L. pertusa* mounds at the northern reef track at Richardson Hills. The ROV landed immediately on coral rubble habitat with abundant live *L. pertusa* colonies. We determined that frequent white balancing of the camera improves the color temperature of the image, particularly when the ROV transitioned from sitting on the seafloor to transiting, or vice versa.

We then began a series of octocoral collections. There were abundant *Plumarella* sp. and neptheids throughout, and occasional patches of a white plexaurid. The first swale was mostly this type of habitat with live *L. pertusa* colonies in the "bush" stage, with some *Madrepora* sp. and a few *Solenosmilia* sp. mixed in. The second swale near WPT 2 was mostly coral rubble with very little live coral consisting of smaller colonies of *L. pertusa* and occasionally *Enallopsamia* sp. The bottom of the swale between WPT 2 and 3 was finer sediments with clear bedforms of sand and small rubble.

As we began to climb up towards WPT 3 with *Jason*, there was mostly rubble with large numbers of small, white plexaurid colonies. At the top near WPT 3, we encountered another field of standing dead coral with numerous live coral colonies interspersed. We set up for the first coral pot sample here, and then made a live coral collection into the biobox.

Upon leaving WPT 3, the coral cover began to decline on the way to WPT 4. We continued along the track from WPT 4 to 5 and observed coral rubble in the swales/furrows between the peaks, with dense live *L. pertusa* on the highs. The structure below the live *L. pertusa* appeared to be a dense matrix of dead *L. pertusa* and fine and sandy sediments. We collected MP2, soft coral, *Plumarella* sp., and *L. pertusa* into a quiver and biobox during the watch. Fish observations included rattails (*Nezumia* sp.), synaphobranchid eels, and a goosefish (*Lophiodes* sp.). Depth ranged from 747 to 773 m. There was a noticeable shimmer in the water around these topographic highs, consistent with water temperature changes.

Near WPT5, on the flank close to the top of a small feature at approximately 780 m, the substrate was mostly coral rubble with white plexurid octocorals plus sponges. We collected one of the white plexurids as representative of this habitat. As we continued up the feature, we came across occasional *Enallopsammia profunda* colonies. Most were the yellow morph, but a few were white. We collected some of each. An invertebrate that was conspicuous was the pinkish *Echinus* sp. urchin.

We continued upslope towards WPT 6. At approximately 750 m, the temperature began to climb sharply from 4.4 to 6.5°C at 760 m, then to about 10 deg at 730 m. We traversed across a swale with coral rubble/sandy substrate before climbing to WPT6, where there was again a higher abundance of large live coral colonies in the warmer waters. Here we began to see occasional *Madrepora oculata*. We collected *M. oculata* and *L. pertusa*, plus *Plumarella* sp. Within 5 minutes we observed three chimeras with black spots. The transit between WP 6 and 7 was mainly along the top of a ridge.

At WPT 7, there were numerous large live *L. pertusa* colonies. Some of these were approaching the thicket stage, with rings or semi-circles of live coral growing around a center consisting of a standing dead skeleton. In some places, these structures were so large that they had tipped over and the live coral continued to grow at the edges.

***Jason*-1129 Dive**: We launched the vehicle about 1.5 nautical miles SW (upstream) of the seafloor target. The *Jason* team wanted to test their level-wind on the way down so we decided to allow for the drift of the ship in the 1-kt surface currents. On the descent, the temperature dropped steadily the entire time. At

450 m, it was approximately 16°C, and at 650 m it was 10°C. On the seafloor at 725 m, it was around 9°C. Occasionally during the dive, the shimmering water of the thermocline was observed at depth.

At 2014 hrs local time, the bottom was in sight. We set up on bottom and immediately looked for a place to deploy the McLean pump. We came across the large 3-m high marker that we had deployed earlier with the coral transplant experiment, but it was in a different location, being just downhill from the deployment site. This was a relatively flat area of rubble surrounded by live coral cover on the side of the coral mound, so we set the McLean pump here at 2046 hrs local time and used the marker to relocate the pump at the end of the dive. As we came off the bottom, we turned towards the transplant target and almost immediately found them. The three cement blocks with the stained coral were retrieved into the starboard biobox without incident. However, we had a difficult time closing the box even though it was not apparently fouled in any way.

Between 2130 and 2200 hrs, we shot a series of highlight video in this area of large live *L. pertusa* colonies on a fairly steep slope. We set down at a new location and collected a series of *Plumarella* sp., *Anthothela* sp., and a few sponges into the quivers. We moved over a bit to a relatively undisturbed location and collected a coral pot sample and a few more collections into the quivers. We then moved again to take another coral pot in a nearby location, and some live *L. pertusa* into the port biobox.

The ROV lifted and traversed to WPT 2 on the north side of the mound, away from the *Alvin* dive tracks in the area. We collected *Madrepora* sp., *Plumarella* sp., an unknown white plexaurid, and a cup coral. We also collected an unknown yellow plexaurid and *Anthomastus* sp. The area was composed of many standing dead *L. pertusa* capped with dense branches of live *L. pertusa*. We also saw a few globular sponges that looked like large golf balls. We saw a few fish while transiting up the slope, including *Nezumia* sp., *Laemonema*? sp., and synaphobranchids.

At 0223 hrs we headed toward the McLane pump to start the multibeam patch test at a known target. The seafloor was visible during the multibeam ops, with dense POM visible in the water column. There was a time code issue with the 4K camera, wherein we had collected some of the initial video with an incorrect time code. We quickly corrected the mistake. During the MB patch test, our plan was to run lines at different elevations at particular headings to calibrate pitch and roll. Overall resolution of the MB was about 0.5 m. At 0345 hrs the survey began, with 5.5 survey lines completed by 0929 hrs. During trackline 6, the current was too fast (0.5 kt to the NE) for the ROV to remain on heading and make way, so we made the decision to break the line. It was not possible to complete the cross line, so we changed the plan and headed to the seafloor and collect samples.

We deployed marker 1 at 31 59.051 N, 77 24.675 W (WGS84) and then collected *Madrepora* sp., *L. pertusa*, and three *Plumarella* sp. colonies into the biobox. We took highlight video in this area after the collections. At 0645 hrs, the wind had come up to about 20 kts with gusts to 25 kts, and the weather was forecast to build throughout the day, so the dive budgeted only 30 minutes before leaving bottom. We took the last mussel pot sample and deployed marker 2 at this location. We then transited over to the pump deployment site, over some very large, tipped-over, live *L. pertusa* colonies, and set up to retrieve the pump. By 0715 hrs, the pump was on board and secure. We attempted to fire all of the Niskin bottles, but only the two smaller bottles actually triggered. At 0730 hrs, we left bottom for retrieval.

***Alvin*-4962 Dive**: This dive was over *L. pertusa* rubble the entire length of the 1.5-km dive track. The currents were very strong, approximately 3 kts at times, and the sub battled them all day. The vehicle reached the bottom nearly 1 km laterally from its launch position, so we began working where we landed rather than chasing the predefined but arbitrary waypoints. The substrate was mainly dead rubble near the bottom of the feature. As we began making our way up the hill, we observed a high density of small plexaurid octocorals. On the leeward side, most of the coral was dead, but at the crests and the windward sides of the mounds, there was a high cover of live coral. We made a series of *L. pertusa* collections,

along with a large *Madrepora* sp. colony, and some smaller *Enallopsamia* sp. colonies. These came with a variety of octocorals and associates including brittle stars and crinoids. Early in the dive, a large swordfish swam around the sub and through the *L. pertusa* reef.

***Alvin*-4963 Dive**: This dive was on coral rubble and live coral the entire time, just as the previous dive. This dive started deeper (over 800 m) in the trough to the west of the line of coral mounds. We expected to find some core-able mud here, but the seafloor was still entirely composed of coral rubble. The submersible climbed from here up to the top of the closest mound in the line of connected mounds. We encountered more live coral as the sub ascended. There appeared to be a higher concentration of particulate material in the water here than there was the day before. We noted a few fish, including roughy and small orange hagfish. There were a few small octocorals, including our first sighting of *Paragorgia* sp. in the area. We located a suitable place for the coral-growth tests and deployed the gear along with a 2–3 m high marker. We made a series of *L. pertusa* collections into the sterilized quivers for microbial work.

2.3.3.3 Richardson West (*Jason*)

***Jason*-1128 Dive**: The rocky seafloor appeared black (727 m), with large amounts of coral rubble and small patches of live *Enallopsammia* sp., *Plumarella* sp., white plexaurids, other octocorals, and sponges. The crusty rock features had dense corals growing with on the edges of ledges (several different species observed, including *L. pertusa* and *Enallopsammia* sp.). Several collections occurred within the first 4 hours of the dive, including plexaurids, primnoids, *Enallopsammia* sp., *Plumarella* sp., cf. *Leiopathes* sp., and crinoids. We attempted push cores, but the sediment was only a fine veneer over hard pavement. We saw several large *Leiopathes* sp. during the dive.

At 660 m near WPT3, we stopped to image the ledges and collect a coral pot within a mixture of live and dead *L. pertusa*. We had a great deal of difficulty with the wire angle due to the swift surface current, so after a few hours of collections, the dive transitioned to an observation-only dive in order to explore more of the seafloor, while minimizing impact on the wire. This mode enabled the ship to maintain heading and provided an opportunity to cover a great deal of ground and observe the transition from rocky ledges and boulders to pavement with many coral colonies.

During the last 3 hours of the dive, the ROV pilots worked in tandem to enabling sample collection while the ROV was in motion. This allowed us to trip the Niskin bottles for water samples and to collect more corals and rock samples. We observed several fish species in the latter part of the dive including *Nezumia* sp., *Chaunax* sp., many *Hoplostethus* sp., and some type of eel, maybe synaphobranchids. We had a successful dive despite the operational limitations. We observed some of the largest *Leiopathes* sp. colonies from all the Deep SEARCH dives at this site.

2.3.3.4 Savannah Bank (*Jason*)

***Jason*-1130 Dive**: During dive descent, there was a striking amount of POM in the water column, as well as squid. On the way to WP1, we saw some octocorals (*Pseudodrifa* sp.) and cup corals and some live and dead *L. pertusa* and collected a coral pot. The sediment had too much coral rubble to enable push coring. Throughout the transit from WPT 1 to WPT 2 there was an increase in coral rubble and live coral density as the ROV moved upslope. During the first portion of the transit there was abundant coral rubble (likely *L. pertusa*) without much live coral except small colonies of stylasterid and nephtheid corals. Then the rubble became denser and the occurrence of live *L. pertusa* thickets increased.

As the ROV continued upslope, the currents increased to around 1 kt and we had several sightings of *Madrepora* sp. and *Enallopsammia* sp. (both yellow and white morphs). As the dive continued, the dominant scleractinian transitioned from *L. pertusa* to *Enallopsammia* sp. (white morph). Amongst the

coral rubble, primnoids (*Plumarella* sp.), cup corals (*Thecapsammia* sp.), Neptheids (*Pseudodrifa* sp.), and sponges were common. There were also several small sharks seen throughout the area.

At WPT 2 (511 m) there were live *Enallopsammia* sp. and the diversity of corals listed above. Downslope from WPT2 the coral diversity suddenly halted and there were almost no live scleractinians and much less rubble. There was very high current with substantial particulate material in the water. Throughout this time, we collected two mussel pots of *L. pertusa*, one large live *L. pertusa* collection, *Madrepora* sp., *Plumarella* sp., *Pseudodrifa* sp., cup corals, *Enallopsammia* sp. (white and yellow), and sponges. While collecting the live *L. pertusa*, we observed a shark eating a squid. We noted that the large urchins were primarily in the rubble areas and not with the live coral.

Overall, we collected several target corals (*Enallopsammia* sp., *Madrepora* sp., *L. pertusa*). Ultimately, we were able to collect push cores in the coral rubble next to the *Pseudodrifa* and near *Enallopsammia* sp. Fish observed included catshark, chimaera, *Nezumia* sp., and scorpaenids. We tripped all four Niskin bottles at the end of the dive near *Enallopsammia* sp., but the aft bottle did not close all the way because it had shifted during the dive. We left bottom at 1138 hrs and saw much POM during ascent.

2.3.3.5 Cape Lookout Deep (*Jason*)

***Jason*-1135 Dive**: We planned a relatively short dive here before the weather started to pick up and push us south. The ROV landed slightly deeper than 1,000 m on soft sediment, with scattered small bacterial mats. We collected push cores within the mats, as well as suction samples. There were few invertebrate megafauna, but moderately abundant fishes of various types (*Nezumia* sp., *Coryphaenoides* sp. and synaphobranchid eels). We transited northwest towards a steeper structure that had been interpreted as a wall. During the transit we came across a pile of boulders of a black material. They were sparsely colonized by sponges, octocorals (*Acanthogorgia* sp., bamboo corals, *Chrysogorgia* sp.) and black corals (*Bathypathes*?). We collected a *Chrysogorgia* sp. colony, a small yellow 'plexaurid' (which resembled *Acanthogorgia* sp.) and a rock with a small single branch bamboo coral colony.

We headed WNW towards the 'wall' and encountered a series of rocks, each with a few coral colonies (bamboo corals, *Anthomastus* sp., black coral, *Acanthogorgia* sp.), and a small yellow plexaurid. We collected highlight imagery of the rock features and associates, then the ROV continued WNW. Continuing to the northeast along the 950-m contour, we encountered some *Nezumia* sp. and other rattails. At 2139 hrs the seas began to build, and we were told by the pilot that the dive would be cut short. While we had collected several *Acanthogorgia* sp. into quivers, attempts were made to collect the unknown yellow plexaurid, but the ROV was pulled off the area and we aborted the collection effort. We fired the Niskin bottles and collected water in them, and then the ROV was recovered to deck.

2.3.3.6 "Stetson Banks" (*Alvin*)

***Alvin*-4965 Dive**: The submersible moved almost 2 km laterally from its launch position to the bottom location due to currents. Rather than attempting to return to our predefined waypoints, we moved straight towards the wall feature that was the subject of the dive. There was a lot of marine snow in the water during the entire dive. On the way to the wall, there were cobble and carbonate pavement with occasional *Leiopathes* sp. colonies and small *L. pertusa* and *Enallopsammia* sp. colonies. There were several squid swimming around the sub during the transit. We collected a variety of scleractinians and octocorals into quivers and we placed an interesting rock in the basket during the run to the wall. The wall came up steeply, with a pile of debris near the foot of the wall and plate-like ledges on the way up. There were few corals near the base of the wall, but higher abundances towards the top, particularly on overhanging ledges. More squid came back to the sub near the top of the wall. The sub transited laterally along the top of the wall for a time, which had a number of *L. pertusa* colonies and small white plexaurids. We collected these along with a bamboo coral. We observed and filmed a large white *Leiopathes* sp. colony

with chirostylid crabs near the top. Near the end of the dive, the sub came to the top of the wall and transited over the plateau. The current was moving quickly on top, and there were occasionally small *L. pertusa* colonies and multiple short white plexaurids. We obtained mussel pot sample over one of the small *L. pertusa* colonies.

***Alvin*-4966 Dive**: The goal of this dive was to locate the ADEON lander at the site and determine the community structure surrounding the area. The submersible was launched over 1 km from the bottom target because of the strong surface currents. When the sub reached the bottom, it was still 1,200 m from the mooring target. There was a hard ground in the pump for the main ballast tank, so that was secured during the dive. The seafloor was a hard carbonate pavement with sponges, small stylasterids, very short octocoral colonies and sargassum. In small depressions in the carbonate, there was a sandy bottom with ripples from the obviously strong currents that are typically present at this site. Further along, there were patches of two different species of primnoids (one may have been a species of *Callogorgia*) and larger yellow *Acanthogorgia* sp. and *Leiopathes* sp. colonies. There were also occasional patches of baseball sized cobble with a heavy manganese crust. In some areas, there were small, interspersed *L. pertusa* and *Enallopsamia* sp. colonies.

During all of the transits the detection range was kept between 50 and 300 m, and the sub maintained a constant scan for the floats of the lander. The sub ran north over the lander target, continuing for about 100 m. The sub then came southeast and then back to the west, running another line of the target, but there was no sign of the mooring. The sub continued to the west another few hundred meters, and then came north and ran another parallel line, all the time scanning with the sonar. An effort was made to circle larger rock outcrops to avoid sonar shadows behind them and complete a thorough search. After running east, the sub went south so that it was about 100 m to the SE of the target. The sub came up off the bottom and drifted with the prevailing current in the hopes of running across the lander, but we never saw the lander. The sub left the bottom at 1500 hrs.

2.3.3.7 Cape Fear Coral Mound (*Alvin*)

***Alvin*-4968 Dive**: The dive started on the western side of the coral mound. The sub approached the mound, going almost straight into the current. We collected a coral pot and a series of cores in coral rubble near the base of the mound. The sub continued upslope, fighting the current the whole way. We obtained a second coral pot sample from standing dead coral skeleton, and we took a series of push cores. We made a few octocoral collections, then the sub made its way to nearly the top of the mound. At this point, its batteries were low on charge. We acquired a final coral pot from mostly live coral, and we collected live coral into the biobox. We also collected a colony of *Paramuricea* sp. before our ascent.

3 Physical Setting

3.1 Oceanographic Setting

Section Authors: Jay Lunden, Furu Mienis, Andrew Davies, Jane Carrick, Alexandra Roads, Jennifer Miksis-Olds

Cold-water coral habitats on the Blake Plateau, such as those of Cape Lookout, are occasionally bathed by Gulf Stream waters, resulting in major fluctuations in environmental conditions (Ross et al. 2009, Mienis et al. 2014). When the Gulf Stream meanders into the area, cold fresh continental slope waters are being replaced by warm, saline Gulf Stream waters, which can result in dramatic temperature changes up to 9°C within 24 hours (Mienis et al. 2014, Brooke et al. 2013). These rapid temperature changes that last from several days up to a week can have a major influence on metabolism of benthic organisms, for example influencing the metabolic and calcification rates of CWCs (Brooke et al. 2013, Lunden et al. 2014).

We conducted a comprehensive study examining the water-column structure and chemical compositions, as well as the near-bed environmental conditions. In this study we compared the hydrographical data collected with shipbound CTD casts acquired during multiple cruises at different times and at different deep-sea biological hotspots. Results mainly focused on the Richardson Reef Complex. Here, our water-column data were accompanied by the data from the long-term deployment of a bottom lander. Long-term measurements of near-bed environmental conditions were taken to study temporal variability near CWC mounds at the Richardson Reef Complex with the aim to identify if the Gulf Stream is a major driver of environmental change and determine how this affects the CWC communities.

3.1.1 Physical Oceanography

3.1.1.1 Methods

Figure 3-1 shows the ALBEX-02 lander location at Richardson Hills Reef area. The lander is indicated by the yellow square (31 53.922 N, 77 21.168 W) and the water-column CTD casts (full water-column data only) locations indicated by circles (red = April 2019 RB1903 cruise, light blue = October 2019 NF1909 cruise).

We collected CTD data for this study in 2018 and 2019 during the following cruises: AT41, BMCC2018, RB1903, and NF1909. See **Figure 3-1** for an overview of CTD casts at the Richardson Reef Complex. During all cruises we made vertical profiles of water-column properties using a CTD-rosette system. We also collected discrete water samples from chosen depths. The CTD system used for this purpose on RV *Atlantis* cruise AT41 (19 August–2 September 2018) consisted of a SBE 911+ deck unit and CTD rosette equipped with 24 10-L Niskin bottles. During the *Brooks McCall* (BMCC) cruise in 2018, we used a Seabird SBE 19+ CTD unit, which recorded data offline with bottom depths being estimated from a paper chart due to malfunctioning of the ship's echosounder. The rosette consisted of 12 10-L Niskin bottles. We also made additional measurements of oxygen (SBE 43) and turbidity (Wetlabs FLNTU). During the RB1903 on the NOAA vessel *Ron Brown* (April 2019), we used a SBE 911+ system with additional sensors for oxygen (SBE 43), fluorescence (Wetlabs ECO-AFL), and turbidity (Wetlabs NTU) to generate water-column profiles (**Figure 3-2**). We collected water samples for water chemistry and microbial diversity with a rosette consisting of 12 10-L Niskin bottles. During the 2019 cruise on board the NOAA vessel *Nancy Foster* (cruise NF1909, October) we acquired CTD casts and discrete water samples at Blake Deep, Cape Lookout Deep, Pamlico Canyon, and the Richardson Reef Complex (**Figure 3-2**). In the Richardson Reef Complex, we conducted a CTD transect across the mounds, and processed raw CTD data using the Seabird SBE Data Processing Software. We averaged downcast data to a 1-m bin size, quality controlled and outliers removed.

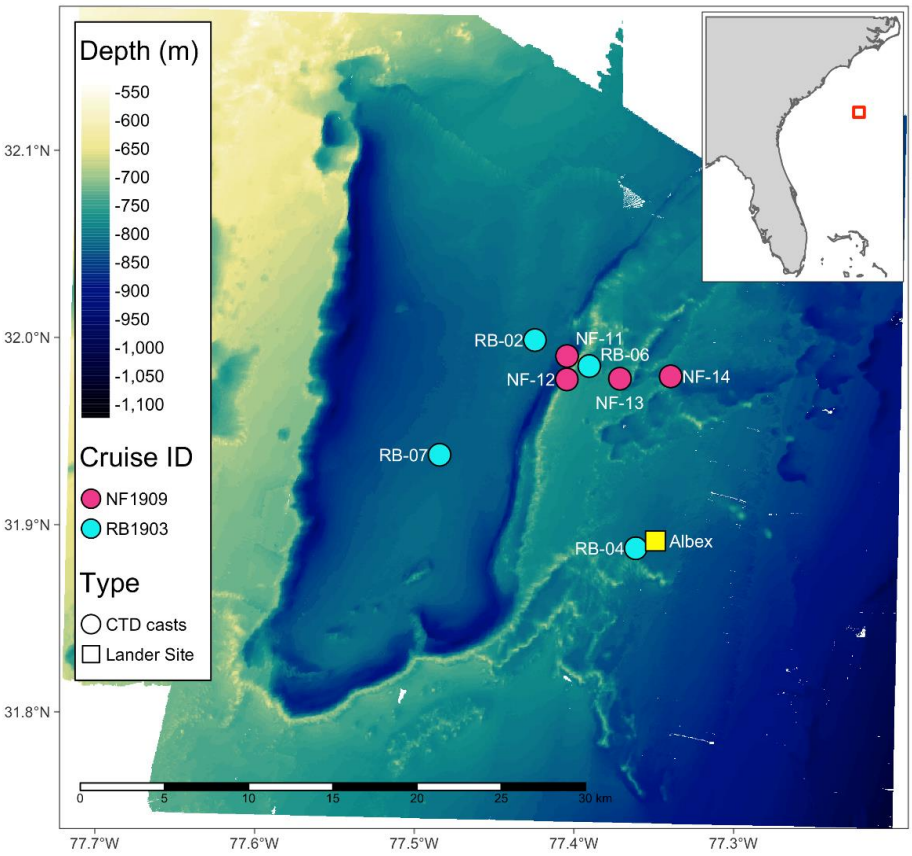

Figure 3-1. ALBEX-02 lander at Richardson Hills Reef area
Lander (yellow square), CTD casts (circles)

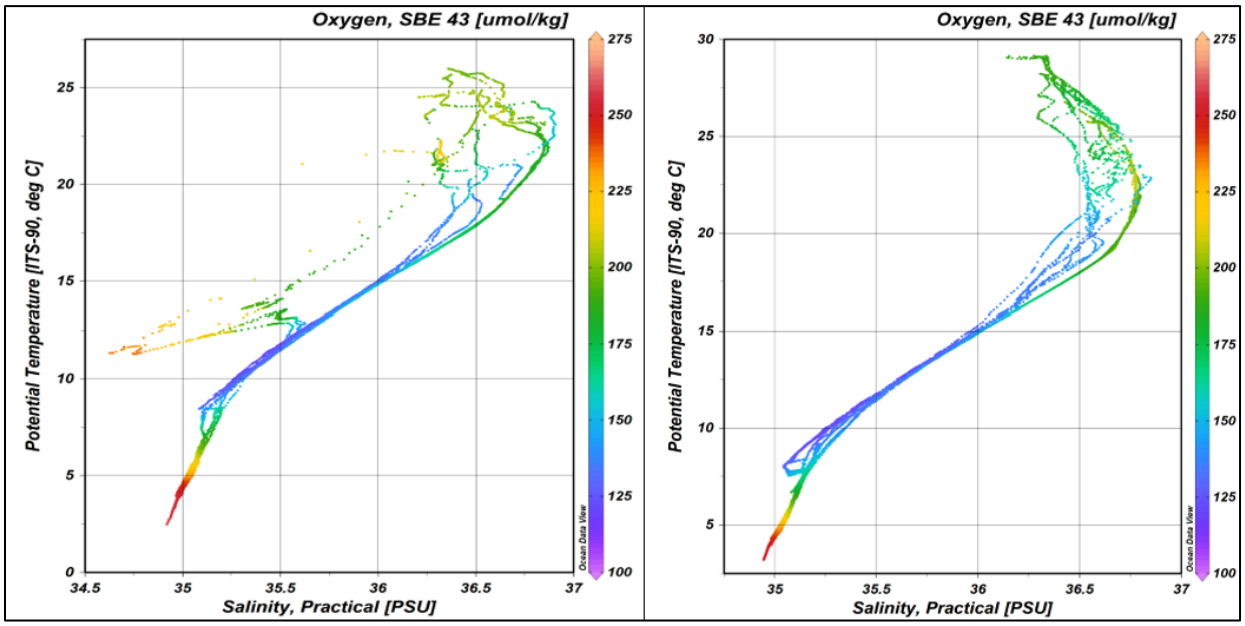

Figure 3-2. Aggregated T-S plots with O_2
From April (left) and October (right); 2019 CDT data.

3.1.1.2 Results

The T-S plots show the presence of the different water masses during the period of observation in April and October 2019. Shallow Gulf Stream Surface and Thermocline Waters are characterized by high temperatures and salinities. AAIW and uLSW are observed below these water masses, showing decreasing temperatures and salinities, but high oxygen levels (**Figure 3-3**, **Figure 3-4**, and **Figure 3-5**).

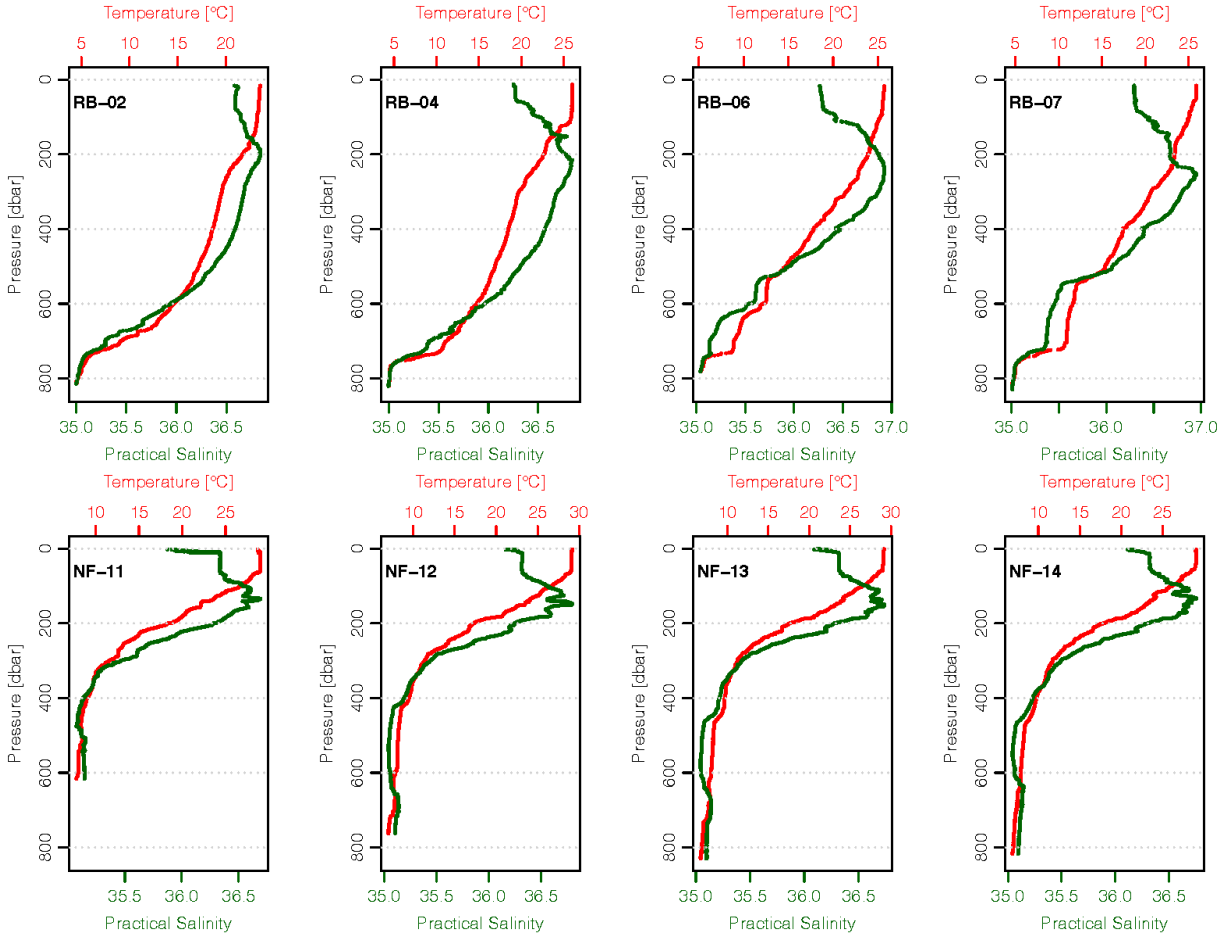

Figure 3-3. Individual temperature and salinity profiles with water depth
Collected in April (top row) and October (bottom row) 2019. Labels correspond to CTD points on map in Figure 3.1.

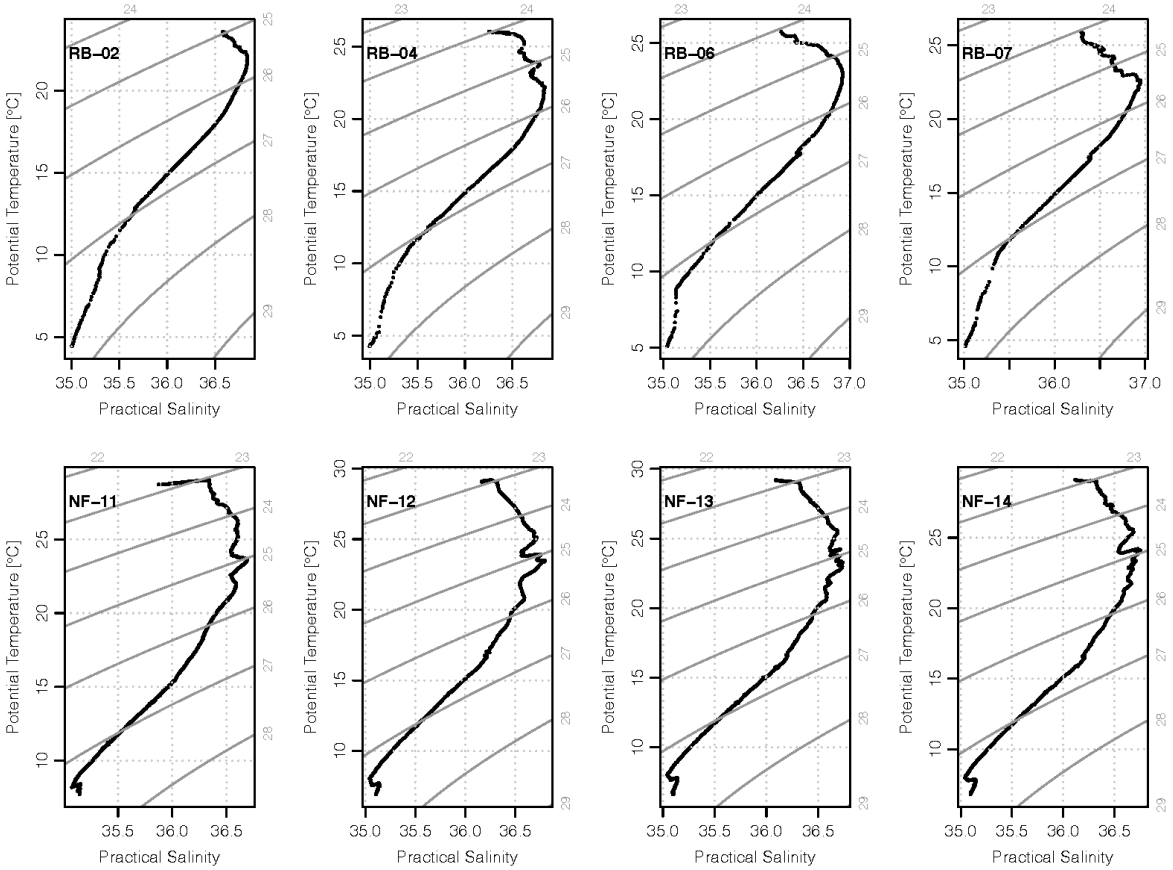

Figure 3-4. Individual T-S plots of CTD profiles
Collected in April (top row) and October (bottom row) 2019. Labels correspond to CTD points on map in Figure 3-1.

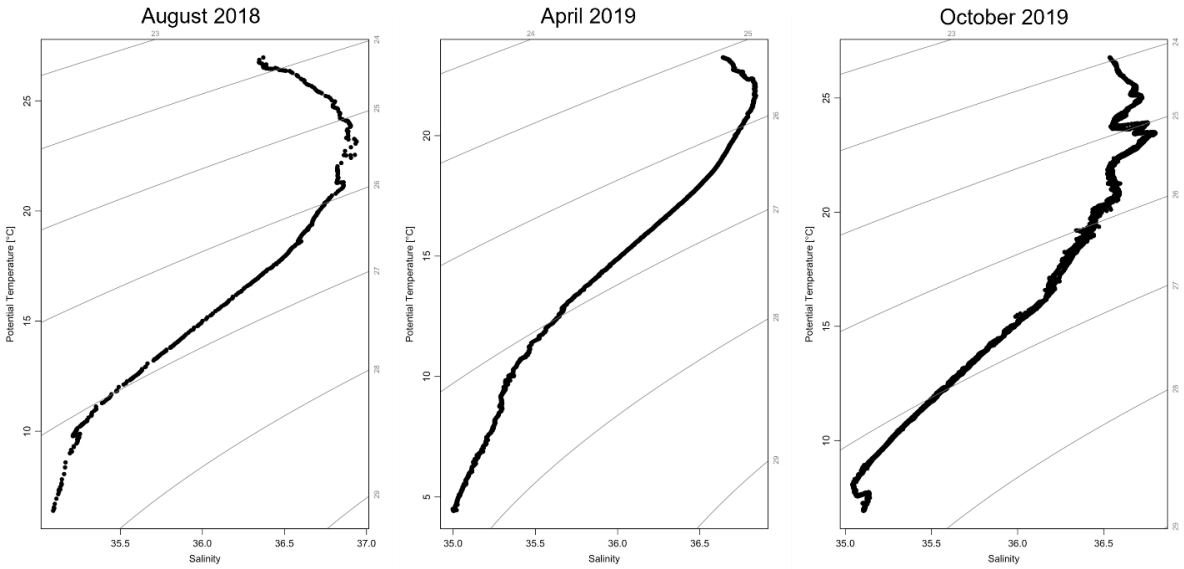

Figure 3-5. Variability in T-S in relation to presence or absence of the Gulf Stream
Within the Richardson Reef Complex (gray lines represent density contours) in August 2018, April 2019, and October 2019.

When comparing the CTD profiles and T-S plots from CTD casts collected near the Richardson Reef Complex during the different cruises the presence of the Gulf Stream is clearly observed during the NF19 cruise, characterized by high bottom water temperatures and corresponding to very strong surface currents (> 4 kts). The Gulf Stream water is characterized by warm and less oxygenated waters, while April 2019 we saw relatively cold, fresh, and well-oxygenated slope waters. We also documented multiple warm Gulf Stream events in the long-term lander data (**Figure 3-6**).

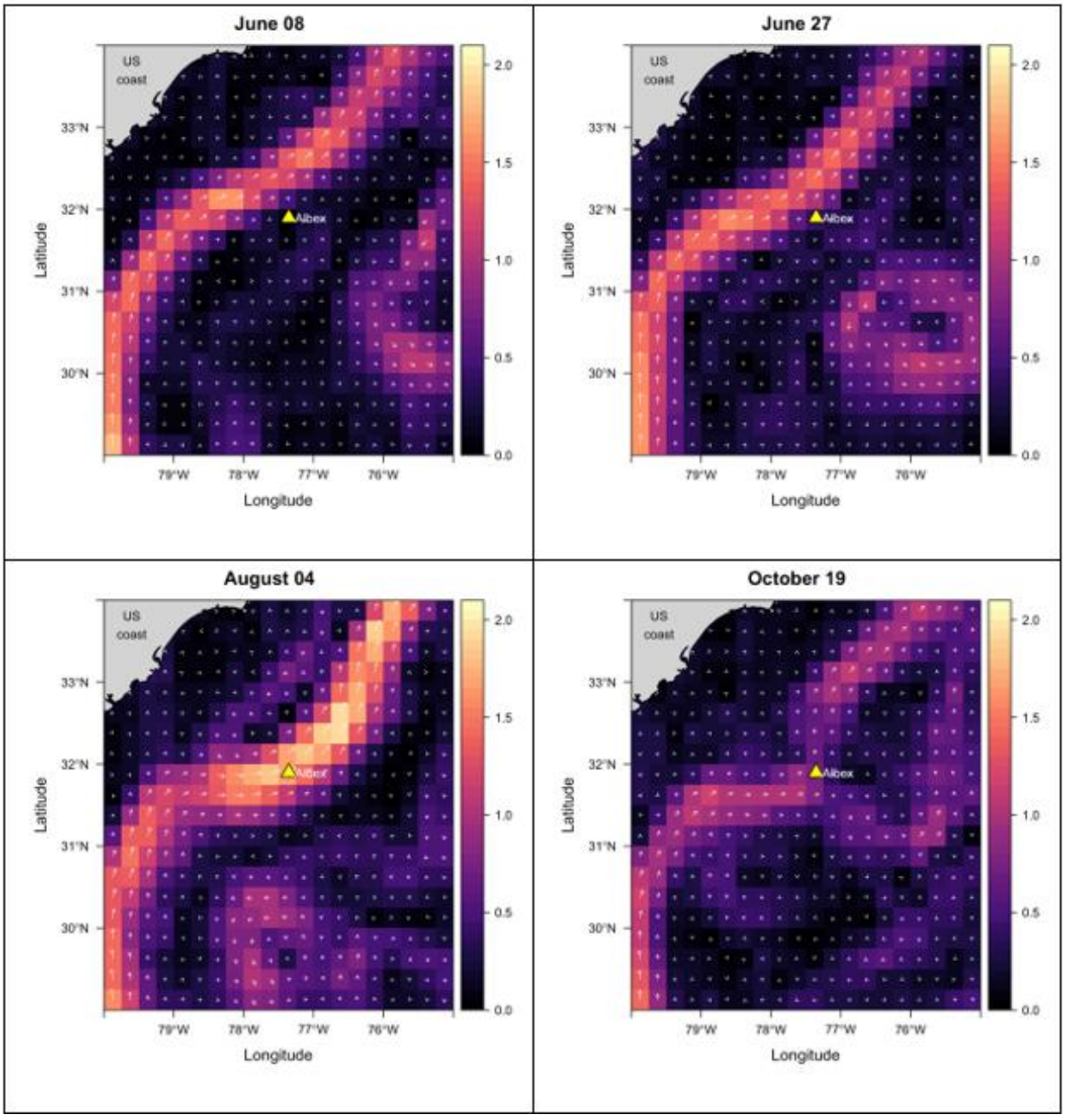

Figure 3-6. Meandering of the Gulf Stream near Richardson Reef
ALBEX lander site shown. Color scale corresponds to surface Geostrophic velocity. Data source: Copernicus Climate Change Service.

3.1.2 Chemical Oceanography

3.1.2.1 Methods

We collected samples from depth and surface waters for aragonite saturation, suspended POM, eDNA, suspended sediment concentration, and inorganic nutrients.

We collected seawater samples onboard the RV *Atlantis* cruise AT-41 in August–September 2018 with a CTD-rosette sampler using 10-L Niskin bottles. During the *Ron Brown* cruise we collected water samples for water chemistry and microbial diversity with a rosette consisting of 12 10-L Niskin bottles. In addition to the these, we collected bottom water samples at Richardson Reef Complex to fill onboard aquarium tanks to maintain live corals.

We acquired data from 16 CTD casts on the *Nancy Foster* in 2019. The system consisted of a rosette containing 12 5-L Niskin bottles. During the cruise very strong surface currents (> 4 kts) were present, which resulted at some stations in greater wire payout compared to the water depth, indicating that actual location of the CTD may not correspond well to the recorded GPS position of the vessel.

Upon recovery of the rosette, we drew seawater samples for various downstream analyses, including nutrient concentrations, POM and stable isotopes, and carbonate chemistry. For carbonate chemistry analysis, we collected samples in 500-mL HDPE bottles and fixed them with saturated mercuric chloride. We measured water pH (total scale) with an Orion 5 Star pH meter with ROSS electrode calibrated against Tris buffer (Dr. Andrew Dickson lab, Batch #33). Preserved samples were shipped to Temple University and measured for total alkalinity by titration. Full methods are available in Lunden et al. (2013) and Georgian et al. (2016). Temperature-salinity diagrams were plotted in Ocean Data View v 5.0, and nutrient profiles were plotted in RStudio and Adobe Illustrator.

For inorganic and organic nutrient and dissolved organic carbon (DOC) analysis, we transferred water from a Niskin bottle to a PETG® bottle (250 mL) that had been prepared by acid-washing, rinsing, and drying. We sample-rinsed each bottle twice and then filled each with sample and stored it on ice. Within 2 hours, we filtered a subsample through a 0.22-µm Target® filter into a 60-mL HDPE bottle. NO_x (nitrate + nitrite), nitrite, and phosphate concentration were determined using an autoanalyzer (Latchat Instruments FIA 8000 Autoanalyzer) and standard protocols 31-107-04-1-A (for NO_x and nitrite) and 31-115-01-1-H (phosphate), with detection limits of 0.4 µM and 0.1 µM, respectively (Rogener et al. 2018). Nitrate concentration was calculated by difference (= NO_x - nitrite). Total dissolved nitrogen (TDN) was quantified via high temperature catalytic oxidation on a TOC-V (Shimadzu Instruments) coupled to a total nitrogen unit; the detection limit was 0.3 µM. The dissolved organic nitrogen (DON) concentration was obtained by difference (= TDN - dissolved inorganic N). Total dissolved phosphorus (TDP) was determined via combustion and hydrolysis followed by spectrophotometry with a minimum detection limit of 0.2 µM (Rogener et al. 2018). The concentration of dissolved organic phosphorus (DOP) was calculated by difference (= TDP - inorganic phosphate). DOC concentration was determined by high temperature catalytic oxidation using the TOC-V system.

3.1.2.2 Results

POM concentrations ranged from 2.49 to 2.7 mg l^{-1} near the surface and 2.52 to 2.77 mg l^{-1} at depth over the reef. Together, the minor increase in C:N ratio of the POM from the surface (6.3) to the reef (8.6) and small changes in the stable carbon isotope values of the POM (surface $\delta^{13}C$ -22.0 to -22.7‰, reef $\delta^{13}C$ -23.4 to -24.3‰) indicate limited aerobic degradation of POM in the water column. Although the concentration of POC was relatively low (5.5-6.1 µg×l^{-1}), the POM is relatively fresh when it arrives at the reef. DOC concentrations were variable but sporadically high (29 to 37 µM) on the reef (**Figure**

3-7b). This elevated DOC is likely a result of rapidly dissolving coral mucous, which, in *L. pertusa*, is released at rates well in excess of those measured for shallow-water corals (Wild et al. 2008).

Nitrate (NO_3) dominated the dissolved inorganic nitrogen pool, and concentrations reached almost 30 µM (**Figure 3-7c**), whereas the previously reported range of NO_3 values for CWC reefs was 2.18–18.8 µM (Findlay et al. 2014, Maier et al. 2011). Regional nitrate concentrations reach a maximum of 25 µM at 800–900 m depth (Williams et al. 2011). Phosphate concentrations over the reef were 1.4–1.8 µM (**Figure 3-7c**), typical of the region (Palter and Lozier 2008), and to those observed near other CWC reefs (0.26–3.59 µM, Findlay et al. 2014, Georgian et al. 2016). DOP concentrations were low (0.2 µM), while DON concentrations (1–2 µM, **Figure 3-7b**) were typical of background concentrations in the area, but there are no published data from other CWC reefs.

In the Gulf Stream, nutrient fluxes are maximal between 500–700 m depth and nutrients increase from 26° to 36°N in denser deepwater layers (Palter and Lozier 2008, Williams et al. 2011). We attributed this increase to the influx of nitrate- and phosphate-rich waters from the subtropical gyre (Palter and Lozier 2008, Williams et al. 2011). However, the nutrient concentrations measured over the reefs here exceed those documented previously in the region, suggesting that the reefs may supply nutrients within the Gulf Stream seascape. This form of nutrient recycling is vital to the productivity of both shallow (de Goeij et al. 2013) and deep reefs (Cathalot et al. 2015, Rix et al. 2018).

Growth of calcifying corals is regulated further by pH (7.68–7.81) and aragonite saturation state (Ω_{arag}, 1.49–1.59). The pH values are lower than those previously measured in the North Atlantic (Georgian et al. 2016); comparable to values from southern California (Gomez et al. 2018). The Ω_{arag} values are extremely low for shallow-water reefs, but within the lower range of values (1.3 to 2.6) typically measured over *L. pertusa* reefs in the North Atlantic (Findlay et al. 2014; Georgian et al. 2016). Saturation state was higher over the reef than in the surrounding water column (1.27 to 1.42), which could result from skeletal dissolution within the reef (Georgian et al. 2016). If locally elevated alkalinity enhances skeletal precipitation rate, net precipitation is positive and the reef structures are accumulating carbon (Titschack et al. 2009), an influential ecosystem service of this deep-sea habitat (Cordes et al. 2016).

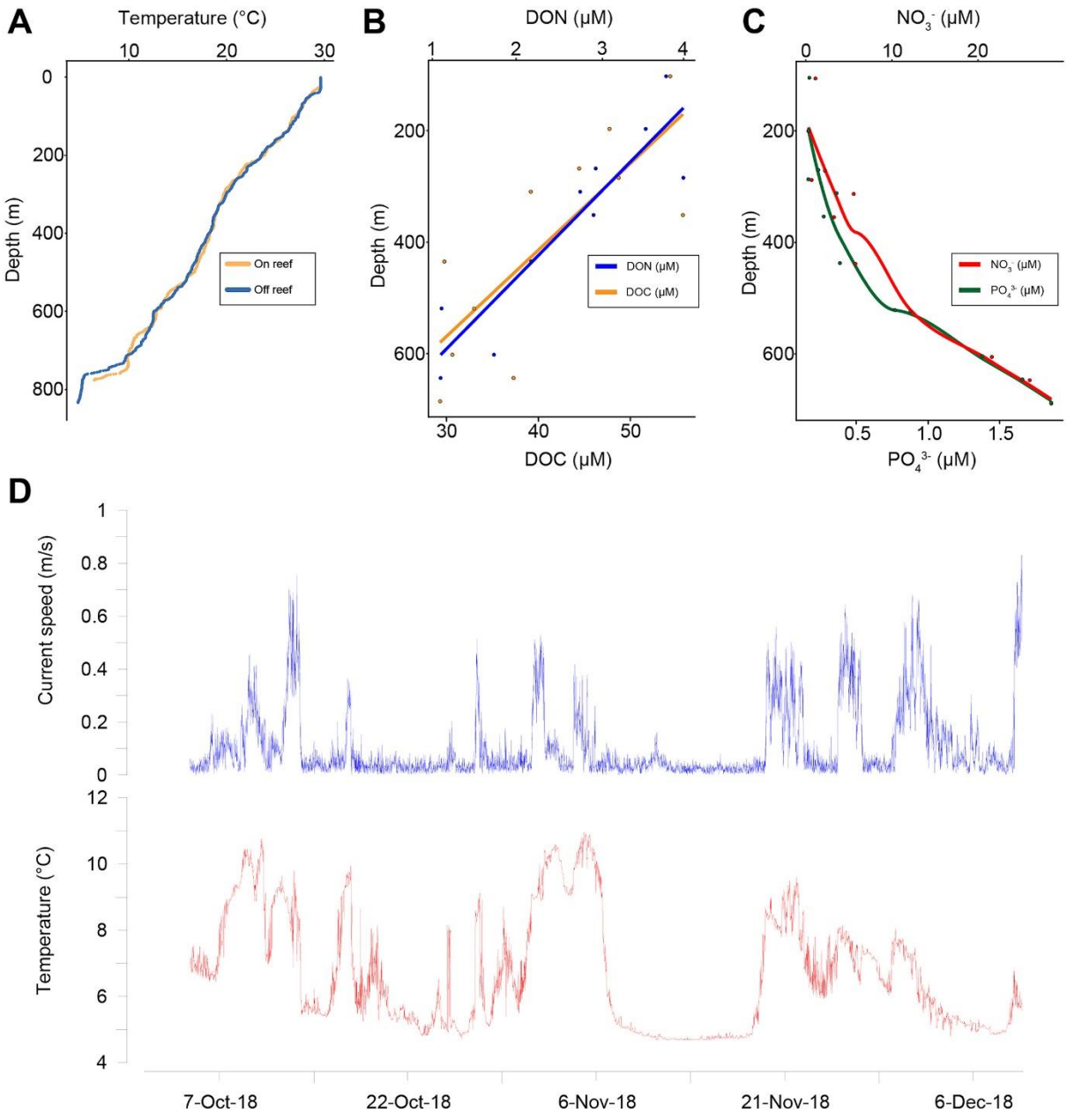

Figure 3-7. Aragonite saturation profiles over the Richardson Reef Complex

3.1.3 Temporal Changes in Oceanographic Parameters

3.1.3.1 Methods

Many of the samples and data for this section come from the benthic landers, the use of which was contributed to the project by our collaborator Furu Mienis from the Netherlands Royal Institute of Oceanography (NIOZ). We used the benthic lander ALBEX to measure temporal variability in near-bed environmental conditions. The lander consisted of an aluminum tripod equipped with 12 glass Benthos™ floats, two IXSEA™ acoustic releases and a single 270-kg ballast weight, necessary for deployment and recovery. We attached an iridium beacon and large orange flag to the frame in order to locate it after

surfacing. Furthermore, the lander was equipped with a Nortek™ Aquadopp current meter to measure current direction and speed, and a combined OBS-fluorometer sensor (Wetlabs™) to measure particle density and fluorescence at 1 m above the bottom. These were connected to a NIOZ-built datalogger and a Technicap PPS4/3 sediment trap, with an aperture at 2.20 m and a rotating carousel of 12 bottles, configured to collect material over a 25-day period. In addition, the lander contained a baited experiment to census fishes and mobile species such as crustaceans at the study site. For this experiment the lander was equipped with a HD video camera (Sony) with infra-red illumination (LED), directed at the bait fitted in a sediment trap carousel (24 bottles), rotating at 14-d intervals. The camera filmed every 2 hours for 15 seconds throughout the deployment period.

We deployed this benthic lander at the Richardson Reef Complex during the BMCC2018 cruise (31 58.9705 N, 77 25.0139 W) for a long-term deployment. Unfortunately, the lander surfaced prematurely in December 2018 and was recovered by the NOAA Ship *Okeanos Explorer* that was fortuitously sailing in the vicinity. All sensors had collected data and the sediment trap collected two samples successfully.

We redeployed the lander near Richardson Reef Complex during the RB19 cruise for a short-term and another long-term deployment (**Figure 3-1**) and then successfully recovered it in October 2019 during the NF19 cruise. During the long-term deployment (192 days, April through October 2019) the lander had the same configuration as described above but was additionally equipped with an oxygen sensor (Advantech ARO-USB) measuring at a 30-minute interval and a hydrophone attached to the frame at 2 m above the bottom. Data from this second, long-term, lander deployment will be discussed here, because they represent the largest dataset with the most parameters monitored, including passive acoustics and oxygen.

The ALBEX lander was instrumented with a hydrophone icListen HF system (OceanSonics, Nova Scotia, Canada) vertically mounted to the top of the lander's frame (approx. 2 m above the bottom) and passively recorded acoustic data for 2 months at a sampling frequency of 128 kHz; therefore, the maximum usable frequency is 64 kHz, half the sampling rate of the recordings (Nyquist frequency). The recorder operated on a duty cycle of 1-minute recording ON, 29 minutes OFF. We compared the acoustic time series to time series of other lander sensors including: acoustic backscatter from the high-frequency ADCP, current speed and direction, optical backscatter (turbidity), temperature, salinity, and dissolved oxygen. The high-frequency ADCP (2 MHz) had a minimum detection limit of particles 24 mm in diameter and reached maximum peak sensitivity for 485-mm sized particles (Lohrmann, 2001, Haalboom et al. 2021). Optical backscatter sensor response is inversely proportional to particle size (Haalboom et al. 2021), therefore the sensitivity decreased over the ADCP sensitivity range (24–485 mm) within those frequency bins (Tonolla et al. 2011, Belleudy et al. 2010).

For temporal alignment with the environmental data, we calculated peak (maximum) sound pressure level (SPL) for each 1-minute sample and 30-minute interval. Peak SPLs were calculated in low (10–100 Hz), mid (100–1,000 Hz), high (1,000 Hz–10 kHz), and ultra-high (10–64 kHz) frequency bands. The majority of analyses used the low-frequency band since most abiotic physical sounds dominate this range (NRC 2003). We analyzed sedimentation events using higher-frequency bins (high and ultra-high), as high velocity particle collisions with the face of the hydrophone or with the benthic lander structure produced sounds. We constructed time series of daily acoustic SPL percentiles (10th, 25th, 50th, 75th, and 90th) from root-mean-square SPLs. A 90th daily percentile indicates that 90% of the day's sound levels did not exceed this amplitude value; conversely, only 10% of the daily values were louder than the 90% percentile value. The lower percentiles capture the sound floor of the soundscape or the quietest ambient conditions that are detectable in passive acoustic recordings. The higher daily percentiles represent the highest levels of sound in a region and provide the potential to identify transient sound sources. We used the 1-minute recordings to construct spectral probability density (SPD) plots showing sound energy levels over the full spectrum of frequencies and the estimated probability of a sound level being encountered at specific amplitude level at a specific frequency. SPD plots were generated for several specific periods in the time series that represented events of interest over two temporal scales: 24 hours and 1 month.

We assessed the capability of the observed environmental variables at predicting the low frequency sound levels using a General Additive Model (GAM) due to the nonlinear relationships between variables. A combination of total current velocity (from all directions), vertical velocity and backscatter, the former two treated isotopically, represented the best fit in predicting the observed low-frequency sound levels, as this model minimized model performance metrics (AIC, GCV, RMSE) and returned the largest adjusted R^2 value. However, due to the strong logistic relationship between optical turbidity and acoustic backscatter, estimates of turbidity from peak SPLs could be predicted. Model fitted values vs. response peak SPL values resembled a linear relationship indicative of good model fit.

We explored whether passive acoustics can be used as a sentinel indicator in the assessment of bottom-current variability in a CWC reef, specifically: 1) detecting and predicting current velocities and 2) detecting particle supply and approximate particle size, and 3) detect complex broad-scale oceanographic processes such as the presence or absence of the Gulf Stream within the Richardson Reef Complex area. These variables are of high importance in many deep-sea ecosystems, as large magnitudes in current velocity shifts will likely affect food particle supply and feeding behavior of CWC through polyp expansion (Orejas et al. 2016), influence replenishment of the coral framework (Van Haren et al, 2014), and impact sedimentation regimes preventing CWCs from burial. A single hydrophone acoustic detection and characterization of high current velocities, sediment loadings, and oceanographic processes can aid in assessing the status of CWC and other deep-sea ecosystems, especially in the absence of multi-parameter fixed platform observatories.

3.1.3.2 Results

We compiled summary data of all environmental parameters (**Table 3-1**) and plotted time series of all environmental parameters including 12-hr rolling means as indicated by the black lines in (**Figure 3-8**) for the approximate 6-month duration of the lander deployment (14 April–23 October, 2019).

Time-series data show major fluctuations in both temperature (°C) and an inverse relationship to DO (mg L^{-1}) (correlation coefficient: -0.98). Temperature data were positively skewed ($\sim\mu_3$ = 3.235), with sporadic peaks of elevated temperature that reached up to eight times the standard deviation (SD) above the mean (max: 10.82°C). Temperature elevations, defined as readings above 1 SD above the mean, occurred as either short-duration fluctuations (less than 30 minutes) or distinct longer periods of ramping and cooling lasting up to 35 hours. Ten distinct peak events occurred within the 6-month deployment, with no detected periodicity between events. Major peak events occurred in early and late May, mid-August, and early September.

Table 3-1. Six-month summary of Richardson Hills ALBEX Lander

Parameter	Mean	SD	Min	Max	Range
Temperature (°C)	5.03	0.75	4.13	10.82	6.69
Dissolved Oxygen (mgO_2l^{-1})	9.47	0.75	4.94	10.32	5.38
Fluorescence (μgl^{-1})	0.0827	0.0098	0	0.285	0.285
Turbidity (NTU)	0.240	0.16	0.132	2.693	2.56
Acoustic Backscatter (mean Amp)	71.2	14	51.3	131.0	79.7
Vertical velocity (ms^{-1})	0.0151	0.042	-0.348	0.397	0.745
Horizontal current speed (ms^{-1})	0.0711	0.053	0	0.513	0.513

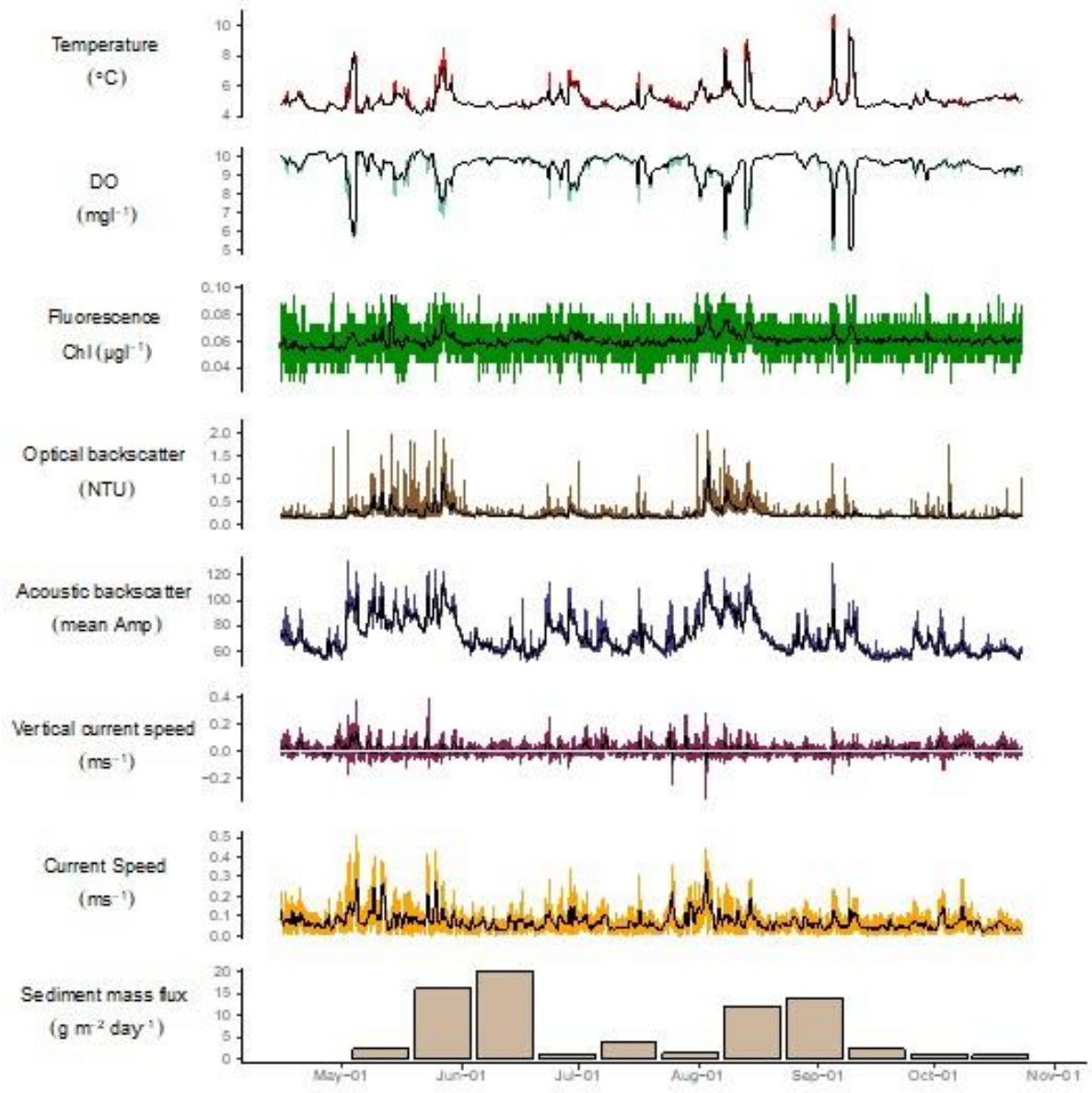

Figure 3-8. Time-series plots for ALBEX lander instruments
April–October 2019. Black lines indicate 12-hr rolling means.

Optical (NTU) and acoustic backscatter (Amplitude), metrics of fine-particle and large-particle turbidity respectively, were variable during late May to early June and mid-August, with elevated readings corresponding to concurrent temperature elevations. Fine-particle turbidity was highly positively skewed ($\sim\mu_3$ = 6.375), while large-particle turbidity was near-normally distributed though still positively skewed ($\sim\mu_3$ = 0.999).

Fluorescent signal (µg l^{-1} Chlorophyll) was low throughout the duration of the time series, with a maximum of 0.263 µg l^{-1}. A 12-hour rolling mean delineated signal pulses in late May and early June, as well as early August and early September, all of which occur during or near the time of substantial temperature elevations.

Vertical velocity (m s^{-1}) and horizontal current speed (m s^{-1}) show patterns of fluctuation coinciding with temperature peaks in early and late May and late July/early August, but with less obvious pattern matching to temperature peaks in the later summer and early fall.

Horizontal current speed did not appear to have strong directional components over the 6-month period, though we found variable patterns within shorter time frames. In May, we observed elevated bimodal current speeds to the NW and SE, a pattern which is not observed in any other month of the deployment period. We observed the greatest overall current speeds during this month, as well as increases in turbidity (optical and acoustic backscatter) and fluorescence. Moreover, Northern velocity components were elevated in the mid-late summer, which suggests intermittent influence of Gulf Stream surface currents to the Richardson Reef region. We conducted a Harmonic Analysis of Least Squares (HAMELs) tidal analysis on horizontal current speed using the 'tidem' tool in the oce package v. 1.4-0 (https://CRAN.R-project.org/package=oce; Kelley and Richards 2020). Results showed some adherence to standard tidal constituent models (**Table 3-1**).

Mass fluxes varied between 0.98 and 20.23 g $m^{-2}day^{-1}$. We saw the highest mass fluxes in late May/early June and in late August/early September, corresponding to fluctuations in temperature, current speed, and turbidity **(Figure 3-9**). During the May period we saw increases in fluorescence, which might indicate that fresh organic matter is delivered to the Richardson Reef Complex. Further analysis of sediment trap samples on organic matter content and pigments are needed to confirm this.

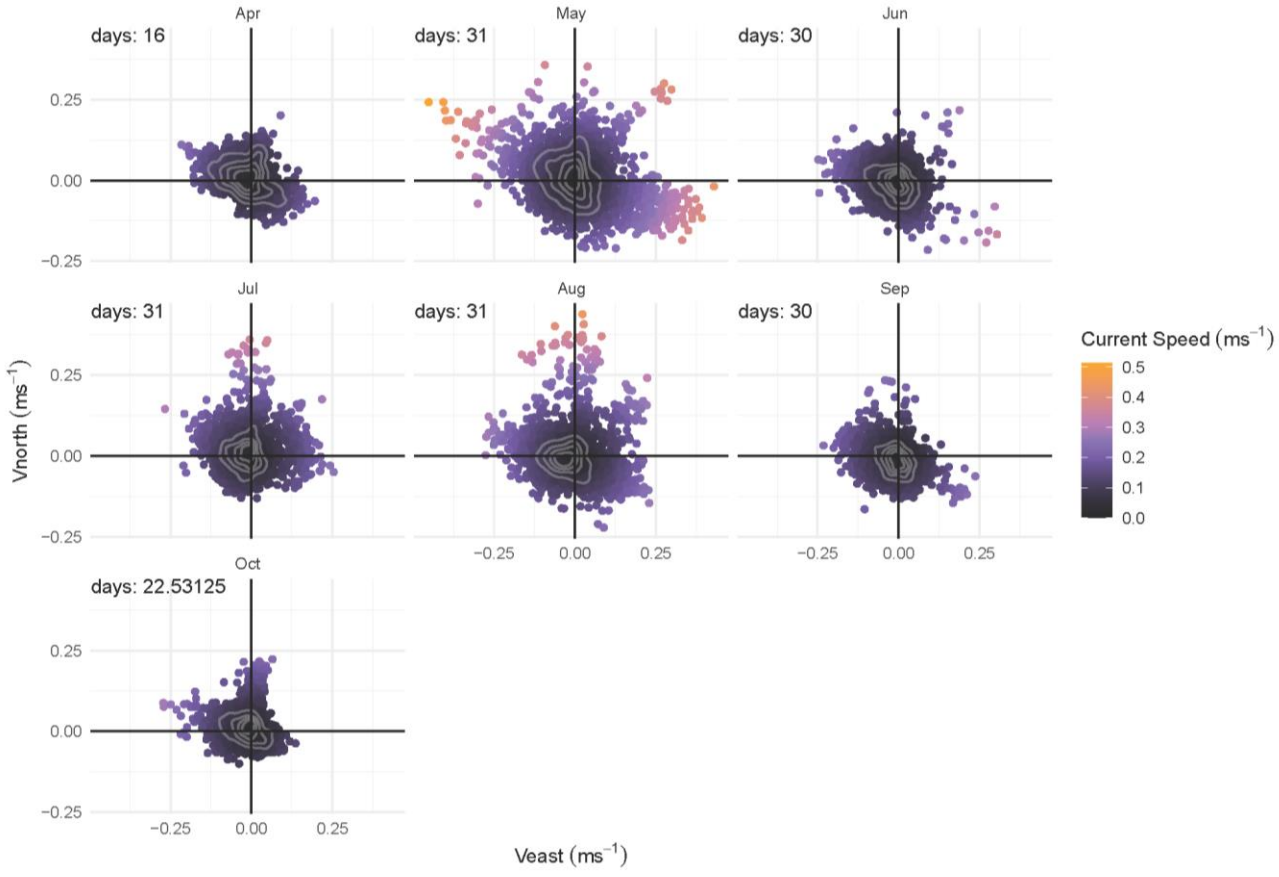

Figure 3-9. Current cloud of North and East velocity components of current speed
For each month during ALBEX lander deployment. Gray lines are 2D kernel density estimate contours scaled to a maximum of 1.

We calculated hourly rates of change for each environmental time series (**Figure 3-10**). Notably, we saw temperature changes up to 3.74°C per hour. As well, high rates of change in temperature appear to correspond to major changes in fluorescence, further suggesting intermittent pulses of warm and relatively nutrient-rich water, possibly driven by meandering incursions of the Gulf Stream and/or its eddies.

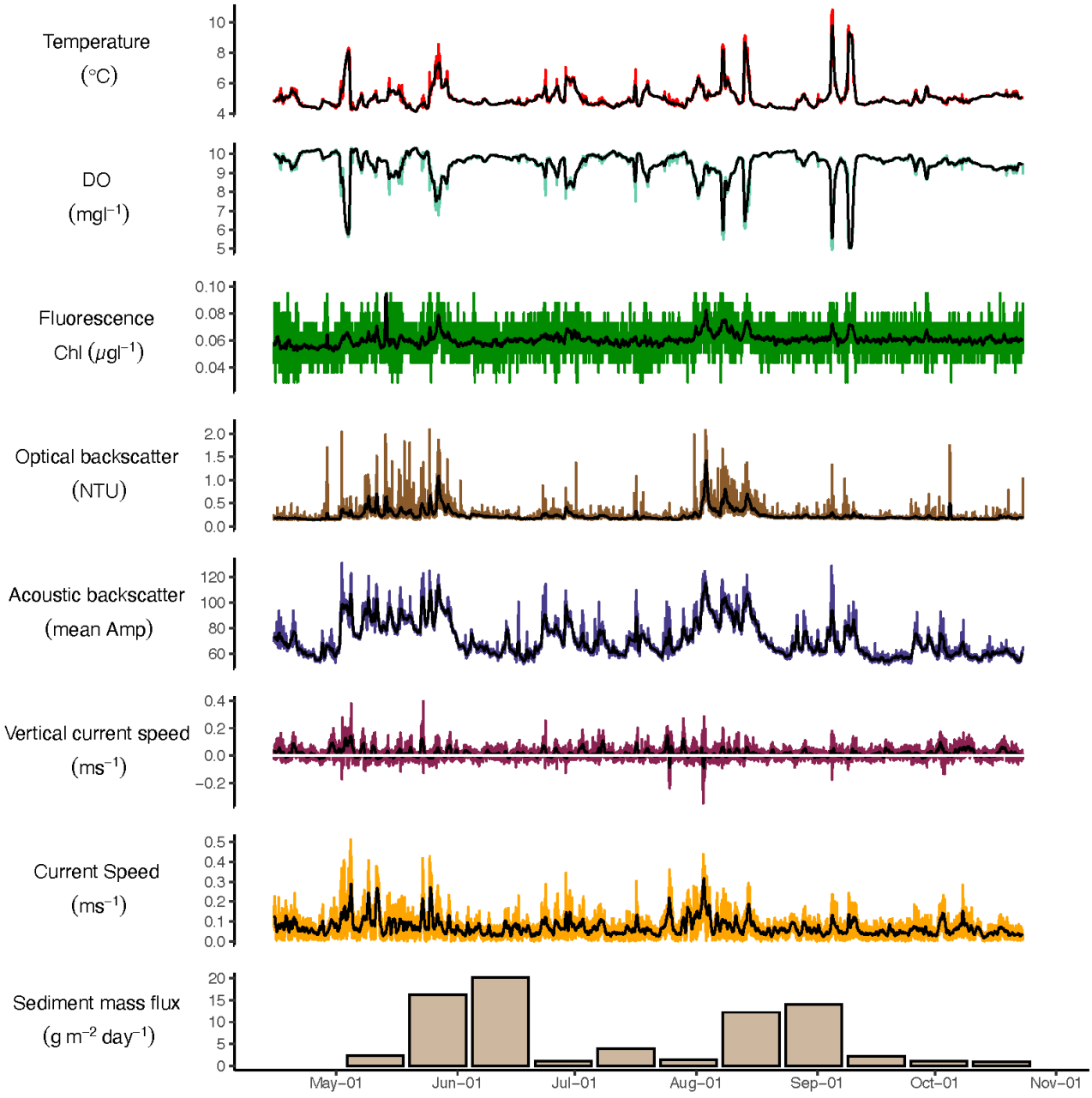

Figure 3-10. Hourly Rate of Change for environmental parameters from ALBEX

We related the largest fluctuations in water-column structure and near-bed environmental conditions to the presence or absence of the Gulf Stream, as confirmed by satellite imagery. Coastward meanders of the Gulfstream lead to rapid rises in bottom water temperature, current speed, and backscatter, resulting in

daily variability in near-bottom environmental conditions as well as mixing of the water column. The influence of the Gulf Stream shows similar changes in temperature as seen in the Cape Lookout CWC area (Mienis et al. 2014), indicating that the coral reefs exist in extreme conditions at the upper thermal range (Brooke et al. 2013). This variability can influence the CWC communities in multiple ways. Large changes in temperature can have major implications on coral physiology (Brooke et al. 2013, Lunden et al. 2014). On the one hand temperature increases of 10°C might lead to a three- to five-fold increase in respiration (Dorey et al. 2020) and when not counterbalanced by enhanced food supply can even lead to increased mortality (Buscher et al. 2017).

On the other hand, more turbulent conditions with enhanced current speed and suspended matter concentrations related to the occasional presence of warm and oligotrophic Gulf Stream water likely lead to enhanced food supply as has been observed in other CWC reef areas (Davies et al. 2009, Mienis et al. 2007, Thiem et al. 2006). We observed high mass fluxes during the Gulf Stream presence, which when enriched in organic matter can compensate stressors like elevated temperature and reduced oxygen conditions (Hanz et al. 2019). Moreover, periods of enhanced current speed and subsequent replenishment can play a role in the nutrient and carbon cycling in the wider MAB region.

Combining observations of acoustic and oceanographic data and the examination of their relationships assisted in identifying short-term changes in the local environment. The rate of change, magnitude, and event duration in environmental and acoustic parameters differed between the early and late May periods, where we saw extreme patterns (**Figure 3-11**). The early May period exhibited substantial deviations in temperature, dissolved oxygen, and acoustic percentiles within a 24-hour period (May 4–5) (**Figure 3-12** and **Figure 3-13**). Temperature and dissolved oxygen fluctuated rapidly during this period, shifting by more than 4 units in under 20 hours. The 90^{th} acoustic RMS SPL percentile increased by 18 dB re 1 mPa2 between May 3–4 reaching a peak of 132.7 dB re 1 mPa2 on May 4 and then decreased by 27 dB re 1 mPa2 between May 4 and 5 coinciding with the deviation in temperature and dissolved oxygen (**Figure 3-12** and **Figure 3-13**). This is an extreme increase as every 3 dB increase is a doubling of sound intensity and a 10 dB increase is a doubling in perceived loudness by a human.

We used SPD plots to assess the impact the high current 24-hour period had on the soundscape (**Figure 3-12**). The low-frequency portion of May 4 showed median SPLs 20 dB re 1 µPa2 Hz-1 higher than the median low-frequency levels of May 5 (**Figure 3-11**, red lines). Transient sounds, likely produced by sediment particles colliding with the lander frame and hydrophone, were also only present on May 4 and manifested in the high-frequency range of the acoustic record (**Figure 3-12**, red rectangle). Acoustic and optical turbidity backscatter measurements suggest the majority of these particles were likely larger in size (**Figure 3-8**). On monthly time scales, low-frequency sound levels in May were higher and more variable compared to the following month of June. Median May current speeds (8.1 cm s^{-1}; SD: 7.5) were nearly double median June current speeds (4.8 cm s^{-1}; SD: 3.2) with May having a larger variation in current speeds. At higher frequencies (100-1,000 Hz), there were peaks in the spectrum in May that were absent in June. We observed this acoustic feature, hypothesized as sediment particle strikes, in the SPD plots on May 4 but it appeared to be less dramatic when visualized at the monthly scale.

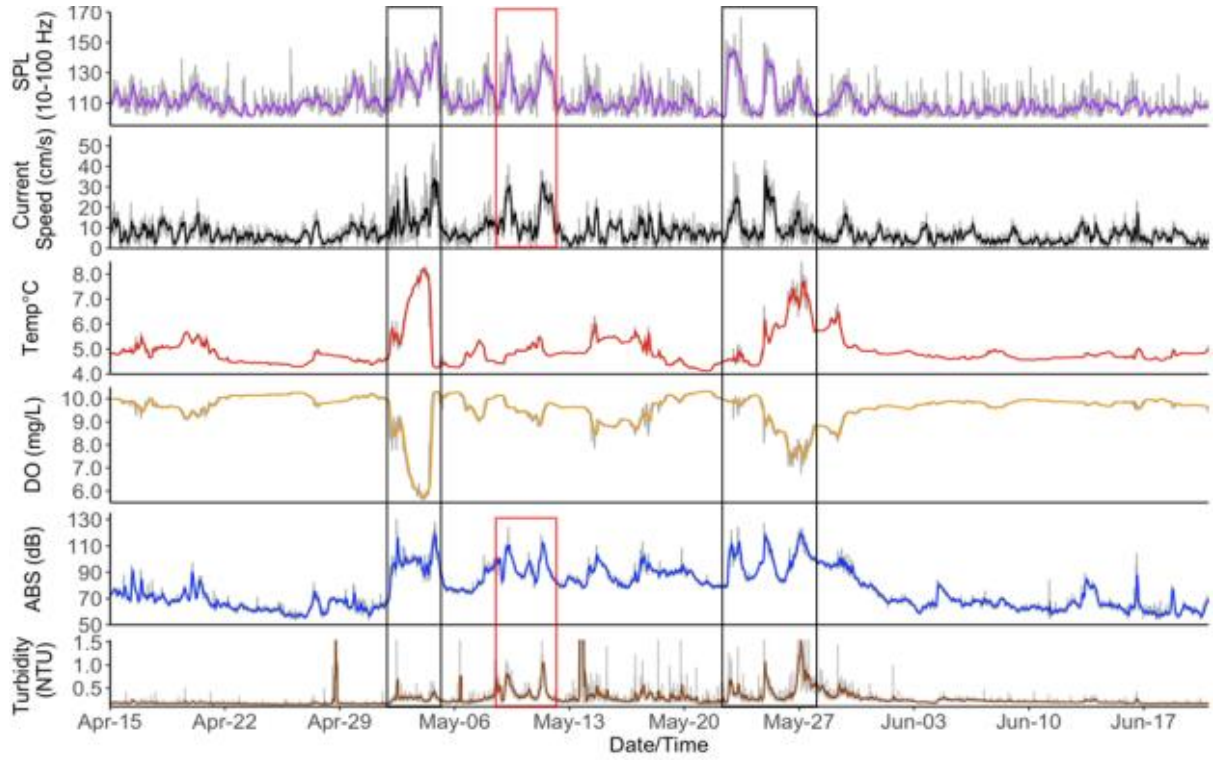

Figure 3-11. Two-month time series of low-frequency peak SPLs (dB re 1 mPa^2)
Also shown are environmental variables (current speed, temperature, dissolved oxygen concentrations, acoustic backscatter, turbidity). Turbidity smoothed with moving average filter (window length = 10). Black rectangular boxes represent May 2–5 and May 22–28 time periods. Red rectangular boxes represent May 9–12 period.

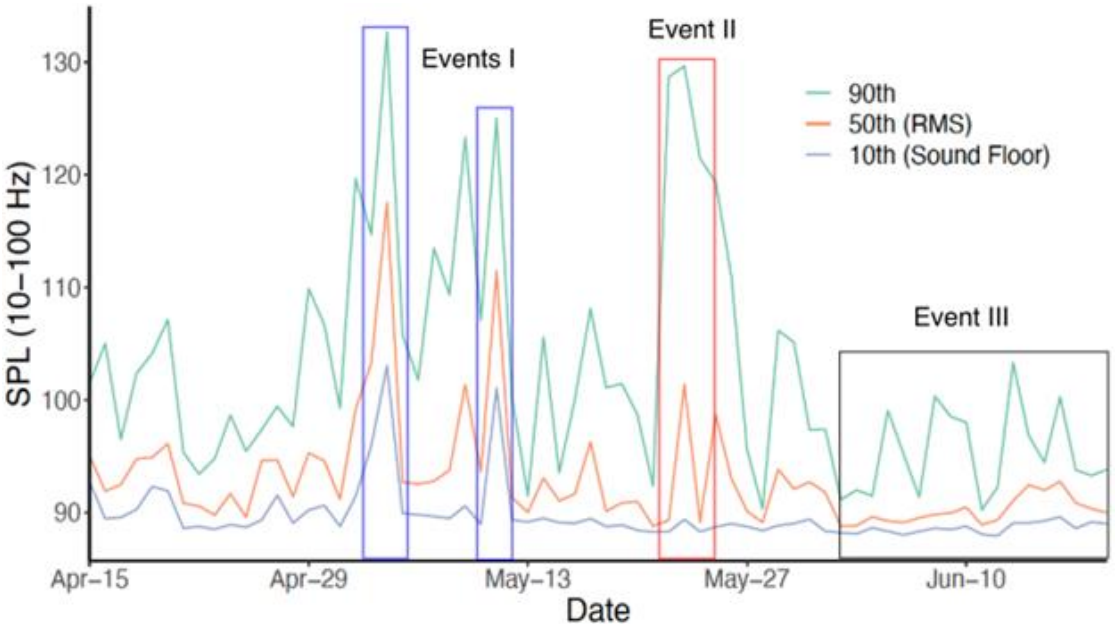

Figure 3-12. Daily time series of 10th, 50th (median), and 90th acoustic percentiles
Based on RMS sound levels (dB re 1 µPa^2) in the low band (10 to 100 Hz) frequency. A percentile spectrum is useful when sound levels vary over time, as it can reveal very loud events that elevate sound floor (events I, blue boxes), loud events not elevating sound floor (event II, red box), or quiet periods (event III, black box).

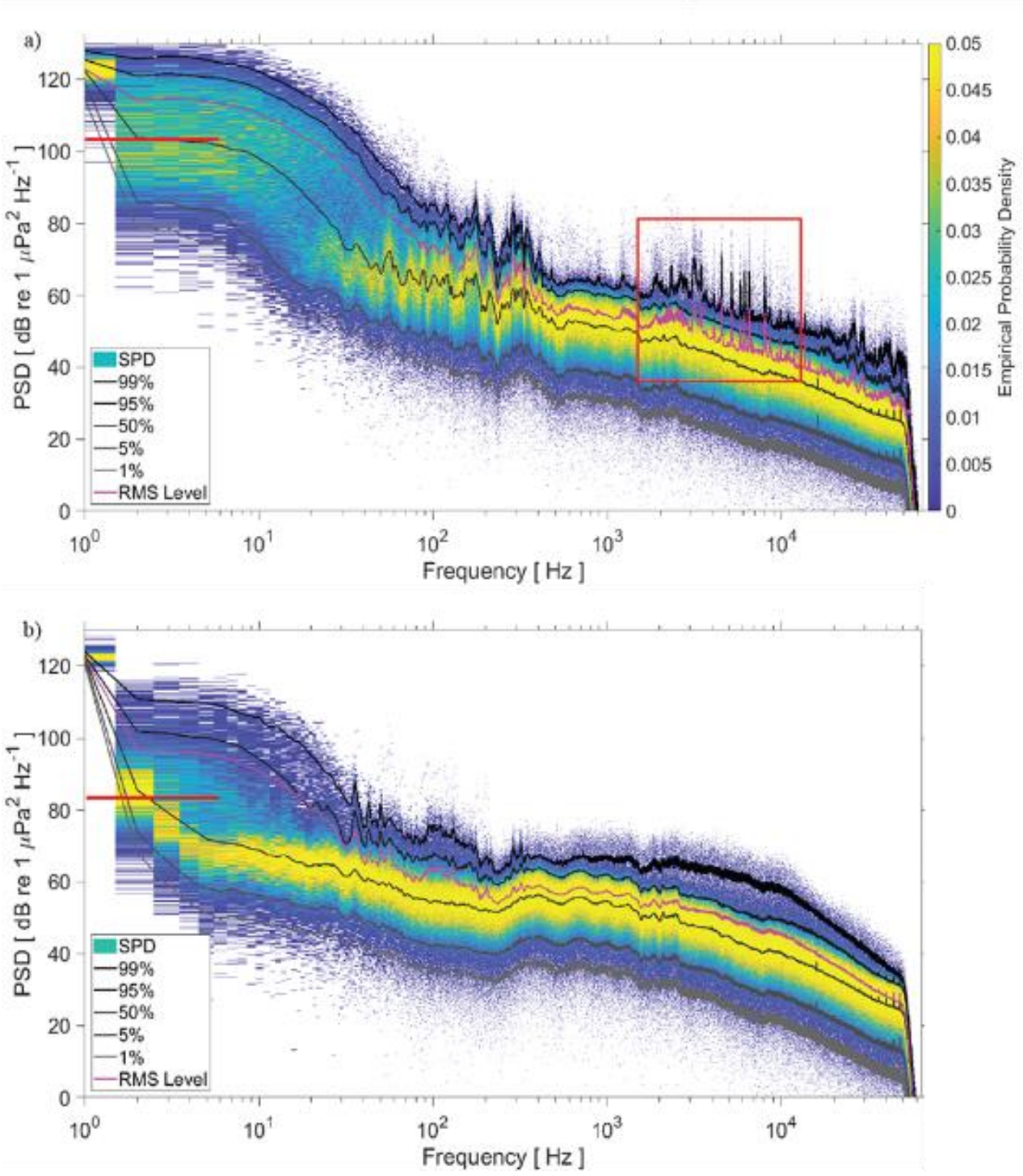

Figure 3-13. SPD plots
For a) May 4 and b) May 5 time domains. Power spectral density levels represented on y-axis and frequency represented on x-axis. Colored based on statistical empirical probability density can be thought of as the rareness of a particular sound at a certain frequency, smaller the value the rarer the sound. Red horizontal lines represent approximately the center of color band. Red box in (a) highlights peaks likely associated with particle collisions against the hydrophone and lander frame.

We assessed the strength of associations between sound level and environmental variables with GAMs and found interesting relationships between sound levels and current velocity, vertical current velocity, and turbidity. The single predictor GAMs constructed to test the ability and effectiveness of using only low-frequency sound levels to estimate environmental conditions showed total current velocity to be best predicted by low-frequency sound levels (adjusted R^2, 0.52). Model response vs. fitted values aligned well on 'perfect fit' line below 15 cm s^{-1}, but at higher current speeds predictions became more variable (**Figure 3-13**).

Changepoint analysis identified material shifts in environmental and acoustic data that revealed the substantial signature of the Gulf Stream on the soundscape at Richardson Reef, as current-driven sound levels increased. While passive acoustic recordings of the deep sea have not previously been used to provide information about current dynamics, we show their real potential for monitoring variability of abiotic environmental parameters in logistically challenging environments.

We related the largest fluctuations in water-column structure to the position of the Gulf Stream with implications on water-column chemistry and coral physiology. A temperature increase of 10°C might lead to a three- to five-fold increase in respiration (Dorey et al. 2020) and when not counterbalanced by enhanced food supply can even lead to increased mortality (Buscher et al. 2017).

Time series of the near-bottom environmental conditions at the Richardson Reef Complex captured substantial temporal variability in both oceanographic and acoustic parameters, supporting observations from other deep-sea acoustic studies (Chen et al. 2021). We identified material relationships between passive acoustics, the local environment, and broad-scale oceanographic conditions, largely driven by the presence of the Gulf Stream This is shown by major changes in temperature and current speed, a major physical oceanographic feature in the region. In the absence of other observing instrumentation, passive acoustics can serve as a sentinel indicator of the physical processes, particularly for variables like food supply, sediment availability, and replenishment which are dependent on currents and their speed as well as the quantity, composition, and size of particles within the current flow.

Multiple analyses demonstrated that passive acoustic recordings at the Richardson Reef Complex correlated with high current velocity and turbid episodes that persisted in some cases for multiple days. Generally, as current speed and particle supply increased, so did low-frequency peak SPLs recorded by the hydrophone, suggesting that current induced physical sounds are potentially a driving factor in the creation of specific local soundscapes (Lin et al. 2019). Here we also recognize that using passive acoustic signals to provide insight into current flow is confounded by turbulence induced noise generated by the physical presence of the hydrophone (and the mounting structure) (Wenz, 1962) particularly in the low-frequency measurements (< 100 Hz; Bassett et al. 2014).

It is generally considered that system noise generated from vortex shedding induced by the physical presence of the hydrophone interferes with measurement of ambient current flow within the system, increasing observed peak SPLs above true ambient levels creating uncertainty in soundscape characterization (Bassett et al. 2014). However, from the perspective of any benthic or pelagic organism that is in the flow environment, this is a true environmental sound pressure and particle motion signal, which can be used by the organism in the same manner the current flow signal would be used if the hydrophone and lander were absent. Using sound levels to predict empirical relationships with current speeds was effective but varied more at higher current velocities. This may be due to lack of observations at higher current speeds or that sound levels in the 10 to 100 Hz range cannot be used effectively to predict very high current speeds as sounds from particles colliding with the hydrophone and mounting infrastructure become louder in this situation and obfuscate the flow velocity acoustic signal.

Low and high-frequency acoustic bands both allowed for the detection of particle activity within the reef area. Such an approach has been used to estimate bedload transport and turbulent flow in rivers (Tonolla

et al. 2011). Tonolla et al. 2011 characterized the high-frequency SPLs as being primarily driven by collisions between sediment particles in transport and the low to mid frequencies capturing turbulence generated by flow interacting with obstacles, in our case the hydrophone, lander structure, and surrounding coral reef structures. However, not all high turbulent flow events produced these sediment collision transient sounds because either particle density was not high enough to observe a detectable acoustic response or velocities must reach a certain level and/or be sustained for a response to be detected in acoustic recordings. Sediment induced turbulence damping may explain lack of elevated peak SPLs during certain high current periods at the reef, as this type of damping has been observed in the high-frequency band in turbulent river habitats during flood conditions with high suspended sediment concentrations (Belleudy et al. 2010).

Given there were relationships between turbidity and low-frequency sound levels, it was possible to estimate the size of particles supplied to the reef through model estimations while taking note of the constraints of the model. Current speeds alter sediment particle size as well; knowing the general magnitudes will help estimate particle sizes, as suspended particles descending from above or laterally transported by local currents will aggregate in moderate currents then be sheared into smaller particles with large increases in current velocity (Thomsen and Gust 2000). Current velocity shifts of this magnitude likely affect food particle access for benthic organisms and also disrupt the effective capture rate of food particles by corals (Orejas et al. 2016), particularly when shearing and re-aggregation into larger flocs may restrict nutrient access (Thomsen and van Weering 1998). Additionally, shifts in current dynamics are also important for the replenishment of the system with nutrients and oxygen (Hanz et al. 2019, Van Haren et al. 2014, Cyr et al. 2016).

The observed elevated sound levels in concurrence with increased temperatures and currents suggest that the dominant oceanographic feature in the region, the Gulf Stream, can be detected with passive acoustic sampling at depth. Two time periods with the largest environmental variations corresponded with Gulf Stream activity at the surface, the later time period saw a lag between sound levels and one of most efficient oceanographic variables for Gulf Stream detection, water temperature. The 72-hour lag suggests sound gives some predictive capability of potential forthcoming Gulf Stream incursions with an increase in current speeds occurring prior to an increase in temperature as the incursion reaches the reef. A lag however does not always occur, as the first time period has temporal alignment between sound and temperature. The presence of a lag may be dependent on the size, the originating direction of incursion, and/or rotational direction of eddy (cyclonic or anticyclonic). Increasing the acoustic sampling rate during Gulf Stream events, in a semi-automated capability, and extending acoustic recording through a whole year would provide additional information on smaller Gulf Stream influences onto the reef and seasonal patterns in which the Gulf Stream may play a role.

Topographically complex CWR systems like the Richardson Reef Complex, generally extend several meters vertically from the seafloor and have a substantial role in driving both physical and biological patterns (Davies et al. 2009, Costello et al. 2005, Henry and Roberts, 2007). These deep reefs likely exhibit distinct soundscapes in a similar fashion to shallow-water coral reefs (Radford et al. 2014). Shallow-water reef soundscapes have been suggested to attract fish and coral larvae through elevated sound levels emanating from reef site, largely those generated directly and indirectly by adult fish and invertebrate species present on reef (Montgomery et al. 2006; Vermeij et al. 2010). Although there may be reduced species richness on a deep-sea reef (Costello and Chaudhary 2017, Smith and Brown 2002) reducing potential sound source signals propagating away from the reef, studies on shallow reefs show that sound propagation distance and off-reef detection is only a few hundred meters mainly due to the presence of surface background sounds (waves, vessel noise) and the way marine species detect sound (Kaplan and Mooney 2016, Raick et al. 2021). We suggest that deep-sea reefs, on the other hand, are hotspots for hydrodynamic generated sounds and may help species detect a reef from a greater distance.

3.2 Geologic Setting

Section Authors: Jason Chaytor, Nancy Prouty, Diana Sahy

3.2.1 Historical Geology

The Deep SEARCH project area of interest spans six-degrees of latitude, or more than 700 km, of the US Atlantic continental margin from the shelf-slope area offshore the North Carolina-Virginia border to the Blake Plateau off the central eastern coast of Florida and out into deepwater settings. Because the project area was so broad, a wide range of antecedent geology and modern seafloor processes combined to shape the diverse seafloor environments investigated. For ease of description and reference, the study area is separated into two primary geologic basins, Carolina Trough and Blake Plateau Basin (**Figure 3-14**), and three morphologic regions: 1) seeps, 2) canyons, and 3) Blake Plateau and adjacent areas.

The modern configuration of the study area is the result of the initial tectonic breakup of the margin during the Triassic and postrift oceanographic and sedimentary processes over the subsequent 215 million years. The initial zone of rifting in the Carolina Trough (shelf/slope) and northern Blake Plateau (Blake Plateau Basin) section of the margin differed considerably along-strike, with the southern segment ultimately becoming wider than the Carolina Basin to the north (**Figure 3-14**) During this initial rift period, evaporites (salt) were deposited in the Carolina Trough, but not the Blake Plateau Basin, possibly a result of variations in crustal thickness and subsidence levels (Dillon et al. 1983, Dillon and Popenoe 1988). During and following breakup (at around 183 Ma), siliciclastic sedimentation processes were active along the entire length of the US Atlantic margin (Poag and Sevon 1989), with periods of carbonate deposition interspersed throughout the time section. Beginning in the middle Jurassic, with all the eastern North America margin at a subtropical latitude, carbonate depositional processes finally overcame siliciclastic processes resulting in the development of carbonate platforms and shelf-edge reefs. Over time, carbonate depositional environments along the margin coalesced to form a near continuous carbonate "gigaplatform" (Poag 1991) from the Bahamas to the Grand Banks offshore Canada.

Termination of large-scale carbonate deposition, resumption of siliciclastic-dominated deposition and continued expansion of accommodation space due to basin subsidence and salt withdrawal occurred along the northern portion of the margin (north of Cape Hatteras) during the middle Early Cretaceous (133 Ma). During the same period and extending until the Late Cretaceous, carbonate deposition largely kept pace with crustal subsidence across the Blake Plateau Basin. In the Late Cretaceous, a major shift in deposition patterns across the Blake Plateau, perhaps resulting from a combination of global sea-level rise and local tectonics, resulted in flooding of the Blake Plateau Basin and development of the current deepwater plateau and initiation of carbonate and clay-rich sediment deposition (marl/carbonate-rich mudstone) (Dillon and Popenoe 1988); the Bahama Banks at the southern end of the Blake Plateau continued to keep pace with sea-level rise (Schlager 1981).

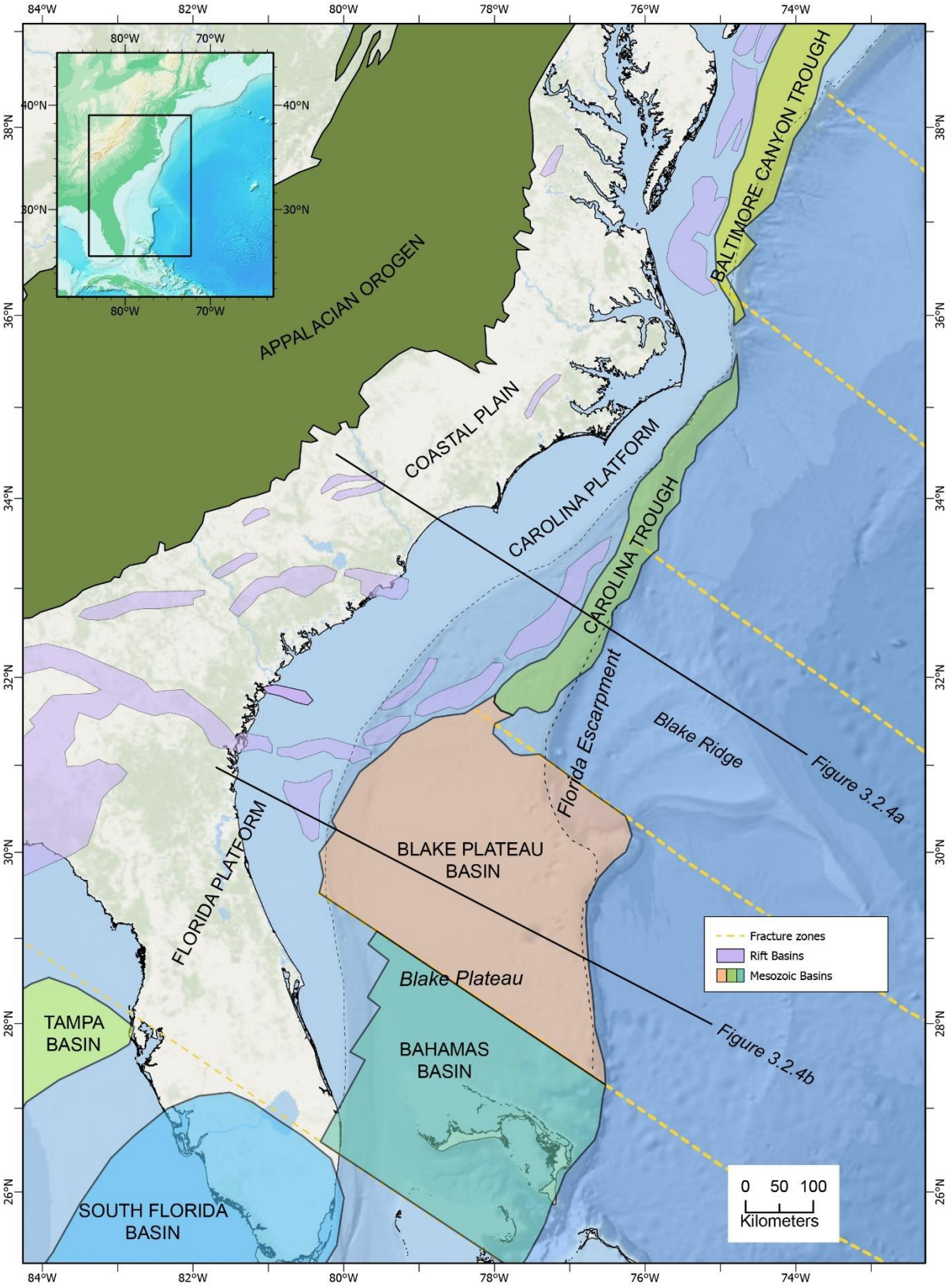

Figure 3-14. Major geologic and tectonic basin features of Deep SEARCH study area
US southeast Atlantic continental margin (simplified Uchupi 1988)

At the end of the Paleocene (56 Ma), overall strengthening of northward-directed surface currents through the Straits of Florida was likely driven by sea-level fall (Hazel et al. 1984) and diversion of the Suwannee Current. This current previously flowed from the GOM to the Atlantic near the current day Florida-Georgia border (**Figure 3-15**) (Pinet and Popenoe 1985, Popenoe 1987). These newly rerouted currents represent the onset of the modern Gulf Stream (Dillon and Popenoe 1988).

While the Suwannee Current carried terrigenous sediments directly from the GOM to the Atlantic, the rerouting of the current flow across the shallow carbonate banks around the south end of Florida removed almost all the sediment load from the Gulf Stream. Starved of terrigenous sediment from both the GOM and the Florida-Hatteras shelf by the north wall of the Gulf Stream, the Blake Plateau continued to subside throughout the early Eocene.

Changes in sea level throughout the remainder of the Eocene and early-Oligocene, switched current flow several times between the Suwannee (Suwannee Strait/Gulf Trough) and Gulf Stream (Straits of Florida), leading to periods of terrigenous sediment accumulation, progradation of the Florida-Hatteras shelf, sediment accumulation in the Carolina Trough and erosion of the Blake Plateau and Blake Escarpment (Paull and Dillon 1980, Sheridan et al. 1981, Pinet et al. 1982, Pinet and Popenoe 1985, Popenoe 1985).

Substantial periods of erosional activity in the late Oligocene and Pliocene scoured the surface of the Blake Plateau and eroded the Blake Escarpment (Paull and Dillon 1980, Sheridan 1981, Dillon and Popenoe 1988), while during the same period, the changes in deep circulation along the western boundary of the Atlantic basin initiated rapid sediment accumulation—forming the deep sediment drifts such as Blake Ridge off the Carolina Trough (Markle and Bryan 1983, Mountain and Tucholke 1985).

The rifting origin and long, complex history of reef building, sediment accumulation, non-deposition and erosion across the Blake Plateau and Carolina Tough have ultimately led to the two distinct margin profiles present today in the study area (**Figure 3-16**). In the north, the margin is formed by the coastal plain (mostly on land), shallow-water insular Carolina platform and the Carolina Trough, before transitioning at the general location of the paleoshelf edge carbonate platform, to canyonized upper continental slope and slope attached contourite drifts.

To the south, the Florida Platform and Blake Plateau Basin extend from the southern end of the Carolina margin to offshore southern Florida, with continued carbonate sediment deposition after the Early Cretaceous and the long-term influence of the Gulf Stream creating a narrow insular shelf, broad gently sloping plateau, and steep escarpment.

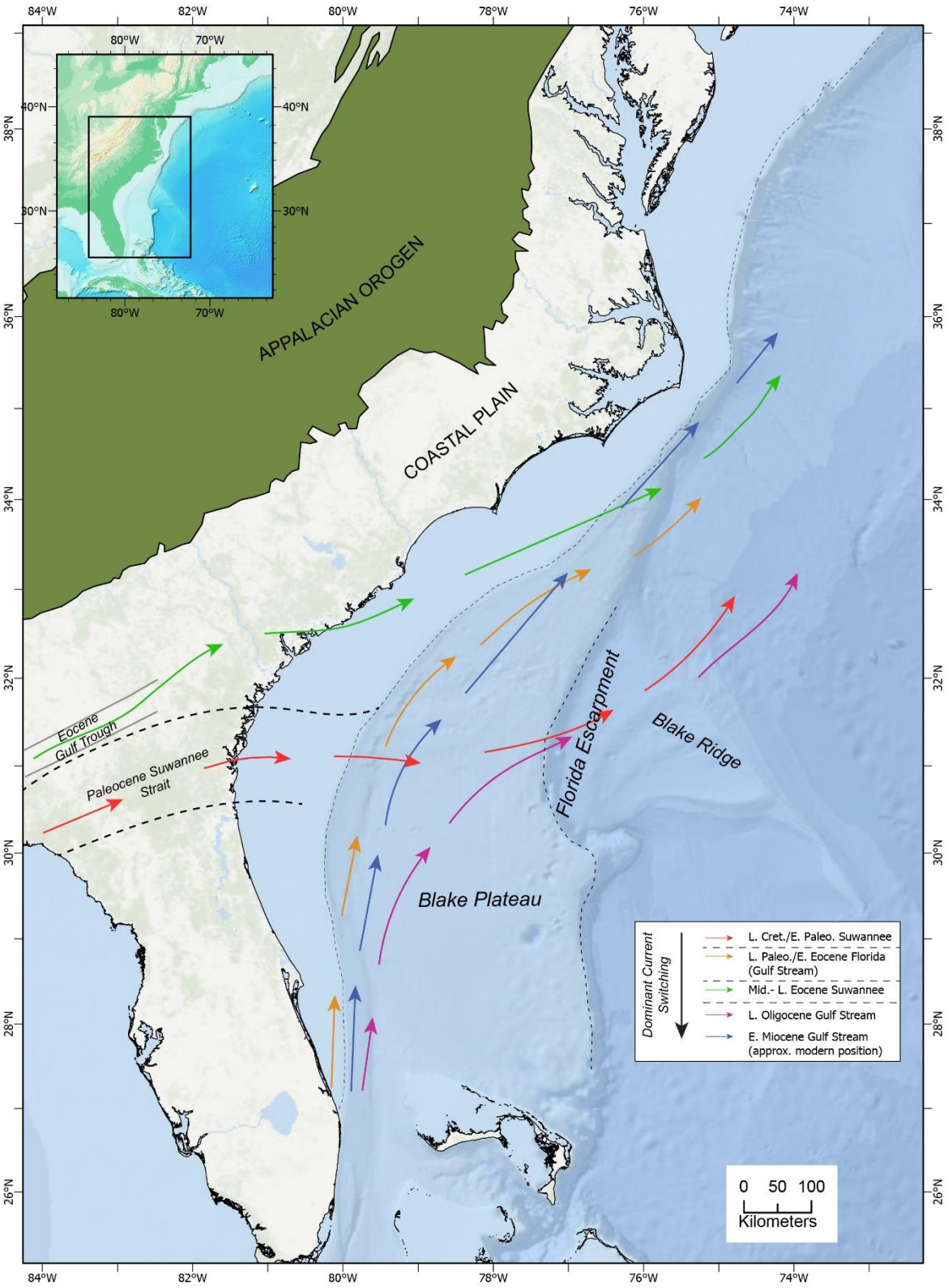

Figure 3-15. Different positions of the Suwannee and Gulf Stream currents over time
Across the Blake Plateau from the Cretaceous through ~ present. Modified from Dillon and Popenoe (1988) and Manheim and Popenoe (2001).

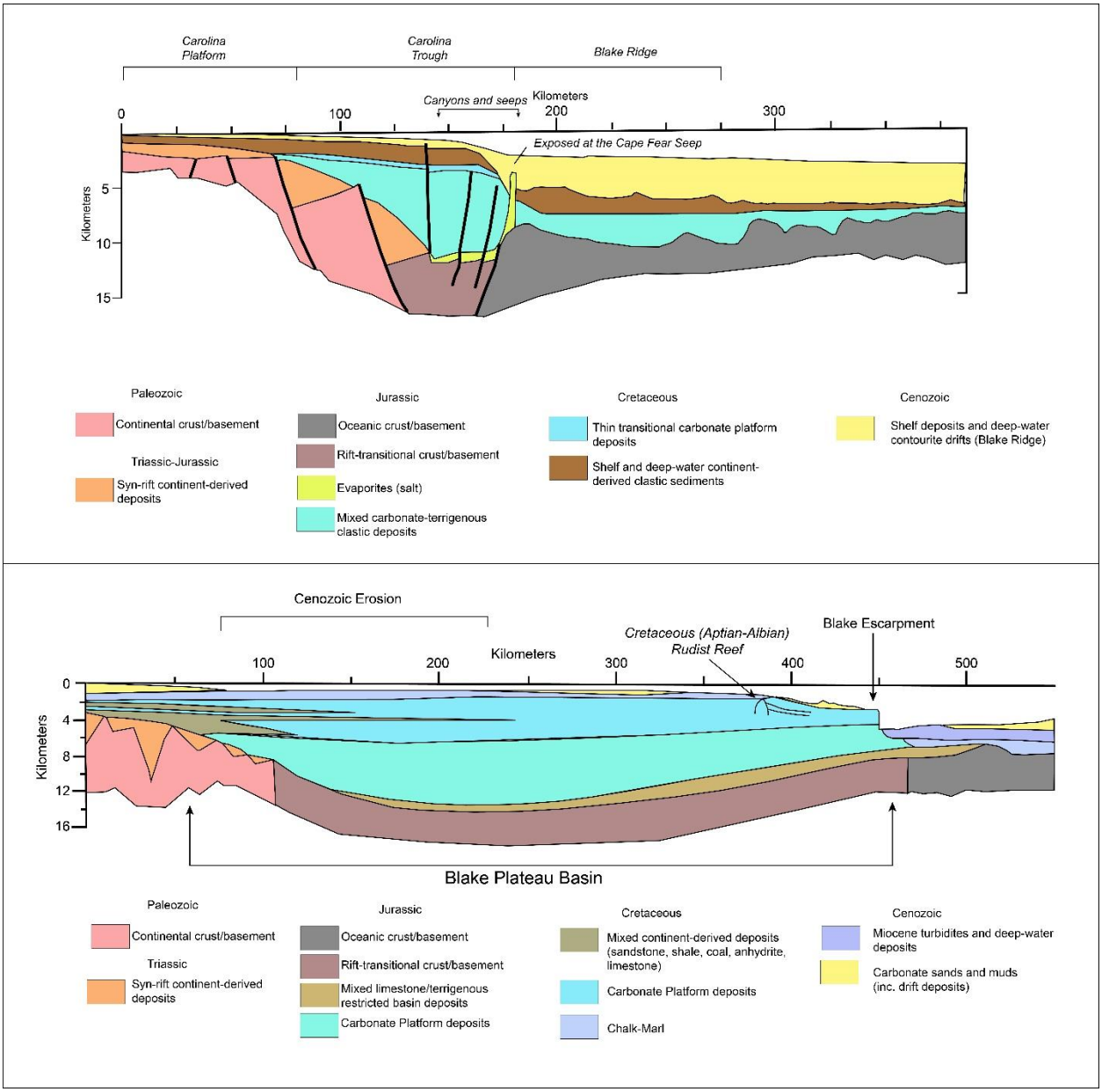

Figure 3-16. Schematic diagrams of the antecedent geology of the Deep SEARCH study area Carolina Trough (A) and Blake Plateau Basin (B) from the coastal plain to the deep sea. Modified from Dillon and Popenoe (1998).

3.2.2 Geomorphology

The regional physiography and geomorphology of the Carolina Margin and Blake Plateau were well established in the literature prior to the Deep SEARCH project as a result of extensive depth soundings (Pratt and Heezen 1964), sidescan (GLORIA; EEZ-SCAN 87, 1991), and seismic studies (Ewing et al. 1966, Popenoe 1980). Extensive ground truthing of seafloor interpretations across the study area revealed by geophysical and other remote sensing data has generally been limited to widely spaced regional seafloor sampling activities (Hollister 1973) or highly focused visual and sampling activities (Stetson et al. 1969, Reed et al. 2006). High-resolution bathymetry (better than 100-m grid resolution) of the upper

slope and shelf in the years prior to this project identified the locations of a large number of seeps, including the Pea Island and Kitty Hawk Seeps. Such also revealed the complete and complex nature of the canyons, gullies and interfluves that shape the slope from Norfolk Canyon in the north to the reentrant adjacent to the Cape Lookout Landslide **(Figure 3-17**). Although the generalized geomorphology of the Blake Plateau has been known for some time due to extensive seismic reflection, single beam echosounder and visual surveys, continuous high-resolution bathymetry data were largely absent from most of the plateau. Extensive bathymetric surveys of the Blake Plateau began in 2018 and still continue, revealing the complexity and diversity of the seafloor across the entire region. The focus here will be in the local geomorphology of the focus areas of the project, with a more detailed description of the regional morphology described by (Dillon and Popenoe 1988, Popenoe 1994, Popenoe and Manheim 2001).

3.2.2.1 Seeps

Seep sites visited during this project occurred in two fundamentally different geologic environments. The Kitty Hawk and Pea Island seeps are located along the shelf-edge and upper slope, adjacent to the heads of slope canyon systems, while the Blake Ridge and Cape Fear seeps are located in deeper water along the Blake Ridge drift and adjacent to the Cape Fear Diapir, respectively.

The shallow-water Pea Island and Kitty Hawk Seeps are located at the continental shelf edge partially within and adjacent to tributaries at the heads of slope canyons. Based on the regional bathymetric and other acoustical imaging data, the seafloor in these areas is generally draped by thick sediments resulting in a smooth and featureless morphology, except for the large canyon system elements. At a local scale, low-relief seep-related authigenic carbonate outcrops and depression (gas release and benthic fauna related) are scattered across broad areas in these shelf-edge environments along the north and mid-Atlantic margin (Prouty et al. 2016).

The Cape Fear and Blake Ridge seeps are found in water depths greater than 2,000 m and are associated with the large SEUS continental margin methane hydrate province (Tucholke et al. 1977, Paull and Dillon 1981). In this region, disturbance of the hydrate stability field by a line of salt diapirs has facilitate development of seafloor chemosynthetic communities across various bottom morphologic regions. The Cape Fear Seep is unique along the US Atlantic continental margin, sitting adjacent to the only salt diapir with material seafloor expression, previously unroofed by seafloor instability and large-scale failure of the region (Cape Fear landslide; Popenoe 1993). The top of the diapir forms a dome-shape mound standing as much as 250 m above the surrounding seafloor and is surrounded by partially sediment draped landslide features (scars and scarps) and the surface expression of faults (Hornbach et al. 2007) within a wider area of bottom-current shaped bedforms. The Blake Ridge Seep is located on the northeastern flank of the Blake Ridge drift over the buried Blake Ridge Diapir 600 m below the seafloor. Faults and other fractures form the fluid migration pathways between the buried diapir and the seafloor seep environment (Paull et al. 1995). The seafloor around the Blake Ridge Seep is generally smooth due to the thick layers of carbonate ridge hemipelagic sediment (Paull et al. 1995), but shallow depressions around the main seep area are visible even in lower-resolution bathymetry. Large-scale contourite bedforms are present to the east of the area.

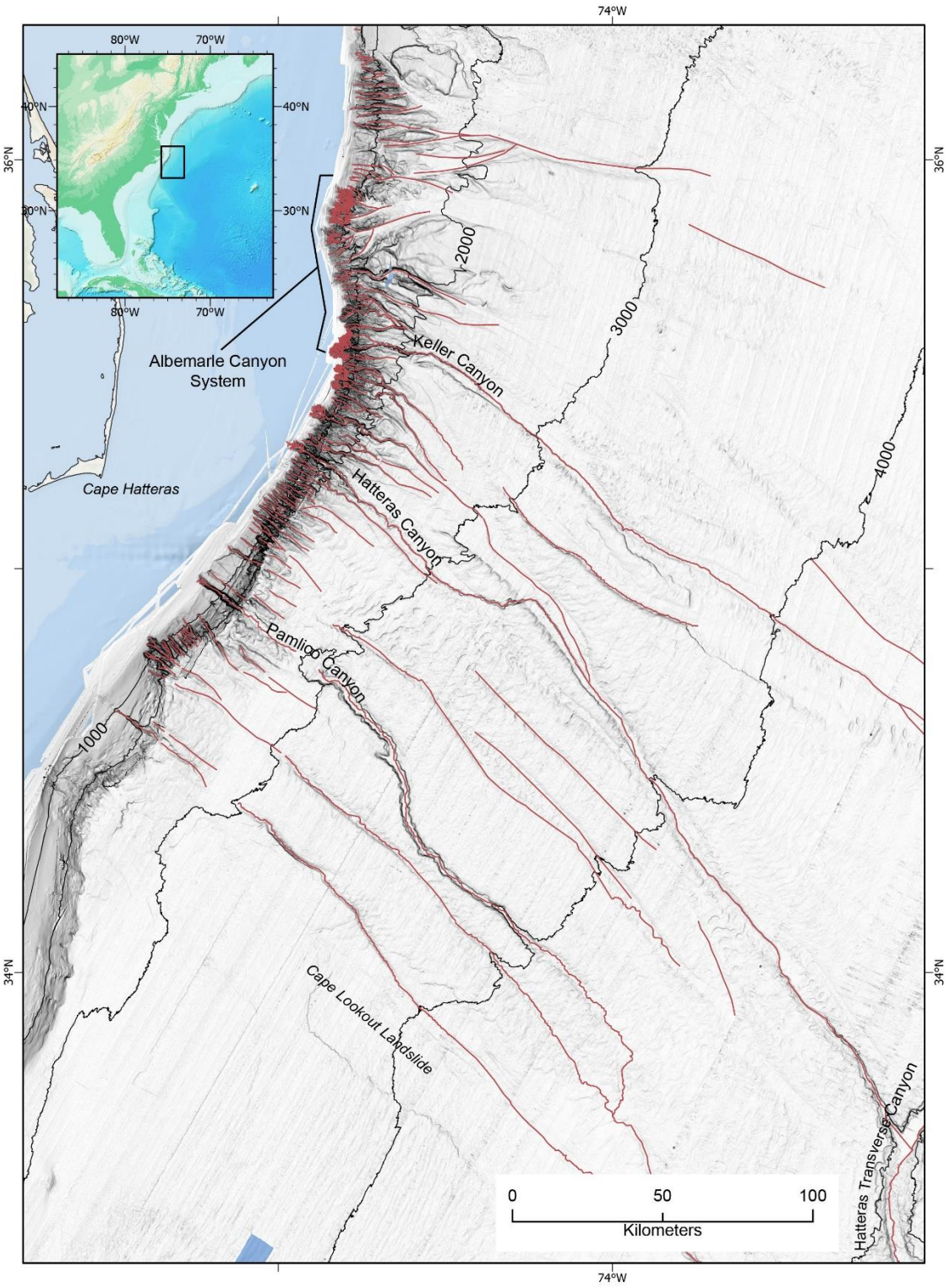

Figure 3-17. Bathymetry and geomorphologic features of canyon systems
Seabed channels (marked in red) within the study area

3.2.2.2 Canyons

Within the study area, canyons and slope gullies are primarily restricted to the section of the margin between Norfolk and Pamlico Canyons. South of Pamlico Canyon, there is evidence of downslope erosive flow, but effective development of transport pathways is largely absent and canyon/gully complexity is greatly reduced. Major named canyon and tributary systems, those with defined shelf-breaching or shelf-edge heads and downslope channels, within the study area include Norfolk, Keller, Hatteras, and Pamlico Canyons, with numerous unnamed canyons and gullies distributed between each (**Figure 3-17**). The "Albemarle canyon system" (ACS), as defined by Popenoe and Dillon (1996), comprises three generally parallel well-defined canyon/channel features draining an approximately 22-km long section of the margin. Keller Canyon is the southernmost and only named canyon within the ACS and the only one that currently has a well-defined channel extending down the lower slope to a deepwater submarine fan.

The heads of Keller and the other ACS canyons, the broadly shelf-indenting drainage just to its north, and immediately adjacent canyons and gullies, deeply dissect a 30-km long section of the shelf and upper slope offshore the northern Outer Banks. High-order dendritic drainage patterns at the canyon and gully heads coalesce within 15 km of the shelf edge into single U-shaped slope- channels. These channels appear to be capturing and storing the bulk of the sediments entering the system. The number and complexity of the gullies and canyons in this region have created an upper-slope morphology characterized by high and steep interfluves, sediment and debris filled canyon floors, and a patchwork of uneroded relict slope sections. South of Keller Canyon, the orientation of the margin changes to NE–SW and the upper-slope, stream-order complexity of the canyon systems drops. Between, and inclusive of, Hatteras and Pamlico Canyons, deep and parallel canyons and gullies heavily dissect the upper slope, often extending downslope only short distances (< 20 km) before appearing to terminate at the base of the steep upper slope section. The canyons and gullies likely extend further downslope but have been filled with down- and along-slope transported sediments. Low-relief ridges and mounds, presumably some of which host seep-related environments (Skarke et al. 2013), are present along the shelf edge above the heads of these canyons and gullies.

Hatteras Canyon is the southernmost of the canyons to have a head defined by prominent dendritic distributaries. These distributaries rapidly coalesce into a generally straight, U-shaped canyon with steep walls and numerous steps in the downslope profile. Previous description of the canyon identified evidence of mass wasting and debris accumulation within the canyon (Popenoe and Dillon 1996). Channel sinuosity increases slightly as the canyon opens out onto the shallow gradient lower slope, and at approximately 3,300 m, the main channel combines with other lower-slope crossing channels before draining into the Hatteras Transverse Canyon.

Early surveys of Pamlico Canyon (Rona, 1970, Stanley et al. 1981, Popenoe and Dillon 1996,) identified the unique morphology of this canyon (relative to other canyons in the study area), with straight but asymmetric shape, no clearly identifiable dendritic distributary channel network at the canyon head, deep incision into the underlying strata, and apparent lack of connection to a lower-slope channel. Bathymetry data collected in the years immediately prior to Deep SEARCH revealed that a broad mass wasting scar encompassed Pamlico Canyon and the upper-slope section to the north (**Figure 3-17**), and that although currently separated by canyon fill and a mix of down- and along-slope transported sediments, a lower-slope channel previously connected Pamlico Canyon to the Hatteras Transverse Canyon. A detailed description of the morphology of Pamlico Canyon is presented in **Section 3.2.3**. Immediately south of Pamlico Canyon, short slope gullies have formed around an amphitheater-shaped reentrant into the margin and on the open slope (**Figure 3-17**). Although these gullies are tightly restricted to the steepest section of the upper slope, the presence of several headless lower-slope canyons 40 km SE of the current mouths of these gullies suggests that they were perhaps much more effective drainages prior to enhancement of along-slope and debris flow deposition in the region.

3.2.2.3 Blake Plateau

As described in **Section 3.2.1**, the Blake Plateau and adjacent areas have been constantly shaped by periods of erosion and deposition for tens of millions of years, driven by shifts in the prevailing oceanographic regime—principally the Gulf Stream. The geomorphology of the Blake Plateau as seen today not only reflects the dynamic nature of these oceanographic and geologic processes (the broader Blake Plateau province within the study area includes antecedent geology related to both the Carolina Trough and Blake Plateau Basin), but also intense biologic construction processes that the unique environment supports. Even though the advances in seafloor mapping have provided an unprecedented view of this dynamic region, the early interpretations of the regional geomorphology remain largely valid.

The most recent compilations of Blake Plateau geomorphology and bottom character (**Figure 3-18** and **Figure 3-19**) are those of Popenoe (1994) and Popenoe and Manheim (2001). These compilations utilized decades of existing seismic-reflection profiles, sidescan mosaics, bathymetric soundings, towed-camera and submersible observations, and bottom sampling (National Ocean Survey 1976, 1979a-e, Pratt 1963, Uchupi 1976) to reveal the nature of the Blake Plateau seafloor and investigate the oceanographic and geologic controls on its formation. Investigators working in the region often separated the Blake Plateau into three morphologic zones: (1) the flat-surfaced and sediment covered southern Blake Plateau (covers Million Mounds), (2) the shallow, rugged and bathymetrically prominent Charleston Bump (Stetson/Savannah Banks, Richardson Hills and Blake Escarpment), and (3) the shallow, down current of the Charleston Bump, and sedimented northern Blake Plateau that overlies the Carolina Trough, rather than the Blake Plateau Basin (Cape Fear coral mounds). While the presence of extensive areas of coral mounds, primarily on the shallower Florida-Hatteras slope, was known as early as 1962 (Stetson et al. 1962, Popenoe 1994), the density and abundance of these features was not appreciated until the availability of modern high-resolution multibeam data across the entirety of the plateau.

Morphologically, the Charleston Bump and adjacent areas to the east dominate the shape of the Blake Plateau within the Deep SEARCH study area. Persistent erosion of the region over millions of years by Gulf Stream currents has dissected the antecedent Blake Plateau Basin stratigraphy, removing thick sections of Paleogene age deposits. Because of the continued focusing of the Gulf Stream through this area, deposition of sediments has been restricted, resulting in complex outcropping of Cretaceous through Oligocene age rocks at the seafloor. Reworking and cementation of phosphate-rich sediments through multiple cycles over millions of years, further add to the ruggedness of the seafloor across the Charleston Bump section of the plateau, resulting in the formation of extremely resistant ferromanganese encrusted phosphorite pavements.

3.2.3 Methods

3.2.3.1 Geology, Mineralogy, and Geochemistry Methods

Our derivation (or update) of regional and site-specific geomorphological interpretations are based on a combination of new and existing bathymetric data, sub-bottom profiles, and dive observations (AT41/RB1903). For regional scale analysis and where higher-resolution data were not available, we used a 25-m resolution (grid cell) bathymetry compilation that merged existing high-quality data with newly collected data from Deep SEARCH (AT41 and RB1903) and NOAA Ocean Exploration (2018 and 2019 NOAA Ship *Okeanos Explorer*) surveys. For the four seeps sites, we used new, from *Sentry* 2017, and existing (Wagner et al. 2013, Brothers et al. 2013) 1- to 2-m resolution *Sentry* AUV acquired bathymetry for interpretation.

Sub-bottom profiles used to support the interpretations are primarily those collected from the hull mounted (Knudsen 3260) chirp sub-bottom profilers installed on the vessels which collected the regional bathymetry data. We used additional sub-bottom profiles collected by the AUV *Sentry* at Pea and Kitty

Hawk Seeps for both investigation of the subsurface and mapping of water-column anomalies at those sites. We used photo transects from the 2017 AUV *Sentry* Deep SEARCH and deep-sea coral surveys of seeps and canyons in the northern segment of the study area to validate interpretations as needed.

We collected sediment cores via a number of methods, including CTD monocorer (MNC-labeled cores), *Alvin* and *Jason* deployed push cores (PU-labeled corers), multicorer (MUC-labeled cores), and piston cores during the 2018 *Brooks McCall* cruise (BMCC PC-labeled cores). We collected rock samples using the manipulators on *Alvin* and *Jason*.

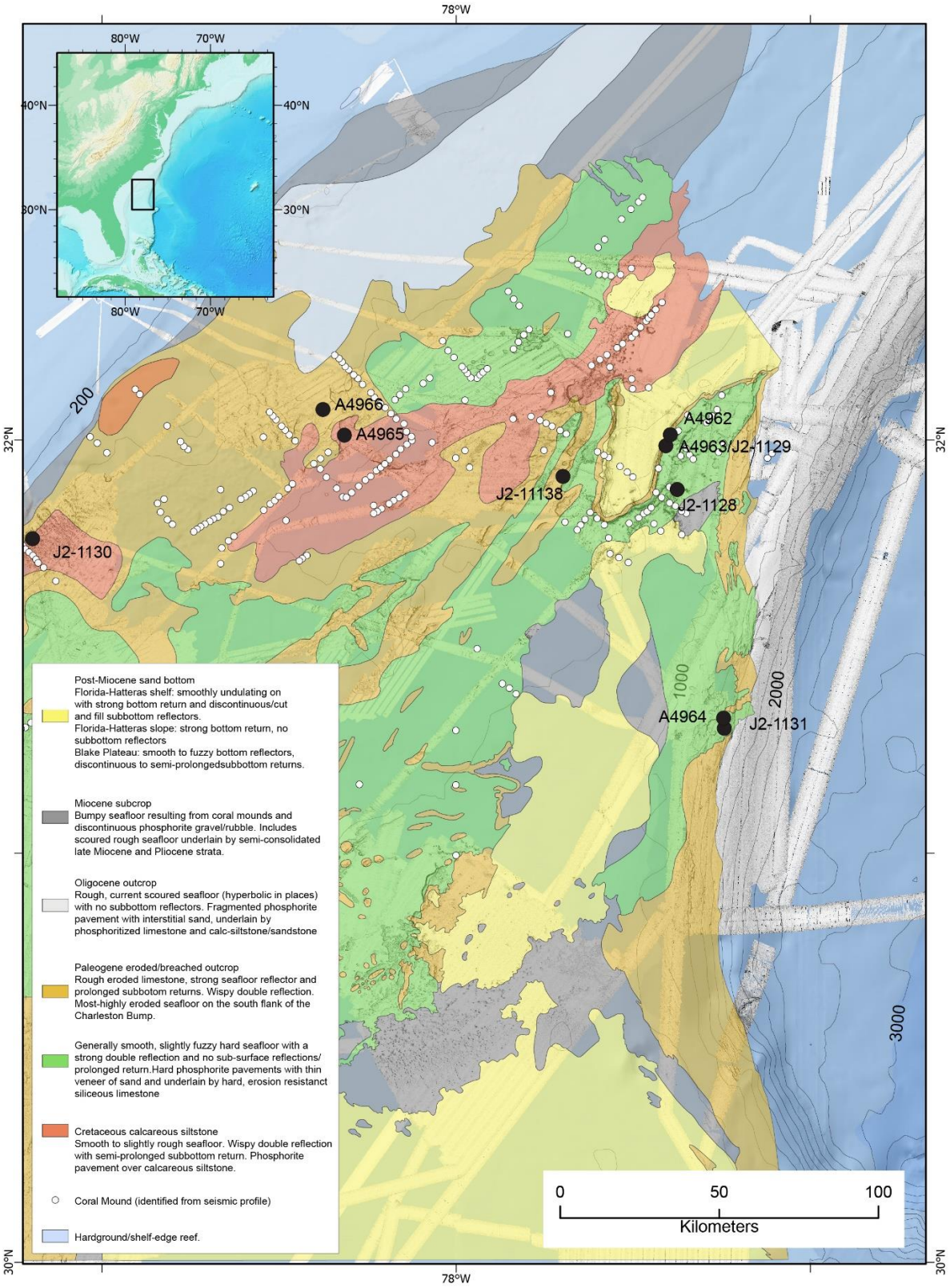

Figure 3-18. Bottom character type of the northern Blake Plateau
From seismic-reflection profiles; 2018 and 2019 dive locations shown. Modified from Popenoe (1993).

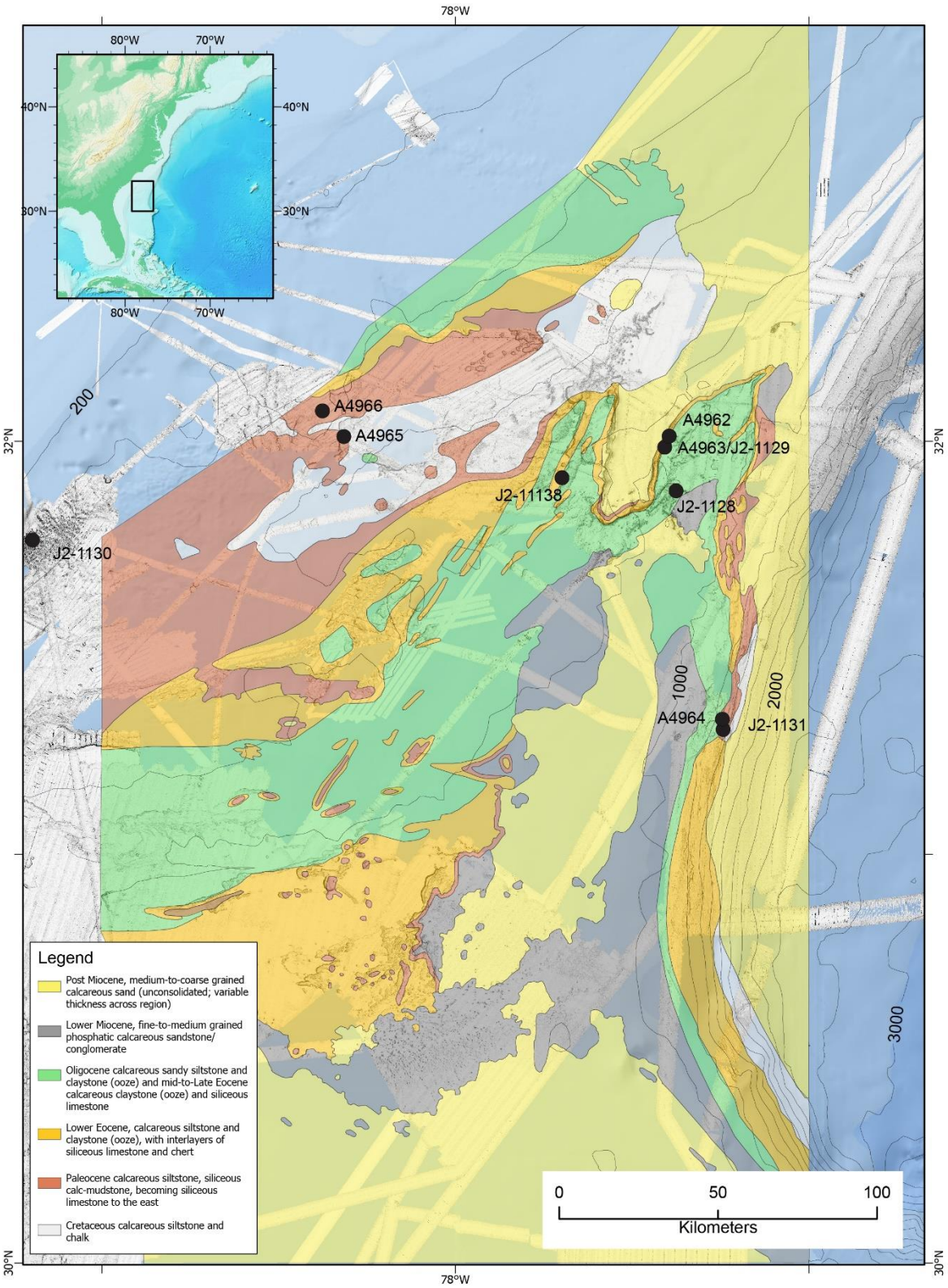

Figure 3-19. Sub-crop morphologic map of the central and northern Blake Plateau
Map shows the surface or near surface exposure of Paleocene through Holocene rock units and sediment accumulation; 2018 and 2019 dive locations shown. Modified from Manheim and Popenoe (2001).

3.2.3.1.1 Sediment Methods

3.2.3.1.1.1 Grain Size

We performed grain size analyses of sediment samples collected during the 2017, 2018, and 2019 cruises in the USGS Woods Hole Coastal and Marine Science Center Sediment Laboratory via laser diffractometry, using established standard operating procedures. Prior to instrument analysis, we weighed the entire sediment sample (or if sample size exceeded 15 g, homogenized subsamples) and then wet-sieved it through a 2-mm (10 US-mesh) sieve into a pre-weighed autosampler vial using distilled water, followed by addition of a small volume of sodium hexametaphosphate to prevent coagulation. If any material was retained by the sieve following wet sieving, the > 2-mm fraction and the vial were placed in an oven until completely dry. After drying, we determined the weight of each fraction, re-wetted the sediment in the vial using distilled water, and passed the > 2-mm fraction through a set of sieves to measure the size distribution of that component.

Once all sample vials were prepared, we sonicated each vial for 10 minutes and loaded into the autosampler of the Horiba LA-960A laser diffractometer. Three analyses of each sample were performed automatically by the instrument. We performed replicate analyses of selected samples at the end of each analysis run. Analysis results from the laser diffractometer and the > 2 mm sieved fractions (if present) are combined and converted to weight percent of primary sediment texture classes of gravel, sand, silt, and clay (Wentworth 1929, Poppe, et al. 2005) and described using the Shepard classification scheme (as modified by Schlee 1973). The final grain size distributions are reported both as 17 size-bins corresponding to phi (ϕ) size classes (Krumbein 1934) between -5 and 11 ϕ (where diameter in mm = 2-ϕ), and as 10x metric size classes between 0.001 µm and 64,000 (µm). We used the logarithmic method of moments technique (Collias et al. 1963) without a "Shepard's Correction" (Kenney and Keeping, 1954) to calculate statistical measures reported in phi-sizes of sample mean, median (D50), SD (sorting), skewness, and kurtosis.

3.2.3.1.1.2 Carbonate Content/Bulk Organic Matter

Calcium carbonate ($CaCO_3$) and bulk organic matter (BOM) content of sediments were determined using a modification of the Loss on Ignition (LOI) method outlined by Dean (1974) that increases heating time at the 550ºC (3 hours) and 950ºC (2 hours) steps. Analyses were made on dried (100ºC for 24 hours), powdered and homogenized subsamples (2–4 g dry weight [DW]) of sediment. The weight differential following the first heating step is assigned entirely to loss of BOM. The weight differential after the second heating step is equated to loss of CO_2 from $CaCO_3$ in the sediment, and the concentration of $CaCO_3$ is calculated by multiplying the weight differential by 2.27. The efficiency of this method is greater than 99% as routinely verified via ignition of a bivalve shell (96–97% $CaCO_3$) standard.

3.2.3.1.1.3 X-Ray Diffraction (XRD) Mineralogy

Quantitative mineralogy of sediments from seep sites and Pamlico Canyon were determined at the USGS Woods Hole Coastal and Marine Science Center via XRD analysis, using a Rigaku Miniflex 600 benchtop x-ray diffractometer utilizing a copper anode tube to generate x-rays operated at 40 kV and 15 mA. Data processing and analysis were performed using the Rigaku PDXL2 software. The Crystallography Open Database (Gražulis et al. 2012), NIST Inorganic Crystal Structure Database (https://icsd.nist.gov/), and the International Centre for Diffraction Data PDF-4/Minerals database (Gates-Rector and Blanton 2019) were used to search and match diffraction patterns and identify component mineral phases. Whole-powder pattern fitting of high-probability candidate phases and Rietveld structure refinement (Bish and Howard 1988) were used for quantitative analysis. Bulk sediments were dried at 100ºC for 24 hrs, powderized using a mortar and pestle and were passed through a 63-µm sieve prior to being packed on aluminum or glass holders as nonselectively oriented powder mounts. Powder mounts

were placed into the internal goniometer and were analyzed at 2θ angles between 3° to 90°, with 0.002° steps/minute. Those samples packed on the aluminum holders were continuously rotated during analysis. At least two powder mounts of each sample were analyzed and processed, with the results averaged in order to minimize spurious peaks or anomalously high peak intensities that would affect the quantitative results. The concentration of different minerals/mineral groups is an average of at least two independent analyses of each sample and reported in weight percent equivalent.

3.2.3.1.1.4 Radiocarbon Dating of Foraminifera

We performed radiocarbon (^{14}C) analysis on single- and mixed species planktonic foraminifera picked from sediment subsamples. Although single-species planktonic foraminifera are preferred for dating, the abundance of foraminifera species within the sediment is highly variable and often necessitated the use of several planktonic species to obtain sufficient material for dating. We submitted samples for Accelerator Mass Spectrometry (AMS) ^{14}C dating at the at the National Ocean Sciences Accelerator Mass Spectrometry facility. The submitted carbonate minerals are directly acidified with strong acid, H_3PO_4, to convert the carbon in the sample to CO_2, educed with use of a catalyst (Fe or Co) in the presence of excess hydrogen ($CO_2 + 2H_2 = C(graphite) + 2H_2O$) to produce graphite for the AMS analysis. Reported radiocarbon age is derived from the $\delta^{13}C$-corrected fraction modern (Fm) (Stuiver and Polach 1977, Stuiver 1980) using a half-life of 5,568 years. Calibrated ages (years before present [YBP]) are calculated using Calib 8.2 (Stuiver et al. 2021) and the Marine20 calibration curve (Heaton et al. 2020), with only the 550-year reservoir correction (no delta-R) applied.

3.2.3.1.2 Rock Methods

We gleaned subsamples of rocks collected during the AT41 and RB1903 cruises for chemical and mineralogic analysis using diamond saws and diamond drill corers. We trimmed slabs cut from the rock samples to remove surface crusts and visible alteration, and further subsampled to target specific lithologies or mineral zones. Samples for chemical and XRD analysis were machine milled, with splits prepared from the homogenized powders. We sent samples for elemental analysis in their original form to facilitate standardized processing.

3.2.3.1.2.1 Major, Minorm and Trace Elemental Composition

We performed analytical geochemistry of rock samples we had collected by the USGS Minerals Resources Analytical Chemistry facility at the Geology, Geophysics, and Geochemistry Science Center in Denver, CO. Unprocessed subsamples of the sampled for XRD analysis were submitted for Wavelength Dispersive X-ray Fluorescence (WDXRF) major element and sixty-element Inductively Coupled Plasma-Optical Emission Spectroscopy-Mass Spectroscopy (ICP-OES-MS) analyses. The samples were prepared by milling to powders of < 150 µm, with the WDXRF slits fused with lithium metaborate/lithium tetraborate flux prior to introduction to the instrument, and ICP-OES-MS samples were fused at 750°C with sodium peroxide with the fusion cake dissolved in a dilute nitric acid to form the analytical solution. Analytical performance is measured by the concurrent analysis of laboratory QAQC samples (including NIST SRM88b) and acceptable comparison (result is no greater than 15% different) of those result with the calculated relative SD of duplicate QAQC samples.

3.2.3.1.2.2 X-Ray Diffraction (XRD) Mineralogy

We performed quantitative mineralogy of authigenic carbonates and other rock samples using the same methods as used for analysis of bulk sediment samples except for additional processing and analysis steps for the low-volume authigenic carbonate cement samples. For these low-volume samples, sample-holder blanks were measured and removed from the resulting patterns, while the Rietveld structural refinement-

WPPF analysis range was restricted to between 2-theta values of 20° and 70° to exclude additional background effects.

3.2.3.1.2.3 Radiocarbon Dating of Authigenic Carbonates

We performed radiocarbon (^{14}C) analysis on splits of the carbonate cement subsamples from authigenic carbonates extracted for XRD analysis. Laboratory analysis methods for authigenic carbonates were the same as for foraminifera as described in Section 3.2.3.1.1.4.

3.2.3.1.2.4 Stable Isotopes of Authigenic Carbonates

Stable carbon ($\delta^{13}C$) and oxygen ($\delta^{18}O$) isotopes were analyzed at the Stable Isotope Geosciences Facility at Texas A&M University and University of Miami. We subsampled authigenic carbonate samples using a hand-held pneumatic drill (a Dremel tool) to sample the authigenic carbonates. We analyzed the resulting powdered carbonate for $\delta^{13}C$ and $\delta^{18}O$ using a Thermo-Finnigan MAT 253 with a Kiel IV Automated Carbonate Prep Device and are reported in per mil (‰) relative to the international reference Pee Dee Belemnite (PDB). Analytical uncertainties (2σ) of 0.04‰ for $\delta^{13}C$ and 0.06‰ for $\delta^{18}O$ are reported based on the long-term daily measurements of the international carbonate standard, NBS-19. We determined carbonate content, reported as weight percent (wt%), using a coulometer at the USGS Pacific Coastal and Marine Science Center, Santa Cruz, CA.

3.2.3.1.2.5 Clumped Isotopes (Δ_{47}) of Authigenic Carbonates

We analyzed authigenic carbonate samples for clumped isotopes (Δ_{47}) using established methods from (Swart et al. 2019) at the University of Miami. Samples weighing between 8 to 10 mg were digested in 105% phosphoric acid (H_3PO_4) held at 90°C. The produced CO_2 was cleaned by passing through a series of traps to remove water. The $\delta^{13}C$ and $\delta^{18}O$ of the CO_2 were calculated from the ratios of masses 45/44 and 46/44 measured using a Thermo 253 and corrected for the typical isobaric interferences using the methods of (Brand et al. 2010). We measured samples against a cryogenically purified in-house reference gas calibrated against NBS 19 and reported relative to Vienna Pee Dee Belemnite (VPDB). Following the methods in (Huntington et al. 2009) raw Δ_{47} values were calculated using the ^{17}O correction values described by (Brand et al. 2010). Final Δ_{47} values (Δ_{47}-processed) were calculated from the Δ_{47}-raw values based on the procedures and standardization methods to place the Δ_{47}-raw values into the carbon dioxide equilibrated scale according to (Dennis et al. 2011). We used the equation of (Swart et al. 2019) to relate Δ_{47} to temperature for the reaction at 90°C (Eq. 1):

$$\Delta_{47}\text{‰} = 0.0392\ (0.0017) * 10^6/T^2 + 0.158\ (0.018)\ (R^2 = 0.985) \qquad \text{(Equation 1)}$$

3.2.3.1.2.6 Uranium-Thorium Dating

We dated U-Th of select authigenic carbonates at the British Geological Survey's Natural Environment Research Council Geochronology and Tracers Facility based on an analytical method modified from Edwards et al. (1987) and Shen et al. (2002), and described in Prouty et al. (2016). Powdered carbonate samples were processed via total dissolution techniques, with isotope ratios measured on a Thermo Neptune Plus multi-collector ICP-MS, relative to a mixed ^{229}Th-^{236}U tracer calibrated against gravimetric solutions of CRM 112a U and Ames laboratory high purity Th. Because authigenic carbonates can incorporate detrital material that carries ^{232}Th, and an associated amount of initial ^{230}Th that is not related to the in situ decay of ^{234}U, a correction was required to calculate a reliable carbonate precipitation age. The detrital isotopic composition was based on measured sediment values from Prouty et al. (2016) from 385 and ~1,600 mbsl along the US Atlantic margin, with the detrital ($^{230}Th/^{238}U$) value for each sample/site interpolated based on water depth. This corrects for both the ^{230}Th contained within the detrital grains, and hydrogenous ^{230}Th produced by the decay of U dissolved in the water column, which

is adsorbed onto the surfaces of sediment particles. Using the decay constants of Cheng et al. (2013), we performed U-Th age calculations using an in-house Excel spreadsheet.

3.2.4 Results

3.2.4.1 Seep Sites

Our work on the local geology at the Cape Fear and Blake Ridge seeps during the Deep SEARCH project was built off of the previous activities at those sites, specifically recent geological and geomorphological analyses based on AUV *Sentry* data by Wagner et al. (2013) and Brothers et al. (2013). The results presented here describing the geology and geochemistry of the Pea Island and Kitty Hawk Seeps represent the first quantitative analysis of these areas. Seabed bathymetries and water-column anomalies from *Sentry* AUV data are shown in **Figure 3-20, Figure 3-21, Figure 3-22, and Figure 3-24** to lay the context for the presence and compositions of authigenic carbonates at these two seep locales.

Overall, the authigenic carbonates at both the upper-slope (Pea Island, **Figure 3-20** and **Figure 3-21**; and Kitty Hawk, **Figure 3-22**) and the deeper diapir-related sites (Blake Ridge, **Figure 3-23**, and Cape Fear, **Figure 3-24**) are quite similar in their mineralogic and geochemical composition, with minor, but obvious variations due to the primary background sedimentation environment.

Calcium carbonate in the form of aragonite ($CaCO_3$) dominates the authigenic carbonate samples recovered (36.6–97%, all samples), with the aragonite content in cements (86–97%) accounting for the higher concentrations. Secondary amounts of low- and high-Mg calcite and dolomite are present, accounting for up to 25% of the groundmass, apart from the single authigenic carbonate sample from the Cape Fear Seep which is composed of 94% dolomite (**Figure 3-24**). Dolomite is present and generally more abundant with the sediments proximal to the authigenic carbonate outcrops (**Table 3-2**). Detrital components, primarily hosted in the groundmass, include quartz, plagioclase and potassium feldspars, micas (muscovite and biotite), pyroxenes, amphiboles, and variable amounts of clay phases.

The concentrations of quartz (SiO_2) and calcite as seen in both the XRD and WDXRF (**Table 3-3**) results reveal the primary mineralogic difference between the shallow shelf edge (higher quartz concentration) and deeper diapir-related site (higher calcite conc.), which are primarily a reflection of the terrigenous-detrital and biogenic components of the surrounding sediments (**Table 3-2, Table 3-3, Figure 3-20, Figure 3-21, Figure 3-22, and Figure 3-24**).

Because of fundamental control that the surrounding sediments have on the final form of the authigenic rock, the texture of the carbonates is best described as a terrigenous-detrital and biogenic clast “breccia” supported by fine-grained aragonite cemented matrix (**Figure 3-25**). Large (> 5 cm long) bivalve shells incorporated into the matrix of the authigenic carbonate were only collected in a single sample, AT41-AL4967-R2 from the Blake Ridge Seep. Voids, fractures and skeletal bioclasts are filled by bladed (fibrous) aragonite (**Figure 3-25**) or aragonite cemented fine-grained sediments. The mineral composition and texture of the carbonates from all visited sites compare closely with those from the Norfolk and Baltimore Canyon seeps as described by Prouty et al. (2016).

Trace element geochemistry of selected bulk samples from the Pea Island, Kitty Hawk and Blake Ridge Seep sites show that the whole-rock composition of the carbonates is closely aligned across the different environments, with variations due to the source of the background sediments. **Table 3-4** shows a comparison of selected trace element concentrations from 11 samples across the three seep sites where these data are available, with the most pronounced, but relatively minor variations between the samples seen for elements predominantly represented in the sedimentary terrestrial detrital mineral fraction (Si, Ti, Zr, Mo, and Hf enhanced at Pea Island and Kittyhawk) or the biogenic fraction (Ca and Sr enhanced at Blake Ridge).

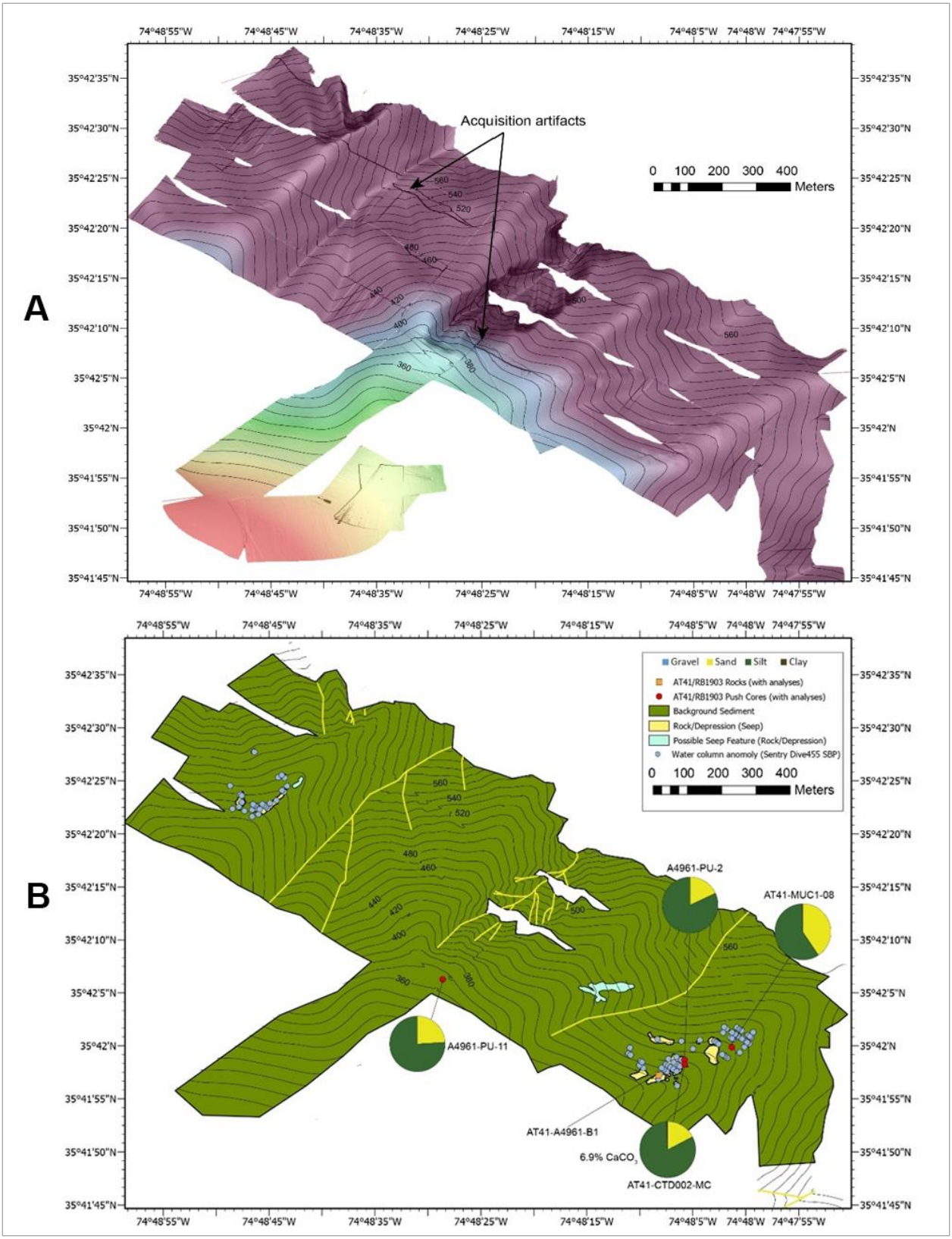

Figure 3-20. Pea Island North bathymetry and water-column anomalies
(A) 1-m resolution AUV *Sentry* bathymetry and (B) interpreted seafloor character and water-column anomalies

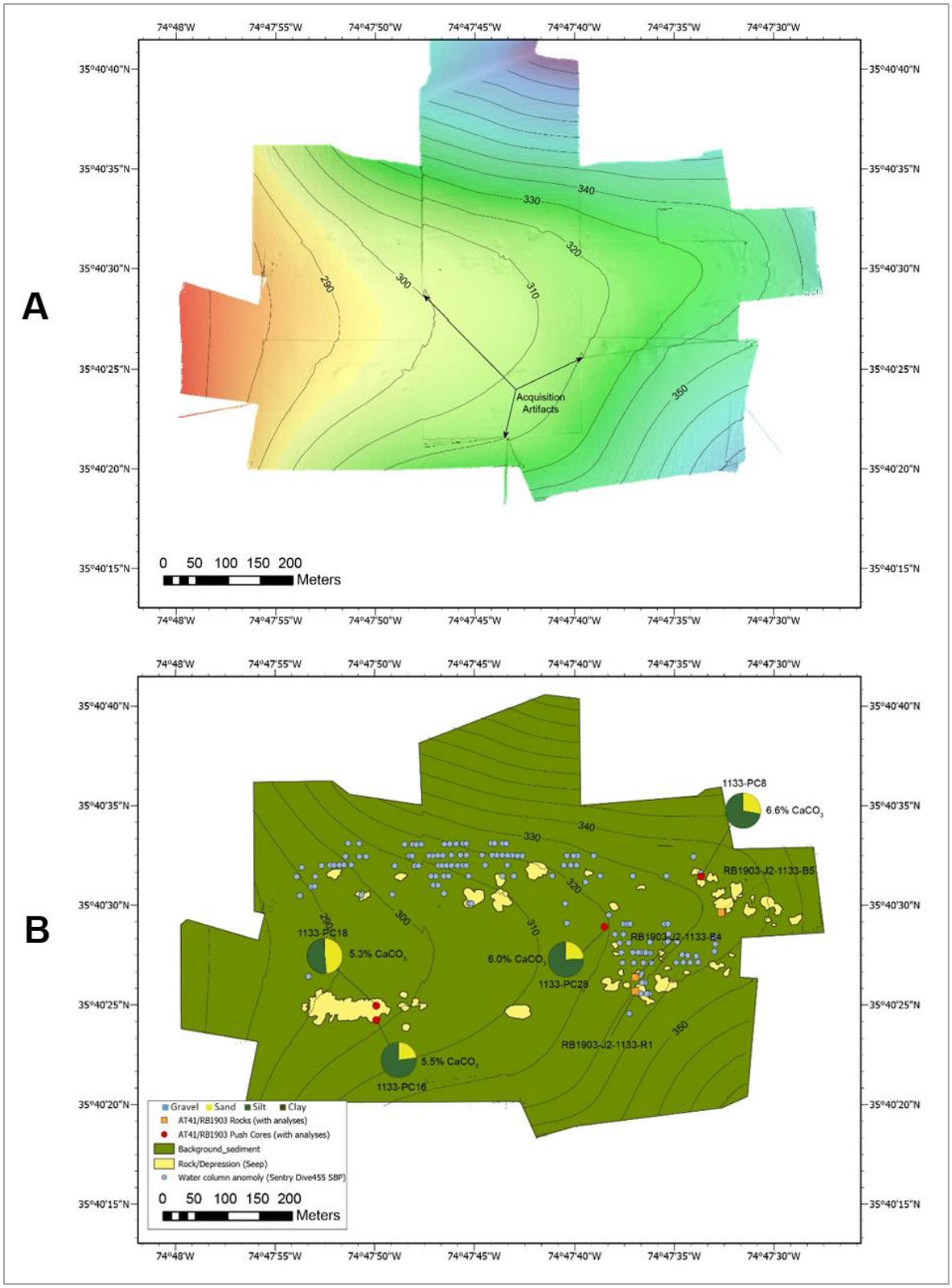

Figure 3-21. Pea Island South bathymetry and water-column anomalies
(A) 1-m resolution AUV *Sentry* bathymetry and (B) interpreted seafloor character and water-column anomalies

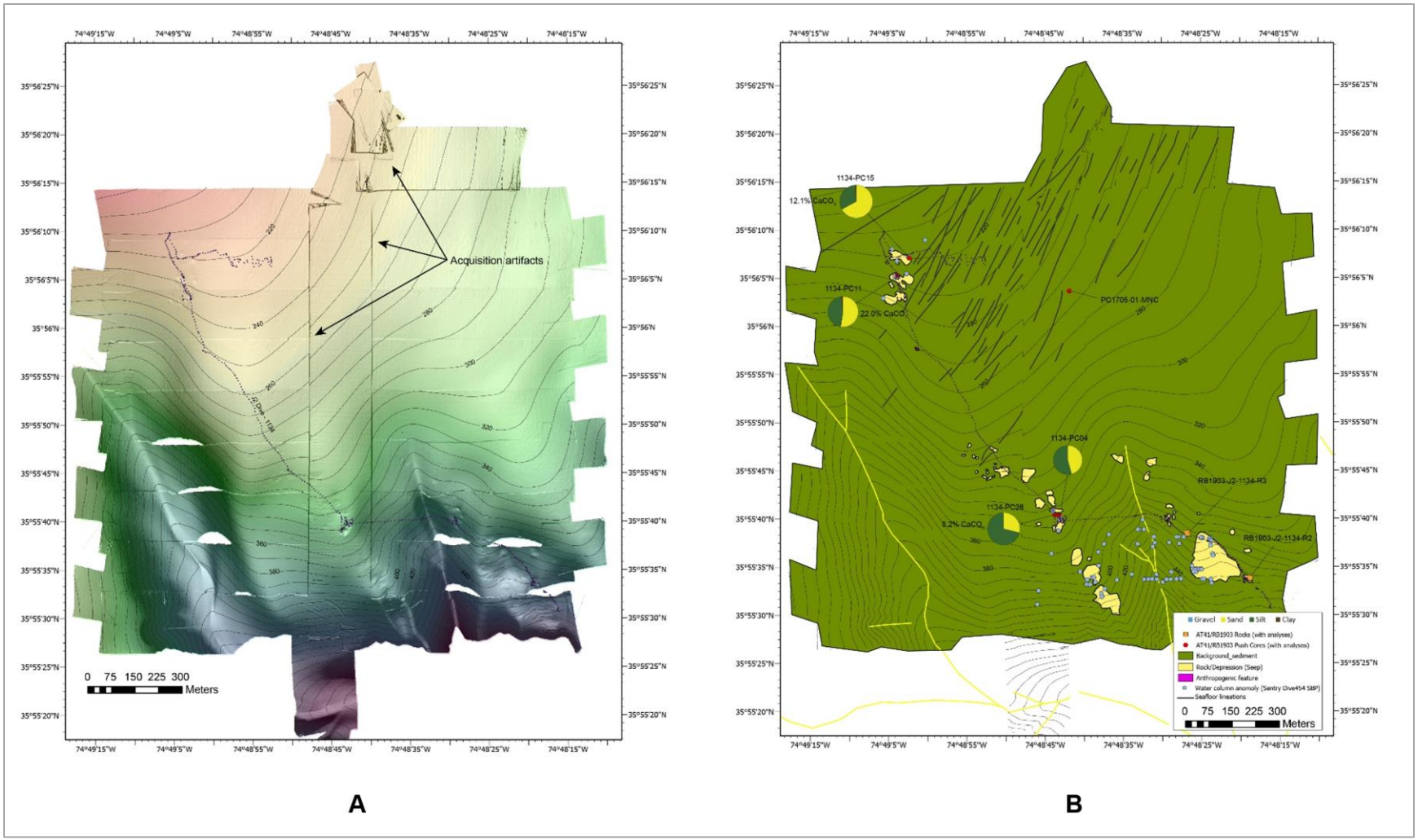

Figure 3-22. Kitty Hawk seep bathymetry and column anomalies
(A) 1-m resolution AUV *Sentry* bathymetry and (B) water interpreted seafloor character and water-column anomalies

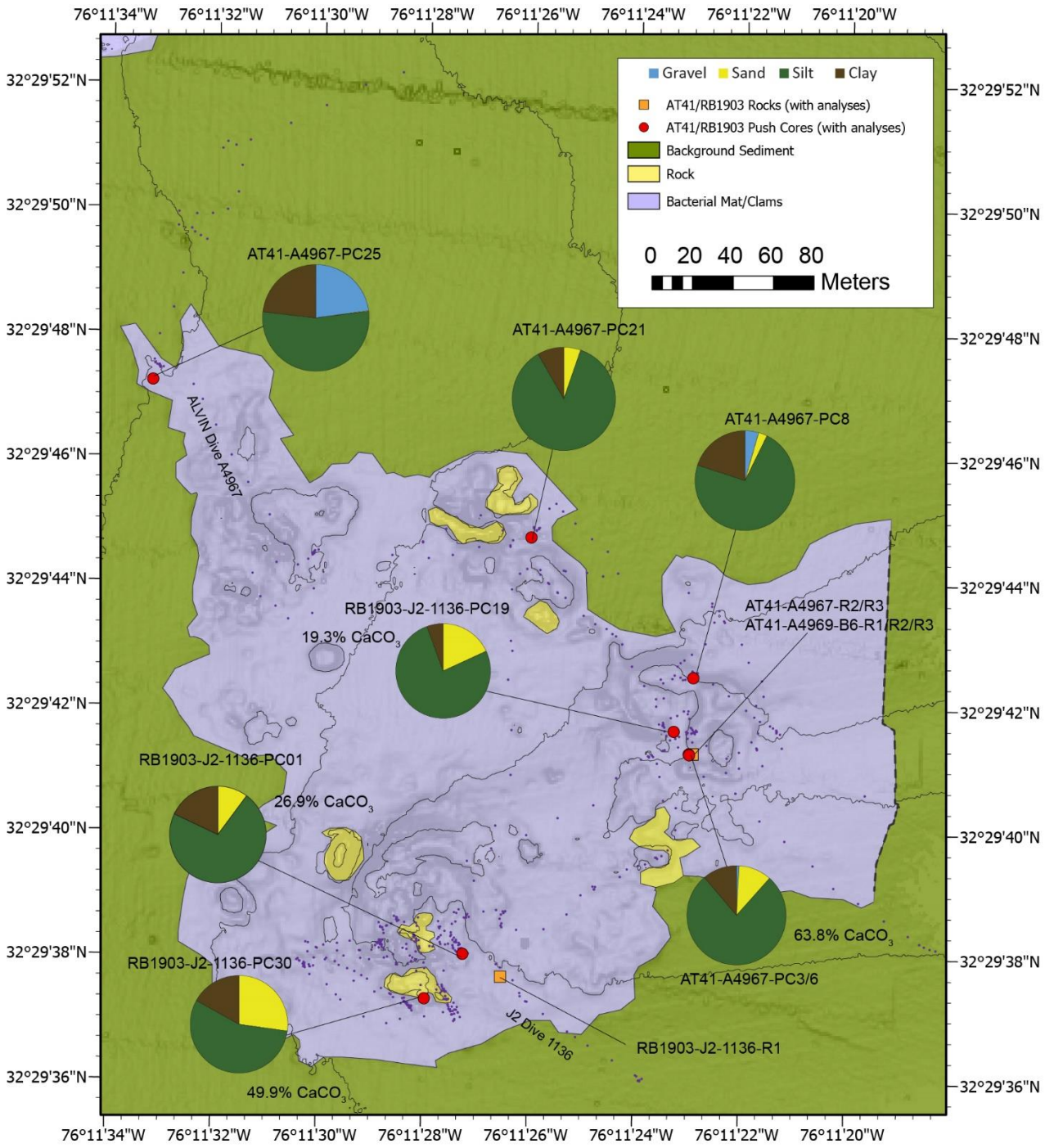

Figure 3-23. Blake Ridge Seep bathymetry and water-column anomalies (1-m resolution)
AUV *Sentry* bathymetry and interpreted seafloor character and sample information (bathymetry data from Van Dover, Duke University, 2018, unpublished data)

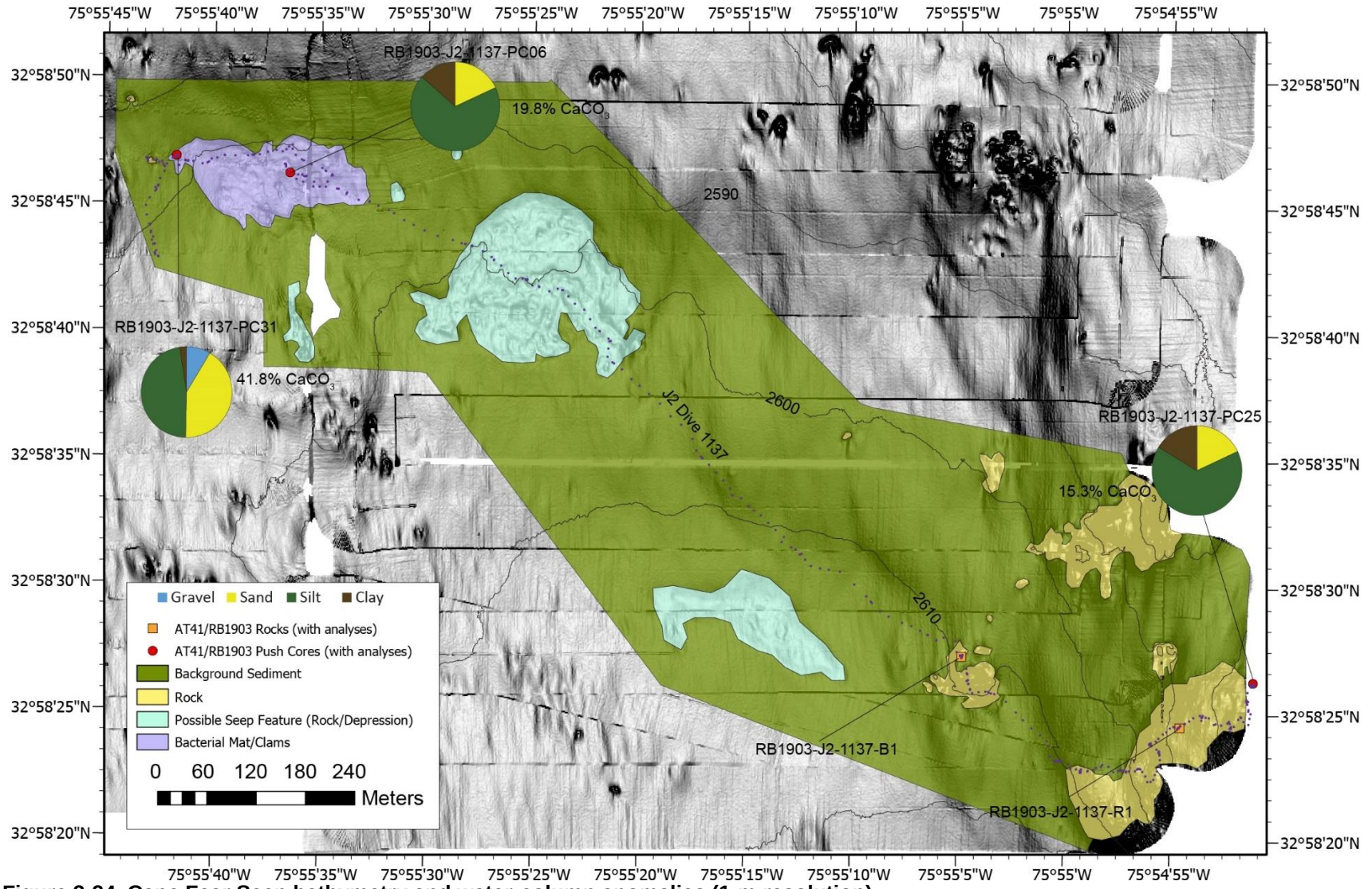

Figure 3-24. Cape Fear Seep bathymetry and water-column anomalies (1-m resolution)
AUV *Sentry* bathymetry and interpreted seafloor character and sample information (data from Van Dover, Duke University, 2018, unpublished data)

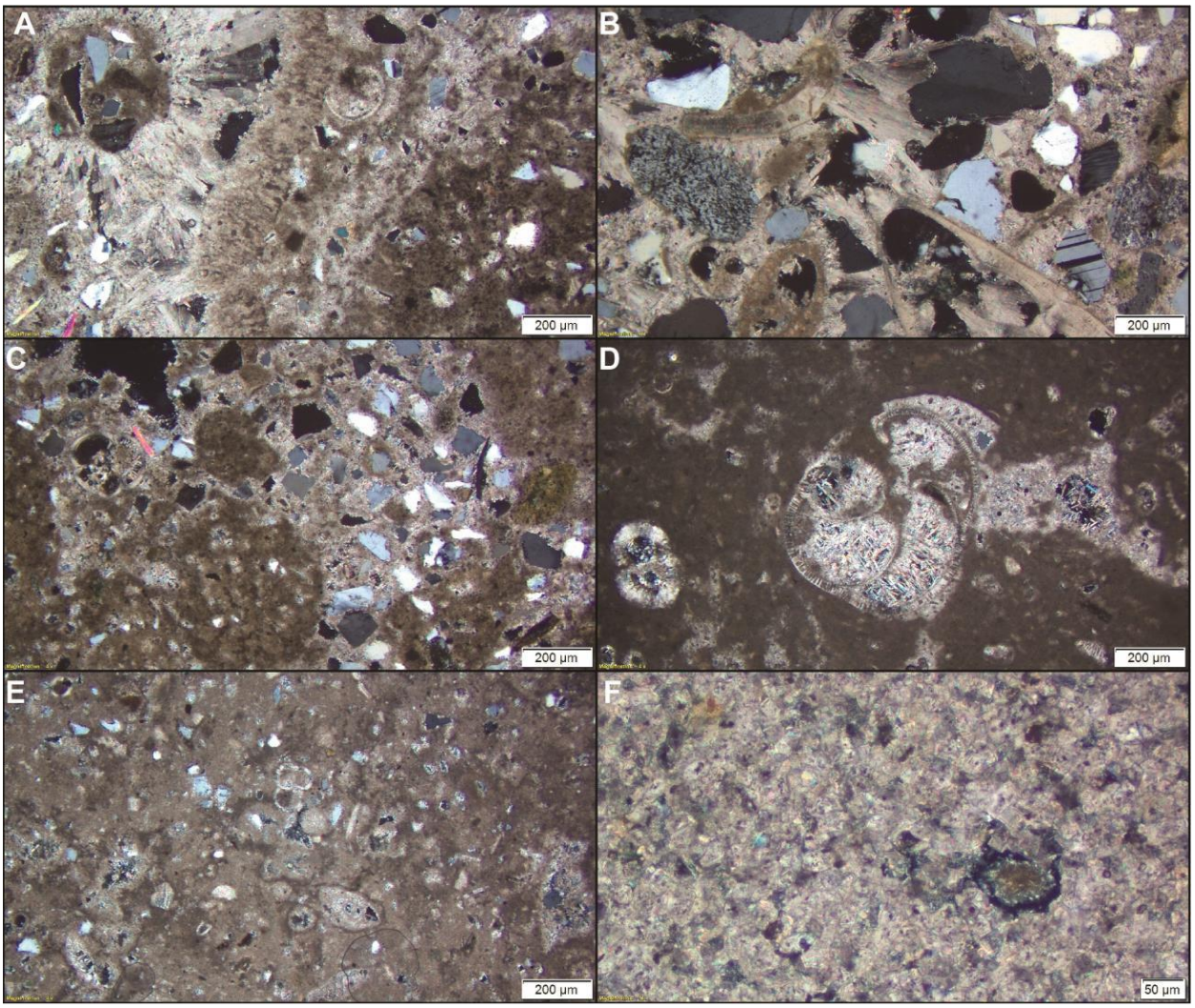

Figure 3-25. Thin section photomicrographs (all cross polarized) of authigenic carbonate samples
(A) Sample RB1903-J2-1133- from the Pea Island Seep with terrigenous components (quartz, feldspars, pyroxenes) and foraminifera tests, bound by a fine-grained aragonite dominated matrix and secondary fibrous aragonite infilling,
(B) Sample RB1903-J2-1134-B4 from the Kitty Hawk seep containing large angular quartz, plagioclase feldspar, heavy and heavy minerals grains, cemented by fibrous aragonite,
(C) Sample RB1903-J2-1134-R2 from the Kitty Hawk seep
(D) Sample RB1903-J2-1136-R1 from the Blake Ridge Seep showing fibrous secondary aragonite formed within a foraminifera test, surrounded by fine-grained carbonate matrix,
(E) Sample AT41-A4967-R2 from the Blake Ridge Seep
(F) Sample RB1903-J2-1137 from the Cape Fear Seep showing the extensive dolomite crystal texture.

Table 3-2. Authigenic carbonate XRD analysis

Results in weight % equivalent units. PI=Pea Island, KW=Kitty Hawk, BR=Blake Ridge and CF=Cape Fear; mica=muscovite/biotite.

Site	Split ID	Sample Type	Quartz	Aragonite	Calcite	High-Mg Calcite	Dolomite	Plag. Feldspar	K Feldspar	Mica	Illite	Chlorite Group	Kaolinite	Smectite/Mont.	Pyroxenes-Titanite	Amphiboles	Other
PI	18042-A4961-B1-X1	Bulk	11.3	70.55	1.21	-	-	10.95	-	1.51	1.25	1.2	-	-	1.3	-	-
PI	18042-A4961-B1-X2	Cement	7.5	86	6	-	-	-	-	-	-	-	-	-	-	-	-
PI	19003-1133-R1-X1	Bulk	18.53	52.367	3.496	-	6.1	4.866	-	2.996	-	1.03	-	-	10.13	0.173	-
PI	19003-1133-R2-X2	Bulk	14.8	67.35	4.515	0.64	0.8	2.45	-	2.77	-	-	-	-	6.45	0.22	-
PI	19003-1133-R1-X3	Cement	3	97	-	-	-	-	-	-	-	-	-	-	-	-	-
PI	19003-1133-B2-X3	Cement	4.5	95.5	-	-	-	-	-	-	-	-	-	-	-	-	-
PI	19003-1133-B5-X1	Bulk	23.45	45.9	2.26	-	4.1	11.61	-	2.285	-	0.65	-	-	8.6	1.385	-
PI	19003-1133-B5-X2	Bulk	21.45	56.7	2.505	-	2.7	7.2	-	1.64	-	0.69	0.55	-	6.55	-	-
KH	19003-1134-R2-X1	Bulk	13.96	62.15	5.2	2.4	2.61	6.05	-	1.855	-	0.595	-	-	4.15	0.75	0.385
KH	19003-1134-R2-X2	Bulk	11.75	67	4.88	2.45	2.09	4.3	-	0.8	-	0.41	-	-	3.55	1.055	2.45
KH	19003-1134-R3-X3	Cement	6.6	93.4	-	-	-	-	-	-	-	-	-	-	-	-	-
KH	19003-1134-B4-X3	Cement	5.8	90.15	3.45	-	-	-	-	-	-	-	-	-	-	-	-
BR	18042-A4967-B6R1	Bulk	5.52	78	4.64	-	-	5.6	-	4.03	-	-	1.3	-	0.3	-	-
BR	18042-A4967-B6R2	Bulk	7.85	75.9	6.3	-	-	4.1	-	4.4	-	-	-	-	1.65	-	-
BR	18042-A4967-R2-X2	Bulk	7.18	67.4	6.07	-	-	7.1	-	2.71	1.1	0.5	0.55	0.99	6.5	-	-
BR	18042-A4967-R2-X3	Bulk	13.05	36.65	7.6	6.6	3	16	-	4.2	-	5.55	-	-	6.45	0.8	-
BR	18042-A4967-R2-X5	Cement	5.5	88.3	6.2	-	-	-	-	-	-	-	-	-	-	-	-
BR	18042-A4967-R3-X1	Bulk	7.7	75	6.2	-	0.55	3.75	-	2.4	-	-	-	-	4.2	-	-
BR	19003-1136-R1-X1	Bulk	3.71	69.6	14	9.75	-	1.01	-	-	-	-	-	-	1.95	-	-
BR	19003-1136-R1-X2	Bulk	3.37	68.55	15.1	10.1	-	0.4	-	-	-	-	-	-	2.5	-	-
BR	19003-1136-R1-X3	Cement	5.15	94.85	-	-	-	-	-	-	-	-	-	-	-	-	-
CF	19003-1137-R1-X1	Bulk	4.55	-	-	-	94.1	-	-	-	-	-	-	1.35	-	-	-

Table 3-3. Major element geochemistry by WDXRF

Oxides in % for selected authigenic carbonate samples (bulk only). PI=Pea Island, KW=Kitty Hawk, BR=Blake Ridge and CF=Cape Fear.

Site	Sample ID	Split ID	Al_2O_3	BaO	CaO	Cr_2O_3	Fe_2O_3	K_2O	LOI	MgO	MnO	Na_2O	P_2O_5	SiO_2	SrO	TiO_2	V_2O_5
PI	AT41-AL4961-B1	A4961.B1.G1	3.04	0.02	35.2	<0.01	1.04	0.7	29.8	0.56	0.02	0.98	0.08	27.7	0.66	0.3	<0.01
PI	RB1903_J2_1133_R1	19003.1133.R1.G1	4.1	0.02	30.2	<0.01	1.47	0.96	24.9	0.79	0.03	0.91	0.1	35.9	0.62	0.33	<0.01
PI	RB1903_J2_1133_B5_01	19003.1133.B5.G1	4.69	0.03	26.8	<0.01	1.76	1.08	22.9	0.97	0.03	1.09	0.12	39.5	0.6	0.37	<0.01
KH	RB1903_J2_1134_RB_02	19003.1134.R2.G1	2.69	0.03	40.2	<0.01	0.96	0.64	33	0.7	0.02	0.7	0.08	21.2	0.81	0.22	<0.01
KH	RB1903_J2_1134_RB_02	19003.1134.R2.G2	2.44	<0.01	41.1	<0.01	0.83	0.61	33.4	0.47	0.02	0.73	0.07	21.2	0.79	0.2	<0.01
KH	RB1903_J2_1134_B4_01	19003.1134.B4.G1	3.14	<0.01	28.5	<0.01	1.38	0.84	23.3	0.49	0.03	0.81	0.08	42.2	0.47	0.29	<0.01
BR	AT41-AL4967-R2	A4967.R2.G1	2.55	0.01	45.4	<0.01	1.07	0.57	37.3	0.64	0.01	0.62	0.06	11.3	0.86	0.14	<0.01
BR	AT41-AL4967-R2	A4967.R2.G3	4.68	0.02	37.1	<0.01	1.85	0.96	31.6	1.59	0.03	1.1	0.07	20	0.75	0.25	<0.01
BR	AT41-AL4967-B6-R1	A4967.B6R2.G1	2.2	<0.01	46.5	<0.01	0.78	0.49	38.9	0.57	<0.01	0.79	0.06	9.31	0.91	0.12	<0.01
BR	AT41-AL4967-B6-R1	A4967.B6R3.G1	3.37	0.01	42.9	<0.01	1.41	0.75	35.8	0.8	0.03	0.78	0.07	14.3	0.82	0.18	<0.01
BR	AT41-AL4967-B6-R1	A4967.B6R1.G1	3.12	<0.01	42.9	<0.01	1.27	0.68	35.9	0.75	0.02	0.81	0.08	14.1	0.82	0.18	<0.01

Table 3-4. ICP-OES-MS Major and trace elements analysis results

For selected authigenic carbonate samples (bulk). Darker shading highlights notably higher concentration in regional seep values relative to the other region (lighter shading). PI=Pea Island, KW=Kitty Hawk, BR=Blake Ridge and CF=Cape Fear.

Site	PI	PI	PI	KH	KH	KH	BR	BR	BR	BR	BR
Sample ID	AT41-AL4961-B1	RB1903_J2_1133_R1	RB1903_J2_1133_B5_01	RB1903_J2_1134_RB_02	RB1903_J2_1134_RB_02	RB1903_J2_1134_B4_01	AT41-AL4967-R2	AT41-AL4967-R2	AT41-AL4967-B6-R1	AT41-AL4967-B6-R1	AT41-AL4967-B6-R1
Split ID	A4961.B1.G1	19003.1133.R1.G1	19003.1133.B5.G1	19003.1134.R2.G1	19003.1134.R2.G2	19003.1134.B4.G1	A4967.R2.G1	A4967.R2.G3	A4967.B6R2.G1	A4967.B6R3.G1	A4967.B6R1.G1
Al %	1.66	2.19	2.49	1.41	1.29	1.62	1.38	2.51	1.16	1.76	1.63
Ca %	23.8	21	18.6	27.8	27.3	19.3	30.1	24.8	31.1	28.2	29.1
Fe %	0.67	1.03	1.22	0.65	0.55	0.93	0.71	1.2	0.52	0.95	0.84
K %	0.65	0.8	0.91	0.55	0.5	0.71	0.52	0.86	0.46	0.69	0.57
Mg %	0.34	0.46	0.56	0.41	0.28	0.3	0.37	0.93	0.32	0.48	0.43
P %	0.04	0.04	0.05	0.03	0.03	0.03	0.03	0.04	0.03	0.03	0.04
S %	0.2	0.3	0.3	0.1	0.1	0.1	<0.1	0.1	<0.1	<0.1	<0.1
Si %	12.5	16.1	17.8	9.57	9.6	18.9	5.04	9.15	4.21	6.55	6.29
Ti %	0.17	0.19	0.22	0.13	0.12	0.16	0.08	0.14	0.07	0.11	0.1
Ag ppm	<1	<1	<1	2	2	<1	<1	<1	<1	<1	<1
As ppm	<5	<5	8	<5	<5	<5	<5	<5	<5	<5	<5
B ppm	28	34	39	27	26	29	27	33	25	36	32
Ba ppm	145	190	213	124	126	190	93	201	79.7	118	111

Site	PI	PI	PI	KH	KH	KH	BR	BR	BR	BR	BR
Sample ID	AT41-AL4961-B1	RB1903_J2_1133_B1	RB1903_J2_1133_B5_01	RB1903_J2_1134_RB_02	RB1903_J2_1134_RB_02	RB1903_J2_1134_B4_01	AT41-AL4967-R2	AT41-AL4967-R2	AT41-AL4967-B6-R1	AT41-AL4967-B6-R1	AT41-AL4967-B6-R1
Split ID	A4961.B1.G1	19003.1133.R1.G1	19003.1133.B5.G1	19003.1134.R2.G1	19003.1134.R2.G2	19003.1134.B4.G1	A4967.R2.G1	A4967.R2.G3	A4967.B6R2.G1	A4967.B6R3.G1	A4967.B6R1.G1
Be ppm	<5	<5	<5	<5	<5	<5	<5	<5	<5	<5	<5
Bi ppm	<0.1	<0.1	0.2	<0.1	0.2	<0.1	<0.1	<0.1	<0.1	<0.1	<0.1
Cd ppm	0.8	0.2	<0.2	<0.2	<0.2	<0.2	<0.2	<0.2	<0.2	0.3	<0.2
Ce ppm	21.5	27.9	30.1	20.2	19.7	21.4	15.2	28.5	14.2	20.6	19
Co ppm	2.7	4.5	4.2	2.4	2	2.7	3.6	6	2.6	4.2	4.1
Cr ppm	14	24	30	17	13	25	17	28	14	22	20
Cs ppm	0.5	1	1	0.6	0.4	0.5	0.9	1.3	0.8	1.2	1
Cu ppm	<5	8	6	8	9	13	7	12	6	9	6
Dy ppm	1.77	2.35	2.48	1.37	1.29	1.63	1.01	1.81	0.95	1.52	1.39
Er ppm	1.09	1.4	1.47	0.79	0.8	0.96	0.58	1.03	0.51	0.8	0.78
Eu ppm	0.46	0.55	0.57	0.31	0.32	0.39	0.29	0.56	0.27	0.39	0.37
Ga ppm	3.83	5.97	6.31	3.6	3.21	4.06	3.27	6.06	2.81	4.13	3.91
Gd ppm	1.97	2.4	2.73	1.72	1.6	1.66	1.34	2.39	1.18	1.74	1.76
Ge ppm	<1	<1	<1	<1	<1	1	<1	<1	<1	<1	<1
Hf ppm	9	7	9	5	6	7	1	2	1	2	2
Ho ppm	0.37	0.47	0.5	0.27	0.25	0.31	0.2	0.35	0.17	0.28	0.27
In ppm	<0.2	<0.2	<0.2	<0.2	<0.2	<0.2	<0.2	<0.2	<0.2	<0.2	<0.2
La ppm	9.8	13.8	14.7	9.7	9.6	10.3	7.6	14.4	7.2	10.7	10.2
Li ppm	12	13	15	<10	<10	<10	14	21	13	17	15
Lu ppm	0.18	0.21	0.23	0.13	0.12	0.15	0.08	0.13	0.07	0.11	0.11
Mn ppm	84	131	148	62	56	172	48	145	<10	74	78
Mo ppm	5	4	6	6	8	3	3	3	<2	2	<2
Nb ppm	4.1	5.7	5.6	3.3	2.7	3.9	2.1	3.4	1.5	2.4	2.4
Nd ppm	10.4	13.9	14.5	9.9	9.9	10.2	7.2	13.9	6.8	9.8	9.4
Ni ppm	6	8	12	10	9	5	9	16	7	10	9
Pb ppm	<5	7	7	<5	<5	11	<5	6	<5	5	6
Pr ppm	2.72	3.6	3.75	2.57	2.52	2.6	1.91	3.53	1.75	2.58	2.41
Rb ppm	20.7	29.5	33	19.3	16.9	22.1	21.9	34.5	18.2	27.3	24.9
Sb ppm	<0.1	0.2	0.1	<0.1	<0.1	0.1	<0.1	<0.1	<0.1	<0.1	<0.1
Sc ppm	<5	<5	<5	<5	<5	<5	<5	<5	<5	<5	<5
Se ppm	<5	<5	<5	<5	<5	<5	<5	<5	<5	<5	<5
Sm ppm	2.1	2.8	2.9	2	2.1	1.9	1.4	2.4	1.3	1.8	1.8
Sn ppm	<1	<1	3	<1	<1	2	<1	<1	<1	<1	<1
Sr ppm	5,460	4,900	4,690	6,320	6,240	3,590	7,000	6,200	7,490	6,770	6,730
Ta ppm	<0.5	<0.5	<0.5	<0.5	<0.5	<0.5	<0.5	<0.5	<0.5	<0.5	<0.5

Site	PI	PI	PI	KH	KH	KH	BR	BR	BR	BR	BR
Sample ID	AT41-AL4961-B1	RB1903_J2_1133_B1	RB1903_J2_1133_B5_01	RB1903_J2_1134_RB_02	RB1903_J2_1134_RB_02	RB1903_J2_1134_B4_01	AT41-AL4967-R2	AT41-AL4967-R2	AT41-AL4967-B6-R1	AT41-AL4967-B6-R1	AT41-AL4967-B6-R1
Split ID	A4961.B1.G1	19003.1133.R1.G1	19003.1133.B5.G1	19003.1134.R2.G1	19003.1134.R2.G2	19003.1134.B4.G1	A4967.R2.G1	A4967.R2.G3	A4967.B6R2.G1	A4967.B6R3.G1	A4967.B6R1.G1
Tb ppm	0.3	0.41	0.39	0.24	0.24	0.25	0.19	0.33	0.16	0.26	0.24
Te ppm	<0.5	<0.5	<0.5	<0.5	<0.5	<0.5	<0.5	<0.5	<0.5	<0.5	<0.5
Th ppm	2.7	3.5	3.9	3	2.3	2.5	2	3.5	2	2.8	2.6
Tl ppm	<0.5	<0.5	<0.5	<0.5	<0.5	<0.5	<0.5	<0.5	<0.5	<0.5	<0.5
Tm ppm	0.16	0.21	0.23	0.14	0.12	0.14	0.09	0.14	0.07	0.12	0.11
U ppm	5.66	3.67	4.98	3.96	5.39	3.42	6.83	7.17	5.59	8.92	5.67
V ppm	20	26	30	18	16	20	25	34	20	36	33
W ppm	<1	<1	<1	<1	<1	<1	<1	<1	<1	<1	<1
Y ppm	9.3	13.5	14	7.8	7.1	8.9	5.1	8.7	4.5	7.3	7.1
Yb ppm	1.1	1.4	1.6	0.8	0.9	1.1	0.6	0.9	0.5	0.8	0.7
Zn ppm	<5	11	15	<5	<5	11	<5	14	<5	6	6
Zr ppm	331	277	312	201	223	276	48	70.2	41.5	61.4	68.1

Table 3-5 shows XRD analysis results from selected sediment samples collected by push core or from sediment removed from recovered rock samples. **Table 3-6.** Shows ICP-OES-MS major and trace elements analysis results for selected authigenic carbonate samples (bulk).

Table 3-5. XRD analysis results from selected sediment samples

Results in weight % equivalent units. collected by push core or from sediment removed from recovered rock samples (BKSED samples). PC= Pamlico Canyon, PI=Pea Island, KH=Kitty Hawk, BR=Blake Ridge and CF=Cape Fear.

Site	Sample ID	Subsample ID	Sediment Depth (cm)	Quartz	Arag.	Calcite	Dolomite	Plag. Feld.		K Feld.	Mica	Illite	Chlorite Group	Kaolinite	Smectite	Pyroxenes	Amphiboles	Garnets	Other Heavy Minerals
PC	At41-A4969-PC02	18042-A4969-2-PU-XRD-1	0	42.65	4.36	13.87	4.09	7.45		0.16	11.47	-	7.20	-	-	5.76	1.37	-	1.62
PC	At41-A4969-PC02	18042-A4969-2-PU-XRD-3	-	32.30	7.19	12.82	--	15.91		1.19	10.28	3.98	0.32	7.80	-	5.73	0.67	1.60	0.21
PC	RB1903-J2-1132-PC07	19003-1132-7-PU-XRD-1	0	32.44	-	9.72		17.25		--	16.85	2.56	2.82	4.50	0.78	6.36	-	3.40	-
PC	RB1903-J2-1132-PC07	19003-1132-7-PU-XRD-2	5	31.52	9.62	10.44	7.66	12.59		2.51	9.51	5.79	0.49	5.79	-	2.37	0.92	0.67	-
PC	RB1903-J2-1132-PC07	19003-1132-7-PU-XRD-3	10	37.27	4.33	13.22	3.25	17.71		2.46	6.23		5.95	4.22	0.32				
PC	RB1903-J2-1132-PC08	19003-1132-8-PU-XRD-1	0	29.67	2.57	13.06	5.04	10.70		3.14	13.21	-	5.27	5.92	-	6.90	1.61	1.23	1.70
PC	RB1903-J2-1132-PC14	19003-1132-14-PU-XRD-1	0	34.61	-	12.24	3.72	13.33		0.41	17.41	-	7.55	-	-	9.24	0.77	0.72	-
PI	RB1903-J2-1133-PC08	19003-1133-8-PU-XRD-1	0	34.60	-	6.27	-	9.59	8.05	17.45	-		6.08	1.13	3.83	4.64	0.41	-	-
PI	RB1903-J2-1133-PC08	19003-1133-8-PU-XRD-2	10	40.58	-	5.19	5.50	14.52	5.35	10.27	1.02		3.45	3.29	-	8.53	2.31	-	-
PI	RB1903-J2-1133-PC16	19003-1133-16-PU-XRD-1	0	44.91	-	6.16	4.03	15.26	4.39	12.57	-		7.66	0.93	-	2.64	1.45	-	-
PI	RB1903-J2-1133-PC16	19003-1133-16-PU-XRD-2	10	37.81	1.18	6.58	6.52	19.47	1.90	9.66	-		5.39	5.45	0.35	0.72	2.92	-	2.05
PI	RB1903-J2-1133-PC28	19003-1133-28-PU-XRD-1	0	39.27	-	4.85	1.65	19.40	5.16	12.05	2.50		8.60	0.94	-	4.54	1.04	-	-
PI	RB1903-J2-1133-PC28	19003-1133-28-PU-XRD-2	10	35.73	-	3.52	9.77	17.76	-	15.88	-		2.44	6.57	-	2.60	2.80	-	-
PI		19003-1133-R1-BKSED	0	33.58	12.21	4.08	11.09	14.40	5.24	8.45	--		3.71	2.39	-	3.56	1.27	-	-
KH	RB1903-J2-1134-PC15	19003-1134-15-PU-XRD-1	0	34.30	6.04	19.72	2.08	8.83	5.94	5.92	-	3.95	0.68	1.50	5.42	5.61	-	-	
KH	RB1903-J2-1134-PC15	19003-1134-15-PU-XRD-2	10	33.49	-	15.86	3.53	15.88	-	14.23	-	5.52	1.41	0.31	9.10	-	0.67	-	
KH		RB1903-J2-1134_BKSED	0	24.61	25.23	9.06	8.23	11.24	4.74	9.06	-	3.08	4.74	-	-	-	-	-	
BR	RB1903-J2-1136-PC01	19003-1136-1-XRD-1	0	19.89	12.91	12.04	9.76	9.39	5.05	8.06	9.58		3.77	8.92	0.61	-	-	-	-
CF	RB1903-J2-1137-PC31	19003-1137-31-PU-XRD-1	0	27.03	11.45	33.12	1.80	4.80	3.76	3.41	4.03		4.03	6.30	-	-	5.00	-	-
CF	RB1903-J2-1137-PC31	19003-1137-31-PU-XRD-2	10	17.04	15.30	26.39	1.07	7.64	4.00	10.98	2.93		4.45	6.90	-	0.78	2.54	-	-

Table 3-6. ICP-OES-MS Major and trace elements analysis results

For selected authigenic carbonate samples (bulk). Elements above the dashed line are reported in %, while those below are in ppm. Darker shading (**) highlights notably higher concentration in regional seep values relative to the other region (lighter shading*).

Site	PI	PI	PI	KH	KH	KH	BR	BR	BR	BR	BR
Sample ID	AT41-AL4961-B1	RB1903_J2_1133_R1	RB1903_J2_1133_B5_01	RB1903_J2_1134_RB_02	RB1903_J2_1134_RB_02	RB1903_J2_1134_B4_01	AT41-AL4967-R2	AT41-AL4967-R2	AT41-AL4967-B6-R1	AT41-AL4967-B6-R1	AT41-AL4967-B6-R1
Split ID	A4961.B1.G1	19003.1133.R1.G1	19003.1133.B5.G1	19003.1134.R2.G1	19003.1134.R2.G2	19003.1134.B4.G1	A4967.R2.G1	A4967.R2.G3	A4967.B6R2.G1	A4967.B6R3.G1	A4967.B6R1.G1
Al	1.66	2.19	2.49	1.41	1.29	1.62	1.38	2.51	1.16	1.76	1.63
Ca	23.8*	21*	18.6*	27.8*	27.3*	19.3*	30.1**	24.8**	31.1**	28.2**	29.1**
Fe	0.67	1.03	1.22	0.65	0.55	0.93	0.71	1.2	0.52	0.95	0.84
K	0.65	0.8	0.91	0.55	0.5	0.71	0.52	0.86	0.46	0.69	0.57
Mg	0.34	0.46	0.56	0.41	0.28	0.3	0.37	0.93	0.32	0.48	0.43
P	0.04	0.04	0.05	0.03	0.03	0.03	0.03	0.04	0.03	0.03	0.04
S	0.2	0.3	0.3	0.1	0.1	0.1	<0.1	0.1	<0.1	<0.1	<0.1
Si	12.5**	16.1**	17.8**	9.57**	9.6**	18.9**	5.04*	9.15*	4.21*	6.55*	6.29*
Ti	0.17**	0.19**	0.22**	0.13**	0.12**	0.16**	0.08*	0.14*	0.07*	0.11*	0.1*
Ag	<1	<1	<1	2	2	<1	<1	<1	<1	<1	<1
As	<5	<5	8	<5	<5	<5	<5	<5	<5	<5	<5
B	28	34	39	27	26	29	27	33	25	36	32
Ba	145	190	213	124	126	190	93	201	79.7	118	111
Be	<5	<5	<5	<5	<5	<5	<5	<5	<5	<5	<5
Bi	<0.1	<0.1	0.2	<0.1	0.2	<0.1	<0.1	<0.1	<0.1	<0.1	<0.1
Cd	0.8	0.2	<0.2	<0.2	<0.2	<0.2	<0.2	<0.2	<0.2	0.3	<0.2
Ce	21.5	27.9	30.1	20.2	19.7	21.4	15.2	28.5	14.2	20.6	19
Co	2.7	4.5	4.2	2.4	2	2.7	3.6	6	2.6	4.2	4.1

Site	PI	PI	PI	KH	KH	KH	BR	BR	BR	BR	BR
Sample ID	AT41-AL4961-B1	RB1903_J2_1133_R1	RB1903_J2_1133_B5_01	RB1903_J2_1134_RB_02	RB1903_J2_1134_RB_02	RB1903_J2_1134_B4_01	AT41-AL4967-R2	AT41-AL4967-R2	AT41-AL4967-B6-R1	AT41-AL4967-B6-R1	AT41-AL4967-B6-R1
Split ID	A4961.B1.G1	19003.11 33.R1.G1	19003.11 33.B5.G1	19003.11 34.R2.G1	19003.11 34.R2.G2	19003.11 34.B4.G1	A4967.R2.G1	A4967.R2.G3	A4967.B6 R2.G1	A4967.B6 R3.G1	A4967.B6 R1.G1
Cr	14	24	30	17	13	25	17	28	14	22	20
Cs	0.5	1	1	0.6	0.4	0.5	0.9	1.3	0.8	1.2	1
Cu	<5	8	6	8	9	13	7	12	6	9	6
Dy	1.77	2.35	2.48	1.37	1.29	1.63	1.01	1.81	0.95	1.52	1.39
Er	1.09	1.4	1.47	0.79	0.8	0.96	0.58	1.03	0.51	0.8	0.78
Eu	0.46	0.55	0.57	0.31	0.32	0.39	0.29	0.56	0.27	0.39	0.37
Ga	3.83	5.97	6.31	3.6	3.21	4.06	3.27	6.06	2.81	4.13	3.91
Gd	1.97	2.4	2.73	1.72	1.6	1.66	1.34	2.39	1.18	1.74	1.76
Ge	<1	<1	<1	<1	<1	1	<1	<1	<1	<1	<1
Hf	9**	7**	9**	5**	6**	7**	1*	2*	1*	2*	2*
Ho	0.37	0.47	0.5	0.27	0.25	0.31	0.2	0.35	0.17	0.28	0.27
In	<0.2	<0.2	<0.2	<0.2	<0.2	<0.2	<0.2	<0.2	<0.2	<0.2	<0.2
La	9.8	13.8	14.7	9.7	9.6	10.3	7.6	14.4	7.2	10.7	10.2
Li	12	13	15	<10	<10	<10	14	21	13	17	15
Lu	0.18	0.21	0.23	0.13	0.12	0.15	0.08	0.13	0.07	0.11	0.11
Mn	84	131	148	62	56	172	48	145	<10	74	78
Mo	5**	4**	6**	6**	8**	3**	3*	3*	<2*	2*	<2*
Nb	4.1	5.7	5.6	3.3	2.7	3.9	2.1	3.4	1.5	2.4	2.4
Nd	10.4	13.9	14.5	9.9	9.9	10.2	7.2	13.9	6.8	9.8	9.4
Ni	6	8	12	10	9	5	9	16	7	10	9
Pb	<5	7	7	<5	<5	11	<5	6	<5	5	6
Pr	2.72	3.6	3.75	2.57	2.52	2.6	1.91	3.53	1.75	2.58	2.41

Site	PI	PI	PI	KH	KH	KH	BR	BR	BR	BR	BR
Sample ID	AT41-AL4961-B1	RB1903_J2_1133_R1	RB1903_J2_1133_B5_01	RB1903_J2_1134_RB_02	RB1903_J2_1134_RB_02	RB1903_J2_1134_B4_01	AT41-AL4967-R2	AT41-AL4967-R2	AT41-AL4967-B6-R1	AT41-AL4967-B6-R1	AT41-AL4967-B6-R1
Split ID	A4961.B1.G1	19003.1133.R1.G1	19003.1133.B5.G1	19003.1134.R2.G1	19003.1134.R2.G2	19003.1134.B4.G1	A4967.R2.G1	A4967.R2.G3	A4967.B6R2.G1	A4967.B6R3.G1	A4967.B6R1.G1
Rb	20.7	29.5	33	19.3	16.9	22.1	21.9	34.5	18.2	27.3	24.9
Sb	<0.1	0.2	0.1	<0.1	<0.1	0.1	<0.1	<0.1	<0.1	<0.1	<0.1
Sc	<5	<5	<5	<5	<5	<5	<5	<5	<5	<5	<5
Se	<5	<5	<5	<5	<5	<5	<5	<5	<5	<5	<5
Sm	2.1	2.8	2.9	2	2.1	1.9	1.4	2.4	1.3	1.8	1.8
Sn	<1	<1	3	<1	<1	2	<1	<1	<1	<1	<1
Sr	5,460*	4,900*	4,690*	6,320*	6,240*	3,590*	7,000**	6,200**	7,490**	6,770**	6,730**
Ta	<0.5	<0.5	<0.5	<0.5	<0.5	<0.5	<0.5	<0.5	<0.5	<0.5	<0.5
Tb	0.3	0.41	0.39	0.24	0.24	0.25	0.19	0.33	0.16	0.26	0.24
Te	<0.5	<0.5	<0.5	<0.5	<0.5	<0.5	<0.5	<0.5	<0.5	<0.5	<0.5
Th	2.7	3.5	3.9	3	2.3	2.5	2	3.5	2	2.8	2.6
Tl	<0.5	<0.5	<0.5	<0.5	<0.5	<0.5	<0.5	<0.5	<0.5	<0.5	<0.5
Tm	0.16	0.21	0.23	0.14	0.12	0.14	0.09	0.14	0.07	0.12	0.11
U	5.66	3.67	4.98	3.96	5.39	3.42	6.83	7.17	5.59	8.92	5.67
V	20	26	30	18	16	20	25	34	20	36	33
W	<1	<1	<1	<1	<1	<1	<1	<1	<1	<1	<1
Y	9.3	13.5	14	7.8	7.1	8.9	5.1	8.7	4.5	7.3	7.1
Yb	1.1	1.4	1.6	0.8	0.9	1.1	0.6	0.9	0.5	0.8	0.7
Zn	<5	11	15	<5	<5	11	<5	14	<5	6	6
Zr	331**	277**	312**	201**	223**	276**	48*	70.2*	41.5*	61.4*	68.1*

Average (±SD) $\delta^{13}C$ and $\delta^{18}O$ isotopes values were -43.33 ± 3.15‰ and 3.70 ±0.42‰, respectively (**Figure 3-27**). While average carbonate $\delta^{13}C$ values at Pea Island (-45.48 ± 2.23‰) are significantly ($p < 0.05$) different than average $\delta^{13}C$ values at Blake Ridge (-41.29 ± 2.99‰) according to one-way analysis of variance (ANOVA) with post-hoc Tukey Honestly Significant Difference (HSD) Test, the difference is less than 4‰. The small range in $\delta^{13}C$ values therefore suggests a common fluid source for carbonate precipitation between Pea Island, Kitty Hawk and Blake Ridge Seep sites. Whereas ^{13}C-enriched values ($\delta^{13}C > -50‰$) indicate a thermogenic methane source, ^{13}C-depleted values ($\delta^{13}C < -50‰$) are indicative of formation from biogenic methane (Bohrmann et al. 1998). Therefore, low $\delta^{13}C$ values are most likely linked to authigenic carbonate precipitation driven by anaerobic oxidation of methane (AOM) via SR ($CH_4 + SO_4^{2-} \rightarrow HCO_3^- + HS^- + H_2O$). This reaction drives an increase in pore water alkalinity by the production of bicarbonate (HCO_3^-) and favors carbonate precipitation.

We investigated the contribution from methane-derived carbon relative to seawater DIC-derived carbon using a two end-member $\delta^{13}C$ mixing model. Using a carbon isotopic composition of methane at Blake Ridge sites of -75‰ and -70‰ from Pea Island methane (Section 3.3.2.4) with a measured seawater DIC value of 0.64‰ (Prouty and Baker 2021), the average contribution from methane is 61% at Pea Island and 57% at Blake Ridge. These results are consistent with previous results along the US Atlantic margin**.** Authigenic carbonate $\delta^{13}C$ values from Norfolk and Baltimore canyons range from -45 to -48‰ with a contribution from methane-derived carbon of ~70% (Prouty et al. 2016). Therefore, results from Pea Island, Kitty Hawk and Blake Ridge are in agreement with $\delta^{13}C$ values at cold-seep sites where microbial AOM is the dominant driver of authigenic aragonite precipitation (Prouty et al. 2020). As discussed in Section 3.3, AOM mediated by methanotrophic archaea and SRB is common in continental margin sediments and plays a key role in the marine carbon cycle. Given the carbonates are aragonite dominated, as presented above, the authigenic carbonates from Kitty Hawk, Pea Island, and Blake Ridge fall into Group I carbonates that typify microbially driven carbonate precipitation within the uppermost few centimeters below the sediment-water interface (Joseph et al. 2013).

Positive $\delta^{18}O$ isotopes values (> 0‰ PDB) characterized the authigenic carbonates with some site-specific differences. According to one-way ANOVA with post-hoc Tukey HSD Test, $\delta^{18}O$ values from Blake Ridge are statistically different from those measured from the Pea Island and Kitty Hawk authigenic carbonates (**Figure 3-27**). Using the aragonite-temperature scale of (Epstein et al. 1953), the authigenic $\delta^{18}O$ values yield temperatures between 1.08 and 7.95°C (**Table 3-7**). In contrast, in situ temperatures measured during ROV dives ranged from 2.5°C at Blake Ridge (2,169 m) to 11.09°C at Pea Island (322 m). The $\delta^{18}O$-aragonite calculated temperatures at Kitty Hawk and Pea Island are lower by ~4°C than in situ temperatures, potentially reflecting input from an ^{18}O-depleted fluid source. In contrast, the $\delta^{18}O$-aragonite calculated temperatures at Blake Ridge are higher than in situ temperatures, reflecting potential input from an ^{18}O-enirched fluid source. However, the average offset at Blake Ridge was 0.58°C, suggesting near isotopic equilibrium.

The clumped isotope (Δ_{47}) values range from 0.6300 to 0.6610‰ with an average (±SD) of 0.6456 ± 0.0408‰, yielding formation temperatures between 5.9 to 15.1°C (**Figure 3-27**). According to one-way ANOVA with post-hoc Tukey HSD Test, there is no statistical difference in the Δ_{47} values between the three seep sites. However, the offset between the Δ_{47}-dervied temperatures (thermometer) and in situ CTD temperatures suggests isotopic disequilibrium (Loyd et al. 2016). The difference between the Δ_{47}-measured and Δ_{47}-expected (based on CTD temperature) values range between -0.0437 to 0.0158‰. The largest consistently negative offset is calculated at Blake Ridge with Δ_{47}-measured values consistently less than Δ_{47}-expected, yielding warmer than expected formation temperatures by more than 12°C (**Table 3-8**). These results are consistent with the results of Loyd et al. (2016) where low Δ_{47} values from modern methane-derived authigenic carbonates from Hydrate Ridge, Eel River Bains, Costa Rica and Norwegian Sea yielded warmer than ambient temperatures. In comparison, the isotopic disequilibrium is smaller at

the Pea Island (-0.0048 to 0.0158‰) and Kitty Hawk (-0.0209 to 0.0065‰) seep sites and the offset is negative and positive respectively (**Figure 3-26**).

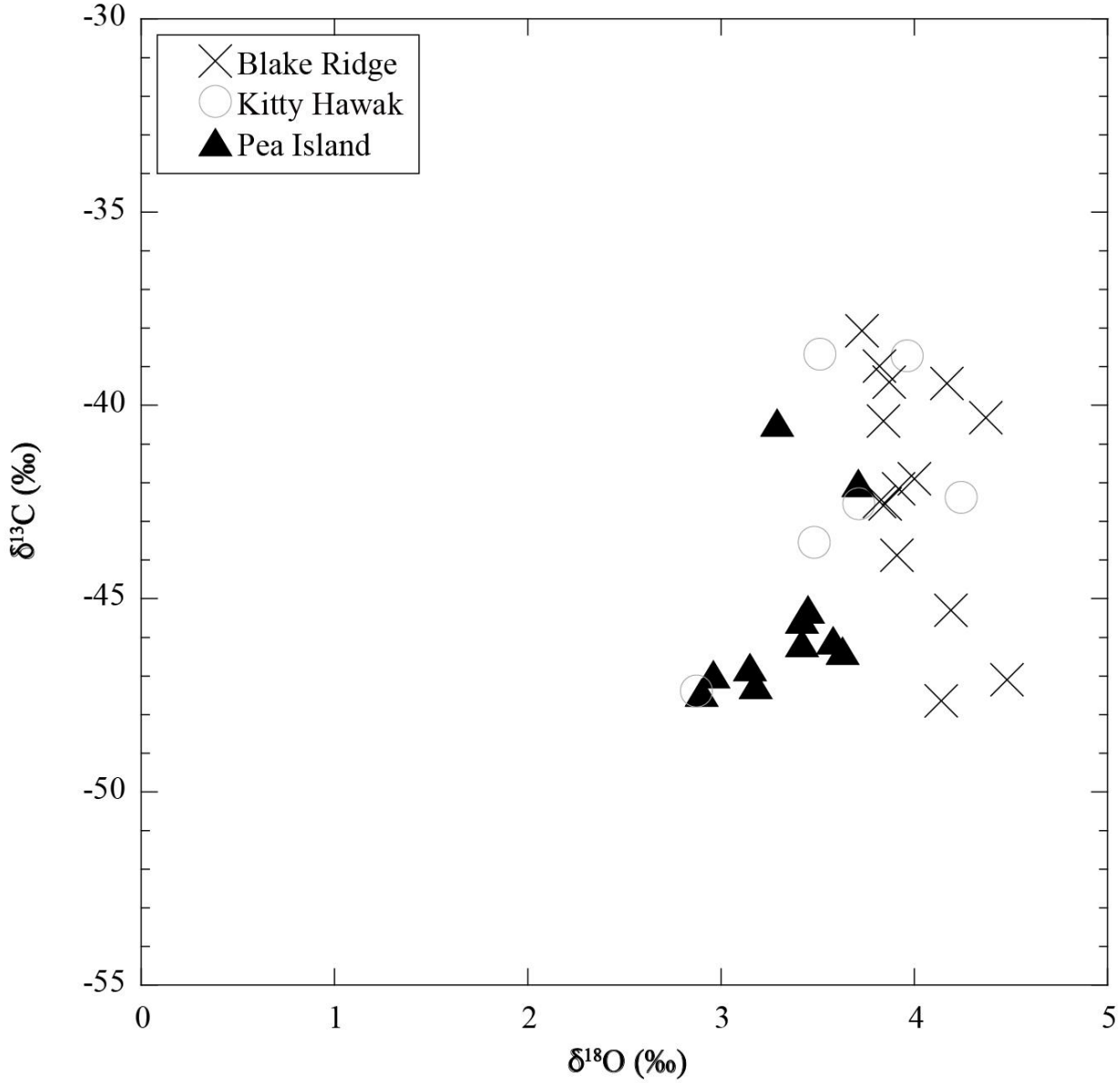

Figure 3-26. Stable carbon vs. oxygen isotopes

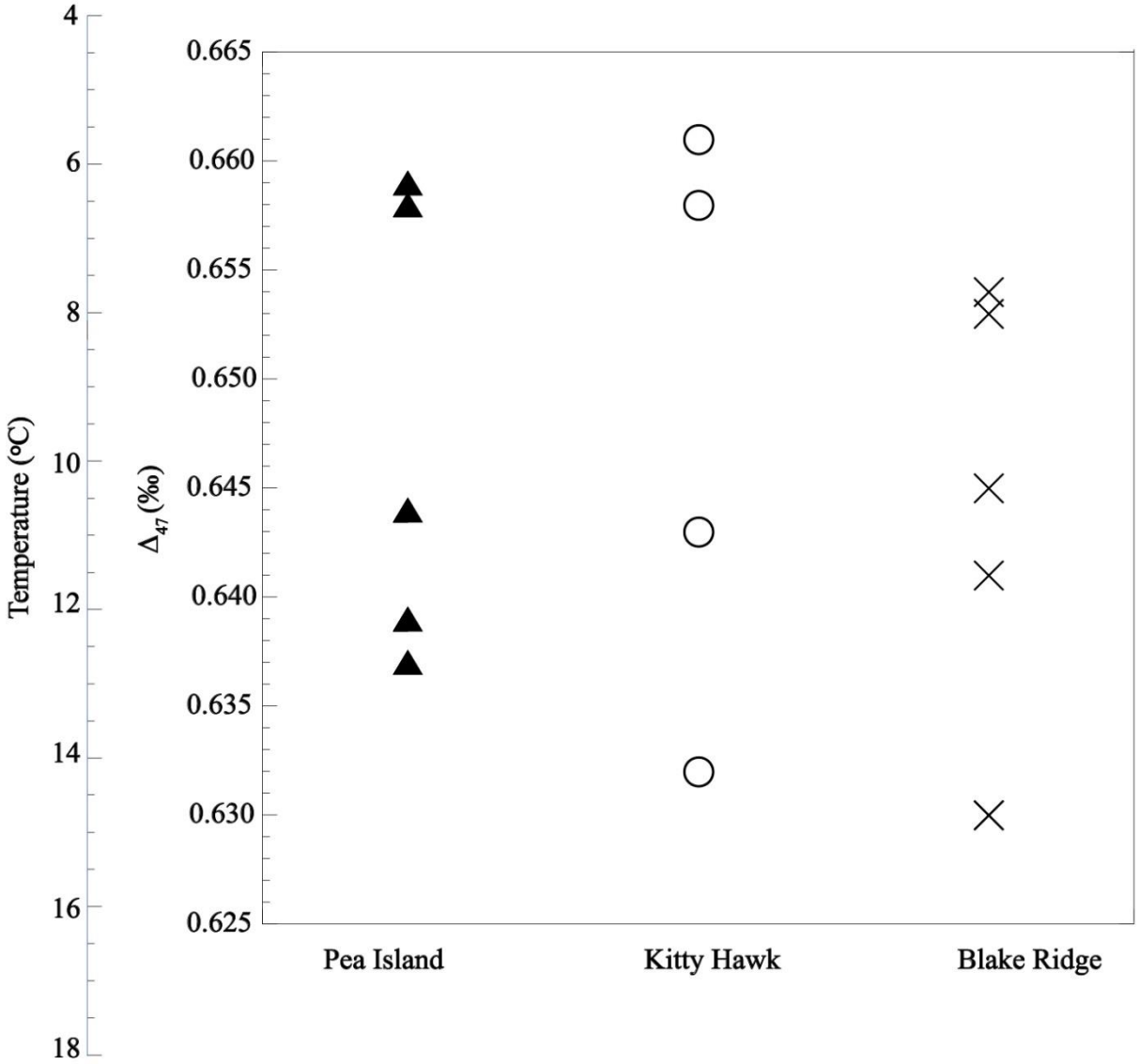

Figure 3-27. Clumped Isotopes

Table 3-7. Composition of selected authigenic carbonates from seep areas.

Percent (%) carbon composition (TC = total carbon, TOC = total inorganic carbon, TIC = Total inorganic carbon, $CaCO_3$ = calcium carbonate), stable carbon ($\delta^{13}C$) and oxygen ($\delta^{18}O$) isotope analysis (per mil; ‰) relative to VPDB, and $\delta^{18}O$-derived temperature (°C; Grossman and Ku 1986) of carbonates from Pea Island, Kitty Hawk, and Blake Ridge seeps.

Split ID	Site	%TC	%TOC	%TIC	%$CaCO_3$	$\delta^{13}C_{VPDB}$	$\delta^{18}O_{VPDB}$	$\delta^{18}O$-derived Temp (°C)
19003-1133-R1-X1	Pea Island	6.801	0.545	6.256	52.132	-47.24	3.18	6.72
19003-1133-R1-X2	Pea Island	8.418	0.431	7.987	66.555	-46.96	2.96	7.69
19003-1133-B5-X1	Pea Island	5.877	0.541	5.336	44.463	-47.44	2.90	7.95
19003-1133-B5-X2	Pea Island	6.258	0.290	5.969	49.736	-46.78	3.15	6.87
AT41-A4961-B1-X1	Pea Island	n.a	n.a	n.a	n.a	-46.15	3.42	5.68
AT41-A4961-B1-X1	Pea Island	7.71	0.29	7.41	61.78	-40.45	3.29	6.24
19003-1133-R1-X1	Pea Island	6.801	0.545	6.256	52.132	-46.08	3.58	4.98
19003-1133-R1-X2	Pea Island	8.418	0.431	7.987	66.555	-46.35	3.63	4.77
19003-1133-B5-X1	Pea Island	5.877	0.541	5.336	44.463	-45.29	3.45	5.55
19003-1133-B5-X2	Pea Island	6.258	0.290	5.969	49.736	-45.54	3.42	5.68
AT41-A4961-B1-X1	Pea Island	7.71	0.29	7.41	61.78	-42.01	3.71	4.42
19003-1134-R2-X1	Kitty Hawk Seep	9.123	0.752	8.371	69.755	-38.66	3.51	5.27
19003-1134-R2-X2	Kitty Hawk Seep	9.082	0.682	8.400	69.998	-43.53	3.48	5.42
19003-1134-R2-X1	Kitty Hawk Seep	9.123	0.752	8.371	69.755	-38.70	3.96	3.33
19003-1134-R2-X2	Kitty Hawk Seep	9.082	0.682	8.400	69.998	-42.53	3.71	4.42
19003-1134-R2-X3	Kitty Hawk Seep	n.a	n.a	n.a	n.a	-42.37	4.24	2.12
19003-1136-R1-X1	Blake Ridge Seep	10.547	0.069	10.478	87.312	-38.07	3.73	4.33
19003-1136-R1-X2	Blake Ridge Seep	10.83	0.247	10.583	88.184	-42.55	3.85	3.81
AT41-A4967-B6-R1-G1	Blake Ridge	9.73	0.24	9.49	79.10	-40.40	3.84	3.85
AT41_A4967-B6-R1-X1	Blake Ridge	n.a	n.a	n.a	n.a	-43.87	3.91	3.55
AT41-A4967-B6-R2-X1	Blake Ridge	9.56	0.14	9.41	78.43	-42.16	3.92	3.51
AT41-A4967-R2-X3	Blake Ridge	7.43	0.31	7.13	59.38	-38.98	3.82	3.94
AT41-A4967-R2-X2	Blake Ridge	9.27	0.11	9.16	76.34	-47.65	4.14	2.55
AT41-A4967-R3-X1	Blake Ridge	9.42	0.28	9.14	76.14	-42.49	3.82	3.94
AT41-A4967-B6-R1-G1	Blake Ridge	9.73	0.24	9.49	79.10	-39.43	4.17	2.42
AT41-A4967-B6-R2-X1	Blake Ridge	9.56	0.14	9.41	78.43	-40.32	4.37	1.55
AT41-A4967-R2-X3	Blake Ridge	7.43	0.31	7.13	59.38	-39.40	3.87	3.72
AT41-A4967-R2-X2	Blake Ridge	9.27	0.11	9.16	76.34	-47.10	4.48	1.08
18042-A4967-R2-X5	Blake Ridge	n.a	n.a	n.a	n.a	-45.30	4.19	2.34
AT41-A4967-R3-X1	Blake Ridge	9.42	0.28	9.14	76.14	-41.90	4.00	3.16

Table 3-8. Clumped isotope (Δ_{47}) values of selected authigenic carbonates from seep areas

From Pea Island, Kitty Hawk, and Blake Ridge seeps. We uses the equation of Swart et al. (2019) to calculate Δ_{47} to temperature (°C).

Split ID	Site	Δ_{47}	Δ_{47} error	Δ_{47}-Temp °C	CTD-Temp °C	Temp °C offset[1]	Predicted Δ_{47}[2]	Δ_{47} offset[3]
19003-1133-R1-X1	Pea Island	0.6580	0.0110	7.0±3.1	11.1	-4.1	0.6432	0.0148
19003-1133-R1-X2	Pea Island	0.6590	0.0090	6.5±2.6	11.1	-4.6	0.6432	0.0158
19003-1133-B5-X1	Pea Island	0.6440	0.0090	10.8±2.5	10.9	-0.1	0.6438	0.0002
19003-1133-B5-X2	Pea Island	0.6390	0.0200	12.3±5.9	10.9	1.4	0.6438	-0.0048
18042-A4961-B1-X1	Pea Island	0.6370	0.0180	11.0	8.3	2.7	0.6530	-0.0160
19003-1134-R2-X1	Kitty Hawk Seep	0.6320	0.0200	14.5±6.0	8.3	6.2	0.6529	-0.0209
19003-1134-R2-X2	Kitty Hawk Seep	0.6430	0.0270	11.2±8.0	8.3	2.9	0.6529	-0.0099
19003-1134-R2-X3	Kitty Hawk Seep	0.6580	n.a.	6.8	8.3	-1.5	0.6529	0.0051
19003-1134-B4-X3	Kitty Hawk Seep	0.6610	n.a.	5.9	7.8	-1.9	0.6545	0.0065
18042-A4967-B6R1-G1	Blake Ridge	0.6530	0.0210	8.4±6.0	2.5	5.9	0.6739	-0.0209
18042-A4967-B6R2-X1	Blake Ridge	0.6300	0.0010	15.1±0.4	2.6	12.5	0.6737	-0.0437
18042-A4967-R2-X3	Blake Ridge	0.6410	0.0260	12.0±7.9	2.6	9.4	0.6737	-0.0327
18042-A4967-R2-X2	Blake Ridge	0.6540	0.2100	8.3±6.4	2.6	5.7	0.6737	-0.0197
18042-A4967-R2-X5	Blake Ridge	0.6450	0.1500	10.5±4.2	2.6	7.9	0.6737	-0.0287
18042-A4967-R3-X1	Blake Ridge	0.6300	0.0090	10.9±6.9	2.6	8.3	0.6737	-0.0437

Several factors can drive disequilibrium, including kinetic isotopic effects during methane oxidation, mixing of inorganic carbon pools, pH and salinity effects and rapid precipitation (Loyd et al. 2016). For example, Zhang et al. (2019) found disequilibrium from the (Loyd et al. 2016) study to be associated with extremely rapid AOM rates. As discussed in Section 3.3, experimental AOM rates vary between sites and within site based on sediment depth. We observed the highest experimental AOM rate at Pea Island (ROV dive J2-1133) at a depth interval of 10–15 cm, reported as 2,235.7 nmol cc^{-1} d^{-1}. We measured the in situ AOM rate to be 20.8 nmol cc^{-1} d^{-1} based. High AOM rates have the potential to introduce mineralogy heterogeneities as a result of various carbonate precipitate rates and multiple stages of precipitation. The latter is consistent with textural and morphological features of the carbonates based on thin sections. Macroporosity with voids and fractures with cross cutting veins and acicular pore filling of highly cemented carbonates is indicative of a high energy environment and multiple stages of precipitation (Prouty et al. 2020, Prouty et al. 2016). The authigenic carbonate texture may result from in situ brecciation of weakly consolidated sediment, possibly linked to venting-induced disturbances such as rapid release of trapped fluids or gases (Matsumoto 1990). Whereas upward flux of methanogenesis-derived DIC could impart a warmer temperature and lower Δ_{47} source (Zhang et al. 2019), the ^{13}C-depleted carbonate values presented here discount methanogenesis, which is characterized by heavier $\delta^{13}C$ (Chatterjee et al. 2011). Multiple factors may influence the isotopic disequilibrium in the Kitty Hawk, Peak Island and Blake Ridge authigenic carbonates, and can reduce the utility of the Δ_{47}-derived paleothermometer as found in this study.

[1] Difference in Δ_{47}-temperature relative to CTD-temperature

[2] Predicted Δ_{47} based on CTD temperature

[3] Difference between measured Δ_{47} vs. predicted Δ_{47}

AMS ^{14}C radiocarbon dating of groundmass (bulk) and cement fractions of authigenic carbonates from the Pea Island, Kitty Hawk and Blake Ridge seeps (**Table 3-9**) were found to have calibrated before present (BP) ages between 15,890 ± 260 years and 25,290 ± 410 years.

Radiocarbon dating of mixed planktonic foraminifera from sediments (**Table 3-11**) at these seep sites and one bivalve shell incorporated into the authigenic carbonate at Blake Ridge (**Table 3-9**) have ages between 950 ± 110 and 1,590 ± 140 YBP (calibrated) for the sediments and 3,340 ± 140 YBP (calibrated) for the bivalve shell.

The marked difference between the sediment and authigenic carbonate ages and the depleted $D^{14}C$ values (-822 ‰ to -933 ‰), suggests that an older source of carbon is incorporated into the aragonite cement. Paired groundmass (bulk) and cement ages from the same subsample show the bulk sample to always be younger, with age differences between 470 and 3,410 years (calibrated), indicating that the sediment calcite is modifying the overall bulk age by adding an impactfully younger fraction to the older carbon contained within the aragonite cement.

Authigenic carbonate cement samples contained 3.51 to 4.94 ppm U, and 0.20 to 1.57 ppm Th **(Table 3-11**). $^{230}Th/^{232}Th$ activity ratios were between 1.57 and 6.28, at the lower end of the range reported from other occurrences of methane-related authigenic carbonates (Teichert et al. 2003, Bayon et al. 2009), suggesting incorporation of detrital material, such as clay minerals, which carry ^{232}Th, and an associated amount of initial ^{230}Th. Therefore, a detrital correction was required and applied based on measured sediment collected from 385 and 1,600 m below sea level along the US from (Prouty et al. 2016). Modeled initial $(^{234}U/^{238}U)_i$ values are similar to the mean modern seawater ($^{234}U/^{238}U$) of 1.1466 (Robinson et al. 2004), meaning that U incorporated in the authigenic carbonates was sourced from seawater, rather than pore waters, which would be comparatively enriched in ^{234}U (Henderson et al. 1999).

The corrected U-Th ages of the authigenic carbonate range between 1.40 ± 1.1 ka at Kitty Hawk to 17.37 ± 4.3 ka at Blake Ridge (**Table 3-11**), supporting earlier work reporting AOM-driven carbonate precipitation since the late Pleistocene and Holocene along the US Atlantic margin (Prouty et al. 2016, Sahy et al. in review). Discrepancies between the ^{14}C and U-Th derived ages is over 20 ka at the Kitty Hawk Seep site and several thousand years at Pea Island and Blake Ridge.

The differences between the ^{14}C and U-Th ages are probably a complex function of absolute age of the authigenic carbonates, and methane flux, and the ^{14}C signature of the source methane. We observed a similar offset at the Norfolk Seep field and attributed it to incorporation of fossil carbon (Prouty et al. 2016). However, incorporation of ^{232}Th-enriched detrital material may also be contributing to younger U-Th dates at Kitty Hawk given $^{230}Th/^{232}Th$ activity ratios less than 2 (**Table 3-11**).

Table 3-9. Authigenic carbonate AMS ^{14}C calibrated radiocarbon ages

Site	Sample ID	Split ID	Type	$\delta^{13}C$	$D^{14}C$	Years (Cal BP) 2-sigma	
						Center Age (rounded)	Age Error (rounded)
Pea Island Seep	RB1903_J2_1133_R1	19003-1133-R1-RC-1	Cement	-49.47	-934.7	19,620	270
Pea Island Seep	RB1903_J2_1133_R1	19003-1133-R1-RC-2	Bulk	-41.27	-931.44	17,470	330
Pea Island Seep	RB1903_J2_1133_B5_01	19003-1133-B5-RC-1	Cement	-8.13	-367.05	19,300	240
Pea Island Seep	RB1903_J2_1133_B5_01	19003-1133-B5-RC-2	Bulk	-50.77	-880.62	15,890	260
Pea Island Seep	RB1903_J2_1133_B4_01 (rock)	19003-1133-B4-RC-1	Cement	-46.53	-848.41	22,170	260
Kitty Hawk Seep	RB1903_J2_1134_RB_02	19003-1134-R2-RC-1	Cement	-50.93	-876.81	21,980	270
Kitty Hawk Seep	RB1903_J2_1134_RB_02	19003-1134-R2-RC-2	Bulk	-46.4	-822.71	19,350	300
Kitty Hawk Seep	RB1903_J2_1134_B4_01	19003-1134-B4-RC-1	Cement	-39.86	-907.77	22,560	270
Blake Ridge Seep	AT41-AL4967-R2	18042-A4967-R2-RC-1	Cement	-45.44	-905.46	25,290	410
Blake Ridge Seep	AT41-AL4967-R2	18002-A4967-R2-RC-2	Bulk	-39.2	-877.79	24,820	410
Blake Ridge Seep	AT41-AL4967-R2	18042-A4967-SHRC-1	Mollusk	-49.16	-911.73	3,340	140
Blake Ridge Seep	RB1903_J2_1136_R1	19003-1136-R1-RC-1	Cement	-49.16	-933.02	24,940	320

Table 3-10. Calibrated AMS ^{14}C radiocarbon ages of foraminifera and coral fragments

Coral fragments from cores and rock-bound sediment. ACS-N = Albemarle canyon System-North, PC = Pamlico Canyon, PI = Pea Island, KH = Kitty Hawk Seep, BR = Blake Ridge Seep. CF = Cape Fear Seep, RH = Richardson Hills

Site	Sample ID	Sub Sample ID	Species	Sediment Depth (cm)	$\delta^{13}C$	$D^{14}C$	Calibrated Age YBP (rounded)	Calibrated Error YBP (rounded)
ACS-N	PC1705-MNC-1	17004-1-MNC-RC-12	*Globigerina **bulloides***	11	-0.32	-265.78	1,880	150
ACS-N	PC1705-MNC-2	17004-2-MNC-RC-16	Mixed Planktonic Foram.	15	-0.05	-79.49	Modern	-
ACS-N	PC1705-MNC-3	17004-3-MNC-RC-19	Mixed Planktonic Foram.	18	0.49	-281.94	2,125	160
ACS	PC1705-MNC-6	17004-6-MNC-RC-19	Mixed Planktonic Foram.	18	0.55	-118.23	390	110
PC	PC1704-MNC-16	17048-16-MNC-RC-8	*Orbulina universa*	14	2	-324.25	2,700	140
PC	PC1704-MNC-17	17048-17-MNC-RC-8	*Orbulina universa*	14	1.82	-144.82	600	100

Site	Sample ID	Sub Sample ID	Species	Sediment Depth (cm)	$\delta^{13}C$	$D^{14}C$	Calibrated Age YBP (rounded)	Calibrated Error YBP (rounded)
PC	PC1704-MNC-19	17048-19-MNC-RC-6	*Orbulina universa*	11	2.17	-153.06	660	120
PC	PC1704-MNC-19	17048-19-MNC-RC-11	*Orbulina universa*	21	2.23	-183.42	940	140
PC	AT41-A4969-PU-08	18042-A4969-PU8-RC-6B	*Orbulina universa*	5	0.77	-64.5	Modern	
PC	AT41-A4969-PU-08	18042-A4969-PU8-RC-16	Mixed Planktonic Foram.	15	1.71	-135.96	540	100
PC	AT41-A4969-PU-14	18042-A4969-PU14-RC-16	Mixed Planktonic Foram.	15	1.82	-187.3	1,000	140
PC	AT41-A4969-PU-20	18042-A4969-PU20-RC-16	Mixed Planktonic Foram.	15	1.43	-91.11	140	130
PC	RB1903-J2-1132-PU-7	19003-1132-7PU-RC-3	*Orbulina universa*	15	2.01	-150.46	630	110
PC	RB1903-J2-1132-PU-14	19003-1132-14-PU-RC-2	*Orbulina universa*	10	2.31	-104.69	280	150
PC	RB1903-J2-1132-PU-24	19003-1132-24-PU-RC-2	*Orbulina universa*	10	2.14	-66.49	Modern	
PC	BMCC-6Oct18-10-PC3	18053-3-P-RC-2	Mixed Planktonic Foram.	100	1.29	-153.89	670	120
PC	BMCC-6Oct18-10-PC3	18053-3-P-RC-4	Mixed Planktonic Foram.	200	2.05	-438.86	4,610	170
PI	RB1903-J2-1133-PU-16	19003-1133-16PU-RC-3	Mixed Planktonic Foram.	11	0.11	-121.61	410	110
KH	RB1903-J2-1134-PU-11	19003-1134-11-PU-RC-3	*Globorotalia inflata*	11	1.1	-119.03	400	110
KH	RB1903-J2-1134-PU-15	19003-1134-15PU-RC-3	Mixed Planktonic Foram.	11	1.57	-168.23	790	120
BR	RB1903-J2-1136-PU-30	19003-1136-30PU-RC-3	*Orbulina universa*	11	2.28	-244.35	1,590	140
CF	RB1903-J2-1137-B1	RB1903-J2-1137-B1	Mixed Planktonic Foram.	rock-surface	-4.88	-986.29	38,410	950
RH	BMCC-3Oct18-05-PC2	18053-2-P-S1-RC-1	*Lophelia* sp.	50	-3.67	-322.23	2,670	150
RH	BMCC-3Oct18-05-PC2	18053-2-P-S2-RC-1	*Lophelia* sp.	200	-3.08	-383.38	3,600	160

Table 3-11. Summary of measured U-Th concentrations

Concentration data for authigenic carbonate samples, and activity ratios (AR) used for age calculation and U-Th ages. (a) Activity calculated using λ^{230}=9.17050E-6, λ234=2.82206E-6 (Cheng et al. 2013), λ^{232}=4.93343E-11 (Holden et al. 1990), λ^{238}=1.55125E-10 (Jaffey et al. 1971), (b) Activity ratios corrected for hydride formation, tailing, fractionation, SEM-Faraday yield, and tracer isotopic composition, and (c) Detrital corrected using from Prouty et al. (2016) on measured sediment collected from 385 and ~1,600 m below sea level along the US.

					MEASURED(a)							CORRECTED(a)							
	Sample Name	Depth (m)	U ppm	^{232}Th ppm	^{230}Th/^{232}Th AR(b)	^{232}Th/^{238}U AR(b)	2s%	^{230}Th/^{238}U AR(b)	2s%	^{234}U/^{238}U AR(b)	2s %	^{230}Th/^{238}U AR(b,c)	2s%	^{234}U/^{238}U AR(b,c)	2s%	Rho 08-48	Age (ka)	^{234}U/^{238}U AR initial	2s
Kitty Hawk	RB1903_J2_1134_B4_01	235	3.83	0.20	1.72	0.01736	0.053	0.02986	0.71	1.143	0.15	0.01462	75.17	1.14519	0.58	0.299	1.40±1.1	1.1458	0.007
Kitty Hawk	RB1903_J2_1134_RB_02	399	4.29	0.23	1.91	0.01760	0.055	0.03368	0.76	1.145	0.15	0.01687	71.93	1.14707	0.59	0.303	1.62±1.2	1.1477	0.007
Pea Island	RB1903_J2_1133_R1	322	4.63	0.31	6.03	0.02221	0.052	0.13397	0.28	1.142	0.12	0.11554	11.86	1.14413	0.71	0.305	11.58±1.4	1.1489	0.009
Blake Ridge	RB1903_J2_1136_R1	2,164	3.51	0.37	6.28	0.03476	0.054	0.21819	0.38	1.129	0.15	0.16715	23.42	1.13185	1.11	0.364	17.37±4.3	1.1385	0.014

:

3.2.4.2 Canyons

Geological sampling and observation activities within the study area canyons were extremely limited, with Pamlico Canyon being the only canyon with detailed geologic observations and collection of a large suite of rock and sediment samples. In addition to samples from Pamlico Canyon, we collected CTD monocores from the heads and upper reaches of four canyons, including Keller and Hatteras canyons (**Figure 3-17**).

Grain size and carbonate content analyses of sediments within and adjacent to the canyons and gullies within the ACS show that the top 10–20 cm of the sediment in the upper 10–15 km of the different channels is dominated by siliciclastic-dominated sand and silts. The clay size fraction is present, but rarely exceeds 5 % of the sediments in the samples from shallower than water depths of 1,000 m. Below 1,000 m, the clay size fraction becomes more abundant but remains a relatively minor component of the sediment, except in monocore PC1705-MNC-03 from 1,350 m within a canyon distributary adjacent to the Kitty Hawk Seep (**Figure 3-28**). BOM concentrations in these sediments remain relatively consistent with depth down core, but the concentrations decrease overall with the water depth and distance from the canyon head of the samples. Calcium carbonate concentration is generally in the 5–10% range regardless of depth down core or position within the canyon, suggesting that the rate of biogenic carbonate formation is relatively fixed across the region and in time, and large-scale transport events which may increase or decrease the concentrations are absent. Discrete layering or other identifiable sedimentary structures are absent within the recovered sections further indicating that discrete sediment-transport events (turbidity currents, debris flows) did not occur over the timespan covered by deposition of these sediments (**Figure 3-28** and **Table 3-10**).

Ship-based sediment sampling in Keller and Hatteras canyons was hampered by the Gulf Stream and we therefore recovered only one CTD monocore from the head of Keller Canyon, while only one of the three CTD monocores in Hatteras Canyon sampled the canyon floor **(Figure 3-29**). Sediments in the heads of both canyons are silty sands to sandy silts, with the clay fraction accounting for less than 3% of the total sediment weight. In Hatteras Canyon, the clay concentration increases with distance down canyon, reaching as much as 8% within core PC1704-MNC-10 at 1,038 m on the south wall of the canyon. BOM and calcium carbonate concentrations in Keller and Hatteras canyons follow similar depth (distance from canyon head) trends as seen in the northern ACS canyons, but there is a notable decrease in BOM and increase in calcium carbonate concentrations in the sediments recovered from Hatteras Canyon when compared with those to the north, suggesting that terrigenous input to the southernmost of the canyons in the system is decreasing.

Visual observations and sampling of several locations within Pamlico Canyon (**Figure 3-30 A**), coupled with additional ship-based sampling and mapping within and adjacent to the canyon, provide the most complete view of the geology and geomorphology of the canyons within the study area. The morphology of Pamlico Canyon is substantially simpler than canyons further north on the margin, with an extremely linear thalweg (axial channel) and limited dendritic distributary channel development at the canyon head. The distributaries at the canyon head and canyon wall gullies are preferentially developed on the southern side of the canyon (**Figure 3-30 B**). Asymmetry of the Pamlico Canyon is further seen with the top of the southern wall consistently at a shallower depth than the northern wall, with a well-developed convex profile suggestive of a levee formation. Although it is possible that the asymmetric cross-canyon profile of the canyon formed in response to the dominant current (Gulf Stream) and sediment-transport regimes, the prominent landslide scar features north of the canyon suggests that post-formation modification of the north wall may have occurred.

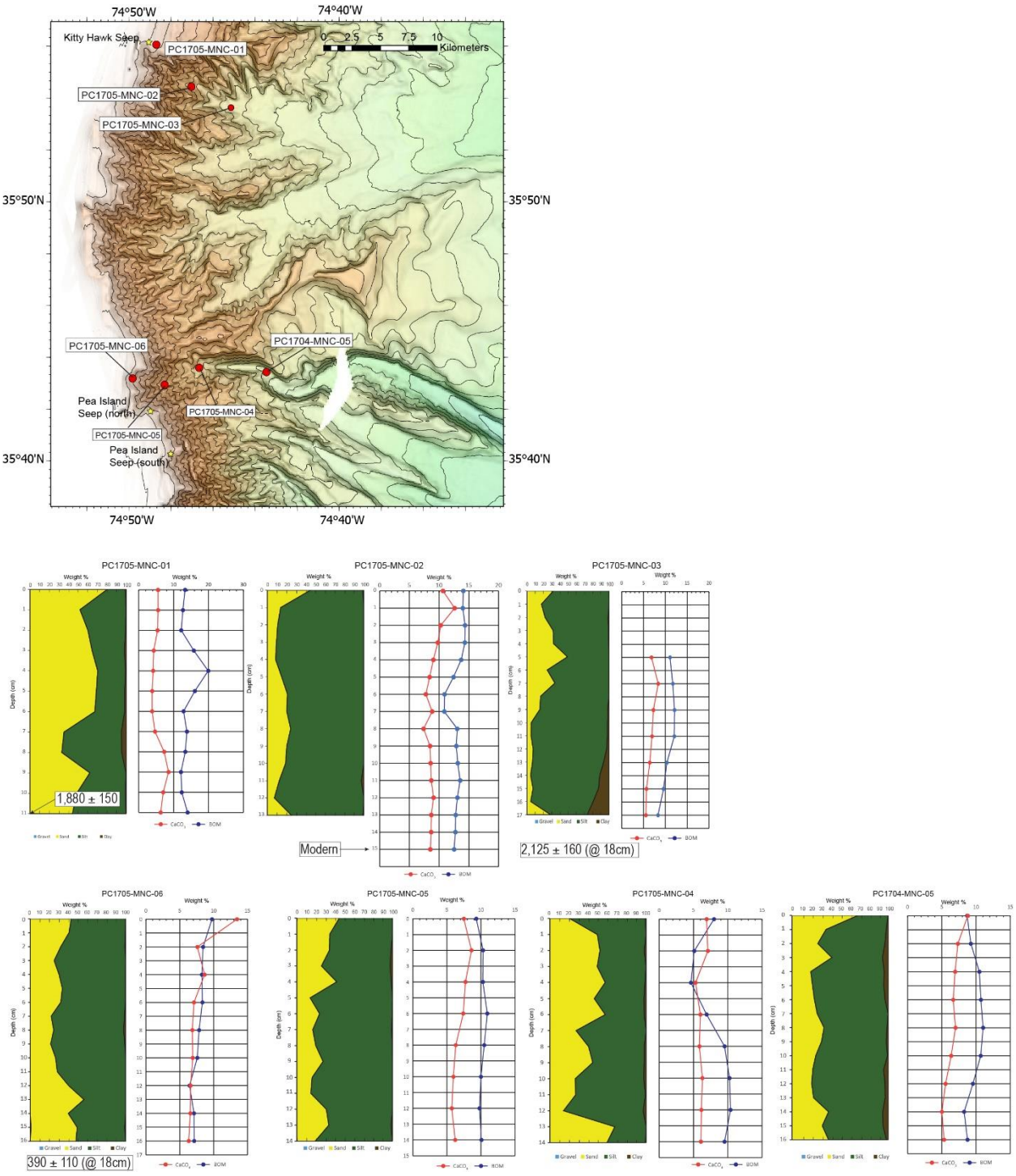

Figure 3-28. Grain size and $CaCO_3$/BOM of north ACS canyon cores
From the north ACS canyons adjacent to the Kitty Hawk and Cape Fear seeps. Calibrated radiocarbon ages for the sediments at the base of cores shown.

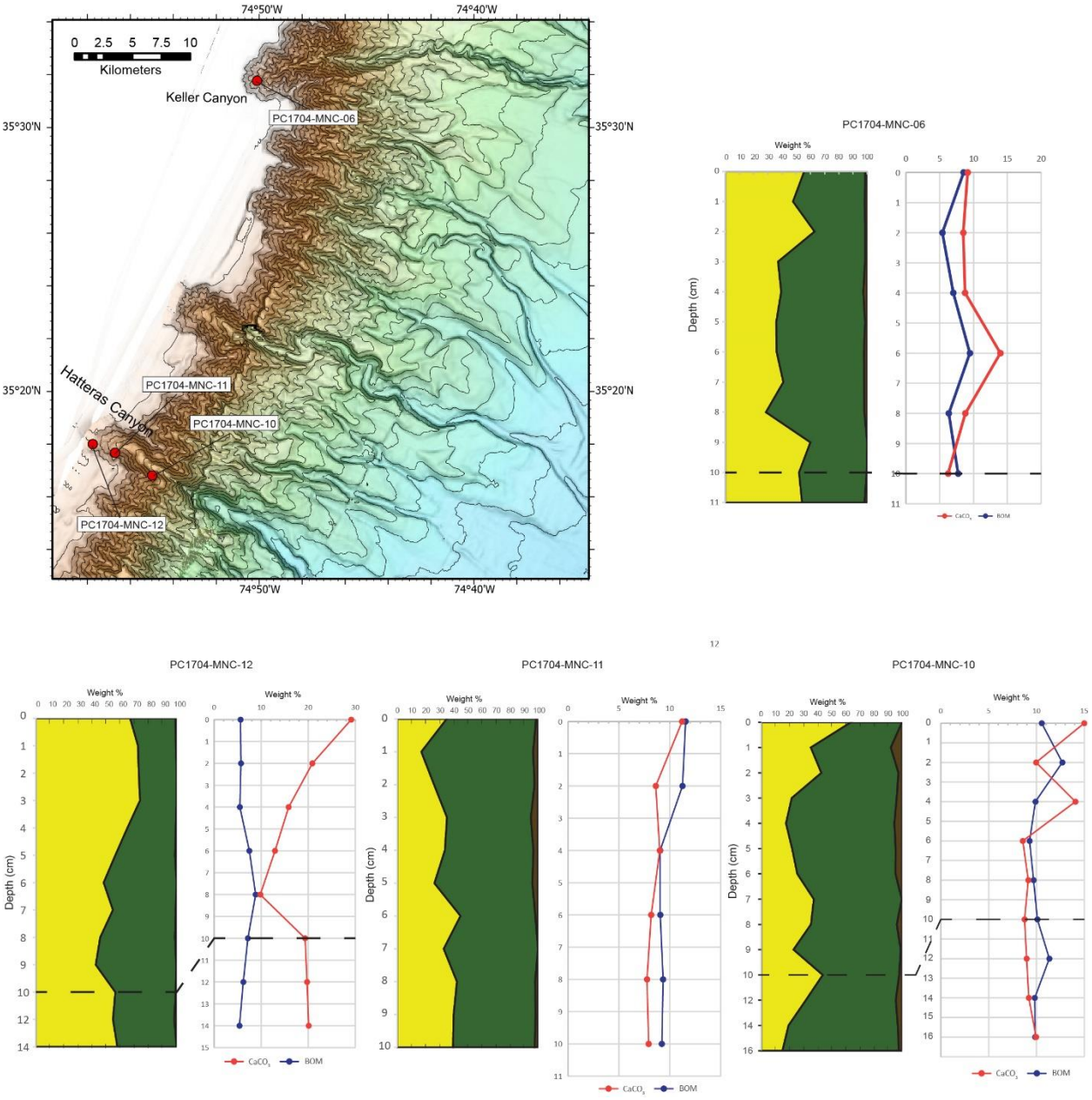

Figure 3-29. Grain size and $CaCO_3$/BOM Keller and Hatteras canyon cores

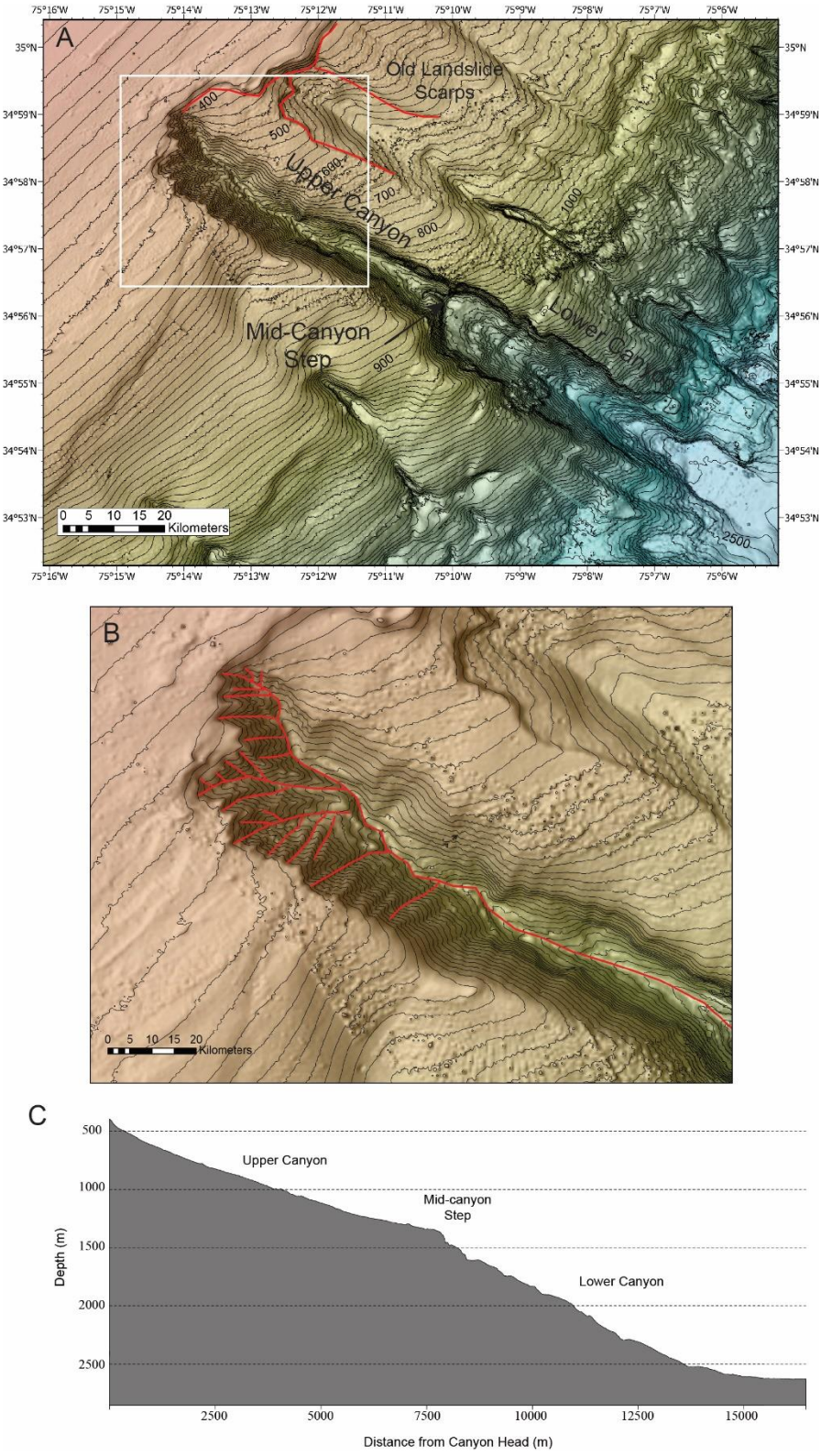

Figure 3-30. Pamlico Canyon map
(A) Bathymetry map of Pamlico Canyon showing deeply incised linear morphology and features on the surround slope. (B) Asymmetric dendritic distributary channel development at the canyon head (location shown by white box on A). (C) Down-channel profile showing the variation on channel floor slope and mid-canyon step.

The axial profile of Pamlico Canyon (**Figure 3-30 C**) comprises two segments; an approximately 7.5-km long upper canyon with a canyon floor gradient of 7–7.5º and a similar length lower canyon with a 9–9.5º floor gradient separated by a prominent, approximately 150 m high, step. The step also marks the point at which the width of the canyon almost doubles from a little of 1 km in the upper canyon to more than 2 km in the lower canyon. The change in profile of the canyon occurs at the projected depth of the mid-late Cretaceous sedimentary sequences (**Figure 3-31**), which showed an increase in siliciclastic components in the deposited sediment in the Esso #1 well drilled at Cape Hatteras (Weems et al. 2019) at that time. Mineralogy of rocks collected at and above the step during *Alvin* dive A4969 contain approximately 10% more quartz (and an associated reduction of the same amount in the calcite content) than those collected from the north wall below the step during *Jason* dive 1132 (**Table 3-12, Figure 3-31**), perhaps reflecting the larger-scale shift in sediment sources and an increase in strength and resistance to erosion of the stratigraphy. Minor shifts in mineral composition of the exposed stratigraphy appear to also control stability of the canyon walls. For example, replacement of less than 10% calcite with dolomite within outcrops of calcareous siltstones may facilitate discernable differences in relative strength in adjacent layers (**Table 3-12, Figure 3-32**). Evidence of localized rockfall, spalling failure and cave development further suggest a level of instability of the canyon walls. Additional sampling and detailed palo-stratigraphic aging of the exposed rocks in the canyon can allow for further stratigraphic correlations and a better understanding of the controls on wall strength due to lithologic variation.

Table 3-12. XRD-derived mineralogy of selected canyon rocks

From Pamlico Canyon, Blake Deep/Blake Escarpment, and the Cape Lookout sites. +lithium minerals are indicated by the XRD pattern, but the mineral phase(s) could not be identified. Minerals expressed in weight percent

Site	Sample ID	Subsample ID	Quartz	Calcite	Dolomite	Mica	Chlorite Group	Mont.	Pyroxenes/Titanite	Ilmenite	Mullite	Lithium Minerals
PC	AT41-A4969-R1	AT41-A4969-R1-X1	14.1	-	-	-	0.5	-	0.7	1.5	77.4	8.5+
PC	AT41-A4969-R3	AT41-A4969-R3-X1	15.3	74.3	1.4	6.3	-	-	-	-	-	-
PC	AT41-A4969-R5	AT41-A4969-R5-X1	14.0	81.9	-	-	-	-	-	-	-	-
PC	RB1903-J2-1132-R4	19003-1132-R4-X1	6.5	87.7	-	4.1	-	-	1.7	-	-	-
PC	RB1903-J2-1132-R4	19003-1132-R4-X2	5.2	80.1	7.1	1.2	-	6.3	-	-	-	-
CL	RB1903-J2-1135-B5_02	19003-1135-B5-X1	5.5	3.8	88.3	-	-	2.8	-	-	-	-
BD	RB1903-J2-1131-R2	19003-1131-R2-X1	1.9	95.0	-	1.7	0.3	-	-	1.2	-	-
BD	RB1903-J2-1131-R2	19003-1131-R2-X2	3.0	89.8	-	-	2.7	-	3.1	1.4	-	-

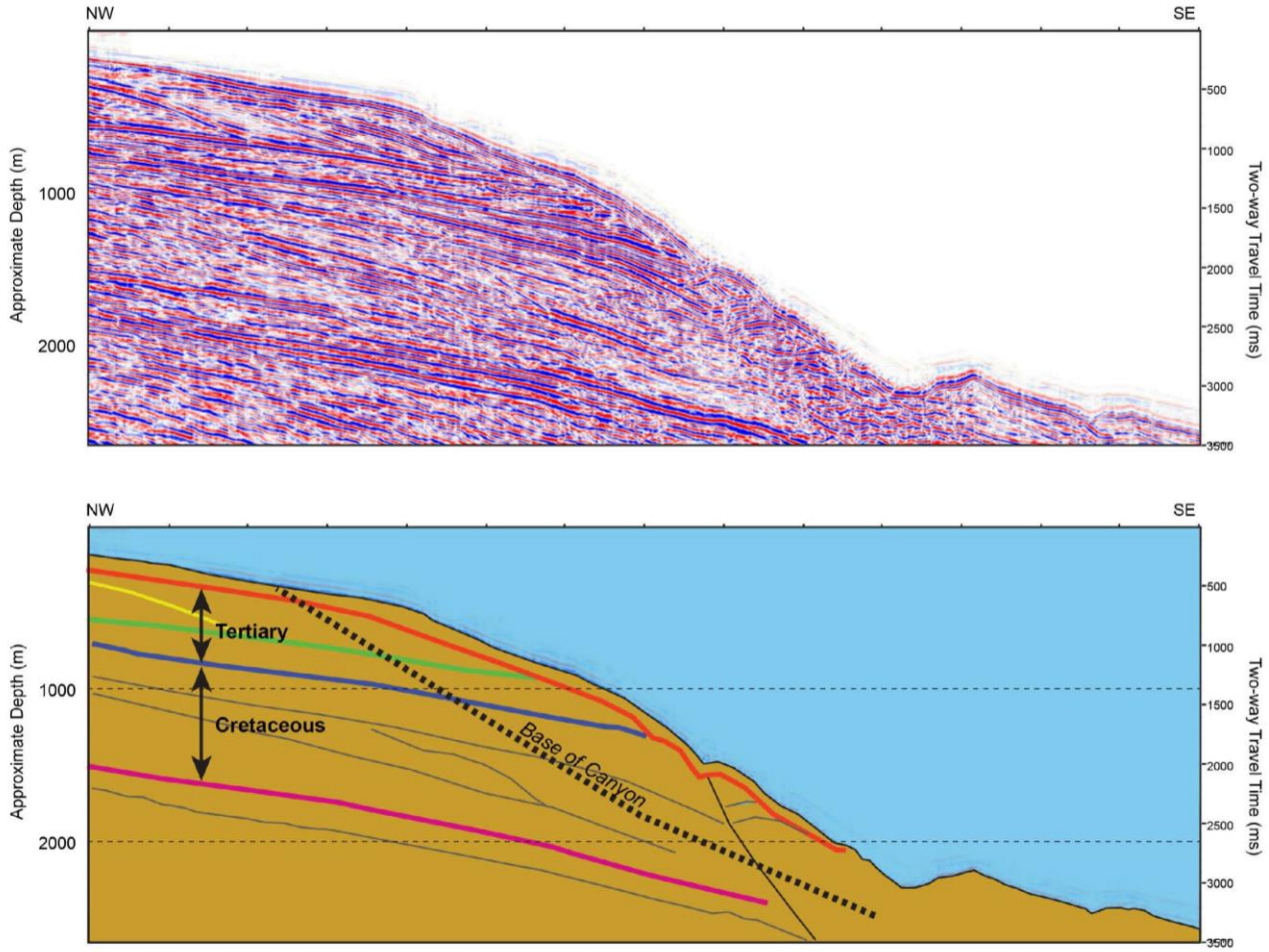

Figure 3-31. Subsurface stratigraphy through which the Pamlico Canyon cuts
(A) Approximately NW-SE multichannel seismic-reflection profile across the upper continental slope adjacent to Pamlico Canyon showing the subsurface stratigraphy through which the canyon cuts. (B) Diagrammatic interpretation of the seismic profile in [A] highlighting the age of the stratigraphic units exposed within the canyon and their approximate depth.

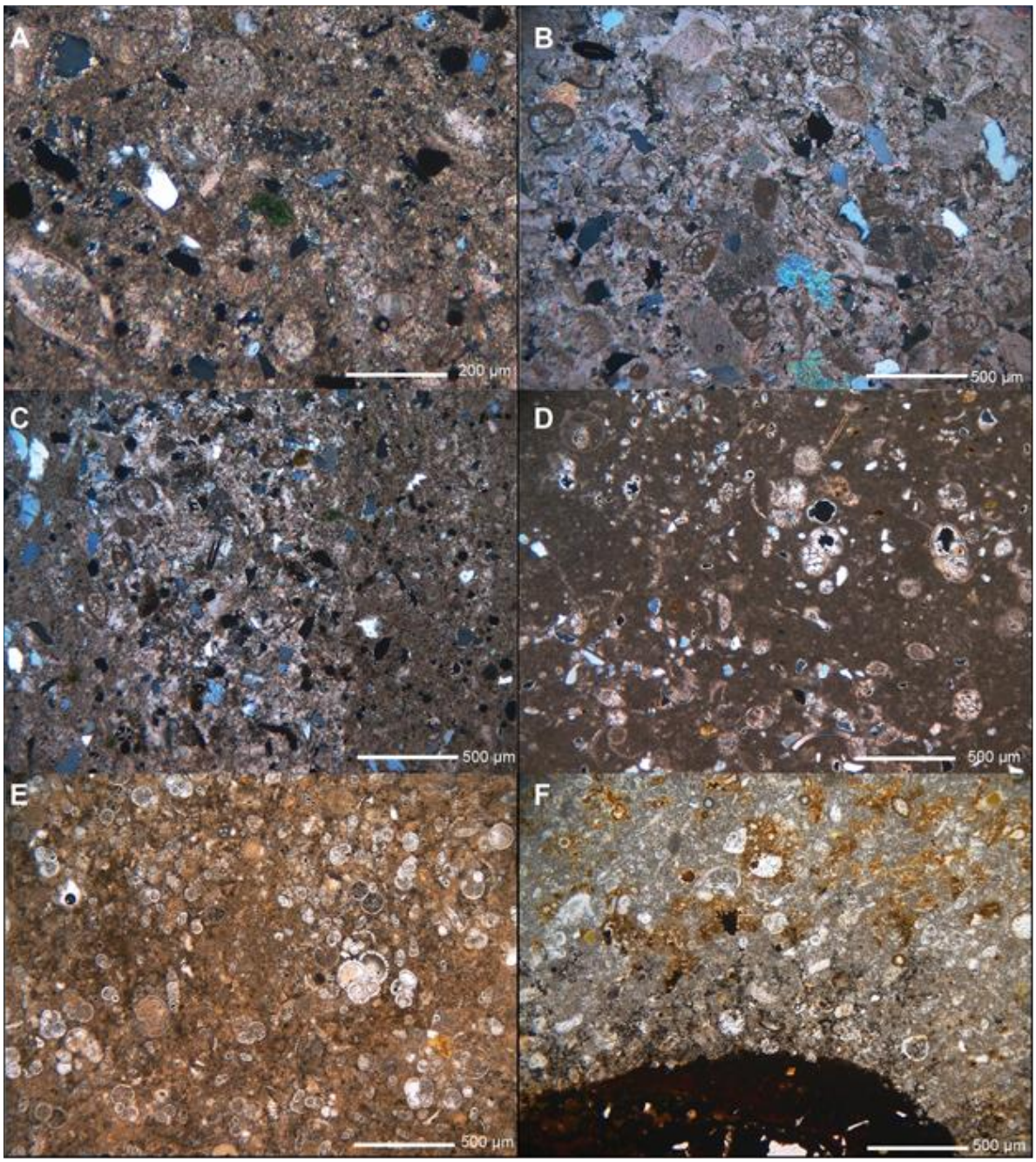

Figure 3-32. Photomicrographs of carbonate-rich canyon lithologies
From Pamlico Canyon, Blake Deep and Cape Lookout Deep. (A) Quartz, pyroxene and mica grains and shell fragments bound with in a calcite fine-grained calcite mud from Pamlico Canyon (Sample AT41-A4969-R3), (B) Calcite cemented terrigenous grains (quartz with minor mica and pyroxene) and biogenic (shell) components from a resistant vein exposed on that wall of Pamlico Canyon (Sample AT41-A4969-R5), (C) Quartz and other terrigenous grains bound with in a calcite cemented vein (top to bottom, center) and fine-grained calcite mud from Pamlico Canyon (Sample RB1903-J2-1132-R3), (D) Quartz and pyroxene grains with foraminifera tests and shell fragments bound within a fine-grained dolomite matrix (Sample RB1903-1135-B5), (E) Bioclastic limestone with foraminifera tests bound by fine-grained calcite mud matrix from Blake Deep (Sample AT41-A4964-Scoop-R1, and (F) Bioclastic limestone with foraminifera tests bound by fine-grained calcite mud matrix from Blake Deep with surficial ferromanganese layer (dark brown) (Sample RB1903-J2-1131-R3).

Temporal and spatial variation of the texture and composition of sediments for core sampling sites within and adjacent to Pamlico Canyon reveal, in part, the complex nature of canyon sedimentation patterns. With the exception of the 5.85-m long piston core (BMCC-6Oct18-10-PC3) collected within the lower canyon at a water depth of 1,940 m, all cores recovered less than 20 cm of the surficial sediments (**Figure 3-33, Figure 3-34**), limiting the extent to which the inferences can be drawn about the longer-term sedimentation and sediment-transport processes active within the canyon. We saw no identifiable sedimentary structures indicative of sediment-transport events (turbidity currents or hurricane driven river plume sedimentation) within the cores from Pamlico Canyon, with the bulk of larger-scale down core and inter-core textural variations (**Figure 3-33, Figure 3-34**) likely resulting from incorporation of material shed from, and accumulating on, canyon walls or larger biogenic components (pteropods, coral skeleton fragments).

The mineralogy of the sediments from all sampling sites reflects primarily terrigenous input, with biogenic and authigenic processes contributing generally less than 20 % of the components. Quartz, plagioclase feldspar and mica are the most abundant components of these sediments (**Table 3-5** shows XRD analysis results from selected sediment samples collected by push core or from sediment removed from recovered rock samples. Table 3-6. Shows ICP-OES-MS major **and trace** elements analysis results for selected authigenic carbonate samples (bulk).

Table 3-5), with calcite and aragonite (as biogenic material), dolomite, mixed amounts of clay minerals (illite, chlorite group, kaolinite) and heavy minerals contributing the remainder of the sediment. Radiocarbon dating of planktonic foraminifera from the base and other intervals of selected short cores (**Table 3-10**) show a wide range of ages from almost 3,000 YBP at a depth of 14 cm in core PC1704-16-MNC at the head of the canyon to a modern age at a depth of 10 cm from core RB1903-J2-1132-PC24 on the lower canyon north wall. Although more comprehensive coring is required to establish more robust sediment geochronology of the canyon system, such variation across the variety of canyon environments may be a result of small-scale down-wall sediment transport, current-driven erosion and redeposition, and biological reworking. Radiocarbon dates from planktonic foraminifera samples at depths of 100 cm and 200 cm within piston core BMCC-6Oct18-10-PC3 (**Table 3-10**) provide a first-order sedimentation rate of 25.4 cm/1,000 years in the lower canyon. Additional analysis of the disturbed sediment within the piston core are needed to confirm this rate.

While the mineralogy and geochemistry of rocks sampled within Pamlico Canyon are consistent with the regional stratigraphy of the Carolina Trough region, one rock sample is sufficiently unusual that it requires special mention. Sample AT41-A4969-R1, collected from the sediment surface immediately below the mid-canyon step is composed of almost 75% mullite (**Table 3-12** and **Table 3-13**), a rare aluminosilicate mineral usually found where high temperatures have metamorphosed clay minerals. In addition to the mullite content, a high concentration of lithium (**Table 3-13**) and a sintered ("clinker") surface on one face of the sample contribute to the uniqueness of the rock in comparison to other rocks collected along the Atlantic margin. While the origin of the sample remains unknown and similar lithologies were not identified in place within the walls of Pamlico Canyon, two hypotheses to explain its presence in the canyon are that it is anthropogenic debris (ship oven brick or trash; Zalasiewicz et al. 2014) or is the product of natural burning of coal adjacent to clay sediment at low-pressures sometime in the past (such as pyrometamorphism, Cosca et al. 1989)

Table 3-13. ICP-OES-MS geochemical analyses of rocks from Blake Escarpment/Blake Deep and Pamlico Canyon

Site	Blake Escarpment	Blake Escarpment	Blake Escarpment	Pamlico Canyon	Pamlico Canyon
Sample ID	AT41-A4964-Scoop-R2	RB1903-J2-1131-R2	RB1903-J2-1131-R3	AT41-A4969-R1	AT41-A4969-R3
Split ID	A4964.SCPR2.G1	19003.1131.R2.G1	19003.1131.R3.G1	A4969.R1.G1	A4969.R3.G1
Sample Type	Calcareous Mudstone	Calcareous Mudstone	Calcareous Mudstone (FeMn Surface)	Unknown	Calcareous mudstone
Al %	0.32	0.35	1.61	15	1
Ca %	34	35.3	1.81	0.23	27.7
Fe %	0.18	0.21	20.2	0.75	0.65
K %	0.12	0.17	0.3	1.84	0.34
Mg %	0.93	0.52	1.48	0.31	0.49
P %	0.27	0.71	0.54	0.03	0.03
S %	0.1	<0.1	0.3	<0.1	<0.1
Si %	1.24	1.98	2.82	27.1	10.4
Ti %	0.02	0.03	0.64	0.73	0.12
Ag ppm	<1	<1	2	<1	<1
As ppm	<5	<5	542	<5	<5
B ppm	15	16	210	80	86
Ba ppm	11.2	18	1,100	379	39.1
Be ppm	<5	<5	10	5	<5
Bi ppm	<0.1	0.2	12.2	<0.1	<0.1
Cd ppm	1.7	0.8	3.6	0.2	<0.2
Ce ppm	4.1	9.8	1,380	130	16.4
Co ppm	1.6	1.4	4,490	5	1.9
Cr ppm	15	19	32	131	28
Cs ppm	0.3	0.3	0.3	19.2	0.7
Cu ppm	7	5	573	36	<5
Dy ppm	0.9	0.87	49.5	6.15	1.03
Er ppm	0.56	0.5	23.7	3.8	0.6
Eu ppm	0.2	0.22	13.6	1.72	0.25
Ga ppm	0.74	1.09	18.5	24.5	2.26
Gd ppm	1.01	1.03	58	7.84	1.35
Ge ppm	<1	<1	2	2	<1
Hf ppm	<1	<1	10	8	4
Ho ppm	0.2	0.18	8.74	1.26	0.2
In ppm	<0.2	<0.2	<0.2	<0.2	<0.2
La ppm	4.6	5.9	278	67.5	8.2
Li ppm	<10	<10	26	207	14
Lu ppm	0.08	0.08	3.05	0.57	0.09
Mn ppm	13	102	116,000	36	21

Site	Blake Escarpment	Blake Escarpment	Blake Escarpment	Pamlico Canyon	Pamlico Canyon
Sample ID	AT41-A4964-Scoop-R2	RB1903-J2-1131-R2	RB1903-J2-1131-R3	AT41-A4969-R1	AT41-A4969-R3
Split ID	A4964.SCPR2.G1	19003.1131.R2.G1	19003.1131.R3.G1	A4969.R1.G1	A4969.R3.G1
Sample Type	Calcareous Mudstone	Calcareous Mudstone	Calcareous Mudstone (FeMn Surface)	Unknown	Calcareous mudstone
Mo ppm	<2	<2	280	<2	<2
Nb ppm	0.4	1.7	73.6	18.7	2.9
Nd ppm	4.3	4.9	264	52.7	8.1
Ni ppm	5	<5	2,060	38	11
Pb ppm	<5	5	1,250	5	<5
Pr ppm	1.05	1.24	65.4	14.6	2.08
Rb ppm	4.2	5.9	7.3	113	16
Sb ppm	<0.1	0.4	38.5	1	<0.1
Sc ppm	<5	<5	14	13	<5
Se ppm	<5	<5	<5	<5	<5
Sm ppm	0.9	0.9	57.5	8.8	1.5
Sn ppm	<1	<1	4	2	<1
Sr ppm	524	439	1,140	115	2,030
Ta ppm	<0.5	<0.5	1.1	1	<0.5
Tb ppm	0.14	0.16	8.55	1.12	0.19
Te ppm	<0.5	<0.5	36.4	<0.5	<0.5
Th ppm	0.7	1	90	17.9	2.5
Tl ppm	<0.5	<0.5	72.6	<0.5	<0.5
Tm ppm	0.08	0.08	3.5	0.54	0.08
U ppm	0.83	3.61	10.6	3.94	0.87
V ppm	8	11	1,120	75	17
W ppm	<1	<1	55	3	<1
Y ppm	6.8	6.2	160	29.6	5.6
Yb ppm	0.5	0.5	22	3.8	0.6
Zn ppm	<5	<5	609	<5	<5
Zr ppm	16.8	22.4	378	253	151

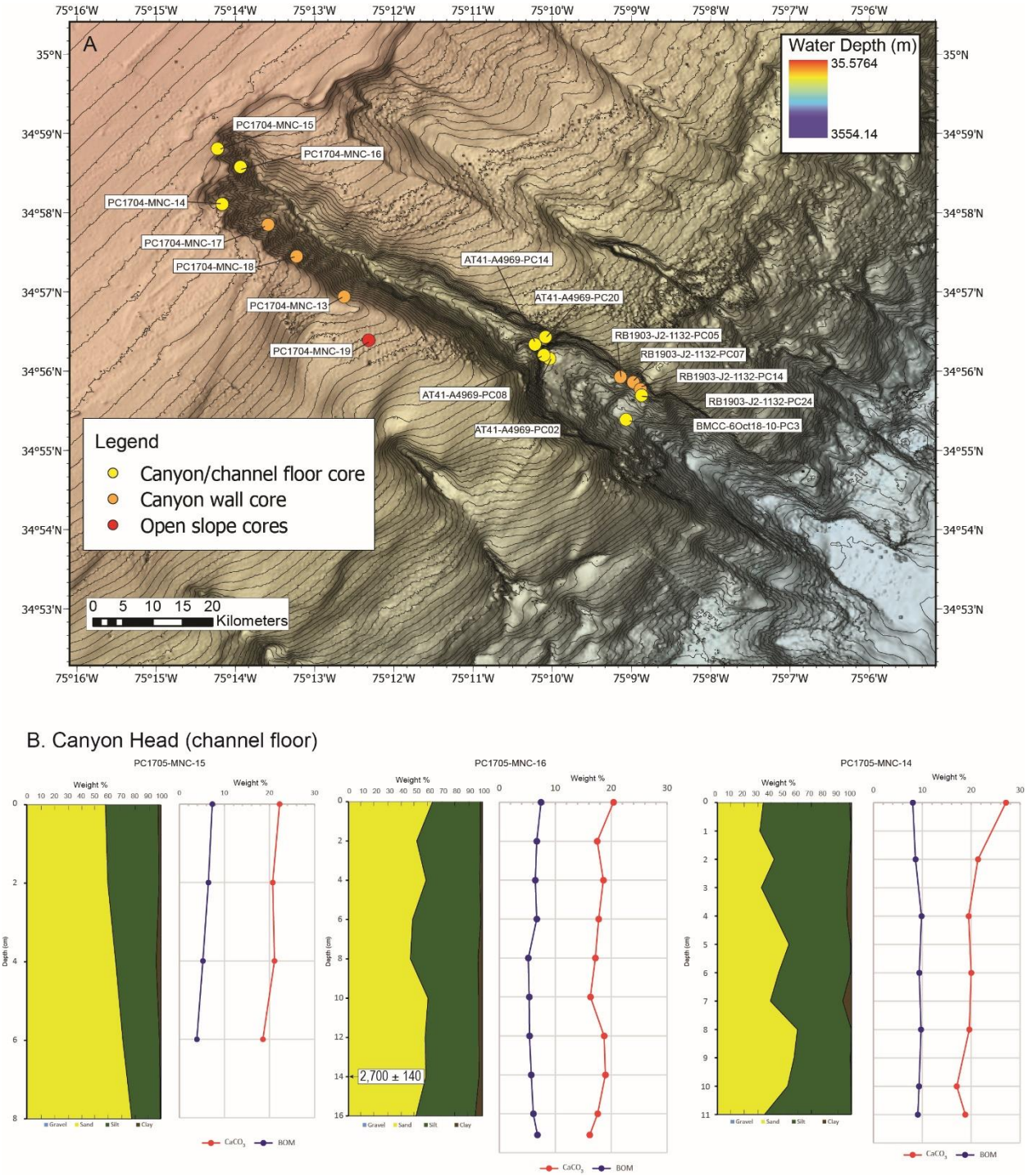

Figure 3-33. Monocore and push core grain size and calcium carbonate A & B
Analysis results Pamlico Canyon, including BOM. A) Distribution of cores within the canyon, separated into the three primary environments sampled. B) Analysis results from the head of Pamlico Canyon, including a radiocarbon age of ~ 2.7 ka for sediments at 14 cm adjacent to the canyon axis.

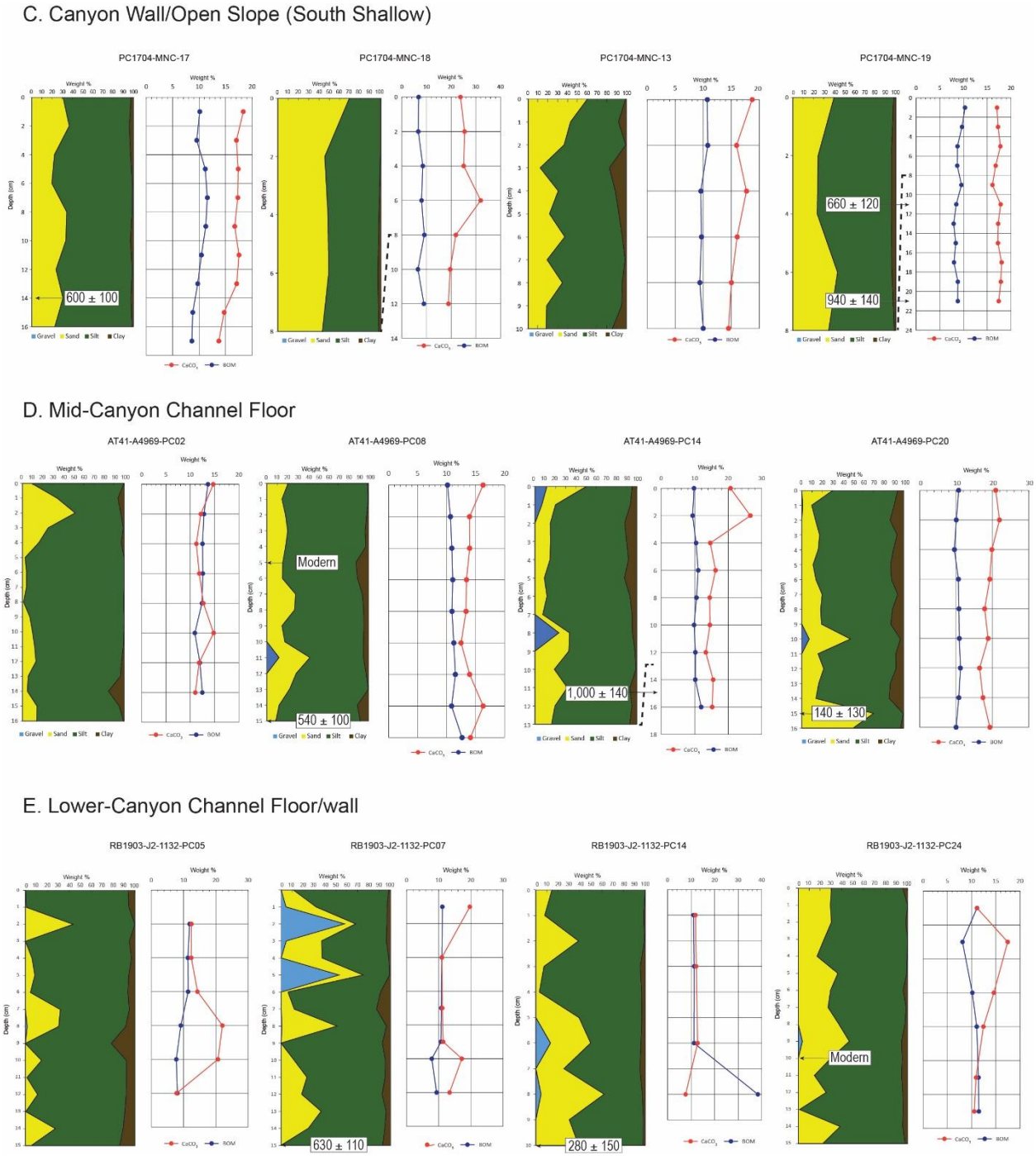

Figure 3-34. Monocore and push core grain size and calcium carbonate C, D, and E
C) Analysis results from the upper canyon walls and open slope south of Pamlico Canyon. D) Analysis results from the floor of the canyon near the mid-canyon step in the channel profile of Pamlico Canyon. E) Analysis results from the lower canyon north wall of Pamlico Canyon, showing that detrital carbonate (wall rock source) and larger biogenic components significantly impacting the grain size distributions.

3.2.4.3 Blake Plateau and Adjacent Areas

Samples collected and observations made of the seafloor character of the study sites on the Blake Plateau have provided the opportunity to evaluate previous interpretation made from lower-resolution imaging or analysis techniques. They further constrain the geologic and oceanographic conditions responsible for the complex and diverse geology and geomorphology of the region (**Figure 3-35**).

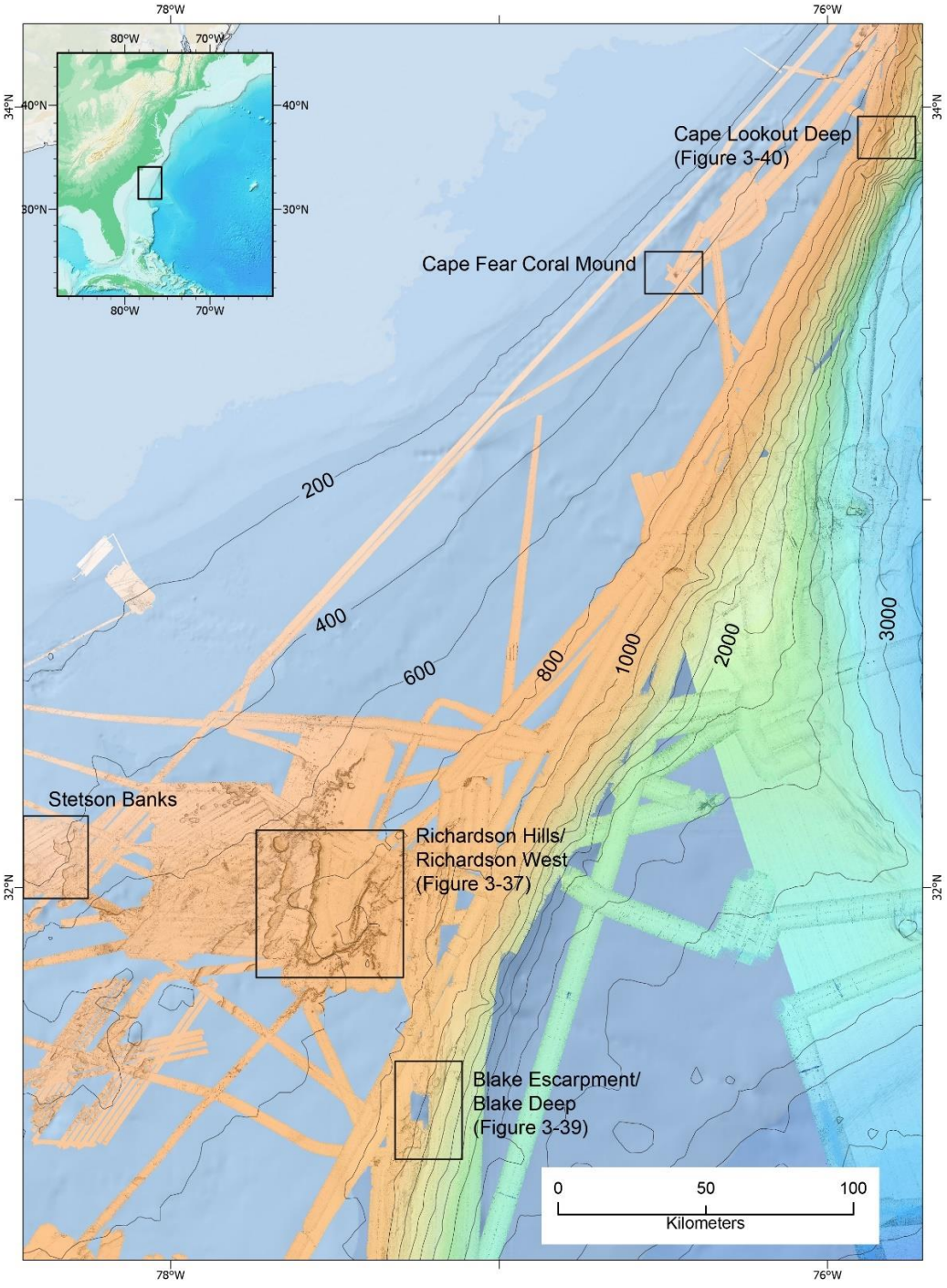

Figure 3-35. Regional map of the northern Blake Plateau and adjacent areas
Regions discussed in the text are highlighted. Contour interval is 200 m.

Limited sediment cover across the central and northern Blake Plateau (the Charleston Bump) hampered sediment sampling at many of the study sites (Richardson Hills and Stetson Banks), so the bulk of the results of geologic sampling are confined to recovered rocks. Results discussed below focus on three areas: 1) Richardson Hills to Stetson Banks, 2) Blake Escarpment, and 3) northern Blake Plateau (Northern Blake Plateau coral mounds and banks).

3.2.4.3.1 Richardson Hills to Stetson Banks

ROV *Jason* and *Alvin* dives in the Richardson Hills to Savannah Banks region (**Figure 3-35**) crossed a variety of rock types and geomorphic terrains. This region has been a focal area of long-term Gulf Stream induced erosion, geochemical overprinting and substantial benthic biological activity. As a result, the seafloor is characterized by rugged and heavily dissected bottom adjacent to areas of prominent scarps and banks (sometimes referred to as buttes or mesas); Popenoe (1994), all of which are separated by areas of smooth seafloor with or without material sediment cover. Although the presence of large mounds of live and dead *Lophelia* sp. has been known since the first detailed investigations of the Blake Plateau in the early 1960's (Stetson 1962; **Section 3.2.2**), the abundance and widespread distribution of the mounds has only recently been revealed by the comprehensive multibeam bathymetric mapping of the region. Using a combination of automated extraction and manual selection on bathymetry data available prior to early 2020, more than 8,900 mound structures have been located within the Savannah Banks to Blake Escarpment section of the Blake Plateau (**Figure 3-36**, mounds). We performed the automated extraction in the Richardson Reef and immediately adjacent areas using morphologic characteristics of the mounds visited during *Alvin* dives A4962 and A4963 as classification criteria and manual review to remove spurious results. Possible coral mounds occurring either as isolated peaks or within more complex ridge structures beyond the Richardson Reef area that were at least 100–125 m in diameter were manually flagged. Detailed statistical analysis of the mound structure dataset is awaiting completion of data collection in the region.

The seafloor underlying the extensive coral mounds of Richardson Reef (**Figure 3-37**) and throughout the central Blake Plateau appear to be largely restricted to exposed hard substrate composed of Cretaceous chalks and claystones, Eocene to Oligocene limestones, and foraminiferal siliciclastic carbonates (Manheim and Popenoe 2001). There are no areas of thick phosphorite pavement exposure. Strong seafloor returns and no subsurface reflections indicate that sediment cover in the region is minimal, at or below the resolution of the hull mounted chirp sub-bottom profilers used during the project (**Figure 3-36 b and c** chirp example). This includes across the smooth seafloor within the U-shaped area ringed by coral mounds and a prominent depression scour, and reefs and surrounding the Richardson Ridge area visited during *Okeanos Explorer* EX1806 (**Figure 3-36**). Limited amounts of sediments collect during *Alvin* dive A4963 on one of the coral mounds and in two of the piston cores collected during the 2018 *Brooks McCall* cruise (BMCC-3Oct18-04-PC1 & BMCC-3Oct18-05-PC2, **Figure 3-37**) recovered sediments dominated by *Lophelia* sp. skeletons (clasts) and a matrix of coarse biogenic carbonate sand. Heavy disturbance of the piston cores prevented most sedimentological analyses, but AMS ^{14}C radiocarbon dating of pieces of *Lophelia* sp. skeleton from 80 cm and 168.5 cm below the top of recovered sediment from piston core BMCC-3Oct18-05-PC2 had calibrated ages of 2,670 ± 150 and 3,600 ± 160 YBP, respectively.

Between Richardson Hills to the east and Stetson to west lies an area of highly dissected seafloor that is characterized by numerous deep erosional scours with steep walls and thin sediment covered floors and extensive outcrops of Oligocene, perhaps through to Paleocene age, limestones and siliciclastic carbonates. Ferromanganese crusts (**Figure 3-38, Table 3-13, Table 3-14**) and encrusted skeletal limestone where collected at the Richardson West site in this region during ROV *Jason II* Dive 1138 (sample RB1903-J2-1138-R1/2/3). Distinct mounds, which are geomorphically very similar to those initially visited at Richardson Hills, are present, but not abundant across this region (**Figure 3-15**). Continuing west, the rugged intensely eroded seafloor changes to relatively flat and smooth seafloor with

abundant mounds and current-rippled seafloor, before further changing to the angular, mesa-like features that characterize the Savannah Banks area (**Figure 3-16**). Two *Alvin* dives in this region found continuously exposed hard seafloor with the bank tops mantled by thick ferromanganese encrusted phosphorite pavement (and little to no sediment accumulation.

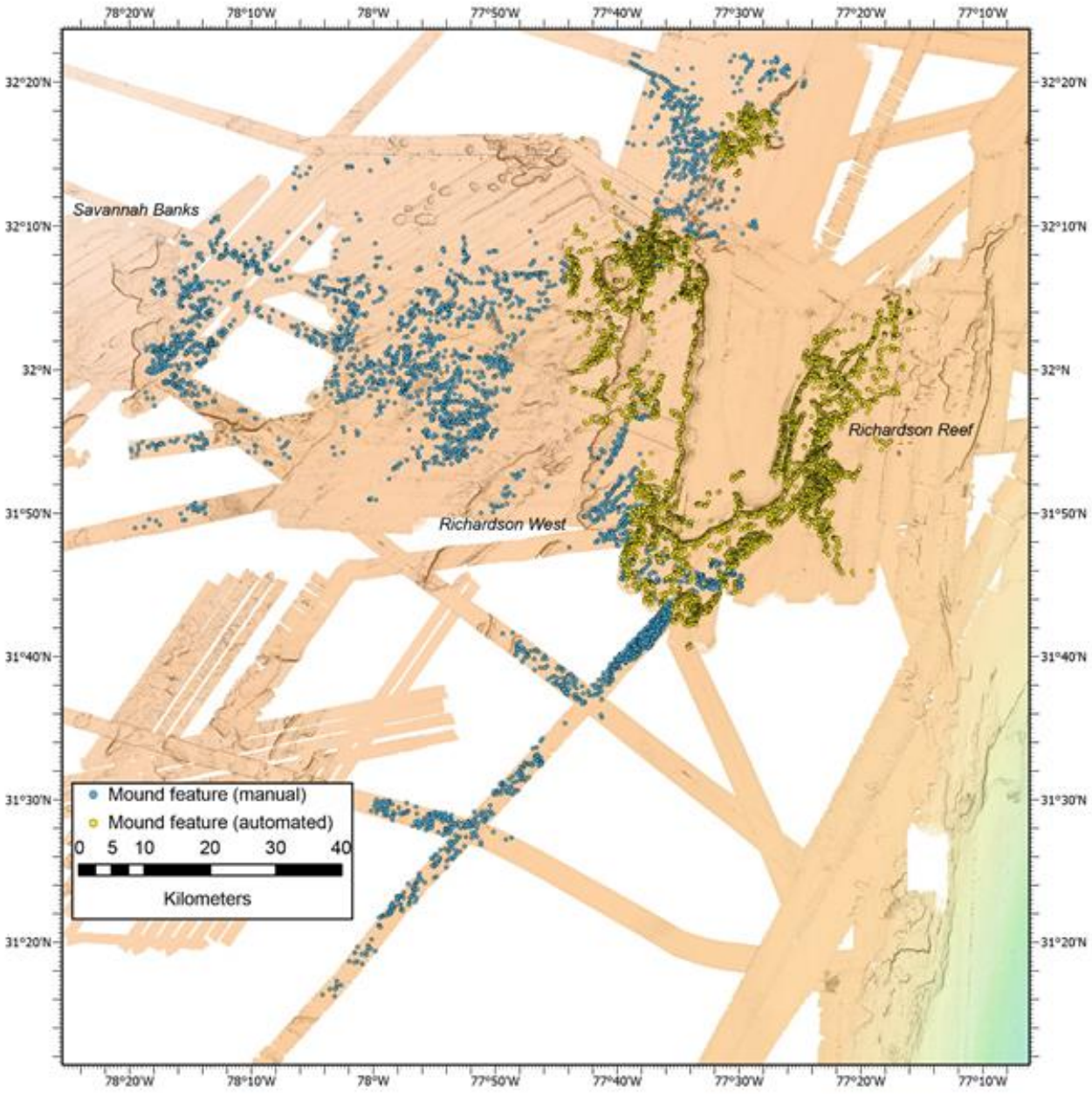

Figure 3-36. Mound features identified in 25-m resolution bathymetry data
In the Stetson Banks to Richardson Reef (Richardson Hills) section of the Blake Plateau. Mounds were picked via a combination of automated (GIS) processes in the Richardson Reef area where morphology of mounds visited during *Alvin* dive A4962 and A4963 confirmed the nature of the features or by manual means outside that region.

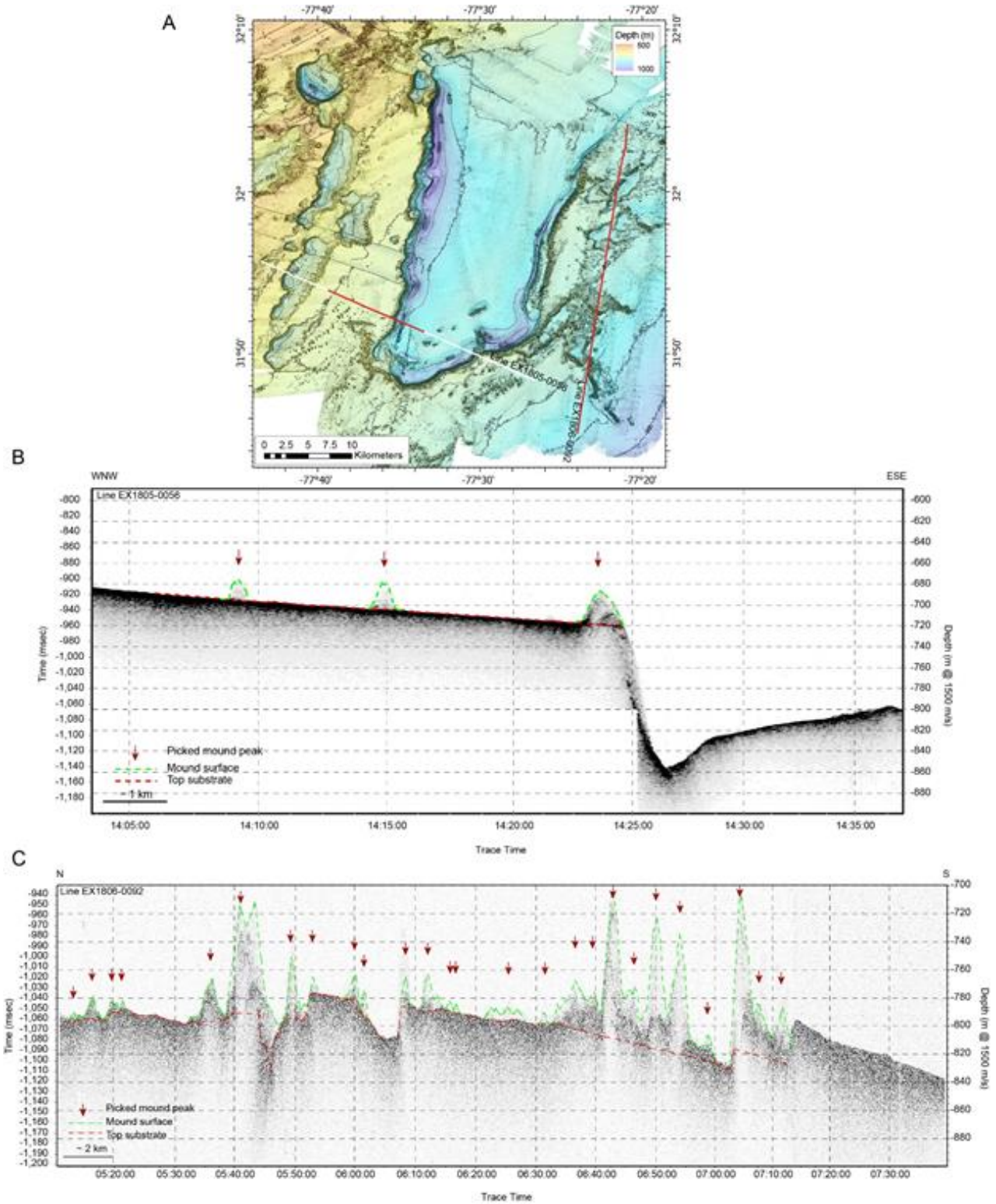

Figure 3-37. Multibeam bathymetry sub-bottom profiles across prominent coral mounds
(A) Geomorphology of the Richardson Hills (Richardson Reef-Richardson West) areas of the Blake Plateau based on 25-m resolution multibeam bathymetry. (B) & (C) Knudsen 3260 (Chirp) sub-bottom profiles across prominent coral mounds in the Richardson Hills.

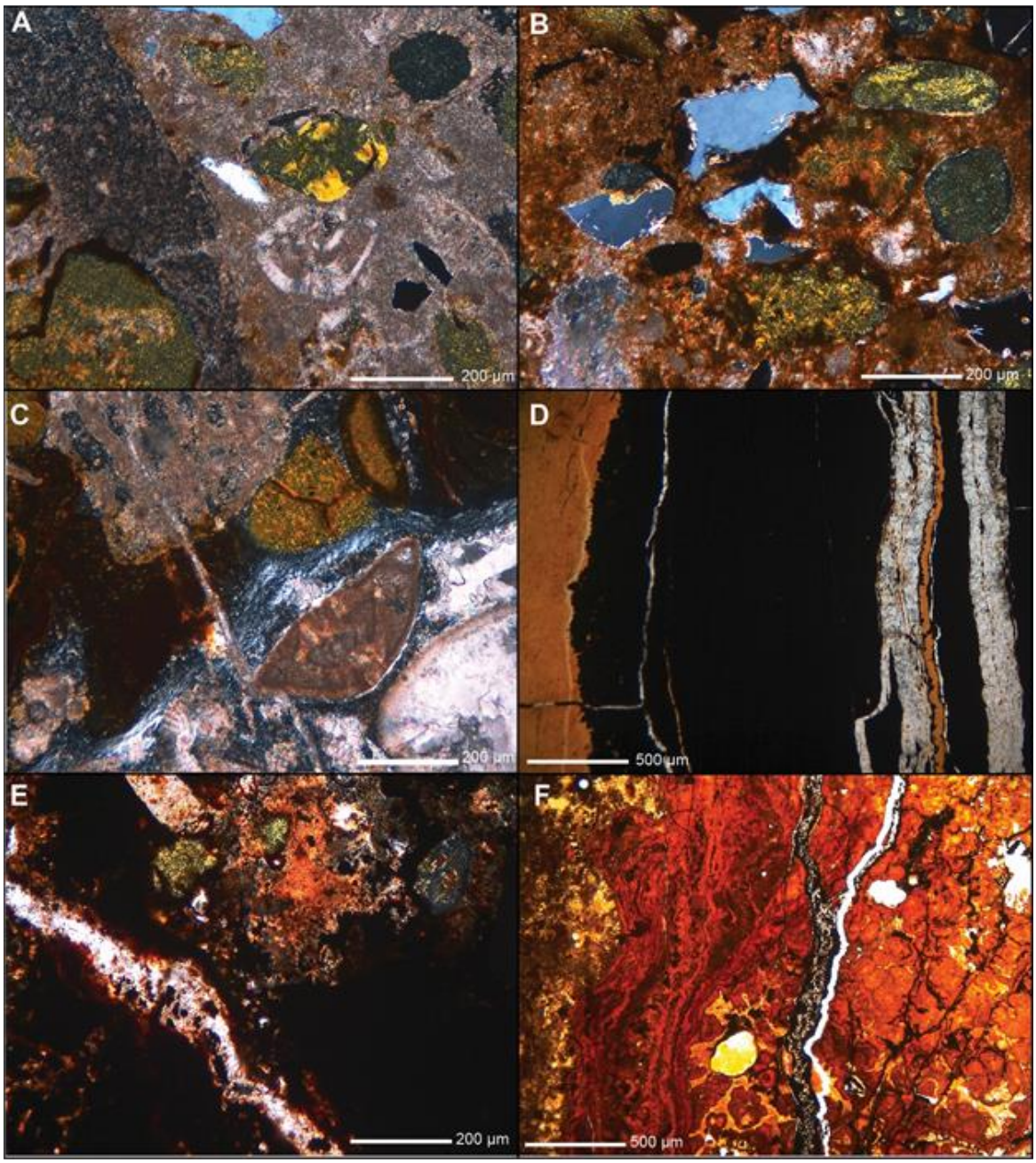

Figure 3-38. Photomicrographs of phosphorite and ferromanganese crusts.
From the Blake Plateau: (A) Phosphorite grains/pellets, foraminifera tests, and terrigenous grains in a matrix of calcite mud/cement (Sample AT41-A4965-R1), (B) Terrigenous (quartz) grains and phosphorite pellets in a matrix of calcite cement and ferromanganese mineral replacement (Sample AT41-A4965-MP1R1), (C) Phosphorite pellets and shell fragments in a matrix of calcite cement and ferromanganese mineral replacement (Sample AT41-A4965-R2), (D) Ferromanganese crust (primarily Todorokite-black) cut by secondary calcite-filled veins (sample AT41-A4966-2), (E) Ferromanganese mineral replacement (dark) and secondary calcite-filled veins from surface region of sample RB1903-J2-1138-R3, and (F) Layered ferromanganese minerals with secondary calcite-filled veins (Sample RB1903-J2-1138-R1)

Table 3-14. XRD-derived mineralogy of phosphorite pavement

From the Stetson Banks (SB) and Richardson West (RW) sites on the Blake Plateau. *XRD patterns indicated the presence of fluorapatite but could not resolve other mineral phases or yield quantitative analysis results. Minerals expressed in weight percent.

Site	Sample ID	Subsample ID	Quartz	Aragonite	Calcite	Glauconite	Fluorapatite	Todorokite	Manganite	Goethite	Fe-oxides & -sulfides
SB	AT41-A4965-R1	18042-A4965-R1-X1	2.09	-	56.10	-	21.80	19.30	-	-	-
SB	AT41-A4965-R2	18042-A4965-R2-X1	-	-	4.50	-	41.00	50.50	5.90	-	-
SB	AT41-A4965-R2	18042-A4965-R2-X2	4.45	-	17.70	-	64.70	9.20	1.50	-	2.20
SB	AT41-A4965-R2	18042-A4965-R2-X3	4.40	-	8.50	-	39.25	46.75	-	-	-
SB	AT41-A4965-R2	18042-A4965-R2-X4	5.81	-	48.95	-	18.75	1.00	-	25.40	-
SB	AT41-A4965-R2	18042-A4965-R2-X5	-	-	4.50	-	47.00	44.25	4.10	-	-
SB	AT41-A4965-MP1R1	AT41-A4965-MP1-R1	5.10	-	33.00	3.10	15.60	39.00	-	-	4.20
SB	AT41-A4966-R1	18042-A4966-1	0.34	-	9.70	-	66.50	23.50	-	-	-
SB	AT41-A4966-R1	18042-A4966-2	9.95	0.95	32.25	-	53.20	-	-	-	3.25
RW	RB1903-J2-1138-R1	19003-1138-R1-X1	-	-	-	-	*	-	-	-	-
RW	RB1903-J2-1138-R1	19003-1138-R1-X2	-	-	-	-	*	-	-	-	-

The mineralogic and geochemical profiles of the recovered samples of the phosphorite pavements and ferromanganese crusts (**Tables 3-11** and **3-12**) are similar to those discussed in detail by Manheim et al. (1980), McArthur and Walsh (1984), and others, but they will be briefly described here. Conglomeritic phosphoritic aggregates composed of pellets and pebbles of carbonate-fluorapatite with calcite, quartz and other minor constituents (**Figure 3-38**), encrusted by a variable thickness of manganese and iron oxide minerals such as Todorokite (**Table 3-6**) were recovered from Stetson Banks (*Alvin* dives A4965 and A4966). Ferromanganese mineral replacement beyond the surface of the rock samples is pervasive, as is fracture-filling secondary calcite. Although generally comparable with both previous phosphorite geochemical analyses conducted on samples from the region (Hein et al. 2016, **Table 3-15**), rare earth elements (including yttrium) and other trace elements values (**Table 3-15**) were significantly higher than previously identified, likely due to significant variability in element incorporation into the ferromanganese phases.

3.2.4.3.1.1 Blake Escarpment (Blake Deep)

Long-term retreat of the Blake Escarpment from its most seaward location in the (early Eocene), has exposed sections of Cretaceous and Paleocene calcareous mudstones/siltstones (bioclastic with limited siliciclastic component; **Table 3-12**), chalks, marls and limestones along irregularly shaped prominent cliffs and benches (**Figure 3-39**). Foraminifera tests and other fossiliferous components are filled by carbonate muds, with secondary calcite cementation (**Figure 3-38**). Ferromanganese crusts have accumulated on exposed outcrops along the sections of the escarpment traversed during J2 Dive 1131 and *Alvin* dive A4964 (**Figure 3-38**). These ferromanganese crusts have geochemical profiles similar to the ferromanganese crusts on the exposed phosphorite pavement at the Stetson Banks dive sites (**Table 3-13**). Overhangs and differential erosion of weaker layers of the exposed stratigraphy, in addition to significant transport of coral debris down the exposed steep cliffs suggests that the escarpment in the region of the dives continues to be actively eroded under the influence of regional currents. That said, the accumulation of ferromanganese crusts on outcrops exposed along the escarpment suggest that they have been relatively stable under current geologic and oceanographic conditions, for some time. Sediments at the two dives sites (**Figure 3-39**) are primarily biogenic silts and with variable amounts of sand and clay (mean grain sizes 3–7 phi) with $CaCO_3$ components accounting for as much as 75 % of the sample mass. Gravel size material in these recovered sediments is primarily coral debris transported down the escarpment cliff outcrops.

3.2.4.3.1.2 Northern Blake Plateau Coral Mounds

The Cape Fear Coral Mound/Lophelia Bank and the Cape Lookout slope bank at the northernmost section of the Blake Plateau (within the Carolina Trough geologic province) were visited during Deep SEARCH dives in 2018 and 2019, respectively. The Cape Fear Coral Mound has been extensively studied (Ross 2006, Quattrini et al. 2012) with its geomorphology and surrounding geologic environment described in detail. Sediments at the Cape Fear Coral Mound site recovered in a single push core and a CTD monocore (**Figure 3-35**), are a mix of medium to coarse grained (mean grain size 0 to 2.5 phi) sand primarily composed of biogenic ($CaCO_3$) shells and tests, authigenic glauconite, and minor terrigenous components.

Table 3-15. ICP-OES-MS analyses of phosphorite pavement samples

From sites on the Blake Plateau (SB=Stetson Banks, RW=Richardson West). The mean values of geochemical analysis of 10 samples from the Blake Plateau by Hein et al. (2016) are included for comparison.

Site	SB	SB	SB	SB	SB	SB	SB	SB	SB	RW	-
Sample ID	AT41-A4965-MP1R1	AT41-A4965-R1	AT41-A4965-R2	AT41-A4965-R2	AT41-A4965-R2	AT41-A4965-R2	AT41-A4965-R2	AT41-A4966-R1	AT41-A4966-R1	RB1903-J2-1138-R1	Hein et al. (2016)
Split ID	A4965.MP1R1.G1	A4965.R1.G1	A4965.R2.G1	A4965.R2.G2	A4965.R2.G3	A4965.R2.G4	A4965.R2.G5	A4966.1.G1	A4966.2.G1	19003.1138.R1.G1	Mean (n = 10)
Al %	0.92	1.14	1.35	2.06	1.34	1.43	1.65	1.4	1.07	0.78	0.71
Ca %	26.7	24.2	20.5	20.8	22.5	22.8	20.9	22.7	26.4	13.9	31.8
Fe %	4.08	3.14	10.3	3.87	4.84	6.47	5.21	5.2	5.99	9.1	2.35
K %	1.08	0.97	1	0.51	0.25	1.04	0.51	0.6	0.98	0.27	0.51
Mg %	1.04	1.15	1.4	2.43	1.66	1.15	1.91	1.63	0.93	1.12	0.65
P %	3.04	4.41	6.05	6.85	8.28	5.7	6.77	7.14	7.36	4.85	8.8
S %	0.2	0.3	0.4	0.5	0.6	0.3	0.5	0.4	0.4	0.4	0.68
Si %	4.82	4.63	4.54	3.39	1.25	5.41	2.42	2.5	3.9	0.88	2.86
Ti %	0.03	0.05	0.08	0.18	0.14	0.07	0.13	0.09	0.06	0.31	0.05
Ag ppm	<1	<1	<1	<1	<1	<1	<1	<1	<1	1	-
As ppm	43	30	128	81	118	101	109	123	97	205	35
B ppm	84	85	133	118	129	108	129	114	109	107	
Ba ppm	1,090	4,440	693	216	1,450	1,620	828	1,460	263	1,540	323
Be ppm	<5	<5	<5	<5	<5	<5	<5	<5	<5	6	-
Bi ppm	0.3	1.3	2.5	3.2	7.6	2.4	3.8	5	2	18.4	-
Cd ppm	1.3	1.1	1.1	2.8	2.4	1	2.6	2.1	0.8	3.1	-
Ce ppm	37.9	86.2	142	165	397	133	229	232	105	1,040	36.2
Co ppm	316	739	692	1,220	1,970	416	1,340	1,210	184	2,490	126
Cr ppm	96	80	217	85	63	129	93	96	119	12	99
Cs ppm	1.6	1.1	1.2	0.5	0.2	1.5	0.4	0.8	1.3	0.2	-
Cu ppm	38	55	129	288	127	71	159	210	53	256	72
Dy ppm	6.72	10.5	26.3	32.9	53	16.7	51	23.6	16.9	30.3	11.8
Er ppm	3.8	6.14	16.2	21.6	38.2	10.3	36.1	15.8	11.2	19.3	7.75
Eu ppm	1.89	3.01	5.67	6.2	9.8	3.94	9.49	4.87	3.48	6.69	2.45
Ga ppm	3.8	5.22	6.95	9.3	9.91	4.87	10.1	7.91	4.17	12.4	-

Site	SB	SB	SB	SB	SB	SB	SB	SB	SB	RW	-
Sample ID	AT41-A4965-MP1R1	AT41-A4965-R1	AT41-A4965-R2	AT41-A4965-R2	AT41-A4965-R2	AT41-A4965-R2	AT41-A4965-R2	AT41-A4966-R1	AT41-A4966-R1	RB1903-J2-1138-R1	Hein et al. (2016)
Split ID	A4965.MP1R1.G1	A4965.R1.G1	A4965.R2.G1	A4965.R2.G2	A4965.R2.G3	A4965.R2.G4	A4965.R2.G5	A4966.1.G1	A4966.2.G1	19003.1138.R1.G1	Mean (n = 10)
Gd ppm	9.29	13.6	32.5	37.2	56.7	21.2	56.5	27.1	19.6	29.7	12.9
Ge ppm	<1	<1	1	1	<1	1	1	1	<1	1	-
Hf ppm	2	5	5	12	6	7	8	6	3	8	-
Ho ppm	1.34	2.19	5.53	7.33	12.3	3.5	11.6	5.12	3.77	6.27	2.58
In ppm	<0.2	<0.2	<0.2	<0.2	<0.2	<0.2	<0.2	<0.2	<0.2	<0.2	-
La ppm	39.1	70.2	151	172	256	112	257	124	101	159	71.1
Li ppm	20	28	30	63	27	23	37	36	16	12	14
Lu ppm	0.4	0.75	1.95	2.67	,5.03	1.26	4.68	1.99	1.43	2.74	1.19
Mn ppm	19,900	48,000	31,700	73,900	85400	17,500	77,300	68,900	7,870	118,000	9,108
Mo ppm	14	46	76	242	147	39	162	102	23	265	22
Nb ppm	1.6	3.5	9.9	20.2	23.6	6.6	20.1	14.1	7.8	42.5	-
Nd ppm	35.7	55.8	118	129	187	79.7	192	97.2	72.7	127	48
Ni ppm	462	1,100	2,110	6,880	4,280	906	5,050	3,830	597	3,250	467
Pb ppm	15	53	125	172	586	121	276	280	74	1,140	19
Pr ppm	8.44	13.3	27.2	29.2	42.2	18.4	42.7	22.2	16.5	29	10.8
Rb ppm	43	34.1	36.9	16.2	6.2	41.1	14.7	21.5	37.4	4.7	-
Sb ppm	6.1	4.6	13.7	9.4	18.1	10.4	13.8	18.9	12.8	34.8	-
Sc ppm	<5	5	8	11	11	8	13	8	6	5	-
Se ppm	<5	<5	<5	<5	<5	<5	<5	<5	<5	<5	-
Sm ppm	7.6	11.1	24.3	26.5	38.5	15.9	39.2	20.4	14.1	26.6	9.09
Sn ppm	<1	<1	1	1	2	<1	1	1	1	4	-
Sr ppm	609	939	1,020	1,320	1,960	827	2,090	1,180	959	1,750	1,376
Ta ppm	<0.5	<0.5	<0.5	<0.5	<0.5	<0.5	<0.5	<0.5	<0.5	0.6	-
Tb ppm	1.18	1.82	4.31	5.05	7.81	2.77	7.78	3.76	2.7	4.75	1.71
Te ppm	0.8	4.8	8.3	14.5	20.4	9	13.8	13.1	6	24.2	-

Site	SB	SB	SB	SB	SB	SB	SB	SB	SB	RW	-
Sample ID	AT41-A4965-MP1R1	AT41-A4965-R1	AT41-A4965-R2	AT41-A4965-R2	AT41-A4965-R2	AT41-A4965-R2	AT41-A4965-R2	AT41-A4966-R1	AT41-A4966-R1	RB1903-J2-1138-R1	Hein et al. (2016)
Split ID	A4965.MP1R1.G1	A4965.R1.G1	A4965.R2.G1	A4965.R2.G2	A4965.R2.G3	A4965.R2.G4	A4965.R2.G5	A4966.1.G1	A4966.2.G1	19003.1138.R1.G1	Mean (n = 10)
Th ppm	3.7	6.5	8.4	8.4	7.1	7	7.4	10.7	4.7	17	-
Tl ppm	1.7	4.8	2	5.4	4.4	1	5.1	3.3	0.8	27	-
Tm ppm	0.47	0.81	2.03	2.86	4.99	1.3	4.63	1.98	1.46	2.92	1.17
U ppm	2.98	3.79	14.4	10.5	11.5	4.61	11.4	7.94	11.9	10.4	62
V ppm	95	185	234	311	355	176	317	320	168	503	113
W ppm	4	14	22	107	61	17	77	35	13	59	-
Y ppm	48.2	82.6	227	317	564	148	521	201	165	208	130
Yb ppm	2.9	5.1	13	17.7	31.7	8.3	30	13.1	9.3	18.5	6.65
Zn ppm	112	161	316	516	598	191	616	487	137	567	87
Zr ppm	74.5	192	176	428	236	215	329	195	94.2	342	73

The bank feature south of Cape Lookout (Cape Lookout North dive site) outcrops from a generally smooth section of the upper slope between water depths of 800 and 1,300 m (**Figure 3-20**). The elongated asymmetric shape of the bank is morphologically distinct from the stratigraphic units of unknown age exposed on the slope below the bank and the smaller tear-drop shaped coral mound in shallower water to the north (**Figure 3-15** map).

Dolomite is the primary component (88.3 weight %) of the mineralogy of the single rock sample (19003-J2-1135-B5; **Table 3-12**; **Figure 3-25**) collected from the bank, but it lacks a well-developed crystalline texture as seen in the dolomite collected at the Cape Fear Seep (**Figure 3-38**). Although the morphology and surficial geology of the site differs from that seen at the shelf-edge and deeper seeps sites, the presence of dolomite-rich lithologies and bacterial mats in the adjacent sediments suggests a seep or seep-related origin for the feature. Multichannel seismic-reflection data collected across the bank (**Figure 3-40**, Triezenberg et al. 2016, line PR82-X249) shows that only a small part of the feature is currently exposed, with the western flank buried below sediments.

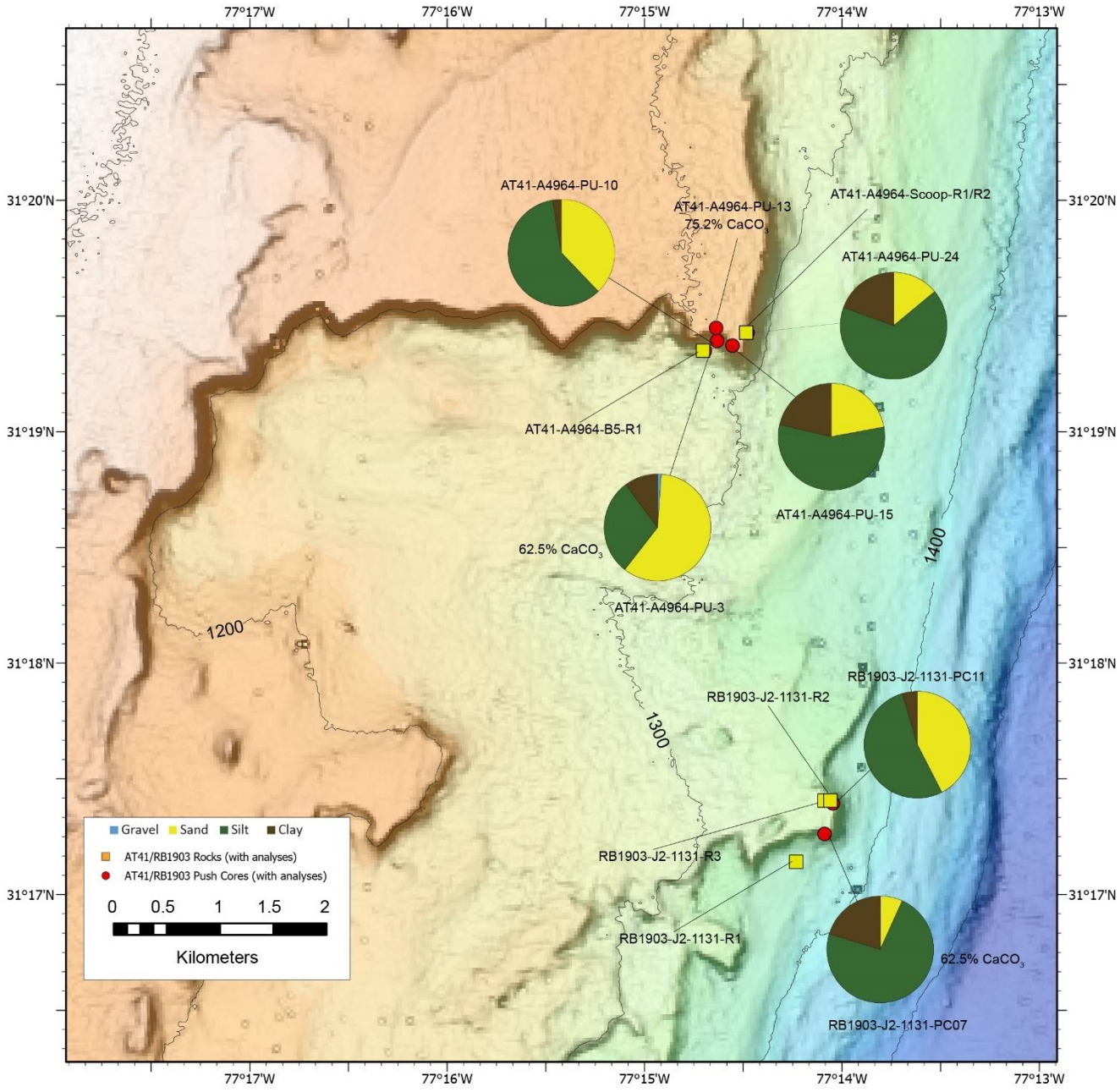

Figure 3-39. Grain size distribution and average $CaCO_3$ content of surficial samples
Seabed samples collected 0–2 cm deep from the Blake Escarpment region.

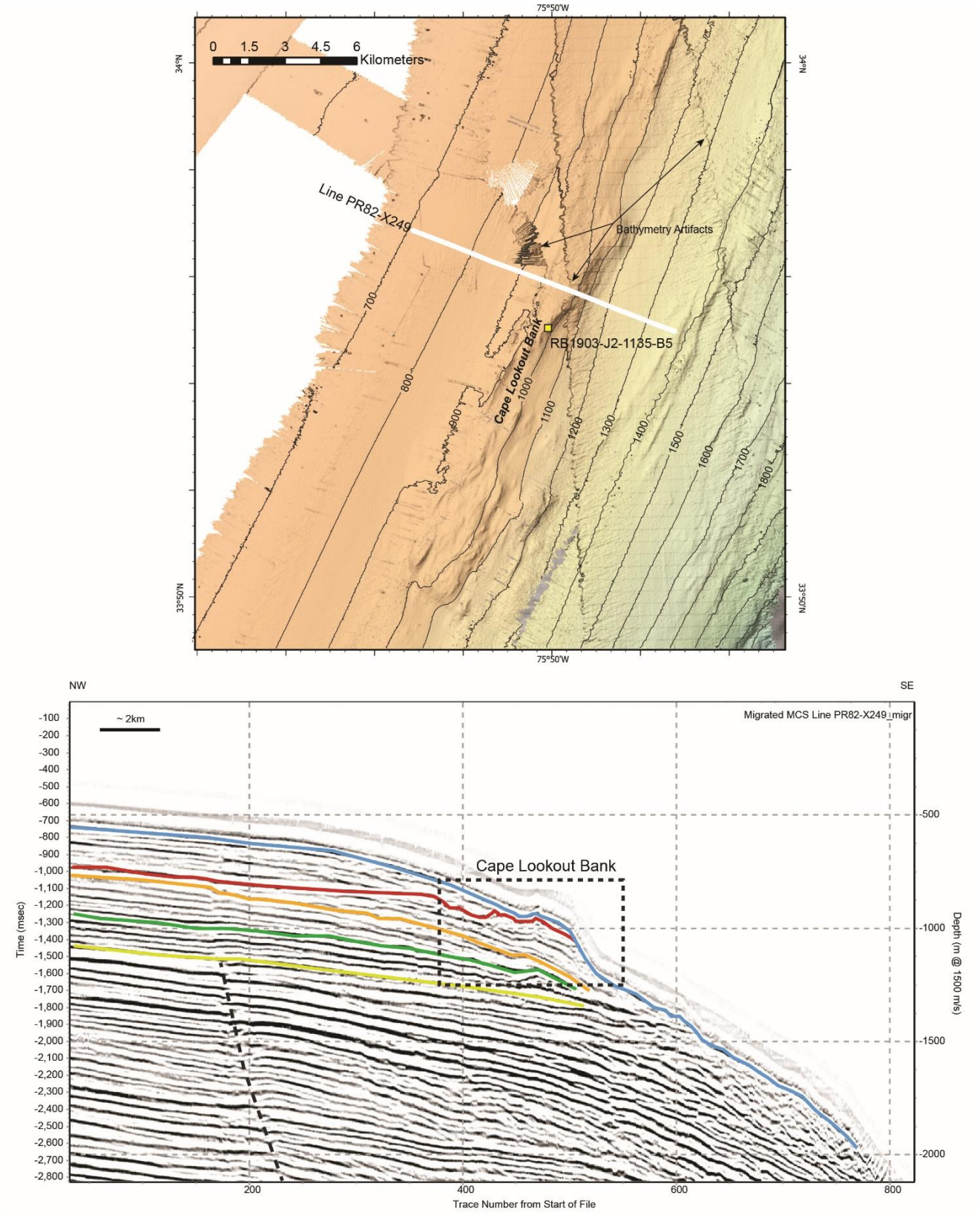

Figure 3-40. Cape Lookout (Deep) bank and multichannel seismic-reflection profile
Shows mostly buried bank structure.

3.3 Biogeochemistry and Microbiology

Section Authors: Samantha Joye, Nancy Prouty, Christina Kellogg, Hannah Choi, Sabrina Beckmann, Guang-Chao Zhuang, Zachary Marinelli, Kimberly Hunter

Microorganisms catalyze elemental cycling in the ocean and help regulate geochemical processes that are crucial for the maintenance of planetary habitability (Joye et al. 2021). Biogeochemical reactions are mediated by microorganisms that couple oxidation and reduction reactions to extract power from chemical disequilibria via thermodynamics (Joye et al. 2021). Biogeochemical cycling varies spatially and temporally as a function of local conditions. Water-column biogeochemistry in the Deep SEARCH domain is influenced strongly by the Gulf Stream. Sediment biogeochemistry across Deep SEARCH sites is modulated by sediment grain size, sediment permeability, and the presence of methane seepage, which is an important modulator of geochemical signatures and microbial activity. Microbial activity plays an important role in both pelagic and benthic environments, shaping patterns of nutrient regeneration and nitrogen to phosphorus ratios and controlling carbon fluxes.

Deep SEARCH biogeochemical studies characterized the geochemical signatures of sediments and carbonates, chemical signatures of the water column, and microbial activity in both sediments and in the water column with a focus on the fate of methane in sediments, carbonates, and in the water column. In total, we collected 272 water-column samples, 85 sediment pore water and 70 sediment solid phase samples from 30 sediment cores during expeditions AT-41 and RB19-03 (**Table 3-16** and **Table 3-17**)

Table 3-16. Deep SEARCH water-column biogeochemistry sample collections

Cruise ID	Sample Type	Number Collected
AT41	CTD Niskin	145
AT41	*Alvin* Niskin	8
BMCC-19	CTD Niskin	15
RB19-03	CTD Niskin	150
RB19-03	*Jason* Niskin	5
NF19-09	CTD Niskin	49

Table 3-17. Deep SEARCH sediment biogeochemistry sample collections

Cruise ID	Sample Type	Number Collected
AT41	Overlying water and pore water	85
AT41	Whole sediment	70
RB19-03	Overlying water and pore water	85
RB19-03	Whole sediment	68

3.3.1 Water-Column Methods

We examined water-column chemistry and methane dynamics at seep sites, at deepwater coral sites, and in canyons (**Table 3-18**). On board the ship, we used hydrographic data to determine sampling depths. At seep sites, we targeted methane plumes as well as control sites some distance from advective discharge. Sampling depths varied across sites, but we typically targeted near surface waters, the deep chlorophyl maximum, other hydrographic anomalies (changes in density or oxygen), and near the seabed, typically

within or near methane plumes. The sampling depths ranged from 400 to 2,800 m (**Table 3-18**). We collected water samples from seep sites, from canyon sites, and from coral sites.

Table 3-18. Detailed summary of pelagic sample collections

Cruise ID	Site	CTD casts	Additional
AT41	Pea Island	3	3 *Alvin* Niskin
AT41	Stetson Deep	2	-
AT41	Richardson Ridge	2	-
AT41	Blake Escarpment	1	-
AT41	Stetson Banks	2	-
AT41	Blake Ridge	1	5 *Alvin* Niskin
AT41	Capre Fear	1	-
AT41	Norfolk	1	-
BMCC-19	Richardson Bend	1	-
BMCC-19	Richardson Hills	1	-
BMCC-19	Pamlico Canyon	1	-
RB19-03	Stetson Banks	1	-
RB19-03	Richardson Hills	3	-
RB19-03	Savannah Banks	1	-
RB19-03	Blake Deep	1	-
RB19-03	Pamlico Canyon	2	-
RB19-03	Pea Island	2	2 *Alvin* Niskin
RB19-03	Kitty Hawk	1	1 *Alvin* Niskin
RB19-03	Lookout Deep	1	-
RB19-03	Blake Ridge	1	-
RB19-03	Cape Fear Seep	1	-
RB19-03	West Richardson Hills	1	-
NF19-09	Blake Ridge	3	-
NF19-09	Pamlico Canyon	1	-
NF19-09	Richardson Hills	5	-

3.3.1.1 Sample Collection

We carried out similar sampling at all sites. We collected samples using a CTD-rosette system with 20-L Niskin bottles equipped with a SBE 911plus CTD profiler, dual SBE 43 DO sensors, dual temperature sensors, and an ECO fluorometer. Biogeochemical sampling proceeded as follows: first, we filled a 1-L PETG® bottle for dissolved methane concentration quantification from the Niskin bottle using silicon tubing according to Rogener et al. (2018, 2021). After filling, bottles were capped headspace-free and without bubbles. We similarly filled a second 1-L PETG to collect waters for determination of methane oxidation rates. Finally, we filled a 1-L PETG bottle to subsample for water-column chemistry. We processed samples for chemical analyses within 1 hour of collection. We processed samples for methane concentration and oxidation rate within 12 hours of collection.

For microbial diversity analyses, we passed approximately 2 L of water through a Sterivex® filter (we noted exact filtered volumes), air-dried filters using sterile-filtered air, sealed and flash-froze each in liquid nitrogen, and stored them at -20ºC shipboard and -80ºC in the laboratory prior to deoxyribonucleic acid (DNA) extraction. DNA was extracted using a Qiagen Dneasy PowerSoil Max extraction kit following the manufacturer's instructions. We measured resulting DNA concentrations using a Qubit (2.0) fluorometer (Thermo Fisher Scientific). Samples were subject to Covaris shearing and metagenomic

libraries were prepared using Kappa DNA library preparation kit and sequenced (2 × 250 bp) on an Illumina HiSeq platform (Illumina Inc.) at COSMOS ID®, Rockville, Maryland. Metagenome sequencing datasets were analyzed using gene-based and genome-based bioinformatics approaches. Results from gene-based approaches are presented here.

Short reads of the 16S rRNA gene in the quality trimmed sequences were identified and taxonomically classified using phyloFlash v3.2, which employs BBMap25 (for identification) and VSEARCH v2.5.026 (for classification) of putative 16S rRNA gene reads using SIVLA 132 (release 27) as the reference database. The relative abundances of each 16S rRNA gene in each sample were normalized by dividing by particular 16S rRNA gene abundance by the total number of read pairs in the trimmed dataset for that specific sample.

3.3.1.2 Chemical Analyses

We removed approximately 60 mL of seawater from each 250-mL PETG sample bottle and filtered that through a pre-cleaned dry 0.2-µm Target® filter. From this volume, we used a 5-mL subsample for ammonium analysis (Rogener et al. 2018, 2021). We froze the remaining samples (ca. 55 mL) in the high density polyethylene bottles and stored them at -20 °C. We determined the ammonium concentration using the phenol hypochlorite method; sample absorbance was quantified using a Shimadzu spectrophotometer (Model UV-1601) that was standardized using reagent grade ammonium chloride; the detection limit was 100 nM (Solorzano 1969).

We conducted other chemical analyses at the University of Georgia (UGA) lab within two months of the cruise. Nitrogen oxides—nitrate + nitrite (NOx)—were reduced to nitric oxide (NO) using acidic vanadium (III); the concentration of NO-N was determined via chemiluminescence using an Antek 7050 nitric oxide detector (Braman and Hendrix 1989). Nitrite concentration was determined using the Greiss method (Grasshoff et al. 1983) and nitrate concentrations were calculated by difference (= [NOx] - [nitrite]). ACS reagent grade KNO_3 and $NaNO_2$ were used to generate standard curves and the detection limits were 150 nM for NOx and 50 nM for nitrite.

We determined DOC concentrations on filtered, acidified, nitrogen-purged water samples using a Shimadzu TOC analyzer. The TOC analyzer was standardized using ACS reagent grade potassium hydrogen phthalate and the detection limit was 300 nM. We determined TDN concentrations in filtered seawater samples using a Shimadzu Instruments TOC-V coupled to Shimadzu Instruments TN unit. The standard was ACS reagent grade glycine and the detection limit was 400 nM. We calculated DON concentrations in the as the difference between TDN and dissolved inorganic N (= NOx + ammonium). We quantified phosphate concentrations using the molybdate blue colorimetric method; the method was standardized using ACS reagent grade potassium orthophosphate solutions and the detection limit of 160 nM (Solorzano and Sharp 1980).

We extracted dissolved methane from a 0.7-L seawater samples using a sonication/vacuum extraction technique (Rogener et al. 2018, 2021). We stored extracted gases in gas-tight vials and we then injected 1-mL gas samples into a gas chromatograph (SRI® model 8610C) outfitted with a HaySep DB® column and a flame ionization detector. We calculated methane concentrations by comparing the integrated areas under the curve for samples to the areas obtained from high purity gas standards of known concentration (Scott Specialty Gases®). The detection limit for the extraction method was 0.5 nM.

3.3.1.3 Methane Oxidation Activity Measurements

We used a tritiated methane (^3H-CH_4) tracer to quantify rates of microbially mediated methane oxidation. In these assays, we determined methane oxidation rates by tracking the conversion of tritium-labeled methane to tritiated water (Eq. 2). The use of high specific activity tritiated methane (~0.7 TBq mmol)

meant that only 0.5 nM methane needed to be added to each sample as tracer. This low addition of methane assured that in situ concentrations were not altered during the incubations, assuring that the measured rates reflect in situ activity instead of potential activity.

$$C^3H_4 + 2\text{-}O_2 \rightarrow CO_2 + 2\,[^3H]\text{-}H_2O \qquad \text{(Equation 2)}$$

We fitted an open large-bore (60-mL) syringe with a section of sterile silicone tubing to subsample PETG bottles for rate incubations; the open bore syringe to ensured that microbial aggregates were not excluded from the incubation vials (Crespo-Medina et al. 2014). We transferred individual samples to a 16-mL Hungate tube and capped headspace-free using deoxygenated Labco® septa. At each depth, we performed rate assays in triplicate alongside a killed control. Killed controls were generated by adding 1.5 mL of 37% formaldehyde to the sample to halt microbial activity; we did this prior to tracer addition. We injected tritiated CH_4 tracer as a 20-µL gas bubble; the final aqueous phase tracer activity was about ~20 kBq. We then incubated samples without bubbles on their sides within 3°C of in situ temperature for 48 hours. Temperature was maintained using an incubator inside the radiation isotope isolation van.

After incubation, we subsampled each vial to determine the total tritium activity, reflecting the sum of ^3H-CH_4 plus ^3H-H_2O. We obtained such by removing a 100-µL subsample, transferring it to a vial containing scintillation cocktail (ScintiSafe Gel®), and quantifying radioactivity on a Hidex 300 SL (ex. AT41) or a Beckman® 6500 (ex. RB19-03, shore-based analyses) liquid scintillation counter. Activity in samples was halted by transferring the sample volume into a 20-mL scintillation vial containing 1.5 mL of 37% formaldehyde, which served to halt microbial activity. After termination, each sample was purged immediately with hydrated air for 60 minutes to remove remaining ^3H-CH_4 tracer. Then, we removed a -mL aliquot and transferred it to a scintillation vial that we had amended with scintillation cocktail. We quantified the ^3H-H_2O activity on the Beckman® 6500 scintillation counter at the UGA laboratory. We calculated methane oxidation rates by multiplying the fractional turnover rate constant (k) by the methane concentration measured for that water sample (Eq. 3, 4).

$$k = (\,{}^3H_2O / (\,{}^3H_2O + C^3H_4\,)\,) / \text{incubation time} \qquad \text{(Equation 3)}$$

In Eq. 3, k is the tracer turnover calculated as the ^3H_2O produced divided by the total tritium injected into the incubation vial (determined as $^3H_2O + C^3H_4$) divided by the incubation time. We then determined the methane oxidation rate by multiplying the fractional turnover rate constant by the sample methane concentration to generate a rate in nmol L^{-1} d^{-1} (Eq. 4). The detection limit for methane oxidation activity was 5 pmol L^{-1} d^{-1}.

$$CH_4 \text{ oxidation} = k\,[CH_4] \qquad \text{(Equation 4)}$$

3.3.2 Water-Column Results

3.3.2.1 Shallow seeps

Methane seeps clearly impacted the water column, especially in shallow waters. Pelagic nutrient concentrations around seeps were depleted at the surface and increased with depth. Concentrations of dissolved inorganic phosphate (DIP) ranged from 0.2 to 3 µM; concentrations of dissolved inorganic nitrogen (DIN = NH_4 + NOx) were zero in surface waters and increased to 30 µM near the seabed. Both DIN and DIP were comparably low in surface waters and DIP was present in excess of DIN, suggesting nitrogen limitation of biological production. At depth, the DIN:DIP ratio was roughly 10, again inferring nitrogen limitation relative to the Redfield DIN:DIP Ratio of 16 (**Figure 3-41**; Redfield 1934, 1958). Concentrations of DIN and DIP exhibited regenerative profiles, characterized by increasing concentration with depth below the surface mixed layer and a stabilization of the profiles by about 300-m depth.

The DIN pool was dominated by nitrate (**Figure 3-42**); ammonium concentrations were less than 0.8 µM and concentrations were typically below 0.4 µM. Concentrations of TDN and TDP followed the profiles of dissolved inorganic nutrients; concentrations of DON and DOP accounted for about 25% of the total dissolved pool (**Figure 3-43**). Concentrations of DOC were generally highest at the surface, exceeding 150 µM (**Figure 3-43**); in one of the Pea Island Seep casts, a peak in DOC was in the midwater, at roughly 250-m depth.

Methane seepage introduces ancient DOC into the ocean (Wang et al. 2001, Pohlman et al. 2010, Hung et al. 2016). At methane seeps in the South China Sea, DOC input via gas seepage exceeds the DOC input from rivers (Hung et al. 2016). DOC concentrations flattened at depth, falling to about 50 µM, which is slightly above the 40-µM DOC average of deep ocean waters (Romera-Castillo et al. 2016, Follett et al. 2014). Patterns and trends in nutrient and DOC distributions differed little between Pea Island Seep and Kitty Hawk Seep sites (data not shown) and no discernable differences were observed between an off-seep control site and an on-seep site with respect to nutrient distributions.

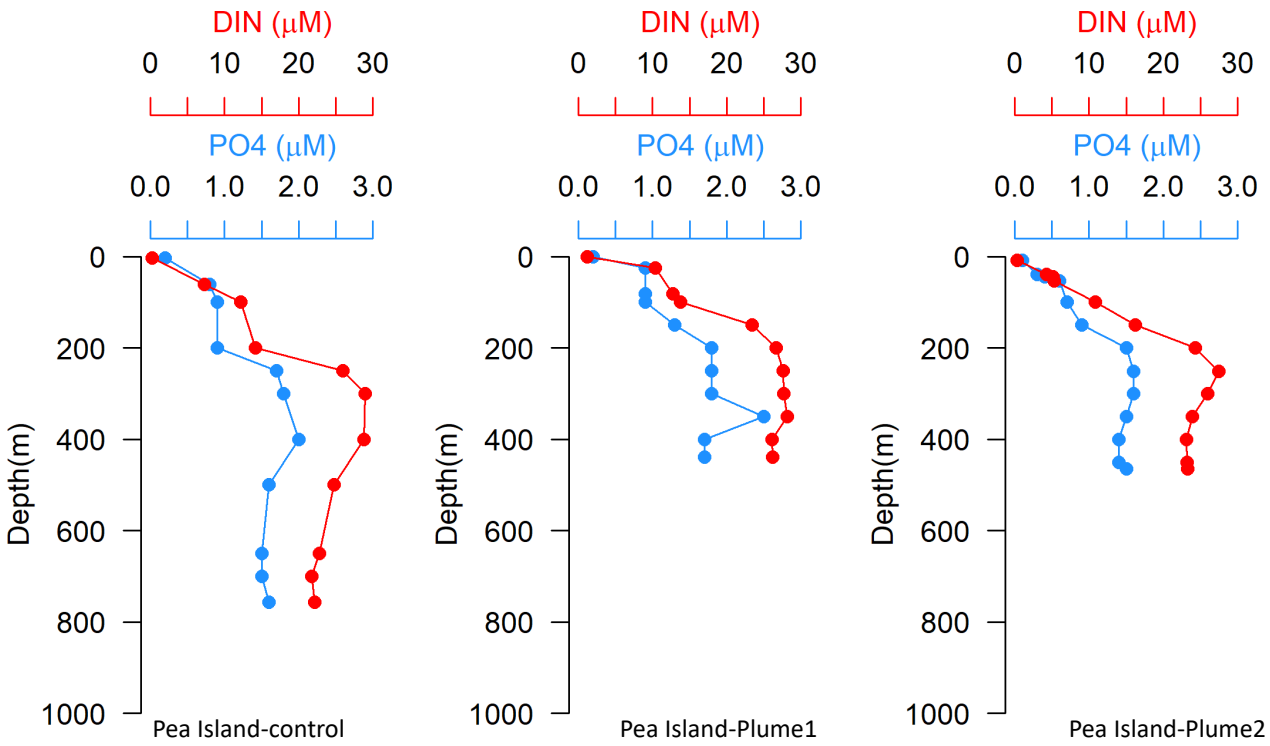

Figure 3-41. Pelagic PO4 & DIN profiles from Pea Island Seep sites, expedition AT41

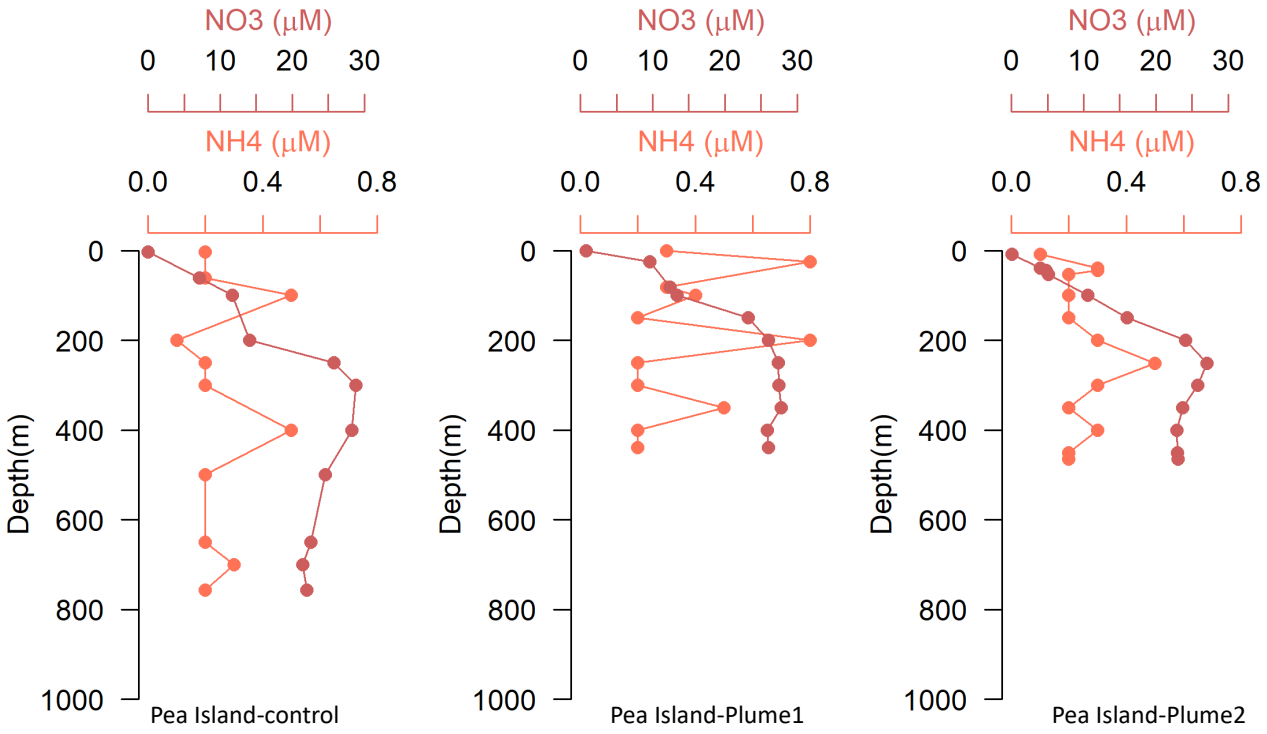

Figure 3-42. Pelagic NH_4 & NO_3 profiles from Pea Island Seep sites, expedition AT41

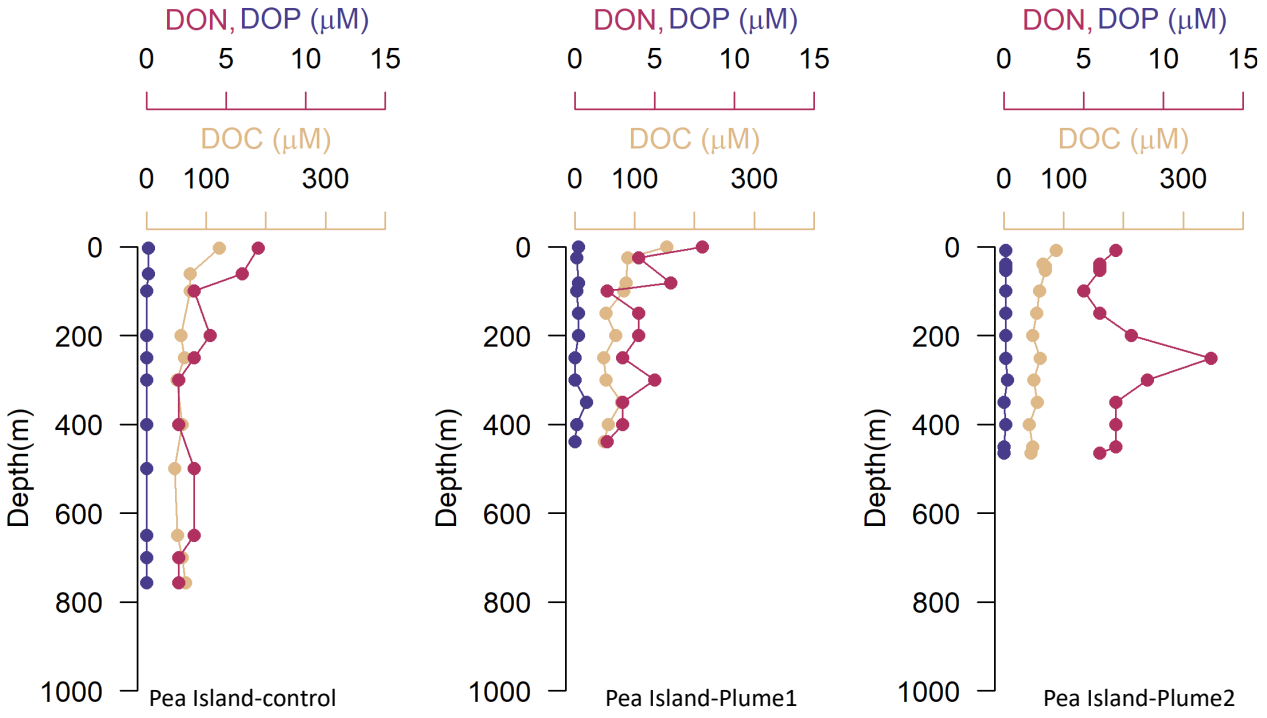

Figure 3-43. Pelagic DOC, DON, & DOP profiles from Pea Island Seep sites, expedition AT41

Methane concentrations and rates of pelagic methane oxidation, in contrast, were much higher at near seeps compared to off-seep control sites (**Figure 3-44**). At the Pea Island off-seep control site, methane concentrations were highest, up to 35 nM, in the upper mixed layer. Methane oxidation rates were higher in the mixed layer and uniformly low in deeper waters. At the Pea Island Seep site, methane concentrations in bottom waters were consistently above 700 nM (**Figure 3-44**). Methane oxidation rates tracked concentrations, peaking at 1.8 nmol L^{-1} d^{-1} in the deepest waters. Elevated rates of methane oxidation, reaching 100's of pmol L^{-1} d^{-1}, were observed in the deepwater column, up to 200 m off the bottom. However, despite elevated rates of methane oxidation activity, the high methane concentrations meant that methane turned over very slowly. Pelagic methanotrophs at shallow seeps were an inefficient sink for methane: the turnover time for methane was from 1 to 2.5 years in bottom waters, meaning that methane was likely advected from the seep domain before being oxidized by methanotrophic microorganisms.

The ability of pelagic methanotrophs to consume methane derived from naturally occurring seepage is poorly constrained, leaving a gap in the global methane cycle (Crespo-Medina et al. 2014, Rogener et al. 2018). Methanotrophs can respond rapidly to seasonal changes in methane concentration (Carini et al. 2005) or to rapid inputs of methane from oil-well inputs (Crespo-Medina et al. 2014), but their ability to modulate natural variations in methane inputs is unknown. Generally speaking, the biomass of methanotrophs usually limit methane oxidation potential. Rogener et al. (2018) showed that methanotrophic biomass can persist for long periods (3–4 years) after a large perturbation (the *Deepwater Horizon* oil well blowout) increasing the baseline potential for methanotrophy in an ecosystem. The dynamic, well-mixed physical environment along the US SE Atlantic margin could make it difficult to accumulate methanotrophic biomass in the vicinity of methane plumes. Still, rates of methane oxidation at US Atlantic margin seeps were almost three times as high as typical rates observed at GOM cold seeps, 750 vs. 275 pmol L^{-1} d^{-1} at Pea Island seeps (**Figure 3-44**) vs. the GC600 seep in the GOM (Rogener et al. 2018), respectively. As observed previously in the GOM, rates of methanotrophy at Pea Island varied substantially over time. Rates and concentrations observed on the *Ron Brown* expedition were much lower than those documented on the *Atlantis* expedition (data not shown).

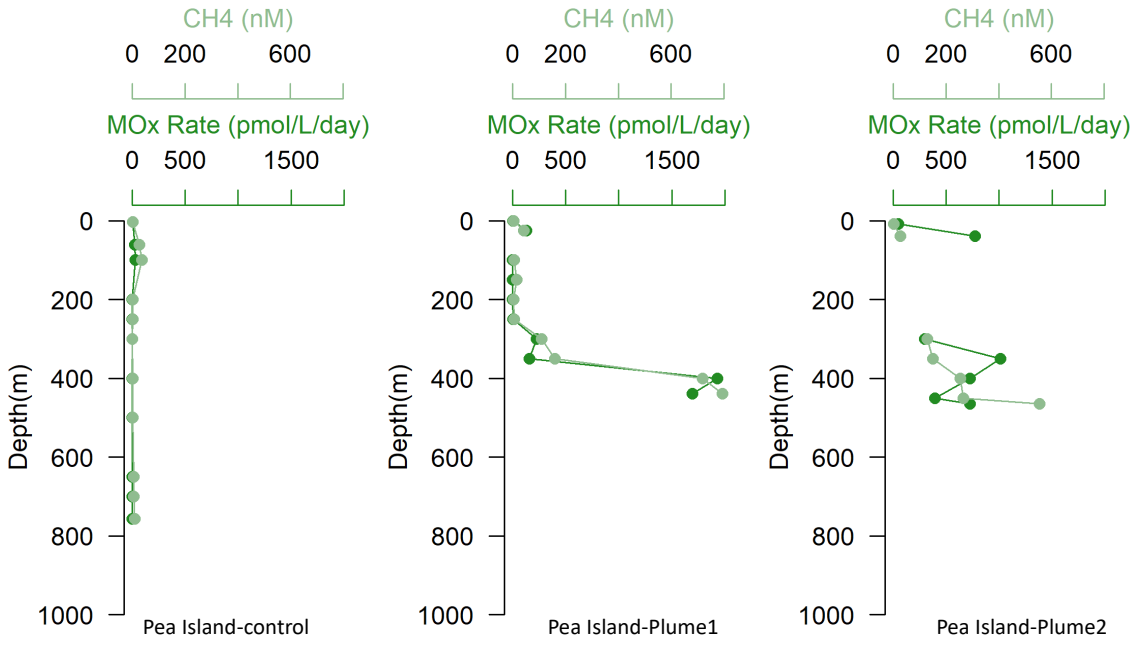

Figure 3-44. Pelagic CH_4 concentration and CH_4 oxidation rate profiles
From Pea Island Seep sites (expedition AT41).

Methane oxidation rates at seep sites along the Atlantic margin, such as at Hudson Canyon, were much higher (0.1 to 22 nmol L^{-1} d^{-1}) than those reported here (Leonte et al. 2017). The difference in activity is likely due a difference in methods; Leonte et al. used $^{13}CH_4$ to track methane oxidation rates. The $^{13}CH_4$ tracer method involves substantial addition of methane, which could increase rates substantially. Such a disparity in activity between the two tracer methods has been previously noted (Rogener et al. 2021, Montgomery et al. 2021). The $C^{14}H_4$ tracer method that we used does not change the methane concentration substantially and thus rates are more reflective of in situ conditions (Rogener et al. 2018).

The high (nM/d) rates reported by Leonte et al. (2017) resulted in calculated turnover times of less than one day, suggesting that Hudson Canyon waters are an efficient sink for methane. The rates reported here (1 to 1,000 pM/d) result in much longer turnover times for the methane pool, suggesting that seeps like Pea Island are inefficient sinks for methane. Identifying and understanding the differences between studies like this is important. Montgomery et al. (2021) showed convincingly that increased methane concentrations resulting from tracer addition substantially increase the observed methane oxidation rate. At this point, it is unclear how efficient Atlantic margin waters are at consuming methane discharging from the seabed.

3.3.2.2 Canyon Habitats and Offshore Sites

Vertical distributions of DIN and DIP were surprisingly variable between canyon sites and between offshore sites (**Figure 3-45**). In Pamlico Canyon (1,250 m water depth), both DIN and DIP were near zero in the upper 100 m of the water column. Concentrations increased gradually between 100 m and 425 m, exhibiting a subsurface maximum there and exhibiting stable profiles to the bottom. In Pamlico Canyon, the DIN:DIP ratio was up to 23 in the upper water column, suggestive of phosphorus limitation; deeper ratios were similarly elevated above the Redfield Ratio.

At the offshore sites, DIN:DIP rates were higher and more skewed towards phosphorus limitation throughout the water column. The ratio of DON:DOP was consistently greater than 16, reflective of nitrogen enrichment, relative to phosphorus, in the dissolved organic matter pool. Generally speaking, the DIN:DIP (>16) and the DON:DOP ratio (> 45) strongly indicated phosphorus limitation of biological production. At the Cape Fear Seep site, DIN and DIP concentrations were depleted to 100 m. Below there, concentrations increased steadily and stabilized by ~700 m. Interestingly, maximal deepwater concentrations of DIN were lower (20–25 µM) at these sites, compared to Pea Island (30 µM) and a mid-depth (~700–800 m) peak in nitrate suggested upwelling intrusion along the shelf break.

Nitrate production, presumably via nitrification, was clearly evident in all profiles, but the shape and depth distribution of the nitracline varied (**Figure 3-46**). The nitracline was steady and steep at Pamlico Canyon and at Cape Fear (150 to 600 m) but the nitracline was broader at Blake Ridge, with nitrate concentrations stabilizing at roughly 900-m depth. Interestingly, nitrite was below detection in all samples, suggesting tight coupling between ammonia oxidation and nitrite oxidation. Ammonium concentrations were low and variable, but never zero, suggesting steady regeneration of ammonium from organic matter and conversion of ammonia to nitrate.

Profiles of DOC, DON, and DOP were unremarkable at these sites, showing little variation across depth or between sites. Concentrations of DON ranged from 5–7 µM, concentrations of DOP ranged from 0.2 to 0.4 µM, and concentrations of DOC were around 50 µM (**Figure 3-47**).

Methane concentrations were extremely low at these three sites (**Figure 3-48**), and at canyon and offshore sites in general (data not shown). In Pamlico Canyon, methane concentrations below 600 m doubled, reaching about 5 nM. Concentrations above that depth were about 2.5 nM, a concentration that would be expected in waters in equilibrium with atmospheric methane. Despite low concentrations of methane, methane oxidation rates in the upper 100 m were up to 60 pmol L^{-1} d^{-1}. Rates below 100 m were very low,

around 10 pmol L^{-1} d^{-1}. Methane oxidation rates at Blake Ridge averaged 20 pmol L^{-1} d^{-1} and activity was most apparent in the upper 600 m. We observed very little methane oxidation at depth and observed no deep methane maxima. No methane oxidation rate data were available for Cape Fear.

Methane oxidation in canyons and at offshore sites is limited by methane concentrations. Aerobic methanotrophy is a first-order process (Chan et al. 2019), meaning that rates are primarily a function of methane concentrations. While absolute concentrations of methane dictate observed rates of methanotrophy in pelagic samples, the flux of methane into the system can constrain accumulation of methanotrophic biomass. In pelagic environments characterized by low concentrations and limited inputs of methane, such as canyons and offshore waters away from seeps, methanotrophic biomass is likely low.

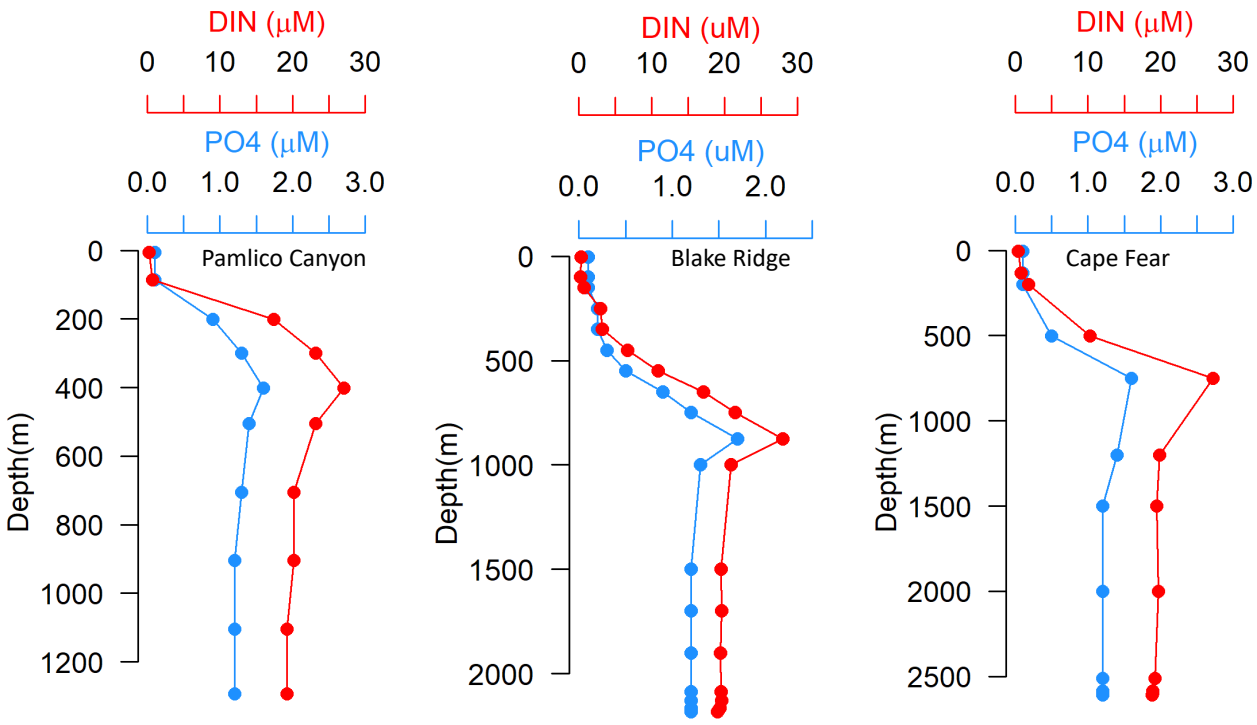

Figure 3-45. Pelagic PO4 & DIN profiles from canyon and offshore sites
Different depth scales for Expedition RB19-03.

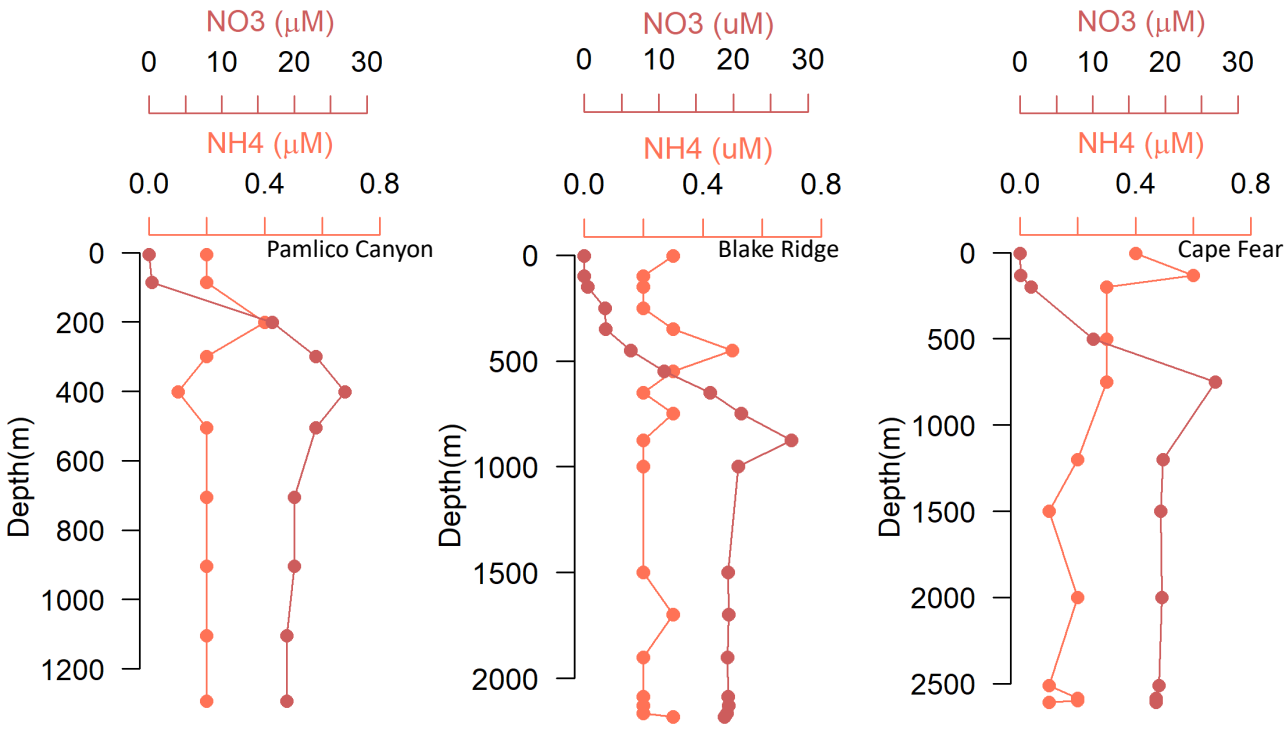

Figure 3-46. Pelagic NH4 & NO3 profiles from canyon and offshore sites
Different depth scales for Expedition RB19-03.

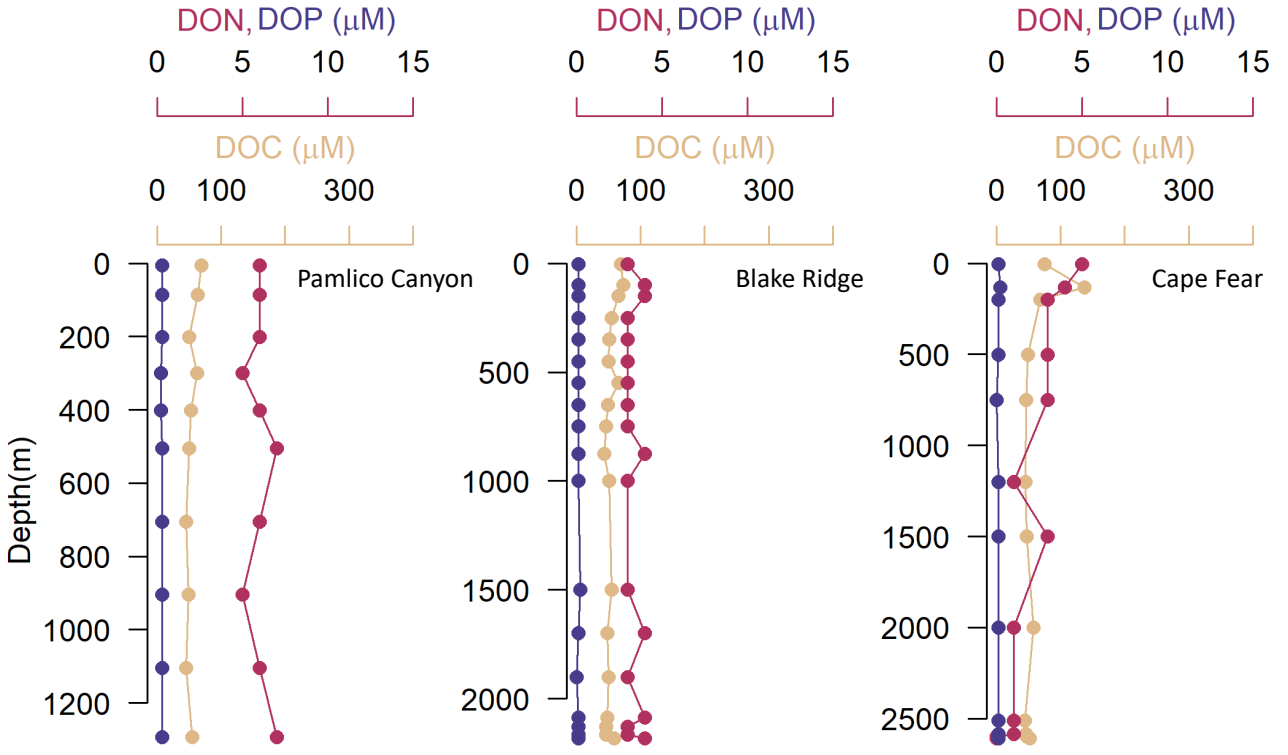

Figure 3-47. Pelagic DOC, DON, and DOP profiles from canyon and offshore sites
Different depth scales for Expedition RB19-03.

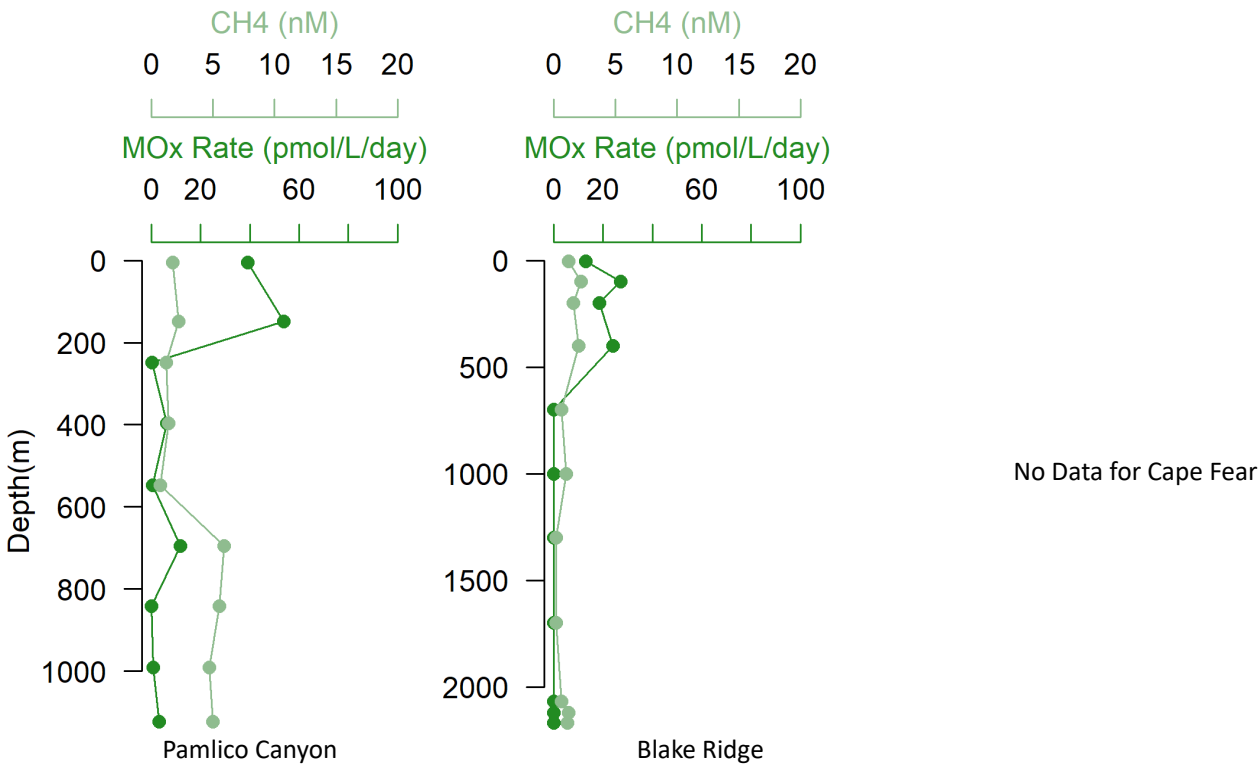

Figure 3-48. Pelagic CH_4 concentrations and CH_4 oxidation rates
From canyon and offshore sites (note diff. depth scales).

One source of methane in such environments is aerobic methanogenesis (Karl et al. 2008), where methylated phosphonates (Repeta et al. 2016) or methylated amines (Wang et al. 2021) can fuel aerobic methane production in nutrient limited waters (Rogener et al. 2018). The potential for pelagic methane oxidation to be coupled tightly to pelagic aerobic production in these and other Deep SEARCH sites is likely (see additional discussion below).

3.3.2.3 Coral Habitats

Vertical profiles of nutrient and organic matter were markedly different at locations overlying or near deepwater coral habitats. Stetson Banks and Savannah Banks were characterized by very oligotrophic surface waters and deep waters enriched in DIN (**Figure 3-49**), mainly nitrate. The nitracline was —shallow—from 150 m to 300 m—at Stetson and Savannah Banks; bottom water nitrate concentrations were 30 µM.

Ammonium concentrations varied between sites, showed little variation over depth, and were not correlated to nitrate concentrations (**Figure 3-50**); nitrite concentrations were usually below detection (data not shown). The regeneration profile was very protracted at these sites, especially the deeper Stetson Deep and Richardson Hills sites. Accumulation of nitrate began at roughly 200 m and continued steadily to 700 m (**Figure 3-50**)

At Stetson Deep and Richardson Hills, DIN concentrations peaked around 700 m. In strong contrast to the other sites, all of the sites within the Gulf Stream exhibited DIN:DIP ratios around Redfield (16:1) but extremely elevated DON:DOP ratios, reflecting DOP levels that approached methodological detection limits regularly. Concentrations of DON (~4 µM) and DOP (< 0.2 µM) were generally low and DOC concentrations were generally low (~50 µM), but DOC was elevated at depth at Stetson Banks (up to

150 µM) (**Figure 3-51**). This enrichment could reflect DOC release by corals, and it is interesting to note that these same waters contained up to 8 µM DON (up to 8 µM) but very low DOP (< 0.15 µM).

The distribution of methane concentrations and methane oxidation rates at coral-associated pelagic waters was distinct from the patterns observed at seep sites (**Figure 3-52**). Methane concentrations were enriched in the upper water column, usually in association with the deep chlorophyll maximum (Karl et al. 2008). Methane concentrations were usually less than 10 nM in the upper water column, but concentrations in the deep chlorophyll maximum were sometimes over 100 nM.

The photic zone supported surprisingly high rates of methane oxidation (up to 80 pmol L^{-1} d^{-1}) at Stetson Banks, Stetson Deep and Richardson Hills (**Figure 3-52**). Rates observed at Savannah Banks was lower but elevated relative to the rates observed in deep waters. The combination of low concentrations and high rates of methane oxidation resulted in rapid turnover of the methane pool; the turnover of methane in these surface waters, especially at Richard Hills and Stetson Banks, occurred on a time scale of 1–2 months. This is remarkable and among the most efficient consumption of methane documented in the pelagic ocean.

The factors that drive such efficient methane oxidation, and presumably production of methanotrophic biomass (see above), in this area is unclear. It is likely that the ultra-oligotrophic conditions present in surface waters above coral habitats fuel methane production via cleavage of methylphosphonate (Karl et al. 2008) and methylamine (Wang et al. 2021) in response to chronic nutrient limitation. Methane production in nutrient limited waters may thus sustain communities of methanotrophic microbes that efficiently consume methane rapidly. Tight coupling between methane production and consumption result in low standing stocks of methane, but a substantial potential for methane consumption.

The rapid turnover times of methane documented in the upper 150 m in coral, canyon, and offshore sites suggests that tight coupling between in situ production and consumption processes is an important—yet poorly recognized—component of the methane cycling in shelf and offshore environments.

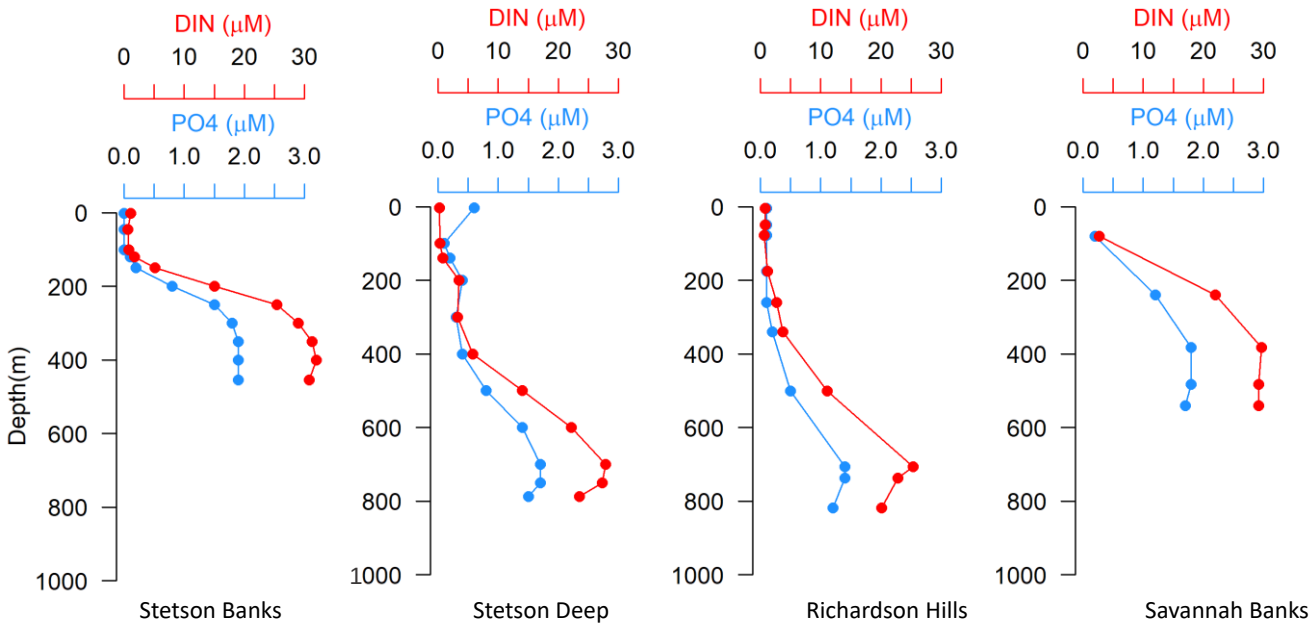

Figure 3-49. Pelagic PO4 & DIN from deepwater coral sites
Note different depth scales.

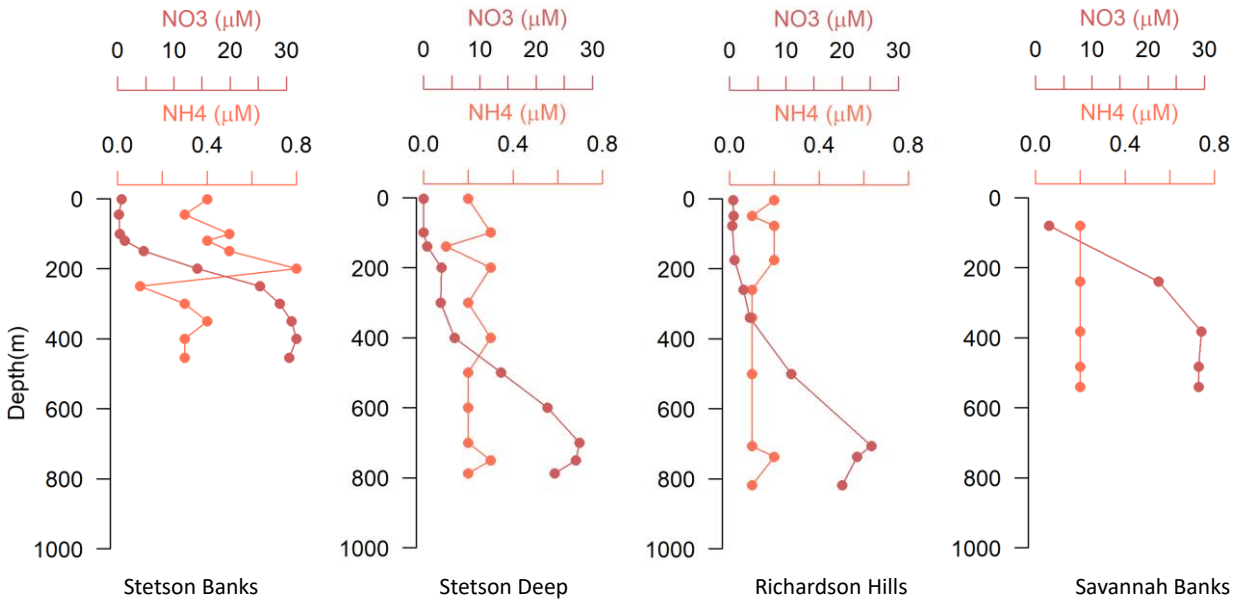

Figure 3-50. Pelagic NH4 & NO3 profiles from deepwater coral sites

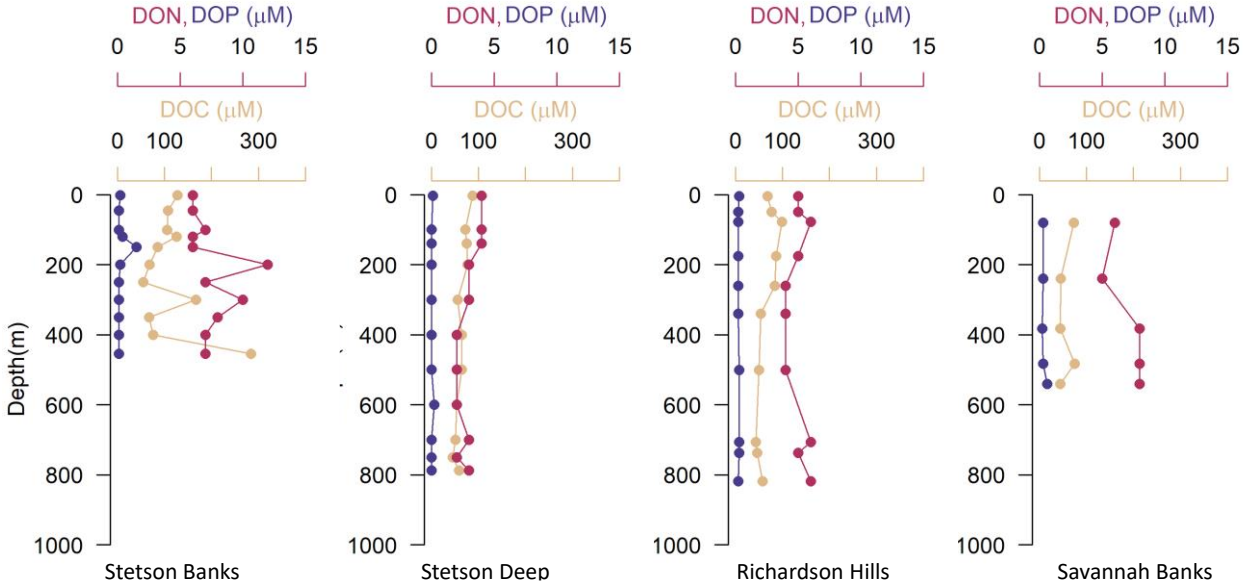

Figure 3-51. Pelagic DOC, DON, and DOP profiles from deepwater coral sites

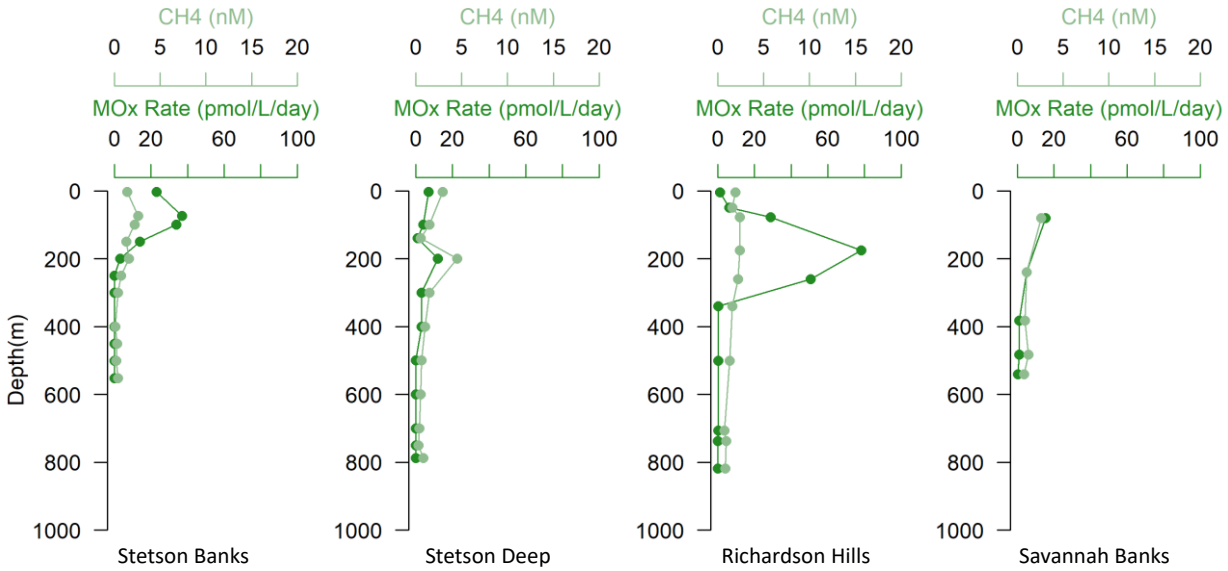

Figure 3-52. Pelagic CH_4 concentration and CH_4 oxidation rate from deepwater coral sites

3.3.3 Methods

3.3.3.1 Sample Collection

Sediment samples for geochemistry and to determine rates of methane oxidation and SR were collected at seep sites, at deepwater coral sites, and in canyons (**Table 3-19**). During expeditions AT41 and RB 19-03, we collected samples from 11 sites in the Deep SEARCH study domain (**Table 3-19**). Here we discuss data from a subset of sites representing shallow seeps, deep seeps, and non-seep areas. We described sediment samples by their ecological or environmental signature, as follows: control (background sediment no visible signs of active seepage or ecological imprint), adjacent to/associated with mussel beds, bacterial mats (sediments with *Beggiatoa* sp. along the surface), coral, or canyon. We collected sediment push cores using the *Alvin* (AT41) and using the ROV *Jason* (RB19-03) (**Table 3-19**). On board the ship, we processed sediment cores in the cold van to collect pore-fluid samples for geochemical analyses and subsamples for rate assays.

Table 3-19. Summary of sediment collections

Cruise ID	Site	CTD casts	Additional
AT41	Pea Island	3	3 *Alvin* Niskin
AT41	Stetson Deep	2	-
AT41	Richardson Ridge	2	-
AT41	Blake Escarpment	1	-
AT41	Stetson banks	2	-
AT41	Blake Ridge	1	5 *Alvin* Niskin
AT41	Cape Fear	1	-
AT41	Norfolk Canyon	1	-
BMCC-19	Richardson Bend	1	-
BMCC-19	Richardson Hills	1	-
BMCC-19	Pamlico Canyon	1	-
RB19-03	Stetson Banks	1	-
RB19-03	Richardson Hills	3	-
RB19-03	Savannah Banks	1	-
RB19-03	Blake Deep	1	-

Cruise ID	Site	CTD casts	Additional
RB19-03	Pamlico Canyon	2	-
RB19-03	Pea island	2	2 *Alvin* Niskin
RB19-03	Kitty Hawk	1	1 *Alvin* Niskin
RB19-03	Lookout Deep	1	-
RB19-03	Blake Ridge	1	1 *Alvin* Niskin
RB19-03	Cape Fear Seep	1	1 *Alvin* Niskin
RB19-03	West Richardson	1	-
NF19-09	Blake Ridge	3	-
NF19-09	Pamlico Canyon	1	-
NF19-09	Richardson Hills	5	-

3.3.3.2 Geochemistry

We carried out similar sampling procedures for all sediments, except those from coral sites. We characterized coral sites by large-grained material, including carbonate clasts, sand, and pebbles that were extremely difficult to sample. Therefore, we centrifuged coral samples to collect pore water. We processed other sediment core samples as follows. The vast majority of sediments were anoxic within millimeters of the sediment-water interface. Upon return to the surface, we transferred cores to a 4°C cold room immediately and processed within 24 hours of collection according to Joye et al. (2010) and Bowles et al. (2016). For each site, we processed two to three replicate cores to obtain sufficient samples for dissolved gases, porewater, and solid phase characterization and microbial activity rates. Sampling depths were 1, 3.5, 7.5, 12.5, and 17.5 cm below the surface (numbers refer to midpoint depth); we collected an overlying water sample 5 cm above the sediment-water interface. We collected five or six samples from each core.

We collected depth-specific samples of pore water using a manual pore water press (Joye et al. 2010). We transferred the sediment from a given depth interval to an Ar-flushed PVC cup and sealed with a PVC piston and cap. We collected porewater into a 60 mL syringe via the application of pressure (manually); we extracted at least 20 mL of porewater per depth horizon. After extraction, we transferred the residual sediment into an Ar-purged Whirl-Pak bag that we had stored in an argon-filled, gas-tight bag, and then we stored the residual frozen at -20°C. We processed the replicate core to obtain dissolved gas, porosity and rate subsamples (Joye et al. 2010, Bowles et al. 2016).

We collected methane samples with a 3-mL, cut-end syringe and ejected each into a 12-mL headspace vial that contained 3 mL methane-free (N_2-purged) 2 M NaOH. We plugged vials with a blue butyl rubber stopper that we had secured using a crimp seal; we vortexed all samples until well mixed and then stored upside-down until analysis.

We collected the hydrogen samples with a 3-mL, cut-end syringe, then ejected each into a 20-mL headspace vial, crimp sealed with a blue butyl rubber stopper, and flushed it immediately with N_2. Next, we collected a 2 cm^3 sample and transferred it to a pre-weighed 7-mL vial with a Teflon-coated cap to determine the porosity.

Then, we collected 3-cm^3 sediment samples (n=4 per depth per rate assay) for methane oxidation and SR measurements using glass cut-end tubes (Bowles et al. 2019). We cut off the base of each Hungate tube and purged the tubes with argon. We added sediment to the tube and inserted a retractable butyl rubber plunger into the open end (Bowles et al. 2011). The stopper was mobile in the tube and permitted compression/expansion. We pushed the sediment up until it was flush with the screw end of the tube and then we sealed the tube as headspace-free using a butyl rubber septa and screw cap. We incubated samples from each site at in situ pressure and temperature and amended all rate samples with 10 mM high purity methane. For more details on this method, see Bowles et al. (2011).

On board the ship, we processed subsamples for dissolved gases and porewater analytes. These included: methane (CH_4), methane isotopic signature ($\delta^{13}CH_4$), alkalinity/dissolved inorganic carbon, hydrogen sulfide (HS^-), ammonium (NH_4^+), nitrate plus nitrite (NO_x^-), nitrite (NO_3^-), phosphate (PO_4^{3-}), DOC, chloride (Cl^-), sulfate (SO_4^{2-}), sodium (Na^+), calcium (Ca^{2+}), magnesium (Mg^{2+}), potassium (K^+). Such were collected and run on board (methane, ammonium) or preserved and analyzed ashore in the UGA laboratory using methods described previously (Joye et al. 2004, 2010; Bowles et al. 2016, 2019).

We measured methane $\delta^{13}C$ using a Picarro G2201-i Isotopic Analyzer cavity ringdown spectrometer equipped with the Small Sample Introduction Module (SSIM). We vortexed methane samples in 20-mL vials (described above) and then injected 2 mL of headspace into the SSIM, where they were diluted with zero air (Airgas) to a 20 mL total volume prior to analysis. We analyzed hydrogen (H_2) samples according to Bowles et al. (2011). We measured cations and anions using ion chromatography (Joye et al. 2010). We collected and processed total carbon (TC) and nitrogen (TN) samples as described previously by Joye et al. (2010).

3.3.3.3 Microbial Activity

We injected, incubated, and preserved samples for SR and AOM rate measurements on board the ship per our standard methods (Joye et al. 2010, Bowles et al. 2011, 2019). For SR, we amended samples with sufficient ultra-high purity methane to return the pore water concentration to those approximating in situ levels (~10 mM). Then, we injected the $^{35}SO_4^{2-}$ tracer solution (200 kBq) through the butyl rubber stopper and placed the samples into a titanium pressure vessel for incubation at in situ temperature for 24 to 48 hours. We ran replicates (n = 3 live samples) and a killed control for each depth horizon in each core. To stop activity, the SR samples was ejected into a 50-mL centrifuge tube containing 10 mL of 20% (w/v) zinc acetate.

At the UGA lab, we recovered radioactive sulfide produced by removing the residual tracer sulfate by centrifuging and amendment with anoxic seawater (repeated 3x). After the first rinse, we collected a subsample to quantify the $^{35}SO_4^{2-}$ tracer activity. The remaining sample was stored in ethanol at -20°C until distillation. We distilled samples via a one-step wet chromous-acid reduction and sulfide was trapped in 5% (w/v) zinc acetate (Canfield et al. 1986, Fossing and Jørgensen 1989). The radioactivity of sulfate and sulfide samples was measured using Bio-Safe II (Research Products International) liquid scintillation cocktail, respectively. We estimated rates of SR using the Eq. 5:

$$\text{SR Rate} = [SO_4^{2-}] \times \alpha / t \times (H_2{}^{35}S / {}^{35}SO_4^{2-} + H_2{}^{35}S) \qquad \text{(Equation 5)}$$

In this equation, the SR rate is the rate of SR in nmol cm^{-3} day^{-1}; $[SO_4^{2-}]$ is the sulfate concentration in nmol cm^{-3} wet sediment which we obtained by multiplying the pore water sulfate concentration times the porosity; the term α reflects the fractionation factor for SR (1.06; Jørgensen 1978), *t* is incubation time (in days); $H_2{}^{35}S$ is the radioactivity present in sulfide (minus activity in killed controls); and $^{35}SO_4^{2-} + H_2{}^{35}S$ reflects the total tracer activity injected.

We amended samples for AOM rate determination with high purity methane, as described above, ^{14}C-CH_4 (16 kBq) and incubated for 24 to 48 hours, after which samples were fixed by mixing with 5 mL of 2-M NaOH in a 50-mL centrifuge tube. We processed samples via acid distillation (Joye et al. 1999, 2010). We distilled samples for at least 6 h and we assessed recovery using $NaH^{14}CO_3$ standards (recovery averaged 99%). We calculated rates of AOM using Eq. 6:

$$\text{AOM Rate} = [CH_4] \times \alpha / t \times ({}^{14}CO_2 / {}^{14}CH_4) \qquad \text{(Equation 6)}$$

The AOM rate is the rate of methane oxidation nmol cm^{-3} day^{-1}; $[CH_4]$ is the concentration of methane in nmol cm^{-3} of wet sediment; α is the fractionation factor (1.018; Alperin et al. 1988); *t* is the incubation

time (days), $^{14}CO_2$ is the radioactivity present in carbon dioxide minus activity from controls, and $^{14}CH_4$ reflects the ^{14}C tracer radioactivity injected.

3.3.4 Sediment Results

3.3.4.1 Shallow Seeps

Cold seeps occur in a variety of settings along active and passive continental margins (Joye 2020, Joye and Bowles 2021). Seeps are driven by the discharge of deeply sourced, chemically altered fluids (Joye 2020). Seeping fluids contain high concentrations of reduced chemicals, including methane, and sometimes other alkanes, like ethane and propane, oil, and DOC (Joye 2020). Atlantic margin seeps discharge methane, but not oil or higher alkanes. Regardless of location, these energy rich fluids influence sediment biogeochemistry and the overlying water column.

The Pea Island Seep field typifies shallow Atlantic seeps examined during this study. Fluid discharge was patchy, as evidence by the sporadic occurrence of *Beggiatoa* mats along the seabed. *Beggiatoa* are large (widths can exceed 100 µm) filamentous sulfide-oxidizing bacteria that couple the oxidation of sulfide with the reduction of oxygen or nitrate (MacGregor et al. 2013). These bacteria are primarily autotrophic, though some strains can also assimilate low molecular weight organic matter (Teske and Nelson 2006). *Beggiatoa* often occur as dense accumulations of filaments—called mats—along the surface of sulfide-rich sediments. They store nitrate in a central vacuole and sediments influenced by *Beggiatoa* often exhibit high concentrations of nitrate in the pore fluid (see DIN, which is mainly nitrate, in **Figure 3-53** Pea Island AT41, RB19-02 panels).

Pore water nitrate concentrations often exceed 200 µM in *Beggiatoa*-influenced sediments; *Beggiatoa* can concentrate nitrate to mM levels in their vacuole. Dissolved inorganic phosphorus concentrations were surprisingly elevated in Pea Island *Beggiatoa* mats (**Figure 3-53**, Pea Island panels). Some strains of *Beggiatoa* can concentrate phosphate intracellularly as polyphosphate (Brock et al. 2012), and it is possible that such a mechanism contributed to the observed DIP profiles at Pea Island. Sediment cores from the Kitty Hawk Seep were not marked by *Beggiatoa* mats, and, as such, pore water concentrations of DIN and DIP were markedly lower and invariable with depth (**Figure 3-53**).

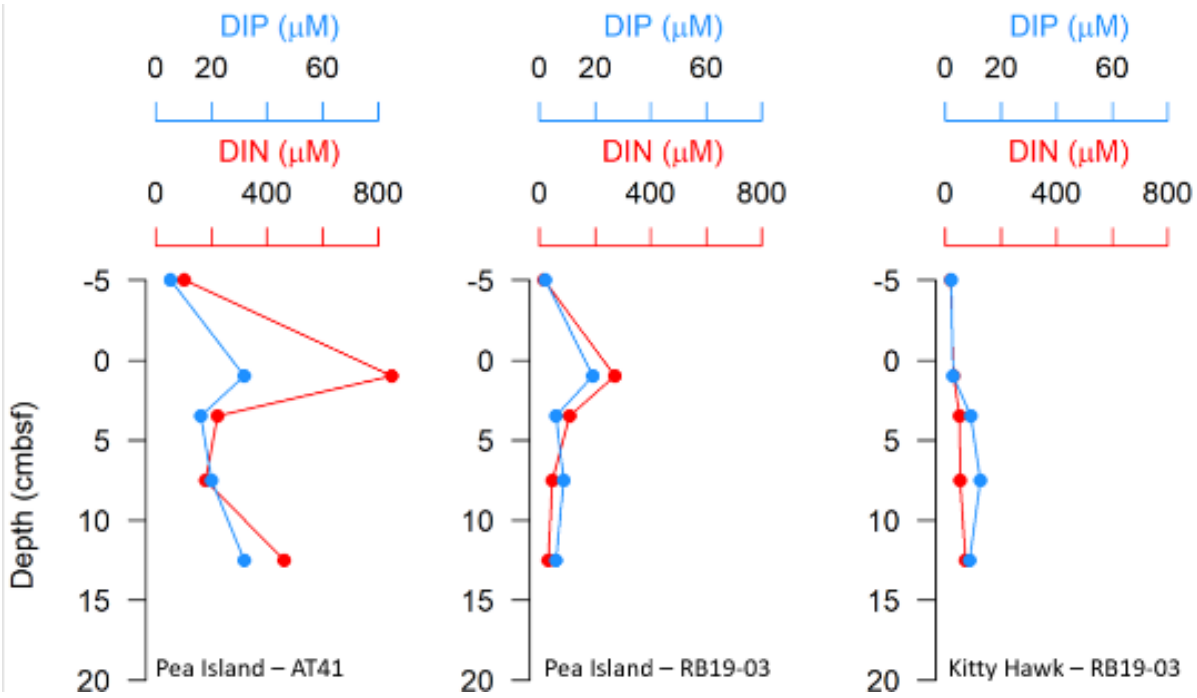

Figure 3-53. Dissolved inorganic N and P from sediments associated with *Beggiatoa*
Beggiatoa microbial mats from shallow-water sites.

Sediments marked by *Beggiatoa* mats at Pea Island were markedly reducing (Eh below -200 mV) and concentrations of hydrogen sulfide exceeded 5 mM. At the Kitty Hawk Seep, sediments were reducing but not nearly as sulfidic. Sulfide only accumulates in pore fluids when the rate of sulfide production from SR exceeds the capacity of sediment iron oxide pools to sequester that sulfide as reduced iron sulfides (Arvidson et al. 2004). Concentrations of reduced iron (Fe(II) were highest in sulfidic sediments; in sediments with low sulfide concentrations, Fe(II) was also low, likely because of FeS mineral formation.

Concentrations of methane, dissolved inorganic carbon, and sulfate exhibited extreme variability across sites (**Figure 3-54**). Methane concentrations in recovered *Alvin* cores degas during recovery, resulting in inaccurate assessment of in situ methane concentrations (Bowles et al. 2010). Methane concentrations in recovered cores always underestimate in situ values. Methane concentrations in Pea Island Beggiatoa mats from the AT41 expedition reached 2.5 mM at 12 cm. This core exhibited a classic SMTZ—as methane concentrations increased, sulfate concentrations decreased, and concentrations of dissolved inorganic carbon increased (**Figure 3-54**). If methane oxidation is coupled to SR, DIC should accumulate with sulfate depletion at a 1:1 stoichiometry based on the Eq. 7:

$$CH_4 + SO_4^{2-} \rightarrow HCO_3^- + HS^- + H_2O \qquad \text{(Equation 7)}$$

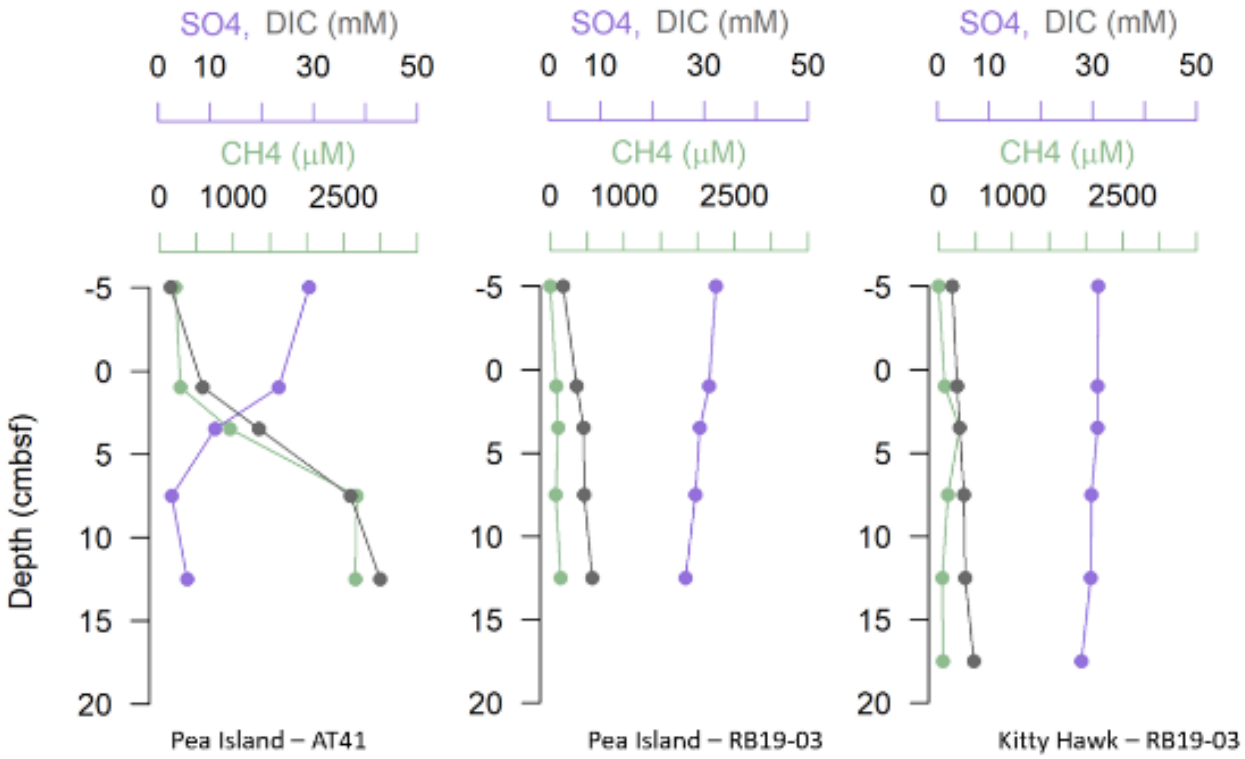

Figure 3-54. Sulfate and methane profiles from sediments associated with *Beggiatoa*
Beggiatoa microbial mats from shallow-water sites.

Sulfate was almost entirely consumed in this core, meaning that roughly 28 mM of DIC would be produced from AOM. However, DIC concentrations reached 40 mM, illustrating that other organic substrates are fueling anaerobic metabolism in these sediments, possibly fueled by other electron acceptors (Bowles et al. 2019). The Pea Island core collected on the RB19-03 expedition contained very low methane concentrations and showed little evidence of sulfate depletion of DIC accumulation. Similarly, the geochemical profiles in the Kitty Hawk core were unremarkable. Cold seeps are known for supporting extensive variability and even sites marked by microbial mats can sometimes contain mundane profiles that lack structure (Joye et al. 2010, Bowles et al. 2016). In some cases, fluid discharge can effectively erase the vertical profiles generated by microbial activity. In other cases, the discharge regime has changed and the Beggiatoa mats are a relic of a previous period of active discharge.

We know that methane oxidation is dependent on the methane concentration (Bowles et al. 2010, 2019). Furthermore, we know that recovery of gas-rich cores from the deep sea leads to loss of methane during degassing. So, we determined rates of microbial methane oxidation and SR in samples amended with 5 mM methane. We did this to mimic the likely high-methane conditions at the seabed. At gas-rich cold seeps, methane concentrations can reach 40 mM or more so 5 mM is a modest addition.

Pea Island and Kitty Hawk sediments exhibited a substantial potential for AOM—rates were greater than 2 µmol/cc/d at both sites (**Figure 3-55**). These rates were comparable to AOM rates documented in gassy sediments from Monterey Bay (Bowles et al. 2019) but lower than rates in gassy, oily sediments from the GOM or Gulf of California (Bowles et al. 2019). Rates of AOM were only loosely coupled to SR (**Figure 3-58**) in most cases, suggesting that other processes, such as denitrification or metal oxide reduction, fueled AOM. Multiple mechanism of AOM has been documented at other seeps (Bowles et al. 2019); such plasticity is likely the rule, rather than the exception.

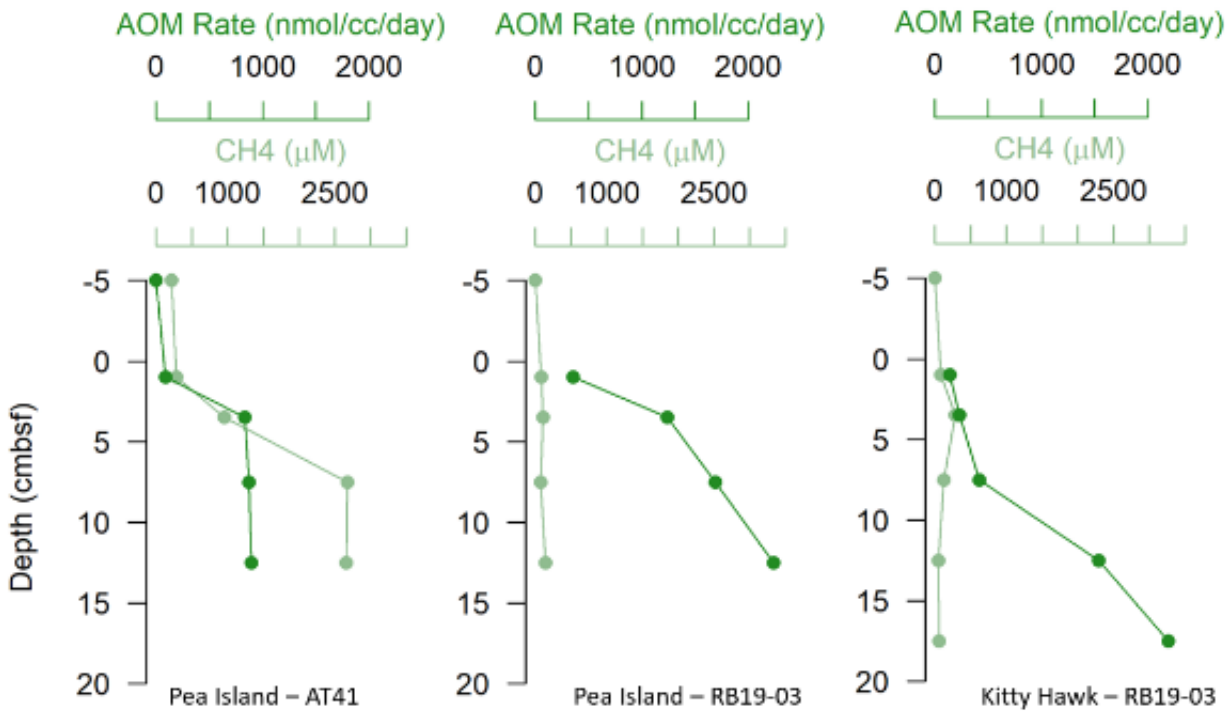

Figure 3-55. Rates of AOM vs. [CH4] in sediments associated with *Beggiatoa*
Beggiatoa microbial mats from shallow-water sites.

3.3.4.2 Canyon Habitats and Offshore Sites

Nutrient inventories were low in cores from Pamlico Canyons (ref. later **Figure 3-69**). Sediments from Cape Lookout and Cape Fear contained more DIN and DIP than Pamlico Canyon cores, but concentrations were lower than in the Pea Island cores. The redox potential in canyon and offshore sediment cores—around -200 mV—was poised by the Fe(III)/Fe(II) redox couple. Pamlico Canyon and Cape Lookout cores contained no detectable hydrogen sulfide. The Cape Fear core, which was marked by a *Beggiatoa* mat, contained high concentrations (> 10 mM) of hydrogen sulfide (**Figure 3-56**). The Pamlico Canyon core exhibited no vertical structure in profiles of methane, sulfate, or DIC (**Figure 3-57**).

The Cape Lookout core contained no methane, exhibited no sulfate depletion, and had modest (10 mM) accumulation of DIC, likely by other modes of anaerobic metabolism. The core from the Cape Fear site exhibited a strong SMTZ. Sulfate was depleted to near-zero values by 5 cm and methane concentrations exceeded 2.5-mM. DIC concentrations were roughly 20-mM. These geochemical profiles are fairly typical for offshore sediments that are not impacted by cold seepage (Pamlico Canyon, Cape Lookout). The Cape Fear site is clearly methane influenced.

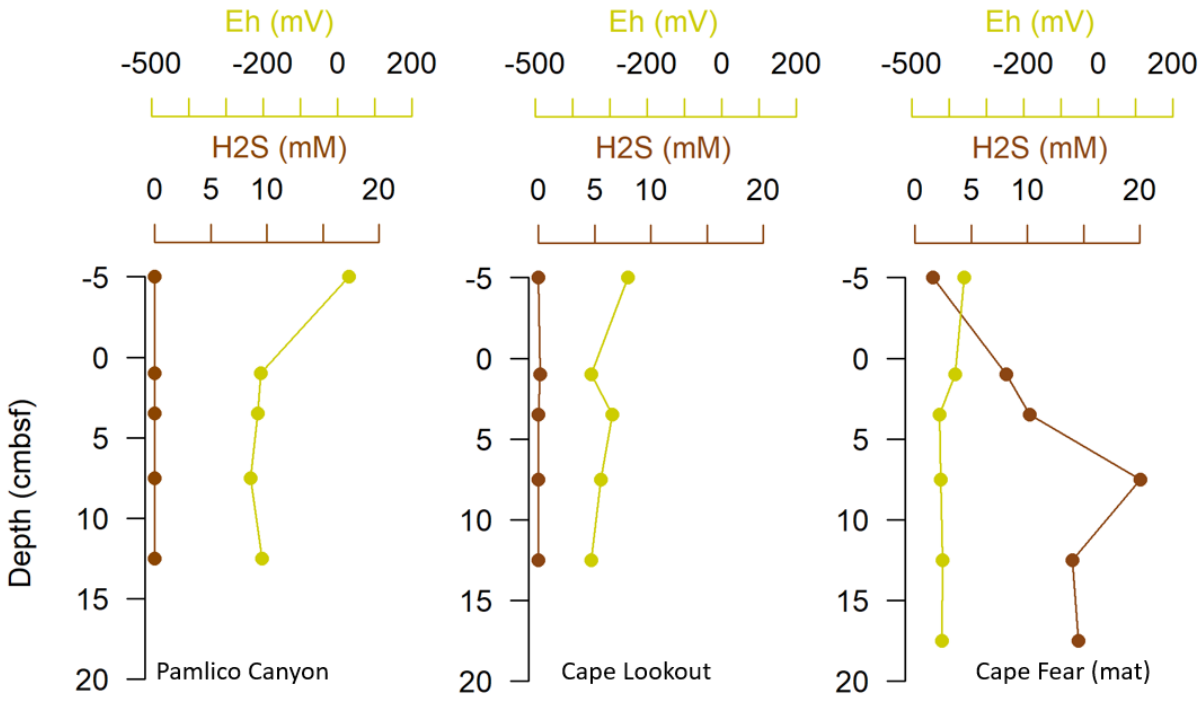

Figure 3-56. Dissolved hydrogen sulfide and Eh in sediments from deepwater sites

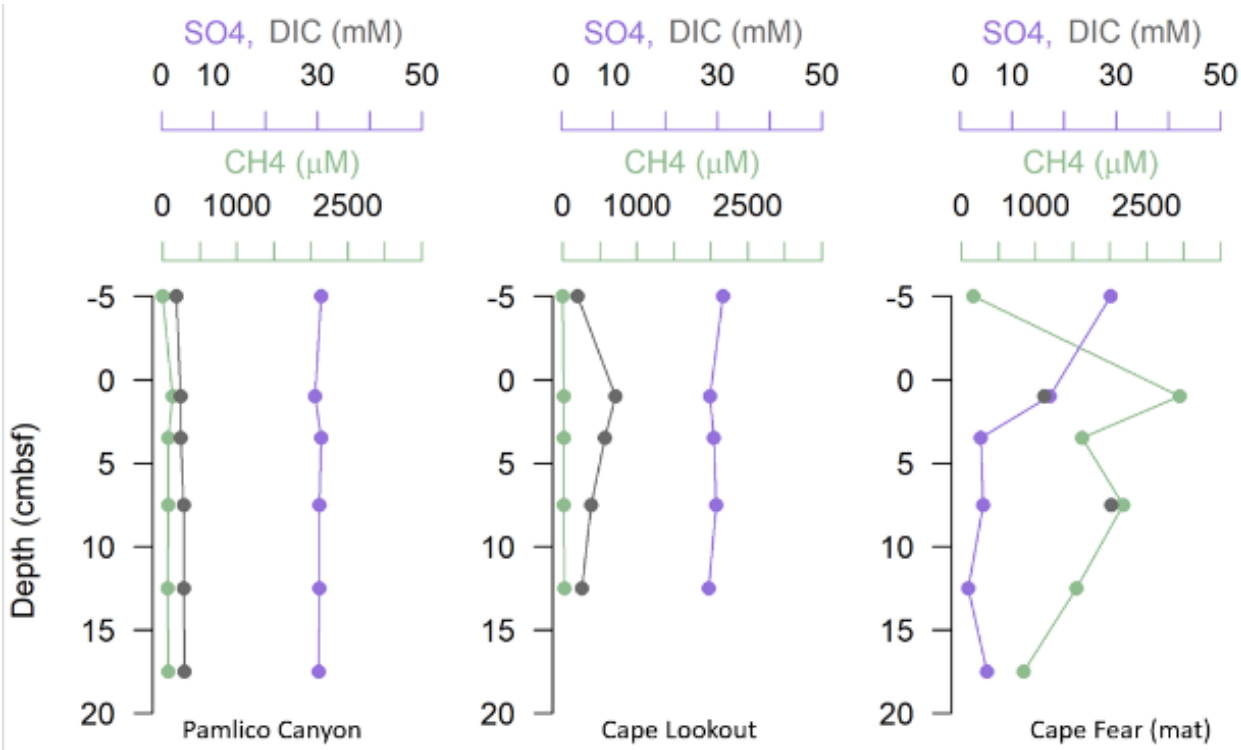

Figure 3-57. Dissolved sulfate and methane in sediments from deepwater sites

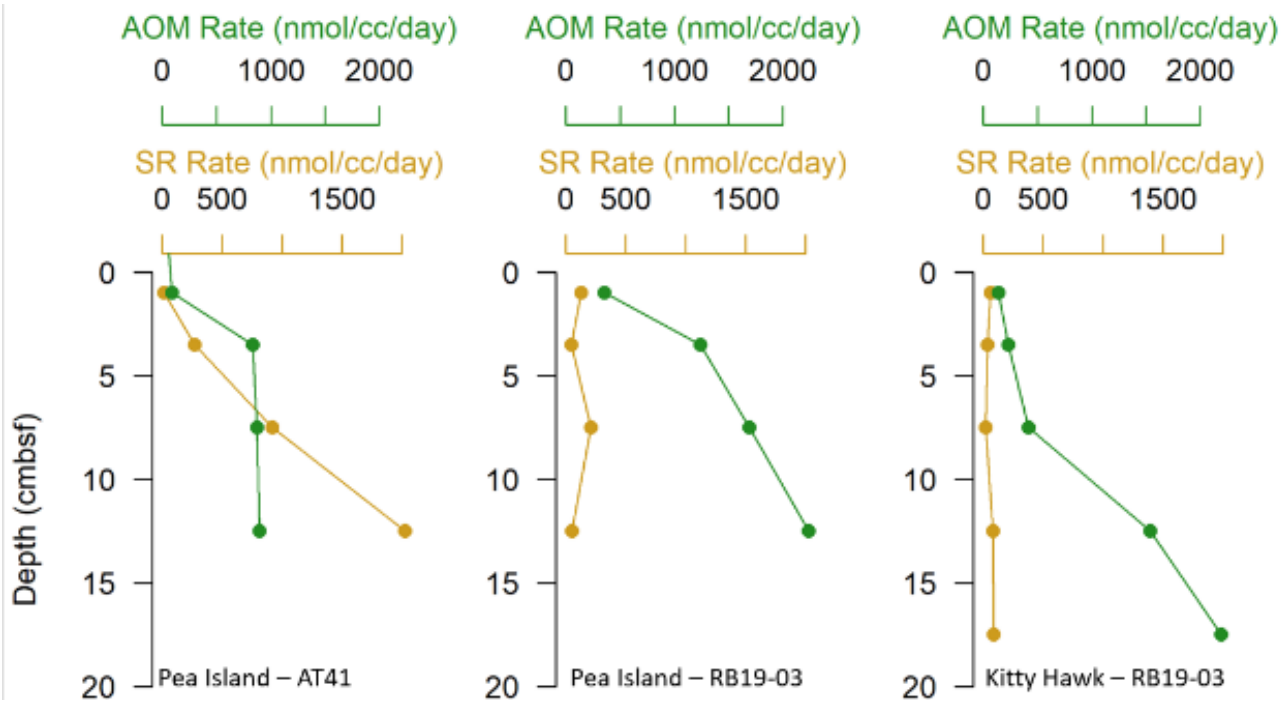

Figure 3-58. Rates of AOM vs. SR in sediments associated with *Beggiatoa*
Beggiatoa microbial mats from shallow-water sites.

As expected, rates of microbial metabolism were low in Pamlico Canyon and Cape Lookout sediments; at Cape Lookout very low SR rates exceeded AOM rates (**Figure 3-59** and **Figure 3-60**). In Cape Fear sediments, the potential for AOM was high and activity tracked the methane profile. As observed at the shallow seep sites, AOM rates exceeded SR rates. Sediments from the region are organic rich (0.5–3% organic carbon and >7% LOI).

While the quality of the organic matter is not fully constrained, there is sufficient organic matter present to fuel heterotrophic metabolism independent of AOM. Seep-influenced sediments are well-poised to consume methane when it becomes available suggesting that seep areas are adapted to variable methane concentrations/fluxes and the microorganisms inhabiting those sediments can rapidly increase activity in response to methane availability. In contrast, sediments from sites that lack seep-influence do not have such a capacity for AOM (see Pamlico Canyon and Cape Lookout panels on **Figure 3-60).** Methane seepage appears to select for a microbial community that is uniquely adapted for efficient methane consumption.

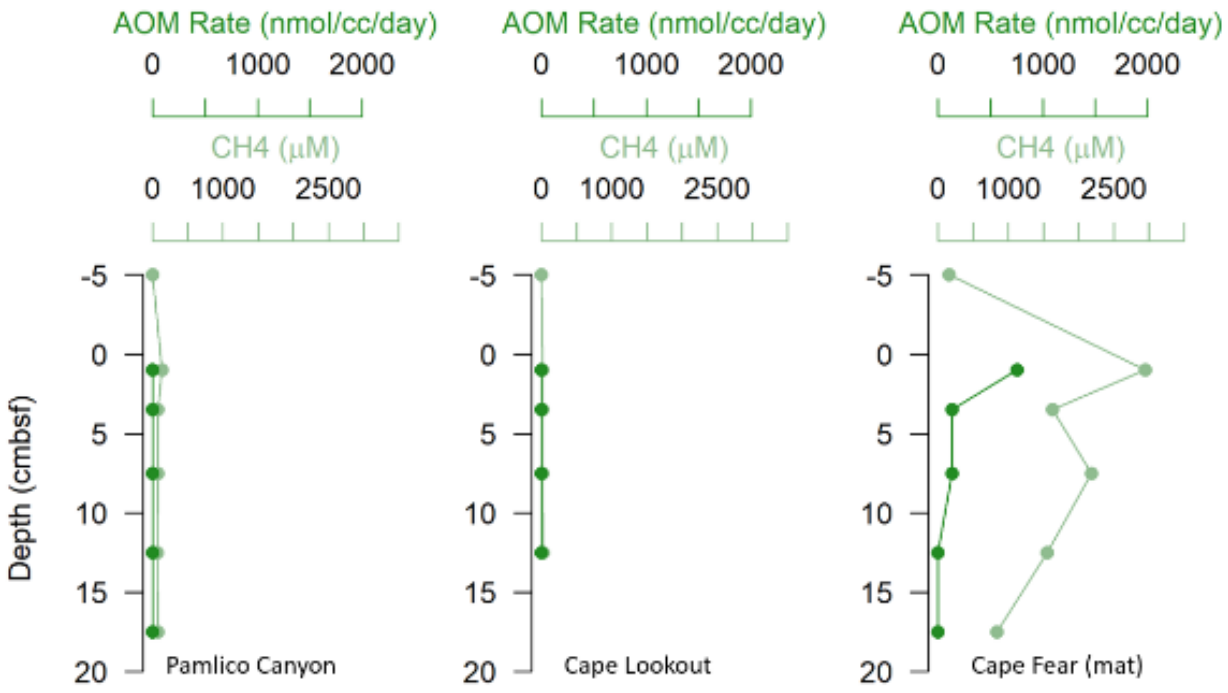

Figure 3-59. Rates of AOM vs. [CH4] in sediments from deepwater sites

Figure 3-60. Rates of AOM vs. SR in shallow sediments from deepwater sites

3.3.4.3 Sediments with Strong SMTZs

Three examples of cores with strong SMTZs are shown in **Figure 3-61** through **Figure 3-65**. The Blake Ridge is a deepwater methane seep characterized by gas hydrate, extensive bathymodiolin mussel beds, and microbial mats. Cores from Blake Ridge sediments contained moderate enrichments of nitrate (about

200 µM) (**Figure 3-61**). A Pea Island core containing ~600 µM nitrate (shown here as DIN) is included for comparison. All three cores were highly reducing and sulfidic (**Figure 3-62**). Some Blake Ridge cores contained 20 mM hydrogen sulfide (middle panel **Figure 3-62**). These three cores contained sharp sulfate-methane transitions; note that on **Figure 3-64** the axis for methane concentration extends to 10,000 µM, whereas 3,500 µM was maximal on the previous plots. Concentrations of methane in Blake Ridge cores were almost 10 mM.

The carbon isotopic composition of methane at Blake Ridge sites was -75‰, whereas Pea Island methane was -70‰; no higher alkanes were observed at either site. We observed steady depletion of sulfate and concomitant production of DIC in all three sets of samples. Sulfate was depleted to zero by 10 cm in Blake Ridge cores; sulfate concentration in Pea Island cores were less than 5 mM. Concentrations of dissolved inorganic carbon exceeded 28 mM at all sites, showing that methane and other organic matter was oxidized via anaerobic metabolisms.

Despite suggestive geochemical signatures of AOM and SR in the sulfate and methane enrichment in Blake Ridge sediment cores, measured rates of AOM with ^{14}C radiotracer were extremely low. SR rates determined independently in separate assays were also near detection limits in paired cores from Blake Ridge. The lack of detectable AOM and SR is surprising, but it could stem from sulfide inhibition. In pure culture, hydrogen sulfide can directly and reversibly inhibit SRB (Reis et al. 1992). The potential for hydrogen sulfide inhibition in natural populations is rarely considered, but this could explain the lack of microbial activity in these sediments. A previous phase of substantial rates of microbial activity would be required to consume sulfate completely and generate 10's of mM of DIC. Future studies should aim to elucidate the factors regulating AOM and SR at Atlantic margin seep sites, including the possibility of hydrogen sulfide inhibition of metabolism.

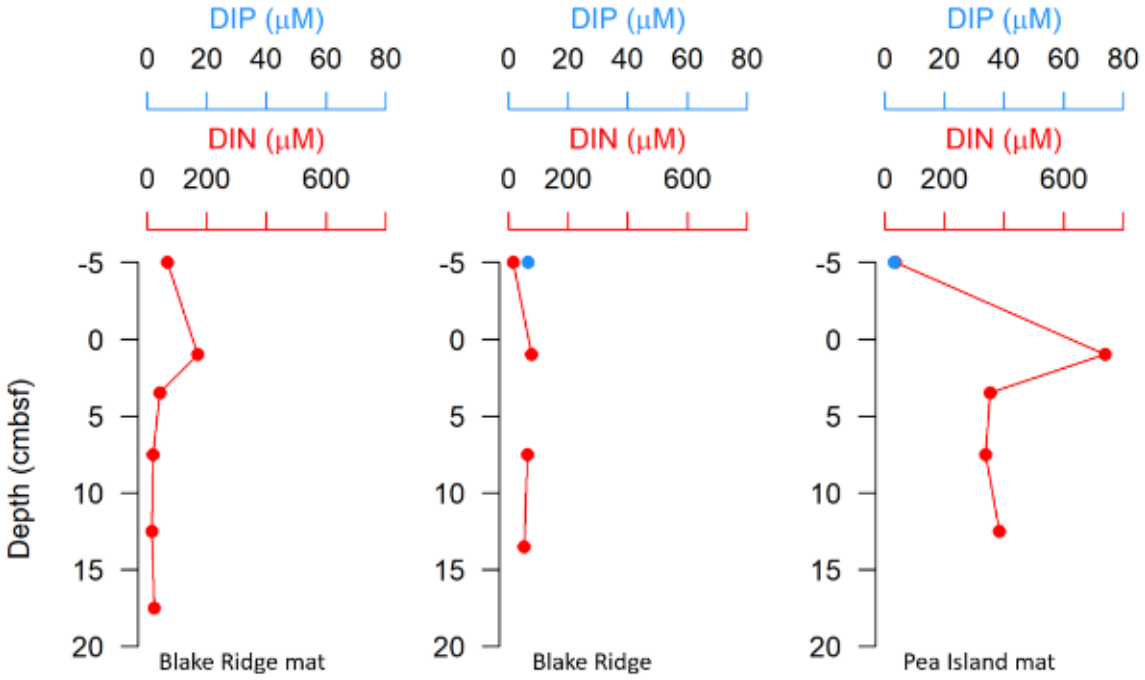

Figure 3-61. Dissolved inorganic N and P in sediments from sites with clear SMTZs

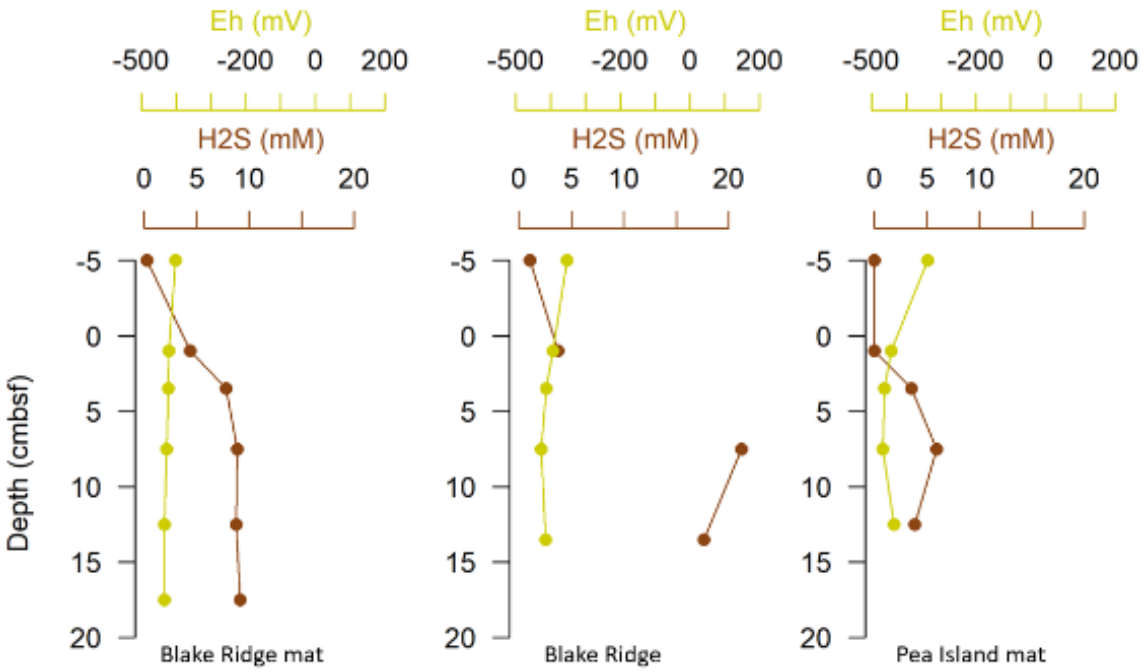

Figure 3-62. Dissolved hydrogen sulfide and Eh in sediments from sites with clear SMTZs

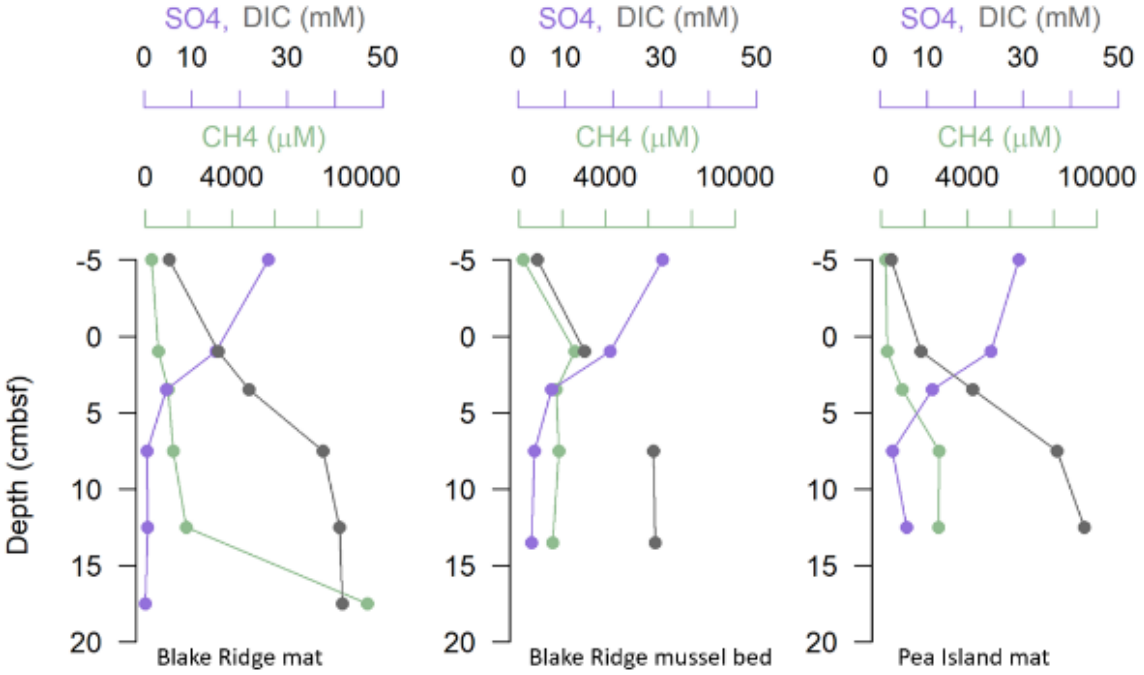

Figure 3-63. Dissolved sulfate, DIC and methane in sediments from sites with clear SMTZs

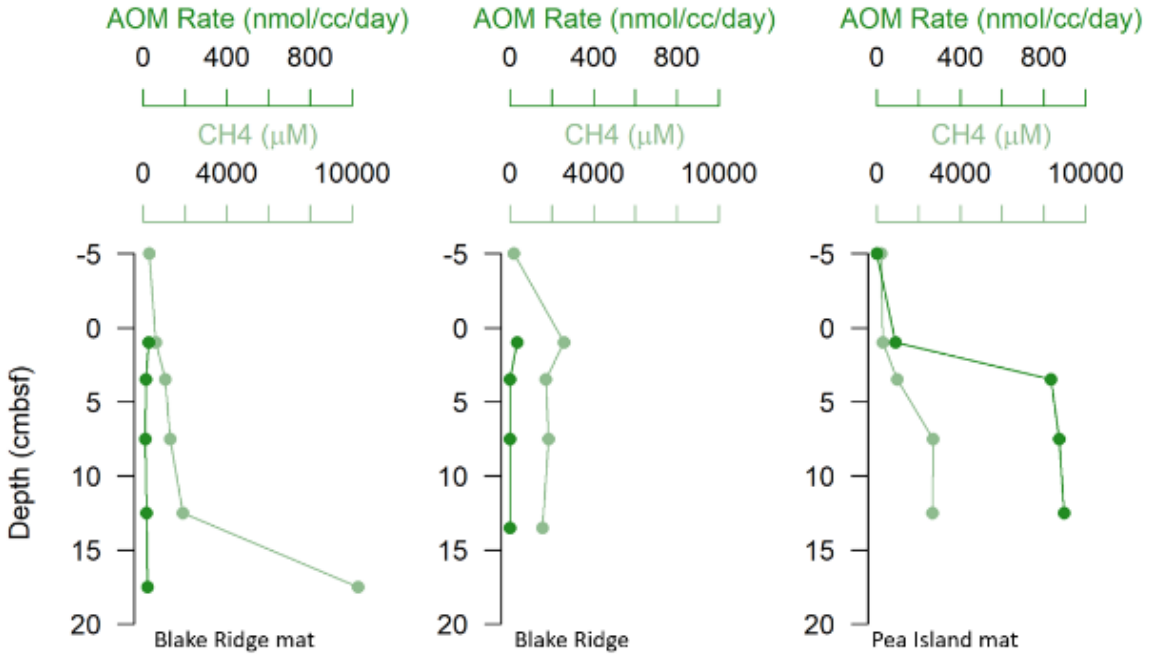

Figure 3-64. Rates of AOM vs. [CH4] in sediments from sites with clear SMTZs

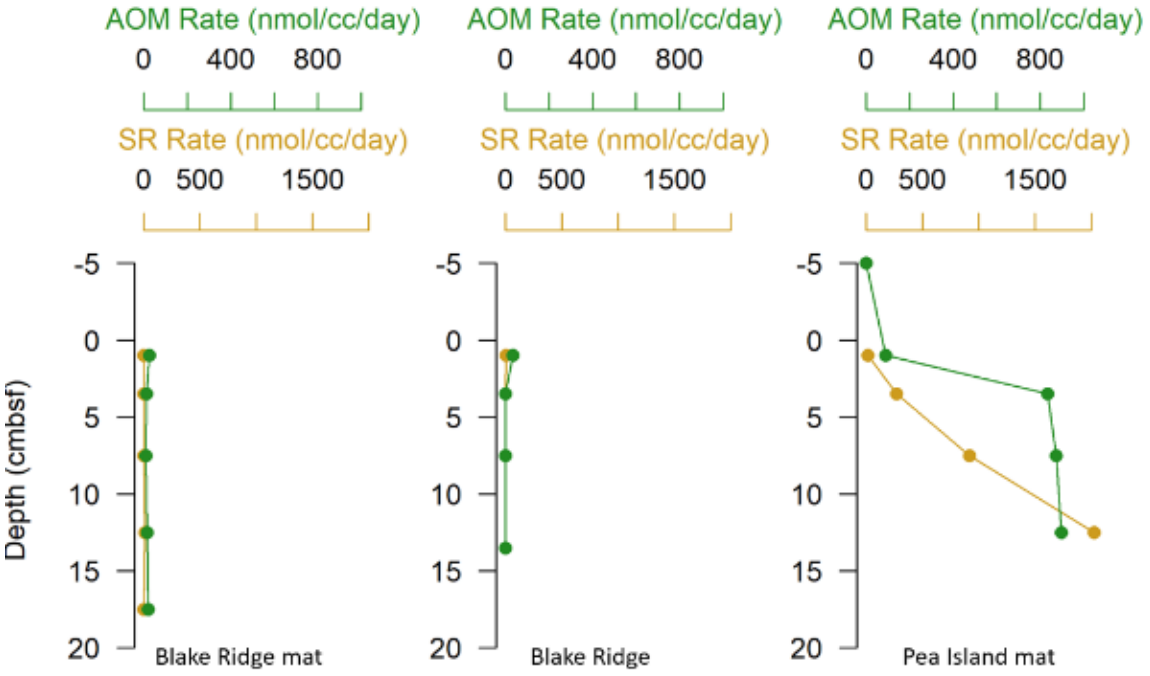

Figure 3-65. Rates of AOM vs. SR in sediments from sites with clear SMTZs

3.3.4.4 Authigenic Carbonates

Methane-derived authigenic carbonates precipitate locally due to oversaturation of bicarbonate ions in pore fluids. At methane-rich cold seeps, methane-derived authigenic carbonates precipitation is driven by the reaction: $CH_4 + SO_4^{-2} \rightarrow HS^- + HCO_3^- + H_2O$ (Reeburgh 1976), which increases pore water alkalinity

via bicarbonate (HCO_3^-) production, which favors carbonate precipitation. This process is mediated by methanotrophic archaea and SRB in continental margin sediments and plays a key role in the marine carbon cycle. Consortia of methane-oxidizing archaea (anaerobic methanotrophs) and SRB have been identified as carrying out AOM (Chevalier et al. 2011, Elvert et al. 2003, Elvert et al. 2005, Hinrichs and Boetius 2002, Hoehler et al. 1994, Knittel and Boetius 2009, Valentine and Reeburgh 2008, Valentine et al. 2000), though other terminal metabolisms may also be coupled to methane oxidation (Bowles et al. 2019, Joye 2020).

The anaerobic methanotrophic archaea (ANME; Orphan et al. 2001) drive net AOM when methane oxidation is coupled to an external electron acceptor such as sulfate, nitrate or metal oxides (see review by Timmers et al. 2017). While authigenic carbonates represent an effective microbial sink for methane, little is known about the microbiome responsible for the methane removal. Previous work by others has demonstrated that DNA associated with carbonates in experiments reflects AOM-mediating microbial communities (Case et al. 2015, Heijs et al. 2006, Marlow et al. 2014a, 2014b, 2021, Stadnitskaia et al. 2005), with recent results from the Atlantic margin demonstrating the fidelity to identify the methanotrophic consortia driving AOM along the Atlantic margin (Beckmann et al. 2021, Prouty et al. 2020). For example, different ANME clades in the Norfolk and Baltimore Seep authigenic carbonates were detected in the phylogenetic analysis. At the Norfolk Seep site, ANME-1a, -1b, 2a-2b, and 2c were detected whereas only the ANME-2 clade was detected at the Baltimore Canyon Seep and present as the subclusters 2a-2b and -2b. The high abundance of Candidatus *Methanoperedens nitroreducens*, (Prouty et al. 2020) suggest the ANME-2d clade may also be present, with AOM potentially linked to nitrate reduction rather than SR.

3.3.5 Microbial Community Assessment Methods

We assessed microbial communities using DNA marker gene sequencing and analysis. We collected carbonate samples in 2018 and 2019 from Pea Island, Blake Ridge, and Kitty Hawk Seeps (**Table 3-20**). Upon collection, we wrapped carbonate samples in sterile foil, then bagged, and stored frozen until analysis. Following methods described in (Beckmann et al. 2021, Prouty et al. 2020), authigenic carbonates were crushed, homogenized aseptically, and transferred to sterile power bead tubes (Qiagen, Hilden, Germany). We extracted DNA using the DNeasy® UltraClean® Microbial Kit according to the manufacturer's instructions (Qiagen). We washed the DNA pellet with 70% (v/v) ethanol and resuspended in 50-µL nuclease free water (Qiagen). DNA concentration and purity were determined by agarose gel electrophoresis and fluorometrically using RiboGreen (Qubit Assay Kit, Invitrogen, LifeTechnologies Corporation, Oregon, USA) according to the manufacturer's instructions.

We used the extracted DNA as a target for bacterial and archaeal 16S rRNA gene sequencing. We generated amplicon libraries from the DNA by following Illumina's 16S Metagenomic Sequencing Library Preparation Protocol. We used the universal primer pair 515F/806R targeting the V4 hypervariable region of the bacterial and archaeal 16S rRNA genes (Apprill et al. 2015, Caporaso et al. 2011, Parada et al. 2016) for the initial amplification.

We purified polymerase chain reaction (PCR) products using the GeneJET Gel Extraction Kit (ThermoFisherScientific, Vilnius, Lithuania) and quantified using a fluorometric RiboGreen kit (Qubit Assay Kit, Invitrogen, LifeTechnologies Corporation, Oregon, USA) according to the manufacturer's instructions. Purified amplicons were multiplex sequenced using the MiSeq platform (Microbial Analysis, Resources, and Services (MARS), UConn Biotechnology Bioservices Center, Stamford, CT, USA) according to (Lange et al. 2014). We performed denoising, chimera removal and trimming of poor quality read ends using QIIME 1.9.1 (https://qiime.org; (Caporaso et al. 2011). Reads were clustered into molecular operational taxonomic units (MOTUs) with > 97% sequence similarity using the uclust_ref algorithm (Edgar 2010) and the SILVA Database (v.119; https://www.arb-silva.de; (Quast et al. 2013).

Table 3-20. Authigenic carbonate samples analyzed for microbial community via DNA marker genes

Site	Sample ID	Lab ID	Date Collected	Depth (m)	Lat.	Long.
Pea Island	18042-A4961-B1-X1	AT41-A4961-B1	08/28/18	424	35.6993	-74.8023
Blake Ridge	18042-A4967-R3-X1	AT41-A4967-R3	08/28/18	2,164	32.4948	-76.1897
Blake Ridge	18042-A4967-B6R2-X1	AT41-A4967-B6-R2	08/28/18	2,164	32.4948	-76.1897
Blake Ridge	18042-A4967-B6R1-G1	AT41-A4967-B6-R1	08/28/18	2,169	32.4948	-76.1897
Pea Island	RB1903_J2_1133_R1	RB1903-J2-1133-R1	04/22/19	322	35.6738	-74.7936
Kitty Hawk	RB1903_J2_1134_RB_02	RB1903-J2-1134-R2	04/24/19	399	35.9274	-74.8079
Kitty Hawk	RB1903_J2_1134_B2_02	RB1903-J2-1134-B2	04/24/19	395	35.9274	74.8075
Blake Ridge	RB1903_J2_1136_R1	RB1903-J2-1136-R1	04/27/19	2,165	32.4938	-76.1907

3.3.6 Microbial Community Assessment Results

We assessed the microbial community composition of the authigenic carbonates collected from the Pea Island, Kitty Hawk and Blake Ridge seeps via 16S rRNA gene sequences. The present work builds upon previous efforts along the Atlantic margin to identify seep microbiome at several seeps (Beckmann et al. 2021, Prouty et al. 2020). Both bacterial and archaeal lineages were represented in the authigenic carbonate samples from the sampling sites listed in **Table 3-20 (Figure 3-66)**.

According to the 16S rRNA phylogeny, ANME comprise less than 2% of the overall microbial communities within the authigenic carbonate samples, with the ANME-1b comprising the majority of Euryarchaeota and ANME-2a-b only detected at Blake Ridge (AT41-A4967-B6-R1; **Figure 3-66**). This is in contrast to authigenic carbonates analyzed from Baltimore and Norfolk seeps where ANME comprised up to 21% of the overall microbial communities (Prouty et al. 2020). We detected SRB belonging to the Deltaproteobacteria and affiliated with the orders Desulfobacterales, Desulfarculales and SEEP-SRB1 with Desulfobulbus sp. and Desulfatiglans sp. in all the samples, except those from Pea Island (RB1903-J2-1133-R1). SRB contributed up to 11% of the overall microbial community in the Blake Ride carbonate from 2,169 m (AT41-A4967-B6-R1).

The presence of SRB is consistent with anoxic conditions and with microbial syntrophy, which allows AOM to occur via reverse methanogenesis whereby electron acceptors, such as sulfate, are readily available and facilitate methane oxidation. However, SRBs contributed less than 5% in the other two Blake Ridge samples, documenting the high degree of variability within a seep site.

In order to evaluate differences between sites in the microbial communities in the authigenic carbonates, we performed nMDS on the microbial abundances obtained from the 16S rRNA gene sequences according to (Clarke 1993, Clarke and Gorley 2015) using PRIMER V6 and XLSTAT (AddinSoftm, Paris, France). nMDS statistical analysis of the microbial community abundance in the authigenic carbonates as determined by 16S rRNA sequencing reveals separation of microbial communities primarily according to seep site (**Figure 3-67**), except for the Pea Island sample collected at 2,169 m (AT41-A4967-B6-R1).

This separation can be attributed to different microbiomes detected at the different seep fields. For example, separation of the Blake Ridge samples may be attributed to higher abundances of *Firmicutes* and *Alphaproteobactria* whereas higher abundance of *Bacteroidetes* helps explain separation of the Kitty Hawk samples **(Figure 3-68**).

According to redundancy analysis (RDA), the samples from Pea Island contain the most diverse group of phyla with potential overlap from the Blake Ridge sample at 2,169 m. However, authigenic geochemical parameters (TOC, TIC, TC, $CaCO_3$, $\delta^{18}O$, and $\delta^{13}C$) may also be influencing microbial community structure. For example, incorporation clays and detrital components relative to quartz and precipitation of dolomite may help explain separation between Kitty Hawk and the Pea Island Seeps. Results from Pea Island, Kitty Hawk and Blake Ridge seeps are consistent with pervious work suggestion that carbonate-hosted microbial assemblages are linked to mineralogy, which may in turn be linked to seep activity (Case et al. 2015).

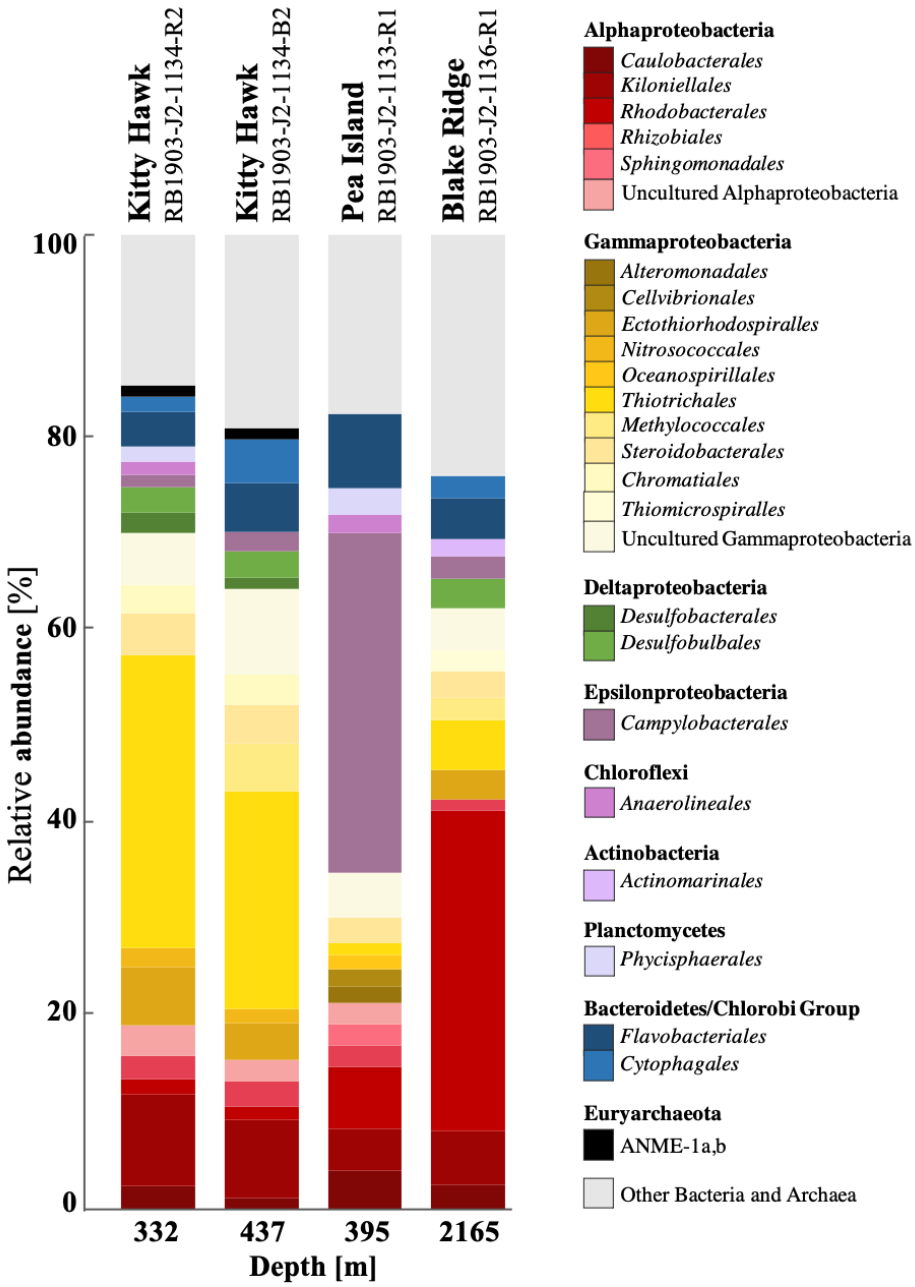

Figure 3-66. Bacterial and archaeal community composition in the authigenic carbonates
From the Pea Island, Blake Ridge, and Kitty Hawk Seeps based on 16S rRNA sequencing.

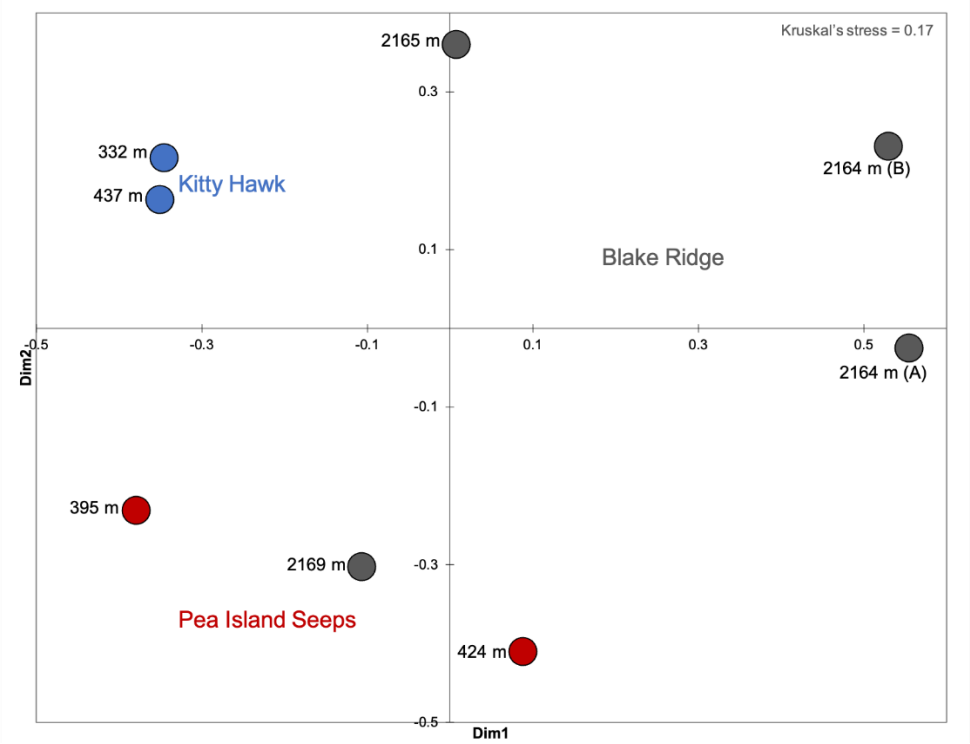

Figure 3-67. Results of multidimensional scaling (MDS) analysis
Includes resulting stress value of 16S rRNA sequencing results of authigenic carbonates collected from the Pea Island, Kitty Hawk and Blake Ridge seeps.

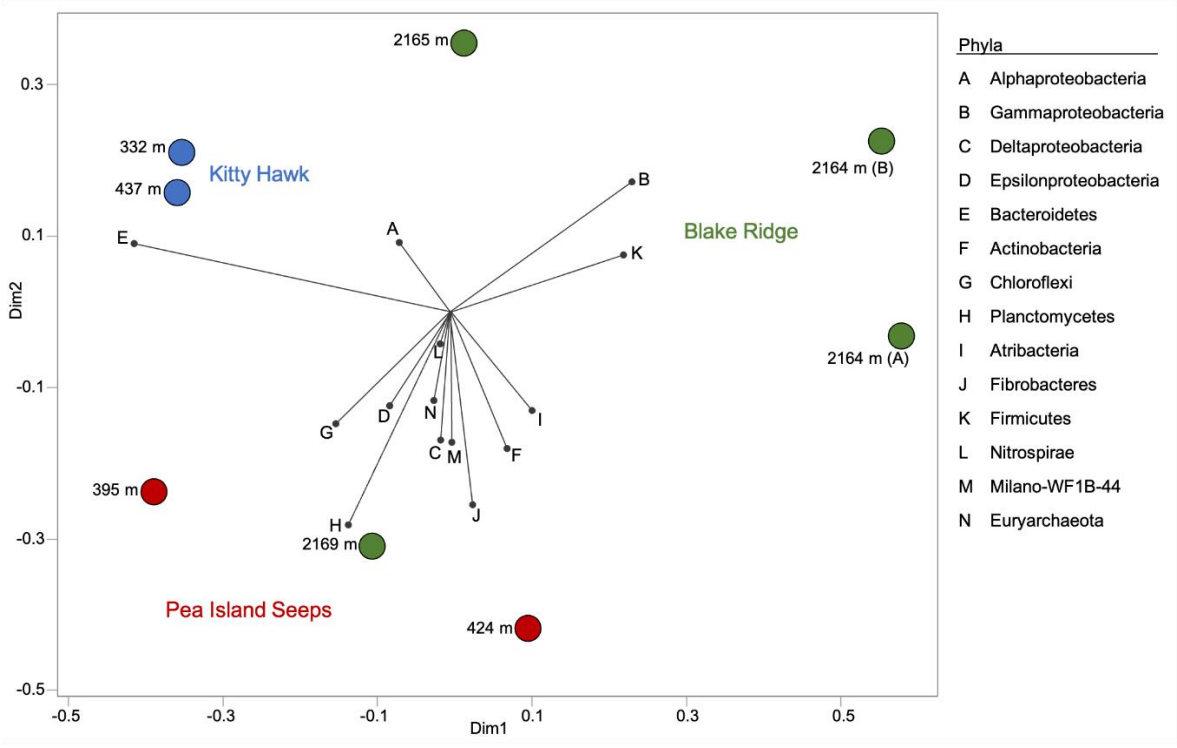

Figure 3-68. Results of RDA, relationship with phyla
Analysis shows the relationship among microbiome assemblage and different microbial phyla.

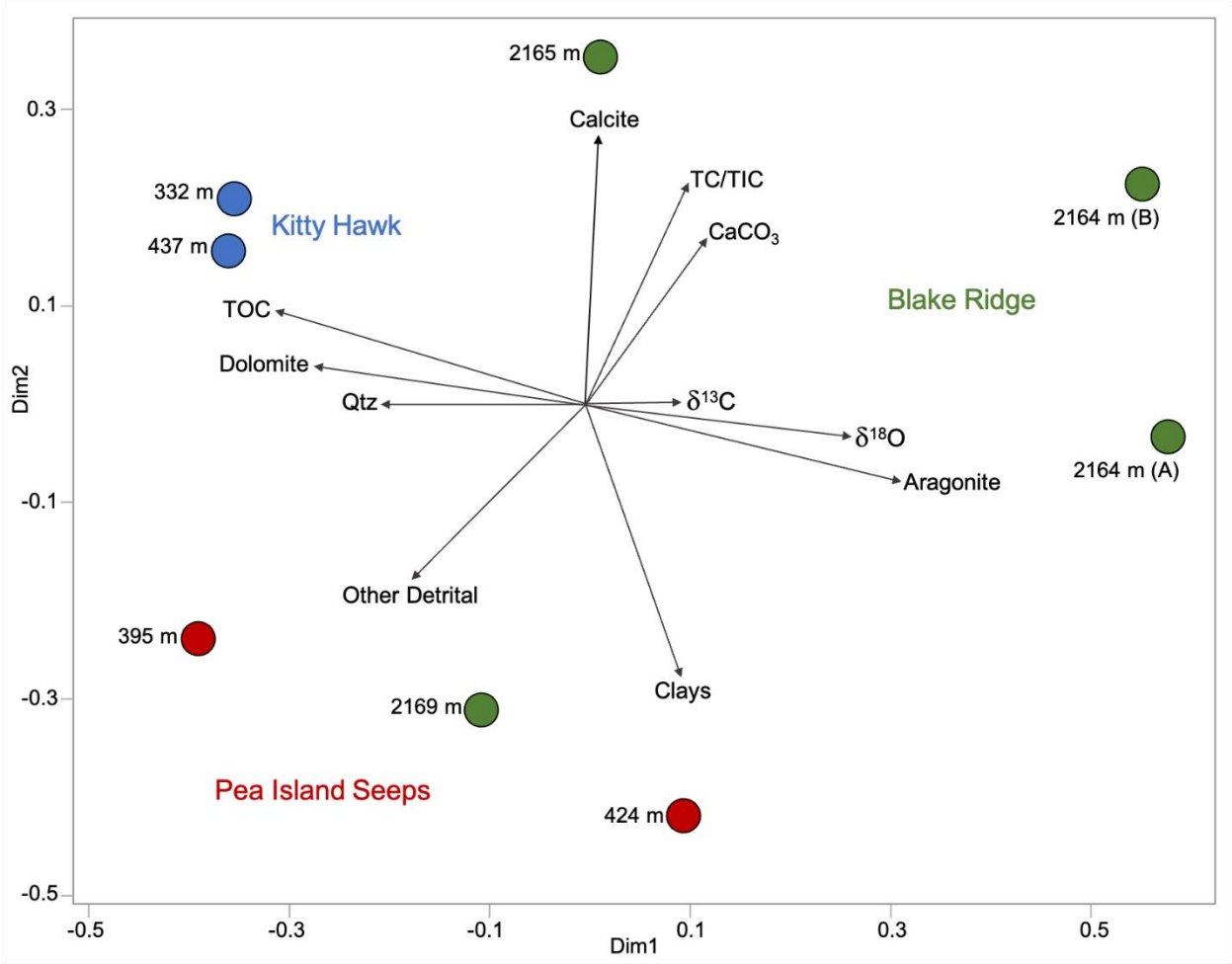

Figure 3-69. Results of RDA, relationship with geochemicals
Analysis shows the relationship among microbiome assemblage and geochemical parameters (TOC, TIC, TC, CaCO3, $\delta^{18}O$, and $\delta^{13}C$; see Section 3.2.3).

4 Community Ecology

In the southern part of the study area, on the Blake Plateau, *L. pertusa*-dominated communities exist that exhibit some similarities to those in south Florida and the GOM, and in the eastern Atlantic from Norway to West Africa. Coral gardens harboring a mixture octocorals and scleractinians are also found on hard substrata from the canyons in the north to the various hard substrata that are predominant on the Blake Plateau. The communities of the canyons are thought to resemble those further north from Virginia to New England. The coral communities in these canyons are composed of the same dominant species, *Paragorgia arborea*, *Primnoa resaedeformis*, and *Paramuricea placomus*, that are observed along the Canadian maritimes and across to the NE Atlantic.

The deeper seeps of the region are dominated by mussel species common to the GOM, and vesicomyid clams are common at the Blake Ridge Diapir. However, the community structure of the shallower seeps that were first documented in the western Atlantic in the early 1980s but were thought to be uncommon in this region, remained undescribed. Recent exploration (Skarke et al 2014), identified ~570 gas plumes along the western Atlantic margin, so these habitats are much more abundant than thought previously. Furthermore, all of the seep sites along the western Atlantic margin appear to lack the vestimentiferan tubeworms that dominate most of the seeps of the Gulf.

The Deep SEARCH study region encompassed vast areas of exposed hardbottom, swept free of sediment by the overlying powerful Gulf Stream. These habitats are morphologically variable and topographically complex, but can be divided into a few broad categories. Coral mounds (bioherms and lithoherms) are abundant along large swaths of the Blake Plateau, created primarily by the cosmopolitan branching scleractinan *Lophelia pertusa*. Less frequently, mounds were formed by *Enallopsammia profunda*, also a branching coral, which is endemic to the western Atlantic. Colonies of *Madrepora oculata* contribute to the scleractinian diversity and structural complexity, but do not create bioherms. The dead coral matrix which forms the underlying structure, provides habitat for abundant and diverse communities of sessile benthic invertebrates (octocorals, hydrocorals, black corals, sponges) and mobile fauna, some of which are economically valuable. Other hardbottom habitats include rocky ledges, pinnacles and escarpments (collectively categorized as 'rocky habitats') carved from the carbonate bedrock by currents and biotic erosion, or lining the walls of the submarine canyons.

Deep-sea octocorals (subclass Anthozoa) are distributed globally across an expansive bathymetric range, where they inhabit seamounts, submarine canyons, slopes, and hardbottom reefs. These long-lived and phenotypically diverse ecosystem engineers build complex heterogeneous structures providing habitat for diverse faunal assemblages (Buhl-Mortensen et al. 2010, Baco & Cairns 2012), engage in symbioses with invertebrates (Buhl-Mortensen and Buhl-Mortensen 2004, Girard et al. 2016), and provide nursery grounds for commercially important fish species (Henderson et al. 2020).

Octocorals underpin vulnerable marine ecosystems, serve as archival windows into past climate cycles (Robinson et al. 2014), and some contain bioactive compounds with potential pharmaceutical applications (Alarif et al. 2019). Despite the integral role octocorals play to the functioning of deepwater ecosystems, only their most fundamental habitat requirements (hardbottom substrate, high nutrient flux, and steady, appropriate temperature schemes) are known to science. A mechanistic understanding of octocoral distribution and biogeography has not yet been achieved due to a lack of studies centering on octocorals, in addition to various logistical and biological challenges specific to the subclass.

To our knowledge, there is no information available on coral-associated sediment communities in the southeast Atlantic region. Similar habitats in the GOM have been found to contain distinct communities with high density and diversity compared to background soft-sediment habitats (Demopoulos et al. 2014, Bourque and Demopoulos 2018). The influence of coral habitats extends outward, with community differences with background soft sediments documented up to 1 km away (Demopoulos et al. 2014).

Sediment communities also differed among coral types, with those associated with *L. pertusa* containing higher proportions of coarse grain sizes that differed from mud-dominated octocoral communities (Bourque and Demopoulos 2018). The high densities and diversities documented in the GOM suggest that coral habitats are important components of regional benthic resources and biodiversity.

Submarine canyons are a source of heterogeneous habitats along continental margins, acting as conduits of organic matter for shallow productive shelves to deep-ocean basins (Harris and Whiteway 2011), and are often described as hotspots of benthic biomass and biodiversity (De Leo 2010; Levin and Sibuet 2012). The southeast Atlantic contains multiple shelf-incising canyons, including Hatteras, Keller, and Pamlico Canyons, as well as multiple smaller unnamed canyons. Previous work in Hatteras and Pamlico Canyons (Rowe 1971) documented distinct epibenthic communities related to canyon topography that differed from adjacent non-canyon areas to the south. Surface sediments within the canyons were dominated by silts and clays, but also contained areas with higher proportions of sand, with the canyon environment exhibiting high sedimentation rates, high influx of organic matter, and deflection up canyon of bottom currents (Rowe 1971).

Although some of the soft-sediment community studies detailed above were conducted in the vicinity of southeast canyons (Blake et al. 1987, Blake & Hilbig 1994), no information is available for infaunal communities residing within southeast canyons. In contrast, Baltimore and Norfolk Canyons in the mid-Atlantic region have been relatively well studied (Robertson et al. 2020; Bourque et al. 2021) where, similar to many canyons worldwide, sediment communities are structured by bathymetric zonation, sediment dynamics, organic enrichment, and disturbance events that differ from adjacent slope habitats.

Seep sediment communities are structured by the flux of methane and porewater sulfide concentrations that can be both spatially and temporally variable (Juniper and Sibuet 1987, Olu et al. 1997, Sibuet and Olu 1998, Levin et al. 2003, Olu-Le Roy et al. 2007). Hard substrata are also created at methane seeps via microbial metabolism, producing authigenic carbonate structures that can be quite large and expansive. These hardbottom habitat types share some common features; they are structurally complex and spatially heterogeneous structures that provide habitat for diverse species assemblages.

At seep habitats in the mid-Atlantic region, macrofaunal communities differ between seep habitat types (microbial mat, mussels) and with background, non-seep communities (Bourque et al. 2018). Microbial mat habitats typically contain high-density and low-diversity macrofaunal communities dominated by tolerant taxa associated with high methane flux and sulfide concentrations (Levin et al. 2003). In contrast, mussel-bed habitats contain high diversity communities associated with likely lower sulfide concentrations (Bourque et al. 2018, Menot et al. 2010). Sediment communities within microbial mat habitats at Blake Ridge contain very low density and diversity of macrofauna and meiofauna (Robinson et al. 2004). In contrast, seep infaunal communities at Cape Fear (Paull et al. 1995) remain unknown.

Sediment infauna are important components of deep-sea ecosystems, supporting benthic biodiversity and providing essential ecosystem functions including transference of energy that reaches the seafloor to higher trophic levels, sediment bioturbation and stabilization, and organic matter decomposition (Gage and Tyler 1991, Danovaro et al. 2008, Gray and Eliot 2009, Thurber et al. 2014). The need for baseline information on deep-sea systems in light of potential oil and gas development led to the US south Atlantic slope and rise study that characterized soft-sediment communities along depth transects near Cape Hatteras, Cape Lookout, and Cape Fear (Blake et al. 1985, Blake et al. 1987). Blake et al. (1987) documented high macrofaunal density and higher diversity than earlier north and mid-Atlantic slope and rise studies (Maciolek et al. 1986, 1987).

Additional studies in the Cape Hatteras region (Blake and Hilbig 1994, Aller and Aller 2002, Schaff et al. 1992, Schaff and Levin 1994, DeMaster et al. 1994) documented high macrofaunal abundances associated with high organic carbon deposition. The Cape Hatteras and Cape Lookout regions are known to be

influenced by the unique combination of narrow shelf and steep slope topography with the Gulf Stream resulting in a zoogeographical break (Blake et al. 1987, Cutler 1975), but potentially not for all taxa (Hilbig 1994).

4.1 Community Structure

Section Authors: Erik E. Cordes, Jill Bourque, Andrea Quattrini, Ryan Gasboro, Sandra Brooke, Amanda Demopoulos

In this study, we tested a series of hypotheses related to the patterns in community structure among all of these habitats. The general Community Hypotheses are listed at the end of **Chapter 1**. Specifically in this section, we examine the following:

1) Do alpha (species richness) and beta (community similarity) diversity vary among habitat types?
2) Does community composition vary with depth?
3) Do other oceanographic or terrain variables influence community structure and diversity?
4) Does abundance/density vary among and within habitat types?

There are differences in depth, topography, and structure across habitats that may influence the species richness and diversity of their associated communities. The composition and diversity of the communities will be described in detail, some for the first time. The primary goal of our video surveys was to understand the influence of habitat and environmental factors on the distribution of megafauna including the seep fauna (primarily bathymodiolin mussels), coral taxa within the Anthozoa (Scleractinia, Alcyonacea, Octocorallia, Antipatharia) and Hydrozoa (Anthoathecatae), as well as the macrofauna species associated with these habitats across the Deep SEARCH study region.

We complimented these studies by quantitative community collections and targeted collections for more precise species identifications, functional trait analyses, and community phylogenetics. The primary goal of the soft-sediment studies was to explore and assess infaunal communities occurring along the southeast Atlantic margin specifically targeting deep-sea coral, chemosynthetic seep, and canyon habitats and their relationship to environmental drivers. Because the data sets and methodology used to characterize the fish assemblages differed from the benthic studies, they are treated separately below.

4.1.1 Methods

4.1.1.1 Video Analysis

We used digital imagery generated by *Alvin* (2018) and ROV *Jason* (2019) to characterize the benthic habitats and their associated communities. During the Deep SEARCH research cruises in 2018 and 2019, we made a total of 14 dives over hardbottom habitats: coral mounds, rocky habitats (ledges, ridges), or canyons. We annotated video from all dives from AT41 and RB1903 at 1s resolution for habitat features (dominant and subdominant substrate percentages) and submersible metadata (whether the vehicle is on bottom, moving, and/or lasers are on). *Alvin* was equipped with a total of five cameras: two Insite Mini Zeus HD cameras mounted on the brow above the port and starboard observer viewpoints, two Kongsberg OE14-522 plan/tilt/zoom HD cameras mounted slightly outboard the forward-facing port and starboard viewpoints, and one SubC imaging 1Cam Alpha camera mounted near the starboard arm in a downward-facing position. *Jason II* was equipped with three mini Zeus HD cameras, configured as two forward-facing (SciCam and Pilot) and one downward-facing cameras. We analyzed video from the starboard Kongsberg camera on *Alvin* and the SciCam on *Jason,* and we used additional cameras as needed to improve faunal identifications. Multiple *Okeanos Explorer* dives of interest to the region (EX1806-7, EX1903L2-4 and EX1903L2-5, EX1907-6) were also analyzed to compliment these data sets (**Table 4-1**).

Table 4-1. Summary of dives conducted during the AT41 and RB19 expeditions

Cruise	Dive #	Site Name	Habitat Feature	On-Bottom Lat	On-Bottom Long	Mean Temp (°C)	Min Depth (m)	Max Depth (m)	Median Depth (m)	Bottom Time	Date
AT41	AL4962	Richardson Reef	coral	32.014	-77.396	9.21	750	820	785	6:33:00	08/23/18
AT41	AL4963	Richardson Reef	coral	31.985	-77.416	9.75	750	820	785	4:35:00	08/24/18
AT41	AL4964	Blake Escarpment Deep	hard bottom	31.323	-77.245	4.32	1,200	1,273	1,237	7:20:00	08/25/18
AT41	AL4965	Stetson Banks	hard bottom	32.012	-78.314	8.47	434	545	490	6:56:00	08/26/18
AT41	AL4966	Stetson Banks	hard bottom	32.07	-78.374	8.36	395	403	399	6:20:00	08/27/18
AT41	AL4968	Cape Fear Coral Mound	coral	33.576	-76.468	10.06	378	458	418	6:29:00	08/29/18
AT41	AL4969	Pamlico Canyon	canyon	34.937	-75.169	-	1,100	1,607	1,354	7:01:00	08/30/18
AT41	AL4970	Norfolk Canyon	canyon	37.043	-74.315	3.72	1,665	1,943	1,804	6:56:00	08/31/18
RB19	J2-1128	Richardson Reef	coral	31.88	-77.374	5.76	731	762	747	9:30:00	04/10/19
RB19	J2-1129	Richardson Reef	coral	31.985	-77.413	9.72	690	708	699	11:15:00	04/13/19
RB19	J2-1130	Savannah Banks	coral	31.754	-79.195	8.55	511	553	532	8:42:00	04/17/19
RB19	J2-1131	Blake Escarpment Deep	hard bottom	31.285	-77.237	4.08	1,306	1,359	1,333	13:27:00	04/17/19
RB19	J2-1132	Pamlico Canyon	canyon	34.914	-75.184	3.90	1,136	1,839	1,488	23:40:00	04/21/19
RB19	J2-1133	Pea Island Seep	seep	35.675	-74.792	11.12	300	353	327	9:28:00	04/23/19
RB19	J2-1135	Cape Lookout Deep	hard bottom	33.916	-75.832	4.48	940	1,029	985	2:40:00	04/25/19
RB19	J2-1136	Blake Ridge Seep	seep	32.493	-76.19	3.28	2,140	2,164	2,152	15:14:00	04/27/19
RB19	J2-1137	Cape Fear Seep	seep	32.979	-75.929	2.68	2,592	2,608	2,600	8:04:00	04/28/19
RB19	J2-1138	Richardson Reef (West)	coral	31.893	-77.699	5.66	658	758	708	8:11:00	04/29/19

We synchronized the ROV navigation files (which recorded latitude, longitude, and depth) with the dive videos via their time codes so that position and depth data could be assigned to observations on the video. We "cleaned" the video data by removing all unusable video footage and sections where the ROV was stationary (usually for sampling). We summarized data at 1-minute intervals for 1) type of video recorded (dead time or unusable video, stopped, transect, or zoomed in), 2) percent coverage (0, < 25%, 25–75%, > 75%) for each habitat type present, and 3) counts of fishes and invertebrates present.

At coral locations, we categorized the video into one of six geological habitat types (**Table 4-2**). In addition to the habitat descriptions, video data were further classified according to percent cover (0%, < 25%, 25% to 75%, > 75%) of structure-forming cnidarians (SFC) and category of SFC (large corals, large anemones/cup corals, and mixed). We used a similar method at seep locations with using slightly different habitat classification types (**Figure 4-1**). The habitat analysis generated georeferenced habitat

types and percent cover of SFC, which were used to create maps of dive tracks with habitat superimposed on bathymetry (**Figure 4-1**).

Table 4-2. Habitat codes used for benthic habitat characterization

Label	Habitat type
S	Soft sediment with no hard substrate visible. Slope may be flat to steep.
SR	Soft sediment with small pieces of rock or emergent hard substrate (EHS). < 50% cover of hard substrate. Slope may be flat to steep.
R	Isolated rock, rubble, EHS. > 50% cover of hard substrate. Slope may be flat to steep.
PB	Large areas of EHS or consolidated sediment that forms hard pavement. >50% cover of hard substrate. Slope may be flat to steep.
W	Walls and steep slopes (rock or consolidated sediment), steep profile.
HC	Hard (stony) coral or coral rubble usually on coral mounds
Label	**Categories of structure-forming cnidarians (SFC)**
1	No SFC
2	< 25% cover
3	25% to 75% cover
4	➢ 75% cover
LC	Large corals: *Paragorgia, Primnoa, Anthothela, Paramuricea, Lophelia, Solenosmilia*
LA	Large anemones and small corals: Cerianthids, *Actinoscyphia, Bolocera,* cup corals
M	Mix of LC and LA

We cross-referenced times with recorded sampling events to ensure accuracy in dive time calculations. We then referenced these calculated dive times to the position to determine the latitude and longitude for each minute interval. We collected data for physical variables around the habitats of interest using CTDs attached to the submersible and ROV. These collected high-frequency data on depth, conductivity, salinity and temperature for the *Alvin* dives, and additional data on dissolved oxygen (mL L^{-1}), and density from *Jason* (DSL SeaBird SBE 19v2 CTD, Omega temperature sensor and Aanderaa oxygen optode 4831). When available, we combined environmental sensor data from the underwater vehicles with the navigation to provide temperature, salinity, eh, pH and dissolved oxygen for each time clip.

When environmental data from *Alvin* or *Jason* were unavailable, we extracted data from the AUV *Sentry* if these data were available, or from the raster layers used for habitat suitability models (see **Chapter 6**) to extract environmental data for points along the vehicle dive tracks. We flagged and excluded data from statistical analyses if the points fell outside the robust portion of the grid domains.

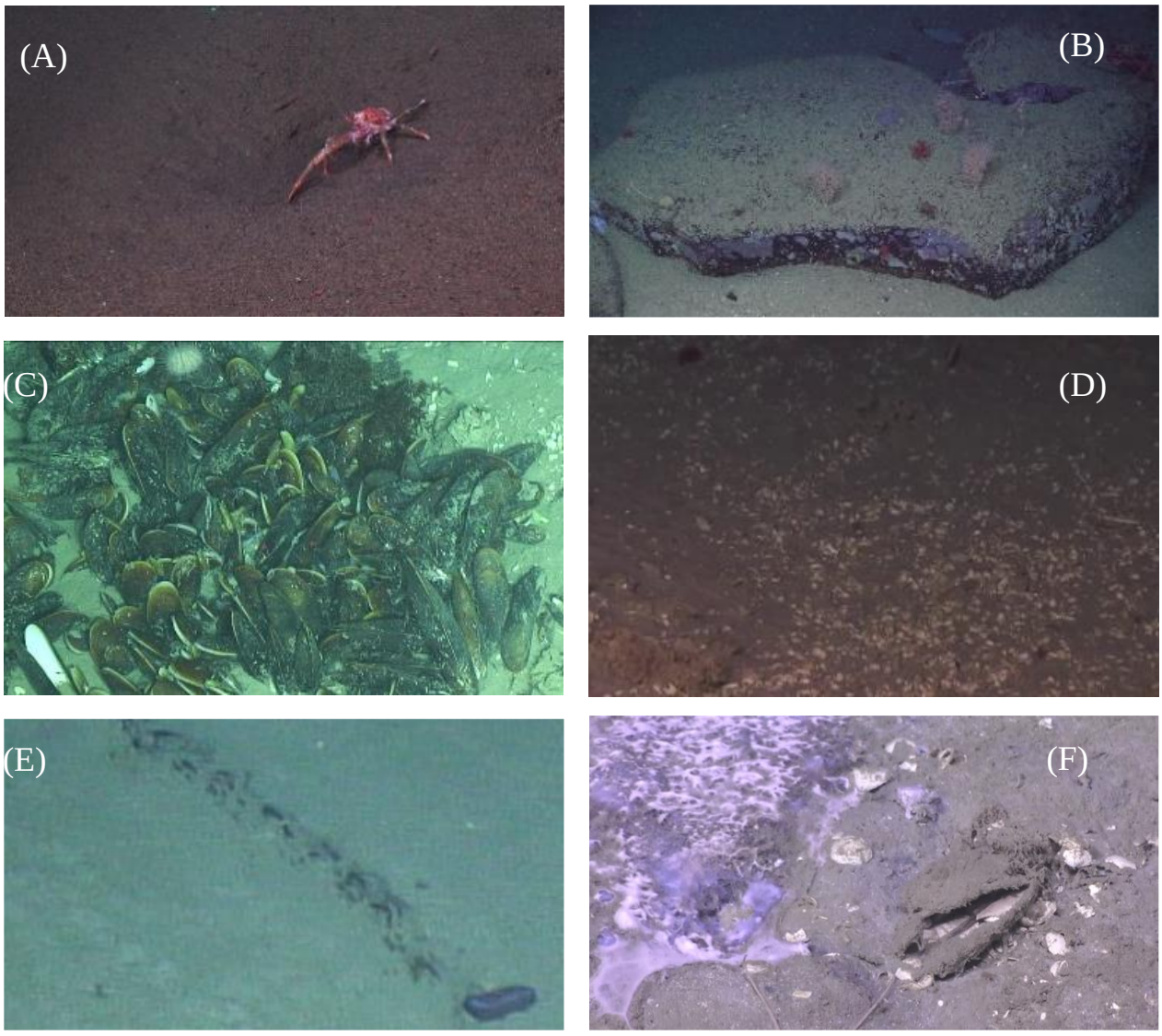

Figure 4-1. Examples of habitat types characterized during video analysis at seep sites
Soft sediment (A), rocks (B), live mussels (C), clams (D), old line debris (E) and bacterial mat (F).

We used high-resolution (1 m) multibeam bathymetry collected during the cruises or in previous expeditions to calculate terrain variables. At local scales, we used bathymetric data collected with *Sentry* when available. We calculated the SD of the depth, slope, and aspect (radians) using ArcGIS 3D Analyst and Spatial Analyst tools. Rugosity (terrain ruggedness), broad BPI, and fine BPI using the Benthic Terrain Modeler package. We calculated tangential curvature using DEM Tools (Jenness 2013).

4.1.1.2 Physical Sampling

We conducted physical sampling during 12 Deep SEARCH cruises from 2016–2019 at 22 main sites (12 coral sites, 4 seep sites, 6 canyons) (**Table 4-3** and **Figure 4-2**). Multiple gear types, including Niskin bottles, Isaacs-Kidd Midwater trawls, tucker trawls, push cores, multicore (MUC), monocore (MC), benthic landers, and underwater vehicles equipped with suction sampling and manipulator arms for sample grabs and quantitative mussel pots, to sample fauna, sediments, and seawater at the study sites. The two underwater vehicles utilized for sampling in this study were the human occupied vehicle *Alvin* in 2018 and the ROV *Jason* in 2019. We collected megabenthic invertebrates (> 2 cm in size) using either

the suction samplers or the manipulator arms, and sediments using push cores (31.65 cm^2 × 30 cm) by underwater vehicles.

Table 4-3. Field Expeditions on Research Vessels

D-Deep SEARCH cruise, C–Collaborative cruise

No.	Year	Date(s)	Field Work	Type	Notes
1	2017	9/10–9/29	*Pisces / Sentry*	D	3 hurricanes
2	2018	03/26–4/25	*Nancy Foster*	D	cancelled
3	2018	05/30–7/1	*Okeanos Explorer / D2*	C	Mapping Blake Plateau / ROV
4	2018	06/6–6/25	*Endeavor*	C	ADEON cruise
5	2018	08/19–9/2	*Atlantis / Alvin*	C	-
6	2018	10/1–10/24	*Okeanos Explorer*	D	Mapping of Blake Plateau
7	2018	10/31–11/16	*Endeavor*	C	ADEON cruise
8	2018	9/27–10/8	*Brooks McCall*	D	lander deployments, sampling
9	2019	04/9–4/30	*Ron Brown / Jason*	D	-
10	2019	10/22–10/30	*Nancy Foster*	D	lander recovery sampling
11	2019	10/22–11/6	*Armstrong*	C	ADEON cruise
12	2019	10/5–11/21	*Okeanos Explorer / D2*	C	Ocean Explorer website

During collection by the submersible, we first imaged coral colonies in situ, then we clipped branches and placed samples in thermally insulated bioboxes onboard the HOV/ROV where they were retained for the remainder of the dive. Once onboard the ship, samples were immediately preserved or stored in a cold room until processing. During sample preservation, we took a photo of each coral specimen then clipped subsamples of tissue measuring 2–3 cm in length, preserved them in both 70% and 95% EtOH and froze them at -80ºC or -20ºC for genetic work. We preserved the remainder of the samples in 95% EtOH as voucher specimens to be deposited at the Smithsonian Natural History Museum.

We identified fauna to the lowest possible taxon using keys and taxonomic expertise within the group when possible, and with external assistance applied when necessary. Later, we verified these morphological identifications with multilocus genetic barcoding and the designation of MOTUs (see below). We sorted fauna collected from trawls and submersibles and either dissected them for stable isotope analyses or froze them for future processing. We preserved vouchers in 95% ethanol and archived them at the Smithsonian.

We collected push cores within microbial mats and within 1 m of targeted habitats (corals, hard substrates, mussel beds). We collected additional sediments with the multicorer (MUC, 71.22 cm^2 x 60 cm) or the monocorer (MC, 22.89 cm^2 x 25 cm) attached to the base of the CTD. We sectioned sediment cores for faunal analyses vertically after recovery as follows: PI-2016 (0-1, 1-2, 2-3, 3-4, 4-5, 5-10 cm) and all other cruises 0–2, 2–5, 5–10 cm. We collected subsamples from geochemistry cores at corresponding vertical depths for stable isotope analysis. We preserved faunal core sections whole in 10% buffered formalin solution until returned to the laboratory and washed them through a 300 µm sieve to retain the macrofauna portion. We sorted macrofauna with a dissecting microscope and identified the macrofauna to the lowest practical taxonomic level, including family level for annelids, peracarid crustaceans, and mollusks. We analyzed homogenized subsamples of geochemistry cores for stable carbon ($\delta^{13}C$) and nitrogen ($\delta^{15}N$) isotopes, and percent organic carbon and nitrogen. We collected POM to characterize the stable isotopic ($\delta^{13}C$, $\delta^{15}N$) composition and total organic carbon and nitrogen. We filtered seawater from the Niskin bottles (1 to 10 L) through a pre-weighed combusted glass microfiber filter (GFF).

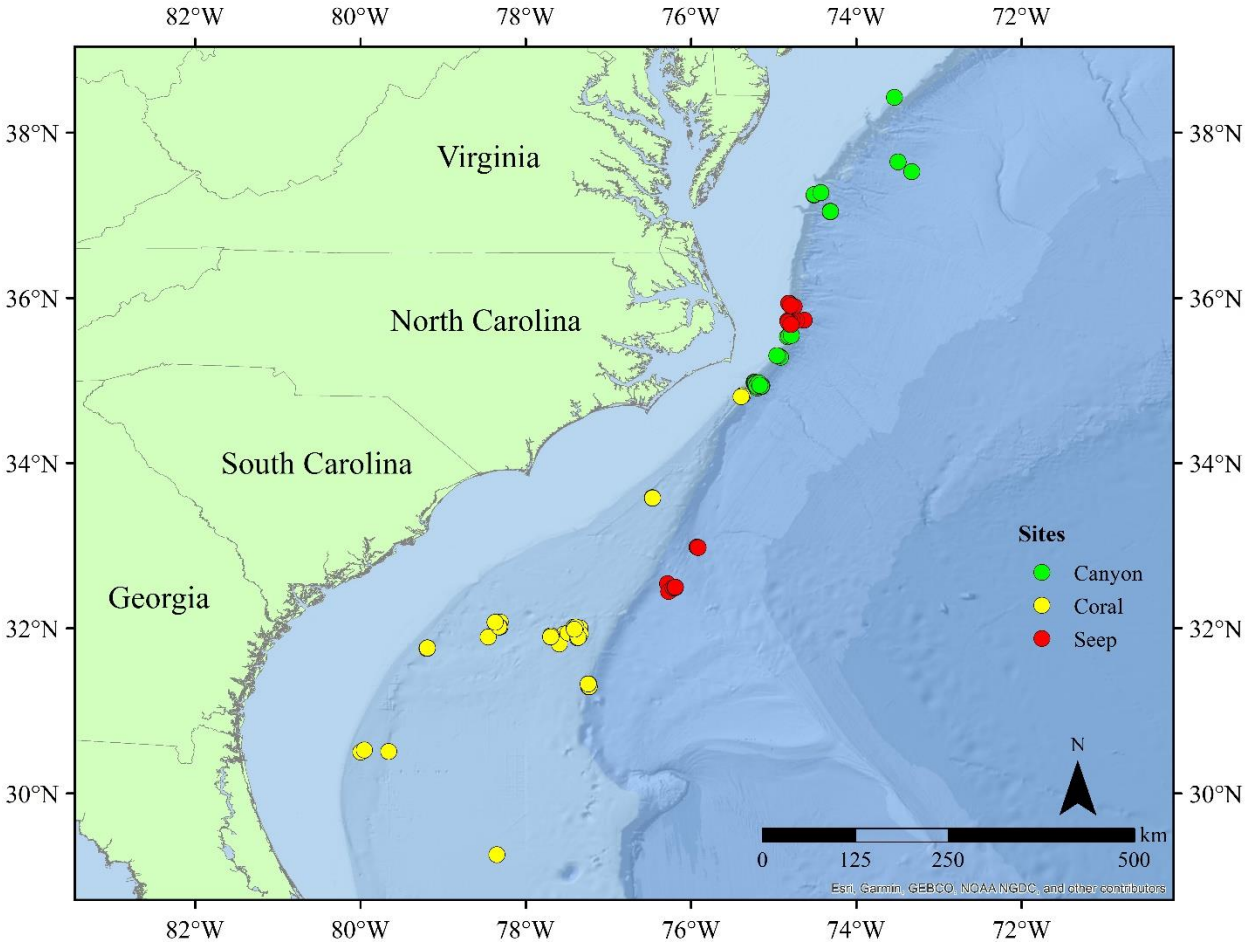

Figure 4-2. Collection locations for Deep SEARCH sites sampled during nine cruises
Deep SEARCH cruises from 2016–2019. Sampling efforts focused on three general habitat types: canyon (green), coral (yellow), and seep (red).

We collected a total of 21 quantitative community samples from eight sites in 10 dives, and depths ranging from 381–2,170 m, on cruises AT41 and RB1903. Fifteen samples were collected in *Lophelia pertusa* coral reef habitats, five from bathymodiolin mussel beds, and one from *Solenosmilia variabilis* coral in Pamlico Canyon. We completed measures of biocomplexity for each of these habitat-forming taxa. For corals this included surface area and volume measurements separately for both live and dead coral; for mussel this included length, height, and width measurements for each shell which can be used to generate volume size-frequency curves. We rinsed and sieved samples to 2 mm onboard; all fauna were separated by morphotype, placed in ethanol, and brought to Temple University. We identified associated taxa to the lowest possible taxonomic category, usually to at least family level. In addition, we completed genetic barcodes of the mitochondrial CO1 gene for macrofauna, allowing for more precise identifications. We sent samples from four abundant/key taxa to the UC Davis Stable Isotope Facility for measures of carbon and nitrogen isotopes for food-web analyses.

4.1.1.3 Genetic Analysis

Epizoic associates commonly occur on octocorals, which offer diverse microhabitats and access to increased food supplies due to their elevated positioning in faster currents above the seafloor (Buhl-Mortensen and Buhl-Mortensen 2004). During the AT41 and RB19 research expeditions, we collected a total of 178 non-octocoral invertebrate specimens. These included octocoral and seep associates such as

ophiuroids (n = 16 individuals) and holothurians (n=20), as well as other anthozoans such as antipatharians (n = 10), scleractinians (n=9), actiniarians (n=31), and zoantharians (n=4). The most abundantly collected species were *Bathymodiolus heckerae* (n=78), *Chiridota heheva* (n=20), and *Ophioctenella acies* (n=8).

For these specimens, we performed DNA extraction, PCR amplification and sequencing following the same protocols as with Octocorallia specimens. We used foot tissue for *Bathymodiolus heckerae*, arm tissue for ophiuroids, and polyps for hydroids. Sponges were PCR amplified for a *28S* barcode, and all other invertebrate associates were amplified for both *28S* and COI barcodes (**Table 4-4**). The COI locus was sequenced for 115 individuals, and the 28S locus for 43 individuals.

Table 4-4. PCR primers and protocols used to amplify target loci in non-octocoral specimens

Gene	Primer	Sequence (5' to 3')	PCR Profile
Ophiuroidea and Aplacophora: COI	jgLCOI[1]	TITCIACIAAYCAYAARGAYATTGG	95°C: 45s, 42°C: 45s, 72°C: 60s (40 cycles)[a]
Ophiuroidea and Aplacophora: COI	jgHCOI[1]	TAIACYTCIGGRTGICCRAARAAYCA	95°C: 45s, 42°C: 45s, 72°C: 60s (40 cycles)[a]
C. heheva: COI	COIef[23]	ATAATGATAGGAGGRTTTGG	95°C: 40s, 45°C: 40s, 72°C: 50s (40 cycles)[a]
C. heheva: COI	COIer[23]	GCTCGTGTRTCTACRTCCAT	95°C: 40s, 45°C: 40s, 72°C: 50s (40 cycles)[a]

[a]PCR began with an initial denaturation of 95°C for 7 min, and concluded with a final extension of 72°C for 5 min
[1]Geller et al. (2013); [2]Arndt et al. (1996); [3]Miller et al. (2017)

4.1.1.4 Statistical Analysis

We visualized all community video segments (n = 883) for coral and canyon ecosystems together via nMDS. To find a convergent solution with such a large ordination with heavily zero-inflated and many low dissimilarity values between CWC and canyon ecosystems, only morphospecies with total counts > 5 were included in this analysis (n = 88). Therefore, actual dissimilarities between the habitat types may be greater than those shown. We used Bray-Curtis dissimilarities for each ordination. We also ran nMDS for each habitat type independently in order to visualize intra-habitat differences between sites.

We used multivariate analyses to examine whether megafaunal communities varied across different seep sites. We summarized video data by dive, square-root transformed and used to generate a Bray-Curtis similarity matrix. We used this matrix to create nMDS ordination plot and dendrograms based on hierarchical cluster with group averaged linkage. A similarity profile analysis (SIMPROF) identified significantly dissimilar clusters, which were then overlaid on the nMDS plot to examine the relationship between significant clusters and specific sites. We used similarity of percentages (SIMPER) to determine which taxa were driving the significant differences among groupings defined by SIMPROF, with the top-ranking taxa contributing to this dissimilarity reported. To assess whether depth, habitat type, or presence of major habitat type influenced the megafaunal community for each dive, we performed an analysis of similarities (ANOSIM), with each run having 999 permutations.

We tested the influence of terrain and environment on coral community composition using a distance-based redundancy analysis (dbRDA) based on Bray-Curtis dissimilarities of Hellinger-transformed morphospecies abundances per 1-minute video. We extracted environmental variables (export carbon, pH, temperature, and dissolved oxygen) from long-term annual mean seafloor conditions from an ensemble of global climate models from the Climate Model Intercomparison Project 6 (Arias et al. 2021).

Where available, in situ data from submersible sensors took precedence over climate model data. We generated all terrain variables from high-resolution (35 m) bathymetry collated by Sowers (2020). These variables included two measures of seafloor aspect (directionality of seafloor measured as northness and eastness), bathymorph, and BPI at both 1-km (broad) and 100-m (fine) neighborhood resolutions, and slope.

After inspection of Pearson's correlation coefficients between all variables, we chose a final suite of variables to include in the models. We removed dissolved oxygen as a variable due to a high correlation coefficient with temperature and pH and the generally normoxic nature of seafloor conditions in this region. We removed Bathymorph and BPI at 100-m resolution due to high Pearson's correlation coefficients that indicated that these variables did not provide unique information in the suite of terrain variables.

We did not include additional variables that did not have full coverage over the study area, particularly the terrain variables, in the dbRDA that covered all sites (those in all three ecosystem types). However, substrate, which is a proxy that is likely driven by local terrain factors such as slope and BPI, was included. We used a reduced model with climate and in-site submersible data for these data.

We assessed infaunal community structure using multivariate analyses and by examining the overall contribution of individual taxa to the community composition. We performed multivariate analysis of community structure across samples on square-root transformed data using Bray-Curtis similarities in PRIMER version 7 (Clarke and Gorley 2015) with the PERMANOVA + add on package (Anderson et al. 2008). We examined infaunal communities using non-metric multidimensional scaling (nMDS) and permutational analysis of variance (PERMANOVA) to test for differences among habitats and sites.

We used cluster analysis (CLUSTER), combined with SIMPROF, to determine similarity groupings among individual samples. We used SIMPER to identify taxa responsible for discriminating between comparison groups and to assess variability of the communities within groups. Specific comparisons are detailed as follows for the coral, canyons, and seep communities.

For coral communities, we made comparisons among sites (Savannah Banks, Cape Fear, Richardson Ridge, Blake Escarpment, and Blake Deep). We compared seep communities among distinct seep attributes (microbial mats, active bubbling near carbonates [bubbles], clam beds, mussel-bed adjacent) and background habitats both within and among sites (Kitty Hawk, Pea Island, Cape Lookout, Cape Fear, Blake Ridge). We compared canyon sediment communities among and within individual canyons, including between near-wall and canyon axis communities in Pamlico Canyon. Canyons included in the analysis were Hatteras, Pamlico, and Keller Canyons and the unnamed, but referred to in this study as North Keller and Amphitheater Canyons.

We examined diversity within (alpha) and between (beta) habitats using the total number of taxa present (Sp), Shannon Diversity (H'loge), taxa richness estimated using Margalef's index (d), and Pielou's evenness (J') based on untransformed abundance data using DIVERSE in PRIMER version 7 (Clarke and Gorley 2015). For push cores, we excluded colonial organisms (Porifera, Bryozoa) from diversity calculations (H'loge, d, J') and multivariate community analysis but included them in overall taxa counts.

We examined beta and regional (gamma) diversity using total taxa counts, shared taxa, and rarefaction curves calculated using the program EstimateS and plotted for each group. We generated species-accumulation curves for each site and combined for all sites (EstimateS, v7.5). We standardized taxa counts recorded for each video clip by dividing counts by the distance traveled (in meters) for each time clip. We calculated distance traveled in ArcGIS Pro using the start and end latitude and longitude for each video clip, with XY points converted to line features and geometry calculated using the field calculator.

We analyzed density of macrofauna and univariate measures of biodiversity using one-way ANOVA followed by post-hoc Tukey's HSD for multiple comparisons, or the Ranks and Dunn's Method for pairwise comparisons in SigmaStat 12.5. We tested all data for normality and heteroscedasticity using Shapiro-Wilk and Levene's tests (Zar 1999), $\log_e$-transformed when necessary. If transformation did not achieve normality or equal variances, we used a non-parametric Kruskal-Wallis test on univariate measures. We tested depth relationships with abundance and diversity measures using Spearman's rank correlation. We used a significance level of $p < 0.05$ in all tests. We computed univariate statistics with the program R (R Development Core Team 2018).

To help identify potential environmental variables driving the patterns in different communities, we performed distance-based linear modeling (DISTLM) and dbRDA using the PERMANOVA + add on package. DISTLM performs nominal tests of each variable's explanatory power on community structure and builds a multivariate statistical model of explanatory power of a suite of variables when considered together. We transformed community transect data to absence/presence to include *Bathymodiolus heckerae* and clams, excluding all fish data. Video clips that did not contain any visible fauna or lacked associated variable data were excluded from statistical analyses.

We excluded variables with strong correlation (> 90%) from the model. Variables included in the model were depth, presence of hard substrate, presence of chemosynthetic-related habitat (bubbles, reduced [dark] sediment, bacterial mats), aspect degrees, slope degrees, SD of the slope, profile curvature, tangential curvature, BPI fine, BPI broad, and rugosity. We averaged push core sediment community data for each sampling location. Variables included were depth, latitude, longitude, coarse sediment content (> 2 mm), mud content (< 63 µm), sediment percent organic carbon (%C), percent nitrogen (%N), stable carbon isotope composition ($\delta^{13}C$), stable nitrogen isotope composition ($\delta^{15}N$), and the carbon to nitrogen ratio (C:N). The explanatory variables used were not correlated to any other variable included in the model and were chosen due to their potential to structure and/or impact sediment communities.

4.1.2 Results

4.1.2.1 Habitat Classifications

The habitat types surveyed in the different types of sites were generally as expected. *L. pertusa* mounds were dominated by hard coral, rock, and coral rubble bottom types with some soft sediment mixed in (**Figure 4-3, Figure 4-4, and Figure 4-5**). Some of the dives on the Lophelia mounds encountered nearly 100% coral cover.

Additional habitat associations with fauna are discussed below. We observed representative chemosynthetic seep features (bacterial mats, active bubbling, reduced sediments, carbonates) during seven dives from five different seep sites (**Figure 4-6).** The shallower sites, Pea Island and Kitty Hawk, had similar general habitat types, which were dominated by soft sediment. We observed only a few bacterial mats and carbonates at Kitty Hawk, with increased occurrences at Pea Island and the deeper sites (Blake Ridge, Cape Lookout, and Cape Fear).

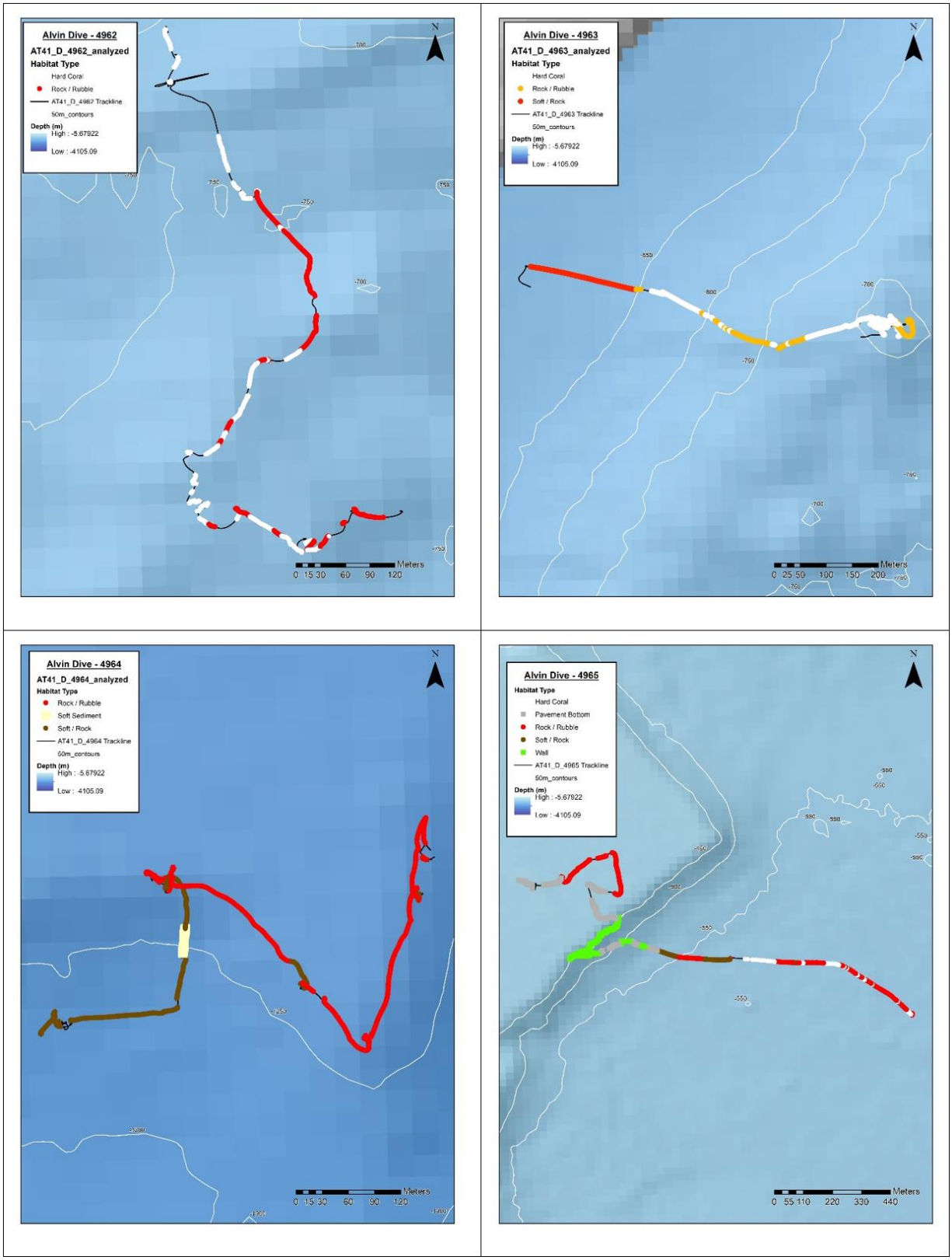

Figure 4-3. Habitat classifications—*Alvin* dives A4962, A4963, A4964, and A 4965

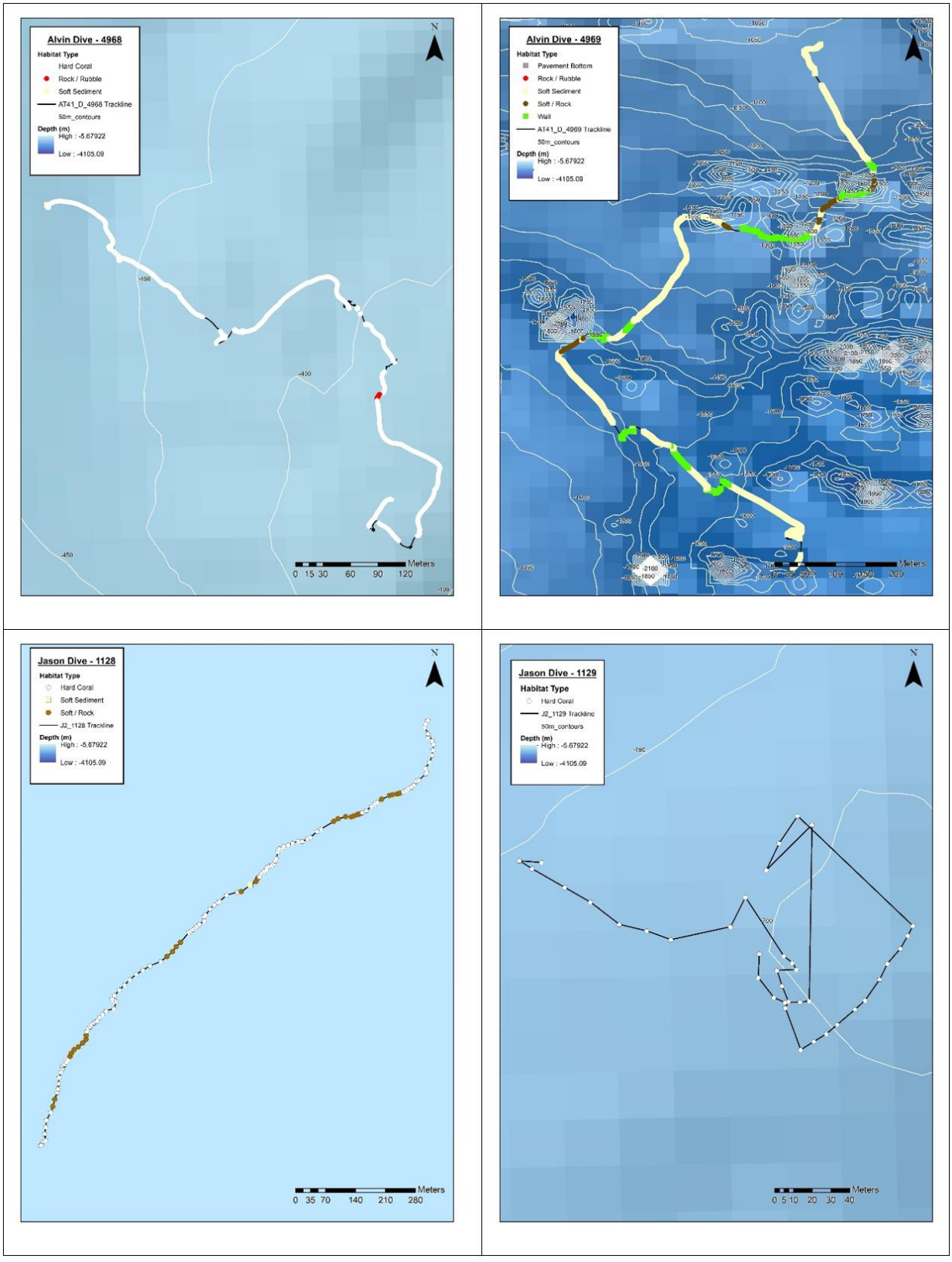

Figure 4-4. Habitat classifications—*Alvin* dives A4968, A4969; *Jason* dives J1128, J1129

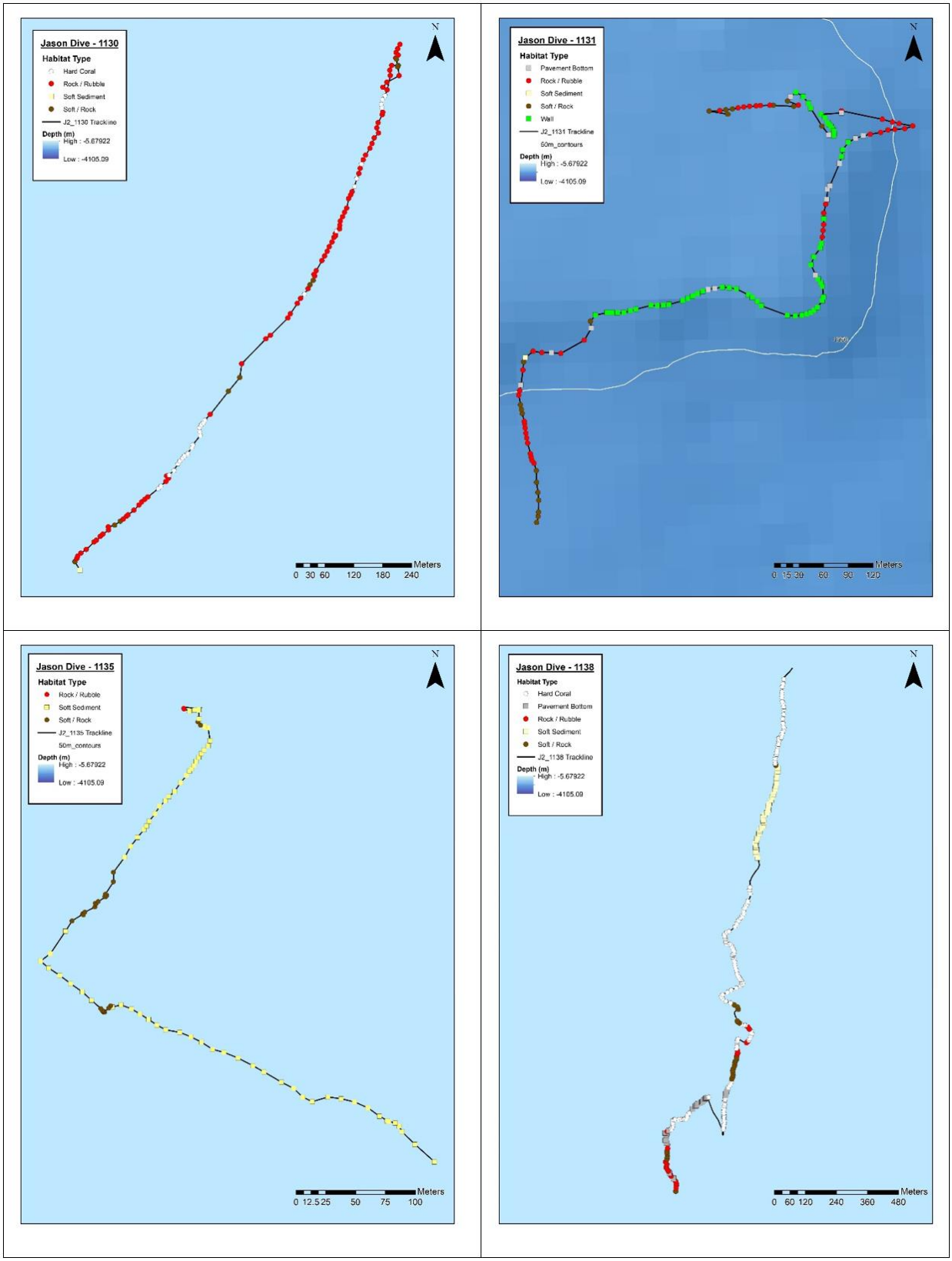

Figure 4-5. Habitat classifications—*Jason* dives J1130, J1131, J1135, and J1138

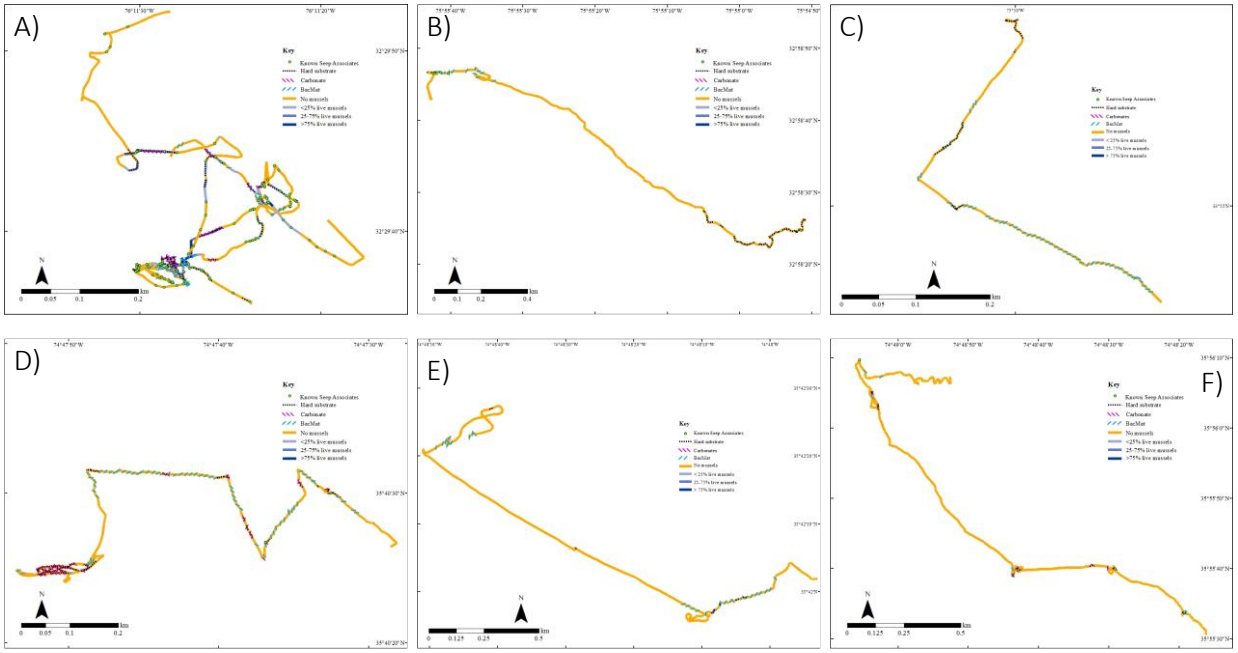

Figure 4-6. Habitat classification for seep sites
A) Blake Ridge, B) Cape Fear, C) Cape Lookout, D) Pea Island 2019, E) Pea Island 2018, F) Kitty Hawk based on video analyses of seeps sites examined during Deep SEARCH from 2018–2019. Solid color lines represent habitat coverage by live mussels, where orange = no mussels, light blue = < 25% live mussel, medium blue = 25–75% live mussel coverage, dark blue = > 75% live mussel coverage. Black dotted lines indicate presence of hard substrate, pink dashed lines indicate carbonates and blue dashed lines indicate presence of bacterial mats. Green points represent locations of where known seep associated fauna (*Escarpia* sp., Alvinocarididae, *Chirodota heheva*, *Ophioctenella acies*, *Sarsiaster griegii*, *Acharax* sp.) were viewed on the video transect.

4.1.2.2 Megafauna

Overall, our surveys of the region have sampled the majority of the species present, as indicated by the leveling off of the species-accumulation curves (**Figure 4-7 A**). The *L. pertusa*-dominated sites (**Figure 4-7 B**) had the most sampling effort and were the most completely characterized, which also is supported by the high rate of initial species accumulation at the Richardson and Central Plateau Mounds sites (**Figure 4-7 C**) that were the location of some of the highly diverse *Okeanos Explorer* dives (**Figure 4-7 D**).

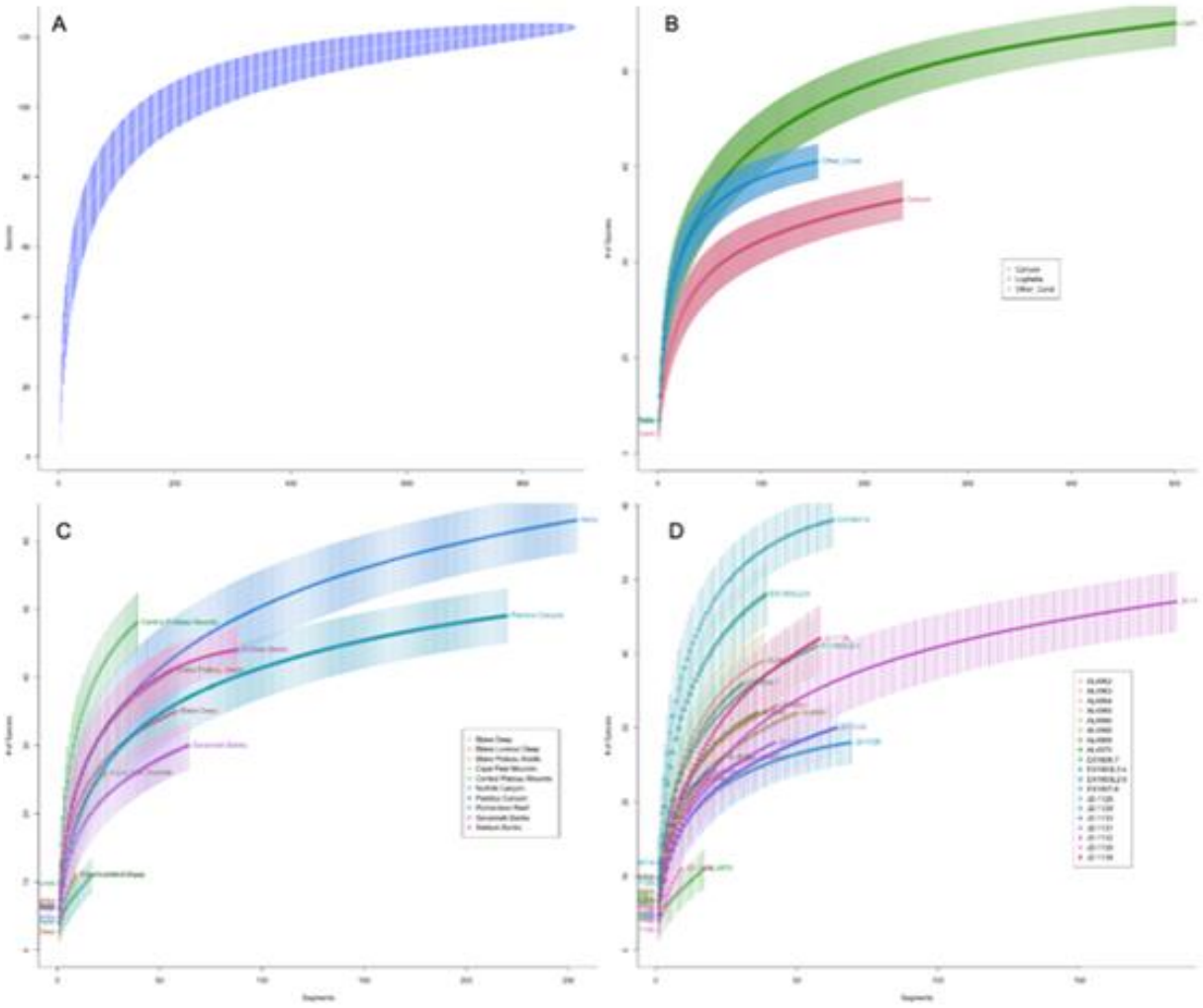

Figure 4-7. Species-accumulation curves for the different sites and habitat types

We analyzed videos of dives (n = 11) in *L. pertusa*-dominated coral habitats in 502 1-minute segments yielding counts of 13,627 individuals of 91 megafaunal (> 5 cm) morphospecies (**Table 4-5**). The ophiuroid *Ophiacantha bidentata*, leptothecate hydroids, and two zoanthid morphospecies, frequently occurred throughout the dives, sometimes in high abundances, but were not feasibly enumerated, and thus were removed from video-based community analyses but were still present in the physical collections. Over 20 megafaunal morphospecies were present in a single 1-minute segment, highlighting the high diversity attained within the reef ecosystems.

Live, dead-standing coral and coral rubble substrates appeared to support high richness and Shannon Diversity on average, although segments with other primary substrates often contained similar diversity values (**Figure 4-8**). Generally, species-accumulation curves suggest that each of the *L. pertusa* sites were relatively well sampled for megafauna, although the curves did not reach an asymptote for multiple sites (**Figure 4-8**). Local topographic highs such as the tops of coral mounds tended to support rich and diverse megafaunal communities (**Figure 4-9**), despite the generally high cover of live *L. pertusa* thickets here that tend to exclude other sessile taxa. Hexactinellid and geodiid sponges were more prominent at these topographic highs where there was a mixture of both living and dead-standing *L. pertusa*. Slopes and flats such as those on coral mound flanks were less diverse, but often supported high abundances of octocorals growing on coral rubble.

Canyon ecosystems yielded 237 video segments across three dives. We counted 6,249 individuals of 22 morphospecies within these ecosystems (**Table 4-5**). Ophiurid brittle stars, the urchin *Phormosoma placenta*, homolid crabs, the sea star *Neomorphaster* spp., and *Acanella arbuscula* were the most abundant morphospecies within the soft-sediment portions of these dives. This included all of dive AL4970 within Norfolk Canyon. On the walls of Pamlico Canyon (dives AL4969 and J2-1132), the scleractinians *Solenosmilia variabilis* and *Desmophyllum dianthus*, *Acesta* spp. clams, and brisingid sea stars were abundant where present. This was typically at microhabitats such as overhangs and ledges where there was little to no sediment drape. Segments within these ecosystems were typically the least speciose and biodiverse **(Figure 4-8, Figure 4-10**), but individual segments often contained high abundances of the primary morphospecies (**Figure 4-11**).

'Other' coral habitats (i.e., those without *L. pertusa* accumulations) contained a wide range of biodiversities within the 155 video segments analyzed. Cape Lookout Deep (J2-1135), for example, was one of the least speciose and diverse sites within the study area, while the Blake Deep site (AL4964), harbored high biodiversity despite occurring at a similar depth (**Figure 4-8**). These sites contained a mosaic of habitats, with primarily hardgrounds such as exposed carbonate outcrops supporting the 4706 individuals of 24 morphospecies observed at these sites. This included over 1,000 colonies of the scleractinian *Enallopsammia* spp., which contributed to the habitat heterogeneity at these sites. We also observed antipatharians genera including *Leiopathes*, *Lepidisis*, *Sticopathes*, and *Bathypathes* at these sites, highlighting a megafauna that was predominantly composed of sessile filter feeders, where the *L. pertusa* sites contained many more mobile fauna.

Table 4-5. List of morphospecies observed

(n = 124) observed in one-minute video segments (n = 893) at SEUS seafloor sites.

Taxonomic Level	Taxonomy
Porifera	-
Demospongiae	-
geodia	*Geodia* sp.
unid_pachastrellid1	Pachastrellidae , unid. sp.
petrosiidae1	Petrosiidae, unid. sp. 1
cladorhizidae	Cladorhizidae, unid. sp.
poecillastra_cf_compressa	*Poecillastra* cf. *compressa*
spongosorites	*Spongosorites* sp.
phakellia_ventilabrum	*Phakellia ventilabrum*
oceanapia	cf. *Oceanapia* sp.
petrosiidae2	Petrosiidae, unid. sp. 1
hymedesmia	*Hymedesmia* sp.
leiodermatium	*Leiodermatium* sp.
demospongiae1	Demospongea, unid. sp.
dercitus	*Dercitus* sp.
raspailiidae	Raspaillidae, unid. sp.
porifera1	Porifera, unid. sp.
demospongiae2	unid. encrusting demosponge
-	-
Hexactinellida	-
hexactinellidae1	Hexactinellidae, unid. sp. 1
euplectillidae	Euplectillidae, unid. sp.
aphrocallistes_beatrix	*Aphrocallistes beatrix*
rosselidae	Rosselidae, unid. sp.

Taxonomic Level	Taxonomy
vazella_pourtalesi	*Vazella pourtalesi*
hertwigia_falcifera	*Hertwigia falcifera*
hexactinellidae2	Hexactinellidae, unid. sp. 2
hyalonema	*Hyalonema* sp.
hexactinellidae3	unid. Hexactinellidae sp. 3
farrea	*Farrea* sp.
hexactinellidae4	unid. Hexactinellidae sp. 4 ('funnel' morph)
hexactinellidae5	unid. Hexactinellidae sp. 5 ('thin' morph common on canyon walls)
-	-
Cnidaria	-
Actinaria	-
actinostolidae	Actinostolidae, unid. sp. 1
actinaria1	Actinostolidae, unid. sp. 2
actinoscyphia_saginata	Actinoscyphia saginata
farrea	Farreidae, unid. sp.
actinaria2	Acinaria, unid. sp. 2
actinaria3	Actinaria, unid. sp. 3
actinaria4	Actinaria, unid. sp. 4
actinaria5	unid. Actinaria sp. 5
actinaria6	unid. Actinaria sp. 6
actinaria7	unid. Actinaria sp. 7
actinaria8	unid. Actinaria sp. 8
-	-
Antipatharia	-
leiopathes_cf_glaberrima	*Leiopathes* cf. *glaberrima*
sticopathes	*Sticopathes* sp.
bathypathes	*Bathypathes alternata*
leiopathes	*Leiopathes* cf. *glaberrima*
umbellapathes	*Umbellapathes* sp.
antipatharia1	Antipatharia, unid. sp.
-	-
Corallimorphia	-
corallium1	Corallidae, unid. sp.
corallimorph	Corallimorpharia, unid. sp.
-	-
Scelactinia	-
madrepora_oculata	*Madrepora oculata*
enallopsammia	*Enallopsammia* sp.
solenosmilia	*Solenosmilia variabilis*
-	-
Octocorallia	-
psuedodrifa_cf_nigra	*Psuedodrifa* cf. *nigra*
swiftia_sp_complex	complex of multiple white octocorals indistinguishable from video: cf. *Swiftia* sp., *Eunicella modesta*, and *Muriceides* sp.
anthomastus	complex of *Anthomastus grandiflorus* and *Pseudoanthomastus* sp. indisinguishable from video
plumarella	white primnoid cf. *Plumarella* sp.

Taxonomic Level	Taxonomy
anthoptilum	Pennatulacea, unid. sp. cf *Anthoptilum* sp.
chrysogorgiidae	Chrysogorgiidae, unid. sp.
keratoisidinae1	Keratoisidinae, unid. sp. (white)
keratoisidinae2	Keratoisidinae, unid. sp. (peach)
anthothelidae1	Anthothelidae, unid. sp.
acanthogorgia_sp_complex	complex of yellow octocorals: *Acnathogorgia* sp. and *Paramuricea* sp.
isidella	*Isidella* sp.
sibogagorgia	*Sibogagorgia* sp.
gersemia_fruticosa	*Gersemia fruticosa*
paragorgiid1	Paragorgiidae, unid. sp. 1
paragorgiid2	Paragorgiidae, unid. sp. 1
primnoidae1	Primnoidae, unid. sp.
pennatulacea1	Pennatulacea, unid. sp.
acanella	complex of octocorals: *Acanella arbascula* and cf. Funiculina
isididae1	unid. Isididae sp. 1
lepidisis	*Lepidisis* sp.
keratoisidinae2	Keratoisidinae, unid. sp. (peach)
unid_octo1	stalked octocoral with three large polyps at end of stalk
-	-
Hydrozoa	-
stylaster	*Stylaster* cf. *erubescens*
hydroid*	unid. Leptothecata
-	-
Zoantharia	-
zoanthid1*	Zoanthidae, unid. sp. (white morph)
zoanthid2*	Zoanthidae, unid. sp. (yellow morph)
-	-
Echinodermata	-
Asteroidea	-
pseudarchaster	*Pseudarchaster* sp.
plinthaster_dentatus	*Plinthaster dentatus*
asteroidea1	Asteroidae, unid. sp. 1
goniasteridae1	Goniasteridae, unid. sp. 1
asteroidea2	*Pseudarchaster* sp.
goniasteridae2	Goniasteridae, unid. sp. 2
solaster	Solasteridae, unid. sp.
brisingida	Brisingida, unid. sp.
chondraster_grandis	*Chondraster grandis*
goniasteridae3	Goniasteridae, unid. sp. 3
gilbertaster_caribbea	*Gilbertaster caribbea*
paxillosida	unid. Paxillosida sp. 1
solaster2	Solasteridae, unid. sp. 2
brisingida2	unid. Brisingidae sp. 2
neomorphaster	*Neomorphaster* sp.
asteroidea2	unid. Asteroid sp. 2
asteroidae3	unid. Asteroid sp. 3
marginaster	*Marginaster* cf. *pectinatus*

Taxonomic Level	Taxonomy
-	-
Ophiuroidea	-
ophiacantha	*Ophiacantha bidentata*
ophiuridae	Ophiuridae, unid. sp.
euryalidae	Euryalidae, unid. sp.
gorgonocephalidae	unid. Gorgonocephalidae sp. 1
-	-
Crinoidea	-
pentametrocrinus_atlanticus	*Pentametocrinus atlanticus*
comatulid	Comatulida, unid. sp.
neocrinus_blakei	*Neocrinus blakei*
endoxocrinus	*Endoxocrinus* sp.
-	-
Holothuria	-
holothuria1	Holothuria, unid. sp. 1
holuthuria2	unid. Holuthurian sp. 2
holothuria3	unid. Holuthurian sp. 3
-	-
Echinoidea	-
gracilechinus	*Gracilechinus* sp.
cidaroididae	Cidaroididae, unid. sp.
araeosoma_belli	*Araeosoma belli*
cidaroid2	unid. Cidaroidae sp. 2
phormosoma	*Phormosoma placenta*
echinoid1	unid. Echinoidae sp. 1
-	-
Arthropoda	-
Crustacea	-
homola	*Homola* sp.
eumunida_picta	*Eumunida picta*
munidopsis_serricornis	*Munidopsis serricornis*
pandalidae	Pandalidae, unid. sp.
chaceon_fenneri	*Chaceon fenneri*
bethynectes_longispina	*Bathynectes longispina*
rochinia_crassa	*Rochinia crassa*
heterocarpus	*Heterocarpus* sp.
cerataspis_monstrosus	*Cerataspis monstrosus*
henricia	*Henricia* sp.
brachyura1	Brachyura, unid. sp.
neomorphaster	*Neomorphaster* sp.
uroptychus	*Uroptychus* sp.
pycnogonid	Pcynogonida, unid. sp. 1
-	-
Bryozoa	
membranipora	*Membranipora* sp.
-	-
Mollusca	-

Taxonomic Level	Taxonomy
graneledone_verrucosa	*Graneledone verrucosa*
bathypolypus_arcticus	*Bathypolypus arcticus*
neogastropoda	Neogastropoda, unid. sp.
-	-
Annelida	-
hyalinoecia_artifex	*Hyalinoecia artifex*
serpulidae	Serpulidae, unid. sp. 1

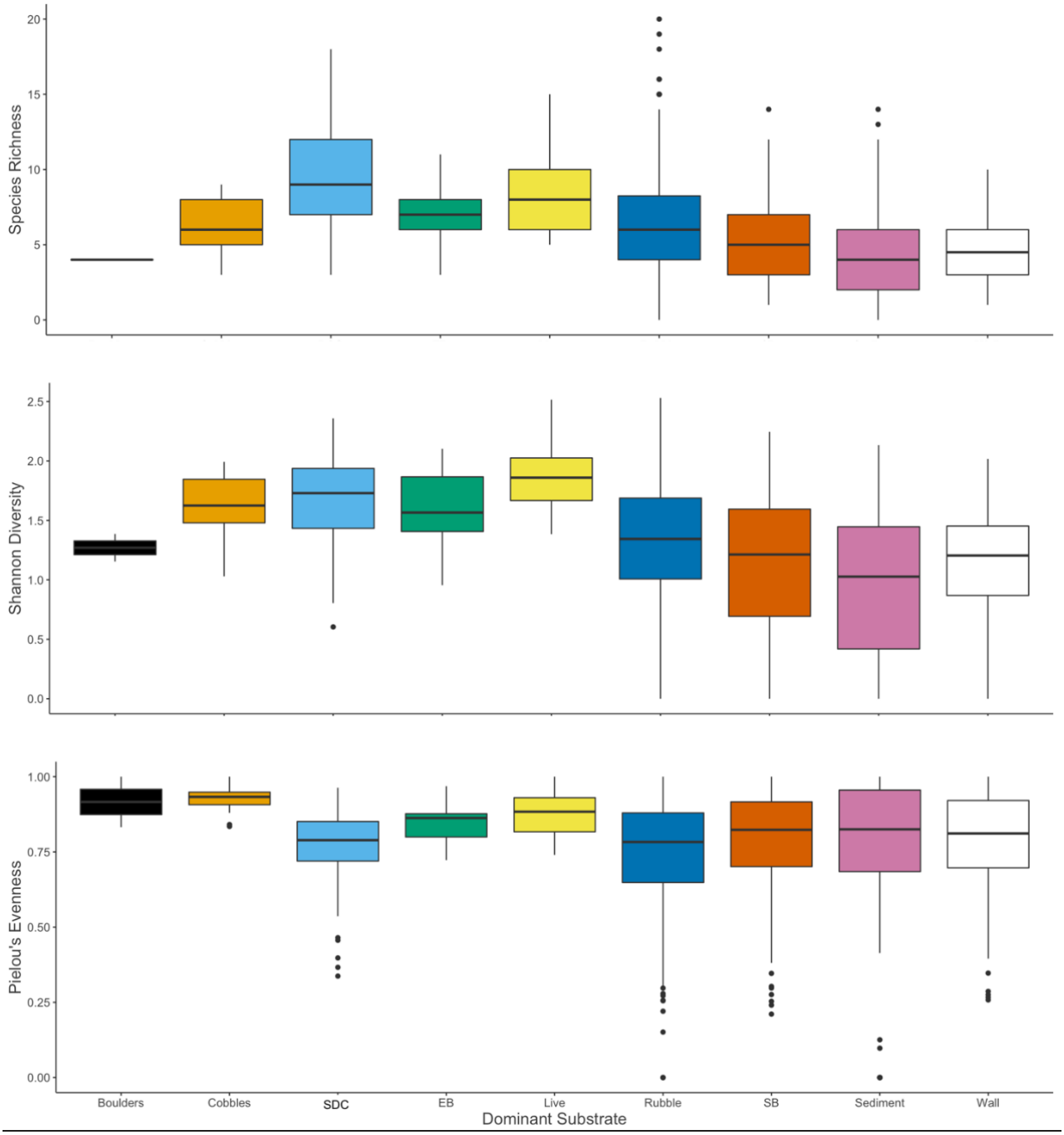

Figure 4-8. Boxplots of species richness, Shannon Diversity, and Pielou's evenness
Richness (top), Shannon Diversity (middle), and Pielou's evenness (bottom) for each 1-minute segment by primary substratum. Substrate categories included boulders, cobbles, standing dead coral (SDC), live coral (Live), coral rubble (Rubble), lightly sedimented bedrock (SB), fully exposed bedrock (EB), and sediment.

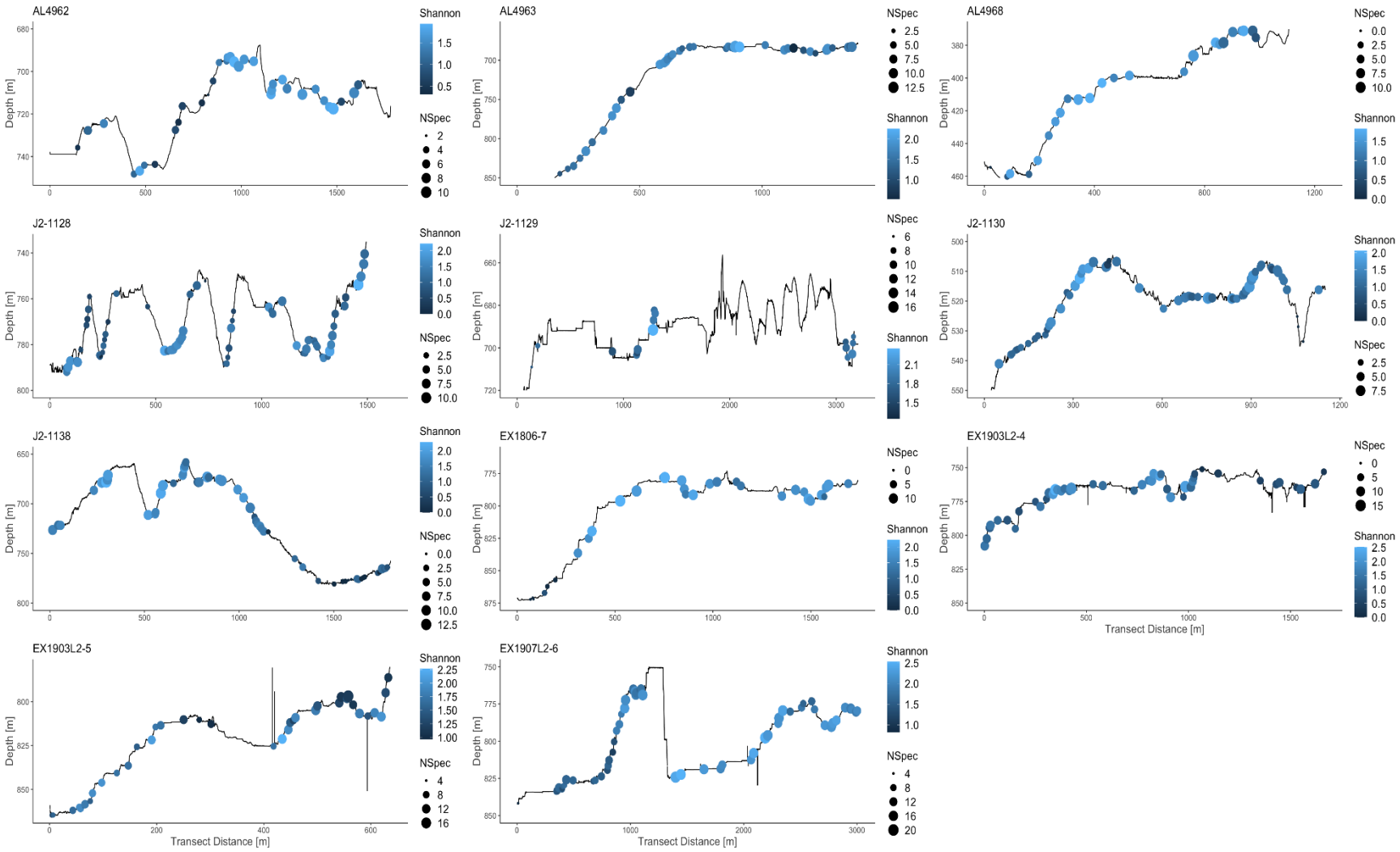

Figure 4-9. Shannon Diversity and Species Richness overlain on the dive tracks
Shannon Diversity (color) and Species Richness (point size) overlain on the dive track (depth vs. distance traveled) for each dive in *Lophelia pertusa* ecosystems.

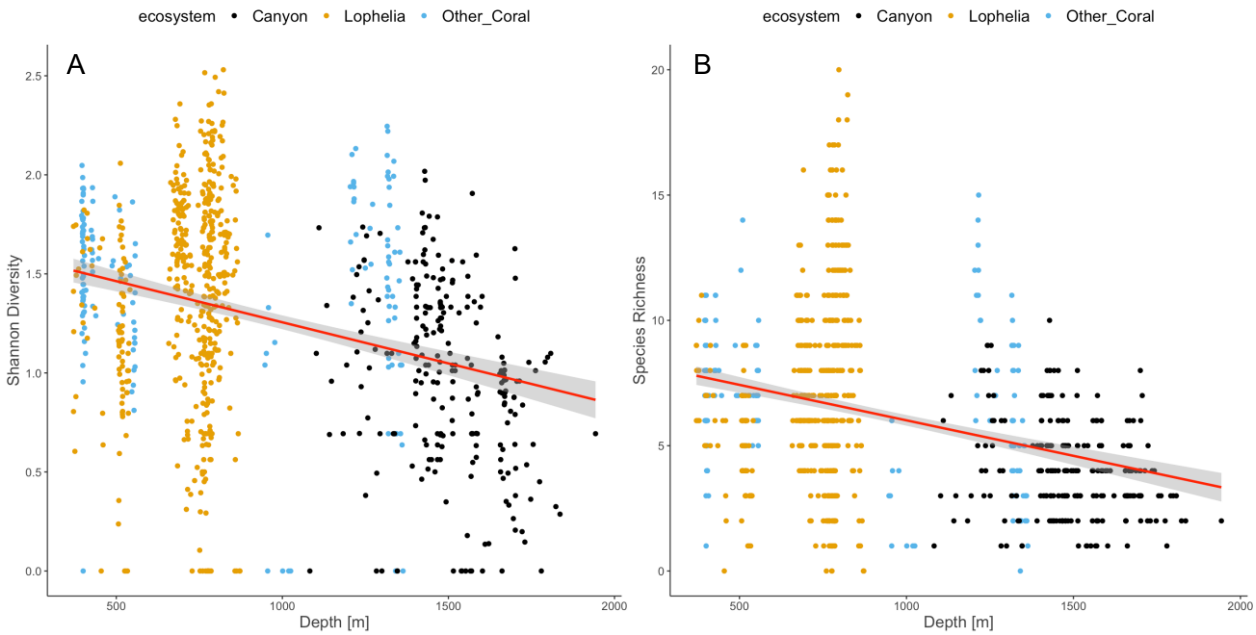

Figure 4-10. Shannon Diversity and Species Richness in each ecosystem type vs. depth
Shannon Diversity (A) and Species Richness (B) per 1-minute segment in each studied ecosystem type (color) vs. depth. The overall relationship between depth and these diversity metrics are shown by red lines, with standard error shown by shading.

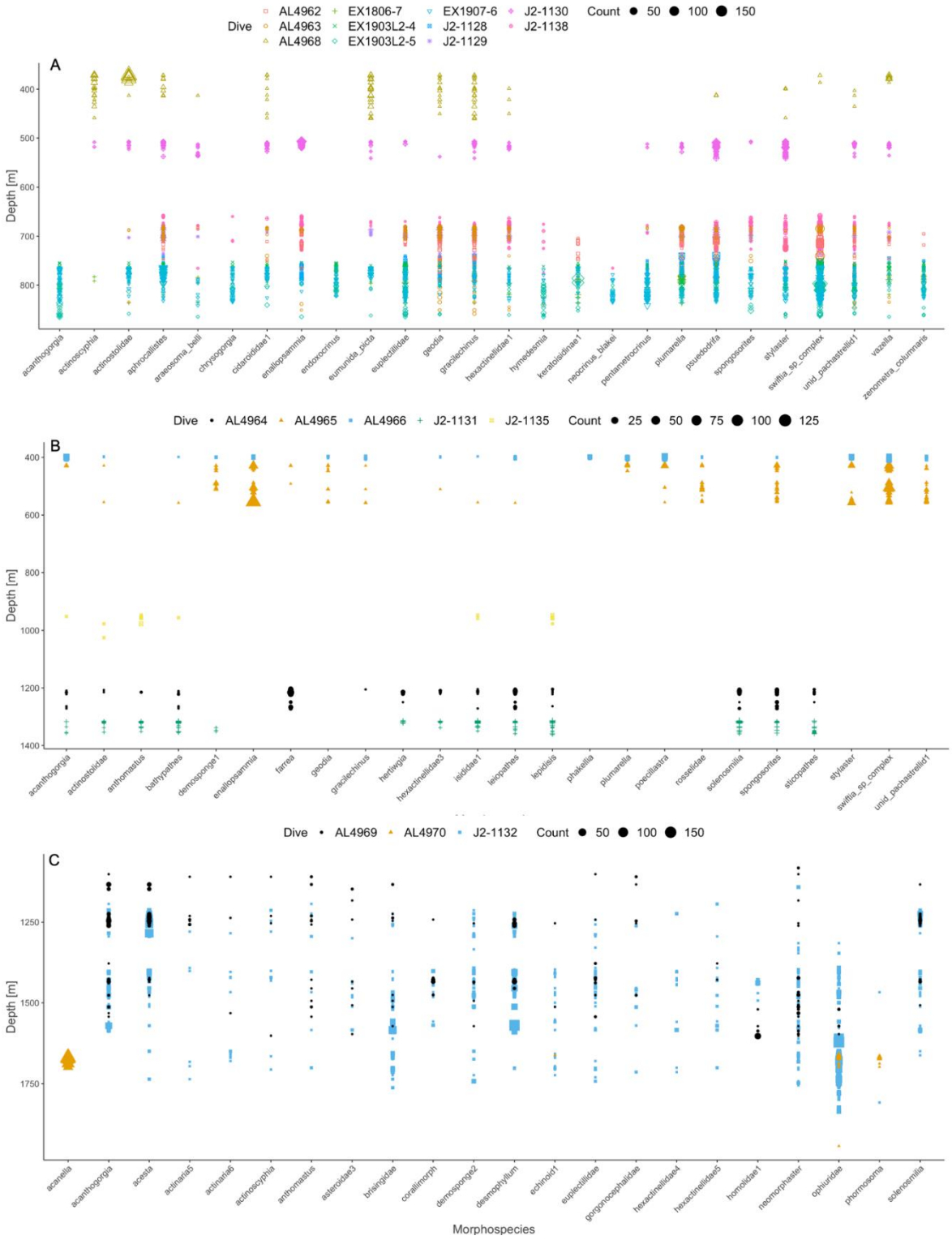

Figure 4-11. Depth distributions of the most abundant morphospecies
(A) *Lophelia pertusa*, (B) other coral, and (C) canyon ecosystems. Plotted morphospecies were present in at least 20, 15, and 10 1-minute video segments for each respective ecosystem type. Discrete dives are represented by symbol color and shape while abundances per segment are represented by symbol size.

Differences between the *L. pertusa* coral, other coral, and canyon habitat types were apparent from the nMDS ordination (Stress = 0.13). Canyon and *L. pertusa* habitats were the most distinct, with each solely occupying territory in the two-dimensional space. Non- *L. pertusa* habitats, on the other hand, overlapped strongly with both canyon and *L. pertusa* habitats with most sites falling within the bounds of the other two habitat-type polygons.

Intra-habitat differences within and between *L. pertusa* (**Figure 4-12**) and canyon (**Figure 4-13**) dives were not apparent, which contrasts with the non-*L. pertusa* habitats (**Figure 4-14**). The centroids for non-*L. pertusa* coral dives AL4965 and AL4966, for example, appeared different than the other dives within that habitat type. This was perhaps driven by depth, as these are the two shallowest non-*L. pertusa* coral habitats in the present study. The *L. pertusa* sites, on the other hand, had a very high degree of overlap (**Figure 4-15**), suggesting a specialized fauna occupying this habitat throughout our study region. Dive J2-1130 at Savannah Banks occupied the most distinct space amongst dives with coral skeleton accumulations. This site was amongst the shallowest sampled (500–550 m) and contained high abundances of actinostoliid anemones in comparison to other sites.

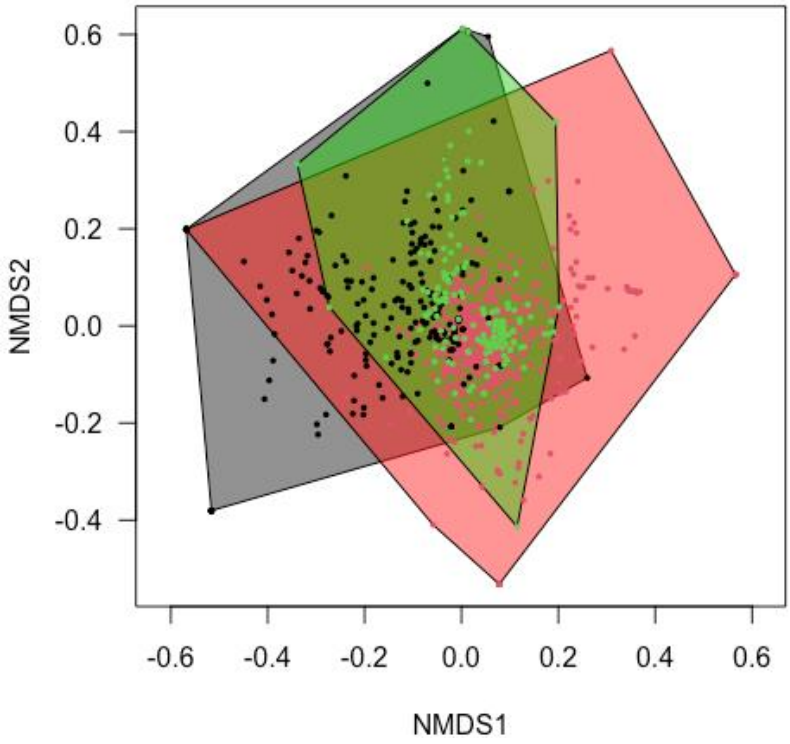

Figure 4-12. nMDS ordination showing dissimilarities of canyon, *L. pertusa*, and coral communities
Dissimilarities between communities in canyons (black), *L. pertusa* reef (red), and other coral habitats (green). Individual video segments are shown with points.

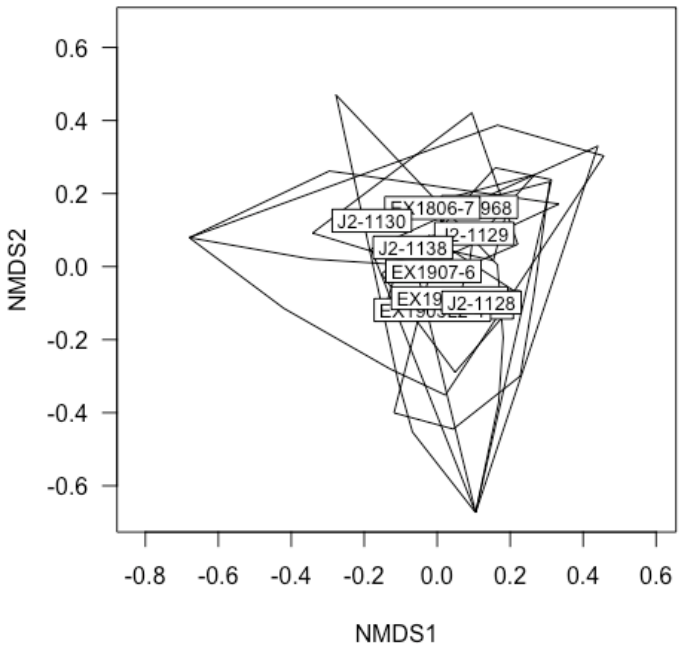

Figure 4-13. nMDS ordination showing dissimilarities within *L. pertusa* reef communities
Dissimilarities between communities sampled from video within *L. pertusa* reef habitats. Note that colors are not displayed per dive due to the high polygon. Text labels for each dive are plotted at the centroid for their respective polygons.

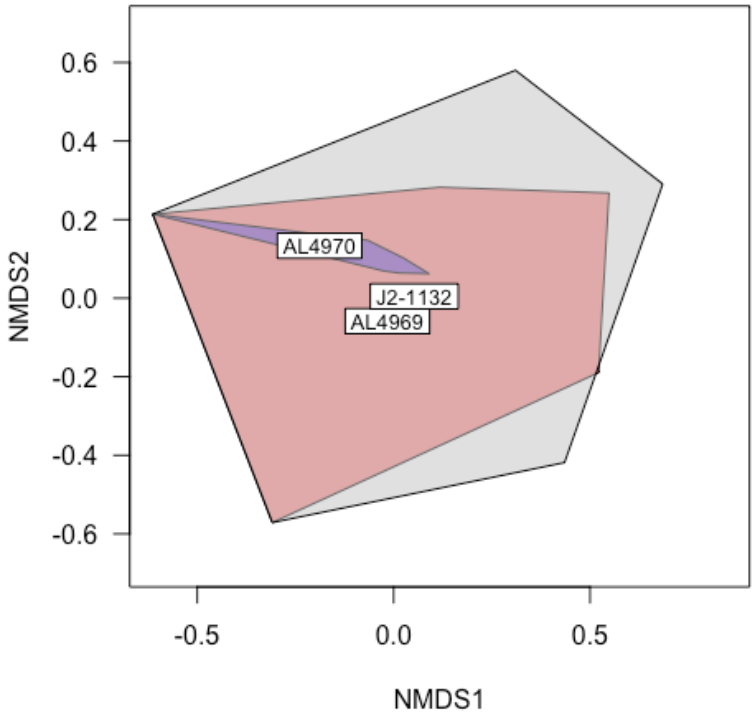

Figure 4-14. nMDS ordination showing dissimilarities between canyon communities
From dives AL4969 (red), AL4970 (blue), and J2-1132 (gray). Text labels for each dive are plotted at the centroid for their respective polygons.

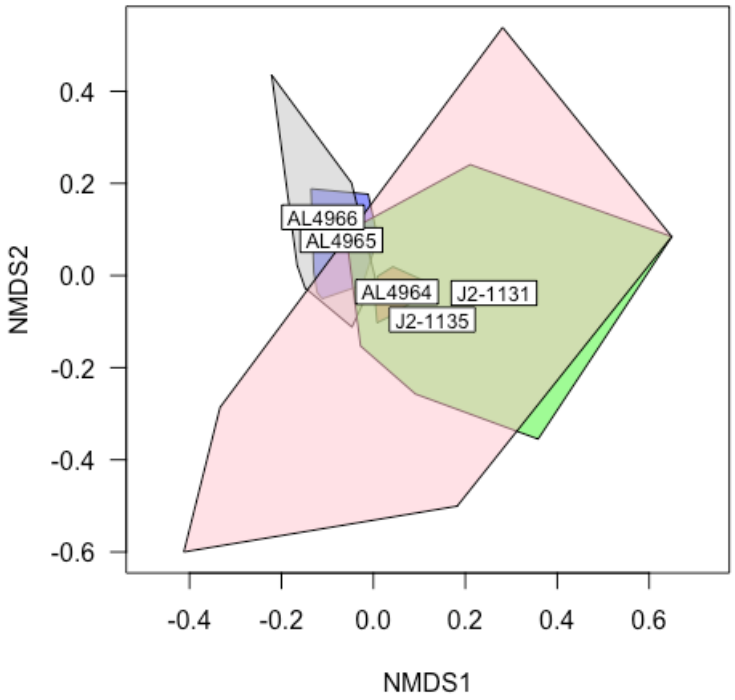

Figure 4-15. nMDS ordination showing dissimilarities between non-Lophelia communities
From dives AL4964 (red), AL4965 (blue), AL4966 (gray), J2-1131 (green), and J2-1135 (pink). Text labels for each dive are plotted at the centroid for their respective polygons.

Overall, the dbRDA models were highly significant for both the *L. pertusa* habitat ($p < 0.001$, $F_{8,493} = 16.03$) and all segments ($p < 0.001$, $F_{13,774} = 15.815$), as were each of the included variables (**Table 4-6** and **Table 4-7**). These models explained 20 and 21% of the variation in communities within all ecosystems and *L. pertusa* reef ecosystems, respectively. Large differences between communities fell along the axes represented by temperature, depth, and export carbon likely due to environmental distinctions between the shallower (350–550 m) and deeper (> 750 m) sites (**Figure 4-16** and **Figure 4-17**). BPI and Eastness both drove another apparent axis of dissimilarity in communities, likely due to the influence that these variables have on local hydrography, and thus, the coral cover that provides invertebrates with three-dimensional habitat. For the model that included all variables, primary substrate was the most important variable in the model, indicating the importance of this variable to community structure especially between sedimented and non-sedimented habitats.

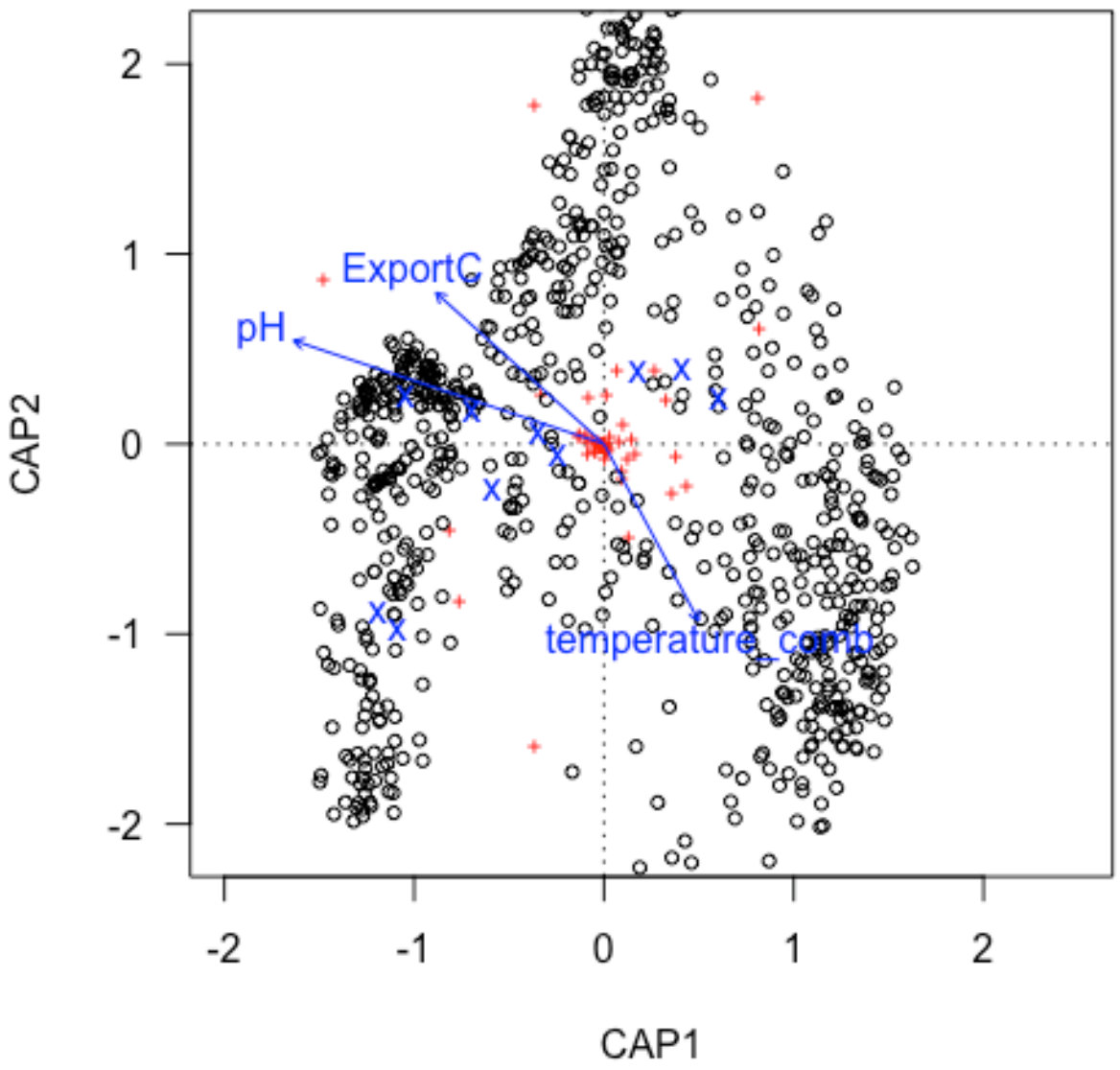

Figure 4-16. dbRDA model showing Bray-Curtis megafaunal community dissimilarities
Visualization of dbRDA model showing Bray-Curtis dissimilarities between all megafaunal communities sampled in *L. pertusa*, canyon, and non- *L. pertusa* coral ecosystems. Variation in species (red crosses) and segments (points) are displayed, along with eigenvectors representing the influence of each variable (blue arrows). Note that different levels of the 'Primary Substrate' factor variable are represented with blue X-marks rather than their full names for clarity.

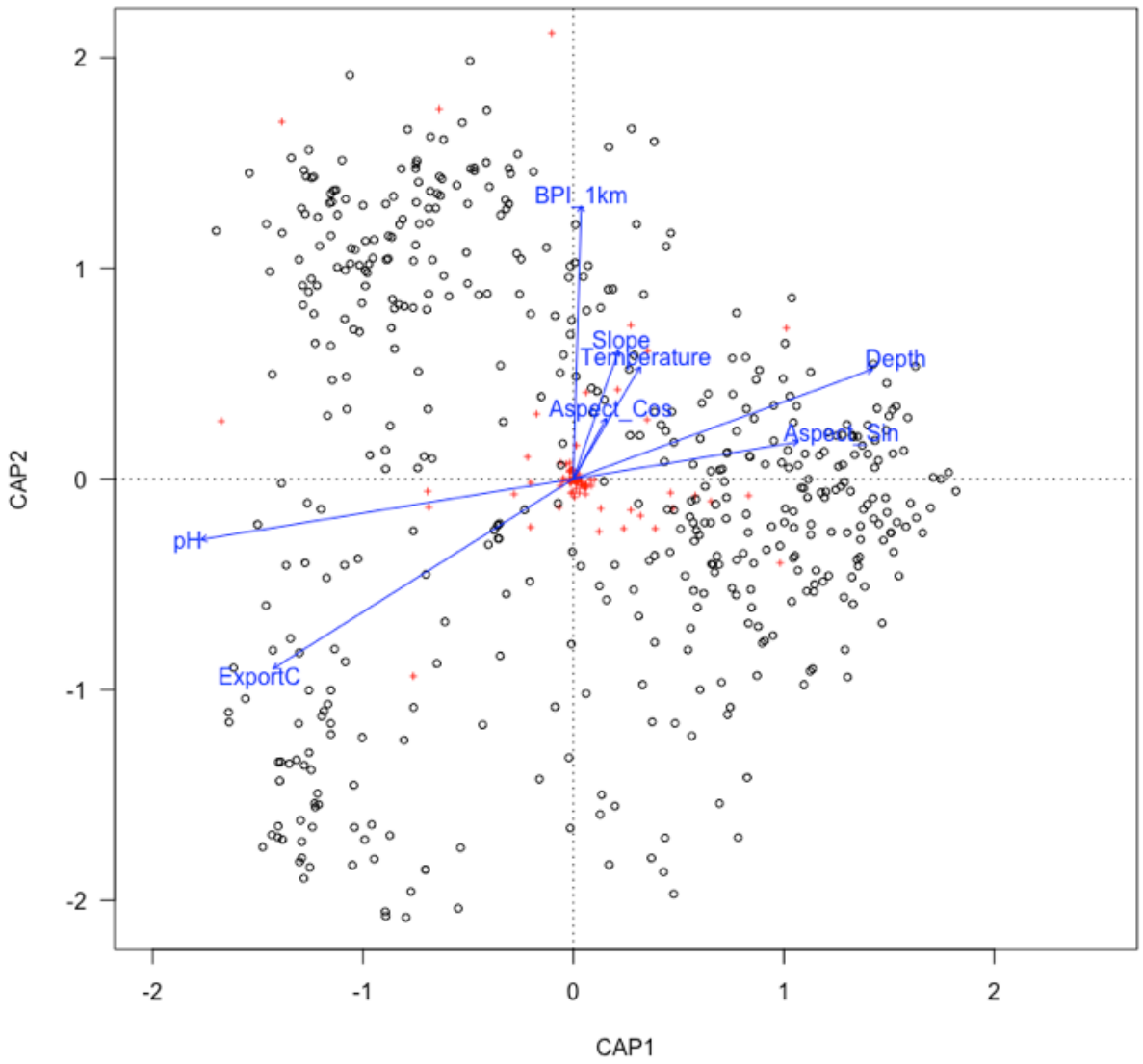

Figure 4-17. dbRDA model showing Bray-Curtis Lophelia community dissimilarities
Visualization of dbRDA model showing Bray-Curtis dissimilarities between *L. pertusa*-associated communities in two-dimensional space. Variation in species (red crosses) and segments (points) are displayed, along with eigenvectors representing the influence of each variable (blue arrows).

Table 4-6. ANOVA results on terms included in the dbRDA model for all habitats
Sum of squares, effect sizes (F-values) and significance (P-values) are shown for each term.

Term	Sum of Squares	F	P
Primary Substrate	46.62	12.14	0.001
Temperature	8.97	21.03	0.001
pH	15.07	35.32	0.001
Export C	12.68	29.73	0.001
Residual	330.62	-	-

Table 4-7. ANOVA results on terms included in the dbRDA model for Lophelia habitats

Sum of squares, effect sizes (F-values) and significance (P-values) are shown for each term.

Term	Sum of Squares	F	P
Export Carbon	14.53	40.94	0.001
pH	13.23	37.28	0.001
Temperature	7.1	19.94	0.001
Northness	1.64	4.62	0.001
Eastness	1.82	5.11	0.001
BPI_1km	2.59	7.30	0.001
Depth	3.68	10.37	0.001
Slope	0.94	2.65	0.003
Residual	**190.922**	**-**	**-**

Known chemosymbiotic organisms were present at all sites, except Cape Lookout, with *Bathymodiolus heckerae* only documented at Blake Ridge, *Acharax* sp. only at Cape Fear, and cf. *Escarpia* sp. observed at both Kitty Hawk and Pea Island. Fewer observations of corals occurred at Pea Island and Kitty Hawk compared to Cape Lookout and Cape Fear, with their presence often coinciding with hard substrates like carbonates (**Figure 4-17**).

We also observed fishes more often at areas with more complex habitat features, including hard substrates and bacterial mats (**Figure 4-18**). We observed over 71,000 megafaunal individuals, encompassing 10 phyla and at least 93 families. With the exception of Annelida, which were only reported at shallow sites Kitty Hawk and Pea Island, similar phyla were present at all seep locations (**Figure 4-19** A).

The composition of Arthropoda and Cnidaria were similar for the shallow sites (20.0–25.0% and 43.8–47.5%), with a decrease in presence at the deeper sites Blake Ridge and Cape Fear (11.6–15.7% Arthropoda, 6–25.6% Chordata, **Figure 4-19 A).** The presence of Echinodermata was higher at deeper sites (24.1–41.9%), with less presence at shallower sites (5.6–7.5%, **Figure 4-19** A). The community at Cape Lookout was unique compared to all other sites, with a large presence of Cnidaria (50.0%) followed by Chordata (25.0%) and Arthropoda (15.0%, **Figure 4-19** A).

Despite the low presence of Annelida at shallow sites (2.5–4.5%, **Figure 4-19** A), we observed thousands of *Hyalinoecia artifex* along the seafloor at Pea Island and Kitty Hawk, with the highest abundance at Pea Island 2018 dive (89.9%, **Figure 4-19** B). There were also a few occurrences of chemosynthetic *Escarpia sp.* tubeworms at Pea Island and Kitty Hawk (**Figure 4-19**).

Similar to the absence/presence data, Echinodermata were most abundant at deep sites (19.6–97.6%) compared to the shallow sites (0.2–13.7%). We observed more fishes (Chordata) at Pea Island 2019 (40.3%) and Cape Lookout (39.1%) compared to all other sites (0.2–2.0%, **Figure 4-19** B), with observations recorded along the majority of the dive track (**Figure 4-18**).

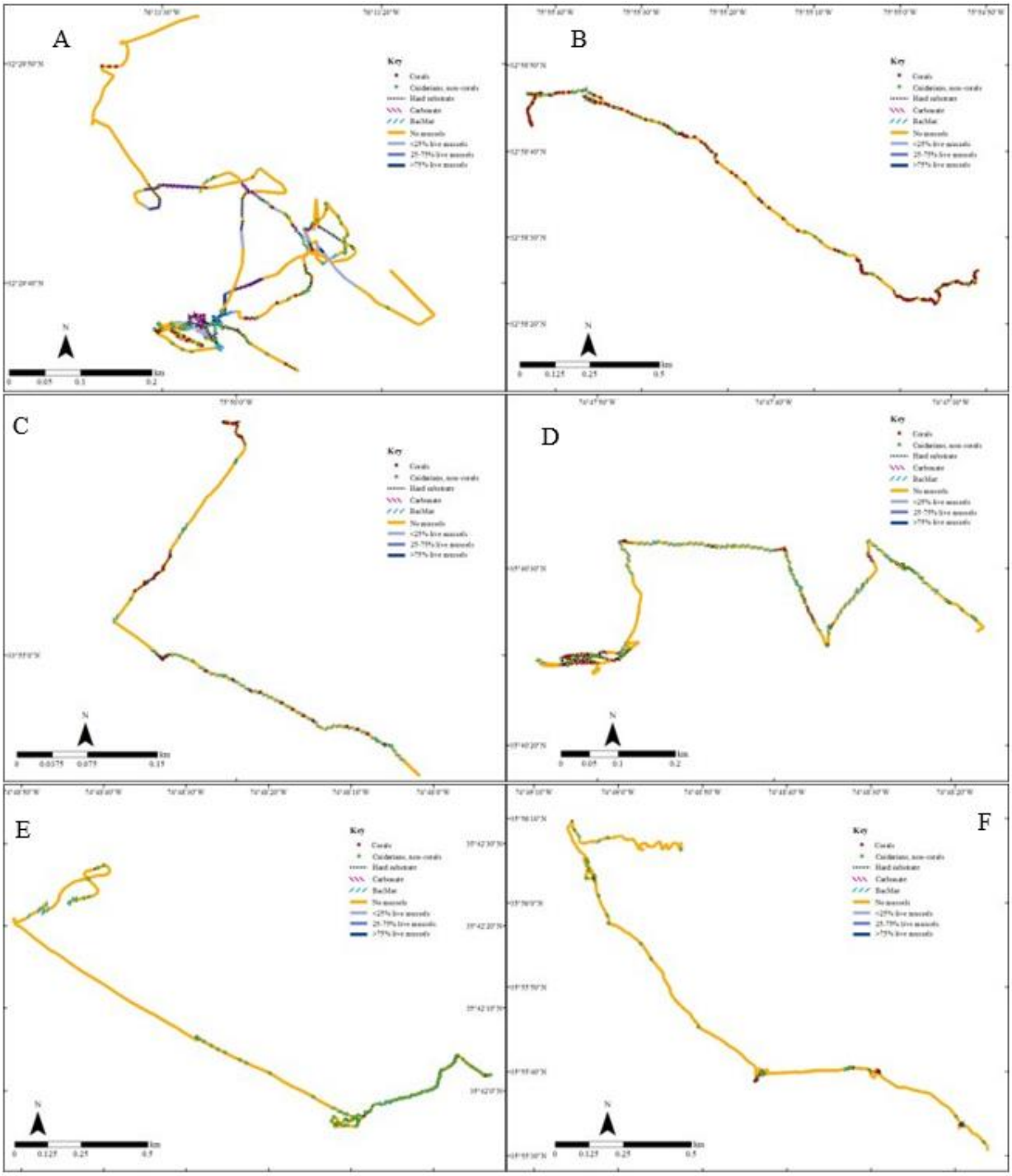

Figure 4-18. Habitat classification of coral communities at seep sites
Habitat classification for A) Blake Ridge, B) Cape Fear, C) Cape Lookout, D) Kitty Hawk, E) Pea Island 2019, F) Pea Island 2018 based on video analyses of seeps sites examined during Deep SEARCH from 2018–2019. Solid color lines represent habitat coverage by live mussels, where: orange = no mussels, light blue = < 25% live mussel, medium blue = 25–75% live mussel coverage, dark blue = > 75% live mussel coverage. Black dotted lines indicate presence of hard substrate, pink dashed lines indicate carbonates, and blue dashed lines indicate presence of bacterial mats. Red points represent the presence of corals, whereas green points represent non-coral cnidarians.

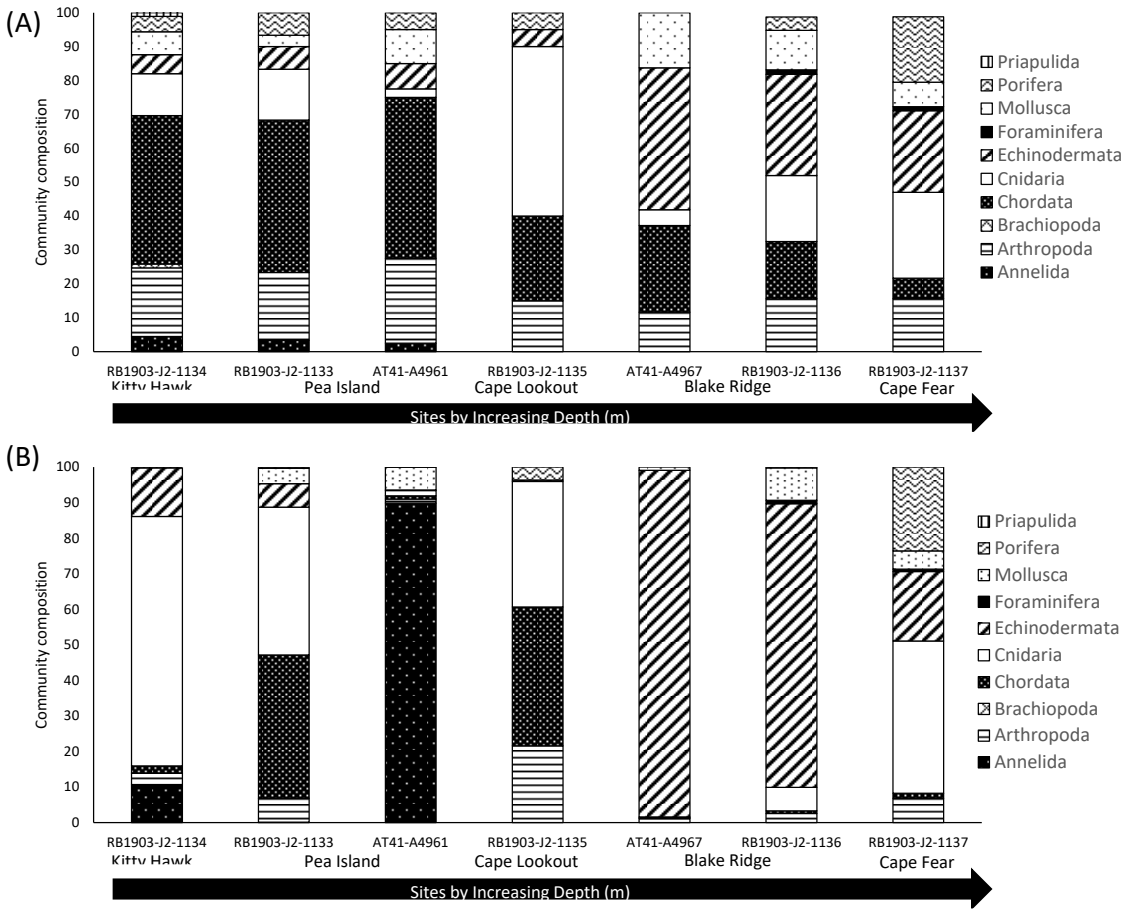

Figure 4-19. Community composition of fauna documented at each site
With taxa grouped at the phylum level based on (A) absence-presence data and (B) taxa counts standardized by distance traveled.

Diversity analysis using species-accumulation curves indicated that Cape Fear and Cape Lookout were undersampled with neither curve reaching an asymptote (**Figure 4-20**). We recorded fewer individuals at these two sites; however, while Cape Lookout had the lowest diversity recorded, with only 40 taxa observed, Cape Fear had higher diversity, with 82 taxa observed, which is similar to the other seep locations (**Figure 4-20**).

Shannon Diversity differed among sites (Kruskal-Wallis, $H = 115.051$, $df = 4$, $p < 0.001$), with diversity at Kitty Hawk significantly lower than Blake Ridge, Cape Fear, Cape Lookout and Pea Island, and Pea Island significantly lower than Blake Ridge (all Dunn's Method with Holm's adjustment, $p < 0.05$). Species richness (d) was also significantly different among sites ($H = 188.998$, $p < 0.001$), with lowest species richness at Pea Island and highest at Cape Fear. Pea Island significantly lower species richness than Blake Ridge, Cape Fear, Cape Lookout and Kitty Hawk ($p < 0.05$); while Kitty Hawk had significantly lower species richness than Blake Ridge, Cape Fear and Cape Lookout ($p < 0.05$), and Blake Ridge had significantly lower richness compared to Cape Fear ($p < 0.05$).

Taxa evenness varied significantly among sites (J', $H = 254.121$, $df = 4$, $p < 0.001$), with Kitty Hawk significantly lower than Pea Island, Blake Ridge, Cape Fear and Cape Lookout, Pea Island significantly lower than Blake Ridge, Cape Fear and Cape Lookout, and Cape Fear significantly lower than Cape Lookout ($p < 0.05$). Overall, we recorded higher taxa evenness for the deeper sites compared to shallower sites.

Dives at seep locations revealed distinctly different megafaunal seep communities (one-way ANOSIM tests, Global R 0.19, p = 0.001), with distinct groups evident from hierarchical clustering and nMDS plots (**Figure 4-21**). SIMPROF identified five statistically different groups. SIMPER analyses reported large differences in megafaunal communities between Pea Island and Blake Ridge (mean dissimilarity = 89.39%) and Kitty Hawk and Blake Ridge (mean dissimilarity = 92.91%). *Hyalinoecia artifex* and *Illex* sp. were only present at Pea Island, representing 19.46% of the dissimilarity between Pea Island and Blake Ridge. Ophiuroids, such as *Ophioctenella acies*, were only present at Blake Ridge and accounted for 16.52% of the dissimilarity. Similarly, the presence of *H. artifex* at Kitty Hawk and absence at Blake Ridge accounted for 8.49% of the dissimilarity. Asteroid seastars and zoanthids were also more abundant at Kitty Hawk than Blake Ridge and accounted for 30.22% of the dissimilarity.

Similar clustering results occurred when we examined these communities using presence/absence data and Sorensen's similarity index, which incorporated mussel and clam data. Dissimilarity increased between Blake Ridge and Pea Island (90.63%) and between Blake Ridge and Kitty Hawk, with clams and mussels accounting for 17.78% and 19.12% of the dissimilarity. One-way ANOSIM tests also reported significant differences in megafaunal seep communities (Global R 0.19, p = 0.001), live mussel coverage (Global R = 0.068, p = 0.001), type of chemosynthetic features present (Global R = 0.038, p = 0.001), and hard-substrate coverage (Global R = 0.037, p = 0.001); however, the low R values reported indicate these factors have only a small effect on the megafaunal community. We also noted variability within a site for sites having multiple dives. Pea Island had higher community variability, with dives conducted at the Pea Island less similar (SIMPER 21.33%) to each other compared to the dives at Blake Ridge (SIMPER 41.10%).

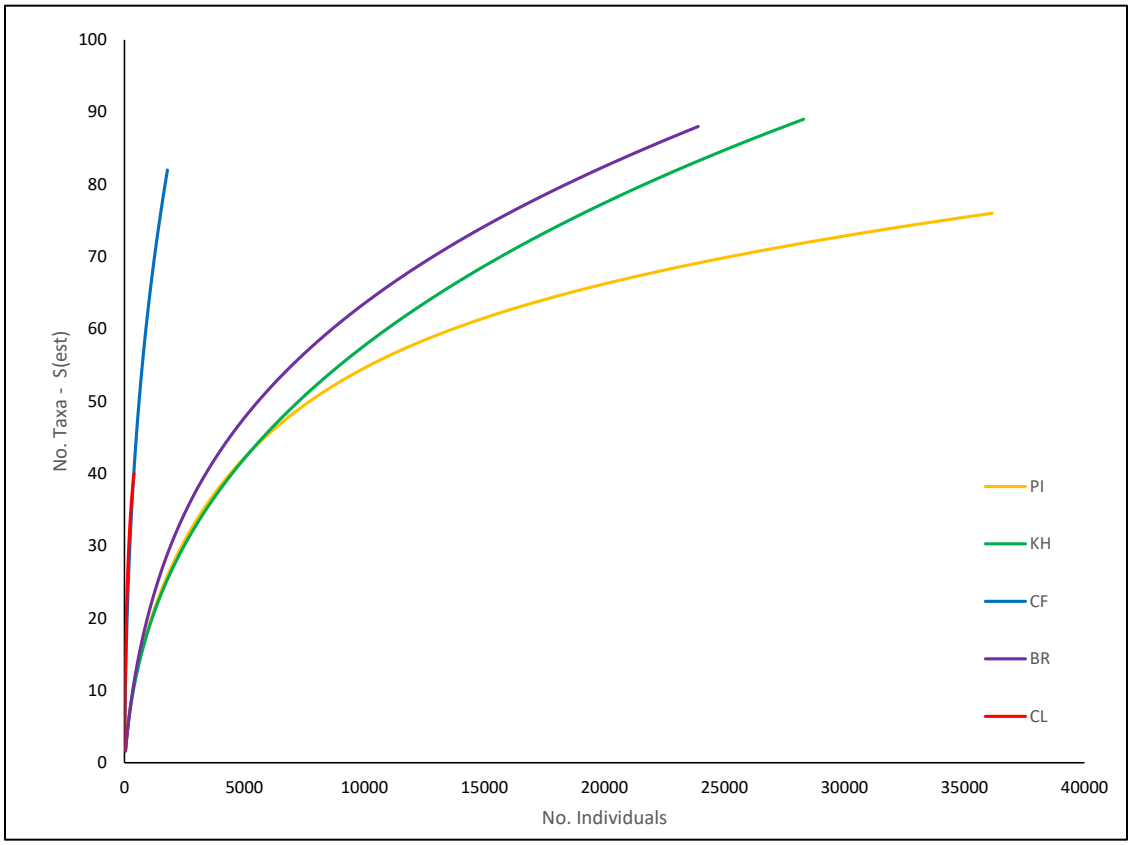

Figure 4-20. Species-accumulation curves for megafauna observed at seep sites
Five seep sites in the western Atlantic. PI = Pea Island, KH = Kitty Hawk, CF = Cape Fear, BR = Blake Ridge, CL = Cape Lookout.

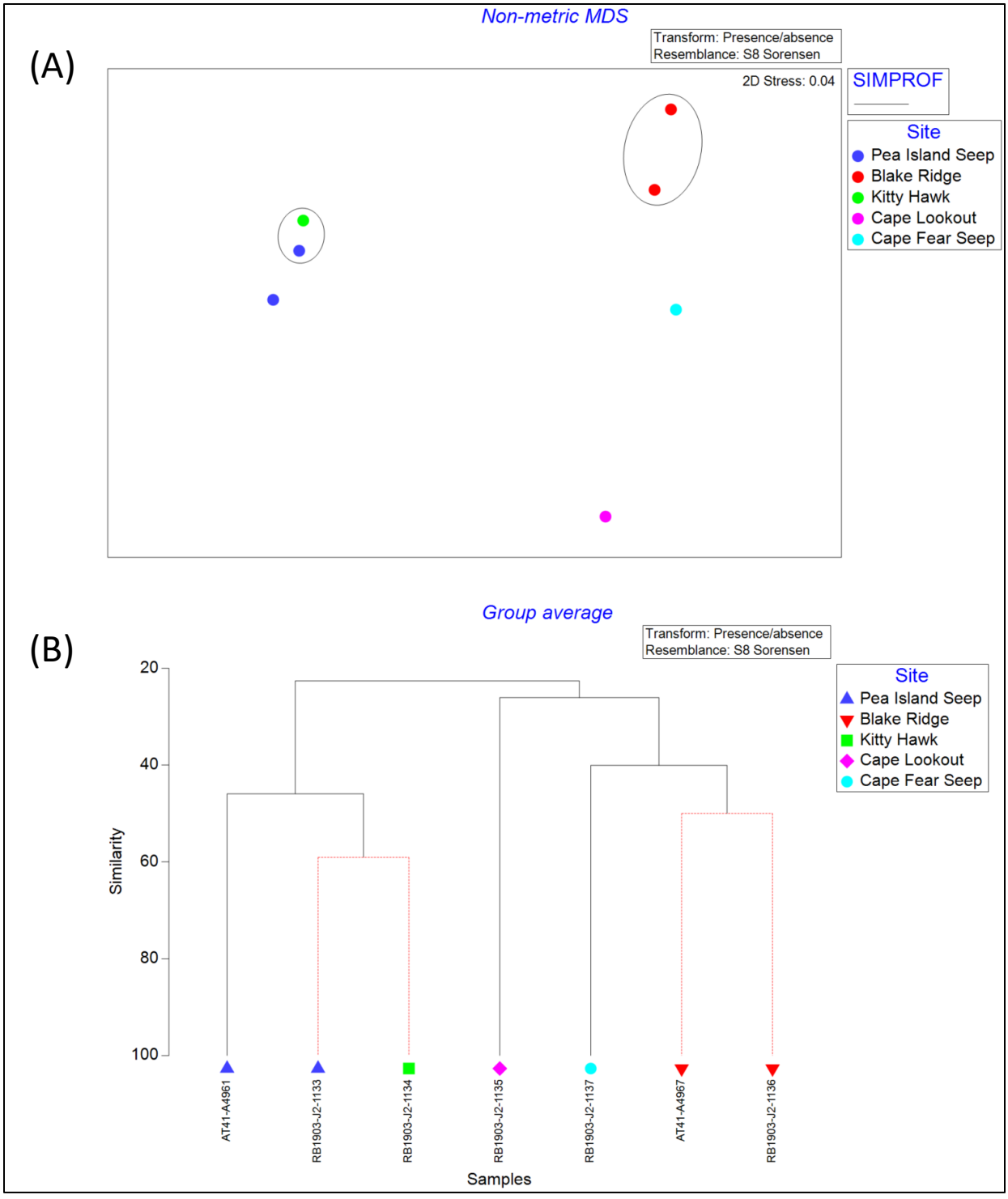

Figure 4-21. A) Non-metric multidimensional scaling (nMDS) plot using Sorensen's Index Among dives conducted at seep sites based on megafauna absence-presence data. Ellipses group statistically similar sites based on SIMPROF results. B) CLUSTER diagram using Sorensen's Index among dives based on absence-presence megafauna data. Black lines connect clusters of samples that are significantly different.

DISTLM analysis (**Figure 4-22**) indicated that all variables except profile curvature (p = 0.851) explained most portions of the seep megafaunal benthic community (0.1–14.5%, p < 0.041), with depth explaining the largest amount of community variation (14.5%) (**Figure 4-9**). The "best" model included only depth (**Table 4-9**), while the "best" two-variable model included both depth and slope degrees (19.5%).

We also analyzed a subset of data from RB1903 (dives RB1903-J2-1133, 1134, 1136, 1137) to allow for the incorporation of oxygen concentration, which was not recorded in AT41 dives. DISTLM analysis indicated that all variables except profile curvature (p = 0.602) and tangential curvature (p = 0.948) explained significant portions of the seep community (0.5–16.2%, p < 0.001), with oxygen concentration (16.2%) and depth (16.0%) explaining the largest amount of community variation (**Table 4-9, Figure 4-22 B**)

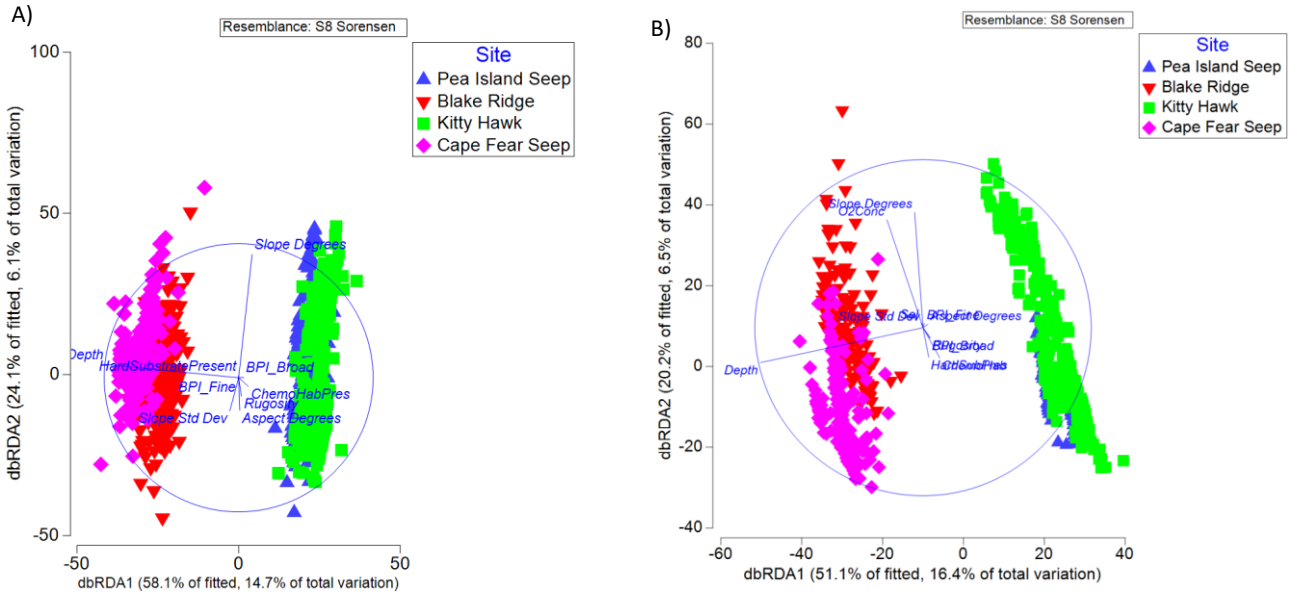

Figure 4-22. dbRDA of Sorensen's Index of absence-presence data from observed megafauna
A dbRDA of Sorensen's Index of absence-presence data from observed megafauna in seep habitats with environmental and terrain vectors overlaid using A) data from AT41 and RB1903 dives and B) using a subset of dives from RB1903 to incorporate additional environmental variables

Table 4-8. DISTLM of environmental and terrain variables using data from AT41 and RB1903 dives

(A) Results from DISTLM of environmental and terrain variables with seep megafaunal communities using the AICc criteria and "best" model selections using data from AT41 and RB1903 dives. SS = sum of squares, P = probability, RSS = residual sum of squares.

Variable	SS(trace)	Pseudo-F	P	Prop.
HardSubPres	1.31E+05	31.223	0.001	0.019759
ChemoHabPres	84,225	19.907	0.001	0.012689
Depth	9.62E+05	262.41	0.001	0.14487
Aspect Degrees	97,687	23.137	0.001	0.014717
Slope Degrees	4.64E+05	116.34	0.001	0.06986
Slope Std Dev	2.57E+05	62.385	0.001	0.038715
Curv Profile	2,324.7	0.54269	0.851	0.0003502
Curv Tangential	8,297.3	1.9387	0.041	0.00125
BPI_Fine	27,707	6.4927	0.001	0.0041741
BPI_Broad	27,752	6.5033	0.001	0.0041808
Rugosity	1.50E+05	35.769	0.001	0.022571

AICc	R^2	RSS	Selections
12730	0.144875	676,300	Depth
12638	0.19525	342,200	Depth, Slope Degrees
12603	0.214115	216,700	HardSubPres, Depth, Slope Degrees
12574	0.22957	114,000	HardSubPres, Depth, Slope Degrees, Slope Std Dev
12555	0.24027	43,000	HardSubPres, Depth, Aspect Degrees, Slope Degrees, Slope Std Dev
12546	0.245555	7,900	HardSubPres, ChemHabPres, Depth, Aspect Degrees, Slope Degrees, Slope Std Dev
12540	0.249194	983,800	HardSubPres, ChemHabPres, Depth, Aspect Degrees, Slope Degrees, Slope Std Dev, Rugosity
12537	0.251954	965,500	HardSubPres, ChemHabPres, Depth, Aspect Degrees, Slope Degrees, Slope Std Dev, BPI_Broad, Rugosity
12535	0.253714	953,800	HardSubPres, ChemHabPres, Depth, Aspect Degrees, Slope Degrees, Slope Std Dev, BPI_Fine, BPI_Broad, Rugosity
12536	0.254174	950,700	HardSubPres, ChemHabPres, Depth, Aspect Degrees, Slope Degrees, Slope Std Dev, Curv Tangent, BPI_Fine, BPI_Broad, Rugosity
12538	0.25454	948,600	HardSubPres, ChemHabPres, Depth, Aspect Degrees, Slope Degrees, Slope Std Dev, Curv Profile, Curv Tangent, BPI_Fine, BPI_Broad, Rugosity

Table 4-9. DISTLM of environmental and terrain variables using a subset of RB1903 dives

(B) Results from DISTLM of environmental and terrain variables with seep megafaunal communities using the AICc criteria and "best" model selections using a subset of dives from RB1903 to incorporate additional environmental variables. SS = sum of squares, P = probability, RSS = residual sum of squares.

Variable	SS(trace)	Pseudo-F	P	Prop.
HardSubPres	154,000	37.44	0.001	0.032804
ChemoHab	101,000	24.274	0.001	0.021515
Depth	748,000	209.65	0.001	0.15959
O_2Conc	757,000	212.77	0.001	0.16159
Sal	98,297	23.656	0.001	0.020978
Aspect Degrees	50,084	11.928	0.001	0.010689
Slope Degrees	251,000	62.486	0.001	0.053568
Slope Std Dev	208,000	51.162	0.001	0.04429
Curv Profile	3,496	0.82424	0.602	0.00074604
Curv Tangential	1,716	0.4045	0.948	0.00036626
BPI_Fine	25,652	6.0771	0.001	0.0054745
BPI_Broad	35,977	8.5422	0.001	0.0076781
Rugosity	121,000	29.196	0.001	0.025764

AICc	R^2	RSS	Selections
9045.9	0.161593	929,000	O_2Conc
8979.8	0.211673	694,000	O_2Conc, Slope Degrees
8923.1	0.252433	503,000	Depth, O2Conc, Slope Degrees
8881.1	0.281563	366,000	HardSubPres, Depth, O_2Conc, Slope Degrees
8862	0.295163	303,000	HardSubPres, Depth, O_2Conc, Slope Degrees, Slope Std Dev
8846.4	0.30633	250,000	HardSubPres, ChemoHab, Depth, O_2Conc, Slope Degrees, Slope Std Dev
8841.3	0.310743	230,000	HardSubPres, ChemoHab, Depth, O_2Conc, Slope Degrees, Slope Std Dev, Rugosity
8837.4	0.314453	212,000	HardSubPres, ChemoHab, Depth, O_2Conc, Slope Degrees, Slope Std Dev, BPI_Fine, Rugosity
8834.4	0.317563	198,000	HardSubPres, ChemoHab, Depth, O_2Conc, Salinity, Slope Degrees, Slope Std Dev, BPI_Fine, Rugosity
8832.9	0.319733	188,000	HardSubPres, ChemoHab, Depth, O_2Conc, Salinity, Aspect Degrees, Slope Degrees, Slope Std Dev, BPI_Fine, Rugosity
8831.9	0.32163	179,000	HardSubPres, ChemoHab, Depth, O_2Conc, Salinity, Aspect Degrees, Slope Degrees, Slope Std Dev, BPI_Fine, BPI_Broad, Rugosity
8833.2	0.322083	177,000	HardSubPres, ChemoHab, Depth, O_2Conc, Salinity, Aspect Degrees, Slope Degrees, Slope Std Dev, Curv Profile, BPI_Fine, BPI_Broad, Rugosity
8834.5	0.322543	174,000	HardSubPres, ChemoHab, Depth, O_2Conc, Salinity, Aspect Degrees, Slope Degrees, Slope Std Dev, Curv Profile, Curv Tangent, BPI_Fine, BPI_Broad, Rugosity

4.1.2.3 Macrofauna—Coral Sites

Quantitative collections, identifications, and counts of the collected fauna revealed 1,480 individuals of 61 taxa from nine phyla associated with the habitat-forming species sampled (**Table 4-10**). *Ophiacantha bidentata* was frequently found and numerically dominant in *Lophelia pertusa* collections, attaining a maximum abundance of 149 individuals in a sample from the Cape Fear Mounds. The holothurian *Chirodota aff. heheva*, ophiuroid *Ophioctenella acies*, polychaetes from the Maldanidae and Cheatopteridae families, and alvinocarid shrimp were all abundant in the seep samples, although none appeared in all five samples. We recorded the most diverse community (207 individuals of 20 morphospecies) at Richardson Reefs West in a sample containing dead and live standing *Lophelia pertusa* and *Enallopsammia* sp.

Density at Savannah Banks was measurably higher than all other coral sites and lowest at Richardson Ridge (**Figure 4-23**). Density at Cape Fear was higher than Blake Escarpment. Density also decreased with depth. We used Raup-Crick dissimilarity, a null-model based method that represents the probability that samples have non-identical compositions, to calculate pairwise beta diversity between samples. Pairwise Raup-Crick values show that there is little overlap between the faunas of different habitat types (**Figure 4-24**), although the canyon habitat was not entirely dissimilar from some samples from coral habitat. Coral sites showed varying degrees of dissimilarity. Mean macrofaunal density in coral-adjacent sediment sites trended as at those sites (**Figure 4-25** as compared to **Figure 4-24**).

For infaunal communities, we collected a total of 261 individuals across five sites (Blake Deep, Blake Escarpment, Cape Fear, Richardson Ridge, Savannah Banks) at 11 sampling locations in coral-adjacent sediments. Density in coral-adjacent sediments differed among sites.

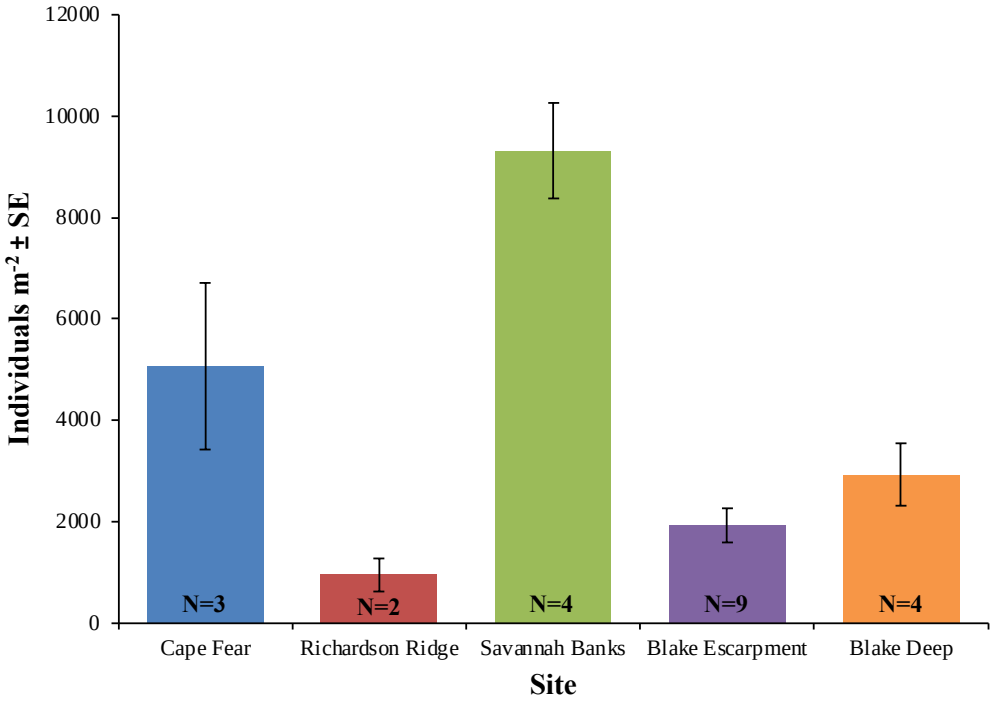

Figure 4-23. One-way ANOVA with density at coral sites
One-way ANOVA, F4-17 = 19.14, $p < 0.0001$), with density at Savannah Banks (9,320 ± 935 individuals m^{-2}) higher than all other coral sites (Tukey HSD $p< 0.014$) and lowest at Richardson Ridge (947 ± 316 individuals m^{-2}). Density at Cape Fear was higher than Blake Escarpment (Tukey HSD $p = 0.046$). Density decreased with depth (Spearman correlation: rho = -0.43, $p = 0.043$), with density at the shallow sites (458–520 m), Cape Fear and Savannah Banks, ranging from 2,212 to 11,374 individuals m^{-2} and density at the deep sites (1,207–1,334 m) ranging from 632 to 4,107 individuals m^{-2}.

Table 4-10. Community collection matrix

Morphospecies	Taxonomy	AL4965-M1	AL4966-M1	AL4967-M1	AL4967-M2	AL4968-M1	AL4968-M2	AL4968-M3	J1128-M1	J1128-M2	J1128-M3	J1129-M1	J1129-M2	J1129-M3	J1130-M1	J1130-M2	J1130-M3	J1132-M1	J1136-M1	J1136-M2	J1136-M3	J1138-M1
Porifera																						
Demospongiae																						
demospongea	unid. Demospongiae	1	1																	1		
cladorhizidae	unid. Cladorhizidae																					1
Hexactinellida																						
lyssacinosida	unid. Lyssacinosida	1					1				3	7										
aphrocallistes	*Aphrocallistes beatrix*													1								9
hertwigia	*Hertwigia falcifera*																					5
Cnidaria																						
Actinaria																						
actinaria1	unid. Actinaria1					16	24		2		2	1		3								1
actinaria2	unid. Actinaria2											2										
actinaria3	unid. Actinaria3																	1	1			
actinaria4	unid. Actinaria4																		1	1		
Scelactinia																						
thecopsammia	*Thecopsammia socialis*	1						1		2			1									
Octocorallia																						
pseudodrifa	*Pseudodrifa* cf. *nigra*	1												1								
clavulariidae	Clavulariidae cf. *Clavularia* sp.	181																				114
plumerella	*Plumerella* cf. *pourtalesii*									2												
Hydrozoa																						
leptothecata	unid. Leptothecata	1	1						6	1	10	18	17	18	1	1	3					55
stylaster	*Stylaster* cf. *erubescens*	1	1				1			2												1
Echinodermata																						
Asteroidea																						
astropecten	*Astropecten* cf. *americanus*						1							1								
Ophiuroidea																						
ophiacantha	*Ophiacantha bidentata*	1					149	4	3	3	33	15	4	29	32	18	2					2
ophiuridae1	unid. Ophiuridae1		3									1				1		2				1
ophioctenella	*Ophioctenella acies*				2														5	35	74	
ophienigma	*Ophienigma spinilimbatum*																			3		
ophiuroidae2	unid. Ophiuroidae2																					1
amphiura	*Amphiura grandisquama*						21															
Crinoidea																						
trichometra	*Trichometra cubensis*										1		4			19	1					
Holothuria																						
chirodota	*Chirodata* aff. *heheva*			1																1	15	
Echinoidea																						
cidaris	*Cidaris rugosa*					1									1							
gracilechinus1	*Gracilechinus tylodes*					1					1					1						
araesoma	*Araesoma belli*										1											
gracilechinus2	*Gracilechinus alexandri*																					1
Arthropoda																						

Morphospecies	Taxonomy	AL4965-M1	AL4966-M1	AL4967-M1	AL4967-M2	AL4968-M1	AL4968-M2	AL4968-M3	J1128-M1	J1128-M2	J1128-M3	J1129-M1	J1129-M2	J1129-M3	J1130-M1	J1130-M2	J1130-M3	J1132-M1	J1136-M1	J1136-M2	J1136-M3	J1138-M1
Crustacea																						
eualus	*Eualus cranchii*		2									2										
amphipoda	unid. Amphipoda			3			1								3	1						6
plesionika	*Plesionika* cf. *martia*						1						1									
spongiocaris	*Spongiocaris* sp.													1								1
arcoscalpellum	*Arcoscalpellum* sp.															6						
munidopsis	*Munidopsis serricornis*															1	1					
uroptychus	*Uroptychus* sp.																1					
alvinocarididae	unid. Alvinocarididae																				1	
alvinocaris	*Alvinocaris cf. muricola*			2	6														10	11	3	
Arthropoda																						
Gastropoda																						
coralliophila	*Coralliophila* cf. *richardi*					10								1								1
diodora	*Diodora tanneri*						1							1								
neogastropoda1	unid. Neograstropoda1																	1	1	1	3	
pertusiconcha	*Pertusiconcha callithrix*																				1	
neogastropoda2	unid. Neograstropoda2																				1	
neogastropoda3	unid. Neograstropoda3																				1	
calliostoma	*Calliostoma stirophorum*																					1
turritellidae	unid. Turritellidae																					1
Bivalvia																						
vesicomya	*Vesicomya venusta*				2																6	
bivalvia	*unid.* Bivalvia																	1				
Bryozoa																						
membranipora	*Membranipora* sp.							3														
Sipuncula																						
apionsoma	*Apionsoma* cf. *murinae*																				3	
Annelida																						
annelida1	unid. Annelida1										1	2		1	1							
Polychaeta																						
polychaeta1	unid. Polychaeta1	1	1			1	2	2														
polychaeta2	unid. Polychaeta2	1					1	1														
eunice	*Eunice norvegica*		3							2	2		1	1	1	1						
polychaeta3	unid. Polychaeta3			2	1																	
chaetopteridae	*Phyllochaetopterus* sp.				10																	
nicomache	*Nicomache lokii*																			132		
polychaeta4	unid. Polychaeta4																			3	26	
polynoidae	unid. Polynoidae																					1
serpulidae	unid. Serpulidae																					1
flabelligeridae	unid. Flabelligeridae																					1
Chordata																						
ascidiacea	unid. Ascidiacea																					1

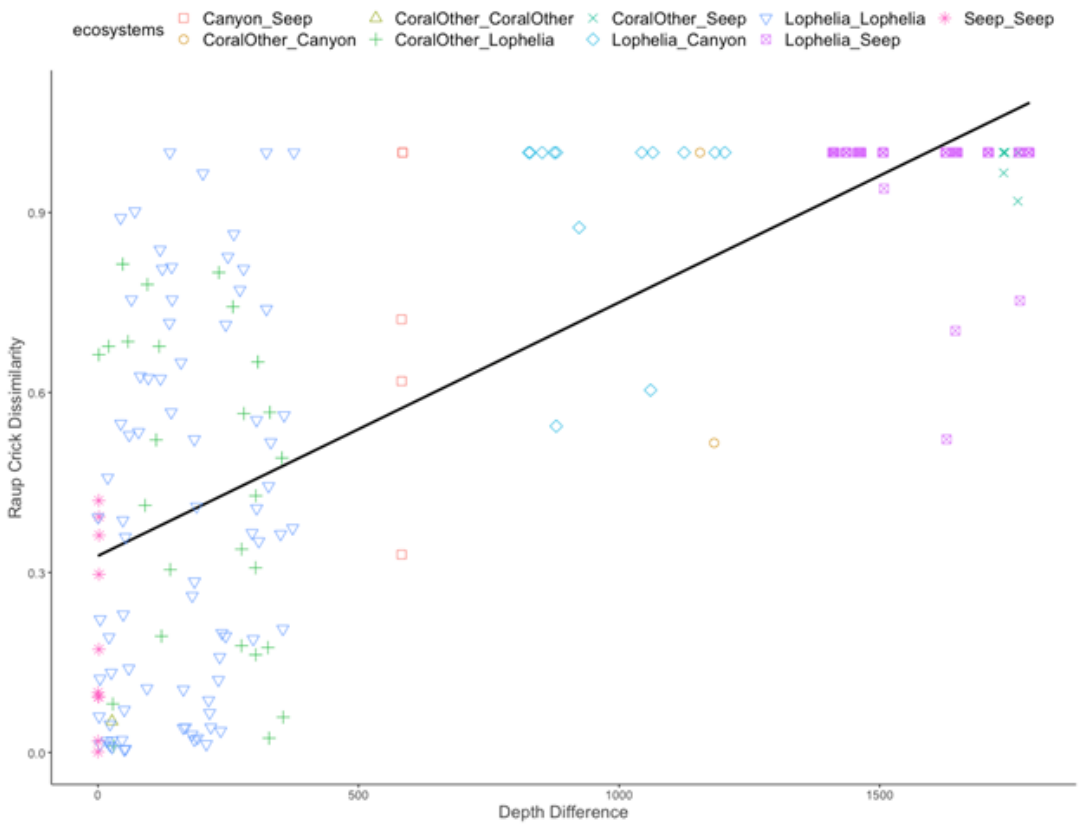

Figure 4-24. Pairwise Raup-Crick Dissimilarity vs. the pairwise difference in sample depth
Pairwise Raup-Crick Dissimilarity between sediment community collections vs. the pairwise difference in sample depth (black line). Symbol color and shape denote different samples from different ecosystem combinations.

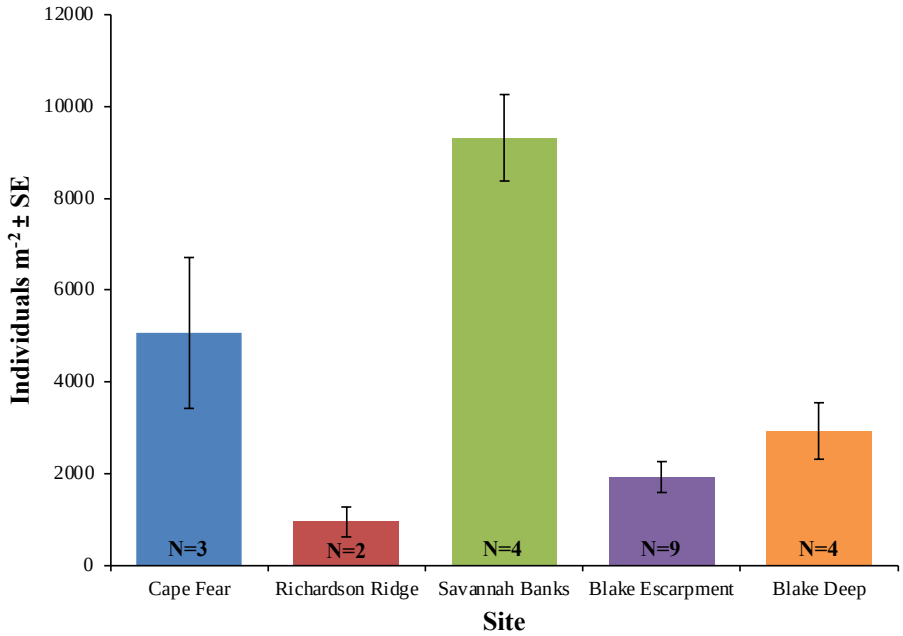

Figure 4-25. Mean macrofaunal density in coral-adjacent sediment sites
Error bars represent the standard error of the mean and N is the number of samples.

Shannon Diversity (H') in coral-adjacent sediments differed from the coral sites (**Figure 4-26**; one-way ANOVA, $F_{4\text{-}17} = 7.08$, $p = 0.0015$). Richardson Ridge had significantly lower H' (0.56 ± 0.56; Tukey HSD, $p < 0.05$) than all other coral sites, but also had the lowest sampling effort (N = 2). The highest H' occurred at Savannah Banks (2.47 ± 0.05), which was also significantly greater than H' at Blake Escarpment (Tukey HSD, $p = 0.03$). There was a general but non-significant decline in H' with depth (Spearman correlation, rho = -0.407, $p = 0.06$).

In contrast, taxa evenness (J') significantly differed among coral sites (**Figure 4-27**; one-way ANOVA, $F_{4\text{-}17} = 10.8$, $p = 0.0002$); evenness was higher at Richardson Ridge than at Cape Fear (Tukey HSD, $p < 0.045$) and lower at Savannah Banks than at Blake Escarpment and Blake Deep (Tukey HSD, $p < 0.042$). In addition, taxa evenness was significantly lower at Cape Fear than at Blake Escarpment and Blake Deep (Tukey HSD, $p < 0.018$). Taxa evenness significantly increased with depth (Spearman correlation, rho=0.51, p=0.018).

Coral-adjacent sediment communities differed among sites (**Figure 4-28**; Pseudo-F = 2.58, $p = 0.0003$). Pairwise comparisons indicated that all sites were distinct from one another ($p < 0.047$) except for Blake Deep which was similar to Blake Escarpment, Cape Fear, and Savannah Banks ($p > 0.07$). Richardson Ridge was distinct from the other sites due primarily to low densities that included only Cirratulidae (Polychaeta) and bivalves (**Figure 4-29).** Cape Fear had the lowest proportion of polychaetes across all coral sites and differed from other sites primarily through high abundances of oligochaetes. Savannah Banks was characterized by high abundances of Cirratulidae and Syllidae (Polychaeta). Blake Escarpment and Blake Deep were distinct from other coral sites due to higher abundances of Spionidae and Sabellidae (Polychaeta).

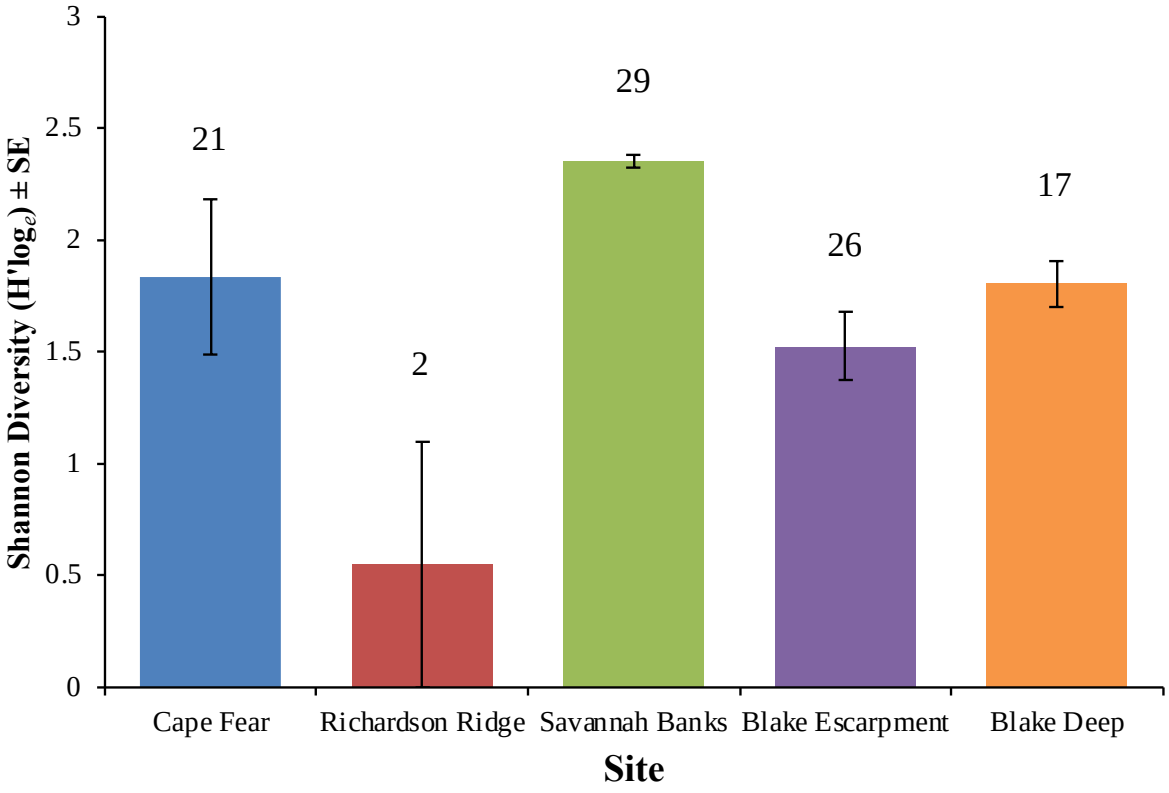

Figure 4-26. Mean Shannon Diversity (H') in coral-adjacent sediment sites
Error bars represent the standard error of the mean.

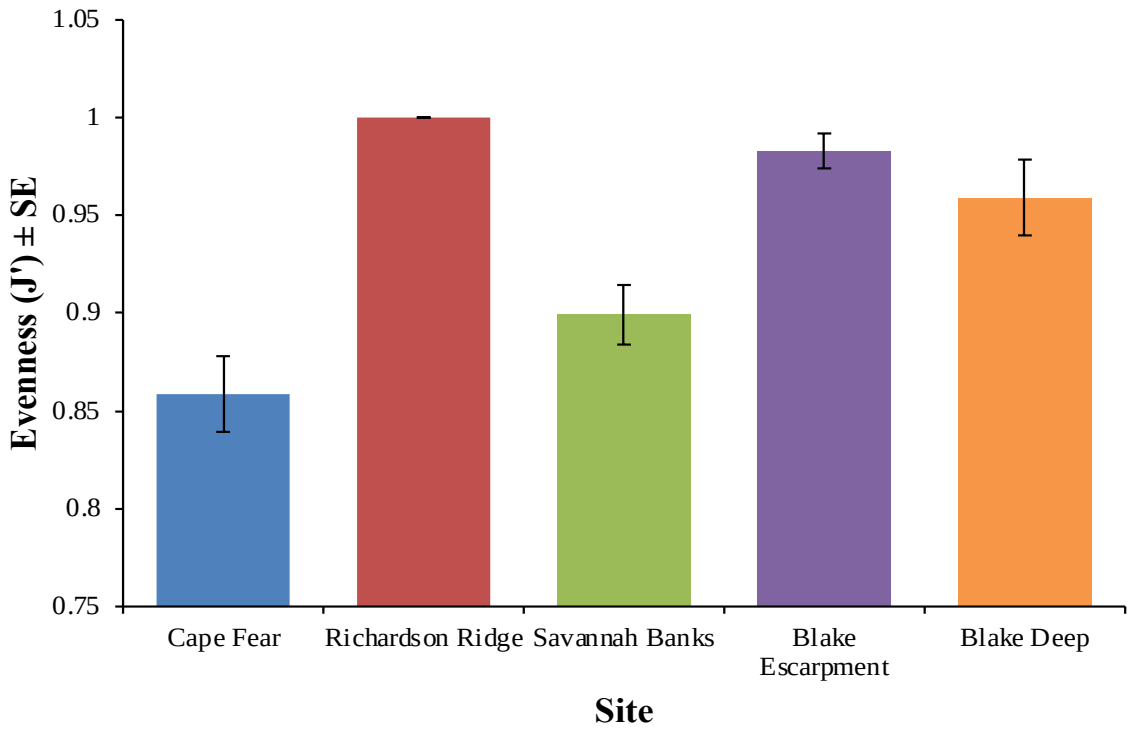

Figure 4-27. Mean taxa evenness (J') in coral-adjacent sediment sites
Error bars represent the standard error of the mean.

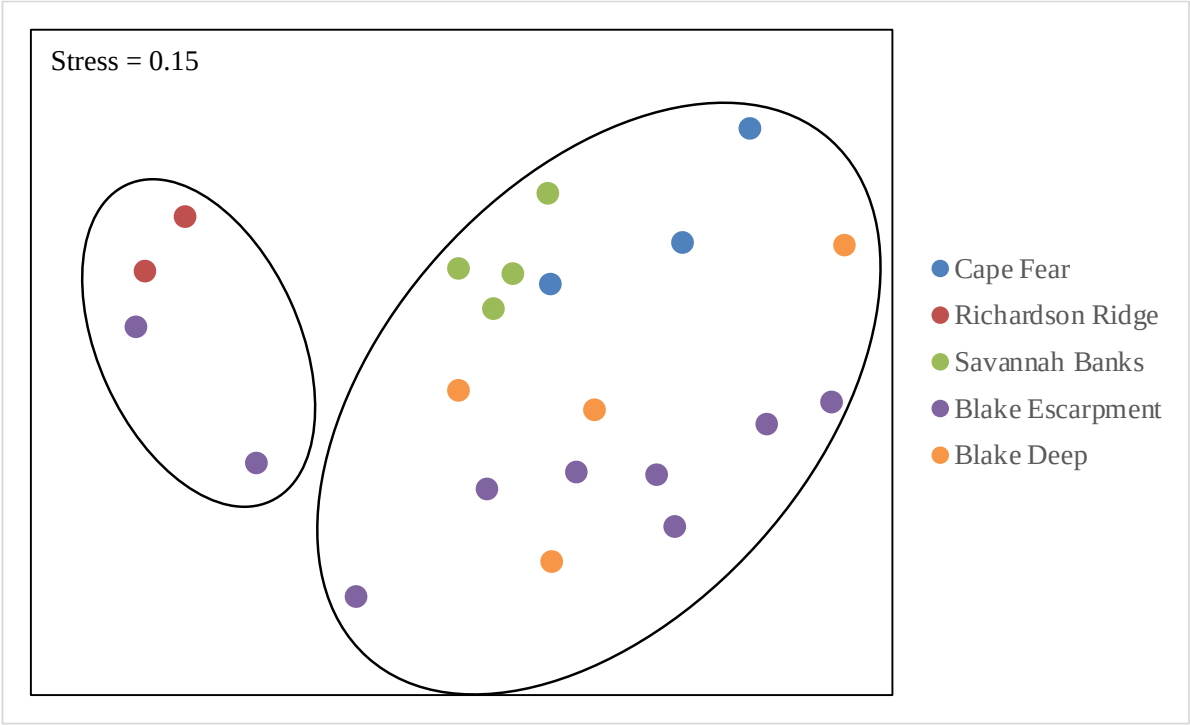

Figure 4-28. Non-metric multidimensional scaling (nMDS) of coral-adjacent infauna in cores
Composition of coral-adjacent habitats based on Bray-Curtis similarities of square-root transformed density data from sediment cores. Ellipses indicate significant groupings based on SIMPROF.

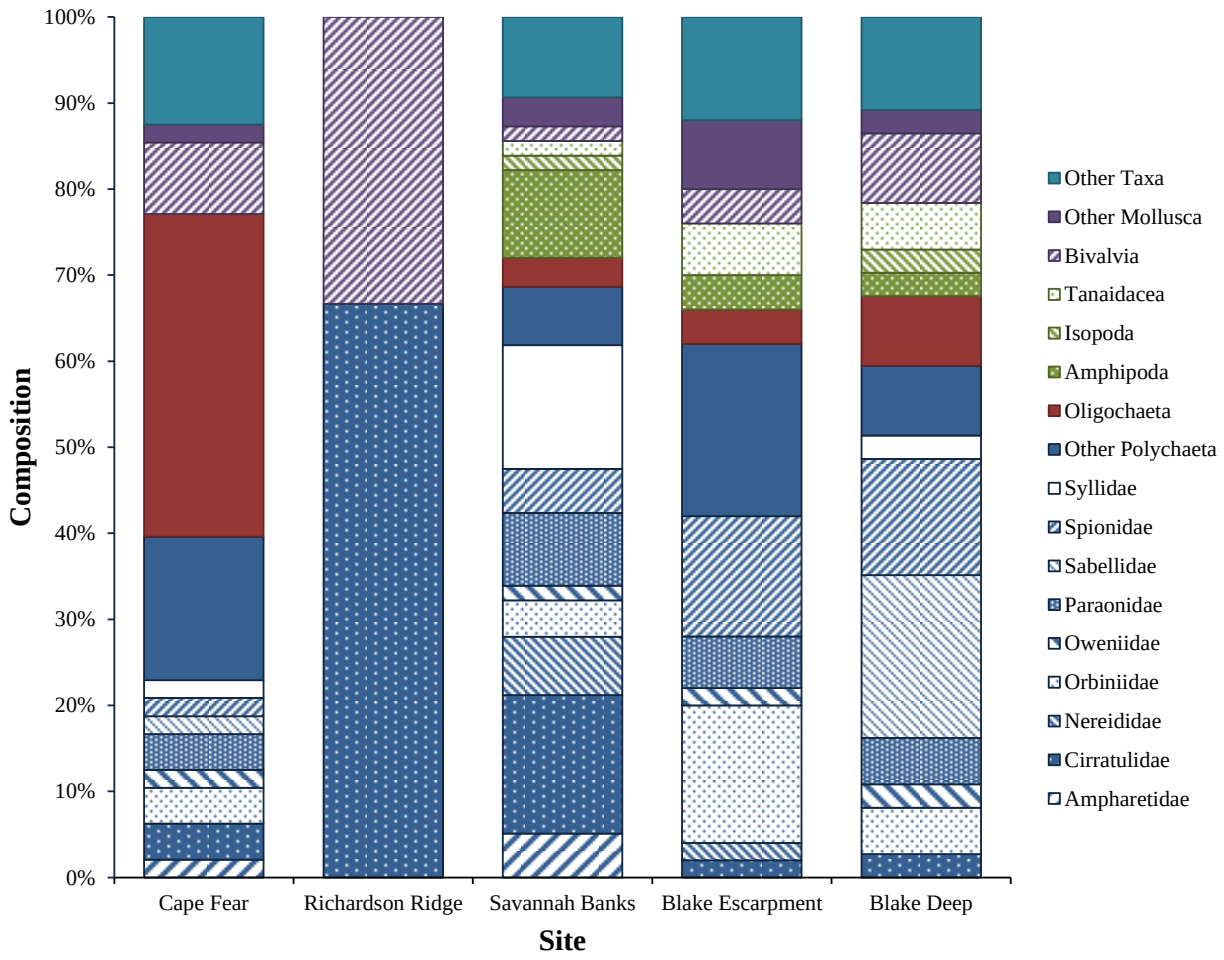

Figure 4-29. Taxonomic composition of dominant macrofauna in coral-adjacent sediments
The "Other Taxa" category includes Halacaridae, Anthozoa, Ophiuroidea, Nemertea, Sipuncula, and Turbellaria.

Environmental parameters differed among the coral sites (**Figure 4-30**). DISTLM analysis indicated that only grain size kurtosis, or the peakedness of the grain size distribution curve where higher values indicate higher sorting, individually explained a large portion (33%) of the coral-adjacent sediment community composition.

Table 4-11. DISTLM of environmental variables with coral-adjacent sediment communities

DISTLM of environmental variables with coral-adjacent sediment communities using the AICc criteria and "best" model selections. SS = sum of squares, P = probability, RSS = residual sum of squares.

Variable	SS(trace)	Pseudo-F	P	Prop.
Coarse Content	3,896	1.450	0.090	0.225
Mud Content	3,579	1.302	0.223	0.207
Sorting	2,121	0.697	0.825	0.122
Skewness	2,867	0.991	0.412	0.165
Kurtosis	**6,574**	**3.056**	**0.017**	**0.379**
Depth	3,691	1.353	0.103	0.213
Latitude	3,206	1.135	0.300	0.185
Longitude	2,226	0.737	0.744	0.128
$\delta^{13}C$	1,682	0.537	0.883	0.097
$\delta^{15}N$	2,670	0.911	0.518	0.154
Percent Carbon	1,543	0.489	0.917	0.089

AICc	R^2	RSS	Selections
58.36	0.3794	10,755	Kurtosis
59.92	0.2248	13,433	Coarse Content
60.02	0.2130	13,638	Depth
60.08	0.2065	13,750	Mud Content
60.27	0.1850	14,123	Latitude
60.43	0.1655	14,462	Skewness
60.53	0.1541	14,659	$\delta^{15}N$
60.74	0.1284	15,103	Longitude
60.79	0.1224	15,208	Sorting
60.99	0.0970	15,648	$\delta^{13}C$
Total SS(trace)	-	17,329	-

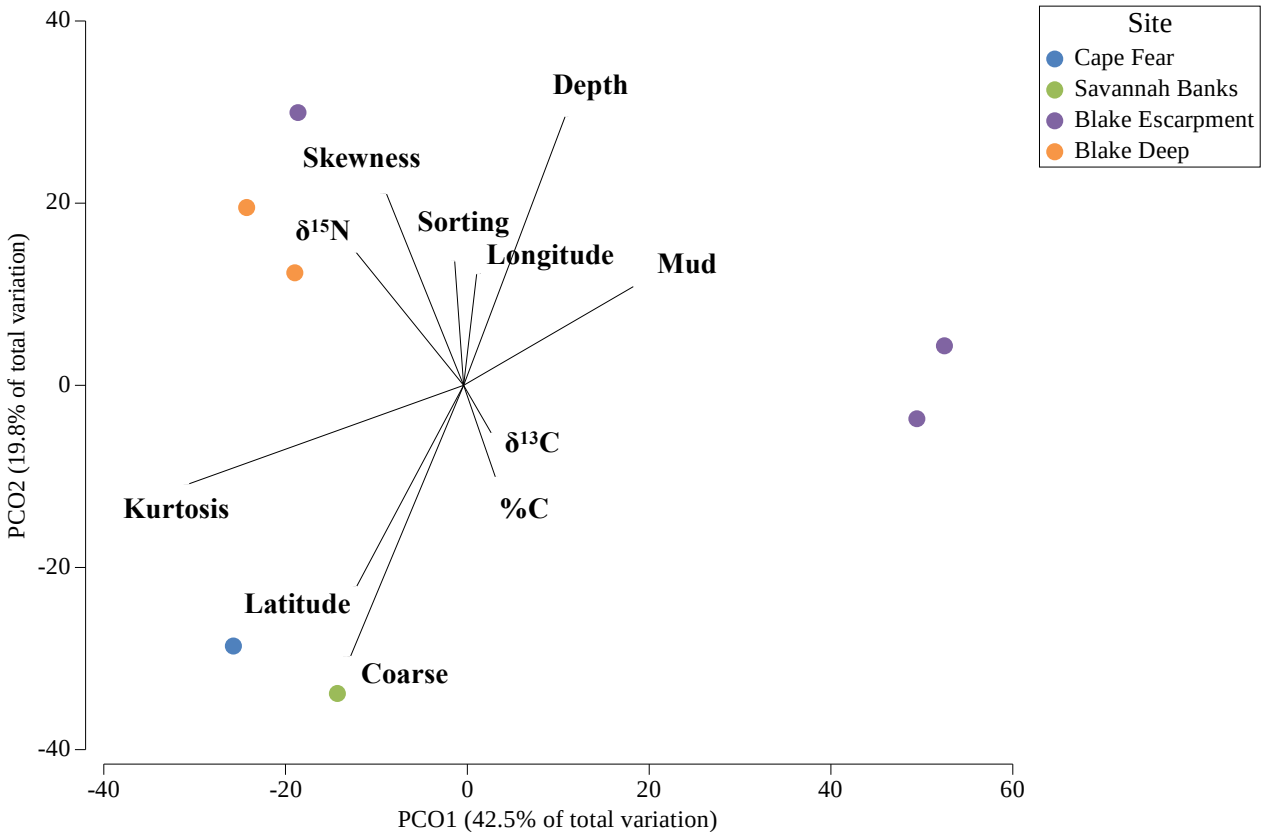

Figure 4-30. Bray-Curtis similarities of abundance data from coral-adjacent push cores
Principal coordinate ordination of Bray-Curtis similarities of square-root transformed abundance data from coral-adjacent sediment push cores with environmental vectors overlaid.

4.1.2.4 Macrofauna—Seep Sites

At the seep sites, we collected a total of 11,501 individuals by push core across five sites (Blake Ridge, Cape Fear, Cape Lookout, Kitty Hawk, Pea Island) that included clam beds, adjacent to mussel beds, microbial mats, active methane bubbling near carbonates, and background soft sediments. We sampled microbial mats at all sites, whereas we sampled mussel and clam beds only at Blake Ridge, and in active bubbling only at Kitty Hawk and Pea Island. We collected background soft sediments at Cape Fear, Kitty Hawk, and Pea Island.

Macro-infaunal density was higher in all habitats at the two northern seeps, Kitty Hawk and Pea Island, than in the southern sites, Cape Lookout, Cape Fear, and Blake Ridge (**Figure 4-31**). We observed the highest densities within microbial mat habitats at Kitty Hawk (319,115 individuals m^{-2}) and Pea Island (303,317 individuals m^{-2}), while microbial mat habitats at Cape Lookout, Cape Fear, and Blake Ridge ranged from 0 to 4,739 individuals m^{-2}. Sediments with active methane bubbling had higher densities at Kitty Hawk than Pea Island, while we observed higher densities in background soft sediments at Pea Island. Clam bed- and mussel bed-adjacent habitats had similar densities at Blake Ridge.

Within sites, infaunal density in microbial mat and active bubbling at Kitty Hawk was significantly higher than in background soft sediments (Tukey HSD, $p < 0.009$). In contrast, there was no difference in macrofaunal density among habitats at Pea Island (one-way ANOVA, $F_{2\text{-}15} = 0.37$, $p = 0.69$) or Cape Fear (one-way ANOVA, $F_{1\text{-}4} = 2.65$, $p = 0.18$). At Blake Ridge, macrofaunal density was significantly lower in microbial mat habitats than in either clam or adjacent to mussel beds (Tukey HSD, $p < 0.0001$).

Macrofaunal density in microbial mats differed among sites (one-way ANOVA, $F_{4\text{-}23} = 9.36$, $p = 0.0001$), with densities at Blake Ridge significantly lower than at Kitty Hawk and Pea Island (Tukey HSD, $p < 0.014$) and Cape Fear significantly lower than at Kitty Hawk (Tukey HSD, $p = 0.001$). Densities were similar in active bubbling sediments between Kitty Hawk and Pea Island (Kruskal-Wallis, chi-squared = 2.4, $p = 0.12$).

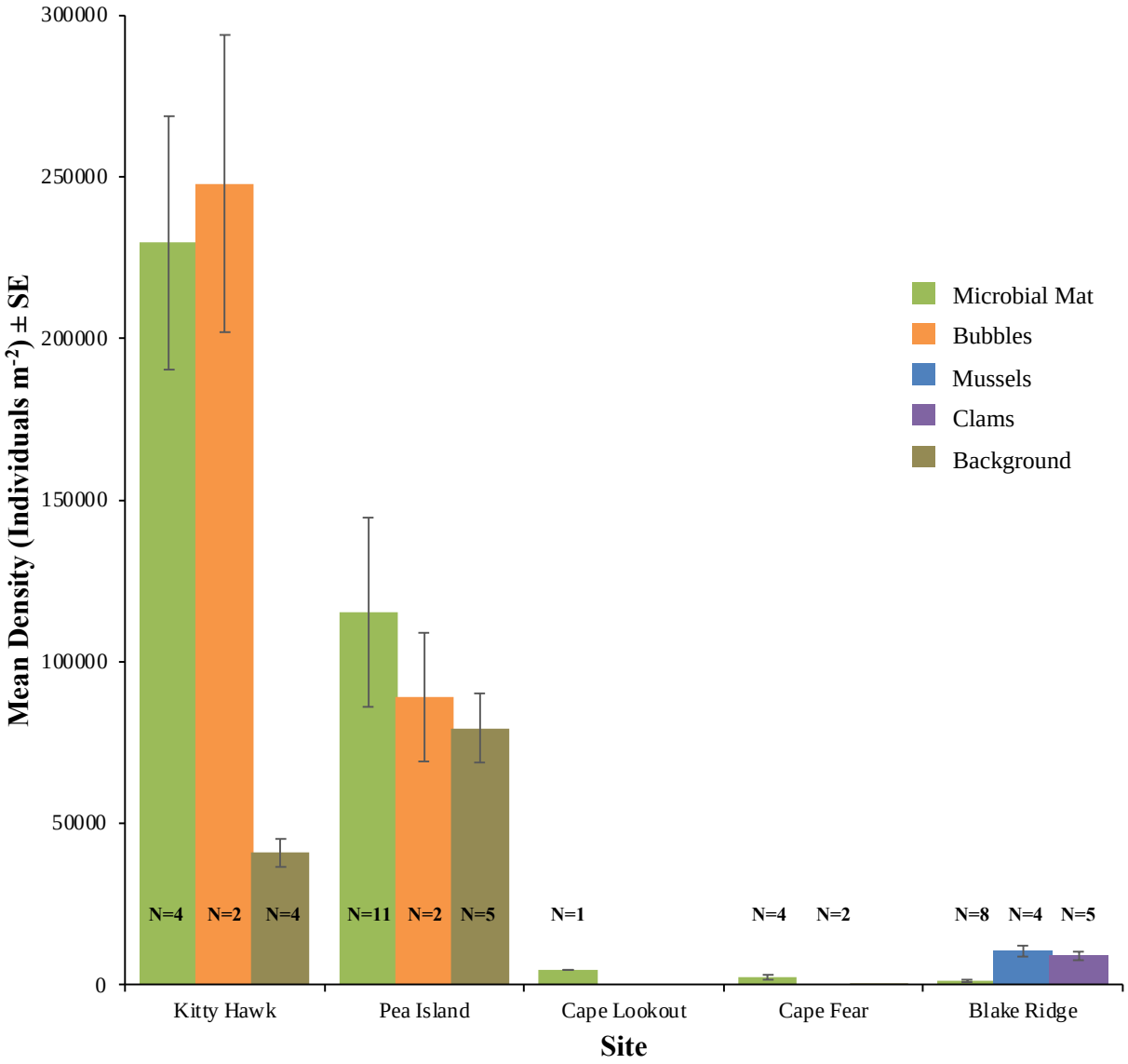

Figure 4-31. Mean macrofaunal density at seep and non-seep habitats and sites
Error bars represent the standard error of the mean, and N indicates the number of samples.

In contrast to density, Shannon Diversity was lowest within microbial mat sediments at all sites except Cape Fear, where diversity was near zero (**Figure 4-32**). Within sites, Shannon Diversity at Kitty Hawk was significantly lower in both microbial mat and active bubbling sediments as compared to background soft-sediment habitats (**Figure 4-32**; Tukey HSD, $p < 0.023$). At Pea Island, Shannon Diversity was significantly lower in microbial mat habitats than in both active bubbling and background soft-sediment habitats (Tukey HSD, $p < 0.005$). Shannon Diversity was also significantly lower in microbial mats at Blake Ridge than in both clam and mussel beds (Tukey HSD, $p < 0.012$). Evenness (J', **Figure 4-33**)

mirrored Shannon Diversity results for both Kitty Hawk and Pea Island. At Blake Ridge, taxa evenness was only significantly lower in microbial mat habitats than in clam beds (Tukey HSD, p = 0.022).

Shannon Diversity differed among sites within microbial mat habitats, with Pea Island significantly lower than at Kitty Hawk (**Figure 4-32**; Wilcox test, p = 0.015). Taxa evenness (J', **Figure 4-33**) was significantly lower in microbial mat habitats at Pea Island and Kitty Hawk than at Cape Fear and Blake Ridge (Tukey HSD, p < 0.005). There was no significant difference in Shannon Diversity (Kruskal-Wallis, chi-squared = 0, p = 1) or taxa evenness (Kruskal-Wallis, chi-squared = 0.6, p = 0.44) within active bubbling habitats between Kitty Hawk and Pea Island.

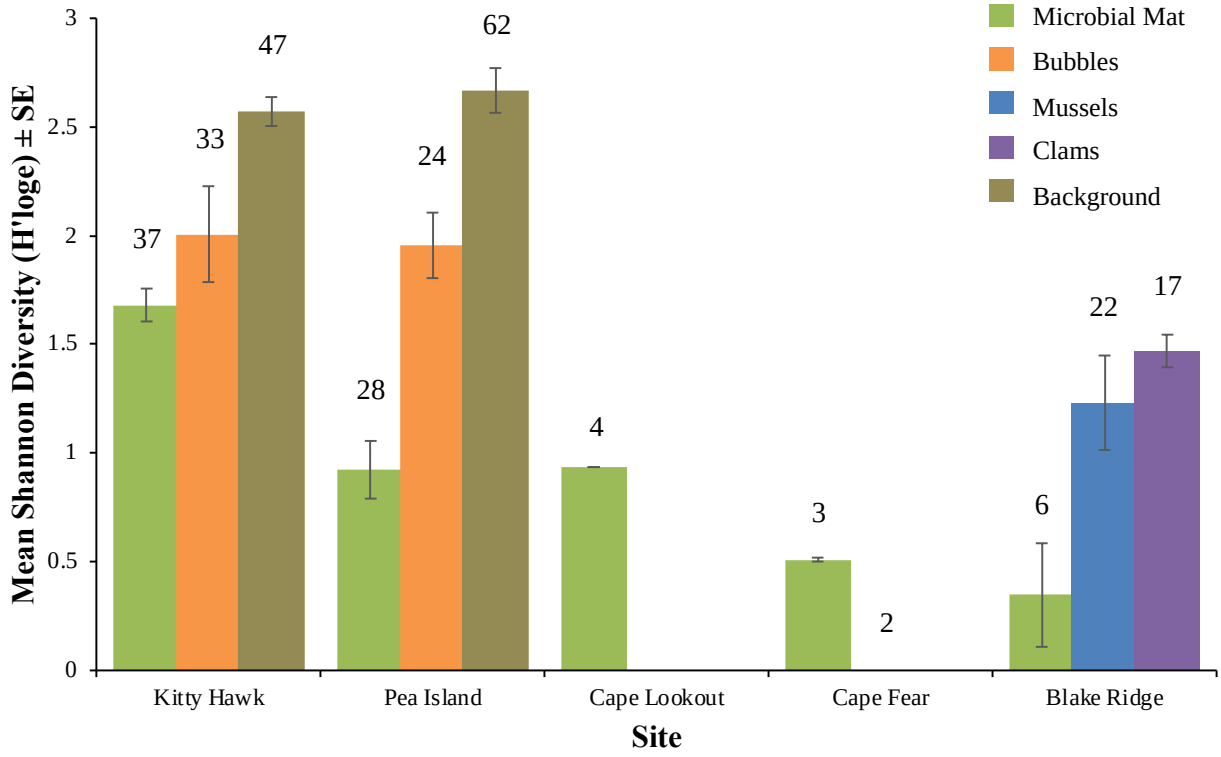

Figure 4-32. Mean Shannon Diversity at seep and non-seep habitats and sites
Error bars represent the standard error of the mean, and N represents the number of samples.

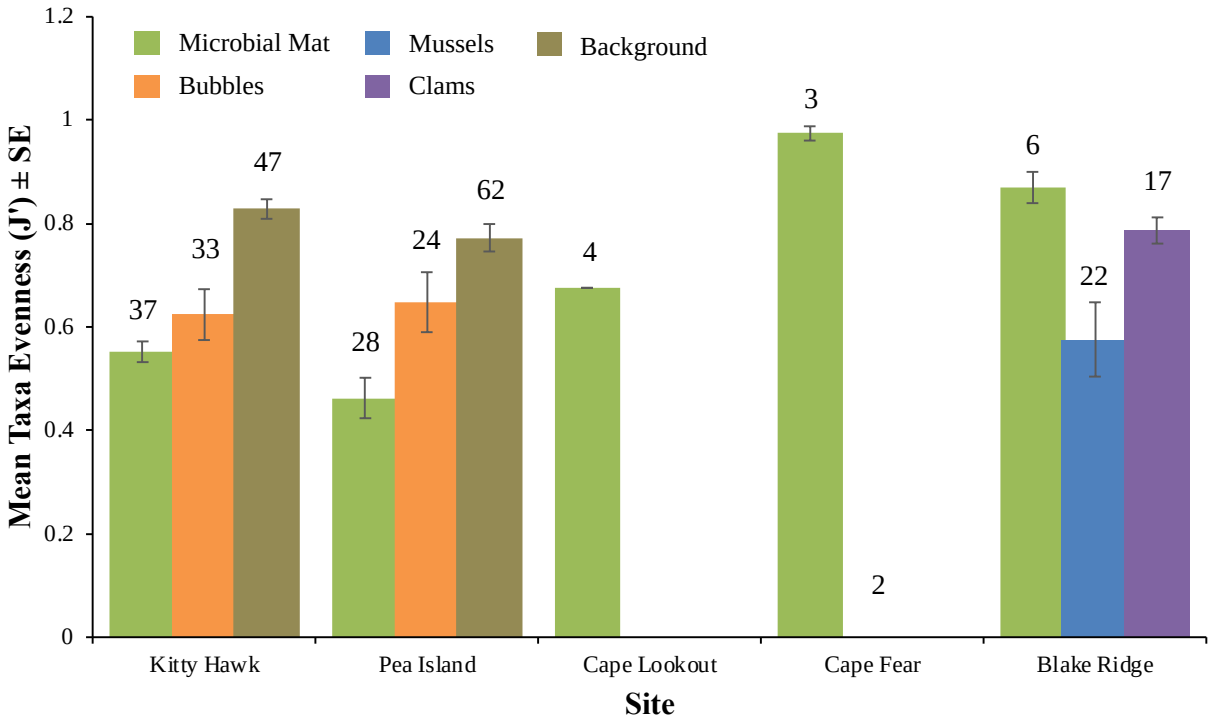

Figure 4-33. Mean taxa evenness (J') at seep sites
Error bars represent the standard error of the mean.

We excluded one core collected within a microbial mat from Blake Ridge (RB1903-J2-1136-PC25) from multivariate analyses as it contained no individuals. Infaunal communities within seep habitats differed among sites and habitat type (**Figure 4-34**, Two-way PERMANOVA, Site: Pseudo-F = 5.059, p = 0.0001; Habitat: Pseudo-F = 5.109, p = 0.0001; Site x Habitat: Pseudo-F = 2.659, p = 0.0001). All habitats were distinct from one another ($p < 0.025$) except for mussel-bed adjacent and clam beds ($t = 1.623$, $p = 0.065$). Comparison among sites indicated that Blake Ridge, Cape Fear, and Cape Lookout were similar to one another ($p > 0.37$) while all other sites were distinct ($p < 0.039$).

CLUSTER and SIMPROF analysis (**Figure 4-35**) indicated there were three outliers: microbial mat cores from Blake Ridge and Cape Fear, and background community at Cape Fear. Otherwise, communities were separated by sites, with Blake Ridge, Cape Fear, and Cape Lookout grouped together, and Pea Island and Kitty Hawk grouped together. Within those two larger groupings, communities exhibited high similarity within habitat types. Clam and adjacent to mussel habitats at Blake Ridge comprised a distinct group (37.7%, p = 0.001; **Figure 4-35**), while the microbial mat communities at Blake Ridge, Cape Lookout, and Cape Fear were similar (18.3%). Within the Pea Island-Kitty Hawk seep complex, active bubbling communities from both sites were a significant group (55.6%, p = 0.0006) and all the background communities grouped together (30.0%, p = 0.002). Nine of the 11 Pea Island microbial mat communities grouped together (44.0%, p = 0.001), while the remaining two grouped with the Kitty Hawk microbial mat communities (59.9%, p = 0.001) that were overall more similar to the communities found active bubbling sediments.

Microbial mat communities at all sites were dominated by polychaetes (59–100%), with high proportions of Capitellidae (21–60%) at all sites except Cape Fear (**Figure 4-36**). Microbial mat communities at Kitty Hawk, Pea Island, and Cape Lookout additionally had high proportions of Dorvilleidae (13–38%). Pea Island microbial mat communities were distinct due to high proportions of oligochaetes (39%). Active

methane bubbling communities also had high proportions of Capitellidae (26–40%), Cossuridae (15–18%), and Dorvilleidae (6–19%).

In contrast, microbial mat habitats at Cape Fear and Blake Ridge had high proportions of Hesionidae (25–40%) and Spionidae (31–57%) polychaetes. Background communities at Pea Island and Kitty Hawk had higher proportions of oligochaetes (8–10%), crustaceans (13–28%), molluscs (7–12%), and other taxa (3–6%). Clam and mussel communities at Blake Ridge had high proportions of isopods (46–70%), tanaids (3–7%), and bivalves (10–13%).

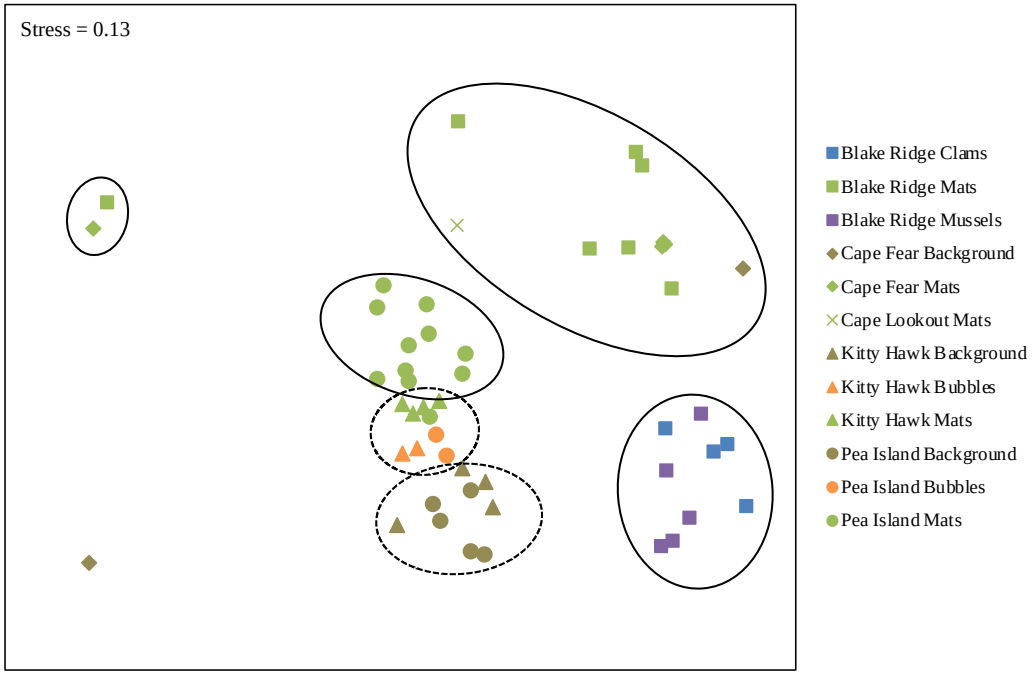

Figure 4-34. Non-metric multidimensional scaling (nMDS) of seep-habitat infauna
Non-metric multidimensional scaling (nMDS) of infaunal community composition of seep habitats based on Bray-Curtis similarities of square-root transformed density data from sediment cores. Solid line ellipses indicate significant groupings from SIMPROF; dashed line ellipses indicate larger groupings of multiple significant groups from SIMPROF.

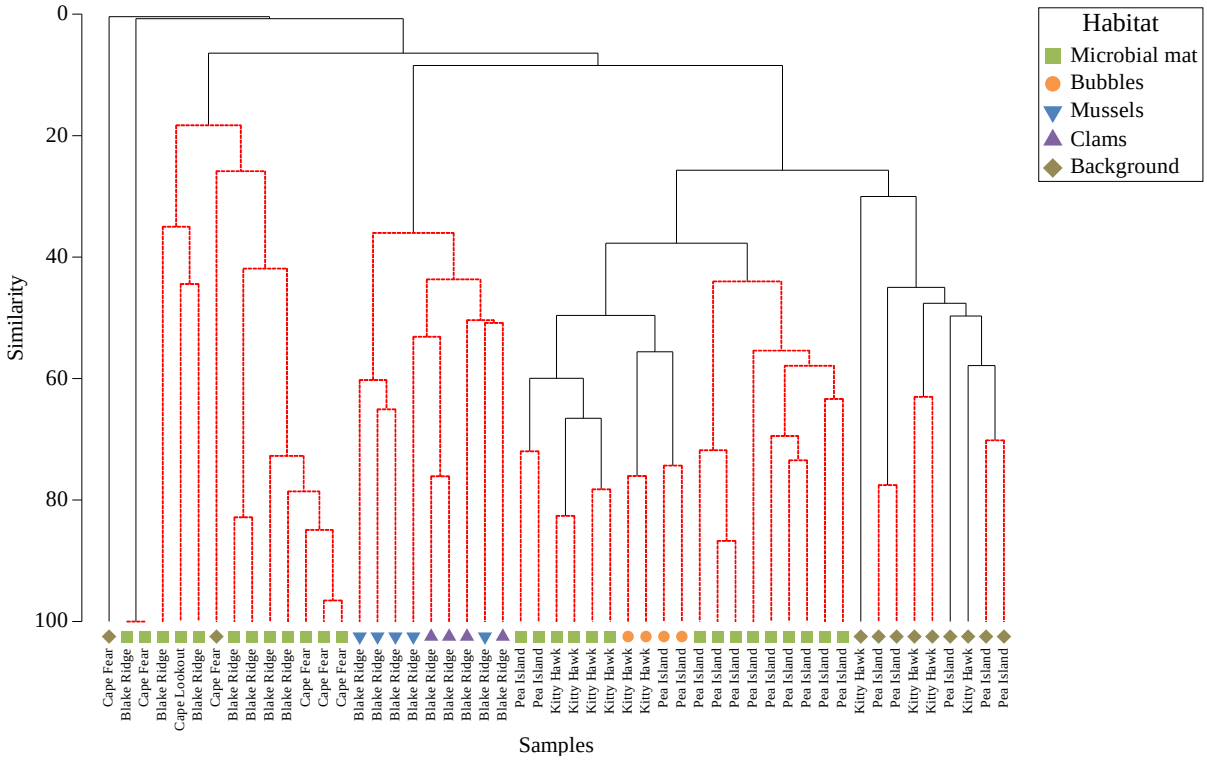

Figure 4-35. CLUSTER analysis of seep sediment communities with SIMPROF groupings indicated

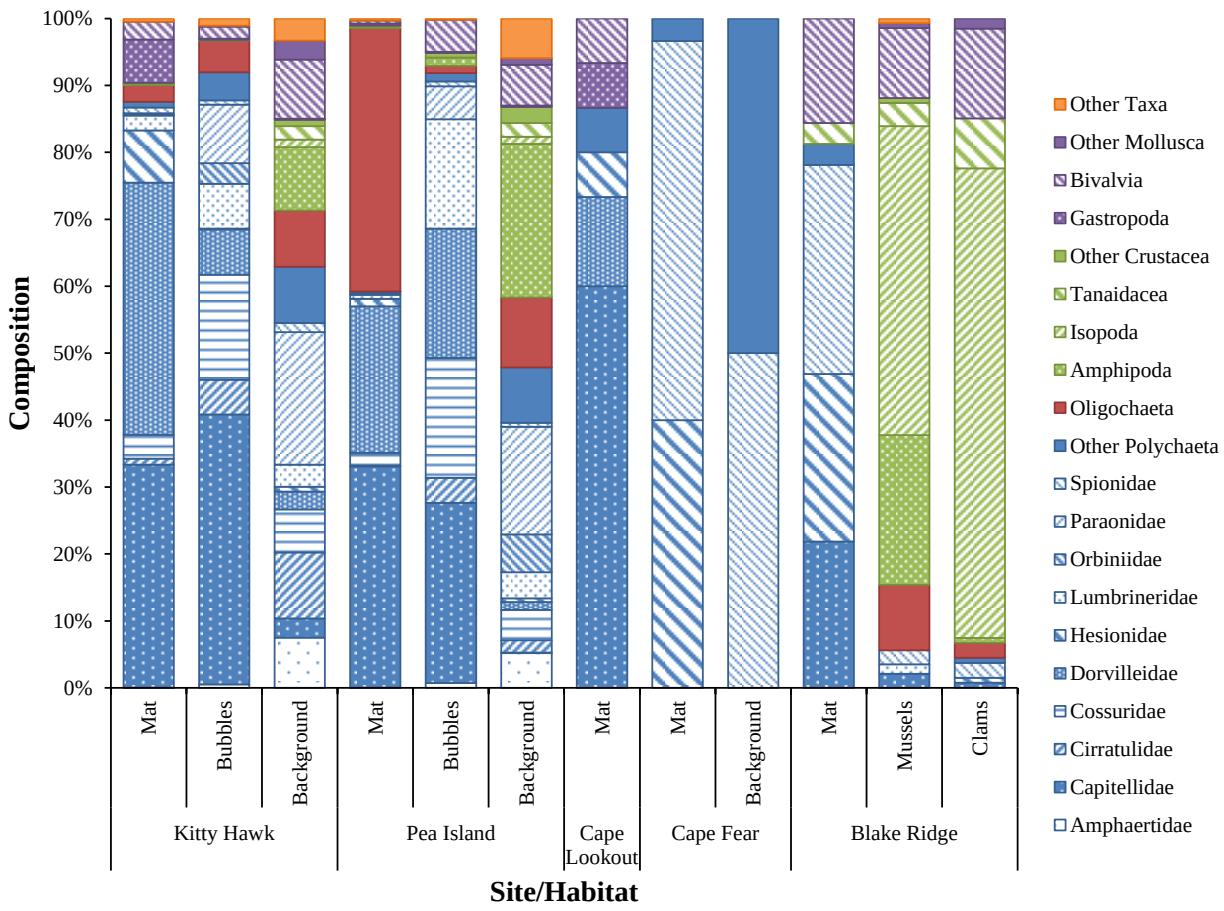

Figure 4-36. Taxonomic composition of dominant macrofauna at seep habitats
The "Other Taxa" category includes Halacaridae, Anthozoa, Hydrozoa, Ophiuroidea, Holothuroidea, Nemertea, Enteropneusta, Sipuncula, and Turbellaria.

Depth correlated well with latitude and longitude (Latitude: Pearson correlation, $\rho = -0.94$, $p < 0.0001$; Longitude: Pearson correlation, $\rho = -0.94$, $p < 0.0001$), thus, we included only depth in the DISTLM analysis. In addition, because the percent sand (< 2 mm, > 63 um) and mud content (< 63 um) were well correlated (Pearson correlation, $\rho = -0.96$, $p < 0.0001$), we included only percent mud content.

DISTLM analysis of locations where data from all environmental variables were available indicated that all environmental variables except C:N ($p = 0.23$) and percent coarse content ($p = 0.16$) individually explained a significant portion of the infauna community (18–38%, $p < 0.049$), with depth explaining the largest amount of community variation (36.9%), while the "best" two-variable model included percent coarse content and depth (43.9%).

Table 4-12. DISTLM of environmental variables for seep sediment communities

Results from DISTLM of environmental variables with seep sediment communities using the AICc criteria and "best" model selections.

Variable	SS(trace)	Pseudo-F	P	Prop.
$\delta^{13}C$	**6,915**	**2.202**	**0.049**	**0.136**
Percent Carbon	**12,798**	**4.704**	**0.001**	**0.252**
$\delta^{15}N$	**9,057**	**3.032**	**0.011**	**0.178**
Percent Nitrogen	**11,384**	**4.035**	**0.001**	**0.224**
C:N	4,260	1.279	0.230	0.084
Coarse Content	4,609	1.395	0.166	0.091
Mud Content	**8,566**	**2.834**	**0.018**	**0.168**
Depth	**18,777**	**8.188**	**0.000**	**0.369**

AICc	R^2	RSS	Selections
126.59	0.36902	32,106	Depth
127.77	0.43968	28,510	Coarse Content, Depth
127.78	0.43912	28,539	Percent Carbon, Depth
127.89	0.43534	28,731	$\delta^{13}C$, Depth
127.97	0.43266	28,868	C:N, Depth
128	0.43157	28,923	$\delta^{15}N$, Depth
128.08	0.54466	23,169	C:N, Coarse Content, Depth
128.28	0.53911	23,451	$\delta^{13}C$, C:N, Depth
128.33	0.41951	29,537	Percent Nitrogen, Depth
128.48	0.41425	29,804	Mud Content, Depth
Total SS(trace)	-	50,882	-

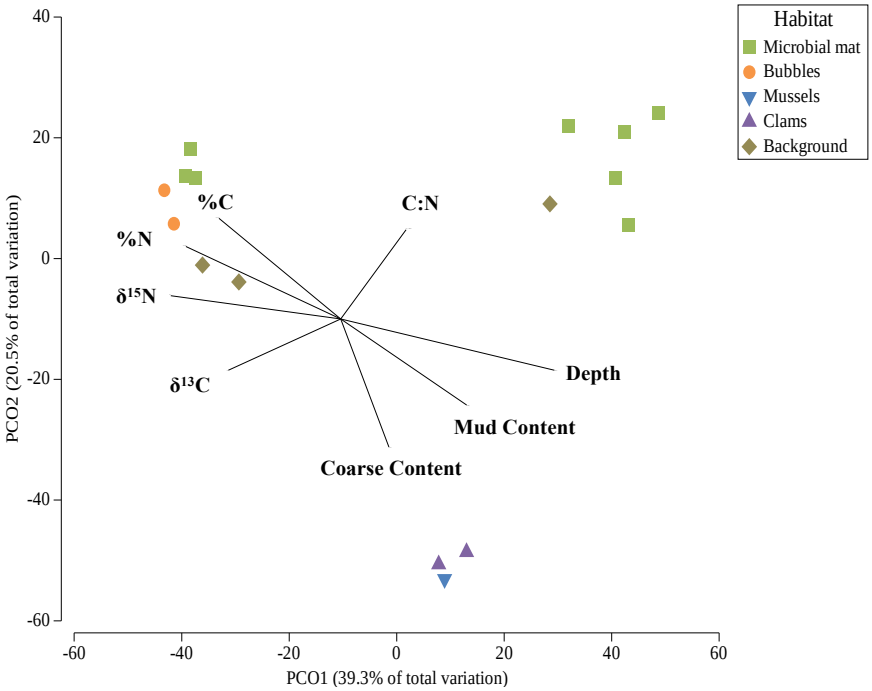

Figure 4-37. Bray-Curtis similarities of abundance data from seep-habitat push cores

Principal coordinate ordination of Bray-Curtis similarities of square-root transformed abundance data from sediment push cores collected in seep habitats with environmental vectors overlaid.

4.1.2.5 Macrofauna—Canyon Sites

We collected a total of 2,095 individuals across five canyons at depths ranging from 281 m to 1,538 m. Macrofaunal density patterns with depth varied among canyons (**Figure 4-38**). Densities were highest within the three northernmost canyon features, "North" Keller, Keller, and Hatteras Canyons, with the highest densities (157,273 individuals m^{-2}) observed at 519–530 m in Hatteras Canyon. Densities were lower in the two southernmost canyons, Pamlico and Amphitheater Canyons, with the maximum density (41,066 individuals m^{-2}) observed at 861 m in Pamlico Canyon.

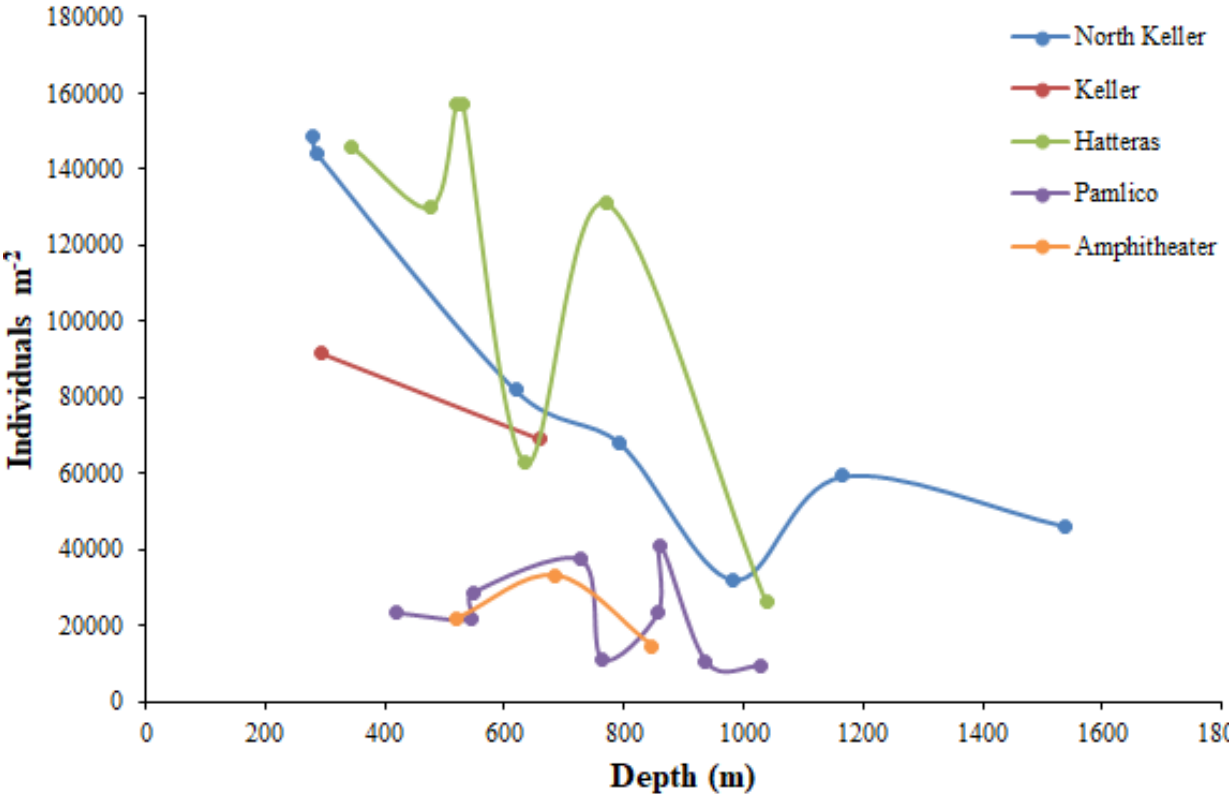

Figure 4-38. Macrofaunal density of canyon habitats with depth

Shannon Diversity generally increased with depth in the three northernmost canyons (**Figure 4-39** A) but decreased or had no change with depth in the two southernmost canyons. Diversity analysis using rarefaction (**Figure 4-39** B) indicated that Keller, Pamlico, and Amphitheater Canyons were undersampled but with high diversity. North Keller had the highest diversity with 46 taxa, while Hatteras had the lowest diversity with only 28 taxa observed. In contrast, taxa evenness (J') generally increased with depth within all canyons (**Figure 4-40**).

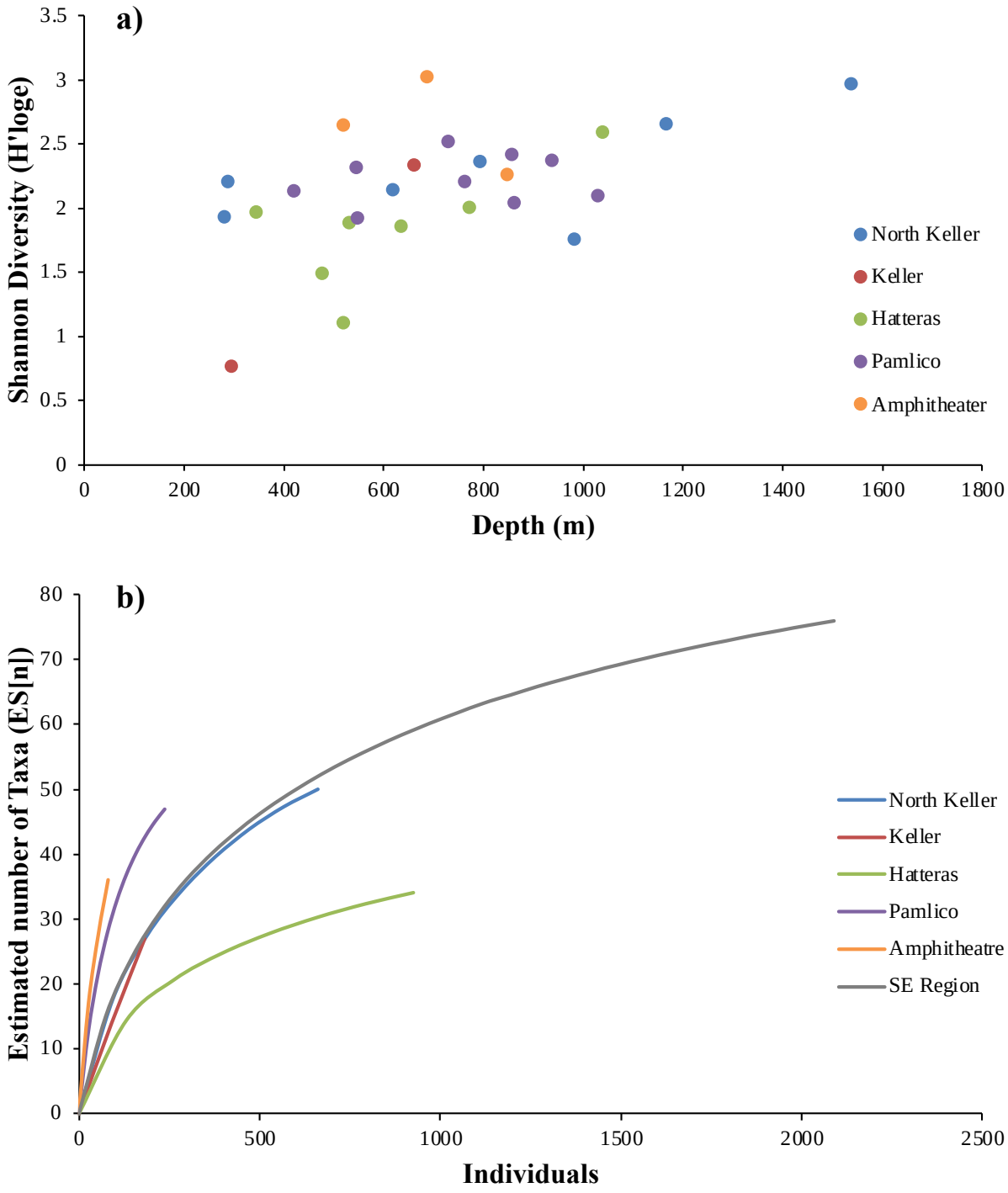

Figure 4-39. Shannon Diversity of canyon habitats with depth and rarefaction of communities
a) Shannon Diversity of canyon habitats with depth, b) Rarefaction of canyon communities.

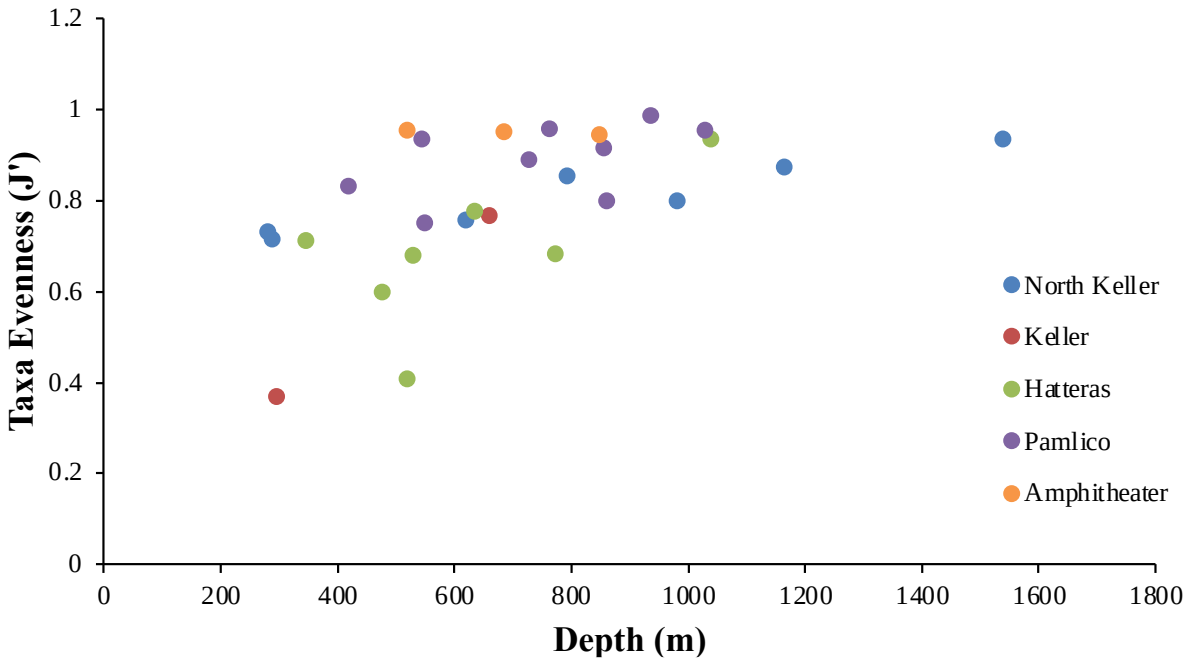

Figure 4-40. Taxa evenness (J') of canyon habitats with depth
Macrofaunal communities differed among SE Atlantic canyons (Figure 4-41, Pseudo-F = 2.06, p = 0.0002). Pairwise comparison indicated that Pamlico Canyon communities differed from both North Keller (t = 1.48, p = 0.006) and Hatteras Canyon (t = 1.89, p = 0.0015), and Amphitheater Canyon differed from both North Keller (t = 1.63, p = 0.029) and Hatteras Canyon (t = 1.99, p = 0.011).

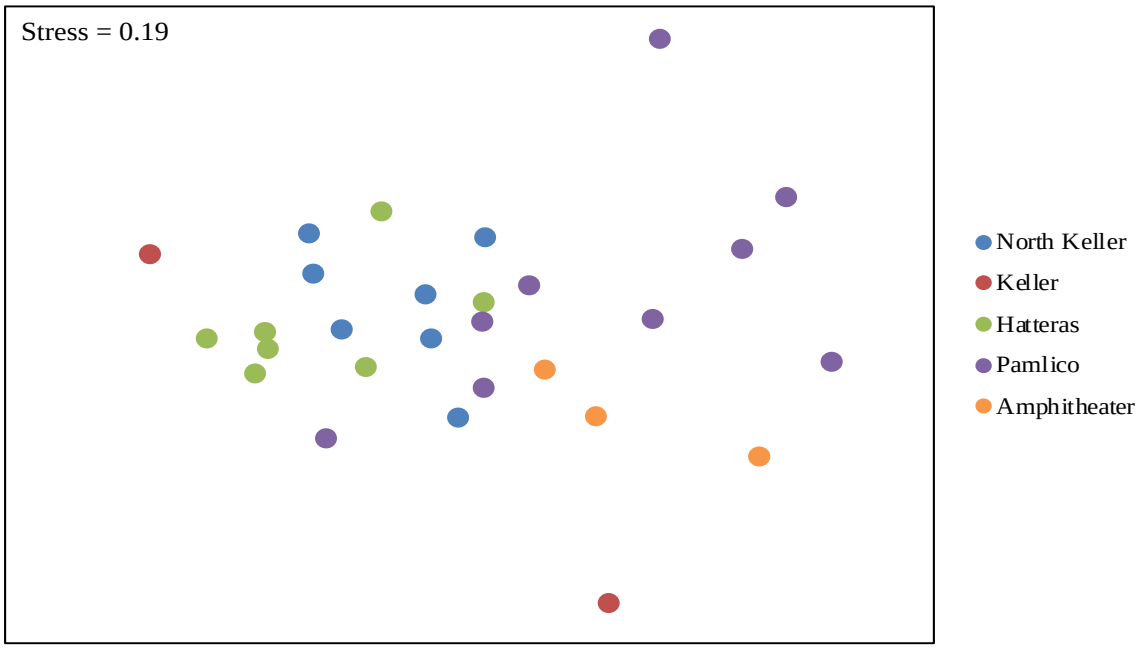

Figure 4-41. Non-metric multidimensional scaling (nMDS) of canyon habitat sediment infauna
Non-metric multidimensional scaling (nMDS) of infaunal community composition of canyon habitats based on Bray-Curtis similarities of square-root transformed density data from sediment cores.

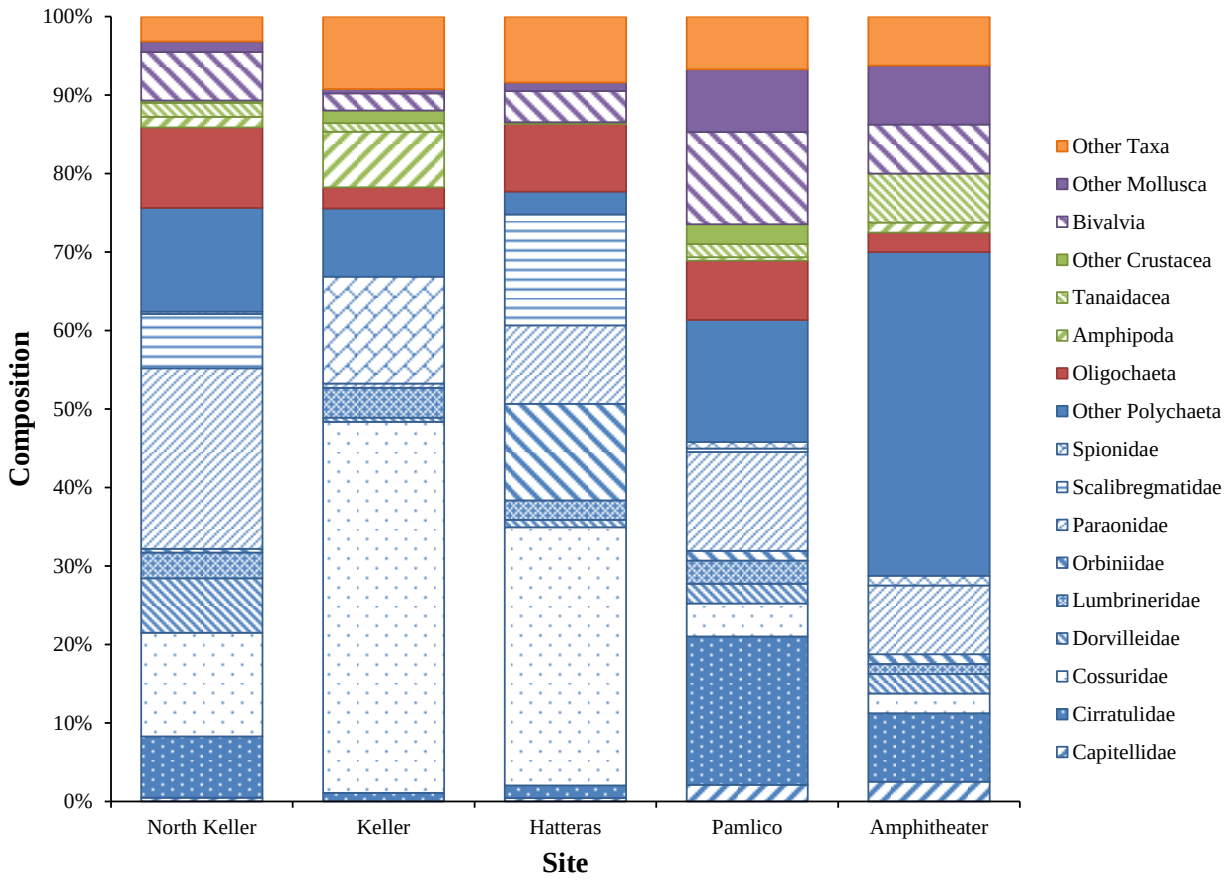

Figure 4-42. Taxonomic composition of dominant macrofauna at canyon habitats
Other Taxa include Halacaridae, Echinodermata, Nemertea, Cnidaria, Enteropneusta, Sipuncula, Turbellaria, and Urochordata

DISTLM analysis indicated that both depth and latitude individually explained significant portions of the community variation, 9 and 11% respectively **(Table 4-13**), and combined provided the second "best" model after latitude alone, explaining 19.7% of the community variation (**Figure 4-43**). However, the top 3-variable model, which also included percent carbon was almost within 1 AICc of the top model, suggesting that this model could be equally as likely, with the 3-variable model explaining 24.9% of the variation.

Table 4-13. DISTLM of environmental variables with canyon sediment communities

Results from DISTLM of environmental variables with canyon sediment communities using the AICc criteria and "best" model selections.

Variable	SS(trace)	Pseudo-F	P	Prop.
Latitude	**6,234**	**2.591**	**0.001**	**0.105**
Depth	**5,229**	**2.133**	**0.004**	**0.088**
$\delta^{13}C$	2,261	0.874	0.611	0.038
$\delta^{15}N$	2,799	1.092	0.355	0.047
Percent Carbon	2,948	1.154	0.285	0.050
Percent Nitrogen	2,820	1.101	0.335	0.048

AICc	R^2	RSS	Selections
189.34	0.10537	52,930	Latitude
189.37	0.19711	47,502	Latitude, Depth
189.79	0.088383	53,935	Depth
190.53	0.15754	49,843	Latitude, Percent Carbon
190.61	0.15455	50,020	Latitude, Percent Nitrogen
190.67	0.24921	44,420	Latitude, Depth, Percent Carbon
190.73	0.24707	44,547	Latitude, Depth, Percent Nitrogen
190.79	0.049821	56,216	Percent Carbon
190.84	0.047659	56,344	Percent Nitrogen
190.85	0.0473	56,366	$\delta^{15}N$
Total SS(trace)	-	59,164	-

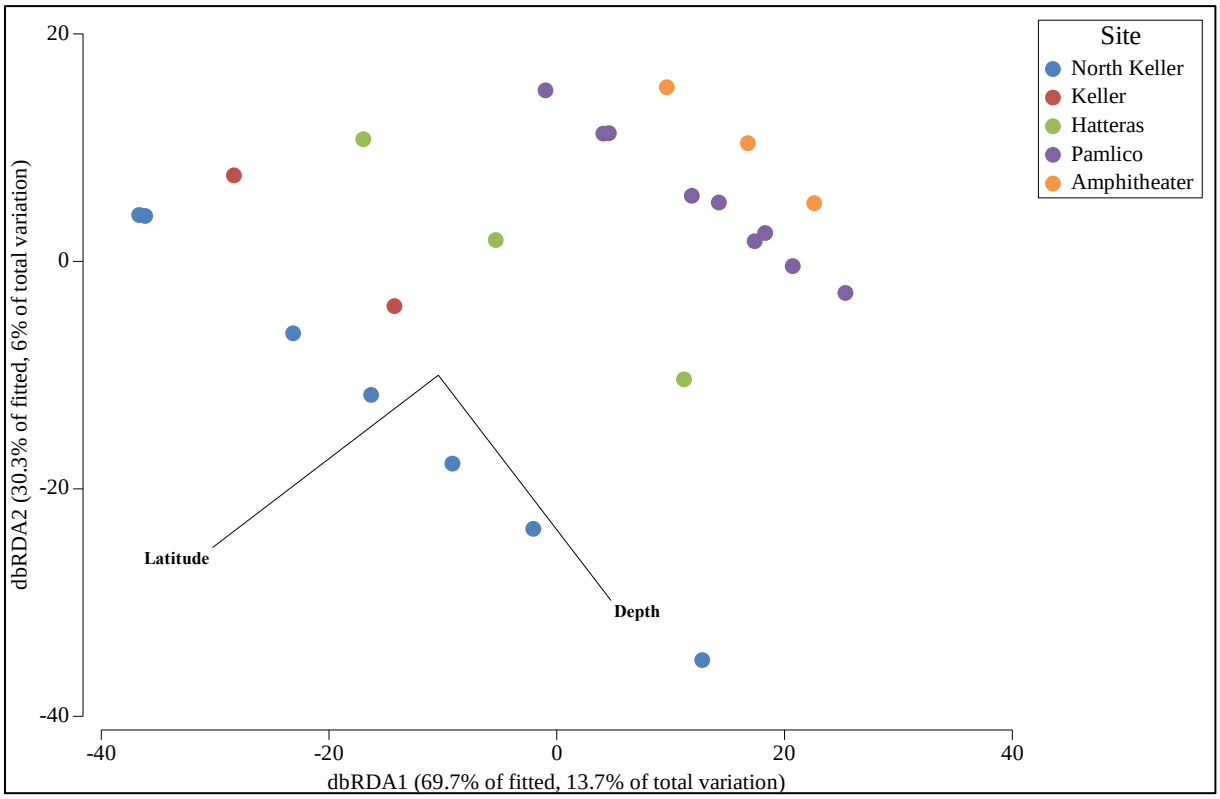

Figure 4-43. dbRDA from the DISTLM analysis

Analysis of the top 2-variable model from the DISTLM analysis.

We collected sediment cores adjacent to hard-substrate habitats in Pamlico (1,263–1,763 m) and Norfolk Canyons (1,667–1,947 m). We collected a total of 372 and 185 individuals in Pamlico and Norfolk Canyons respectively. Overall density was significantly lower in the deeper Norfolk sediments (ANOVA, $F_{1\text{-}25} = 7.37$, $p = 0.012$). Density significantly decreased with depth for the Norfolk habitats ($R^2 = 0.41$, $p = 0.035$) while a unimodal pattern was suggested for Pamlico habitats with a maximum around 1,650 m ($R^2 = 0.23$, $p = 0.18$, **Figure 4-44**).

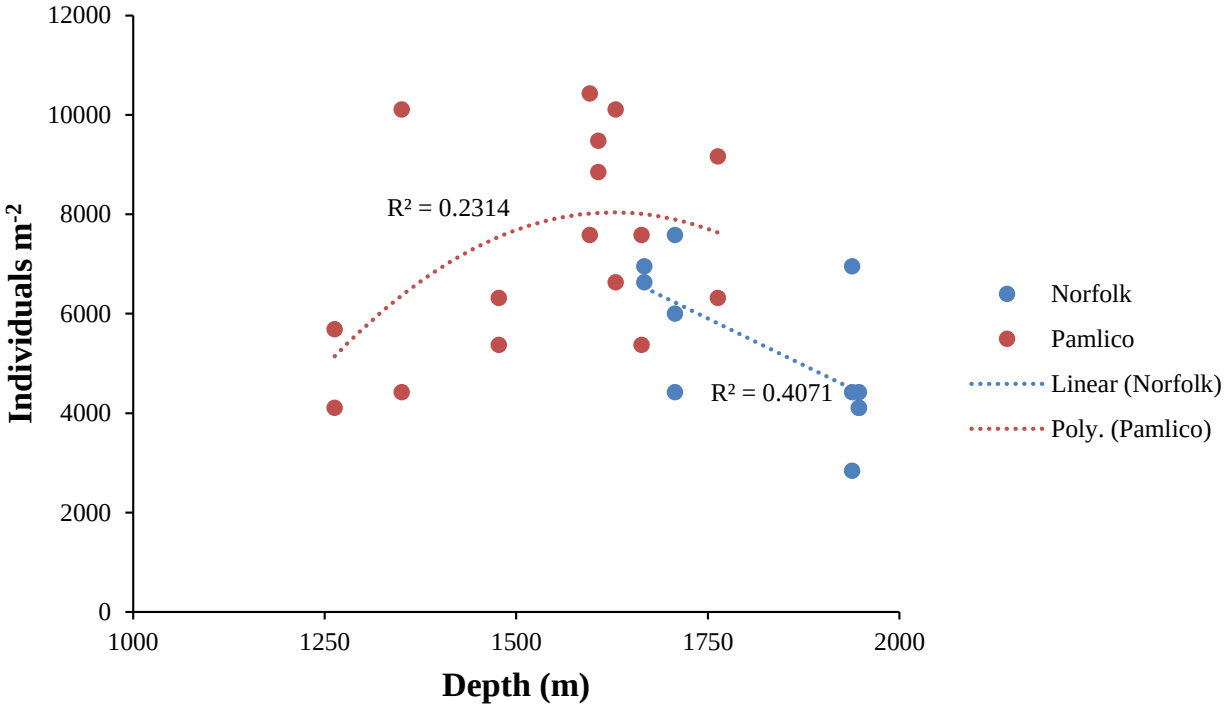

Figure 4-44. Macrofaunal density of canyon hard-substrate habitats with depth

Shannon Diversity exhibited a similar pattern with depth as infaunal density, with diversity significantly decreasing with depth within Norfolk habitats ($R^2 = 0.53$, $p = 0.007$) and a unimodal pattern suggested for Pamlico habitats ($R^2 = 0.22$, $p = 0.13$) (**Figure 4-45**). However, overall Shannon Diversity was similar between Pamlico (2.44 ± 0.07) and Norfolk (2.34 ± 0.08) (ANOVA, $F_{1\text{-}25} = 1.54$, $p = 0.23$).

In contrast, there was no pattern in taxa evenness (J') with depth (**Figure 4-46**) for either Pamlico or Norfolk habitats and taxa evenness was similar between the two sites (ANOVA, $F_{1\text{-}25} = 0.52$, $p = 0.48$).

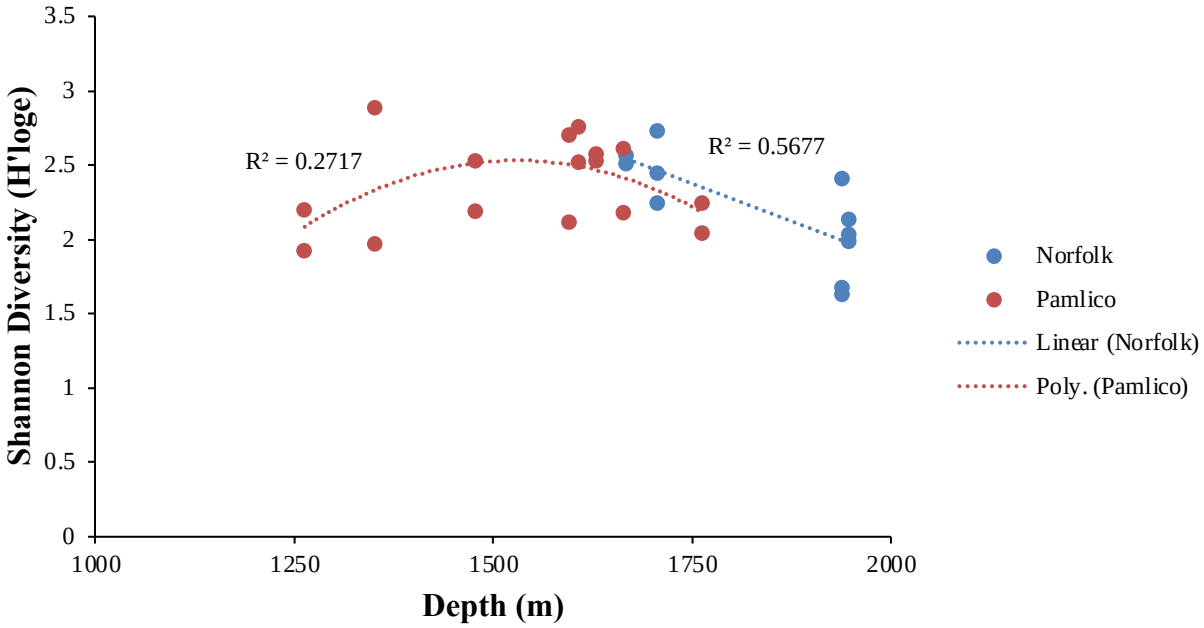

Figure 4-45. Shannon Diversity of canyon hard-substrate habitats with depth

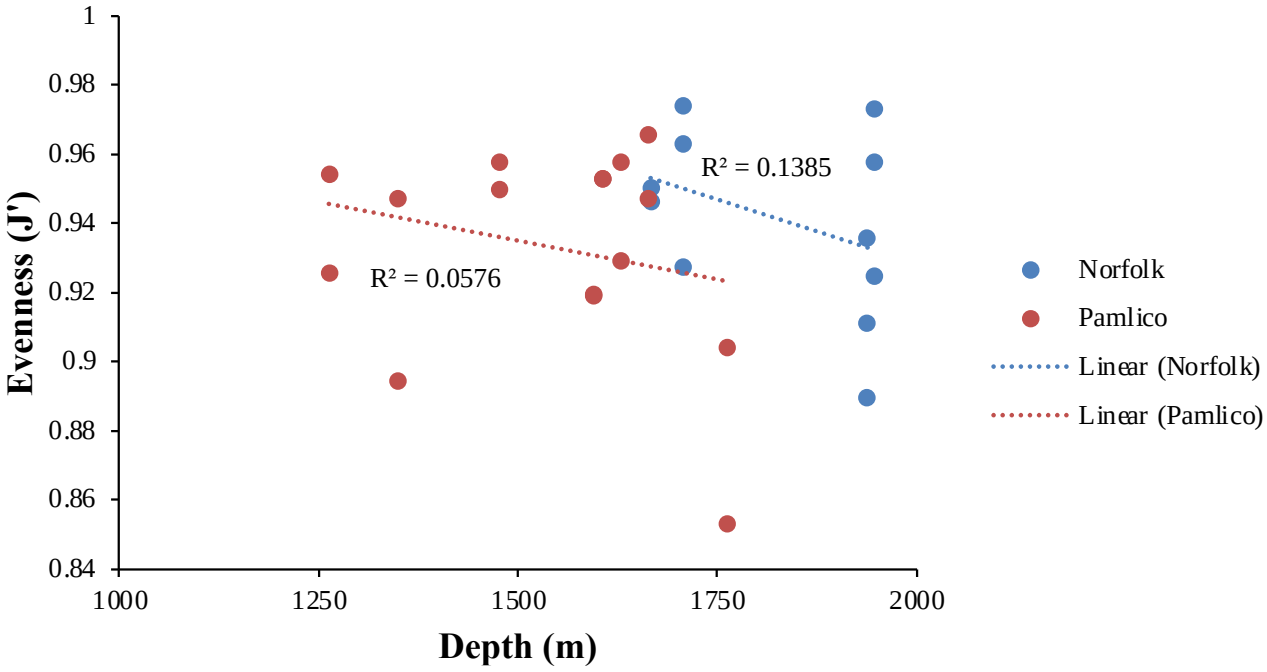

Figure 4-46. Evenness of canyon hard-substrate habitats with depth

Macrofaunal communities differed between the Pamlico and Norfolk hard-substrate habitats (**Figure 4-47**, Pseudo-F = 5.75, p = 0.0001). Community differences were influenced by higher abundances of Cossuridae (Polychaeta), Thyasiridae (Bivalvia), Sigalionidae (Polychaeta), and Sipuncula within Pamlico habitats and higher abundances of Spionidae and Paraonidae (Polychaeta) in Norfolk habitats (**Figure 4-48**), with those taxa accounting for 27% of the dissimilarity.

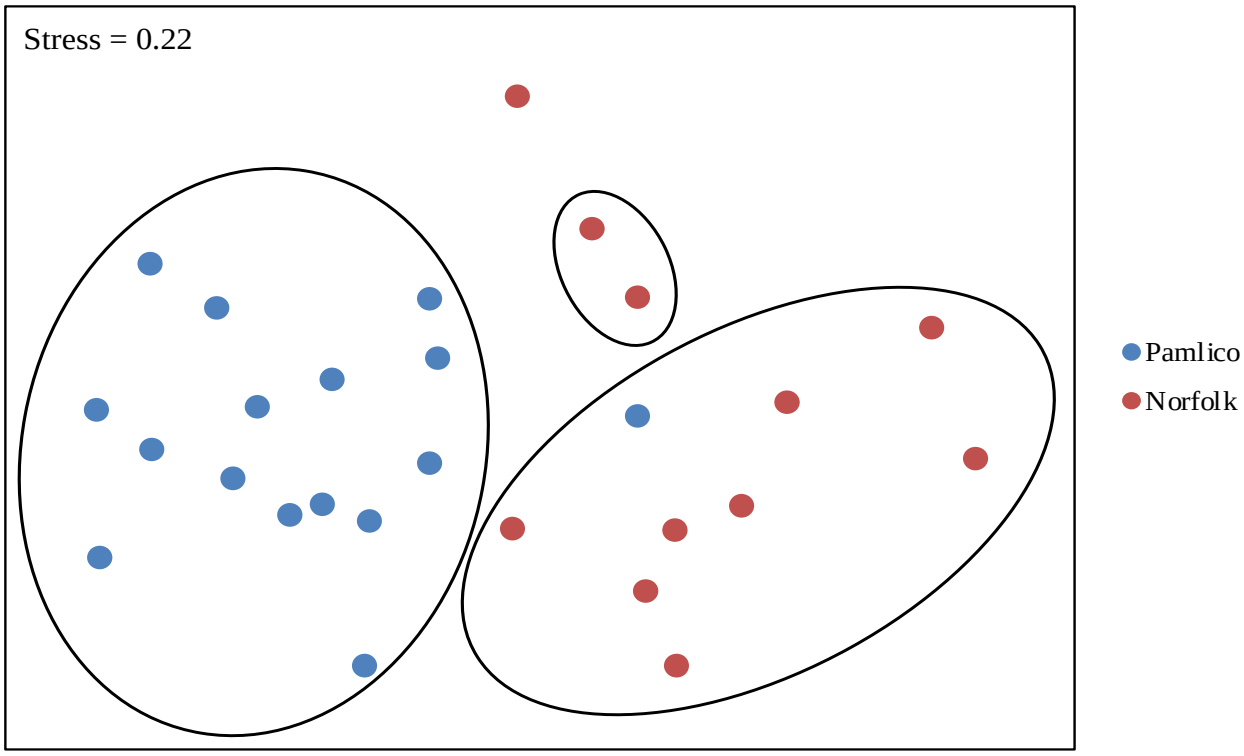

Figure 4-47. Non-metric multidimensional scaling (nMDS) of canyon hard-substrate infauna
Non-metric multidimensional scaling (nMDS) of infaunal community composition of canyon hard-substrate habitats based on Bray-Curtis similarities of square-root transformed density data from sediment cores. Ellipses indicate significant groupings based on SIMPROF.

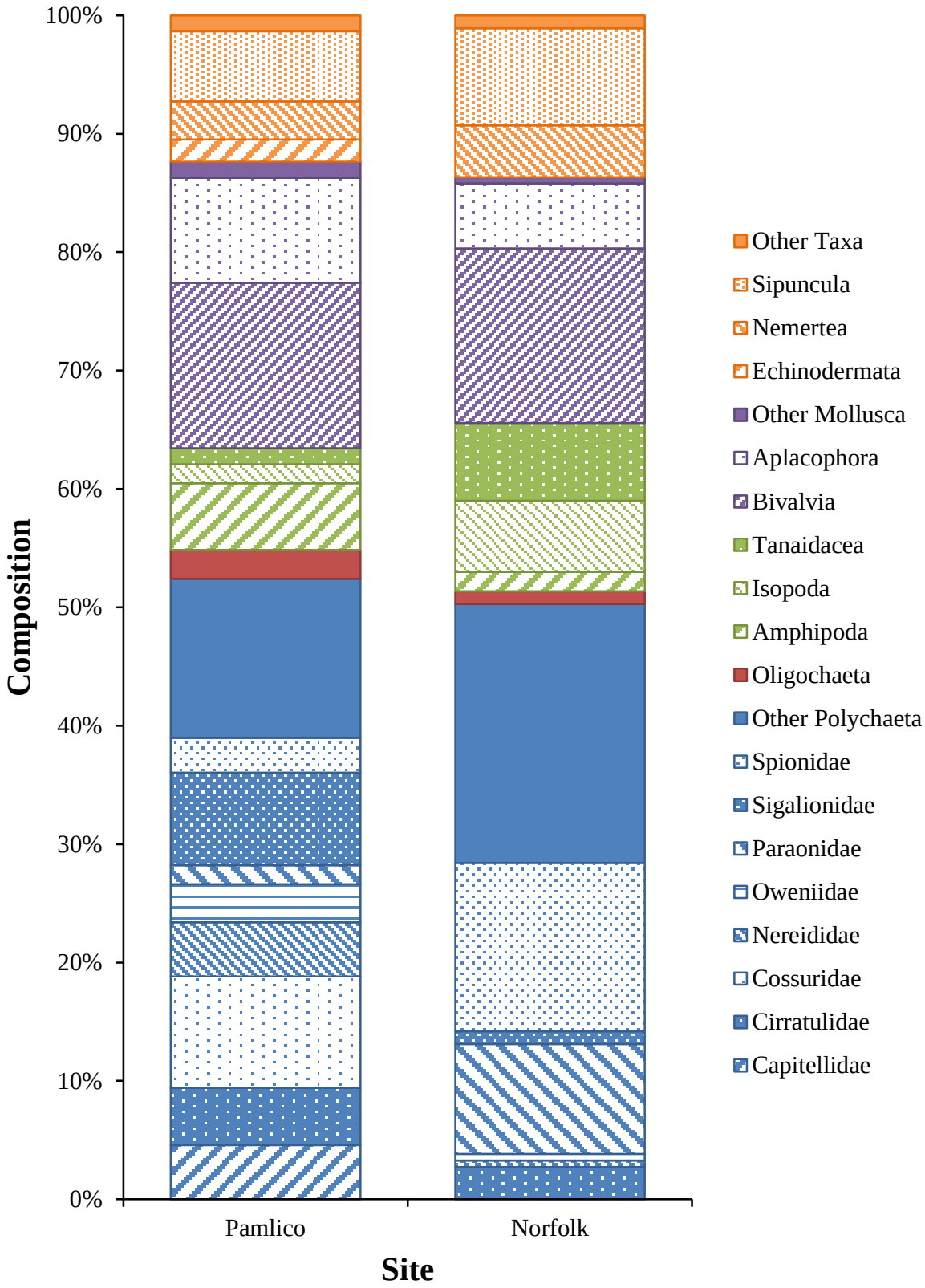

Figure 4-48. Taxonomic composition of dominant macrofauna at canyon hard-substrate habitats
Other Taxa include Halacaridae, Cnidaria, Enteropneusta, and Urochordata.

DISTLM analysis indicated that both percent carbon (27%) and percent nitrogen (22%) individually explained significant portions ($p < 0.001$) of the community variation, 22–27% (**Table 4-14**), also providing the top 2 "best" models. Percent carbon and percent nitrogen were both higher in Pamlico as compared to Norfolk hard-substrate habitats (**Figure 4-49**).

Table 4-14. DISTLM of environmental variables with canyon hard-substrate communities

Results from DISTLM of environmental variables with canyon hard-substrate sediment communities using the AICc criteria and "best" model selections. Significant individual variables are shown in bold.

Variable	SS(trace)	Pseudo-F	P	Prop.
Depth	3,016	1.722	0.075	0.147
Coarse	1,958	1.054	0.360	0.095
Sand	2,131	1.158	0.304	0.104
Mud	2,573	1.433	0.141	0.125
$\delta^{13}C$	1,571	0.828	0.629	0.076
$\delta^{15}N$	3,099	1.777	0.056	0.151
Percent Carbon	**5,510**	**3.667**	**0.001**	**0.268**
Percent Nitrogen	**4,547**	**2.844**	**0.004**	**0.221**
C:N	2,063	1.117	0.314	0.100

AICc	R^2	RSS	Selections
90.924	0.26831	15,025	Percent Carbon
91.669	0.22144	15,987	Percent Nitrogen
92.34	0	12,455	Mud, Percent Carbon
92.662	0.37694	12,794	Sand, Percent Carbon
92.71	0.15089	17,436	$\delta^{15}N$
92.765	0.3716	12,904	Coarse, Percent Carbon
92.767	0.14687	17,519	Depth
2.814	0.36902	12,957	$\delta^{15}N$, Percent Carbon
93.066	0.12531	17,962	Mud
93.189	0.34896	13,369	Mud, Percent Nitrogen
Total SS(trace)	-	20,535	-

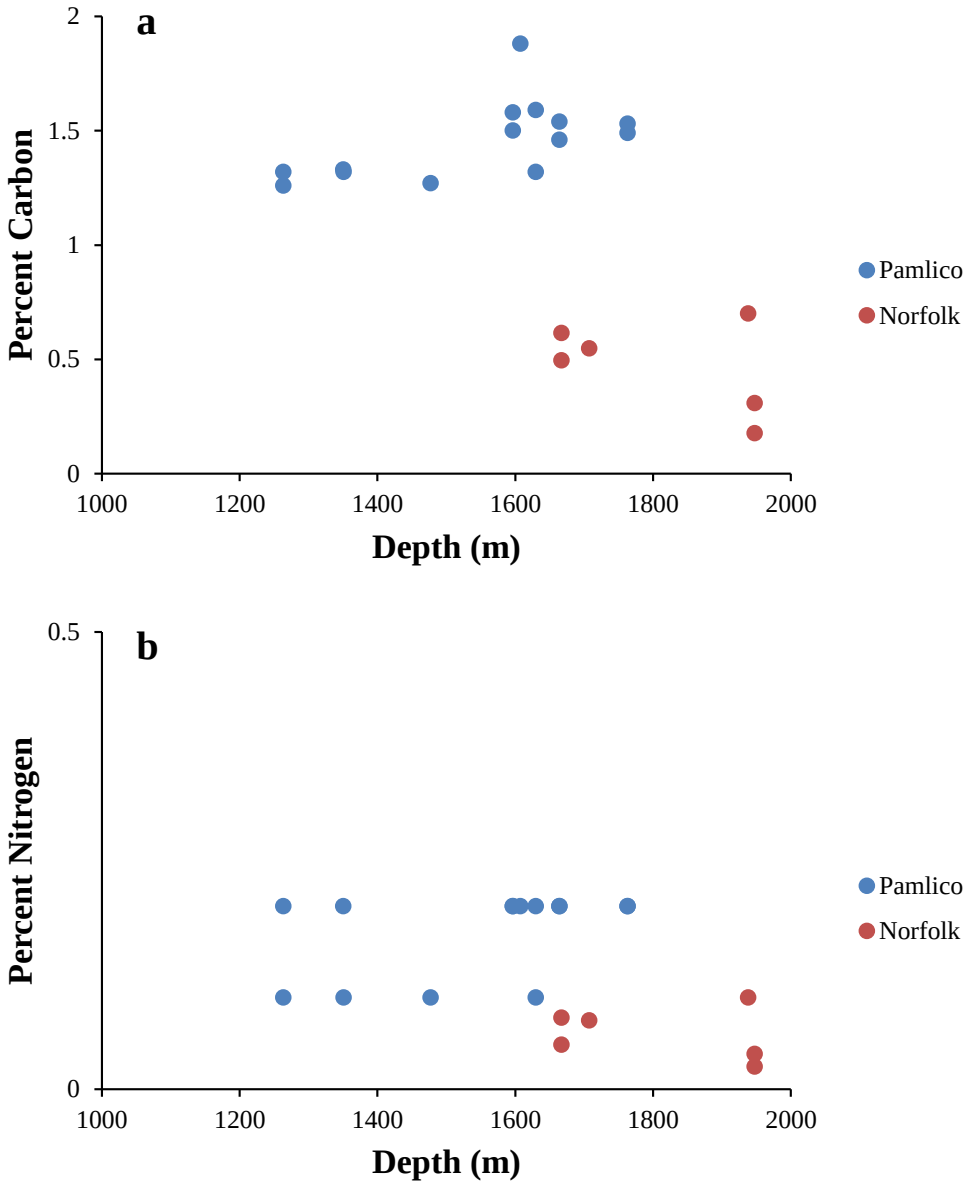

Figure 4-49. Carbon and nitrogen compositions vs. depth at hard-substrate habitats
a) Percent carbon and b) percent nitrogen with depth at Pamlico and Norfolk hard-substrate habitats.

4.1.3 Discussion

4.1.3.1 Megafauna

The megafaunal assemblages associated to coral and canyon environments in the Deep SEARCH study area were fairly well-characterized through video annotations but species-accumulation curves from individual dives and sites reveal that some areas warrant further investigation, particularly within the canyons (**Figure 4-7 B-D**). The canyon megafauna consisted of 51 morphospecies, while the non-*L. pertusa* reef hard-ground sites on the Blake Plateau consisted of 61 morphospecies, with 24 of these taxa shared between the habitats. These morphospecies include representatives from four phyla and comprised mostly cnidarians (n = 11). Species-level similarity may be lower between canyon and non-canyon sites

as many of the shared taxa were those with coarse identifications from video (three unidentified actinarians, euplectellid glass sponges).

We also compared Deep SEARCH canyon megafaunal data to the species list from Brooke et al (2017, video data) and Robertson et al. (2020, box core data) from Baltimore and Norfolk Canyons. Similarity between these data sets was qualitatively assessed due to the different methods of data collection (box cores vs. video transects). Despite this, there were multiple shared taxa between the lists including all of the scleractinian and octocoral species, astropectinid sea stars, gastropods, and holothurians. This suggests relatively high faunal similarity between these canyons, specifically assemblages with high abundances of *D. dianthus*, *Acesta* sp. bivalves, and brisingid asteroids. However, these taxa were rare (in the case of brisingids) or absent in non-canyon Deep SEARCH sites. Together, these lines of evidence indicate high faunal connectivity between canyons on the US Atlantic margin, with lower overlap between canyon and non-canyon sites.

In general, the sites characterized by cover of *L. pertusa* were the most speciose and diverse, but some dive segments on octocoral-dominated hardgrounds had similar diversities. Despite this, compositional differences between the ecosystem types in the current study were apparent. *L. pertusa* reef inhabitants appeared to have a more diverse set of inhabitants including many species of motile scavengers and predators within the three-dimensional coral matrix. While some motile species—primarily echinoderms and crustaceans—were seen at the canyon and non-*L. pertusa* coral sites, the assemblages here were numerically dominated by sessile filter feeders. Thus, functional diversity differences between the ecosystem types may be more apparent than the differences in traditional diversity metrics (species richness, Shannon Diversity) presented here.

Most of the fauna from *L. pertusa* sites are members of the regional species pool with occasional endemics as documented by baseline studies in the region (Reed et al. 2006). Comparisons with *L. pertusa* reef assemblages in the GOM (Cordes et al. 2008) and Northeast Atlantic (Roberts et al. 2009) reveal many regional similarities, including shared key taxa at broad (Family and higher) levels (*Eumunida* spp. galatheids, geodiid and hexactinellid sponges). The reef fauna in our study region, however, appears to be less speciose on than these regions, perhaps due to differences in the size of regional species pools or to the oceanography of our region. A topographic (BPI) and depth-driven distinction in *L. pertusa* communities was apparent in the video data, however, suggesting environmental control of the coral reef fauna (**Figure 4-9**).

At sites in the high velocity and temperature core of the Gulf Stream on the western Blake Plateau (Cape Fear Mounds), actinostolid and *Actinoscyphia* sp. anemones formed dense mats that at times appeared to overgrow and/or exclude other attached species, but these morphospecies were rare at deeper sites (**Figure 4-11 a**). Multiple crinoid, hexactinellid, and octocoral morphospecies showed the opposite pattern, and were only present on deep mound sites. This distinction suggests a sensitivity to warm near-shelf conditions in some taxa, and that deep mound sites may represent refugia for these species. Conversely, warming-tolerant opportunists may be favored at the shallower sites and may encroach on the deeper sites as warming continues.

The high megafaunal abundances and diversities occurring at reef tops (**Figure 4-7**) where live *L. pertusa* is most abundant also suggests that warming-driven declines in coral cover will affect the coral-associated assemblages negatively. The additional stress of habitat degradation that occurs more rapidly on dead coral (Hennige et al. 2020) is also likely to negatively affect these communities. Thus, the high biodiversity and distinct assemblages of the deep eastern sites at Richardson Reef Complex and the Central Plateau Mounds warrant additional protection as many of them fall outside of current bottom-contact fishing closures.

To test the hypothesis that communities associated with deep-coral habitat in the southern part of the study area are more similar to those of the east and west Florida slope and northern GOM than the NE Atlantic, we compared presence/absence checklists from the west Florida slope and GOM (Reed et al. 2006, Demopolous et al. 2017) and the Mingulay Reef Complex in the Northeast Atlantic (Roberts et al. 2009) to those obtained during Deep SEARCH. Of the 18 putative morphospecies observed during submersible dives on the west Florida slope by Reed et al. (2006), we observed 15 during Deep SEARCH. Morphospecies observed by Reed et al. (2006) but not during Deep SEARCH included two coral taxa (*Bathypsammia?* sp. and *Placogorgia mirabilis*) and one demosponge (*Siphonodictyon* sp.). This suggests a large degree of faunal overlap between the Florida slope and the Blake Plateau, as hypothesized. The checklist of species from *L. pertusa* habitats in the GOM obtained during the Lophelia *II* project (Demopolous et al. 2017) contained 195 morphospecies total—66 from the west Florida slope. Video segments from Deep SEARCH contained ~31% of those 195 morphospecies, and ~65% of the west Florida slope morphospecies. Most of the species not found in the SEUS but present in the GOM came from a few invertebrate groups including dendobranch decapods and galatheid crabs. While these groups appear more speciose in the GOM, coral diversity between the two regions is roughly similar.

Roberts et al. (2009) contains a checklist of 368 morphospecies collected at the Mingulay Reef Complex in the Northeast Atlantic. There were very few taxa at the genus or species level shared between this checklist and the SEUS (n = 15), indicating that faunal overlap between these two regions is much lesser at high taxonomic resolutions. Of the 29 cnidarian taxa present at the Mingulay Reef Complex, only 5 were present in the SEUS. A few broad taxonomic groups such as bryozoans were in the northeast Atlantic such as (n = 36 morphospecies) but relatively rare in the SEUS (n = 1 morphospecies), while others such as echinoderms were more equivalent (n = 18 in both regions); brachiopods were only represented in the northeast Atlantic.

Overall, these assessments are hampered by a lack of taxonomic resolution and the lower number of samples in the Deep SEARCH study region compared to the GOM and northeast Atlantic, but represent a first-order estimate of faunal similarity between regions. Despite this, the comparisons suggest that the deep coral fauna of the SEUS are more similar to the GOM than the northeast Atlantic, likely due to oceanographic connectivity within the Gulf Stream.

Seeps along the eastern US coast support a diverse group of species. While some similar chemosynthetic habitat features (bacterial mat, reduced sediments, carbonates) existed at each site, we classified the megafaunal communities into five distinct groups. Depth explained the most megafaunal variability among the different seep communities along the western Atlantic and has been previously recognized as a driving force influencing patterns in deep-sea communities (Hernandez-Avila et al. 2018, Cordes et al. 2007, Ross and Quattrini 2009, Levin et al. 2001). The two shallowest dives (one at Pea Island and another at Kitty Hawk) were more similar than the two dives at Pea Island, indicating a high degree of within-site community heterogeneity. Generally, the shallow sites had fewer echinoderms and were the only sites with annelids observed in the video. *Hyalinoecia artifex,* one of the species influencing differences between the shallow and deep sites, are known to be highly abundant in the western Atlantic between ~300-500 m (Mangum and Rhodes 1970, Meyers et al. 2016) and in soft-sediment habitat (Cleland et al. 2021, Meyers et al. 2016), which corresponds to the depths and habitat types reported at these shallow sites.

In contrast, at the deeper seep site Blake Ridge, there was a high abundance of ophiuroids, including *Ophioctenella acies*, which is a known associate of bathymodiolin mussels (Stohr and Segonzac 2005), and we also saw them in *B. heckerae* beds at Blake Ridge (Van Dover et al. 2003, this study). This pattern was similar to seep communities in the GOM, with increased abundances of *O. acies* reported at deep seep locations, while polychaetes were more abundant at shallower seep locations (Cordes et. al. 2010).

Habitat heterogeneity can influence megafaunal communities, with a variety of geomorphic and biological features ultimately shaping biodiversity (Cordes et al. 2009). Whereas we determined depth to be one of the most important factors influencing megafaunal communities, multiple terrain variables, including slope and the presence of hard substrate, also explained some of the megafaunal community variance. The seafloor environment at Kitty Hawk and Pea Island predominately comprised soft-sediment habitat, and in general had lower megafaunal diversity compared to the deeper sites (Cape Fear, Cape Lookout, Blake Ridge) with more habitat complexity, including mussel beds or large areas of hardbottom habitat. Increased habitat complexity can lead to higher species richness, which has been reported for the deeper sites in this study and is consistent with previous studies of seeps in the GOM (Cordes et al. 2010) and Atlantic (Cleland et al. 2021).

Sedimentation may also influence megafaunal community structure in a number of ways, but in particular as many deep-sea corals and sponges depend on hardbottom habitat. Both occurred in greater abundance at Cape Fear and Cape Lookout as compared to Pea Island and Kitty Hawk. Both Kitty Hawk and Pea Island were located farther north near Cape Hatteras, a hydrographically and topographically complex area with anomalously high sediment accumulation rates (Rhoads and Hecker 1994). High sedimentation rates can result in smothering and inhibit coral settlement by reducing the availability of hard substrate (Brooke et al. 2009, Roberts et al. 2006, Hubbard 1997).

Sediment composition and quality can also impact coral health, with larger particles being hard to expel and high organic content leading to increased bacterial activity and lower oxygen levels, which can stress corals (Larsson and Purser 2011). While this high sedimentation may not be ideal for corals, it can explain the increased presence of *H. artifex*, which prefer soft sediments and shallower depths (Meyers et al. 2016, this study). As food availability can decrease with depth (Carney 2005), shallower depths with high sedimentation may provide a variety of food resources and explain the increased frequency of fishes observed at the shallow sites. These shallow seep sites appear similar in species composition to shelf seeps located in the Sea of Okhotsk, which consist mainly of patchy bacterial mats (Sahling et al. 2003).

In addition to habitat heterogeneity, variations in the type and magnitude of venting affect seep community populations (Olu et al. 2010). For example, species richness was higher at seep sites associated with higher methane concentrations found in Japan (Nakajima et al. 2014). Similar dynamic venting was observed at the seep sites studied here, which may help explain the site-variation in species diversity observed. The presence of authigenic carbonates dating back thousands of years (see Chapter 3), along with the consistent presence of chemosynthetic bivalves, *Bathymodiolus heckerae*, at Blake Ridge (Van Dover et. al. 2003, Paull et al. 1995, this study) indicate a sustained methane source, providing a potential distinction between the shallow and deep seep sites in the study area.

With a reliable methane source, Blake Ridge has been able to support large mussel-bed communities, as well as a more diverse seep megafaunal community, whereas only sporadic chemoautrophic megafauna (*Escarpia* sp.) were reported at the shallow sites. However, mussel beds have been documented in shallower seeps in the northeast Atlantic (Bodie Seep, NOAA), indicating that at least some mussel species are not limited to deeper depths. Clearly geochemical features can be a driving force in structuring the biological community.

One key finding from this study was our discovery of the vestimentiferan tubeworm *Escarpia* sp. at the shallow seeps; this genus of tubeworm is found at seep locations worldwide (Olu et al. 2010). These gutless annelids rely on thiotrophic endosymbionts for energy and reside in habitats with high subsurface sulfide concentrations (Childress and Fisher 1992). While its presence off the northern US Atlantic Coast was not previously reported (McVeigh et al. 2018), we observed multiple individuals of *Escarpia* sp. at both Kitty Hawk and Pea Island during this study. This unique finding disproves the previously held hypothesis that their absence may be due to insufficient larval supply (McVeigh et al. 2018, Quattrini et al. 2014). Given the presence of these tubeworms, there are clearly sufficient concentrations of sulfide at

the shallow seeps to support *Escarpia* and its symbiotic bacteria; sulfide concentrations within the seeps are variable and high (see Chapter 3, this volume). However, the absence of tubeworms at the deeper seeps cannot be explained by chemistry alone, given the substantial sulfide concentrations found at Blake (see Chapter 3). Also, this site is closer to known source larvae then the shallow seeps. Their apparent absence may be due to insufficient exploration of this seep, although it is considered one of the most studied seeps in the US Atlantic margin. Improved connectivity models of these annelids will help clarify their distribution in this region and identify sites where they may occur, to be explored in the future.

We best explain megafaunal community variability at US Atlantic seeps investigated here by depth, and such provides further support for depth-driven influences on seep communities reported in the GOM and along the equatorial Atlantic (Olu et al. 2010). However, depth only explained roughly 15% of the community variability. Clearly additional variables are needed to further explain the differences among seep communities. Oxygen concentration data were not available for all dives but has been suggested to affect seep biota distribution (Sahling et al. 2003). Data related to the geochemical processes (methane and sulfide concentrations) may also provide additional insights on the variability of seep communities and the habitat heterogeneity that can influence fauna distributions. Inclusion of the environmental and geological parameters are essential to improve understanding of seep community structure and to better predict areas that may support these biologically diverse communities.

4.1.3.2 Macrofauna—Coral Sites

Macrofaunal assemblages in the deep sea are generally limited by the availability of organic matter (Rowe et al. 1982, Billet et al. 1983, Rex et al. 2005, Smith et al. 2008) resulting in declining densities with depth and distance from shore (Rowe et al. 1982, Houston and Haedrich 1984, Rex et al. 2005). Atlantic margin coral-adjacent sediment communities had overall low densities that declined with depth, and depth was one of the main structuring factors for the community structure. Densities at Cape Fear were lower than those recorded at the closest soft-sediment habitats (10,188–16,337 individuals m^{-2}; 583–800 m depth; 66–122 km; Blake et al. 1987). Densities at Richardson Ridge were also lower than the nearest recorded soft-sediment habitats (2,351 individuals m^{-2}; 600 m depth; 75 km; Blake et al. 1987). In contrast, the deeper sites Blake Escarpment and Blake Deep had higher densities compared to the closest historical samples (1,311 individuals m^{-2}; 134 km) which were from a deeper depth (1,993 m).

There is no historical information available in the vicinity of the coral site with the highest densities, Savannah Banks. Macrofaunal densities for all the Atlantic coral-adjacent habitats were much lower than those reported adjacent to both *D. pertusum* and octocoral habitats across similar depth ranges in the GOM (Demopoulos et al. 2014, Bourque and Demopoulos 2018). Environmental variables, including hydrodynamic regimes, sedimentation rates, and food availability, and habitat parameters, such as coral type and patch size, may play an influential role in structuring differences between the two regions (GOM vs. Atlantic).

The lack of a clear pattern of Shannon Diversity with depth is consistent with regional studies of soft sediments (Blake et al. 1987) where species diversity with depth was location specific, with some areas exhibiting the highest diversities at middle slope depths (800–1,500 m) but with the southern areas containing the lowest diversity. Although we did not assess taxa to the species level for this study for comparison to historical sampling programs (Blake et al. 1987), coral-associated sediments in the GOM are known to support diverse communities at the family level compared to nearby soft-sediment habitats (Demopoulos et al. 2014, Bourque and Demopoulos 2018). Given that 43% of the species documented in the historical regional sampling program (Blake et al. 1987) were new to science, there is a high likelihood that the unique habitats documented in this study will provide additional new taxa that contribute to the regional diversity pool.

Depth is a common variable that affects community composition, typically relating to the amount of organic matter flux to the sea floor (food availability). The type and amount of food available to sediment communities influences the functional trait characteristics capable of occupying a specific location, and thus the individual taxa. However, neither the percent organic carbon, an estimation of the amount of food available, or the $\delta^{13}C$, an estimation of the "freshness" of the organic matter, were material factors structuring our observed communities. Other studies have suggested that measured percent organic carbon is not an accurate estimate to the food availability, as it can contain both refractory and labile organic carbon (Schaff et al. 1992, Sanders et al. 1965, Rowe et al. 1974), which may explain the lack of correlation with our results. Grain size composition can be an indicator of the hydrodynamic environment in an area. The higher proportions of gravel-sized sediments and poor sorting at the shallow-coral sites suggests high current velocities and/or the fragmentation of stony corals that were only present at the shallow sites.

Of the coral sites sampled, Richardson Ridge was the most notable in that it had very low density and diversity, with the observed community comprised only two taxa. Richardson Ridge was also the most distinct habitat, consisting of expansive stony coral habitats with few soft-sediment patches to sample. In addition, we collected only two cores at Richardson Ridge, which we split for community and sediment characteristics analysis. Overall, the samples at Richardson Ridge facilitate a very preliminary look at the communities residing in the coral-associated sediments.

4.1.3.3 Macrofauna—Seep Sites

Visible seep habitats, including microbial mats, mussel beds, clams, and active methane bubbling are indicative of distinct infaunal communities, suggesting similar geochemical environments to support those communities. Microbial mat habitats typically contain high sulfide concentrations and methane flux (Sahling et al. 2002) and are characterized by high dominance and densities of tolerant taxa (Bernardino et al. 2012; Levin et al. 2003, 2006, 2013; Bourque et al. 2017). Communities in microbial mat habitats at Kitty Hawk and Pea Island were consistent with previous studies in microbial mat habitats worldwide with high densities of Capitellidae and Dorvilleidae polychaetes and low densities of crustaceans (Bernardino et al. 2012, Bourque et al. 2017, Levin & Mendoza 2007).

We observed record high densities of macrofauna for any seep habitat worldwide (Bourque et al. 2017) at Kitty Hawk (319,115 individuals m^{-2}) and Pea Island (303,317 individuals m^{-2}), with the previous record recorded from a GOM microbial mat habitat (277,100 individuals m^{-2}; Robinson et al. 2004). Overall densities of macrofauna in microbial mat habitats at Kitty Hawk were twice those observed at Baltimore Seep in the mid-Atlantic region, while those at Pea Island were similar to those at the Baltimore Seep (Bourque et al. 2017), all at similar depths (366–400 m).

There was some variation in communities among the microbial mat habitats sampled, which are likely related to small-scale variations in the geochemical environment (see Chapter 3 for sediment geochemical results). Microbial mat habitats at Pea Island had higher subsurface concentration of hydrogen sulfide (H_2S) than Kitty Hawk. Methane concentrations varied among Pea Island microbial mats, with those from 2018 containing higher methane concentrations than those collected 2019, possibly accounting for the higher variability in Pea Island microbial mat communities. Methane concentrations were similar between microbial mats at Pea Island and Kitty Hawk in 2019, contributing to the observed similarities between the two sites. For habitat-specific sediment geochemical results, see **Chapter 3**.

We observed mussels and clam beds at Blake Ridge only in the southeast region and those beds contained similar communities, suggesting overall similar geochemical environments. Mussel and clam habitats had higher infaunal densities than microbial mat habitats at Blake Ridge, and overall similar densities to shallower (1,482–1,585 m) mussel-bed habitats at the Norfolk Seep (Bourque et al. 2017). Densities adjacent to mussel beds observed in this study were higher than those observed in both microbial mats

and mussel beds by Robinson et al. (2004) at Blake Ridge, possibly due to increased sample size in this study or potential variations in the sizes of the mussel beds sampled. Community composition in both mussel bed-adjacent sediments and clam beds observed in this study were similar to Robinson et al. (2004) with high proportions of crustaceans adjacent to mussel beds.

Active methane bubbling habitats exhibited similarities to both microbial mat and background sediments, possibly a presenting a temporary phenomenon where microbial mats have yet to form. The active methane bubbling sites support similarly high densities as microbial mats at both Pea Island and Kitty Hawk, but higher diversity than microbial mats, and some community similarity to background soft sediments. Additionally, the bubbling habitats contained taxa that were also dominant in both microbial mat and background sediments, including Capitellidae and Paraonidae (Polychaeta).

There was a separation in communities between the shallow northern sites Kitty Hawk and Pea Island and the southern deeper sites Cape Fear and Blake Ridge across all habitat types, with depth identified as the primary structing factor explaining 37% of the community variation. As depth and latitude were significantly correlated, we are unable to determine which factor is the primary cause for separation among our sites. The higher densities observed at the shallow sites compared to deep sites is consistent with previous work in the mid-Atlantic region (Bourque et al. 2017); however, the very low densities at Blake Ridge and Cape Fear are consistent with regional low densities previously observed in both seep (Robinson et al. 2004) and soft-sediment (Blake et al. 1987) habitats.

The high densities observed at shallow sites have been hypothesized to be due to added input from surface productivity to the organic matter pool providing additional food sources for infauna, while those in deeper habitats may be more heavily reliant on seep productivity (Bourque et al. 2017) resulting in lower densities. Added complexity to the separation in our sites is the potential zoogeographic barrier offshore of Cape Hatteras (Blake et al. 1987, Cutler 1975). Although assessed at a different taxonomic level, this study also documented higher abundances of sipunculans, cumaceans, and aplacophorans at the northern Pea Island and Kitty Hawk sites compared with the southern sites, consistent with the specific taxa identified as exhibiting zoogeographic limits (Blake et al. 1987, Cutler 1975).

Community patterns at each of the sites with seep habitats vary in relation to nearby historical samples (Blake et al. 1987, Schaff et al. 1992), providing regional biogeographic context. Communities at Blake Ridge had higher densities in mussel and clam bed habitats but similar densities in microbial mat habitats to nearby shallower samples (1,993–1,996 m; Blake et al. 1987), while sediments adjacent to mussel beds and in clam beds had similar densities to sediments found at 850 m (Schaff et al. 1992). Microbial mat habitats at Cape Fear had similar densities to the nearest soft sediments; however, background sediments were much lower (Blake et al. 1987). For both Cape Fear and Blake Ridge, low sedimentation rates and carbon flux (0.6 g C m^{-2} y^{-1}) estimated nearby (within 60 km, Schaff et al. 1992) combined with lower observed sediment percent carbon content (0.5–0.98% this study; 1.2–1.6% Schaff et al. 1992) may help explain the low densities of infauna found at these seeps.

For Cape Lookout microbial mat habitats, densities were lower than those found at similar depths (1,000 m; Blake et al. 1987), but similar to deeper locations (1,500 m; Blake et al. 1987). Carbon flux estimates from sites nearby suggest high rates (20 g C m^{-2} y^{-1}, Schaff et al. 1992) in this area which does not help explain the lower densities observed in this study. The northern shallow sites, Pea Island and Kitty Hawk, were closest to the same historical sampling locations (within 75 km, Blake et al. 1987; Schaff et al. 1992). Background sediments at Kitty Hawk had similar densities to the historical samples, while those at Pea Island were higher. Of note is that sediment methane concentrations up to 4–5 µM were detected during historical sampling (Schaff et al. 1992), suggesting the previously high densities observed in this region may have contained seep habitats. Overall, seep habitats on the Atlantic margin represent areas of extremely high productivity compared to surrounding areas.

4.1.3.4 Macrofauna—Canyon Communities

Macrofaunal densities varied with depth in all of the southeast canyon features studied, with fluctuating highs and lows in North Keller, Hatteras, and Pamlico Canyons, corresponding to variable environmental conditions throughout the canyons. Submarine canyons are dynamic environments, often with gradients in food resources, sediment resuspension and deposition, resulting in differing benthic communities along the canyon axis (De Leo et al. 2010, Puig et al. 2014, Robertson et al. 2020). Hatteras, Keller, and North Keller canyons all had higher abundances than the previously studied mid-Atlantic canyons, Baltimore and Norfolk (Robertson et al. 2020), contributing to the idea that no two canyons are alike (De Leo et al. 2010).

High abundances have been documented in non-canyon sediments near Hatteras Canyon (Blake et al. 1987, Schaff et al. 1992). The canyons with the highest abundances also had overall lower diversity, suggesting organically enriched environments. The high influence of percent organic carbon on macrofaunal community variation suggests that productivity is a driver in all the canyons studied. The southeast canyons overall had similar diversity as the mid-Atlantic canyons, 65 and 66 taxa respectively. However, combined, the SE canyons increase margin-wide diversity in canyon habitats alone by 35%, indicating they are important contributors to regional biodiversity.

In addition, the individual differences among the southeast canyons, there appears to be regional differences among the five canyons studied, with the two southernmost canyons, Pamlico and Amphitheater, differing from the northern three canyons. These differences correspond to the zoogeographical break associated with Cape Hatteras (Blake et al. 1987, Cutler 1975) suggesting regional patterns in oceanography, hydrography, productivity and transport of organic matter to deep-sea areas that affects both canyon and non-canyon environments.

Historical sampling programs (Blake et al. 1987, Blake and Hilbig 1994, Aller and Aller 2002) have included non-canyon habitats nearby some of the canyons studied, providing important comparative data to the communities observed here. For example, infaunal communities from a non-canyon habitat (804 m) located 3.4 km south of North Keller Canyon (793 m) were previously described in Blake and Hilbig (1994). Densities within the canyon were more than twice the density in the non-canyon habitat but were dominated by similar taxa, including Cossuridae, Scalibregmatidae, and oligochaetes (Blake and Hilbig 1994) suggesting higher productivity within the canyon, resulting in higher densities, but potentially similar, family-level, taxonomic composition. For the undersampled Keller Canyon (n = 2 cores), the 660 m station was within 5.4–5.9 km of historical samples (530–651 m; Aller and Aller 2002, Blake and Hilbig 1994). Densities were similar (Blake and Hilbig 1994) or higher (Aller and Aller 2002) than non-canyon sediments; however, oligochaetes dominated the historical sites while Cossuridae dominated locations in this study.

The closest historical samples to our Hatteras Canyon stations were 12–13 km to the north (590–785 m; Blake and Hilbig 1994). Densities in Hatteras Canyon were much higher than the nearby non-canyon habitat but exhibited some similarities in dominant taxa, including Cossuridae, Scalibregmatidae, Orbiniidae, and Paraonidae (Blake and Hilbig 1994). A single station from Blake et al. (1987) was located between Pamlico and Amphitheater canyons but at much deeper depths (2,004 m; 14–17km) providing the only comparison for these canyons. Densities within Pamlico and Amphitheater canyons was higher than in non-canyon habitats; however, this pattern may be a function of sampling depths, given densities typically decline with depth. Our results support that submarine canyons are hotspots of benthic densities and differ from non-canyon habitats.

There are few studies highlighting hard-substrate-associated sediment communities within canyon environments despite the fact that canyon hard substrates are known to support high level of biodiversity (Pierdomenico et al. 2017, Huvenne et al. 2011, Orejas et al. 2009, Quattrini et al. 2015). Previous work

in Norfolk Canyon (Bourque et al. 2021) found similar densities but distinct community structure and higher diversity in hard substate associated sediment communities compared to those in the canyon axis. While the hard-substrate sediment communities observed in this study were at deeper depths than previously studied in Norfolk Canyon (Bourque et al. 2021) or sampled within the soft sediments found along the Pamlico Canyon axis (this study), some comparisons can be made. Hard-substrate communities in Norfolk and Pamlico Canyons (this study) did not exhibit any clear pattern with depth, similar to previous studies in Norfolk Canyon (Bourque et al. 2021).

Food availability, inferred from percent organic carbon in sediments, was a primary structuring factor in previous studies (Bourque et al. 2021) and this study, highlighting the importance of the availability of organic matter for infaunal communities. There were also some similarities in community composition, including similar proportions of Paraonidae, Cossuridae, and Bivalvia (Bourque et al. 2021). Hard-substrate habitats support high biodiversity that adds to the overall regional taxa pool (Bourque et al. 2021), and the hard substrates in deeper Norfolk and Pamlico Canyons likely also contribute to both the local and regional biodiversity.

4.2 Fish Communities

Section Authors: Andrea Quattrini, Tracey Sutton, Tara McIver, Joe Warren, Jennifer Miksis-Olds

4.2.1 Introduction

Deep-sea ecosystems along the US continental margin support a complex mixture of coastal, benthic, and open-ocean fishes, yet they remain inadequately inventoried and quantified. Off the US East Coast, this high diversity is driven by the intersection of oceanic waters with numerous topographically complex and rugged continental margin features, such as submarine canyons, cold seeps, lithoherms capped with corals, and coral-formed bioherms. These features influence the distribution and abundance of pelagic and demersal fishes, including many of commercial importance, while increasing both local and regional biodiversity.

Hardbottom habitats along the continental margin are also thought to play a role in the evolution and diversity of deep-sea fishes, facilitating the dispersal and maintenance of communities and providing sites for feeding, spawning, nursery habitat, and refugia from predation. Thus, we need to better characterize faunal and habitat distributions, determine the processes that differentiate ‘oceanic rim’ population and community structure, and determine the linkages between physical, chemical, and biological processes to better understand ecosystem structure and function.

The Mid-Atlantic Planning Area contains a variety of seafloor features across a broad depth range, and therefore provides a remarkable setting to determine how habitat and other environmental conditions influence fish communities in the deep sea. Deep SEARCH is a rarity among US deep-benthic habitat studies in its inclusion of a deep-pelagic (open ocean, greater than 200-m depth) component. Demersal fishes were previously surveyed throughout the region, and various degrees of habitat-specific associations have been noted. Ross and Quattrini (2007) determined there was a characteristic reef fish fauna in the region, which differed from the fish assemblages in off-reef habitats. Ross et al. (2015) noted that fishes were specific to macro or microhabitat features in submarine canyons and cold seeps north of Cape Hatteras (Norfolk and Baltimore canyons).

Although microhabitat associations of many fish species have been well documented on the upper to middle continental slope in the region, it remains unknown whether fish communities differ among broader-scale habitat features, such as submarine canyons, coral reefs, hardbottoms and cold seeps. Furthermore, it is unknown whether the multiple dimensions of biodiversity (taxonomic, functional,

phylogenetic) differ among the habitat types. Thus, we addressed these questions and examined the environmental factors that contribute to the variation in fish communities along the US Atlantic margin, from the FLS to the MAB, north of Cape Hatteras. Our investigations have revolved around the ecological connectivity between pelagic and deep coral/canyon/cold-seep (DCCC) habitats, specifically "boundary community" dynamics (what pelagic taxa occur over DCCC habitats, what functional groups do they represent, and do these assemblages differ from those occurring further offshore?), pelagic habitat use by early life history stages of DCCC fauna, and trophic resources provided to DCCC communities by DSL impingement.

4.2.2 Methods

We divided the fish components of this project into two main components: pelagic fishes (those taxa observed or collected in midwater, not specifically associated with the seafloor) and demersal fishes (those taxa observed on or just off the bottom; *sensu* Drazen and Sutton, 2017). As methodology and sampled size varied greatly between the two components, each is treated separately.

4.2.2.1 Pelagic Fishes

Our pelagic fish surveys focused on the intermediate-trophic-level fauna ('oceanic micronekton'), the dominant components of acoustically detected DSLs throughout the World Ocean, and the prey of deep-demersal megafauna. Oceanic micronekton can be quantitatively sampled by midwater trawling and semi-quantitatively sensed by acoustic echosounding. The former precisely determines what and how much is there, and the latter informs the distributions of whole assemblages over fine vertical scales (1 m) and large horizontal scales (> 1 km). Work package adjustment was required due to a series of unavoidable early project set-backs (Hurricane Irma prevented pelagic team participation on the 2017 *Pisces* cruise, a ship's accident cancelled the 2018 *Nancy Foster* cruise, and ship's technical limitations prevented water-column sampling on the 2018 *Brooks McCall* cruise). That said, component focus was placed on midwater trawl samples and acoustic echograms collected during the 2019 *Nancy Foster* cruise as well as a collaborative project involving midwater trawl samples collected during four ADEON cruises.

We deployed Isaacs-Kidd Midwater trawls (2.5 m^2, 3-mm net mesh with 1-mm cod-end mesh) during ADEON and towed for approximately 1–5 hours at approximately 2 kts ground speed to sample midwater fauna, whereas We deployed tucker trawls (6 m^2, 3-mm mesh) during *Nancy Foster* cruises for approximately 1–5 hours at ~1.5 kts ground speed. We quantitatively processed tucker trawl samples at sea. Isaacs-Kidd Midwater trawl samples were shipped to Sutton's lab for detailed taxonomic analysis and then returned to the ADEON Co-PI, Dr. Joseph Warren. ADEON is led by Dr. Jennifer Miksis-Olds, a Deep SEARCH Co-PI, while members of Deep SEARCH Co-PI Sutton's lab participated on three ADEON cruises. In total, we collected 60 trawl samples, with concomitant echosounding, at 10 stations within the Deep SEARCH/ADEON research area. A complete inventory of taxa collected during these surveys is presented in **Table 4-15** and **Table 4-16**.

4.2.2.2 Demersal Fishes

Our demersal fish surveys centered on the analysis of video from submersible and ROV dives use to determine if fish assemblages vary among benthic habitat types (coral vs. canyon vs. seep vs. hardbottom vs. soft sediment). Once the submersible/ROV reached near-bottom depths, we identified all fishes and enumerated them until the submersible/ROV ascended. Additionally, we documented time, microhabitat, macrohabitat and habitat type for each fish observed. We took high-resolution, still frames and video clips from the original videos to aid in further identification of fishes and to use for publication purposes. Fishes were enumerated and identified from all of the video collected during dives on the cruises AT41, RB1903, OE-EX1903-L2, OE-EX1907, and from 11 dives on the cruise OE-EX1806 (**Table 4-17**). We also created a fish identification guide (see Appendix). We created species-accumulation curves for each

macrohabitat type (canyon, coral, seep, hardbottom, soft sediment) in *R* using vegan (Oksanen et al. 2020).

Table 4-15. Summary of submersible and ROV dives analyzed for demersal fish surveys

Cruise	Date	Dive #	Site Name	On-Bottom Latitude	On-Bottom Longitude	Mean Temp (°C)	Min Depth (m)	Max Depth (m)	Median Depth (m)	Bottom Time (h)
AT41	20-Aug-2018	AL4960	Wilmington Canyon	38.4294	-73.536	-	656	688	672	3:25:00
AT41	21-Aug-2018	AL4961	Pea Island Seep	35.705	-74.813	7.59	408	511	460	7:28:00
AT41	23-Aug-2018	AL4962	Richardson Reef	32.014	-77.396	9.21	750	820	785	6:33:00
AT41	24-Aug-2018	AL4963	Richardson Reef	31.985	-77.416	9.75	750	820	785	4:35:00
AT41	25-Aug-2018	AL4964	Blake Escarpment Deep	31.323	-77.245	4.32	1,200	1,273	1,237	7:20:00
AT41	26-Aug-2018	AL4965	Stetson Banks	32.012	-78.314	8.47	434	545	490	6:56:00
AT41	27-Aug-2018	AL4966	Stetson Banks	32.070	-78.374	8.36	395	403	399	6:20:00
AT41	28-Aug-2018	AL4967	Blake Ridge Seep	32.495	-76.190	3.35	2,162	2,169	2,166	5:48:00
AT41	29-Aug-2018	AL4968	Cape Fear Coral Mound	33.576	-76.468	10.06	378	458	418	6:29:00
AT41	30-Aug-2018	AL4969	Pamlico Canyon	34.937	-75.169	-	1,100	1,607	1,354	7:01:00
AT41	31-Aug-2018	AL4970	Norfolk Canyon	37.043	-74.315	3.72	1,665	1,943	1,804	6:56:00
RB1903	10-Apr-2019	J2-1128	Richardson Reef	31.880	-77.374	5.76	731	762	747	9:30:00
RB1903	13-Apr-2019	J2-1129	Richardson Reef	31.985	-77.413	9.72	690	708	699	11:15:00
RB1903	17-Apr-2019	J2-1130	Savannah Banks	31.754	-79.195	8.55	511	553	532	8:42:00
RB1903	17-Apr-2019	J2-1131	Blake Escarpment Deep	31.285	-77.237	4.08	1,306	1,359	1,333	13:27:00
RB1903	21-Apr-2019	J2-1132	Pamlico Canyon	34.914	-75.184	3.90	1,136	1,839	1,488	23:40:00
RB1903	23-Apr-2019	J2-1133	Pea Island Seep	35.675	-74.792	11.12	300	353	327	9:28:00
RB1903	24-Apr-2019	J2-1134	Kitty Hawk Seep	35.926	-74.805	9.93	214	476	345	14:56:00
RB1903	25-Apr-2019	J2-1135	Cape Lookout Deep	33.916	-75.832	4.48	940	1,029	985	2:40:00
RB1903	27-Apr-2019	J2-1136	Blake Ridge Seep	32.493	-76.190	3.28	2,140	2,164	2,152	15:14:00
RB1903	28-Apr-2019	J2-1137	Cape Fear Seep	32.979	-75.929	2.68	2,592	2,608	2,600	8:04:00
RB1903	29-Apr-2019	J2-1138	Richardson Reef (West)	31.893	-77.699	5.66	658	758	708	8:11:00
EX1903L2	21-Jun-2019	01	Canaveral Deep	28.1506	-79.3607	7.13	697	805	751	5:26:41
EX1903L2	22-Jun-2019	02	Stetson Mesa South Mounds	29.0664	-79.2670	8.33	712	784	748	5:44:30
EX1903L2	23-Jun-2019	03	Stetson Mesa South Scarp	29.4525	-79.3426	7.37	757	893	825	5:18:22
EX1903L2	24-Jun-2019	04	Blake Plateau Knolls	29.3915	-78.2699	10.57	738	827	783	6:53:08
EX1903L2	25-Jun-2019	05	Central Blake Plateau Mounds	30.3221	-78.1278	10.16	772	866	819	4:31:26
EX1903L2	27-Jun-2019	06	Stetson Mesa Potential Seep	30.2606	-79.3492	7.48	730	841	786	5:52:05
EX1903L2	28-Jun-2019	07	Savannah Banks	31.3542	-79.0660	10.71	424	461	443	7:04:50
EX1903L2	29-Jun-2019	08	Central Blake Plateau Scarp	30.5507	-78.0523	6.13	846	1,008	927	5:19:04
EX1903L2	30-Jun-2019	09	Blake Escarpment Mid	31.3173	-77.0929	4.07	1,295	1,426	1,361	6:26:49
EX1903L2	1-Jul-2019	10	Richardson Reef	32.0574	-77.4008	8.46	574	886	730	7:02:08
EX1903L2	3-Jul-2019	11	Deep "Dodge" Canyon, NC	35.3748	-74.4491	4.20	1,166	1,348	1,257	3:29:40
EX1903L2	4-Jul-2019	12	Pamlico Canyon Deep	34.3471	-74.4062	2.32	3,082	3,498	3,290	4:13:43
EX1903L2	5-Jul-2019	13	Roanoke Minor Canyon	35.5550	-74.4605	4.56	832	1,056	944	6:34:53
EX1903L2	6-Jul-2019	14	Bodie Island Seep	35.4411	-74.4874	7.72	333	446	390	7:44:55

Cruise	Date	Dive #	Site Name	On-Bottom Latitude	On-Bottom Longitude	Mean Temp (°C)	Min Depth (m)	Max Depth (m)	Median Depth (m)	Bottom Time (h)
EX1903L2	7-Jul-2019	15	Currituck Landslide Base	36.2113	-74.3756	3.97	1,457	1,645	1,551	4:13:31
EX1903L2	8-Jul-2019	16	Washington Canyon	37.2438	-74.2489	5.82	300	996	648	5:16:30
EX1903L2	9-Jul-2019	17	Wilmington Canyon	38.1895	-73.2607	3.83	1,376	1,541	1,459	06:26:39
EX1903L2	10-Jul-2019	18	Baltimore Canyon	38.0758	-73.5087	5.36	477	770	624	06:52:07
EX1903L2	11-Jul-2019	19	Norfolk Deep Seep	36.5190	-74.2914	3.84	1,508	1,623	1,566	05:58:32
EX1907	1-Nov-2019	01	Blake Plateau South	28.2593	-79.0284	6.69	800	870	835	06:50:33
EX1907	2-Nov-2019	02	Stetson Mesa East	29.3514	-79.0722	8.49	729	826	778	09:05:30
EX1907	3-Nov-2019	03	Stetson Mesa West	29.5181	-79.2731	8.57	744	809	777	03:51:34
EX1907	4-Nov-2019	04	Stetson Mound Field	30.2416	-79.1656	8.49	801	836	819	06:56:52
EX1907	5-Nov-2019	05	Stetson Mound Field	30.2519	-79.1356	8.57	794	830	812	02:36:26
EX1907	6-Nov-2019	06	Central Blake Plateau Mound	30.4555	-78.4478	9.42	743	842	793	08:57:21
EX1907	7-Nov-2019	07	Northern Blake Plateau	31.0101	-78.2320	8.97	778	807	793	06:41:22
EX1907	15-Nov-2019	08	Miami Terrace	25.3377	-79.5273	7.40	473	564	519	07:27:06
EX1907	16-Nov-2019	09	Key Largo Deep	24.4613	-80.0868	6.45	559	642	601	06:26:59
EX1907	17-Nov-2019	10	Pourtalès Terrace	24.2235	-80.4245	9.85	309	404	357	08:08:48
EX1907	18-Nov-2019	11	Key West Deep	23.5856	-81.5593	4.31	1,108	1,218	1,163	06:08:43
EX1907	19-Nov-2019	12	“Berg Bits”	23.5905	-83.2317	4.81	904	973	939	06:51:56
EX1806	14-Jun-2018	01	Blake Escarpment North	32.0524	-76.8446	3.88	1,675	1,736	1,706	05:20:55
EX1806	17-Jun-2018	04	Blake Escarpment South	30.9401	-77.3285	4.10	1,246	1,321	1,284	05:52:57
EX1806	19-Jun-2018	05	Stetson Mesa South	29.3708	-79.7293	9.20	705	734	720	06:35:35
EX1806	20-Jun-2018	06	Stetson Mesa North	30.4034	-79.5982	8.68	709	789	749	05:16:55
EX1806	21-Jun-2018	07	Richardson Ridge	31.7708	-77.3643	6.73	778	873	826	03:36:40
EX1806	22-Jun-2018	08	Richardson Scarp	32.0930	-77.1595	4.50	868	1,006	937	06:29:10
EX1806	24-Jun-2018	10	Cape Fear	33.5785	-76.4629	8.62	370	454	412	07:02:43
EX1806	28-Jun-2018	14	Hatteras Canyon	35.2964	-74.9468	7.61	302	510	406	07:17:54
EX1806	29-Jun-2018	15	Keller Canyon	35.5563	-74.7931	5.64	506	728	617	05:18:02
EX1806	30-Jun-2018	16	Pea Island Seep	35.7077	-74.8128	7.60	328	521	425	06:58:39
EX1806	1-Jul-2018	17	Currituck Landslide	36.2284	-74.4646	3.65	1,747	1,881	1,814	06:09:45

Table 4-16. Traits examined in functional diversity analyses

Trait	Levels
Maximum size	centimeters
Gregariousness	singleton, paired to small schools, always schooling
Motility level	swimming, crawling, sedentary/lying, sessile
Trophic guild	planktivore, carnivore, scavenger, benthic invertivore, unknown
Feeding mechanism	benthic forager, surface deposit feeder, predatory, scavenger, filter feeder, benthopelagic forager
body shape	laterally compressed, fusiform, laterally depressed, anguilliform, elongate, globiform
Reproduction	benthic eggs, pelagic eggs, live birth, unknown
Eye size/body size ratio	small, moderate, large

**Traits were compiled from FishBase, FAO, FWNA*

4.2.2.2.1 Multivariate Analyses of Demersal Fish Assemblage Structure

The large number of spatially discrete observations of demersal fishes accompanied with environmental data facilitated community analysis across a range of benthic habitat types. We used multivariate analyses to determine differences in demersal fish assemblages between regions (MAB: north of Cape Hatteras; SEUS: Cape Canaveral FL to Cape Hatteras NC; FLS: Key Largo, FL, to Cape Canaveral, FL), habitats (canyon, seep, hardbottom, coral reef [*L. pertusa*], soft sediment), and depth ranges (200-m intervals; PRIMER 6, Clarke and Warwick 2001, Clarke and Gorley 2006). We created a non-metric, MDS ordination plot and a dendrogram based on hierarchical clustering of group average linking from a Bray-Curtis similarity matrix based on square-root transformed relative abundances per dive; similarity clusters from the clustering were overlain onto the MDS plots.

We used two-way crossed ANOSIM tests to determine whether there were significant differences in fish assemblages among habitats or depth ranges while allowing for the possibility of differences among regions. R values closer to 1 indicated stronger dissimilarities among communities. Following these analyses, we conducted a dbRDA and a DISTLM test on the Bray Curtis similarity matrix to determine the proportion of variation in fish assemblages explained by the following factors: median depth of dive, mean bottom temperature of dive, habitat (coral, canyon, seep, hardbottom, soft sediment) and region (MAB, SEUS, FLS).

Temperature and depth were log-transformed prior to analyses and AIC was used to choose the best model of environmental (predictor) variables. On the dbRDA, we plotted the variables (as vectors) responsible for the variation in assemblages; we color-coded each dive to habitat type and region. We duplicated the dbRDA to overlay median depth and mean temperature of each dive (as bubbles) and species (as vectors) that were important contributors to the assemblage differences; species vectors were chosen with a Pearson correlation coefficient (> 0.5).

4.2.2.2.2 Functional Diversity Analyses of Demersal Fish Assemblages

We conducted functional diversity estimates in *R* using the *FD* package (Laliberté et al. 2015) to examine whether habitats in particular depth ranges (500-m depth intervals down to 2,000 m, then 2000–3,500 m depth) had higher functional diversity. We examined eight traits in the analysis, including: maximum size,

gregariousness, motility level, trophic guild, feeding mechanism, body shape, reproduction, and eye size **(Table 4-16**).

We coded maximum size and gregariousness as continuous traits whereas the others were categorical and were coded as binary data. We used Gower's dissimilarity measure, which is appropriate for continuous and categorical variables, with a podani method for ordinal variables to calculate dissimilarity among species based on the trait data. We used the dbFD function, which employs principal coordinates analysis (PCoA) to return PCoA axes, which are then used as 'traits,' to calculate several functional diversity indices. Such indices included the functional richness, functional evenness, functional divergence, and functional dispersion (Laliberté and Legendre 2010).

Indices were weighted by species abundances as appropriate. We also calculated functional diversity using Picante (Kembel et al. 2010) and a clustering algorithm based on group average linking based on Petchey and Gaston (2002). We created box plots of functional diversity results in *R* using ggplot2.

4.2.3 Results and Discussion

4.2.3.1 Pelagic Fishes

Pelagic sampling and acoustic sensing detected dense aggregations of water-column taxa in close proximity with numerous abrupt topographic features, suggesting widespread pelagic-benthic coupling over deepwater features of interest along the US Atlantic OCS. Spatial interactions between DSL and DCCC features were readily apparent from *Nancy Foster* water-column acoustic surveys (**Figure 4-50**). During both ADEON and Deep SEARCH sampling, the majority of fish taxa (55 and 56%, respectively) and highest numbers (58 and 42%) collected during midwater surveys were primarily mesopelagic, confirming that these layers comprised pelagic taxa, not deep-demersal or coastal taxa. Thus, trophic subsidy from pelagic resources is undoubtedly an integral component of DCCC community ecology.

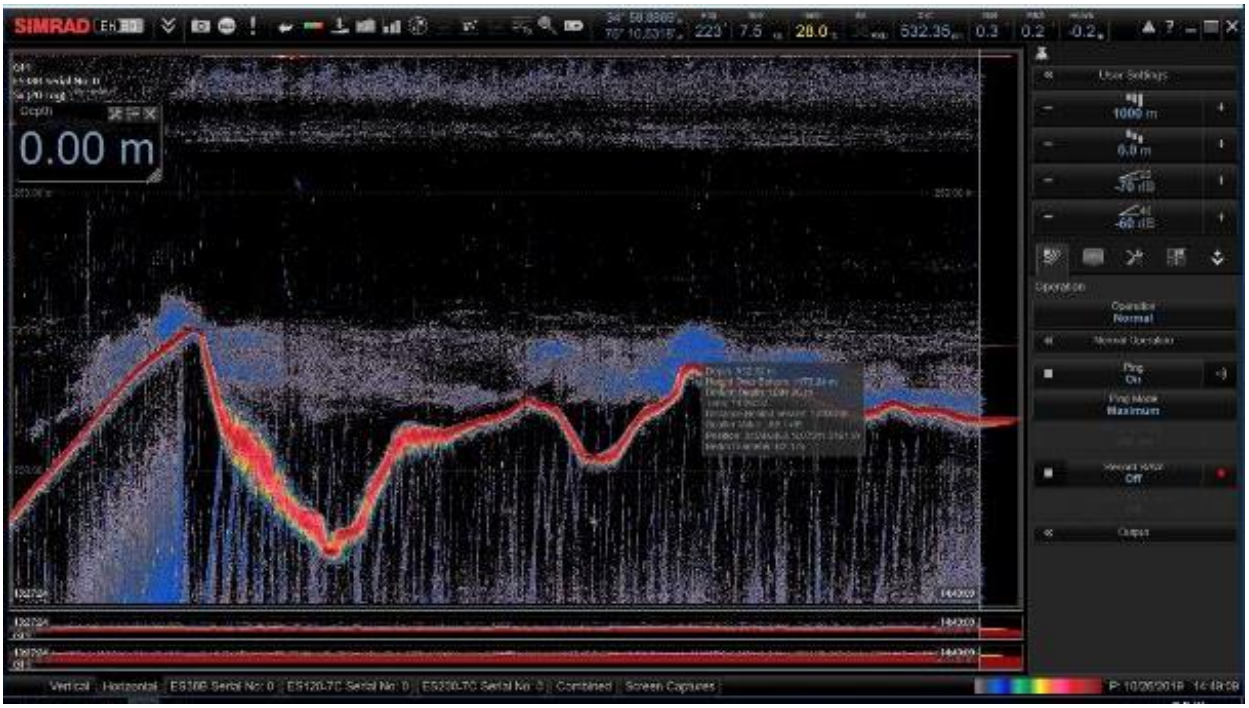

Figure 4-50. DSL association with bottom topography at Pamlico Canyon

DSL (upper blue and gray band) association with bottom topography (irregular red band) at Pamlico Canyon. Echogram was derived from 18-kHz acoustic sensing aboard the 2019 *Nancy Foster* research cruise.

From the benthic to pelagic perspective, sample analyses revealed that the water column over DCCC features serves as habitat for juvenile life stages of reef-associated fauna. Here we note an important early life-history distinction between juveniles (represented in these data) and larvae (represented in many pelagic surveys), as the former more closely represent the recruitment base for DCCC habitats than the latter, given that juveniles have survived the "99% mortality gauntlet" experienced by larvae. Thus, distributions of juveniles is more indicative of direct recruitment processes than those of larvae. Among fishes, approximately one in eight species collected were taxa considered reef-associated as adults. Perhaps no benthic fish taxon makes better use of pelagic habitat than eels. During both field campaigns, eel leptocephalus larvae were either the first- (*Nancy Foster*, **Table 4-18)** or second-ranked (ADEON, **Table 4-17**) taxon numerically. Many of the eel species represented by these larvae are reef- and/or canyon-associated as adults.

We concluded that interactions with the overlying water column are integral to the structure, complexity, and functioning of benthic communities in the Deep SEARCH study area. Trawl- and acoustic-based results reveal a rich mesopelagic micronekton assemblage overlying Deep SEARCH topographic features of interest, and in many locations, we observed direct impingement of dense layers of pelagic fauna with such features. Direct trophic studies are outside the scope of analyses in this chapter, but Deep SEARCH midwater trawling provided a large amount of material for stable isotope studies being conducted in other labs, particularly the Demopoulos and Morrison Labs at USGS (Chapter 4.4). We also found ample evidence of benthic connectivity with the water column; late juveniles of reef-associated taxa were conspicuous components of the pelagic assemblage, indicative of a key recruitment pathway.

Table 4-17. Fishes collected and identified during ADEON pelagic sampling

ADEON pelagic sampling in the Deep SEARCH project area. n = number of specimens collected; juv = juvenile.

Taxon	n	Adult habitat
Cyclothone spp.	2,003	Meso- and bathypelagic
Elopomorpha (larvae)	1,019	Coastal and deep benthic
Pleuronectiformes (larvae)	841	Coastal
Benthosema glaciale	205	Mesopelagic
Cyclothone braueri	190	Mesopelagic
Paralepididae	100	Mesopelagic
Perciformes	100	Coastal and deep reef
Myctophidae	98	Mesopelagic
Acanthurus spp.	61	Coastal reef
Scorpaeniformes (juv)	44	Coastal and deep reef
Diaphus dumerilii	35	Mesopelagic
Gonostoma atlanticum	33	Mesopelagic
Pollichthys mauli	31	Mesopelagic
Chauliodus sloani	29	Mesopelagic
Maurolicus weitzmani	28	Mesopelagic
Nesiarchus nasutus	28	Mesopelagic
Ophidiiformes (juv)	28	Deep demersal
Stomiiformes	27	Mesopelagic
Stomiidae	26	Mesopelagic

Taxon	n	Adult habitat
Antigonia combatia (juv)	25	Deep reef
Bonapartia pedaliota	24	Mesopelagic
Carangidae (juv)	23	Epipelagic
Chlorophthalmus agassizi	21	Deep demersal
Tetraodontiformes (juv)	21	Coastal reef
Melamphaes spp.	19	Mesopelagic
Vinciguerria poweriae	19	Mesopelagic
Canthigaster spp.	18	Coastal reef
Melamphaidae	18	Mesopelagic
Trachurus lathami	18	Epipelagic
Valenciennellus tripunctulatus	18	Mesopelagic
Ceratoscopelus maderensis	16	Mesopelagic
Lobianchia dofleini	16	Mesopelagic
Notolychnus valdiviae	16	Mesopelagic
Argyropelecus hemigymnus	15	Mesopelagic
Scorpaenidae (juv)	14	Deep reef
Lampanyctus (Nannobrachium) sp.	13	Mesopelagic
Sigmops elongatus	13	Mesopelagic
Sternoptyx diaphana	13	Meso- and bathypelagic
Synodontidae (juv)	13	Coastal
Teleostei	13	---
Argyropelecus aculeatus	12	Mesopelagic
Bolinichthys supralateralis	12	Mesopelagic
Diplospinus multistriatus	12	Mesopelagic
Lepidophanes guentheri	12	Mesopelagic
Pomacanthidae (juv)	11	Coastal reef
Scombridae (juv)	11	Epipelagic
Vinciguerria nimbaria	10	Mesopelagic
Selene vomer (juv)	9	Coastal
Ceratoscopelus warmingii	8	Mesopelagic
Bramidae	7	Mesopelagic
Diaphus splendidus	7	Mesopelagic
Lampanyctus cuprarius	7	Mesopelagic
Bolinichthys photothorax	6	Mesopelagic
Cyclothone pallida	6	Mesopelagic
Gobiidae (larvae)	6	Coastal reef
Myctophum affine	6	Mesopelagic
Nessorhamphus ingolfianus	5	Mesopelagic
Balistes capriscus	5	Coastal reef
Benthosema suborbitale	5	Mesopelagic
Diaphus spp.	5	Mesopelagic
Dysommina rugosa	5	Deep reef

Taxon	n	Adult habitat
Gadiformes (juv)	5	Deep demersal
Holocentridae (juv)	5	Coastal reef
Scopelogadus mizolepis	5	Mesopelagic
Stephanolepis hispidus	5	Coastal reef
Vinciguerria attenuata	5	Mesopelagic
Auxis thazard	4	Epipelagic
Bregmaceros spp.	4	Mesopelagic
Chaetodontidae (juv)	4	Coastal reef
Cyclothone microdon	4	Meso- and bathypelagic
Hygophum macrochir	4	Mesopelagic
Hygophum taaningi	4	Mesopelagic
Idiacanthus fasciola	4	Mesopelagic
Nemichthys scolopaceus	4	Mesopelagic
Omosudis lowii	4	Mesopelagic
Serrivomer beanii	4	Meso- and bathypelagic
Caulolatilus spp.	3	Deep demersal
Diogenichthys atlanticus	3	Mesopelagic
Lampanyctus alatus	3	Mesopelagic
Lampanyctus ater	3	Mesopelagic
Lampanyctus pusillus	3	Mesopelagic
Lutjanidae (juv)	3	Coastal reef
Monacanthidae (juv)	3	Coastal reef
Notosudidae	3	Mesopelagic
Pomacentridae (juv)	3	Coastal reef
Sphoeroides sp. (juv)	3	Coastal reef
Stephanolepis sp.	3	Coastal reef
Triglidae (juv)	3	Coastal
Benthodesmus simonyi	2	Mesopelagic
Carapidae (juv)	2	Coastal
Centrobranchus nigroocellatus	2	Mesopelagic
Derichthys serpentinus	2	Mesopelagic
Engraulidae (juv)	2	Coastal
Eurypharynx pelecanoides	2	Meso- and bathypelagic
Fistulariidae (juv)	2	Coastal reef
Howella atlantica	2	Mesopelagic
Hygophum benoiti	2	Mesopelagic
Ichthyococcus ovatus	2	Mesopelagic
Lampanyctus lineatus	2	Mesopelagic
Lampanyctus photonotus	2	Mesopelagic
Nealotus tripes	2	Mesopelagic
Parasudis truculenta (juv)	2	Deep demersal
Polymixia lowei (juv)	2	Deep demersal

Taxon	n	Adult habitat
Pterois spp. (juv)	2	Coastal reef
Scopelarchidae	2	Mesopelagic
Selene vomer (juv)	2	Coastal
Stomias affinis	2	Mesopelagic
Thunnus spp.	2	Epipelagic
Astronesthes similus	1	Mesopelagic
Bolinichthys sp.	1	Mesopelagic
Carapus bermudensis (juv)	1	Coastal
Chaunacidae (juv)	1	Deep demersal
Coryphaena hippurus (juv)	1	Epipelagic
Dactylopterus volitans (juv)	1	Coastal
Diaphus brachycephalus	1	Mesopelagic
Diaphus lucidus	1	Mesopelagic
Diaphus mollis	1	Mesopelagic
Dolicholagus longirostris	1	Mesopelagic
Echeneidae (juv)	1	Coastal
Euthynnus alletteratus (juv)	1	Epipelagic
Evermannella indica	1	Mesopelagic
Evermannellidae	1	Mesopelagic
Exocoetidae (juv)	1	Epipelagic
Gadella imberbis (juv)	1	Deep demersal
Hippocampus erectus (juv)	1	Coastal
Istiophoridae (larvae)	1	Epipelagic
Katsuwonus pelamis	1	Epipelagic
Liopropoma sp.	1	Coastal and deep reef
Lobianchia gemellarii	1	Mesopelagic
Lophiiformes	1	Meso- and bathypelagic
Margrethia obtusirostra	1	Mesopelagic
Nemichthys sp.	1	Mesopelagic
Nomeidae (juv)	1	Mesopelagic
Nomeus gronovii	1	Mesopelagic
Photonectes achirus	1	Mesopelagic
Photostomias guernei	1	Mesopelagic
Poromitra sp.	1	Mesopelagic
Priacanthidae (juv)	1	Coastal reef
Prionotus sp. (juv)	1	Coastal
Scopeloberyx sp.	1	Mesopelagic
Serranidae (juv)	1	Coastal reef
Sigmops bathyphilus	1	Meso- and bathypelagic
Sphyraena barracuda	1	Coastal reef
Sphyraenidae (juv)	1	Coastal reef
Sternoptyx sp.	1	Meso- and bathypelagic

Taxon	n	Adult habitat
Symbolophorus veranyi	1	Mesopelagic
Synaphobranchidae	1	Deep demersal
Trichiuridae (juv)	1	Deep demersal
Vinciguerria sp.	1	Mesopelagic
Zoarcidae (juv)	1	Deep demersal

Table 4-18. Fishes collected and identified during 2019 *Nancy Foster* sampling

Sampling in the Deep SEARCH project area. n = number of individuals collected.

Fish Taxa	n	Adult Habitat
Elopomorpha (larvae)	195	Coastal
Teleost	101	--
Pleuronectiformes	78	Coastal
Cyclothone braueri	55	Mesopelagic
Acanthurus sp.	22	Coastal reef
Diaphus dumerilii	17	Mesopelagic
Stomiiformes	17	Mesopelagic
Gempylidae	14	Mesopelagic
Myctophidae	14	Mesopelagic
Cyclothone microdon	13	Meso- and bathypelagic
Dicrolene nigra	12	Deep demersal
Diaphus sp.	11	Mesopelagic
Paralepididae	11	Mesopelagic
Sternoptyx diaphana	11	Meso- and bathypelagic
Scorpaenidae	9	Deep demersal
Cyclothone sp. DAM	8	Meso- and bathypelagic
Notolychnus valdiviae	8	Mesopelagic
Melamphaes sp.	6	Mesopelagic
Pollichthys mauli	6	Mesopelagic
Scopelarchidae	6	Mesopelagic
Bolinichthys supralateralis	5	Mesopelagic
Carangidae	5	Coastal
Gobiidae	5	Coastal reef
Canthigaster sp.	5	Coastal reef
Antigonia combatia	4	Deep reef
Chauliodus danae	4	Mesopelagic
Chlorophthalmus agassizi	4	Deep demersal
Cyclothone pallida	4	Mesopelagic
Foetorepus sp.	4	Coastal reef
Photostomias guernei	4	Mesopelagic
Sigmops elongatus	4	Mesopelagic
Stomiidae	4	Mesopelagic
Valencienellus tripunctulatus	4	Mesopelagic
Chauliodus sloani	3	Mesopelagic
Cyclothone pseudopallida	3	Mesopelagic
Lophiiformes	3	Deep demersal
Lutjanidae	3	Coastal reef

Fish Taxa	n	Adult Habitat
Nannobrachium cuprarium	3	Mesopelagic
Nezumia bairdii	3	Deep demersal
Aldrovandia phalacra	2	Deep demersal
Bolinichthys photothorax	2	Mesopelagic
Bramidae	2	Mesopelagic
Bregmaceros atlanticus	2	Mesopelagic
Diaphus mollis	2	Mesopelagic
Lampanyctus alatus	2	Mesopelagic
Lepidophanes guentheri	2	Mesopelagic
Liopropoma sp.	2	Deep reef
Myctophum affine	2	Mesopelagic
Notosudidae	2	Mesopelagic
Seriola rivoliana	2	Coastal and deep reef
Sphoeroides sp.	2	Coastal reef
Vinciguerria nimbaria	2	Mesopelagic
Antigonia combatia	1	Deep reef
Apogonidae	1	Coastal reef
Astronesthes similis	1	Mesopelagic
Benthosema suborbitale	1	Mesopelagic
Caranx sp.	1	Epipelagic
Conger sp.	1	Deep reef
Diaphus brachycephalus	1	Mesopelagic
Diretmidae	1	Mesopelagic
Etelis oculatus	1	Deep reef
Eustomias sp.	1	Mesopelagic
Idiacanthus fasciola	2	Mesopelagic
Melamphaidae	1	Mesopelagic
Nemichthys curvirostris	1	Mesopelagic
Psenes arafurensis	1	Mesopelagic
Sphyraena sp.	1	Coastal reef
Stephanolepis sp.	1	Coastal reef
Syngnathidae	1	Coastal reef
Synodontidae	1	Coastal
Tetraodontidae	1	Coastal reef

4.2.3.2 Demersal Fishes

We analyzed a total of 569:05:17 hours of video from 11 *Alvin* submersible dives (Cruise AT41), 11 ROV *Jason II* dives (Cruise RB1903), 19 EX1903-L2 ROV dives, 12 EX1907 ROV dives, and 11 EX1806 ROV dives. We observed a total of 15,317 fishes during all dives, representing 189 species from 76 families. Synaphobranchidae (17%), Bramidae (16%), Scorpaenidae (15%), Macrouridae (12%), and Zoarcidae (12%) were the most abundant families observed. *Brama* sp. (17%), *Synaphobranchus* cf. *kaupii* (17%), *Helicolenus dactylopterus* (16%), *Lycenchelys verrillii* (8%), *Nezumia bairdii* (7%), *Hoplostethus occidentalis* (3%), *Phycis chesteri* (3%), *Laemonema barbatulum* (3%), and *Nezumia sclerorhynchus* (3%) were the most abundant species observed in the videos.

Notably, 24 fish taxa observed in the videos were previously not known to occur in the study areas, and thus represent geographical range extensions (**Figure 4-51, Figure 4-52**), including Alepocephalidae, *Bassozetus taenia, Brosme brosme, Carcharhinus altimus, Cataetyx laticeps, Centrophorus granulosus, Chimaera cubana, C. monstrosa, Cottunculus thomsonii. C. microps. Cruriraja poeyi, C. rugosa, Epigonus occidentalis, Eustomias acinosus, Gadomus arcuatus, Gaidropsaurus argentatus, G. ensis, Laemonema robustum, Lepidion schmidti, Lycodes esmarkii, Neocyttus helgae, Nezumia longebarbata, Rajella fuliginea, Scyliorhinus hesperius, Somniosus microcephalus,* and *Squalogadus modificatus*. Most of these are southern range extensions for the species reported.

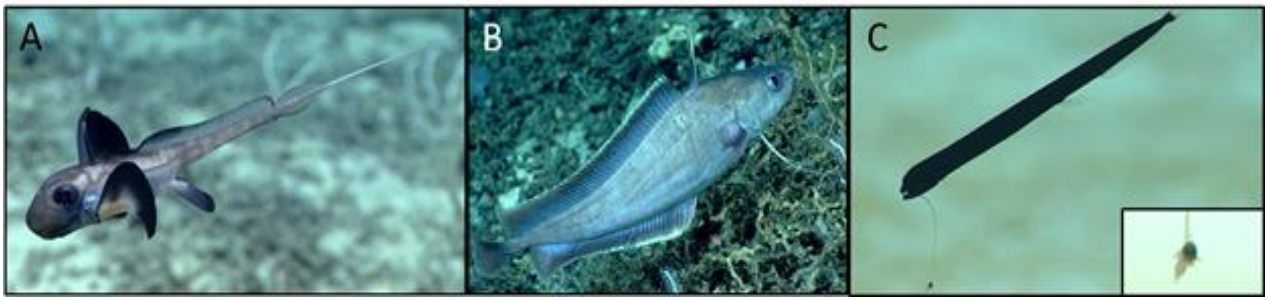

Figure 4-51. In situ frame grabs of fish species representing new records for the study areas
A= *Chimaera cubana* observed from OE-EX1907-DD-D04, B= *Laemonema robustum* observed from OE-EX1903L2-DD-D05, C= *Eustomias acinosus* observed from OE-EX1907-DD-D07.

Figure 4-52. In situ frame grabs of fish species representing range extensions for the study areas
A= *Brosme brosme* observed from OE-EX1903L2-DD-D18, B= *Cottunculus microps* observed from OE-EX1903L2-DD-D13, C= *Gaidropsaurus argentatus* observed from OE-EX1903L2-DD-

Ten submersible/ROV dives occurred in canyon habitats and the most abundant fish species observed were *Lycenchelys verrillii* (24%), *Nezumia bairdii* (21%), *Synaphobranchus* cf. *kaupii* (21%), *L. paxillus* (7%) and *Lycodes terraenovae* (6%). Seventeen submersible/ROV dives occurred in coral habitat. The most abundant fish species observed in coral habitat were *Synaphobranchus* cf. *kaupii* (35%), *Hoplostethus occidentalis* (18%), *N. sclerorhynchus* (10%), *Laemonema melanurum* (6%), and *H. mediterraneus* (4%). Twenty-six submersible/ROV dives occurred in hardbottom habitat. The most abundant fish species observed in hardbottom habitat were *Synaphobranchus* cf. *kaupii* (32%), *N. sclerorhynchus* (7%), *Dicrolene* sp. (7%), *L. barbatulum* (5%), *L. melanurum* (4%), and *Beryx decadactylus* (4%). Eight submersible/ROV dives occurred in seep habitat. The most abundant fish species observed in seep habitat were *Brama* sp. (36%), *H. dactylopterus* (33%), *Phycis chesteri* (5%), *L. barbatulum* (4%), and *Merluccius* cf. *albidus*/*bilinearis* (4%). From three submersible/ROV dives over soft-sediment habitats, the most abundant fish species observed were *Coryphaenoides armatus* (64%), *Peristedion truncatum* (8%), and *Bathypterois bigelowi* (7%).

Although species-accumulation curves indicated that further characterization of fish assemblages in the region is necessary to document the regional species pool, species richness appeared to differ among

some habitats (**Figure 4-53**). Canyons and cold seeps appear to harbor higher species richness than coral and hardbottom habitats, and all complex habitats appear to have higher species richness as compared to soft-sediment habitats.

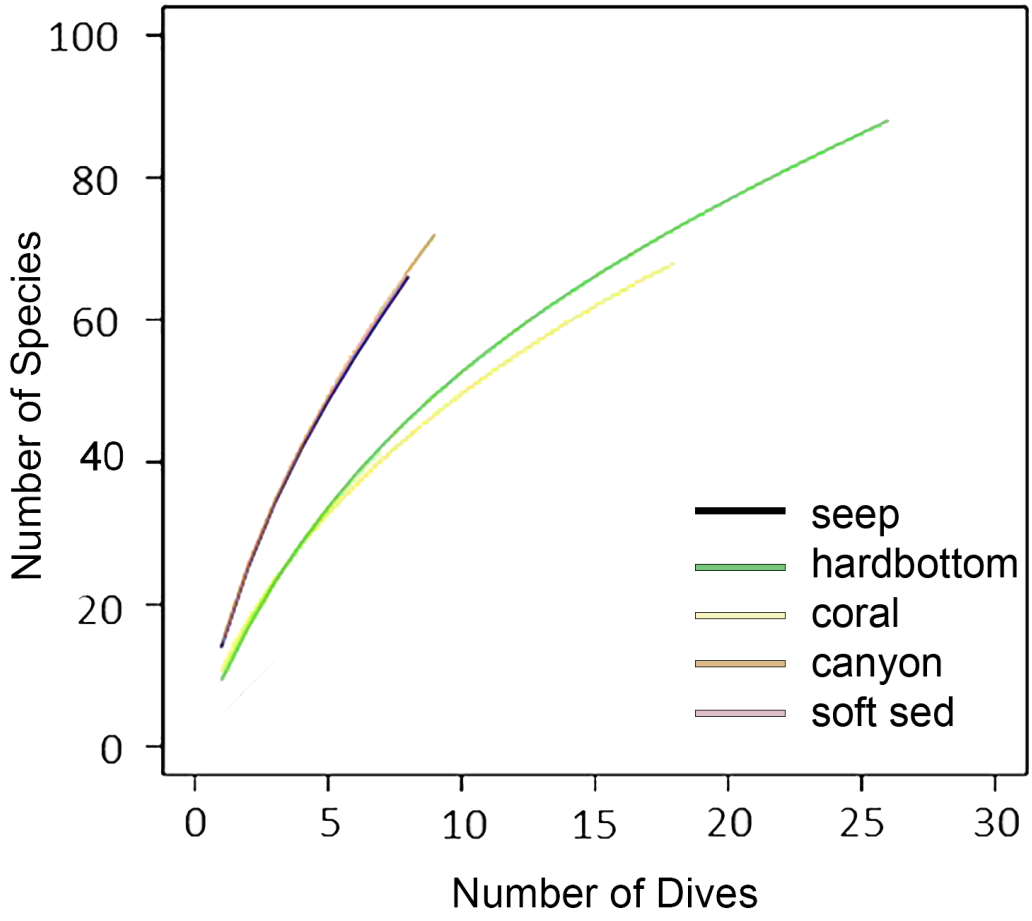

Figure 4-53. Species-accumulation curves by habitat

MDS ordination of demersal fish assemblages based on Bray-Curtis similarity matrices calculated from standardized, square-root transformed data for all fishes from all regions and habitat types indicated nine groupings at a 25% similarity level (**Figure 4-54, Figure 4-55).**

The majority of coral- and hardbottom-habitat fish assemblages clustered into two main groups, segregated by temperature and depth. This is seen clearly in the MDS plots that summarize the data in 200 m depth bins per habitat type and region **(Figure 4-56, Figure 4-57)**. Canyon habitats grouped together along with a few hardbottom habitats. Fish assemblages at seep habitats also differed, with shallower seeps in the SEUS different from deeper seeps in the MAB. A two-way ANOSIM test indicated differences among habitat types (Global R = 0.36, p = 0.001) and region (Global R = 2.4, p = 0.041).

Communities in the MAB were similar to those in SEUS and FLS, whereas communities in FLS differed slightly from those in the SEUS (R = 0.33, p = 0.03). Assemblages were significantly different among habitats, with the largest differences between seeps (R = 0.49 to 0.66) and all other habitats. Notably, canyon communities differed from coral habitats (R = 0.9), whereas assemblages at hardbottoms and coral reefs were highly similar (R = 0.1). Assemblages were also significantly dissimilar among depth ranges (Global R = 0.82, p = 0.001), with the largest differences between the shallowest and deepest depths. Notably, however, there were large differences (R = 0.5–0.6) in assemblages between adjacent

depth ranges on the upper to middle slope (300–900 m) and these tended to become less pronounced on the middle to lower slope (**Figure 4-56, Figure 4-57**).

When controlling for depth, regional differences became more apparent (Global R = 0.7, p = 0.1) with the largest differences between the FLS and SEUS (R = 0.94) fish assemblages.

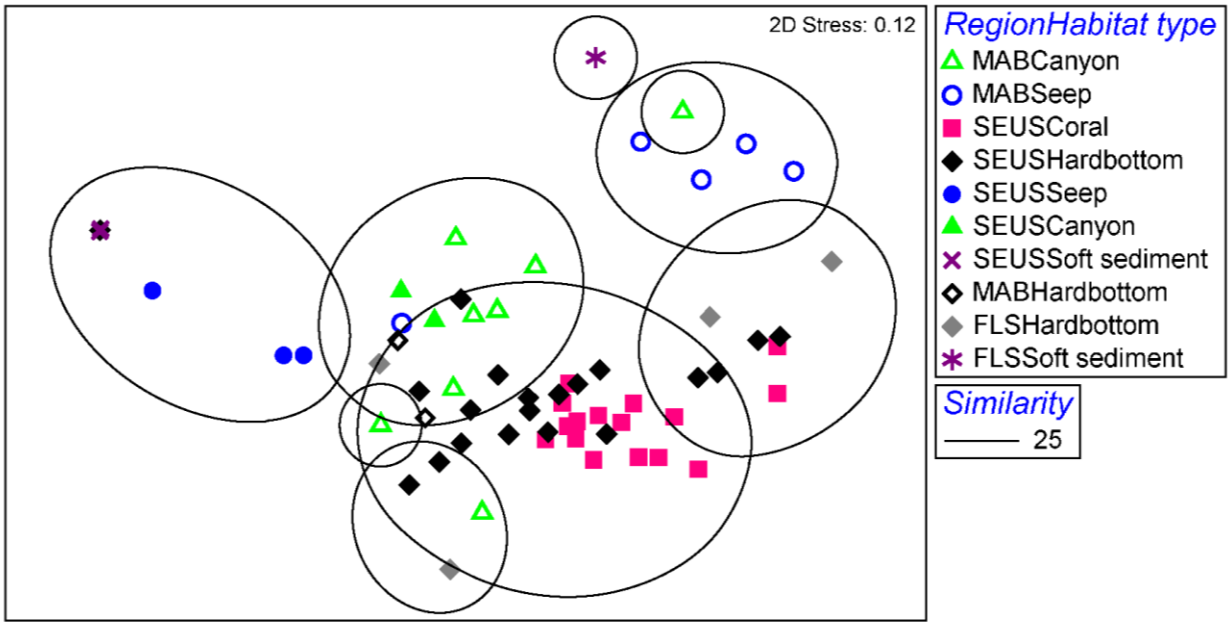

Figure 4-54. Non-metric multidimensional scaling ordination plot of fishes by habitat type
With each dive color coded to habitat and region based on Bray-Curtis similarity of log-transformed relative abundances.

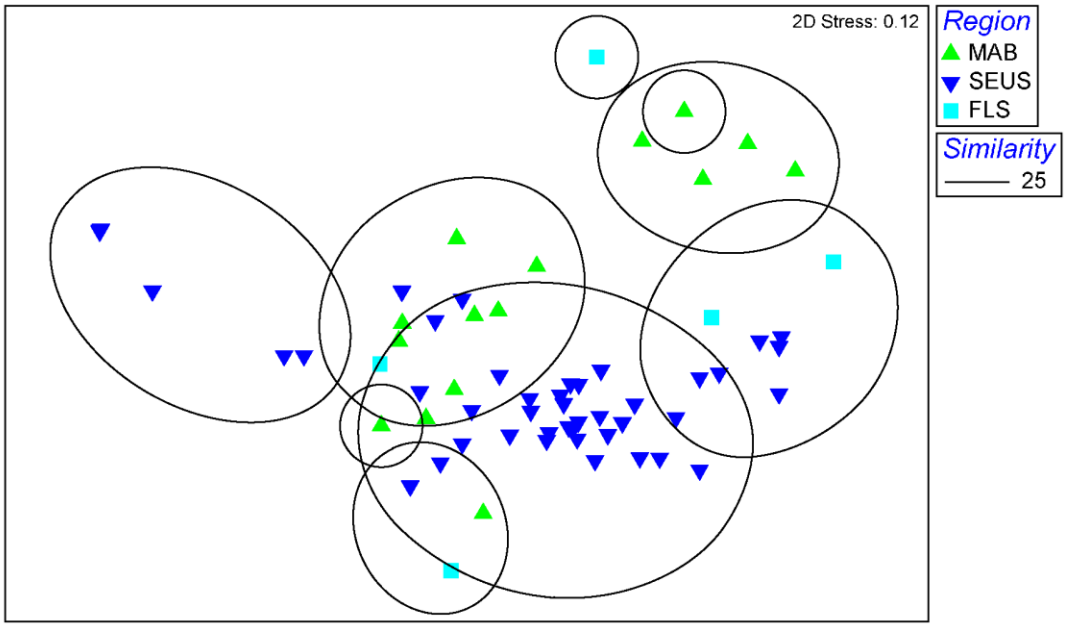

Figure 4-55. Non-metric multidimensional scaling ordination plot of fishes by region
With each dive color coded to region based on Bray-Curtis similarity of log-transformed relative abundances.

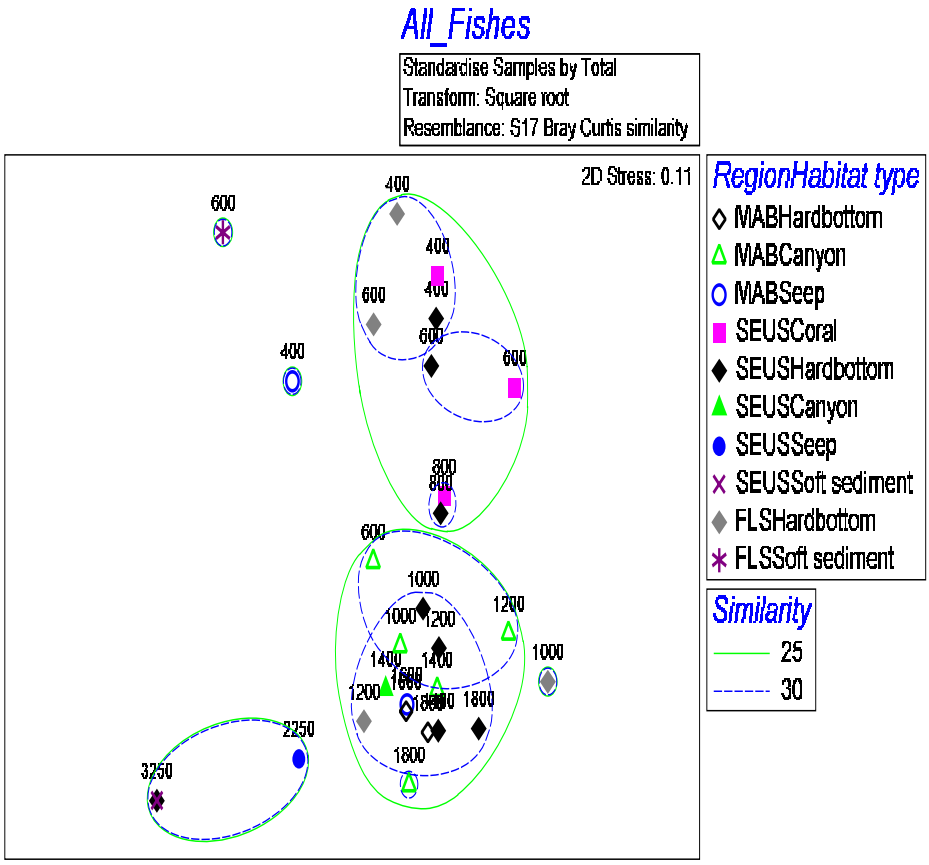

Figure 4-56. Non-metric multidimensional scaling ordination plot of fish habitat type with depth
Based on Bray-Curtis similarity of log-transformed relative abundances per depth-region-habitat type. Symbols represent region and habitat, and labels represent median depth (m) per 200-m depth bin.

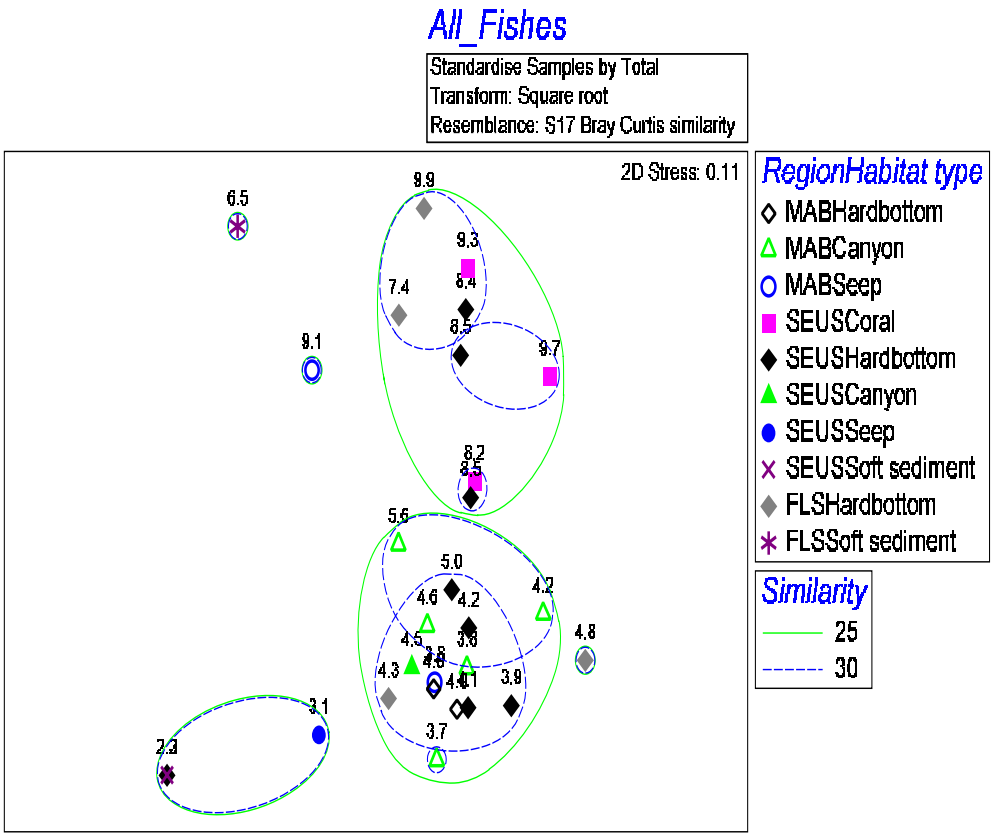

Figure 4-57. Non-metric multidimensional scaling ordination plot of region with depth
Based on Bray-Curtis similarity of log-transformed relative abundances per depth bin-region-habitat type. Symbols represent region and habitat, and labels represent median temperature (C) per 200-m depth bin.

We conducted distance-based Redundancy Analyses (dbRDA) combined with DISTLM to determine what environmental factors explain the variation in communities (**Figure 4-58** through **Figure 4-61**). We chose all environmental variables as the best model (AIC = 504, R^2 = 0.43), explaining 43% of the total variation in the dataset.

Habitat and depth explained the largest proportion of variation (30%) followed by temperature and region (13%). The first two axes of the dbRDA plot explained 66% of the fitted variation, and 27% of the total variation. There was a negative relationship between depth and both axes, with deeper sites found on the left and bottom of the graph and shallow sites found in the upper right.

There was a positive relationship between temperature and axis 1, with dives in warmer temperatures along the positive of axis 1. Habitat was largely associated with axis 2, with seep and soft-substrate habitats along the positive portion of axis 2 and the majority of hardbottom, canyon, and coral habitats along the negative portion of axis 2; those that were along the positive axis were in shallower depths. Canyon sites were also associated with the negative portion of axis 1.

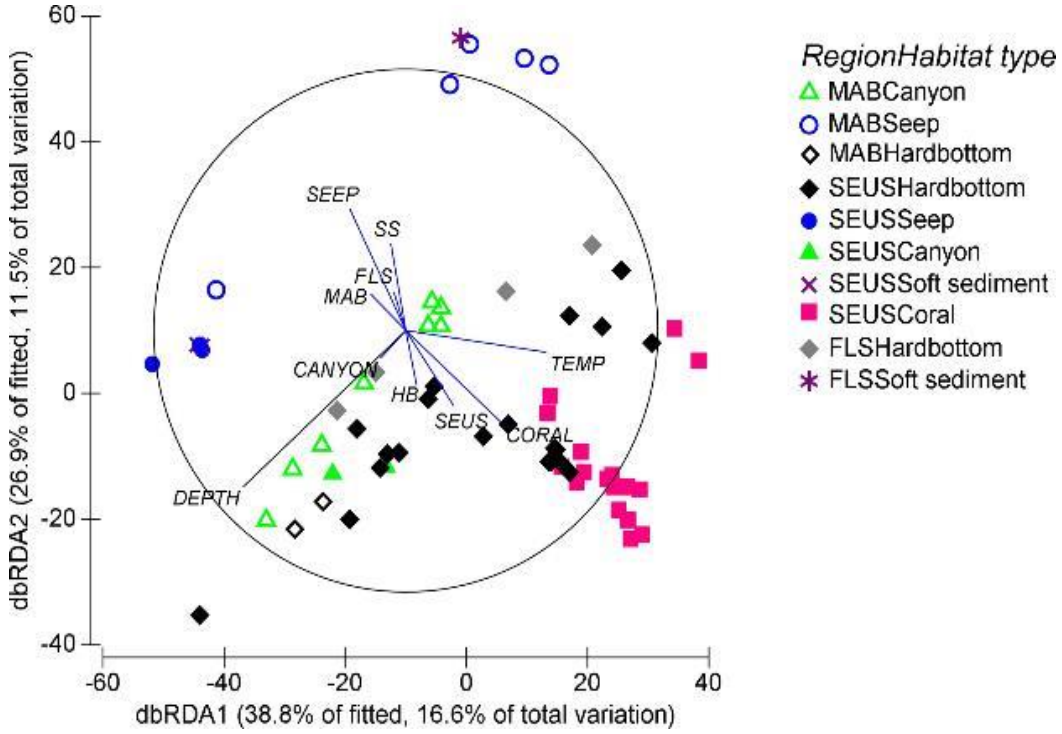

Figure 4-58. dbRDA ordination plot of habitat and region
Each dive is color coded by habitat and region. Environmental factors that explain the fitted variation are included as vectors.

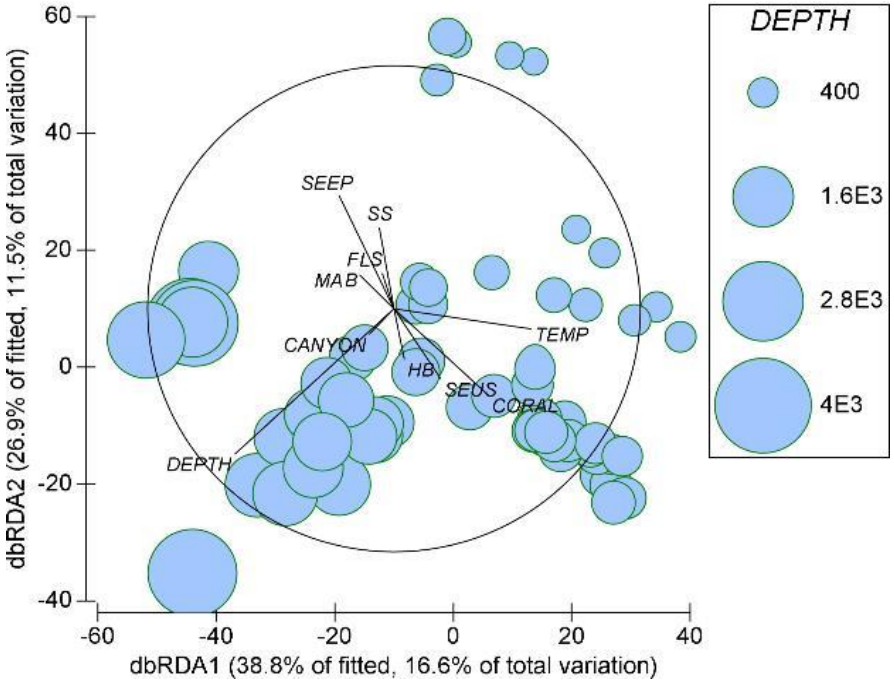

Figure 4-59. dbRDA ordination plot of depth
Median depth (as bubbles) of each dive is overlain onto the plot. Environmental factors that explain the fitted variation are included as vectors.

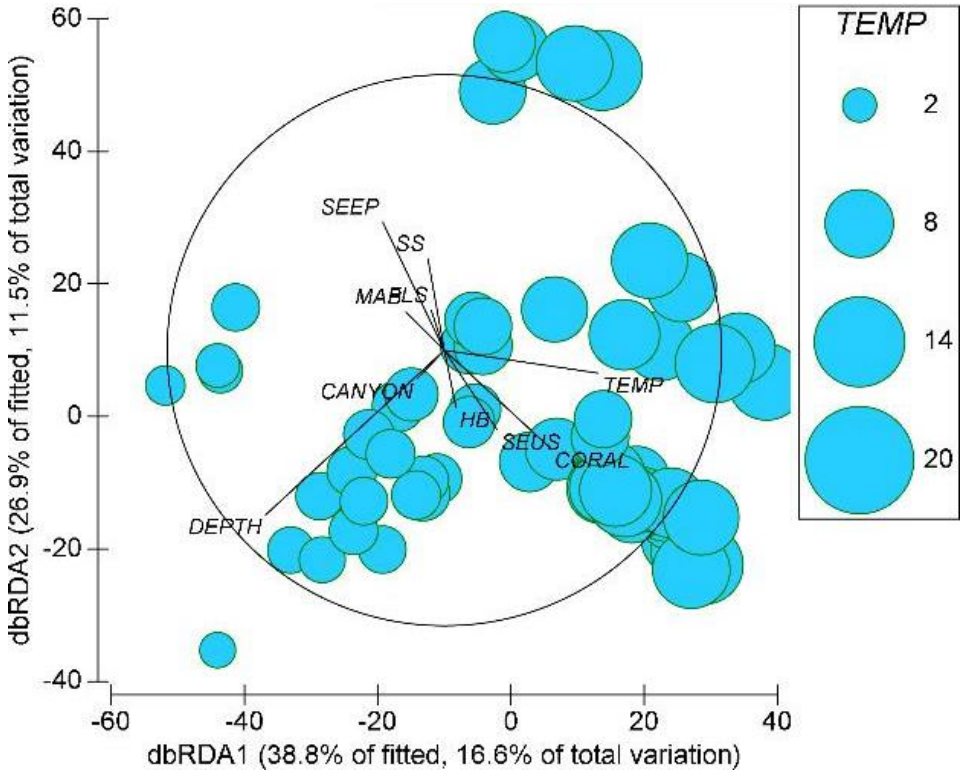

Figure 4-60. dbRDA ordination plot of temperature
Mean temperature (as bubbles) of each dive is overlain onto the plot. Environmental factors that explain the fitted variation are included as vectors.

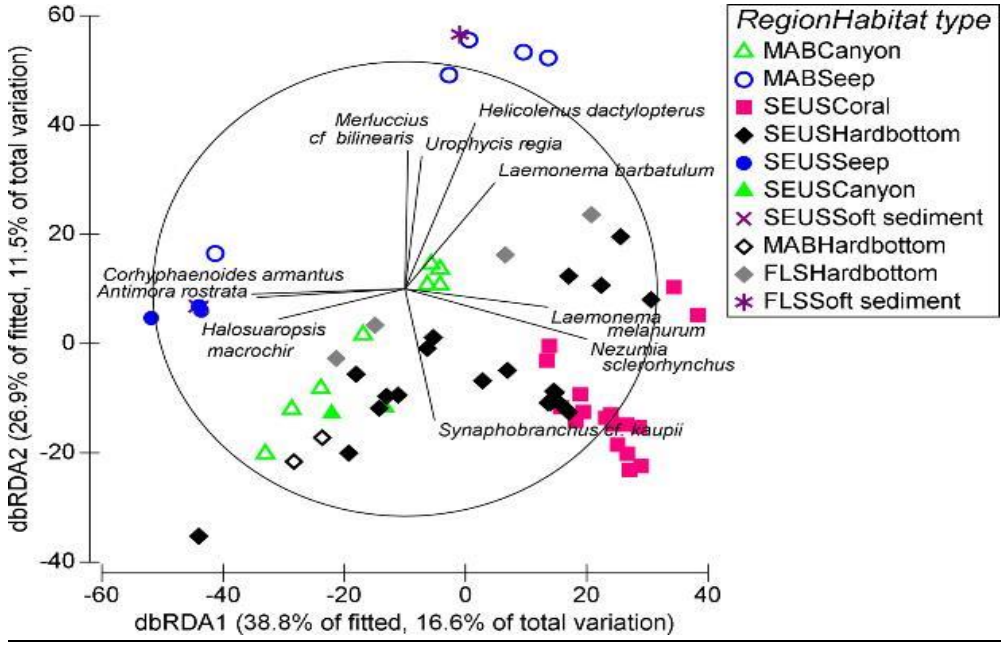

Figure 4-61. dbRDA ordination plot of species
Each dive is color coded by habitat and region. Vectors are species with Pearson correlation coefficients r > 0.5.

Several species were correlated with the axes in the dbRDA plot. *Coryphaenoides armatus, Halosauropsis macrochir,* and *Antimora rostrata* were correlated with axis 1, and thus were species associated with deeper seep, soft-sediment, and canyon habitats. *Laemonena melanurum* and *Nezumia sclerorhynchus* were also correlated with axis 1, discriminating assemblages in shallower coral and hardbottom habitats. *Synaphobranchus* cf. *kaupii* was correlated with axis 2, and was found in deeper canyon, hardbottom and coral habitats. *Helicolenus dactylopterus, Urophycis regia, Laemonema barbatulum, and Merluccis cf. bilinearis/albidus* were correlated with axis 2 with high abundances in seep habitats.

We calculated functional diversity estimates for each site and grouped in boxplots across habitat and depth range to examine if all deep-sea habitats across the study region are functionally equivalent. Both functional diversity and functional richness (amount of niche space filled by members of community) of fishes at cold-seep and canyon habitats were higher than other habitats in similar depth ranges (**Figure 4-62** through **Figure 4-64**). In addition, there was a general trend of decreasing functional diversity and functional richness with increasing depth. Both of these indices corresponded to the volume of functional space occupied by species (Mouchet et al. 2010). In contrast, functional dispersion, which is dispersion of species in functional space independent of species richness, was fairly similar across all habitats and depths, except that functional diversity is in soft sediments was low (**Figure 4-65).** Estimates of functional evenness and functional divergence were somewhat opposite of the pattern seen in diversity and richness, with an overall increase with increasing depth. In addition, the lowest values of functional evenness and functional divergence (**Figure 4-66**) were found in seep habitats in 0–500 m depth, whereas both of these estimates were generally higher in hardbottoms compared to other habitats in similar depth ranges.

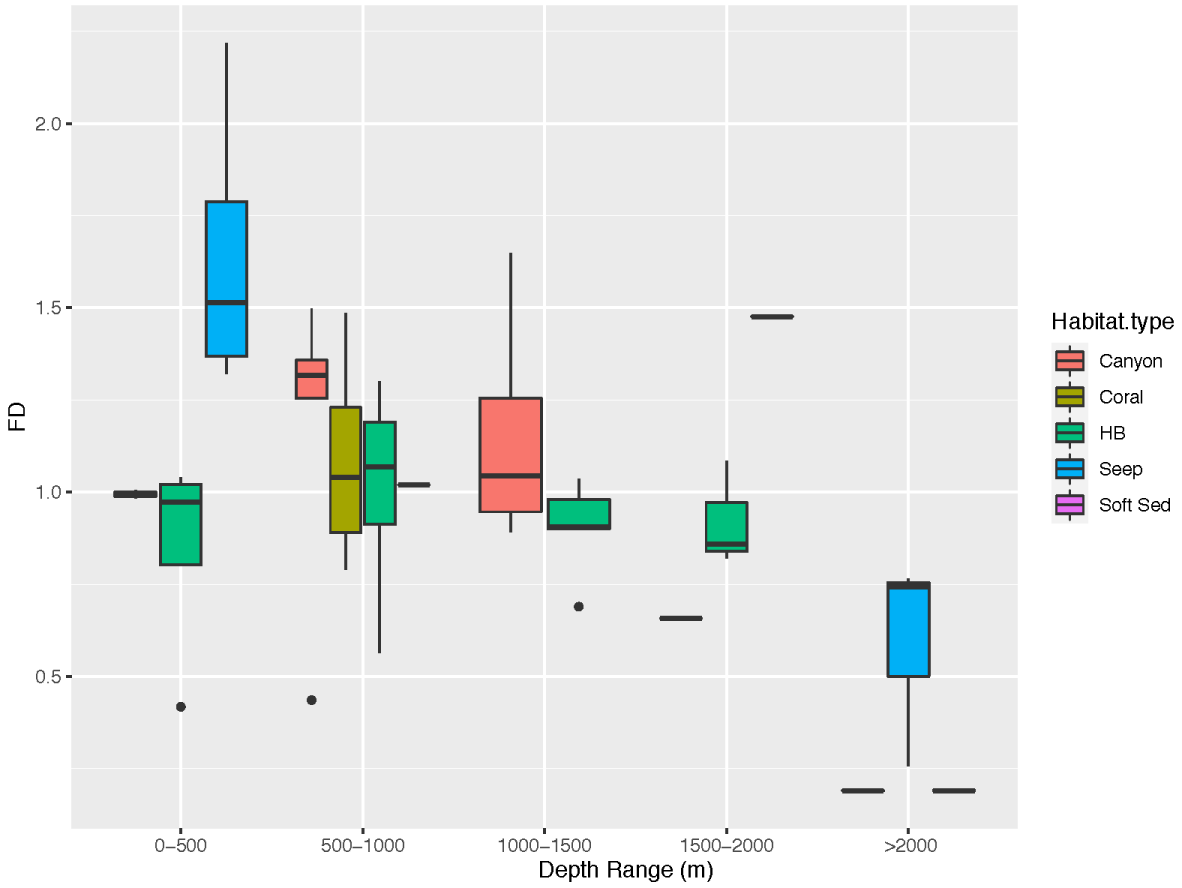

Figure 4-62. Functional diversity estimates of fish assemblages across depth and habitat

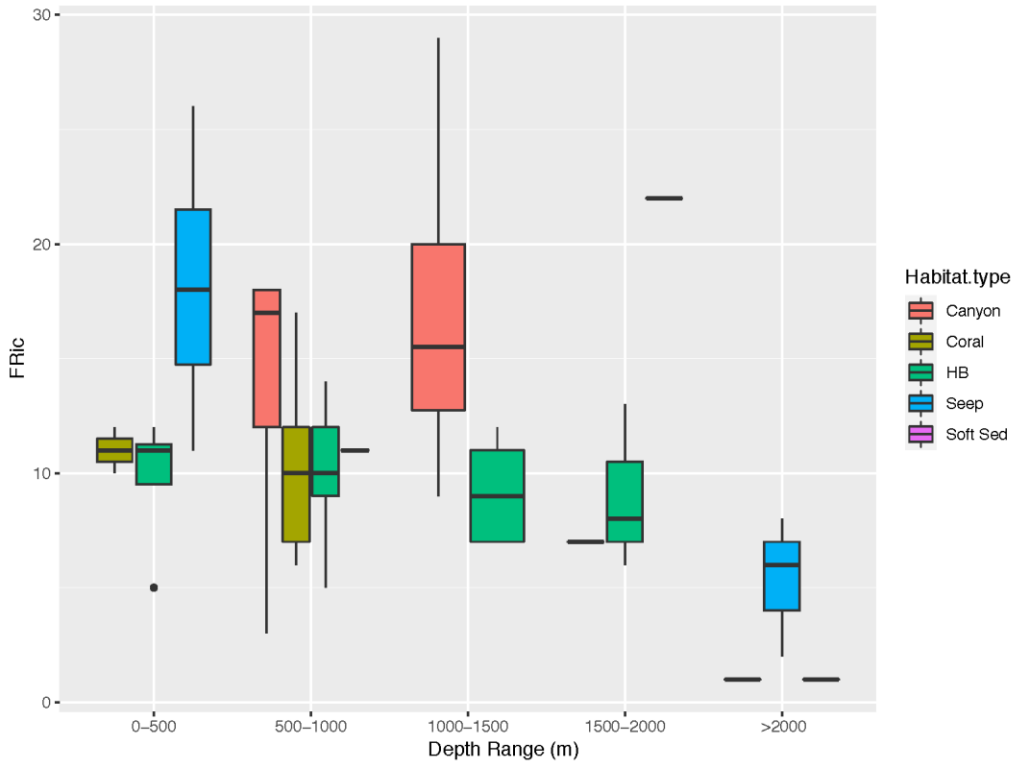

Figure 4-63. Functional richness estimates of fish assemblages across depth and habitat

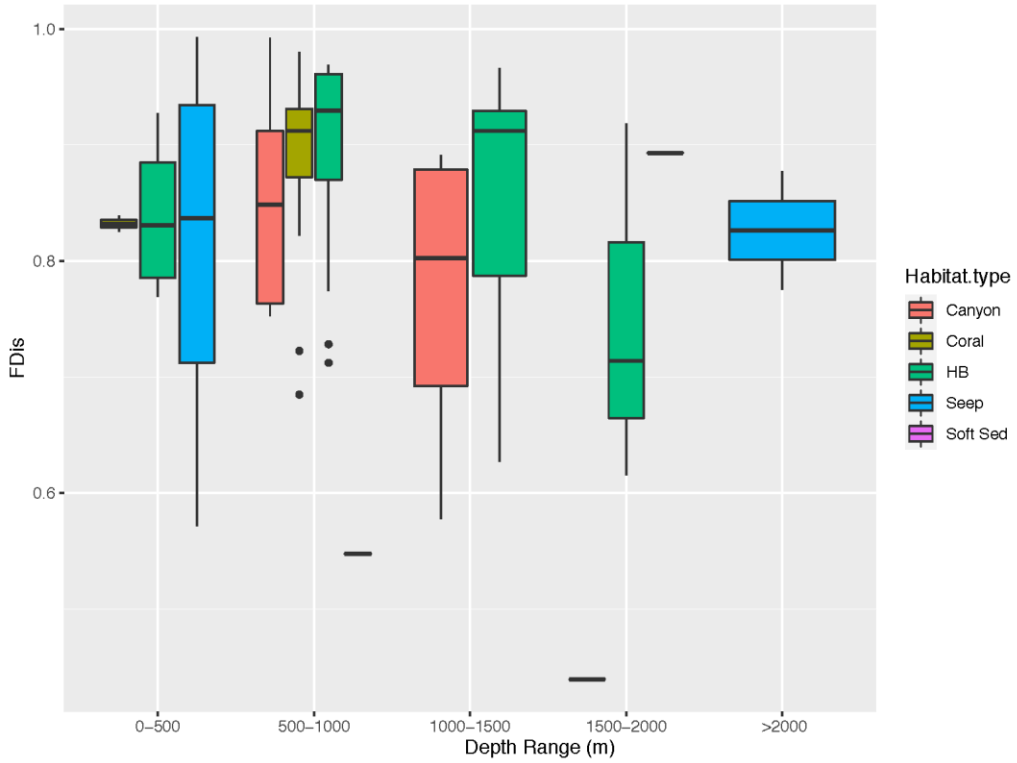

Figure 4-64. Functional dispersion estimates of fish assemblages across depth and habitat

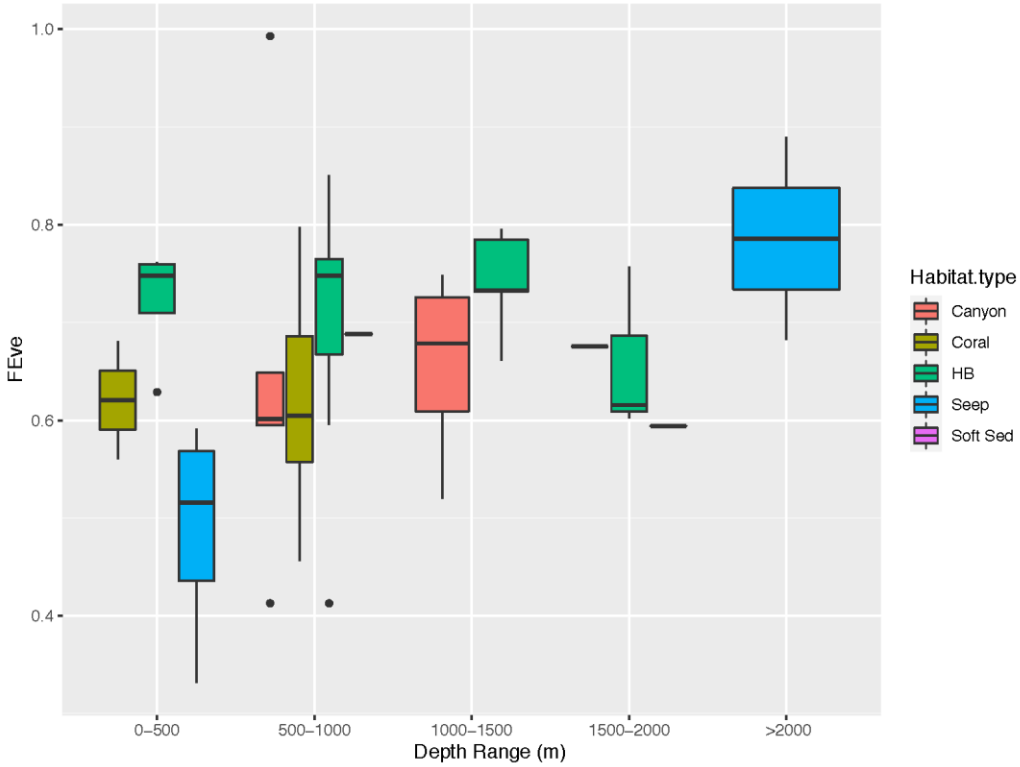

Figure 4-65. Functional evenness estimates of fish assemblages across depth and habitat

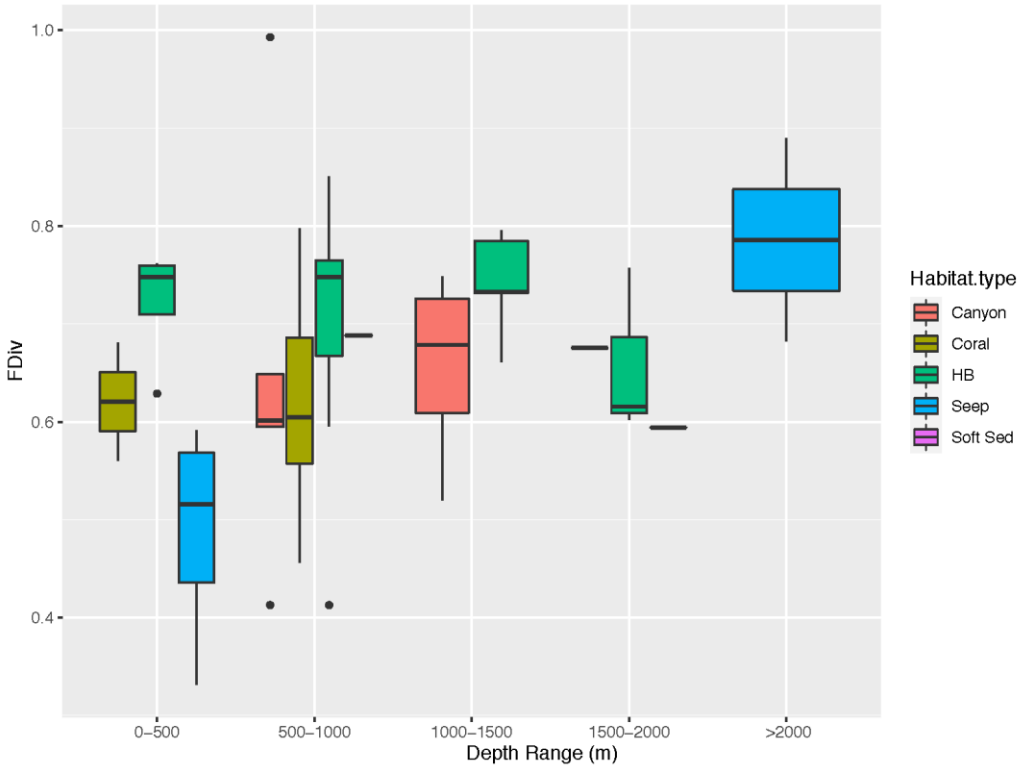

Figure 4-66. Functional divergence estimates of fish assemblages across depth and habitat

4.2.3.3 Demersal Fish Assemblage Summary

Previous studies in the region (Ross and Quattrini 2007, Ross et al. 2015) have noted species-specific habitat associations. We have built on this prior work by taking a broad-scale approach and examining habitat equivalency among macrohabitat categories, including coral reef, cold seep, submarine canyon, and soft sediment. Our results indicate that variation in demersal fish assemblages in the region is driven primarily by habitat type, and that depth and habitat are not functionally synonymous. Some habitats harbor more species and higher abundances of fishes, even at similar depths.

Notably, cold seeps in shallow regions of the MAB harbor high species richness, functional diversity, and abundances of fishes compared to other habitats examined; both Pea Island and Bodie Seeps are quite distinct and unique habitats. The area of the continental slope just north of Cape Hatteras is hydrographically unique due to convergence of the southward-flowing Labrador Current and northward flowing Gulf Stream (Csanady and Hamilton 1988). This region includes the highest abundances of benthic infauna, carbon flux, and particulate sedimentation rates of anywhere along the US Atlantic margin (see Sulak and Ross 1996). It is likely that the combination of high photosynthetic and chemosynthetic productivity fuel abundant and diverse demersal fish assemblages in this region.

Canyon habitats also appear to differ from other habitats, even when controlling for regional differences. Canyons appear to have higher species richness and functional diversity than coral reefs and hardbottoms in similar depths. Hardbottom habitats of the region have high functional divergence, indicating that species in the assemblage occupy disparate areas of the niche space, perhaps due to the numerous microhabitats that hardbottoms provide (coral gardens, stony coral bushes, caves, walls). Finally, we note that demersal fish assemblages at CWR composed of *Lophelia pertusa* did not emerge as exceptionally unique or diverse as compared to other complex habitats along the US Atlantic margin. Coral reefs and hardbottom habitats with coral gardens do, however, contain characteristic reef species, including the coral hagfish (*Rubicundus lopheliae),* the roughtip grenadier (*Nezumia sclerorhynchus),* and the coral hake (*Laemonena melanurum).*

4.3 Octocoral Community Phylogenetics

Section Authors: Andrea Quattrini, Emma Saso, Erik E. Cordes

The complete assessment of community structure and community similarity among sites requires a number of different approaches. The previous portions of this chapter focused on direct assessments of diversity and abundance of species through video and physical sampling. In this section, we apply new approaches to the determination of diversity where the genetic distance among species is taken into consideration. This provides another level of nuance beyond the simple presence/absence and abundance analyses. Taken together, all of these approaches provide a more comprehensive view of community structure in the study area.

4.3.1 Introduction

Global biogeographic patterns of octocoral distribution and community assembly are informed by the interplay of biotic (larval dispersal) and abiotic (seafloor topography, temperature, oxygen, currents, and mineral saturation states) factors which co-vary with depth and water masses (Radice et al. 2016, Auscavitch et al. 2020). Species distribution models have elucidated certain environmental variables to be strong determinants of octocoral distribution (Yesson et al. 2012, Baker et al. 2012, Bracco et al. 2019, Summers and Watling 2021), albeit these models remain error prone. While it is known that many deep-sea animals sort along depth gradients (Rex and Etter 2010), details of assembly by depth are typically species or region-specific and not generalizable. In Octocorallia, species of the genus *Paramuricea* have

been seen to occupy wide depth ranges in the well-mixed deep North Atlantic (Radice et al. 2016), whereas octocoral species inhabiting the stratified deep GOM are confined to narrower depth ranges (Quattrini et al. 2014, Doughty et al. 2014). In addition to depth, habitat type has been shown to influence the diversity and distribution of deep benthos (Quattrini et al. 2015) and has a potential impact on octocoral biogeography. Octocorals are distributed across a myriad of habitat types including coral-formed bioherms, submarine canyons, hardbottom substrate, and cold seeps, each habitat offering a unique set of environmental parameters and requiring a subset of adaptations. Octocoral species' ranges and patterns of community assembly are likely determined by a combination of the distinct oceanographic and environmental parameters that define each region, and the evolutionary histories within the subclass. While research on North Atlantic octocorals dates back three decades (Tendal 1992), no community-level study to date has centered the SEUS region where the Gulf Stream current plays an integral role in global ocean circulation and connectivity.

Slow-growing and long-lived, octocorals are highly adapted to deep-sea environments and are susceptible to ocean change and anthropogenic disturbance (Sherwood and Edinger 2009, Watling et al. 2011). Investigating the biogeographical patterns of octocoral distribution and diversity is a crucial first step towards effective management of these species.

While recent technological advances have facilitated sampling of deep benthos, questions of octocoral biogeography and endemicity are complicated still by the existence of morphologically plastic traits, cryptic species and unresolved taxonomy. For instance, the considerable ecophenotypic variability within Octocorallia often leads to erroneous species identifications, causing inaccurate assessments of species ranges and population connectivity (Baco and Cairns 2012, McFadden et al. 2019). Thus, molecular barcoding of informative loci can be used in complement with morphological species designations to achieve accurate species identifications, which take into consideration phylogenetic relatedness in addition to morphology.

With these DNA barcodes, taxa can be classified into MOTUs using appropriate genetic distance thresholds (McFadden et al. 2014, 2019). Not only do these molecular methods have the power to confirm species and account for the misleading presence of phenotypically plastic traits, but they also provide a phylogenetic framework to understanding community diversity. This phylogenetic lens incorporates species relatedness into analyses of community similarity, resulting in a more holistic view of functional diversity within communities. With a clear understanding of community diversity on a genetic scale, more accurate assessments can be made regarding the biogeographic and evolutionary factors which work to shape community structure and diversity.

Our goals were to

1) Determine octocoral distribution, species richness and phylogenetic alpha diversity across the region,
2) Assess community assembly and species turnover across sites, and
3) Edentify biogeographical provinces into which species are sorting.

With regards to species distribution, we hypothesized that a combination of depth-related environmental variables (temperature, habitat type, currents, and depth) and biotic factors (larval dispersal) influence octocoral distribution, and therefore suggest that depth and water mass are key predictors of distribution.

At the community level, we hypothesized that taxonomic and phylogenetic community similarity can be explained by three factors: habitat type, depth, and distance. Lastly, we expected to observe a biogeographic break at Cape Hatteras such that octocoral communities north of Hatteras will be more similar to each other and will differ significantly from communities to the south of Cape Hatteras.

4.3.2 Methods

4.3.2.1 Molecular Barcoding and MOTU Delimitation

Two Deep SEARCH cruises (RV *Atlantis* AT-41 and RV *Ron Brown* RB19) in the western North Atlantic off the US eastern seaboard targeted octocorals for collection (**Table 4-19**) by submersible and ROV. We clipped off small pieces of each coral colony and preserved them in 95% EtOH stored at -20°C. We extracted total genomic DNA using AutoGenPrep 965 (Autogen, Holliston, MA) or DNeasy Blood & Tissue Kit (Qiagen). Following DNA extraction, octocorals were PCR amplified for portions of two mitochondrial genes (mt*MutS*, *COI*+igr) and one nuclear ribosomal gene (*28S*) (**Table 4-20**) (McFadden et al. 2011).

Table 4-19. Summary of dives octocoral collections during AT41 and RB19 expeditions

Cruise	Dive #	Site Name	Habitat Feature	On-Bottom Lat	On-Bottom Long	Mean Temp (°C)	Min Depth (m)	Max Depth (m)	Median Depth (m)	Bottom Time	Date
AT41	AL4962	Richardson Reef	coral	32.014	-77.396	9.21	750	820	785	6:33:00	08/23/18
AT41	AL4963	Richardson Reef	coral	31.985	-77.416	9.75	750	820	785	4:35:00	08/24/18
AT41	AL4964	Blake Escarpment Deep	hard bottom	31.323	-77.245	4.32	1,200	1,273	1,237	7:20:00	08/25/18
AT41	AL4965	Stetson Banks	hard bottom	32.012	-78.314	8.47	434	545	490	6:56:00	08/26/18
AT41	AL4966	Stetson Banks	hard bottom	32.07	-78.374	8.36	395	403	399	6:20:00	08/27/18
AT41	AL4968	Cape Fear Coral Mound	coral	33.576	-76.468	10.06	378	458	418	6:29:00	08/29/18
AT41	AL4969	Pamlico Canyon	canyon	34.937	-75.169	-	1,100	1,607	1,354	7:01:00	08/30/18
AT41	AL4970	Norfolk Canyon	canyon	37.043	-74.315	3.72	1,665	1,943	1,804	6:56:00	08/31/18
RB19	J2-1128	Richardson Reef	coral	31.88	-77.374	5.76	731	762	747	9:30:00	04/10/19
RB19	J2-1129	Richardson Reef	coral	31.985	-77.413	9.72	690	708	699	11:15:00	04/13/19
RB19	J2-1130	Savannah Banks	coral	31.754	-79.195	8.55	511	553	532	8:42:00	04/17/19
RB19	J2-1131	Blake Escarpment Deep	hard bottom	31.285	-77.237	4.08	1,306	1,359	1,333	13:27:00	04/17/19
RB19	J2-1132	Pamlico Canyon	canyon	34.914	-75.184	3.90	1,136	1,839	1,488	23:40:00	04/21/19
RB19	J2-1133	Pea Island Seep	seep	35.675	-74.792	11.12	300	353	327	9:28:00	04/23/19
RB19	J2-1135	Cape Lookout Deep	hard bottom	33.916	-75.832	4.48	940	1,029	985	2:40:00	04/25/19
RB19	J2-1136	Blake Ridge Seep	seep	32.493	-76.19	3.28	2,140	2,164	2,152	15:14:00	04/27/19
RB19	J2-1137	Cape Fear Seep	seep	32.979	-75.929	2.68	2,592	2,608	2,600	8:04:00	04/28/19
RB19	J2-1138	Richardson Reef (West)	coral	31.893	-77.699	5.66	658	758	708	8:11:00	04/29/19

Table 4-20. PCR primers and protocols used to amplify target loci in collected specimens (Cnidaria)

Gene	Primer	Sequence (5' to 3')	PCR Profile
mtMutS	ND42599F[1]	GCC ATT ATG GTT AAC TAT TAC	94°C: 30s, 50°C: 45s, 72°C: 45s (40 cycles)[a]
mtMutS	AnthoCorMSH[2]	AGG AGA ATT ATT CTA AGT ATG G	same as above
mtMutS	Mut3458R[1]	TSG AGC AAA AGC CAC TCC	same as above
COI	COII-8068F[3]	CCA TAA CAG GRC TWG CAG CAT C	same as above
COI	COI-LA-8398-F[3]	GGA ATG GCG GGG ACA GCT TCG AGT ATG TTA ATA CGG	same as above
COI	COIoct-R[3]	ATC ATA GCA TAG ACC ATA CC	same as above
28S	Far[4]	CAC GAG ACC GAT AGC GAA CAA GTA	94°C: 30s, 55°C: 45s, 72°C: 45s (35 cycles)[a] or touchdown protocol[b]
28S	Rab[4]	TCG CTA CGA GCT TCC ACC AGT GTT T	same as above

[a]PCR began with an initial denaturation of 94°C for 7 min, and concluded with a final extension of 72°C for 5 min
[b]Touchdown protocol: annealing temperature began at 60°C and decreased 1°C per cycle until reaching 55°C. Following this, an additional 25 cycles were performed at 55°C.
[1](France & Hoover 2001); [2](Herrera et al. 2010); [3](McFadden et al. 2011); [4](McFadden & van Ofwegen 2012)

Once we competed sequencing octocoral *28S* (n = 140) and mt*MutS* (n = 152) we aligned both barcodes by the L-INS-i method in MAFFT (Katoh and Standley 2013), trimmed to 746 bp and 853 bp respectively, and visually adjusted in Aliview using the amino acid viewer (Larsson 2014). We also concatenated the two genetic barcodes into a single 1,572 bp multilocus barcode with the program Mesquite (Maddison and Maddison 2019).

Due to the differing evolutionary rates between genomic and mitochondrial genes in octocorals (Shearer et al. 2002), the *28S* and *MutS* barcodes each require individualized genetic distance thresholds to appropriately delimit MOTUs. Therefore, we first delimited MOTUs for the two loci separately at their respective genetic distance thresholds using the program MOTHUR v 1.44.3 (Schloss et al. 2009), resulting in two sets of preliminary MOTUs. We used a genetic distance threshold of 0.3% for MOTU delimitation with *MutS*, and a threshold of 0.8% for *28S* (McFadden et al. 2014, 2019). We constructed maximum-likelihood phylogenetic trees for *28S* and *MutS* in IQ-TREE v 2.0.7 (Minh et al. 2020) and visualized them with FigTree v 1.4.4 (Rambaut 2018) to compare each set of MOTUs. We also constructed a phylogenetic tree for the multilocus barcode. Final MOTUs were then assigned based upon congruency between *MutS* and *28S* preliminary MOTUs, and based upon taxonomic relatedness as observed in the multilocus molecular phylogeny. We individually analyzed specimens with only one of two loci available (n = 30) and grouped them into MOTUs based on the available sequence data.

4.3.2.2 Community Assembly Analyses

In order to assess sampling effort of octocorals in the study region, we created a species-accumulation curve using MOTU assignments in R using the package VEGAN (Oksanen et al. 2020). To examine the degree of community similarity among sites, we calculated Sorensen's Index of similarity between pairs of sites in PRIMER (Clarke and Gorley 2006) based on presence/absence of MOTUs. We then assessed differences in octocoral community composition across sites with analysis of similarity (ANOSIM) tests, hierarchical clustering and non-metric multidimensional scaling ordinations (nMDS) in PRIMER (Clarke and Gorley 2006). In order to evaluate our hypothesis that octocoral community composition is influenced by habitat type, depth, and geographic distance, we conducted several ANOSIM tests, each run with 999 permutations. We ran a one-way ANOSIM test to determine if octocoral communities inhabiting various depth ranges (0–999 m, 1,000–1,999 m, and 2,000–3,000 m) were compositionally different.

Similarly, we conducted a one-way ANOSIM test to analyze the differences in community composition among habitat types (hardbottom, coral, canyon, and seep). To account for the interrelatedness of depth and habitat type and to determine if one of the two factors is responsible for driving differences in community structure, we isolated the effects of both depth and habitat type using two-way nested ANOSIM tests. We plotted associations between groups of samples using nMDS ordinations to visualize any patterns related to depth, temperature and/or habitat feature. In addition to hypothesis testing, we explored the data *a priori* to identify any existing community assembly patterns we had not anticipated. To this end, we ran hierarchical cluster analysis followed by SIMPROF tests to identify groupings of sites with statistically different ($p < 0.05$) compositional structure. Finally, we ran similarity percentage (SIMPER) tests to identify species contributing most notably to the differences in community structure between depth groups, and between SIMPROF groups.

4.3.2.3 Phylogenetic Diversity Analyses

We calculated phylogenetic alpha diversity at each site based on the *MutS + 28S* concatenated barcode using Faith's Index (FI) of diversity (Faith 1992) with the package Picante (Kembel et al. 2010). FI calculates alpha diversity by summing the branch lengths in a phylogenetic tree connecting all species occurring at a given site (Faith 2002). Thus, FI adds to traditional species richness measures by considering the genetic makeup of communities when estimating diversity. In addition to FI, we calculated species richness at each site using MOTUs as species. To analyze patterns of phylogenetic diversity in the context of environmental variables, we compared alpha diversity across depth ranges, habitat types and SIMPROF groups.

4.3.3 Results and Discussion

We collected and preserved 185 octocoral samples during 18 dives at 11 distinct sites during the AT41 and RB1903 research expeditions off the US eastern seaboard. Collections were composed of 13 octocoral families, the most abundant being Plexauridae followed by Primnoidae and Nephtheidae. The species-accumulation curve to assess octocoral sampling effort is approaching an asymptote, indicating that the regional species pool has been relatively well sampled. However, additional species of octocoral are still likely to be found with further sampling, particularly from deeper depth zones (**Figure 4-67)**.

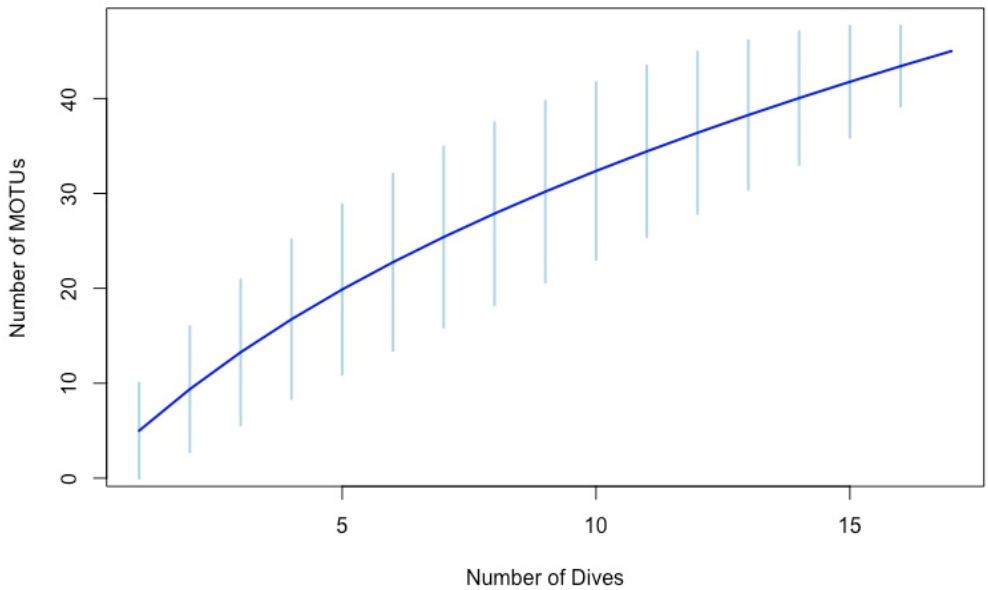

Figure 4-67. Species-accumulation curve of octocoral sampling In the North Atlantic off the US eastern seaboard with 95% confidence intervals

4.3.3.1 Octocoral Phylogenetic Diversity

Octocoral species richness was highest at Richardson Reef, (n = 42) followed by Blake Escarpment Deep (n = 31), Pamlico Canyon (n = 21) and Richardson Reef West (n = 19). The lowest observed species richness was at Blake Ridge Seep (n = 1), Cape Lookout Deep (n = 3) and Cape Fear Mounds (n = 3; **Figure 4-68 a**). In general, species richness correlated with FI of phylogenetic α-diversity, wherein higher species richness at a site corresponds to greater α-diversity (**Figure 4-68 c**). FI was highest at Richardson Reef, then Stetson Banks, Blake Escarpment Deep, and Richardson Reef West (**Figure 4-68 b**). For certain sites, such as Stetson Banks, the lower species count (n = 17) relative to FI measure reflects a community composed of octocoral species that are more distantly related. When the phylogenetic relatedness of communities is considered in addition to traditional species counts, community composition can be understood with the greater nuance of an evolutionary perspective.

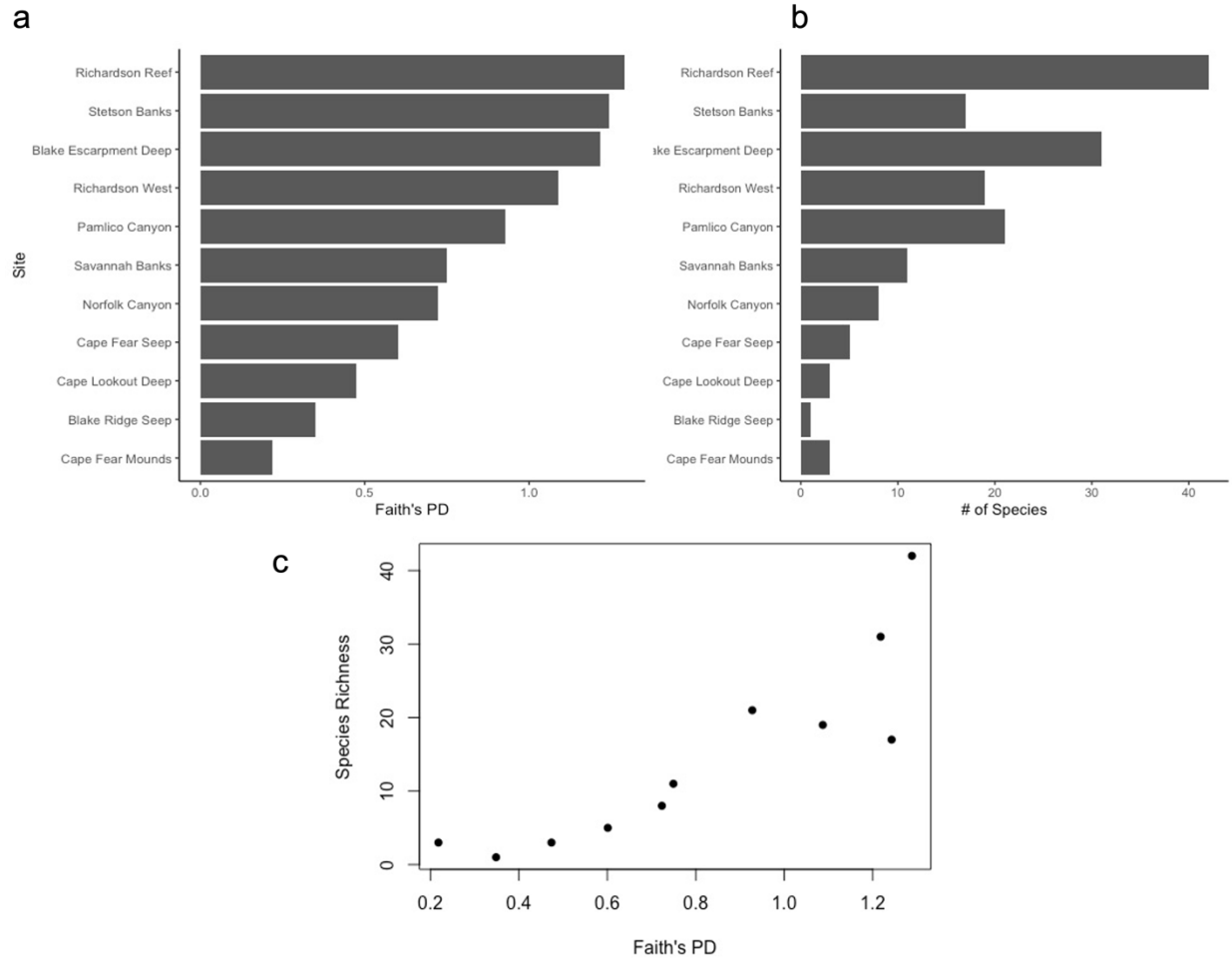

Figure 4-68. Species richness and FI of phylogenetic diversity across 11 sites
Species richness (a, c) and FI of phylogenetic α-diversity (b, c) across 11 sites in the North Atlantic.

Sites within the 0–1,000 m and 1,000–2,000 m depth ranges had similar average FI measures, both higher than α-diversity at sites occupying the 2,000–3,000 m range (**Figure 4-69 a**). Out of the four habitat types, we observed the highest average α-diversity in coral habitats, and the lowest diversity was observed in seep habitats (**Figure 4-69 b**). We observed the highest FI measure of all SIMRPOF groups in group *b*, which includes Richardson Reef, Richardson Reef West, Stetson Banks and Savannah Banks, all of which are coral or hardbottom sites inhabiting the 0–1,000 m depth range (**Figure 4-69 c**).

In contrast, the lowest average α-diversity occurred in SIMPROF group *d* which includes Blake Ridge and Cape Fear seeps. The deepest sites (2,000–3,000 m), as well as the Norfolk Canyon site, contained only species from the Calcaxonia-Pennatulacea clade with no members from the Holaxonian-Alcyoniina clade (**Figure 4-70**). This could be due to the expanse of soft sediment rather than hard substrate of these sites, which is conducive to the proliferation of sea pens. All other sites contained species from both clades, with the exception of Cape Fear Mounds, which was only composed of species from the Holaxonian-Alcyoniina clade.

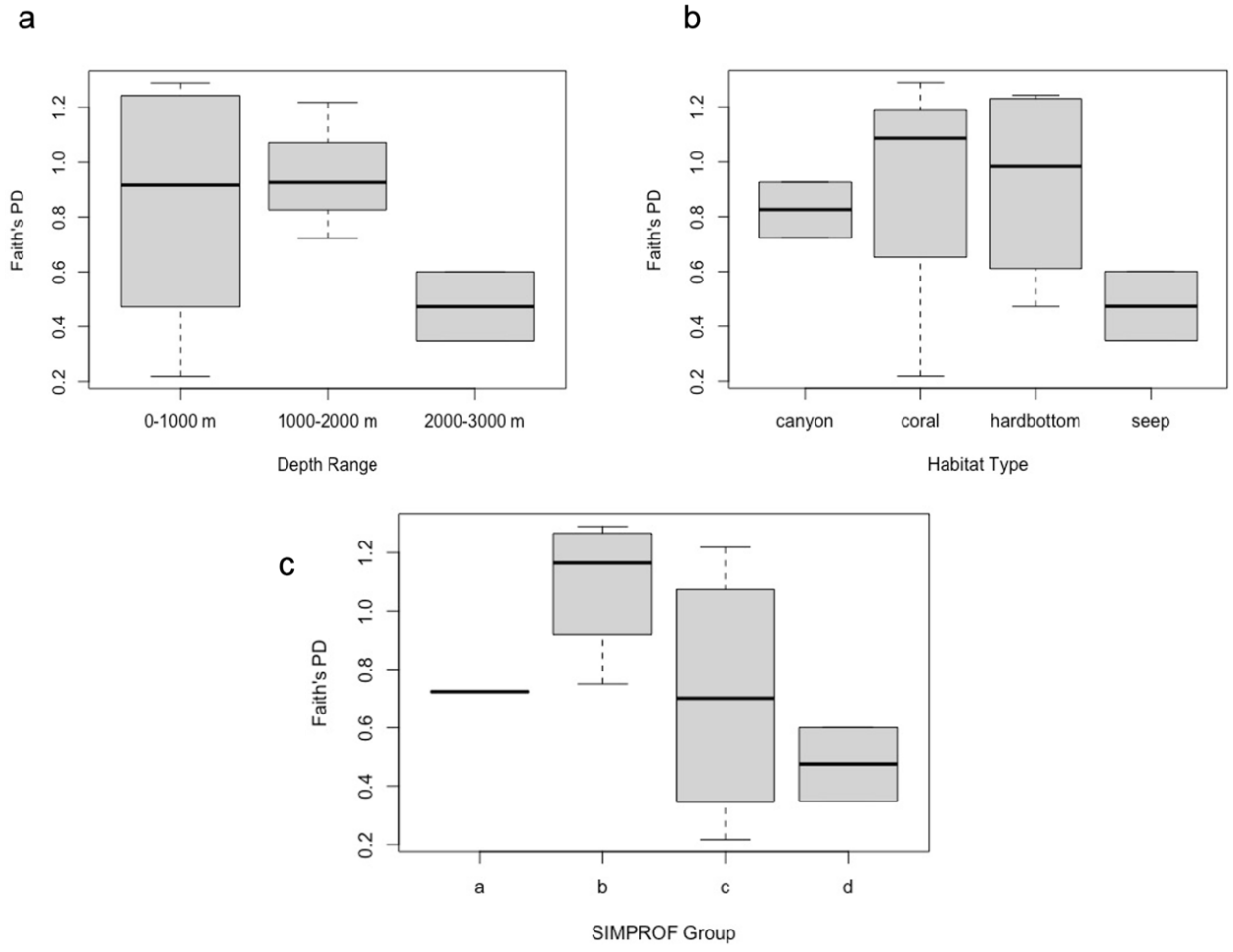

Figure 4-69. FI of PD based on (a) depth (b) habitat type, and (c) SIMPROF group

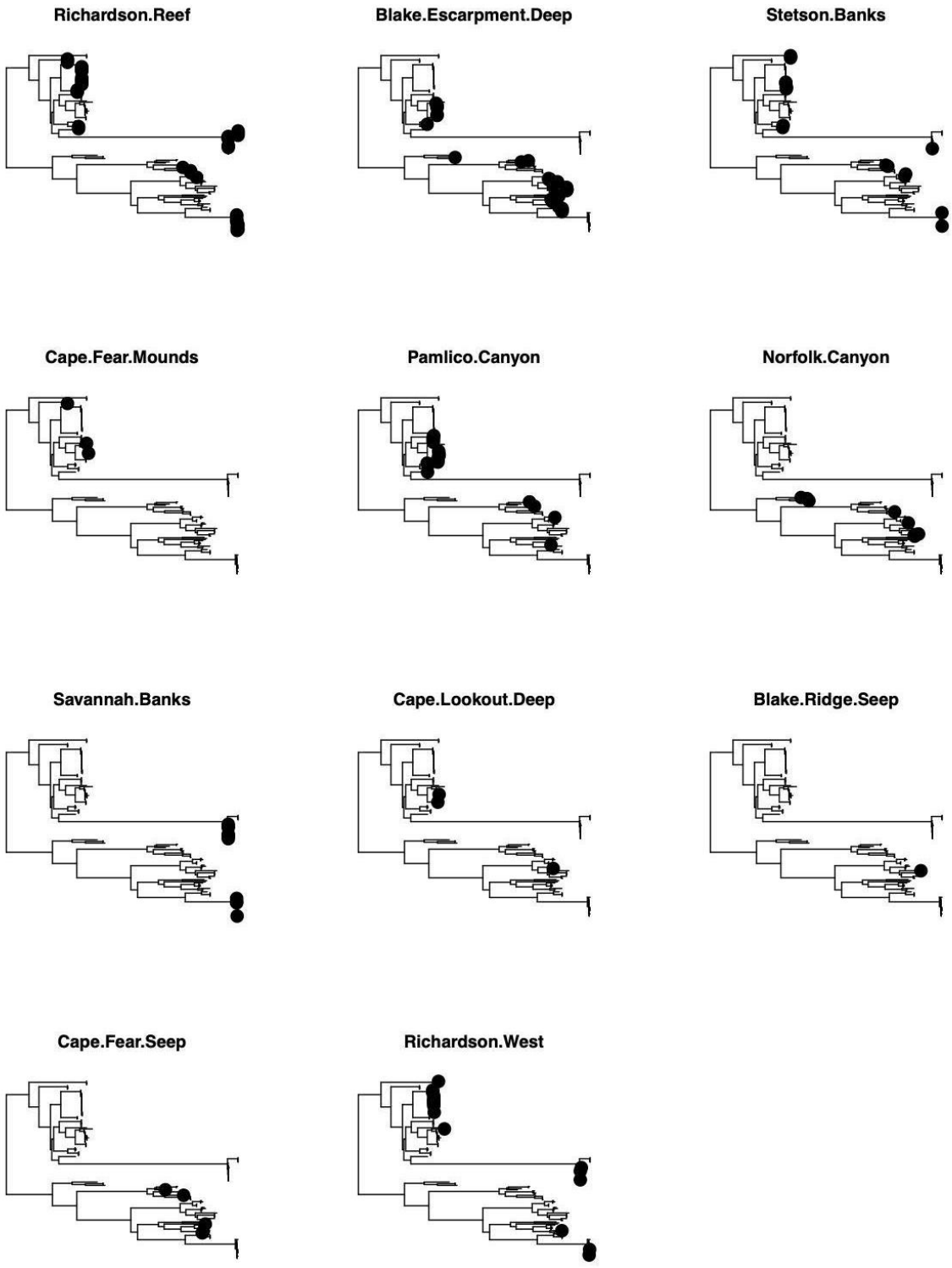

Figure 4-70. Community composition of each site mapped onto a mutS + 28S phylogeny
Note that mutS + 28S phylogeny is rooted at the midpoint. The top clade contains Holaxonian-Alcyoniina taxa, and the bottom clade contains Calcaxonia-Pennatulacea taxa. Species occurring at each site appear as black dots on the tree.

4.3.3.2 Community Assemblages

Molecular barcodes of at least one gene were successfully sequenced for 161 individuals. For 131 of these individuals, barcodes of both *28S* and mt*MutS* loci were successfully sequenced. An additional 30 specimens were sequenced at only one of the two molecular loci (i.e., either *28S* or *mutS*). In addition, we sequenced a *COI* barcode for 123 octocorals.

Based on the *MutS* barcode alone, at a genetic distance threshold of 0.3% octocorals sorted into 41 distinct MOTUs (**Figure 4-71**). From the *28S* barcode alone, at the genetic distance threshold of 0.8% octocorals were assigned to 49 MOTUs **(Figure 4-72**).

Two distinct clades—Calcaxonia-Pennatulacea and Holaxonian-Alcyoniina—were well supported in the multilocus phylogeny (**Figure 4-71**). According to information from the two sets of MOTUs and from phylogenetic relatedness, octocorals were finally assigned to one of 45 unique MOTUs (**Figure 4-73**).

For the majority of specimens, morphological identifications made in the field matched MOTU assignments, and phylogenetic relatedness of individuals comprising a given MOTU was as anticipated.

Figure 4-71. Maximum likelihood phylogeny of the MutS barcode rooted at the midpoint
Taxa names include preliminary MOTUs delimited by MutS.

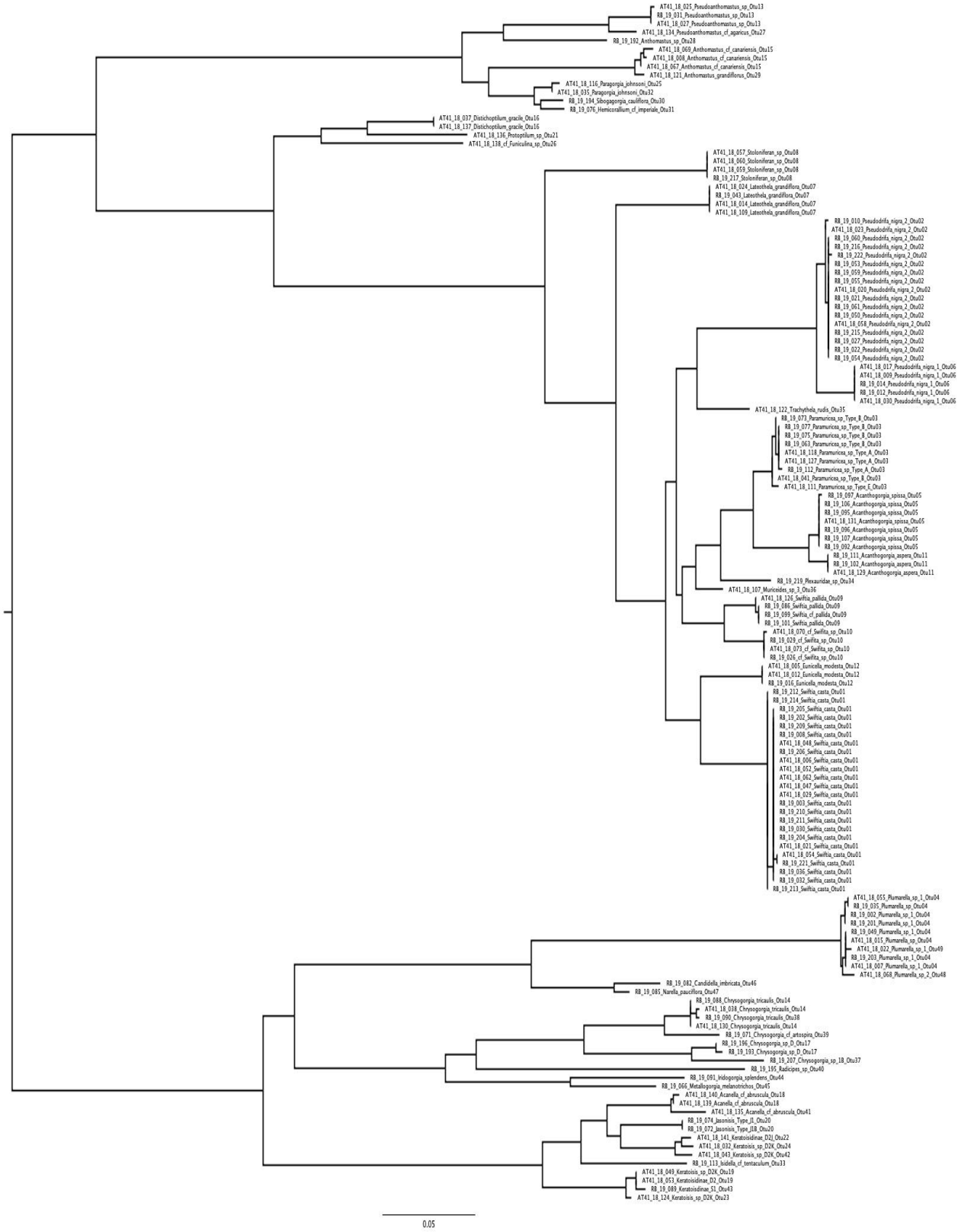

Figure 4-72. Maximum likelihood phylogeny of the 28S barcode rooted at the midpoint
Taxa names include preliminary MOTUs delimited by 28S. *(continued next page.)*

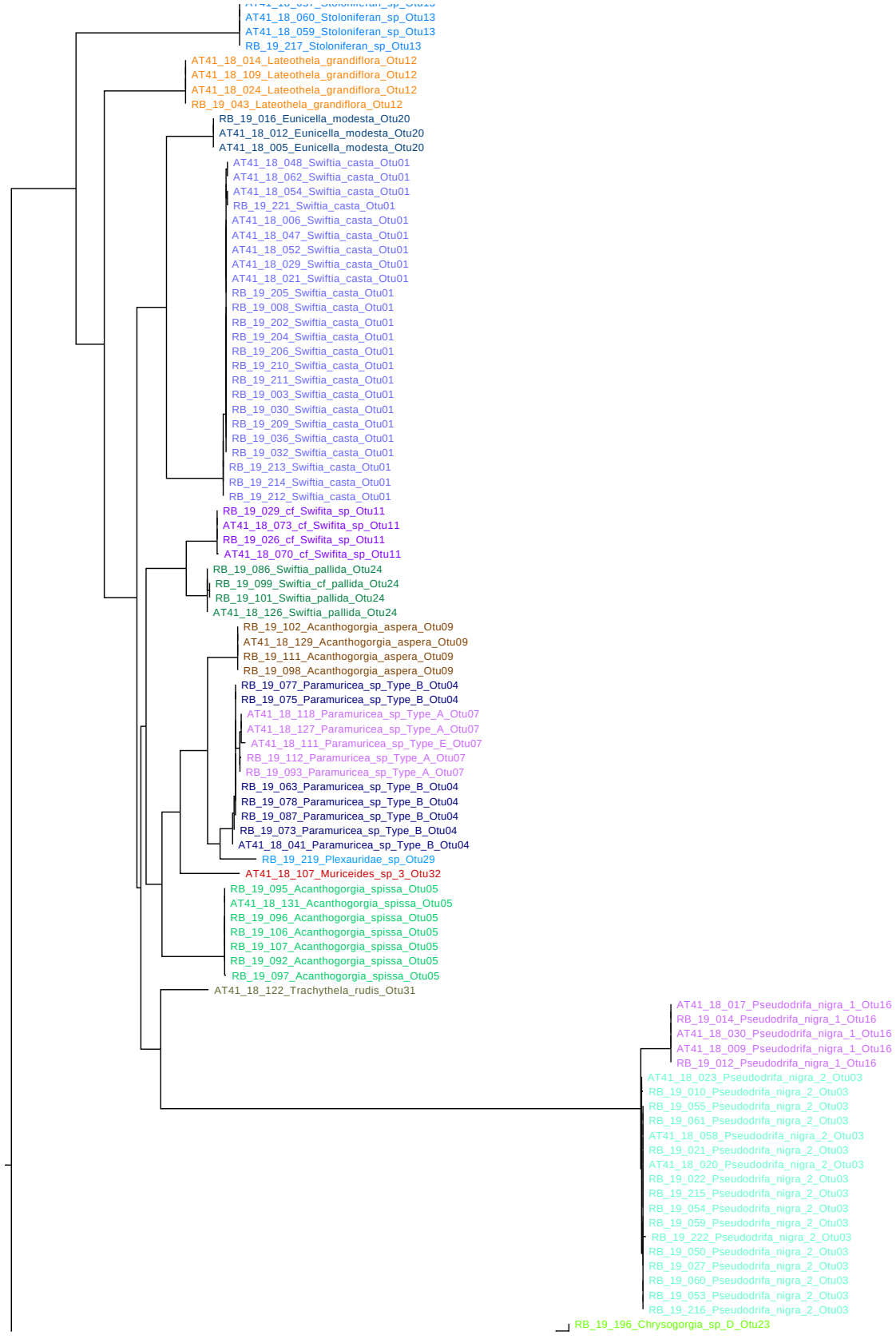

(continued next page)

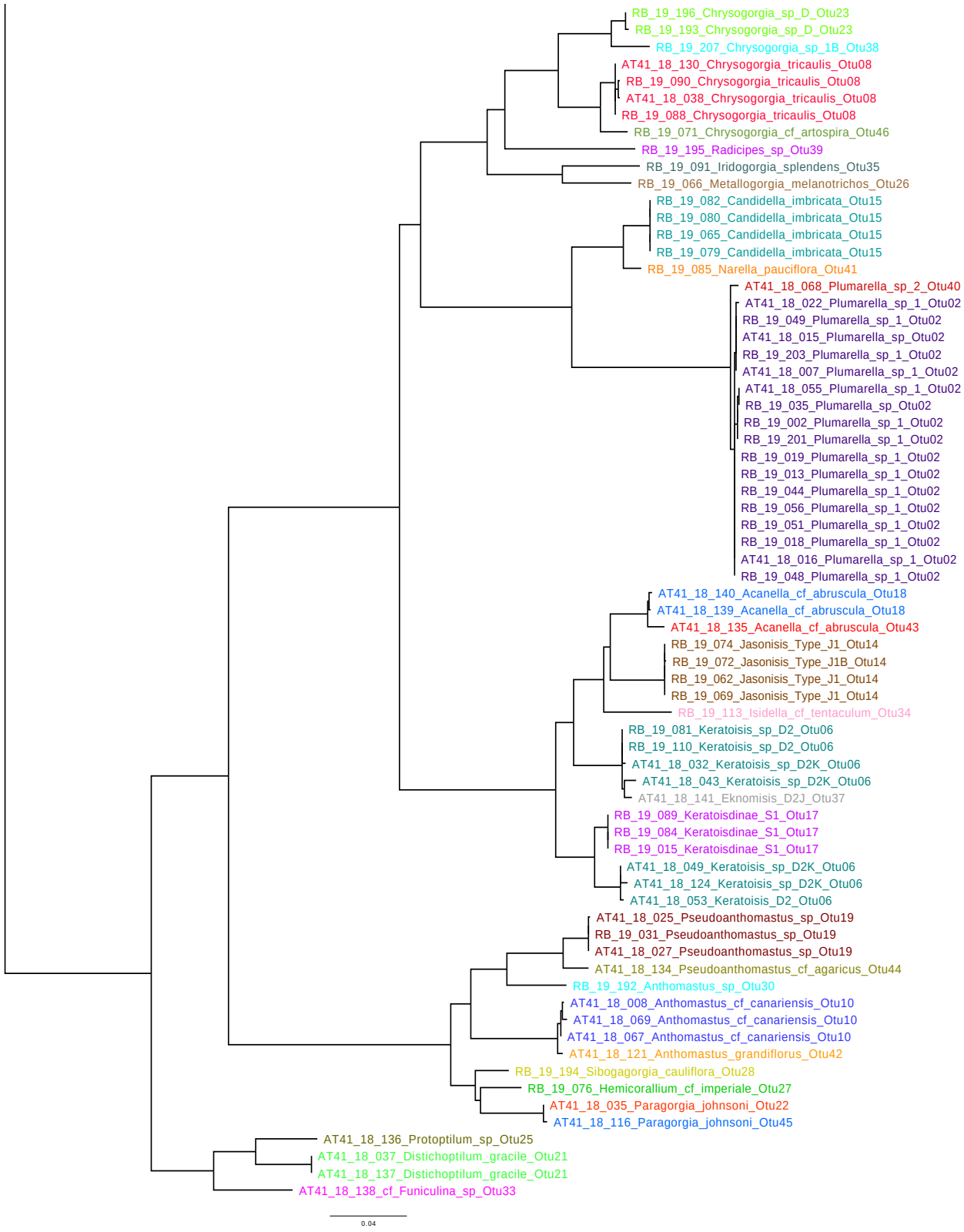

Figure 4-73. Maximum likelihood phylogeny of the multilocus (MutS + 28S) barcode
Barcode is rooted at the midpoint. Taxa names include final MOTUs assignments, and colors represent unique MOTUs (continued from previous page).

Patterns of octocoral community assembly across the western North Atlantic emerged from hierarchical cluster and multidimensional scaling analyses (**Figure 4-74**). Differences in community structure between habitat types (Global R = 0.26, p = 0.042; **Figure 4-75**) and between depth ranges (Global R = 0.472, p = 0.001; **Figure 4-76**) were suggested according to one-way ANOSIM tests. Out of the four habitat types surveyed, the greatest dissimilarities occurred between seep and hardbottom habitats (R = 0.571, p = 0.067) and between seep and coral habitats (R = 0.5, p = 0.1), although these differences were not statistically significant at p <0 .05. In contrast, communities were similar between hardbottom and coral (R = 0.019, p = 0.486) and between hardbottom and canyon habitats (R = 0.018, p = 0.40).

An nMDS ordination of community similarity in relation to habitat-type-grouped hardbottom sites with both coral and canyon sites, suggesting that these habitat types are compositionally similar (**Figure 4-76**). Despite a statistically significant one-way ANOSIM for habitat type, when controlling for the effect of depth in a two-way nested ANOSIM test, no habitat type differed significantly from any other (Global R = 0.556, p = 0.3; **Figure 4-77**). This result suggests that the differences between habitat types indicated by the one-way ANOSIM can be explained by patterns of depth distribution. This pattern is well illustrated by the two cold-seep sites (Blake Ridge Seep and Cape Fear Seep), which are simultaneously the only sites included within the 2,000–3,000 m depth category. Although these seeps share a common habitat, compositional similarities between the two cannot simply be attributed to habitat type alone. Habitat type (coral reef, canyon, seep, hardbottom) is thus not a key driver of octocoral community composition.

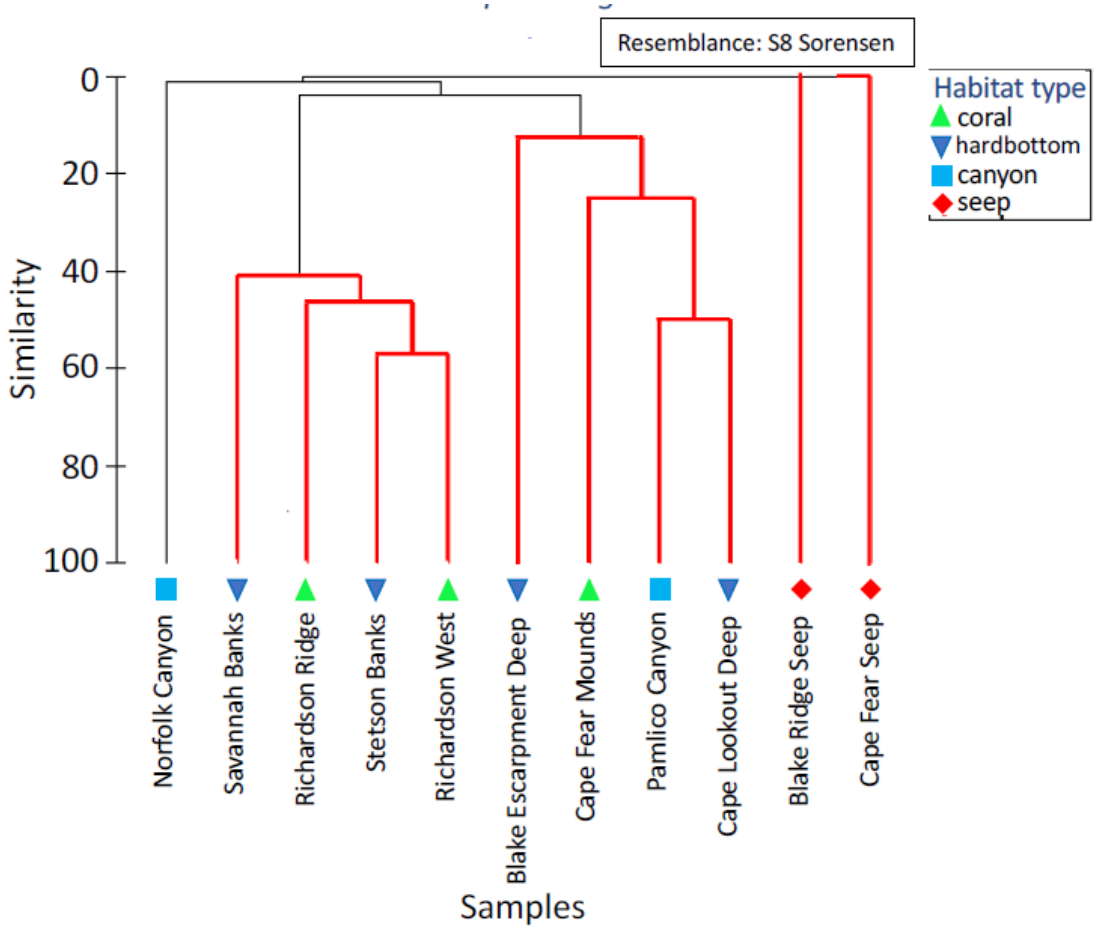

Figure 4-74. CLUSTER analysis of 11 dive sites

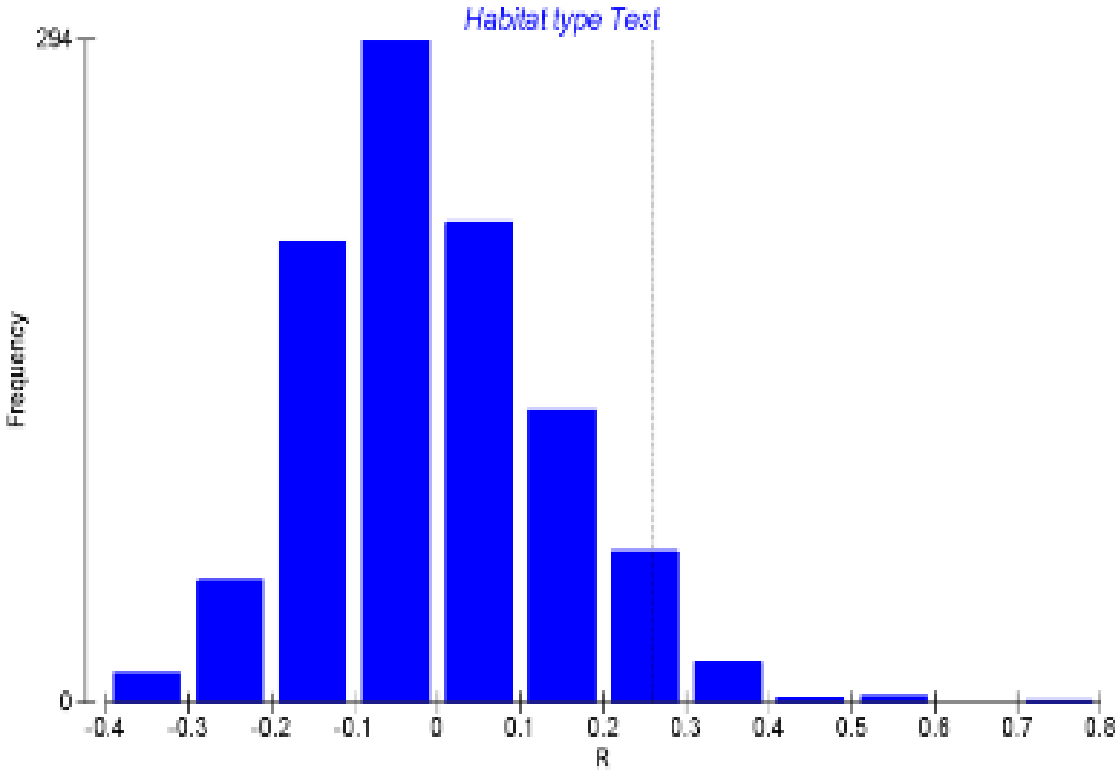

Figure 4-75. Histogram of habitat type permutations from one-way ANOSIM analysis

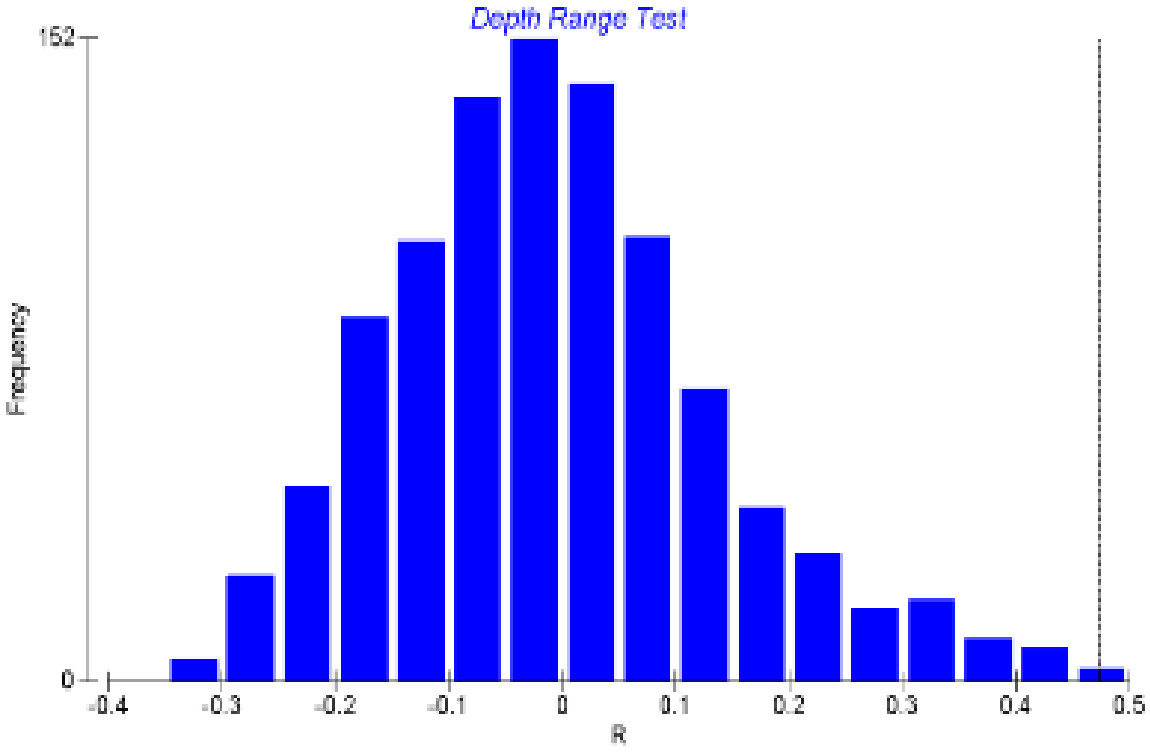

Figure 4-76. Histogram of depth range permutations from one-way ANOSIM analysis

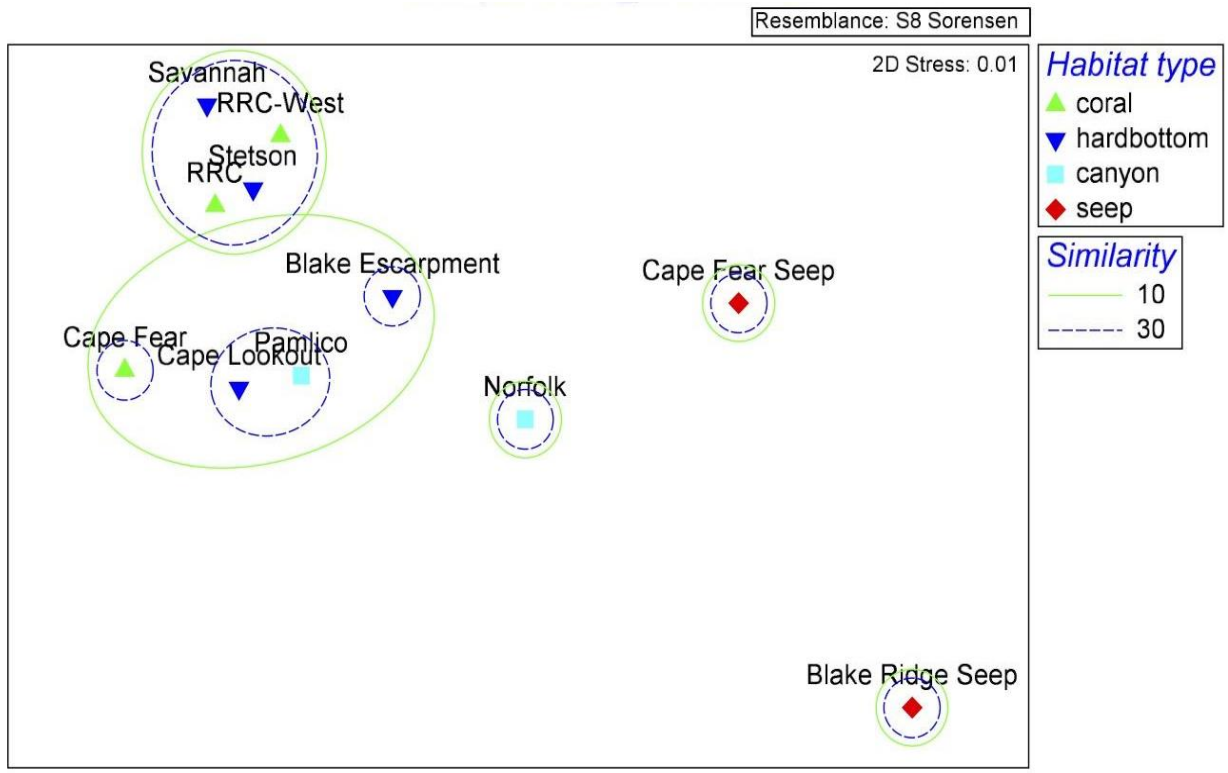

Figure 4-77. Multidimensional scaling ordination of samples coded to habitat type
Based on Sorenson's Index. Solid green circles indicate > 10% and black dotted circles indicate > 30% compositional similarity.

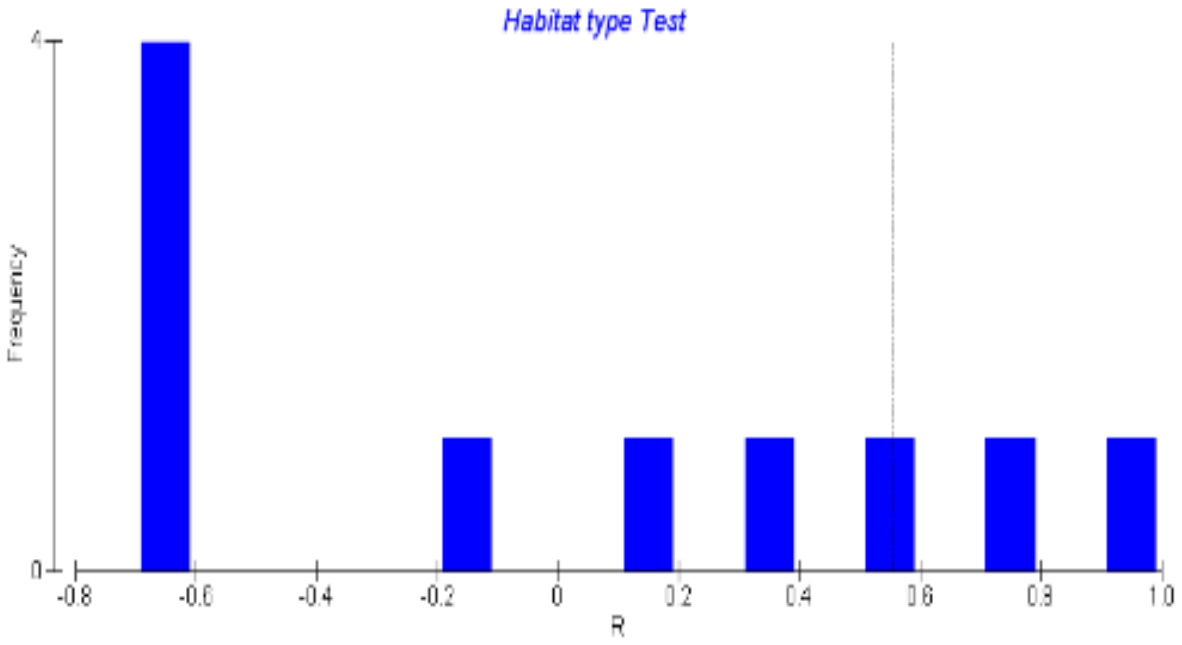

Figure 4-78. Histogram of habitat-type permutations
From a two-way nested ANOSIM controlling for depth range.

A pattern of community differentiation based on depth range emerged from ANOSIM analyses (Global R = 0.472, p = 0.001; **Figure 4-79**). We observed significant differences in community assembly between the 0–1,000 m depth range and the deeper two depth ranges: 1,000–2,000 m (R = 0.404, p = 0.024), and 2,000–3,000 m (R = 0.563, p = 0.036). The average dissimilarity between sites of the shallowest (0–1,000 m) and middle (1,000–2,000 m) depth categories was 94.0%, and average dissimilarity between the shallowest and deepest depth categories was 100% (SIMPER). The two deepest depth ranges did not differ significantly from one another (R = 0.5, p = 0.1). To control for the impact of habitat type on these results, we ran a two-way nested ANOSIM testing community differences among depth groups (Global R = 1, p = 0.067; **Figure 4-79**). While we did not find the differences to be statistically significant, the notably high global R-statistic and lower p-value of this test suggest that some differences do exist between depth ranges when controlling for habitat type, albeit they are marginally significant. This result which minimizes the impact of depth on community assembly is likely due in part to the constraints of a small sample size.

The nMDS ordination of community similarity with median depth overlain illustrated a pattern of grouping by depth (**Figure 4-80**). Specifically, four sites with >30% community similarity (SIMPROF group *b*) are among the shallowest in the study, with median depths ranging from 437 to 771 m. A second group containing four shallow-to-middle depth sites is > 10% similar (SIMPROF group *c*).

The three deepest sites, namely Blake Ridge Seep, Cape Fear Seep and Norfolk Canyon, each remain distinct in the plot from all other sites. To assess which species were the greatest contributors to similarities and differences across depth ranges, we conducted SIMPER analyses for using the Bray-Curtis measure of similarity.

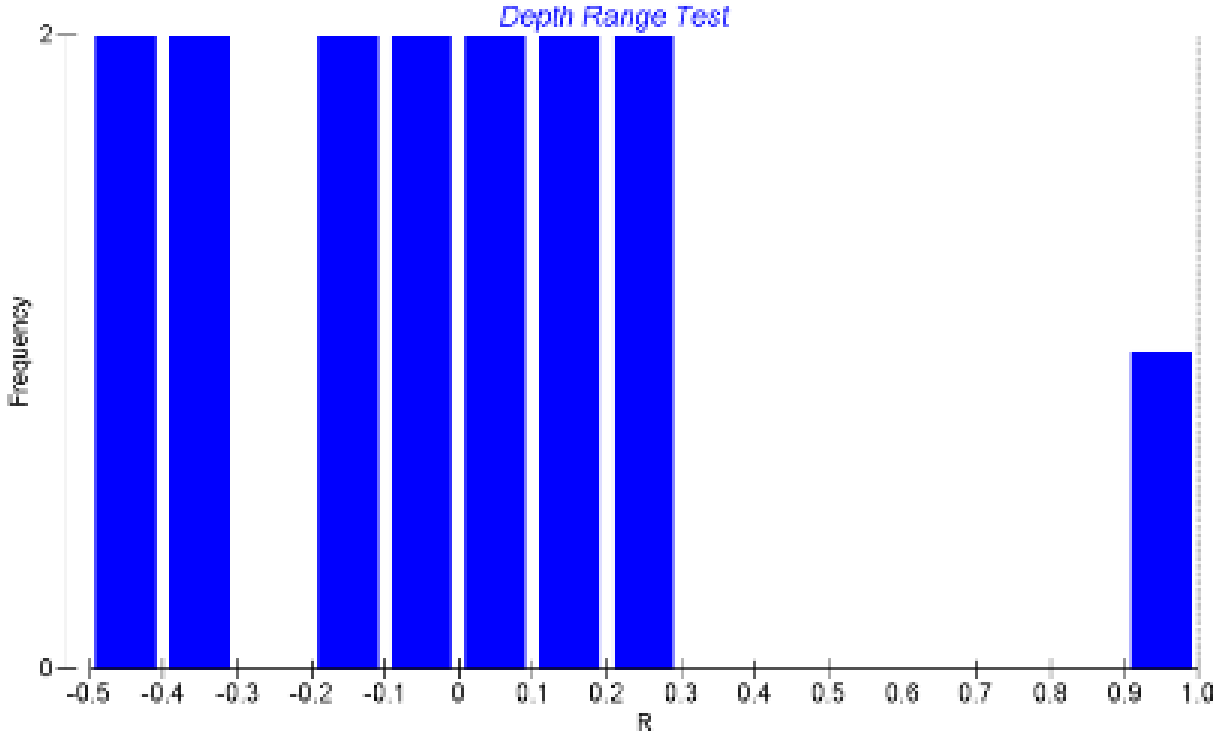

Figure 4-79. Histogram of depth range permutations
From a two-way nested ANOSIM controlling for habitat type.

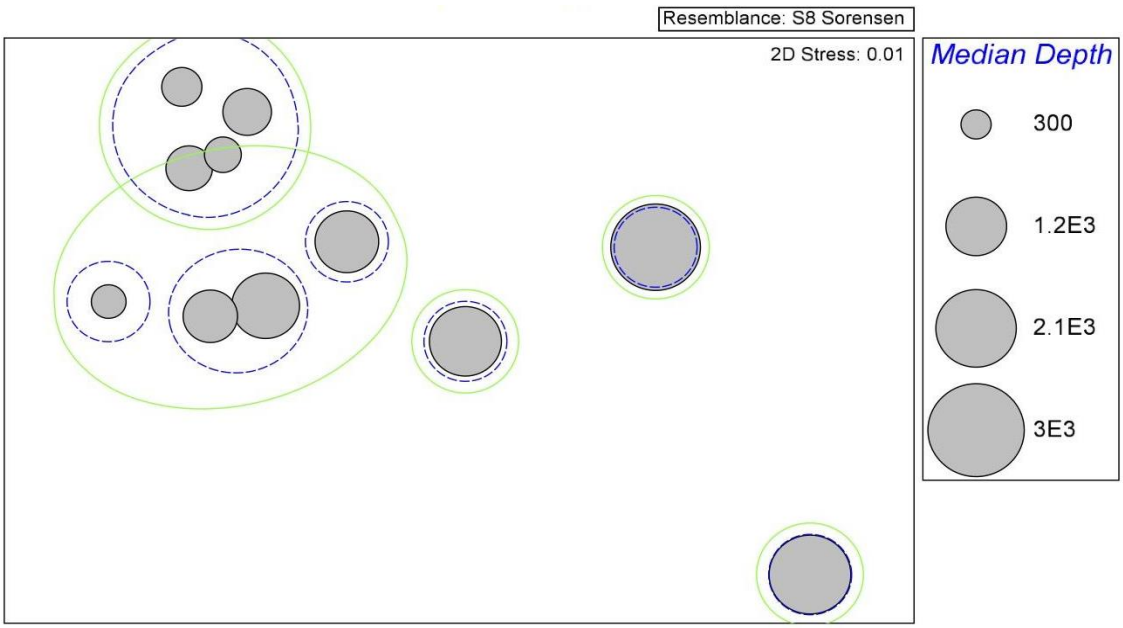

Figure 4-80. Multidimensional scaling ordination of site depth
Based on Sorenson's Index Solid green circles indicate > 10% and blue dotted circles indicate > 30% compositional similarity.

In terms of within-group similarity, sites within the 0–1,000 m depth range (n = 6) were found to be 22.7% similar to one another on average. The MOTUs driving similarity within the shallowest depth category include *Plumarella sp. 1* (MOTU 02) and *Pseudodrifa nigra sp. 2* (MOTU 03), each contributing 29.3% to the total similarity. *Swiftia casta* (MOTU 01) and *Paramuricea Type A/E* (MOTU 07) were the next highest contributors within this group, constituting 11.1 and 9.8% similarity, respectively. Sites occupying the middle depth range group of 1,000–2,000 m (n = 3) were 11.9% similar on average. From the middle depth category, *Distichoptilum gracile* (MOTU 21) contributed 26.7% to the total similarity, and three additional MOTUs each contributed 24.4%: *Keratoisis sp D2/D2K* (MOTU 06), *Chrysogorgia tricaulis* (MOTU 08) and *Swiftia pallida* (MOTU 24). Sites within 2,000–3,000 m (n = 2) were 0% similar to one another on average, and no MOTUs were shared across sites. Overall, within-group similarity was lowest for the deepest depth range and highest for the shallowest depth category of 0–1,000 m, where the largest number of MOTUs co-occurred.

Differences between community composition at shallow and middle depths were driven by a large number of species. *Distichoptilum gracile* (MOTU 21), *Plumarella sp. 1* (MOTU 02), *Pseudodrifa nigra sp. 2* (MOTU 03), *Chrysogorgia tricaulis* (MOTU 08) and *Swiftia pallida* (MOTU 24) accounted for the greatest dissimilarities between these depth groups, each contributing between 4 and 5% dissimilarity. Species accounting for differences between the shallowest and deepest depth categories were *Isidella cf tentaculum* (MOTU 34) which contributed 9.8%, and *Plumarella sp. 1* (MOTU 02) and *Pseudodrifa nigra sp. 2* (MOTU 03), which both contributed 9.2% to the total dissimilarity. Lastly, differences between the middle and deepest depth categories were driven by *Distichoptilum gracile* (MOTU 21), *Keratoisis sp D2/D2K* (MOTU 06), *Chrysogorgia tricaulis* (MOTU 08), *Swiftia pallida* (MOTU 24) and *Isidella cf tentaculum* (MOTU 34), which each contributed between 4 and 5% to the total dissimilarity. From these results, several taxa have emerged as drivers of similarity and difference in community composition in the study region, including *Distichoptilum gracile* (MOTU 21), *Pseudodrifa nigra sp. 2* (MOTU 03), *Plumarella sp. 1* (MOTU 02) and *Chrysogorgia tricaulis* (MOTU 08).

In addition to habitat type and depth, we examined the influence of temperature on community similarity in the nMDS plot (**Figure 4-81**). Temperature, an abiotic factor that can be informative to the distribution of coral communities (Yesson et al. 2012), co-varies with depth and water mass. To an extent, we can therefore hypothesize community assemblage patterns to run in parallel across depth and temperature. The group of four shallow sites of > 30% compositional similarity also has similar average temperatures. These range from 5.66 to 8.55°C and are elevated in comparison to all other sites (with the exception of Cape Fear Mounds, the other shallow-water site; **Figure 4-81**).

An *a priori* evaluation of compositional patterns across 11 sites resulted in the creation of four SIMPROF groups (**Figure 4-74**). Analyzing these clusters enabled us to recognize additional patterns and variables potentially involved in shaping octocoral community assembly across the region. SIMPROF group *b* includes four sites off the coast of South Carolina (Richardson Reef, Richardson Reef West, Stetson Banks and Savannah Banks). These sites all belong to the 0–1,000 m depth range group and are an average of 45.6% similar to one another (**Figure 4-74**). Sites within cluster *b* are geographically close, just south of the Charleston Bump, a deep-sea topographical feature which rises steeply from the seafloor causing the Gulf Stream to deflect seaward and form a series of eddies and currents. The exclusion of the deeper (1,327 m) Blake Escarpment Deep site from this group—despite its geographic closeness to the other sites in this cluster—highlights the potential importance of depth in shaping community structure. The MOTUs driving similarity among SIMPROF group *b* sites include *Plumarella sp. 1* (MOTU 02) and *Pseudodrifa nigra sp. 2* (MOTU 03), attributing 36.4% each to the total similarity.

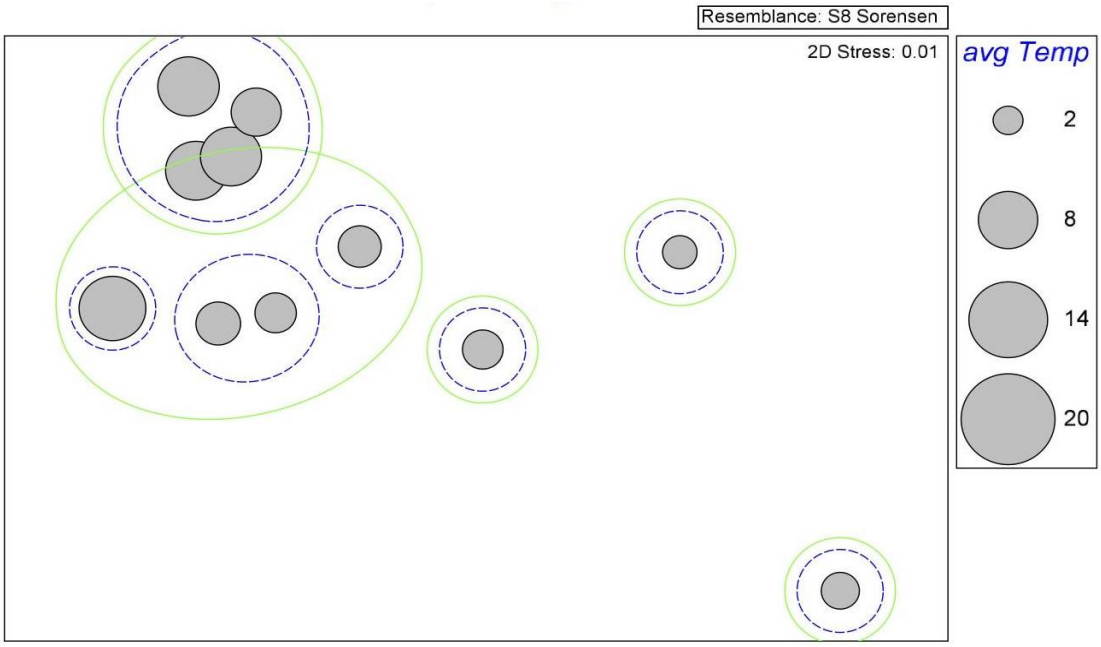

Figure 4-81. Multidimensional scaling ordination of average temperature
Based on Sorenson's Index. Solid green circles indicate > 10% and blue dotted circles indicate >3 0% compositional similarity.

Another four-site cluster is SIMPROF group *c* (Blake Escarpment Deep, Cape Fear Mounds, Cape Lookout Deep, and Pamlico Canyon), which has an average similarity of 23.0% (**Figure 4-74**) and is located primarily off North Carolina (with the exception of Blake Escarpment Deep, which is located off South Carolina). These sites occupy deeper water on average than group *b*, with median depths of 391 to 1,494 m. Similarities within group *c* are driven by *Paramuricea Type A/E* (MOTU 07), accounting for 48.4% of the total similarity, followed by *Keratoisis sp D2/D2K* (MOTU 06), contributing an additional 26.9%.

Despite their relatively close proximity, North Carolina group *b* and South Carolina group *c* are an average of 96.1% dissimilar from one another (**Figure 4-74**). Given the northward movement of the Gulf Stream current along the US eastern seaboard and therefore its potential to transport and disperse larvae throughout the region, we expected greater similarity across the sites composing these two groups. Instead, a high dissimilarity over a short geographic distance could in part be due to local changes in the Gulf Stream current as it passes over the Charleston Bump. This topographical feature and the oceanographic dynamics associated with it could promote local larval retention and inhibit dispersal, effectively isolating neighboring communities from one another and driving internal community similarity.

SIMPROF cluster *a* contains only Norfolk Canyon, the northernmost site in the present study and the only site located in the MAB rather than the SEUS (**Figure 4-82).** This canyon is 100% dissimilar from clusters *b* and *d*, and 97.6% dissimilar from cluster *c* (**Figure 4-74**). The taxa contributing mostly to dissimilarities between Norfolk Canyon cluster *a* and all other clusters are *Acanella cf abruscula* (MOTU 18 and MOTU 43), *Pseudoanthomastus cf agaricus,* (MOTU 44), *Distichoptilum gracile* (MOTU 21), *Protoptilum sp* (MOTU 25), *cf Funiculina sp* (MOTU 33) and *Keratoisidinae D2J* (MOTU 37).

The separate grouping of Norfolk Canyon from all other sites, notably those of the same depth range, complements our hypothesis that this canyon is dissimilar from other sites in the SEUS due to a biogeographic break located at Cape Hatteras. Due to the geomorphology of the cape and the resulting divergent movement of the Gulf Stream, larval flow between the MAB and SEUS is likely impeded. Thus, the biogeographic break that occurs at Cape Hatteras in shallow-water taxa can also be extended to deep-sea octocorals, driving dissimilarity between the two regions and explaining the compositional distinctiveness of Norfolk Canyon. Further support for this scenario is the high dissimilarity between Pamlico and Norfolk Canyons; two canyon features in similar depths but located south and north of Cape Hatteras, respectively.

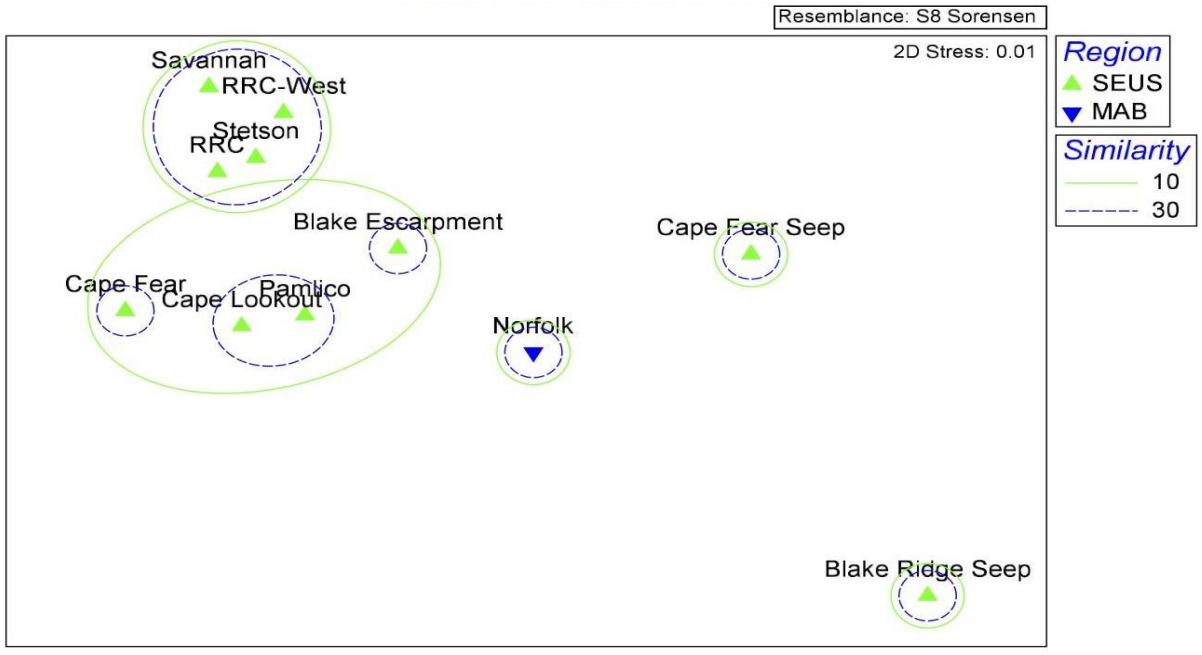

Figure 4-82. Multidimensional scaling ordination of region
Based on Sorenson's Index. Triangles represent unique sites. Green solid lines indicate 10% similarity and blue dotted lines indicate 30% similarity of species composition.

SIMPROF group *d* contains Blake Ridge Seep and Cape Fear Seep, two sites sharing a common habitat type and similar depth. Although these seep communities cluster together in the SIMPROF, their within-group similarity is 0% (**Figure 4-74**). This is likely an effect of a small sample size, particularly from Blake Ridge Seep (n =1). Group *d* is 100% dissimilar from all other clusters, driven by the MOTUs *Isidella cf tentaculum* (MOTU 34), *Chrysogorgia sp D* (MOTU 23), *Sibogagorgia cauliflora* (MOTU 28), *Anthomastus sp* (MOTU 30), *Radicipes sp* (MOTU 39). Corals found in these areas included those that can anchor in soft substrates as well as the hardbottom colonizers of authigenic carbonates present at the seep sites; hardbottom habitat was not extensive at these seeps.

Molecular barcoding and MOTU delimitation offer a proxy for species identification that can guide species diversity and distribution analyses while octocoral taxonomy is concurrently resolved. These genetic tools should continue to be used alongside morphological species assignments to assure relative consistency over time. According to the species-accumulation curve, future research expeditions in the SEUS region will likely lead to the discovery of additional species, particularly with sampling at deeper depths, but the upper bathyal octocoral assemblages have been adequately represented in the Deep SEARCH program.

Our results suggest community assembly is influenced in part by depth and associated variables (temperature), but not by habitat type. Therefore, we suggest that canyon, coral reef, and seep habitats in similar depths are equivalent habitats for octocoral establishment and persistence in the region. The Gulf Stream is also an important factor that shapes octocoral distribution via promoting or inhibiting dispersal; sites to the north of Charleston Bump were dissimilar to those from the south while Norfolk Canyon (in the MAB) was significantly dissimilar from all other sites. Future analyses could investigate the influence of conduits for dispersal on community composition in the SEUS region and throughout the greater Atlantic, in order to gain a more holistic view of the parameters shaping deepwater octocoral diversity and distribution. A refined understanding of community structure and improved habitat mapping capabilities can help to inform effective management of these vulnerable foundation species and the ecosystems they underpin.

4.4 Trophic Ecology

Section Authors: Amanda Demopoulos, Jennifer McClain-Counts, Jill Bourque

4.4.1 Background

The US Atlantic continental margin encompasses diverse habitat types over a range of depths (**Chapter 1**). For the purposes of generalizing the trophic ecology, we focused on three primary environments: coral habitats, seeps, and canyons, as well as site-specific analysis of the trophic function of midwater communities.

Deep-sea corals and their habitats are tightly dependent on the vertical or advected flux of organic matter transported via rapid currents. Deep-sea corals typically occur in areas of dynamic currents, sufficient food supply, poised over hard substrates to maximize access to food supplied via fast moving currents. In the mid-Atlantic region, Demopoulos et al. (2017) characterized deep-sea corals and other suspension feeders found in canyons and slope environments relying on surface-derived organic matter, consistent with work conducted elsewhere (Sherwood et al. 2009, Duineveld et al. 2012). The current study focused on expanding that effort to include several additional deep-sea coral habitats and hardbottom features found throughout the region (**Figure 4-83**). These features punctuate the otherwise flat seafloor, providing habitats for a variety of organisms, including sessile coral species and associates. Within these environments, we focused on a wide range of taxa and feeding groups in order to discern spatial and

interspecific patterns in the stable isotope values of corals, their associates, and estimate dominant nutritional resources.

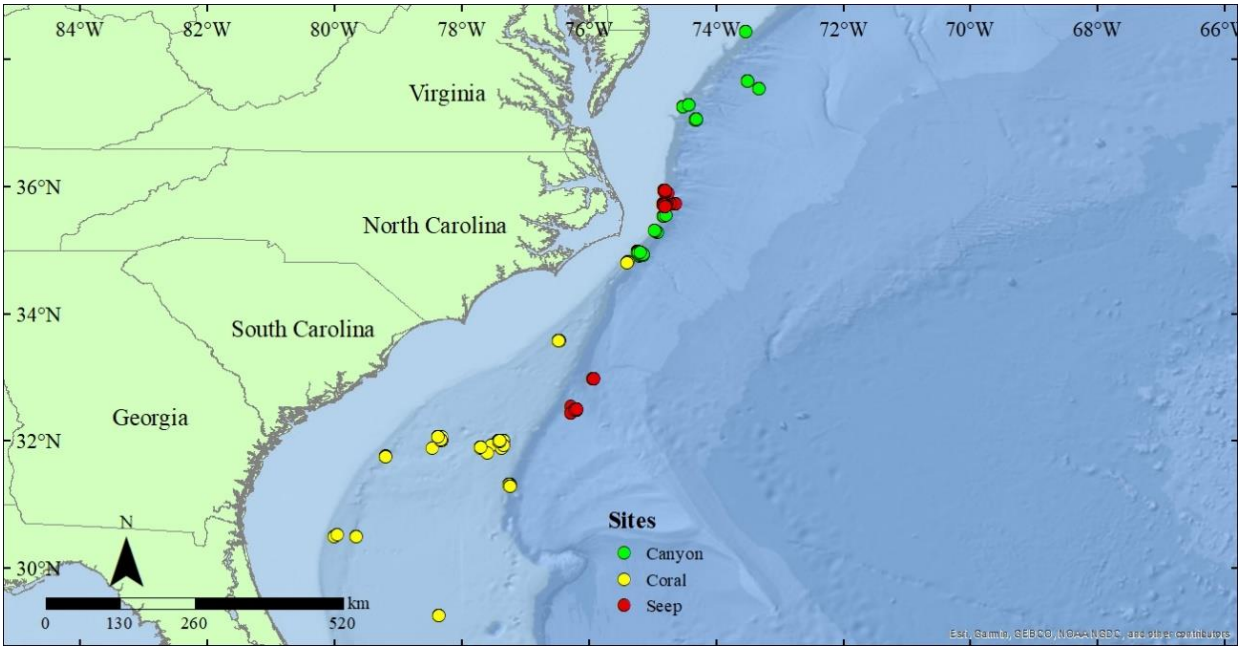

Figure 4-83. Collection locations for sites sampled during nine cruises from 2016–2019
NOTE: Sampling efforts focused on three general habitat types: canyon (green), coral (yellow) and seep (red).

The US Atlantic region is known to be a gas-hydrate province and a source for cold seeps. Early work characterized methane seepage in the SE region at the Blake Ridge Diapir followed by Cape Fear, associated with subsurface diapirs (Paull et al. 1995). More recently, multibeam sonar acoustic surveys from 2012 to present revealed several hundred discrete acoustic anomalies in the water column, which reflect bubble streams emanating from the seafloor and provide clues into locations of seep environments (Skarke et al. 2014). However, detailed geological and geophysical context to these recently discovered shallow and deep seeps, including methane sources and conduits for fluid flow, and their co-association with canyon features, remains unexplored.

The region has numerous chemosynthetic environments, some of which have been investigated in detail (Van Dover et al. 2003; Heyl et al. 2007; Brothers et al. 2013; Ross et al. 2015; Bourque et al. 2017; Prouty et al. 2016, 2020; Cleland et al. 2021; Quattrini et al. 2015; McVeigh et al 2018). Only a handful of studies within the region have examined the trophic ecology and estimated the reliance on chemosynthetically derived organic matter fueling surrounding seafloor inhabitants (Van Dover et al. 2003, Demopoulos et al. 2019, Turner et al. 2020, Vokhshoori et al. 2021). These areas are characterized by a variety of habitat types (mussel beds, tubeworms, microbial mats, authigenic carbonate), high degree of heterogeneity (including variable patch sizes), successional stages, and specialized organisms that can capitalize on the extreme environments, often with high concentrations of toxic sulfides.

Questions remain regarding whether these patterns are consistent at other US Atlantic seeps. By using stable isotope analysis, our goal was to identify primary carbon and energy sources for seep inhabitants. This expands upon previous work to provide more regional context to seep food webs and trophic diversity, with the ultimate goal to examine the role seeps play in fueling Atlantic margin environments.

Much like deep-sea coral habitats, benthic and pelagic communities residing within submarine canyons depend on particulate flux from surface waters for energy (Gage and Tyler 1991, Klages et al. 2003, De

Leo et al. 2010). Submarine canyons represent spatially heterogeneous environments in terms of faunal composition and food resource utilization. Much like terrestrial canyons, submarine canyons exhibit a high degree of topographic complexity, influencing variability in fluid flow and transport of particles, including food (Gibbs et al. 2020), which contrasts with the generally quiescent deep sea. Differences in flow can influence food quality and supply to consumers within canyons and in adjacent slope environments. Resuspension of material due to local hydrodynamics (internal tides) often create nepheloid layers at discrete depths; these layers are concentrated suspended material that includes POM, serving as a food source for deep-sea fauna (Demopoulos et al. 2017).

The consolidation and settlement of organic matter, both influenced by canyon morphology, may increase benthic productivity (Duineveld et al. 2001) and trophic complexity (Stefanescu 1994, Cartes and Sorbe 1999, Cartes et al. 2010, Romero-Romero et al. 2016). Thus, canyon-driven controls on the quality and quantity of food supply to the seafloor environments, may influence ecological niche space and biodiversity in submarine canyons (Dell'Anno et al. 2013). However, only a few studies have examined submarine-canyon, trophic complexity (Duineveld et al. 2001, Fanelli et al. 2009, Cartes et al. 2010, Jeffreys et al. 2011, Demopoulos et al. 2017). In this study, we examined stable isotopes, feeding groups, and trophic function of seafloor and pelagic communities within Norfolk and Pamlico Canyons in detail.

Midwater communities represent key components of oceanic food webs, serving as vectors for organic matter transport from surface to bottom, as well as food for demersal species (Hidaka et al. 2001, McClain-Counts et al. 2017). Their consumption of POM influences the available food supply to benthic communities. This study examined stable isotopes, in combination with available information on midwater feeding group classification, to characterize the trophic structure of mesopelagic communities at one representative site per habitat: seep, canyon, and deep-sea corals. We examined the isotope data in concert with benthic community isotopic composition to further understand long-term trophic transfer from surface through midwater environments to seafloor habitats.

The primary goal of this study element was to examine deep-sea food-web structure and trophic niches in deep-sea coral, canyon, and seep environments along the US mid- and south Atlantic margin using stable isotope analysis. We hypothesized that there would be distinct differences among these environments in terms of isotopic composition (across taxa and within feeding groups), given variability in the physics, chemistry, and dominant food-supply mechanisms which influence the quality and quantity of organic matter available to seafloor communities.

4.4.2 Methods

4.4.2.1 Stable Isotope Analysis

We dissected fish and invertebrate tissues for stable isotope analysis prior to preservation for vouchers. For consistency, we removed the subject tissue from similar body regions based on taxa (muscle from the dorsal region of fishes, caudal tissue of shrimps, leg muscle for crabs, mantle, gill and adductor muscle for mollusks, legs for brittle stars, gonads for urchins and polyps for corals). We dried tissue samples to a constant weight at 50–60°C, ground the samples to a fine powder and weighed them into tin capsules. We acidified invertebrate samples with 2N phosphoric acid to remove inorganic carbon. We dried POM filters and treated them with 1.0 N hydrochloric acid, then transferred the filters into tin boats. We homogenized sediment samples prior to drying, acidified them with 1.0 N phosphoric acid, re-homogenized the material then encapsulated it in tin capsules.

We analyzed samples for stable carbon and nitrogen isotope composition referenced to Vienna PeeDee Belemnite and atmospheric nitrogen gas, respectively. Samples from AT41-2018 and PC1704-2017 were analyzed at Washington State University using a Costech (Valencia, USA) elemental analyzer interfaced with a GV instruments (Manchester, UK) Isoprime isotope ratio mass spectrometer. Precision was

verified using egg albumin calibrated against National Institute of Standards reference materials and reproducibility was monitored using organic reference standards (Fry 2007) and duplicate samples. Samples from RB1903-2019, NF1909, BM-2018, EN615-2018, PI-2016, EN626-2018, and all sediments from AT41-2018 were analyzed at University of California Davis Stable Isotope Facility.

Fauna were analyzed using a PDZ Europa ANCA-GSL elemental analyzer interfaced to a PDZ Europa 20-20 isotope ratio mass spectrometer (Sercon Ltd., Cheshire, UK), whereas POM filters and sediments were analyzed either using an Elementar Vario EL Cube or Micro Cube elemental analyzer (Elementar Analysensysteme GmbH, Hanau, Germany) interfaced to either an Isoprime VisION IRMS (Elementar UK Ltd, Cheadle, UK) or a PDZ Europa 20-20 isotope ratio mass spectrometer (Sercon Ltd., Cheshire, UK). Precision and reproducibility were monitored using several reference standards calibrated again international reference materials, including IAEA-600, USGS-40, USGS-41, USGS-42, USGS-43, USGS-61, USGS-64, and USGS-65, and duplicate samples.

We finalized values by correcting the entire batch based on the known values of the included laboratory reference materials. We expressed isotope ratios in standard delta notation, $\delta^{13}C$ and $\delta^{15}N$, in per mil (‰). We analyzed a bovine liver standard at both labs with a SE of < 0.1% at Washington State University and at UC Davis for both carbon and nitrogen. There was no statistical difference between the two labs for carbon (Welch t-test, $p = 0.62$) or nitrogen (Welch t-test, $p = 0.54$). Reported $\delta^{13}C$ and $\delta^{15}N$ values are from acidified and non-acidified samples, respectively, in order to avoid the potential artefact to ^{15}N associated with acidification (Pinnegar and Polunin 1999). The long-term SD is 0.2‰ for $\delta^{13}C$ and 0.3‰ for $\delta^{15}N$.

We analyzed a subset of fauna from seep sites for sulfur isotopes ($\delta^{34}S$) at the Washington State University Stable Isotope Core Laboratory using an elemental analyzer (ECS 4010, Costech Analytical, Valencia, CA) coupled to a Delta PlusXP Thermo-Finnigan continuous flow isotope ratio mass spectrometer. Sulfur isotope ratios ($\delta^{34}S$) are reported in per mil (‰) relative to Vienna Canyon Diablo Troilite and analytical accuracy was determined by replicate analysis of internal lab standard referenced to seven international standards (Silver sulfide IAEA S-1, IAEA S-2, IAEA S-3, IAEA S-4) and barium sulfates (IAEA SO5, IAEA SO6, NBS127), the inclusion of bovine liver standard, and duplicate samples in every run. The long-term SD is 0.5‰ for $\delta^{34}S$.

4.4.2.2 Statistical Analysis

All data are reported in McClain-Counts et al. (2022). We tested isotope data for normality (Shapiro-Wilk) and equal variance (Levene's test) in SigmaStat 12.5. We analyzed comparisons among feeding groups at canyon and seep sites using one-way ANOVA followed by Holm-Sidak post-hoc pairwise comparisons, or ANOVA on the Ranks followed by Dunn's Method pairwise comparisons when data failed normality or equal variance tests. When data failed normality or equal variance tests, a t-test, or Mann-Whitney Rank Sum Test, was used to determine differences between feeding groups at the two canyon sites. We examined depth relationships to carbon and nitrogen isotope data using Spearman's rank correlation. A significance level of $p < 0.05$ was used for all tests.

4.4.3 Results

4.4.3.1 Coral Communities

We analyzed a total of 467 samples (7 sediment, 46 POM, and 414 fauna samples) for $\delta^{13}C$ and $\delta^{15}N$ isotopes from six coral sites. Fauna represented six phyla and encompassed four feeding groups (Benthic, Benthic/Pelagic, Benthic/Suspension, and Suspension). Despite the coral sites occurring at a wide depth range (Cape Fear [381–407 m] to Blake Deep [1,318–1,336 m]), there was overlap in POM $\delta^{13}C$ across the sites sampled, suggesting a consistent isotopic signal of this baseline carbon source, primarily derived

from photosynthetic material (**Figure 4-84, Table 4-21**). POM samples covered a broad range of $\delta^{15}N$ values (Surface: 1.7 to 4.0‰, Bottom: 5.8 to 9.1‰) with average bottom and midwater POM enriched in ^{15}N compared to surface POM (**Figure 4-84**).

Faunal $\delta^{13}C$ values indicated the primary carbon source was likely photosynthetic material, with fauna ranging from -21.4 ± 0.2‰ (Lysianassoidea sp.) to -15.7‰ (Ophiuroidea, n = 1, [Richardson], Gastropoda [Stetson], **Figure 4-84, Table 4-21**). *Eumunida picta* (benthic feeder) had the highest $\delta^{15}N$ value (15.8‰), whereas the stony coral, *Madrepora oculata*, had the lowest $\delta^{15}N$ values (7.0 ± 0.4‰); both taxa were from Richardson Reef Complex.

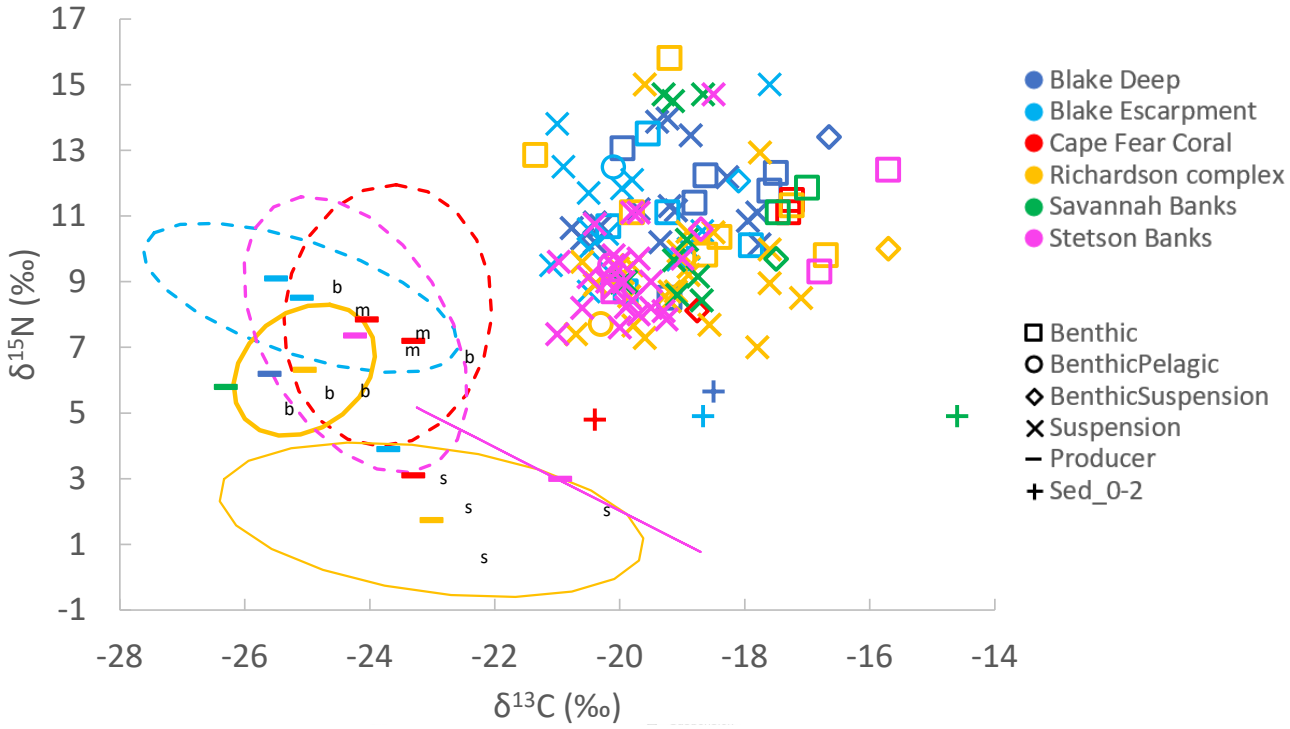

Figure 4-84. Average $\delta^{13}C$ and $\delta^{15}N$ of fauna, producers, and sediment at coral locations
Average $\delta^{13}C$ and $\delta^{15}N$ ± 1SD isotope values of fauna, producers (POM) and sediment (0–2 cm) collected at coral locations during cruises from 2016–2019. Colors represent different sampling locations and symbols differentiate feeding groups, producers (POM) and sediment. POM is separated into bottom, midwater, and surface values with averages and when possible, 95% confidence intervals. Thick solid lines represent (b)ottom POM, thin solid lines represent (s)urface POM and dashed lines represent (m)idwater POM.

Table 4-21. Mean $\delta^{13}C$ and $\delta^{15}N$ for fauna, POM, and sediment collected from coral sites

Mean isotope values of $\delta^{13}C$ and $\delta^{15}N$ (‰, SD, and range [min/max]) for fauna, POM (b= bottom, m=midwater, s=surface) and surface sediment (0–2 cm) collected from coral sites using underwater vehicles and CTDs during research cruises from 2018–2019. FG represent the different feeding groups: BE = benthic, BP-btm = Benthic/Pelagic bottom collection, BS = Benthic/Suspension, SS = Suspension. PR = producer, NA = not applicable.

-		Blake Deep			Blake Escarpment			Cape Fear			Richardson complex			Savannah Banks			Stetson Banks		
Taxon	**FG**	**n**	**$\delta^{13}C$ ‰**	**$\delta^{15}N$ ‰**	**n**	**$\delta^{13}C$ ‰**	**$\delta^{15}N$ ‰**	**n**	**$\delta^{13}C$ ‰**	**$\delta^{15}N$ ‰**	**n**	**$\delta^{13}C$ ‰**	**$\delta^{15}N$ ‰**	**n**	**$\delta^{13}C$ ‰**	**$\delta^{15}N$ ‰**	**n**	**$\delta^{13}C$ ‰**	**$\delta^{15}N$ ‰**
Annelida																			
Annelida	**BE**	**2**	**SD = -18.8 (0.6) Range = -19.2 / -18.4**	**SD = 11.4 (1.3) Range = 10.5 / 12.3**	**-**	**-**	**-**	**-**	**-**	**-**	**-**	**-**	**-**	**-**	**-**	**-**	**-**	**-**	**-**
Bylgides sp.	BE	-	-	-	1	SD = -19.9	SD = 8.7	-	-	-	-	-	-	-	-	-	-	-	-
Dasybranchus sp.	BE	-	-	-	-	-	-	-	-	-	-	-	-	-	-	-	1	SD = -16.8	SD = 9.3
Eunice norvegica	BE	-	-	-	-	-	-	1	SD = -17.3	SD = 11.1	7	SD = -17.2 (0.8) Range = -18.4 / -15.9	SD = 11.3 (0.7) Range = 10.1 / 12.4	3	SD = -17.5 (0.3) Range = -17.7 / -17.2	SD = 11.1 (0.3) Range = 10.8 / 11.4	-	-	-
Eunicidae	BE	-	-	-	-	-	-	-	-	-	-	-	-	2	SD = -17.0 (0.4) Range = -17.3 / -16.7	SD = 11.9 (0.2) Range = 11.7 / 12.0	-	-	-
Eunoe sp.	BE	-	-	-	3	SD = -19.2 (0.8) Range = -20.1 / -18.7	SD = 11.1 (0.4) Range = 10.7 / 11.4	-	-	-	-	-	-	-	-	-	-	-	-
Harmothoe sp.	BE	-	-	-	-	-	-	-	-	-	2	SD = -18.4 (0.4) Range = -18.7 / -18.1	SD = 10.4 (0.4) Range = 10.1 / 10.6	-	-	-	-	-	-
Hesionidae	BE	-	-	-	1	SD = -17.9	SD = 10.1	-	-	-	-	-	-	-	-	-	-	-	-
Malmgreniella sp.	BE	-	-	-	5	SD = -20.2 (0.4) Range = -20.4 / -19.5	SD = 10.7 (0.6) Range = 10.2 / 11.6	-	-	-	-	-	-	-	-	-	-	-	-
Polychaeta	BE	1	SD = -19.2	SD = 8.5	-	-	-	-	-	-	-	-	-	-	-	-	-	-	-
Polynoidae	BE	4	SD = -18.6 (1.2) Range = -19.8 / -17.1	SD = 12.2 (1.5) Range = 10.8 / 14.3	-	-	-	-	-	-	-	-	-	-	-	-	-	-	-

-		Blake Deep			Blake Escarpment			Cape Fear			Richardson complex			Savannah Banks			Stetson Banks		
Taxon	**FG**	**n**	**δ13C ‰**	**δ15N ‰**	**n**	**δ13C ‰**	**δ15N ‰**	**n**	**δ13C ‰**	**δ15N ‰**	**n**	**δ13C ‰**	**δ15N ‰**	**n**	**δ13C ‰**	**δ15N ‰**	**n**	**δ13C ‰**	**δ15N ‰**
Sabellidae	SS	-	-	-	-	-	-	1	SD = -17.1	SD = 11.3	-	-	-	-	-	-	-	-	-
Arthropoda																			
Amphipoda	BP-btm	-	-	-	-	-	-	-	-	-	1	SD = -20.3	SD = 7.7	-	-	-	2	SD = -20.2 (0.1) Range = -20.2 / -20.1	SD = 9.5 (0.6) Range = 9.1 / 9.9
Cirripedia - Barnacle	SS	-	-	-	3	SD = -20.0 (0.5) Range = -20.4 / -19.5	SD = 11.8 (2.0) Range = 10.2 / 14.1	-	-	-	-	-	-	-	-	-	1	SD = -19.7	SD = 8.0
Dynameniscus carinatus	BE	-	-	-	2	SD = -19.6 (0.1) Range = -19.6 / -19.5	SD = 13.5 (0.1) Range = 13.4 / 13.6	-	-	-	-	-	-	-	-	-	-	-	-
Eumunida picta	BE	-	-	-	-	-	-	-	-	-	1	SD = -19.2	SD = 15.8	-	-	-	1	SD = -20.1	SD = 8.7
Galatheidae sp.	BE	-	-	-	-	-	-	-	-	-	1	SD = -16.7	SD = 9.8	-	-	-	-	-	-
Lysianassoidea	BE	-	-	-	-	-	-	-	-	-	2	SD = -21.4 (0.2) Range = -21.5 / -21.2	SD = 12.9 (1.3) Range = 11.9 / 13.8	-	-	-	-	-	-
Rhachotropis oculata	BP-btm	-	-	-	6	SD = -20.1 (0.2) Range = -20.3 / -19.9	SD = 12.5 (0.9) Range = 11.8 / 14.2	-	-	-	-	-	-	-	-	-	-	-	-
Cnidaria																			
Acanthogorgia sp.	SS	-	-	-	1	SD = -19.8	SD = 12.1	-	-	-	-	-	-	-	-	-	-	-	-
Actiniaria sp 2	SS	-	-	-	-	-	-	-	-	-	-	-	-	-	-	-	1	SD = -19.0	SD = 9.7
Actinioidea sp	SS	-	-	-	-	-	-	-	-	-	-	-	-	-	-	-	1	SD = -20.1	SD = 9.8
Alcyonacea sp.	SS	-	-	-	-	-	-	-	-	-	-	-	-	4	SD = -18.9 (0.7) Range = -19.7 / -18.1	SD = 10.3 (0.7) Range = 9.5 / 11.0	-	-	-
Amphianthidae sp 1	SS	-	-	-	-	-	-	2	SD = -19.1 (0.7) Range = -19.6 / -18.6	SD = 8.8 (0.5) Range = 8.4 / 9.1	-	-	-	-	-	-	2	SD = -19.3 (0.1) Range = -19.3 / -19.2	SD = 7.9 (0.1) Range = 7.8 / 7.9

-		Blake Deep			Blake Escarpment			Cape Fear			Richardson complex			Savannah Banks			Stetson Banks		
Taxon	**FG**	**n**	**δ13C ‰**	**δ15N ‰**	**n**	**δ13C ‰**	**δ15N ‰**	**n**	**δ13C ‰**	**δ15N ‰**	**n**	**δ13C ‰**	**δ15N ‰**	**n**	**δ13C ‰**	**δ15N ‰**	**n**	**δ13C ‰**	**δ15N ‰**
Anemone	SS	-	-	-	3	SD = -20.1 (0.6) Range = -20.8 / -19.8	SD = 9.2 (0.3) Range = 8.9 / 9.5	1	SD = -19.1	SD = 8.0	1	SD = -18.9	SD = 9.2	-	-	-	1	SD = -19.5	SD = 8.2
Bamboo coral	SS	1	SD = -19.2	SD = 11.3	-	-	-	-	-	-	-	-	-	-	-	-	-	-	-
cf. Bathypathes sp.	SS	-	-	-	1	SD = -19.2	SD = 8.4	-	-	-	-	-	-	-	-	-	-	-	-
cf. Plexauridae sp 1	SS	-	-	-	-	-	-	-	-	-	2	SD = -20.0 (0.2) Range = -20.1 / -19.8	SD = 9.3 (0.5) Range = 8.9 / 9.6	-	-	-	-	-	-
Chrysogorgia	SS	2	SD = -19.4 (2.1) Range = -20.8 / -17.9	SD = 10.2 (0.8) Range = 9.6 / 10.8	-	-	-	-	-	-	-	-	-	-	-	-	-	-	-
Chrysogorgia cf. artospira	SS	1	SD = -20.4	SD = 10.8	-	-	-	-	-	-	-	-	-	-	-	-	-	-	-
Chrysogorgia tricaulis	SS	3	SD = -20.8 (0.4) Range = -21.1 / -20.4	SD = 10.6 (1.2) Range = 9.3 / 11.7	1	SD = -20.5	SD = 8.7	-	-	-	-	-	-	-	-	-	-	-	-
Cup coral	SS	-	-	-	-	-	-	-	-	-	-	-	-	-	-	-	1	SD = -21.0	SD = 7.4
Desmophyllum sp.	SS	6	SD = -17.8 (2.7) Range = -20.6 / -14.0	SD = 10.1 (0.9) Range = 8.9 / 11.4	-	-	-	-	-	-	-	-	-	-	-	-	-	-	-
Enallopsammia rostrata	SS	-	-	-	1	SD = -21.1	SD = 9.5	-	-	-	-	-	-	-	-	-	-	-	-
Enallopsammia sp.	SS	-	-	-	-	-	-	-	-	-	2	SD = -19.9 (0.5) Range = -20.2 / -19.5	SD = 8.6 (0.5) Range = 8.2 / 8.9	6	SD = -19.1 (1.0) Range = -20.1 / -17.4	SD = 9.7 (0.4) Range = 9.1 / 10.1	5	SD = -20.5 (0.6) Range = -21.5 / -20.1	SD = 9.1 (0.5) Range = 8.4 / 9.7
Epizoanthus cf. corallizoanthus	SS	-	-	-	-	-	-	-	-	-	-	-	-	-	-	-	5	SD = -19.9 (0.1) Range = -20.0 / -19.7	SD = 8.2 (0.2) Range = 8.0 / 8.5
Epizoanthus cf. illorciatus	SS	-	-	-	-	-	-	1	SD = -19.2	SD = 10.0	-	-	-	-	-	-	-	-	-

-		Blake Deep			Blake Escarpment			Cape Fear			Richardson complex			Savannah Banks			Stetson Banks		
Taxon	**FG**	**n**	**δ13C ‰**	**δ15N ‰**	**n**	**δ13C ‰**	**δ15N ‰**	**n**	**δ13C ‰**	**δ15N ‰**	**n**	**δ13C ‰**	**δ15N ‰**	**n**	**δ13C ‰**	**δ15N ‰**	**n**	**δ13C ‰**	**δ15N ‰**
Eunicella modesta	SS	-	-	-	-	-	-	-	-	-	1	SD = -20.7	SD = 7.4	-	-	-	-	-	-
Hormathiidae sp 1	SS	-	-	-	-	-	-	4	SD = -19.5 (0.4) Range = -19.9 / -19.0	SD = 9.7 (0.7) Range = 8.9 / 10.4	-	-	-	-	-	-	-	-	-
Hydroid	SS	5	SD = -18.3 (0.7) Range = -19.5 / -17.7	SD = 12.2 (0.5) Range = 11.4 / 12.7	5	SD = -18.7 (0.4) Range = -19.3 / -18.3	SD = 10.5 (1.1) Range = 8.9 / 11.9	7	SD = -19.8 (0.5) Range = -20.7 / -19.2	SD = 8.0 (0.3) Range = 7.6 / 8.5	-	-	-	10	SD = -18.7 (0.6) Range = -20.0 / -18.2	SD = 8.4 (0.4) Range = 7.7 / 9.1	8	SD = -19.8 (1.0) Range = -21.5 / -18.9	SD = 8.4 (0.9) Range = 7.4 / 10.4
Isidella sp. S1	SS	-	-	-	-	-	-	-	-	-	1	SD = -20.6	SD = 9.6	-	-	-	-	-	-
Jasonisis Type J1	SS	2	SD = -20.6 (0.3) Range = -20.8 / -20.4	SD = 10.3 (0.1) Range = 10.2 / 10.4	-	-	-	-	-	-	-	-	-	-	-	-	-	-	-
Jasonisis Type J1b	SS	1	SD = -20.4	SD = 10.2	-	-	-	-	-	-	-	-	-	-	-	-	-	-	-
Keratoisidinae S1	SS	1	SD = -19.7	SD = 11.2	-	-	-	-	-	-	-	-	-	-	-	-	1	SD = -20.2	SD = 9.0
Keratoisis sp. Type D2K	SS	-	-	-	2	SD = -20.2 (0.1) Range = -20.3 / -20.1	SD = 10.5 (0.5) Range = 10.1 / 10.8	-	-	-	-	-	-	-	-	-	1	SD = -20.0	SD = 7.6
Keratoisis type D2	SS	1	SD = -20.3	SD = 10.7	-	-	-	-	-	-	-	-	-	-	-	-	-	-	-
Lateothela grandiflora	SS	-	-	-	-	-	-	1	SD = -19.6	SD = 10.0	2	SD = -19.2 (0.7) Range = -19.7 / -18.7	SD = 8.7 (1.3) Range = 7.8 / 9.6	-	-	-	-	-	-
Leiopathes cf. montana	SS	-	-	-	-	-	-	-	-	-	-	-	-	-	-	-	1	SD = -20.6	SD = 8.2
Leiopathes sp.	SS	-	-	-	-	-	-	-	-	-	-	-	-	-	-	-	1	SD = -20.1	SD = 8.8
Leptothecata incertae sedis	SS	-	-	-	-	-	-	-	-	-	10	SD = -19.8 (0.6) Range = -21.1 / -19.1	SD = 7.7 (0.5) Range = 6.7 / 8.4	-	-	-	-	-	-
Lophelia pertusa	SS	-	-	-	-	-	-	4	SD = -20.3 (0.4) Range = -20.6 / -19.9	SD = 11.7 (1.8) Range = 9.5 / 13.8	16	SD = -18.6 (1.5) Range = -20.6 / -15.9	SD = 7.7 (2.0) Range = 3.5 / 10.3	2	SD = -18.8 (0.5) Range = -19.1 / -18.4	SD = 9.2 (0.1) Range = 9.1 / 9.2	4	SD = -20.4 (0.4) Range = -20.9 / -20.0	SD = 10.8 (1.4) Range = 9.3 / 12.6

-		Blake Deep			Blake Escarpment			Cape Fear			Richardson complex			Savannah Banks			Stetson Banks		
Taxon	**FG**	**n**	**δ13C ‰**	**δ15N ‰**	**n**	**δ13C ‰**	**δ15N ‰**	**n**	**δ13C ‰**	**δ15N ‰**	**n**	**δ13C ‰**	**δ15N ‰**	**n**	**δ13C ‰**	**δ15N ‰**	**n**	**δ13C ‰**	**δ15N ‰**
Madrepora oculata	SS	-	-	-	-	-	-	-	-	-	2	SD = -17.8 (3.3) Range = -20.1 / -15.5	SD = 7.0 (0.4) Range = 6.7 / 7.3	-	-	-	-	-	-
Madrepora sp.	SS	-	-	-	1	SD = -20.9	SD = 12.5	2	SD = -20.0 (0.4) Range = -20.3 / -19.7	SD = 9.2 (1.3) Range = 8.2 / 10.1	4	SD = -17.6 (1.9) Range = -18.9 / -14.8	SD = 10.0 (0.8) Range = 9.1 / 11.0	-	-	-	-	-	-
Muriceides cf. hirta	SS	-	-	-	-	-	-	1	SD = -20.5	SD = 8.4	-	-	-	-	-	-	-	-	-
Paragorgia johnsoni	SS	-	-	-	1	SD = -20.5	SD = 10.6	-	-	-	-	-	-	-	-	-	-	-	-
Paramuricea	SS	1	SD = -17.8	SD = 11.1	-	-	-	-	-	-	-	-	-	-	-	-	-	-	-
Paramuricea sp. Type B	SS	-	-	-	1	SD = -20.5	SD = 11.7	-	-	-	-	-	-	-	-	-	-	-	-
Paramuricea sp. Type E	SS	-	-	-	-	-	-	1	SD = -20.2	SD = 9.6	-	-	-	-	-	-	-	-	-
Paramuricea type B	SS	3	SD = -19.1 (0.8) Range = -20.0 / -18.4	SD = 11.2 (0.3) Range = 10.9 / 11.4	-	-	-	-	-	-	-	-	-	-	-	-	-	-	-
Plexauridae	SS	-	-	-	-	-	-	-	-	-	-	-	-	-	-	-	1	SD = -20.0	SD = 9.6
Plumarella sp.	SS	-	-	-	-	-	-	-	-	-	1	SD = -19.8	SD = 9.5	1	SD = -19.9	SD = 9.0	-	-	-
Plumarella sp. 1	SS	-	-	-	-	-	-	-	-	-	14	SD = -20.0 (0.4) Range = -20.8 / -19.4	SD = 9.4 (0.4) Range = 8.8 / 10.3	4	SD = -20.0 (0.3) Range = -20.2 / -19.6	SD = 9.0 (0.3) Range = 8.5 / 9.3	1	SD = -19.3	SD = 8.1
Plumarella sp. 2	SS	-	-	-	-	-	-	-	-	-	-	-	-	-	-	-	1	SD = -19.7	SD = 11.1
Pseudoanthomastus sp.	SS	-	-	-	-	-	-	1	SD = -19.2	SD = 8.4	-	-	-	-	-	-	-	-	-
Pseudodrifa nigra	SS	-	-	-	-	-	-	2	SD = -17.6 (1.7) Range = -18.8 / -16.4	SD = 9.0 (0.1) Range = 8.9 / 9.0	-	-	-	-	-	-	-	-	-
Pseudodrifa nigra 1	SS	-	-	-	-	-	-	2	SD = -18.5 (0.3) Range = -18.7 / -18.3	SD = 10.5 (0.1) Range = 10.4 / 10.6	-	-	-	-	-	-	-	-	-
Pseudodrifa nigra 2	SS	-	-	-	-	-	-	6	SD = -18.9 (0.4) Range = -19.2 / -18.2	SD = 10.5 (0.6) Range = 9.9 / 11.2	-	-	-	-	-	-	1	SD = -19.8	SD = 11.1

-		Blake Deep			Blake Escarpment			Cape Fear			Richardson complex			Savannah Banks			Stetson Banks		
Taxon	**FG**	**n**	**δ13C ‰**	**δ15N ‰**	**n**	**δ13C ‰**	**δ15N ‰**	**n**	**δ13C ‰**	**δ15N ‰**	**n**	**δ13C ‰**	**δ15N ‰**	**n**	**δ13C ‰**	**δ15N ‰**	**n**	**δ13C ‰**	**δ15N ‰**
Pseudodrifa sp.	SS	-	-	-	-	-	-	5	SD = -19.1 (0.3) Range = -19.4 / -18.6	SD = 9.9 (0.6) Range = 9.1 / 10.6	-	-	-	-	-	-	-	-	-
Solenosmilia sp.	SS	4	SD = -18.0 (1.5) Range = -18.8 / -15.7	SD = 10.9 (0.7) Range = 10.1 / 11.6	1	SD = -21.0	SD = 13.8	-	-	-	-	-	-	-	-	-	-	-	-
Stauropathes cf. punctata	SS	-	-	-	1	SD = -18.9	SD = 10.0	-	-	-	-	-	-	-	-	-	-	-	-
Stauropathes sp.	SS	-	-	-	3	SD = -19.1 (0.5) Range = -19.6 / -18.6	SD = 9.7 (1.0) Range = 8.6 / 10.5	-	-	-	-	-	-	-	-	-	-	-	-
Stichopathes dissimilis	SS	-	-	-	1	SD = -20.5	SD = 10.0	-	-	-	-	-	-	-	-	-	-	-	-
Stolonifera	SS	-	-	-	-	-	-	-	-	-	-	-	-	-	-	-	1	SD = -19.7	SD = 9.7
Stoloniferan sp. (nov?)	SS	-	-	-	-	-	-	-	-	-	-	-	-	-	-	-	3	SD = -20.1 (0.5) Range = -20.5 / -19.5	SD = 9.5 (0.2) Range = 9.3 / 9.6
Swifita nov. sp?	SS	-	-	-	-	-	-	-	-	-	1	SD = -20.4	SD = 8.9	-	-	-	1	SD = -19.5	SD = 9.0
Swiftia casta	SS	-	-	-	-	-	-	-	-	-	15	SD = -20.4 (0.7) Range = -21.6 / -18.8	SD = 9 (0.6) Range = 7.6 / 9.9	-	-	-	5	SD = -19.9 (0.6) Range = -20.8 / -19.3	SD = 9.0 (0.6) Range = 8.2 / 9.7
Swiftia cf. casta	SS	-	-	-	-	-	-	-	-	-	2	SD = -18.9 (1.6) Range = -20.0 / -17.8	SD = 9.5 (0.4) Range = 9.2 / 9.7	-	-	-	-	-	-
Thecopsammia sp.	SS	-	-	-	-	-	-	2	SD = -20.7 (0.1) Range = -20.8 / -20.6	SD = 8.9 (0.4) Range = 8.6 / 9.1	-	-	-	-	-	-	4	SD = -21.0 (0.2) Range = -21.2 / -20.9	SD = 9.6 (0.7) Range = 8.5 / 10.1
Echinodermata																			
Asteroschema sp.	BE	3	SD = -17.6 (0.4) Range = -18.0 / -17.2	SD = 11.8 (0.3) Range = 11.4 / 12.0	-	-	-	-	-	-	-	-	-	-	-	-	-	-	-

-		Blake Deep			Blake Escarpment			Cape Fear			Richardson complex			Savannah Banks			Stetson Banks		
Taxon	**FG**	**n**	**δ13C ‰**	**δ15N ‰**	**n**	**δ13C ‰**	**δ15N ‰**	**n**	**δ13C ‰**	**δ15N ‰**	**n**	**δ13C ‰**	**δ15N ‰**	**n**	**δ13C ‰**	**δ15N ‰**	**n**	**δ13C ‰**	**δ15N ‰**
Crinoidea sp.	SS	-	-	-	-	-	-	-	-	-	1	SD = -19.1	SD = 8.7	10	SD = -19.1 (0.2) Range = -19.3 / -18.8	SD = 8.6 (0.3) Range = 8.1 / 9.1	-	-	-
Ophiacantha bidentata	BE	-	-	-	-	-	-	-	-	-	7	SD = -18.6 (0.6) Range = -19.4 / -17.6	SD = 9.8 (0.7) Range = 8.8 / 10.7	-	-	-	-	-	-
Ophiocreas oedipus	BE	1	SD = -17.5	SD = 12.3	-	-	-	-	-	-	-	-	-	-	-	-	-	-	-
Ophiuroidea	BS	2	SD = -16.7 (1.6) Range = -17.8 / -15.5	SD = 13.4 (1.6) Range = 12.3 / 14.5	3	SD = -18.1 (2.2) Range = -20.4 / -16.0	SD = 12.1 (1.1) Range = 10.8 / 12.9	10	SD = -18.8 (1) Range = -20.5 / -17.5	SD = 8.1 (1.1) Range = 5.9 / 9.5	1	SD = -15.7	SD = 10.0	10	SD = -17.5 (0.4) Range = -18.0 / -16.5	SD = 9.7 (0.4) Range = 9.1 / 10.2	10	SD = -18.7 (1.1) Range = -21.2 / -17.5	SD = 10.6 (0.5) Range = 9.7 / 11.2
Trichometra cubensis	SS	-	-	-	-	-	-	-	-	-	6	SD = -19.6 (0.9) Range = -20.3 / -17.8	SD = 7.3 (0.6) Range = 6.6 / 8.2	-	-	-	-	-	-
Mollusca																			
Aplacophora	BE	4	SD = -20.0 (0.2) Range = -20.2 / -19.7	SD = 13.1 (0.5) Range = 12.5 / 13.6	-	-	-	-	-	-	-	-	-	-	-	-	-	-	-
Coralliophila cf. richardi	BE	-	-	-	-	-	-	-	-	-	1	SD = -19.8	SD = 11.1	-	-	-	-	-	-
Gastropoda	BE	-	-	-	-	-	-	5	SD = -17.2 (1.6) Range = -19.8 / -16.1	SD = 11.5 (0.3) Range = 11.1 / 11.9	-	-	-	-	-	-	1	SD = -15.7	SD = 12.4
Unidentified Mussel - Gill	SS	-	-	-	-	-	-	1	SD = -16.6	SD = 9.6	-	-	-	-	-	-	-	-	-
Unidentified Mussel - Mantle	SS	-	-	-	-	-	-	1	SD = -16.7	SD = 10.0	-	-	-	-	-	-	-	-	-
Unidentified Mussel - Muscle	SS	-	-	-	-	-	-	1	SD = -16.5	SD = 10.3	-	-	-	-	-	-	-	-	-
NA																			
POMb	PR	1	SD = -25.6	SD = 6.2	1	SD = -25.5	SD = 9.1	1	SD = -23.3	SD = 7.2	5	SD = -25.0 (0.5) Range = -25.4 / -24.1	SD = 6.3 (0.9) Range = 5.0 / 7.1	1	SD = -26.3	SD = 5.8	-	-	-

-		Blake Deep			Blake Escarpment			Cape Fear			Richardson complex			Savannah Banks			Stetson Banks		
Taxon	**FG**	**n**	**δ13C ‰**	**δ15N ‰**	**n**	**δ13C ‰**	**δ15N ‰**	**n**	**δ13C ‰**	**δ15N ‰**	**n**	**δ13C ‰**	**δ15N ‰**	**n**	**δ13C ‰**	**δ15N ‰**	**n**	**δ13C ‰**	**δ15N ‰**
POMm	PR	-	-	-	6	SD = -25.1 (1.1) Range = -26.9 / -23.8	SD = 8.5 (1.0) Range = 6.6 / 9.3	9	SD = -24 (0.7) Range = -25.6 / -23.4	SD = 7.9 (1.7) Range = 4.3 / 10.9	-	-	-	-	-	-	9	SD = -24.2 (0.8) Range = -25.8 / -23.1	SD = 7.4 (1.8) Range = 4.9 / 10.3
POMs	PR	-	-	-	1	SD = -23.7	SD = 3.9	1	SD = -23.3	SD = 3.1	9	SD = -23.0 (1.5) Range = -26.0 / -20.8	SD = 1.7 (1.0) Range = -0.1 / 3.2	-	-	-	2	SD = -21.0 (1.3) Range = -21.9 / -20	SD = 3.0 (1.3) Range = 2.1 / 3.9
Sed_0-2	NA	2	SD = -18.5 (4.4) Range = -21.6 / -15.4	SD = 5.7 (0.5) Range = 5.3 / 6.0	3	SD = -18.7 (1.9) Range = -20.2 / -16.5	SD = 4.9 (0.2) Range = 4.7 / 5.0	-	SD = -20.4	SD = 4.8	-	-	-	1	SD = -14.6	SD = 4.9	-	-	-
Porifera																			
Aphrocallistes sp.	SS	-	-	-	-	-	-	-	-	-	1	SD = -19.6	SD = 15.0	-	-	-	-	-	-
Cladorhizidae	SS	3	SD = -19.4 (0.6) Range = -19.9 / -18.7	SD = 13.9 (0.5) Range = 13.5 / 14.4	-	-	-	-	-	-	-	-	-	-	-	-	-	-	-
Geodia sp.	SS	-	-	-	-	-	-	-	-	-	1	SD = -17.1	SD = 8.5	-	-	-	-	-	-
Glass sponge	SS	6	SD = -19.2 (1.0) Range = -19.8 / -17.3	SD = 14.0 (2.2) Range = 10.7 / 15.8	-	-	-	-	-	-	-	-	-	1	SD = -19.3	SD = 14.7	-	-	-
Hexactinellida	SS	-	-	-	-	-	-	-	-	-	-	-	-	-	-	-	2	SD = -19.2 (0.1) Range = -19.2 / -19.1	SD = 14.5 (0.4) Range = 14.2 / 14.8
Sponge	SS	6	SD = -18.9 (0.5) Range = -19.7 / -18.3	SD = 13.5 (2.9) Range = 8.3 / 16.0	1	SD = -17.6	SD = 15.0	-	-	-	7	SD = -17.8 (0.6) Range = -18.3 / -17.0	SD = 12.9 (3.3) Range = 6.2 / 15.6	3	SD = -18.7 (0.8) Range = -19.2 / -17.8	SD = 14.7 (1.1) Range = 13.6 / 15.8	4	SD = -18.5 (1.2) Range = -20.1 / -17.2	SD = 14.7 (4.0) Range = 9.1 / 18.1

Across the coral sites, there was no significant relationship between fauna $\delta^{13}C$ values and depth (correlation coefficient = 0.0334, p = 0.501); however, $\delta^{15}N$ was positively correlated with depth (R = 0.413, $p < 0.001$). There were also isotopic differences among coral sites within feeding groups. For benthic feeders, $\delta^{13}C$ values differed among sites (H = 19.404, df = 5, p = 0.002), where Blake Escarpment had lower $\delta^{13}C$ values than Savannah Banks (Q = 3.395, $p < 0.05$) and Cape Fear (Q = 3.400, $p < 0.05$). $\delta^{15}N$ was not significantly different among sites for benthic feeders **(**ANOVA on ranks across sites: H = 10.513, df = 5, p = 0.062).

For suspension feeders, $\delta^{15}N$ was significantly different among sites (H = 76.569, df = 5, $p < 0.001$); Blake Deep and Blake Escarpment were significantly higher in $\delta^{15}N$ compared to Richardson (Q = 7.783, $p < 0.05$ [Deep], Q = 4.265, $p < 0.05$ [Escarpment]) and Stetson Banks (Q = 6.629, $p < 0.0.5$ [Deep], Q = 3.670, $p < 0.05$ [Escarpment]). Blake Deep was also significantly higher than Savannah Banks (Q = 5.603, $p < 0.05$) and Cape Fear (Q = 5.146, $p < 0.05$). Suspension feeder $\delta^{13}C$ values were also significantly different among sites (H = 31.258, df = 5, $p < 0.001$), with Savannah Banks having higher $\delta^{13}C$ values than both Stetson Banks (Q = 4.935, $p < 0.05$) and Blake Escarpment (Q = 3.034, $p < 0.05$), while Stetson Bank suspension feeders had significantly lower $\delta^{13}C$ values compared to Blake Deep (Q = 3.975, $p < 0.05$) and Richardson (Q = 3.497, $p < 0.05$).

For the mixed feeding group (B/S: Benthic/Suspension), $\delta^{15}N$ among sites was distinct (ANOVA, F = 29.674, df = 4, $p < 0.001$), with post-hoc tests revealing site differences between Cape Fear and Blake Deep **(**t = 8.529, $p < 0.001$), Blake Escarpment (t = 7.502, $p < 0.001$), Stetson Banks (t = 6.939, $p < 0.001$), and Savannah Banks (t = 4.121, p = 0.003), with the lowest $\delta^{15}N$ values reported for Cape Fear. Further, $\delta^{15}N$ values from Savannah Banks were significantly lower than Blake Deep (t = 6.029, $p < 0.001$) and Blake Escarpment (t = 4.567, $p < 0.001$). Lastly, B/S from Blake Deep had significantly higher $\delta^{15}N$ values compared to Stetson Banks (t = 4.523, $p < 0.001$) and Richardson (t = 3.474, p = 0.013), similar to the patterns for the suspension feeders. While there was a significant difference in $\delta^{13}C$ among sites for this mixed feeding group (H = 15.725, df = 5, p = 0.008), post-hoc tests did not reveal any significant differences between specific site pairs. Lastly, for the mixed feeding group, Benthic/Pelagic, there were no among site differences in either $\delta^{15}N$ (H = 5.695, df = 2, p = 0.054) or $\delta^{13}C$ (F = 1.448, df = 1, p = 0.274).

4.4.3.2 Seep Communities

We analyzed a total of 582 samples (60 sediment, 84 POM, and 438 fauna samples) from four primary seep sites for $\delta^{13}C$ and $\delta^{15}N$ isotope values. Fauna represented eight phyla and encompassed six general feeding groups (Benthic, Benthic/Pelagic, Benthic/Suspension, Chemosynthetic, Pelagic, and Suspension). Bottom water POM samples were depleted in ^{13}C and enriched in ^{15}N relative to surface POM collected in the same locations (**Figure 4-85, Table 4-22**).

Most fauna had stable isotope values that fell between two primary endmembers, photosynthetically derived carbon ($\delta^{13}C > -25$ ‰) and methane-derived carbon (< -50‰). Fauna with the highest $\delta^{13}C$ included several benthic feeders from Pea Island and Kitty Hawk Seeps, including the seastar, *Plutonaster* sp. 1 (-17.6 ± 0.1‰, n = 2). Sponges had the highest $\delta^{15}N$, including those collected from Cape Fear Seep (15.1 ± 0.6‰, n = 2). Bivalves had the lowest $\delta^{13}C$ values (*Bathymodiolus heckerae*, -52.8 ± 5.8‰) and $\delta^{15}N$ values (*Isorropodon*, -3.5‰, n = 1), both from Blake Ridge Seep.

Fauna with chemosynthetic endosymbionts had distinct isotope values from many of the heterotrophic species (**Figure 4-85**, triangle symbols). Chemosynthetic bivalves collected at Blake Ridge Seep had variable isotope values, with the mussel *Bathymodiolus heckerae* depleted in ^{15}N (all tissues: muscle, mantle, gills) compared to clams (*Acharax* sp. and *Isorropodon* sp.). There were among tissue differences within the bivalves, with muscle tissue typically enriched in ^{13}C relative to gill or mantle (**Table 4-22**). The tubeworms, cf. *Escarpia* sp. also had low $\delta^{13}C$ values (across tissues analyzed), with more depleted

^{13}C values at Pea Island compared to Kitty Hawk (**Figure 4-85, Table 4-22**). Certain benthic, suspension and mixed feeders (benthic/suspension) also exhibited low δ^{13}C values suggesting use of chemosynthetic carbon sources (**Figure 4-85, Table 4-22**). There was a significant negative correlation between depth and both δ^{13}C ($R = -0.651$, $p < 0.001$) and δ^{15}N ($R = -0.455$, $p < 0.001$). Most of the fauna collected from Blake Ridge were depleted in ^{13}C relative to the other seep sites. Benthic feeders were significantly different among sites for both isotopes (δ^{13}C: $H = 59.159$, $df = 2$, $p < 0.001$; δ^{15}N: $H = 59.936$, $df = 2$, $p < 0.001$), with those from Blake Ridge significantly lower in δ^{13}C and δ^{15}N then Pea Island (δ^{13}C: $Q = 7.247$, $p < 0.05$, δ^{15}N: $Q = 7.461$, $p < 0.05$) and Kitty Hawk (δ^{13}C: $Q = 4.987$, $p < 0.05$, δ^{15}N: $Q = 4.584$, $p < 0.05$).

Suspension feeders also exhibited significant differences among the sites (δ^{13}C: $H = 29.343$, $df = 3$, $p < 0.001$, δ^{15}N: $H = 32.740$, $df = 3$, $p < 0.001$), with Blake Ridge having the lowest values relative to Pea Island (δ^{13}C: $Q = 2.991$, $p < 0.05$, δ^{15}N: $Q = 4.442$, $p < 0.05$), Kitty Hawk (δ^{13}C: $Q = 4.527$, $p < 0.05$, δ^{15}N: $Q = 2.661$, $p < 0.05$), and Cape Fear (δ^{13}C: $Q = 4.524$, $p < 0.05$, δ^{15}N: $Q = 5.283$, $p < 0.05$).

Likewise, benthic/pelagic mixed feeders had different δ^{13}C values among sites ($H = 12.005$, $df = 3$, $p = 0.007$), with fauna from Blake Ridge significantly lower in δ^{13}C then Pea Island (δ^{13}C: $Q = 3.032$, $p < 0.05$) and Kitty Hawk (δ^{13}C: $Q = 2.660$, $p < 0.05$). δ^{15}N values also varied among sites (δ^{15}N: $F = 14.952$, $df = 2$, $p < 0.001$), with lower values at Blake Ridge compared to Pea Island ($t = 4.671$, $p = 0.003$) and Cape Fear ($t = 3.932$, $p = 0.010$). Also, δ^{15}N values at Kitty Hawk were significantly lower compared to Pea Island ($t = 3.120$, $p = 0.035$) and Cape Fear ($t = 2.647$, $p = 0.042$). Chemosynthetic feeders were significantly different among sites for both isotopes (δ^{13}C: $H = 20.168$, $df = 2$, $p < 0.001$; δ^{15}N: $H = 13.289$, $df = 2$, $p = 0.001$) with those from Blake Ridge significantly lower than Kitty Hawk (δ^{13}C: $Q = 3.853$, $p < 0.05$; δ^{15}N: $Q = 3.271$, $p < 0.05$).

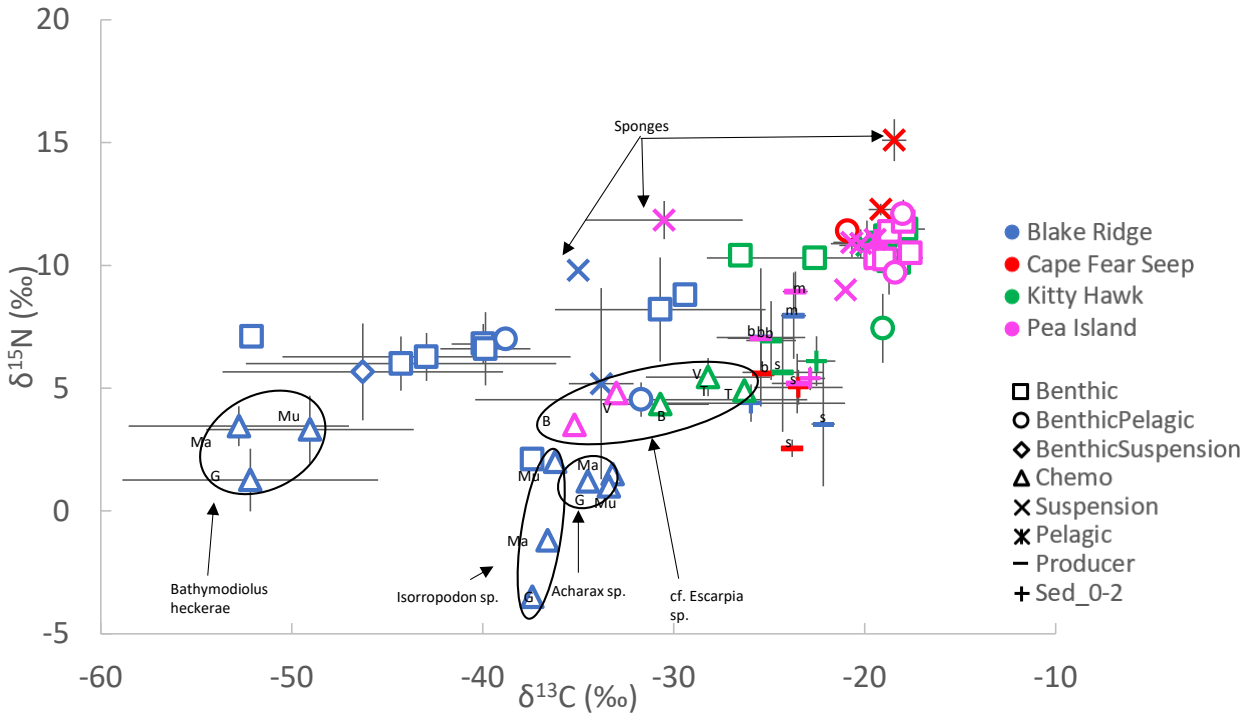

Figure 4-85. Average δ^{13}C and δ^{15}N of fauna, POM, and sediment collected at seeps
Average δ^{13}C and δ^{15}N (‰ ± SD) isotope values of fauna, POM (b = bottom, m = midwater, s = surface) and sediment collected at seep locations during research cruises from 2016–2019. Colors represent different sampling locations and symbols differentiate feeding groups, POM, and sediment. For chemosynthetic feeders, letters designate the different tissue types, with bivalves (G)ill, (Ma)ntle and (Mu)scle analyzed, and tubeworms (B)ranchiae, (T)rophpsome and (V)estimentum analyzed.

Table 4-22. Mean $\delta^{13}C$ and $\delta^{15}N$ for fauna, POM, and sediment collected from seeps

Mean isotope values of $\delta^{13}C$ and $\delta^{15}N$ (‰, SD, and range [min/max]) for fauna, POM (b = bottom, m = midwater, s = surface), and surface sediment (0–2 cm) collected from seep sites using underwater vehicles and CTDs during research cruises from 2018–2019. FG represent the different feeding groups: BE = benthic, BP-btm = Benthic/Pelagic bottom collection, BS = Benthic/Suspension, CH = chemosynthetic, SS = Suspension. PE = pelagic, PFS = potential food source, NA = not applicable.

-		Blake Ridge			Cape Fear			Kitty Hawk			Pea Island		
Taxon	**FG**	**n**	**$\delta^{13}C$ ‰**	**$\delta^{15}N$ ‰**	**n**	**$\delta^{13}C$ ‰**	**$\delta^{15}N$ ‰**	**n**	**$\delta^{13}C$ ‰**	**$\delta^{15}N$ ‰**	**n**	**$\delta^{13}C$ ‰**	**$\delta^{15}N$ ‰**
Annelida													
cf. *Escarpia* sp. Branchiae	CH	-	-	-	-	-	-	2	SD = -30.7 (2.5) Range = -32.5 / -28.9	SD = 4.4 (0.2) Range = 4.2 / 4.5	1	SD = -35.2	SD = 3.5
cf. *Escarpia* sp. Trophosome	CH	-	-	-	-	-	-	1	SD = -26.3	SD = 4.9	-	-	-
cf. *Escarpia* sp. Vestimentum	CH	-	-	-	-	-	-	2	SD = -28.2 (3.3) Range = -30.5 / -25.9	SD = 5.5 (0.8) Range = 4.9 / 6.0	1	SD = -33.0	SD = 4.8
cf. *Harmothoe* sp.	BE	-	-	-	-	-	-	-	-	-	2	SD = -19.4 (0.3) Range = -19.6 / -19.2	SD = 10.4 (0.1) Range = 10.3 / 10.5
Eunice norvegica	BE	-	-	-	-	-	-	1	SD = -18.2	SD = 10.1	-	-	-
Eunice sp.	BE	1	SD = -29.4	SD = 8.8	-	-	-	-	-	-	-	-	-
Harmothoe sp.	BE	-	-	-	-	-	-	2	SD = -22.6 (5.7) Range = -26.6 / -18.6	SD = 10.3 (0.1) Range = 10.2 / 10.4	7	SD = -18.7 (0.7) Range = -20.0 / -17.9	SD = 11.4 (0.4) Range = 10.6 / 11.8
Hesionidae	BE	-	-	-	-	-	-	1	SD = -18.9	SD = 11.2	-	-	-
Hyalinoecia artifex	BE	-	-	-	-	-	-	4	SD = -18.7 (0.6) Range = -19.5 / -18.2	SD = 10.2 (1.4) Range = 9.0 / 12.1	16	SD = -18.0 (0.6) Range = -19.3 / -16.9	SD = 11.8 (0.9) Range = 10.7 / 13.6
Maldanidae	BE	-	-	-	-	-	-	1	SD = -26.5	SD = 10.4	-	-	-
Terebellidae	BE	-	-	-	-	-	-	-	-	-	2	SD = -19.0 (0.9) Range = -19.6 / -18.3	SD = 10.3 (0.6) Range = 9.8 / 10.7
Arthropoda													
Amphipoda	BP-btm	-	-	-	1	SD = -20.9	SD = 11.4	-	-	-	-	-	-
Decapoda - Crab	BE	-	-	-	-	-	-	-	-	-	1	SD = -19.4	SD = 10.3
Decapoda - Shrimp	BP-btm	1	SD = -38.8	SD = 7.0	-	-	-	-	-	-	-	-	-
Decapoda - Shrimp_Benthic	BP-btm	3	SD = -31.7 (8.7) Range = -41.4 / -24.6	SD = 4.5 (0.7) Range = 3.8 / 5.2	-	-	-	9	SD = -19.0 (0.4) Range = -19.6 / -18.3	SD = 7.4 (1.4) Range = 5.7 / 9.1	1	SD = -18.0	SD = 12.1

-		Blake Ridge			Cape Fear			Kitty Hawk			Pea Island		
Taxon	**FG**	**n**	**δ13C ‰**	**δ15N ‰**	**n**	**δ13C ‰**	**δ15N ‰**	**n**	**δ13C ‰**	**δ15N ‰**	**n**	**δ13C ‰**	**δ15N ‰**
Galatheidae sp.	BE	2	SD = -30.7 (5.5) Range = -34.6 / -26.8	SD = 8.2 (2.1) Range = 6.7 / 9.7	-	-	-	4	SD = -17.8 (1.0) Range = -19.1 / -17.0	SD = 11.5 (0.9) Range = 10.8 / 12.7	-	-	-
Chordata													
Unidentified Fish	BP-btm	-	-	-	-	-	-	-	-	-	1	SD = -18.4	SD = 9.7
Cnidaria													
Anemone	SS	10	SD = -33.8 (1.7) Range = -35.3 / -30.3	SD = 5.2 (3.9) Range = 1.0 / 9.9	-	-	-	9	SD = -19.9 (1.5) Range = -23.6 / -18.8	SD = 10.8 (1.0) Range = 9.9 / 13.2	10	SD = -20.2 (1.6) Range = -22.1 / -17.2	SD = 10.9 (0.6) Range = 9.7 / 11.8
Hormathiidae sp. 1	SS	1	SD = -35.0	SD = 9.8	-	-	-	-	-	-	-	-	-
Hydroid	SS	-	-	-	4	SD = -19.2 (0.6) Range = -19.6 / -18.2	SD = 12.3 (0.2) Range = 12.1 / 12.6	-	-	-	1	SD = -21.0	SD = 9.0
Hydroid/Zooanthid	SS	-	-	-	-	-	-	1	SD = -18.4	SD = 10.2	-	-	-
Metridioidea sp 1	SS	-	-	-	-	-	-	-	-	-	3	SD = -20.7 (1.0) Range = -21.5 / -19.6	SD = 10.9 (0.6) Range = 10.3 / 11.5
Echinodermata													
Chiridota heheva	BE	13	SD = -44.3 (8.1) Range = -52.3 / -32.4	SD = 6.0 (1.1) Range = 4.7 / 8.2	-	-	-	-	-	-	-	-	-
Echinus sp.	BE	1	SD = -52.1	SD = 7.1	-	-	-	-	-	-	-	-	-
Ophioctenella acies	BE	4	SD = -40.0 (1.7) Range = -41.0 / -37.5	SD = 6.8 (0.8) Range = 6.3 / 8.0	-	-	-	-	-	-	-	-	-
Ophiuroidea	BS	6	SD = -46.3 (7.3) Range = -49.8 / -31.3	SD = 5.7 (2.0) Range = 4.1 / 9.6	-	-	-	-	-	-	-	-	-
Plutonaster sp.	BE	-	-	-	-	-	-	-	-	-	2	SD = -17.6 (0.1) Range = -17.7 / -17.5	SD = 10.5 (0.1) Range = 10.4 / 10.6
Urchin	BE	7	SD = -42.9 (7.5) Range = -52.2 / -34.3	SD = 6.3 (1.0) Range = 4.9 / 7.5	-	-	-	-	-	-	-	-	-
Mollusca													
Acharax sp. Gill	CH	1	SD = -34.5	SD = 1.2	-	-	-	-	-	-	-	-	-

-		Blake Ridge			Cape Fear			Kitty Hawk			Pea Island		
Taxon	**FG**	**n**	**$\delta^{13}C$ ‰**	**$\delta^{15}N$ ‰**	**n**	**$\delta^{13}C$ ‰**	**$\delta^{15}N$ ‰**	**n**	**$\delta^{13}C$ ‰**	**$\delta^{15}N$ ‰**	**n**	**$\delta^{13}C$ ‰**	**$\delta^{15}N$ ‰**
Acharax sp. Mantle	CH	1	SD = -33.2	SD = 1.5	-	-	-	-	-	-	-	-	-
Acharax sp. Muscle	CH	1	SD = -33.4	SD = 1.0	-	-	-	-	-	-	-	-	-
Bathymodiolus heckerae Gill	CH	104	SD = -52.2 (6.7) Range = -62.3 / -32.4	SD = 1.3 (1.3) Range = -2.5 / 3.9	-	-	-	-	-	-	-	-	-
Bathymodiolus heckerae Mantle	CH	68	SD = -52.8 (5.8) Range = -61.9 / -40.1	SD = 3.5 (0.8) Range = 2.2 / 5.3	-	-	-	-	-	-	-	-	-
Bathymodiolus heckerae Muscle	CH	99	SD = -49.0 (5.4) Range = -57.5 / -37.8	SD = 3.3 (1.4) Range = -0.9 / 6.0	-	-	-	-	-	-	-	-	-
Gastropoda	BE	1	SD = -37.4	SD = 2.1	-	-	-	-	-	-	-	-	-
Illex sp.	PE	-	-	-	-	-	-	-	-	-	2	SD = -19.5 (0.4) Range = -19.7 / -19.2	SD = 11.1 (0.4) Range = 10.8 / 11.3
Isorropodon sp. Gill	CH	1	SD = -37.4	SD = -3.5	-	-	-	-	-	-	-	-	-
Isorropodon sp. Mantle	CH	1	SD = -36.6	SD = -1.2	-	-	-	-	-	-	-	-	-
Isorropodon sp. Muscle	CH	1	SD = -36.2	SD = 2.0	-	-	-	-	-	-	-	-	-
Nudibranchia	BE	-	-	-	-	-	-	1	SD = -19.2	SD = 10.9	-	-	-
NA													
POMb	PFS	3	SD = -25.4 (2.3) Range = -27.9 / -23.3	SD = 7.1 (2.8) Range = 4.1 / 9.7	1	SD = -25.3	SD = 5.6	5	SD = -24.9 (1.3) Range = -26.9 / -23.4	SD = 6.9 (1.6) Range = 5.6 / 9.3	21	SD = -25.4 (1.7) Range = / -22.7	SD = 7.0 (1.2) Range = 5.3 / 9.4
POMm	PFS	6	SD = -23.7 (0.6) Range = -24.5 / -22.8	SD = 8.0 (1.8) Range = 4.6 / 9.2	-	-	-	-	-	-	15	SD = -23.6 (0.6) Range = -24.7 / -22.8	SD = 8.9 (0.8) Range = 7.8 / 10.5
POMs	PFS	3	SD = -22.2 (0.6) Range = -22.7 / -21.5	SD = 3.5 (2.5) Range = 0.8 / 5.8	2	SD = -23.8 (0.0) Range = -23.8 / -23.8	SD = 2.6 (0.4) Range = 2.3 / 2.8	10	SD = -24.3 (2.1) Range = -29.8 / -22.8	SD = 5.6 (2.4) Range = 1.9 / 10.7	18	SD = -23.5 (1.3) Range = -27.8 / -21.5	SD = 5.2 (1.2) Range = 2.5 / 6.9
Sed_0-2	NA	8	SD = -26.0 (4.9) Range = -31.4 / -18.8	SD = 4.4 (0.8) Range = 3.5 / 5.6	3	SD = -23.5 (2.3) Range = -25.9 / -21.3	SD = 5.0 (0.7) Range = 4.4 / 5.8	4	SD = -22.5 (1.0) Range = -24.0 / -21.9	SD = 6.1 (0.2) Range = 5.9 / 6.4	8	SD = -22.9 (0.8) Range = -23.9 / -21.8	SD = 5.4 (0.5) Range = 4.6 / 6.1
Porifera													
Sponge	SS	-	-	-	2	SD = -18.5 (0.6) Range = -18.9 / -18.0	SD = 15.1 (0.8) Range = 14.5 / 15.7	-	-	-	9	SD = -30.5 (4.1) Range = -36.0 / -23.7	SD = 11.8 (0.8) Range = 11.1 / 13.6

We analyzed a subset of 104 fauna samples for $\delta^{34}S$ composition to further differentiate the reliance on chemosynthetically vs. photosynthetically derived food resources. Fauna represented eight phyla and encompassed five feeding groups (Benthic, Benthic/Pelagic, Chemosynthetic, Pelagic, and Suspension). $\delta^{34}S$ values were variable across taxa (**Table 4-23, Figure 4-86**). Chemosynthetic feeders had some of the lowest $\delta^{34}S$ isotopes values, with negative values reported for *Acharax* sp. (-12.4‰) collected at Blake Ridge and cf. *Escarpia* sp. (ranging -11.3 to -1.3‰) collected at Kitty Hawk. Low values are consistent with reliance on hydrogen sulfide as a sulfur source. Several taxa, including benthic, pelagic, and benthic/pelagic feeders had $\delta^{34}S$ values similar to or lower than values typical for seawater sulfate (18–20‰). This suggests some reliance on chemosynthetic-derived production, whether through consumption of free-living microbes or resuspended organic matter.

Benthic and Suspension feeders had a large range in $\delta^{34}S$ values (**Figure 4-86**), but in general, $\delta^{34}S$ values were lower in fauna collected at Blake Ridge (circles) compared to Pea Island (triangles) or Kitty Hawk (squares). Fauna with higher $\delta^{13}C$ values (> -25‰) often had higher $\delta^{34}S$ values (> 15‰) compared to fauna with depleted ^{13}C values (< -25‰) (**Figure 4-86**).

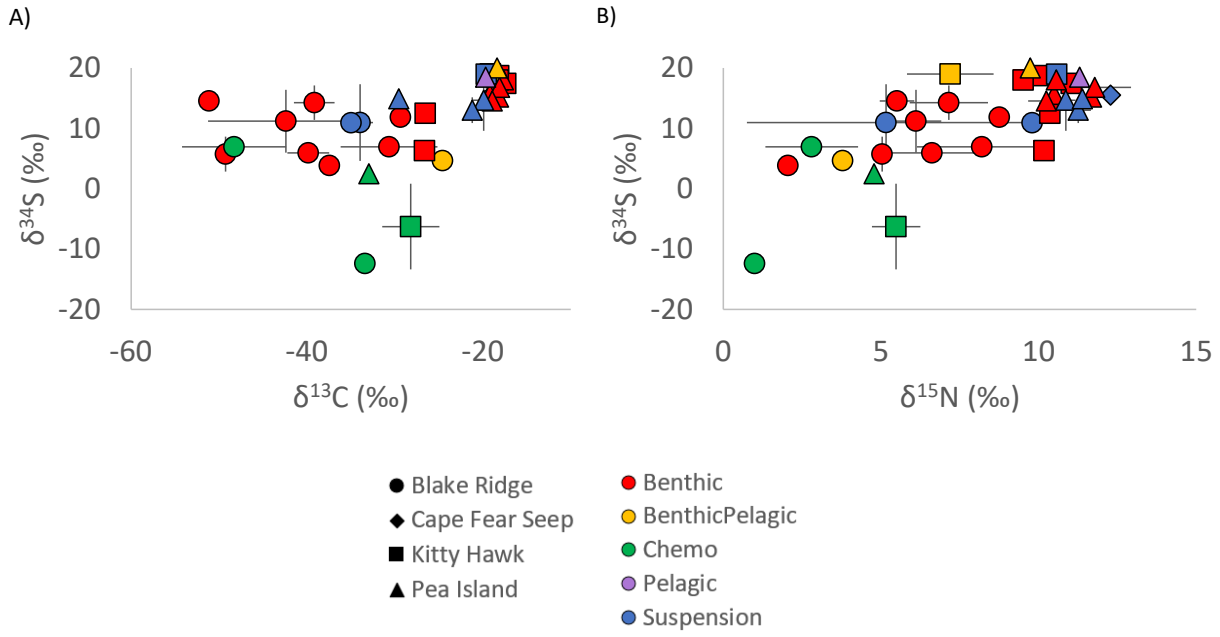

Figure 4-86. Average isotope values for of a subset of fauna, plotting $\delta^{34}S$ vs. $\delta^{13}C$ and vs. $\delta^{15}N$
Average isotope values (‰ ± SD) for of a subset of fauna examining $\delta^{34}S$ and A) $\delta^{13}C$ isotope values and B) $\delta^{15}N$ isotope values. Colors represent different feeding groups and symbols represent different locations.

Table 4-23. Values of δ34S and percent sulfur for a subset of fauna collected at seeps

Isotope values of δ34S and percent sulfur (mean, SD, and range) for a subset of fauna collected at seep locations during Deep SEARCH from 2018–2019.

-	-	Blake Ridge			Cape Fear			Kitty Hawk			Pea Island		
Taxon	**FG**	**n**	**$\delta^{13}C$ ‰**	**$\delta^{15}N$ ‰**	**n**	**$\delta^{13}C$ ‰**	**$\delta^{15}N$ ‰**	**n**	**$\delta^{13}C$ ‰**	**$\delta^{15}N$ ‰**	**n**	**$\delta^{13}C$ ‰**	**$\delta^{15}N$ ‰**
Annelida													
cf. Harmothoe sp.	BE	-	-	-	-	-	-	-	-	-	1	SD = 15.6	SD = 1.3
Eunice norvegica	BE	-	-	-	-	-	-	1	SD = 18.7	SD = 1.9	-	-	-
Eunice sp.	BE	1	SD = 11.9	SD = 1.2	-	-	-	-	-	-	-	-	-
Harmothoe sp.	BE	-	-	-	-	-	-	1	SD = 6.3	SD = 1.7	2	SD = 15.2 (0.4) Range = 14.9 / 15.5	SD = 1.1 (0.0) Range = 1.1 / 1.2
Hyalinoecia artifex	BE	-	-	-	-	-	-	1	SD = 18	SD = 1.3	5	SD = 16.8 (0.5) Range = 16.3 / 17.5	SD = 1.3 (0.2) Range = 1.2 / 1.6
Maldanidae	BE	-	-	-	-	-	-	1	SD = 12.5	SD = 1.7	-	-	-
Terebellidae	BE	-	-	-	-	-	-	-	-	-	2	SD = 14.5 (1.2) Range = 13.6 / 15.4	SD = 1 (0.2) Range = 0.9 / 1.2
cf. Escarpia sp. vestimentum	CH	-	-	-	-	-	-	2	SD = -6.3 (7.1) Range = -11.3 / -1.3	SD = 3.0 (0.2) Range = 2.9 / 3.1	1	SD = 2.5	SD = 3.2
Arthropoda													
Galatheidae sp.	BE	2	SD = 6.9 (0.2) Range = 6.8 / 7.1	SD = 0.9 (0.0) Range = 0.8 / 0.9	-	-	-	3	SD = 17.4 (0.3) Range = 17.2 / 17.8	SD = 1.0 (0.0) Range = 1.0 / 1.0	-	-	-
Decapoda - Shrimp_Benthic	BP	1	SD = 4.6	SD = 0.6	-	-	-	5	SD = 19.0 (0.6) Range = 18.2 / 19.7	SD = 1.3 (0.1) Range = 1.2 / 1.4	-	-	-
Chordata													
Fish	BP	-	-	-	-	-	-	-	-	-	1	SD = 20	SD = 1.2
Cnidaria													
Actiniaria	SS	6	SD = 11.0 (6.4) Range = 1.1 / 16.8	SD = 1.7 (0.5) Range = 1.1 / 2.2	-	-	-	5	SD = 19.0 (2.4) Range = 15.9 / 20.9	SD = 2.3 (0.7) Range = 1.5 / 2.9	5	SD = 14.6 (5.0) Range = 6.2 / 18.6	SD = 1.3 (0.1) Range = 1.1 / 1.4
Hormathiidae sp. 1	SS	1	SD = 10.9	SD = 1.5	-	-	-	-	-	-	-	-	-
Hydrozoa	SS	-	-	-	3	SD = 15.5 (0.6) Range = 15.2 / 16.2	SD = 1.0 (0.1) Range = 1.0 / 1.1	-	-	-	-	-	-

-	-	Blake Ridge			Cape Fear			Kitty Hawk			Pea Island		
Taxon	**FG**	**n**	**$\delta^{13}C$ ‰**	**$\delta^{15}N$ ‰**	**n**	**$\delta^{13}C$ ‰**	**$\delta^{15}N$ ‰**	**n**	**$\delta^{13}C$ ‰**	**$\delta^{15}N$ ‰**	**n**	**$\delta^{13}C$ ‰**	**$\delta^{15}N$ ‰**
Metridioidea sp 1	SS	-	-	-	-	-	-	-	-	-	2	SD = 13.0 (2.1) Range = 11.5 / 14.5	SD = 1.2 (0.3) Range = 0.9 / 1.4
Echinodermata													
Chiridota heheva	BE	5	SD = 14.5 (1.6) Range = 13.1 / 17.3	SD = 1.7 (0.3) Range = 1.2 / 2.0	-	-	-	-	-	-	-	-	-
Ophioctenella acies	BE	2	SD = 14.3 (2.9) Range = 12.2 / 16.3	SD = 0.4 (0.3) Range = 0.2 / 0.6	-	-	-	-	-	-	-	-	-
Ophiuroidea	BE	3	SD = 5.7 (2.9) Range = 2.5 / 8.1	SD = 1.0 (0.3) Range = 0.6 / 1.3	-	-	-	-	-	-	-	-	-
Plutonaster sp.	BE	-	-	-	-	-	-	-	-	-	1	SD = 18	SD = 0.3
Spatangoida	BE	4	SD = 11.2 (5.2) Range = 4.4 / 16.7	SD = 1.1 (0.4) Range = 0.5 / 1.4	-	-	-	-	-	-	-	-	-
Mollusca													
Gastropoda	BE	1	SD = 3.9	SD = 1.4	-	-	-	-	-	-	-	-	-
Acharax sp.	CH	1	SD = -12.4	SD = 1.3	-	-	-	-	-	-	-	-	-
B. heckerae muscle	CH	26	SD = 6.9 (3.0) Range = -1.0 / 11.8	SD = 0.8 (0.1) Range = 0.7 / 0.9	-	-	-	-	-	-	-	-	-
Illex sp.	PE	-	-	-	-	-	-	-	-	-	1	SD = 18.5	SD = 1.7
Porifera													
Porifera	SS	-	-	-	-	-	-	-	-	-	1	SD = 14.9	SD = 0.5
Sipuncula													
Sipunculidea	BE	7	SD = 6.0 (1.4) Range = 3.6 / 7.7	SD = 0.9 (0.1) Range = 0.7 / 1.0	-	-	-	-	-	-	-	-	-

4.4.3.3 Canyon Communities

We analyzed a total of 204 samples (23 sediment, 46 POM, and 135 fauna samples) for $\delta^{13}C$ and $\delta^{15}N$ isotope values from two canyons. Fauna represented seven phyla and encompassed four primary feeding groups (Benthic, Benthic/Pelagic, Benthic/Suspension, and Suspension). POM $\delta^{13}C$ values fell within the range of photosynthetic-based material. POM samples covered a broad range of $\delta^{15}N$ values (Surface: 2.3 to 6.2‰, Bottom: 5.9 to 8.6‰, **Table 4-24**, **Figure 4-87**), with average bottom POM enriched in ^{15}N compared to surface and midwater POM. Fauna $\delta^{13}C$ values reflected material originating in the euphotic zone as the primary carbon source.

The bamboo coral, *Keratoisis* sp. Type D2K from Pamlico Canyon had the highest $\delta^{13}C$ values (-16.4‰) and the lowest value was from *Protoptilum* sp. (-20.6‰) collected at Norfolk Canyon. An unidentified ophiuroid (benthic-suspension feeder) had the highest $\delta^{15}N$ value (17.2‰, n = 1), whereas *Eumunida picta* (9.0 ‰) and Sipuncula (9.0‰ ± 0.2‰) had the lowest $\delta^{15}N$ values. Overall, fauna collected from the two canyons had overlapping isotope values, and there was no significant pattern with canyon depth in either $\delta^{15}N$ (R = 0.0706, p = 0.417) or $\delta^{13}C$ (R = 0.0319, p = 0.714), but this might have been a consequence of limited sampling depths.

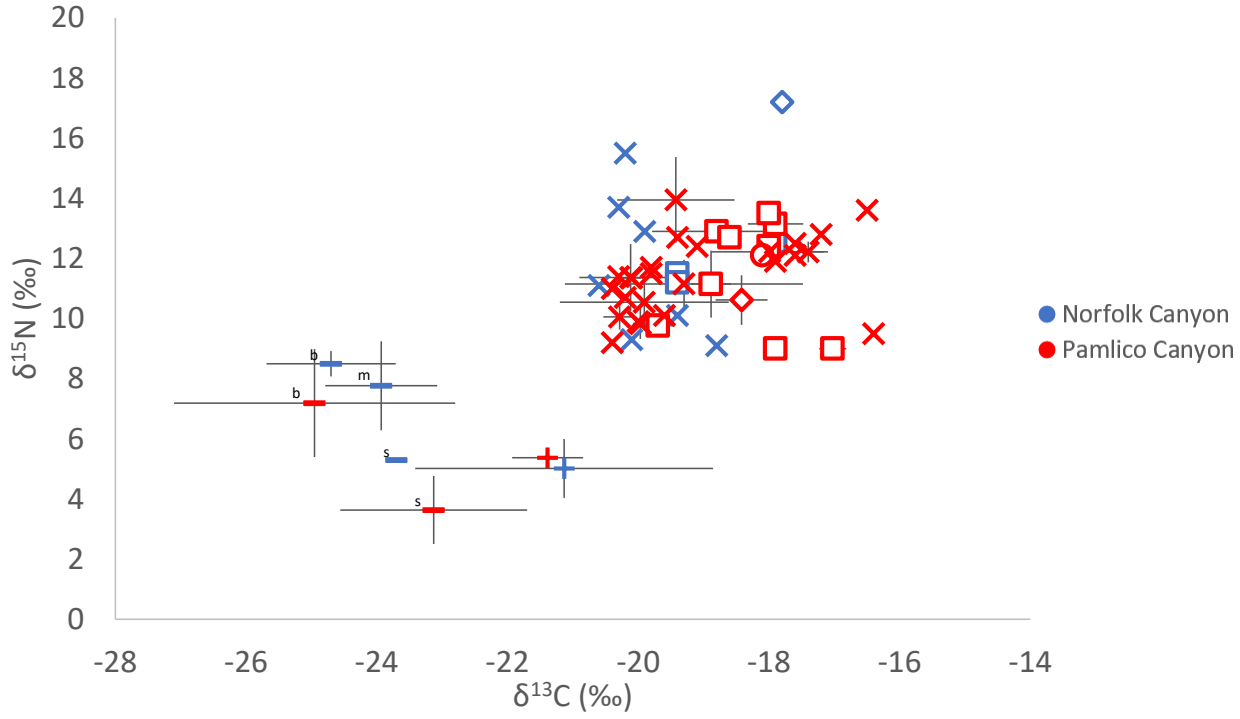

Figure 4-87. Average $\delta^{13}C$ and $\delta^{15}N$ of fauna, POM and sediment from canyons
Collected at canyon locations during research cruises from 2016–2019. Colors represent different locations.

Table 4-24. Values of $\delta^{13}C$ and $\delta^{15}N$ for fauna, POM and sediment collected at canyons

Isotope values of $\delta^{13}C$ and $\delta^{15}N$ (mean, SD, and range) for fauna, POM and sediment collected at canyon locations during research cruises from 2016–2019.

-		Norfolk Canyon			Pamlico Canyon		
Taxon	**FG**	**n**	**$\delta^{13}C$ ‰**	**$\delta^{15}N$ ‰**	**n**	**$\delta^{13}C$ ‰**	**$\delta^{15}N$ ‰**
Annelida							
Annelida	BE	-	-	-	3	SD = -19.7 (0.3) Range = -20.0 / -19.5	SD = 9.8 (0.4) Range = 9.5 / 10.2
Eunicidae	BE	-	-	-	2	SD = -18.8 (1.0) Range = -19.5 / -18.1	SD = 12.9 (0.1) Range = 12.8 / 13.0
Eunoe sp.	BE	1	SD = -19.4	SD = 11.5	8	SD = -18.9 (0.3) Range = -19.3 / -18.4	SD = 11.2 (1.1) Range = 8.9 / 12.3
Polynoidae	BE	1	SD = -19.4	SD = 11.2	1	SD = -18.0	SD = 12.4
Arthropoda							
Cirripedia - Barnacle	SS	-	-	-	1	SD = -20.4	SD = 11.0
Decapoda - Shrimp	BP-btm	-	-	-	1	SD = -18.1	SD = 12.1
Eumunida picta	BE	-	-	-	1	SD = -17.9	SD = 9.0
Paguroidea	BE	-	-	-	1	SD = -18.6	SD = 12.7
Cnidaria							
Acanella abruscula	SS	1	SD = -20.3	SD = 13.7	-	-	-
Acanella sp. n	SS	1	SD = -20.2	SD = 15.5	-	-	-
Acanthogorgia aspera	SS	-	-	-	3	SD = -20.0 (0.1) Range = -20.1 / -19.9	SD = 9.8 (0.5) Range = 9.3 / 10.3
Acanthogorgia sp.	SS	-	-	-	1	SD = -20.2	SD = 10.7
Acanthogorgia spissa	SS	-	-	-	7	SD = -20.3 (0.2) Range = -20.6 / -20.0	SD = 10.1 (0.4) Range = 9.5 / 10.6
Actiniaria sp 1	SS	-	-	-	1	SD = -17.6	SD = 12.1
Anthomastus grandiflorus	SS	-	-	-	1	SD = -20.0	SD = 9.9
Anthoptilum sp.	SS	1	SD = -19.4	SD = 10.1	-	-	-
cf. *Alternatipathes* sp.	SS	-	-	-	1	SD = -19.8	SD = 11.7
cf. *Bathypathes* sp.	SS	-	-	-	1	SD = -19.6	SD = 10.1

-		Norfolk Canyon			Pamlico Canyon		
Taxon	**FG**	**n**	**$\delta^{13}C$ ‰**	**$\delta^{15}N$ ‰**	**n**	**$\delta^{13}C$ ‰**	**$\delta^{15}N$ ‰**
Chondrophellia cf. *orangina*	SS	-	-	-	1	SD = -19.1	SD = 12.4
Chrysogorgia tricaulis	SS	-	-	-	1	SD = -20.4	SD = 9.2
Desmophyllum sp.	SS	-	-	-	13	SD = -19.9 (1.3) Range = -21.7 / -17.3	SD = 10.5 (0.9) Range = 8.2 / 11.6
Distichoptilum gracile	SS	1	SD = -20.1	SD = 9.3	-	-	-
Eknomisis sp. Type D2J	SS	1	SD = -18.8	SD = 9.1	-	-	-
Hydroid	SS	-	-	-	6	SD = -20.1 (0.8) Range = -21.2 / -19.2	SD = 11.4 (1.1) Range = 10.0 / 12.6
Keratoisis sp. Type D2K	SS	-	-	-	1	SD = -16.4	SD = 9.5
Paragorgia johnsoni	SS	-	-	-	1	SD = -19.8	SD = 11.5
Paramuricea sp. Type A (cf. *placomus*)	SS	-	-	-	2	SD = -20.1 (0.1) Range = -20.2 / -20.0	SD = 11.4 (0.1) Range = 11.3 / 11.4
Protoptilum sp.	SS	1	SD = -20.6	SD = 11.1	-	-	-
Pseudoanthomastus cf. *agaricus*	SS	1	SD = -19.9	SD = 12.9	-	-	-
Solenosmilia sp.	SS	-	-	-	9	SD = -19.3 (1.8) Range = -23.7 / -17.4	SD = 11.2 (0.8) Range = 10.2 / 13.0
Swiftia pallida	SS	-	-	-	1	SD = -20.3	SD = 11.4
Swiftia sp.	SS	-	-	-	1	SD = -17.9	SD = 11.9
Trachythela rudis	SS	-	-	-	1	SD = -19.4	SD = 12.7
Echinodermata							
Asteroschema clavigerum	BE	-	-	-	2	SD = -17.9 (0.4) Range = -18.2 / -17.6	SD = 13.2 (0.2) Range = 13.0 / 13.3
Asteroschema sp. (nov?)	BE	-	-	-	1	SD = -18.0	SD = 13.5
Holothuroidea	BE	2	SD = -17.9 (0.1) Range = -18.0 / -17.8	SD = 12.6 (0.1) Range = 12.5 / 12.6	-	-	-
Ophiuroidea	BS	1	SD = -17.8	SD = 17.2	16	SD = -18.4 (0.4) Range = -19.2 / -17.9	SD = 10.6 (0.8) Range = 8.8 / 11.9
Mollusca							
Acesta sp. Gill	SS	-	-	-	1	SD = -17.6	SD = 12.5

-		Norfolk Canyon			Pamlico Canyon		
Taxon	**FG**	**n**	**$\delta^{13}C$ ‰**	**$\delta^{15}N$ ‰**	**n**	**$\delta^{13}C$ ‰**	**$\delta^{15}N$ ‰**
Acesta sp. Mantle	SS	-	-	-	1	SD = -17.2	SD = 12.8
Acesta sp. Muscle	SS	-	-	-	1	SD = -16.5	SD = 13.6
Acesta sp. Whole	SS	-	-	-	9	SD = -18.0 (0.9) Range = -19.7 / -16.6	SD = 12.2 (0.5) Range = 11.2 / 13.0
Scallop Mantle	SS	-	-	-	10	SD = -17.4 (0.2) Range = -17.8 / -17.1	SD = 12.2 (0.3) Range = 11.5 / 12.6
NA							
POMb	PR	2	SD = -24.7 (1.0) Range = -25.4 / -24.0	SD = 8.5 (0.4) Range = 8.2 / 8.8	15	SD = -25.0 (2.2) Range = -29.6 / -21.8	SD = 7.2 (1.8) Range = 3.3 / 11.1
POMm	PR	6	SD = -23.9 (0.9) Range = -25.0 / -22.5	SD = 7.8 (1.5) Range = 4.8 / 8.8	-	-	-
POMs	PR	1	SD = -23.7	SD = 5.3	20	SD = -23.1 (1.4) Range = -26.3 / -20.9	SD = 3.6 (1.1) Range = 1.3 / 5.5
Sed_0-2	NA	6	SD = -21.1 (2.3) Range = -23.5 / -17.7	SD = 5.0 (1.0) Range = 3.2 / 5.9	17	SD = -21.4 (0.5) Range = -22.0 / -20.2	SD = 5.4 (0.2) Range = 4.9 / 5.8
Porifera							
Sponge	SS	-	-	-	8	SD = -19.4 (0.9) Range = -20.2 / -17.4	SD = 14.0 (1.4) Range = 12.2 / 16.3
Sipuncula							
Sipuncula	BE	-	-	-	4	SD = -17.0 (0.2) Range = -17.2 / -16.8	SD = 9.0 (0.2) Range = 8.7 / 9.2

Coral isotope values within coral and canyon environments exhibited a large spread in both $\delta^{13}C$ and $\delta^{15}N$ (**Figure 4-88**). The bamboo coral, *Keratoisis* type D2K (-16.4‰, n = 1) and *Pseudodrifa nigra* (-17.6‰ ± 1.7‰) had the highest $\delta^{13}C$ values from canyon and coral sites, respectively. Whereas the seapen, Protoptilum sp. (-20.6‰, n = 1, canyon) and stony coral, *Enallopsammia rostrata* (-21.1‰, n = 1, coral habitat) had the lowest $\delta^{13}C$ values. The bamboo corals, *Acanella* sp. n (15.5 ‰, n = 1, canyon) and *Eknomisis* sp. Type D2J (9.1‰, n = 1), had the highest and lowest $\delta^{15}N$ values from the canyons. For coral habitats, *Acanthogorgia* sp. (12.1‰, n = 1) and *Solenosmilia* sp. (13.8‰) had the highest $\delta^{15}N$, while an unidentified primnoid had the lowest $\delta^{15}N$ value (4.5‰, n = 1).

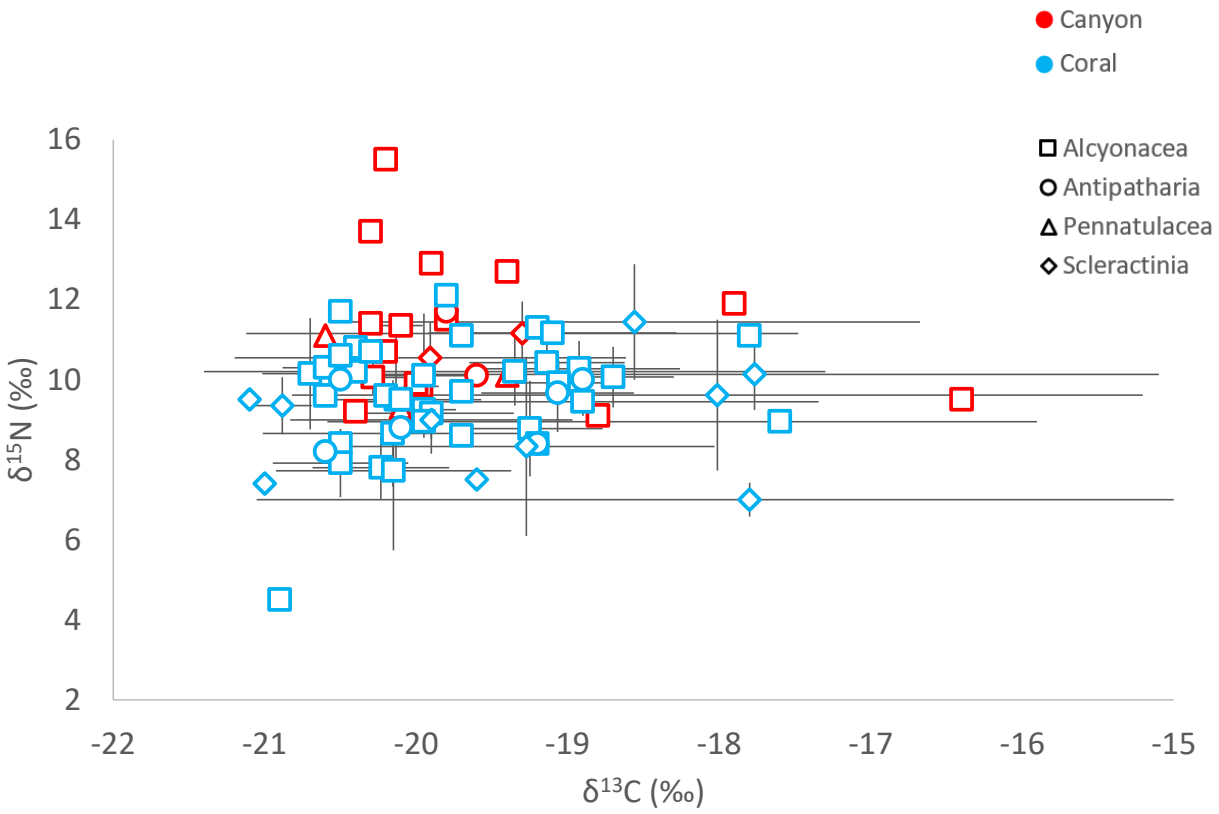

Figure 4-88. Average $\delta^{13}C$ and $\delta^{15}N$ values of corals from canyon and coral habitats
Average $\delta^{13}C$ and $\delta^{15}N$ ± 1 SD isotope values of corals collected from canyon (red) and coral (blue) habitats. Symbols represent different orders of corals.

4.4.3.4 Midwater Communities

We collected midwater fauna primarily during three research cruises, with 13 total trawls in total. A total of 381 samples (seven phyla) were analyzed from five feeding groups (Benthic, Benthic/Pelagic, Benthic/Suspension, Pelagic, and Suspension). Specific areas targeted included seep (Blake Ridge, 200 and 650 m, N = 2 trawls), coral habitats (Richardson Reef complex, Million Mounds, 200–550 m, N = 5), and canyon environments (Pamlico Canyon, Virginia InterCanyon, 559 m, N = 6). $\delta^{13}C$ values were similar across sites and indicate reliance on photosynthetically derived carbon sources (**Figure 4-89; Table 4-25**), with the exception of a single specimen of *Gastropoda* sp. 2 that was depleted in ^{13}C (-44.3‰) and ^{15}N (-6.9‰).

Across the sites, *Pleuronectiformes* sp. (flatfishes) (Richardson Reef Complex) and stomatopods (Pamlico Canyon) had the lowest $\delta^{13}C$ values, (-22.5 ± 0.3‰ and -21.7 ± 1.5‰, respectively). In contrast, unidentified shrimp, *Pteropoda*, and *Gastropoda* sp. 1, all from Pamlico Canyon, had the highest $\delta^{13}C$

values (-16.5 ± 0.6‰, -16.4 ± 2.3‰, -16.4 ± 0.1‰). $\delta^{15}N$ values of both Chordata (2.9 to 14.1‰) and Arthropoda (3.1 to 14.1‰) exhibited a large range (**Figure 4-89**). Ctenophores from Pamlico Canyon and stomatopods from Richardson Reef Complex had the lowest $\delta^{15}N$ values (0.5 ± 2.6 ‰ and 3.1 ± 1.9‰, respectively). Taxa with the highest $\delta^{15}N$ values included echinoderm larvae from Richardson Reef Complex (11.1 ± 0.5‰), *Nezumia bairdii* (14.1 ± 0.5‰) and shrimp (14.1 ± 0.8‰), both from Pamlico Canyon.

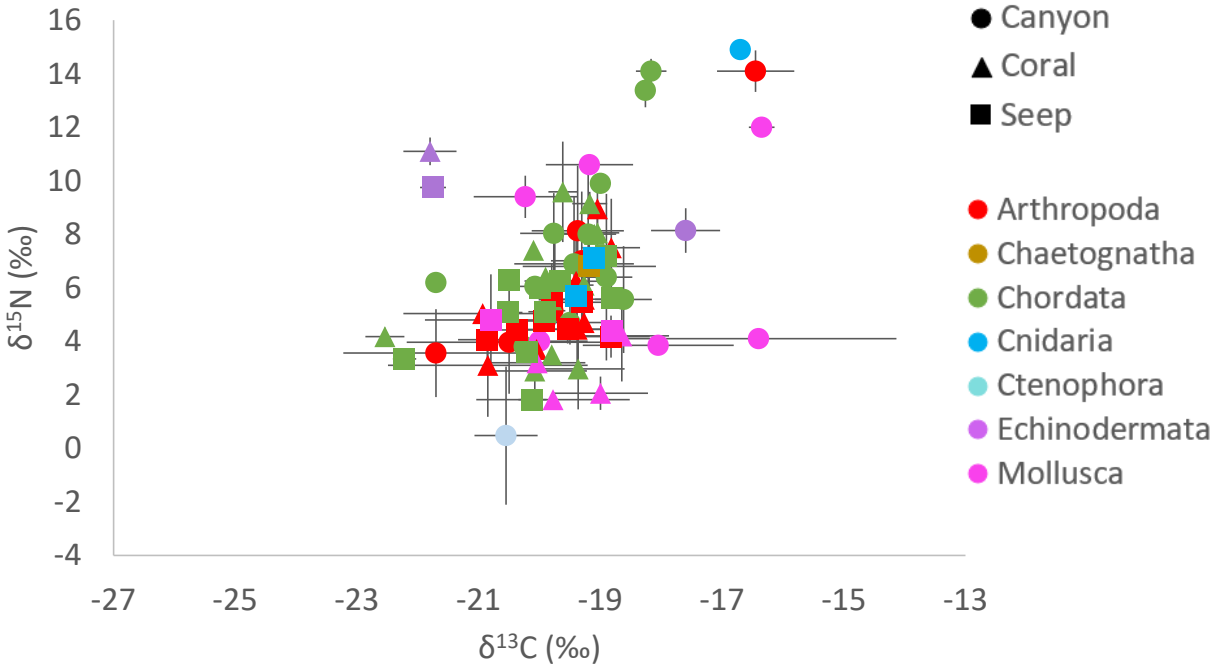

Figure 4-89. Average $\delta^{13}C$ and $\delta^{15}N$ values of midwater fauna from coral, seep, and canyon sites
Average $\delta^{13}C$ and $\delta^{15}N$ isotope values of fauna collected in midwater trawls from coral, seep, and canyon sites during research cruises from 2016–2019. Colors represent different phyla and symbols represent the different habitat types.

Table 4-25. Mean values of $\delta^{13}C$ and $\delta^{15}N$ for fauna collected with trawls

Mean isotope values of $\delta^{13}C$ and $\delta^{15}N$ (‰, SD, and minimum/maximum) for fauna collected with trawls during research cruises from 2018–2019. FG represent the different feeding groups: BE = benthic, BP-mid = Benthic/Pelagic midwater collection, BS = Benthic/Suspension, PE = Pelagic, and SS = Suspension.

-		Pamlico Canyon			Virginia InterCanyon			Richardson Complex			Million Mounds			Blake Ridge		
Taxon	**FG**	**n**	**$\delta^{13}C$ ‰**	**$\delta^{15}N$ ‰**	**n**	**$\delta^{13}C$ ‰**	**$\delta^{15}N$ ‰**	**n**	**$\delta^{13}C$ ‰**	**$\delta^{15}N$ ‰**	**n**	**$\delta^{13}C$ ‰**	**$\delta^{15}N$ ‰**	**n**	**$\delta^{13}C$ ‰**	**$\delta^{15}N$ ‰**
Arthropoda																
Amphipoda	BP-mid	5	SD = -19.8 (0.2) Range = -20.0 / -19.6	SD = 5.1 (0.6) Range = 4.4 / 5.9	-	-	-	8	SD = -19.3 (0.4) Range = -20.0 / -18.8	SD = 5.6 (1.2) Range = 3.7 / 7.1	-	-	-	5	SD = -19.9 (0.7) Range = -20.8 / -18.9	SD = 4.8 (0.8) Range = 3.6 / 5.9
Copepoda	PE	-	-	-	-	-	-	3	SD = -20.9 (1.3) Range = -22.4 / -19.9	SD = 5.0 (0.2) Range = 4.8 / 5.2	-	-	-	4	SD = -19.8 (0.5) Range = -20.4 / -19.3	SD = 5.7 (1.2) Range = 4.2 / 6.8
Decapoda - Lobster larvae	PE	-	-	-	-	-	-	-	-	-	-	-	-	4	SD = -20.4 (0.6) Range = -21.1 / -19.6	SD = 4.4 (0.6) Range = 3.6 / 5.0
Decapoda - Shrimp	BP-mid	4	SD = -16.5 (0.6) Range = -17.4 / -16.1	SD = 14.1 (0.8) Range = 13.0 / 14.8	-	-	-	6	SD = -19.4 (0.4) Range = -19.8 / -18.7	SD = 4.5 (1.4) Range = 3.1 / 7.0	-	-	-	4	SD = -18.8 (0.5) Range = -19.5 / -18.4	SD = 4.2 (0.8) Range = 3.0 / 4.6
Euphausiacea	PE	-	-	-	-	-	-	9	SD = -19.4 (0.4) Range = -20.0 / -18.7	SD = 6.2 (2.0) Range = 3.1 / 8.9	-	-	-	9	SD = -19.3 (0.6) Range = -20.0 / -18.4	SD = 5.5 (1.1) Range = 3.4 / 6.9
Euphausiidae	PE	-	-	-	-	-	-	-	-	-	2	SD = -19.1 (0.1) Range = -19.1 / -19.0	SD = 9.0 (0.9) Range = 8.3 / 9.6	-	-	-
Gennadas sp.	PE	-	-	-	17	SD = -19.3 (0.5) Range = -20.6 / -18.6	SD = 7.0 (2.6) Range = 3.4 / 10.0	-	-	-	-	-	-	-	-	-

-		Pamlico Canyon			Virginia InterCanyon			Richardson Complex			Million Mounds			Blake Ridge		
Taxon	**FG**	**n**	**δ13C ‰**	**δ15N ‰**	**n**	**δ13C ‰**	**δ15N ‰**	**n**	**δ13C ‰**	**δ15N ‰**	**n**	**δ13C ‰**	**δ15N ‰**	**n**	**δ13C ‰**	**δ15N ‰**
Oplophoridae	PE	-	-	-	3	SD = -20.5 (1.7) Range = -22.4 / -19.2	SD = 4.0 (1.9) Range = 1.8 / 5.5	-	-	-	-	-	-	-	-	-
Ostracoda	PE	-	-	-	-	-	-	-	-	-	-	-	-	2	SD = -20.1 (0.1) Range = -20.1 / -20.0	SD = 3.7 (0.3) Range = 3.5 / 3.9
Sergestidae	PE	-	-	-	29	SD = -19.4 (0.8) Range = -21.9 / -18.3	SD = 8.1 (2.4) Range = 1.7 / 10.3	3	SD = -19.3 (0.5) Range = -19.7 / -18.7	SD = 4.7 (0.2) Range = 4.5 / 4.8	17	SD = -18.8 (0.5) Range = -19.5 / -17.9	SD = 7.5 (1.8) Range = 4.5 / 9.4	-	-	-
Sergia sp.	PE	-	-	-	-	-	-	-	-	-	-	-	-	5	SD = -19.5 (0.3) Range = -19.9 / -19.1	SD = 4.4 (0.5) Range = 4.0 / 5.1
Stomatopoda	BP-mid	5	SD = -21.7 (1.5) Range = -22.6 / -19.0	SD = 3.6 (1.6) Range = 2.1 / 5.4	-	-	-	6	SD = -20.9 (1.6) Range = -22.4 / -19.0	SD = 3.1 (1.9) Range = -0.4 / 5.0	-	-	-	5	SD = -20.9 (1.6) Range = -22.8 / -19.1	SD = 4.1 (1.0) Range = 2.9 / 5.2
Chaetognatha																
Chaetognatha	PE	-	-	-	-	-	-	-	-	-	-	-	-	6	SD = -19.2 (1.1) Range = -20.0 / -17.0	SD = 6.8 (1.3) Range = 4.3 / 8.1
Chordata																
Acanthurus sp.	PE	4	SD = -20.3 (0.1) Range = -20.4 / -20.2	SD = 3.8 (0.3) Range = 3.3 / 4.1	-	-	-	1	SD = -19.8	SD = 3.5	-	-	-	-	-	-
Aldrovandia phalacra	BE	1	SD = -21.7	SD = 6.2	-	-	-	-	-	-	-	-	-	-	-	-

-		Pamlico Canyon			Virginia InterCanyon			Richardson Complex			Million Mounds			Blake Ridge		
Taxon	**FG**	**n**	**δ13C ‰**	**δ15N ‰**	**n**	**δ13C ‰**	**δ15N ‰**	**n**	**δ13C ‰**	**δ15N ‰**	**n**	**δ13C ‰**	**δ15N ‰**	**n**	**δ13C ‰**	**δ15N ‰**
Benthosema glaciale	PE	-	-	-	24	SD = -19.2 (0.5) Range = -20.1 / -17.9	SD = 8.0 (2.3) Range = 3.4 / 10.2	-	-	-	-	-	-	-	-	-
Canthigaster sp.	PE	-	-	-	-	-	-	-	-	-	-	-	-	2	SD = -19.9 (0.3) Range = -20.1 / -19.7	SD = 5.1 (0.7) Range = 4.6 / 5.6
Ceratoscopelus maderensis	PE	-	-	-	3	SD = -19.8 (0.6) Range = -20.4 / -19.4	SD = 8.0 (1.5) Range = 6.3 / 8.9	-	-	-	-	-	-	-	-	-
Ceratoscopelus warmingii	PE	-	-	-	2	SD = -18.9 (0.4) Range = -19.2 / -18.6	SD = 6.4 (3.1)	-	-	-	-	-	-	-	-	-
Chauliodus danae	PE	-	-	-	-	-	-	1	SD = -20.1	SD = 7.4	-	-	-	-	-	-
Cyclothone braueri	PE	-	-	-	-	-	-	-	-	-	-	-	-	5	SD = -19.7 (0.2) Range = -19.9 / -19.4	SD = 6.3 (0.3) Range = 6.0 / 6.6
Cyclothone microdon	PE	-	-	-	-	-	-	-	-	-	-	-	-	6	SD = -19.6 (0.2) Range = -19.9 / -19.4	SD = 9.6 (1.9) Range = 5.8 / 10.8
Diaphus dumerilii	PE	4	SD = -20.1 (0.4) Range = -20.5 / -19.7	SD = 6.1 (0.2) Range = 5.8 / 6.2	5	SD = -18.6 (0.5) Range = -19.3 / -18.2	SD = 5.6 (2.0) Range = 4.2 / 9.0	2	SD = -19.8 (0.5) Range = -20.1 / -19.4	SD = 6.3 (1.6) Range = 5.1 / 7.4	-	-	-	-	-	-

-		Pamlico Canyon			Virginia InterCanyon			Richardson Complex			Million Mounds			Blake Ridge		
Taxon	**FG**	**n**	**δ13C ‰**	**δ15N ‰**	**n**	**δ13C ‰**	**δ15N ‰**	**n**	**δ13C ‰**	**δ15N ‰**	**n**	**δ13C ‰**	**δ15N ‰**	**n**	**δ13C ‰**	**δ15N ‰**
Dicrolene nigra	BE	5	SD = -18.3 (0.1) Range = -18.4 / -18.1	SD = 13.4 (0.6) Range = 12.3 / 13.8	-	-	-	-	-	-	-	-	-	-	-	-
Etelis oculatus	PE	-	-	-	-	-	-	-	-	-	-	-	-	1	SD = -18.9	SD = 7.2
Lampanyctus alatus	PE	-	-	-	-	-	-	1	SD = -19.3	SD = 5.6	1	SD = -19.9	SD = 6.4	-	-	-
Lepidophanes guentheri	PE	-	-	-	-	-	-	-	-	-	8	SD = -19.1 (0.4) Range = -19.7 / -18.5	SD = 8.1 (1.2) Range = 6.0 / 9.5	-	-	-
Leptocephalus	PE	-	-	-	-	-	-	10	SD = -20.1 (0.9) Range = -21.2 / -18.6	SD = 2.9 (1.3) Range = 0.9 / 4.9	-	-	-	1	SD = -20.5	SD = 6.3
Nezumia bairdii	BP-mid	3	SD = -18.2 (0.3) Range = -18.4 / -17.9	SD = 14.1 (0.5) Range = 13.7 / 14.6	-	-	-	-	-	-	-	-	-	-	-	-
Notolychnus valdiviae	PE	-	-	-	-	-	-	-	-	-	-	-	-	5	SD = -20.5 (0.2) Range = -20.8 / -20.2	SD = 5.1 (0.2) Range = 4.9 / 5.5
Photostomias guernei	PE	-	-	-	-	-	-	-	-	-	-	-	-	1	SD = -20.2	SD = 3.6
Pleuronectiformes sp.	PE	-	-	-	-	-	-	5	SD = -22.5 (0.3) Range = -23.0 / -22.2	SD = 4.2 (0.3) Range = 3.7 / 4.5	-	-	-	5	SD = -22.2 (0.2) Range = -22.5 / -22.0	SD = 3.3 (0.2) Range = 3.1 / 3.5
Pollichthys mauli	PE	-	-	-	-	-	-	-	-	-	-	-	-	1	SD = -20.0	SD = 6.0
Psenes arafurensis	PE	-	-	-	-	-	-	-	-	-	-	-	-	1	SD = -18.8	SD = 5.6
Pyrosoma atlanticum	PE	-	-	-	12	SD = -19.4 (1.0) Range = -21.6 / -17.7	SD = 6.9 (2.5) Range = 3.9 / 10.6	-	-	-	4	SD = -19.2 (0.3) Range = -19.5 / -18.8	SD = 9.2 (0.4) Range = 8.5 / 9.4	-	-	-

-		Pamlico Canyon			Virginia InterCanyon			Richardson Complex			Million Mounds			Blake Ridge		
Taxon	**FG**	**n**	**δ13C ‰**	**δ15N ‰**	**n**	**δ13C ‰**	**δ15N ‰**	**n**	**δ13C ‰**	**δ15N ‰**	**n**	**δ13C ‰**	**δ15N ‰**	**n**	**δ13C ‰**	**δ15N ‰**
Salpida	SS	-	-	-	-	-	-	14	SD = -19.4 (0.8) Range = -20.3 / -17.1	SD = 3.0 (1.5) Range = 1.4 / 5.7	-	-	-	6	SD = -20.1 (0.2) Range = -20.5 / -19.8	SD = 1.8 (0.4) Range = 1.4 / 2.3
Serrivomer beanii	BP-mid	-	-	-	-	-	-	-	-	-	-	-	-	3	SD = -19.5 (0.1) Range = -19.6 / -19.4	SD = 4.7 (0.8) Range = 4.0 / 5.6
Sigmops elongatus	PE	1	SD = -19.2	SD = 6.8	-	-	-	-	-	-	1	SD = -19.1	SD = 8.0	1	SD = -19.1	SD = 7.1
Sternoptychidae	PE	-	-	-	-	-	-	3	SD = -19.3 (0.2) Range = -19.4 / -19.1	SD = 6.1 (1.2) Range = 5.1 / 7.4	-			-	-	-
Sternoptyx diaphana	PE	-	-	-	1	SD = -19.0	SD = 9.9	4	SD = -19.8 (0.2) Range = -20.1 / -19.6	SD = 5.6 (0.7) Range = 4.5 / 6.1	-	-	-	-	-	-
Cnidaria																
Anemone	SS	1	SD = -16.7	SD = 14.9	-			-	-	-	-	-	-	-	-	-
Siphonophore sp.2	PE	-	-	-	-	-	-	-	-	-	-	-	-	1	SD = -19.4	SD = 5.7
Siphonophore sp.7	PE	-	-	-	-	-	-	-	-	-	-	-	-	1	SD = -19.1	SD = 7.1
Ctenophora																
Ctenophora	PE	4	SD = -20.6 (0.5) Range = -20.9 / -19.8	SD = 0.5 (2.6) Range = -1.2 / 4.3	-	-	-	-	-	-	-	-	-	-	-	-

-		Pamlico Canyon			Virginia InterCanyon			Richardson Complex			Million Mounds			Blake Ridge		
Taxon	**FG**	**n**	**$\delta^{13}C$ ‰**	**$\delta^{15}N$ ‰**	**n**	**$\delta^{13}C$ ‰**	**$\delta^{15}N$ ‰**	**n**	**$\delta^{13}C$ ‰**	**$\delta^{15}N$ ‰**	**n**	**$\delta^{13}C$ ‰**	**$\delta^{15}N$ ‰**	**n**	**$\delta^{13}C$ ‰**	**$\delta^{15}N$ ‰**
Echinodermata																
Echinodermata larvae	PE	-	-	-	-	-	-	5	SD = -21.8 (0.4) Range = -22.2 / -21.1	SD = 11.1 (0.5) Range = 10.3 / 11.6	-	-	-	2	SD = -21.8 (0.2) Range = -21.9 / -21.6	SD = 9.8 (0.2) Range = 9.6 / 9.9
Ophiuroidea	BS	5	SD = -17.6 (0.6) Range = -18.3 / -17.1	SD = 8.1 (0.8) Range = 6.7 / 8.8	-	-	-	-	-	-	-	-	-	-	-	-
Mollusca																
Bivalvia	BS	5	SD = -19.2 (0.7) Range = -20.0 / -18.2	SD = 10.6 (0.3) Range = 10.2 / 11.0	-	-	-	-	-	-	-	-	-	-	-	-
Gastropoda sp.1	BE	2	SD = -16.4 (0.2) Range = -16.5 / -16.2	SD = 12.0 (0.1) Range =11.9 / 12.1	-	-	-	-	-	-	-	-	-	-	-	-
Gastropoda sp.2	BE	4	SD = -26.3 (12.1) Range = -44.3 / -19.6	SD = 5.3 (8.2) Range = -6.9 / 10.0	-	-	-	-	-	-	-	-	-	-	-	-
Pteropoda	PE	-	-	-	-	-	-	-	-	-	-	-	-	3	SD = -20.8 (1.1) Range = -22.0 / -19.9	SD = 4.8 (1.7) Range = 3.1 / 6.5
Pteropoda sp.1	PE	2	SD = -16.4 (2.3) Range = -18.0 / -14.8	SD = 4.1 (0.3) Range = 3.9 / 4.3	-	-	-	-	-	-	-	-	-	-	-	-
Pteropoda sp.10	PE	5	SD = -20.0 (0.8) Range = -21.0 / -18.8	SD = 4.0 (0.5) Range = 3.4 / 4.6	-	-	-	-	-	-	-	-	-	-	-	-
Pteropoda sp.11	PE	-	-	-	-	-	-	5	SD = -20.0 (0.8) Range = -20.8 / -18.8	SD = 3.2 (0.3) Range = 2.9 / 3.7	-	-	-	-	-	-

-		Pamlico Canyon			Virginia InterCanyon			Richardson Complex			Million Mounds			Blake Ridge		
Taxon	**FG**	**n**	**$\delta^{13}C$ ‰**	**$\delta^{15}N$ ‰**	**n**	**$\delta^{13}C$ ‰**	**$\delta^{15}N$ ‰**	**n**	**$\delta^{13}C$ ‰**	**$\delta^{15}N$ ‰**	**n**	**$\delta^{13}C$ ‰**	**$\delta^{15}N$ ‰**	**n**	**$\delta^{13}C$ ‰**	**$\delta^{15}N$ ‰**
Pteropoda sp.2	PE	-	-	-	-	-	-	5	SD = -19.0 (0.8) Range = -19.7 / -18.1	SD = 2.1 (0.6) Range = 1.3 / 3.0	-	-	-	-	-	-
Pteropoda sp.4	PE	-	-	-	-	-	-	2	SD = -18.7 (0.8) Range = -19.2 / -18.1	SD = 4.2 (1.7) Range = 3.0 / 5.4	-	-	-	-	-	-
Pteropoda sp.6	PE	-	-	-	-	-	-	5	SD = -19.8 (1.3) Range = -20.6 / -17.6	SD = 1.8 (0.1) Range = 1.7 / 1.9	-	-	-	-	-	-
Pteropoda sp.9	PE	4	SD = -18.1 (1.2) Range = -19.7 / -17.0	SD = 3.9 (0.2) Range = 3.7 / 4.1	-	-	-	-			-	-	-	-	-	-
Pterotracheoidea	PE	-			-	-	-	-	-	-	-	-	-	1	SD = -18.8	SD = 4.4

Several fish families were present at multiple sites and isotope results (**Figure 4-90**) illustrate clear overlap among families analyzed. In addition, a narrow range in $\delta^{13}C$ values indicates similar food sources and/or consistent $\delta^{13}C$ values of their primary food source across sites. Acanthuridae from Richardson Reef Complex had the lowest $\delta^{15}N$ value (3.5‰, n = 1) and Sternoptychidae had the highest $\delta^{15}N$ value (9.9 ‰, n = 1, Virginia InterCanyon). Sternoptychidae from the Virginia InterCanyon also had the highest $\delta^{13}C$ value (-19.0‰, n = 1), whereas Myctophidae had the lowest $\delta^{13}C$ values (-20.5 ± 0.2‰, Blake Ridge).

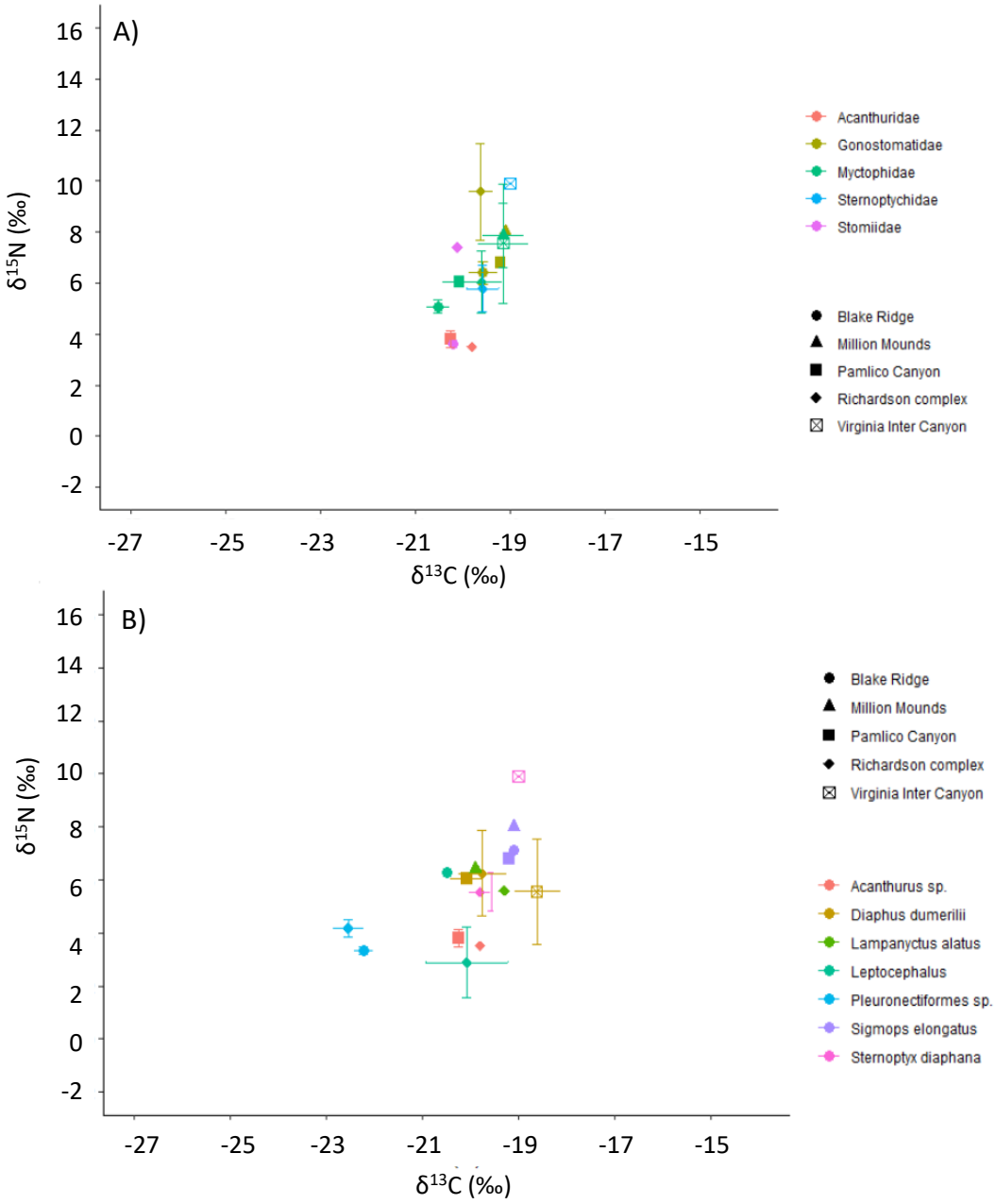

Figure 4-90. Mean stable isotope values for fish families by species/taxa
Mean stable isotope values for fish A. families and B. species/taxa (mean ± SD) that were collected at different locations. Data were based on nine trawls (two Blake Ridge, one Million Mounds, one Pamlico, three Richardson, two Virginia InterCanyon)

Table 4-26. Mean values of $\delta^{13}C$ and $\delta^{15}N$ for fishes collected across multiple sites

Mean isotope values of $\delta^{13}C$ and $\delta^{15}N$ (‰, SD, and minimum/maximum) for fishes collected across multiple sites during research cruises from 2018–2019 at A) family level and B) taxa/species level. FG represent the different feeding groups: BE = benthic, BP-mid = Benthic/Pelagic midwater collection, BS = Benthic/Suspension, PE = Pelagic and SS=Suspension.

Level	Order	Taxon	FG	n	$\delta^{13}C$ ‰ Mean (SD)	$\delta^{13}C$ ‰ Range	$\delta^{15}N$ ‰ Mean (SD)	$\delta^{15}N$ ‰ Range	C:N Mean (SD)	C:N Range
Blake Ridge										
Family	Myctophiformes	Myctophidae	PE	5	-20.5 (0.2)	-20.8 / -20.2	5.1 (0.2)	4.9 / 5.5	4.7 (0.3)	4.4 / 5.2
	Perciformes	Acanthuridae	PE	-	-	-	-	-	-	-
	Stomiiformes	Gonostomatidae	PE	6	-19.6 (0.3)	-19.9 / -19.1	6.4 (0.4)	6.0 / 7.1	4.1 (0.1)	4.0 / 4.2
	Stomiiformes	Sternoptychidae	PE	-	-	-	-	-	-	-
	Stomiiformes	Stomiidae	PE	1	-20.2	-	3.6	-	4.8	-
Taxa/Species	-	*Leptocephalus*	PE	1	-20.5	-	6.3	-	4.4	-
	Myctophiformes	*Diaphus dumerilii*	PE	-	-	-	-	-	-	-
	Myctophiformes	*Lampanyctus alatus*	PE	-	-	-	-	-	-	-
	Pleuronectiformes	Pleuronectiformes sp.	PE	5	-22.2 (0.2)	-22.5 / -22	3.3 (0.2)	3.1 / 3.5	6.3 (0.2)	6.1 / 6.5
	Perciformes	*Acanthurus* sp.	PE	-	-	-	-	-	-	-
	Stomiiformes	*Sigmops elongatus*	PE	1	-19.1	-	7.1	-	4.2	-
	Stomiiformes	*Sternoptyx diaphana*	PE	-	-	-	-	-	-	-
Million Mounds										
Family	Myctophiformes	Myctophidae	PE	9	-19.1 (0.4)	-19.9 / -18.5	7.9 (1.3)	6.0 / 9.5	3.8 (0.0)	3.7 / 3.8
	Perciformes	Acanthuridae	PE	-	-	-	-	-	-	-
	Stomiiformes	Gonostomatidae	PE	1	-19.1	-	8.0	-	3.8	-
	Stomiiformes	Sternoptychidae	PE	-	-	-	-	-	-	-
	Stomiiformes	Stomiidae	PE	-	-	-	-	-	-	-
Taxa/Species	-	*Leptocephalus*	PE	-	-	-	-	-	-	-
	Myctophiformes	*Diaphus dumerilii*	PE	-	-	-	-	-	-	-
	Myctophiformes	*Lampanyctus alatus*	PE	1	-19.9	-	6.4	-	3.7	-
	Pleuronectiformes	Pleuronectiformes sp.	PE	-	-	-	-	-	-	-
	Perciformes	*Acanthurus* sp.	PE	-	-	-	-	-	-	-
	Stomiiformes	*Sigmops elongatus*	PE	1	-19.1	-	8.0	-	3.8	-
	Stomiiformes	*Sternoptyx diaphana*	PE	-	-	-	-	-	-	-
Pamlico										
Family	Myctophiformes	Myctophidae	PE	4	-20.1 (0.4)	-20.5 / -19.7	6.1 (0.2)	5.8 / 6.2	4.7 (0.2)	4.4 / 4.9
	Perciformes	Acanthuridae	PE	4	-20.3 (0.1)	-20.4 / -20.2	3.8 (0.3)	3.3 / 4.1	4.6 (0.2)	4.3 / 4.7
	Stomiiformes	Gonostomatidae	PE	1	-19.2	-	6.8	-	4.2	-
	Stomiiformes	Sternoptychidae	PE	-	-	-	-	-	-	-
	Stomiiformes	Stomiidae	PE	-	-	-	-	-	-	-
Taxa/Species	-	*Leptocephalus*	PE	-	-	-	-	-	-	-
	Myctophiformes	*Diaphus dumerilii*	PE	4	-20.1 (0.4)	-20.5 / -19.7	6.1 (0.2)	5.8 / 6.2	4.7 (0.2)	4.4 / 4.9

Level	Order	Taxon	FG	n	$\delta^{13}C$ ‰ Mean (SD)	$\delta^{13}C$ ‰ Range	$\delta^{15}N$ ‰ Mean (SD)	$\delta^{15}N$ ‰ Range	C:N Mean (SD)	C:N Range
	Myctophiformes	*Lampanyctus alatus*	PE	-	-	-	-	-	-	-
	Pleuronectiformes	Pleuronectiformes sp.	PE	-	-	-	-	-	-	-
	Perciformes	*Acanthurus* sp.	PE	4	-20.3 (0.1)	-20.4 / -20.2	3.8 (0.3)	3.3 / 4.1	4.6 (0.2)	4.3 / 4.7
	Stomiiformes	*Sigmops elongatus*	PE	1	-19.2	-	6.8	-	4.2	-
	Stomiiformes	*Sternoptyx diaphana*	PE	-	-	-	-	-	-	-
Richardson										
Family	Myctophiformes	Myctophidae	PE	3	-19.6 (0.4)	-20.1 / -19.3	6.0 (1.2)	5.1 / 7.4	4.3 (0.1)	4.2 / 4.4
	Perciformes	Acanthuridae	PE	1	-19.8	-	3.5	-	5.3	-
	Stomiiformes	Gonostomatidae	PE	6	-19.6 (0.2)	-19.9 / -19.4	9.6 (1.9)	5.8 / 10.8	4.6 (0.2)	4.3 / 5.0
	Stomiiformes	Sternoptychidae	PE	7	-19.6 (0.3)	-20.1 / -19.1	5.8 (0.9)	4.5 / 7.4	4.1 (0.2)	4.0 / 4.5
	Stomiiformes	Stomiidae	PE	1	-20.1	-	7.4	-	4.7	-
Taxa/Species	-	*Leptocephalus*	PE	10	-20.1 (0.9)	-21.2 / -18.6	2.9 (1.3)	0.9 / 4.9	4.7 (0.4)	4.2 / 5.2
	Myctophiformes	*Diaphus dumerilii*	PE	2	-19.8 (0.5)	-20.1 / -19.4	6.3 (1.6)	5.1 / 7.4	4.3 (0.1)	4.2 / 4.4
	Myctophiformes	*Lampanyctus alatus*	PE	1	-19.3	-	5.6	-	4.2	-
	Pleuronectiformes	Pleuronectiformes sp.	PE	5	-22.5 (0.3)	1.0	4.2 (0.3)	3.7 / 4.5	7.0 (0.2)	6.8 / 7.4
	Perciformes	*Acanthurus* sp.	PE	1	-19.8	-	3.5	-	5.3	-
	Stomiiformes	*Sigmops elongatus*	PE	-	-	-	-	-	-	-
	Stomiiformes	*Sternoptyx diaphana*	PE	4	-19.8 (0.2)	-20.1 / -19.6	5.6 (0.7)	4.5 / 6.1	4.2 (0.2)	4.0 / 4.5
Virginia InterCanyon										
Family	Myctophiformes	Myctophidae	PE	34	-19.1 (0.5)	-20.4 / -17.9	7.6 (2.3)	3.4 / 10.2	4.0 (0.1)	3.9 / 4.1
	Perciformes	Acanthuridae	PE	-	-	-	-	-	-	-
	Stomiiformes	Gonostomatidae	PE	-	-	-	-	-	-	-
	Stomiiformes	Sternoptychidae	PE	1	-19.0		9.9		4.1	
	Stomiiformes	Stomiidae	PE	-	-	-	-	-	-	-
Taxa/Species	-	*Leptocephalus*	PE	-	-	-	-	-	-	-
	Myctophiformes	*Diaphus dumerilii*	PE	5	-18.6 (0.5)	-19.3 / -18.2	5.6 (2)	4.2 / 9.0	3.9 (0.0)	3.9 / 3.9
	Myctophiformes	*Lampanyctus alatus*	PE	-	-	-	-	-	-	-
	Pleuronectiformes	Pleuronectiformes sp.	PE	-	-	-	-	-	-	-
	Perciformes	*Acanthurus* sp.	PE	-	-	-	-	-	-	-
	Stomiiformes	*Sigmops elongatus*	PE	-	-	-	-	-	-	-
	Stomiiformes	*Sternoptyx diaphana*	PE	1	-19.0	-	9.9	-	4.1	-

Isotopic overlap among taxa found at different sites also mimicked the patterns in the family-level data (**Figure 4-90 B, Table 4-26**). *Sternoptyx diaphana* from Virginia InterCanyon had the highest $\delta^{15}N$ value (9.9‰, n = 1), whereas leptocephalus (eel larvae representing several possible taxa) from Richardson Reef Complex had the lowest $\delta^{15}N$ values (2.9 ± 1.3‰). *Diaphus dumerilii* (-18.6 ± 0.5‰, n = 5) had the highest and Pleuronectiformes sp. (-22.5 ± 0.3‰, n = 5) had the lowest $\delta^{13}C$ values. Several species/taxa collected at the different locations that had overlapping $\delta^{13}C$ and $\delta^{15}N$ values, including *Acanthurus* sp., *D. dumerilii*, *Lampanyctus alatus*, Pleuronectiformes sp., *Sigmops elongatus*, and *Sternoptyx diaphana*.

Limited sample sizes precluded statistical analysis to determine if there were intra-species isotopic differences among sites. Across all fishes collected, there was a strong positive correlation between depth and $\delta^{15}N$ (**Figure 4-91 B**, R = 0.332, p = 0.007), but this pattern did not hold for $\delta^{13}C$ (R = 0.168, p = 0.191) (**Figure 4-91 A**).

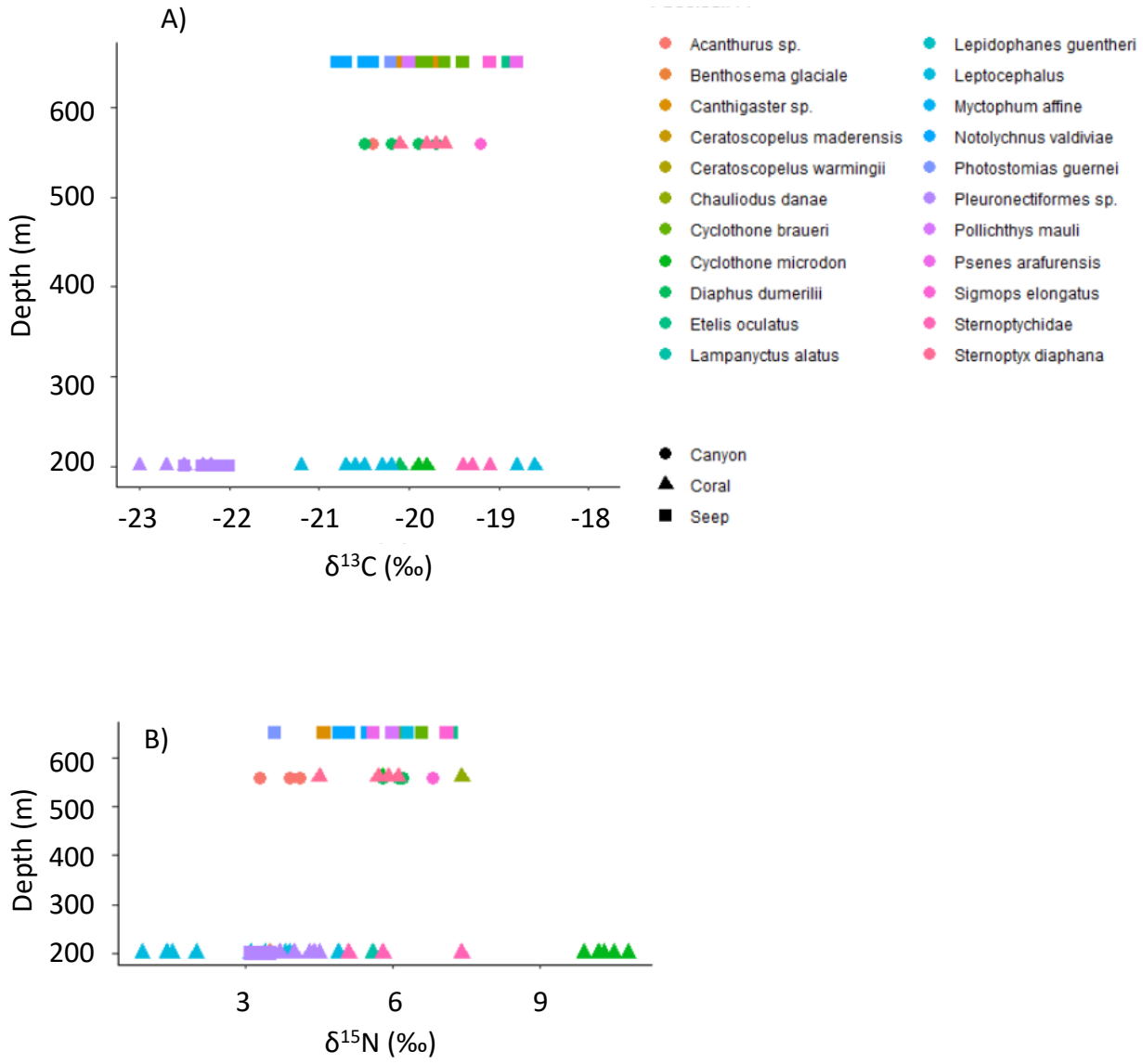

Figure 4-91. Average $\delta^{13}C$ and $\delta^{15}N$ values vs. depth for midwater trawl fishes
Average A. $\delta^{13}C$ and B. $\delta^{15}N$ isotope values vs. depth for midwater trawl fishes. Colors represent different species and symbols represent the different habitat types.

We compared a subset of isotope data from midwater collections to areas where seafloor organisms were also analyzed, specifically at Richardson Reef Complex (coral), Blake Ridge (seep), and Pamlico Canyon, and these comparisons are summarized below.

At Richardson Reef Complex, the distance from midwater trawls to the closest fauna collections from submersible dives ranged from 1.3 to 11 km (**Figure 4-92**). While the basal carbon source for all the taxa was likely derived from photosynthetic material, animals collected in the midwater were depleted in ^{15}N relative to the bottom dwellers, indicating either unique nitrogen isotopic composition of their food source, feeding location, and/or feeding at lower trophic levels (**Figure 4-93**, triangle symbols).

The isotopic niche of midwater taxa, as illustrated by the 95% CI ellipses around the mean (dashed ellipses, **Figure 4-94**), indicates some overlap among pelagic, suspension, and mixed feeding types (benthic/pelagic feeders), with the greatest overlap between suspension feeders on the seafloor (yellow, solid ellipse) with pelagic feeders collected via midwater trawl (light blue, dashed ellipse). This overlap might reflect assimilation of similar food resources over time, or sources with consistent isotopic values.

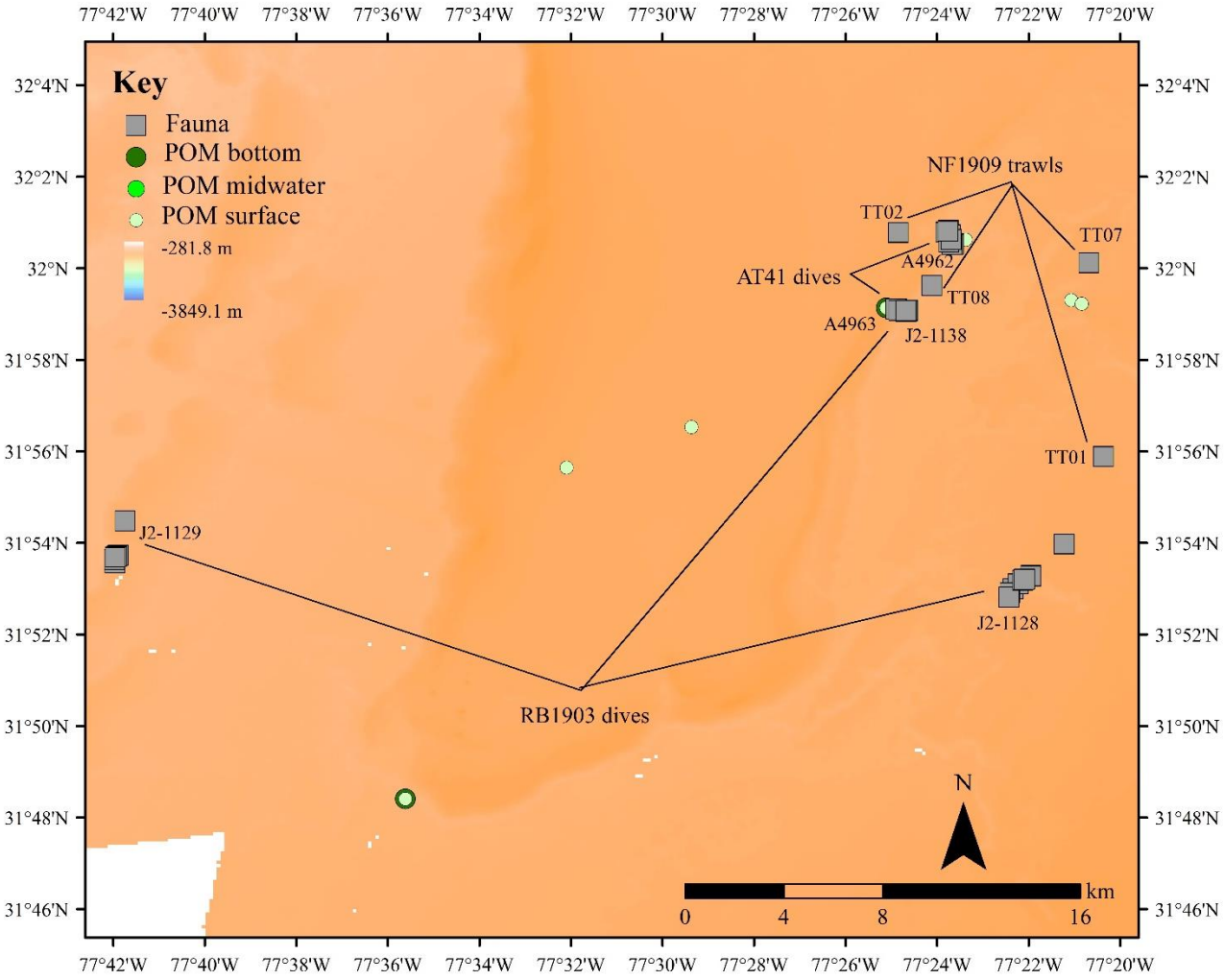

Figure 4-92. Locations of the midwater trawls at Richardson Reef Complex
Relative to submersible dives

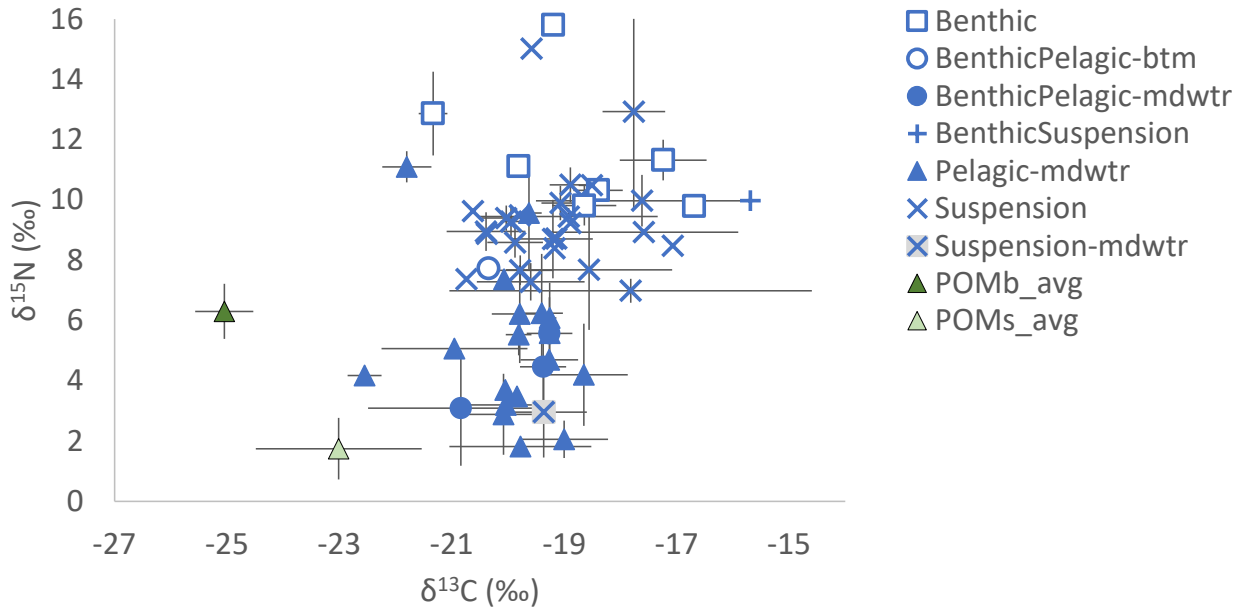

Figure 4-93. Average $\delta^{13}C$ and $\delta^{15}N$ values of fauna and POM collected from Richardson Reef
Average $\delta^{13}C$ and $\delta^{15}N$ isotope values (± SD) of fauna and POM collected from Richardson Reef Complex. Symbols represent the different habitat types and colors represent the type of sample (fauna, POM, sediment). POM was separated into bottom (POMb) and surface (POMs) samples.

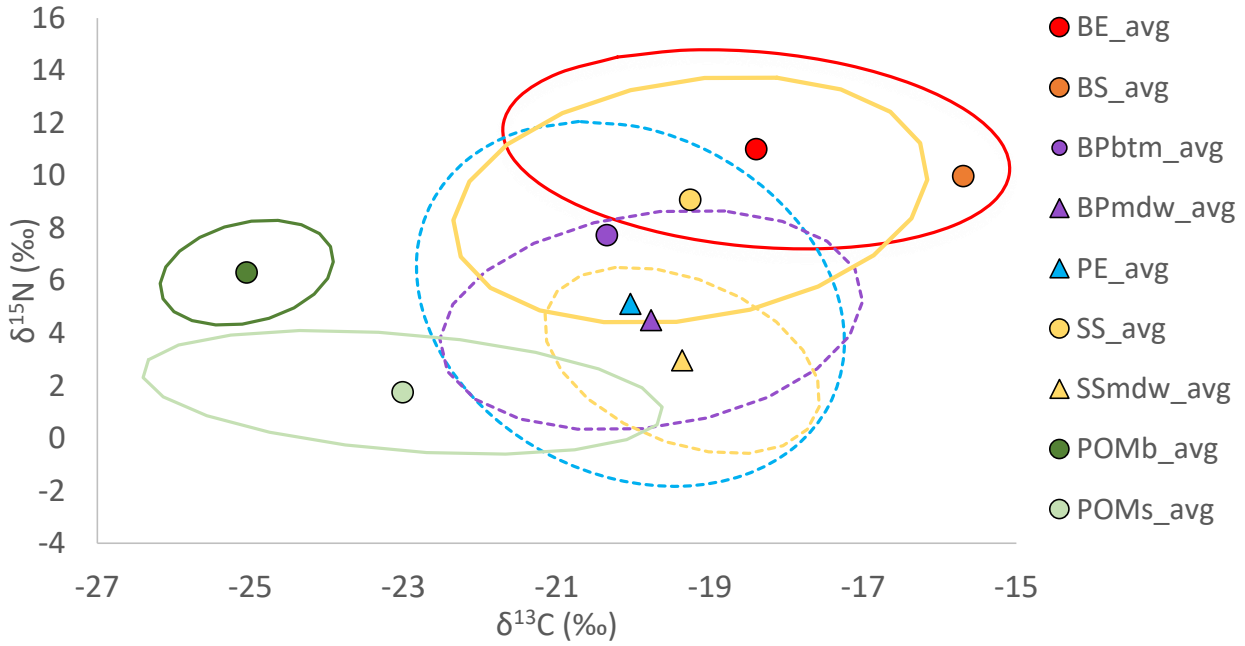

Figure 4-94. Average $\delta^{13}C$ and $\delta^{15}N$ values with 95% CI ellipses for each feeding group
Average $\delta^{13}C$ and $\delta^{15}N$ values (point) with 95% CI (ellipses) for each feeding group: red = benthic (BE), purple = benthic/pelagic (BP), orange = benthic/suspension (BS), gray = chemo, blue = pelagic (PE), yellow = suspension (SS), green = POM, and black = sediment 0–2 cm. Solid lines and ellipses indicate seafloor (submersible) collections, whereas dashed lines and triangles indicate midwater collections.

At Blake Ridge seeps, we collected midwater trawls (200 and 500 m water depth) approximately 0.7–2.8 km from where we collected seep fauna via submersible at 2,150 m water depth (**Figure 4-95**). Midwater communities were isotopically enriched in ^{13}C relative to those collected near or on the seafloor and had isotope values reflecting photosynthetically derived carbon. In contrast, most of the taxa collected from the seep area, regardless of feeding group were relatively depleted in ^{13}C (**Figure 4-96**). This pattern is further reflected in the feeding niches (**Figure 4-97**), where some overlap occurred between mixed feeding groups (benthic/pelagic, purple dashed and solid ellipses) found on the seafloor and midwater, but the other midwater and seafloor feeding groups were isotopically distinct.

There was also more spread in the $\delta^{13}C$ and $\delta^{15}N$ among the groups collected on the seafloor (solid lines) compared to the midwater, indicating a greater diversity of isotope values, and possible availability of food sources available, at the seeps.

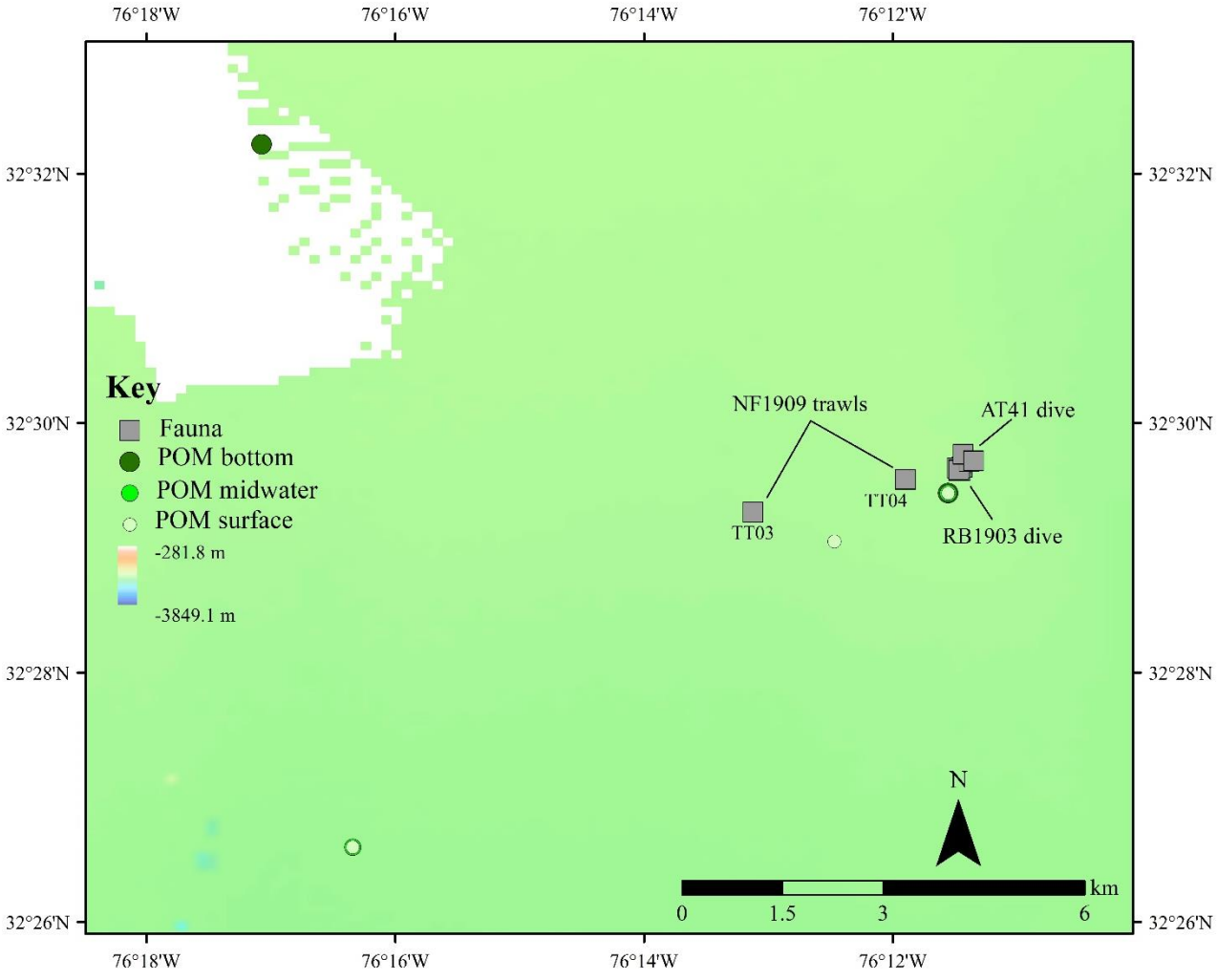

Figure 4-95. Locations of the midwater trawls at Blake Ridge Seep
Relative to submersible dives

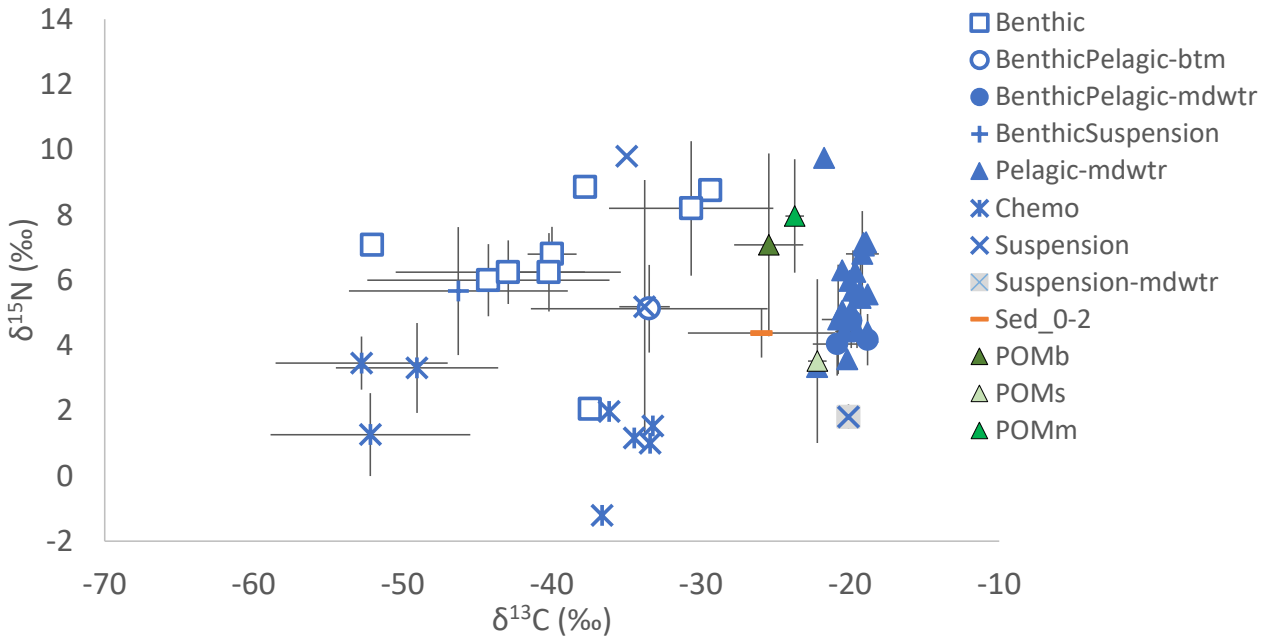

Figure 4-96. Mean $\delta^{13}C$ and $\delta^{15}N$ values of fauna, POM, and sediment from Blake Ridge
Mean $\delta^{13}C$ and $\delta^{15}N$ isotope values (‰ ± SD) of fauna, POM (b = bottom, m = midwater, s = surface) , and surface sediment (0–2 cm) collected from Blake Ridge. Symbols represent the different feeding groups with btm indicating fauna collected from benthic gear and mdwtr representing fauna collected from trawls. POM was separated into bottom (POMb), midwater (POMm) and surface (POMs) samples.

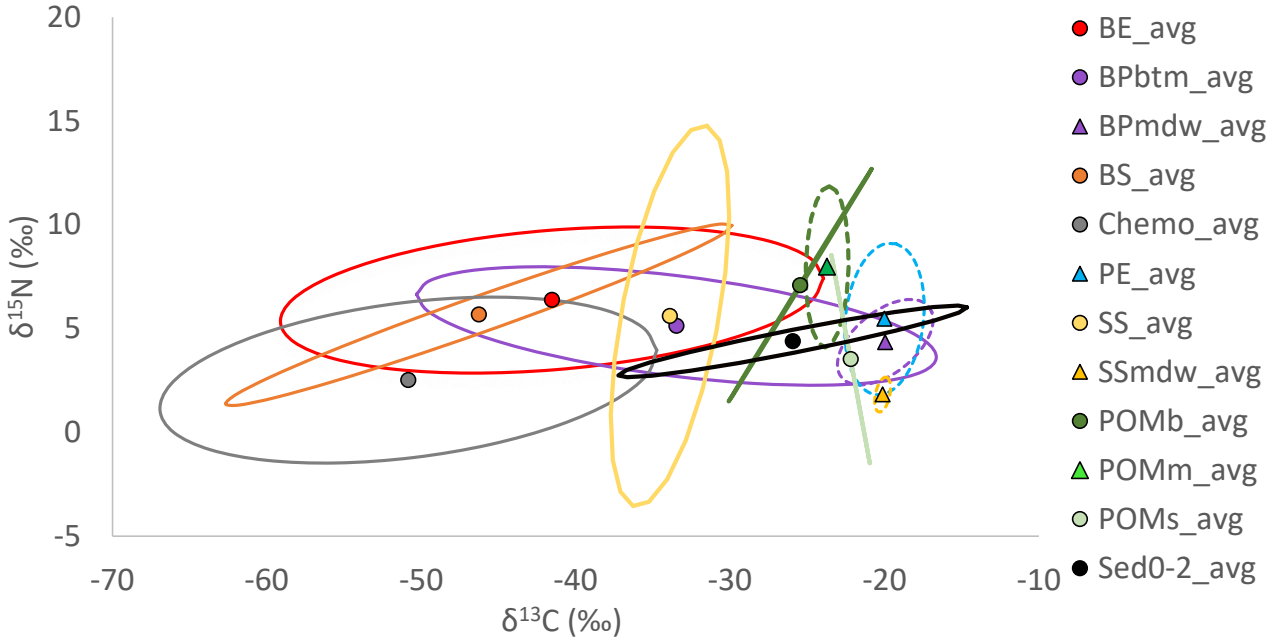

Figure 4-97. Average $\delta^{13}C$ and $\delta^{15}N$ values with 95% CI for each feeding group from Blake Ridge
Average $\delta^{13}C$ and $\delta^{15}N$ isotope values (point) with 95% CI (ellipses) for each feeding group. from Blake Ridge Seep. Symbols represent the different habitat types and colors represent the type of sample (fauna, POM, sediment). POM was separated into bottom (POMb) and surface (POMs) samples.

Finally, we also sampled midwater communities in proximity to seafloor benthos at Pamlico Canyon, between 3.4 and 7.0 km from the submersible dives (**Figure 4-98**). At Pamlico Canyon, *Nezumia* sp. and decapod shrimp collected within the midwater trawls had similar $\delta^{15}N$ and $\delta^{13}C$ values compared to benthic feeders and higher $\delta^{15}N$ values compared to other mixed feeding groups (benthic/pelagic feeders) collected at the seafloor (**Figure 4-99**). Overlap in isotopic ellipses for all the feeding groups suggests some similarities in baseline carbon sources and/or the use of benthic resources by diel vertical migrators present in the midwater communities (**Figure 4-100**). Of note is that one of the trawls in Pamlico Canyon hit the bottom, so it is possible that a few of the taxa collected via trawl actually live near or at the seafloor rather than the water column.

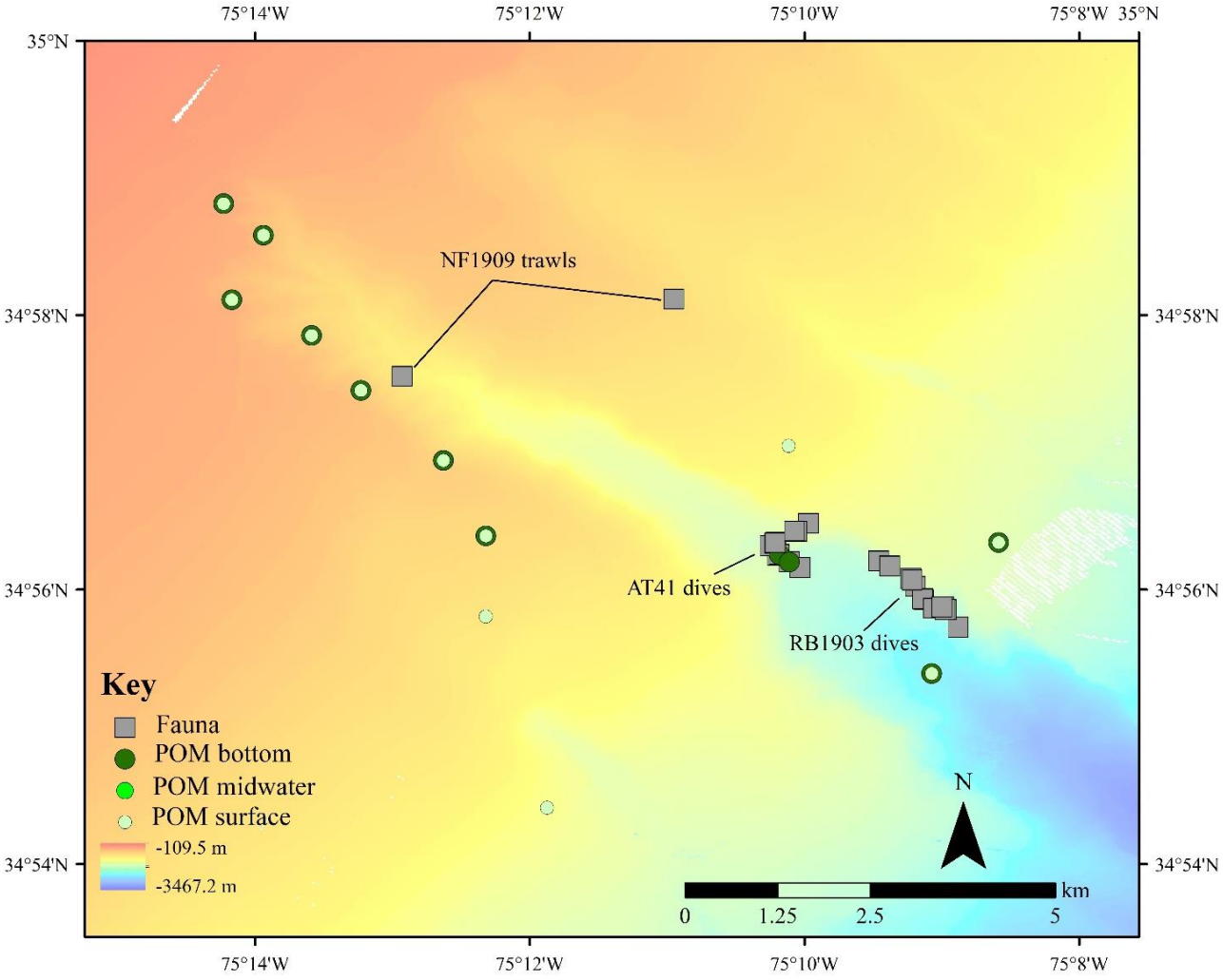

Figure 4-98. Locations of the midwater trawls at Pamlico Canyon
Relative to submersible dives

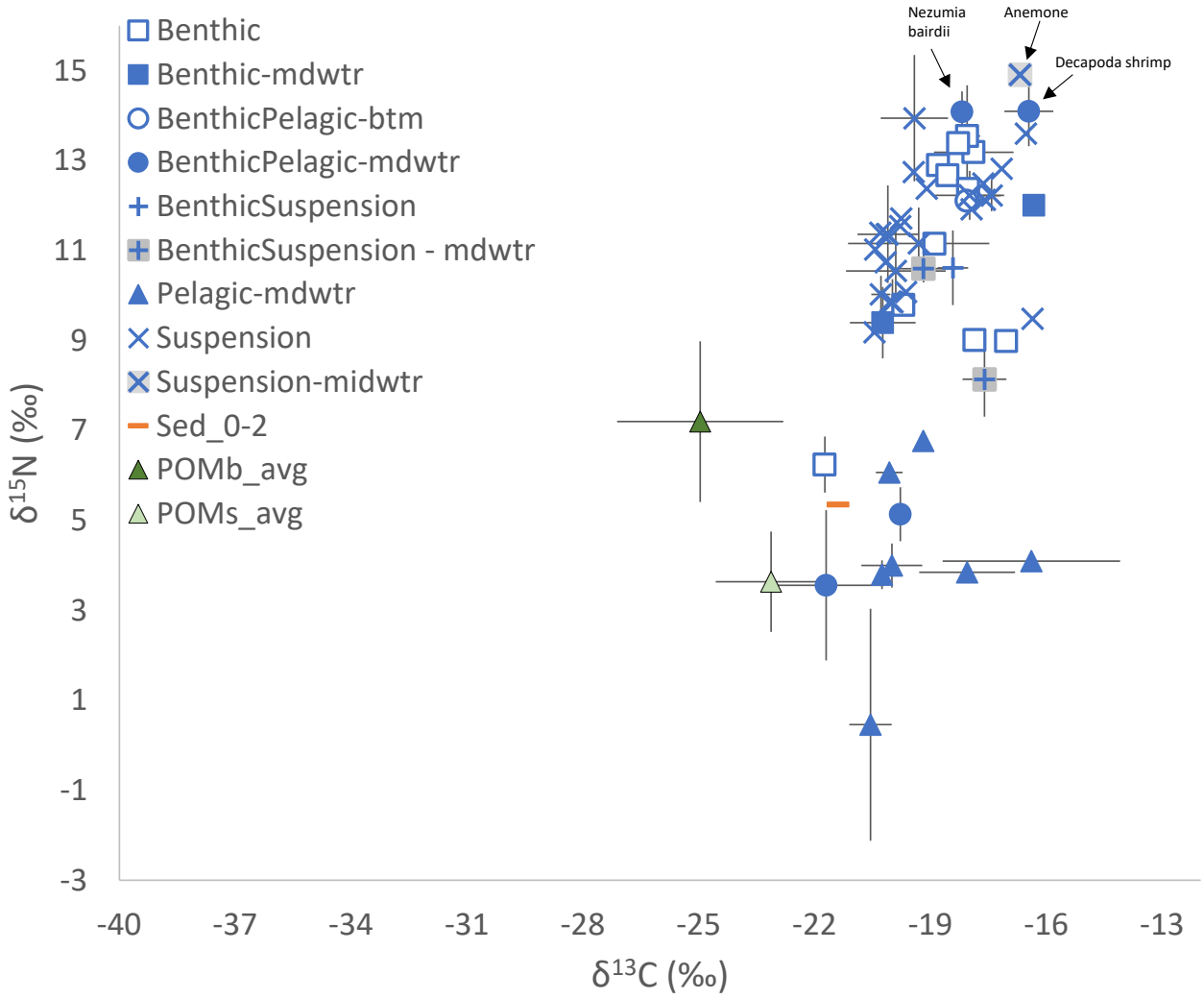

Figure 4-99. Average $\delta^{13}C$ and $\delta^{15}N$ values of fauna, POM and Pamlico Canyon sediment
Average $\delta^{13}C$ and $\delta^{15}N$ isotope values (± SD) of fauna, POM and surface sediment (0–2 cm) collected from Pamlico Canyon. Symbols represent the different habitat types and colors represent the type of sample (fauna, POM, sediment). POM was separated into bottom (POMb) and surface (POMs) samples.

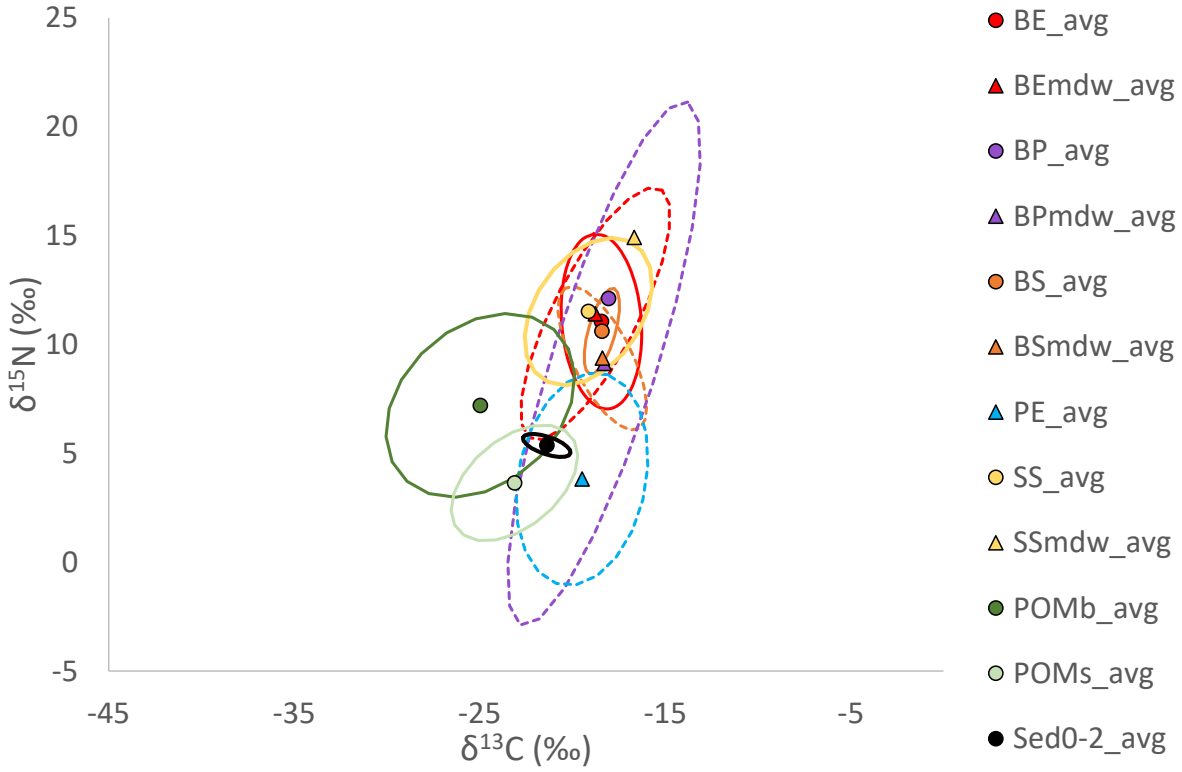

Figure 4-100. Average $\delta^{13}C$ and $\delta^{15}N$ values with 95% CI for each feeding group at Pamlico Canyon
Average $\delta^{13}C$ and $\delta^{15}N$ isotope values (point) with 95% CI (ellipses) for each feeding group. red = benthic (BE), purple = benthic pelagic (BP), orange = benthic suspension (BS), blue = pelagic (PE), yellow = suspension (SS), green = POM.

4.4.4 Discussion

4.4.4.1 Nutrition of Deep-Sea Coral Habitats

Coral habitats encompassed a wide range of isotope values indicative of relying on photosynthetically derived material. The range in isotope values from the six habitats examined overlapped with previous isotopic surveys conducted within Norfolk and Baltimore Canyon environments to the north (Demopoulos et al. 2017). Across these habitats and feeding groups, there was isotopic overlap, suggesting some consistency in the isotopic composition of the primary food sources over time and space.

However, significant differences among sites within feeding groups suggested some spatial variability in the baseline composition and/or variation in food selection by suspension feeders in particular. For example, suspension feeders from deeper coral sites located at Blake Deep and Escarpment (1,300 m) had higher $\delta^{15}N$ values then from shallower sites at Richardson and Stetson Banks. Stable nitrogen isotope values can change with depth due to increased microbial reworking of the organic material as it descends through the water column (Mintenbeck et al. 2007); thus, higher $\delta^{15}N$ values may represent feeding on degraded POM that is ^{15}N enriched. Similar patterns with depth and increased isotopic composition of suspension feeders has also been documented in other deep-sea environments (Bergmann et al. 2009), suggesting a consistent pattern with functional grouping rather than species-specific relationship with depth.

Suspension-feeding corals are known to consume zooplankton (Kiriakoulakis et al. 2005, Duineveld et al. 2007, 2012) and feeding at higher trophic levels can also result in higher $\delta^{15}N$ values (Sherwood et al. 2009, Demopoulos et al. 2017). The stable isotope results reported here were based on bulk analysis, which averages the isotopic composition of all the biochemical components of an organism's diet (Peterson and Fry 1987). Further work using compound specific stable isotope analysis would refine our understanding of whether isotope patterns are due to differences in source or trophic level, or a combination of both.

Notably, there were differences among suspension-feeding taxa across sites, with corals having lower isotopic values compared to sponges. Lower $\delta^{15}N$ values for certain corals, *Madrepora oculata*, may result from many factors, including symbiotic nitrogen fixation and/or direct consumption of bacteria by these suspension feeders (Mueller et al. 2014, Middelburg et al. 2015). Polyp size may influence food selection and capture ability, which in turn effects corals' functional niche (Quattrini et al. 2017). In contrast, sponges maybe assimilating a wide range of organic material of various sources, ages, and lability.

There are also sponge-associated microorganisms which may influence assimilation pathways (cf. Taylor et al. 2007), which may, in turn, lead to higher $\delta^{15}N$ of sponges (Iken et al. 2001, Becker et al. 2009, Bergmann et al. 2009). Sponge specimens included various hexactinellids (glass sponges), as well as the carnivorous cladorhizids, which are known to feed at higher trophic levels. Variable isotope values of sponges have been reported in several deep-sea food-web studies, but more details of the isotope-effects of food-selection and assimilation pathways are needed. It is noted that we cleaned sponge samples and all associated metazoan fauna, often present within sponge tissues, were removed via dissection prior to isotopic analysis to reduce their contribution to the sponge isotopic signal.

4.4.4.2 Nutrition of Deep-Sea Seep Habitats

4.4.4.2.1 Isotopic Composition for the Known Symbiont Bearing Fauna

Several taxa known to house chemosymbiotic microbes were present along the seeps examined in this study, including the bivalves, *Bathymodiolus heckerae*, *Acharax* sp., and *Isorropodon* sp., and tubeworms (cf. *Escarpia* sp.). Although *B. heckerae* were found in abundance at Blake Ridge Seep and are known to occur near Norfolk Canyon Seep (Coykendall et al. 2019), they were not visibly present at any of the other seeps examined in this study. These mussels house four phylotypes of symbionts, with two that are apparent thiotrophs, one that groups with methanotrophs, and one that groups with methylotrophs (Duperron et al. 2007, 2009).

Mussel isotopic composition reflects their primary reliance on biogenic methane, and or inorganic carbon derived from biogenic methane, ($\delta^{13}C$ ~< -50‰, Paull et al. 2000) as primary carbon sources fueling their microbial symbionts. Results were similar to previous work in the Atlantic (Van Dover et al. 2003, Demopoulos et al. 2019) and GOM seeps (Becker et al. 2010). Recent work at Baltimore and Norfolk seeps (Demopoulos et al. 2019) indicated that the stable isotope variation in *Gigantidas* [*Bathymodiolus*] *childressi* mussels was correlated with the size and extent of the mussel beds; where high-density mussels had overall lower $\delta^{13}C$ and $\delta^{15}N$ values, whereas low density patches had higher isotope values. Vohkshoori et al. (2021) using compound specific stable isotope analysis identified methane as the dominant carbon source at Baltimore, Norfolk, and Chincoteague seeps, and found the degree of venting intensity (whether major geysers or diffuse flow) and bed size influences the compound specific results.

Isotopic variation among mussel patch size remains to be examined. In addition, isotopic variation also occurred across tissue types, indicating variation due to isotopic routing among tissues, and possible influence of the bacterial symbionts to the mussel bulk isotope values. The range in sulfur isotopic composition present in the *B. heckerae* muscle tissues (**Table 4-23**) provides support for this differential

role of the mussel symbionts in accessing and utilizing various energy sources available in the environment.

In contrast, chemosymbiotic tubeworms (cf. *Escarpia* sp.), vesicomyid (*Isorropdon* sp.), and solemyid (*Acharax* sp.) clams were ^{13}C-enriched relative to mussels present at Blake Ridge, with $\delta^{13}C$ and $\delta^{34}S$ values indicative of their different carbon fixation pathways and thiotrophic endosymbionts, consistent with previously published isotope values from the GOM (Becker et al. 2014) and Atlantic margin seeps (Van Dover et al. 2003). The *Escarpia* sp. specimens were relatively small, where small individuals use their plume to access seawater carbon dioxide (Becker et al. 2011). Given the large range in *Escarpia* sp. $\delta^{34}S$ values (**Table 4-23**), the small dataset suggests high variability in the inorganic sulfur pools present at Kitty Hawk and Pea Island seeps. Tubeworms can access carbon sources required for their endosymbionts through their plumes (CO_2) and their "roots" (bicarbonate) (Freytag et al. 2001, Becker et al. 2011).

If they assimilate porewater bicarbonate via root acquisition, we expect the $\delta^{13}C$ of the tissues to be lower than the clams, because the isotopic composition of porewater bicarbonate present reflects the source material, of which methane ($\delta^{13}C < -50‰$) is the dominant substrate. Given the similar $\delta^{13}C$ composition of both the tubeworms and clams, results support utilization of seawater CO_2 via plumes. Isotope values differed by tissue type for both mussels and tubeworms, possibly due to variations in isotopic routing among the tissues, tissue-specific turnover time, and the contribution of endosymbionts (Van Dover et al. 2003, Demopoulos et al. 2019).

4.4.4.2.2 Utilization of Chemosynthetic Production by Heterotrophic Fauna

Seep communities examined in this study exhibited a wide range of stable isotope values, consistent with diverse food resources available along the margin (Demopoulos et al. 2019). Taxa associated with Blake Ridge Seep had notably the largest range in isotope values (**Figure 4-101**) and taxa were lower in both $\delta^{13}C$ and $\delta^{15}N$ relative to those collected from the other seep sites; these results suggest greater utilization of isotopically depleted seep resources over the long term. Few studies have examined seep food webs in the US Atlantic region (Demopoulos et al. 2019, Turner et al. 2020, Vohkshoori et al. 2021), all building on the foundational work by Van Dover et al. (2003) at Blake Ridge Diapir. There, seep communities exhibited variable reliance on methanotrophic and thiotrophic bacteria fueling the food-web base.

Most of the associated organisms analyzed in the current study relied upon seep-derived carbon, including biogenic methane, for a basal food source. Since the bottom water POM was depleted in ^{13}C at all the seep sites, consumers may also rely on the contribution of isotopically light, free-living microbes that reside in the bottom water and/or resuspension of organic matter from surface sediments. Given the range in isotope values present in each of the seep environments, methane plays an important role in fueling these food webs. Future applications of mixing models, combined with habitat analysis, will improve estimates of the proportional contribution of methane and its spatial variation within seep habitats and adjacent environments. Because food webs from several hundred seeps has not been characterized, margin-wide contribution of seep primary production remains unknown

4.4.4.3 Nutrition of Canyon Communities

Canyon food-web studies were limited to Norfolk and Pamlico Canyons at depths ranging from 1,100 to 1,800 m. There was substantial isotopic overlap among suspension feeders found within both canyons (**Figure 4-101**) and the range in values was consistent with those found at other canyons in the region (Demopoulos et al. 2017). Suspension feeders had the largest range in $\delta^{13}C$ and $\delta^{15}N$ values, indicating high variability in their primary food source, including mixed feeding at different trophic levels (Fanelli et al. 2009, Jeffreys et al. 2009). Some suspension feeders feed on POM and zooplankton prey resources. Particle size selection can also influence the $\delta^{13}C$ values, where larger particles are enriched in heavy

isotopes relative to the smaller particles (Rau et al. 1990, Gage and Tyler 1991, Tyler et al. 1995). The sizes of particles captured may differ among suspension feeders. Isotopic differences among suspension feeders may indicate assimilation of organic matter along a freshness gradient, from highly labile and fresh (low $\delta^{13}C$/ $\delta^{15}N$) to degraded (high $\delta^{13}C/\delta^{15}N$, Jeffreys et al. 2009). Thus, isotopic variabilities across suspension feeders are likely a function of multiple factors, including food selection, lability, particle size, as well as localized variability in the baseline carbon sources.

Coral isotope data from canyon and coral environments exhibited a continuum of values, from depleted to enriched ^{13}C and ^{15}N data, with no obvious pattern based on species/family level or environment (coral vs. canyon). Future examination of the imagery coupled with the isotope data may reveal isotopic differences based on the dynamic nature of the environment, similar to results found in Demopoulos et al. 2017, where lower values were associated with species residing on high-profile hard substrates (*L. pertusa*, *Paragorgia sp.*) and higher isotope values present in species residing in less dynamic, more quiescent sedimented environments (seapens).

4.4.4.4 Nutrition of Midwater Environments

While limited studies have examined stable isotopes of mesopelagic species, comparable studies in the GOM have indicated key functional roles of midwater communities in (Ross et al. 2010, McClain-Counts et al. 2017). The range in isotope values across environments (canyons, corals, and seeps) overlap with those found from similar environments in the GOM (McClain-Counts et al. 2017) and are consistent with photosynthetically derived organic matter serving as the primary food source. Similar isotopic composition for fishes co-occurring in multiple sites (**Figure 4-101**) suggest some consistency in the isotopic composition of the basal food source in space and time, where isotope data reflect time-integrated diets mixed over longer time periods (weeks to months).

Copepods have been identified as important to the diets for many mesopelagic fish species (McClain-Counts et al. 2017); those analyzed in this study had isotope values consistent with serving as a food source for mesopelagic fishes. Also, this previous work has identified non- crustacean prey items, such as salps and pteropods, as potentially important prey items for mesopelagic fishes, including *Sternoptyx* spp. Though there was no direct measure of mesopelagic fishes assimilating chemosynthetic material, detection of infrequent consumption of this food resource may be hindered by the assimilation of isotopically enriched photosynthetic organic matter.

Several mesopelagic fishes represented juvenile forms of demersal species typically found near the seabed, including Pleuronectiformes, Perciformes, and *Acanthurus* sp. Many of these fishes will settle at some future time, serving as important vectors of energy flow to the seafloor. Future analysis using isotope mixing models, as well as the migration status (diel vertical migrators, weak migrators, non-migrators) can help to improve our understanding of the trophic structure of mesopelagic communities, and the influence they have in transport of energy to the seafloor communities residing in the three environments examined.

4.4.5 Conclusions

In conclusion, this study examined the trophic structure in several coral, canyon, and seep environments using both stable isotopes along the US Atlantic margin. SIA and isotope niches revealed high trophic diversity in these food webs based on analysis of many different taxa and feeding groups, which may be a function of diverse food sources available, as well as habitat complexity. Habitat heterogeneity, methane flux rates, and depositional dynamics may play a role in diversifying associated food webs and niche specialization identified for the different feeding groups represented.

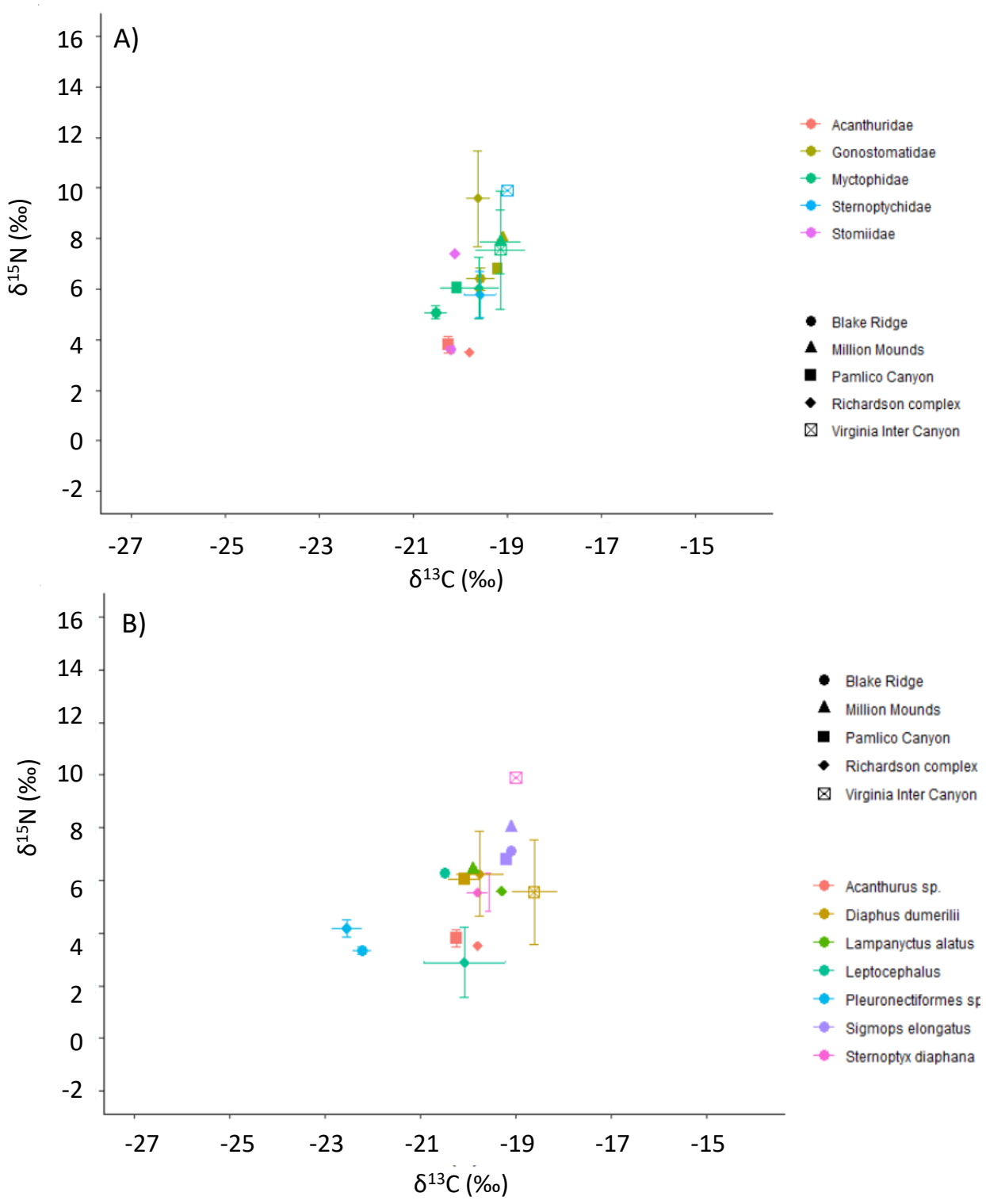

Figure 4-101. Mean $\delta^{13}C$ and $\delta^{15}N$ of fishes at family level and species level
Mean $\delta^{13}C$ and $\delta^{15}N$ isotope values (‰ ± SD) of fishes collected at different locations at the A) family level and B) species level. Data based on nine trawls (two Blake Ridge, one Million Mounds, one Pamlico, three Richardson, two Virginia InterCanyon)

4.5 Remote Sensing of Deep-Sea Habitats

Section Authors: Dylan Wilford, Jennifer Miksis-Olds

4.5.1 Soundscape Ecology

Passive acoustic technology can be used non-invasively to assess underwater sound levels, surface conditions, human activity, and the distribution and biodiversity of vocalizing marine life. The ability to obtain passive acoustic measurements contemporaneously, along with ancillary data to validate and enhance interpretations, can be a powerful tool facilitating insight into ocean and ecosystem dynamics. However, acoustic observation has not, in general, been a part of many previously established, large-scale oceanographic observatories, such as the International Ocean Observation System and Pacific Coast Ocean Observation System systems. Even when present, it usually records at frequencies below those of importance to most marine organisms (Tyack et al. 2015).

A great deal of information related to ocean dynamics and use can be gained simply by listening to the ambient sound. Information contained in soundscapes provide a means to better understand the influence of environmental parameters on local acoustic processes (Miksis-Olds et al. 2013, McWilliams & Hawkins, 2013, Staaterman et al. 2014), to assess habitat quality and health (Staaterman et al, 2014; Parks and Tyack 2014), and to better understand the impacts and risks of human contributions to the soundscape on marine life. Sound is a critical component in the lives of marine organisms, which rely on it for a number of different life functions. Although we know much about how marine mammals interact acoustically with their environment, we know far less about how the more numerous fish and invertebrate species perceive and generate sound. Shallow-water coral reefs have unique acoustic signatures (Bertucci et al. 2015), and these signatures are utilized by a variety of marine animals in selecting an appropriate habitat or substrate for settlement (Parmentier et al. 2015). It is currently unknown whether deep-sea, cold-water coral reefs also have unique acoustic soundscapes.

Examination of the soundscape in its entirety can be an indicator of habitat function or overall ecosystem quality and health. Indicators of habitat quality and biodiversity that were developed for terrestrial applications are now being applied to marine habitats and soundscapes (Staaterman et al. 2014, Denes et al. 2014, Parks et al. 2014). Rapid acoustic analysis of a habitat's soundscape through the calculated acoustic complexity index (ACI), acoustic entropy index, or acoustic dissimilarity index (diversity) is providing a quantitative way to assess biodiversity and compare/contrast soundscapes of different terrestrial and marine areas (Sueur et al, 2008, Staaterman et al. 2014). Sound travels further underwater than it does in air, so distant sound sources that overlap in frequency with local or regional signals often complicate interpretation of the calculated indices and limit the use of filtering techniques. The soundscape ecology effort executed under the Deep SEARCH project developed a multidimensional soundscape code framework that we applied to a comparison of four deep-sea and one shallow reef soundscape.

4.5.2 Methods

The overall goal of the Deep SEARCH soundscape ecology effort was to develop and apply a quantitative method of analyzing, visualizing, and comparing underwater acoustic environments across habitat types with the objectives of:

1. Determining the optimal suite of metrics that comprehensively capture the salient properties of a marine soundscape, and
2. Comparing/contrasting soundscapes from five locations corresponding to habitats varying in depth and coral content

The details of the multidimensional soundscape code developed as part of this project was published as Open Access in July 2021 in a special issue of Frontiers in Marine Science focusing on underwater soundscapes (Wilford et al. 2021). The abstract is provided below as a summary of this work (**Figure 4-102**).

Quantitative Soundscape Analysis to Understand Multidimensional Features

Dylan Charles Wilford[1,2,3], Jennifer L. Miksis-Olds[2], S. Bruce Martin[4], Daniel R. Howard[2,5], Kim Lowell[3], Anthony P. Lyons[2,3] and Michael James Smith[3]*

[1] School of Marine Science and Ocean Engineering, University of New Hampshire, Durham, NH, United States, [2] Center for Acoustics Research and Education, Institute for the Study of Earth, Oceans, and Space, University of New Hampshire, Durham, NH, United States, [3] Center for Coastal and Ocean Mapping, University of New Hampshire, Durham, CA, United States, [4] JASCO Applied Sciences (Canada) Ltd., Victoria, BC, Canada, [5] Department of Biological Sciences, College of Life Sciences and Agriculture, University of New Hampshire, Durham, NH, United States

A methodology for the analysis of soundscapes was developed in an attempt to facilitate efficient and accurate soundscape comparisons across time and space. The methodology consists of a collection of traditional soundscape metrics, statistical measures, and acoustic indices that were selected to quantify several salient properties of marine soundscapes: amplitude, impulsiveness, periodicity, and uniformity. The metrics were calculated over approximately 30 h of semi-continuous passive acoustic data gathered in seven unique acoustic environments. The resultant metric values were compared to *a priori* descriptions and cross-examined statistically to determine which combination most effectively captured the characteristics of the representative soundscapes. The best measures of amplitude, impulsiveness, periodicity, and uniformity were determined to be SPLrms and SPLpk for amplitude, kurtosis for impulsiveness, an autocorrelation based metric for periodicity, and the Dissimilarity index for uniformity. The metrics were combined to form the proposed "Soundscape Code," which allows for rapid multidimensional and direct comparisons of salient soundscape properties across time and space. This initial characterization will aid in directing further analyses and guiding subsequent assessments to understand soundscape dynamics.

Keywords: soundscape, kurtosis, Dissimilarity Index, ocean sound, metrics, marine acoustics

Figure 4-102. Title and abstract of Wilford et al (2021)

We then applied the Wilford et al (2021) soundscape code (SSC) to a shallow coral reef (GBR), two deep cold-water reefs (Savannah Deep [SAV] and Richardson Hills [RH]), and two deep sandy bottom marine environments (Wilmington [WIL] and Blake Escarpment [BLE]). WIL, SAV, BLE, and RH are sites along the OCS being studied in the ADEON and Deep SEARCH projects (**Figure 4-103** and **Figure 4-104**). GBR is the designation for Wheeler Reef, a shallow tropical reef that is part of the GBR chain.

GBR as a whole is one of the largest reef systems of the world, supports billions of dollars of annual revenue for Australia, and provides a range of ecosystem goods and services (McCook et al. 2010, Stoeckl et al. 2011). The five selected sites differ in habitat type, depth, and proximity to the US mid-Atlantic coast. Comparing the soundscapes at five locations using the SSC methodology provided a rapid assessment of the soundscapes highlighting salient differences in acoustic properties, which are connected to both the function of the environments and transient sound sources.

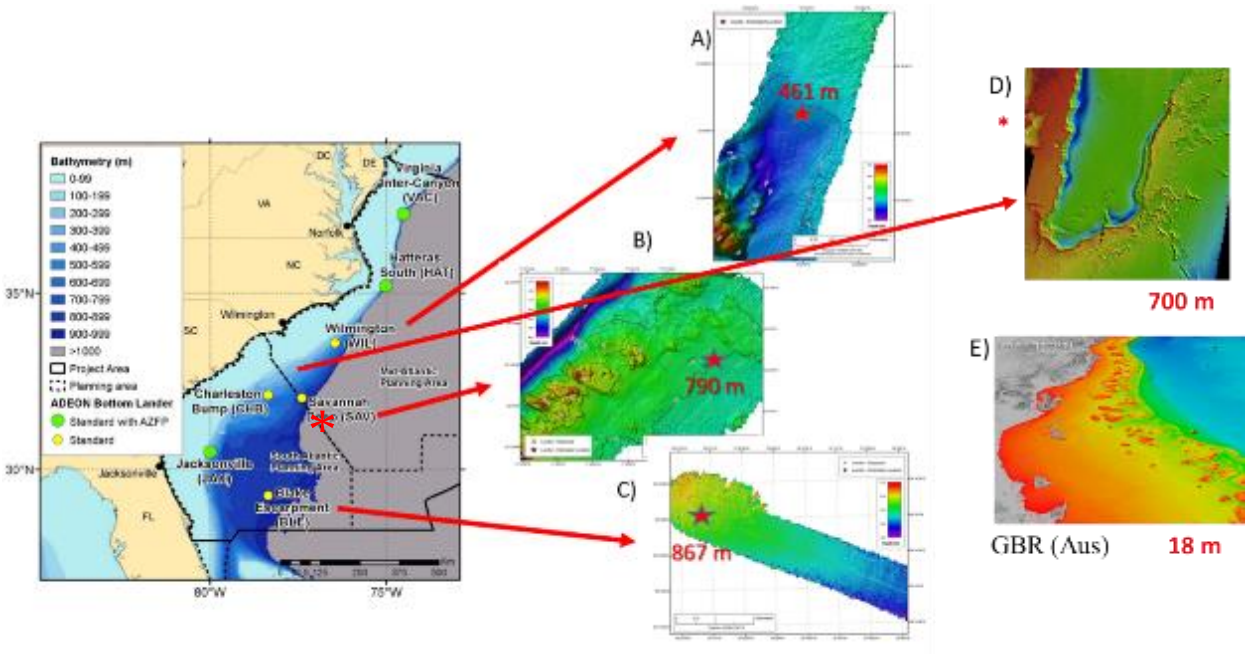

Figure 4-103. Site locations, depths, and bathymetry for Soundscape Code locations
Site locations, depths, and bathymetry for (A) WIL, (B) SAV, and (C) BLE. D) RH location in close proximity to the SAV lander, and E) is the GBR location depth and bathymetry off Australia but is not indicated on this map.

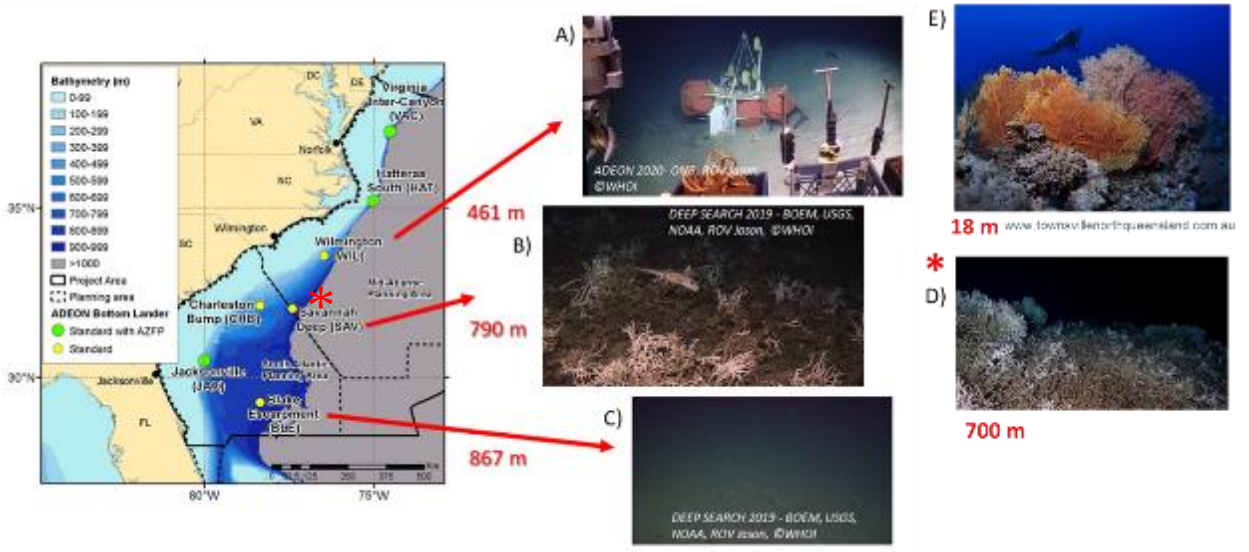

Figure 4-104. Bottom habitat images for each of the five soundscape code locations
Bottom habitat images for each of the five locations: A) WIL, B) SAV, C) BLE, D) RH, and E) GBR.

We chose a winter period consisting of the months December through February 2017 for analysis of the WIL, SAV, and BLE sites. This 3-month period consists of about 5,960 minutes of passive acoustic data per site sampled at 375 kHz. We recorded data from the RH site on an icListen Smart Hydrophone (Ocean Sonics, Truro Heights, NS, Canada) between 14 April 2019 and 20 June 2019 and consist of about 3,220 minutes of passive acoustic data sampled at 126 kHz. We recorded data from the GBR site on

an AMAR G3 recorder (JASCO Applied Sciences, Dartmouth, NS, Canada) between 27 April 2013 and 31 May 2013 and consists of about 6,480 minutes of passive acoustic data. (**Table 4-27**).

Table 4-27. Long-term dataset information and data collection parameters

Data set	Ecosystem Type	Latitude (° North)	Longitude (° East)	Depth (m)	Sample Rate (kHz)	Duration (min)	Duty cycle (min)
Wilmington (WIL)	Deep, Sandy	33.6	-76.4	461	375	5,964	1/20
Savannah Deep (SAV)	Deep, Coral	32	-77.3	790	375	5,966	1/20
Blake Escarpment (BLE)	Deep, Sandy	29.2	-78.3	872	375	5,966	1/20
Richardson Hills (RH)	Deep, Coral	31.5	-77.2	700	128	3,222	1/30
Great Barrier Reef (GBR)	Shallow, Coral	-18.8	147.5	18	375	6,486	1/20

We calculated 1-minute SSC metrics over the acoustic recordings for amplitude, impulsiveness, periodicity, and uniformity. We reported SSC metrics by the median (med) and central 95th percentage (C95) of the 1-minute SSC metrics of SPL for amplitude, kurtosis for impulsiveness, an autocorrelation-based metric for periodicity, and the acoustic dissimilarity index (D-Index) for uniformity. A summary for the calculation of each metric is provided below from Wilford et al. (2021).

- Amplitude: SPL root-mean-square (SPL_{rms}) (Eq. 8)

$$SPL_{rms} = 10\,log_{10}\left(\sqrt{\frac{1}{T}\int_0^T \frac{p^2(t)}{p_{ref}^2}dt}\right) \qquad \text{(Equation 8)}$$

where P_{ref} is reference pressure, $p(t)$ is the instantaneous pressure at time (t), and T is the analysis window duration.

- Amplitude: SPL peak (SPL_{pk}) (Eq. 9)

$$SPL_{pk} = 10\,log_{10}\left(\frac{p_{max}^2(t)}{p_{ref}^2}\right) \qquad \text{(Equation 9)}$$

- Impulsiveness: kurtosis defined below for the pressure time series $p(t)$ as (Eq. 10–12).

$$Kurtosis = \frac{\mu_4}{\mu_2^2} \qquad \text{(Equation 10)}$$

$$\mu_2 = \frac{1}{t_2 - t_1}\int_{t_1}^{t_2}[\,p(t) - \bar{p}\,]^2 \qquad \text{(Equation 11)}$$

$$\mu_4 = \frac{1}{t_2 - t_1}\int_{t_1}^{t_2}[\,p(t) - \bar{p}\,]^4 \qquad \text{(Equation 12)}$$

- Periodicity: We set the threshold for periodicities using autocorrelation, a minimum peak prominence of ρyy (t, t + τ) = 0.5 using the MATLAB function findpeaks, and any autocorrelation coefficient peaks in the 1-min time window above this threshold were counted (ppm). We considered a sum of 420 lags (70%) in the selected autocorrelation metric using a 0.1 sec average.
- Uniformity: Acoustic Dissimilarity Index (D-index). The amplitude envelope is given by the absolute value of the analytic signal ζ(t), which is defined as (Eq. 13):

$$\zeta(t) = p(t) + ip_H(t) \qquad \text{(Equation 13)}$$

where $i = \sqrt{-1}$, and $p_h(t)$ is the Hilbert transform of the real valued signal *p(t)*. Probability mass functions (PMF) give the probability that a discrete, random variable is exactly equal to some value, and the PMF of the amplitude envelope *A(t)* and PMF of the mean spectrum *S(f)* is given by (Eq. 14):

$$A(t) = \frac{|\zeta(t)|}{\sum_{t=1}^{n}|\zeta(t)|} \qquad \text{(Equation 14)}$$

$$S(f) = \frac{|\overline{s(f)}|}{\sum_{t=1}^{n}|\overline{s(f}|} \qquad \text{(Equation 14)}$$

and is used to quantify envelope dissimilarity where $\overline{s(f)}$ is the mean spectrum. Envelope dissimilarity is estimated between two signals by computing the difference between their envelope PMFs (Eq. 15 & 16):

$$D_t = \frac{1}{2}\sum_{t=1}^{n} |\, A_1(t) - A_2(t)| \qquad \text{(Equation 15)}$$

$$D_f = \frac{1}{2}\sum_{t=1}^{n} |S_1(f) - S_2(f)| \qquad \text{(Equation 16)}$$

where *A(t)* is the PMF of the amplitude envelope and S(f) is PMF of the mean spectrum. Dissimilarity Index (D-index) (Eq. 17) is the product of the temporal dissimilarity (D_t) and spectral dissimilarity(D_f):

$$D = D_t \times D_f \qquad \text{(Equation 17)}$$

The D-index is a between-group (β) index originally developed to measure differences between communities. In the context of this study element, the D-index was used to quantify differences in the soundscape across time by calculating it over consecutive acoustic recordings.

We calculated all metrics over five frequency bands: 1) 10–100 Hz (Low), 2) 100–1,000 Hz (Mid), 3) 1–10 kHz (High), 4) 10 kHz and above (Ult-High), and 5) 10 Hz and above (broadband; BB). We chose these frequency bands because the dominant frequencies of many signals can be isolated into a single soundscape code frequency band.

4.5.3 Results

The SSCs (**Figure 4-105**), provide a wealth of information about the soundscapes and produce results that set the stage for subsequent analysis. GBR amplitude metrics are much larger in frequencies over 1 kHz than in frequencies under 1 kHz. The GBR amplitude metrics are also much larger in the Broadband, High, and Ultra-High bands than the OCS sites, which suggests GBR is driven by acoustic activity in the High and Ultra-High bands. This differs from what we observed in the OCS sites, which appear to be driven by acoustic activity in the Low, Mid, and High bands. All OCS site Broadband amplitude metric medians are within 3 dB of each other (across site), but nuanced differences in the amplitude metric medians across frequency bands (within site) suggest fundamental soundscape differences. At SAV, WIL, and RH the respective 1-month SSC SPL_{rms} medians in the Low, Mid, and High bands are within 3 dB of each other and are between 4 dB and 7 dB larger than median SPL_{rms} values in the Ultra-High band.

At BLE, the 1-month SSC Low band amplitude metrics (both SPL_{rms} and SPL_{pk}) are substantially larger than the Mid, High, and Ultra-High bands, which are all within 4 dB of each other. The 1-month GBR SSC reports the smallest variability of amplitude metrics in almost all frequency bands, and RH reports the largest variability of amplitude metrics in all frequency bands. Variability of BLE, SAV, and WIL amplitude metrics was considerably different across frequency band and site, with an interesting similarity between GBR and BLE, SAV, and WIL. In the Ultra-High band, 1-month SSCs corresponding to GBR, BLE, SAV, and WIL all report SPL_{rms} variability within 2 dB of each other (across site), although the variability of the SPL_{pk} metric indicates there are substantial differences in the maximum sound levels that occur among these sites, especially in the Ultra-High band.

BLE	BB		Low		Mid		High		Ult-High	
	med	C95	med	C95	med	C95	med	C95	med	C95
Amplitude	103	16	101	17	92	18	93	23	89	7
	118	26	114	18	107	21	108	27	106	34
Impulsiveness	3	14	3	3	3	6	3	17	3	875
Uniformity	0.015	0.045	0.023	0.03	0.018	0.046	0.012	0.016	0.013	0.038
Periodicity	0	3	0	3	0	12	0	1	0	2

SAV	BB		Low		Mid		High		Ult-High	
	med	C95	med	C95	med	C95	med	C95	med	C95
Amplitude	102	24	94	30	97	24	97	23	90	6
	118	26	109	34	111	27	112	23	108	21
Impulsiveness	3	17	3	20	3	25	3	1	3	5
Uniformity	0.016	0.055	0.028	0.078	0.017	0.094	0.012	0.018	0.012	0.029
Periodicity	0	16	0	15	0	21	0	0	0	1

WIL	BB		Low		Mid		High		Ult-High	
	med	C95	med	C95	med	C95	med	C95	med	C95
Amplitude	103	18	98	23	96	20	98	19	92	8
	120	25	112	24	110	21	113	19	113	30
Impulsiveness	3	10	3	4	3	4	3	2	3	366
Uniformity	0.015	0.046	0.03	0.053	0.014	0.054	0.012	0.012	0.013	0.028
Periodicity	0	9	0	9	0	7	0	0	0	1

RH	BB		Low		Mid		High		Ult-High	
	med	C95	med	C95	med	C95	med	C95	med	C95
Amplitude	100	32	94	34	94	26	94	27	87	14
	118	39	110	41	111	36	111	36	108	38
Impulsiveness	3	964	3	153	3	188	3	506	3	1546
Uniformity	0.015	0.078	0.025	0.091	0.015	0.095	0.011	0.034	0.012	0.044
Periodicity	0	5	0	5	0	11	0	3	0	2

GBR	BB		Low		Mid		High		Ult-High	
	med	C95	med	C95	med	C95	med	C95	med	C95
Amplitude	116	6	73	6	84	5	107	6	115	7
	160	12	98	16	118	16	146	9	159	13
Impulsiveness	585	2532	21	217	102	1307	334	1168	585	2532
Uniformity	0.017	0.003	0.015	0.018	0.014	0.005	0.017	0.003	0.016	0.003
Periodicity	0	1	0	2	0	2	0	1	0	1

RANGE	BB		Low		Mid		High		Ult-High	
	min	max	min	max	min	max	min	max	min	max
Amplitude	100	116	73	101	84	97	93	107	87	115
	118	160	98	114	107	118	108	146	106	159
Impulsiveness	3	585	3	21	3	102	3	334	3	585
Uniformity	0.015	0.017	0.015	0.03	0.014	0.018	0.011	0.017	0.012	0.016
Periodicity	0	0	0	0	0	0	0	0	0	0

Figure 4-105. One-month soundscape codes for deep/shallow, coral/sandy bottom sites
The ranges reported in the lower right panel indicate the range of 1-month SSC medians. The total range of the SSC medians and C95s was divided into quartiles, and the cell colors correspond to which quartile the value falls into from low to high: blue, green, yellow, red. This figure follows the format of Figure 11 in Wilford et al (2021).

GBR is also the most impulsive site, which is identified by the largest impulsiveness metric medians and variability. The remaining sites all report identical impulsiveness metric medians, so we used the variability to assess soundscape impulsiveness. RH is the second most impulsive site and does not surpass GBR. WIL and BLE that report large (kurtosis > 350) impulsiveness values in the Ultra-High band. This

suggests that BLE and WIL were being influenced by some impulsive acoustic activity in the Ultra-High bands, while SAV appears to be influenced by broadband transient acoustic activity. The Broadband kurtosis variability at SAV is the largest of these three sites, followed by BLE.

The dominant acoustic activity at GBR was not periodic in nature, as the periodicity values for GBR are the lowest of all the sites. Periodic signals appear to be well represented in the OCS sites, as all the sites report considerable variability in periodicity metric values in a variety of frequency bands. At SAV, this trend is most obvious, and the variability of periodicity metric values in the Broadband, Low, and Mid bands is the highest out of all the sites. The 1-month periodicity metric ranges suggest some periodic sound component is present and influential at SAV and WIL, and that in general that periodic signals influence the soundscapes of the OCS sites. The SSCs also suggest that among the OCS sites, there is a disparity in the content of periodic signals. The deep-sea coral sites at SAV and RH are the most periodic of the five sites, followed by WIL, BLE, and GBR.

The median values of the uniformity D-index at GBR reported that the minute-to-minute changes in acoustic activity are greatest at this location in the Broadband, High, and Ultra-High frequency bands. However, the C95 of the D-index values at GBR are substantially lower than the other sites. Instead of a conflicting assessment, the reality is that the median and the C95 of the D-index are capturing and reporting different aspects of what has been defined in this project as acoustic uniformity. The relatively small C95 of almost all metrics at GBR describe the low variability of the soundscape, while the median D-index values appear to describe the chaotic nature of the acoustic activity in frequencies above 1 kHz.

While the minute-to-minute changes at GBR are greater than the other sites in the Broadband, High, and Ultra-High bands, the consistency with which these changes occur make the site acoustically uniform. RH reports the largest ranges in the D-index but also the smallest medians. This suggests that at RH, there are more transient events that shift the D-index to values higher than the other sites, but not enough to result in a larger median. SAV D-index ranges are the second largest behind RH, and while the median D-index values at SAV are never the largest among the sites, they come close (within D = .002), and no other site produces a combination of high D-index medians and C95s like SAV in the Broadband, Low, and Mid bands.

The broadband D-index medians and ranges suggest WIL and BLE are the most uniform behind GBR. However, WIL reports the highest median of the five sites in the Low band along with low-moderate variability (0.056), and BLE reports the highest median in the Mid band also accompanied by low-moderate variability (0.046). BLE also reports the second highest D-index C95 in the Ultra-High band (0.038). D-index results for BLE, SAV, and WIL are similar, but there are nuanced differences in where the dynamic acoustic activity occurs in frequency space, which suggests differences in respective soundscape.

In summary, the tropical, shallow GBR soundscape generated a remarkably different SSC from the other sites in terms of all soundscape code properties. The GBR soundscape is far more consistent than the OCS sites, which is most clearly reflected in the narrow range of the SSC metrics calculated over the 1-month analysis period. The high median amplitude, impulsiveness, and uniformity metric values in the High and Ultra-High bands suggest that GBR is dominated by acoustic activity in the higher frequencies (> 1 kHz). In comparison, SSCs corresponding to SAV, WIL, and BLE suggest that dominant acoustic activity is in the mostly lower frequencies (Low, Mid, and High bands), with a nuanced OCS SSC comparison suggesting BLE is dominated by activity in the Low band. RH is intermediate in its characteristics between GBR and the other OCS sites. Large impulsiveness ranges in all frequency bands, and large amplitude ranges in frequencies over 1 kHz suggest RH is more similar to GBR, but large periodicity and uniformity metric ranges, and large amplitude metric medians in frequencies under 1 kHz suggest RH is more like the OCS soundscapes. Periodicity appears to be a distinguishing feature of the

OCS sites, and a disparity among the OCS sites in terms of periodicity suggests some fundamental difference in the respective soundscapes.

4.5.4 Discussion

The most obvious differences in respective SSCs group all the deep-ocean soundscapes in one group and the shallow, tropical reef soundscape in another. The SSC features that distinguish these two groups are the range of all SSC metrics, impulsiveness values, periodicity values, and which frequency bands the largest amplitude metric median and range occur in. The low variability of the biological signals of GBR produced SSC metric ranges in amplitude, periodicity, and uniformity that were very small compared to the OCS sites, with kurtosis the only exception. The impulsiveness of the shallow, tropical coral reef environment, most likely driven by snapping shrimp, was the highest of all the sites. RH also exhibited impulsive tendencies, but in a much-reduced manner relative to GBR. The other OCS soundscapes (BLE, SAV, and WIL) also indicated some influence by impulsive signals, but in mostly solitary frequency bands (WIL & BLE), or in a magnitude so small that it suggests only transient acoustic activity (SAV).

The SSCs of the OCS sites suggest the soundscapes may have unique acoustic signatures or properties. Periodic signals were well represented in the OCS sites, with SAV reporting the most substantial presence of these types of signals. The frequency band in which these metrics peaked also indicated a nuanced difference between the shallow and OCS sites, especially in terms of sound amplitude. At the shallow-coral environment, the maximum sound amplitude occurred in frequencies above 1 kHz, while at the OCS sites the maximum amplitudes occurred in frequencies below 1 kHz. Uniformity as indicated by the D-index was difficult to interpret and appeared well correlated with other metric values.

SSC results both provide valuable soundscape information and highlight areas that subsequent analysis should explore to better understand the soundscape dynamics of the five sites. Determining the sound sources responsible for the elevated periodicity metrics in the OCS sites would help to understand the deep-sea environments and could illuminate connections between the OCS sites across bottom type. It would also be beneficial to explore what is driving the RH impulsiveness values, as a distinguishing feature of the GBR soundscape is also the large impulsiveness values. Determining what is driving sound levels in all frequency bands at the deep-ocean sites would also help to understand if dominant acoustic activity of the deep-ocean sites is different across bottom types, or if there is a connection between increased sound amplitude and habitat quality/bottom type. The uniformity metric suggested a clear distinction between GBR and the OCS sites and exploring the driving sources for the uniformity metric would help to understand what has impacts on the variability of the OCS soundscapes across deep-sea bottom type.

4.6 Environmental DNA Analysis of Deep-Sea Habitats

Section Authors: Aaron Aunins, Cheryl Morrison

4.6.1 Introduction

Environmental DNA (eDNA) is DNA extracted from bulk environmental samples such as water without first isolating specific target organisms or their parts (Turner et al. 2014). In marine environments, there are multiple sources of eDNA. Larger fauna such as fish and marine mammals release sloughed cells and secrete wastes containing DNA, invertebrates such as corals secrete mucus and metabolic wastes into the surrounding water that may contain DNA, and whole live and dead organisms such as diatoms and bacteria also serve as sources of DNA. This eDNA can be concentrated from the water using filtration or flocculation and sequenced to see what organisms contributed to the eDNA pool. This use of eDNA to develop community profiles of environments is referred to as biomonitoring (Baird and Hajibabaei 2012).

Approaches for eDNA-based biomonitoring are most commonly performed through eDNA metabarcoding, where a short DNA barcode region is amplified from the eDNA and sequenced on a high-throughput sequencer. The resultant reads are compared to a reference database of barcode sequences using bioinformatics.

The metabarcoding primers can be tuned to be narrowly selective for specific taxa (a group of coral genera at the mitochondrial *mutS* gene), or broadly amplify multiple metazoan groups (fishes, corals, crustaceans) by amplifying a conserved DNA region, such as the nuclear 18S rRNA gene. Less common is shotgun metagenomic sequencing, in which no specific sequences are enriched for amplification. Given the lack of PCR amplification in the shotgun metagenomic approach, a major benefit is no issue of primer amplification bias. However, a major drawback (at least presently) is the lack of reference data in genomic databases for eukaryotic taxa, and the cost to obtain sufficient read depth of each sample.

Because eDNA is relatively easy to collect from the deep sea (Niskin bottles on a rosette lowered to depth) vs. traditional deep-sea monitoring methods such as trawling, benthic landers, and ROVs, there have been numerous recent studies assessing the potential for eDNA to serve as a high-throughput and sensitive means for deep-sea biomonitoring (Everett and Park 2018, Djurhuus et al. 2018, Djurhuus et al. 2020, Laroche et al. 2020). Everett and Park (2018) demonstrated that numerous octocoral species identified visually could be simultaneously sequenced from their eDNA in the water at deep-sea sites in the Pacific. Similarly, Laroche et al. (2020) found significant differences in taxon richness among polymetallic nodules, sediments, and water between seamount and plain habitats in the Clarion Clipperton Zone using *cox1* mitochondrial and 18S nuclear metazoan metabarcoding.

When community composition change inferred through eDNA metabarcoding is coupled with environmental data through time, complex community networks can be constructed to examine trophic linkages and seasonal shifts in poorly accessible habitats such as the mesopelagic or deep sea (Djurhuus et al. 2020). While there is no substitute for traditional monitoring, sampling, and exploration of marine habitats, tools such as eDNA analyses offer exciting applications for biomonitoring at a time when environmental degradation is outpacing efforts to survey extant biodiversity. All of these studies show great promise for integration of eDNA biomonitoring into surveys of both novel and well-studied marine habitats.

Most eDNA metabarcoding studies to date of deep-sea habitats have focused on particular taxonomic groups such as corals (Everett and Park 20187), fishes (McClenaghan et al. 2020), or eDNA within sediments (Cowart et al. 2020, Brandt et al. 2020). However, the broader metazoan communities characterized by eDNA in near-bottom water in a biomonitoring framework are beginning to receive more attention (Laroche et al. 2020, Brandt et al. 2020), yet remain poorly described. Our main objectives were to:

- Assess variation of metazoans and micro-eukaryotes among deep-sea cold-seep, CWC, and canyon habitats using metabarcoding of eDNA isolated from near-bottom water collected by ROV mounted Niskin bottles
- Identify taxa driving among community differences
- Evaluate the impact of a pre-filtering step and different volumes of water filtered on the community recovered

4.6.2 Methods

4.6.2.1 Study Area

Environmental DNA sequencing results were generated from samples from eight ROV dives and are thus the focus of this analysis (**Figure 4-106**). We generalized habitat types into six major categories including

deep cold seep, shallow cold seep, coral, scarp, and sediment at 1,000 and 2,600 m (**Table 4-28**). While we refer here to habitats called "sediment," it is important to note these samples were water collected above sediments and *not* DNA extracted from actual sediment samples. Details regarding the characteristics of each dive are in **Table 4-28**.

Table 4-28. Metadata for dives where bottom water was collected for eDNA extraction

Dive	Site	Depth (m)	Habitat Type	Habitat characteristics
RB1903-J2-1128	Richardson Hills	731	Coral	Lophelia mound
RB1903-J2-1130	Savannah Bank	516	Coral	Coral rubble with a few live stony corals
RB1903-J2-1131	Blake Deep	1,318	Scarp	Coral ledge
RB1903-J2-1133	Pea Island Seep	298	Shallow cold seep	White bacterial mats
RB1903-J2-1134	Kitty Hawk Seep	274	Shallow cold seep	Bacterial mats and bubbles
RB1903-J2-1135	Cape Lookout	948	Sediment 1000*	Expansive flat sediment
RB1903-J2-1136	Blake Ridge Seep	2,164	Deep cold seep	Live mussel bed adjacent to hydrate mound
RB1903-J2-1137	Cape Fear Seep	2,571	Sediment 2600*	Expansive flat sediment, not near seep fauna

NOTE: *denotes water sampled above a sediment bottom habitat, *not* DNA from actual sediments.

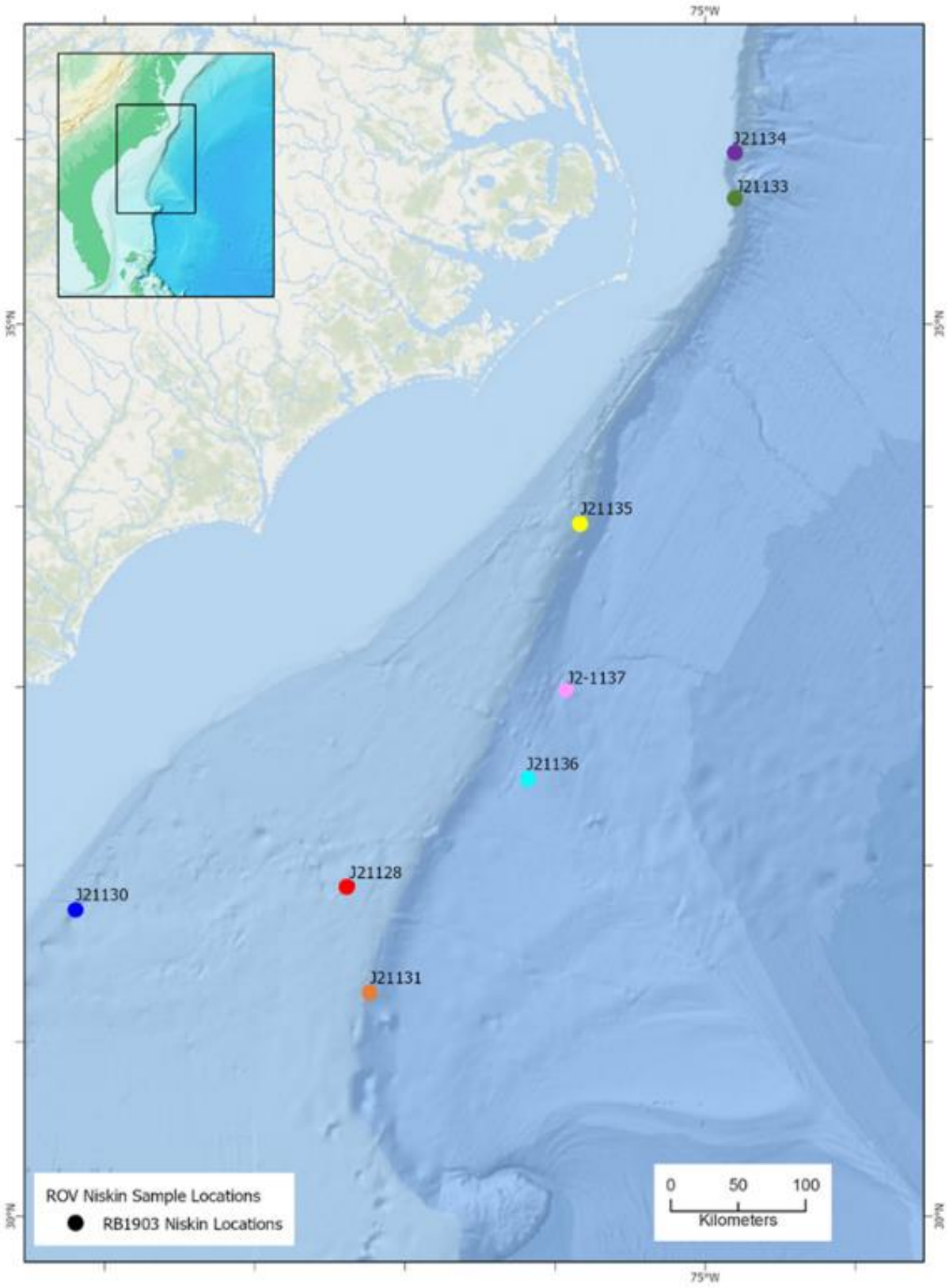

Figure 4-106. Map of the dive sites from cruise RB1903 where bottom water was collected
Dots indicate dive locations along with the abbreviated name.

4.6.2.2 eDNA Sample Collection

We utilized two 12-L Teflon-lined Niskin bottles (named Darya and Sedna) for collecting bottom water samples (General Oceanics, Miami, FL). Before the first deployment and prior to each dive, we filled each Niskin bottle with 12 L of freshly made 10% bleach and soaked between 30–60 minutes to denature any residual seawater derived eDNA. We rinsed each bottle two times from a deck hose utilizing the ship's freshwater supply by completely filling the bottle, then releasing the water from the bottom. A final spray rinse using the hose followed the two fill and release rinses.

We mounted the bottles next to each other to the bottom frame of *Jason* in a bracket holding the bottles at an angle to reduce sediment retention such that for each Niskin one opening was 15 cm off the seafloor and the other was 47 cm off the seafloor (**Figure 4-107).** We configured the triggering mechanism to be fired remotely by the ROV. In most cases, the bottles were closed within 2 hours of the end of the dive at the bottom to minimize the time the captured water spent in the bottles. The habitat type chosen for closure of the Niskin bottles is listed in (**Table 4-28**).

Figure 4-107. Mounting and orientation of the Niskin bottles on *Jason* for collections
Collection of deep-sea bottom water. Niskin bottles on the side of the ROV were not used for eDNA collection, and openings of the two eDNA bottles are visible on the bottom center left. Photo: C. Kellogg.

Once the ROV was secured back on deck, we detached the bottles from the ROV and drained them within 15–35 minutes. We collected subsamples of 1 L of water with gloved hands from each bottle into 2-L Whirl-Pak bags from the Niskin bottle spigot. After collection of the 1 L subsamples, we attached a section of silicon tubing to the spigot and dispensed the remainder of water into two separate 20 L bleach-sterilized Nalgene carboys. Prior to use, we filled the carboys with 10 L of 10% bleach and soaked them

for 30 min, then rinsed three times with shipboard freshwater. Once each carboy was filled to 10 L with Niskin water as determined by a mark on their sides, we placed all Whirl-pak and carboy samples into a 4°C walk-in refrigerator until they could be processed. Prior to deployment on the first day of the cruise, and after the final dive on the last day of the cruise, we filled each bleached and rinsed Niskin with 12 L of Milli-Q deionized water brought in a bleach-sterilized carboy from an onshore lab. We then collected this deionized water as above to serve as pre- and post-cruise negative controls.

4.6.2.3 Water Filtering

We processed water from each Niskin bottle to obtain 1 L filtered through a 0.2 µM PES Sterivex filter capsule, 10 L through a 0.8 µM cellulose acetate prefilter. The 10 L of prefiltered water was subsequently filtered through a 0.2-µM PES Sterivex filter capsule (**Figure 4-108**). We performed this processing on water from each Niskin for a total of three samples per Niskin bottle. The six samples among the two bottles at each site served as replicates.

Figure 4-108. Laboratory setup for water filtration of 10 L seawater from Niskin bottles
Filtration through the clear acrylic prefilter, then through a terminal 10-L Sterivex filter plumbed after the prefilter. Photo: C. Kellogg.

We individually filtered the 1-L samples within the Whirl-pak bags through 0.2-µM PES Sterivex filter capsules (one Sterivex per Whirl-pak). We used new vinyl tubing for each 1-L sample, along with a new barbed fitting to attach the Sterivex to the tubing. We used a peristaltic pump to draw the water out of the Whirl-Pak and through the Sterivex filter. We used gloved hands to handle the filters and tubing. To measure the volume filtered, we directed the outlet of the Sterivex into a 1,000 mL graduated cylinder. When the target volume was reached, we lifted the tubing out of the sample bag and the peristaltic pump

was allowed to push air through the filter capsule to empty any residual water. We capped each end of the Sterivex with a new Luer fitting and placed it in a labeled Whirl-pak bag. The filter was immediately placed into a -20°C walk-in freezer. Each 1-L filtering event was accomplished within approximately 15 minutes. In cases where there was a high particulate load in the samples, 500 mL was filtered through two separate Sterivex filters per sample.

Filtering of the 10 L samples utilized different equipment than for the 1-L samples. A Geotech 142-mm, in-line acrylic filter holder (Model 83150004) was disassembled and immersed in a 10% bleach solution for 1 minute. Using gloved hands and the ship's fresh water supply, we thoroughly rinsed the filter holders, followed that by a final rinse in Milli-Q deionized water, and reassembled them utilizing an autoclaved cellulose acetate 0.8-µM filter (Advantec C080A142C) inserted into the holder. Once reassembled, we attached a section of bleach sanitized silicone tubing to the inlet of the in-line filter holder, through a peristaltic pump head and into the carboy with the water sample. On the outlet end of the in-line filter holder, we attached a section of bleach-sterilized silicon tubing and connected it to a 0.2-µM PES Sterivex capsule utilizing a new barb fitting.

Because the volume of the water in the carboy was known, the outlet of the Sterivex was allowed to empty directly into a sink. Once 10 L of water (the full volume of water in the carboy) was processed through the Sterivex filter, the in-line filter was disassembled using gloved hands. We used forceps soaked in 10% bleach and rinsed with DNA-free DI water to gently roll the filter up and insert it into a 50-mL conical tube. No preservative was added to the filter. We then placed it into a -20°C freezer. The Sterivex filters through which 10 L was filtered were capped, sealed inside tubes of heatshrink plastic, placed into labeled Whirl-Pak bags and then flash-frozen and stored in liquid nitrogen for the duration of the cruise. In some cases, it was necessary to utilize two prefilters and two Sterivex to obtain the target volume of 10 L through both media. In these cases, we handled the filters in the same manner and placed each into individual conical tubes, though the exact volume filtered through each filter was unknown (approximately 5 L). The time taken to process the 10-L samples ranged between 40 and 85 min.

4.6.2.4 DNA Extraction

We extracted DNA from Sterivex filters utilizing the PowerSterivex DNA kit (Qiagen) following the manufacturer's instructions. One-L Sterivex and 10-L prefilter samples were extracted at the USGS Eastern Ecological Science Center at the Leetown Research Laboratory, Kearneysville, WV, whereas the 10-L Sterivex samples were extracted at the USGS St. Petersburg Coastal and Marine Science Center, St. Petersburg, FL. The prefilters were adapted for use with the Sterivex extraction kit by performing the following steps. We used a sterile scalpel to cut one quarter of the prefilter in a laminar flow hood and sterile plastic dish. We placed this filter piece within a 5-mL screw top plastic vial with a volume similar to that of a Sterivex capsule. These samples were then processed using the PowerSterivex protocol and reagent volumes, except that we performed pipetting by unscrewing the lid of the vial to access the liquid. Extraction blanks for one Sterivex and one prefilter utilizing a new Sterivex and unused prefilter respectively were processed alongside other DNA extractions to assess contamination. DNA extracts were stored at -20°C.

4.6.2.5 Metabarcoding Library Preparation

We used two different primer pairs to assess the metazoan and micro-eukaryotic community composition and diversity among the sites (**Table 4-29**). These included one primer pair targeting the mitochondrial gene *cox1,* and a marker targeting metazoan nuclear 18S rRNA.

To generate libraries compatible with sequencing on the Illumina MiSeq, we followed the Illumina 16S metagenomics sequencing protocol (Illumina 2016) for both primer pairs, where we ordered each primer with the following adapter sequences attached to the 5' end of the primers for the incorporation of

Nextera indices and flowcell adapters (5'–3'): F-TCGTCGGCAGCGTCAGATGTGTATAAGAGACAG R-GTCTCGTGGGCTCGGAGATGTGTATAAGAGACAG (Illumina 2016). The amplicon size listed in **Table 4-29** does not include the length of the primers, or any Illumina sequencing adapters added to the primers for high-throughput sequencing (HTS). Reaction conditions for the *cox1* marker consisted of 1 µL template, 2.5 µL F primer at 1 µM stock concentration, 2.5 µL R primer at 1 µM stock concentration, 6.25 KAPA HiFi in a total volume of 12.25 µL. We set up three replicate PCRs for each individual sample and thermal cycled each as follows: 95°C for 10 min; 16 cycles of 94°C for 10 s, 62°C for 30 s, 68°C for 30 s; then 25 cycles of 94 for 10 s, 46 for 30 s, 68 for 60 s; final extension of 72°C for 10 min; hold at 12°C for inf.

We pooled each set of triplicate PCRs into a composite sample of 36 µL, then we used 25 µL of this composite sample for Ampure cleanup, following Illumina (2016) with no modifications. The 18S reaction conditions were the same, with the exception of the thermal cycling parameters: 95°C for 3 min; 27 cycles of 95°C for 30 s, 63°C for 30 s, 72°C for 30 s; final extension of 72°C for 5 min; hold at 12°C for inf. We performed dual indexing of all amplicons following the Illumina instructions with no changes. We ran each set of amplicons at the USGS-EESC-LSC on separate MiSeq V3 600 cycle cartridges at a concentration of 12 pM (*cox1*) and 15 pM (18S) with 10% PhiX spike-in.

Table 4-29. Gene regions and associated metabarcoding primer pairs utilized

Primer pairs utilized for characterizing eDNA within deep-sea communities.

Gene Region	F and R primer (5'–3' orientation)	Amplicon Size	Reference
Mitochondrial cox1	mlCOIintF: GGWACWGGWTGAACWGTWTAYCCYCC HCO2198: TAAACTTCAGGGTGACCAAAAAATCA	313 bp	Folmer et al. (1994), Leray et al. (2013)
Nuclear 18S rRNA	1391F: GTACACACCGCCCGTC EukBr: TGATCCTTCTGCAGGTTCACCTAC	~120 bp	Amaral-Zettler et al. (2009)

4.6.2.6 Shotgun Metagenomic Library Preparation

We used only the DNA extracted from the 10-L Sterivex samples for shotgun metagenomics. The DNA was shipped on dry ice to a sequencing vendor. The DNA concentrations for the samples were very low, so the two technical replicates (from the two Niskin bottles) were combined for each site and concentrated by evaporation. The samples were run on an Illumina HiSeq 4000 without amplification.

4.6.2.7 Amplicon Dataset Bioinformatics

We demultiplexed samples by Illumina software using default settings, output the data to Illumina's cloud storage system BaseSpace, and downloaded it. We looked for any residual adapter sequences and removed such using the bbduk.sh script of the BBMap software (Bushnell et al. 2017). Forward and reverse primers were also removed from all samples using bbduk.sh.

We imported all amplicon datasets into Qiime2 for analyses and visualization (Bolyen et al. 2019). We performed read pair merging and de-noising into amplicon sequence variants (ASVs; Callahan et al. 2016) using the 'qiime dada2 denoise-paired' script. We aligned all ASVs with mafft (Katoh et al. 2002) and used it to construct a phylogeny using fasttree2 (Price et al. 2010) with 'qiime phylogeny align-to-tree-mafft-fasttree'.

4.6.2.8 Taxonomic Assignment

Various curated eukaryotic metabarcoding gene reference databases do exist for taxonomic assignment of eukaryotic barcoding gene sequence regions such as Silva 18S (Quast et al. 2013), and Midori *cox1* (Leray et al. 2018). One benefit of these databases is that the curation provides some level of quality control over the taxonomic annotations. However, we chose to utilize the National Center for Biotechnology Information (NCBI) nt database (downloaded in May 2021) for taxonomic assignment of *cox1* and 18S ASVs while acknowledging the potential for some errors in the taxonomic assignments by the sequence authors (Mioduchowska et al. 2018). This is because it is not limited taxonomically, which is an important consideration when sequencing samples from poorly described habitats such as the deep-sea that may contain substantial and novel diversity and non-target reads co-amplified by the markers.

Both the *cox1* and 18S ASVs were locally blasted against the NCBI nt database using blastn and the default output format (Altschul et al. 1990). The blastn output file was imported in MEGAN Community Edition (version 6.20.19) for taxonomic annotation based on the NCBI taxonomy (Huson 2016). Settings for the least common ancestor (LCA) parameters in MEGAN for 18S were Min score: 100; Max expected: 0.01; Min percent identity: 85.0; Top percent: 10.0; Min support percent: 0.01; Min support: 1.0; Use Min complexity filter: 0; LCA algorithm: weighted; Percent to cover: 80.0; Assignment mode: readcount.

The MEGAN settings for *cox1* were the same except that we adjusted the Min score to 450. We selected all nodes with a taxonomy assigned in MEGAN and then we exported the taxonomy in the format Kingdom;Phylum;Class;Order;Family;Genus;Species (KPCOFGS), including ASVs, with no taxonomic assignment ('Unassigned') or no hit ('No_hit') to the nt database. We then imported these taxonomies into Qiime2 for additional analysis using the 'qiime tools import –type 'FeatureData[Taxonomy]' command. Due to constant revisions of the taxonomy within multiple eukaryotic lineages, exported levels of taxonomy often did not match 'KPCOFGS', though there were usually still seven levels of taxonomy for these taxa.

4.6.2.9 Diversity Analyses and Among Sample Comparisons

The ASVs assigned to the following taxa were considered contaminants (Djurhuus et al. 2018) and filtered from each dataset based on a name search of taxonomic assignments from each dataset prior to additional analysis: cox1 – Insecta, Rodentia, Primates, Bacteria, Archaea; 18S – Bacteria, Insecta, Archaea. In addition, any ASVs present within extraction or field controls and deep-sea Niskin samples had their counts adjusted as follows: if the count was greater in the control, we adjusted the number of reads in the sample to zero. Similarly, if the number of reads was less in the control, the control count was subtracted from the field sample.

We performed rarefaction analyses in Qiime2 to assess whether the biological diversity was sampled sufficiently using 'qiime diversity alpha-rarefaction'. To enable comparisons of diversity across samples with different numbers of reads within the *cox1* and 18S marker datasets, we rarefied reads to a common depth. Depending on the comparison among samples being made, we changed the rarefaction depth and we noted where this was performed.

To assess whether diversity and evenness of taxa was different between the 1-L Sterivex verus the 10-L prefilter, we calculated Shannon's index (Shannon and Weaver 1949) and Pielou's evenness (Pielou 1966) and compared them by pooling all samples across sites (all PF vs. all Sterivex) using the 'qiime diversity core-metrics-phylogenetic' plugin. Statistical significance between pooled Sterivex vs. prefilter was assessed using a Kruskal-Wallis test implemented in Qiime2.

We generated PCoA plots in Qiime for all samples at each metabarcoding marker using Bray-Curtis indices after rarefying to a common depth to visualize clustering among habitat types.

4.6.2.10 Analysis of Differentially Abundant Taxa

We made pairwise comparisons between a subset of sites to investigate what taxa are more highly represented in a specific habitat using Analysis of Composition of Microbiomes (ANCOM; Mandal et al. 2015) implemented in Qiime2. ANCOM can be used to draw inferences regarding taxa abundance at the ecosystem level using the specimen level relative abundance data (Mandal et al. 2015). Comparisons for ANCOM included: "Deep cold seep (1136)" vs. "Shallow cold seeps (1133 and 1134 pooled)" and "Coral (1128 and 1130 pooled)" vs. "Scarp (1131)".

We also ran analyses of similarity percentages (SIMPER; Clarke 1993) run in R with the 'simper' function within the VEGAN package to identify ASVs with higher representation in either habitat type (R core team 2021; Oksanen et al. 2020). Briefly SIMPER performs pairwise comparisons of groups and finds the contribution of each unit (in this case, ASVs) to the average between-group Bray-Curtis dissimilarity (Oksanen et al. 2021). We recorded the taxa accounting up to ~70% of the variation among habitats. We implemented 1,000 permutations to evaluate whether species contributing to the between-group dissimilarity were significant.

4.6.2.11 Taxonomic Representation

We exported ASV tables and taxonomies from Qiime2 for visualization in the R package Phyloseq (McMurdie and Holmes 2013). We generated barplots by collapsing the data to a common taxonomic level using the 'tax_glom' function. To get an overview of general diversity of taxa among habitats, we chose the top 20 most relative abundant taxa for visualization from each sample to allow them to fit within the plot. These were pooled as "Coral and Scarp", "Deep and Shallow Seeps", and "Sediments 1,000 and 2,600 m". For the *cox1* data only, we generated plots without inclusion of unassigned taxa, as the number of unassigned taxa greatly outnumbered annotated taxa hindering their observation. We did not rarefy ASV tables for these visualizations.

Focusing on the top 20 taxa may help identify major taxonomic groups among habitats, but obscures more fine-scale patterns in representation of taxa, such as scleractinians and mollusks, of particular interest to Deep SEARCH scientists. Therefore, we investigated the relative abundance of taxa assigned to Mollusca, Arthropoda, Cnidaria, and Annelida at the deep and shallow seep sites at the 18S marker as an example of how our data can be mined for specific animals of interest. We chose these sites because of their apparent differentiation, and the 18S marker because of the greater number of assigned taxa vs. the *cox1* marker (see **Results** section).

4.6.3 Results

4.6.3.1 General Results

We collected paired samples from replicate Niskin bottles at 7 sites, with the exception of site 1130 where only one Niskin bottle was sampled due to a malfunction with the closing mechanism on Darya (**Table 4-30**). Preliminary screening of the shotgun metagenomic data from the 10 L Sterivex samples indicated that after quality control, 94% of the sequence reads were from the control (deionized water) sample. Only three of the samples (1135, 1136, and 1137) returned any sequences, but in all cases, they were very few and had considerable overlap with the control. No gene-based analysis of this dataset was possible. We made a further attempt to examine metagenome assembled genomes in these samples, however again, there was not sufficient coverage, and results of shotgun metagenomic sequencing are not discussed further.

Table 4-30. Read pairs retained for analysis at the *cox1* and 18S metabarcoding marker

PF refers to samples where 10 L was filtered through the 0.8-micron prefilter, and 1 L refers to 1 L through a 0.2-micron Sterivex. EB denotes extraction blank. Initial refers to the number of primer-trimmed read pairs input into dada2, and final refers to the number of merged read pairs remaining after denoising, contaminant removal, and subtraction of control reads (see main text for additional details).

Name	Dive number	Niskin	*cox1*	-	-	-	18S	-	-	-
-	-	-	1 L initial	1 L final	PF initial	PF final	1 L initial	1 L final	PF initial	PF final
Pre-cruise ctl	NA	Darya	80,163	46,218	218,786	199,009	59,127	52,720	259,701	194,195
“	“	Sedna	86,754	77,085	135,323	106,477	31,107	26,852	96,796	78,252
Richardson Hills	RB1903-J2-1128	Darya	9,5826	87,848	108,412	90,971	224,967	152,545	481,964	381,480
“	“	Sedna	151,798	120,030	144,641	106,988	286,088	193,523	317,145	263,618
Savannah Bank	RB1903-J2-1130	Sedna	142,425	128,988	216,138	198,836	329,570	235,784	600,339	497,209
Blake Deep	RB1903-J2-1131	Darya	121,455	110,577	80,536	72,933	323,677	225,455	240,656	205,486
“	“	Sedna	149,347	136,976	244,166	233,495	267,548	204,033	298,247	241,124
Pea Island	RB1903-J2-1133	Darya	101,592	93,691	142,164	133,347	428,337	381,046	286,895	234,727
“	“	Sedna	183,583	171,723	130,223	121,295	132,117	106,124	272,356	221,482
Kitty Hawk	RB1903-J2-1134	Darya	157,902	145,918	738,137	692,793	311,115	247,157	385,217	321,746
“	“	Sedna	165,542	154,832	192,362	181,699	356,206	276,103	342,183	281,927
Cape Lookout	RB1903-J2-1135	Darya	137,501	128,998	141,793	131,559	273,789	198,979	332,235	271,262
“	“	Sedna	190,811	177,284	186,998	165,965	309,204	235,719	619,844	319,321
Blake Ridge	RB1903-J2-1136	Darya	169,326	160,397	168,273	156,385	267,377	185,979	239,649	190,375
“	“	Sedna	178,301	169,168	174,082	164,804	306,036	238,448	323,969	254,210
Cape Fear	RB1903-J2-1137	Darya	215,629	202,071	133,016	122,235	521,912	424,036	412,491	341,487
“	“	Sedna	192,855	181,944	126,844	118,491	264,124	205,959	301,623	244,411
Post-cruise ctl	NA	NA	183,365	172,499	211,017	197,616	351,553	215,424	165,241	122,243
“	“	NA	66,359	217	15,669	1,882	2,657	880	13,939	10,222
Sterivex EB	-	-	7,364	94	-	-	993	2	-	-
Prefilter EB	-	-	-	-	38,768	334	-	-	2	0
-	-	Avg.	156,926	144,684	195,186	179,453	306,804	234,059	363,654	284,658
-	-	SD	33,813	33,362	155,959	148,075	87,814	80,010	118,486	78,864

We sequenced all prefilter and 1-L Sterivex samples at four metabarcoding markers, though only 18S and *cox1* are discussed here (**Table 4-30**). Results of a microbial 16S, and 16S mitochondrial marker are forthcoming (Aunins et al. *in prep*, 2021). We identified 37,861 18S, and 13,241 *cox1* ASVs, respectively, after denoising and chimera removal in Qiime2 (**Table 4-31**). After filtering for ASVs assigned to taxa we considered contaminants in each dataset (see methods), there were 32,834 18S and 13,217 cox1 ASVs (**Table 4-31**). "Post-filtering" refers to the number of ASVs remaining after removal of contaminant taxa as described above. "Unassigned" refers to an ASV that had a hit to the nt database but did not meet the settings in MEGAN for a putative taxonomic assignment. "No hit" refers to ASVs with no hit to the nt database meeting. All subsequent analyses/discussion consider only the final contaminant filtered datasets (see methods for information regarding contaminant filtering).

Table 4-31. ASVs counted in each metabarcoding set after denoising with dada2.

Set	ASVs	Post-filtering	Unassigned	No_hit
cox1	13,241	13,217	12,235	674
18S	37,861	32,834	7,150	1,174

4.6.3.2 Controls

Nearly all extraction control samples (Sterivex and Prefilter) had positive numbers of reads, which is a common occurrence in studies using general metabarcoding markers that amplify many diverse targets from environmental samples (**Table 4-31**). Of primary concern for the two laboratory extraction controls was evidence of amplification of taxa expected from marine environments, which would suggest cross-contamination of the samples at some stage of laboratory processing (DNA extraction through library construction). In the 18S dataset, n = 4 ASVs (4 Sterivex ASVs among 721 reads) were found in the negative and environmental samples, but no reads were present in the prefilter extraction control.

The highest represented ASV (336 reads) was assigned to Mammalia, and most likely represents human or mouse contamination, as this ASV was poorly represented in the field samples. Subtraction of these contaminant taxa left two reads. In the *cox1* dataset, n = 22 ASVs (12 prefilter ASVs among 337 reads, and 9 Sterivex ASVs among 102 reads) were found in the negative and environmental samples. We were unable to assign most of these ASVs a taxonomy in MEGAN, and the most highly represented ASV in the controls was not present in any environmental sample. Ninety-four reads were left in the 18S Sterivex extraction control. Thus, we concluded contamination from laboratory processing was extremely low and negligible.

In contrast to the lab extraction controls, some of the pre- and post-cruise Niskin controls had read counts approaching those observed in the deep-sea samples. The most parsimonious explanation for this occurrence is due to DNA being introduced into the Niskin bottles through rinsing of the bleach water with a deck hose and shipboard water supply and creating a ship tank metagenomic sample. In most cases, the taxonomic assignment of the ASV present in the controls and field samples was unassigned or mostly present in only the control sample. We performed ordinations of the controls with the field samples, and they did not cluster close together for 18S or *cox1*, further indicating there was no appreciable field contamination through the collection process.

4.6.3.3 Rarefaction

Rarefaction curves appeared to approach an asymptote around 70,000–80,000 reads (**Figure 4-109**), with an outlier sample or two in each that appeared to still be climbing. Thus, since no samples had less reads than this range, analyses rarefying to read counts near that depth should still be representative of the diversity present in most of the samples.

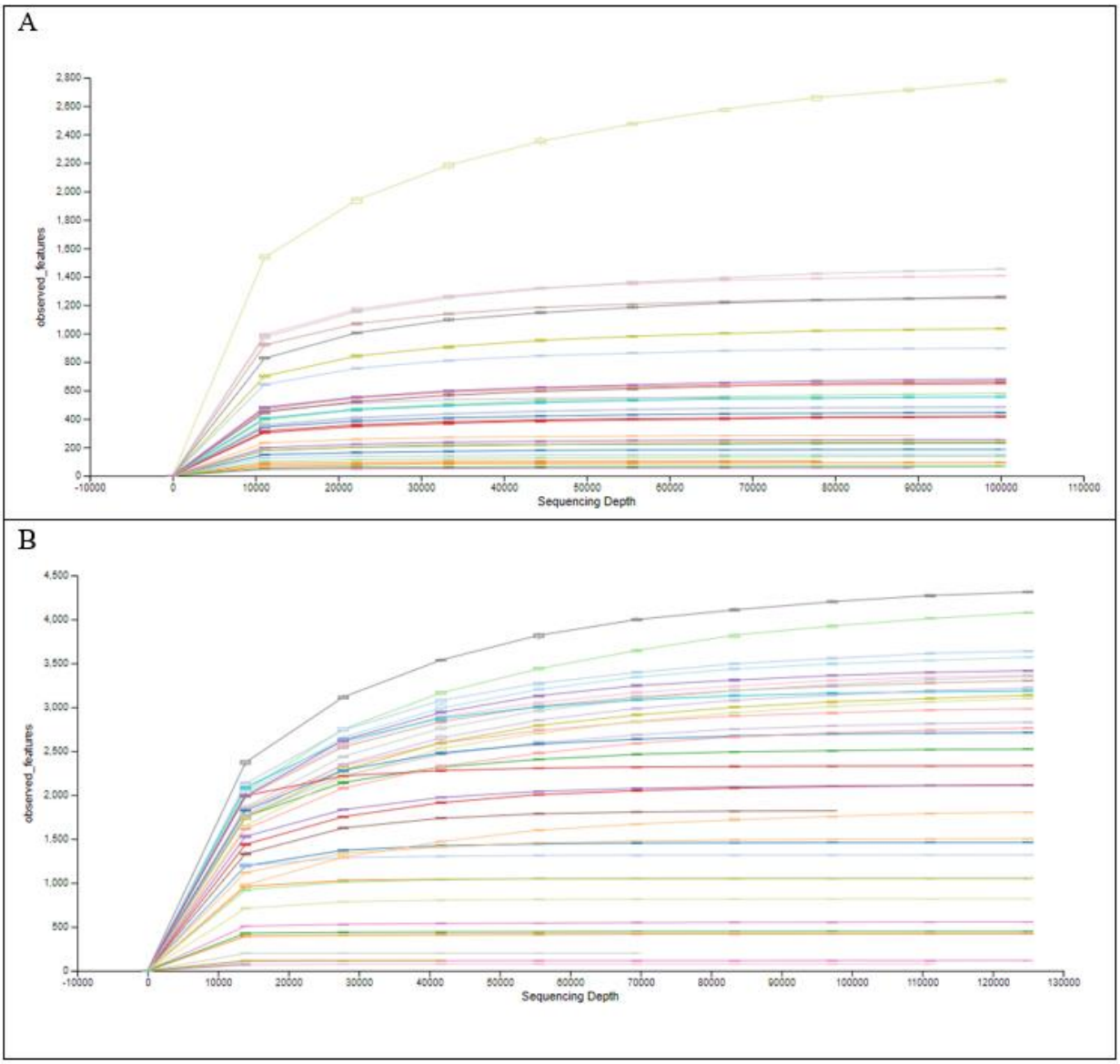

Figure 4-109. Rarefaction curves of all field collected samples in the cox1 (A) and 18S (B) metabarcoding datasets

4.6.3.4 Diversity Among Filter Types

There were no significant differences in richness measured by Shannon (Kruskal-Wallis H = 0.4684, *P* = 0.49) and Pielou's evenness (Kruskal-Wallis H = 0.1552, *P* = 0.69) indices between the prefilter and Sterivex samples each pooled across all sites at the 18S marker (**Figure 4-110**). However, both diversity measures were significantly different between filter types at the *cox1* marker (**Figure 4-111**), with the prefilter samples having greater richness as measured by Shannon (Kruskal-Wallis H = 5.1101, *P* = 0.02) and Pielou's evenness (Kruskal-Wallis H = 6.0908, *P* = 0.01).

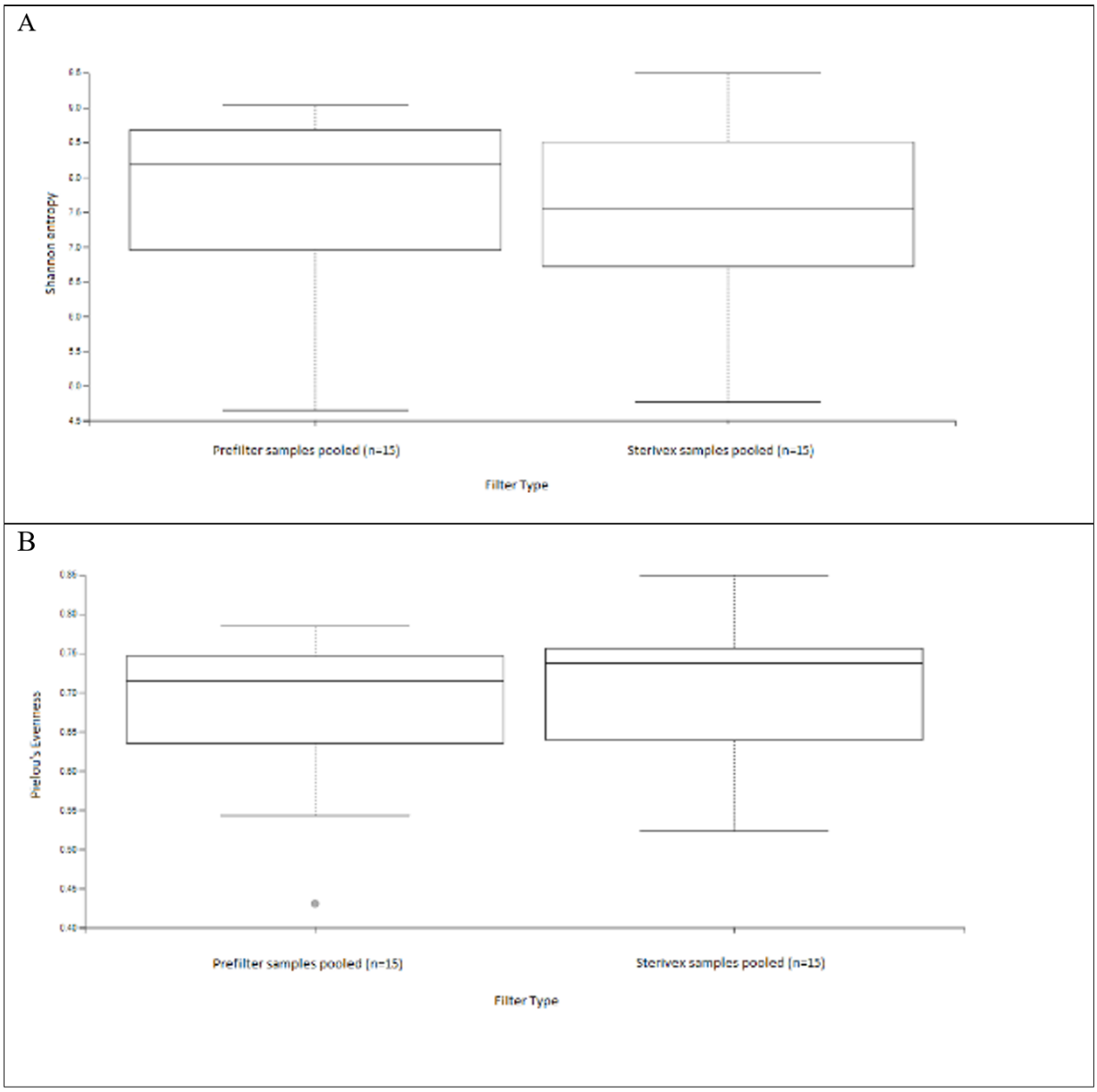

Figure 4-110. Shannon entropy and Pielou's evenness at 18S marker rarefied to 106,124 reads
Shannon entropy (A) and Pielou's evenness (B) across all pooled 10-L prefilter and 1-L Sterivex samples at the 18S marker rarefied to 106,124 reads.

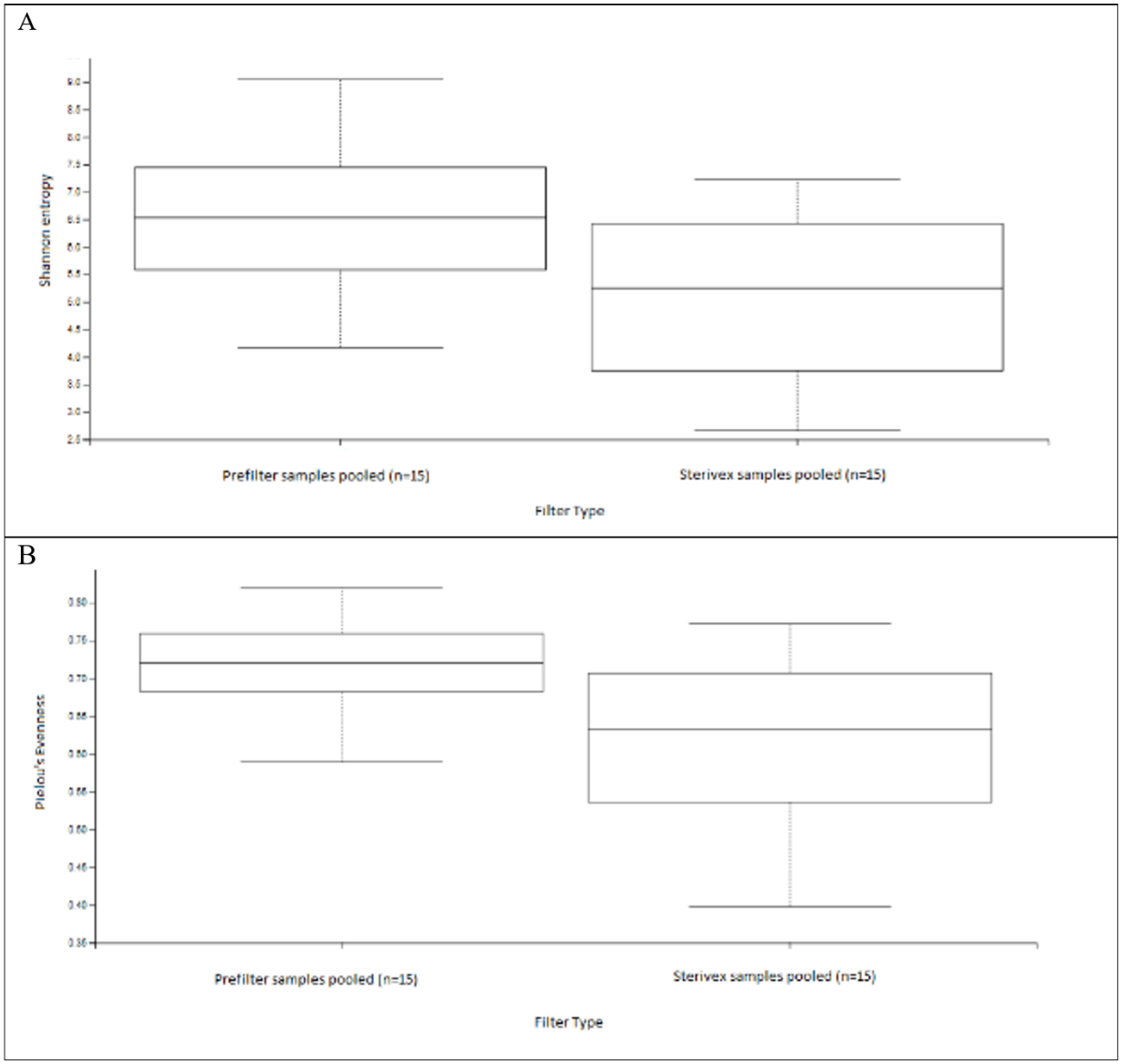

Figure 4-111.Shannon entropy and Pielou's evenness at *cox1* marker rarefied to 72,933 reads
Shannon entropy (A) and Pielou's evenness (B) across all pooled 10-L prefilter and 1-L Sterivex samples at the *cox1* marker rarefied to 72,933 reads.

4.6.3.5 Ordinations

PCoA plots of Bray-Curtis dissimilarity are shown for *cox1* in **Figure 4-112** (samples rarefied to 46,052 reads) and 18S in **Figure 4-113** (samples rarefied to 106,124 reads), where Sterivex samples are represented as cones, and prefilter samples as spheres. The PCoA plots revealed similar separation among habitat types at both the *cox1* and 18S markers. The Coral, Scarp, and Sediment 1000 samples clustered closer together than to other habitat types. The shallow and deep seeps appeared most divergent. Generally clustering was more evident in the 18S dataset than within *cox1*. The Coral, Sediment 1000, and Scarp communities clustered closer to each other than to either Seep community.

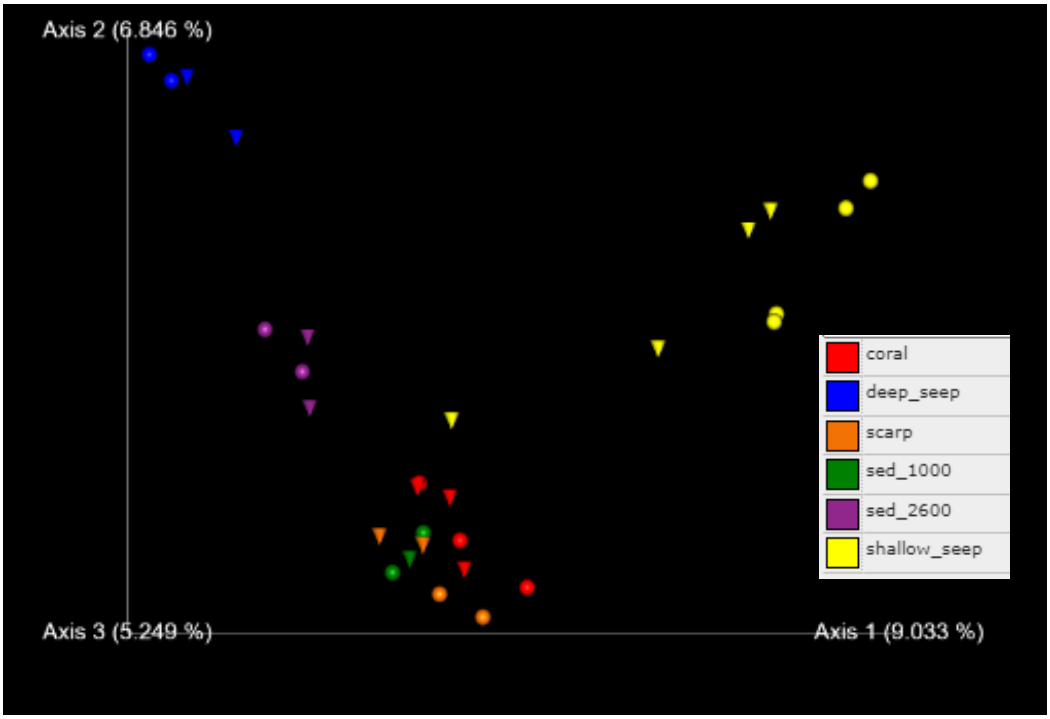

Figure 4-112. Principal coordinate plot based upon a Bray-Curtis dissimilarity matrix, *cox1*
Among samples sequenced with a *cox1* marker targeting the metazoan community, with circles representing 10-L prefilters and triangles representing 1-L Sterivex filters.

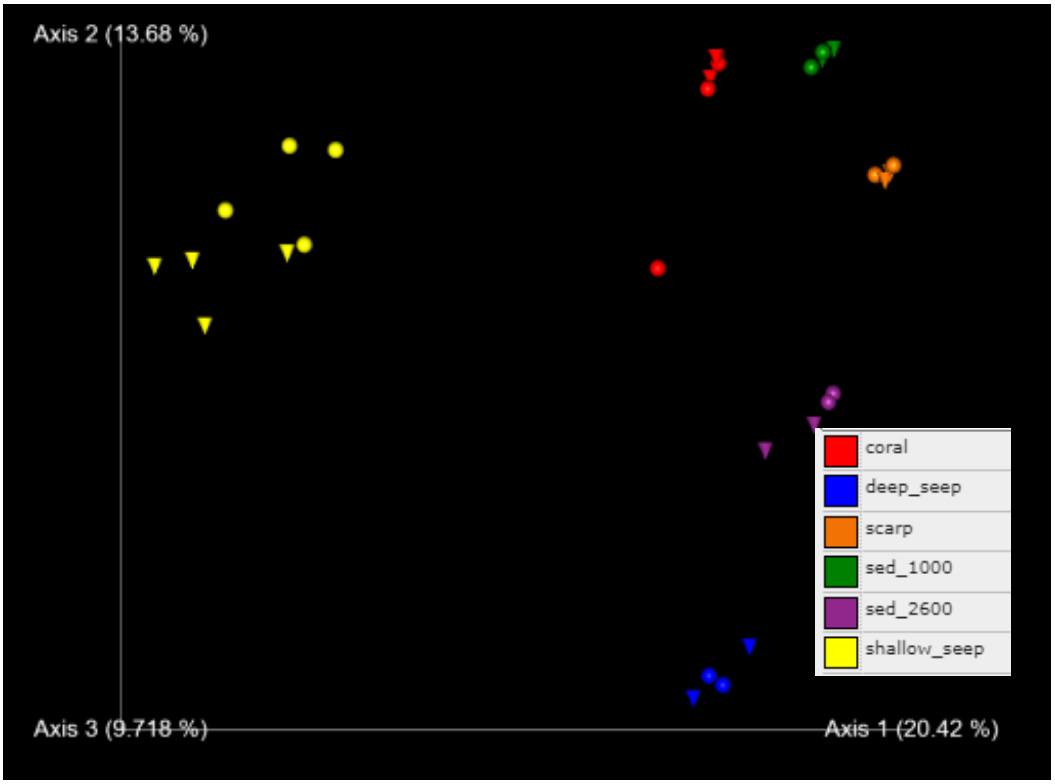

Figure 4-113. Principal coordinate plot based upon a Bray-Curtis dissimilarity matrix, 18S
Among samples sequenced with an 18S marker targeting the metazoan community, with circles representing 10-L prefilters and triangles representing 1-L Sterivex filters.

4.6.3.6 Taxonomic Assignment

The *cox1* dataset had 12235/13217=92.6% of the ASVs with hits to the nt database, but unassigned a taxonomy using our settings for MEGAN (**Table 4-32**). In many cases, a marine taxon was among the top hits for an ASV but matches to other marine and non-marine taxa resulted in an 'Unassigned' assignment due to application of the LCA. In other cases, the ASV was less than 85% similar to anything in the nt database and was not annotated. There were 329 ASVs assigned to Eukaryota, of which 176 were assigned as metazoans. 674 ASVs in the *cox1* dataset had no hit to the nt database from the blastn search, suggesting these are either novel taxa recovered or a result of sequencing error.

The 18S dataset had 7,150/37,861=18.9% of the ASVs with hits to the nt database, but not assigned a taxonomy (**Table 4-32**). 24,129 ASVs were assigned to Eukaryota, of which 1,463 were assigned to Metazoa. There was a sizeable number of ASVs that were assigned to Bacteria (4,320) and Archaea (664). 1,174 ASVs had no hit to the nt database suggesting these are either novel taxa recovered or sequencing error.

4.6.3.7 Analysis of Differentially Abundant Taxa

ANOSIM analysis of the 18S "Coral vs. Scarp" (**Table 4-32,**

Deep vs. Shallow Seep ASV ID, 106124 Rarefaction Depth	**Deep 100 Percentile**	**Shallow 100 Percentile**	**Taxonomic Assignment**
39e47e583c5859f7422f0d370a90f91c	32,582	1	*Bathymodiolus* sp.
5af6b3d8eae82dd53c7879865ce1ad08	7,637	1	Uncultured ciliate associated with deep-sea sediments
8e21bd8c3d890b27a5b041dae497de6f	9,678	20	Metazoan
655834c590d3c5a821db9dc68acf4ffe	2,545	1	Uncultured Eukaryote
92e7ee1254ad6aecccd98b04f24dd5d3	1,158	1	Eukaryota
f48c7ff4dd1d6d3a1ead453918801ae7	1,164	1	Philasterida
922719b901363656475a9bd55175b2a7	1	5,034	Uncultured eukaryote
f874cc41d9cd9c2a584e12e381729125	768	1	Ciliophora
2fbfe0c5eca8070edbf0ae17980c66e7	3,104	1	Eukaryota
aaf265b4a4d9d656f8ecdba49147b826	708	1	Echinoidea
23ac09b228a3cad21155008d5868fda2	1,178	1	Spionidae

Table 4-33) identified three differentially abundant ASVs, though we were unable to assign a taxonomy more specific than "Unassigned" or "Eukaryota". Eleven ASVs were identified as differentially abundant in the "Deep vs. Shallow Seep" comparison, though taxonomic assignments were at generally high levels, with only one genus-level assignment (*Bathymodiolus*). Multiple taxa were identified as more abundant at the Deep Seep, including commonly observed *Bathymodiolus* sp. mussels. SIMPER analysis of the 18S "Coral vs. Scarp" identified up to seven taxa contributing up to 73% of the variation between habitats, but none were statistically significant, and we identified no taxa in common with the ANOSIM results. Nine ASVs from SIMPER accounted for up to 71% of the variation observed between the "Deep vs. Shallow Seeps", but none were significantly different. Two ASVs identified were shared as being differentially abundant in both the SIMPER and ANOSIM results for the "Deep vs. Shallow Seeps" and include *Bathymodiolus* sp. and an uncultured ciliate.

Table 4-32. ASVs identified as differentially abundant at the 18S marker through ANCOM

The numbers represent abundance of the feature within the 100.0 percentile.

Coral vs. Scarp ASV ID, 152545 Rarefaction Depth	Coral 100 Percentile	Scarp 100 Percentile	Taxonomic Assignment
eb0afd31eb99b44776caa0a268cc1f6e	1	1,618	Unassigned
9d542a29a6e478240b9318a3cac99097	1	1,514	Unassigned
0586edc72b15d2b29101c573f1a9be86	2,078	1	Eukaryota

Deep vs. Shallow Seep ASV ID, 106124 Rarefaction Depth	Deep 100 Percentile	Shallow 100 Percentile	Taxonomic Assignment
39e47e583c5859f7422f0d370a90f91c	32,582	1	*Bathymodiolus* sp.
5af6b3d8eae82dd53c7879865ce1ad08	7,637	1	Uncultured ciliate associated with deep-sea sediments
8e21bd8c3d890b27a5b041dae497de6f	9,678	20	Metazoan
655834c590d3c5a821db9dc68acf4ffe	2,545	1	Uncultured Eukaryote
92e7ee1254ad6aecccd98b04f24dd5d3	1,158	1	Eukaryota
f48c7ff4dd1d6d3a1ead453918801ae7	1,164	1	Philasterida
922719b901363656475a9bd55175b2a7	1	5,034	Uncultured eukaryote
f874cc41d9cd9c2a584e12e381729125	768	1	Ciliophora
2fbfe0c5eca8070edbf0ae17980c66e7	3,104	1	Eukaryota
aaf265b4a4d9d656f8ecdba49147b826	708	1	Echinoidea
23ac09b228a3cad21155008d5868fda2	1,178	1	Spionidae

Table 4-33. ASV's contributing up to 70% if the variation between habitats at the 18S marker

Through SIMPER. 'c_sum' represents the proportion of variance accounted for by the feature, and P is a probability calculated through 1,000 permutations. Taxonomic assignments represent the top blast hit to attempt to find the most specific taxonomy.

Coral vs. Scarp ASV ID, 152545 Rarefaction Depth	Coral c_sum	Scarp P	Taxonomic Assignment
e3465e90d58164c7764641b515b1ac8a	0.2416	0.04950	Uncultured eukaryote
8c9f0fa5a4197d1ecdd91b978edf1126	0.3938	0.07921	Metazoan
508881c0d6da9ce264bbad39f9edd039	0.5061	0.01980	Eukaryota
fb924282d29b8c99830862e936b37a56	0.6059	0.33663	Actinopteri
d4ec5146f19bcf66630db61cdda3e19e	0.6521	0.52475	Ptychogastria
e60a6a2702900664e07976636b152625	0.6957	0.27723	Hexanauplia
d426cb12c3c2995a68c278376b69d40e	0.7309	0.27723	Unassigned

Deep vs. Shallow Seep ID, 106124 Rarefaction Depth	Coral c_sum	Scarp P	Taxonomic Assignment
cd9d4ddac0d434e918573af4c3ee8213	0.1887	0.52475	Calanoida
4015a786a3a8cf4b1f64dbdd714a19e4	0.2974	0.02970	Eukaryota
0eec2ed064698ec92a180a4d748abc8f	0.3839	0.21782	Hexanauplia

Deep vs. Shallow Seep ID, 106124 Rarefaction Depth	Coral c_sum	Scarp P	Taxonomic Assignment
5af6b3d8eae82dd53c7879865ce1ad08	0.4567	0.22772	Uncultured ciliate associated with deep-sea sediments
a7a3f74af544f21456d1a57ca53a3b56	0.5251	0.08911	Cyclopoida
39e47e583c5859f7422f0d370a90f91c	0.5901	0.08911	*Bathymodiolus*
70feea438d55de2fcbdfc39e4643fe9d	0.6406	0.38614	Euphausiidae
d800f1bba18646f12b119a0d5531d4a8	0.6798	0.22772	Nerillidae
0c27f0e562c08056ef996c02f262507e	0.7160	0.55446	Unassigned

ANOSIM analysis of the *cox1* "Coral vs. Scarp" dataset identified one ASV as more abundant in the scarp community, and it was unassigned a taxonomy (**Table 4-34**). Similarly, three unassigned *cox1* ASVs were differentially abundant between the "Deep vs. Shallow Seeps". SIMPER analysis identified three ASVs accounting for 82% of the variation between the "Coral vs. Scarp" communities, and three ASVs accounting for 76% of the variation between the "Deep vs. Shallow Seep" communities (**Table 4-35)**. One ASV assigned as Genus *Emiliania* was shared between the "Coral vs. Scarp" and "Deep vs. Shallow Seep" comparisons.

Table 4-34. ASVs identified as differentially abundant through ANCOMs at the *cox1* marker

For ANCOM, the numbers represent abundance of the feature within the 100.0 percentile.

Coral vs. Scarp ASV ID, 72933 Rarefaction Depth	Coral 100 percentile	Scarp 100 percentile	Taxonomic Assignment
bb6b707a4bb9d916a25ade7a363462c5	1	5,634	Unassigned

Deep vs. Shallow Seep ASV ID, 93691 Rarefaction Depth	Deep	Shallow	Taxonomic Assignment
b2ece110be2f193cda6a7e62244b3adf	36,243	1	Unassigned
d58d69709acfc55fd7d4b48364289747	35,349	3	Unassigned
de5a5b6e9edd4e569824d1ec97afba09	11,363	1	Unassigned

Table 4-35. ASV's contributing up to 70% if the variation between habitats at the cox1 marker

Through SIMPER. 'c_sum' represents the proportion of variance accounted for by the feature, and P is a probability calculated through 1,000 permutations. Taxonomic assignments represent the top blast hit to attempt to find the most specific taxonomy.

Coral vs. Scarp ASV ID, 72933 Rarefaction Depth	Coral c_sum	Scarp P	Taxonomic Assignment
b338383086c829ce9a410ff83cda11b0	0.4412	0.1584	Unassigned
64642f3e2d9638171133588a53ee7af5	0.6516	1.0000	Mikroconchoecia
c803ea9d79a5b3065bf594d68c5126cc	0.8253	1.0000	*Emiliania* sp.

Deep vs. Shallow Seep, 93691 Rarefaction Depth	Deep c_sum	Shallow P	Taxonomic Assignment
8444c18568ac69a7f0c9b98d61f2ec85	0.4084	0.415842	Unassigned
c803ea9d79a5b3065bf594d68c5126cc	0.6753	0.207921	*Emiliana*
723493cbaa0f9c6f1a9961653a416eee	0.7626	0.009901	*Prionospio* sp.

4.6.3.8 Taxonomic Representation

A broad range of taxa were represented among the top 20 18S and *cox1* ASVs (**Figure 4-114** and **Figure 4-115**, respectively). The majority of ASVs were identified as metazoans, including annelids (polychaetes), crustaceans (copepods and malacostracans such as amphipods, sergestid shrimps and euphausiid krill), cnidarians (hydrozoans and octocorals), molluscs (bivalves and a cephalopod), echinoderms and chordates (fishes and sharks). Also represented were phyla known from the plankton, such as Polycystinea (radiolarians), Dinophyceae (dinoflagellates), Foraminifera (forams), and Haptista (coccolithophores). Together, these eDNA barcoding loci provide an efficient survey of a component of the biodiversity present at the habitat types examined.

Taxa well represented in 18S ASVs included Annelida (Terebellida, Spinoida, Paranida, Nerillidae, and Polychaeta), Mollusca (Mytilloida mussels), Cnidaria (Alcyonacea octocorals, Ctenophora, and Trachymedusa), and Arthropoda (crustaceans including Hexanauplia, Harpacticoida, Calanoida and Cyclopoida copepods, plus Euphausiacea (krill) and Halocypida (ostracod), **Figure 4-114**). Also represented were Platyhelminthes (flatworms), Echinodermata (Holothuroidea), and Chordata (Actinopteri, fishes).

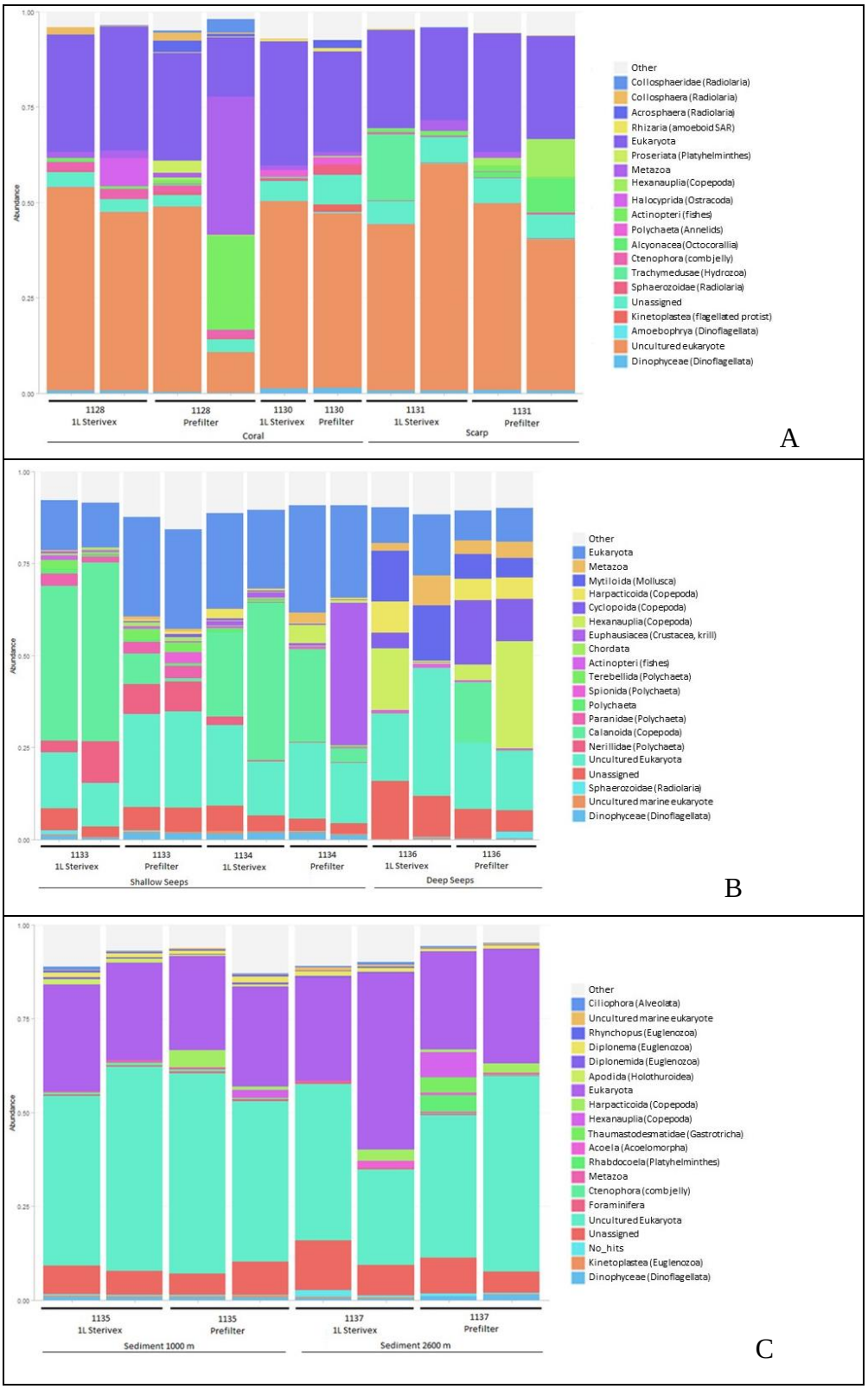

Figure 4-114. Relative abundance of the top 20 taxa in the 18S dataset
Collapsed at level 6 of the taxonomy for the A) coral and scarp, B) deep and shallow seeps, C) sediment_1000 and sediment_2600.

Copepods were among the top 20 ASVs detected at all habitat types and were especially diverse at the deep seep site (**Figure 4-114 B**). Several families of polychaetes were also detected, with highest diversity at the shallow seep sites (**Figure 4-114 B**). At both coral and scarp sites, Alcyonacean octocorals were detected and observed with the ROV prior to eDNA water collections (**Figure 4-114 A**). At sediment habitats, fewer metazoans were among the top ASVs detected, and instead several types of Euglenozoa, Alveolata, and Gastrotricha were detected and unique to these habitats.

Though paired samples (two niskins triggered simultaneously, biological replicates) generally had similar representation of 18S ASVs, this was not always the case. For example, paired prefilters at a coral habitat (J2-1128, **Figure 4-114 A**) and at a shallow seep habitat (J2-1134, **Figure 4-114 B**) had many ASVs detected for fish and an unknown metazoan (coral habitat) and krill (seep habitat) that were not present in other samples from these habitats. Differences in detection of ASVs among water samples may result from actual differences in DNA representation, as heterogenous partitioning of eDNA in water samples is common (Pilliod et al. 2013). The larger volume of water (10 L) filtered through the prefilters vs. the Sterivex filters may increase the likelihood of detecting differences in presence of DNA between samples, if they exist.

Using the *cox1* barcode, we detected similar major taxonomic groups as with the 18S barcode, but often could be assigned to lower taxonomic rank (**Figure 4-115**). For example, while the 18S barcode detected Actinopteri (fishes) at coral sites, the *cox1* barcode enabled resolution to Scyliorhinidae (cat shark) and Synaphobranchidae (cutthroat eels; **Figure 4-115 A**). At shallow seep sites, we detected and observed sergestid shrimp and squid ASVs with the ROV.

We recovered a diversity of diatoms (seep and sediment habitats, **Figure 4-115 B and C**) and siphonophores (coral/scarp and sediment habitats, **Figure 4-115 B and C**). The common marine diatom *Pseudo-nitzschia* sp. was detected with *cox1* at all habitat types. Though the *cox1* barcode often produced better taxonomic resolution than 18S, general biodiversity patterns between sites were not as obvious. There was also more variability between paired samples and less diversity detected within a sample relative to the 18S ASV data. For example, the paired samples from a coral site on dive J2-1128 varied dramatically in the dominant taxa recovered (**Figure 4-115A**).

In all benthic water samples and with both eDNA barcoding loci, the majority of ASVs could not be identified to a specific taxon (categories of Other, Eukaryota, Metazoa, Unassigned, Uncultured eukaryote), which reflects a known shortcoming of deep-sea and planktonic taxa representation in reference databases to date (see Discussion). This was especially true for the sediment habitats (**Figure 4-114 C** and **Figure 4-115 C**).

Investigation of Annelida, Cnidaria, Arthropoda, and Mollusca at the shallow and deep seep sites revealed numerous taxa that made biological sense given the habitat and also showed differences in relative abundance (**Figure 4-116**). For Annelida, we identified multiple orders and some family assignments, with Nerillidae having higher representation at the shallow seep site, and Spionida and Golfingiida at higher relative read abundance at the deep seep. The high biomass of Mytilidae, which had a top blast hit (not shown) to *Bathymodiolus* sp., was evident at high relative abundance at the deep seep site and absent at the shallow seep, consistent with their known distribution. Similarly, the presence of Solemyidae was higher at the shallow seep, but it is unclear if the genus is *Acharax* sp. or *Solemya sp*. For Cnidaria, we observed Scleractinia only at the shallow seep site consistent with ROV observation and expectation. Why we only observed Scleractinia on the prefilter vs. the Sterivex at the shallow seep is unknown. Alcyonacean corals were more highly represented at the deep seep consistent with visual observations. We detected a wide diversity of Arthropod fauna, but the most abundant taxon at the shallow seeps were Calanoid copepods.

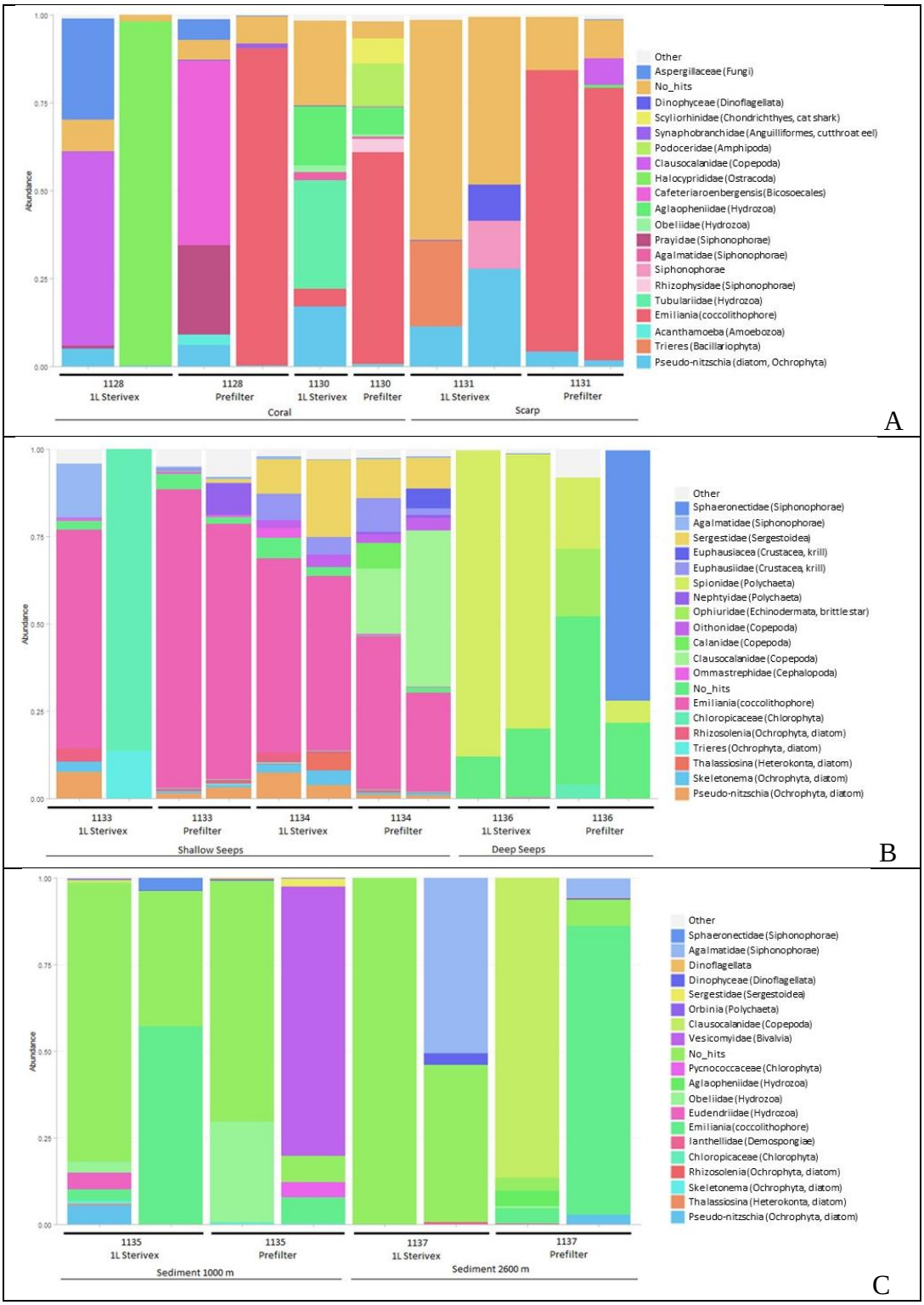

Figure 4-115. Relative abundance of the top 20 taxa in the *cox1* dataset
Collapsed at level 6 of the taxonomy for the A) coral and scarp, B) Deep and shallow seeps, C) sediment_1000 and sediment_2600.

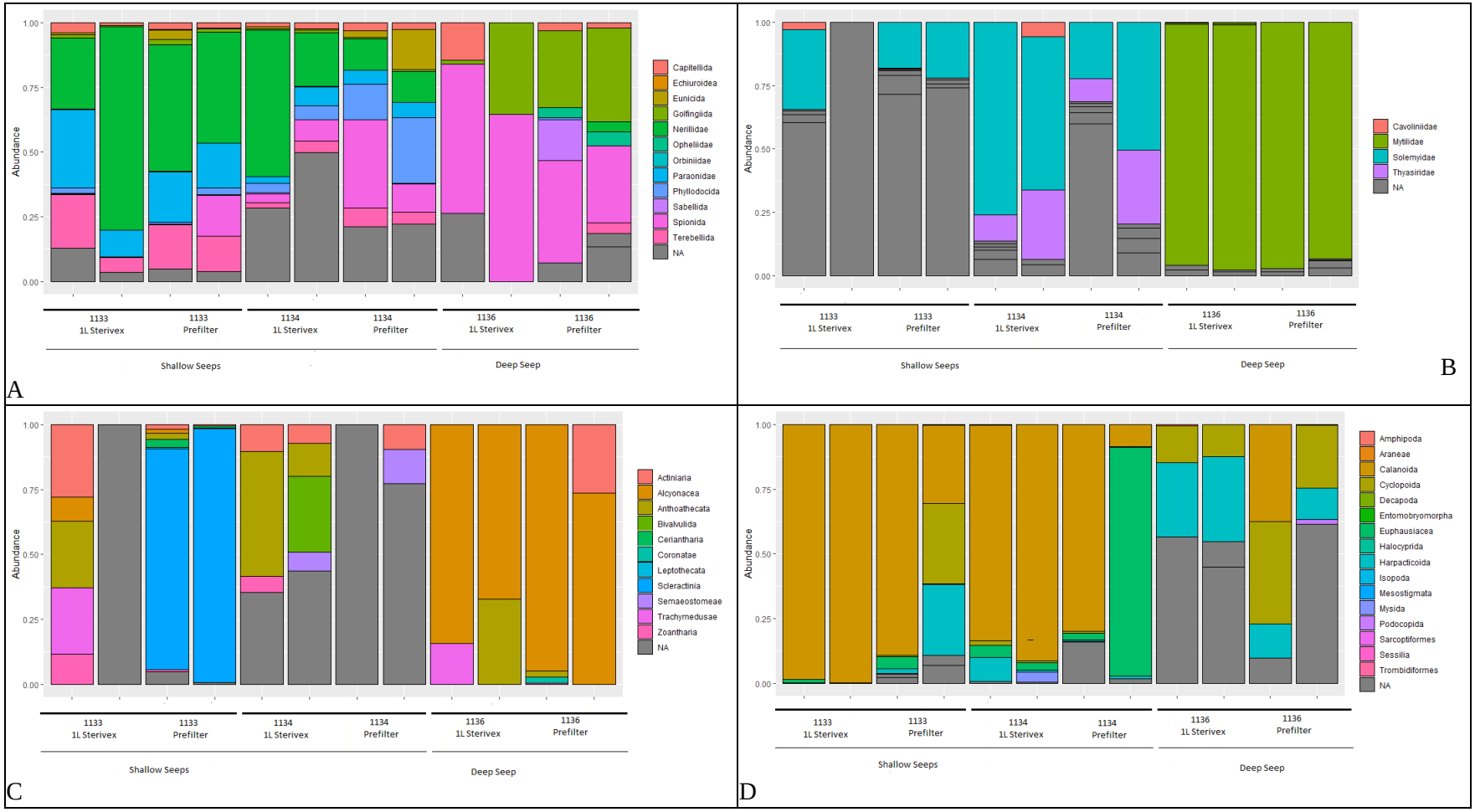

Figure 4-116. Relative abundance of Annelida, Mollusca, Cnidaria, and Arthropoda
Relative abundance of A) Annelida, B) Mollusca, C) Cnidaria, and D) Arthropoda at the shallow and deep seep sites sequenced at 18S. 'NA' taxa are part of the phyla examined but have a less specific taxonomic assignment.

4.6.4 Discussion

The deep sea presents unique challenges for biomonitoring vs. more easily accessible habitats such as estuarine or freshwater aquatic environments, and our study represents some of the first data examining whether patterns in biodiversity are detectable through eDNA filtered from visually targeted near-bottom water samples. Indeed, we found distinct clustering among habitat types, as well as a relatively large amount of eDNA biodiversity as estimated through ASV recovery. For example, in deep-sea, marine sediments collected among five different habitat types in Brandt et al. (2020), 4,333 *cox1* ASVs were obtained vs. 13,241 in this study using the same primer pair. Govindarajan et al. (2021) detected 8,417 18S ASVs, of which 351 were metazoans among samples collected in 5 CTD casts in the mesopelagic zone using the same primer set we did, whereas we detected 1,463 metazoan taxa.

It is important to note these are not direct comparisons, as the number of reads and ASVs recovered is influenced by sample volume, extraction method, sequencing depth, sequence quality, habitat type (water vs. sediment, geographic location, biodiversity hotspot like a reef or seep, etc.), and whether ASVs are subjected to additional clustering as in Brandt et al. (2020), etc. Nevertheless, the apparent diversity we recovered is notable and demonstrates proof of concept for eDNA sequencing in the deep sea.

While we recovered multiple ASVs at both markers, many remained unassigned with our taxonomic annotation approach. Initial efforts using the Midori database and Silva 18S for taxonomic assignment using a Bayesian Classifier built in Qiime2, often resulted in non-sensical taxonomic assignments for an ASV. This appears to be a consequence of forcing comparison of sequences to a reduced set of taxa that may not include any close relatives that may be a better match. Comparing the data to the entire nt database as performed in this study alleviates that limitation, but poses potential new problems, such as wrong taxonomic assignments based on incorrect annotations by the sequence authors (Sidall et al. 2009, Bucklin et al. 2021).

In the present study, manual blasting of sequences from SIMPER and ANCOM analyses compared to the results obtained from MEGAN were always in agreement (results not shown), suggesting our approach is relatively robust provided the original sequence annotations are correct. In addition, application of the LCA with results from blasting against the entire nt database result in taxonomic assignments that are more conservative and reduce the chance of misassignment.

Our study reinforces the value of future coordinated efforts to augment eukaryotic reference databases for metabarcoding studies, including detailed metadata and deposition/storage of vouchers where possible (Bucklin et al. 2021). One valuable result of our study is the ASV sequences themselves, that can be re-examined in the future as databases become more complete. Nevertheless, taxonomic identity and resolution using these markers will remain limited until more voucher sequencing is completed. Metabarcoding primers should also continually be adjusted to reflect newly available sequence data and tailored to specific research questions. For example, if only corals are of interest, a targeted coral metabarcoding primer (Everett and Park 2018) would be more appropriate than the 18S marker used in this study, which amplifies a broader range of taxa and has less taxonomic resolution. Part of the reason we employed the *cox1* marker was because we anticipated a higher level of taxonomic resolution to complement the 18S data, but the apparent lack of present reference sequences limited this capability.

Incremental optimization of methods for filtering seawater and preservation of filters at sea is an active area of research (Djurhuus et al. 2018, Torres Beltran et al. 2019). Part of the consideration driving this methods development is resource dependent and includes factors such as lab space suitable for filtering eDNA from water, cold-storage, and ship-time. The other primary consideration is what aspects of the actual filtering protocol (pore size, filter material, volume of water filtered) influence target recovery. At the two metrics of diversity we measured, there was no significant difference in richness or evenness between 10 L filtered through a 0.8-micron or 1 L through a 0.2-micron Sterivex for the 18S data.

However, there was a significant difference in recovery between the *cox1* filter types, with the prefilter having significantly higher richness. It is not clear why richness was higher in the *cox1* dataset. The particle size of eDNA in the deep sea has not been rigorously investigated sensu Turner et al. (2014), and metazoan eDNA targeted by the *cox1* primers may be of a larger size and enriched on the 0.8-micron filter, though this is speculative.

We demonstrated that metabarcoding of bottom water can uncover patterns in community structure among habitats. However, investigation of several factors is needed to better understand how metabarcoding results such as ours can be interpreted so the technique can be applied most effectively. Implicit in our analysis is that the patterns represent the community at the site where the water was sampled. At bottom water sites where there are strong water currents, such as several of the shallower sites in this study within or in close proximity to the Gulf Stream (dives 1130, 1133, 1134), there is the consideration of whether the eDNA signal is attributable to local taxa or those from up-current.

Water temperatures in the deep sea are conducive to preservation of eDNA and there is no risk of UV degradation (Brandt et al. 2020). Thus, it is reasonable to expect that eDNA could be transported far from its source. Everett and Park (2018) reported that they detected some deep-sea octocorals not observed at the eDNA collection site, hypothesizing they may have originated up-current. Everett and Park (2018) also noted that studies in nearshore habitats (O'Donnell et al. 2017) predicted that eDNA remains within 100 m of the source, but no such studies exist describing fate and transport of deep-sea eDNA.

Allan et al. (2021) developed the first model to simulate transport of eDNA vertically in the mesopelagic and concluded based on a stringent set of assumptions that it likely does not move more than 60 m from the source. However, they acknowledge that horizontal currents are not accounted for in the model, and the model was not intended to characterize transport of eDNA near-bottom habitats. Clearly, fate and transport of eDNA in the deep sea still represents a knowledge gap and may ultimately be hard to generalize given the variations among deep-ocean habitats and ocean circulation patterns. We attempted to compare video data with the eDNA in our study, but due to limitations of the reference databases and possible primer bias for some taxonomic groups, a meaningful comparison was not possible (data not shown). Additional investigations, perhaps using ddPCR or qPCR for a single target species with a sampling grid different distances from the target (up and down current) at different deep-sea sites could help determine the spatial extent of the eDNA signal.

While we examined water samples in our study, we collected all samples in close proximity to the seafloor, where natural currents or disturbance from something like the ROV during sample collection can re-suspend sediment particles. Brandt et al. (2020) note that up to 125,000-year-old ancient DNA has been reported in oxic and anoxic sediments at various depths. Thus, resuspension of sedimentary eDNA could confound interpretation of the contemporary community in water samples collected from near bottom. Collection of replicate water samples at different distances from the seafloor along with sediment samples may help determine if there is a "sediment signature" at water close to the seabed interface.

For our comparison of diversity and evenness between the prefilter and Sterivex samples, we pooled all samples together to increase statistical power. However, it was obvious from taxonomic bar charts that prefilter and Sterivex samples from the same site often recovered different taxa or different relative abundances of the same taxa. Thus, more rigorous testing is needed to assess eDNA stochasticity among sample replicates and filter types at each of the different habitats. Nevertheless, we were encouraged that 1 L of water did not grossly under-sample diversity relative to the 10 L prefilter. Though we targeted 1 L of unfiltered water through our Sterivex filters, it would have been possible to increase the volume filtered at many sites from a filter capacity standpoint, but we were often time limited. In contrast to the Sterivex filters, the prefilters required more handling of the filter, and bleach and rinse steps among samples. Additional research could help to identify the appropriate balance of volume filtered and pore size for this application.

Results from this study are promising for the utility of targeted eDNA sampling for biomonitoring at vulnerable deep-sea habitats. This work provides baseline characterizations of several habitats that are complementary to observations and collections. Additionally, community analyses such as those described, in combination with environmental data, may provide information on key taxa in deep-sea food webs.

5 Biology of Coral and Seep Fauna

5.1 Organismal Physiology

Section Authors: Carlos Gomez, Andrea Gori, Alexis Weinnig, Adam Hallaj, Hee Jin Chung, Erik E. Cordes

5.1.1 Introduction and Context

Lophelia pertusa dominates the coral habitats of the Blake Plateau. In this region, this species of scleractinian coral forms massive frameworks and reef structures that we now recognize as being among the largest CWC reefs in the world. Therefore, we focused much of the physiology work in this project on this species.

Globally, *L. pertusa* has been reported growing under thermal conditions from 4ºC (Greenland) to 14ºC (Mediterranean Sea) with clear temporal variability within regions (Mienis et al. 2007, 2014; Davies et al. 2010; Kenchington et al. 2016; Dorey et al. 2020). Data collected with landers in the northeast Atlantic Ocean, at depths between 570 and 677, showed *L. pertusa* to be exposed to average temperatures between 8 and 9ºC with intra-annual variation of up to 2.6ºC (Mienis et al. 2007, Dullo W et al. 2008). In the GOM, high-resolution data for *L. pertusa* reefs (Viosca Knoll 450–500-m depth) have shown similar average temperatures with variations up to 5ºC, with minimum values corresponding to the winter season (6.5ºC) and maximum values corresponding to summer season (11.6ºC) (Mienis et al. 2012). In the Deep SEARCH study area, long-term (6 months) data collected close to *L. pertusa* reefs in this study and in previous work have highlighted unusual events of high temperatures with increased flow that caused peak temperatures of 15ºC within short periods, and temperature fluctuations up to 9°C within a day for unpredictable periods of time (Brooke et al. 2013, Mienis et al. 2014). These fluctuations are caused by the direct influence of the Gulf Stream that meanders over the Blake Plateau causing warm water incursions into the deep-coral mounds (Brooke et al. 2013, Matos et al. 2015).

Physiological studies can provide useful information to understand the mechanisms a species uses to cope with environmental change (increasing temperature), in order to predict future climate-change outcomes such as species survival and adaptation potential (Somero 2010). In most ectotherms there is a distinct "thermal curve" that defines the effects of temperature on physiological performance and homeostatic mechanisms (Schulte 2015). Studies performed on CWC species show a general pattern where temperature increase has a negative effect on survival (Brooke et al. 2013, Lunden et al. 2014) as well as in maintaining physiological functions by increasing oxygen consumption and metabolic rates (Dodds et al. 2007, Dorey et al. 2020). Studies indicate that metabolic functions in *L. pertusa* can be maintained across a range of temperatures from 5 to 14°C, and an upper temperature of 15°C could be considered the tipping point, beyond which survival is impacted (Brooke et al. 2013). This is further supported for populations from the GOM where corals can tolerate temperatures up to 14°C for two weeks, but total mortality results from prolonged exposure to a temperature of 16°C (Lunden et al. 2014).

Multi-stressor experiments performed on CWC indicate that metabolic functions appear to be more sensitive to changes in temperature than to ocean acidification, and that a clear synergistic impact would result in a severe reduction of coral metabolism under future climate-change scenarios (Gori et al. 2016). Moreover, recent evidence shows that in *L. pertusa*, increased temperature causes more stress under the combined influence of other stressors such as oil spills and dispersant exposure (Weinnig et al. 2020). Results from studies that have replicated natural thermal variability using controlled experiments (Dodds et al. 2007, Brooke et al. 2013, Naumann et al. 2014, Dorey et al. 2020) indicate that *L. pertusa* can tolerate a wide range of temperatures from 5 to 14ºC, but at the expense of increasing respiration and excretion rates as temperature increases (Dorey et al. 2020).

The aim of this study element was to explore the ecophysiological response of *L. pertusa* to natural short-term increases in temperature up to sub-lethal conditions, in order to understand species performance within natural thermal variability. We conducted a series of experiments under controlled conditions that simulated in situ temperature shifts that are naturally experienced by *L. pertusa* on the Blake Plateau. We hypothesized that corals experiencing rapid temperature variation would show a more stressful metabolic response than those at a single ambient temperature, but that coral colonies will survive within the homeostatic range expected for this population. Our results inform our understanding of the response of corals to future climate change, both in terms of maximum temperature and the frequency of severe episodic events, which is crucial to understanding the whole deep-sea ecosystem response in the western Atlantic and beyond.

5.1.2 Methods

5.1.2.1 Study site and Sample Collection

On expedition AT-41 in August 2018, we collected colonies of *Lophelia pertusa* (syn. *Desmophyllum pertusum* - Linneus, 1758) at Richardson Reef Complex (31.98°–32.00°N and 77.39°–77.41°W) in the northwestern Atlantic Ocean between 684 and 696 m using the manned Deep Submergence Vehicle (DSV) *Alvin* (Woods Hole Oceanographic Institution). We placed different collections in separate temperature-insulated compartments on the submersible and kept them separate throughout relocation and experimentation. We kept all corals onboard the ship inside a cold room with constant temperature of 8ºC using recirculating containers with natural seawater.

We transported corals to Temple University (Philadelphia, PA), where all the experiments were performed. At the time of arrival, we split collections into two 550-L recirculating systems with custom-made artificial seawater (ASW) prepared using B-ionic®, and maintained at a temperature of 8ºC, salinity 35 psu, and total alkalinity 2,300 µmol kg^{-1}. We fed coral fragments five times per week with a mixture of zooplankton-phytoplankton (Fauna Marin®, Holzgerlingen, Germany) and artificial Marine Snow® (Two Little Fishies, Miami Gardens, FL), and allowed them to acclimate to laboratory aquaria conditions for a period of approximately 2 months prior to the start of experiments. We ran our experiments from October to November 2018 using independent 55-L aquaria.

5.1.2.2 Physiological Measurements

At the time of the experimental trials, we nonselectively split a total of 21 coral fragments consisting of an average of 8 polyps each (range of 5 to 11) between the three independent 55-L tanks (seven fragments per tank) and maintained each for 1 week before the start of the experiments. We replaced approximately 20% of the water every other day in order to maintain good water conditions for the corals. We monitored temperature with data loggers (Onset-HOBO) in each experimental tank and maintained the target temperature (8ºC or 14ºC). We took water samples and determined total alkalinity, pH_T, and salinity regularly throughout the period to monitor water quality. On average, total alkalinity in the tanks was 2,265 ± 17 µmol kg^{-1}, pH_T 7.95 ± 0.03, and salinity 35 psu (**Table 5-1**).

We used nonselectively chosen coral fragments for physiological measurements (respiration and excretion rates, feeding): 5 fragments per tank for respiration and excretion (15 total) and 2 per tank for feeding rates (6 total). We first set tanks to the lower temperature range (8ºC), and left corals for an additional 7 days before the first physiological trials. After this period, we increased the temperature to the maximum range (14ºC) within 4 days at a rate of 1.5ºC day^{-1} and left the tanks at this temperature for seven more days before performing the second set of physiological trials.

Table 5-1. Average of the different physical and chemical parameters measured

Average ± SD of the different physical and chemical parameters measured during the experimental trials. The pH is reported in total scale (pHT).

Temperature	Tank	Temperature °C	Total alkalinity (µmol Kg^{-1})	pH_T	Salinity (psu)
8ºC	1	8.49 ± 0.09	2.264 ± 21	7.91 ± 0.01	35
8ºC	2	8.33 ± 0.10	2.274 ± 10	7.91 ± 0.01	35
8ºC	3	8.25 ± 0.10	2.279 ± 19	7.90 ± 0.00	35
14ºC	1	14.19 ± 0.10	2.266 ± 10	7.96 ± 0.05	35
14ºC	2	14.17 ± 0.07	2.247 ± 15	7.97 ± 0.03	35
14ºC	3	14.03 ± 0.09	2.262 ± 13	7.95 ± 0.02	35

All coral fragments used for the trials were deprived of food for 24 h. We performed experiments independently for eight hours in 700-mL plastic containers filled with water from the tank in which we maintained the coral fragment, sealed with no headspace, and placed in a water bath to avoid temperature variation. We ensured constant water movement inside each container by a Teflon-coated magnetic stirrer. To determine respiration rates, we assessed oxygen concentration before and after the incubation period using an optode (Hach-Lange HQ 40b, Loveland, USA, precision 0.2 mg L^{-1}). As a control to account for microbial respiration, we subtracted oxygen uptake values in a container without coral (0.39 ± 0.09 µmol O_2 h^{-1}) from the values in containers with coral fragments. We determined excretion rates as change in ammonium concentrations (NH_4^+) by sampling 20 mL of sterile-filtered (0.2 µm) seawater before and after the incubation period which was kept frozen until further analysis. We standardized respiration and excretion rates to DW of the individual coral fragments.

We calculated the atomic ratio of oxygen to nitrogen (O:N) for each independent incubation from the oxygen consumed and ammonium excreted using Eq. 18:

$$O{:}N = \frac{(2 * O_2)}{(NH_4\ excretion)} \qquad \text{(Equation 18)}$$

This ratio can elucidate the primary type of substrate being catabolized by the corals. Depending on the value it can indicate whether corals are mainly relying on protein/protein-lipid (O:N = 15–40) or lipid-dominated catabolism (O:N > 50) (Sabourin and Stickle 1981, Mayzaud and Conover 1988). Finally, to determine the effect of temperature on metabolic performance, the Q_{10} value quantifies temperature dependence across a limited temperature range of 10ºC (Gillooly 2001) according to Eq. 19:

$$Q_{10} = \left(\frac{k_2}{k_1}\right)^{10/(t_2 - t_1)} \qquad \text{(Equation 19)}$$

where k_1 and k_2 are the initial and final oxygen consumption respectively, and t is the initial (t_1) and final (t_2) temperature.

5.1.2.3 Feeding Experiments

We used live *Artemia salina* nauplii (0.5-mm length) to assess the feeding rates of *L. pertusa* at the different temperatures. We used the same setup used for physiological measurements for the feeding experiments, except the containers were not sealed. We took coral fragments in non-selective order from the aquaria and placed them inside the containers to allow conditioning of the coral, as indicated by the expansion of their polyps. After conditioning, all trials lasted four hours. We introduced an initial concentration of 1,018 ± 148 nauplii L^{-1} (Purser et al. 2010, Gori et al. 2015) into the containers at the beginning of the experiment. We then took five replicated 10-mL seawater samples immediately from the container just after the start of the experiment (30 s), and every hour until the end of the trials. *A. salina* nauplii were counted and immediately returned to the chambers to avoid any concentration decrease. We performed six control trials with dead skeletal fragments devoid of polyp cavities (corallites filled with epoxy) in the same way as the coral trials to account for possible concentration decrease due to the *A. salina* nauplii becoming trapped within the coral fragment structure (initial concentration of 1,020 ± 70 nauplii L^{-1}).

5.1.2.4 Data Analysis

To test for the effects of increased temperature on the physiological performance of *L. pertusa*, dry-weight (DW) standardized respiration (µmol O_2 g^{-1} h^{-1}), excretion (µmol NH_4 g^{-1} h^{-1}) and feeding capture rates (*A. salina* nauplii $polyp^{-1}$ h^{-1}) were treated as response (dependent) variables and temperature as an independent variable (two levels). We averaged the responses of individual coral fragments within each tank (n = 3). To test for the assumptions of normality and homoscedasticity, we used the Shapiro-Wilk test and Bartlett tests, respectively. Values for normality ($p > 0.05$ for all response variables) and homogeneity of variances ($p > 0.05$ for all response variables) validated the assumptions of the one-way ANOVA test.

We calculated capture rates as the decrease in prey concentration at the end of the incubation time, normalized to the number of polyps per fragment. We used changes in *A. salina* nauplii concentration during the control experiments as a correction factor and we subtracted such from the trials with coral fragments. We did this based on the observation that the skeletal framework of the fragment is causing a net loss of nauplii (105 ± 81) not being captured by the live polyps (repeated measures ANOVA, $F_{3,15} = 7.91$, $p < 0.01$). We reported results as mean ± SD and for all analyses we considered $p < 0.05$ to be statistically significant.

5.1.3 Results

We found 100% survival of coral fragments for the length of the exposure to the temperature range tested. We detected no observable physical stress signs and all the coral fragments showed polyp expansion throughout the experimental period.

5.1.3.1 Respiration Rates

In all experimental trials we detected a decrease in oxygen concentration attributable to the metabolic activity of *L. pertusa*. These values never fell below 90% oxygen saturation during incubations, which is within the conservative threshold for *L. pertusa* respiration measurements (Dodds et al. 2007). Average respiration rates (oxygen consumption) for corals experiencing normal temperature (8°C) was 0.13 ± 0.02 µmol O_2 g^{-1} h^{-1} (**Figure 5-1**, **Table 5-2**).There was a significant effect of temperature on oxygen consumption (one-way ANOVA $p = 0.03$, **Table 5-3**), where coral fragments exhibited more than 60% increase in respiration at 14°C with an average rate of 0.21 ± 0.03 µmol O_2 g^{-1} h^{-1} (**Figure 5-1**).

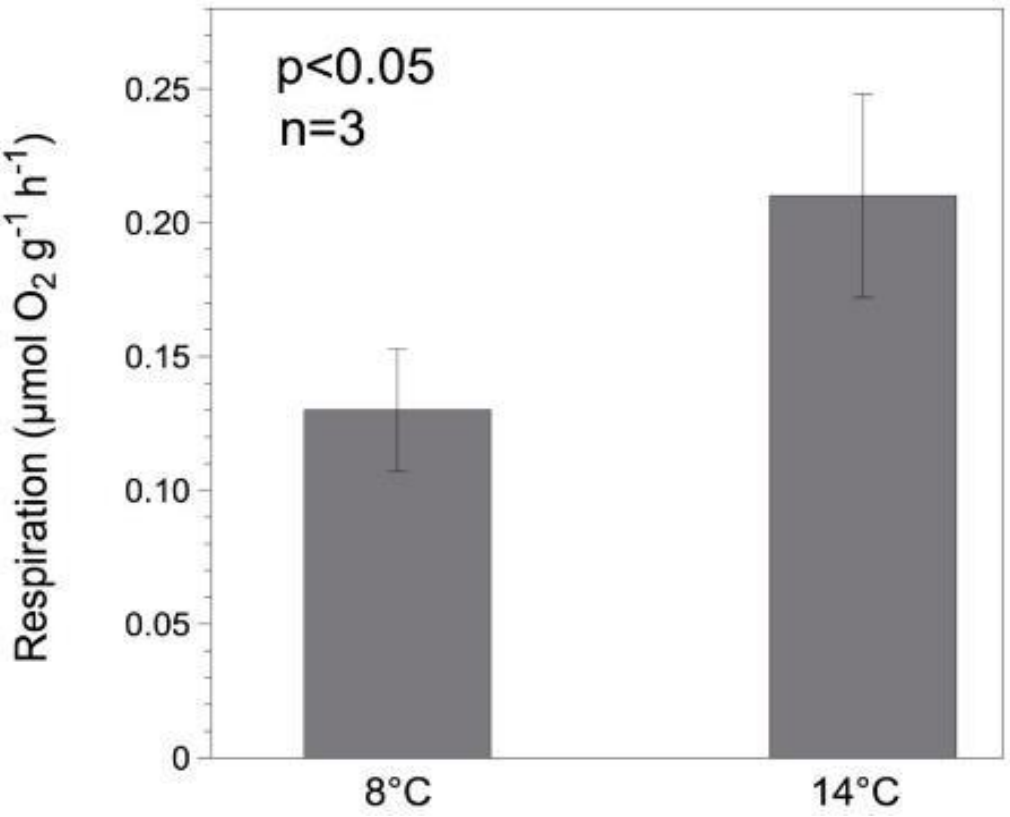

Figure 5-1. Respiration rates for *Lophelia pertusa* exposed to the different temperatures
Values are expressed as average ± SD of oxygen consumption standardized by coral DW.

Table 5-2. Average respiration, excretion, and feeding rates, and oxygen to nitrogen ratio

Average standardized (dry weight) ± SD of the respiration rates (oxygen consumed), excretion rates (ammonium excreted), feeding rates (*A. salina* nauplii capture), and oxygen to nitrogen ratio (O:N) for each independent tank at the different temperature treatments.

Temperature	Tank	Respiration (µmol O_2 g^{-1} h^{-1})	Excretion (µmol NH_4 g^{-1} h^{-1})	Capture rate (*A. salina* nauplii $polyp^{-1}$ h^{-1})	O:N
8ºC	1	0.141 ± 0.106	0.004 ± 0.004	18.33 ± 0.00	63.607
	2	0.152 ± 0.224	0.005 ± 0.004	26.83 ± 0.00	61.563
	3	0.108 ± 0.037	0.003 ± 0.001	18.21 ± 0.18	77.985
14ºC	1	0.247 ± 0.164	0.007 ± 0.007	8.33 ± 0.00	66.894
	2	0.235 ± 0.275	0.010 ± 0.011	6.61 ± 0.00	48.961
	3	0.175 ± 0.071	0.011 ± 0.005	4.14 ± 3.11	32.566

Table 5-3. One-way ANOVA table of dependent variables results between two temperatures

One-way ANOVA table showing the statistical results of the dependent variables (respiration, excretion, and feeding) between the two different temperatures (8ºC and 14ºC). Significant differences when p < 0.05 (bold).

Variable	df Between Groups	df Total	SS Between Groups	SS Total	MS	F	*p*-value
Respiration	1	5	0.011	0.015	0.011	10.61	0.031
Excretion	1	5	0.023	0.28	0.023	19.29	0.012
Feeding	1	7	425.75	550.358	425.752	20.51	0.004

To further understand if the observed response to the increase in temperatures was within the expected range for *L. pertusa*, we calculated the Q_{10} value, which is a measure of the temperature sensitivity of a physiological process due to an increase in temperature by 10°C. Our results showed a $Q_{10} = 2.3$, which means that for a 10°C increase in temperature, we should expect a greater-than-two-fold increase in metabolic rate. The normal Q_{10} range for most biological systems is between 2 and 4, which indicates that the corals are responding as expected and show some degree of homeostasis at higher temperatures (Schulte 2015).

5.1.3.2 Excretion Rates

Average excretion rates for corals at 8°C was 0.004 ± 0.001 µmol NH_4 g^{-1} h^{-1}. There was a significant effect of temperature on excretion rates (one-way ANOVA $p = 0.01$, **Table 5-3**), with a 44% increase (0.009 ± 0.002 µmol NH_4 g^{-1} h^{-1}) when we increased temperature to 14°C (**Figure 5-2**). These values were positively correlated with respiration rates ($R = 0.47$; $p = 0.010$). The oxygen to nitrogen atomic ratio (O:N) decreased at elevated temperatures, from 67.71 ± 8.94 at 8°C to 49.47 ± 17.16 at 14°C, indicating an increase in the rate of nitrogen production. This could be a result of a change in the substrate for catabolism from lipids and carbohydrates to a mix of proteins and lipids at higher temperatures (**Figure 5-2, Table 5-2**).

5.1.3.3 Feeding Rates

Average feeding (capture) rates for corals experiencing the control temperature (8ºC) was 20 ± 4 *A. salina* nauplii $polyp^{-1}$ h^{-1} decreasing to 6 ± 3 nauplii $polyp^{-1}$ h^{-1} at increased temperature (14°C) (**Figure 5-4**). This decrease represents more than a three-fold change (one-way ANOVA $p < 0.01$, **Table 5-3**), providing further evidence for the negative effect of temperature on feeding rates.

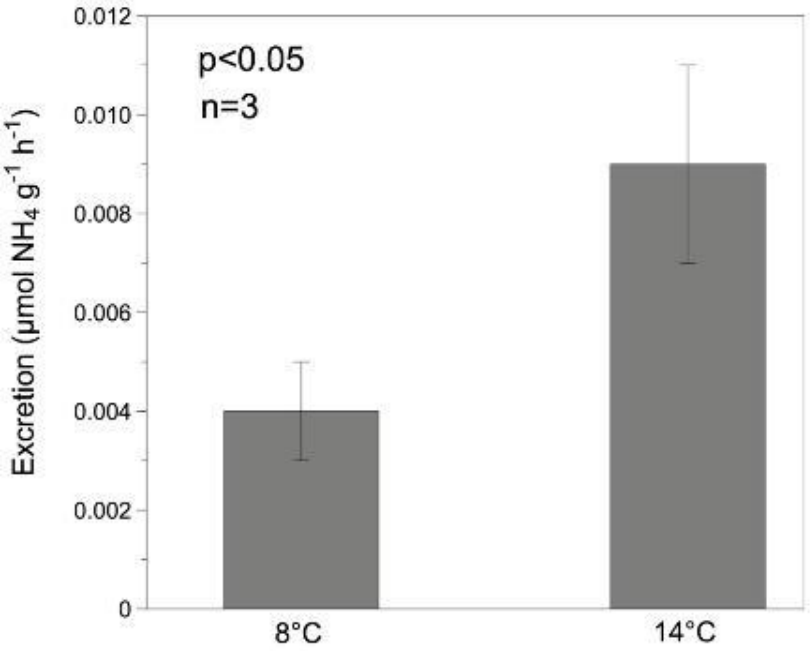

Figure 5-2. Excretion rates for *Lophelia pertusa* exposed to two different temperatures
Values are expressed as average ± SD of ammonium excretion standardized by coral DW.

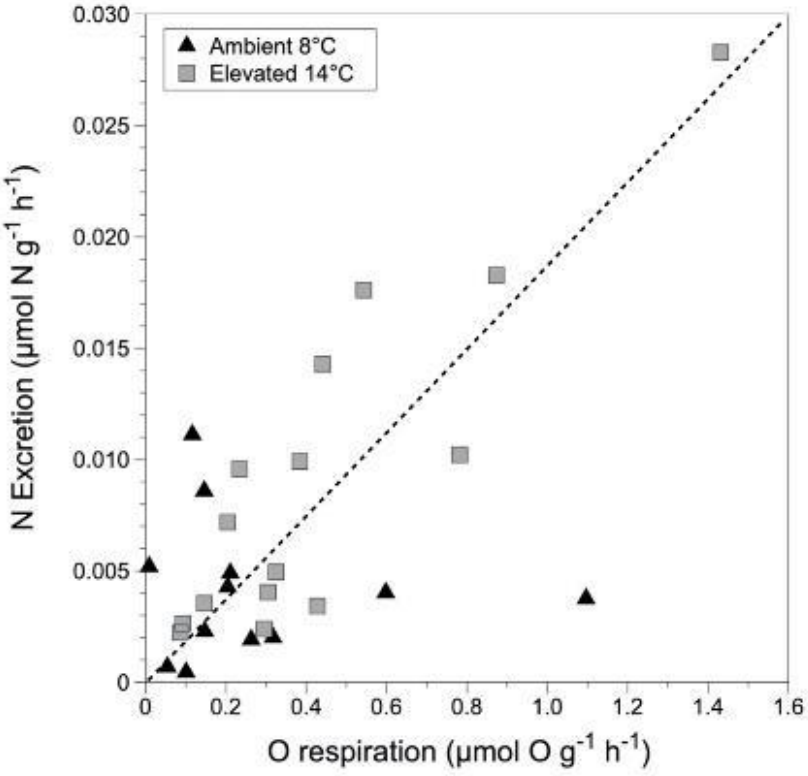

Figure 5-3. O:N for *Lophelia pertusa*
Values are oxygen respiration and ammonium excretion standardized by coral DW.

5.1.4 Discussion

This study examined the metabolic response of the CWC *Lophelia pertusa* to a short-term temperature increase of 6°C (from 8°C to 14°C) that simulated the natural thermal environment experienced by this coral in the South Atlantic Bight (northwestern Atlantic Ocean), where the Gulf Stream has a direct influence on the CWC communities dwelling below it (Matos et al. 2015, Cordes et al. submitted). High-frequency temperature data has shown unusual extreme temperature events year-round recorded in *L. pertusa* habitats (Brooke et al. 2013, Mienis et al. 2014, Cordes et al. in press). Coral respiration and excretion rates increased more than two-fold in the temperature range tested, accompanied by an almost three-fold decrease in feeding rate. Together, these effects compromise the physiological performance of *L. pertusa* when exposed to the regular arrival of warm surface waters from the Gulf Stream.

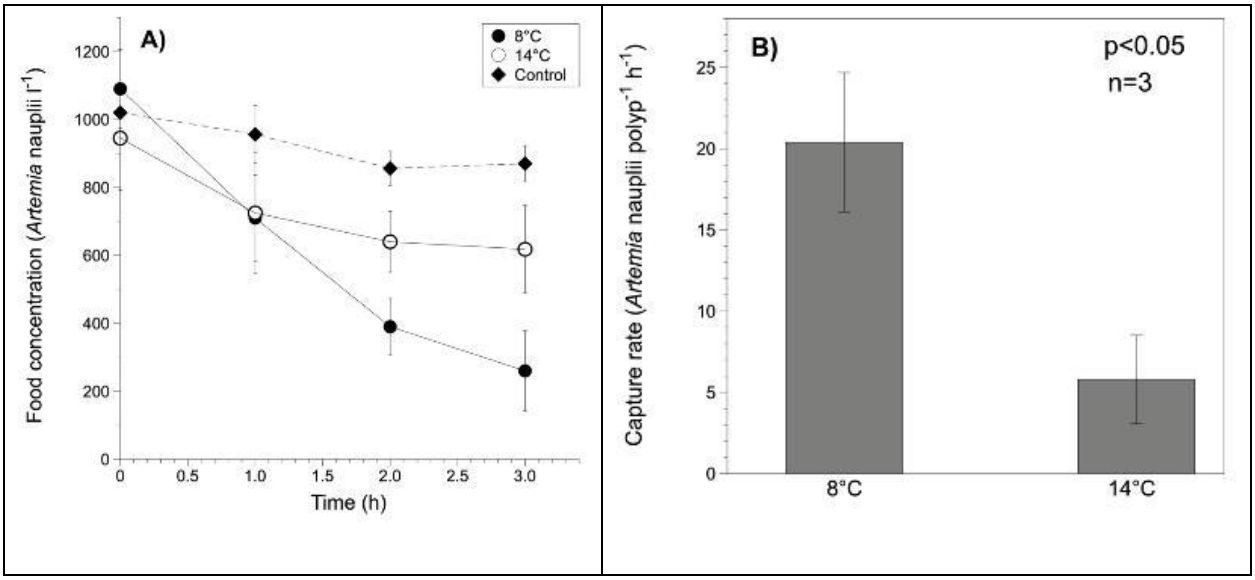

Figure 5-4. Decrease in nauplii over time in the different temperature treatments
Raw concentration of *Artemia* nauplii for each time point (average ± SD), showing the decrease in nauplii over time in the different temperature treatments, including the controls performed to account for the 3D shape of the coral fragment. B) average ± SD of feeding rates in the two different temperatures standardized to number of polyps within each fragment.

The elevated temperature tested in this study (14ºC), which is within the natural maximum variability experienced by this species in situ, caused an approximately 60% increase in respiration and ammonium excretion rates. *Lophelia pertusa* is distributed worldwide in waters from ~4ºC to 14ºC (Rogers 1999, Roberts et al. 2009), and different studies have indicated thermal acclimation, in which respiration rates are not affected by changes in temperature, in the range from 6 to 12ºC (Naumann et al. 2014). *L. pertusa* is able to survive short-term (< 24 h) temperature increases up to 20ºC, while sustained (7 days) exposures to temperatures of 15ºC (Brooke et al. 2013) and 16ºC (Lunden et al. 2014) caused measurable mortality. When exposed to short-term temperature increases within its natural thermal range, for example, 6.5°C to 11°C (Dodds et al. 2007), and 5°C to 15ºC (Dorey et al. 2020), *L. pertusa* has been able to maintain physiological function without cellular damage or oxidative stress response at the expense of increasing oxygen consumption by 50% from 9°C to 11°C (Dodds et al. 2007) and 150% from 5ºC to 15°C (Dorey et al. 2020).

Metabolic alterations driven by temperature have been widely compared using the Q_{10} index, which indicates the proportional change of respiration of biological systems to a temperature increase of 10ºC (van't Hoff and Arrhenius Q_{10} rule). Normally, respiration within a physiologically tolerable temperature range has a Q_{10} of around 2–3 (two to three-fold change in respiration), assuming a linear response (Kruse

et al. 2011). Higher values suggest sensitivity to temperature perturbations and inability to compensate for these changes (Dodds et al. 2007, Q_{10} = 6–8.3). The Q_{10} of 2.3 found in the present study indicates that *L. pertusa* from the Richardson Reef Complex can compensate for the thermal variation within the expected range of temperatures experienced in the natural habitat. This has also been shown for populations of *L. pertusa* from the fjords of Norway (Dorey et al. 2020, Q_{10} = 3) and the warmer Mediterranean Sea (Maier et al. 2019, Q_{10} ~4). Increased respiration and excretion rates will also be expected for *L. pertusa* (and ectotherms in general) under a metabolic curve model (Schulte 2015). However, if energy demand is increasing, feeding ability must increase too (Georgian et al. 2016), otherwise this may threaten the sustainability and functionality of the population (Morato et al. 2020).

The increase in excretion (NH_4) rates with the increase of respiration rates found at the higher temperature conforms to what has been reported for different taxa of marine organisms (Martin et al. 2006), including CWC's (Dorey et al. 2020). Similar patterns have been documented for *L. pertusa* where excretion rates increased with increasing temperature (Dorey et al. 2020). We found that coral fragments exposed to the higher temperature more than doubled their excretion rate compared to ambient temperature, leading to a change in average O:N ratio from 67.7 to 49.5 at elevated temperature (**Table 5-2**). This ratio has been used to explain the proportions and type of substrate being catabolized (protein relative to lipids and carbohydrates) (Mayzaud and Conover, 1988).

Although there was high variability in the O:N observed, the decrease in the ratio at 14ºC is indicative of a shift from a use of lipid-dominated catabolism to a mix of protein and lipid, with some coral fragments relying exclusively on the less efficient protein-dominated catabolism for energy (Pillai and Diwan 2002; Yu et al. 2013). Recent studies with CWCs have found that increasing temperatures from 5°C to 15°C alter the ratio from lipid-dominated to lipid/protein mix (Dorey et al. 2020), while synergistic effects of temperature and ocean acidification interact to shift coral metabolism to a protein-dominated metabolism (Gori et al. 2016). *L. pertusa* could be using its energy reserves (Larsson et al. 2013, Maier et al. 2019) to overcome the increased metabolism driven by the arrival of warm surface waters.

Feeding rates decreased by nearly three-fold at 14°C compared to 8ºC. Tsounis et al. (2010) found capture rates on the order of ~280 *Artemia* nauplii polyp^{-1} h^{-1} at ambient control temperature (12ºC, Mediterranean Sea temperature), compared to ~20 *Artemia* nauplii polyp^{-1} h^{-1} at ambient control temperature (8ºC) from this study. This difference might arise from the higher initial concentration used by Tsounis (10–15 nauplii ml^{-1}) compared to ~1 nauplii ml^{-1} used in the present study. Average capture rates found by Purser et al. (2010), who investigated the influence of flow velocity and food concentration on captures rates of *L. pertusa* from the northeast Atlantic, are comparable to the present study with a similar initial concentration of 1,035 *Artemia* nauplii l^{-1}. Orejas et al. (2016) also found similar capture rates for *L. pertusa*, which ranged between 10 and 22 zooplankton polyp^{-1} h^{-1} .

Feeding performance in CWC strongly depends on food availability, but also on polyp behavior such as polyp expansion and mucus production (Mortensen 2001, Murray et al. 2019). Seawater temperature may affect feeding success in coral species since polyp contraction and nematocyst function could be slower under abnormally high (Ferrier-Pagès et al. 2010) or low temperatures (Johannes and Tepley 1974, Palardy et al. 2005). In this sense, decreased feeding success observed under sub-lethal high temperature (14ºC) may result from reduced polyp expansion and capture efficiency. Even though we did not quantify polyp behavior or mucus production in the present study, these behaviors likely contribute to the energetic unbalance and are probably driving the observed reduction in feeding performance under the natural short-term exposure to high temperatures.

Reduced feeding will ultimately result in unbalanced energetics, where an increase in metabolic rate is not being compensated for by increased food intake, eventually affecting cellular homeostasis and biochemical processes (Gillooly 2001, Schulte 2015). It has been demonstrated that animals can cope with environmental stress if they can access additional energy to maintain homeostasis (Cohen and

Holcomb 2009, Sokolova et al. 2012). It is interesting to note that some CWC communities dwelling in areas considered non-favorable in terms of, for example, calcium carbonate saturation states (Baco et al. 2017, Gómez et al. 2018) or temperature (Mienis et al. 2014), are in areas of high food availability driven by surface primary productivity. Moreover, the abundance and richness of benthic fauna has been shown to correlate with food availability in the water column (Jansen et al. 2018). However, given the 60% increase in metabolic activity with the three-fold decrease in feeding ability found in the present study at elevated temperatures, food supply alone may not be able to provide the extra energy required for physiological adjustments to increasing temperature.

It has been shown that food availability in CWC habitats undergoes complex seasonal dynamics due to hydrodynamic processes, which normally results in discrete pulses of food delivered over short periods of time (Maier et al. 2020). Evidence indicates that food supply around the collection site is dependent on the temperature fluctuations where an increase in temperature is associated with a reduction in high-quality phytodetritus (Mienis et al. 2014), which is an important component of the diet of *L. pertusa* (Maier et al. 2019). However, other hydrodynamic processes (internal waves, upwelling of deeper water masses, advection) can supplement food sources with zooplankton or derived products that coincide with the warmer events recorded in the area (Mienis et al. 2014), which might offer an alternative resource to support the survival of this CWC population.

5.2 Coral Symbiosis and Microbiome

Section Author: Christina Kellogg

At its simplest, symbiosis can be defined as an interaction between two different organisms living together. Within the term exists a continuum defined by the interactions between symbiont and host: mutualism, commensalism, and parasitism. Where on that continuum the relationship exists at any given time may be influenced by environmental conditions. This concept includes the microorganisms associated with a coral, present in its mucus, tissue, and skeleton, otherwise known as the microbiome. By broadest definition this means the coral microbiome includes all three domains of life (Eukaryota, Archaea, and Bacteria), as well as viruses capable of infecting the host animal and all the other cellular microbes (Rosenberg et al. 2007, Vega Thurber and Correa 2011).

Microbial associates have been shown to perform ecosystem services for corals, including fixing nitrogen, cycling waste products, and producing antibiotics to keep unwanted microbes from infecting the coral (Kimes et al. 2010, Olson et al. 2009, Raina et al. 2009, Ritchie 2006). Characterizing the microbial communities associated with deep-sea corals increases our knowledge of biodiversity and can provide insight into the variability or uniqueness of the corals in different habitat types. The coral's microbiome is considered the most genetically adaptable part of the coral, capable of changing its taxonomic composition and functionality in response to environmental change on the order of hours to days (Voolstra and Ziegler 2020, Ziegler et al. 2019). Shifts in the coral-associated microbial community can also be used to detect or monitor coral stress, so it is critical to obtain benchmark datasets that can be used as comparative baselines against future changes, either anthropogenic or environmental, that may affect these deep ecosystems.

Coral bacterial microbiomes have been shown to be distinct from the water column, sediments, and nearby corals of other species (Hansson et al. 2009, Neulinger et al. 2008). Although there has been considerable attention focused on the microbiome of the deep-sea coral *Lophelia pertusa* (*Desmophyllum pertusum*), the microbial associates of most other deep-sea stony corals and octocorals remain unknown (Chapron et al. 2020, Galand et al. 2020, Galkiewicz et al. 2011, Galkiewicz et al. 2012, Kellogg et al. 2017, Kellogg et al. 2009, Meistertzheim et al. 2016, Neulinger et al. 2008, Schöttner et al. 2009, van Bleijswijk et al. 2015, Yakimov et al. 2006).

5.2.1 Methods

5.2.1.1 Culturing Coral-Associated Bacteria

Based on prior research that indicated a *Propionibacterium* sp. could be a conserved coral symbiont (Kellogg 2019), during cruise AT-41 we used two types of agar media to try and isolate this bacterium. The base medium, yeast extract sodium lactate (YESL; **Table 5-4**) is recommended for the isolation and cultivation of *Propionibacterium* species (Atlas 2010), however it is not necessarily a selective medium. Guided by Kishishita et al. (1980), we added 0.02% bromocresol purple to one batch of plates (YESL+BP) and per Forget and Fredette (1962) we added 0.05% sodium azide to a second batch of plates (YESL+SA) in an effort to create more selective media. Further, we added oxyrase enzyme (Oxyrase, Inc., Mansfield, OH) to both media prior to pouring the agar into Oxydish Petri dishes. This enzyme scavenges oxygen, and the shape of the dish removes air headspace, such that each dish functions as an individual anaerobic chamber. A third medium, Czapek Dox, was also inoculated in an effort to isolate filamentous fungi (Zhang et al. 2013).

We processed samples from three separate *L. pertusa* colonies collected at the Richardson Ridge Complex (dives A4962, A4963). We placed a piece of coral in a sterile aluminum weigh boat and crushed using a sterile hammer to expose tissue and then we made a slurry by adding 5 mL of sterile buffer containing 0.5% KH_2PO_4, 0.4% Na_2HPO_4 and 0.1% Tween 80 (Kishishita et al. 1980). Aliquots (100 µL) of slurry were then spread-plated in triplicate on each of the three media. We incubated these agar plates at 4°C for 3 months after inoculation, but we observed no growth.

During cruise RB1903 we made another attempt at culturing bacteria from *L. pertusa*, focused again on *Propionibacterium* and nitrogen fixers. We used two media, YESL and Propionibacterium Agar (**Table 5-4**; Atlas 2010), trying to isolate *Propionibacterium*, and three media, Jensen's, Burks, and Paul & Newton (**Table 5-4**; Atlas 2010, Paul and Newton 1961, Rao 1977) trying to isolate bacteria capable of nitrogen fixation. In all cases, instead of Petri dishes, the media were made as semi-soft agar by adding 1.5 grams of agar per liter and sterilized in glass culture tubes. The idea of semi-soft agar in tubes is that a stabbed inoculum allows motile bacteria to choose the level of oxygen they prefer by moving to the surface of the agar or growing at some depth within it.

We inoculated all tubes from two *L. pertusa* colonies collected in biobox compartments 3 and 6 at 756 m during dive J2-1128 at Richardson Hills. We rinsed the coral pieces each with 5 mL of sterile solution of phosphate buffered saline (1xPBS) to remove any loosely adhered microbes and mucus. For each biobox sample, we placed a piece of coral roughly 20 polyps in size in a sterile aluminum weigh boat, crushed it using a sterile hammer to expose tissue and then we made a slurry by adding 10 mL of sterile 1xPBS. We transferred this slurry to a sterile 15-mL tube and then vortexed and inverted the tube for 5 minutes to mix it well. We kept slurry tubes on ice to keep them cool during inoculations. For each semi-soft agar tube, we used a single-use sterile plastic inoculating loop to pick up a loopful of slurry and then plunged it into the agar in the tube.

We incubated agar tubes at 4°C for 5 weeks at which point growth was visible in all tubes. Material from each agar tube was isolation-streaked onto full-strength (15%) agar Petri dishes of each of the original media (**Table 5-4**) and then incubated at 10°C. The two *Propionibacterium* media grew what appeared to be a single colony phenotype while the three nitrogen-fixer media grew three to four colony phenotypes, with overlap in phenotype between media. Ultimately, we isolated 64 colonies across all media. Of those, we were able to successfully amplify the 16S rRNA genes from the 42 colonies isolated on nitrogen-fixer media. All 42 colonies were identified as *Pseudomonas*, despite having four different colony morphologies. We were unable to maintain or archive these cultures.

Table 5-4. Semi-soft nutrient agars tested for bacterial isolation from *L. pertusa*

Target	Medium	Ingredient	Per Liter
Propionibacterium	Propionibacterium Agar	Digest of casein	10.0 g
		Sodium lactate	10.0 g
		Yeast extract	5.0 g
Propionibacterium	Yeast Extract Sodium Lactate	digest of casein	10.0 g
		Yeast extract	10.0 g
		Sodium lactate	10.0 g
		KH2PO4	2.5 g
		MnSO4	5.0 mg
Nitrogen-fixing bacteria	Jensen's Medium	Sucrose	20.0 g
		K2HPO4	1.0 g
		MgSO4	0.50 g
		NaCl	0.50 g
		FeSO4	0.10 g
		Na2MoO4	0.005 g
		CaCO3	2.0 g
Nitrogen-fixing bacteria	Burks Medium	MgSO4 * 7H2O	0.20 g
		K2HPO4	0.80 g
		KH2PO4	0.20 g
		CaSO4 * 2H2O	0.130 g
		FeCl3	0.00145 g
		Na2MoO4 * 7H2O	0.000253 g
		Sucrose	20.0 g
Nitrogen-fixing bacteria	Paul and Newton	K2HPO4	0.5 g
		MgSO4 * 7H2O	0.2 g
		NaCl	0.2 g
		CaSO4 * 2H2O	0.1 g
		FeSO4 * 7H2O	0.1 g
		Na2MoO4 * 7H2O	0.05 g
		2% Mannitol	20.0 g

A master's student from Western Carolina University, S. Gold, also provided some culture media for cruise RB1903 in the form of both liquid media and agar plates of a dilute general medium, a medium targeting chitin-digesters, and a medium targeting ammonia-oxidizers (Gold 2020). We inoculated these various media from the same coral slurries described above (*L. pertusa* biobox samples 3 and 6) and from identically generated slurries from *L. pertusa* sample RB1903-J2-1129-Q4. The media were returned to Gold on 16 April 2019 during a port day and all subsequent processing and isolation were conducted at Western Carolina University. A total of 27 bacterial isolates were characterized, with 80% being *Pseudoalteromonas* spp., and the rest a collection of *Enterobacter*, *Enterococcus*, *Pantoea*, *Photobacterium*, *Serratia*, and *Vibrio* (Gold 2020).

5.2.1.2 Coral-Associated Microbial Diversity (16S Amplicon Surveys)

One of the most widely used methods to capture an overview of the bacterial and archaeal diversity present in a coral's microbiome is to conduct an amplicon survey of the 16S ribosomal RNA gene

(Pollock et al. 2018b). This metabarcoding approach provides a list of prokaryotic taxa and some sense of their relative abundance. This furnishes a foundation of "who is there" upon which further hypotheses and research can be built to determine "what are they doing."

5.2.1.3 Method Comparison of Preservation and Extraction Methods

We used samples of *L. pertusa* and *Paragorgia johnsoni* that we had collected during cruise AT-41 in conjunction with several tropical coral genera to test the effects of three preservatives commonly used for environmental microbiome preservation (RNAlater, DNA/RNA Shield, and liquid nitrogen), and two extraction kits (the Qiagen DNeasy PowerBiofilm kit and the Promega Maxwell RBC kit with modifications) (Pratte and Kellogg 2021). Our results indicated that there was no single combination of preservative and extraction method (of those tested) that was superior to the others across all coral species.

The combination of DNA/RNA Shield and PowerBiofilm appeared to perform best for *L. pertusa* and *P. johnsoni* samples in terms of a greater number of ASVs (**Figure 5-5**). However, these small differences were not statistically significant; in fact, there were not statistically significant differences in any alpha or beta diversity metrics and preservative. Some loss of diversity was indicated in liquid nitrogen preserved samples, based on significantly lower detection of SAR202 clade, Nitrospinae, and Syntrophobacterales. The variance among preservation types and extraction methods within each genus were less than the variance detected among microbial communities between coral genera (**Figure 5-6**) indicating that comparisons between coral species are less affected by differing preservation/extraction methods than comparisons within a coral species, because the more subtle intra-species differences would be of similar magnitude to methodological effects.

Our study also confirmed the importance of including positive and negative controls (known mock community and kit extraction blanks) to allow for assessing bias and contamination. Given that methods are rapidly evolving, and no combination of preservation and extraction is without bias, it is expected that method testing will be on-going in the microbiome community. Based on this experiment, RNAlater or DNA/RNA Shield followed by freezing, and any extraction method that included both physical and chemical lysis (bead-beating) appears sufficient for most interspecies coral microbiome comparisons (Pratte and Kellogg 2021). The sequencing data associated with the methodology comparison are available as a USGS data release (Kellogg et al. 2021) or from the NCBI Sequence Read Archive as BioProject PRJNA544686.

5.2.2 Results

5.2.2.1 Microbiomes of Four Deep-Sea Corals

The microbiomes of the majority of azooxanthellate CWC species remain undescribed. This project provided the opportunity to characterize the bacterial and archaeal communities of a pair of octocoral species within the genus *Acanthogorgia* (*A. aspera* and *A. spissa*) and compare them against a pair of scleractinian species that have recently been combined into a single genus (*L. pertusa* (=*Desmophyllum pertusum*) and *Desmophyllum dianthus*; Addamo et al. 2016).

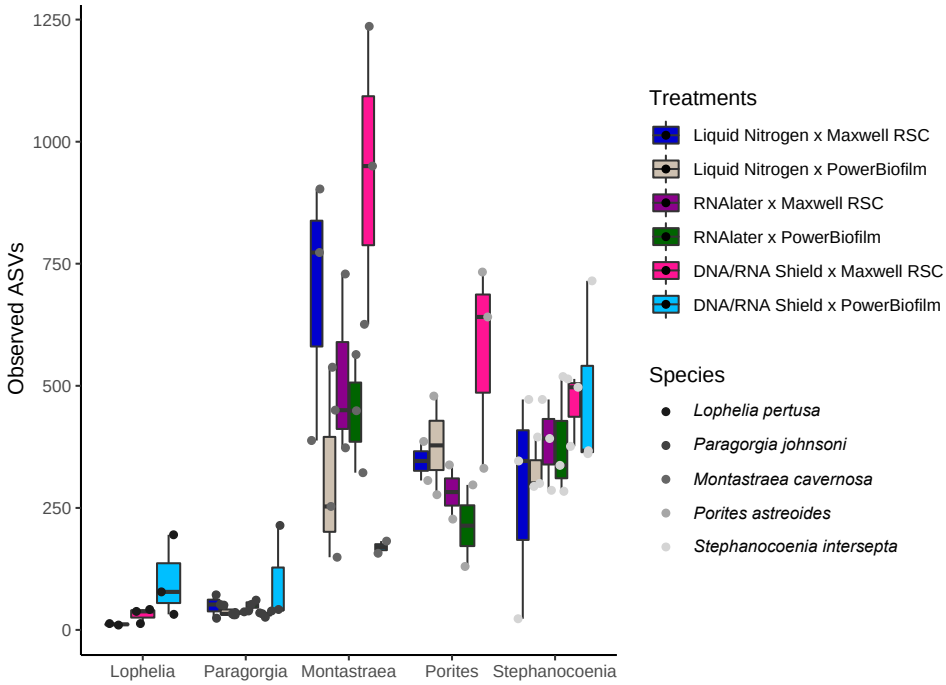

Figure 5-5. Method comparison observed ASVs for each coral by genus
Preservative x extraction method treatments (from left to right for each coral): dark blue = liquid nitrogen x Maxwell RSC; gray = liquid nitrogen x PowerBiofilm; purple = RNAlater x Maxwell RSC; green = RNAlater x PowerBiofilm; pink = DNA/RNA Shield x Maxwell RSC; light blue = DNA/RNA Shield X PowerBiofilm.

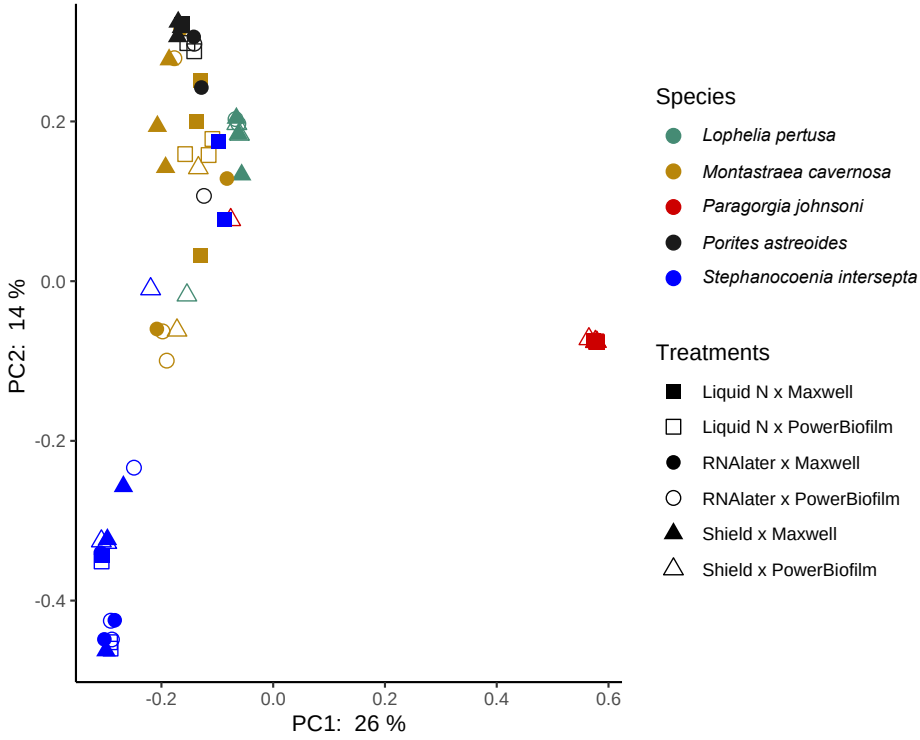

Figure 5-6. Method comparison observed ASVs for each coral by genera
Principal coordinate plots based upon a Bray-Curtis dissimilarity matrix of all coral species and treatments (preservative x extraction method). Microbial communities clustered strongly according to coral species rather than treatment.

Table 5-5. Coral samples processed for microbiome characterization

Sample ID	Date	Site	Coral	Depth (m)	Latitude	Longitude	Temp (°C)
685Q3	5/11/13	Norfolk Canyon	*A. aspera*	1,336	37.04989	-74.51357	4.2
685Q5	5/11/13	Norfolk Canyon	*A. aspera*	1,311	37.04991	-74.51234	4.2
RB1903-J2-1132-Q1	4/22/19	Pamlico Canyon	*A. spissa*	1,476	34.93145	-75.15013	3.9
RB1903-J2-1132-Q2	4/22/19	Pamlico Canyon	*A. spissa*	1,476	34.93145	-75.15013	3.9
RB1903-J2-1132-Q5	4/22/19	Pamlico Canyon	*A. spissa*	1,476	34.93145	-75.15013	3.9
RB1903-J2-1132-Q6	4/22/19	Pamlico Canyon	*A. spissa*	1,402	34.93160	-75.15148	4.0
AT41-A4964-Q1	8/25/18	Blake Escarpment	*D. dianthus*	1,216	31.32269	-77.24234	4.3
RB1903-J2-1131-Q4	4/18/19	Blake Deep	*D. dianthus*	1,321	31.28760	-77.23677	4.1
RB1903-J2-1131-Q6	4/18/19	Blake Deep	*D. dianthus*	1,320	31.28767	-77.23660	4.2
RB1903-J2-1131-Q8	4/18/19	Blake Deep	*D. dianthus*	1,321	31.28762	-77.23677	4.1
RB1903-J2-1132-Q3	4/22/19	Pamlico Canyon	*D. dianthus*	1,567	34.93077	-75.15035	3.9
RB1903-J2-1132-Q4	4/22/19	Pamlico Canyon	*D. dianthus*	1,567	34.93077	-75.15035	3.9
RB1903-J2-1132-Q8	4/22/19	Pamlico Canyon	*D. dianthus*	1,567	34.93077	-75.15035	3.9
AT41-A4962-Q2	8/23/18	Richardson Ridge	*L. pertusa*	695	32.00998	-77.39507	9.2
AT41-A4963-Q2	8/24/18	Richardson Ridge	*L. pertusa*	827	31.98494	-77.41471	5.0
AT41-A4963-Q3	8/24/18	Richardson Ridge	*L. pertusa*	789	31.98449	-77.41393	6.8
AT41-A4963-Q8	8/24/18	Richardson Ridge	*L. pertusa*	684	31.98459	-77.41106	10.9
AT41-A4963-Q10	8/24/18	Richardson Ridge	*L. pertusa*	685	31.98450	-77.41122	10.9
AT41-A4968-Q1	8/29/18	Cape Fear Coral	*L. pertusa*	381	33.57256	-76.46505	7.0
AT41-A4968-Q2	8/29/18	Cape Fear Coral	*L. pertusa*	460	33.57551	-76.46792	7.7
RB1903-J2-1133-Q3	4/23/19	Pea Island Seep	*L. pertusa*	296	34.67360	-75.79777	11.4
NF1708-10-01	8/19/17	Many Mounds	*L. pertusa*	480	26.20755	-84.72610	ND
NF1708-10-08	8/19/17	Many Mounds	*L. pertusa*	496	26.20576	-84.72679	ND
NF1708-11-04	8/19/17	Many Mounds	*L. pertusa*	432	26.20725	-84.71101	ND
NF1708-12-01	8/20/17	Okeanos Ridge	*L. pertusa*	521	25.66988	-84.58431	7.1

In addition to the collections during the two Deep SEARCH cruises (AT-41 and RB1903), we included some additional samples of *L. pertusa* from the GOM and *A. aspera* from Norfolk Canyon (**Table 5-2**). We sampled branches of each coral colony using the manipulator arm of an undersea vehicle and placed into individual, thermally insulated containers that had been specially cleaned to reduce microbial contamination (Kellogg and Pratte 2021).

Onboard ship, we lightly rinsed the coral samples with sterile 1xPBS and preserved in RNAlater at -20°C. Subsequently, we extracted DNA from the coral samples using the Qiagen DNeasy PowerBiofilm kit and sequenced using primers 341F/806R targeting the V3-V4 region of the 16S rRNA gene. These sequence data are available as a USGS data release (Kellogg and Voelschow 2021) or from the NCBI Sequence Read Archive as BioProject PRJNA699458. An initial attempt at sequencing using V4 primers 515F/806R failed because they almost exclusively amplified coral mitochondrial DNA rather than microbial DNA. We conducted data analysis using QIIME2 (Bolyen et al. 2019, Estaki et al. 2020) and MEGA X (Kumar et al. 2018); specific details can be found in Kellogg and Pratte (2021).

Some prior work on tropical scleractinian corals has indicated conservation of the bacterial community composition at the host genus level (Littman et al. 2009) and that parts or all of the coral microbiome follows host phylogeny (Pollock et al. 2018a, Sunagawa et al. 2010). This would imply that there should be a fair amount of similarity in the microbiomes of *L. pertusa* and *D. dianthus*, since they have been combined into one genus based on their genetic similarity (Addamo et al. 2016). In fact, there was more taxonomic richness in the bacterial communities associated with *D. dianthus* compared to the community associated with *L. pertusa* (**Figure 5-7**).

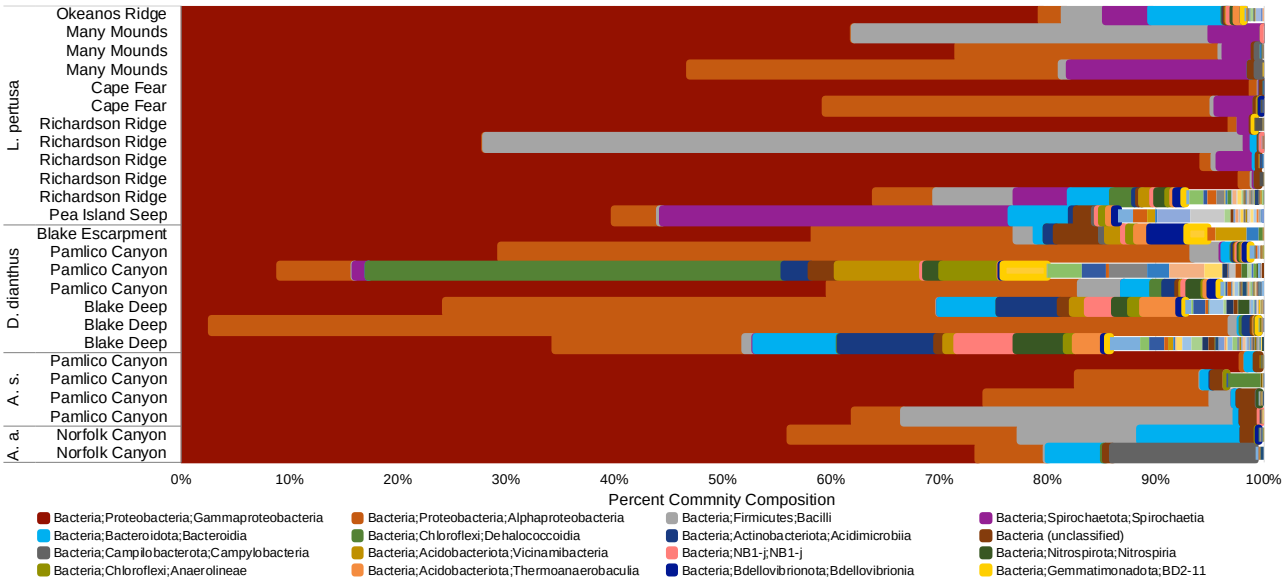

Figure 5-7. Bacterial community composition at the class level for four corals
From top to bottom: *L. pertusa, D. dianthus, Acanthogorgia spissa* (abbreviated A.s.), and *A. aspera* (abbreviated A.a.). Only the top 16 classes are listed in the legend (thickened bars).

Moreover, the microbial communities of *L. pertusa* and *D. dianthus* were significantly different. A pairwise comparison of Faith's Phylogenetic Diversity resulted in a p-value of 0.007, and an analysis of similarity (ANOSIM) resulted in a p-value of 0.002 (r = 0.648). This difference is also reflected in the separation between the two corals in **Figure 5-8 B**. The one exception is the *L. pertusa* sample from Pea Island Seep, which clusters with *D. dianthus*; this sample was collected from a shallow depth and high temperature (**Table 5-2**), so that may explain its unusual microbiome.

An obvious caveat to this work is that in the western Atlantic, we typically encountered these two corals in different depth zones (**Table 5-2**) and habitats: *L. pertusa* mounding on hardbottom vs. *D. dianthus* on vertical walls and underhangs. Differing habitats, which likely also translates into different diets, may have a substantial effect on the coral microbiomes (Galand et al. 2020, Hernandez-Agreda et al. 2016, Pantos et al. 2015).

In contrast, the two *Acanthogorgia* spp. clustered much more closely **Figure 5-7, Figure 5-8 A**) and were not statistically differentiable. This echoes similar work that found microbiomes of two deep-sea octocorals in the genus *Anthothela* to be indistinguishable (Lawler et al. 2016).

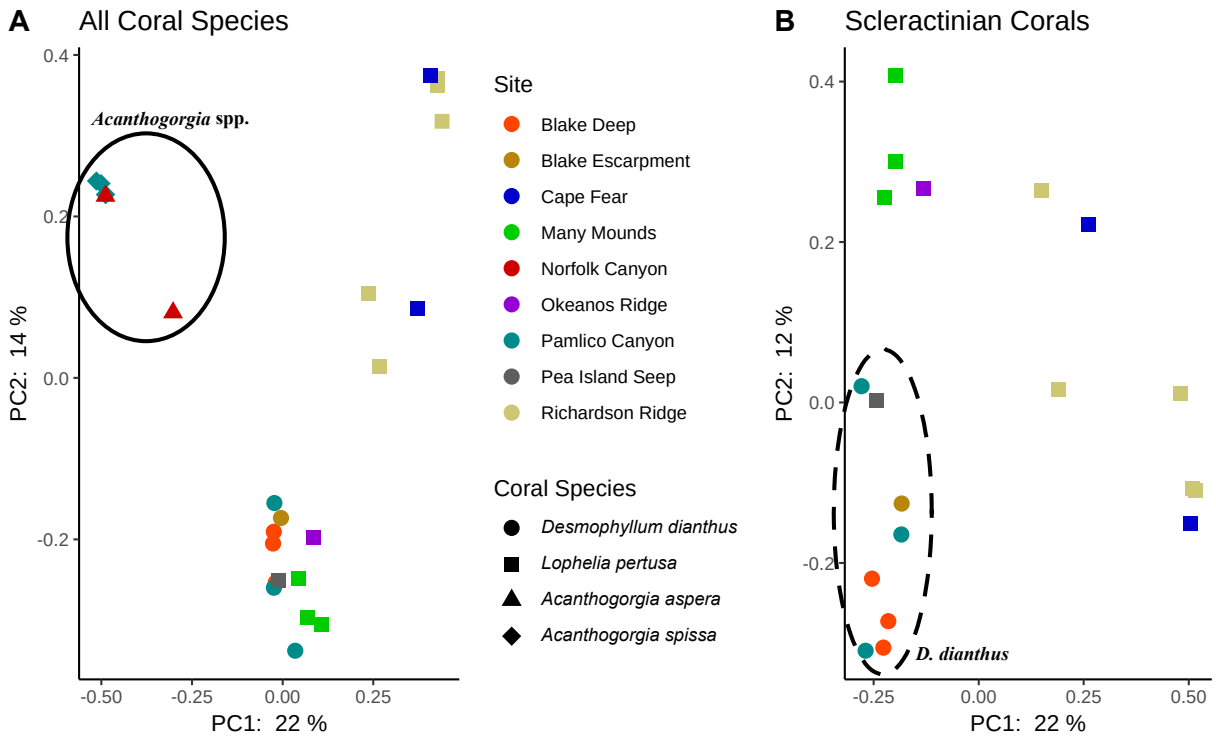

Figure 5-8. PCoA for four deep-sea coral microbiome samples
The PCoAs are based upon Bray-Curtis dissimiliarity matrices. Panel A includes all coral species, with a black oval indicating the cluster of the two *Acanthogorgia* spp. Panel B independently analyses only the two scleractinians, *D. dianthus* and *L. pertusa*, with a dashed elipse indicating the cluster of *D. dianthus* samples. A version of this figure was previously published in Kellogg and Pratte (2021).

Our most exciting finding was the dominance of the bacterial group *Endozoicomonas* in both *Acanthogorgia* spp. microbiomes and, even more unusual, in the microbiomes of *L. pertusa* from Richardson Ridge and Cape Fear sites (Kellogg and Pratte 2021). This bacterial group has been commonly associated with (and often dominates) the microbiomes of tropical scleractinian corals as well as octocorals in tropical and temperate waters (Apprill et al. 2016; Bayer et al. 2013a, 2013b; Gignoux-Wolfsohn et al. 2017; McCauley et al. 2020; Morrow et al. 2012; Pogoreutz et al. 2018; Reigel et al. 2020; Roder et al. 2015; Speck and Donachie 2012; van de Water et al. 2016; Vezzulli et al. 2013). However, these bacteria have been notably uncommon in deep-sea, CWCs.

A comparison of the microbiomes of six deep-sea octocoral species found *Endozoicomonas* to be rare in *Anthothela* spp. and undetectable in the rest (Kellogg 2019). A key exception is *Madrepora oculata*, whose microbiome has been shown to be dominated by *Endozoicomonas* (Galand et al. 2018, Hansson et al. 2009, Meistertzheim et al. 2016). Those same three studies also examined *L. pertusa* collected from the same sites at the same time as *M. oculata* via the same methods and found few or no *Endozoicomonas*; this implies that it is not an environmental limitation but likely driven by the coral host. Prior microbiome studies of *L. pertusa* from the Mediterranean (Galand et al. 2018, Meistertzheim et al. 2016, Yakimov et al. 2006), a Norwegian fjord (Neulinger et al. 2008), Rockall Bank (Hansson et al. 2009; van Bleijswijk et al. 2015), and GOM/western Atlantic (Galkiewicz et al. 2011, Kellogg et al. 2017, Kellogg et al. 2009) have either not detected *Endozoicomonas* or found it to be in extremely low abundance.

There were differences in *Endozoicomonas* sequence variants (genotypes) present in *L. pertusa* and *Acanthogorgia* spp. microbiomes, represented by the different color blocks in **Figure 5-9**. It is not unusual for scleractinians and octocorals to host different types of *Endozoicomonas* (Kellogg 2019). The

Endozoicomonas from *L. pertusa* at Richardson Ridge and Cape Fear sites clustered together and were most similar to a sequence from *L. pertusa* mucus obtained from Rockall Bank in the eastern Atlantic (van Bleijswijk et al. 2015). The sequences from *L. pertusa* in the GOM clustered separately. The *Endozoicomonas* from *Acanthogorgia* spp. were most similar to sequences from the Caribbean seafan *Gorgonia ventalina* (Sunagawa et al. 2010).

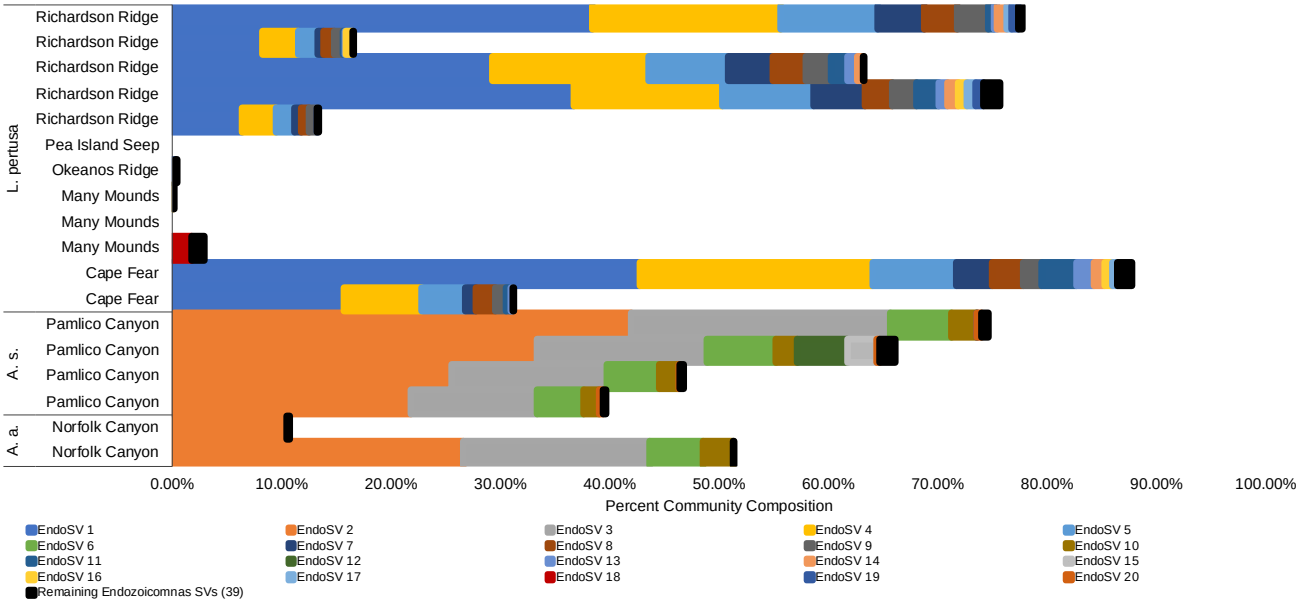

Figure 5-9. Relative abundance of *Endozoicomonas* sequence variants
Variants present in three deep-sea coral microbiomes. The top 20 most common *Endozoicomonas* genotypes are shown, the remaining 39 were combined. *Acanthogorgia spissa* is abbreviated A.s. and *A. aspera* as A.a. A version of this figure was previously published in Kellogg and Pratte (2021).

It is unclear what is driving the unexpected diversity and dominance of *Endozoicomonas* in *L. pertusa* at the Richardson Ridge and Cape Fear sites. These sites are known to be affected by the Gulf Stream even at depth (Bane and Brooks 1979, Legeckis 1979, Popenoe 1994, Stetson et al. 1962, Bane and Brooks 1979, Legeckis 1979, Popenoe 1994), resulting in extreme variability of water temperature, salinity, nutrients, and current speeds (Mienis et al. 2014). These environmental factors have been shown to affect coral microbiomes in tropical systems (Guppy and Bythell 2006, Lee et al. 2017, Littman et al. 2009, Zaneveld et al. 2016). However, shallow-water coral studies have consistently shown that *Endozoicomonas*-dominated microbiomes lose these putative symbionts when under stress, shifting towards a more diverse microbiome (Maher et al. 2019, Morrow et al. 2015, Neave et al. 2016, Shiu et al. 2020, van de Water et al. 2016, Vezzulli et al. 2013).

Moreover, the majority of coral-associated *Endozoicomonas* are sensitive to temperatures outside their optimal range of 15–30°C (Kellogg 2019, Shiu et al. 2020). There are no prior examples of a coral that did not normally host a multitude of *Endozoicomonas* gaining them as a high proportion of the microbiome. Yet, *L. pertusa* at two highly variable sites have become dominated by unusual *Endozoicomonas* genotypes, implying that these bacteria are atypical in their compatibility with rapid temperature shifts and may be capable of novel biogeochemical services to the coral (Kellogg and Pratte 2021).

5.2.2.2 Microbial Functions in Coral Microbiomes

Nitrogen and carbon fixation and translocation to coral tissue has been shown for *L. pertusa* (Middelburg et al. 2015). Several studies of deep-sea coral microbiomes have identified the possibility for complete or

near-complete nitrogen cycling based on the known functional capabilities of certain taxa of bacteria (Kellogg et al. 2016, Lawler et al. 2016). Further, predictive functional profiling has indicated the potential for chemoautotrophy, nutrient cycling, and antibiotic production by *L. pertusa*'s microbiome (Kellogg et al. 2017). However, much remains to be learned about the actual functional capacity of microbes in these corals.

The GeoChip 5.0S microarray contains approximately 60,000 gene probes that detect microbial enzyme-encoding genes involved in biogeochemical cycling (carbon, nitrogen, phosphorus, sulfur), as well as categories like virulence, antibiotic resistance, and metal resistance (Wang et al. 2014). We made attempts to extract and apply both RNA and DNA from coral samples to the microarrays (to distinguish between genes actively being transcribed vs. those that are simply present). Unfortunately, the complimentary DNA (cDNA) that was reverse transcribed from the RNA extractions did not support adequate labeling so we were only able to assay the original DNA.

Table 5-6. Coral samples processed for microarray analysis

Sample ID	Date	Site	Coral	Depth (m)	Latitude	Longitude	Temp (°C)
RB1903-J2-1135-Q3	4/25/19	Cape Lookout	*A. aspera*	944	33º 55.135	-75º 50.010	4.5
RB1903-J2-1132-Q1	4/22/19	Pamlico Canyon	*A. spissa*	1,476	34.93145	-75.15013	3.9
AT41-A4964-Q1	8/25/18	Blake Escarpment	*D. dianthus*	1,216	31.32269	-77.24234	4.3
RB1903-J2-1131-Q4	4/18/19	Blake Deep	*D. dianthus*	1,321	31º 17.256	-77º 14.206	4.1
RB1903-J2-1132-Q8	4/22/19	Pamlico Canyon	*D. dianthus*	1,567	34º 55.846	-75º 9.021	3.9
RB1903-J2-1130-Q1	4/17/19	Savannah Bank	*E. profunda*	509	31º 45.289	-79º 11.639	8.6
RB1903-J2-1130-Q2	4/17/19	Savannah Bank	*E. profunda*	519	31º 45.524	-79º 11.481	8.6
RB1903-J2-1130-Q4	4/17/19	Savannah Bank	*E. profunda*	509	31º 45.278	-79º 11.645	8.6
AT41-A4963-Q2	8/24/18	Richardson Ridge	*L. pertusa*	827	31.98494	-77.41471	5.0
AT41-A4963-Q8	8/24/18	Richardson Ridge	*L. pertusa*	684	31.98459	-77.41106	10.9
RB1903-J2-1133-Q3	4/23/19	Pea Island Seep	*L. pertusa*	296	34.67360	-75.79777	11.4

Samples of three colonies each of scleractians *Desmophyllum dianthus*, *Enallopsammia profunda*, and *L. pertusa*, plus samples from one colony each of *Acanthogorgia aspera* and *A. spissa* (**Table 5-4**) were processed for application to microarrays. We preserved the samples in liquid nitrogen and extracted DNA from two replicate subsamples per coral using the Qiagen PowerBiofilm kit, then combining to increase DNA concentrations. The DNA samples were sent to Glomics, Inc for labeling, incubation, hybridization, and scanning.

The intention of this study element was to assess the metabolic potential of the microbial communities (bacterial, archaeal, eukaryotic) associated with deep-sea corals and determine how the metabolic potential differs between different life-history traits, including skeleton type and colonial structure. These data and full results are published (Pratte et al. 2023) and raw data are available from a USGS data release (Kellogg and Voelschow 2023).

5.2.3 Conclusions

Cataloging microbial baselines for these CWC species is a critical first step to understanding and predicting the ecosystem services their microbiomes contribute, as well as providing a benchmark against which to measure changes in response to environmental change or anthropogenic impacts.

5.3 Scleractinian Growth Rate

Section Authors: Nancy Prouty, John Schiff, Sandra Brooke

Several authors have described the formation of growth bands in shallow-water corals (Barnes and Lough 1989, 1993; Taylor et al. 1993; Le Tissier et al. 1994), but there is less information on growth and skeletal structure in azooxanthellate scleractinians (Freiwald et al. 1997, Nagelkerken et al. 1997). Growth rates of *Lophelia* (patterns and rate of corallite extension) have been studied using growth bands and/or stable oxygen isotope analysis (Wilson 1979b, Mikkelsen et al. 1982, Freiwald et al. 1997, Mortensen and Rapp 1998). Mean annual linear extension (LE) rate varies between 2 and 25 mm/yr (average 11 mm/yr) for *Lophelia* sampled from Atlantic coral structures (Wilson 1979b, Mikkelsen et al. 1982, Freiwald et al. 1997, Mortensen and Rapp 1998).

A growth study on *Lophelia* maintained in aquaria (Mortensen 2000) showed a similar LE rate of 9.4 mm/yr using growth bands and direct measurement. Mortensen (2000) suggested that growth line formation in *Lophelia* is correlated with seasonal temperature variations but also noted that temperature may co-vary with other factors such as food supply. Aquarium studies of *Lophelia* in Norway and Scotland (Mortenson 2000, Roberts and Anderson 2002) indicated that increased food supply was followed by high extension rates. Therefore, seasonal changes in food supply, rather than temperature directly, may be controlling growth rates of *Lophelia* in the field. During the 2018 Deep SEARCH cruise, we explored an unusual series of coral mounds on the eastern Blake Plateau. These mounds, named the Richardson Hills, were deeper than most, and had anomalous water-column conditions that ranged from ~ 5ºC at the base of the mound at 1,000 m to 11ºC at the top (800 m). The corals were abundant and appeared healthy, but the conditions were unlike those observed elsewhere in the region.

We deployed the transplant experiment within the coral habitat on one of these mounds. The objective of this experiment was to assess growth and survival of selected species of deep-sea scleractinians using in situ deployment of coral fragments. In addition to the traditional staining techniques used to assess transplant growth rates (Brooke and Young 2009), we used a novel photogrammetric approach to test whether this is an effective non-destructive method of assessing volumetric and linear growth.

5.3.1 Methods

5.3.1.1 Experiment Deployment

Fragments of *Lophelia pertusa, Enallopsammia* cf. *profundai,* and *Madrepora oculata* were collected on 22 August, 2018 using the DSV *Alvin* (dive A4962) from a coral mound in the Richardson Hills area of the study site. We maintained the fragments in the ship cold room at -7ºC and stained them for 8 hours in water baths containing a 10-ppm solution of calcein, which is incorporated into the coral skeleton. After staining, we mounted each fragment on the upper part of a ¾ inch PVC union fitting using cyanoacrylate glue and Two Little Fishes aquatic epoxy. We counted and documented the number of live and dead polyps to assess survival, and logged the fragments attached to one of four (A, B, C, D) transplant units for deployment back on the collection reef. Each transplant unit had two fragments of *L. pertusa* and one each of the other two species. Prior to mounting on the transplant units for deployment, we photographed each fragment from multiple angles for subsequent generation of 3D models. We recovered the transplant units on 14 April 2019 using the ROV *Jason II* (dive J-1129) and removed the fragments. We counted the number of live and dead polyps on each fragment for comparison with pre-deployment data and the coral tissue was removed for transport of the skeleton to the lab for further processing.

5.3.1.2 Image Capture

We placed each coral fragment on a turntable inside an 18-in^3 photo light box, against a non-reflective, black background. We marked the base of each fragment with identifiable markings, using multi-colored permanent ink pens, prior to image acquisition. These markings are beneficial to software-generated and manual alignment during modeling. We measured marking lengths and spacing at various locations, to aid scaling during modeling. The photo light box was equipped with LED lights, which we adjusted to illuminate the fragment, without overexposing any structural features. We captured at least fifty 45.7 megapixel RAW-format images of each fragment, using a Nikon Z7 camera mounted to a tripod. We rotated coral fragments between images, ensuring at least 50% overlap between images. We adjusted the tripod height and camera positioning periodically during photographing, to capture the fragment from above and below, which is necessary to create 360° structural models.

5.3.1.3 Photo Processing and Masking

We sorted RAW images by sample using Adobe® Bridge 2019. We opened images in groups, by fragment sample, in Adobe® Camera RAW, we used a photo processing program accessible from Adobe® Bridge Camera RAW to adjust image properties prior to photogrammetric modeling. Contrast, texture, white balance, shadows, highlights, sharpening, and noise reduction properties were adjusted, when necessary, to enhance image details, while minimizing noise. All image properties were equally adjusted for each photo in the sample, in order to maintain comparable pixel-to-pixel similarities between photos. We exported adjusted images as .TIFF files—Agisoft Metashape's preferred file type for photogrammetry—at 300 pixel per inch resolution, without image resizing or compression. We repeated this process for each fragment sample.

We created masks to isolate the fragment in each image, which assists photo alignment during modeling. Although the Agisoft Metashape program has masking capabilities, masking in Adobe® Photoshop resulted in more precise subject identification; improving the accuracy of image masks and minimizing the amount of accidental background pixels that were included in resulting models.

To create masks, we first opened each TIFF image file in Adobe® Photoshop. The "Select Subject" tool was used to select the fragment from the image. "Add selection" and "Remove Selection" features were used to fine tune the fragment selection, making sure all fragment portions were included and background portions were excluded. We deleted the selected fragment, and a white (#FFFFFF) "New Fill Layer" was created in its place. We then selected the inverse (background) region of the image, and a black (#000000) "New Fill Layer" was created to take its place. The resulting black (background, or mask) and white (fragment, or subject) version of the image is read by Agisoft Metashape as areas of the image to mask or observe when modeling. We exported the resulting mask as a .PNG file at maximum resolution, using the same image file name as the original. We repeated this process for each TIFF image.

5.3.1.4 Photogrammetry

We modeled fragments using Agisoft Metashape 2019. Camera settings and Agisoft parameters were checked for accuracy prior to starting each model. We then added all images associated with an individual fragment to the workspace and checked for image quality. Images with quality levels lower than 0.50 were disabled or removed, and no longer used in model creation. All masks were imported at once, by entering "{filename}.PNG" as the mask file name, which associates each image with its affiliated mask. Models were created for each fragment, following the workflow procedure (**Figure 5-10)**.

Figure 5-10. Schematic of workflow for creating models of coral fragments

5.3.1.5 Model Repair and Quantification

We imported completed models into Autodesk® Netfabb 2018 as .STL files. We used Netfabb tools to close holes and detect and remove any intersecting surfaces, which can artificially inflate surface area measurements. We used the Netfabb "Standard Analysis" tool to quantify the meshed model's surface area and volume. Netfabb measurement tools were used to measure the average LE of each sample. We quantified LE by measuring the planar distance (D) between two points located at the base and top of a polyp (p) on the triangulated mesh. We measured planar distances for each recognizable coral polyp. The average planar distance of all coral polyps (n_p) was used as the LE for that sample:

$$LE = \frac{\sum D_{p1} + D_{p2} + D_{p3} + D_{pn\ldots}}{n}$$

Growth metrics can be measured by subtracting measurements of the "after deployment" models from initial "before deployment" models. Image acquisition, photogrammetric modeling, and triangulated mesh measurement methods must remain consistent during final and initial measurements in order to derive growth metrics. These methods can be used to quantify changes in surface area, volume, or LE over time.

5.3.1.6 Analysis of Growth Using Stain Bands

After we completed the images for the models, we analyzed the fragments for growth using the calcein staining protocols. We exposed each fragment to a fluorescent light (465–495 nm) to identify stained areas. We cut slices of skeleton (2–3 mm) showing staining (usually younger polyps and branch tips) perpendicular to the longitudinal axis of stained polyps using a diamond blade and slices were mounted on microscope slides using cyanoacrylate glue. We viewed the sections under a dissecting microscope using florescent light, with the objective of assessing radial growth measurements using the Calcien bands.

5.3.2 Results

During transfer from the cold room to the submersible biobox, transplant unit B was accidentally broken, leaving only A, C, and D units for deployment. The post-deployment fragments for the remining units showed very high survival overall (**Figure 5-11A, B**), with *M. oculata* showing the highest (99.14%), followed by *E. profunda* (98.47%) and *L. pertusa* (97.51%). A one-way ANOVA showed no significant difference in mean survival among species ($F = 0.354$; $p = 0.711$). Survival was high, but there was a small net loss of polyps, indicating little or no growth during the deployment period.

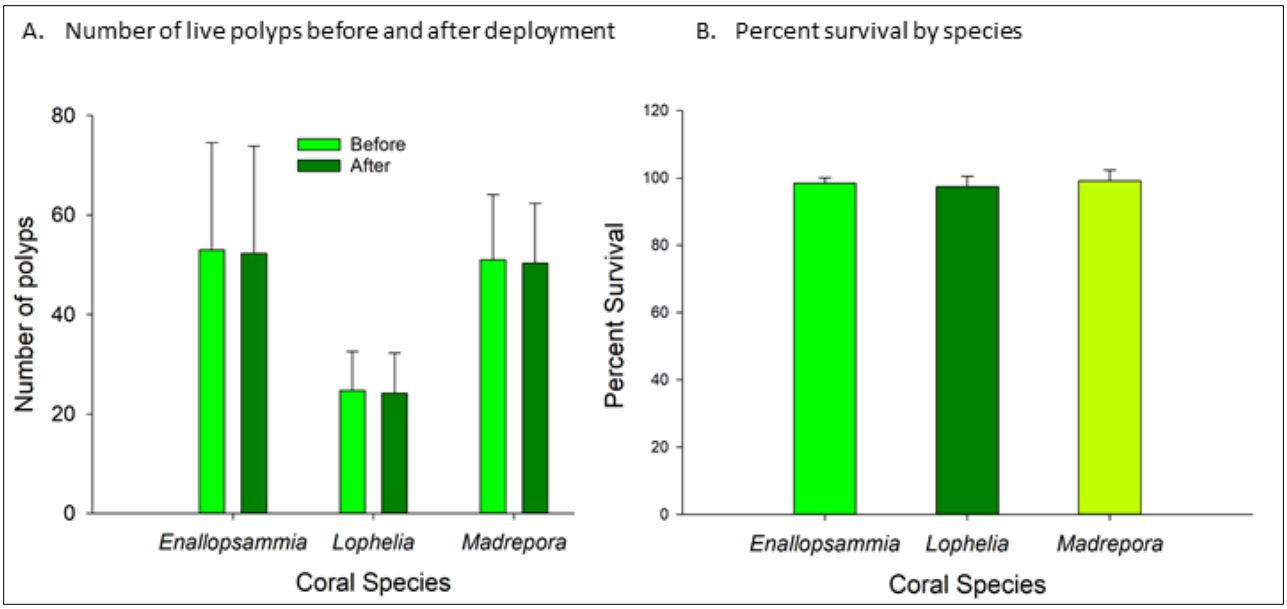

Figure 5-11. Survival of coral fragments deployed August 2018–April 2019
A) average number of live polyps by species before and after deployment; B) percentage of live polyps by species.

We attempted an assessment of transplant growth using two techniques: photogrammetry and calcein staining. The transplant photographs taken prior to deployment were inadequate for the creation of usable models (this will be discussed further in the summary). Growth comparisons could not be derived without pre-deployment models, but the post-recovery model development (and metrics measurement) was completed as a "proof of concept" and to refine methodology.

We developed models for each transplant (**Figure 5-12**), but it was a challenging task due to the complexity and fine-scale structure of the coral skeleton, especially for species such as *M. oculata* that have very fine branches.

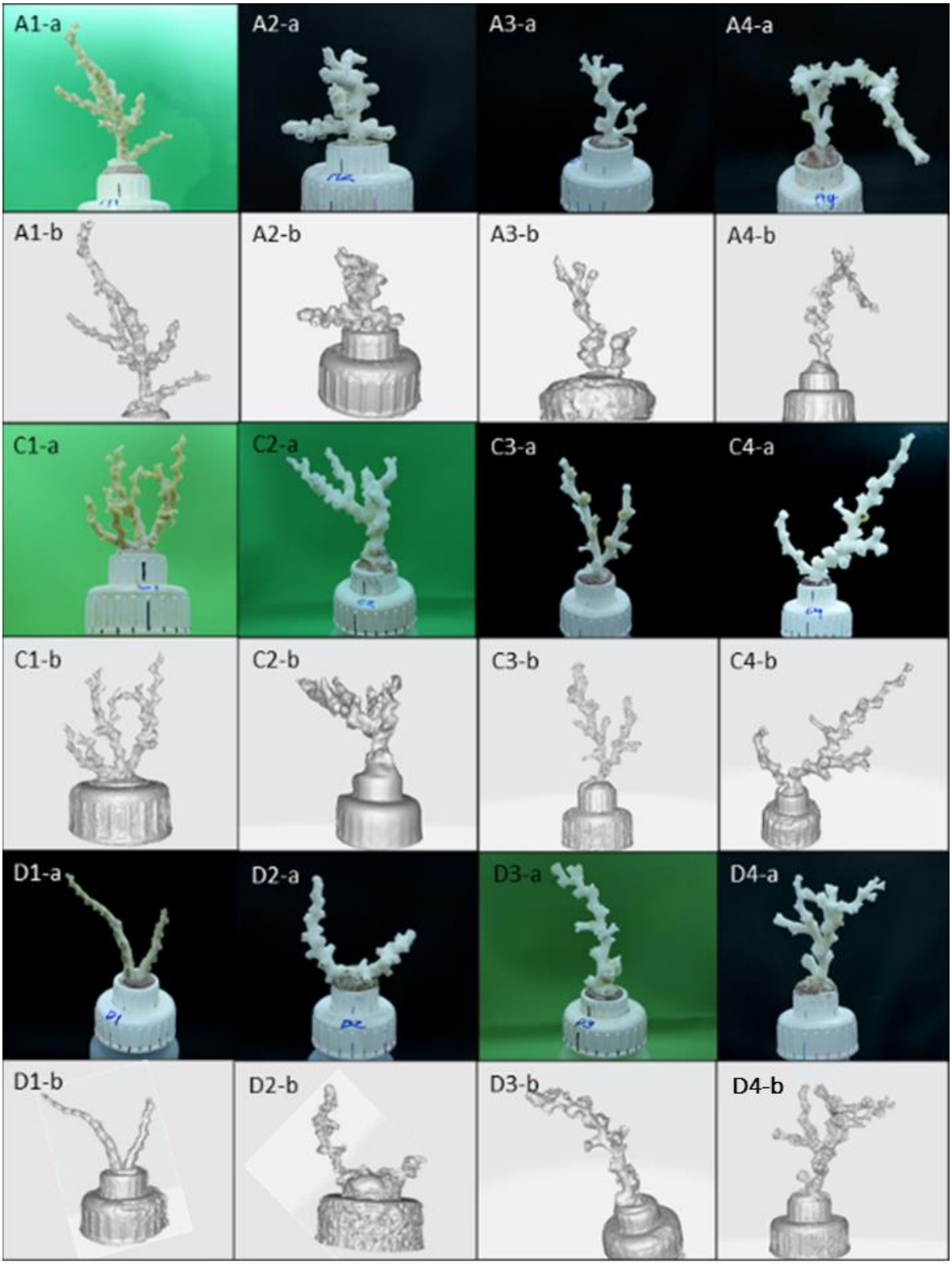

Figure 5-12. Images of coral fragments after recovery and removal of tissue
Plate shows images of coral fragments after recovery and removal of tissue for each transplant unit (images A1-a–A4a; C1-a–C4-a; D1-a–D4-a) and their corresponding digital models that were used to derive skeletal metrics (images A1-b–A4b; C1-b–C4-b; D1-D4-b).

Once the models were complete, the skeletal metrics were readily derived using Autodesk Netfab software (**Table 5-7**).

Table 5-7. Metrics for deployed fragments derived from models using Autodesk Netfab

Fragment	Species	Ave. Linear Ext (mm)	Area (cm^2)	Volume (cm^3)
A1	*Madrepora oculata*	3.090	168.34	29.80
A2	*Enallopsammia profunda*	5.780	429.99	305.18
A3	*Lophelia pertusa*	4.378	223.05	69.37
A4	*Lophelia pertusa*	10.199	459.50	384.39
C1	*Madrepora oculata*	2.706	185.69	85.36
C2	*Enallopsammia profunda*	6.123	345.92	227.14
C3	*Lophelia pertusa*	9.124	238.59	105.45
C4	*Lophelia pertusa*	7.319	415.65	281.37
D1	*Madrepora oculata*	3.096	241.37	171.77
D2	*Enallopsammia profunda*	9.669	501.33	429.53
D3	*Lophelia pertusa*	13.936	595.42	488.31
D4	*Lophelia pertusa*	6.979	319.20	177.31

After the models were complete, we exposed the transplants to fluorescent light to illuminate the stained parts of the skeletons. We targeted stained polyps for sectioning and growth measurements. The *L. pertusa* polyps were large and robust and could be sliced perpendicular to the growth axis. The *E. profunda* polyps were smaller and had limited vertical relief; perpendicular slices were not possible, so we sliced polyps lengthwise along the axis of the calices. The *M. oculata* skeletons were so fragile that they could not be sectioned directly, but were mounted in plastic resin prior to sectioning. Despite the additional support, this species was too insubstantial for sectioning.

Although the calcein was taken up by the skeletons (Error! Reference source not found.), the skeletal sections showed inconsistent staining, unclear banding and/or no discernible growth over the deployment period and growth assessments could not be completed.

Figure 5-13. Images of stained coral skeleton from a recovered fragment of *Lophelia pertusa*
The right panel shows new polyp growth from the calyx of an existing polyp, as indicated by the calcein staining.

5.3.3 Conclusions

Survival of the transplants was high for all species, with no significant differences observed among species. Fragment growth can be accomplished through size increase of existing polyps, but more importantly, through production and growth of new polyps. There was some polyp mortality over the deployment period (7 months); however, this loss was not compensated for by addition of new polyps indicating that new polyp production was minimal.

The original intent of the modeling approach was to compare changes in branch length (i.e., LE), polyp size, area and volume metrics of the models before and after deployment. This is a new approach to assessing transplant growth rates and we refined techniques throughout the process. One of the "lessons learned" was that we took too few images of the fragments prior to deployment, with too few markers to allow the software to recreate such complex structures. The pre-deployment models could not be completed adequately, and without the pre-deployment metrics, growth rates could not be established. We processed post-deployment fragments as a "proof of concept," and metrics were derived from their models.

Skeletal metrics can be readily derived using this technique, which has potential for taking measurements and assessing changes in complex structures created by corals and other taxa. Current growth analyses measure radial growth of tree corals and changes linear dimensions of stony coral colonies. Neither of approaches measures overall changes in colony size, nor do they capture phenotypic variation among colonies of the same species. With continued improvements in underwater image capability, photogrammetric techniques have the potential for non-destructive assessment of size and growth of complex taxa for research, monitoring and restoration. This technique has important management implications as it allows for assessment of restoration success and non-destructive monitoring of growth rates of long-lived colonies.

The skeletal analysis was unsuccessful as indicated in the **Results** section. The limited banding supported the conclusion that growth/new polyp production during the deployment period was minimal. Similar experiments conducted elsewhere in the SEUS (Brooke et al. 2013) show similar high survival with very low numbers of new polyps. Transplant experiments from the GOM, however, show an average of three to four new polyps per fragment (Brooke and Young 2009). These experiments were similar in design to the current experiment, with the exception of the staining protocol. The previous experiments used Alizarin, which is taken up quickly and leaves clear bands that are readily visible. This stain fell out of favor after a coral-growth study indicated it may cause short-term growth inhibition (Holcomb et al 2013).

For long-term studies such as in situ deployments the benefits of using a visible stain may outweigh any minor short-term impacts. While there are undoubtedly artefacts associated with transplants, they can provide useful information on growth rates between species and locations; however, development of in situ techniques such as photogrammetry could avoid such artifacts and increase the scope of metrics that can be used (volume increase).

5.4 Coral Size Distributions

Section Authors: Nancy Prouty, John Schiff, Sandra Brooke

5.4.1 Introduction

The goal of this study element was to measure by analysis of video surveys the height and width (where possible) of coral colonies in the class Anthozoa (orders Scleractinia, Alcyonacea, Pennatulacea) and examine potential relations between colony size to depth and temperature. Understanding the demography of a population can provide insights into recruitment dynamics and system stability. For example, a population dominated by young/small colonies with very few mature individuals may be indicative of a recent new colonization event, or a population recovering from mortality. Conversely, a population dominated by large colonies may indicate low or sporadic recruitment.

Understanding how these populations are structured may provide insight into their vulnerability to natural and anthropogenic stressors and their potential for population recovery after a mortality event. Given the spatial and temporal heterogeneity of deep-coral systems, particularly in the SEUS where the influence of the Gulf Stream can cause extreme temperature variability (Brooke et al 2013), there may be regional differences in population structure, which can be assessed if there is sufficient data for each region. As temperature directly influences metabolism, the deeper depths that are colder may show an overall smaller colony size than those in shallower, warmer waters. Food delivery to the seafloor also generally decreases with depth which could contribute to differences in colony demographic structure across a wide depth range.

5.4.2 Methods

We analyzed videos from five cruises in the Deep SEARCH study area in 2018 (At-41, Ex-1806) and 2019 (RB-1903, Ex-1903L2, Ex-1907). We measured coral colonies that were within the same plane as the lasers, or an object of known dimensions (such as the manipulator claw or biobox of the vehicle). For those colonies with two well-defined dimensions (Stony coral colonies, bushy octocorals and stylasters), we measured colony height and width. For other colony morphotypes (single or few branches), we recorded height alone. We created colony size-frequency distributions for each taxa overall, and we subsequently broke them down by depth and location if sufficient samples were available.

5.4.3 Results

Several hundred height and width measurements have been extracted from the video data. We documented demographic metrics such as average and SDs of colony height, width (if appropriate) and maximum observed colony size. Here we present the size (height) frequency distributions for the most abundant taxa that can confidently be identified to species. These include the scleractinians *Enallopsammia profunda*, *Madrepora oculata* and *Solenosmilia variabilis*. *L. pertusa* was not analyzed as this species does not generally occur as individual colonies. **Table 5-8** shows summary statistics for these three species of scleractinians.

Table 5-8**. Metrics of size measurements for three species of scleractinians from five research cruises in the study region in 2018 and 2019**

Species	No. Records	Ave. Height	Ave. Width	S. D. Height	S. D. Width	Max. Height	Max. Width
Madrepora oculata	46	31.14	25.02	18.54	18.66	121.15	110.46
Enallopsammia profunda	231	15.40	14.72	7.24	7.79	53.80	58.09
Solenosmillia variabilis	165	18.44	13.60	8.12	5.59	53.2	37.50

We binned the size distribution data (height only) for all locations into 5-cm categories for each species and translated this into percentage frequency to facilitate comparisons between species (**Figure 5-12**). Both *E. profunda* and *S. variabilis* have unimodal distributions with peaks in the same size category (10–14.9 cm colony height). *M. oculata* distribution is less well defined, with two less pronounced peaks than the other two species. Combining sites masked any site-specific differences among the populations but several dives have low sample numbers, which decreases statistical power, so we treated the data set as a single population for the purposes of this analysis.

We applied a regression analysis of colony height on depth and temperature to each species. Depth is often used as a proxy for temperature but this is not always a linear or predictable relationship. The Richardson Hills sites where we observed some of the colonies had unusual temperature-depth profiles so both relationships are presented (**Figure 5-15 A-F**). *Madrepora oculata* colony height was not significantly related to either depth ($R^2 = 0.01$, $t = 0.633$, $p = 0.53$) (**5 A**) or temperature ($R^2 = 0.04$, $t = 1.31$, $p = 0.195$) (Error! Reference source not found. **B)**. *Enallopsammia profunda* colony size was positively related to depth ($R^2 = 0.04$, $t = 4.15$, $p < 0.01$) (**Figure 5-15 C)** and temperature ($R^2 = 0.11$, $t = 3.59$, $p < 0.001$) (**Figure 5-15 D)**. *Solenosmillia variabilis* height was negatively related to depth ($R^2 = 0.22$, $t = 11.41$, $p < 0.01$) (**Figure 5-15 E**) but not significantly related to temperature ($R^2 = 0.007$, $T = 1.07$, $P = 0.286$) (**Figure 5-15 F**).

5.4.4 Conclusions

We used three common species of stony corals for demographic assessment. These species were readily identified from video, found across wide depth range and in sufficient numbers to generate a sufficient data set for analysis. These species also occur as discrete colonies, unlike *L. pertusa* where colonies overlap and make measurement of individuals challenging. The size-frequency distribution of *M. oculata* indicate a double peak in colony height at 15–25 cm and another at 30–35 cm. Both *E. profunda* and *S. variabilis* show a single peak in the size-frequency analysis, with peak colony height of 10–15 cm and 15–20 cm respectively.

Small individual colonies of *E. profunda* were abundant on the plateaus of the Richardson Hills bioherms as a yellow morphotype that is not usually seen elsewhere. These small colonies contributed to the dominance of small colonies in the data set which drive the depth relations to colony height for this

species. The unusually high temperatures on Richardson Hills (up to 11°C), which was also where many of the deeper living colonies of *E. profunda* and *M. oculata* were collected may have contributed to the generally low R^2 values in correlations between colony height with temperature and depth.

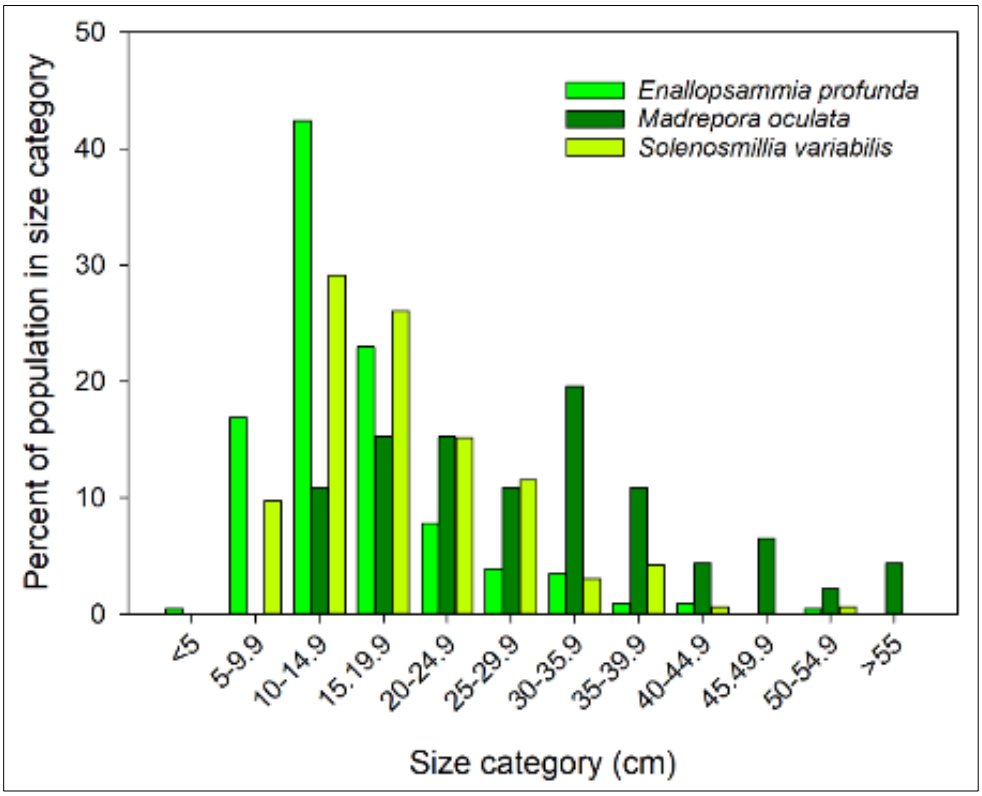

Figure 5-14. Size-frequency distribution of coral colony heights for three species of scleractinians
Species shown: *Enallopsammia profunda, Madrepora oculata,* and *Solenosmillia variabilis.*

The negative relationship between *S. variabilis* colonies and depth can be explained by the attenuation of food and reduced water temperature, both of which can reduce growth. This species was collected from a wider and deeper depth range, where temperature variation is lower, which may also have contributed to this significant and easily explained relation.

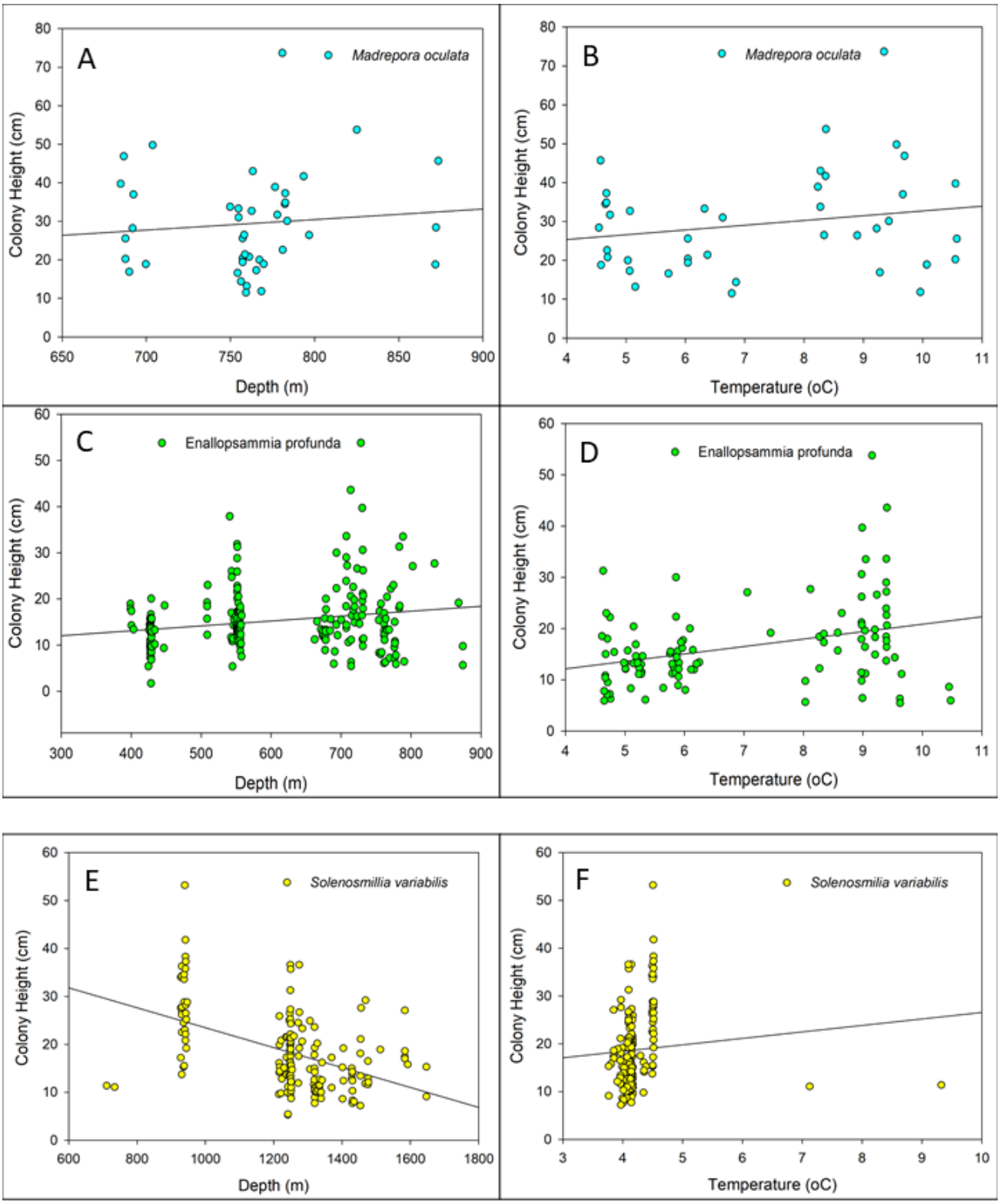

Figure 5-15. Graphs showing relationship between depth and colony height
For A) *Madrepora oculata*, C) *Enallopsammia profunda*, E) *Solenosmilia variabilis*, and between temperature and colony height for B) *Madrepora oculata*, D) *Enallopsammia profunda*, F) *Solenosmilia variabilis.*

5.5 Coral Reproductive Biology

Section Author: Sandra Brooke

5.5.1 Introduction

Environmental drivers of reproductive processes in shallow-water species include changes in temperature, currents, daylength and lunar/tidal signals (Harrison 2011). These signals become attenuated or absent with depth. It was originally thought that the deep sea was environmentally homogeneous, resulting in continuous reproduction in deep-benthic invertebrates; however, Tyler et al (1982) documented several examples of seasonal reproduction in bathyal echinoderms. Since then, many more taxa, including corals, have demonstrated seasonal reproductive cycles. Gametogenesis in deep-sea benthic organisms is probably driven by the seasonal influx of particulate organic carbon (Tyler et al. 1993, Witte 1996) derived from surface blooms of phytoplankton and zooplankton.

Monthly samples collected over several years are required to accurately describe the gametogenic cycles of a species; however, in the deep sea, expense and logistical constraints often preclude such sampling. Gametogenic cycles can be derived from sporadic sampling over several years, providing different time periods are covered. It is possible that organisms within similar taxonomic and trophic groups with similar reproductive strategies will use the same environmental factors as reproductive cues, in which case, fauna with the same reproductive strategies (broadcast spawning or brooding) from the same depth and location may have similar reproductive cycles. If the reproductive cycles vary across taxa, we can conclude that different species use different cues or food sources, and/or that reproduction is genetically predetermined by internal rhythms. Some species may exhibit continuous reproduction, as in many chemosynthetic species that have a continuous food supply and stable environment (Tyler and Young 1999), or species that have taxonomic constraints on their reproductive strategies.

There has been a proliferation of research on deepwater corals over the past 15 years that has focused primarily on structure-forming species such as *Lophelia pertusa*. Despite this increase in effort, information on the reproductive biology of *L. pertusa* was not published until quite recently (Waller and Tyler 2005, Brooke and Jarnegren 2013). Using samples collected from the northeast Atlantic, these authors reported a seasonal reproductive cycle with one cohort per year, culminating in a protracted spawning period of several weeks beginning in late January. Waller and Tyler (2005) also reported information on gametogenic cycles of *Madrepora oculata*, suggesting two cohorts per year. In contrast to structure-forming colonial species, which appear to be uniformly gonochoric (separate sexes) broadcast spawners, cold-water solitary scleractinians, such as *Flabellum* sp., (Waller and Tyler 2011, Mercier et al. 2011), *Caryophyllia* sp. (Waller et al. 2005) and *Fungiacyathus* sp. (Waller et al. 2002, Flint et al. 2007), have various reproductive strategies including hermaphroditism (simultaneous and sequential), gonochorism, brooding, and broadcast spawning.

The octocorals (subclass Alcyonaria) comprise three suborders (Alcyonacea, Pennatulacea, and Helioporacea), of which the Alcyonacea is the largest and most diverse. The sea pens are all broadcast spawners, which suggests that this strategy may be phylogenetically constrained (Watling et al. 2011). The majority of the octocorals belong to the Alcyonacea, which includes the gorgonian type taxa with an internal skeleton and the true soft corals, which have hydrostatic skeletons. Despite their widespread distribution and often high abundance, there has been very little research on reproductive biology of octocorals, particularly those at mesophotic or deep depths. However, the limited published material shows some consistencies among the taxa studied. The soft corals (suborder Alcyoniina) studied to date are gonochoric brooders with either continuous (Cordes et al. 2001, Sun et al. 2010) or seasonal gametogenesis (Mercier and Hamel 2011). Reproductive traits of Antarctic gorgonians described in the older literature (Brito et al. 1997, Versluys 1906) suggest that gonochorism and brooding are common features of cold-water octocorals. However, some gorgonians (members of the Primnoidae and Isididae)

are broadcast spawners that release gametes to be fertilized in the water column (Beazley and Kenchington 2012, Mercier and Hamel 2011, Orejas et al. 2002). Broadcast-spawning species generally either reproduce periodically (Orejas et al. 2002, Mercier and Hamel 2011) or annually (Mercier and Hamel 2011).

The overall goal of this study element was to provide information on the reproductive biology (strategy and timing) of dominant and/or habitat-forming corals in the study area. Such data enhance our understanding of deepwater coral ecology and contribute to a broader study on spatial and temporal differences among dominant deepwater scleractinian populations.

5.5.2 Methods

Samples of corals collected during the August 2018 and April 2019 sampling cruises are shown in **Table 5-9** (2018) and **Table 5-10** (2019). Each sample comprised several small branches (colonial corals) or several individuals (solitary corals), which were placed in 5% buffered formalin. Samples remained in formalin for the duration of the cruises but were transferred into 70% ethanol in the laboratory. Prior to histological processing, we dissolved the calcified skeleton of each sample in 10% hydrochloric acid for 2 to 12 hours depending on the degree of calcification. We cut the large solitary corals into halves or quarters using a diamond band saw prior to decalcification. After decalcification, we rinsed the polyps in distilled water then dehydrated them through a series of ethanol concentrations (70%, 95%, and 100%).

The tissues were then cleared overnight using Histoclear and embedded in paraffin wax, then sliced into 8-µm sections using a microtome. We mounted the sections onto microscope slides, dried for 12 hours, and stained using Mayer's Haematoxylin (which stains DNA dark blue) and Eosin B (which stains cytoplasmic proteins bright pink). After staining, the sections were mounted and left to dry. We took sequential images of all the sections using either an AmScope or Optronics digital camera attached to an Olympus BX50 compound microscope. These methods represent standard histological techniques (Waller et al 2005, Brooke and Jarnegren 2013).

In female gametogenesis (oogenesis), the eggs increase in size as they mature from the initial oogonia (stage I) to the pre-vitellogenic stage (II) when yolk deposition begins. Vitellogenesis increases as the oocytes mature and the oocytes reach their maximum size (stage III). A granular cortical layer may develop prior to spawning. After spawning, the females are in stage IV ('spent'). Some species have overlapping gametogenic cycles, so there may be multiple stages in a single colony or polyp. Female maturity can be assessed according to stage, and/or oocyte diameter.

For this project, we measured oocytes from each female fragment from 5–10 polyps in an effort to reach 50 oocytes. We measured only those oocytes with visible nucleoli. This ensured that the same egg was not measured more than once, as the nucleolus is so small (approximately 9-µm diameter) that it only appears in one 8-µm slice. We measured the oocyte area and recorded using ImageJ image analysis software. We calculated oocyte "feret" diameter using Eq. 20, which estimates the diameter of a hypothetical circle with the same area as the object measured.

$$\text{Feret diameter} = \frac{2\sqrt{\text{area}}}{\pi} \qquad \text{(Equation 20)}$$

Male gamete development (spermatogenesis) is initiated when aggregations of spermatocytes appear around the outer edges of the spermatocysts, leaving an open lumen in the center (stage I). As the spermatocytes mature, the lumen fills in and a few spermatozoa are visible (stage II). The mature stage III is indicated by densely packed spermatocytes with mature spermatozoa within the lumen. After spawning the spent spermatocytes contain relict spermatozoa (stage IV). Although the spermatocysts increase in

size as they mature, size alone is not a good indicator of maturity so male gametogenesis is assessed by stage rather than size. Male staging follows Waller et al. 2002.

Table 5-9. Number of coral samples processed for gametogenetic analysis from August 2018 cruise

Species	Collection Date	Dive No.	No. of Samples
Alcyonacea			
Acanthogorgia spissa	29-Aug-2018	4969 (Pamlico Canyon)	3
Lateothela grandiflora	29-Aug-2018	4968 (Cape Fear)	1
Paragorgia johnsoni	29-Aug-2018	4969 (Pamlico Canyon)	1
Paramuricea sp.	29-Aug-2018	4968 (Cape Fear)	1
Paramuricea sp.	29-Aug-2018	4969 (Pamlico Canyon)	1
Scleractinia			
Desmophyllum dianthus	29-Aug-2018	4969 (Pamlico Canyon)	2
Enallopsammia profunda.	23-Aug-2018	4962 (Richardson Hills)	5
Enallopsammia profunda	24-Aug-2018	4963(Richardson Hills)	2
Enallopsammia profunda	25-Aug-2018	4964 (Richardson Ridge)	1
Enallopsammia profunda	26-Aug-2018	4965 (Stetson Banks)	6
Lophelia pertusa	23-Aug-2018	4962 (Richardson Hills)	8
Lophelia pertusa	24-Aug-2018	4963 (Richardson Hills)	9
Lophelia pertusa	26-Aug-2018	4965 (Stetson Banks)	2
Lophelia pertusa	29-Aug-2018	4968 (Cape Fear)	3
Madrepora oculata	23-Aug-2018	4962 (Richardson Hills)	1
Madrepora oculata	24-Aug-2018	4963 (Richardson Hills)	2
Madrepora oculata	25-Aug-2018	4964 (Richardson Ridge)	1
Madrepora oculata	29-Aug-2018	4968 (Cape Fear)	1
Solenosmilia variabilis	25-Aug-2018	4964 (Richardson Ridge)	1
Solenosmilia variabilis	29-Aug-2018	4969 (Pamlico Canyon)	4
Zoantharia			
Zoantharia sp.	27-Aug-2018	4966 (Stetson Banks)	1

Table 5-10. Number of coral samples processed for gametogenetic analysis from April 2019 cruise

Species	Collection Date	Dive No.	No. of Samples
Alcyonacea			
Acanthogorgia spissa	18-Apr-2019	J2-1132 (Pamlico Canyon)	7
Acanthogorgia spissa	21-Apr-2019	J2-1135 (Cape Lookout Deep)	1
Lateothela grandiflora	11-Apr-2019	J2-1129 (Richardson Hills)	1
Paragorgia johnsoni	17-Apr-2019	J2-1136 (Blake Ridge Seep)	1
Paramuricea sp.	29-Apr-2019	J2-1131 (Blake Deep)	6
Swiftia casta	11-Apr-2019	J2-1128 (Richardson Hills)	4
Swiftia casta	14-Apr-2019	J2-1129 (Richardson Hills)	4
Swiftia casta	17-Apr-2019	J2-1135 (Cape Lookout Deep)	1
Swiftia casta	22-Apr-2019	J2-1138 (Richardson West)	2

Species	Collection Date	Dive No.	No. of Samples
Plumarella sp.	29-Apr-2019	J2-1128 (Richardson Hills)	5
Plumarella sp.	11-Apr-2019	J2-1129 (Richardson Hills)	7
Plumarella sp.	14-Apr-2019	J2-1130 (Savannah Banks)	5
Plumarella sp.	29-Apr-2019	J2-1138 (Richardson West)	2
Pseudodrifa nigra.	11-Apr-2019	J2-1128 (Richardson Hills)	3
Pseudodrifa nigra	14-Apr-2019	J2-1129 (Richardson Hills)	1
Pseudodrifa nigra	17-Apr-2019	J2-1130 (Savannah Banks)	1
Scleractinia			
Desmophyllum dianthus	18-Apr-2019	J2-1131 (Blake Deep)	4
Desmophyllum dianthus	21-Apr-2019	J2-1132 (Pamlico Canyon)	35
Enallopsammia profunda.	11-Apr-2019	J2-1128 (Richardson Hills)	4
Enallopsammia profunda.	17-Apr-2019	J2-1130 (Savannah Banks)	8
Enallopsammia profunda	29-Apr-2019	J2-1138 (Richardson West)	3
Lophelia pertusa	11-Apr-2019	J2-1128 (Richardson Hills)	5
Lophelia pertusa	14-Apr-2019	J2-1129 (Richardson Hills)	3
Lophelia pertusa	17-Apr-2019	J2-1130 (Savannah Banks)	3
Lophelia pertusa	22-Apr-2019	J2-1133 (Pea Island Seep)	1
Lophelia pertusa	29-Apr-2019	J2-1138 (Richardson West)	1
Madrepora oculata	11-Apr-2019	J2-1128 (Richardson Hills)	2
Madrepora oculata	14-Apr-2019	J2-1129 (Richardson Hills)	2
Madrepora oculata	17-Apr-2019	J2-1130 (Savannah Banks)	1
Solenosmilia variabilis	18-Apr-2019	J2-1131 (Blake Deep)	7
Solenosmilia variabilis	21-Apr-2019	J2-1132 (Pamlico Canyon)	9

5.5.3 Results

We calculated the average feret diameter and SD from the mean for the female gametes for each year for each species (**Table 5-11**). To examine the size distribution, we split oocytes from each female within a species and sampling period into size categories (of either 10 µm or 20 µm, depending on the total oocyte size range) and the relative frequency calculated for each category. We used oocyte diameters and size-frequency distributions to infer the timing and periodicity of female gametogenic cycles. We classified male reproductive stages for each species with males and are shown in **Table 5-11** and **Table 5-12.**

The numbers of samples for most species were too low, or too incomplete (due to only one gender and/or time point) for a meaningful assessment of reproductive strategy or gametogenesis. However, for those species that had males and female gametes for the same time period, or at least one gender for both time periods, the data provided some useful information. These included the scleractinians *D. dianthus, E. profunda, L. pertusa, M. oculata* and *S. variabilis* and the octocorals *A. spissa, Plumarella* sp., *P. nigra* and *S. casta* (**Table 5-11** and **Table 5-12**).

Table 5-11. Average feret diameter of female oocytes from corals

From corals processed from the August 2018 and April 2019 cruises (± SD). The t-statistic and p-values represent comparisons of oocyte diameter between years. Significant difference between years shown by *

Species	Avg. ± SD 2018	Avg. ± SD 2019	t-statistic	p-value
Desmophyllum dianthus	No females	57.19 ± 13.37	-	-
Enallopsammia profunda	257.58 ± 74.34	289.00 ± 10.06	-1.37	0.199
Lophelia pertusa	65.56 ± 24.47	No females	-	-
Madrepora oculata	No females	119.99 ± 35.82	-	-
Solenosmilia variabilis	90.29 ± 15.69	42.37 ± 10.30	8.97	<0.001*
Acanthogorgia spissa	85.13 ± 30.88	128.24 ± 47.82	-1.94	0.114
Lateothela grandiflora	80.97 ± 35.14	No samples	-	-
Paramuricea sp.	No females	73.97 ± 48.27	-	-
Plumarella sp.	No samples	72.45 ± 38.65	-	-
Pseudodrifa nigra	No samples	45.20 ± 19.44	-	-
Swiftia casta	No samples	107.85 ± 12.51	-	-
Zoantharia sp.	65.56 ± 13.84	No samples	-	-

Table 5-12. Gametogenic stages of male spermatocysts from corals

Processed from the 2018 and 2019 sampling cruises. Stages follow Waller et al. 2002.

Species	August 2018	April 2019
Desmophyllum dianthus	II-III	II
Enallopsammia sp.	II-IV	II-III
Lophelia pertusa	II-III	II
Madrepora oculata	III	No males
Solenosmilia variabilis	II-III	I-II
Acanthogorgia spissa	No males	II-III
Plumarella sp.	No samples	I-III
Paragorgia johnsonii	I-II	No males
Pseudodrifa nigra	No samples	1-IV
Swiftia casta	No samples	II-III

5.5.3.1 *Desmophyllum dianthus*

During the RV *Atlantis* cruise in August 2018, we collected two samples of the cup coral *D. dianthus* from Pamlico Canyon; both were males showing mature (stage III) spermaries. During the NOAA Ship *Ron Brown* cruise in April 2019, we collected 35 individuals from Pamlico Canyon and both genders were represented in the sample.

Males collected in August 2018 showed mostly mature stage III spermaries (**Figure 5-16A**), with a few less mature stage II. Females from April 2019 showed an average oocyte diameter of 57.19 (SD = 13.37; **Table 5-11**). The size-frequency distribution (**Figure 5-17**) showed a wide range of oocyte sizes (20–109 µm), with dominant categories in the center of the distribution, indicating a single cohort of developing eggs. Oocytes from the April samples were primarily immature vitellogenic oocyte (VO) stages (**Figure 5-16B**) with a small number of larger and more mature eggs. Males collected in April 2019 showed only immature (stage II) spermaries (**Figure 5-16C**), which is also consistent with a single cohort of gametes

within each time period. There were no indications of hermaphroditism or brooding in these samples, indicating that *D. dianthus* is a gonochoristic broadcast-spawning species.

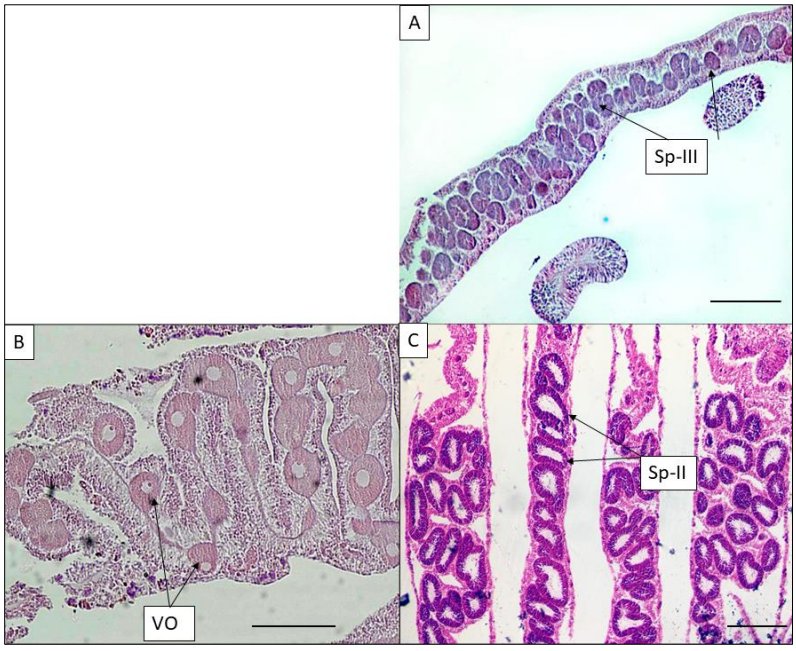

Figure 5-16. *Desmophyllum dianthus* thin section slides
A) Male collected in August 2018 showing stage III spermaries (Sp-III), B) female collected April 2019 showing VO, C) male collected April 2019 showing primarily stage II spermaries (Sp-II). No females were collected in August 2018. Scale bars: 100 µm.

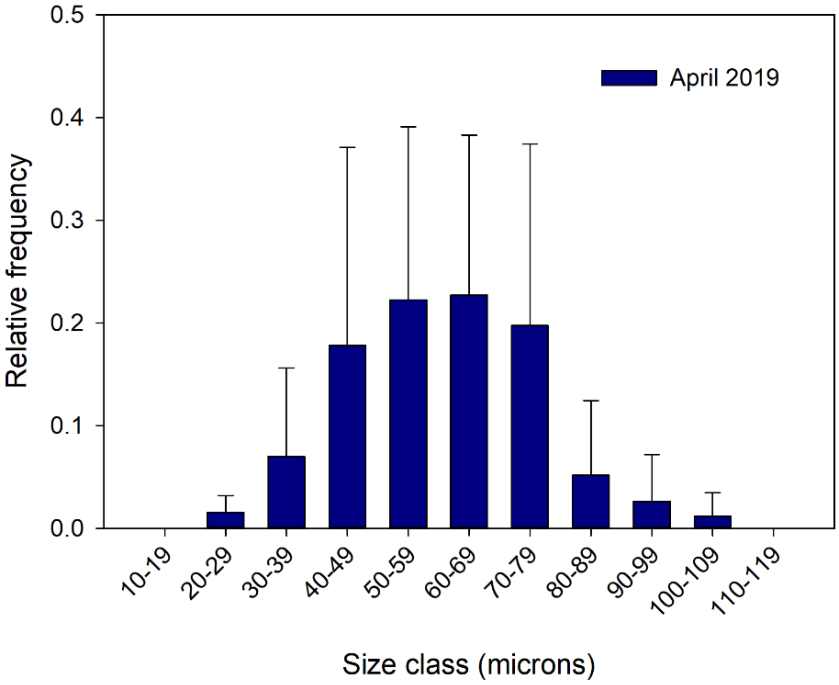

Figure 5-17. *Desmophyllum dianthus* oocyte size-frequency distribution for April 2019 samples
The x-axis shows oocyte size category and the y-axis shows relative frequency of oocytes within each category.

5.5.3.2 *Enallopsammia profunda*

This species is endemic to the western Atlantic and is one of two reef-building species in the region, with the other being *L. pertusa*. Samples collected during the 2018 and 2019 cruises came primarily from the Richardson Hills/Ridge area, with additional samples from Stetson and Savannah Bank (**Figure 5-11** and **Figure 5-12**). Although this species can create reef structures, the samples collected during the cruises were all from small (< 0.5 m), discrete colonies, most of which were yellow, rather than the more common cream or white color.

Both sampling periods contained male and female colonies (**Table 5-11** and **Table 5-12**). The range of egg sizes was broader in August 2018 than in April 2019 (**Figure 5-18**), with some smaller immature oocytes present in August, although both time periods showed the presence of large (> 250 µm) mature oocytes (**Figure 5-18** and **Figure 5-19 A, C**). The male samples showed similar trends to the females as the males showed a wider range of spermary stages (stages II to IV) in August 2018 (**Figure 5-19B**) than the males from April 2019 (**Figure 5-19D**), which showed predominantly stage III, with a few stage II (not shown in figure).

We used a t-test to compare oocyte sizes from 2018 and 2019 and showed no significant difference between time periods (**Table 5-11**). These data indicate there may be some seasonality with more mature gametes in spring than fall, or this species could reproduce continuously. Fecundity seems to be lower than other scleractinians, as far fewer (and larger) eggs were encountered during histological processing, but this has not been rigorously examined. There were no indications of hermaphroditism in these samples and we observed no planulae, but brooding cannot not be eliminated as a reproductive strategy in this species, given the large egg size and lack of clear synchronized cohorts.

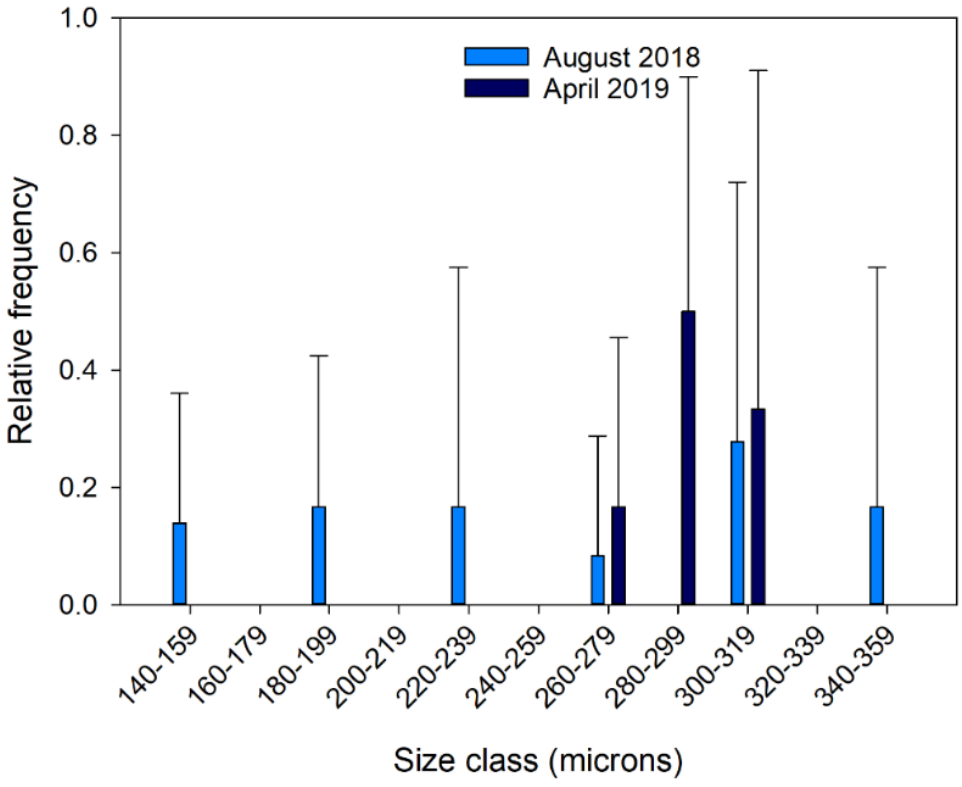

Figure 5-18. *Enallopsammia profunda* oocyte size-frequency distribution for August 2018 and April 2019 samples
The x-axis shows oocyte size category and the y-axis shows relative frequency of oocytes within each category.

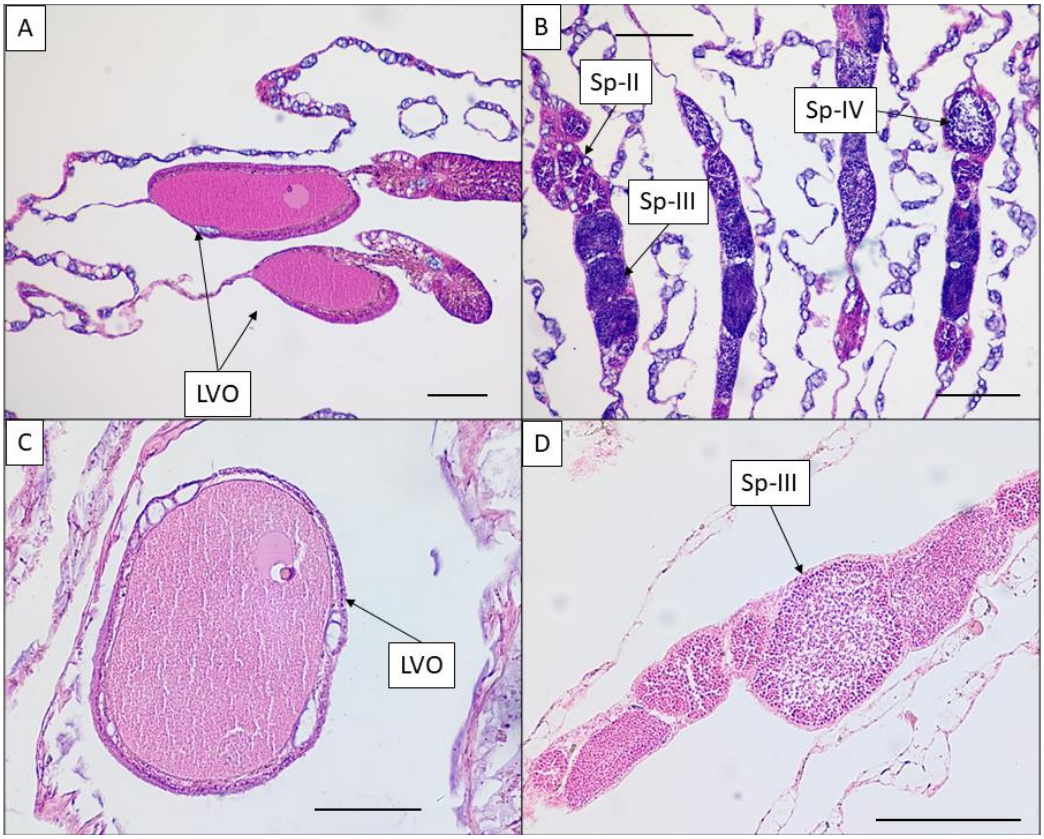

Figure 5-19. *Enallopsammia profunda* thin section slides
A) Female collected in August 2018 showing late vitellogenic oocytes (LVO), B) male collected August 2018 showing developmental stages II, III and IV (Sp-II, Sp-III, Sp-IV respectively), C) female collected April 2019 showing a large individual LVO, D) male collected April 2019 showing predominantly stage III spermaries (Sp-III). Scale bars: 100 µm.

5.5.3.3 *Lophelia pertusa*

This reef-building scleractinian is one of the most extensively studied of all deep/cold-water coral species. It is known to be a gonochoristic broadcast-spawning species with a single annual spawning period that occurs in the early spring in the northeastern Atlantic (Waller and Tyler 2005, Brooke and Jarnegren 2013), and in the late fall in the western Atlantic (Brooke and Sogluizzo 2017).

The majority of samples collected during the cruises in 2018 and 2019 were from the newly explored Richardson Hills reefs on the eastern extent of the Blake Plateau. Females collected in August 2018 had an average oocyte diameter of 65.56 µm (SD 24.47); the large variance in the sample data can be explained by the size-frequency distribution **(Figure 5-20**), which shows a wide range of size categories. The dominant size class is 70–79 µm, but there is also a peak of smaller oocytes at 30–39 µm.

This pattern of oocyte size distribution indicates two cohorts within the sample, with one more advanced than the other. **Figure 5-21A** shows the larger LVO. The males from August 2018 are predominantly mature stage III spermaries, with some stage II (**Figure 5-21 B**). This development pattern also supports two gamete cohorts within the sample. There were no females with gametes in April 2019, but males we observed exhibited predominantly immature stage II spermaries (**Figure 5-21 C**).

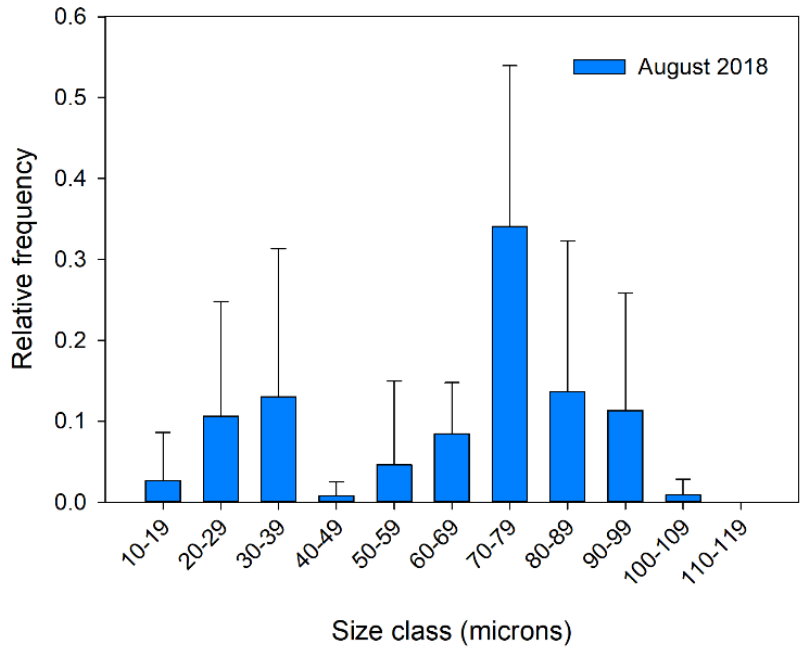

Figure 5-20. *Lophelia pertusa* oocyte size-frequency distribution for August 2018 samples
The x-axis shows oocyte size category and the y-axis shows relative frequency of oocytes within each category.

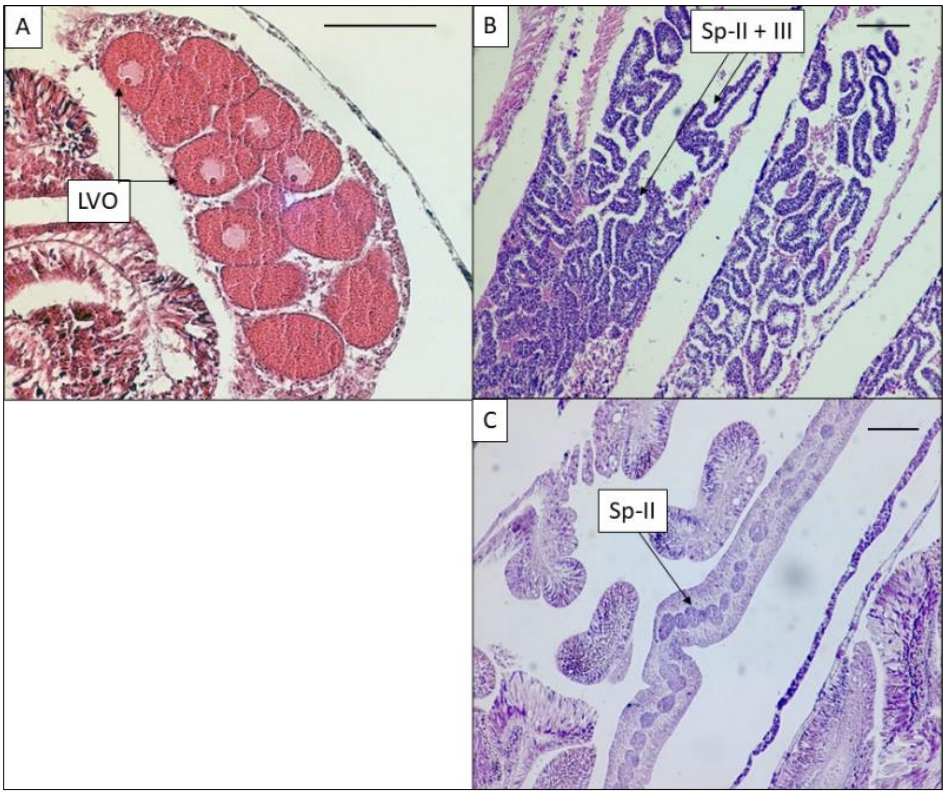

Figure 5-21. *Lophelia pertusa* thin section slides
A) Female collected in August 2018 showing LVO, B) male stage II and III spermaries from male collected August 2018, C) early stage II spermaries from male collected April 2019. No females were obtained from 2019. Scale bar: 100 µm.

5.5.3.4 *Madrepora oculata*

This stony coral is not a reef-building species but can form large individual colonies that contribute to overall habitat complexity. It is broadly distributed and is common on deep reefs throughout the North Atlantic and elsewhere.

We collected five samples of *M. oculata* during the August 2018 and April 2019 cruises. These few samples yielded two males in 2018 and two females in 2019. The average oocyte diameter was 119.99 (SD 35.82, **Table 5-11**), which indicates high variation in oocyte size. The size-frequency distribution (**Figure 5-22**) shows two or possibly three cohorts of eggs, with peak size categories of 70–79 µm, 100–109 µm, and 140–149 µm.

Each female had VO (immature) LVO (mature) **(Figure 5-23**), and the males from August 2018 had mature spermatocytes (Sp-III). The presence of mature gametes in both August and April also indicate multiple cohorts are present rather than a single synchronous cohort. These samples were all separate genders and showed no indications of brooding, therefore this species is most likely a gonochoristic broadcast-spawning species with unclear spawning periodicity.

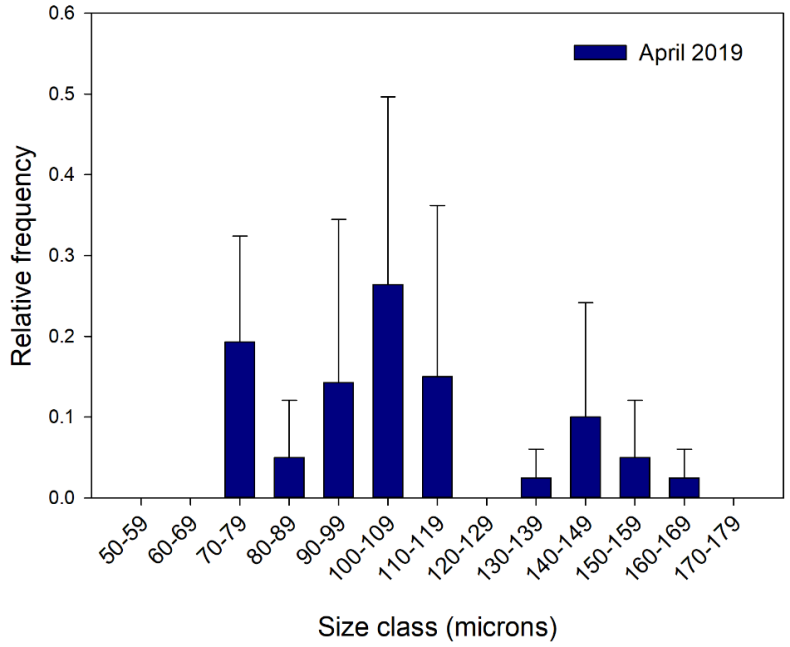

Figure 5-22. *Madrepora oculata* oocyte size-frequency distribution for April 2019 samples
The x-axis shows oocyte size category and the y-axis shows relative frequency of oocytes within each category.

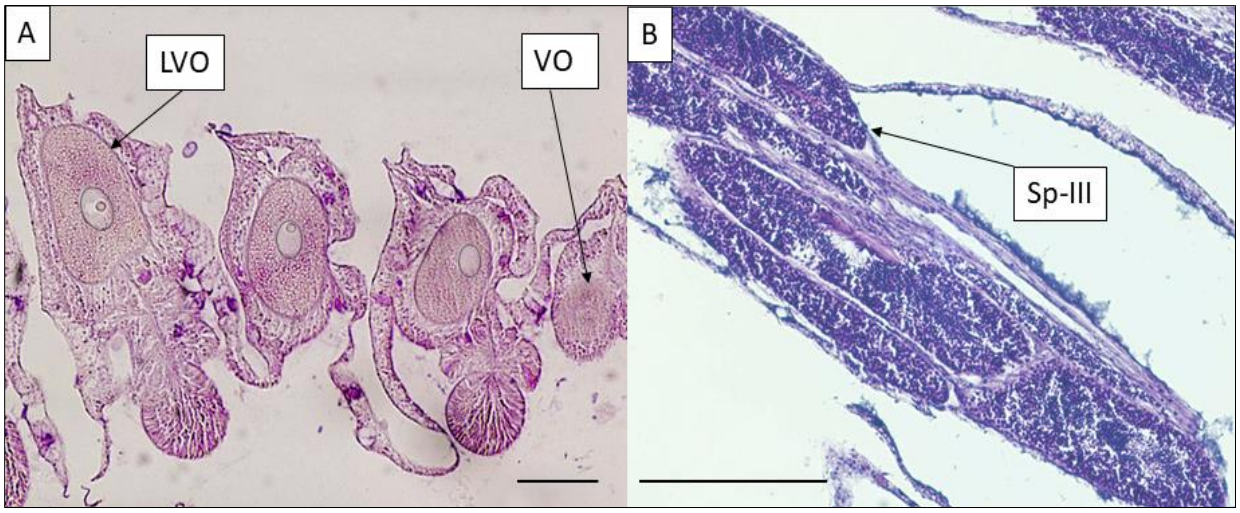

Figure 5-23. *Madrepora oculata* thin section slides
A) Female collected in April 2019 showing VO and LVO, B) male collected August 2018 showing stage III (Sp-III) spermaries. No females were obtained from 2018, or males from 2019. Scale bar: 100 µm.

5.5.3.5 *Solenosmilia variabilis*

This stony coral is generally found on deep (> 800 m) rocky habitats as isolated colonies or small thickets. In the Pacific however, *S. variabilis* is one of the major reef-building species and is particularly abundant on the tops and flanks of seamounts (Roberts et al 2009). We collected 5 samples of this species in August 2018 and 16 in April 2019. These samples yielded both males and females in both time periods (**Table 5-11, Table 5-12**). The average oocyte diameter for August was 90.29 (SD 15.69) and for April 42.37 (SD 10.30). We compared these data using a t-test and showed a significant difference between the two time periods ($t = 8.97$; $p < 0.001$, **Table 5-11**).

The size-frequency distribution (**Figure 5-24**) showed very clear cohorts of oocytes, with a peak in smaller eggs at 40–49 µm in April, and a peak in larger oocytes (90–99 µm) in August. This pattern can be seen in the different gamete stages from the two time periods (**Figure 5-25**). Samples from August show mature LVO and mature stage III (Sp-III), spermaries (**Figure 5-25 A, B**) whereas the samples from April show immature VO and immature stage II spermaries (**Figure 5-25 C, D).** This pattern supports an annual seasonal cycle that begins sometime in the spring and culminates in spawning in the fall. All samples were separate genders and no indications of brooding we evident; this species is most likely a gonochoristic broadcast spawner.

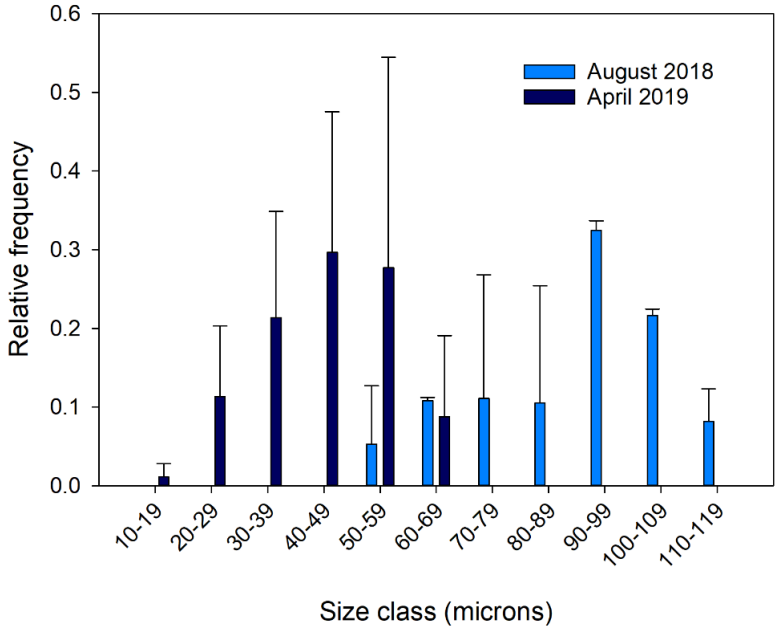

Figure 5-24. *Solenosmilia variabilis* oocyte size-frequency distribution for August 2018 and April 2019 samples
The x-axis shows oocyte size category and the y-axis shows relative frequency of oocytes within each category.

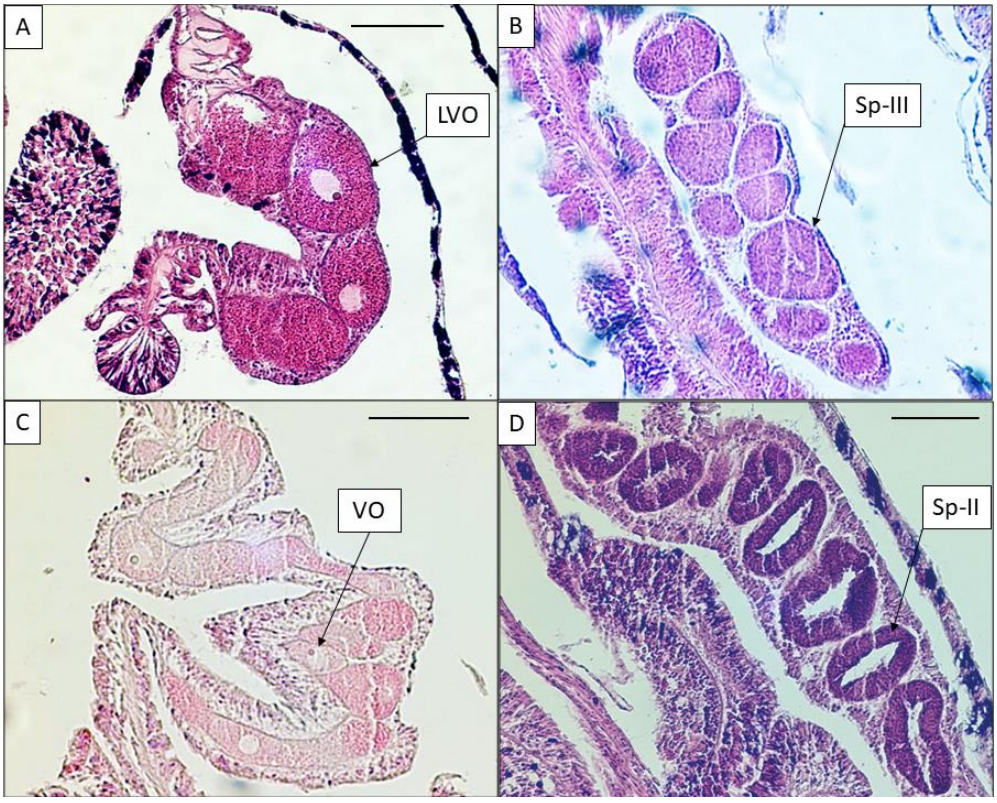

Figure 5-25. *Solenosmilia variabilis* thin section slides
A) Female collected in August 2018 showing LVO, B) male collected August 2018 showing stage III (Sp-III) spermaries, C) female collected April 2019 with VO, D) male collected April 2019 showing stage (Sp-II) spermaries. Scale bar: 100 µm.

5.5.3.6 *Acanthogorgia spissa*

The octocoral genus Acanthogorgia (family Acanthogorgiidae) is moderately common on exposed hardbottom habitats such as canyons and rocky ledges. There are three species that look very similar and have overlapping distributions along the western Atlantic margin; these are *A. armata*, *A. aspera* and *A. spissa*. We collected two species during the 2018 and 2019 research cruises that were identified using genetic barcoding. The more common *A. spissa* samples were processed for histological analysis. The majority of the samples collected in August 2018 and April 2019 were from Pamlico Canyon, with a single specimen in 2019 collected from Cape Lookout Deep site. These samples yielded females in both years, and males in 2019. The average oocyte diameter in August 2018 was 85.13 (SD 30.88) and 128.24 (SD 47.82) in April 2019 (**Table 5-11**). The high variance among sizes indicates lack of synchrony within time periods and a t-test showed no significant difference in oocyte diameters between sampling periods ($t = -1.94$, $p = 0.114$).

The August 2018 sample has a peak oocyte diameter of 80–99 µm, but the most abundant oocytes in the April 2019 were in the 160–179 µm size category. The size-frequency distribution (**Figure 5-26**) shows considerable overlap between time periods, Females in August 2018 contained primarily VO with some mature LVO (**Figure 5-27 A**). The April 2019 samples had more LVO (**Figure 5-27 B**). There were no male samples in 2018, but in April 2019, male specimens had some stage II (Sp-II), but predominantly stage III (Sp-III) spermaries (**Figure 5-27 C**) These data could be interpreted as an annual cycle with overlapping cohorts that culminates in the spring/summer, or a continuous reproductive cycle with some size categories not represented.

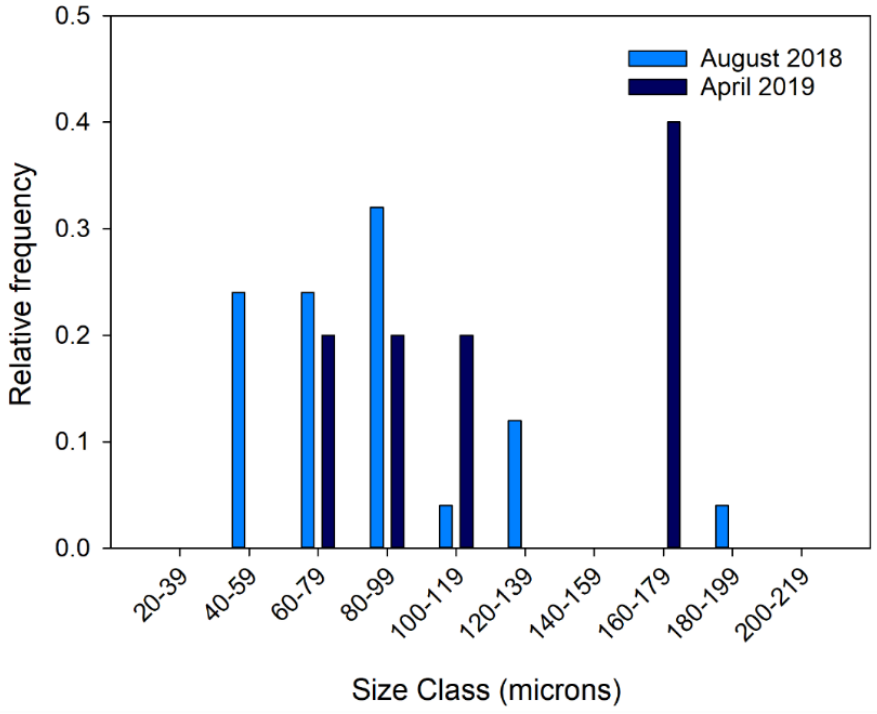

Figure 5-26. *Acanthogorgia spissa* oocyte size-frequency distribution for August 2018 and April 2019 samples
The x-axis shows oocyte size category and the y-axis shows relative frequency of oocytes within each category.

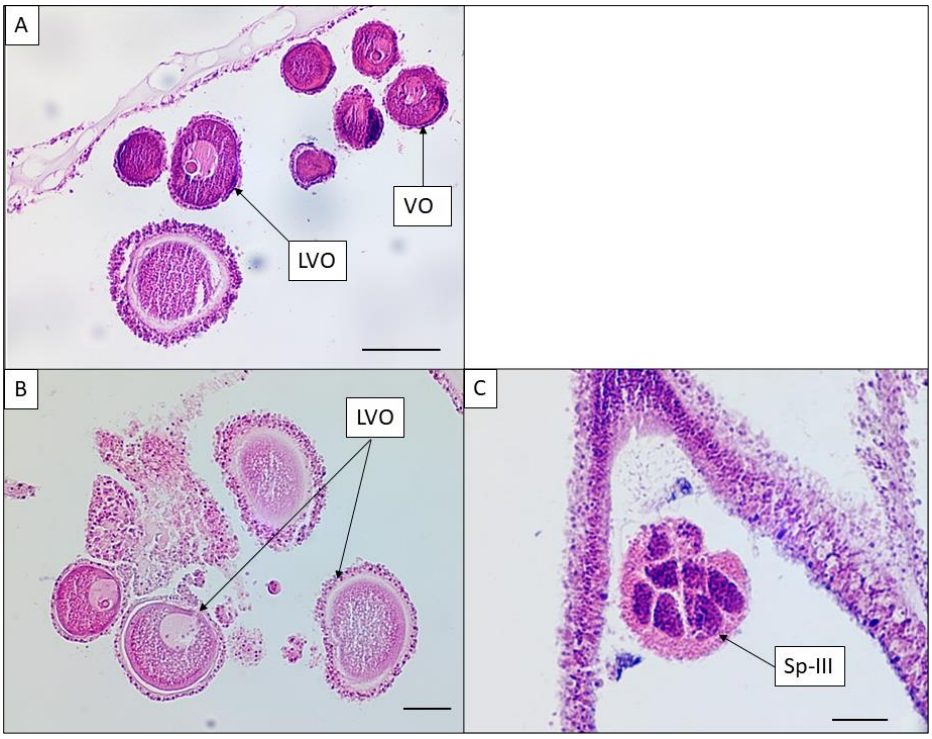

Figure 5-27. *Acanthogorgia spissa* thin section slides
A) Female collected in August 2018 showing LVO and VO, B) female collected April 2019 with VO, C) male collected April 2019 showing stage (Sp-II) spermaries. Scale bar: 100 µm.

5.5.3.7 *Plumarella* sp.

This species is a small octocoral (Family Primniodae) that is common on deep-coral reefs in the SEUS and can be found in high abundance on dead coral skeleton. We collected 19 samples of this species in 2019 from Richardson Hills, Richardson West and Savannah West, and the effort yielded both males and females. The oocyte size-frequency distribution (**Figure 5-28**) was dominated by small immature eggs (40–69 µm), but with a few large (200–219 µm) LVO (**Figure 5-29 A**). The male samples (**Figure 5-29 B**) also showed a range of spermatocyte stages (Sp-I to Sp-III). All samples were either male or female; there was no indication of hermaphroditism or brooding. The gamete data indicate the possibility of one or more annual cohorts with mostly small, developing oocytes in the spring, with a few large oocytes that may be remnants of an earlier spawning event.

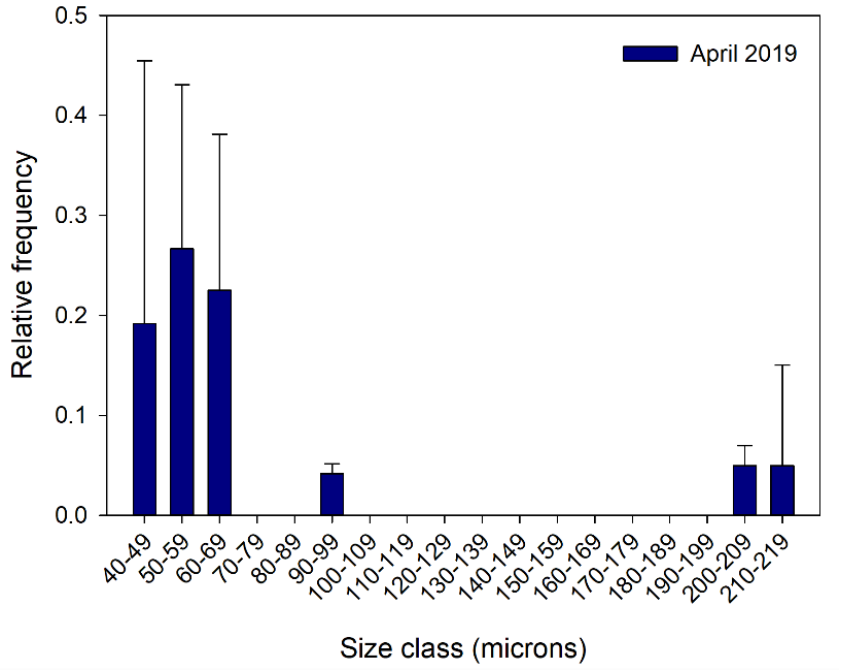

Figure 5-28. *Plumarella sp.* oocyte size-frequency distribution for April 2019 samples
The x-axis shows oocyte size category and the y-axis shows relative frequency of oocytes within each category.

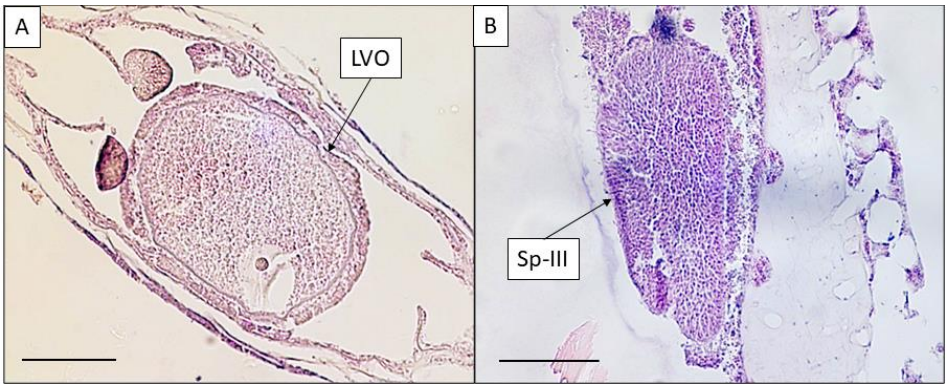

Figure 5-29. *Plumarella sp.*: thin section slides
A) Female collected in April 2019 showing LVO, B) male collected April 2019 showing stage III (Sp-III) spermaries. Scale bar: 100 µm

5.5.3.8 *Pseudodrifa nigra*

This soft coral (family Nephtheidae) can be locally abundant on deep reefs and hardbottoms in the SEUS and GOM. We collected no samples in 2018 but we sampled five colonies in April 2019 from Richardson Hills and Savannah Banks (**Figure 5-30**). The samples yielded females with an average oocyte diameter of 45.20 µm (SD 19.44) and males with a range of spermatocyte stages (Sp-I to Sp-IV). There were no indications of hermaphroditism or brooding so this species appears to be a gonochoristic broadcast-spawning species. The April sample was dominated by small eggs with a peak size category of 30–39 µm with a few mature gametes, which were still rather small (80–99 µm) (**Figure 5-31 A**). The male samples also showed a range of developmental stages including early spermatogonia (Sp-I) and spent spermaries (Sp-IV) as well as the intermediate (Sp-II and Sp-III) stages (**Figure 5-31 B**)

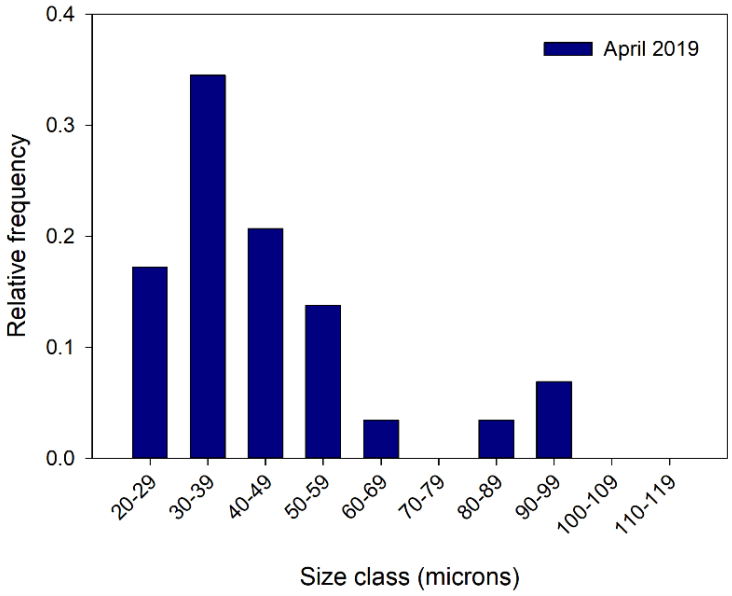

Figure 5-30. *Pseudodrifa nigra* oocyte size-frequency distribution for April 2019 samples
The x-axis shows oocyte size category and the y-axis shows relative frequency of oocytes within each category.

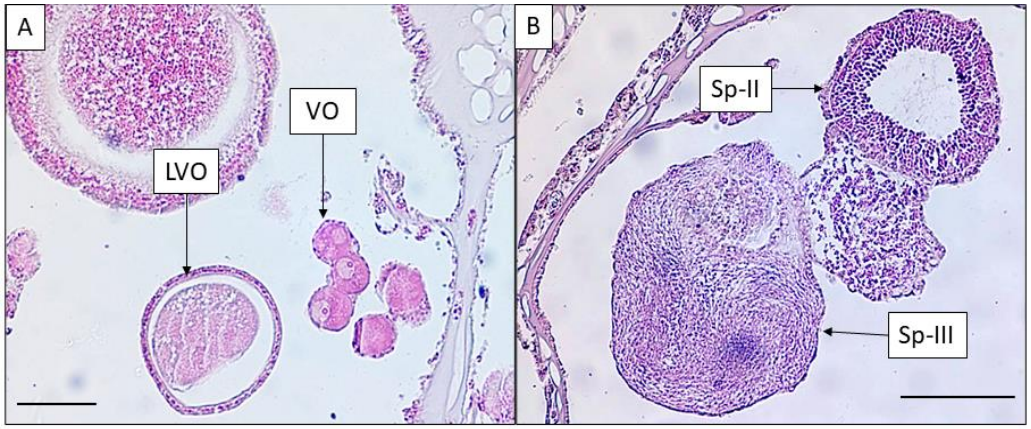

Figure 5-31. *Pseudodrifa nigra* thin section slides
A) Female collected April 2019 with VO and LVO, B) male collected April 2019 showing stage II (Sp-II) and stage III (Sp-III) spermaries. Scale bar: 100 µm.

5.5.3.9 *Swiftia casta*

This small white octocoral was very abundant in the Richardson Hills area, and we collected samples in April 2019 from Richardson Hills and Cape Lookout coral mounds and Richardson West rocky ledges. This species co-occurred with two other small white octocorals that appeared very similar but belonged to different taxa (*Muriceides cf hirta* and *Eunicella modesta*). The samples were identified through genetic barcoding to ensure samples from different species were not mixed. *Swiftia casta* was the most common species collected and the only one that had gametes. The six females had an overall average oocyte diameter of 107.85 µm (SD 12.51), but oocytes covered a wide range of sizes (20–340 µm). The size-frequency distribution (**Figure 5-32**) shows potentially four cohorts of increasing oocyte diameters with peaks at 60–80 µm, 100–120 µm, 140–160 µm, and a small peak at 260–280 µm. VO and LVO were present in the female samples (**Figure 5-33 A**). We classified male spermaries (**Figure 5-33 B**) as stage I (Sp-I) to stage III (Sp-III). These data indicate several rapidly developing cohorts terminating in release of large mature eggs.

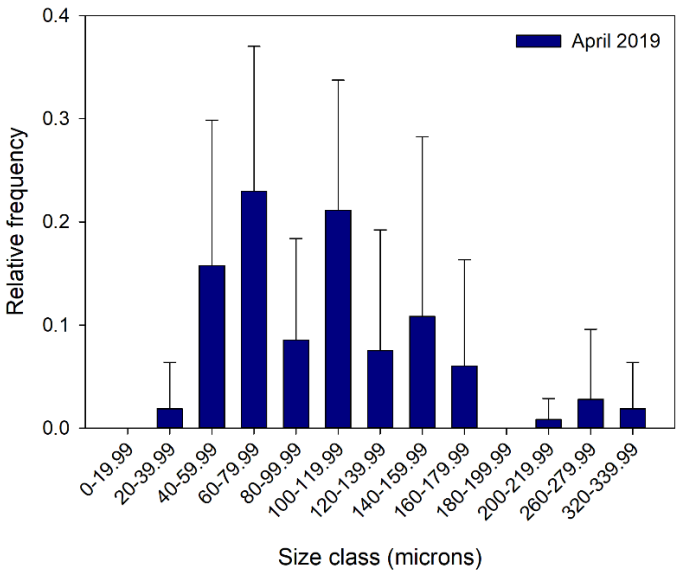

Figure 5-32. *Swiftia casta* oocyte size-frequency distribution for April 2019 samples
The x-axis shows oocyte size category and the y-axis shows relative frequency of oocytes within each category.

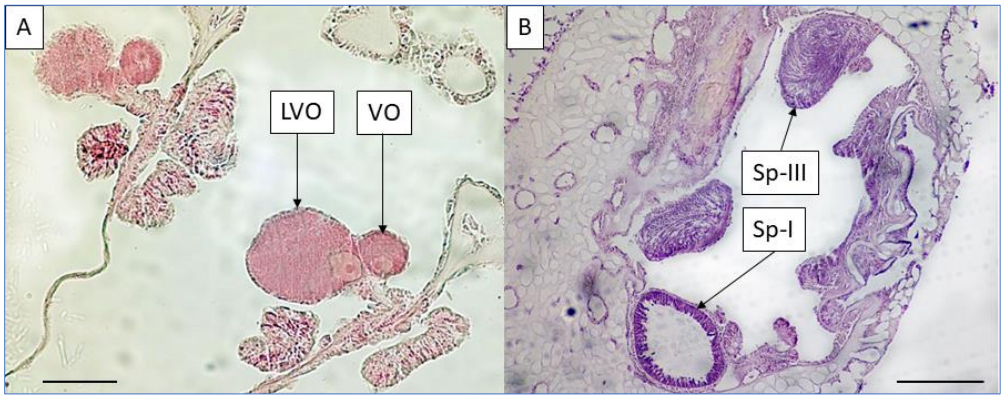

Figure 5-33. *Swiftia casta* thin section slides
A) Female collected April 2019 with VO and LVO, B) male collected April 2019 showing stage I (Sp-I) and stage III (Sp-III) spermaries. Scale bar: 100 µm.

5.5.4 Conclusions

Reproductive ecology knowledge of deepwater coral species is relatively scarce; research cruises are sporadic, usually occur during seasonal good weather periods, and often use vehicles with limited sampling capacity. Samples for reproductive studies are often collected opportunistically and data compiled 'piecemeal' from multiple cruises. Information collected during the August 2018 and April 2019 cruises builds on existing information on some species and creates starting points for others.

Information on reproductive strategy and gametogenic cycles is presented for five common scleractinian (*D. dianthus, E. profunda, L. pertusa, M. oculata* and *S. variabilis*) and four Alcyonacean species (*A. spissa, Plumarella sp., P. nigra* and *S. casta*). The most well studied of these is *Lophelia pertusa*; the reproductive strategy, gametogenic cycles and early life-history stages were described several years ago for populations in the northeastern Atlantic (Waller et al 2005, Brooke and Jarnegren 2013, Larsson et al 2014), western Atlantic margin (Brooke and Sogluizzo 2017), and GOM (Demopoulos et al 2017).

These studies show that *Lophelia pertusa* is a gonochoristic broadcast spawner with an annual protracted spawning period. Reproductive timing differ among populations, with spawning occurring off the northeastern Atlantic in February–March, and the western Atlantic/GOM in October–November. We had collected samples of *L. pertusa* from the mid-Atlantic canyons in September 2012 and May 2013; both of these sampling periods were one month later than the Deep SEARCH cruises (August 2018, April 2019). There were no females from spring 2019, but the August 2018 Deep SEARCH samples showed similar size distribution as the September 2012 canyons samples. However, the Deep SEARCH samples showed a smaller peak of small eggs in August that were not present in the September 2012 canyons samples. This indicates overlapping cohorts, with the larger eggs developing for release in the late fall, and smaller oocytes developing for the following fall spawning season.

We have also observed this phenomenon in samples from the Norwegian fjords but had not been previously observed in the western Atlantic. A study of four scleractinians from the southwestern Atlantic off Brazil (Pires et al 2014) concluded that *Lophelia pertusa* spawns May–July (late autumn/winter) also with some overlap in cohorts. Oocyte production is energetically costly, so hypothetically a higher food input would be required to support overlapping oocyte development. How timing and quantity of food supply vary across the different study regions is unknown but an important avenue of study as food supply has been shown to influence reproduction in the deep sea (Tyler et al 1982) and has been suggested as a driver of deep-sea octocoral reproduction (Lawson 1991).

The stony corals *D. dianthus* and *S. variabilis* are gonochoristic broadcast-spawning species with a single annual cohort. Samples of these species were also collected from the mid-Atlantic canyons, so provided a comparison for the Deep SEARCH data. The spring samples of *D. dianthus* showed an average oocyte diameter of 57.19 µm (SD 13.37) in April 2019, and 60.2 µm (SD 3.96) in May 2013, indicating a comparable gametogenic cycle for this species between the two regions. A study on reproduction of *D. dianthus* from the Chilean fjords indicated that oocyte production began in the Austral spring (September) culminating in spawning almost a year later in August when oocyte diameters reached 300 µm (Feehan et al. 2019). If the western Atlantic populations followed this pattern, this species would have maximum egg size and spawn in Feb–March. No samples were available for this time period for the western Atlantic to verify the extrapolation. Collecting deep-sea samples during the winter season is challenging, but fjords provide an opportunity to collect samples across a broader time period as they are more sheltered and accessible than offshore areas.

Samples of *S. variabilis* had an average oocyte diameter of 42.37 µm (SD 10.30) in April 2019 and 55.2 µm (SD 12.4) in May 2013. Neither species was collected in the fall from the mid-Atlantic canyons for comparison but the spring samples aligned well indicating similar reproductive cycles between the two regions. The available samples support an interpretation of a single cohort with seasonal reproduction. Analysis of a samples from New Zealand also supported this conclusion (Burgess and Babcock 2005), but sampling was limited to April (fall). From their analysis of samples from southwestern Atlantic population, Pires et al (2014) concluded that this species has continuous reproduction with a peak in September. Average oocyte diameters aligned with those from other locations, but maximum sizes observed by Pires (336 µm) were larger than previously documented.

Samples of *Madrepora oculata* from the SEUS show no clear seasonal signal but appear to have a series of cohorts that are produced either continuously, or over an extended period. This species had larger eggs (120 µm) than *D. dianthus*, or *S. variabilis* for the same April time period (57.19 µm 42.37µm respectively). Studies of this species from the northeastern Atlantic also concluded a periodic gametogenic cycle for *M. oculata* with larger eggs (405 µm) than *L. pertusa* (140 µm) for the fall time period. For the southwestern Atlantic populations, Pires et al (2014) concluded that *M. oculata* has a continuous reproductive cycle with maximum oocyte diameter of 650 µm, which is much larger than documented elsewhere.

There is very little information on the reproduction of *E. profunda*, which has a limited distribution and is not as common as the other species. Samples from August and April both had larger average oocyte diameter (257.58 and 289 µm respectively) than the other species studied, and possibly a continuous or extended spawning period. Congeneric species *E. rostrata* from the southwestern Atlantic (Pires et al 2014), also showed continuous reproduction and very large eggs (average mature oocyte diameter 457.60 µm). Large eggs and continuous gametogenic cycles are often indicative of a brooding strategy rather than broadcast spawning, although this is not always the case. If *E. profunda* is a brooder, it would be the only reef-building stony coral species known that is not a broadcast spawner, but more data is needed before reproductive strategy can be established.

Octocorals are the most diverse deep-coral taxa; they have a global distribution and are found in all depth zones. There are at least 2,000 known species, but the taxonomy of many families remains unresolved so the exact number of species in unknown. There is less known of the reproductive ecology of octocorals than for scleractinians; this holds true for shallow-water species as well as the deep sea. Octocorals have a range of reproductive strategies but they fall into broad categories of synchronous broadcast spawning or brooding, which may be synchronous or asynchronous. Larger egg sizes are generally characteristic of brooding species but this is not always the case. Reproductive cycles are not always clear from the distribution of oocyte sizes.

Four species from the Deep SEARCH octocoral collections had sufficient samples to provide useful data. The small bushy *Acanthogorgia* genus (Family Acanthogorgiidae) is moderately abundant on deep rocky habitats. There are three species in the western Atlantic (*A. armata*, *A. aspera* and *A. spissa*) that overlap in distribution (World Register of Marine Species). The multi-species complex potentially confounded description of species-specific reproduction, but the samples were resolved using genetic barcoding. The most abundant was *A. spissa*, and samples from both August 2018 and April 2019 contained gametes. Samples from both time periods showed separate sexes with no indications of hermaphroditism. The females from both time periods contained a range of oocyte sizes (40–200 µm) with no clear pattern. The males also showed a range of spermatocyte maturity (Sp-II/Sp-III). Continuous reproduction is often associated with brooding, but there were no indications of embryos or planulae in these samples.

We observed a similar pattern of quasi-continuous oocyte sizes in congener *A. aspera* from the mid-Atlantic canyons (Brooke and Sogluizzo 2017). Many shallow gorgonian species maintain a pool of intermediate sized oocytes, that continuously or periodically develop into mature gametes for release (Excoffen et al 2004, Zeevi and Benayahu 1999). Some deep-sea gorgonian octocorals may have similar complex reproductive cycles but more data is needed before conclusions can be drawn for most deep octocoral species.

The dead skeletons of deep stony corals offshore southeastern US are often colonized by the small Primoid octocoral *Plumarella* sp. The samples used for the reproductive analysis were all identified by genetic barcoding as *Plumarella sp. 1*. This species appears to be gonochoristic with no indications of hermaphroditism. The female samples were dominated by small (40–70 µm) oocytes with a small number of larger oocytes (>200 µm), which may have represented the beginning and end respectively of an annual gametogenic cycle.

Studies of three species of Antarctic primnoids revealed that all were either confirmed or likely brooders with large eggs (Orejas et al 2002, Brito et al 1997). A common primnoid from the mid-Atlantic canyons *Primnoa resedaeformis*, showed a larger (but non-significant) average oocyte diameter in September than in May, indicating some level of seasonality, but a wide range of oocyte classes were present in both time periods (40–400 µm in May, 40–600 µm in September); we observed no evidence of brooding (Brooke and Sogluizzo 2017). The reproductive cycles of species within a taxon can vary, but the gametogenic data from *Plumarella* sp. 1 indicate a very different reproductive strategy from the other primnoids cited

above. However, the *Plumarella sp. 1* data are preliminary, and more information is needed before conclusions can be drawn about this species.

Several tropical soft coral families (including the Nephtheidae) are capable of asexual propagation via non-reproductive budding or fragmentation (Benayahu and Loya 1987). This process can facilitate high population growth and rapid colonization, resulting in high local abundance and rapid post-disturbance recovery (Dahan and Benayahu 1997). The soft coral *Pseudodrifa nigra* (Family Nephtheidae) occurs on deep rocky habitats and coral reefs off the east coast of Florida and GOM. It is relatively uncommon but as with the shallow tropical species, can be locally abundant.

It is plausible that deep- water members of these families also use asexual propagation to expand population size. Sexual reproduction strategies in Nephtheids include broadcast spawning and brooding. A shallow tropical nephtheid, *Dendronephthya hemprichi* from the Red Sea was found to be a gonochoric broadcast-spawning species with small oocytes (< 100 µm), which are abundant year-round (Dahan and Benayahu 1997). Samples of *P. nigra* collected during the April 2019 cruise, showed a limited range of oocyte sizes (20–100 µm) but a wide range of maturity levels in both males and females. The small terminal ooyctes and no indication of brooding indicate that *P. nigra* is a broadcast spawner and given that all maturity levels were present in the same time period, possibly a continuous reproducing species like other members of the Neptheidae. More data are needed to confirm (or refute) this conclusion.

The small white octocoral, *Swiftia casta* (Family Plexauridae) occurs in deep water along the western Atlantic and GOM. Other members of this family are broadcast spawners, internal brooders or in one documented case (*Paramuricea clavata*), external brooders (Coma et al 1995). Samples of *S. casta* collected in April 2019 show a wide range of oocyte size classes (20–400 µm) and maturity levels, indicating a continuous reproductive cycle, terminating in either broadcast spawning or brooding. There were no indications of internal brooding in samples of this species, but external brooding is a possibility.

Broadcast spawning vs. brooding in octocorals can vary by taxonomic order (Babcock 1990, Ecklebarger et al 1998), and may be phylogenetically constrained or influenced by environmental conditions. There is also evidence that some octocorals can propagate vegetatively, which has implications for post-impact recovery and population resilience. Information on reproduction and early life histories of the Octocorallia, particularly cold and deepwater taxa is a major information gap and will hamper any efforts to restore or understand community dynamics of these ecologically important groups.

5.6 Seep Mussel Reproductive Biology

5.6.1 Introduction

Methane seeps were first discovered in the GOM at the base of the West Florida Escarpment in 1984 (Paull et al 1984, Hecker 1985), although Hecker had seen mussel beds in Baltimore Canyon in 1982 using a towed camera but was unaware of their significance at the time. These seeps were ‘re-discovered’ and explored in 2011 during the mid-Atlantic canyons study (Ross et al. 2017).

Chemosynthetic (methanotropic and thiotrophic) mussels (Mytilids in the subfamily Bathymodiolinae) are often the dominant fauna at methane seeps and hydrothermal vents (MacDonald et al 1990), with *G. childressi* the most common species in the shallow GOM and western Atlantic. In 2012, the US Geological Survey discovered hundreds of gas plumes along the western Atlantic margin (Skarke et al 2014), most of which have not been surveyed. Some of these newly discovered seeps (Norfolk Canyon) have extensive areas of seepage supporting dense mussel fields and other seep-endemic fauna (Ross et al. 2017).

Two deep (> 2,000 m) seeps (Blake Ridge and Cape Fear) off North Carolina had been discovered in the 1990s during a drilling survey. The seep mussels at these sites are *B. heckerae*, which are larger and do not occur as shallow as *G. childressi*. The primary source of energy for cold-seep mussels is methane and/or sulfides, which are processed by bacteria in the gills, although *G. childressi* are also capable of heterotrophy by filtering phytodetritus and bacteria from the water (Page et al. 1990, Pile and Young 1999). Most shallow-water mytilid mussels have seasonal reproductive cycles culminating in broadcast-spawning and plantotrophic larvae. Reproductive cycles of *G. childressi* in the GOM also have a seasonal gametogenic cycle (Tyler et al 2006), which was not expected given the continuous food supply and attenuation of seasonal environmental signals; however reproductive seasonality was found in hydrothermal vent Bathymodiolinae (Colaco et al 2006, Hessler et al 1988). Despite continued research efforts on many aspects of chemosynthetic ecosystems, there are still data gaps in some aspects of Bathymodiolin reproductive ecology.

The objective of this study element was to describe the gametogenic cycles of *B. heckerae* at the deep cold seeps off North Carolina and determine whether seasonal signals exist in this data set.

5.6.2 Methods

We collected the methane-seep mussels *Bathymodoilus heckerae* from Blake Ridge Seep (32.494N, 76.191W; depth 2,155 m) in August 2018 (*DSV Alvin* dive 4967) and April 2019 (ROV *Jason* dive 1136). We photographed and measured each individual mussel before removing one valve and preserving them in 10% fully buffered formalin for reproductive analysis. Our histological methods were similar to those described for corals in **Section 5.2.1.2**, except there was no need for the decalcification step, and we dissected the gonad material from the rest of the body prior to further histological processing. We conducted an analysis of female gametogenesis by using oocyte size and maturity, but we assigned the male stages based on Tyler et al. (2007), as follows:

- Stage I: Onset of spermatogenesis. Proliferation of spermatogonia around the edge of the acinus (sack-like cavities within the gonad)
- Stage II: Appearance of spermatids in the lumen of the acinus
- Stage III: Lumen of acinus fills with spermatids and spermatozoa
- Stage IV: Lumen is full of spermatozoa and begin to appear as whorls in the acinus.
- Stage V: Whorls of spermatozoa fill the acinus lumen and are ready for spawning
- Stage 0: Post spawning—deflated/empty acinus surrounded by somatic cells

For each time period, we documented the oocyte diameter and male stages, and such are reported below.

5.6.3 Results

We calculated the average feret diameter and SD from the mean for the female gametes (**Table 5-12**). To examine the size distribution, we split oocytes from each female and sampling period into size categories (10 µm) and calculated the relative frequency for each category. We used oocyte diameters and size-

frequency distributions to infer the timing and periodicity of female gametogenic cycles. We classified male reproductive stages, and these are also shown in **Table 5-14.**

Table 5-13.Summary of gamete stages from *Bathymodiolus heckerae* from Blake Ridge Seep

Collected in August 2018 and April 2019. Average oocyte diameter (± SD) and male spermatocyte stages are shown for each time period.

Sampling period	Oocyte diameter (µm)	Male stages
August 2018	42.80 ± 7.78	II–V
April 2019	40.31 ± 1.18	II–V

Size-frequency distributions of the mussel population (**Figure 5-34**) showed a distribution greatly skewed towards the smaller sizes in the population. The August samples were clearly dominated by 25–75 mm individuals, whereas in April the peak sizes were similar but less pronounced. Individuals greater than 150 mm comprised 8% and 13% of the population for August 2018 and April 2019 respectively.

The average oocyte diameters and the male gamete stages were very similar for both time periods (**Table 5-13**). The oocyte size-frequency distribution (**Figure 5-34**) was dominated by 30–50 µm oocytes for both time periods and the histological analysis shows the co-occurrence of immature and mature eggs in both time periods (**Figure 5-35 A, C**). The males also show a range of spermatocyte stages (**Figure 5-35 B, D**)

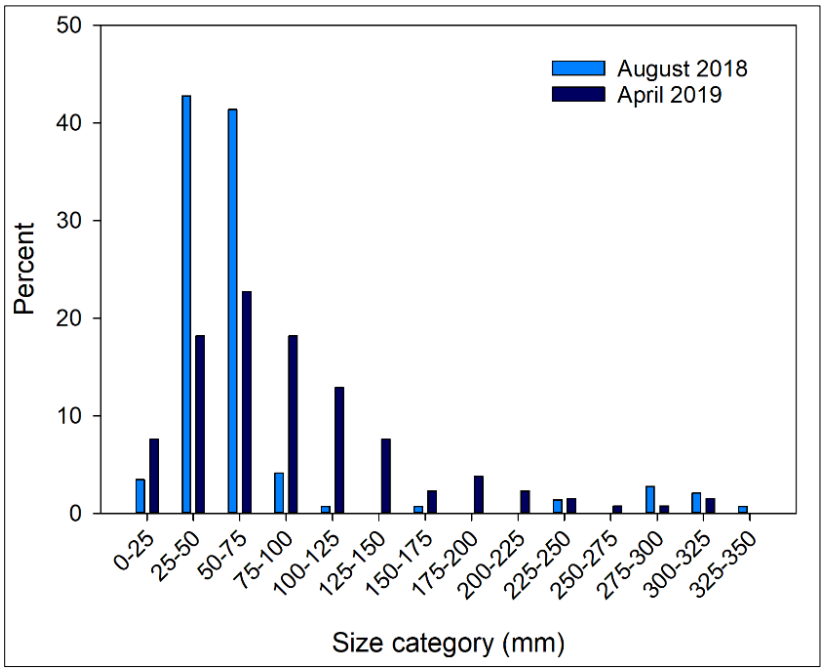

Figure 5-34. *Bathymodiolus heckerae* size-frequency distribution of samples collected in August 2018 and April 2019 from Blake Ridge Seep

The x-axis shows mussel size (length) category, and the y-axis shows percentage of mussels within each category.

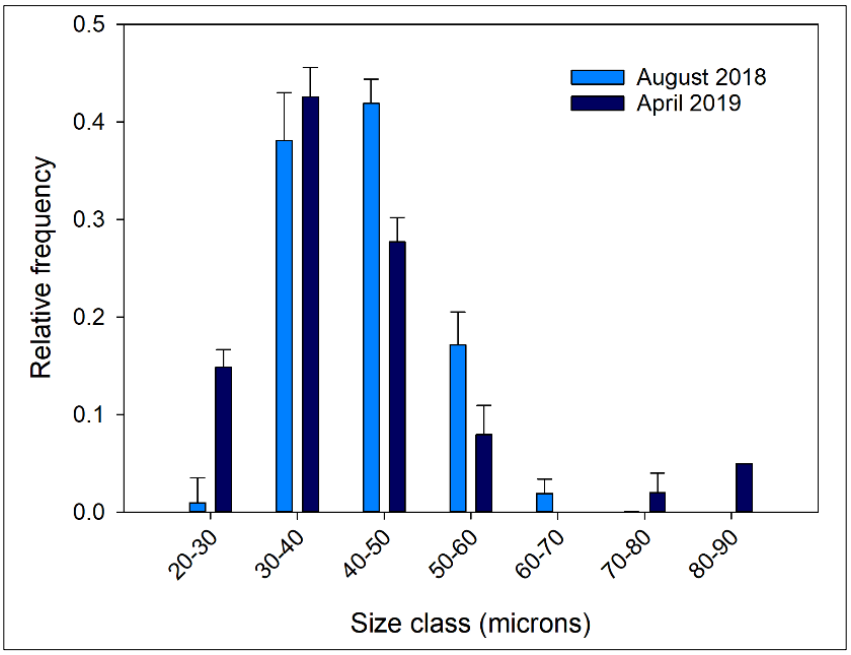

Figure 5-35. *Bathymodiolus heckerae* oocyte size-frequency distribution for August 2018 and April 2019 samples
The x-axis shows oocyte size category and the y-axis shows relative frequency of oocytes within each category

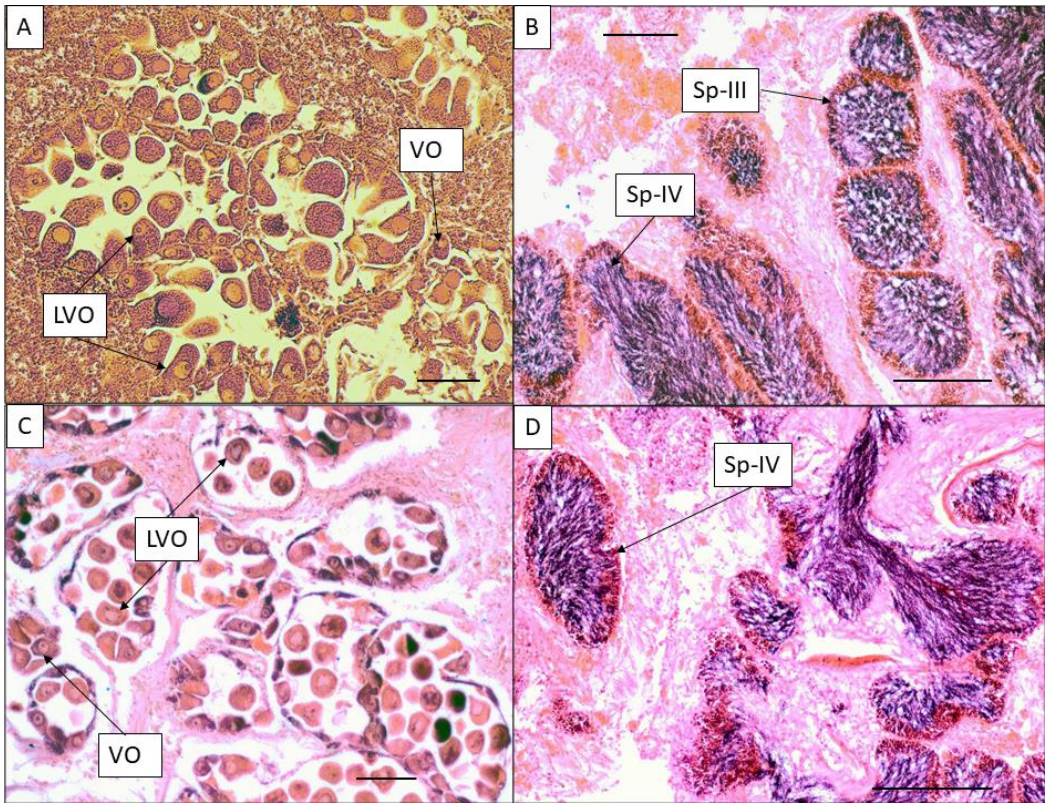

Figure 5-36. *Bathymodiolus heckerae* thin section slides
A) Female collected in August 2018 showing LVO, B) male collected August 2018 showing stage III (Sp-III) and stage IV (Sp-IV) spermatocysts, C) female collected April 2019 with VO, D) male collected April 2019 showing stage IV (Sp-IV) spermatocysts. Scale bar: 100 µm.

5.6.4 Conclusions

The mussel length distribution from both time periods was skewed significantly towards the smaller individuals, with a low percentage contribution by animals > 15 cm. It is not unusual to see smaller numbers of the large individuals in any species distributions; however, this species can reach lengths > 35 cm in some habitats and the size-frequency distribution (**Figure 5-34**) shows a sharp reduction in animals less than half the maximum size. Age, growth and mortality of this species has not been elucidated so population dynamics are unclear. The size-frequency distribution was generated with a limited sample size (two time periods), and it is unclear whether the pronounced peak in small size classes in August 2018 reflects a recruitment event, or simple variation in the population.

The presence of mature and immature gametes in both genders and time periods indicates that reproduction is continuous, but the majority of gametes are small/immature and there are clear peaks in size distribution. Continuous reproduction can be represented by gametes consistently present across size classes, with mature gametes released continuously in small quantities as they mature. This kind of reproduction is generally found in brooding species. Broadcast-spawning species need synchronization of gamete maturity among part or all of the population to ensure fertilization success. The size-frequency distribution curves show clear peaks in oocyte distribution, but no clear seasonal spawning period. This may indicate continuous cohorts of eggs that are released in batches within the population.

A similar reproductive strategy was observed in *G. childressi* from the mid-Atlantic canyons (Brooke and Sogluizzo 2017). However, con-specifics in the GOM showed strong developmental synchrony between males and females, which began gametogenesis in November, followed by oocyte growth and proliferation of spermatozoa from February to September, with spawning occurring from October to February (Tyler et al 2007). A review of bathymodiolin reproduction from seeps in the western Atlantic and GOM (Plowman 2017) showed peaks in oocyte size classes, with few exceptions. The author concluded that all species reproduced periodically and synchronously, but the clear seasonality observed in the GOM could not be confirmed elsewhere. Patterns of reproduction in the Bathymodiolinae may reflect their ability to filter feed and therefore be influenced by surface productivity.

5.7 Population Connectivity

Section Authors: Andrea Quattrini, Heather Shull, Makiri Sei, Cheryl Morrison, Martha Nizinski

5.7.1 Introduction

Larval dispersal plays a key role in connecting populations in the marine environment. As larvae are dispersed with ocean currents, there are many opportunities to colonize new areas and exchange gametes, leading to seemingly “open” populations (Cowen et al. 2007). Population genetic and oceanographic modeling data, however, have also shown that populations can be more “closed” than previously recognized (Cowen et al. 2007), revealing that local or self-recruitment can be quite high.

Local recruitment, inbreeding, genetic drift, and selective forces can all contribute to differentiation of populations (Baums et al. 2005). Thus, measuring larval dispersal solely via dispersal models does not always correspond to *realized* connectivity and differentiation within and among natural populations (Jahnke et al. 2017). Instead, by using genetics, estimates of realized connectivity (both historical and contemporary), or effective gene flow, can be obtained while simultaneously revealing the importance of additional evolutionary processes (selection and drift) that shape populations. Realized connectivity depends on the interaction between oceanographic features and abiotic conditions and species-specific life-history traits that affect dispersal and population demography.

Determining the levels and pathways of realized genetic connectivity and other evolutionary processes that shape connections among populations is not only important for understanding how marine biodiversity is generated, knowledge of these evolutionary forces is also critical for conservation as they play a role in the resiliency of populations to human and environmental disturbances.

Understanding the extent to which populations are connected is vital to the development and implementation of effective management and conservation efforts. Assessing population connectivity in marine environments is challenging, especially in the deep sea, but genetic and genomic analysis can illuminate patterns that were previously undetectable across depth and geographic distance or boundaries. In addition to unveiling patterns in population dynamics, genomic-level analysis enables fine-scale taxonomic assessments and can potentially reveal hidden (cryptic) species, even within well-studied groups (Herrera and Shank 2016).

While there are many methods to obtain genome-wide informative markers, restriction-site associated DNA (RAD) sequencing (RAD-seq) has emerged as a popular method for marker discovery in population genomics (Miller et al 2007, Davey and Blaxter 2010). RAD-seq relies on restriction enzymes and HTS to produce 1,000s of genomic markers, from which single nucleotide polymorphisms (SNPs) can be attained and subsequently used in downstream analyses. SNPs can not only be used to determine levels of genetic diversity and rates of gene flow, but they can also be used, for example, to discover genes that are potentially under selection and indicative of adaptation to environmental conditions. We used RAD-seq to obtain SNPs from a variety of invertebrates in deep-sea habitats along the US Atlantic margin, including samples from the GOM for some taxa (**Figure 5-37).** We focused our investigation on critically important foundation species and their associated invertebrates, including bathymodiolin mussels (*Gigantidas childressi, B. heckerae)*, octocorals (*Plumarella* sp., *Paramuricea* spp.*)*, scleractinians (*Lophelia pertusa)*, ophiuroid brittle stars (*Asteroschema* spp., *Ophioctenella acies*), and sea cucumbers (*Chiridota heheva)*.

Chemosynthetic seeps along the US Atlantic margin are thought to be numerous (Skarke et al. 2014), though they remain poorly characterized. The bathymodiolin mussels that dominate many cold-seep communities serve as characteristic indicator fauna for methane and/or sulfide-rich environments (reviewed in Sibuet and Olu 1998). This includes the seep communities found along the Blake Ridge Diapir, where one of the first seeps was discovered in the region- in the deep waters off the coast of South Carolina (Paull et al. 1995, Van Dover et al. 2003). More recently, cold-seep communities were discovered among the submarine canyons off the coast of Baltimore, Maryland and Norfolk, Virginia (Skarke et al. 2014, Bourque et al. 2017, Demopoulos et al. 2017). Characterization of the population dynamics and connectivity for bathymodiolins, an ecologically important group of deep-sea mussels, is timely as resource (mineral, oil and gas) extraction efforts continue in deep waters. Understanding connectivity in the region can help in establishing conservation areas or potential protection measures for cold-seep fauna.

Benthic ecosystems supported by CWCs are distributed throughout the world's oceans and can be found along continental slopes, canyon walls, and seamounts (Freiwald et al. 2004, Roberts et al. 2009). Evidence of CWC populations in US waters continues to accumulate but there are still large knowledge gaps pertaining to the overall functionality of CWCs in broader biogeochemical cycles, the extent of the ecosystem services they provide, and the regional and global population dynamics of these ecosystem engineers. Given that CWCs can occur over large, spatially fragmented, geographic scales, it is important to understand the degree of connectivity among existing populations. The degree of connectivity contributes to the resiliency of each population and the probability of recovery from potential natural or anthropogenic impacts.

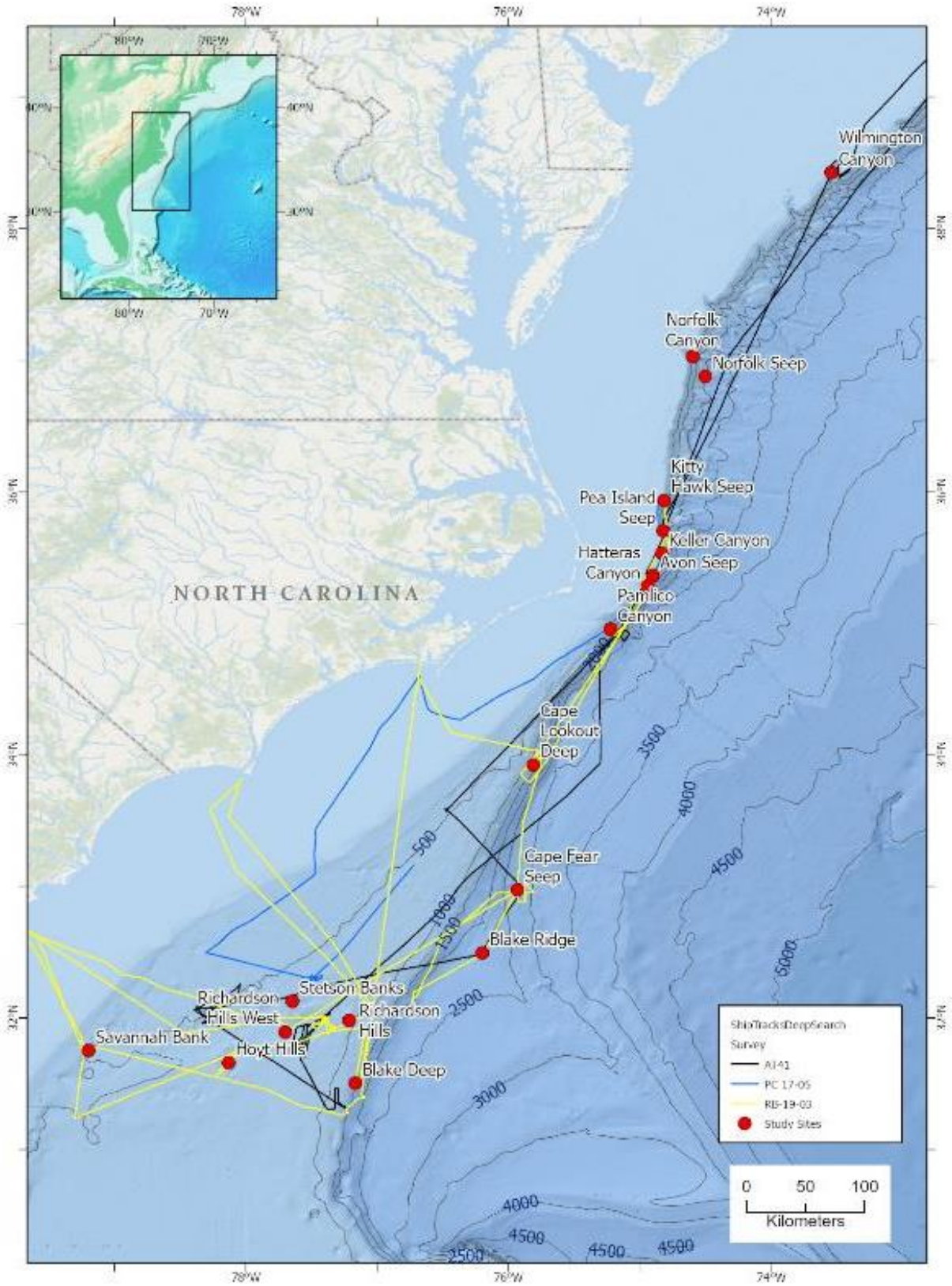

Figure 5-37. Map of study area marked with deep-sea sites used for population genomics

5.7.2 Bathymodiolinae

Gigantidas childressi (Gustafson et al. 1998), which dominates the Baltimore and Norfolk Canyon Seep sites (Coykendall et al. 2019), is typically found between 400 and 2,200 m, while *Bathymodiolus heckerae* (Gustafson et al. 1998) is the dominant species found among deeper cold seeps between 2,200 and 3,300 m (Cordes et al. 2009), including Blake Ridge (Van Dover et al. 2003).

In general, bathymodiolin species found at cold-seep habitats have high dispersal capabilities (Arellano et al. 2009, Young et al. 2012) and high estimated rates of gene flow (Craddock et al. 1995, Thaler et al. 2017) suggesting highly connected populations throughout the region. However, due to the limitations of sampling in deep waters and the previous molecular and sequencing methodology used (Sanger sequencing of a few mitochondrial genes, allozyme or microsatellite scoring), the rates and directions of gene flow (level of connectivity) between spatially discrete cold-seep sites in the region are unknown.

As several bathymodiolin mussel species are believed to be panmictic (Craddock et al. 1995, Carney et al. 2006, Breusing et al. 2015) with long-range dispersal capabilities (Arellano and Young 2009), underlying genetic differences may be influencing the fitness of one or both species and their ability to colonize and thrive at different depths. Of particular note, some bathymodiolins host a variety of different chemosynthetic endosymbiotic bacteria (Duperron et al. 2007) that may enable optimal utilization and turnover of chemical nutrients for energy.

In addition to nutrient type and availability, the depth segregation previously observed among cold-seep communities between 1,000 and 2,000 m (Olu et al. 2010) suggests potential barriers to dispersal across depth or depth-related adaptations among species inhabiting specific depth niches. Therefore, genetic differences likely exist among bathymodiolins that are influenced by environmental differences like those associated with depth (temperature and pressure) and/or seepage composition. With the continual optimization of HTS approaches for non-model organisms, genome-wide diversity assessments could clarify how selective pressures have influenced diversification within this group.

Here, we present a connectivity assessment of the recently discovered bathymodiolin cold-seep communities along the US Atlantic margin, dominated by *G. childressi* along the upper to middle continental slope and *B. heckerae* in lower-slope depths at Blake Ridge. We also examined whether genes potentially under selection in bathymodiolins would be related to the different depths that they inhabit, thus providing further insight into molecular underpinnings of niche ranges in cold-seep mussels.

5.7.2.1 Bathymodiolin Methods

We extracted DNA from all bathymodiolin mussels collected on the *Ron Brown* and *Atlantis* cruises. Mussel samples from Norfolk Canyon Seep (NCS), Baltimore Canyon Seep (BCS), and Chincoteague Seep (CTS) collected on prior cruises of USGS collaborators Demopoulos and Morrison were included to augment analyses. In total, we obtained high molecular weight DNA from 183 mussels (**Table 5-14**). *G. childressi* and *B. heckerae* gDNA were quantified with Qubit dsDNA BR Assay Kit (Thermo Fisher), and the presence of high molecular weight DNA was confirmed with 0.8% agarose gel electrophoresis, using GelRed® DNA stain (Biotium, Fremont, CA) for visualization. We diluted the genomic DNA (gDNA) to 20 ng/µL in 50 µL volumes and sent it to Floragenex (Beaverton, OR) for RAD-seq. We constructed DNA libraries using the 6-cutter *PstI* enzyme, followed by sequencing 100 bp SE reads across four lanes of an Illumina HiSeq4000 (University of Oregon's Genomics and Cell Characterization Core Facility lab).

Table 5-14. Bathymodiolin mussel samples collected

From the study area from either (*G. childressi*) Norfolk Canyon Seep (NCS), Baltimore Canyons Seep (BCS), or Chincoteague Seep (CTS) or (*B. heckerae*) from Blake Ridge Seep (BRS). The asterisk (*) denotes samples used in selection analyses, while the (x) denotes samples excluded from analyses based on sequencing results.

Sample ID	Species	Site	Depth (m)
HRS-1704-CM-4*	*G. childressi*	NCS	1,482
HRS-1704-CM-5*	*G. childressi*	NCS	1,482
HRS-1704-CM-7(x)	*G. childressi*	NCS	1,482
HRS-1704-CM-9	*G. childressi*	NCS	1,482
HRS-1704-CM-11	*G. childressi*	NCS	1,482
HRS-1704-CM-15	*G. childressi*	NCS	1,491
HRS-1704-CM-17	*G. childressi*	NCS	1,491
HRS-1704-CM-19	*G. childressi*	NCS	1,491
HRS-1704-CM-21	*G. childressi*	NCS	1,491
HRS-1704-CM-23	*G. childressi*	NCS	1,491
HRS-1704-CM-25	*G. childressi*	NCS	1,491
HRS-1704-CM-28	*G. childressi*	NCS	1,491
HRS-1704-CM-29	*G. childressi*	NCS	1,491
HRS-1704-CM-31	*G. childressi*	NCS	1,491
HRS-1704-CM-33*	*G. childressi*	NCS	1,494
HRS-1704-CM-37	*G. childressi*	NCS	1,494
HRS-1704-CM-39*	*G. childressi*	NCS	1,494
HRS-1704-CM-41*	*G. childressi*	NCS	1,494
HRS-1704-CM-43	*G. childressi*	NCS	1,494
HRS-1704-CM-45	*G. childressi*	NCS	1,494
HRS-1704-CM-47	*G. childressi*	NCS	1,494
HRS-1704-CM-49	*G. childressi*	NCS	1,494
HRS-1704-CM-51	*G. childressi*	NCS	1,494
MAS283	*G. childressi*	NCS	1,570
MAS284	*G. childressi*	NCS	1,570
MAS285	*G. childressi*	NCS	1,570
MAS286	*G. childressi*	NCS	1,574
MAS288	*G. childressi*	NCS	1,574
MAS289	*G. childressi*	NCS	1,574
MAS290	*G. childressi*	NCS	1,574
MAS291	*G. childressi*	NCS	1,574
MAS292	*G. childressi*	NCS	1,570
MAS293	*G. childressi*	NCS	1,570
MAS294(x)	*G. childressi*	NCS	1,570
MAS295*	*G. childressi*	NCS	1,570
MAS296(x)	*G. childressi*	NCS	1,570
MAS297	*G. childressi*	NCS	1,570
MAS298	*G. childressi*	NCS	1,570
MAS299	*G. childressi*	NCS	1,570
MAS306	*G. childressi*	NCS	1,570
MAS310	*G. childressi*	NCS	1,570
MAS311	*G. childressi*	NCS	1,587
MAS313*	*G. childressi*	NCS	1,570
MAS314*	*G. childressi*	NCS	1,548
MAS320	*G. childressi*	NCS	1,594
MAS321*	*G. childressi*	NCS	1,594

Sample ID	Species	Site	Depth (m)
MAS322	*G. childressi*	NCS	1,535
MAS323*	*G. childressi*	NCS	1,535
MAS326*	*G. childressi*	NCS	1,,612
MAS327	*G. childressi*	NCS	1,612
MAS338*	*G. childressi*	NCS	1,457
MAS339*	*G. childressi*	NCS	1,457
MAS340	*G. childressi*	NCS	1,457
MAS341	*G. childressi*	NCS	1,457
MAS343*	*G. childressi*	NCS	1,457
HRS-1704-CM-55	*G. childressi*	CTS	1,037
HRS-1704-CM-58*	*G. childressi*	CTS	1,037
HRS-1704-CM-61*	*G. childressi*	CTS	1,037
HRS-1704-CM-63*	*G. childressi*	CTS	1,037
HRS-1704-CM-65(x)	*G. childressi*	CTS	1,037
HRS-1704-CM-67*	*G. childressi*	CTS	1,037
HRS-1704-CM-69	*G. childressi*	CTS	1,037
MAS537*	*G. childressi*	BCS	362
MAS538(x)	*G. childressi*	BCS	362
MAS539	*G. childressi*	BCS	364
MAS540	*G. childressi*	BCS	364
MAS541*	*G. childressi*	BCS	364
MAS542*	*G. childressi*	BCS	364
MAS543	*G. childressi*	BCS	364
MAS544*	*G. childressi*	BCS	364
MAS545	*G. childressi*	BCS	400
MAS546(x)	*G. childressi*	BCS	400
MAS547	*G. childressi*	BCS	400
MAs548*	*G. childressi*	BCS	400
MAS549	*G. childressi*	BCS	401
MAS550	*G. childressi*	BCS	401
MAS551*	*G. childressi*	BCS	401
MAS552*	*G. childressi*	BCS	401
MAS553*	*G. childressi*	BCS	401
MAS554	*G. childressi*	BCS	401
MAS555	*G. childressi*	BCS	401
MAS556	*G. childressi*	BCS	401
MAS557*	*G. childressi*	BCS	401
MAS561	*G. childressi*	BCS	401
MASm32	*G. childressi*	BCS	407
MASm36*	*G. childressi*	BCS	407
CM-00128*	*B. heckerae*	BRS	2,168
CM-00129	*B. heckerae*	BRS	2,168
CM-00130	*B. heckerae*	BRS	2,168
CM-00131	*B. heckerae*	BRS	2,168
CM-00132	*B. heckerae*	BRS	2,168
CM-00133	*B. heckerae*	BRS	2,168
CM-00134	*B. heckerae*	BRS	2,168
CM-00135*	*B. heckerae*	BRS	2,168
CM-00136	*B. heckerae*	BRS	2,168
CM-00137*	*B. heckerae*	BRS	2,168

Sample ID	Species	Site	Depth (m)
CM-00138	*B. heckerae*	BRS	2,168
CM-00139*	*B. heckerae*	BRS	2,168
CM-00140	*B. heckerae*	BRS	2,168
CM-00141	*B. heckerae*	BRS	2,168
CM-00142	*B. heckerae*	BRS	2,168
CM-00143	*B. heckerae*	BRS	2,168
CM-00144	*B. heckerae*	BRS	2,168
CM-00146(x)	*B. heckerae*	BRS	2,168
CM-00148*	*B. heckerae*	BRS	2,168
CM-00149*	*B. heckerae*	BRS	2,168
CM-00150*	*B. heckerae*	BRS	2,168
CM-00151	*B. heckerae*	BRS	2,168
CM-00153	*B. heckerae*	BRS	2,168
CM-00154*	*B. heckerae*	BRS	2,168
CM-00155*	*B. heckerae*	BRS	2,168
CM-00157	*B. heckerae*	BRS	2,168
CM-00158	*B. heckerae*	BRS	2,168
CM-00160	*B. heckerae*	BRS	2,168
CM-00161	*B. heckerae*	BRS	2,168
CM-00163	*B. heckerae*	BRS	2,168
CM-00165	*B. heckerae*	BRS	2,168
CM-00166	*B. heckerae*	BRS	2,168
CM-00167	*B. heckerae*	BRS	2,168
CM-00168	*B. heckerae*	BRS	2,168
CM-00169(x)	*B. heckerae*	BRS	2,168
HRS-1704-CM-35*	*B. heckerae*	NCS	1,494
RB-19-114	*B. heckerae*	BRS	2,166
RB-19-115	*B. heckerae*	BRS	2,166
RB-19-116	*B. heckerae*	BRS	2,166
RB-19-117	*B. heckerae*	BRS	2,166
RB-19-118	*B. heckerae*	BRS	2,166
RB-19-119	*B. heckerae*	BRS	2,166
RB-19-120	*B. heckerae*	BRS	2,166
RB-19-121*	*B. heckerae*	BRS	2,166
RB-19-122(x)	*B. heckerae*	BRS	2,166
RB-19-123	*B. heckerae*	BRS	2,166
RB-19-124	*B. heckerae*	BRS	2,166
RB-19-125	*B. heckerae*	BRS	2,166
RB-19-126*	*B. heckerae*	BRS	2,166
RB-19-127	*B. heckerae*	BRS	2,166
RB-19-128	*B. heckerae*	BRS	2,166
RB-19-129	*B. heckerae*	BRS	2,166
RB-19-130	*B. heckerae*	BRS	2,166
RB-19-131	*B. heckerae*	BRS	2,166
RB-19-132	*B. heckerae*	BRS	2,166
RB-19-133*	*B. heckerae*	BRS	2,166
RB-19-134(x)	*B. heckerae*	BRS	2,166
RB-19-135(x)	*B. heckerae*	BRS	2,166
RB-19-136	*B. heckerae*	BRS	2,166
RB-19-137*	*B. heckerae*	BRS	2,166

Sample ID	Species	Site	Depth (m)
RB-19-138	*B. heckerae*	BRS	2,166
RB-19-139	*B. heckerae*	BRS	2,166
RB-19-140	*B. heckerae*	BRS	2,166
RB-19-141(x)	*B. heckerae*	BRS	2,166
RB-19-142	*B. heckerae*	BRS	2,166
RB-19-143	*B. heckerae*	BRS	2,166
RB-19-144	*B. heckerae*	BRS	2,166
RB-19-145	*B. heckerae*	BRS	2,166
RB-19-150(x)	*B. heckerae*	BRS	2,166
RB-19-151	*B. heckerae*	BRS	2,166
RB-19-152(x)	*B. heckerae*	BRS	2,166
RB-19-153*	*B. heckerae*	BRS	2,166
RB-19-154*	*B. heckerae*	BRS	2,166
RB-19-155*	*B. heckerae*	BRS	2,166
RB-19-156	*B. heckerae*	BRS	2,166
RB-19-157*	*B. heckerae*	BRS	2,166
RB-19-158	*B. heckerae*	BRS	2,166
RB-19-159	*B. heckerae*	BRS	2,166
RB-19-160	*B. heckerae*	BRS	2,166
RB-19-161*	*B. heckerae*	BRS	2,166
RB-19-162*	*B. heckerae*	BRS	2,166
RB-19-163(x)	*B. heckerae*	BRS	2,166
RB-19-164*	*B. heckerae*	BRS	2,166
RB-19-165	*B. heckerae*	BRS	2,166
RB-19-166*	*B. heckerae*	BRS	2,166
RB-19-167	*B. heckerae*	BRS	2,166
RB-19-168	*B. heckerae*	BRS	2,166
RB-19-169*	*B. heckerae*	BRS	2,166
RB-19-170	*B. heckerae*	BRS	2,166
RB-19-171*	*B. heckerae*	BRS	2,166
RB-19-172*	*B. heckerae*	BRS	2,166
RB-19-173*	*B. heckerae*	BRS	2,166
RB-19-174*	*B. heckerae*	BRS	2,166
RB-19-175	*B. heckerae*	BRS	2,166
RB-19-176	*B. heckerae*	BRS	2,166
RB-19-177	*B. heckerae*	BRS	2,166
RB-19-178	*B. heckerae*	BRS	2,166

We quality-checked raw data using the program FASTQC (Andrews 2010) and de-muliplexed it using the program STACKS (*process_radtags,* -e pstI --inline_null) with default parameters to clean the data (-c: removing any read with an uncalled base and -q: discarding reads with low quality scores) (Catchen et al. 2013). We assembled RAD-seq data for bathymodiolin mussels with ipyrad v 0.9.12 (Eaton and Overcast 2020) using the genome of *Gigantidas platifrons* (=*Bathymodiolus platifrons,* Hashimoto & Okutani, 1994) as a reference (Sun et al. 2017). We did this using default parameters with a sequence similarity *clust threshold* = 0.95, allowing for 20% missing data *min_samples_locus* = 61–72 for *G. childressi and B. heckerae* respectively and a maximum number of heterozygous sites *max_shared_Hs_locus* = 0.5. To maximize the loci recovered, we excluded individuals with < 1,000k assembled contigs (*G. childressi* n = 6 and *B. heckerae* n = 9) from the analyses.

To examine genetic population structure based on allele frequencies within and among the seep sites for *G. childressi*, we conducted a STRUCTURE v.2.3.4 analysis on unlinked SNPs. We assigned hypothetical population information (imap directory) based on seep locality (NCS, BCS or CTS) for *G. childressi* individuals only, requiring 50 percent of coverage in each group (*minmap* = 0.5). SNPs were further filtered by removing those that were not shared across 90 percent of all samples (*mincov* = 0.9). STRUCTURE was run in replicate (n = 10, *burnin* = 20,000, *numreps* = 100,000) using several population (K) values (K=1–4). We averaged these results over the replicates for each K value (1–4) and used the package toyplot to assess the likelihood of each K value and plot the results.

Further assessment of genetic differentiation among *G. childressi* and *B. heckerae* was done in R (v.3.5.0) with custom scripts and the package *adegenet* (Jombart 2008). For *G. childressi*, we examined population structure between seep sites (Norfolk, Baltimore, or Chincoteague). As we sampled almost all *B. heckerae* samples (except one individual) from the same locality (Blake Ridge Seep), sampling methods were instead added to examine whether there was any local-scale population structure as reflected in the sampling methods (ROV, slurp or mussel pot). We calculated genetic diversity statistics (using the *basic.stats* function from the package *hierfstat*) according to Nei (1987) including the population differentiation fixation index (Fst), inbreeding coefficient (Fis), mean observed heterozygosity (Ho), mean gene diversities within populations (Hs), mean gene diversity overall (Ht), and a measure of population differentiation (Dest). We also computed pairwise Fst comparisons between the sampling localities (*G. childressi*) or methods (*B. heckerae*). We also ran a principal components analysis (PCA) in R using the package *ade4* (Dray and Dufour 2007) to visualize the genetic differentiation captured among sampling localities.

To assess relatedness among (*G. childressi*) and within (*B. heckerae*) seep communities, we conducted kinship analyses in SEQUOIA (Huisman 2017) which performs pedigree reconstruction based on SNP data. Parameter thresholds included: for missingness (*--geno* 0.2), minor allele frequency (*--maf* 0.3) and the sliding window (*--indep* 50 5 1), to subset a few hundred SNPs (300–700 total). The subsets of SNPs (*G. childressi* n = 669 and *B. heckerae* n = 628) were then used for pedigree reconstruction (*sequoia*, *MaxSibIter* = 40, *Err* = 0.001, *FindMaybeRel* = TRUE). For each pair of individuals, likelihoods are calculated in terms of them being parent-offspring (PO), full siblings (FS), half siblings (HS), grandparents (GP), full avuncular (niece/nephew - aunt/uncle; FA), half avuncular (great-grandparental/cousins; HA), or unrelated (U). Kinship assignments are made if the (log10) likelihood ratio (LLR) between a given relationship and the most likely alternative exceeds a default threshold.

To further assess connectivity and the directionality of gene flow among *G. childressi* communities, we calculated migration rates between the three sampling localities (NCS, CTS, BCS) using unlinked SNPs in BayesAss v3.04 (BA3) (Wilson and Rannala 2003). BA3 assumes that first generation immigrants can be detected and mean immigration rates for each population can be estimated. First, loci were removed if missing in more than 50% of individuals (*missingno,* type = "loci", cutoff = 0.5). We then ran the filtered dataset in BA3 using 10,000,000 iterations, with a burnin of 250,000 and sampling the chain every 100 generations. We set parameters to ensure acceptance rates between 20-60% for all adjustable parameters (according to Wilson and Rannala 2003), with allele (-a) frequencies at 0.3, inbreeding coefficients (-f) at 0.02, and migration rates (-m) at 0.1 (default). We examined convergence by analyzing the trace file using the Tracer program v1.7.2 (Rambaut and Drummond 2009).

To examine loci under potential selection in each species that inhabit distinct depth ranges (*G. childressi* [shallower seeps, 400–2,200 m] vs. *B. heckerae* [deeper seeps, 2,200 to 3,300 m]), we used a subset of samples in ipyrad (Eaton and Overcast 2020) to create an assembly for bathymodiolin mussels (see

Table 5-1). We ran the genus-level assembly in reference mode using the genome of *G. platifrons* with default parameters and 28 individuals from each species. We chose individuals based on the number of loci assembled in each species-specific assembly (*G. childressi* > 28K, with spread across all three sampling localities [NFC = 14, BTC = 10, CTS = 4]; *B. heckerae* > 3.8K). We ran samples with a clustering threshold = 0.85, missing data set at 20% and a maximum shared heterozygosity of 0.25. We then analyzed these data in R using the program *pcadapt* (Luu et al. 2017) to detect genetic markers under putative selection using statistical tests based on PCA. Pcadapt calculates test statistics for each SNP based on the PCA, and outliers are identified based on Mahalanobis distance— a multidimensional approach to measure distance from the mean (Luu et al. 2017). Bonferroni correction, considered the conservative approach for p-value correction, was applied and SNPs were considered outliers based on the adjusted p-values ($\alpha \leq 0.05$). Corresponding SNP and genome annotations were identified for the outlier SNPs via custom scripts using biopython (Cock et al. 2009) to link SNPs back to the scaffolds with annotation information from the *G. platifrons* genome. We then used Bedtools (Quinlin and Hall 2010) to extract gene information from the corresponding genome GFF annotation file, which has gene ontology and KEGG orthology information. We then used REVIGO (Supek et al. 2011) to produce a reduced visualization of the biological processes and molecular functions under putative selection between the Bathymodiolins. We further used KEGG reconstruction pathway mapper (Kanehisa and Sato 2020) to elucidate corresponding pathways associated with the outlier SNPs.

5.7.2.2 Bathymodiolin Results

An average of 96.2% of reads were retained after demultiplexing and filtering with *STACKS.* This includes 4.27M (± 2.18M) reads for *G. childressi* and 4.18M (± 3.63M) for *B. heckerae.*

5.7.2.2.1 Gigantidas childressi

On average ~99.9% of reads for *G. childressi* passed the additional filtering step in ipyrad, which generated an average of ~271.4K total clusters per individual with an average heterozygosity estimate of 0.01 and error estimate of 0.002. Following assembly, there were 21,292 filtered loci remaining of the 417,015 assembled in total using the genome of *G. platifrons*, yielding 283,754 total SNPs (39.0% missing sites and 21,220 unlinked SNPs).

Assessments of genetic differentiation among *G. childressi* yielded an overall Fst of ~0.002 with a low overall mean observed heterozygosity (Ho = ~0.09), within population gene diversity (expected heterozygosity, Hs = ~0.13) and overall gene diversity (Ht = ~0.13) (**Table 5-15**). These results indicate low heterozygosity and relatively equal allele frequencies among *G. childressi* individuals collected from the different seep sites along the mid-Atlantic margin. Further, *G. childressi* had an overall inbreeding coefficient (Fis) of approximately 0.33, indicating a high level of inbreeding among the total population of sampled individuals.

Table 5-15. Overall summary statistics for Bathymodiolin mussels across loci

N = number of individuals, Fst = Fixation Index, Ho = mean observed heterozygosity, Hs = within population gene diversity or expected heterozygosity, Ht = overall gene diversity, Dst = amount of gene diversity among samples (Ht-Hs), Fis = inbreeding coefficient, and Dest = measure of population differentiation.

Species	N	Ho	Hs	Ht	Dst	Fst	Fis	Dest
G. childressi	81	0.0860	0.1276	0.1278	0.0003	0.0022	0.3260	0.0005
B. heckerae	87	0.0743	0.1064	0.1064	0.0000	0.0000	0.3015	-

Likewise, pairwise Fst values between the collection localities were low and ranged from 0.003 to 0.006 (**Table 5-16**). The highest pairwise Fst value was between BCS and CTS, followed by NCS and CTS

indicating relatively larger genetic differences between the canyon seeps with CTS, though this is likely due to the low number of samples available for this locality (n = 6).

Table 5-16. Pairwise Fst values for *G. childressi*

Collected from three cold-seep communities along the mid-Atlantic margin: Norfolk Canyon Seep (1,485–1,600 m), Chincoteague Seep (1,000 m), and Baltimore Canyon Seep (360–430 m). Values represent putative population differentiation based on genetic structure i.

Site	Norfolk Canyon	Chincoteague	Baltimore Canyon
Norfolk	-	0.005	0.003
Chincoteague	0.005	-	0.006
Baltimore	0.003	0.006	-

We used PCA to visualize this genetic differentiation among *G. childressi* individuals and across collection localities also shows a considerable amount of overlap among samples (1: NCS [n = 53], 2: CTS [n = 6], 3: BCS [n = 22]) (**Figure 5-38**). Genetic similarity among sites is apparent by the lack of clustering among individuals collected from the same seep community. STRUCTURE analyses further indicate there is no population structure among *G. childressi* samples and that all individuals likely belong to one population (k = 1) (**Figure 5-39**).

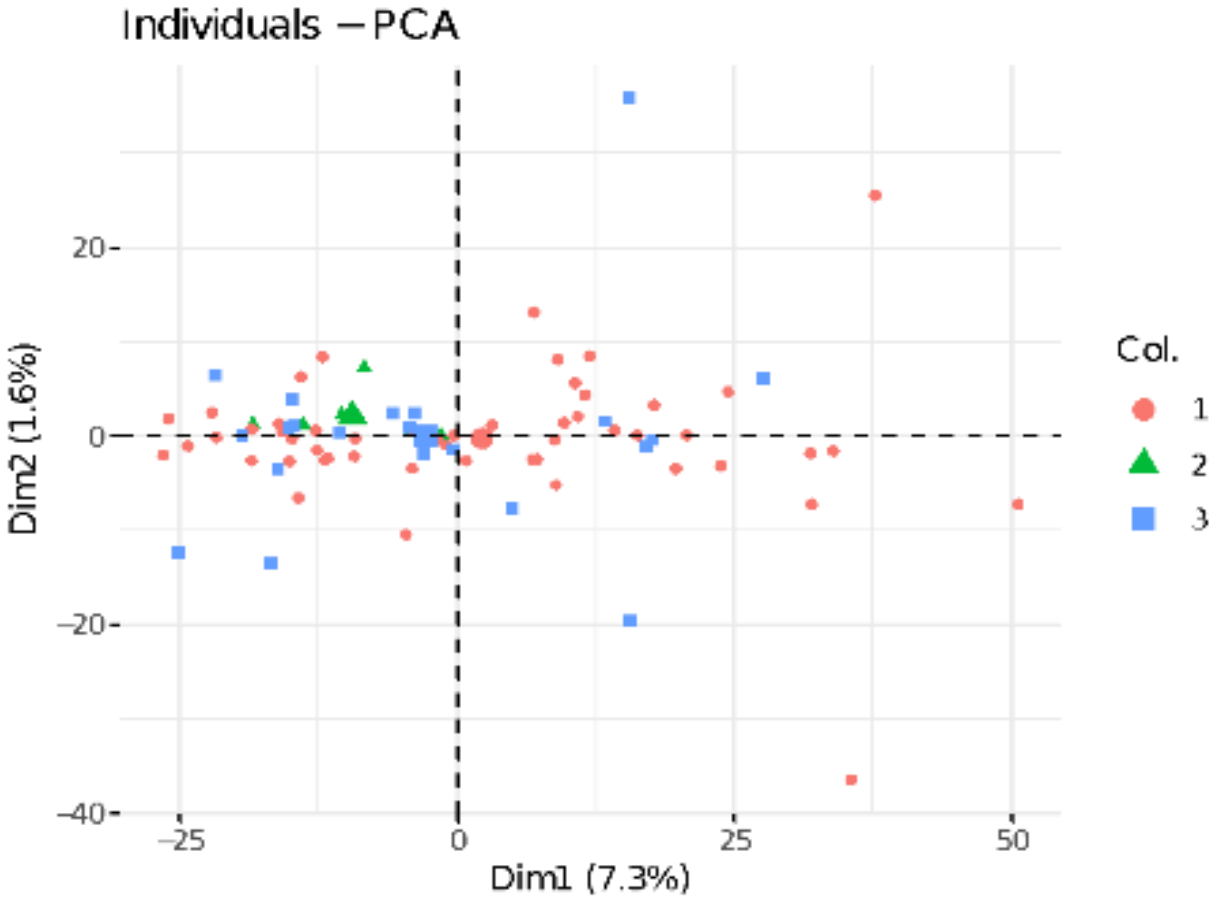

Figure 5-38. PCA plot representing genetic differentiation among *G. childressi* samples

Samples collected from Norfolk Canyon Seep (1: red circles), Chincoteague Seep (2: green triangles), and Baltimore Canyon Seep (3: blue squares).

Kinship analyses (via SEQUOIA) revealed approximately 45% of individuals were related (36 probable relationships among the 81 samples), including parent-offspring (PO = 2), full siblings (FS = 3), grandparent (GP = 29), and half avuncular (HA = 2)—great-grandparents/cousins (**Table 5-17**). The relationships predicted across the three sites is indicative of gene flow between the locations and suggest BCS (shallowest and northernmost seep) serves as a source population, supplying recruits to NCS (deepest and southernmost seep), though there does appear to be local recruitment and some directionality of gene flow from Norfolk to Chincoteague Seep (intermediate depth).

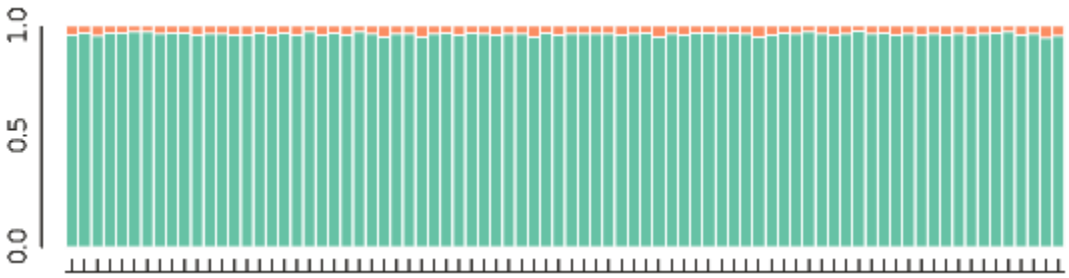

Figure 5-39. Average probability of membership graph for *G. childressi*
CLUSTER as identified by STRUCTURE. K = 1, n = 81.

Table 5-17. Kinship associations and log-likelihood ratios among *G. childressi* individuals

Associations and log-likelihood ratios (LLR) among individuals (ID) collected from the three different seep sites as predicted by SEQUOIA. TopRel = second column ID relative to first column ID and includes parent-offspring (PO), full siblings (FS), grandparent (GP), and half avuncular (HA)—great-grandparental/cousins.

ID1	ID2	TopRel	LLR	Site 1	Site 2
MAS339	**MAS541**	PO	0.72	Norfolk C.	Baltimore C.
MAS321	**MAS544**	PO	0.08	Norfolk C.	Baltimore C.
MAS338	**MAS541**	FS	0.51	Norfolk C.	Baltimore C.
HRS-1704-CM-041	**MAS545**	FS	0.24	Norfolk C.	Baltimore C.
MAS298	**MAS557**	FS	0.1	Norfolk C.	Baltimore C.
HRS-1704-CM-069	**MAS322**	GP	7.83	Chincoteague S.	Norfolk C.
HRS-1704-CM-069	**MAS297**	GP	6.05	Chincoteague S.	Norfolk C.
MAS289	**MAS299**	GP	5.04	Norfolk C.	Norfolk C.
MAS341	**MAS556**	GP	4.58	Norfolk C.	Baltimore C.
MAS293	**MAS544**	GP	4.01	Norfolk C.	Baltimore C.
HRS-1704-CM-011	**MAS284**	GP	3.8	Norfolk C.	Norfolk C.
MAS291	**MAS561**	GP	3.76	Norfolk C.	Baltimore C.
HRS-1704-CM-011	**MAS288**	GP	3.32	Norfolk C.	Norfolk C.
HRS-1704-CM-009	**HRS-1704-CM-039**	GP	2.99	Norfolk C.	Norfolk C.
MAS291	**MAS556**	GP	2.95	Norfolk C.	Baltimore C.
MAS290	**MAS341**	GP	2.78	Norfolk C.	Norfolk C.
MAS555	**MAS557**	GP	2.58	Baltimore C.	Baltimore C.

ID1	ID2	TopRel	LLR	Site 1	Site 2
MAS297	**MAS321**	GP	2.55	Norfolk C.	Norfolk C.
MAS290	**MAS327**	GP	2.33	Norfolk C.	Norfolk C.
HRS-1704-CM-031	**MAS553**	GP	2.22	Norfolk C.	Baltimore C.
HRS-1704-CM-009	**MAS298**	GP	2.15	Norfolk C.	Norfolk C.
MAS299	**MAS540**	GP	2.01	Norfolk C.	Baltimore C.
HRS-1704-CM-031	**HRS-1704-CM-041**	GP	1.94	Norfolk C.	Norfolk C.
HRS-1704-CM-031	**MAS545**	GP	1.89	Norfolk C.	Baltimore C.
MAS299	**MAS327**	GP	1.53	Norfolk C.	Norfolk C.
HRS-1704-CM-015	**MAS545**	GP	1.33	Norfolk C.	Baltimore C.
MAS322	**MAS340**	GP	1.3	Norfolk C.	Norfolk C.
HRS-1704-CM-011	**HRS-1704-CM-025**	GP	1.29	Norfolk C.	Norfolk C.
MAS284	**MAS544**	GP	1.17	Norfolk C.	Baltimore C.
MAS292	**MAS553**	GP	0.98	Norfolk C.	Baltimore C.
HRS-1704-CM-015	**MAS311**	GP	0.78	Norfolk C.	Norfolk C.
HRS-1704-CM-043	**MAS537**	GP	0.77	Norfolk C.	Baltimore C.
HRS-1704-CM-017	**MAS541**	GP	0.67	Norfolk C.	Baltimore C.
HRS-1704-CM-009	**MAS283**	GP	0.58	Norfolk C.	Norfolk C.
HRS-1704-CM-021	**MAS555**	HA	1.33	Norfolk C.	Baltimore C.
HRS-1704-CM-039	**HRS-1704-CM-069**	HA	1.13	Norfolk C.	Chincoteague S.

Further assessments of gene flow with BA3 between the three seep sites (NCS, CTS, BCS) dominated by *G. childressi* indicate a large fraction of non-migrants at each seep site, suggestive of local recruitment (**Table 5-18**). Those that were migrants appear to be sourced from the shallower and northernmost BCS site. Furthermore, inbreeding coefficients were relatively high at BCS (Fis = ~0.10) relative to the other sites (~0.04) (**Table 5-19**).

Table 5-18. Inferred (posterior mean) migration rates from the BayesAss analysis

Values represent the proportion of individuals from each site (row) that are either non-migrants (bold) or migrants derived from another site. Migrant sources are listed at the top of the table.

Site	NFC	CTS	BTC
NFC	0.7809	0.0061	0.2130
CTS	0.0398	0.7705	0.1896
BCT	0.0668	0.0133	0.9200

Table 5-19. Estimated inbreeding coefficients (Fis) at each site with standard error

Site	Inbreeding Coefficient (Standard Error)
NFC	0.041 (0.065)
CTS	0.041 (0.048)
BTC	0.104 (0.021)

5.7.2.2.2 Bathymodiolus heckerae

On average, 99.9% of reads for *B. heckerae* passed the additional filtering step in ipyrad, which generated an average of 98.4K total clusters per individual with a heterozygosity estimate of 0.01 and an error estimate of 0.003. Following assembly, there were 4,142 filtered loci remaining of the 259,443 assembled in total using the *G. platifrons* genome, yielding 52,904 total SNPs (37.31% missing sites and 4,114 unlinked SNPs).

Assessments of site-wide genetic differentiation among *B. heckerae* individuals collected at Blake Ridge Seep yielded an overall Fst of 0 and an inbreeding coefficient (Fis) of approximately 0.30 (**Figure 5-40**), similar to the high level of inbreeding found among *G. childressi* individuals collected across sites. The low overall mean observed heterozygosity (Ho= ~0.07), within population gene diversity (expected heterozygosity, Hs = ~0.10) and overall gene diversity (Ht = ~0.10) also indicate low heterozygosity and relatively equal allele frequencies among *B. heckerae* individuals collected in the Blake Ridge region. Grouping *B. heckerae* by discrete collections yielded a higher overall Fst of 0.02 and Fis coefficient of 0.35.

However, the PCA to visualize genetic differentiation among *B. heckerae* individuals—with samples grouped by collection—shows genetic similarity among the discrete collections via a considerable amount of overlap and a lack of distinct clustering by group (**Table 5-20**). Pairwise Fst values between the discrete collections reveal relatively high Fst values between sample *HRS-1704-CM-35* collected via ROV and all other collections (**Table 5-21**); we collected this sample from a shallower region near NCS and is the only *B. heckerae* individual in this study not collected from Blake Ridge. We also observed relatively high pairwise Fst values (0.04–0.09) for sample *RB-19-114* collected discretely via slurp (SBlue_02) relative to samples collected via mussel pots B1, B4 and B6, but not B2 (0.006).

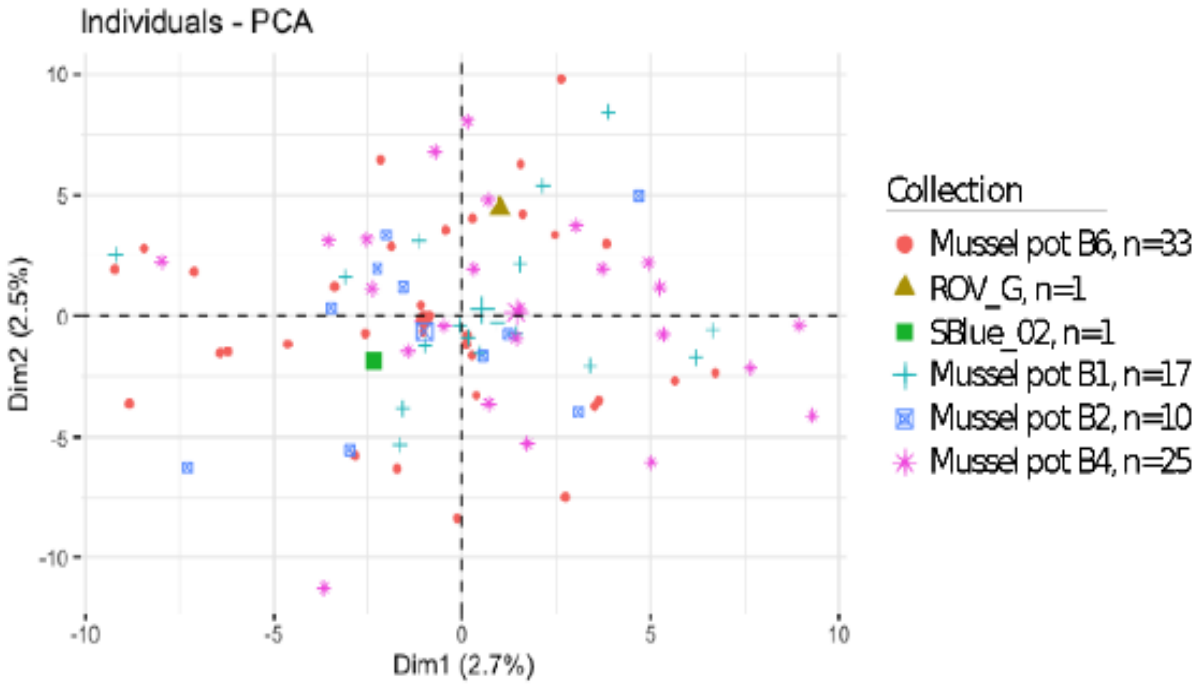

Figure 5-40. PCA plot representing genetic differentiation among *B. heckerae* samples
From six discrete collections along Blake Ridge Seep (1, red circle: mussel pot B6 [n = 33], 2, yellow triangle: ROV_G [n = 1], 3, green square: SBlue_02 [n = 1], 4, blue cross: mussel pot B1 [n = 17], 5, blue square: mussel pot B2 [n = 10], 6, pink asterisks: mussel pot B4 [n = 25]).

Table 5-20. Pairwise Fst values for *B. heckerae* collected from Blake Ridge Seep

Discrete collections are listed in the top row. Values represent differentiation between the collections based on genetic structure. The highest levels of differentiation are shown in bold.

Collections	Mussel Pot B6	ROV_G	SBlue_02	Mussel Pot B1	Mussel Pot B2	Mussel Pot B4
MP- B6	-	0.1332	0.0355	-0.0121	8.00E-04	0.0082
ROV_G	0.1332	-	NA	0.1213	0.1273	0.147
SBlue_02	0.0355	NA	-	0.0847	0.006	0.0889
MP- B1	-0.0121	0.1213	0.0847	-	-0.0055	0.0028
MP- B2	8.00E-04	0.1273	0.006	-0.0055	-	0.0016
MP- B4	0.0082	0.147	0.0889	0.0028	0.0016	-

The kinship analyses (via SEQUOIA) revealed approximately 10% of the sampled *B. heckerae* individuals were related (8 probable relationships among the 87 samples), including grandparent (GP=6) and half avuncular (HA=2)—great-grandparental/ cousins (**Table 5-21**). This includes a probable grandparental relationship between sample *HRS-1704-CM-35* collected near NCS (with the highest levels of genetic differentiation we detected for this species), and individual *CM-00151* collected with mussel pot B6 at Blake Ridge Seep.

This relationship suggests high dispersal and gene flow capabilities for *B. heckerae*, similar to what was observed for *G. childressi*. These results further suggest the individual collected from the Norfolk Canyon region (and discussed in Coykendall et al. 2019) is a possible recruit from Blake Ridge Seep or an undiscovered site near Norfolk Canyon with genetic connectivity to Blake Ridge.

Table 5-21. Kinship associations and associated LLR among *B. heckerae*

Individuals (ID) collected from Blake Ridge Seep, with one individual collected near Norfolk Canyon, as predicted by SEQUOIA. TopRel = second column ID relative to first column ID and includes grandparent (GP) and half avuncular (HA) - great-grandparents/cousins.

ID1	ID2	TopRel	LLR	Sites
CM-00167	**RB-19-136**	GP	28.01	Blake Ridge
CM-00157	**RB-19-119**	GP	27.34	Blake Ridge
RB-19-125	**RB-19-154**	GP	14.26	Blake Ridge
RB-19-132	**RB-19-168**	GP	13.09	Blake Ridge
CM-00134	**CM-00157**	GP	9.48	Blake Ridge
CM-00151	**HRS-1704-CM-35**	GP	6.32	Blake Ridge / Norfolk C.
CM-00149	**RB-19-130**	HA	6.17	Blake Ridge
RB-19-157	**RB-19-171**	HA	0.67	Blake Ridge

5.7.2.3 Bathymodioline Signatures of Selection

Using conservative methods for outlier detection among bathymodiolin mussels, we identified 3,429 outlier SNPs using an adjusted p-value cutoff of 0.05 (**Figure 5-41 A**). The score plot from pcadapt (**Figure 5-41 B**) reveals species structure among the SNP outliers but a lack of population structure among *G. childressi* sampled at the different canyon sites. These data suggest that there is no evidence for adaptation with gene flow between Baltimore Canyon, Norfolk Canyon and Chincoteague seeps. Analysis of SNP outliers specific to *G. childressi* also confirmed a lack of population structure among the sampled SNPs. Further assessment of the outlier SNPs revealed an association with the first principal component only, which separates *G. childressi* from *B. heckerae* individuals, further indicating the SNPs are likely associated with interspecies divergence (**Table 5-22**).

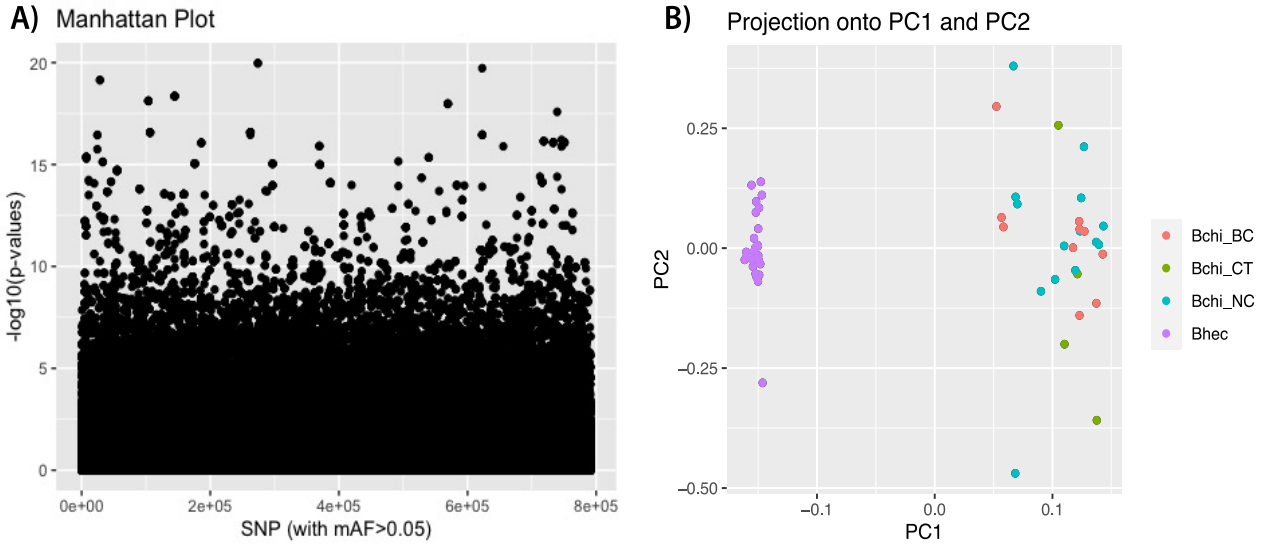

Figure 5-41. Manhattan plot and score plot for *G. childressi* by site
A) Manhattan plot revealing outlier SNPs. B) a score plot displaying the projection of each sample onto the principal components of the PCA conducted in pcadapt. Samples are color coded by site for G. childressi (Baltimore Canyon [BC] Seep, red); Norfolk Canyon [NC] Seep, blue; and Chincoteague [CT] Seep, green) and/or species *B. heckerae* (Blake Ridge Seep, purple).

Table 5-22. Overall population statistics for the Bathymodiolin mussels
For n = 57 dataset across 3,191 loci. Ho = mean observed heterozygosity, He = expected heterozygosity or within population gene diversity, Ht = overall gene diversity, Dst = amount of gene diversity among samples

ID1	ID2	TopRel	LLR	Site(s)
CM-00167	RB-19-136	GP	28.01	Blake Ridge
CM-00157	RB-19-119	GP	27.34	Blake Ridge
RB-19-125	RB-19-154	GP	14.26	Blake Ridge
RB-19-132	RB-19-168	GP	13.09	Blake Ridge
CM-00134	CM-00157	GP	9.48	Blake Ridge
CM-00151	HRS-1704-CM-35	GP	6.32	Blake Ridge / Norfolk C.
CM-00149	RB-19-130	HA	6.17	Blake Ridge
RB-19-157	RB-19-171	HA	0.67	Blake Ridge

Based on the *G. platifrons* genome, we obtained annotation information for 1,259 of the outlier SNPs, which corresponded to 427 unique genes. Among those annotated genes are a variety of known environmental response genes including a probable cytochrome p450, ABC transporters, collagens, various zinc finger proteins, solute carriers, serine-threonine kinases and ion receptors, glutathione S-transferase, heat shock protein 70, carbonic anhydrases and the stress response protein nhaX, a diagnostic cancer biomarker protein Cubillin, a developmental homeobox gene Hox-A9, the transcription factor SOX-30 involved in Wnt signaling and spermatid development, and sulfite oxidase involved in sulfur metabolism.

Gene ontology analyses indicate that the loci under putative selection in bathymodiolins are associated with a variety of biological processes including ATP and carbohydrate metabolism, response to ionizing radiation, inhibition of coagulation, toxin transport, microtubule based movement, protein folding, epigenetic modifications such as methylation, phosphorylation and ubiquitination, cellular response to starvation, nitrate assimilation, Wnt signaling, establishment of an endothelial barrier, and organelle and cytoskeletal organization (**Figure 5-42**).

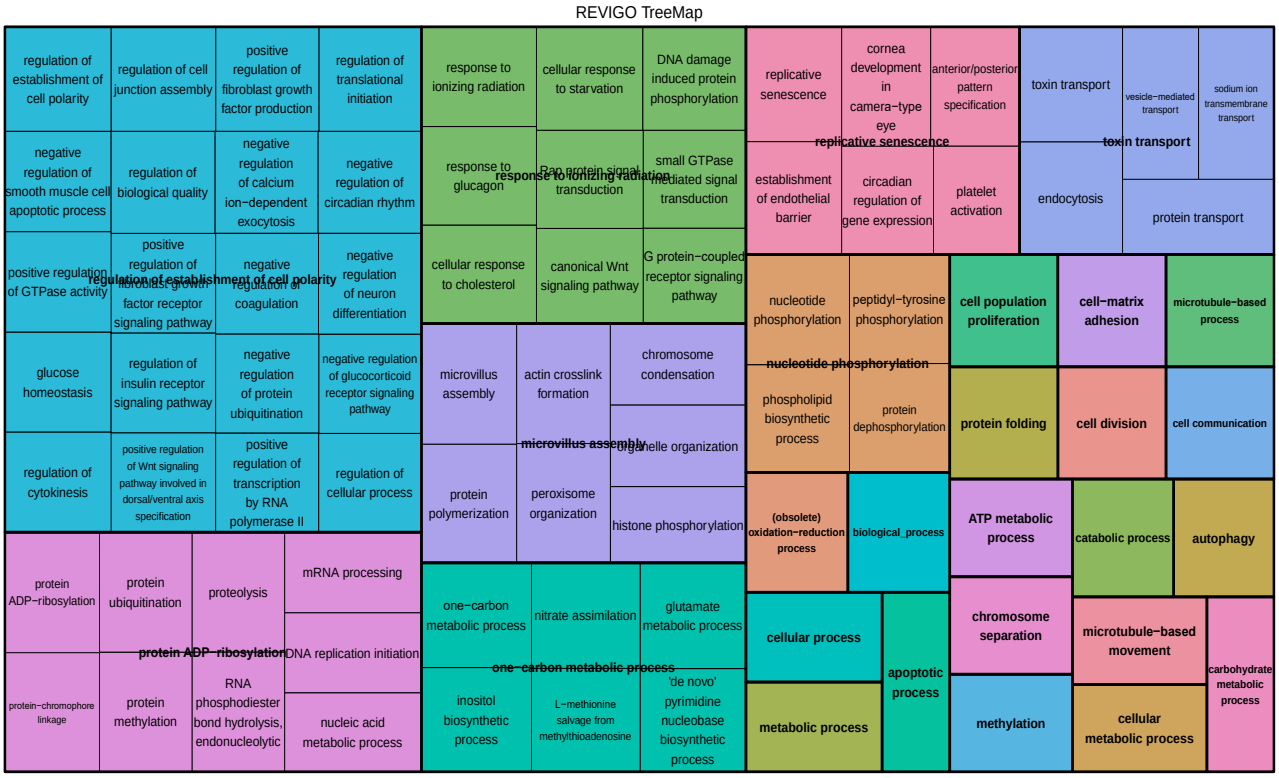

Figure 5-42. REViGO treemap produced by the REVIGO server
Summarizes and visualizes gene ontology information for biological processes associated with the outlier SNPs for *Bathymodiolus* spp. Server at http://revigo.irb.hr/.

5.7.2.4 Bathymodiolin Connectivity

Populations of *G. childressi* are highly connected between sites in the MAB. Gene flow is apparent between BCS, NCS, and CTS populations. Both migration rate and kinship analyses indicated that gene flow occurs from Baltimore to Norfolk seeps, in a shallow/north to deep/south direction. BayesAss analysis, which can infer gene flow rates and directionality over the last two generations (Wilson and Rannala 2003), indicated that a 25% fraction of migrants moved from the shallower Baltimore Canyon site to the deeper Norfolk Canyon site and ~20% moved from Baltimore Canyon to the intermediate

Chincoteague Seep site. We found a negligible fraction (8%) of migrants from Norfolk and Chincoteague seeps at Baltimore.

This pattern in gene flow is consistent with an onshore to offshore or downslope pattern of dispersal, which has been hypothesized to be a predominant mode of genetic diversification in deep-sea taxa (Jablonski et al. 1983, Hessler and Wilson 1983, Little and Vrijenhoek 2003). However, this directionality in gene flow is also oriented in a north to south direction, which corresponds with the prevailing current structure in the region. The Labrador Current (and derived Labrador Slope water) is the predominant current along the shelf and slope off the northeastern US, bringing cold waters from the northern Labrador Sea southward to an area off Cape Hatteras North Carolina, where the Labrador Current converges with the Gulf Stream (Frantoni and Pickart 2007, New et al. 2021). Collectively, our results indicate that Baltimore is an important source of genetic material to downstream and deeper sites in the region.

No genetic structure of *B. heckerae* among sampling locations was apparent at Blake Ridge Seep, indicating that cohorts of larvae are not found in spatially discrete patches and that collection location does not bias the results. The inbreeding coefficient at this site was relatively high, suggesting some degree of local recruitment. This is also supported by the kinship analyses, which suggest that at least 10% of the sampled population was closely related to one another.

The high levels of kin not only at Blake Ridge (10%) but also at Norfolk Canyon (17%) are actually quite surprising, and indicative of some degree of local recruitment. Thus, we hypothesize that a proportion of planktotrophic larvae are likely entrained in local hydrographic conditions, in Gulf Stream eddies or submarine-canyon circulation patterns, that serve to retain and transport larvae back to natal (or near natal) sties in the region. We suggest that future studies incorporate more spatially discrete mussel beds along the US Atlantic margin and beyond to fully understand the source-sink dynamics and level of local recruitment in the region.

Finally, selection tests indicated that *G. childressi* and *B. heckerae* harbor >400 genes under potential directional selection. These genes were related mainly to metabolism, cellular signaling and genetic information processing. Notably, sulfite oxidase, which is involved in sulfur metabolism, was found to be under selection. In cold seeps, reduced sulfur (hydrogen sulfide) can be oxidized via seafloor-living bacteria and via thiotrophic symbionts that live within the gill tissues of some bathymodiolin mussel species (Distel et al. 1988, Levin 2005, Dupperon et al. 2007, Coykendall et al. 2019). Thus, sulfite oxidase is potentially under selection in bathymodiolins to help convert sulfite produced by thiotrophic symbionts or from exongenous uptake (via filter feeding) in the environment.

It has been previously hypothesized that the non-overlapping distributions of *B. heckerae* and other seep bivalves (vesicomyid clams) may be due to competition for sulfide (Van Dover et al. 2003). It is therefore possible that the non-overlapping distributions of *B. heckerae* and *G. childressi* are associated with sulfide seepage or utilization. Further investigation could help to elucidate the differences in seepage conditions between the ridge (deeper) and canyon (shallower) seeps. Likewise, it is possible that dual symbiosis (thiotrophy and methanotrophy) has led to additional adaptations among *B. heckerae*, including those associated with metabolism, that enable these mussels to thrive in deeper, sulfide-rich seep habitats.

5.7.3 Corals

With ongoing advances in technology (both ship and shore-based) scientists are able to access deep-sea ecosystems, including CWCs, to conduct, collect, analyze, and synthesize ecosystem-based baseline information. Benthic ecosystems supported by CWCs are distributed throughout the world's ocean and can be found along continental slopes, canyon walls, and seamounts (Freiwald et al. 2004, Roberts et al. 2009).

Evidence of CWC populations in US waters continues to accumulate but there are still large knowledge gaps pertaining to the overall functionality of CWCs in broader biogeochemical cycles, the extent of the ecosystem services they provide, and the regional and global population dynamics of these important ecosystem engineers. Given that CWCs can occur over large, spatially fragment, geographic scales, it is important to understand the degree of connectivity among existing populations. The degree of connectivity contributes to the resiliency of each population and the probability of recovery from potential natural or anthropogenic impacts.

5.7.3.1 Lophelia pertusa

Lophelia pertusa, is known to occur in all oceans except for the polar regions, including the deep waters of the GOM, along the US Pacific margin, on the continental slope of the SEUS, in canyons in the MAB and off the NEUS (Cordes et al. 2008, Morrison et al. 2011, Brooke and Ross 2014, Caldow et al. 2015). In the western North Atlantic, genetic connectivity studies have been carried out for only a few CWC species, including *Lophelia pertusa* (Morrison et al. 2011), *Callogorgia delta* (Quattrini et al. 2015), and *Leiopathes glabberima* (Ruiz-Ramos et al. 2015).

We observed different patterns in population connectivity among species, and included regional panmixia in *L. pertusa,* population divergence by depth in *C. delta,* and a mixture of long-distance dispersal with high rates of self-recruitment in *L. glabberima.* Although divergence across depth is a common theme in deepwater populations (Rex and Etter 2010), these studies show that patterns of connectivity cannot be generalized across different deepwater coral taxa or different regions.

5.7.3.1.1 *Lophelia pertusa* Methods

We extracted DNA from 157 *L. pertusa* individuals collected on the RV *Ron Brown* and ROV *Jason II*, RV *Henry Bigelow*, and ROV *ROPOS*, RV *Seward Johnson* and the *Johnson-Sea-Link* submersible, and RV *Atlantis* and *Alvin* submersible. Samples represent sites located in the GOM and in the western Atlantic Ocean (off the coast of the US in the Mid- and South Atlantic Bights and NEUS intercanyons off New England; see Morrison et al. [2023] for sample details). Because sample tissue age and quality varied, we employed several DNA extraction methods to obtain the high quality and quantity required for RAD-seq, including Qiagen PureGene, the Qiagen DNeasy Blood & Tissue Kit (Qiagen, Hilden, Germany), and a modified cetyltrimethylammonium bromide (CTAB) method (McFadden et al. 2001).

We quantified the DNA from each sample using the Qubit dsDNA BR Assay Kit (ThermoFisher) and verified it to be high molecular weight via 2.0% agarose gel electrophoresis, visualized using GelRed® DNA stain (Biotium, Fremont, CA). We then cleaned the samples with adequate quality DNA using either the Qiagen DNeasy PowerClean Pro Cleanup Kit (Qiagen, Hilden, Germany) or Ampure magnetic beads (Agencourt Bioscience Corporation, Beverly, MA). Those with lower quantification values underwent bead cleaning to minimize loss of DNA quantity.

To test that cleaning removed enzymatic inhibitors, each sample was run through a test enzyme digestion using mseI restriction enzyme (New England Bio), following the New England Biolabs Optimizing Restriction Endonuclease Reactions protocol. We then reran each sample on the Qubit prior to normalization to 20 ng/µL in 50 µL and sending them to Floragenix (Beaverton, OR) for library prep and RAD sequencing. We constructed DNA libraries using the 6-cutter PstI enzyme, followed by sequencing 100 bp SE reads on an Illumina HiSeq4000 (University of Oregon's Genomics and Cell Characterization Core Facility lab).

We demultiplexed RAD-seq data from 157 *L. pertusa* individuals and assembled them using ipyrad v.0.9.81 in de novo mode (ipyrad -p params-lophelia_all.txt -s 1234567). The default parameters were used in the assembly including *clust_threshold* = 0.85 and a maximum number of heterozygous sites

max_shared_Hs_locus = 0.5. The percent of missing data (*min_sample_locus* = 4) was set relatively high with the intention of retaining as much data through the assembly process as possible, then applying post-assembly filtering to the dataset. Following the assembly, we recovered loci and SNP information in a variant call format (vcf) file and used vcftools v.0.1.16 to examine and filter the data to retain only high-quality samples and SNPs.

Using vcftools, we used the thin function to retain one SNP per locus to obtain unlinked SNPs. The --missing-indv function calculated the percent of missing data of each individual. We removed individuals with more than 90% missing data (n = 100) (--remove) from the dataset, leaving 57 individuals for further analysis. Further filtering was applied to only keep variants that successfully genotyped to 50% of individuals (--max-missing 0.5) and a minimum allele count of 3 (--mac 3). The sequencing data associated with the methodology comparison are available as a USGS data release (Morrison et al. 2023) or from the NCBI Sequence Read Archive.

We input the resulting vcf file containing filtered information for the 57 *L. pertusa* individuals into various programs to visualize the genetic population structure and assess genetic differentiation between the various sampling sites. We used the API: ipyrad-analysis toolkit, a Python interface tool in jupyter notebook, to generate a PCA and to run STRUCTURE. We first compressed the vcf file and converted it to a SNP database file (snps.hdf5) using the ipa.vcf_to_hdf5() tool. We input the snps.hdf5 file into the ipa.pca() tool and we assigned the individuals to populations based on the collections sites (imap directory). Through a minmap directory we required that 10% of samples have data in each population. Additionally, we invoked the mincov option to filter SNPs that are shared across less than 10% of all of the samples. These filtering steps were non-constraining because filtering had been applied previously through vcftools.

The pca.run() call generated the PC axes and the variance explained by each axis. We visualized the PCA results using the pca.draw() call. The default subsampling parameter and no subsampling (subsample = False) were both performed and produced very similar results. We input the same snps.hdf5 file into ipyrad-analysis toolkit: STRUCTURE v.2.3.4 to examine population genetic structure based on allele frequencies within and among populations. We applied the same population information (imap directory), minmap, and mincov parameters to the STRUCTURE run. We ran the struct.run() call in replicate (n = 3, burnin = 20,000, numreps = 100,000) using population (K) values up to one more than the number of populations (K = 2–10). We averaged the results over the replicates (n = 3) for each K value (2–10) and visualized them using the package toyplot to assess the likelihood of each K value.

We calculated basic genetic diversity statistics in R (v.4.1.1) using the packages adegenet and hierfstat. First, we imported SNP data as a genind object from the vcf file containing filtered information for the 57 *L. pertusa* individuals using the package adegenet. We assigned individuals to populations based on the collection sites (genind@pop) to examine genetic diversity between the different site collections. We calculated genetic diversity statistics (basic.stats) for the whole dataset and for each population including the mean observed heterozygosity (Ho), mean expected heterozygosity (Hs), overall gene diversity (Ht), amount of gene diversity among samples (Dst = Ht-Hs), and the inbreeding coefficient (Fis). We calculated pairwise Fst (genet.dist) between the assigned populations and plotted it using the ggplot2 package, where higher Fst indicates larger genetic differentiation between populations. We calculated the basic statistics according to Nei (1987) and computed pairwise Fst according to Weir and Cockerham (1984).

5.7.3.1.2 *Lophelia pertusa* Results

The assembly of 157 *Lophelia pertusa* samples generated 144,682 loci (57% of prefiltered loci) following the trimming and filtering steps carried out by ipyrad. The assembly generated between 757–187,331 clusters per individual. Following filtering with vcftools, 57 individuals (containing < 90% missing data)

and 3,191 unlinked SNPs (successfully genotyped to 50% of individuals and a minimum allele count of 3) were retained for further analysis.

We visualized estimates of genetic differentiation across 57 *L. pertusa* individuals at 3,191 unlinked SNPs with a PCA (**Figure 5-43**). The PCA displayed samples from the Blake Plateau populations (Cape Fear, Stetson Bank, Savannah Banks, Richardson Reef, and Canaveral) as one grouping, Norfolk Canyon and the GOM as a second group, NEUS intercanyons as a third group, while the single Pea Island Seep *L. pertusa* sample fell between the Blake Plateau and GOM/NEUS intercanyons groups. Diversity statistics for this data included observed heterozygosity (Ho) of 0.106, expected heterozygosity (He) of 0.269, overall gene diversity (Ht) of 0.281, an inbreeding coefficient (Fis) of 0.606, and an overall Fst of 0.04 (**Table 5-23).** The mean Ho for the different sites ranged from 0.05–0.15, the mean He ranged from 0.23–0.29, and the inbreeding coefficient ranged from 0.356–0.739 (**Table 5-24**). It is noteworthy that both the NEUS intercanyons and GOM populations had the highest levels of inbreeding (0.739 and 0.621, respectively), followed by Richardson Reef (0.599). Given the single sample representing the Pea Island population, diversity statistics could not be calculated.

Pairwise Fst between the sites ranged from -0.058–0.139 (**Figure 5-44**). Genetic differentiation was detected between many of the sites, with the highest overall Fst values involving comparisons with Norfolk Canyon, ranging from 0.045 (GOM) to 0.139 (Cape Fear). Pairwise Fst values were also high for several comparisons involving the NEUS intercanyons (Norfolk Canyon = 0.112, GOM = 0.067), but were surprisingly low for comparisons with several Blake Plateau populations including Savannah Banks, Cape Fear, and Canaveral (0–0.004). We detected only minimal genetic differentiation between the Blake Plateau populations (Fst range 0–0.007), suggesting high connectivity. Specifically, the Richardson Reef does not appear to be differentiated from Canaveral, Savannah Banks, and Cape Fear. The single Pea Island sample had lowest pairwise Fst with the GOM (0.017) and highest with Norfolk Canyon (0.122), despite relatively small geographic distance (x) with the latter population.

The Structure analysis indicated that structuring existed in the *L. pertusa* SNP data, which was best explained by four genetic clusters (K = 4) (**Figure 5-43**). At the K = 4 level of clustering, individuals from Norfolk Canyon, Pea Island, and the GOM shared common genetic ancestry (blue bars, (**Figure 5-43**); while several individuals from the NEUS intercanyons clustered with most of the Blake Plateau populations (orange bars, (**Figure 5-43**), including Cape Fear, Stetson Banks, Savannah Banks, Richardson Reef, and Canaveral. The final two clusters included two individuals each from the NEUS intercanyons (green, RB2008-09 and RB2008-10, (**Figure 5-43**) and Richardson Reef (pink, CM-00048 and CM-00058, (**Figure 5-43**). With the addition of one or two more clusters (K=5 and 6) the clustering patterns are consistent with K = 4, yet additional admixture at the individual level was apparent within the broad clusters, especially in the Blake Plateau and NEUS intercanyons populations, possibly indicating additional source populations.

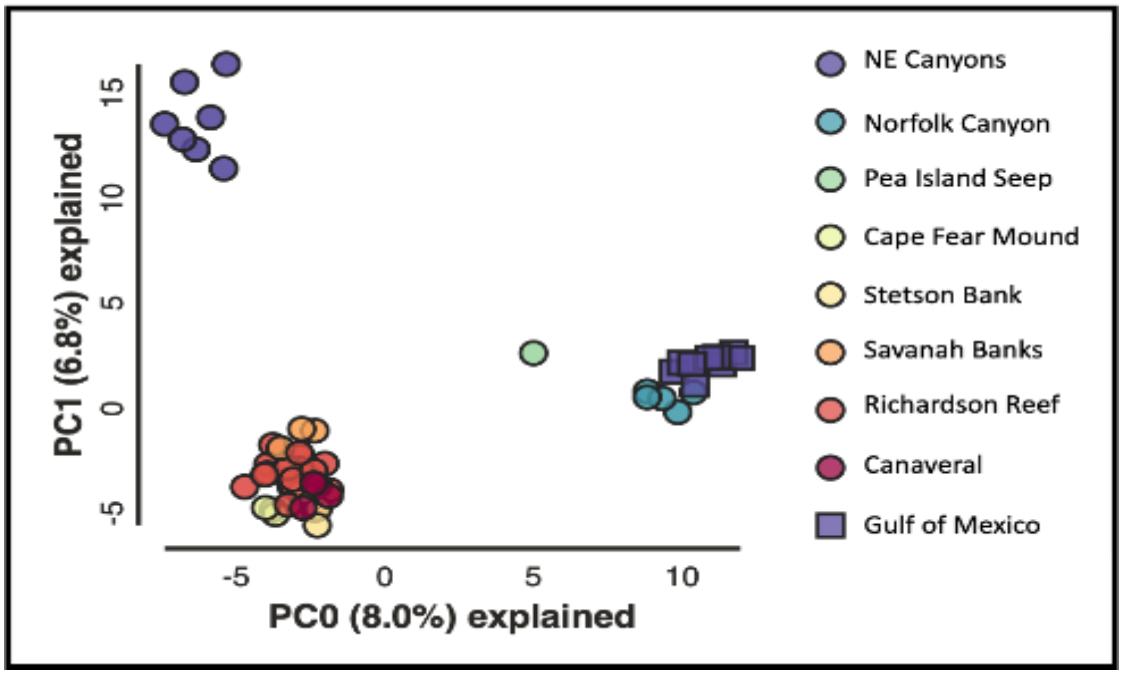

Figure 5-43. PCA plot of genetic differentiation
Genetic differentiation among L. *pertusa* samples collected from nine populations.

Table 5-23. Overall statistics for *Lophelia pertusa*

For n = 57 dataset across 3,191 loci. Ho = mean observed heterozygosity, He = expected heterozygosity or within population gene diversity, Ht = overall gene diversity, Dst = amount of gene diversity among samples (Ht-Hs), Fst = fixation index, Fis = inbreeding coefficient, and Dest = measure of population differentiation.

Ho	He	Ht	Dst	Fst	Fis	Dest
0.1062	0.2693	0.2805	0.0112	0.0401	0.6056	0.0177

Table 5-24. Overall population-level statistics for the *L. pertusa* sample sites

N = number of individuals, Ho = observed heterozygosity, He = expected heterozygosity or within population gene diversity, and Fis = inbreeding coefficient.

Site	N	Mean Ho	Mean He	Mean Fis
NEUS Canyons	7	0.05	0.29	0.739
Norfolk Canyon	5	0.13	0.23	0.356
Pea Island	1	0.06	Na	Na
Cape Fear	4	0.12	0.25	0.384
Richardson Reef	24	0.10	0.27	0.599
Savannah Banks	3	0.15	0.26	0.366
Canaveral	4	0.14	0.26	0.356
Gulf of Mexico	9	0.08	0.27	0.621

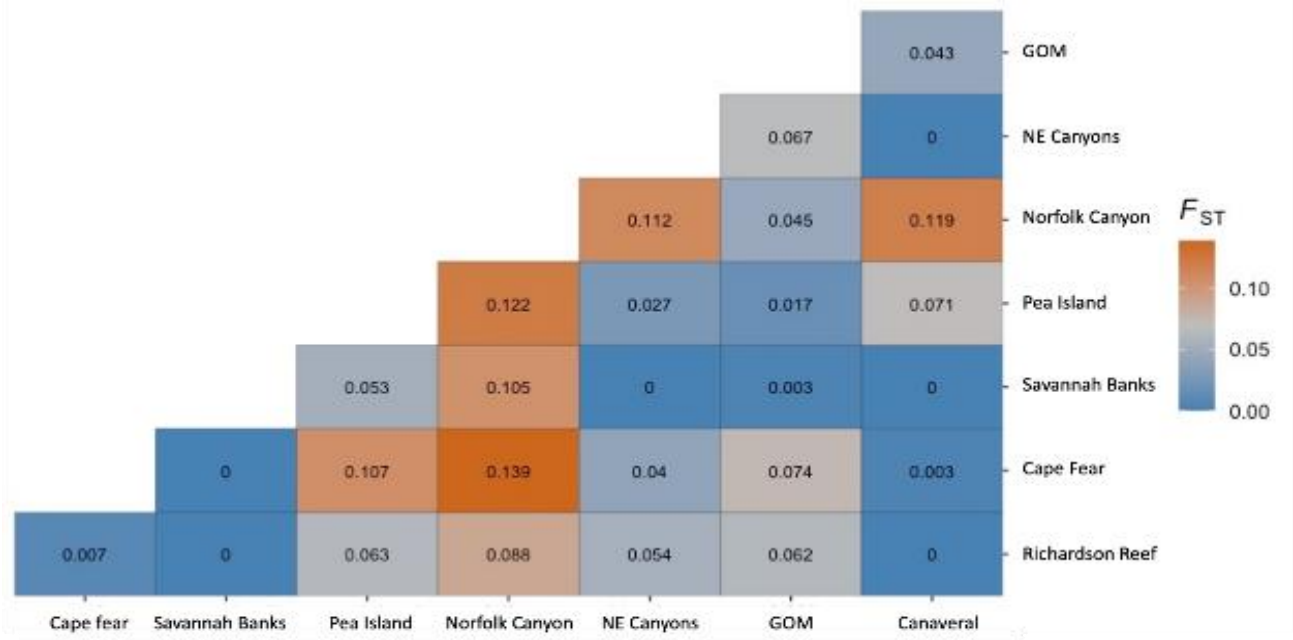

Figure 5-44. Pairwise Fst values for *L. pertusa* individuals
Collected from nine communities ranging from the New England Canyons, through the Mid-Atlantic and Blake Plateau, and to the GOM. For values < 0, a 0 was applied.

5.7.3.2 *L. pertusa* Connectivity

These analyses are the first to utilize genomic SNP data for Northwestern Atlantic *L. pertusa*, and generally confirm regional structuring between *L. pertusa* populations on the Blake Plateau, Norfolk Canyon, and populations found to the north (NEUS intercanyons) and southwest (GOM) that had been ascertained previously by microsatellite analyses (Morrison et al. 2011, 2017; Lunden et al. 2014). Regional genetic structuring in *L. pertusa* has also been concordant with coral-defined biogeographic provinces (Morrison et al. 2011). The concordance with deepwater scleractinian provinces suggests that oceanographic processes may influence coral larvae in a similar manner, restricting gene flow between provinces.

The PCA, pairwise Fst values, and Structure analysis (**Figure 5-43, Figure 5-44, Figure 5-45**) all indicated that the Blake Plateau populations (Cape Fear, Stetson Banks, Savannah Banks, Richardson Reef, Canaveral) were all relatively genetically similar to each other but were differentiated from *L. pertusa* populations found at Norfolk Canyon, Pea Island, the NEUS intercanyons, and the GOM. Fst values were highest in comparisons involving Norfolk Canyon. This pattern of highest isolation north of Cape Hatteras follows findings by Wang et al. (2021) that used larval dispersal models to determine potential connectivity of glass sponge larvae along the US Atlantic Coast and found it unlikely that populations north and south of Cape Hatteras were physically connected.

The genetic similarity at SNP loci between the Norfolk Canyon (in the MAB) *L. pertusa* populations and those from the GOM was also detected using microsatellites (Morrison et al. 2017). While hydrodynamic connections with the GOM are not obvious, intrusions of Gulf Stream ring waters occasionally move onshore and may facilitate the migration of marine species to the MAB (Zhang and Gawarkiewicz 2015, Wang et al. 2021). Given the rarity of *L. pertusa* in the MAB canyons and the various colony sizes encountered (suggestive of numerous recruitment events; Brooke and Ross 2014), occasional long-distance dispersal events may be possible, delivering *L. pertusa* larvae from either the GOM or bioherms off the SEUS via the Gulf Stream. Such onshore intrusions likely influence long-distance

dispersal of several fishes as well, such as bluefish (Hare and Cowan 1996) and American eel from the Sargasso Sea (Rypina et al. 2014). Additionally, gaps in sampling *L. pertusa* may also explain the apparent gulf-like signature of the MAB samples. There may be additional, unsampled *L. pertusa* populations in the western Atlantic that would be a closer larval source yet have more gulf-like genetic characteristics (off the Bahamas or the Caribbean). Sampling of additional potential *L. pertusa* source populations (Caribbean) could help refine estimates of larval sources.

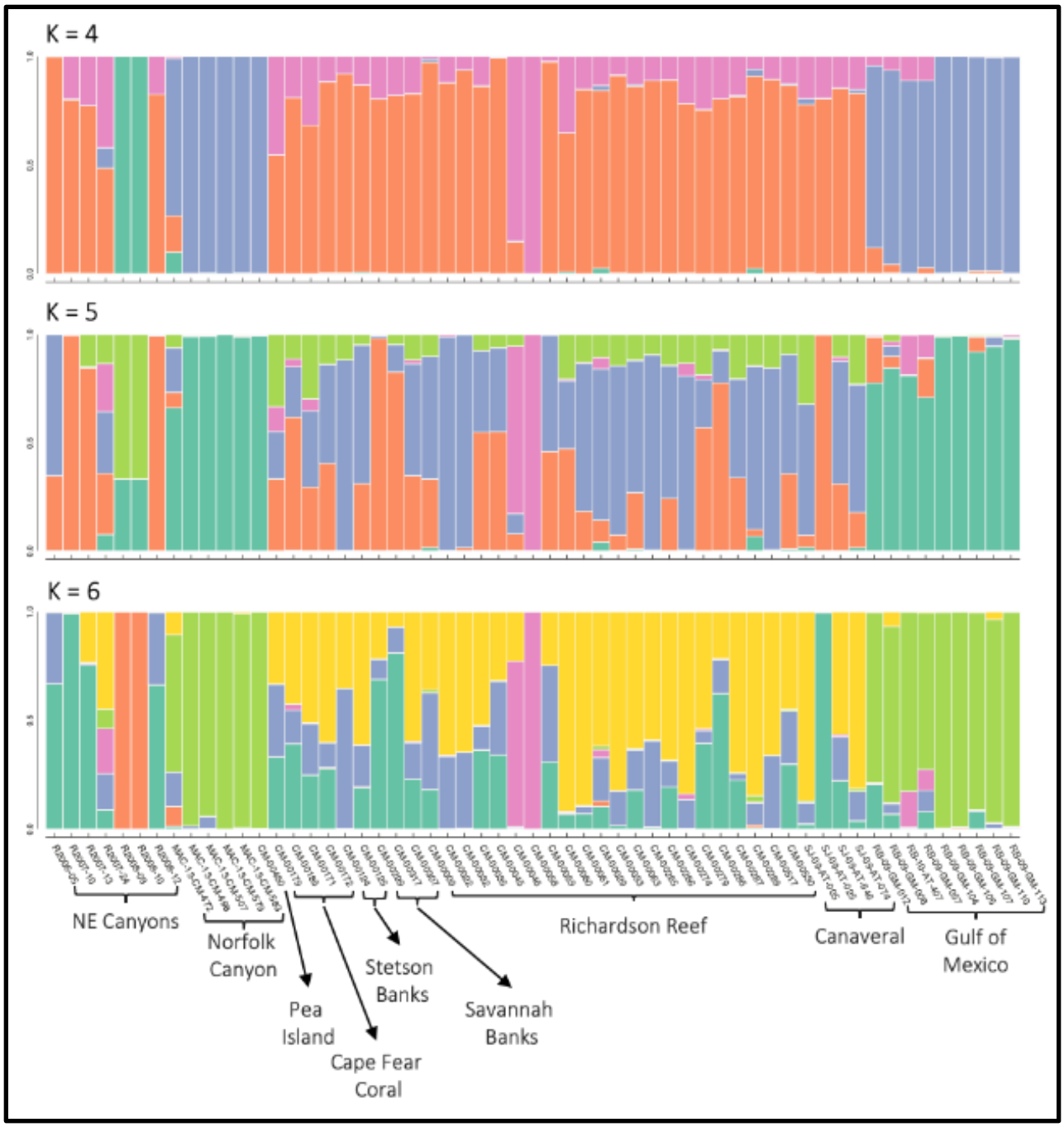

Figure 5-45. Structure results (K=4, 5, 6) for *Lophelia pertusa* across nine sites
Includes Northeast (NE) Canyons and the GOM. Analysis is based on ~3,000 SNPs.

While genetic structuring patterns were similar between the two marker types (microsatellites vs. SNPs), we obtained higher resolution by SNPs, revealing fine-scale details not available previously. For example, in the Structure analysis, both Richardson Reef and the NEUS intercanyons had two individuals each that formed unique genetic clusters, suggesting migration from unsampled populations. Additionally, at higher levels of *K* (*K* = 5–6), populations from the Blake Plateau appeared more genetically differentiated and admixed than in previous analyses involving microsatellites. Again, a pattern of high connectivity among Blake Plateau populations, yet with potential for influence from outside populations, follows findings by Wang et al. (2021). Similarly, larvae sourced from the northeast were likely to reach the NEUS intercanyons in larval dispersal models for the glass sponge *Vazella pourtalesii* (Wang et al. 2021). A larval source of *L. pertusa* further to the northeast from the NEUS intercanyons may explain the unique signature of two individuals.

While these are encouraging preliminary results, a note of caution involving small sample sizes for several *L. pertusa* populations is warranted. To achieve accuracy in defining population structuring, larger sample sizes and lower sequencing depth has been suggested (Fumagalli 2013). Next steps are planned including refining the extraction and sequencing methods and selecting more individuals to add to the analysis, from both Deep SEARCH archives and other collaborators.

5.7.4 Plumarella spp.

We chose *Plumarella* for a population genomic study as it is an abundant octocoral throughout the SEUS region, colonizing both *L. pertusa* skeletons and rocky reefs. This octocoral, with indetermined reproductive mode, provides a contrasting model of connectivity from the other species examined.

5.7.4.1 *Plumarella* spp. Methods

We quantified DNA samples using a Qubit fluorometer, and we checked the DNA checked for quality using a NanoDrop spectrophotometer and agarose gel electrophoresis. We prepared libraries and target-enriched them by Arbor Biosystems (Ann Arbor, MI) following the protocol outlined in Quattrini et al. (2018, 2020). We used the octocoral (Erickson et al. 2021) baitset to target-enrich non-coding and coding regions of genomes. Pooled, enriched libraries were sequenced on an Illumina HiSeq or NovaSeq (150 bp PE reads). Reads were processed using the Phyluce pipeline (Faircloth, 2016) as outlined in Quattrini et al. (2018), with some modifications. Briefly, reads were cleaned using illumiprocessor (Faircloth, 2013) and Trimmomatic v 0.35 (Bolger et al. 2014) and then assembled using SPAdes v 3.1 (Bankevich et al. 2012; with the --careful and --cov-cutoff two parameters). We used the *phyluce_assembly_match_contigs_ to_probes* command to match the octocoral (Erickson et al. 2021) baits to contigs to identify loci with a minimum coverage of 70% and a minimum identity of 70%. Loci were then extracted using *phyluce_assembly_get_fastas_from_match_counts* and aligned with MAFFT v7.130b (Katoh et al. 2002). Edges of the aligned loci were then trimmed using *phyluce_align_seqcap_align*.
SNPs were extracted following methods outlined in previous studies (Derkarabetian et al. 2019; Zarza et al. 2016, 2018) using modified scripts from Zarza et al. (2016). We chose the individual with the largest number of loci as identified by *phyluce_assembly_get_match_counts* as a reference individual for SNP calling. The commands *phyluce_assembly_get_match_counts* and *phyluce_assembly_get_fastas_from_match_count* were rerun on the reference individual to create a fasta file of loci found only in the reference. We indexed reference loci using bwa version 0.7.7 (Li and Durbin 2009).

We created BAM files for each individual by mapping their cleaned, trimmed reads to the reference using bwa-mem (Li 2013), sorting the reads using samtools, and removing duplicates using picard version 1.106-0 (http://picard.sourceforge.net). We then used gatk version 3.4 (McKenna et al. 2010) to realign BAM files around indels, call variants and filter variants based on vcf tools (Danecek et al. 2011). SNPs

were called at loci for which all taxa were represented and for which each locus had at least 25X coverage. We converted SNP files to a Structure-formatted file using phyluce_snp_convert_vcf_to_structure.

Structure (Pritchard et al. 2000) uses a Bayesian clustering approach to probabilistically infer population structure given *K*. We ran Structure in parallel using StrautoParallel (Chhatre and Emerson 2017, generations = 1 million, burnin = 250,000) with *K* = 7 populations on all 28 individuals and on the 27 individuals of *Plumarella* sp. 1 only. Five runs were completed at each value of *K*. Genetic diversity statistics (using the *basic.stats* function from the package *hierfstat*) according to Nei (1987) were also calculated. We used IQ-TREE to generate a phylogenetic tree of all *Plumarella* spp.

5.7.4.2 *Plumarella* spp. Results

The IQ-TREE and Structure analysis on all 29 individuals supports two species: *Plumarella* sp. 1 and 2 (OCT009, **Figure 5-46**). Further analyses on *Plumarella* sp. 1 demonstrate gene flow occurs among all sites sampled in the region **(Figure 5-47).** However, pairwise Fst values indicated significant genetic differentiation as well (**Figure 5-47**), yet this differentiation was not structured by depth or geographic distance (**Figure 5-48**). This apparent genetic differentiation could be due to some unique alleles present in individuals at each site, and these perhaps are related to either genetic drift of small founder populations or adaptive alleles. Alternatively, these significant results could be reflective of the overall small sample sizes used in these preliminary analyses **Figure 5-48).** More individuals are required to corroborate the results. BayesAss analysis was not performed due to the overall low sample size.

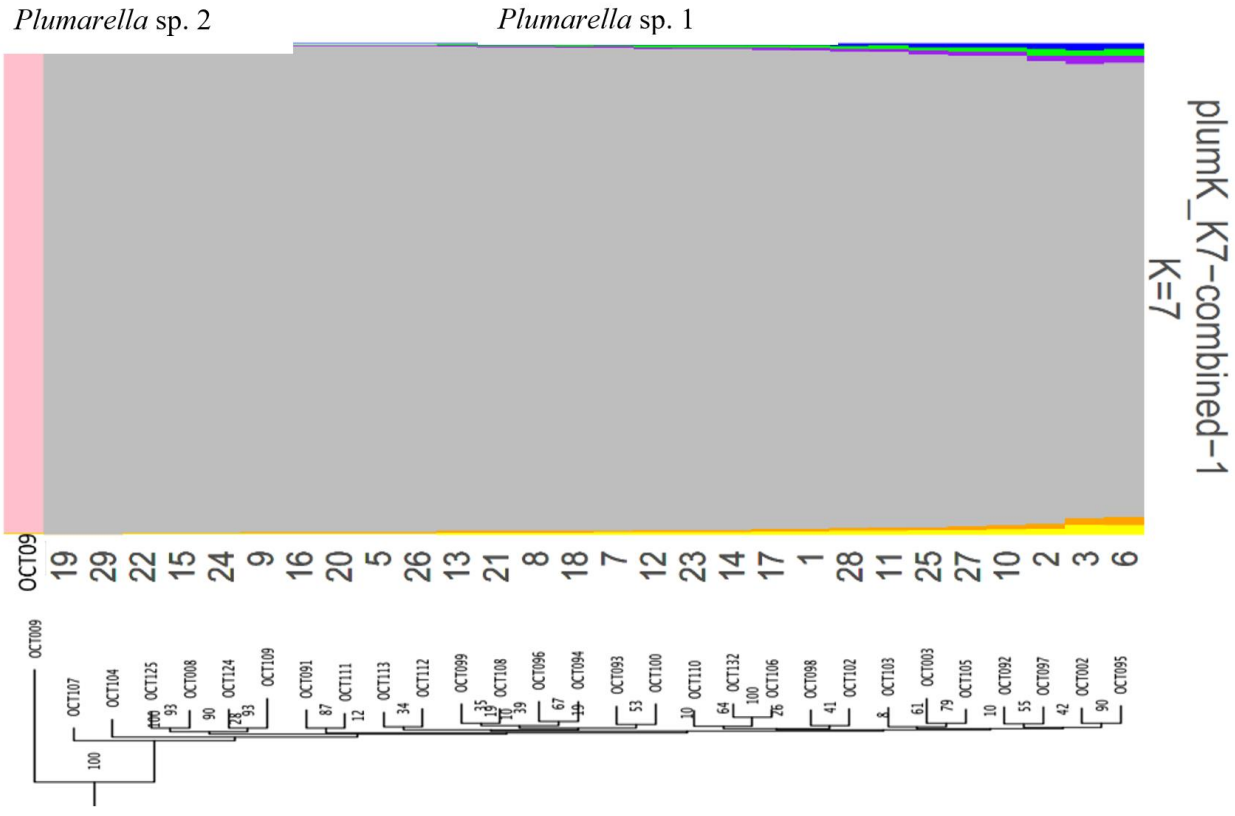

Figure 5-46. Structure and phylogenetic analyses for *Plumarelia* spp.
Structure (top, K = 7) and phylogenetic (bottom) analyses for the full *Plumarella* spp. dataset (n =28 individuals).

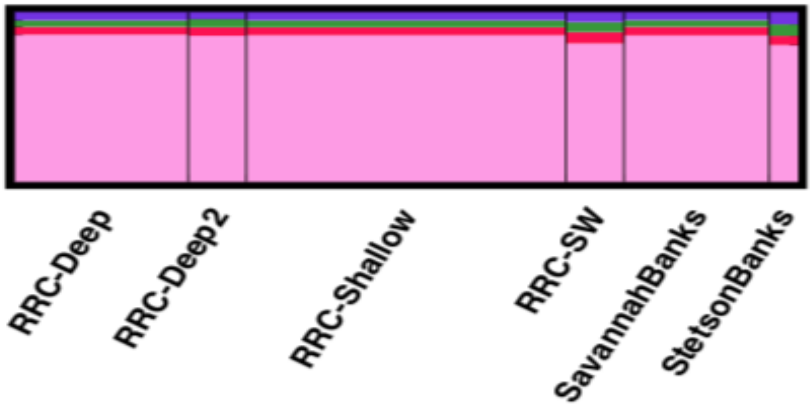

Figure 5-47. Structure results (K=4) for *Plumarella* spp. across the six sites
Based on 20K SNPs at 25X coverage. We further divided Richardson Reef into deep and shallow sites, with two sampling sites for each. RRC=Richardson Reef.

Table 5-25. Pairwise Fst values and corresponding p-values for *Plumarella* spp.

Pairwise Fst values (lower left) and corresponding p-values (upper right) determined by bootstrapping over loci in StAMPP for *Plumarella.*

Location	RRC Deep n = 6	RRC Deep2 n = 2	RRC Shallow n = 11	RRC SW n = 2	Savannah Banks n = 5	Stetson Banks n = 1
RRC-Deep	-	0.154	0.001	< 0.001	< 0.001	< 0.001
RRC-Deep2	0.00360	-	0.244	< 0.001	0.009	< 0.001
RRC-Shallow	0.00359	0.00211	-	< 0.001	< 0.001	< 0.001
RRC-SW	0.04253	0.03555	0.05270	-	< 0.001	0.194
SavannahBanks	0.01176	0.00857	0.01295	0.04361	-	< 0.001
StetsonBanks	0.06972	0.06262	0.06345	0.00809	0.06099	-

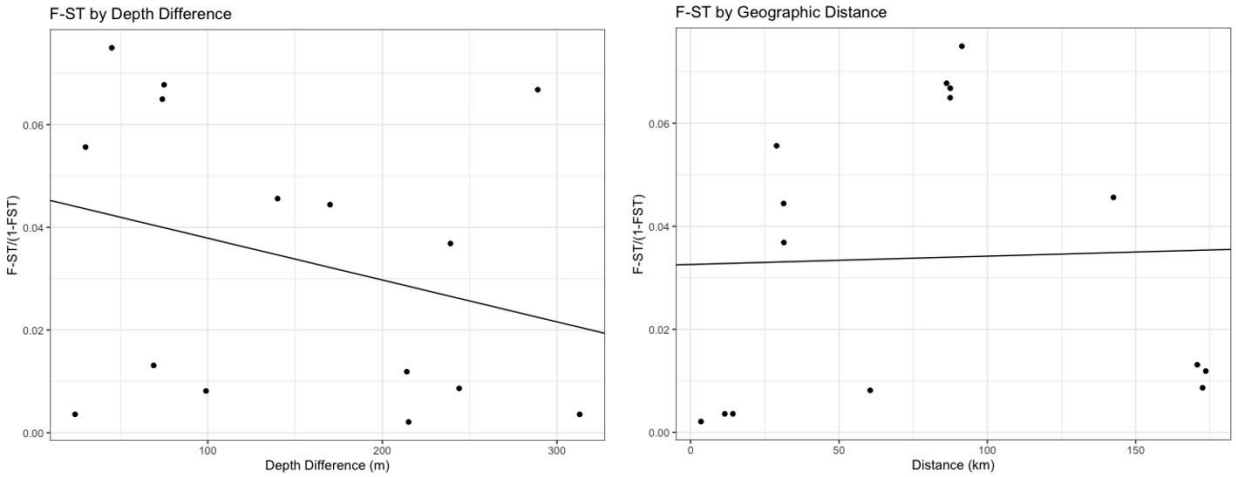

Figure 5-48. Pairwise transformed Fst values for *Plumarella* spp.
\ Pairwise transformed Fst values (Fst/(1-Fst)) plotted by differences in depth (left) and geographical distance (right) for *Plumarella*. Adjusted R2 values are 0.0124 and -0.0755 for depth and distance, respectively, with p-values of 0.298 and 0.899.

5.7.4.3 *Plumarella* spp. Connectivity

Target-capture genomics is an effective method to assess population genetics of deep-sea octocorals. This method enabled us to unlock the utility of the historical collection at the Smithsonian National Museum of Natural History (NMNH) and use specimens not preserved specifically for genomics in population genetic studies. Our results suggest substantial gene flow among sites, which are not isolated by depth or distance. However, Fst values also suggest some genetic differentiation occurring between sites as well. Perhaps this pattern is related to genetic drift of populations with low effective population sizes, selection of depth-adaptive alleles, or small sample size of our Deep SEARCH samples. Museum specimens can be leveraged in the future to corroborate these preliminary conclusions.

5.7.5 Paramuricea spp.

Ten *Paramuricea* spp. specimens from the Deep SEARCH study area were analyzed for population genomics. This genus has undergone ample work in recent years because of its abundance at the sites impacted by the Deepwater Horizon oil spill in the GOM (Doughty et al. 2014, Quattrini et al. 2022). The specimens examined here belonged to four putative species: *P. biscaya, P. aff. biscaya, P.* sp. 2, and *P.* sp. 4 (**Figure 5-49**) each from Pamlico Canyon, Blake Escarpment Deep, Cape Fear, and Cape Lookout Deep, respectively. None of the species were found to overlap at any of the sites.

5.7.5.1 *Paramuricea* spp. Methods

We extracted DNA using a modified CTAB protocol or a Qiagen eDNEasy kit. We normalized genomic DNA to 20 ng/µL in 50 µL and sent to Floragenex (Beaverton, OR) for RAD-seq. We made libraries with the 6-cutter *PstI* enzyme and sequenced on a single lane of an Illumina 4000 (100 bp, single end reads) with other *Paramuricea* spp. samples from a companion study. Raw data were quality checked using the program FASTQC (Andrews 2010) and de-multiplexed using the program STACKS (*process_radtags,* -e pstI --inline_null) with default parameters to clean the data (-c: removing any read with an uncalled base and -q: discarding reads with low quality scores) (Catchen et al. 2013). We assembled and clustered RAD-seq data using the ipyrad v 0.9.12 (Eaton and Overcast 2020) pipeline and integrated with *Paramuricea* spp. RAD-seq data from the North Atlantic Ocean in an ongoing study by Quattrini. We set the clustering threshold at 0.85, heterozygosity at 0.5, and min-samples at 75% taxa present per locus; the rest of the parameters were kept at defaults.

We constructed a phylogeny using IQ-TREE on a concatenated alignment of 125 taxa and 463,322 bp alignment with 1,000 bootstraps using the best model of nucleotide substitution and the ultrafast bootstrapping method. We displayed the tree in FigTree and rooted to a Plexauridae outgroup. We performed Structure analysis on *Paramuricea biscaya* and *Paramuricea* aff. *biscaya,* as eight of the nine Deep SEARCH samples were of these two species. Unlinked SNPs (4,488 SNPs) for this *Paramuricea* spp. subset (n = 45 individuals) were selected with the criterion of only 20% missing data and were subsequently used in the analysis (100,000 generations, 10% burning, 5 runs of K, K =1 through 6). We used the Evanno method in Structure Harvester to choose the optimal value of K. Following this output, we selected unlinked SNPs (25% missing data) from each species (n = 29, 12,515 SNPs for *P. biscaya,* n = 16, 11,184 SNPs, *P.* aff. *biscaya)* separately using ipyrad and re-performed the Structure analysis as described above. BayesAss and Fst statistical analyses were not conducted because of the few individuals collected in the Deep SEARCH study area.

5.7.5.2 *Paramuricea* spp. Results

We demultiplexed and trimmed reads using STACKS, with approximately 30% being discarded due to low quality reads or absence of the cut site. For *Paramuricea* spp. from the Deep SEARCH study area, this resulted in an average of 4.13 + 2.38 SD million reads per individual.

The phylogenetic analysis indicated that four phylogenetic lineages, which match distinct morphospecies, had been collected in the Deep SEARCH study area. *Paramuricea* sp 1 had been collected from Cape Fear; to date this species has been collected in the GOM from similar depth ranges (~300–450 m). *Paramuricea* sp. 4 had been collected from the Cape Lookout Deep area, also found off Canada in similar depths (900–1,200 m).

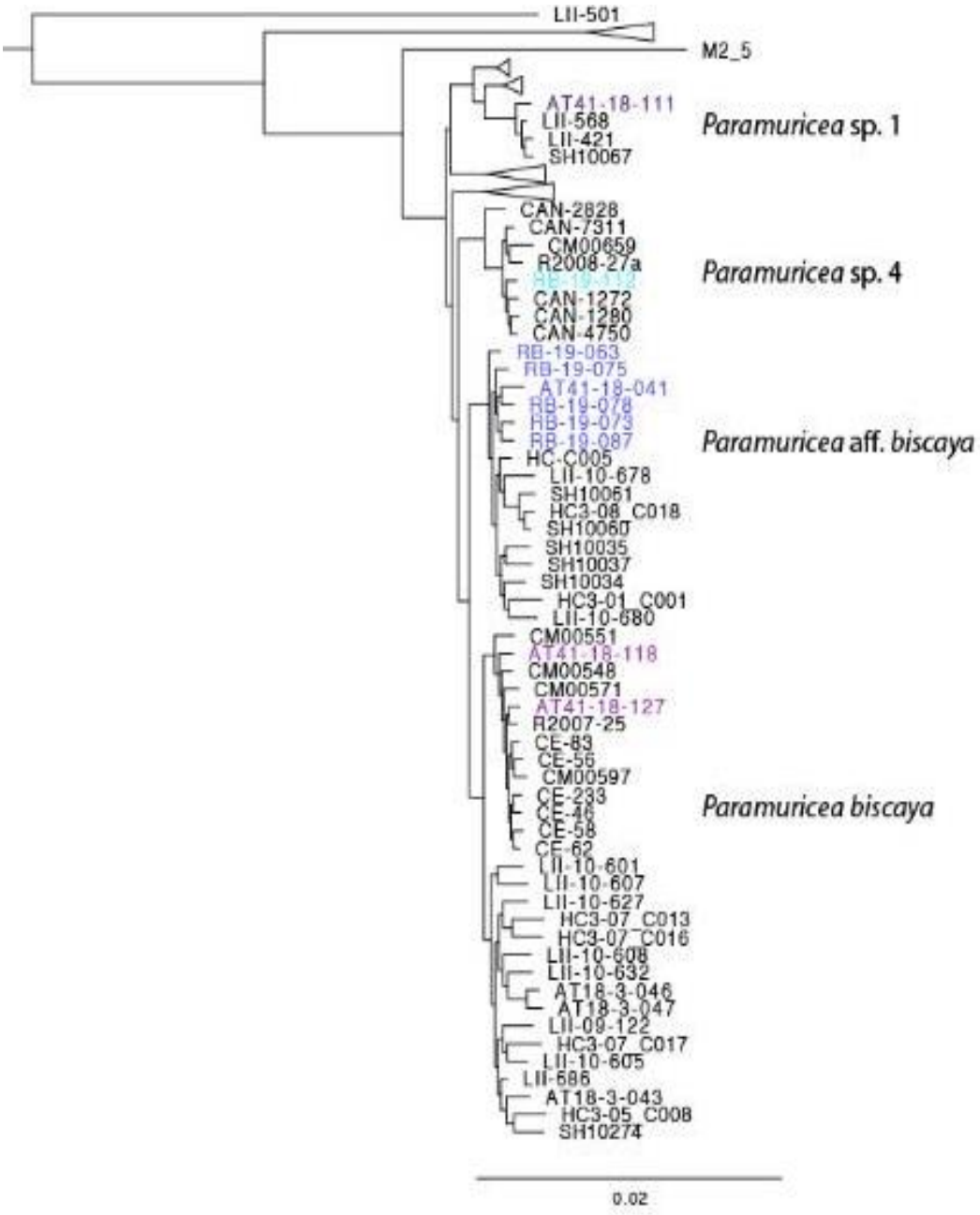

Figure 5-49. Phylogeny (IQ-TREE) of *Paramuricea* throughout the N. Atlantic Ocean
Color-highlighted specimen labels are of Deep SEARCH samples.

Two sister species, *P. biscaya* and P. aff *biscaya*, were more common in Deep SEARCH collections. Both species appear to be widespread in deep waters throughout the North Atlantic Ocean. *Paramuricea* aff. *biscaya* has been collected at depths ~1,000–1,500 m in the GOM. In the Deep SEARCH study area, we

collected *P.* aff. *biscaya* from Blake Escarpment Deep in similar depths (1,200–1,333 m). *Paramuricea biscaya* appears to be the deepest occurring species. We collected this species in Pamlico Canyon at depths > 1,500 m. Similarly, it has been collected in the GOM and in the eastern North Atlantic at depths of ~1,500–2,500 m.

We further examined the population structure of both *P. biscaya* and *P.* aff. *biscaya* using a Structure analysis, which indicated clear separation (K = 2, Structure Harvester) of these species with little to no admixture between them (**Figure 5-50).** Within *P.* aff. *biscaya,* Structure Harvester indicated that the number of likely populations (K) is 3; with the Deep SEARCH samples from the Blake Escarpment clustering together with samples from the GOM, although there does appear to be some differentiation in the GOM samples. Within *P. biscaya,* we found there are most likely two clusters (K = 2). Pamlico Canyon samples clustered with those from the NEUS canyon area and the eastern North Atlantic; this metapopulation was differentiated from the GOM.

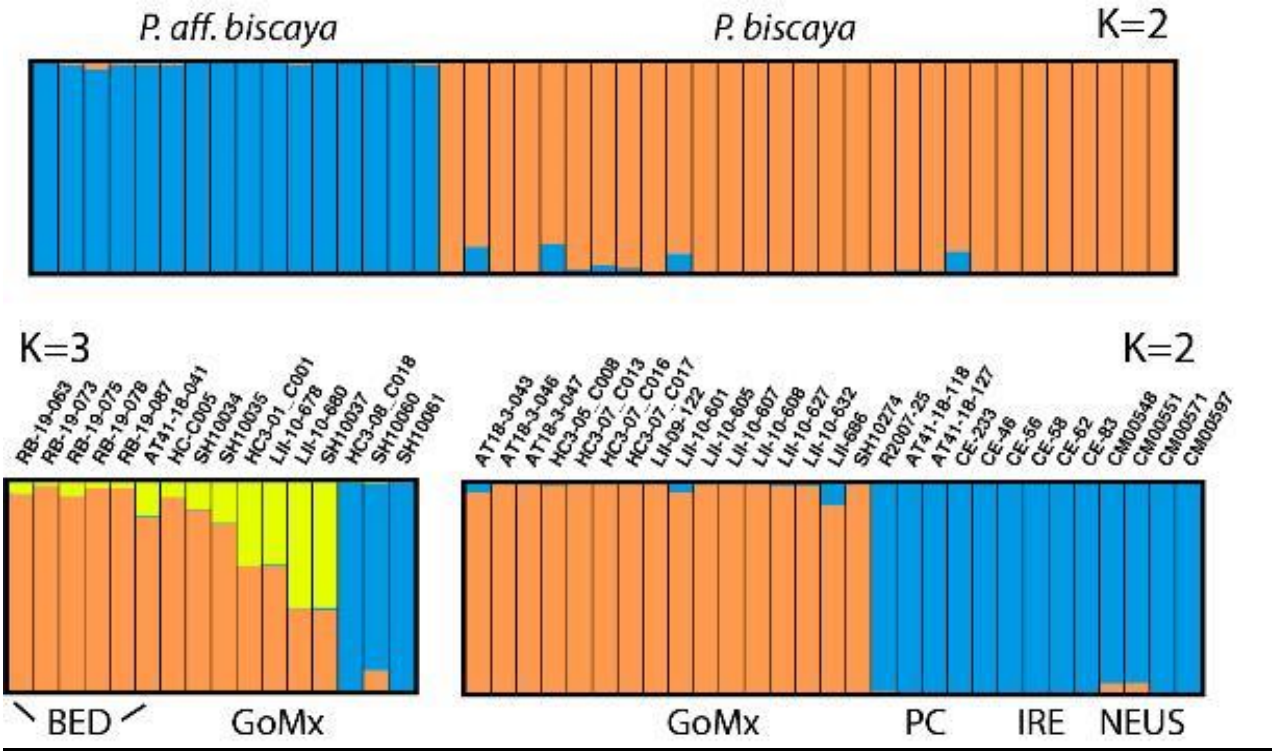

Figure 5-50. Membership of probability graphs from a Structure analysis of *Paramuricea* spp. Structure analysis of *Paramuricea biscaya* and *P.* aff. *biscaya*. Analysis on both species on the top row and analysis on each species separately in the bottom row. BED = Blake Escarpment Deep, GoMX = Gulf of Mexico, PC = Pamlico Canyon, IRE = eastern North Atlantic, NEUS = northeastern US canyons area.

5.7.5.3 *Paramuricea* spp. Connectivity

The population genetic analysis indicates two distinct lineages that are morphollogcally different and likely represent different species: *P. biscaya and P. aff biscaya,* which correspond with recent results from a RAD-seq study in the GOM (Galaska et al. 2021). However, that study found a small degree of admixture between them, whereas our results indicate that there is little to no admixture between them. Our results could be driven by the additional populations from the North Atlantic included in our analyses. Further research could help to determine whether these two species represent incipient species or not (Galaska et al. 2021).

Notably, species-specific population structure occurs between regions within this genus, although we note that sample sizes from the Deep SEARCH study area are small (and too low for gene flow analysis). Populations of the shallower of the two species, *P. aff. biscaya*, were not differentiated between the GOM and the Deep SEARCH study area south of Cape Hatteras. In contrast, we found that populations of the deeper-occurring *P. biscaya* were differentiated between the GOM and the Deep SEARCH study area north of Cape Hatteras. *Paramuricea biscaya* samples from Pamlico Canyon also clustered together with those from the NEUS canyons area and the eastern North Atlantic.

The population structure pattern observed in *P. biscaya* is not too surprising as there is a strong biogeographic break at Cape Hatteras, which is commonly observed in shallow-water taxa (Pappalardo et al. 2014). At Cape Hatteras, currents converge, reducing the larval exchange around the cape as most larvae are transported offshore (Savidge and Bane 2001). Although this biogeographic break has been studied primarily for coastal and shallow-water taxa (Pappalardo et al. 2014) it is possible that this can be extended to deepwater corals as well. Analysis of more samples throughout the study area could help to to explore and confirm results presented here with additional data.

5.7.6 Other Invertebrates

We targeted coral- and mussel-associated invertebrates for population genomic analyses. Our target taxa included ophiuroid brittle stars (*Asteroschema* spp.) commonly associated with corals. We conducted population genomic analyses on six specimens collected from *Paramuricea* spp.colonies in Pamlico Canyon, an NEUS intercanyon, and Blake Escarpment Deep. We also opportunistically collected and subsequently sequenced one *Ophiocreas oedipus* from a *Metallogorgia melanotrichos* coral colony. In addition to coral-associates, we focused population genomic efforts on two invertebrate species common to cold-seep habitats: the brittle star *Ophioctenella acies* (n=8 individuals) and the sea cucumber *Chiridota heheva* (n = 16 individuals), both collected from Blake Ridge Seep.

5.7.6.1 Other Invertebrates Methods

We extracted DNA using either a AutoGenPrep 965 Kit or a Mag Attract high molecular weight kit. We normalized gDNA to 20 ng/µL in 50 µL and sent to Floragenex (Beaverton, OR) for RAD-seq. We made libraries with the 8-cutter *sbfI* enzyme and sequenced across two lanes of an Illumina 4000 (100 bp, single end reads). We demultiplexed raw data using the program STACKS (*process_radtags*, -e sbfI --inline_null) with default parameters to clean the data (-c: removing any read with an uncalled base and -q: discarding reads with low quality scores) (Catchen et al. 2013). We assembled and clustered RAD-seq data using the ipyrad v 0.9.12 (Eaton and Overcast, 2020) pipeline for each target taxon. We set the clustering threshold at 0.85–0.92, heterozygosity at 0.5, and min-samples at 50-80% taxa present per locus; the rest of the parameters were kept at defaults.

We constructed a phylogeny using IQ-TREE on concatenated alignments of ophiuroids (654,684 bp) and sea cucumbers (159,789 bp), using the best model of nucleotide substitution and the ultrafast bootstrapping method (-bb 1,000). We displayed the tree in FigTree and rooted to the midpoint. We performed structure analyses on *Asteroschema* spp., *O. acies* and *Chiridota heheva*. For *Asteroschema* spp., We performed Structure analysis (100,000 generations, 10% burning, 5 runs of *K*, *K* =1 to 6) on 713 unlinked SNPs (n = 6 individuals) with the criterion of only 20% missing data. For *O. acies*, we performed structure analysis (100,000 generations, 10% burning, 5 runs of *K*, *K* = 1 to 8) on 4,902 unlinked SNPs (n = 8 individuals). For *C. heheva*, we performed structure analysis (100,000 generations, 10% burning, 5 runs of *K*, *K* = 1 to 6) on 548 unlinked SNPs (n = 6 individuals). We used the Evanno method in Structure Harvester to choose the optimal value of *K*. BayesAss. Analyses of Fst statistics were not conducted because of the few individuals collected in the Deep SEARCH study area.

5.7.6.2 Other Invertebrates Results

We demultiplexed and trimmed reads using STACKS, with approximately 13% being discarded due to low quality reads or absence of the cut site in reads. For ophiuroids, this resulted in an average of 2.70 + 1.38 SD million reads per individual. RAD-seq performed much worse for *C. heheva.* Following demultiplexing and trimming in STACKS, only 356,363 ± 287,773 SD reads were retained.

The phylogenetic analysis for the ophiuroids was well supported at deeper nodes in the phylogeny and indicated that there are at least four lineages that represent distinct species and/or genera (**Figure 5-51**). Within the *Asteroschema* spp., an unidentified species (potential new species) from Blake Escarpment Deep was found to be sister to the *A. clavigerum* group (**Figure 5-51**). Structure analysis also indicated that this individual was distinct from the others. The Evanno method revealed that the most likely number of *K* clusters was 4 for *Asteroschema* spp.

The Structure analysis also suggested that *A. clavigerum* individuals from Pamlico Canyon were differentiated from those in an intercanyon area to the north (**Figure 5-51**), suggesting that populations of *Asteroschema* spp. might be differentiated over relatively short geographic distances (10s km) as the depth ranges of these sites were similar. We based this result, however, on few individuals and this could be explored with more data in future studies. *Ophioctnella acies* at Blake Ridge Seep appear to be well admixed, suggesting no cryptic species present.

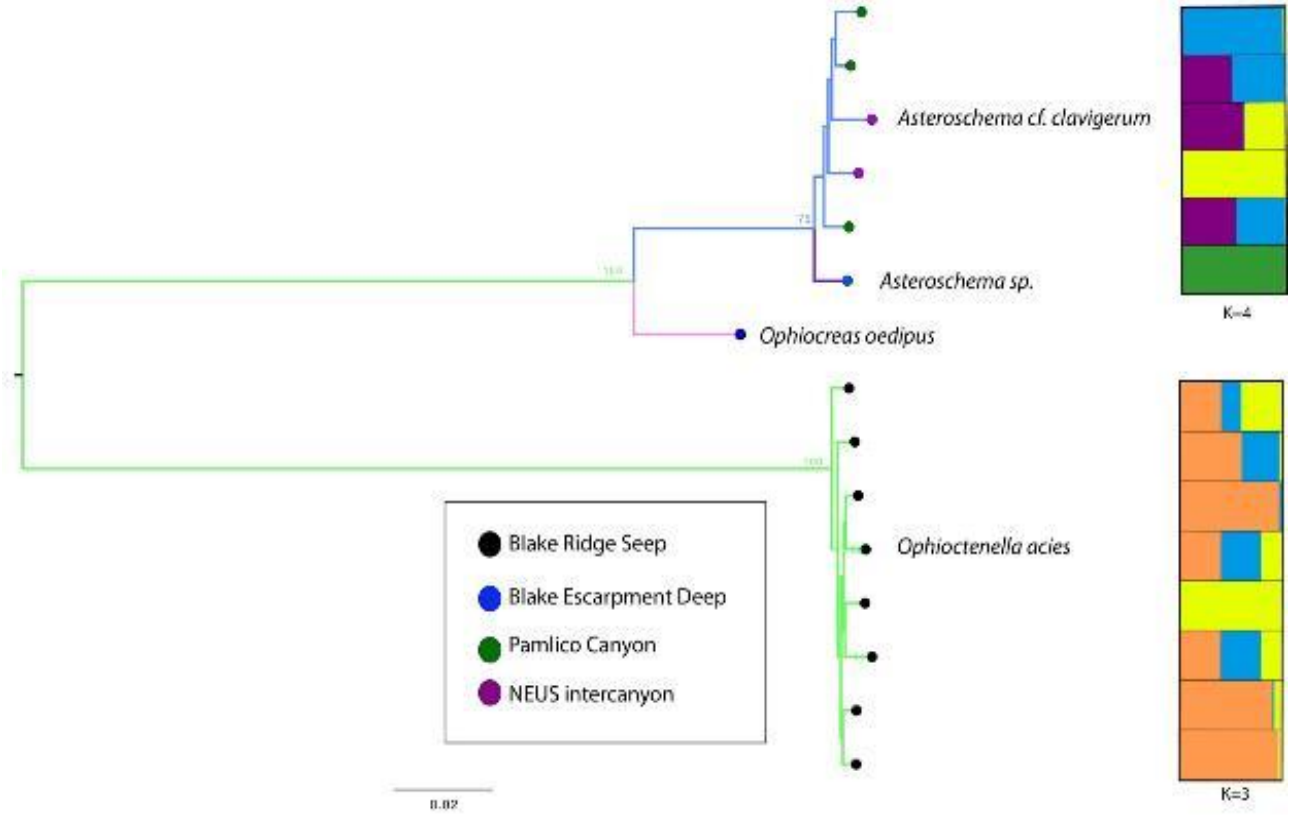

Figure 5-51. Phylogeny and membership of probability graphs of ophiuroid brittle stars
Phylogeny (IQ-TREE) of ophiuroid brittle stars (left) and membership of probability graphs from structure analyses (right).

The sea cucumber phylogeny was rooted at the midpoint, thus two distinct clades were recovered (**Figure 5-52**). However, these two groups were also recovered in the Structure analysis. Using the Evanno

method, the most likely number of *K* clusters was 2 for *C. heheva*. This result was a bit surprising, but suggests perhaps a sympatric, cryptic *Chiridota* species is present in cold seeps in the region. Upon further analysis of COI barcode data, we also found that there are two groups of *C. heheva* based on the COI data and these were ~1% different (p-distance) from one another, which is within the normal level of intraspecific variation within a species (**Figure 5-53**). Therefore, morphological analysis combined with species delimitation methods are necessary for confirmation.

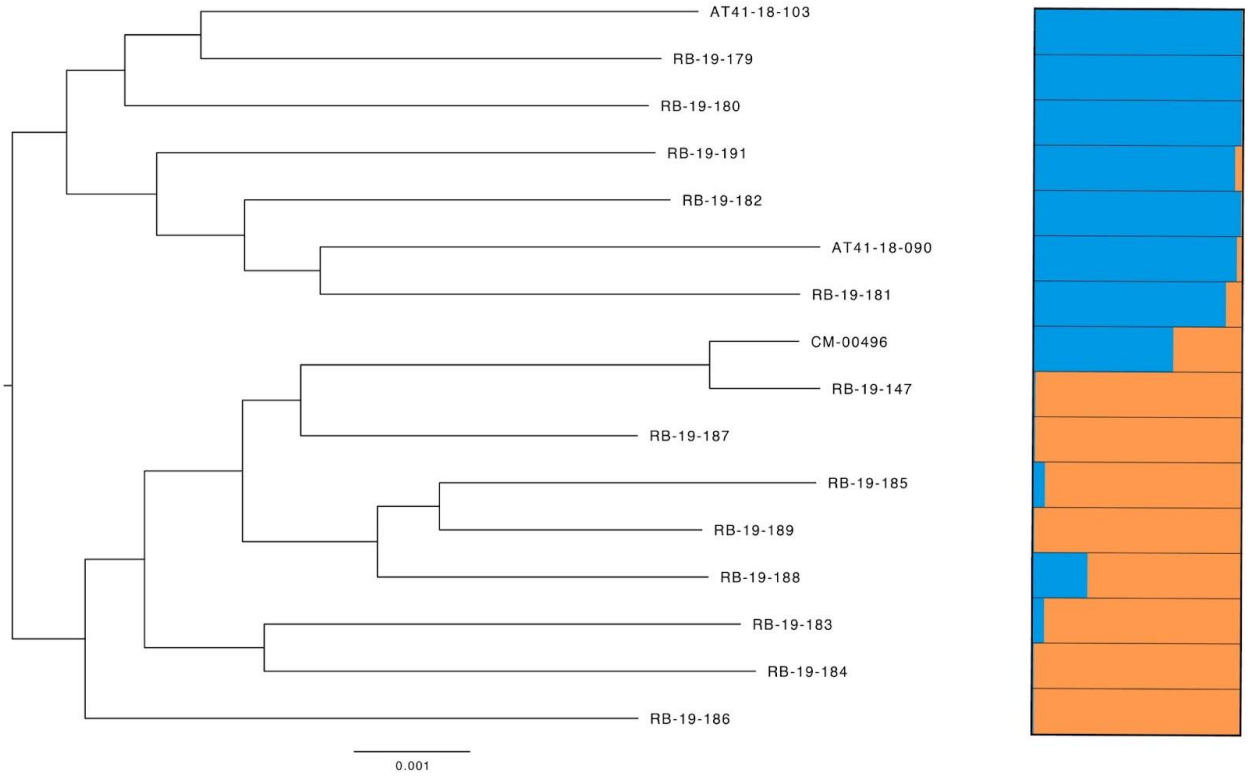

Figure 5-52. Phylogeny and membership of probability graph of sea cucumbers
Phylogeny (IQ-TREE) (left) and membership of probability graph from structure analysis (right) of *Chiridota heheva* sea cucumbers.

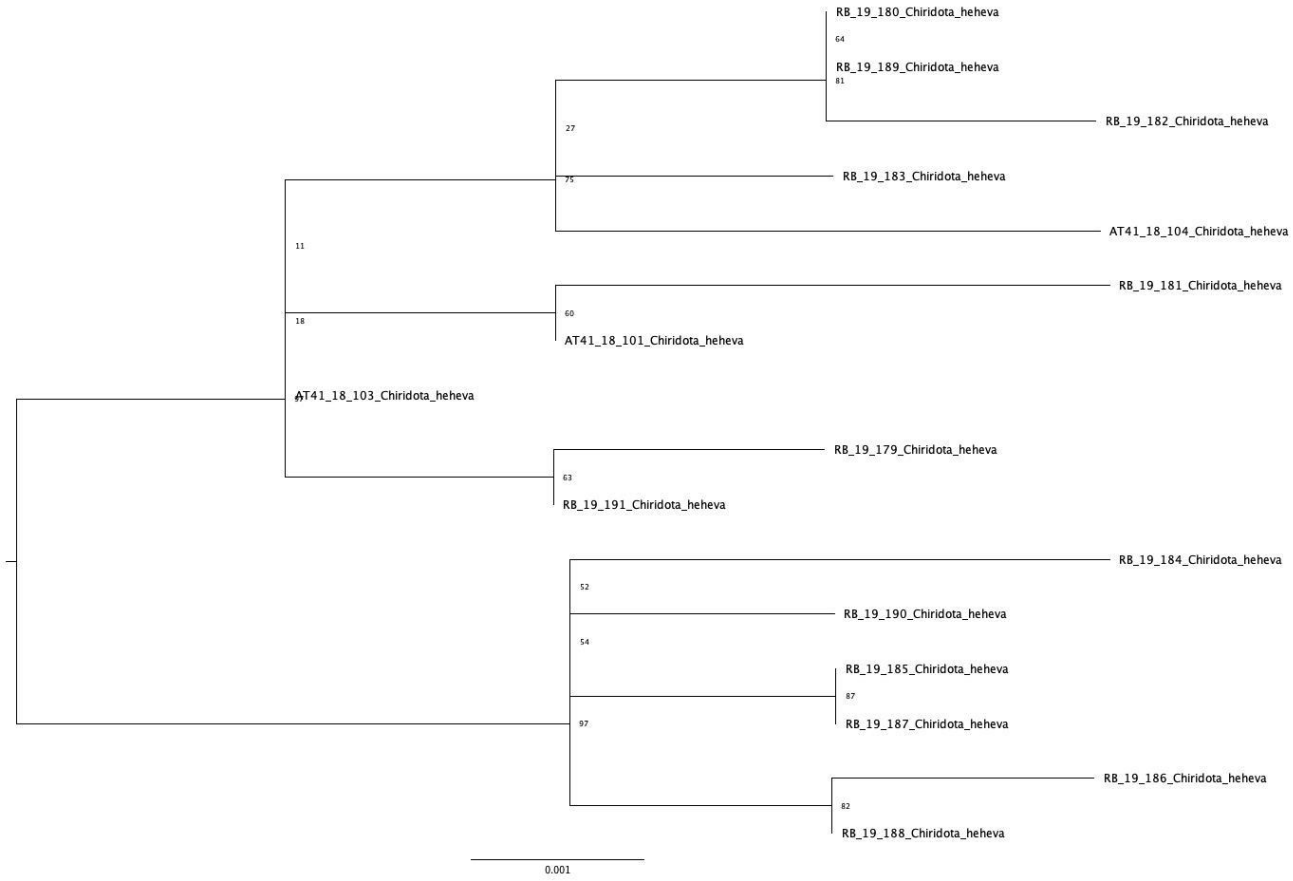

Figure 5-53. Phylogeny (IQ-TREE) of *C. heheva* based on an alignment of COI data (652 bp)

5.7.6.3 Other Invertebrates Connectivity

Although we collected few individuals from the Deep SEARCH study area for phylogenomic and population genomic analysis, results on the other invertebrates indicated the likelihood of cryptic species and population differentiation. There is some evidence for population structure in *A.* cf. *clavigerum*, with Pamlico Canyon and intercanyon area further to the north likely harboring different populations. Isolation by distance has been noted in populations of this species before (Cho and Shank 2010). Population differentiation within this species might also be tied to its habitat, as it is a symbiont on octocorals, likely in a mutualistic relationship (Girard et al. 2016). Therefore, gene flow between different locations would likely also depend on host availability. In contrast, *O. acies*, which is a brittle star found only in chemosynthetic habitats, appeared to consist of well-admixed individuals at Blake Ridge Seep.

This brittle star occurs in high densities at vents along the Mid-Atlantic Ridge and at seeps in the western North Atlantic (Stohr and Segonzac 2005), suggesting potential for high gene flow among sites. Finally, the presence of two lineages of the sea cucumber *C. heheva*, a widespread cosmopolitan species (Thomas et al. 2020) was surprising. The 1% divergence observed between two groups at the COI barcode is indicative of intraspecific variation, but the RAD-seq data based on 548 SNPs suggests that there is more genetic variation than what COI barcode data demonstrate. Further genomic and morphological data for all these invertebrates from multiple sites in the region could help to confirm population structure and accurately delimit species.

5.7.7 Conclusions

Determining the scale of connectivity for benthic deep-sea invertebrates is a complex task due to the many environmental and biological processes that may influence dispersal distances of larvae but are difficult to measure directly (Cowen and Sponaugle 2009). Highly connected networks of populations improve resiliency to increasing anthropogenic resource exploitation in the deep sea and the projection of escalated habitat fragmentation (Hilário et al. 2015), and studies of connectivity can help to inform future management decisions (Kinlan et al. 2005, Gaines et al. 2007, Baco et al. 2016, Metaxas et al. 2019).

In this study element, we utilized high-resolution population genomics techniques to estimate realized connectivity among benthic invertebrates from both coral and cold-seep habitats along the US Atlantic margin. Taken together, our estimates of realized genetic connectivity provide insights into the forces shaping genetic diversity, population structuring, and potential for adaptation in vulnerable deep-sea habitats and may provide information crucial for guiding management efforts.

Our genetic connectivity data provides insights into several hypotheses that were proposed for key CWC and cold-seep taxa in the Deep SEARCH study area. First, we expected that our collections and analyses may result in the discovery of new and/or cryptic species. Although sample sizes were small, analysis of SNP data detected a potential new species of *Astroschema* brittle star at the Blake Escarpment, as well as a potential cryptic species of sea cucumber *Chiridota* at the Blake Ridge Seep. Additional collections and morphological analyses are needed to confirm these findings.

Another hypothesis we tested was the existence of a break in genetic connectivity in populations north and south of Cape Hatteras, NC. This area is a biogeographical province boundary separating water masses of the Virginian and Carolinian provinces that differ sharply in temperature (Briggs 1974, Briggs and Bowen 2012). The Hatteras area is a known biogeographic break for fishes (Avise et al. 1987, McCartney et al. 2013, Boehm et al. 2015) as well as biogeographical province boundary for CWC species (Cairns and Chapman, 2001).

Two species targeted for genetic analyses, *Lophelia pertusa* and *Paramuricea biscaya,* had populations on either side of Hatteras, and both showed evidence of restricted gene flow north and south of Cape Hatteras. SNP data for *L. pertusa* confirmed regional structuring for the scleractinian *L. pertusa,* with differentiation among SEUS (South of Hatteras) and Norfolk Canyon (North of Hatteras), populations, as well as GOM and NEUS intercanyon populations, confirming previous genetic analyses of microsatellite loci (Morrison et al. 2011, 2017; Lunden et al. 2014). Similarly, GOM and MAB populations of the octocoral *P. biscaya* were genetically unique. For species that inhabit the MAB north of Cape Hatteras, hydrodynamic conditions may isolate populations, as seen in larval dispersal models for the glass sponge *Vazella pourtalesii* (Wang et al. 2021).

Within regions, we hypothesized that rates and directions of gene flow would correspond with predominant currents. This hypothesis held for several species within the Blake Plateau or MAB. In the MAB, three *G. childressi* populations were well connected genetically, with gene flow from onshore to offshore, following the prevailing Labrador Current. On the Blake Plateau, gene flow appears to connect populations of the octocoral *Plumarella* spp. as well as the scleractinian coral *L. pertusa*, with larval dispersal likely following the Gulf Stream in a stepping-stone fashion.

This result may be expected given the larval dispersal models that indicate strong unidirectional flow following the Gulf Stream (Wang et al. 2021). The larval dispersal models (Wang et al. 2021) also suggest the potential for occasional gene flow from outside the Blake Plateau; concordantly, the *L. pertusa* Structure analysis (**Figure 5-47**) suggested that a few individuals likely originated from an unsampled population. As suggested by Wang et al. (2021), it is likely that considerable redundancy in

larval supply from downstream (lithoherms off the coast of Florida) may confer higher resilience through genetic mixing of multiple source populations.

6 Prediction Modeling

Chapter Authors: Erik E. Cordes, Ryan Gasboro, Andrew Davies, Amanda Demopoulos

Deep-sea ecosystems along the US continental margin support enhanced biodiversity and sensitive biological communities, yet they remain poorly understood. The maintenance of biodiversity is critical to the function and sustainability of these deepwater ecosystems that provide numerous ecosystem services (Thurber et al. 2014). Loss of deep-sea biodiversity could have long-term, damaging effects to large expanses of the deep seafloor, the overlying water column, and to human health. The data gathered throughout the Deep SEARCH project has been essential for predicting organism and ecosystem-level responses to potential anthropogenic impacts and for assessing the severity of different impact types on sensitive deep-sea communities.

Through this study, we have filled major data gaps for poorly known deepwater ecosystems in order to refine regional management measures in the deep sea. The improved understanding of the habitats and communities in offshore areas of the Atlantic Large Marine Ecosystem can help to augment the capacity to predict the distribution of sensitive areas with respect to the potential development of energy and marine minerals managed by the Bureau of Ocean Energy Management and their concurrent mission to protect the environment.

6.1 *Lophelia pertusa* Mounds as Suitable Habitats

On the continental margin off the SEUS, azooxanthellate coral reef ecosystems dominated by the cosmopolitan CWC *Lophelia pertusa* have long been known to exist (Stetson 1962) and a rich associate fauna has been documented (Hourigan et al. 2017). Despite this, only select sites—primarily coral mounds off of Florida and the western Stetson Banks—had previously been imaged (Reed et al. 2006, Partkya et al. 2007).

At the onset of this project, we began to assemble *L. pertusa* predictive habitat models, which were first generated in April 2018 (**Figure 6-1**). These models suggested that there were relatively high-probability coral sites further east on the Blake Plateau than previous studies had focused. This guided the mapping of the *Okeanos Explorer* that summer, which led to the first high-resolution bathymetry in the area. This revealed a number of features that we then explored on one dive during the *Okeanos Explorer* cruise and later with the *Alvin* in August 2018 in the area that we now refer to as the Richardson Reef Complex.

Indeed, much of the Blake Plateau has been mapped in high resolution using shipboard multibeam echosounders for the first time during this project on the *Pisces*, *Atlantis*, *Ron Brown*, and *Nancy Foster* cruises as well as through our collaborative work with the *Okeanos Explorer* program. During the Deep SEARCH project, we ground-truthed these maps, and our visual surveys confirmed the presence of numerous CWC-formed mounds and reef tracts that previous, lower-resolution surveys had not detected. We found many of these features on the Blake Plateau, an area long presumed to be relatively featureless and where predictive models for CWCs placed a low-to-moderate probability of suitable habitat (Guinotte et al. 2017).

Here, we present updated ensemble habitat suitability models for three coral taxa of interest—*L. pertusa*, Octocorallia (gorgonian sea fans and soft corals), and Antipatharia (black corals)—on the SEUS margin using the latest high-resolution terrain data, coral occurrence data obtained during the Deep SEARCH surveys, and climate models as explanatory data in order to create high-quality baseline distributional maps for the region. The main reef-forming taxon, *L. pertusa*, is modeled by itself in order to best define the environmental niche and geographic distribution of this important species. These models represent notable expansions of our knowledge of distribution of these taxa, and the model outputs contained herein

are relevant to conservation and exploration of both CWC habitats and the wider SEUS margin ecosystem.

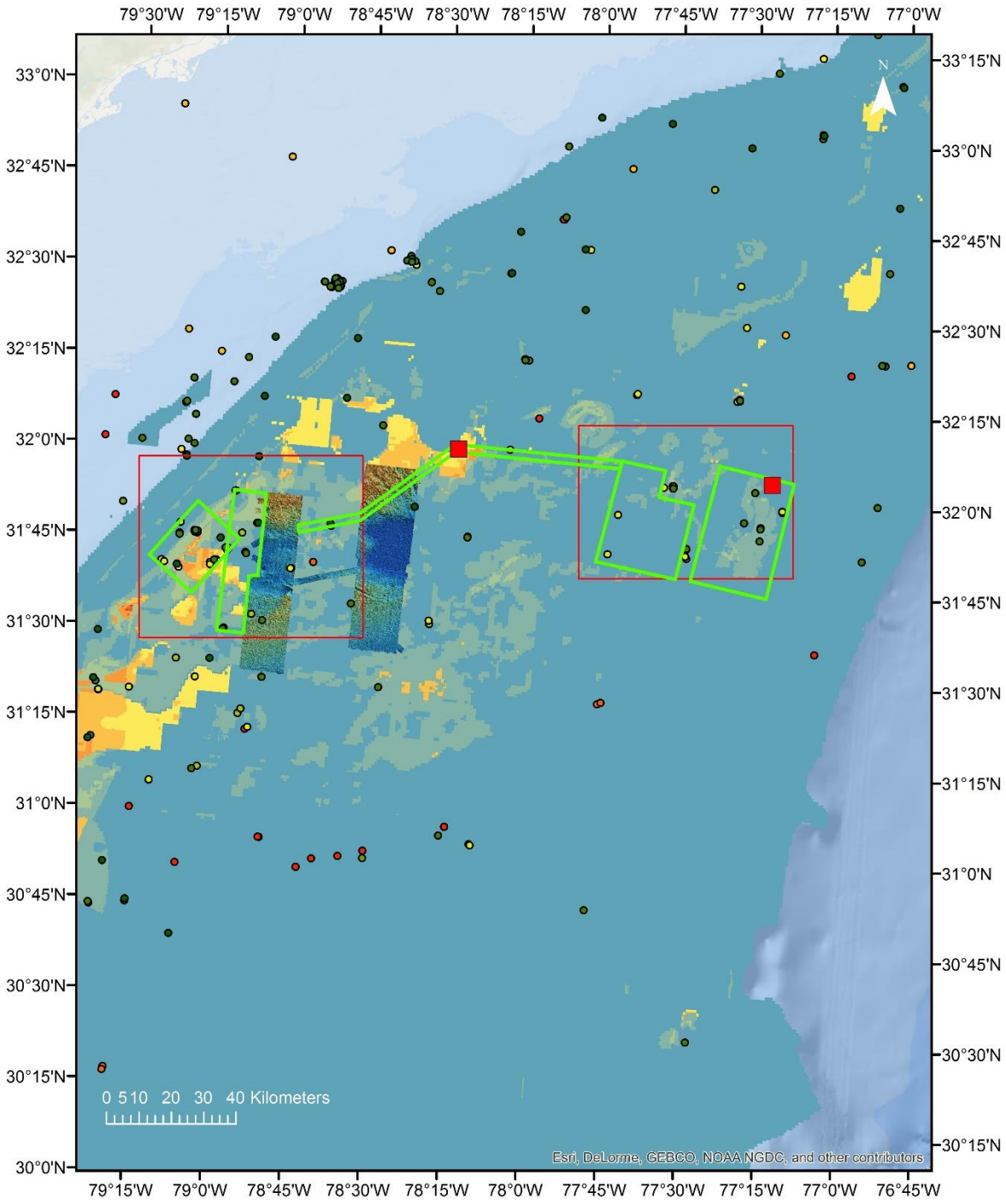

Figure 6-1. Results of the early *Lophelia pertusa* predictive habitat models
Generated in April of 2018 for the Stetson Banks area of the Blake Plateau. Background coloration indicates probability of occurrence of *L. pertusa*, with warmer colors indicating higher probability. Open red boxes indicate areas of interest for mapping and subsequent visual surveys, while bright green boxes are refined plans for the *Okeanos Explorer* bathymetric surveys. The green box to the furthest east is the site of the Richardson Reef Complex discovery. Small red squares indicate the positions of the ADEON landers in the area.

6.1.1 Methods

6.1.1.1 Presence Data

We downloaded presence data from the October 2020 version of the NOAA deep-sea coral database (https://deepseacoraldata.noaa.gov/). Additionally, points were excluded from analyses if their location accuracy was greater than 1,000 m; this excluded older, less reliable records (e.g., dredge and trawl records) that likely have lower fidelity to gridded environmental data. We also generated presence points from submersible dive imagery obtained in 2018–19 during Deep SEARCH cruises AT41 and RB1903, using the *Alvin* and ROV *Jason II*, respectively. We annotated video imagery from submersible dives and we recorded abundances of each taxon at min^{-1} resolution; we converted all abundance data to binary (1 = presence) data before modeling. Additional presence points came from dives executed on the Blake Plateau from the NOAA Ship *Okeanos Explorer* using the ROV *Deep Discoverer*. To prevent spatial autocorrelative bias in the results, we merged all points that fell within the same grid cell. The data were then filtered into one of three taxa: *Lophelia pertusa*, Octocorallia, or Antipatharia.

6.1.1.2 Terrain & Environmental Data

A bathymetric dataset covering much of the Blake Plateau—generated by collating and cleaning both publicly available multibeam echosounder data and that collected during the Deep SEARCH expeditions (Derek Sowers et al. [Ocean Exploration Trust], unpubl. data, [2019])—was used to create the high-resolution (35 m) terrain variables used in this study. Slope, aspect (both N-S and E-W), three types of curvature, fine (100 m) and broad-scale (1,000 m) bathymetric position indices comprised the terrain variables used in subsequent analyses. In addition, we classified the terrain into valley, flat, slope, ridge, and peak landforms or 'bathymorphons' by Sowers et al. (unpubl. data); we included this layer as a categorical variable. We generated all variables besides depth and bathymorphon with Benthic Terrain Modeler v3.0 (Walbridge et al. 2018) in ESRI Arcmap software.

A number of environmental or climate variables were also included to model suitable coral habitat (**Table 6-1**). We downloaded data in four-dimensional (X, Y, depth, time) netCDF format from the Earth System Grid Federation as either monthly or annual means from 1950–2014. We used the command-line Climate Data Operators tool (Schulzweida 2019) to convert all data to annual means and to re-grid from curviliear to 0.25º lat/long grids using bilinear interpolation. We extracted bottom-most (= benthic) data using the 'nctoolkit' v.0.3.0 in Python.

We sequentially removed variables with VIF > 5 and/or were highly correlated (Pearson's R > 0.9) from the models in order to minimize multicollinearity. The final variables (Table 6-1) still included a few highly correlated variables (temperature, pH), but were included in the model for their known biological relevance to the studied taxa.

Table 6-1. Summary of variables included in habitat suitability models

All terrain variables were derived from [1]. Variables selected for final models are in bold.

Variable	Short_name	Type	Nominal Resolution	Units	Reference(s)
Depth	Depth	Terrain	35 m	m	[1a]
Bathymorphon	Bathymorph	Terrain	35 m	Landform	[1b]
Slope	Slope	Terrain	35 m	º	-
BPI_1000m	BPI_1000m	Terrain	35 m	-	-
BPI_100m	BPI_100m	Terrain	35 m	-	-
Aspect (sin)	Aspect_sin	Terrain	35 m	º	-
Aspect (cos)	Aspect_cos	Terrain	35 m	º	-
Curvature (general)	Curv_gen	Terrain	35 m	-	-
Curvature (plan)	Curv_plan	Terrain	35 m	-	-
Curvature (profile)	Curv_prof	Terrain	35 m	-	-
Temperature	Temp	Climate	7–50 km	ºC	[2], [3], [4], [5]
pH	pH	Climate	50 km	pH	[2]
Dissolved Oxygen (mean)	DO	Climate	50 km	µmoL L^{-1}	[2]
Dissolved Oxygen (min)	DOmin	Climate	50 km	µmoL L^{-1}	[2]
Zooplankton Carbon Conc.	Zooc	Climate	50 km	mol m^{-3}	[2]
Export Carbon	ExpC	Climate	50 km	mol m^{-3}	[2]

[1a] Derek Sowers et al. (2020; Ocean Exploration Trust, unpubl. data); [1b] Sowers et al. (2020; unpubl. data)
[2] Müller et al. (2018)
[3] Hurrel et al. (2020)
[4] Alexander et al. (2020)

6.1.1.3 Habitat Suitability Models

We created an ensemble habitat suitability model for each of the three taxa using the 'biomod2' package (Thuiller et al. 2016) in the R statistical environment (R Core Team 2019). We chose two machine-learning algorithms, Random Forest (RF) and Maximum Entropy (MaxEnt), for the analyses based on their flexibility and past predictive performance in similar terrain-based habitat suitability models for CWCs (Cordes et al. submitted). We generated three sets of 1,000 random pseudoabsences, or background points, for each taxon to compare that taxon's niche at the presence points to the wider regional environment. We executed three evaluation runs for each presence-pseudoabsence dataset, with 70% of the data used to train the model and 30% set aside for model evaluation using receiver-operating characteristic (ROC) and true-skill statistic (TSS) scores.

We also created an additional model that was trained and evaluated on the entire dataset for each presence-pseudoabsence set. In total we created 24 individual models per taxon. A cutoff of 0.8 ROC was used to filter for high-performing models. We weighted the remaining models by ROC and created an ensemble-mean model for each taxon. We then projected each ensemble-mean model back onto the environmental grid space.

6.1.2 Results

We used a total of 736, 557, and 72 unique presence points respectively to model *L. pertusa*, Octocorallia, and Antipatharia (**Figure 6-2**). Most coral presences fell on slope or ridge bathymorphs, but octocorals appeared to have less of a defined preference for these geomorphologies and for steep slopes (**Figure 6-3**).

6.1.2.1 Lophelia pertusa

The mean ensemble model showed suitable habitat for *L. pertusa* occurring throughout the Blake Plateau, but concentrated at areas characterized by rugged terrain; BPI at both scales and slope explained most of the variation in the *L. pertusa* niche, with some additional (< 5 % each) variation explained by the environmental variables (**Figure 6-4** and **Figure 6-5**).

The models for *L. pertusa* performed the best of all the taxa, perhaps in part due to the large number of recorded presences for this species. While both algorithms performed well, the RF models had extremely high values for both ROC and TSS (> 0.9), suggesting excellent performance in both predictive and explanatory capacities. However, it does appear that the model may suffer from a degree of overfitting, as suitable habitat tended to be concentrated around areas with more known coral presences and extended submersible sampling (the Richardson Reef Complex).

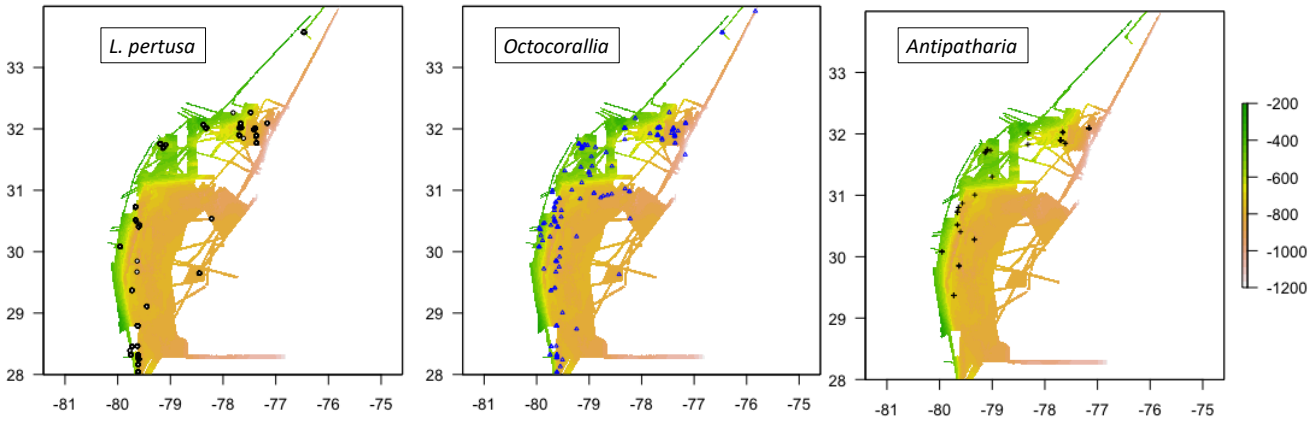

Figure 6-2. Presence points for *L. pertusa*, Octocorallia, and Antipatharia
Presence points for *L. pertusa* (n = 736), Octocorallia (n = 557), and Antipatharia (n = 72) overlain on the 35-m Blake Plateau bathymetry grid.

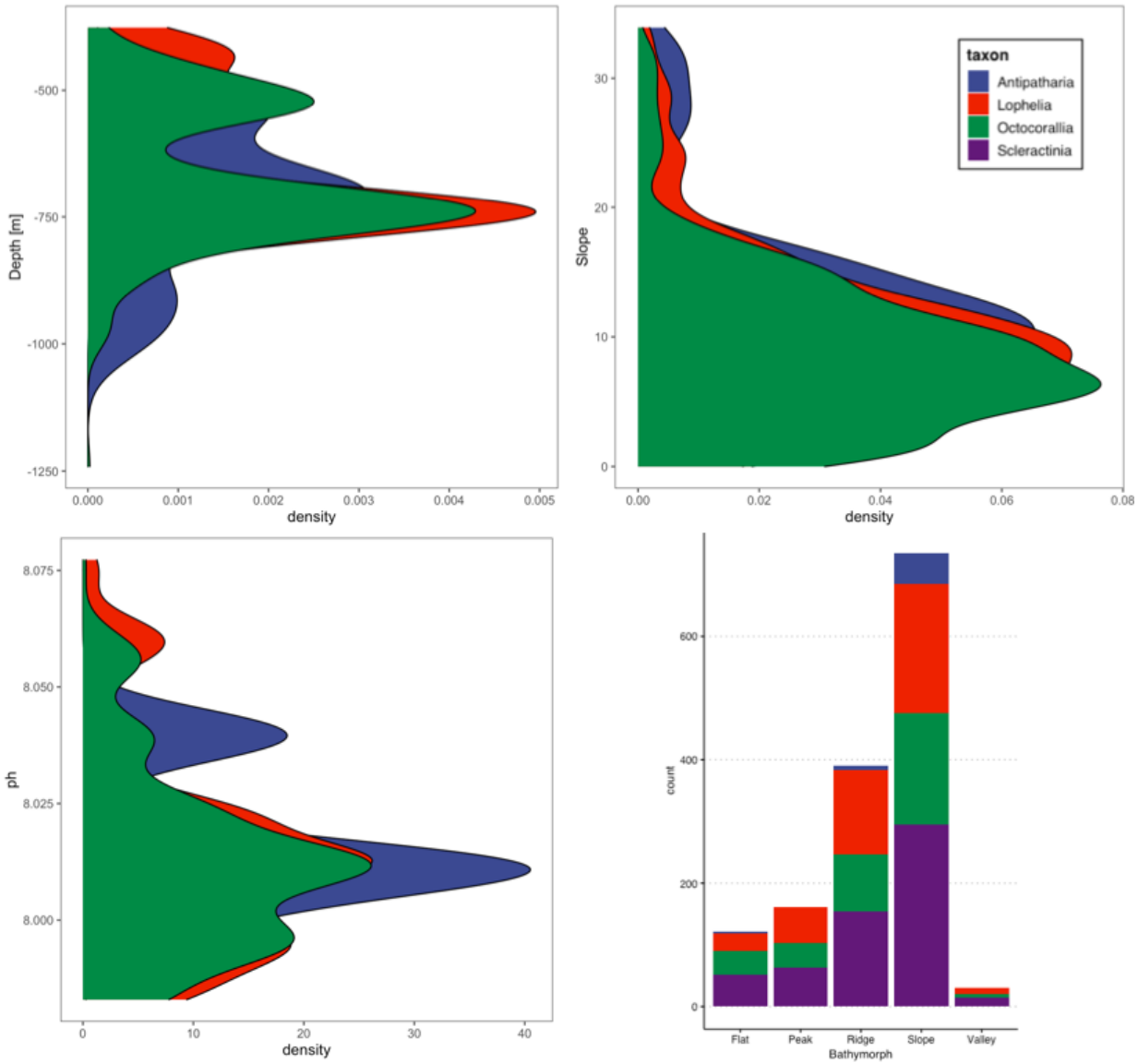

Figure 6-3. Taxon-environment relationships and Kernel density plots by taxon
Taxon-environment relationships. Kernel density plots by taxa for Depth, Slope, and pH. Bar plot showing the count of occurrences per bathymorphon for each taxon.

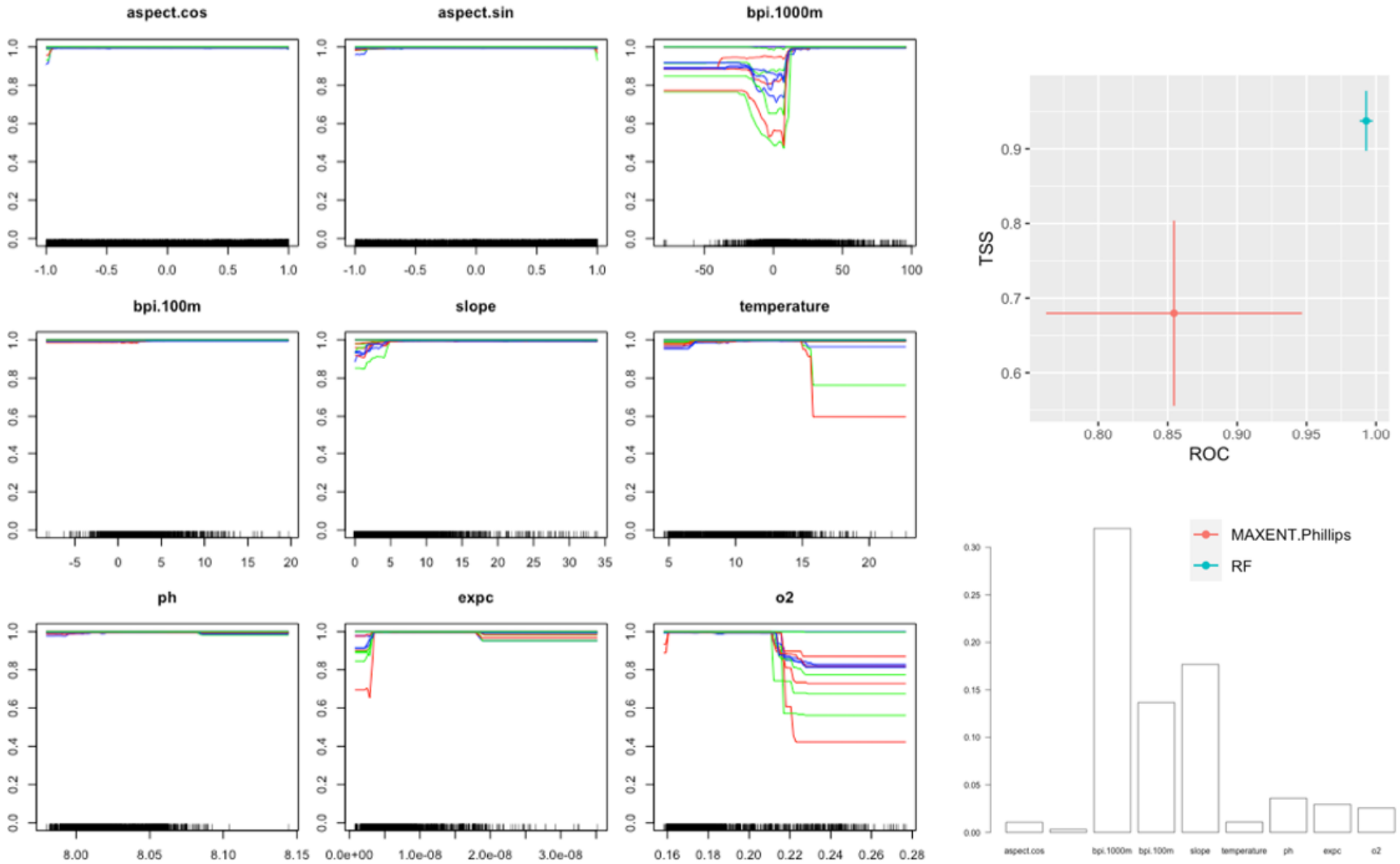

Figure 6-4. RF variable response curves, evaluation and importance for *L. pertusa*
RF variable response curves (left), model evaluation (ROC and TSS scores; top right) and variable importance (bottom right) results for L. pertusa. Colored lines represent individual model runs that contributed to the ROC-weighted ensemble-mean model.

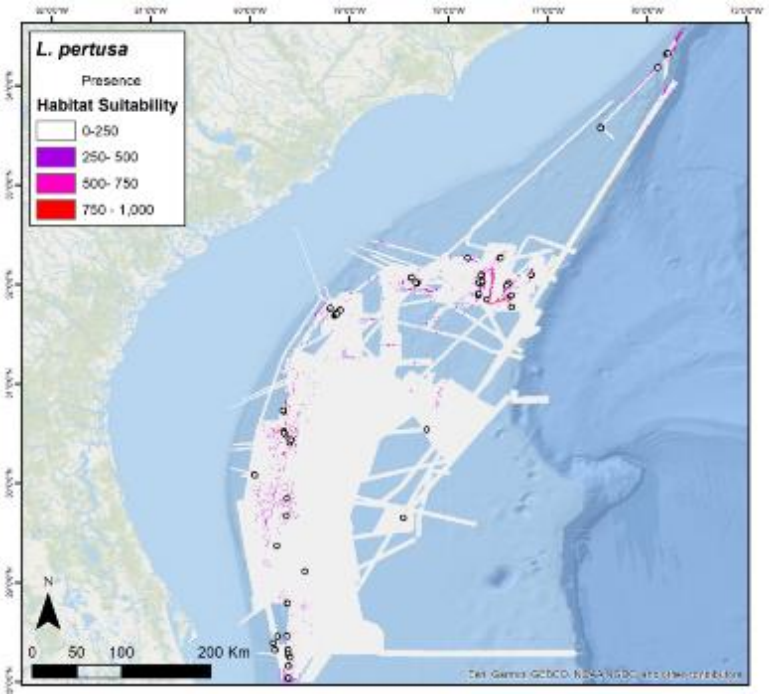

Figure 6-5. Ensemble-mean habitat suitability predictions for *L. pertusa* throughout the Blake Plateau
Presence points are shown with points, and colored grid cells show habitat suitability scores.

6.1.2.2 Octocorallia

Octocorals had the widest environmental preferences of the modeled taxa, perhaps owing to the great diversity of lifestyles and physiological tolerances of the component taxa of this group when compared to the other taxa. However, the models still performed with good (> 0.75 mean ROC for MaxEnt) to excellent (> 0.9 mean ROC for RF) discriminatory power, although predictive power as measured by TSS was lesser for this group (mean TSS ~= 0.65).

Variable response curves show strong and consistent responses to BPI and slope, with corals preferring elevated slopes and local topographic highs (**Figure 6-6**). Although not exerting a strong influence on the model and not entirely consistent across all model runs, temperatures < 10–12 ºC, pH > 8–8.1, and relative highs in O_2 and export carbon appeared to favor octocoral presence (**Figure 6-6**). Accordingly, suitable habitat for this species was predicted across large regions of the Blake Plateau, with visible hotspots at the Richardson Reef, Savannah Banks, and Million Mounds regions (**Figure 6-7**).

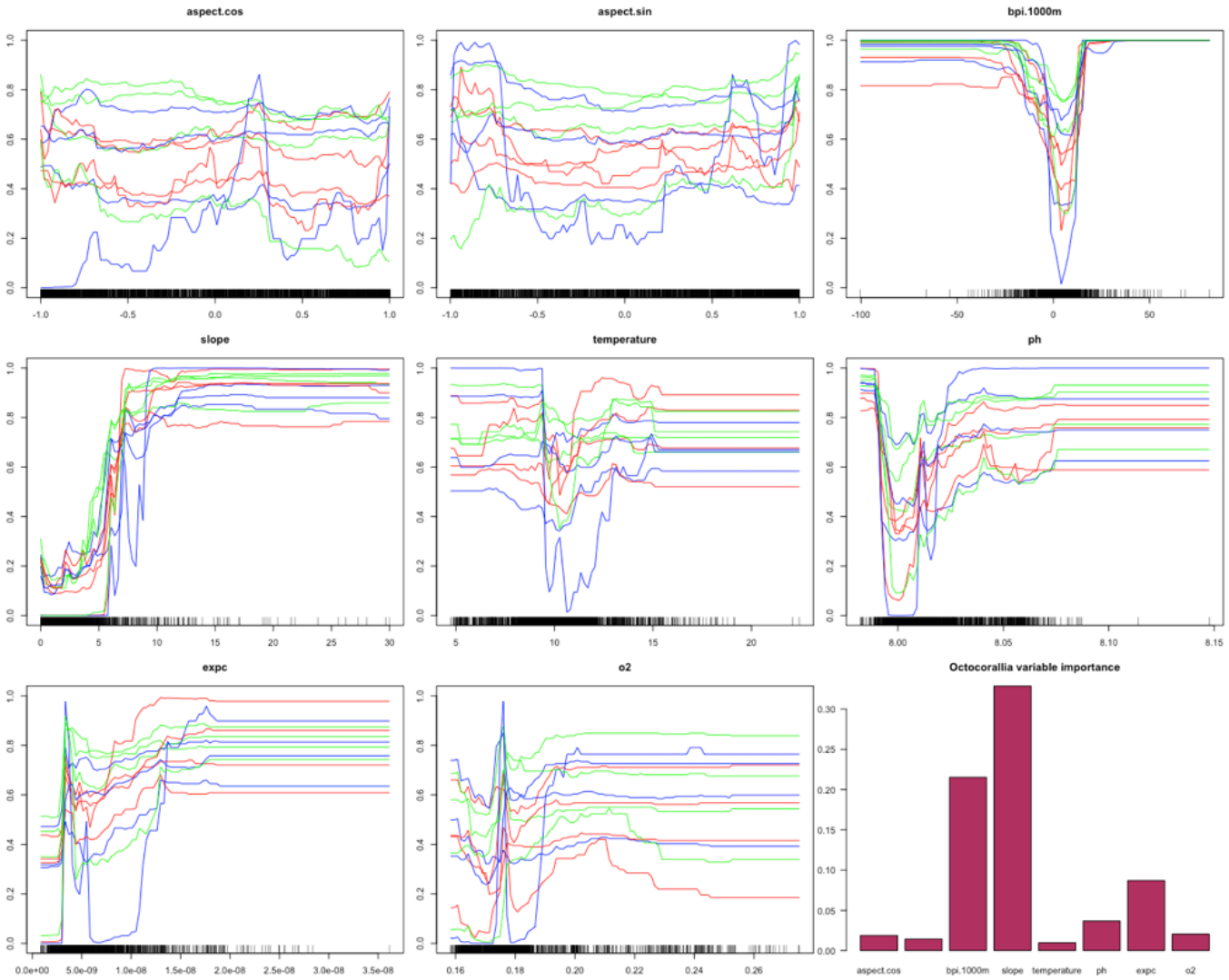

Figure 6-6. RF variable response curves, evaluation, and importance for Octocorallia
RF variable response curves (line plots) and variable importance results (barplot) for Octocorallia. Colored lines represent individual model runs that contributed to the ROC-weighted ensemble-mean model.

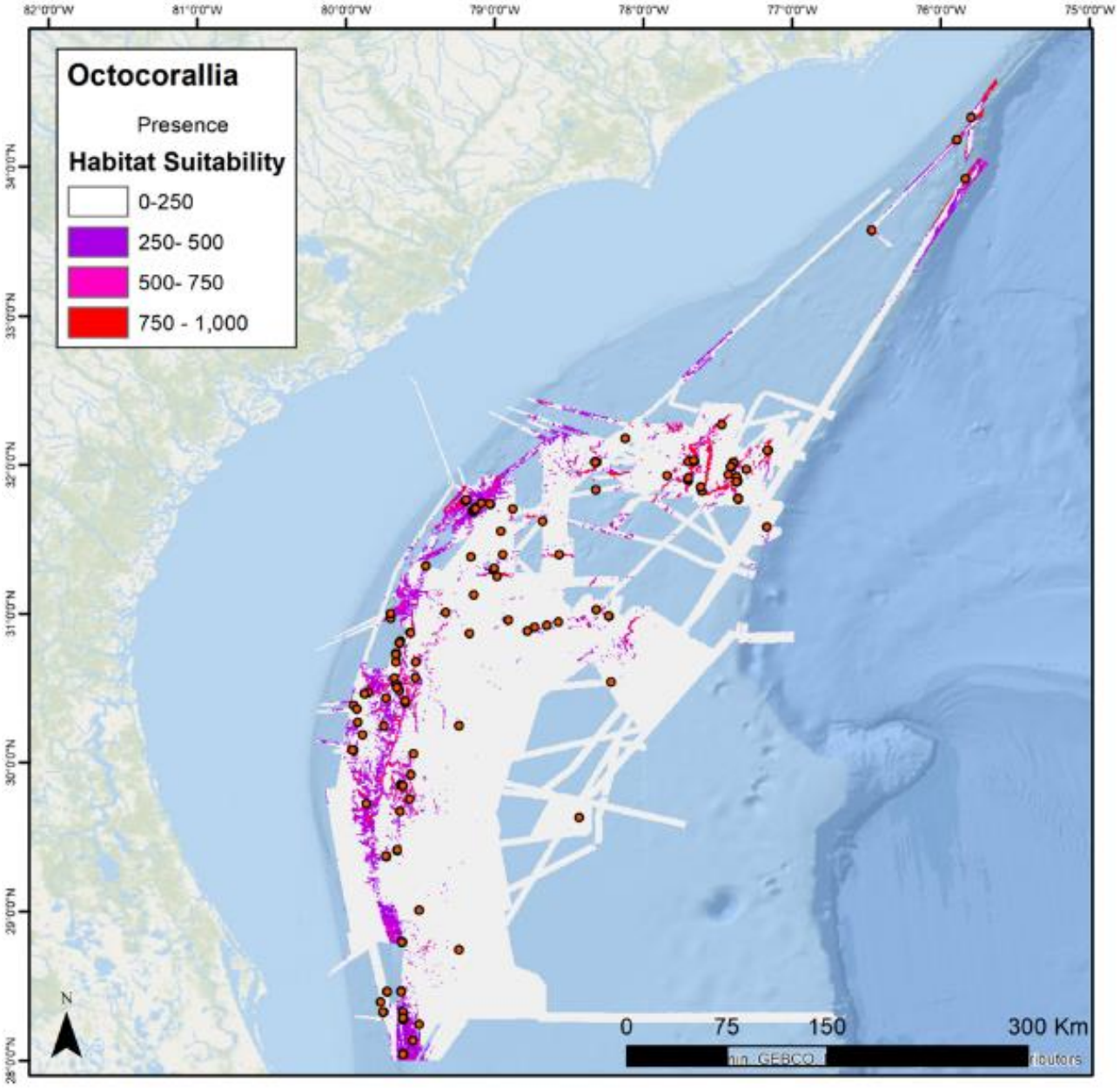

Figure 6-7. Ensemble-mean habitat suitability predictions for Octocorallia throughout the Blake Plateau
Presence points are shown with points, and colored grid cells show habitat suitability scores.

6.1.2.3 Antipatharia

Despite having the least known presence points (n = 72), the models were able to discriminate potential suitable habitat with good discrimination (ROC > 0.7), revealing swaths of suitable habitat concentrated at elevated topographies in the deeper portions (> ~500 m) on the Blake Plateau, although some shallower areas appear also to be suitable for antipatharians (**Figure 6-8**). The most important variables in the model were once again slope and BPI_1000m, respectively. This is unsurprising as the mode of occurrence for slope is greater than the other taxa (**Figure 6-3**). The model may have also suffered from issues of

overfitting and/or inadequate sample coverage, as suitable habitat was restricted to larger features (Richardson Reef Complex, a large ridge at the Central Plateau Mounds).

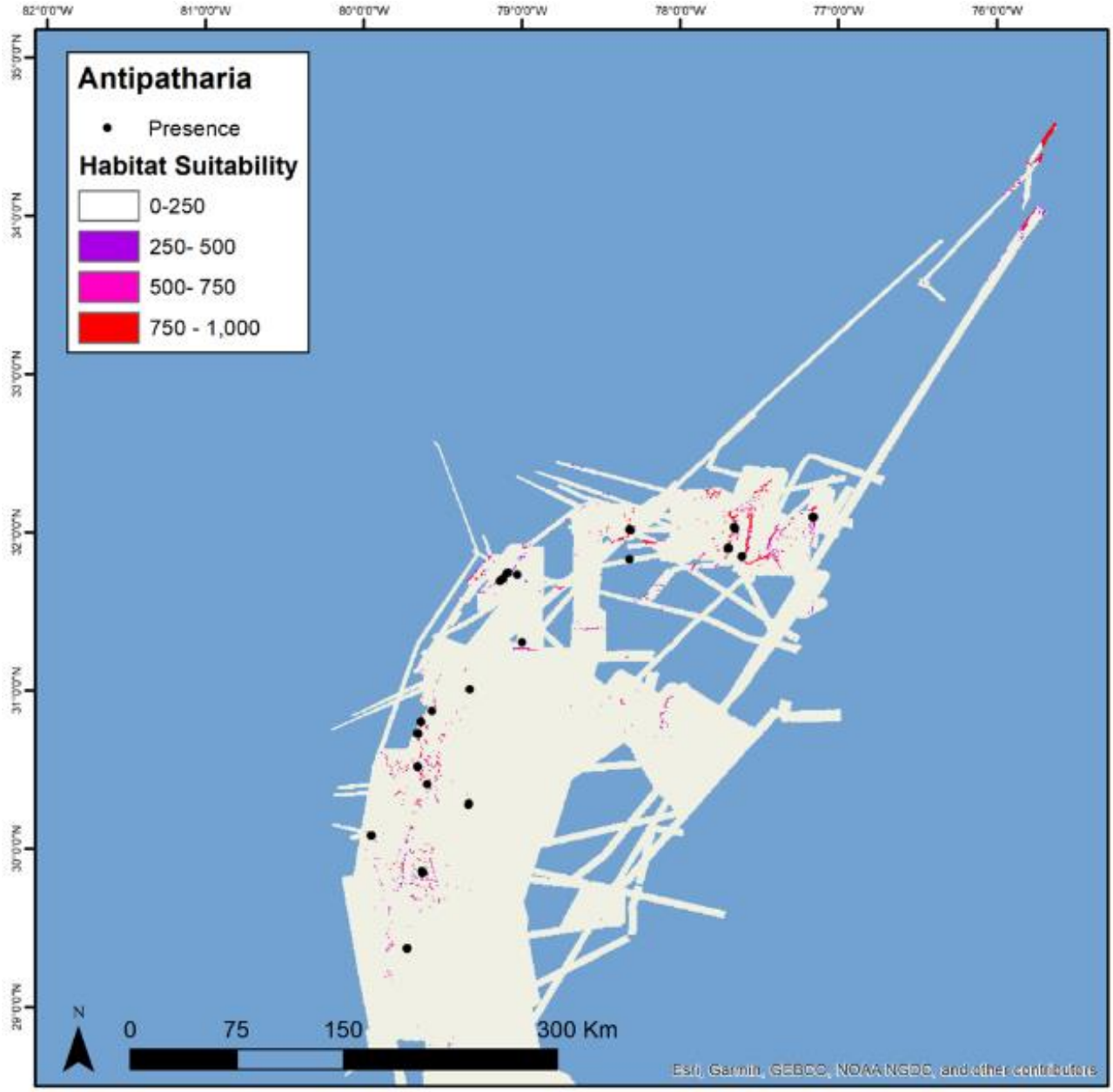

Figure 6-8. Ensemble-mean habitat suitability predictions for Antipatharia throughout the Blake Plateau
Presence points are shown with points, and colored grid cells show habitat suitability scores.

6.2 Predicting *L. pertusa* Habitat Suitability

In the marine realm, climate change manifests primarily through warming, acidification, deoxygenation, and alterations in hydrography affecting food supply (Doney et al. 2012. Levin and Bris 2015). In surface waters, models predict large expanses with either novel or disappearing climates by 2100, yet little is known about no-analogue climates in the deep ocean (> 200 m depth), where most of the planet's

habitable area exists. However, in situ trends (Desbruyères et al. 2016, Meinen et al. 2020), and climate models (Sweetman et al. 2017, Morato et al. 2020) suggest rapid seafloor climate changes will accumulate this century.

Vibrant CWC ecosystems flourish underneath the Gulf Stream due to elevated currents and pulses of fresh phytodetritus to the seafloor (Mienis et al. 2014). However, climate change may cause the Gulf Stream to deliver increasingly warm and acidic subtropical waters to their depth range (500–900 m) (Saba et al. 2016) but potentially at lower velocities (Boers 2021, Caesar et al. 2021), simultaneously lowering the rate of food delivery. All CWC ecosystems of this region may not be affected equally by climate changes, as many shallower sites near the shelf break sit directly underneath the Gulf Stream's main axis whiles deeper sites on the eastern Blake Plateau are affected more intermittently by Gulf Stream meanders.

In this section, we present a novel biogeographic, geomorphological, and climatic data synthesis to build ensemble, multi-scale habitat suitability models for *Lophelia pertusa*. We project these models onto the present-day SEUS margin and two future timepoints (2050, 2100) under four climate-change scenarios in order to characterize the extent of critical CWC ecosystems in the region and test several hypotheses critical to their future.

6.2.1 Methods

6.2.1.1 Biological Data

We downloaded *L. pertusa* occurrence data from the NOAA Deep-sea Coral Research & Technology Program database (v102020; https://deepseacoraldata.noaa.gov/), which includes all of the *L. pertusa* presence points generated as part of Deep SEARCH. We excluded points from analyses if their location accuracy was > 1,000 m, which generally excludes older, less reliable records (dredge and trawl records) that likely have lower fidelity to gridded environmental data. We also generated presence points from submersible dive imagery (see **Table 6-1**). We annotated video from submersible dives for *L. pertusa* presence and georeferenced it by timestamp. All points falling within the same grid cell were merged to curtail pseudoreplication.

We generated abundance (= percent cover) data from analysis of 1-minute video segments during the dives. We took five non-selective screenshots during each 1-minute segment, and then 50 random points overlain on each screenshot in ImageJ software. We counted points falling on live *L. pertusa* giving an estimate of percent cover for each screenshot and a mean and SD for each one-minute segment. Again, segments falling within the same grid cell on the bathymetry were removed to prevent pseudoreplicates, giving a total of n = 516 estimates of *L. pertusa* percent cover to be used in abundance modeling.

6.2.1.2 Terrain, Climate & Velocity

We used the bathymetric dataset covering much of the Blake Plateau generated by Sowers (2020) to create high-resolution (35 m) terrain variables (**Table 6-1**). Slope, aspect [both cosine (N-S) and sine (E-W)], three types of curvature (see **Table 6-1**), fine (100 m) and broad-scale (1,000 m) bathymetric position indices comprised the initial set of terrain variables. We generated all terrain variables from the bathymetric data with Benthic Terrain Modeler v3.0 (Walbridge et al. 2018). In addition, we classified the terrain into valley, flat, slope, ridge, and peak landforms or 'bathymorphons' by Sowers (2020); this classification was used post-hoc to test whether suitable terrain was concentrated on particular bathymorphon types.

We used a number of variables to model climatic suitability for *L. pertusa* (**Table 6-1**). Global Atmosphere/Ocean General Circulation Model data were downloaded in 4D (X, Y, depth, time) netCDF

format from the Earth System Grid Federation as either monthly or annual means. All data come from Climate Model Intercomparison Project 6 (CMIP6; Eyring et al. 2016), allowing for higher-resolution models than in basin-scale models for *L. pertusa* based on CMIP5-era data (Morato et al. 2020). CMIP6 models used in this study were forced under Shared Socioeconomic Pathways (SSPs). These SSPs range from the SSP1-2.6 "Sustainable Future" to the SSP5-8.5 "Business As Usual" scenarios with two intermediate pathways (SSP2-4.5, SSP3-7.0). The SSPs incorporate revised emission and land use pathways than those in the Representative Concentration Pathways of CMIP5 (see O'Neill et al. 2016, Riahi et al. 2017).

We averaged data for each SSP into current (1995–2014), mid-century (2031–2050), and end-of-century (2081–2100) timepoints, giving a rough estimate of the time of emergence for suitability changes. CMIP6 data included the variables pH, mean and minimum dissolved oxygen, zooplankton carbon concentration and export carbon from the high-resolution implementation of the Max Planck Institute's MPI-ESM1-2-HR model (Müller et al. 2018).

Bottom temperatures were available from several modeling groups; thus, we used a multi-model CMIP6 ensemble (see **Table 6-1** for climate metadata). We used Climate Data Operators (Schulzweida 2019) to convert data from each model to annual means where necessary, re-grid from curvilinear to lat/long grids, and to extract bottom-most (= benthic) data at their native resolution (**Table 6-1**). We cropped these data and re-gridded them at 700 m for the SEUS using bilinear interpolation.

CMIP6 bottom temperature data for the SEUS were compared to data from Alexander et al. (2020) implementation of an eddy-resolving Regional Ocean Modeling System that covered the study area with comparable data for the historical and 2100 business-as-usual scenarios at a higher native resolution. In addition, we compared the data from climate layers to in situ data collected during the Deep SEARCH and *Okeanos Explorer* expeditions and from the 2018 World Ocean Atlas (Boyer et al. 2018; Supplementary Materials 2).

We also used the Alexander et al. (2020) temperature data to calculate distance-based climate-change velocity, i.e., the distance to the geographically closest thermal analogue in the SEUS in the year 2100 using the R package 'VoCC' (Molinos et al. 2019). We used a climate tolerance of 0.25ºC and margin-wide search radius to find analogous cells. Thermal trajectories were overlain on the velocity map in order to visualize general trends of isotherm movement in the region.

6.2.1.3 Habitat Suitability and Abundance Modeling

We sequentially removed variables with VIF > 5 and/or highly correlated (Pearson's R > 0.9) before the modeling process in order to minimize multicollinearity. The final variable set (**Table 6-1**) still included a few highly correlated variables (temperature, pH) that were included in the model because of their ecological relevance to *L. pertusa* (Brooke et al. 2013, Hennige et al. 2014, Lunden et al. 2016).

We used a multi-scale framework to model the distribution of *L pertusa* to incorporate the variation in the species' ecological response to both terrain and climate at relevant scales. That is, we captured the fine-scale (35 m) landscape morphology that is fundamental in predicting CWC distributions by proxying hydrodynamics (Rengstorf et al. 2013), while separately modeling climatic suitability at a downscaled, but lower resolution. Suitability of both terrain and climate is a prerequisite for *L. pertusa* presence (Georgian et al. 2016), and so decreasing the terrain resolution would smooth over important information and decrease model performance (Miyamoto et al. 2017).

We first constructed the climatic niche of *L. pertusa* for the whole of the North Atlantic on the native resolution grid, then projected it onto each of the scenario climate grids for the SEUS (n = 9). as the entirety of their niche was not represented in the SEUS. For example, pH is relatively high in the region.

Thus, SEUS data would not capture a lower limit for *L. pertusa* suitability and a model trained solely on current SEUS climatology would not predict an influence of pH declines in future scenarios, despite the known relevance of pH in this range to the species' distribution and survival (Davies et al. 2008; Georgian et al. 2016, Lunden et al. 2014, Hennige et al. 2020, Morato et al. 2020). Thus, there may be regional variability in *L. pertusa* climate-stressor tolerance in the SEUS that was not captured in our models.

We computed suitability scores with one regression (Generalized Linear Models [GLM]) and two machine-learning algorithms (RF and Gradient Boosting Machines [GBM]). For both the terrain and climate models, three presence/background replicates were run with a set of 10,000 pseudoabsences each. We used repeat split-sample cross validation (70/30 testing/training splits) to evaluate the models, as it is the most widely used approach in modeling studies (Santini et al. 2021). We computed five evaluation runs computed for each pseudoabsence set and algorithm combination for a total of 45 models for each of terrain and climate.

We generated response curves according to Elith et al. (2005) and inspected for biologically plausible responses for each algorithm. Then, we calculated ensemble means and variances from model runs across algorithms to minimize individual model biases (Buisson et al. 2010). We assessed individual and ensemble model discrimination accuracy with TSS (Lawson et al. 2014) and area under the ROC metrics. We assessed relative variable importance in the models by the variable randomization approach recommended in Guisan et al. (2017).

We compared projected scenario climatic suitability scores to scores from the present-day model and suitability scores at known *L. pertusa* sites and regressed these against depth to test the hypothesis that the deepest, eastward sites containing *L. pertusa* will act as climate refugia. The combined terrain-climatic suitability scores were then used to model the areal percent cover for each scenario using the RF regression as in Hill et al. (2017). We performed all computations in R version 4.0.5 (R Core Team 2021) on Temple University's High-Performance Computing server cluster. We used the R packages 'biomod2' (v. 3.5.1; Thuiller et al. 2009) and 'randomForest' (Liaw and Wiener 2002) for terrain/climatic suitability and abundance modeling, respectively.

6.2.2 Results

6.2.2.1 Terrain Suitability

We incorporated GBM, GLM, and RF runs into the ensemble terrain model, with TSS and ROC scores showing excellent discrimination capacity (both > 0.9 on average) in recreating the *L. pertusa* distribution (**Figure 6-4**). One km BPI, slope, and depth were respectively the most important variables in defining suitable terrain, with high BPIs and slopes favored along with a depth range of ~200–1,000 m (**Figure 6-5**).

Broad expanses of suitable habitat were predicted by the model (**Figure 6-6**), including a large reef complex (henceforth referred to as the Richardson Reef Complex; notable mound provinces with many mounds topped by live *L. pertusa*, and ridge and terrace features along the southwestern portion of the mapped area. Much of this habitat fell outside of the South Atlantic Fisheries Management Council's 'Stetson Banks-Miami Terrace HAPC' (**Figure 6-6**). Flats and valleys typically had lower suitability scores, while peaks, ridges, and slopes each contained a sizeable portion of the areas with suitability scores > 750 (**Figure 6-7**). Peaks, which included the tops of mounds of all size ranges shown in **Figure 6-2**, generally had the highest suitability scores.

6.2.2.2 Climatic Suitability

We observed notable changes in temperature and pH at *L. pertusa* sites in the CMIP6 data by 2100, with more modest changes in dissolved oxygen and export carbon (**Figure 6-8**). All sites with current *L. pertusa* populations experienced pH levels below which there is a current SEUS analogue in each scenario besides SSP1-2.6. These conditions are highly unfavorable for the species based on the climatic response curves for the N. Atlantic. We used only RF and GBM runs algorithms in the ensemble model due to biologically implausible responses in the GLM runs (**Figure 6-9**). Despite this, TSS and ROC scores show that the two algorithms reproduced current distributions in the North Atlantic with excellent discrimination capacity (TSS & ROC > 0.9; **Figure 6-4 C and D**).

Ensemble projection onto the SEUS showed that almost all of the region from the shelf break to 1,000 m is currently climatically suitable (**Figure 6-9**). This was not the case in the climate-change scenarios, however, which showed distinct patterns of suitability declines (**Figure 6-10**). In the 2050 timepoint, ~20% declines in suitability on the Blake Plateau were apparent near the shelf break and appeared regardless of SSP. Lesser declines extended onto the Blake Plateau in a similar way in all scenarios, with the southernmost Blake Plateau a notable exception. At the 2100 timepoint, suitability declines were more severe and widespread. Near the shelf break, 80% declines were projected, and the extent of these declines increased with increasing emissions in the SSPs. In SSP1-2.6, however, the spatial extent of these declines was notably lesser than the other three scenarios (**Figure 6-10**).

A distinct pattern emerged with suitability declines significantly correlated with depth at both known *L. pertusa* sites (**Figure 6-11 A**) and peak grid cells (**Figure 6-11 B**). The slope and variance explained by this relationship increased in each successively higher emissions scenario. A notable exception to this pattern occurred at *L. pertusa* sites in SSP1-2.6, where the decline in suitability with depth was not significant.

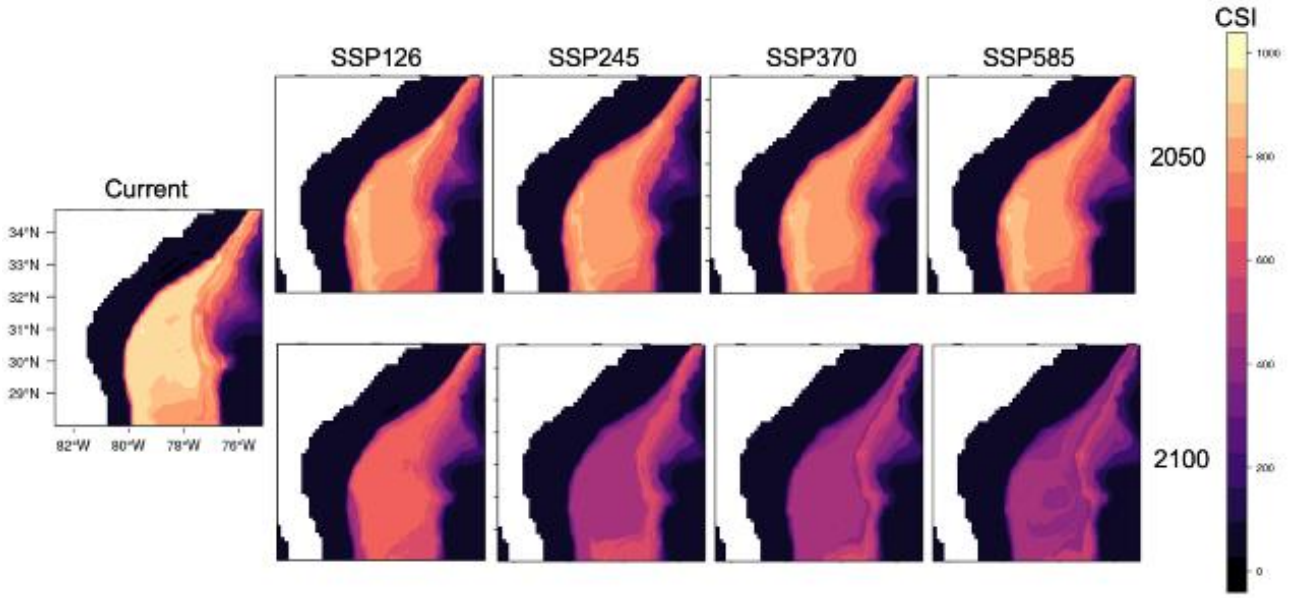

Figure 6-9. Projected climatic suitability index (CSI) of *Lophelia pertusa* habitat
On the SEUS margin in the current (left) and four SSPs in 2050 (top row) and 2100 (bottom row).

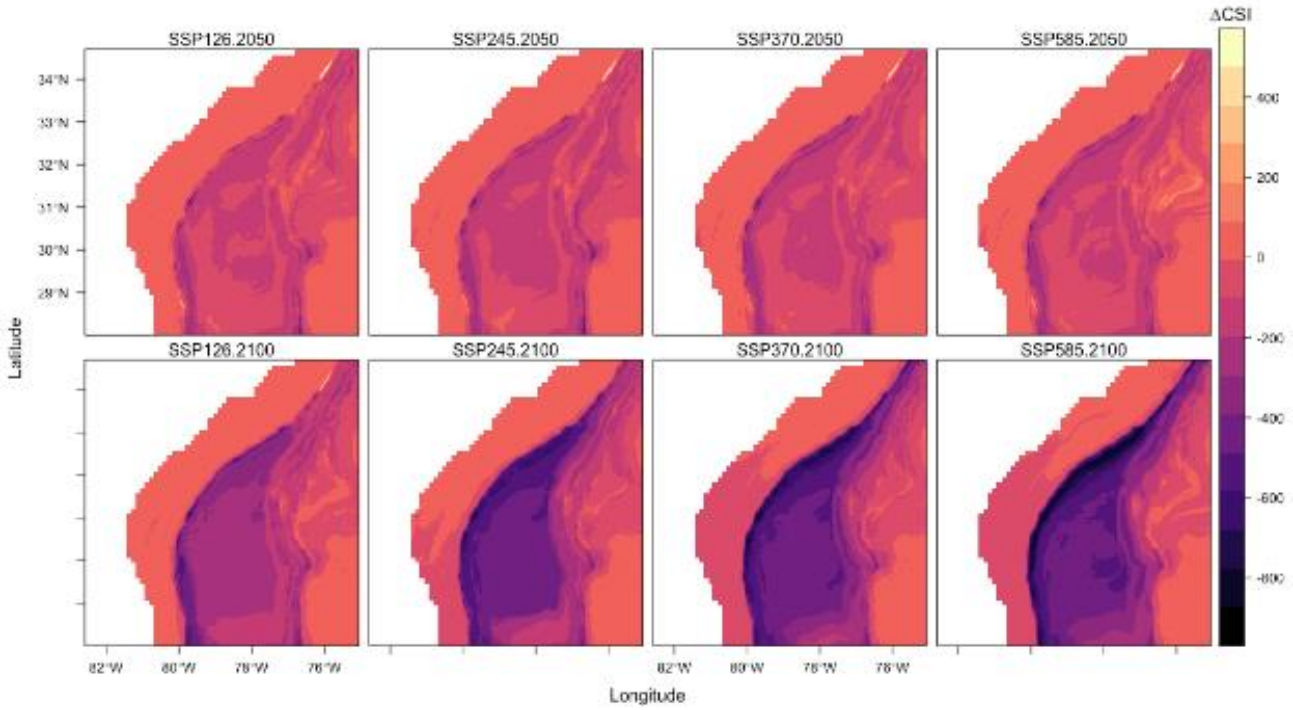

Figure 6-10. Change in climatic suitability (ΔCSI) maps for the SEUS margin
In each SSP in 2050 (top row) and 2100 (bottom row).

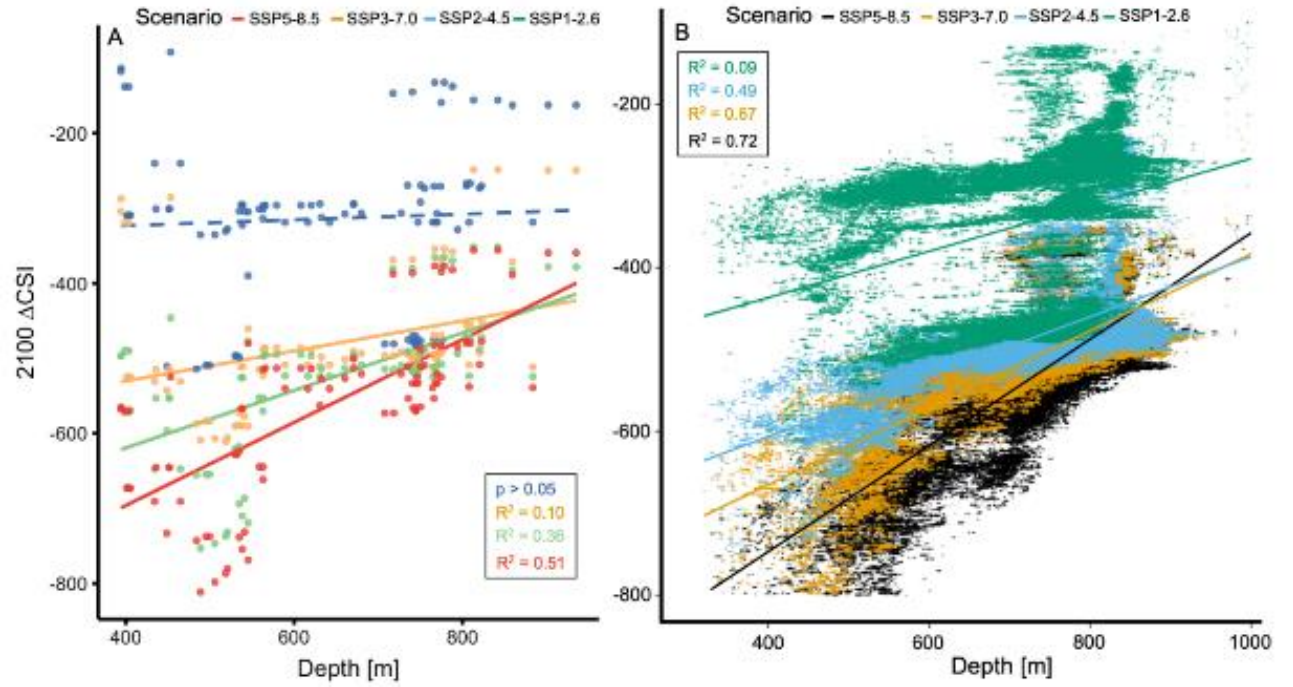

Figure 6-11. Change in climatic suitability index (ΔCSI)
(A) Unique SEUS margin *Lophelia pertusa* sites on 700-m grid and (B) all grid cells classified as peaks on mapped SEUS region (n = 262,822) in each 2100 SSP scenario regressed against depth. Solid and dashed lines represent significant and insignificant linear trends, respectively.

6.2.2.3 Predicted vs. Observed Abundance of *L. pertusa*

We found a range of coral cover at sites on the SEUS margin, ranging from zero to over 40% mean cover. We observed the highest coral cover on a coral mound at ~770 m on the central Blake Plateau. Observed abundances were significantly correlated with those predicted by terrain-climate suitability (RF regression; p << 0.01, R2 = 0.55, RMSE = 8.53; Error! Reference source not found. **A**). Future projections show that sites predicted to have greater than ~20% coral cover cease to exist in SSP5-8.5 but are still present in SSP1-2.6 (Error! Reference source not found. **B**). The sites predicted to retain relatively high cover were concentrated on the eastern Blake Plateau, with the Richardson Reef Complex maintaining the largest areal extent of high cover while more isolated individual mounds maintained lesser abundances.

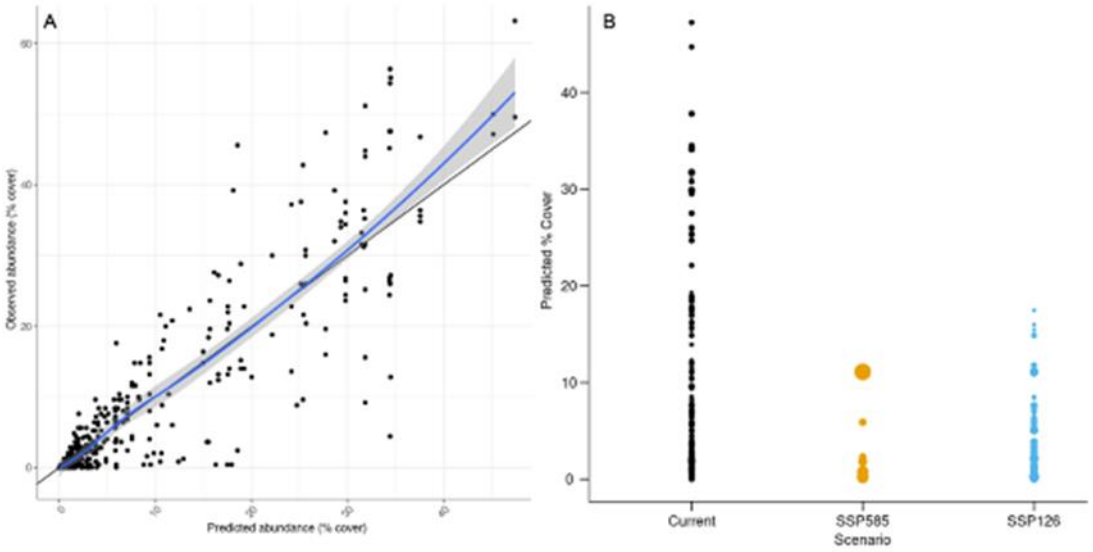

Figure 6-12. (A) Predicted vs. Observed Results of RF regression (B) Changes in the distribution of predicted abundances (= % cover) of *Lophelia pertusa* in each scenario at the 2100 timepoint
1:1 line is shown in black and LOESS smoother in blue.

6.2.2.4 Climate Velocity Predictions

Climate velocities varied throughout the region, with some of the highest velocities occurring just off the shelf break where many of the shallower *L. pertusa* sites occur (**Figure 6-13**). Here, isotherms moved at approximately four kilometers per year ($km \cdot y^{-1}$) from 2015 to 2100, while isotherms at sites on the eastern Blake Plateau (e.g., Richardson Reef Complex, Central Plateau Mounds) moved at less than one $km \cdot y^{-1}$. Velocities were also lower to the north, with sites off Cape Fear and Cape Lookout, VA experiencing similarly low velocities. While these sites are predicted to experience severe warming, they are closer to deep areas, lowering their velocities. Isotherm trajectories show a general eastward pattern towards the deep (> ~750 m) Blake Plateau, which is predicted to offer a more similar thermal environment to what currently occurs at the *L. pertusa* sites near the shelf break.

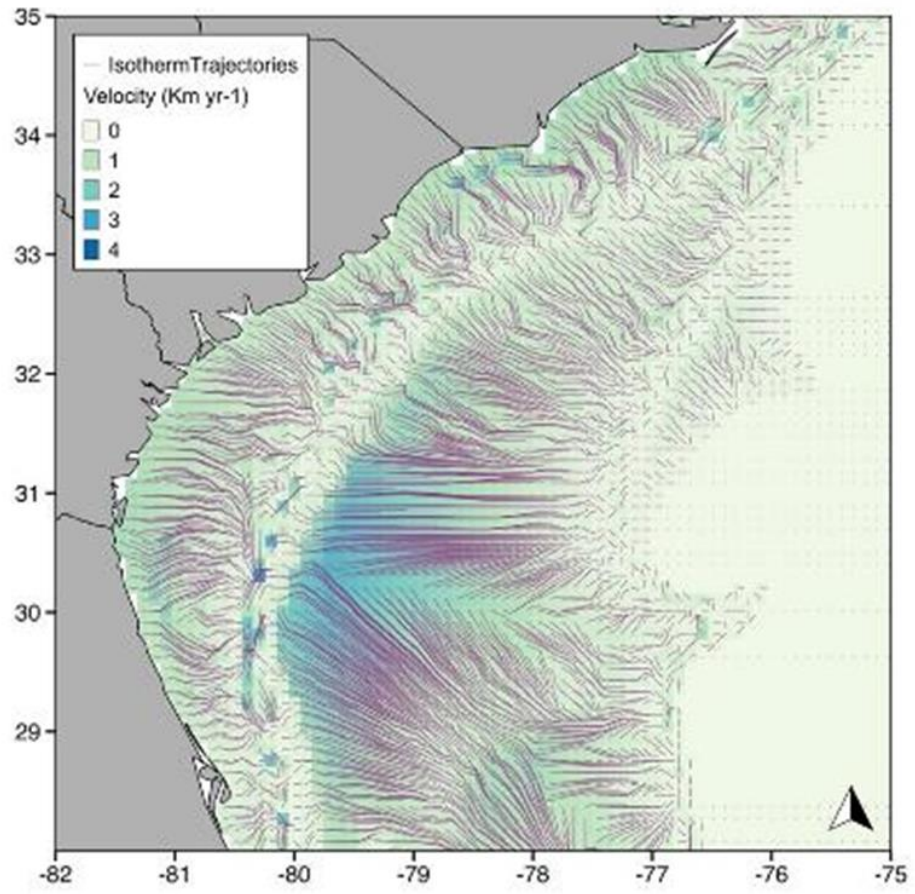

Figure 6-13. Climate velocity based off regional ocean model data
Distance to nearest thermal analogue cell in km year-1 from 2015 to 2100, based off regional ocean model data (Alexander et al. 2020). Trajectory lines tracking isotherms from each grid cell are overlain and display.

6.2.3 Discussion

Our terrain suitability models predict a previously underappreciated extent of suitable *L. pertusa* habitat in the SEUS, including outside of the boundaries of protected areas that are closed to bottom-contact fishing due to the presence of CWC habitat (coral HAPC; **Figure 6-2**). While there are > 50,000 apparent CWC mounds in the region—with many predicted to be topped with live coral by our models (**Figure 6-6**)—some of the Blake Plateau remains unmapped, and the coral mounds are predominantly unvisited. Future expeditions to the region will help ground-truth the models presented in this study. The spatial predictions arising from our models, in conjunction with the suitability differences observed between bathymorphon types (**Figure 6-7**), allow for the fullest characterization of *L. pertusa* habitat in the SEUS to date.

Currently, most of the SEUS is climatically suitable for *L.* pertusa (**Figure 6-14**). However, the waters overlying most of the suitable terrain will become climatically unfavorable by 2100 (**Figure 6-15**). Shallower sites near the shelf break will be the first to feel climate-induced stress and will experience the most acute long-term reductions in climatic suitability. Coral mounds in the northern parts of the region (known reefs off Cape Lookout and Cape Fear, VA) are predicted to be among the sites with the fastest warming. These sites also experience frequent short-term (days-to-weeks) temperature spikes associated with Gulf Stream dynamics and/or downfluxes of surface waters (Mienis et al. 2014). While similar temperature spikes have been observed at the deeper sites in the region (Richardson Reef Complex), their

lower mean temperatures give them a buffer against shorter-term spikes. Experimental work that investigates the effects of both the long-term 'press' and shorter-term 'pulse' dynamics (*sensu* Harris et al. 2018) of climate in dictating CWC physiology over ecological timescales is needed. The incorporation of environmental data over these timescales into models may reveal further vulnerable and/or refugia areas for CWCs, but is currently beyond the purview of large-scale correlative models such as the ones we present here.

Our models are in step with the growing consensus on temperature as a major biodiversity driver in the ocean (Hunt et al. 2005, Yasuhara and Danovaro 2016), although more data is needed and exceptions exist in certain taxa and regions. The Northwestern Atlantic is a hotspot of warming (Saba et al. 2016). Accordingly, our models predict a warming-driven deepening of the distribution of *L. pertusa* will occur this century, and that the eastern Blake Plateau sites may be critical climate refugia. Interestingly, at the 2050 timepoint some suitability declines emerged but noticeable differences between scenarios did not (**Figure 6-15**). By 2100, the depth-driven refugia effect increased with increasing emissions in each scenario. In fact, SSP1-2.6 was the only scenario in which many of the Blake Plateau coral sites retained suitability scores > 700 (**Figure 6-14**) and cover of ~20% (**Figure 6-16**).

These sites are especially notable because they may not only be climate refugia, but submersible dives at these sites depict thriving reef environments with some of the highest coral cover and megafaunal biodiversity observed in the SEUS. Biodiversity would be impacted by our predicted declines, as it is positively associated with percent cover of live coral, with a relationship that tends to saturate at ~20% cover (Rowden et al. 2020).

The losses of living coral we project may also lead to positive feedbacks of declining geomorphological complexity, as dead skeleton is more susceptible to dissolution and colonization by bioeroding species (Freiward and Wilson 1998, Hennige et al. 2020), flattening the habitat and making it even less suitable for CWC growth and the maintenance of biodiversity.

While there was a significant positive relationship between our abundance predictions and those observed, there is a notable amount of variance, particularly at high cover values. This may be caused by species interactions or finer-scale environmental dynamics not incorporated in the present model. As more mapping is completed for the region and complete, high-resolution maps of the seafloor (as laid out by the Seabed 2030 initiative, Mayer et al. 2018) are created, our models of *L. pertusa* abundance could be combined with laboratory and/or i carbon and nitrogen flux measurements to refine first-order estimates of the contributions of these ecosystems to margin- and even basin-wide functioning.

Somewhat surprisingly, oxygen and export carbon flux were not significant environmental drivers in our models. CWCs may be more resilient to deoxygenation if other conditions such as food supply are well met (Hebbeln et al. 2020), or oxygen limitation may be a more regional phenomenon where availability is lower than in the North Atlantic, such as in the North Pacific (Auscavitch et al. 2020).

However, low oxygen does affect *L. pertusa* metabolic function (Dodds et al. 2007, Lunden et al. 2014) and the window for metabolically viable habitat will be narrowed by deoxygenation and warming in concert (Pörtner 2017, Deutsch et al. 2015). Thus, more research is needed into the additive and/or synergistic effects of deoxygenation as warming continues. Our data suggests that the SEUS, however, will be bathed in normoxic waters until at least the end of this century.

Export carbon, however, will likely decline, particularly under the main Gulf Stream axis (**Figure 6-8**). The degree to which CWC distributions are influenced by large-scale export carbon patterns is a matter of debate and projected declines in open-ocean productivity may be somewhat alleviated by increasing terrigenous carbon inputs (Lacroix et al. 2021). While pH did not have as strong an effect on climatic suitability as temperature, its importance may have been masked by their correlation. In the

Mediterranean, where temperatures are also high, pH does appear to be a critical driver of *L. pertusa* reef persistence (Matos et al. 2021).

6.3 Seeps Occurrence Predictions

Areas of fluid expulsion of methane gas are numerous (> 10,000) and widespread on continental margins (Seuss et al. 2014), yet great uncertainty exists around their regional distributions and what drives them (Phrampus et al. 2020). This uncertainty hampers assessments of biogeochemical budgets (Kastner et al. 1991) and biodiversity (Sibuet and Olu 1998, Cordes et al. 2010) due to the strong influence that seepage exerts on the surrounding seafloor (Levin et al. 2016). Currently, methane seeps are identified by direct observation of bubble plumes, authigenic carbonate rocks, or chemosynthetic fauna or by geophysical methods such as sonar.

Thousands of new sites of methane seepage have been discovered as more of the seabed is mapped in high resolution. This data can be leveraged by habitat suitability models to create continuous spatial predictions of the probability of seep presence. To date, estimates of seep distributions has been limited to extremely coarse, global predictions (Phrampus et al. 2021). Here, we compile both published and unpublished records of seep presence in the northwest Atlantic along with gridded terrain data in order to build ensemble habitat suitability models for seep presence in the region and to test the hypothesis that they are geomorphologically controlled in the region despite occurring on a passive margin.

6.3.1 Methods

Records of seep occurrence were first compiled in the open-source of SEAfloor FLuid Expulsion Anomalies (SEAFLEAS) database (Phrampus et al. 2020), which contains the many occurrences of methane seepage along the US Atlantic margin described in Skarke et al. (2014). Locations of additional bubble plumes that had not yet been entered into SEAFLEAS, including the many shallower seep sites surveyed by Deep SEARCH and NOAA's *Okeanos Explorer* program since 2018, were provided by Skarke (Mississippi State University 2020, unpublished data). In total, 996 seep occurrences fell within our study region (**Figure 6-2**).

Because high-resolution multibeam bathymetry does not cover much of the areas with active seeps north of Cape Hatteras, VA, we generated a suite of terrain variables from the global 15 arc second (~450 m) grid (GEBCO 2021). A simpler, but similar, suite of terrain variables was generated for the seep-terrain models than for the coral-terrain models due to this coarser nature of the bathymetry. These variables included cosine and sine of the seafloor aspect which respectively describe the direction the seafloor is facing in northness and eastness, slope, roughness, and BPI representing the height of each pixel relative to a given spatial radius. We used the Horn (1981) 8-cell algorithm for slope and aspect. We generated all terrain variables as in Wilson et al. (2007) with the *terrain()* function in the 'raster' R package (Hijmans 2021).

As with the models for coral taxa, we created a multi-model ensemble to account for biases with individual algorithms. We computed suitability scores with one regression (GLM) and two machine-learning algorithms (RF and GBM). We ran three presence-background replicates for each algorithm with 10,000 pseudoabsences generated for each. Model fits were assessed with repeat split-sample cross validation; for each evaluation run 70% of the data were used to train the model, with 30% set aside for testing. We computed five evaluation runs for each pseudoabsence set and algorithm combination, generating 45 models in total.

We generated response curves according to Elith et al. (2005) and inspected them for biologically plausible responses for each algorithm. Then, we calculated ensemble means and variances from model

runs across algorithms to minimize biases from individual model types (Buisson et al. 2010). We assessed individual and ensemble model discrimination accuracy with TSS (Lawson et al. 2014) and area under the ROC metrics. We estimated relative variable importance in the models by the variable randomization approach recommended by Guisan et al. (2017).

6.3.2 Results and Discussion

Across the Deep SEARCH study region there are large expanses of terrain that the models predict are suitable for seep occurrence as indicated by mean Habitat Suitability Index (**Figure 6-14**). These areas are concentrated on areas with high-relief topography such as the shelf break, the Blake Escarpment, ridge-like topographies on the Blake Plateau, and the shelf-incising canyons north of Cape Hatteras, VA where most of the known seep sites in the region occur. Prediction uncertainty as assessed by the SD of the Habitat Suitability Index was low in most areas, indicating agreeance between models. Indeed, evaluations of all three algorithms indicate a well-fitted model with mean ROC and TSS scores respectively greater than 0.95 and 0.85 (**Figure 6-15 A**). The RF model performed the best, as in the models for coral taxa.

Terrain roughness was by far the most important variable in the model, with an average relative importance score of 0.61 while all other variable scores were well below 0.2 (**Figure 6-15 B**). Slope contributed the second most to the model, with BPI and both measures of seafloor aspect relatively unimportant. This is in contrast to models for coral taxa, which were driven by BPI. Response curves for slope and roughness (**Figure 6-16**) indicate that there was a consistent negative response to low values for both of these variables, indicating that seep presence is more likely on rugose, sloped terrain.

When compared directly to the seeps located by the presence of bubble plumes, these models clearly overpredict seep presence. However, there are likely to be numerous, smaller seeps that are not easily visualized by the acoustic data, which suggests that continued exploration of the study region may be met by new discoveries of cold seeps. Notably, the model predicts large expanses of suitable terrain south of Cape Hatteras, VA, where cold seeps are not widely known outside of the Blake Ridge Seep at 2,170 m off the Blake Escarpment (Van Dover et al. 2003). If seeps do exist here, they may represent important stepping stones between regional cold-seep faunas (Olu et al. 2010). However, ground-truthing data will be critical in refining these models, as habitat suitability models, especially where data are sparse and irregular, tend to overpredict (Rowden et al. 2017).

Future iterations of this model may benefit from the incorporation of additional data reflecting sub-surficial geology and oceanography/biogeochemistry. While Phrampus et al. (2020) conclude from their global models that sites of seafloor fluid expulsions are likely not driven by oceanographic variables such as temperature or current magnitudes, several chemical (particulate organic carbon content) and biological (chlorophyll, biomasses of fish and meiofauna) variables emerged as highly important to seep distributions. This suggests that future iterations of the models we present herein could be improved by incorporating remotely sensed and or modeled parameters related to ocean biogeochemistry.

However, while temperature may not drive global models of seafloor fluid expulsions (Phrampus et al. 2020), temperature may constrain seep distributions in the future. Indeed, some of the shallower (< 500 m) seep sites in the region are within areas expected to be hotspots of warming (Alexander et al. 2020), and even some of the deeper sites (Blake Ridge at 2,170 m) may be affected as the near-seabed conditions could destabilize the large outcroppings of methane hydrate there (Van Dover et al. 2003). These uncertainties in the environmental controls of seafloor methane emissions, particularly at shallow seeps, may not be resolvable using global-scale models. Therefore, regional-scale models such as the ones we present here represent critical first steps towards creating frameworks for seep prediction.

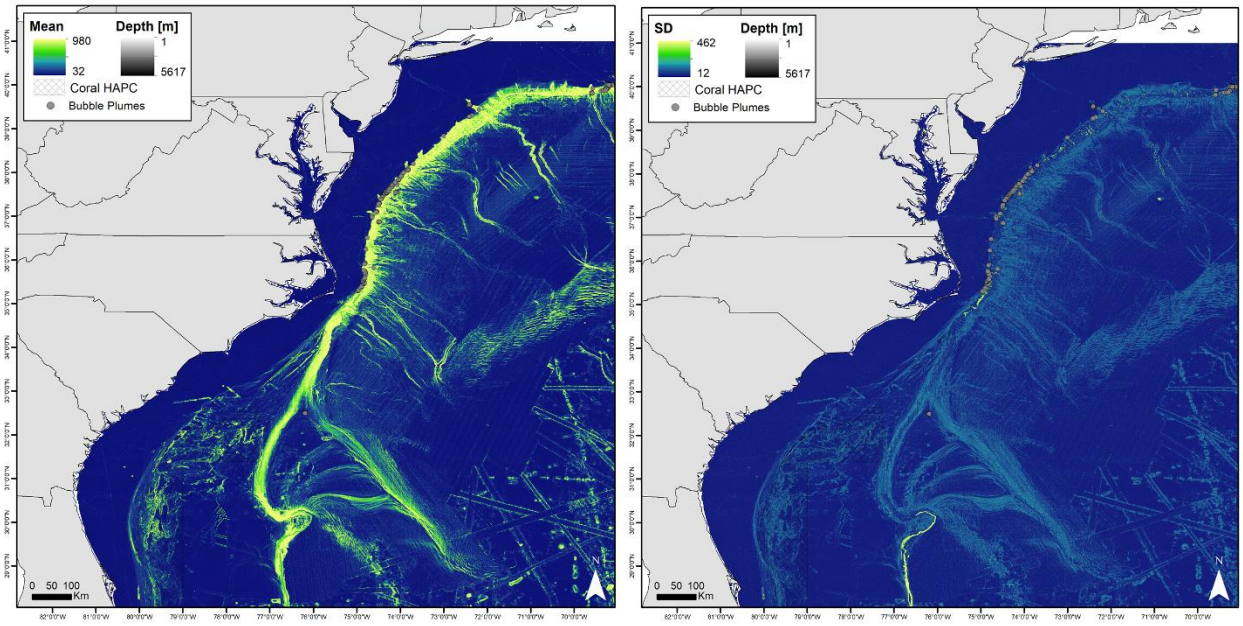

Figure 6-14. Mean and SD of the Habitat Suitability Index in the study area
Mean (left) and SD (right) of the Habitat Suitability Index in the study area. Locations of bubble plumes included in the model are overlain (gray points).

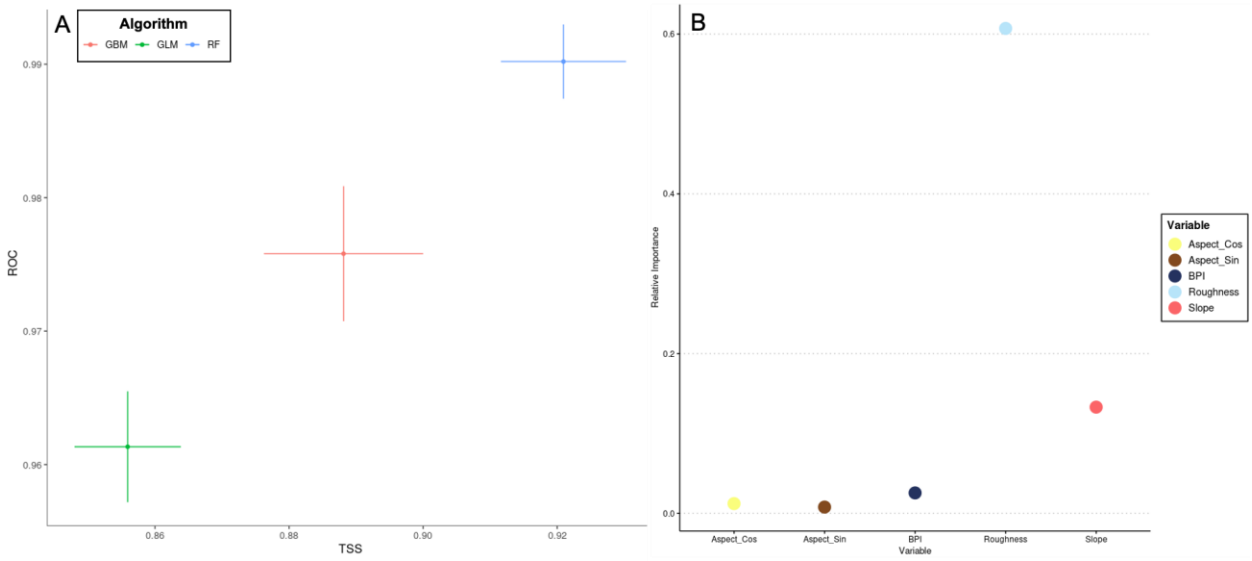

Figure 6-15. Seep model diagnostics
(A) Mean (point) and SD (lines) TSS & ROC values for each algorithm. (B) Relative importance of each variable as assessed by permutational removals of each variable.

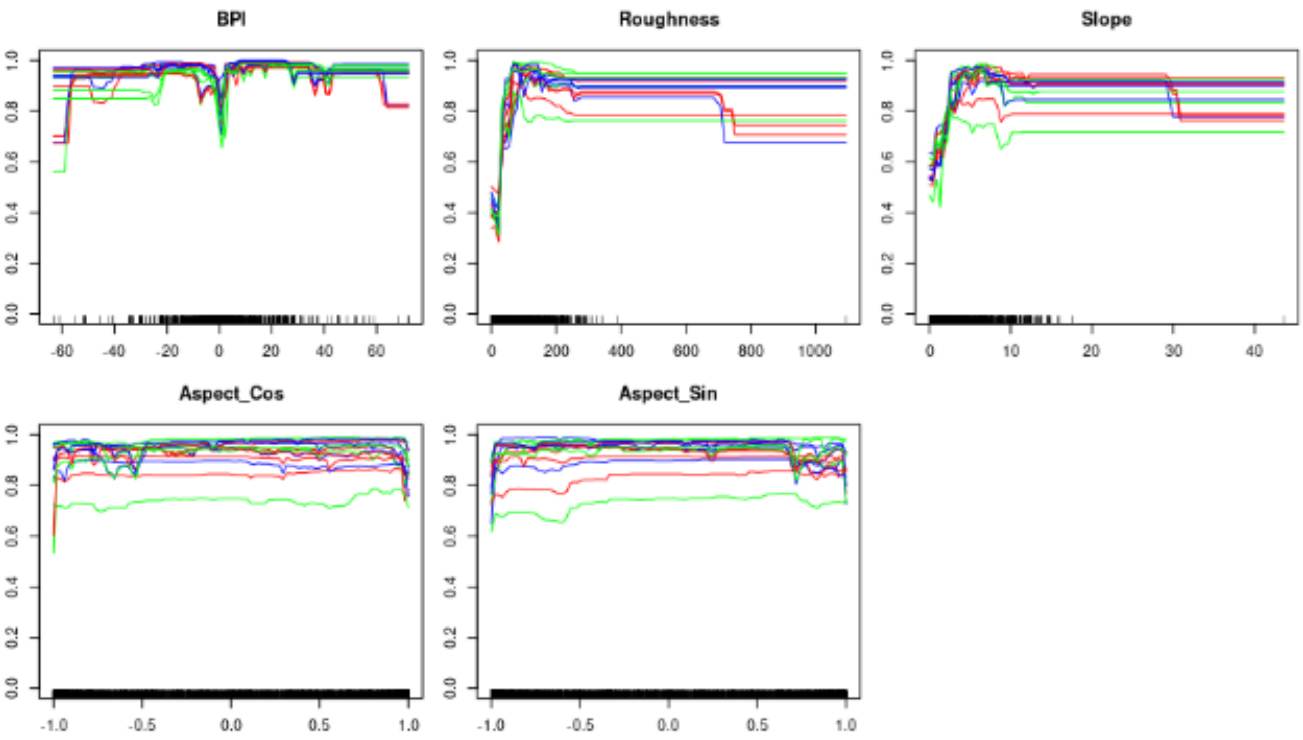

Figure 6-16. Terrain response curves from RF model runs
Scores for each model run (lines) and plotted across the range of each variable, with higher scores indicating suitability.

7 Synthesis of Study Results

7.1 Major Findings of This Study

Section Authors: All

The Deep SEARCH study was a five-year, collaborative scientific research program focused on the OCS between Virginia and Georgia that surveyed that region's deep-sea coral, cold-seep, and canyon communities. The overall goal of the study was to better inform natural resource management by increasing our scientific understanding of the ecology and environmental conditions of the region. The intended application of the new science was to develop better predictive capacities for the occurrence of these community types. Indeed, in the course of this research, these important findings have come to light among others:

- Within the three major habitat types of this study, some sites exhibited remarkable characteristics. The newly named Richardson Reef Complex is now understood to be one of the largest CWC reef complexes in the world. Furthermore, the Richardson Reef Complex is part of one of the largest coral mound provinces in the world, the Million Mounds, which extends from Richardson in the northeast and south across the entire Blake Plateau, and down along the Florida coast to the Jacksonville Mounds.
- The seeps along the continental shelf edge, visited here for the first time, are remarkable for their extremely high rates of methane release and oxidation. Their chemistry fuels biological productivity that appears to also subsidize local pelagic communities. We also characterized Pamlico Canyon for the first time and found it to be home to a very high diversity coral assemblage, to have high overall diversity of infauna, and to exhibit some of the highest densities of sediment infauna we have observed at this depth.
- One of the most important findings of this study is the numerous pieces of evidence throughout our data sets indicating the high connectivity among all habitat and community types within the region. This is highlighted, for example, by the interactions between the diel vertical-migrating midwater community and the benthic zone of the Richardson Reef Complex in the southern part of the study area, as well as by the interaction of midwater organisms with the walls of the canyons and relatively shallow seep sites to the north.
- The unique oceanographic conditions in the region have a corresponding influence on the various communities. The Gulf Stream cuts through the center of the study area, causing vertical mixing in its core down to 1,000 m. This promotes a rapid translation of food to depth and nutrients to the surface, and brings elevated trophic and genetic connectivity of the components of the ecosystem. These currents can be highly variable on the seafloor, as measured using passive acoustic data. This variability also appears to impart a high degree of adaptive resilience of the deep-sea corals of the region in the face of to rapidly changing environmental conditions, specifically examined in live coral experiments with *Lophelia pertusa*.

7.1.1 Habitat Characterization

Mapping was a major focus of the Deep SEARCH project team. We accomplished our goals directly through our dedicated cruises and with our partners at NOAA Ocean Exploration. During the two primary Deep SEARCH expeditions, we mapped 8,938 km^2 during AT41 and 6,733 km^2 were mapped during RB1903. Deep SEARCH PIs also worked closely with NOAA Ocean Exploration at all stages from cruise planning through at-sea execution to use the NOAA Ship *Okeanos Explorer* to map the entirety of the Blake Plateau. This addition of high-resolution mapping data revealed large features like the Richardson Reef Complex on the outer Blake Plateau, and hundreds of smaller, isolated coral mounds on

the central Blake Plateau. While this was already known to be an area of coral abundance, we now have a much better appreciation of the size of the deep-coral ecosystem in this region, making it one of the largest CWC mound provinces in the world.

The oceanographic conditions over the Richardson Reef Complex became a major focus of the study after the discovery of the size and contiguous nature of this feature with the augmented multibeam bathymetric data from this study and the collaborative NOAA Ship *Okeanos Explorer* work in the region. On the seafloor, the measured environmental conditions (backscatter, current, temperature, fluorescence) over the 6-month lander deployment were both highly variable and rapidly changing, with no apparent tidal regularity. Water temperature was especially dynamic, fluctuating up to 10.8°C (mean: 5.03°C) at a rate of up to 3.74°C per hr. Major temperature peaks (> 2 SD above the mean) lasted up to 36 hrs, occurring in May, and in early August and September. Changes in water conditions were primarily linked to the meandering activity of the Gulf Stream, which nears its greatest transport capacity and current speed as it flows over the study site. This is supported by the co-occurrence of elevated measurements in turbidity and fluorescence with temperature peaks, indicating vertical transport/mixing from warm waters entrained in the Gulf Stream.

This program conducted the first visual surveys of the shallow seep sites near the shelf break in the northern canyons portion of the study area. Sampling at these sites revealed areas of seafloor influenced by rapid emission of methane, with bubble streams and authigenic carbonates commonly observed in the center of the sites. Authigenic carbonates from Kitty Hawk, Pea Island, and Blake Ridge typify carbonate precipitation of microbial origin within the uppermost few centimeters below the sediment-water interface. Corrected U-Th ages of the authigenic carbonates ranged between 1.40 ± 1.1 ka at Kitty Hawk to 17.37±4.3 ka at Blake Ridge indicating AOM-driven carbonate precipitation since the late Pleistocene and Holocene at these sites.

7.1.2 Community Ecology

The Deep SEARCH program conducted detailed, standardized sampling across habitat types within the study area. This sampling effort provided the data required to perform a regional comparison of community types at different scales and within different biological size classes.

Variation in demersal fish assemblages in the region were driven primarily by habitat type and depth. The different habitats were not functionally equivalent. Cold seeps in shallow regions of the MAB harbored high species richness, functional diversity, and abundances of fishes compared to other habitats examined; both Pea Island and Bodie Seeps are quite distinct and unique habitats. It is likely that the combination of high photosynthetic and chemosynthetic productivity lead to abundant and diverse fish communities in the region off Cape Hatteras. Canyon habitats also appear to differ from other habitats, even when controlling for regional differences. Canyons had higher species richness and functional diversity of demersal fish than coral reefs and hardbottoms at similar depths.

Pelagic communities were more similar to one another than the demersal fish assemblages. Acoustic investigations of benthopelagic coupling revealed rich aggregations of pelagic organisms around reef structures throughout the study area, while direct pelagic sampling revealed a high degree of pelagic habitat use by early life stages of reef-associated benthic and demersal taxa. Among the most interesting results of the study was that organisms such as the bathypelagic bristlemouth fish, *Cyclothone microdon*, which generally occurs below 1,000 m depth in the Atlantic, were collected over reef structures in less than 600 m bottom depth in our study sites, suggesting that their pelagic distributions may have been altered above these habitats.

The larger benthic megafauna were video-surveyed at a number of different sites across the study area. In general, diversity declined with depth for all types of coral sites. The coral mounds had the highest diversity for benthic megafauna, with the isolated mounds on the central plateau among the most diverse followed by the Richardson Reef Complex, while the canyon sites were less diverse. The seep sites had the highest combined density and biomass of all fauna, particularly the deep sites where mussel beds represented the highest biomass sites surveyed during Deep SEARCH. Contrary to the coral results, diversity and community evenness of larger benthic megafauna increased with site depth.

For the infaunal communities, the shallower Savannah Banks sites had a distinct community with high abundance and diversity, while the deeper Richardson Reef Complex had a lower diversity and abundance but higher evenness in the community structure. Infaunal composition of these communities was best characterized by depth and the distribution of sediment grain sizes in the samples. The seep infauna were more abundant at the shallower sites, with extremely high abundance (over 200,000 individuals m^{-2}) in microbial mats and active bubble streams at the Kitty Hawk seep.

The seep infaunal communities were best defined by depth, with clear differences between the shallow and deep sites, and next by habitat type within depth range, including background sediments, bacterial mats, bubble streams, and (at the deep sites) clam and mussel beds. At the canyon sites, density of infauna declined with depth, while diversity increased. Pamlico Canyon had a distinct, high diversity infaunal community, which correlates with our general observations during the dives and in the video analysis. Additional variability among infaunal communities in the canyons was best described by the percent of organic carbon in the sediments.

Our study provides some of the first data examining whether patterns in biodiversity are detectable through eDNA and from passive acoustic soundscape data. In the eDNA from visually targeted near-bottom water samples, we found distinct clustering among habitat types (shallow and deep seeps, corals and sediment), and the high diversity sampled at these sites was reflected in the ASV recovery from the eDNA sequencing, providing a proof of concept for eDNA sequencing for biomonitoring at deep-sea habitats.

Application of the soundscape code illustrates that deep-ocean soundscapes are very different from shallow, tropical reef soundscapes in terms of frequency, amplitude, periodicity, and uniformity, which may indicate that deep-sea coral reefs have different ecological dynamics compared to shallow coral reefs. We observed strong linkages between the ambient soundscape and the local environmental conditions in the region, principally driven by the Gulf Stream.

7.1.3 Biology of Coral and Seep Fauna

Throughout the Deep SEARCH study, investigations of genetic and trophic connectivity, coral physiology, age and growth, and microbial associations provided a comprehensive view of the deep-sea fauna of the MAB. *Lophelia pertusa* was the most common coral of the study region, and was the subject of the live coral experiments. In this study, we simulated an incursion of warm water in the laboratory and the subject corals responded by increasing their respiratory and excretion rates, which was fueled by digesting their own proteins rather than increasing their feeding rate. Although they are capable of surviving these marine “heat waves” there is a material energetic cost in doing so, and this may not be sustainable in the future with increasing frequency and duration of exposure to warmer waters.

Distinct and diverse genotypes of Endozoicomonas unexpectedly dominated the microbiome of *L. pertusa* at Richardson Reef Complex and Cape Fear coral sites. All prior studies of *L. pertusa* in other regions of the world found this bacterial group to be rare or absent, even when present in neighboring corals. The unusual microbiomes at these two sites may be linked to the extreme variability experienced by these

corals due to interactions with the Gulf Stream. This study also represented the first application of functional gene microarrays to compare deep-sea coral microbiome functions between stony and soft corals, and between deep and tropical species.

We collected new information about the reproductive patterns of key coral species. Many of the species examined exhibited seasonal reproduction, including *Desmophyllum dianthus*, *Lophelia pertusa*, and *Solenosmilia variabilis* and possibly *Plumarella* sp. and *Pseudodrifa nigra*; while other species, such as *Madrepora oculata*, *Acanthogorgia* spp., and *Swiftia casta* appeared to have continuous spawning. Additional samples at different time periods are required to verify the reproductive patterns of these and other species.

The genetic structuring patterns were similar to previous microsatellite analyses, but the SNP data presented here provided higher resolution, revealing fine-scale details and suggesting that some of the genetic diversity observed likely originates from populations outside of the current sampling scheme. Analysis of genomic SNP data from 57 *Lophelia pertusa* polyps aligned with previous microsatellite data to indicate that deepwater scleractinian populations exhibit regional structuring. The Blake Plateau populations (Cape Fear, Stetson Banks, Savannah Banks, Richardson Reef, Canaveral) are likely connected by larval dispersal in Gulf Stream currents. We found them to all be genetically relatively similar. However, they were notably differentiated from populations found at Norfolk Canyon, Pea Island, the intercanyon populations off New England, and the GOM.

Populations of *G. childressi* were highly connected between sites in the MAB. Although inbreeding coefficients and kinship analyses suggested some degree of local recruitment, gene flow was apparent between Baltimore Canyon Seep, Norfolk Canyon Seep, and Chincoteague Seep populations. Both migration rate and kinship analyses indicated that gene flow occurs from Baltimore to Norfolk seeps, in a north to south (and shallow to deep) direction.

7.1.4 Improved Prediction of Occurrence

In **Chapter 6**, we detail how we assembled biogeographic, geomorphological, and climatic data to build ensemble, multi-scale, habitat suitability models for *L. pertusa* on the continental margin of the SEUS. The models reveal the extent of suitable reef habitat in the SEUS and corroborate it as the largest known CWC reef province on earth. We also predict abundance (= % cover) of *L. pertusa.* This information can help to identify key areas of predicted occurrence, including some areas located outside of bottom-contact-fishing restricted zones managed by NOAA and the Fishery Management Council (South and Mid-Atlantic).

We also projected our models out to two timepoints (2050, 2100) with four climate-change scenarios in order to characterize changes in the extent of CWC habitat into the future. Drastic reductions in habitat suitability emerged primarily at the later time point and were most severe at the shallower end of the regional species distribution under the main axis of the Gulf Stream. Our results thus suggest a depth-driven climate refugia effect where deeper, cooler reef sites experience lesser suitability declines. Taken as a whole, our study findings can help to inform the regional and global management of this species, including subsequent changes in the biodiversity reliant on *L. pertusa.*

7.2 Conclusions and Recommendations for Management

Section Author: Erik E. Cordes

The habitats within the study area comprise a combination of hard and soft substrata inhabited by a fauna that can be generally characterized as sensitive to disturbance. Of course, there is a variety of specific

habitat types that vary in their potential vulnerability to anthropogenic impacts. Certain areas of the Blake Plateau contain ferromanganese encrusted phosphorite deposits that are sometimes occupied by habitat-forming octocorals, solitary corals, and sponges. This biodiversity has ecological value, as each species plays a specific role in the ecosystem. In addition, certain deepwater species (in particular sponges) show promise of biopharmaceutical utility that may potentially lead to future commercial collection.

At depths below approximately 500 m, there are vast areas of CWC mounds created primarily by *Lophelia pertusa*, along with *Madrepora oculata*, *Enallopsammia rostrata*, and *Solenosmilia variabilis*. that host added biodiversity of associated fauna. Along the margin of the Blake Plateau are two influential hydrocarbon seep sites, the Blake Ridge and Cape Fear seeps, which are primarily inhabited by large mussel beds of *Bathymodiolus heckerae* and associated fauna. As the Blake Plateau drops off to the steep continental slope, there are diverse assemblages of octocorals, black corals, and sponges that can be hundreds to thousands of years old. Further to the north, the Blake Plateau gives way to a series of submarine canyons that incise the shelf break to different degrees and have limestone walls of varying composition and stability. On the walls of the canyons are numerous octocorals and cup corals that add to the heterogeneity of the substrate and the biodiversity of the coral assemblage in the region.

Along the shelf break in this area are numerous seeps that can be visualized by the acoustic opacity of the methane bubble streams that they are actively emitting. Those observed to date have been in fairly shallow water (200–300 m) and are very different in composition from the deeper seeps to the south. Together, these habitats contribute to a continental margin that is complex and heterogenous in both geology and biology.

Salient to BOEM's mission are the oil and gas (including gas hydrate) accumulations within the study area. These hydrocarbon reservoirs primarily lie beneath the seep sites investigated during this study, but also overlap some of the coral sites and intersect some of the canyons. The large area of ferromanganese encrusted phosphorite deposits, along with localized areas of manganese nodules on the Blake Plateau, are also within the jurisdiction of BOEM and may become of commercial interest in the future.

The majority of areas of interest for fixed platform wind power development are shallower and shoreward of the study area (**Figure 7-1**). It is conceivable that wind energy development could extend onto the Blake Plateau in the future if there are OCS spatial-use conflicts elsewhere and depending on what happens with the nascent technological development of floating wind turbines, which can be anchored to the seabed in deeper regions of the OCS than current, fixed US OCS wind turbines.

Any of the above resource development activities would require additional, precise ecological surveys prior to activity implementation in order to avoid or minimize negative impacts to the coral, seep, and canyon habitats presented here.

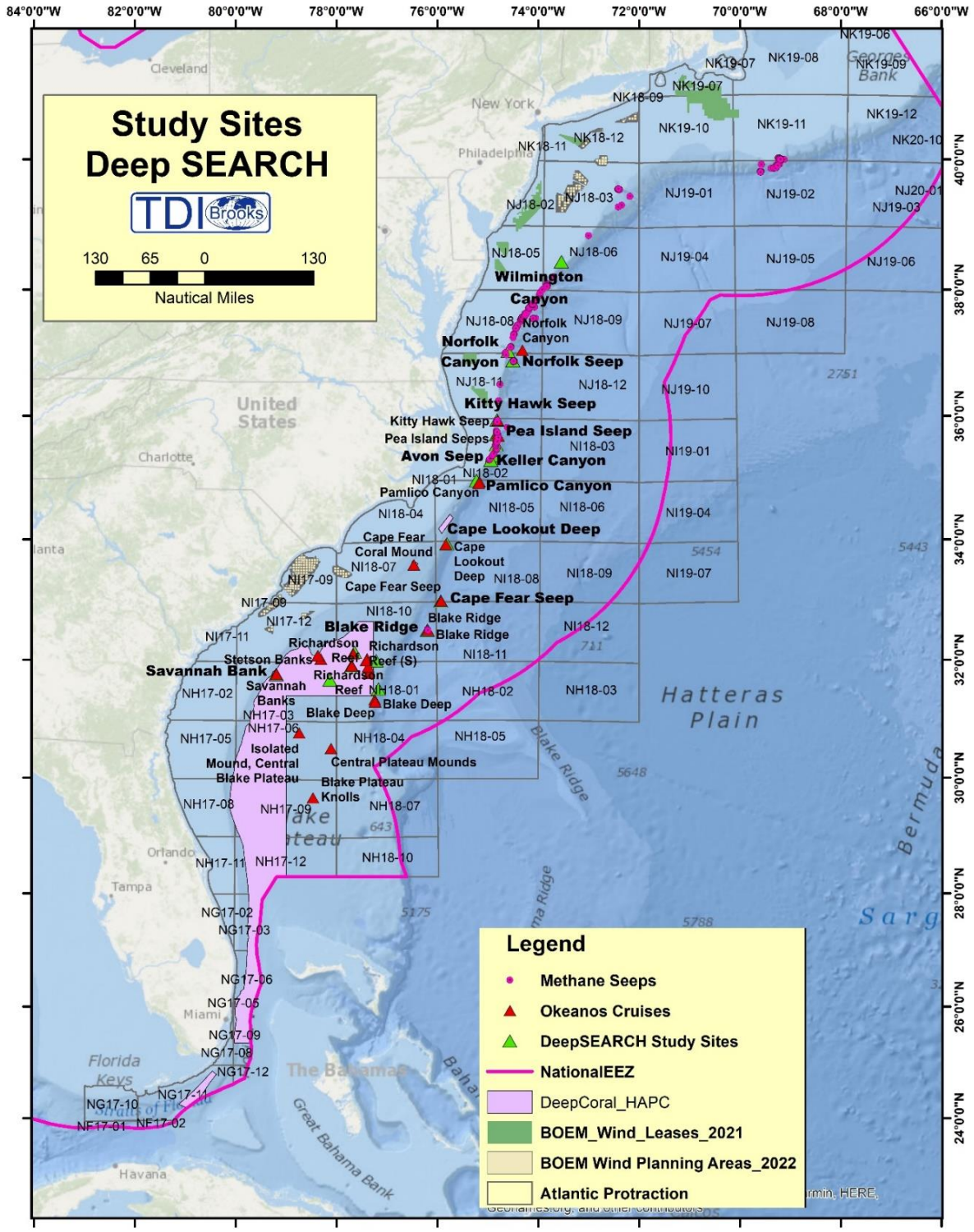

Figure 7-1. Deep SEARCH area showing BOEM wind leases
Along with protraction areas, methane seeps, *L. pertusa* sites, and deep-sea coral Habitat Area of Particular Concern.

The extensive mapping effort, sampling, visual surveys, and predictive modeling studies presented here revealed that the CWC mound province in the study area is one of the largest in the world. It extends from the Cape Lookout mounds and the Richardson Reef Complex in the north, to the Million Mounds area in the south. The coral mounds are usually solitary in much of the Blake Plateau but are observed in high densities along the eastern edge of the Plateau at the Savannah, Jacksonville, and Miami Terrace sites that have been studied for decades within the Million Mounds area. In the Richardson area these mounds have coalesced into a continuous reef complex consisting of over 200 km of mounds and ridges. Our study focus on these habitats is already influencing regulation and management, with the addition of a "live hard-bottom" category of habitat in the "*Protective Measures Assessment Protocol*" used by the US Navy (https://nwtteis.com/Environmental-Stewardship/Protective-Measures-Assessment-Protocol).

CWC mounds are internationally recognized as "ecologically and biologically sensitive habitats" as defined by the U.N. Convention on Biological Diversity, and "vulnerable marine ecosystems" in the parlance of international fisheries management organizations. In the US, these features are considered "essential fish habitat" (EFH). Some specific EFH areas are further protected through designation as HAPCs under the Magnuson-Stevens Fishery Conservation and Management Act. The coral mounds in the study area are known to harbor numerous fisheries species of potential commercial importance, including the swordfish, blackbelly rosefish, and golden crab in the study area and the South Atlantic Fishery Management Council designated the Stetson-Miami Terrace as an HAPC. Most of the coral mounds explored in this study are already within this HAPC, but many of the more isolated mounds in the central Blake Plateau had gone unnoticed in earlier, coarser-resolution surveys.

The canyon sites within the study area, including Norfolk, Keller, Hatteras, and Pamlico, are similar to the canyon sites further north along the shelf break (including Wilmington Canyon, which we also visited during AT-41) in that they support coral communities on their walls that support elevated biomass. During this program, an important achievement was the amount of data collected at Pamlico Canyon, which had not been previously visited by ROV or other submersible. This was the site of extremely high octocoral diversity and concentrations of mesopelagic fauna. Benthopelagic coupling was apparent in the acoustic data obtained at all of the canyon sites (see **Chapter 4.2**), and further supports the conceptualization of their significance to regional fisheries. The canyon sites to the north, including Norfolk and Wilmington Canyons, are designated as deep-sea coral HAPCs by the Mid-Atlantic Fishery Management Council. Any impactful activities permitted to occur near the heads of the canyons (where the coral assemblages are diverse, the seeps are nearby, and benthopelagic coupling is strong) would therefore need to be carefully assessed and managed.

At our shallower, intercanyon seep sites, we discovered a visually apparent and unexpectedly high degree of benthopelagic coupling. These are some of the most active seeps ever directly measured (see **Chapter 3.3**), with methane fluxes highly elevated in the water column and occasionally measurable at the air-sea interface. This area is known to have one of the highest abundances of benthic infauna, carbon flux, and particulate sedimentation rates of anywhere along the US Atlantic margin (Sulak and Ross 1996). The seep sites exhibit localized areas of chemosynthetic productivity at the seafloor and in the water column and could augment the delivery of nutrients to the photic zone, as has been observed in the GOM (D'Souza et al. 2016).

The seep sites were occupied by numerous species of demersal fishes and squid, further contributing to the linkage with the overlying pelagic communities. The full role of the seeps in the larger mid-Atlantic and SEUS seascape remains to be revealed, but this study has provided a wealth of data that begins to tell the story. Already, seeps are considered EFH on the west coast of the US and may be considered for fishery management designation in the study area and further to the north (Grupe et al. 2015). In the context of BOEM management decisions, biodiverse seep sites would likely be considered "high density" benthic communities that must be avoided in the GOM.

These sites can be precisely located through the use of seabed reflectivity anomalies in the industry-generated 3D seismic data that are housed at BOEM. In the Atlantic study area considered here, there are insufficient seismic data to utilize such methods, but the detection of water-column bubble plumes by multibeam echosounder sonars can be another effective way to locate the active seeps. Additional ground-truthing data would be required to extend this methodology and ensure that other influential seep sites do not go undetected.

Looking ahead and informed by this study's results, BOEM may consider requesting site-specific surveys that operators could provide with environmental baseline information to accurately assess and manage potential activity impacts. One way this could be accomplished is through physical distancing or other mitigations via site-specific conditions of approval for permits. Methods and information requirements for these surveys could include some shared characteristics, whether they be conducted for oil and gas, marine mineral mining, or renewable energy (wind, wave, solar, and/or ocean thermal energy conversion) infrastructure installation. All of these types of activities may include some disturbance of the seafloor. As such, high-resolution multibeam echosounder sonar bathymetric and backscatter data could first be acquired from surface ships or vehicles (if not already available) and then at higher resolution over specific areas interest, likely using AUVs. A resolution of site-specific data approaching 1 m^2 could help to reliably detect rugose topography and high backscatter features or areas that are most likely to represent hard substrata. During the bathymetric surveys, water-column data could be acquired by CTD rosette to measure certain water-column conditions in the area, including particulate loads, trace metal abundance, hydrocarbon concentrations, and the composition of the microbial community. These data could feed the generation of potential impact models for areas of focus for the specific activity proposed.

After the mapping data and model results are reviewed, benthic sampling could be conducted to provide information about the benthic community that may be impacted by the activity. Soft-sediment benthic sampling could be accomplished by multicore seafloor sediment sampling deployments from surface ships. These could be analyzed for both geological characteristics and biological community characterization to the macrofauna level (at a minimum). Any areas that are likely to contain hard substrata, revealed by the bathymetric surveys or 3D seismic data if available, could be surveyed visually by ROV and/or AUV. Random transect design can be employed though heavy stratification could help to include the vast majority, if not all, of the detected hard substrata within the zone predicted to be impacted by the industrial activity. If these surveys reveal any potentially sensitive habitats in the area (see further discussion below), subsequent activities can avoid them with appropriate distancing of infrastructure (see additional information in Cordes et al. 2016).

Climate change is a focus in the SEUS. The Gulf Stream has a major influence on the oceanographic conditions at depth in the region, frequently bringing warm temperatures (> 12 to 15°C) to the depths under consideration here. While our predictive habitat modeling and projections indicate that the deeper sites will see less warming in the future, the shallower coral sites in the western portion of Stetson Banks and Savannah Banks could be exposed to temperatures above their thermal limits (approximately 15°C for *L. pertusa*, see **Chapter 5**).

As global and ocean water temperatures continue to climb and is translated to depth, some gas-hydrate accumulations along the shelf break may further destabilize, potentially releasing additional methane to the ocean and atmosphere (see **Chapter 3**) and causing localized benthic habitat disturbance. Global use of fossil fuels will continue to contribute to these ongoing ocean temperature, acidification, and other relevant global change trends. Analyzing and considering these factors can help to inform stability impacts of the living resources investigated in this study.

8 Deep SEARCH Outreach

Education and outreach were key components of the Deep SEARCH mission. The PIs put great emphasis on the effective communication of our results to the general public, starting with the coverage of the expeditions on the NOAA Ocean Explorer web site, and finishing with the production of the 20-minute summary video for the project.

We participated in numerous public presentations and interactions, highlighted by the use of the "Ocean Discovery Zone" booth at various science festivals and institutional open houses during the project. Below is a (non-exhaustive) list of the media coverage and educational activities of the members of Deep SEARCH.

8.1 Individual PI Contributions

8.1.1 Cheryl Morrison – USGS

ADEON Blog

Earth Day 2018 & 2019

Presentations & Symposiums – 2020 Ocean Sciences, 2020 GEOBON Open Science, 2019 ASLO, 2019 Deep-Sea Coral Symposium, 2018 Deep-Sea Biology Symposium.

Seminars – 2019 LSC Lunch and Learn, 2019 LSC Evening Seminar, 2019 College of Charleston invited seminar, 2021 MBARI Seminar series

Webinar – 2019 NOAA Deep Sea Coral coordination meeting

Workshop – 2018 Second Environmental DNA Technical Exchange Workshop

8.1.2 Jennifer Miksis-Olds

UNH Ocean Discovery Day 2018, 2019

ADEON blog – Tracey Sutton and Cheryl Morrison labs highlighted on expeditions

8.1.3 Tracey Sutton

Web coverage Deep SEARCH Expedition, RV *Nancy Foster* 2019

Public seminar Research in the NSU Oceanic Biology Lab 2018

ADEON Blog

8.1.4 Samantha Joye

Featured Scientist – Creatures of the Deep, "Expert is In" Program, 2019, Smithsonian National Museum of Natural History, Washington, D.C

Web coverage – Deep SEARCH expedition, NOAA Ship Ronald Brown,2019, NOAA Ocean Explorer (signature expedition)

Web coverage – Deep SEARCH expedition, RV *Atlantis*, 2018, NOAA Ocean Explorer

8.1.5 Erik Cordes

Featured Scientist – Creatures of the Deep, "Expert is In" Program, 2019, Smithsonian National Museum of Natural History, Washington, D.C, Invited Speaker Cephalopod Movie Night

Science Friday @ Johnny Brenda's
Philadelphia, PA

Web coverage – Deep SEARCH expedition, NOAA Ship Ronald Brown 2019
NOAA Ocean Explorer (signature expedition)

Public seminar Bringing Light to the Depths of the Ocean 2018

"Starry Night" benefit for Star Island Corporation
Portsmouth, NH

Web coverage Deep SEARCH expedition, RV *Atlantis* 2018
NOAA Ocean Explorer

8.1.6 Andrea Quattrini

NMNH Director's Discovery Series - Presentation to NMNH donors with director Kirk Johnson, 21 April, 2021

NMHN Senate of Scientists - Lightning talk on "Fieldwork", 15 May 2020

Smithsonian Institution Ocean Portal Article - Optimism in the Deep Sea. Provided interview and edited written content.

Participated in "Expert is in" at NMNH, 20 May 2020 - 30 minute discussion with Education Specialists, ~300 participants

Mentoring - Intern Emma Saso (2020-present) and PostDoc Dr. Danielle DeLeo (2020-present)

8.1.7 Ivan Hurzeler

Video report (3 minutes) from Deep SEARCH AT-41 on finding Richardson Hills, featuring Dr. Samantha Joye and Dr. Erik Cordes

Video report (5 minutes) on Deep SEARCH AT-41, posted by BOEM. A summary of work done on the cruise featuring Dr. Cordes, Dr. Demopoulos and Dr. Michael Rasser of BOEM. Video highlights and stories from the *Alvin* dives during AT-41.

Video report (5 minutes) on Deep SEARCH RB-1903, posted by BOEM. A summary of work done on the cruise featuring Dr. Cordes, Dr. Demopoulos and Dr. Michael Rasser of BOEM. Video highlights and stories from *Jason* dives during RB-1903.

Video report (25 minutes) on the Deep SEARCH program, posted by BOEM. A summary of work done on the cruises featuring Dr. Cordes, Dr. Demopoulos and Dr. Michael Rasser of BOEM. Video highlights and stories from the field effort.

8.2 Outreach Through NOAA Platforms

Education Module - https://oceanexplorer.noaa.gov/explorations/17Deep SEARCH/background/edu/edu.html

2017 –https://oceanexplorer.noaa.gov/explorations/17Deep SEARCH/background/plan/plan.html

2018 – https://oceanexplorer.noaa.gov/explorations/18Deep SEARCH/welcome.html

2019 – https://oceanexplorer.noaa.gov/explorations/19Deep SEARCH/welcome.html

8.3 Outreach Through Press Releases

8.3.1 General Press

Press Release (Bureau of Ocean Energy Management), 12 September, 2017: "Federal Ocean Partnership Launches Deep SEARCH Study Off the Mid- and South Atlantic Coast"

Press Release (USGS), 13 September 2017: "Federal Ocean Partnership Launches Deep SEARCH Study of Coral, Canyons and Seeps Off the Mid- and South Atlantic Coast"

TDI-Brooks International Deep SEARCH Announcement

BOEM Announcement of August/September 2018 *Atlantis* Expedition

BOEM Announcement of April 2019 Expedition

https://www.huffpost.com/entry/methane-hydrate-atlantic-samantha joye_n_5d681737e4b0488c0d117841

https://www.huffpost.com/entry/scientists-exploring-uncharted-ecosystems-atlantic-ocean_n_5b7b12e4e4b0a5b1febde68f

https://www.huffpost.com/entry/scientists-discover-giant-deep-sea-coral-reef-off-atlantic-coast_n_5b81c298e4b0cd327dfd415e

https://www.huffpost.com/entry/tubeworm-discovery-atlantic-ocean_n_5cd2f021e4b07ce6ef790fd3

https://www.huffpost.com/entry/atlantic-coral-reef-seismic-surveys-oil-gas_n_5c09b43ce4b04046345a87ee

8.3.2 Press Specifically Regarding the Aug/Sep 2018 *Atlantis* Expedition

Charleston Post Courier https://www.postandcourier.com/news/south-carolina-s-deep-ocean-is-home-to-vast-/article_e9e34724-aa1e-11e8-bec3-839607de538d.html *South Carolina's deep ocean is home to vast, 85-mile-long stretch of coral,* August 29, 2018

Charlotte Observer https://www.charlotteobserver.com/news/local/article217444020.html *Divers find mysterious mounds 1/2 mile under sea near SC. They're massive coral reefs,* August 28, 2018

CNN https://www.cnn.com/2018/08/27/us/giant-coral-reef-atlantic-coast-trnd/index.html *Scientists discover hidden deep-sea coral reef off South Carolina Coast,* August 28, 2018

Daily Mail http://www.dailymail.co.uk/news/article-6099969/Scientists-uncover-85-mile-long-coral-reef-Atlantic-Ocean.html *Scientists uncover massive 85 mile long coral reef deep in the Atlantic off the coast of South Carolina,* August 26, 2018

Forbes https://www.forbes.com/sites/priyashukla/2018/08/30/scientists-discovered-a-massive-deep-sea-coral-reef-near-south-carolina/#1bbc1ca377cc *Scientists Discovered A Massive Deep Sea Coral Reef Near South Carolina,* August 30, 2018

Forbes https://www.forbes.com/sites/priyashukla/2018/09/10/why-the-discovery-of-the-deep-sea-coral-reef-near-south-carolina-matters/#c7179fd6c373 *Why the discovery of the deep sea coral reef near South Carolina matters,* September 10, 2018

Huffington Post (original article) https://www.huffingtonpost.com/entry/scientists-discover-giant-deep-sea-coral-reef-off-atlantic-coast_us_5b81c298e4b0cd327dfd415e *Deep SEARCH Scientists Discover Giant Deep-Sea Coral Reef Off Atlantic Coast,* August 25, 2018

IFL Science https://www.iflscience.com/plants-and-animals/massive-deepsea-coral-reef-discovered-off-the-coast-of-south-carolina/ *Massive Coral Reef Discovered Off the Coast of the USA,* August 29, 2018

The Independent https://www.independent.co.uk/news/world/americas/south-carolina-deep-sea-coral-reef-deep-search-noaa-trump-offshore-drilling-a8511996.html *Scientists discover 'unbelievable' deep-sea coral reef off coast of South Carolina,* August 29, 2018.

Interesting Engineering https://interestingengineering.com/lengthy-85-mile-stretch-of-coral-reef-discovered *Lengthy 85 Mile Stretch of Coral Reef Discovered,* August 31, 2018

International Business Times, India Edition https://www.ibtimes.co.in/ahead-oil-drill-move-coral-reef-measuring-85-miles-discovered-off-south-carolina-779084 *Ahead of oil drill move, coral reef measuring 85 miles discovered off South Carolina,* August 30, 2018

https://www.livescience.com/63442-new-coral-reef-found.html *85 Miles of Atlantic Coral Reef Stayed Hidden Until Now,* August 27, 2018

NBC https://www.nbcnews.com/mach/science/huge-deep-sea-coral-reef-discovered-south-carolina-coast-ncna904821 *Huge deep-sea coral reef discovered off the South Carolina coast,* August 29, 2018

Ocean Conservancy Blog https://oceanconservancy.org/blog/2018/09/04/secret-garden-atlantic/ *A secret garden in the Atlantic* September 4, 2018

https://www.simplemost.com/scientists-discovered-coral-reef-coast-south-carolina/ *Scientists Just Discovered a Coral Reef Off the Coast of South Carolina,* August 31, 2018

Sputnik News https://sputniknews.com/environment/201808301067583455-cold-water-coral-reef-south-carolina/ *Massive deep-water coral reef uncovered off US East Coast,* August 30, 2108

Tech Times https://www.techtimes.com/articles/233854/20180831/scientists-find-previously-unknown-coral-reef-in-deep-waters-near-south-carolina-coast.htm *Scientists Find Previously Unknown Coral Reef in Deep Waters Near South Carolina Coast,* August 31, 2018

The Times https://www.thetimes.co.uk/article/unknown-85-mile-coral-reef-stands-in-path-of-oil-drillers-gc2dpmnwv *Unknown 85-mile coral reef stands in path of oil drillers,* September 1, 2018

Washington Post https://www.washingtonpost.com/science/2018/08/28/scientists-discovered-coral-reef-almost-long-delaware-hidden-off-coast-charleston/?utm_term=.9fd30b21403a *Scientists discovered a coral reef — almost as long as Delaware — hidden off the coast of Charleston,* August 28, 2018

The Weather Channel https://weather.com/science/nature/news/2018-08-29-deep-coral-reef-south-carolina-coast *'Unbelievable' Deep Coral Reef Discovered Off South Carolina Coast,* August 29, 2018

https://e360.yale.edu/digest/scientists-find-a-massive-deep-sea-reef-off-the-u-s-east-coast *Scientists Find a Massive Deep Sea Reef Off the U.S. East Coast,* August 29, 2018

Business Insider https://www.businessinsider.com/scientists-discovered-deep-sea-coral-reef-2018-9?r=UK&IR=T *Scientists discovered 85 miles of deep-sea coral reef hidden off the US East Coast -- here's what it looks like*, September 22, 2018 (same article re-posted on CT Post):

https://www.theinertia.com/environment/researchers-found-an-85-mile-long-centuries-old-coral-reef-in-the-atlantic/ *Researchers Found n 85-Mile Long, Centuries-Old Coral Reef in the Atlantic,* October 2, 2018

http://templeupdate.com/temple-professor-discovers-new-corral-reef/

Temple Professor Discovers Coral Reef, September 27, 2018

https://www.surfer.com/environmental-news/coral-reef-discovered-south-carolina/

Previously unknown coral reef discovered off South Carolina, November 24, 2018

Press Specifically Regarding Discoveries on the April 2019 Expedition:

NOAA social media:

https://t.co/YdYpfaubYp

https://twitter.com/oceanexplorer/status/1113822159493898242

https://www.facebook.com/OceanExplorationResearch/photos/a.1962817740488242/1962817860488230/?type=3&theater

https://oceanexplorer.noaa.gov/explorations/19Deep SEARCH/background/explorers/explorers.html

8.4 Outreach Through BOEM Platforms

https://www.boem.gov/note04092019a/

The State: https://www.thestate.com/latest-news/article229617829.html

Huffington Post: https://www.huffpost.com/entry/tubeworm-discovery-atlantic-ocean_n_5cd2f021e4b07ce6ef790fd3

Fox News: https://www.foxnews.com/science/bizarre-deep-sea-tubeworms-discovered-off-north-carolina-popped-out-like-a-jack-in-the-box

Newsweek: https://www.newsweek.com/strange-deep-sea-tube-worms-north-carolina-atlantic-coast-1420761

ECO Magazine: https://www.ecomagazine.com/news/industry/boem-and-research-partners-resume-southeast-atlantic-exploration

Coral Issue: http://digital.ecomagazine.com/publication/frame.php?i=664239&p=&pn=&ver=html5

9 References

Addamo AM, Vertino A, Stolarski J, Garcia-Jimenez R, Taviani M, Machordom A. 2016. Merging scleractinian genera: the overwhelming genetic similarity between solitary *Desmophyllum* and colonial *Lophelia*. Bmc Evolutionary Biology. 16.

Alarif WM, Abdel-Lateff A, Alorfi HS, Alburae NA. 2019. Alcyonacea: a potential source for production of nitrogen-containing metabolites. Molecules. 24.

Alexander MA, Shin S, Scott JD, Curchitser E, Stock C. 2020. The response of the northwest Atlantic Ocean to climate change. Journal of Climate. 33:405–428.

Allan EA, DiBenedetto MH, Lavery AC, Govindarajan AF, Zhang WG. 2021. Modeling characterization of the vertical and temporal variability of environmental DNA in the mesopelagic ocean. Scientific Reports. 11:21273. doi:10.1038/s41598-021-00288-5.

Aller JY, Aller RC, Green MA. 2002. Benthic faunal assemblages and carbon supply along the continental shelf/shelf break-slope off Cape Hatteras, North Carolina. Deep Sea Research Part II: Topical Studies in Oceanography. 49(20):4599–4625.

Alperin MJ, Reeburgh WS, Whiticar MJ. 1988. Carbon and hydrogen isotope fractionation resulting from anaerobic methane oxidation. Global Biogeochemical Cycles. 2(3):279–288.

Altschul SF, Gish W, Miller W, Myers EW, Lipman DJ. 1990. Basic local alignment search tool. Journal of Molecular Biology. 215:403–410. doi:10.1016/S0022-2836(05)80360-2

Amaral-Zettler LA, McCliment EA, Ducklow HW, Huse SM. 2009. A method for studying protistan diversity using massively parallel sequencing of V9 hypervariable regions of small-subunit ribosomal RNA Genes. PloS ONE. 4:1–9.

Anderson M, Gorley RN, and Clarke KR. 2008. PERMANOVA+ for PRIMER: guide to software and statistical methods. Plymouth (UK):PRIMER-e Ltd.

Andres M, Donohue KA, Toole JM. 2020. The Gulf Stream's path and time-averaged velocity structure and transport at 68.5 degrees W and 70.3 degrees W. Deep-Sea Research Part I-Oceanographic Research Papers 156.

Andrews S, Krueger F, Segonds-Pichon A, Biggins L, Krueger C, Wingett S. 2010. FastQC. A quality control tool for high throughput sequence data. https://www.bioinformatics.babraham.ac.uk/projects/fastqc/.

Apprill A, McNally S, Parsons R, Weber L. 2015. Minor revision to V4 region SSU rRNA 806R gene primer greatly increases detection of SAR11 bacterioplankton. Aquatic Microbial Ecology. 75(2):129–137.

Apprill A, Weber LG, Santoro AE. 2016. Distinguishing between microbial habitats unravels ecological complexity in coral microbiomes. mSystems. 1(5):e00143–e00116.

Arellano SM, Young CM. 2009. Spawning, development, and the duration of larval life in a deep-sea cold-seep mussel. The Biological Bulletin. 216(2):149–162.

Arias PA, Bellouin N, Coppola E, Jones RG, Krinner G, Marotzke J, Naik V, Palmer MD, Plattner G-K, Rogelj J, et al. 2021. Technical summary. In: Masson-Delmotte V, Zhai P, Pirani A, Connors SL, Péan C, Berger S, Caud N, Chen Y, Goldfarb L, Gomis MI, et al., editors. Climate change 2021: the physical science basis. Contribution of Working Group I to the Sixth Assessment Report of the Intergovernmental Panel on Climate Change. Cambridge (UK): Cambridge University Press. p. 33−144. doi:10.1017/9781009157896.002.

Arndt A, Marquez C, Lambert P, Smith MJ. 1996. Molecular phylogeny of Eastern Pacific sea cucumbers (echinodermata: holothuroidea) based on mitochondrial DNA sequence. Molecular Phylogenetics and Evolution. 6:425–437.

Arvidson RS, Morse JW, Joye SB. 2004. The sulfur biogeochemistry of chemosynthetic cold seep communities, Gulf of Mexico, USA. Marine Chemistry. 87(3-4):97–119.

Atlas RM. 2010. Handbook of microbiological media. Boca Raton (FL): CRC Press.

Aunins AW, Morrison CL. 2023. Deep SEARCH eDNA metabarcoding Data. US Geological Survey Data Release. doi:10.5066/P9EAY8JD

Auscavitch SR, Deere MC, Keller AG, Rotjan RD, Shank TM, Cordes EE. 2020. Oceanographic drivers of deep-sea coral species distribution and community assembly on seamounts, islands, atolls, and reefs within the Phoenix Islands Protected Area. Frontiers in Marine Science. 7:42.

Avise JC, Reeb CA, Saunders NC. 1987. Geographic population structure and species differences in mitochondrial DNA of mouthbrooding marine catfishes (Ariidae) and demersal spawning toadfishes (Batrachoididae). Evolution. 41:991–1002.

Babcock RC. 1991. Comparative demography of three species of scleractinian corals using age- and size-dependent classifications. Ecological Monographs. 61(3):225–244.

Baco AR, Cairns SD. 2012. Comparing molecular variation to morphological species designations in the deep-sea coral *Narella* reveals new insights into seamount coral ranges. PLoS ONE. 7:e45555.

Baco AR, Etter RJ, Ribeiro PA, Heyden SD, Beerli P, Kinlan BP. 2016. A synthesis of genetic connectivity in deep-sea fauna and implications for marine reserve design. Molecular Ecology. 25:3276–3298.

Baco AR, Morgan N, Roark EB, Silva M, Shamberger KEF, Miller K. 2017. Defying dissolution: discovery of deep-sea scleractinian coral reefs in the North Pacific. Scientific Reports. 7:5436.

Baird DJ, Hajibabei M. 2012. Biomonitoring 2.0: a new paradigm in ecosystem assessment made possible by next-generation DNA sequencing. Molecular Ecology. 21:2039–2044.

Baker K, Wareham V, Snelgrove P, Haedrich R, Fifield D, Edinger E, Gilkinson K. 2012. Distributional patterns of deep-sea coral assemblages in three submarine canyons off Newfoundland, Canada. Marine Ecology Progress Series. 445:235–249.

Baker MC, Ramirez-Llodra E, Tyler PA, German CR, Boetius A, Cordes EE, Dubilier N, Fisher CR, Levin L, Metaxas A, et al. 2010. Biogeography, ecology and vulnerability of chemosynthetic ecosystems in the deep sea. In: McIntyre AD, editor. Life in the world's oceans. Blackwell Publishing Ltd.

Bane Jr. JM, Brooks DA. 1979. Gulf Stream meanders along the continental margin from the Florida Straits to Cape Hatteras. Geophysical Research Letters. 6(4):280–282.

Bankevich A, Nurk S, Antipov D, Gurevich AA, Dvorkin M, Kulikov AS, Lesin VM, Nikolenko SI, Pham S, Prjibelski AD, et al. 2012. SPAdes: a new genome assembly algorithm and its applications to single-cell sequencing. Journal of Computational Biology. 19(5):455–477.

Barnes DJ, Lough JM. 1989. The nature of skeletal density banding in scleractinian corals: fine banding and seasonal patterns. Journal of Experimental Marine Biology and Ecology. 126:119–134.

Barnes DJ, Lough JM. 1993. On the nature and cause of density banding in massive coral skeletons. Journal of Experimental Marine Biology and Ecology. 167:91–108.

Bassett C, Thomson J, Dahl PH, and Polagye B. 2014. Flow-noise and turbulence in two tidal channels. Journal of the Acoustical Society of America. 135(4):1764–1774.

Baums IB, Miller MW, Hellberg ME. 2005. Regionally isolated populations of the imperiled Caribbean coral, *Acropora palmata*. Molecular Ecology. 14:1377–1390.

Bayer T, Arif C, Ferrier-Pagès C, Zoccola D, Aranda M, Voolstra CR. 2013a. Bacteria of the genus *Endozoicomonas* dominate the microbiome of the Mediterranean gorgonian coral *Eunicella cavolini*. Marine Ecology Progress Series. 479:75–84.

Bayer T, Neave MJ, Alsheikh-Hussain A, Aranda M, Yum LK, Mincer T, Hughen K, Apprill A, Voolstra CR. 2013b. The microbiome of the Red Sea coral *Stylophora pistillata* is dominated by tissue-associated *Endozoicomonas* bacteria. Applied and Environmental Microbiology. 79(15):4759–4762.

Bayon G, Henderson GM, Bohn M. 2009. U–Th stratigraphy of a cold seep carbonate crust. Chemical Geology. 260(1-2):47–56.

Beazley LI, Kenchington EL. 2012. Reproductive biology of the deep-water coral *Acanella arbuscula* (phylum Cnidaria: class Anthozoa: order Alcyonacea), northwest Atlantic. Deep-Sea Research II. 68:92–104.

Becker EL, Cordes EE, Macko SA, Fisher CR. 2009. Importance of seep primary production to *Lophelia pertusa* and associated fauna in the Gulf of Mexico. Deep-Sea Research I. 56:786–800.

Becker EL, Cordes EE, Macko SA, Lee RW, Fisher CR. 2014. Spatial patterns of tissue stable isotope contents give insight into the nutritional sources for seep communities on the Gulf of Mexico lower slope. Marine Ecology Progress Series. 498:133–145.

Becker EL, Lee RW, Macko SA, Faure BM, Fisher CR. 2010. Stable carbon and nitrogen isotope compositions of hydrocarbon-seep bivalves on the Gulf of Mexico lower continental slope. Deep Sea Research Part 2: Topical Studies in Oceanography. 57(21-23):1957–1964.

Becker EL, Macko SA, Lee RW, Fisher CR. 2011. Stable isotopes provide new insights into vestimentiferan physiological ecology at Gulf of Mexico cold seeps. Naturwissenschaften. 98(2):169–174.

Beckmann S, Farag I F, Zhao R, Christman G D, Prouty NG, Biddle JF. 2021. Expanding the repertoire of electron acceptors for the anaerobic oxidation of methane in carbonates in the Atlantic and Pacific Ocean. The ISME Journal. 15:2523–2536.

Belleudy P, Valette A, Graff B. 2010. Passive hydrophone monitoring of bedload in river beds: first trials of signal spectral analyses. Report No.: U.S. Geological Survey Scientific Investigations Report 2010-5091.

Benayahu Y, Loya Y. 1987. Long-term recruitment of soft corals (Octocorallia: Alcyonacea) on artificial substrata at Eilat (Red Sea). Marine Ecology Progress Series. 38:161–167.

Bennett RH, Lehman L, Hulbert MH, Harvey GR, Bush SA, Forde EB, Crews P, Sawyer WB. 1985. Interrelationships of organic carbon and submarine sediment geotechnical properties. Marine Geotechnology. 6(1):61–98.

Bergmann M, Dannheim J, Bauerfeind E, Klages M. 2009. Trophic relationships along a bathymetric gradient at the deep-sea observatory HAUSGARTEN. Deep-Sea Research Part I: Oceanographic Research Papers. 56(3):408–424.

Bergquist DC, Ward T, Cordes EE, McNelis T, Howlett S, Kosoff R, Hourdez S, Carney R, Fisher CR. 2003. Community structure of vestimentiferan-generated habitat islands from Gulf of Mexico cold seeps. Journal of Experimental Marine Biology and Ecology. 289(2):197–222.

Bernardino AF, Levin LA, Thurber AR, Smith CR. 2012. Comparative composition, diversity and trophic ecology of sediment macrofauna at vents, seeps and organic falls. PLoS ONE. 7(4):e33515.

Bertucci F, Parmentier E, Berten L, Brooker RM, Lecchini D. 2015. Temporal and spatial comparisons of underwater sound signatures of different reef habitats in Moorea Island, French Polynesia. PLoS ONE. 10(9): e0135733. doi:10.1371/journal.pone.0135733.

Bish DL, Howard SA. 1988. Quantitative phase analysis using the Rietveld method. Journal of Applied Crystallography. 21:86–91.

Blake JA, Hecker B, Grassle JF, Brown B, Wade M. 1987. Study of biological processes on the US South Atlantic slope and rise. Phase 2. Volume 1. Executive summary. Report for November 1985–March 1987. Duxbury (MA): Battelle New England Marine Research Lab.

Blake JA, Hecker B, Grassle JF, Maciolek-Blake N, Brown B. 1985. Study of biological processes on the US South Atlantic slope and rise. Phase 1: Benthic characterization. Volume 2. Final report. Duxbury (MA): Battelle New England Marine Research Lab.

Blake JA, Hilbig B. 1994. Dense infaunal assemblages on the continental slope off Cape Hatteras, North Carolina. Deep Sea Research Part II: Topical Studies in Oceanography. 41:875–899.

Boehm JT, Waldman J, Robinson JD, Hickerson MJ. 2015. Population genomics reveals seahorses Hippocampus erectus of the western mid-Atlantic coast to be residents rather than vagrants. PLoS ONE. 10:e0116219.

BOEM. 2015. 2017–2022 Outer Continental Shelf Oil And Gas Leasing Draft Proposed Program. https://www.boem.gov/2017-2022 -DPP/.

Boers N. 2021. Observation-based early-warning signals for a collapse of the Atlantic Meridional Overturning Circulation. Nature Climate Change. 11:680–688. doi:10.1038/s41558-021-01097-4.

Bohrmann G, Greinert J, Suess E, Torres M. 1998. Authigenic carbonates from the Cascadia subduction zone and their relation to gas hydrate stability. Geology. 26(7):647–650.

Bolger AM, Lohse M, Usadel B. 2014. Trimmomatic: a flexible trimmer for Illumina sequence data. Bioinformatics. 30(15):2114–2120.

Bolyen E, Rideout JR, Dillon MR, Bokulich NA, Abnet CC, Al-Ghalith GA, Alexander H, Alm EJ, Arumugam M, Asnicar F. 2019. Reproducible, interactive, scalable and extensible microbiome data science using QIIME 2. Nature Biotechnology. 37(8):852–857.

Bourque JR, Demopoulos AWJ. 2018. The influence of different deep-sea coral habitats on sediment macrofaunal community structure and function. PeerJ. 6:e5276.

Bourque JR, Demopoulos AWJ, Robertson CM, Mienis F. 2021. The role of habitat heterogeneity and canyon processes in structuring sediment macrofaunal communities associated with hard substrate habitats in Norfolk Canyon, USA. Deep Sea Research Part I. 170:103495.

Bourque JR, Robertson CM, Brooke S, Demopoulos AW. 2017. Macrofaunal communities associated with chemosynthetic habitats from the US Atlantic margin: a comparison among depth and habitat types. Deep Sea Research Part II: Topical Studies in Oceanography. 137:42–55.

Bowles MW, Hunter KS, Samarkin VA, Joye SB. 2016. Patterns and variability in geochemical signatures within and between diverse cold seep habitats along the lower continental slope, Northern Gulf of Mexico. Deep Sea Research II. 129:31–40.

Bowles MW, Samarkin VA, Hunter KS, Finke N, Teske AP, Girguis PR, Joye SB. 2019. Remarkable capacity for anaerobic oxidation of methane at high methane concentration. Geophysical Research Letters. 46:12192–12201.

Bowles MW, Samarkin VA, Joye SB. 2011. Improved measurement of microbial activity in deep-sea sediments at in situ pressure and methane concentration. Limnology and Oceanography: Methods. 9(10):499–506.

Boyer TP, García HE, Locarnini RA, Zweng MM, Mishonov AV, Reagan JR, Weathers KA, Baranova OK, Paver CR, Seidov D, et al. 2018. World Ocean Atlas. https://repository.library.noaa.gov/view/noaa/49137.

Bracco A, Liu G, Galaska MP, Quattrini AM, Herrera S. 2019. Integrating physical circulation models and genetic approaches to investigate population connectivity in deep-sea corals. Journal of Marine Systems. 198:103189.

Braman RS, Hendrix SA. 1989. Nanogram nitrite and nitrate determination in environmental and biological materials by vanadium(III) reduction with chemiluminesence detection. Analytical Chemistry. 61:2715–2718.

Brand WA, Assonov SS, Coplen TB. 2010. Correction for the ^{17}O interference in $\delta(^{13}C)$ measurements when analyzing CO_2 with stable isotope mass spectrometry (IUPAC technical report). Pure and Applied Chemistry. 82(8):1719–1733.

Brandt MI, Trouche B, Henry N, Liautard-Haag C, Maignien L, et al. 2020. An assessment of environmental metabarcoding protocols aiming at favoring contemporary biodiversity in inventories of deep-sea communities. Frontiers in Marine Science. doi:10.3389/fmars.2020.00234.

Breusing C, Johnson SB, Tunnicliffe V, Vrijenhoek RC. 2015. Population structure and connectivity in Indo-Pacific deep-sea mussels of the *Bathymodiolus septemdierum* complex. Conservation Genetics. 16(6):1415–1430.

Briggs JC. 1974. Marine zoogeography. New York (NY): McGraw-Hill.

Briggs JC, Bowen BW. 2012. A realignment of marine biogeographic provinces with particular reference to fish distributions. Journal of Biogeography. 39:12–30.

Brito MR, Chávez EL, Quiroz AJ, Yukich JE. 1997. Connectivity of the mutual *k*-nearest-neighbor graph in clustering and outlier detection. Statistics & Probability Letters. 35(1):33–42.

Brock J, Rhiel E, Beutler M, Salman V, Schulz-Vogt HN. 2012. Unusual polyphosphate inclusions observed in a marine Beggiatoa strain. Antoine van Leeuwenhoek. 101:347–157.

Brooke S, Järnegren J. 2013. Reproductive periodicity of the scleractinian coral *Lophelia pertusa* from the Trondheim Fjord, Norway. Marine Biology. 160:139–153.

Brooke S, Ross SW, Bane JM, Seim HE, Young CM. 2013. Temperature tolerance of the deep-sea coral *Lophelia pertusa* from the southeastern United States. Deep Sea Research Part II: Topical Studies in Oceanography. 92:240–248.

Brooke S, Ross SW. 2014. First observations of the cold-water coral *Lophelia pertusa* in mid-Atlantic canyons of the USA. Deep Sea Research Part II: Topical Studies in Oceanography. 104:245–251.

Brooke S, Sogluizzo A. 2017. Chapter 11: invertebrate reproductive biology. In: CSA Ocean Sciences, editor. Exploration and research of mid-Atlantic deepwater hard bottom habitats and shipwrecks with emphasis on canyons and coral communities. Report No.: OCS Study BOEM 2017-060. U.S. Department of the Interior, Bureau of Ocean Energy Management, Atlantic OCS Region. p. 537–577.

Brooke S, Young CM. 2009. Direct measurements of in situ survival and growth of *Lophelia pertusa* in the northern Gulf of Mexico. Marine Ecology Progress Series. 397:153–161.

Brooke SD, Holmes MW, Young CM. 2009. Sediment tolerance of two different morphotypes of the deep-sea coral *Lophelia pertusa* from the Gulf of Mexico. Marine Ecology Progress Series. 390:137–144.

Brooke SD, Watts MW, Heil AD, Rhode M, Mienis F, Duineveld GCA, Davis AJ, Ross SW. 2017. Distributions and habitat associations of deep-water corals in Norfolk and Baltimore Canyons, Mid-Atlantic Bight, USA. Deep Sea Research Part II. 137:131–147.

Brothers LL, Van Dover CL, German CR, Kaiser CL, Yoerger DR, Ruppel CD, Lobecker E, Skarke AD, Wagner JKS. 2013. Evidence for extensive methane venting on the southeastern US Atlantic margin. Geology. 41(7):807–810.

Bucklin A, Peijnenburg KTCA, Kosobokova K, O'Brien TD, Blanco-Bercial L, Cornils A, Falkenhaug T, et al. 2021. Toward a global reference database of COI barcodes for marine zooplankton. Marine Biology. 168. doi:10.1007/s00227-021-03887-y.

Buhl-Mortensen L, Mortensen PB. 2004. Symbiosis in deep-water corals. Symbiosis. 37:33–61.

Buhl-Mortensen L, Vanreusel A, Gooday AJ, Levin LA, Priede IG, Buhl-Mortensen P, Gheerardyn H, King NJ, Raes M. 2010. Biological structures as a source of habitat heterogeneity and biodiversity on the deep ocean margins. Marine Ecology. 31:21–50.

Buisson L, Thuiller W, Casajus N, Lek S, Grenouillet G. 2010. Uncertainty in ensemble forecasting of species distribution. Global Change Biology. 16(4):1145–1157.

Burgess SN, Babcock RC. 2005. Reproductive ecology of three reef-forming, deep-sea corals in the New Zealand region. Cold-Water Corals and Ecosystems. p. 701–713.

Busby MS, Orr JW, Blood DM. 2006. Eggs and late-stage embryos of *Allocareproctus unangas* (family Liparidae) from the Aleutian Islands. Ichthyological Research. 53:423–426.

Buscher JV, Form AU, Riebesell U. 2017. Interactive effects of ocean acidification and warming on growth, fitness and survival of the cold-water coral *Lophelia pertusa* under different food availabilities. Frontiers in Marine Science. 4.

Bushnell B, Rood J, Singer E. 2017. BBMerge – accurate paired shotgun read merging via overlap. PLoS ONE. doi:10.1371/journal.pone.0185056.

Caesar L, McCarthy GD, Thornalley DJ, Cahill N, Rahmstorf S. 2021. Current Atlantic Meridional Overturning Circulation weakest in last millennium. Nature Geoscience. 14(3):118–120.

Cairns SD, Chapman RE. 2001. Biogeographic affinities of the North Atlantic deep-water Scleractinia. In: Proceedings of the First International Symposium on Deep-Sea Corals, Ecology Action Centre and Nova Scotia Museum, Halifax, Nova Scotia, Canada.

Caldow C, Monaco ME, Pittman SJ, Kendall MS, Goedeke TL, Menza C, Costa BM. 2015. Biogeographic assessments: a framework for information synthesis in marine spatial planning. Marine Policy. 51:423–432.

Callahan BJ, McMurdie PJ, Rosen MJ, Han AW, Johnson AJA, Holmes SP. 2016. DADA2: high-resolution sample inference from Illumina amplicon data. Nature Methods. 13:581–583. doi:10.1038/nmeth.3869.

Canals M, Puig P, de Madron XD, Heussner S, Palanques A, Fabres J. 2006. Flushing submarine canyons. Nature. 444(7117):354–357.

Canfield DE, Raiswell R, Westrich JT, Reaves CM, Berner RA. 1986. The use of chromium reduction in the analysis of reduced inorganic sulfur in sediments and shales. Chemical Geology. 54(1-2):149–155.

Caporaso JG, Lauber CL, Walters WA, Berg-Lyons D, Lozupone CA, Turnbaugh PJ, Fierer N, Knight R. 2011. Global patterns of 16S rRNA diversity at a depth of millions of sequences per sample. Proceedings of the National Academy of Sciences. 108(Supplement 1):4516.

Carini S, Bano N, LeCleir G, Joye SB. 2005. Aerobic methane oxidation and methanotroph community composition during seasonal stratification in Mono Lake, California (USA). Environmental Microbiology. 7(8):1127–1138.

Carney R. 1994. Consideration of the oasis analogy for chemosynthetic communities at Gulf of Mexico hydrocarbon vents. Geo-Marine Letters. 14:149–159.

Carney RS. 2005. Zonation of deep-sea biota on continental margins. Oceanography and Marine Biology: Annual Review. 43:211–279.

Carney SL, Formica MI, Divatia H, Nelson K, Fisher CR, Schaeffer SW. 2006. Population structure of the mussel *"Bathymodiolus" childressi* from Gulf of Mexico hydrocarbon seeps. Deep Sea Research Part I: Oceanographic Research Papers. 53(6):1061–1072.

Cartes JE, Fanelli E, Papiol V, Maynou F. 2010. Trophic relationships at intrannual spatial and temporal scales of macro and megafauna around a submarine canyon off the Catalonian coast (western Mediterranean). Journal of Sea Research. 63(3-4):180–190.

Cartes JE, Sorbe JC. 1999. Estimating secondary production in bathyal suprabenthic peracarid crustaceans from the Catalan Sea slope (western Mediterranean; 391–1255 m). Journal of Experimental Marine Biology and Ecology. 239(2):195–210.

Case D, Pasulka AL, Marlow JJ, Grupe BM, Levin LA, and Orphan VJ. 2015. Methane seep carbonates host distinct, diverse, and dynamic microbial assemblages. mBio. 6(6):e01348–e01315.

Catchen J, Hohenlohe PA, Bassham S, Amores A, Cresko WA. 2013. Stacks: an analysis tool set for population genomics. Molecular Ecology. 22(11):3124–3140.

Cathalot C, Van Oevelen D, Cox TJS, Kutti T, Lavaleye M, Duineveld G, Meysman FJR. 2015. Cold-water coral reefs and adjacent sponge grounds: hotspots of benthic respiration and organic carbon cycling in the deep sea. Frontiers in Marine Science. 2.

Chan EW, Shiller AM, Joung D-J, Arrington EC, Valentine DL, Molly MC, Breier JA, Socolofsky SA, Kessler JD. 2019. Investigations of marine methane oxidation in two marine seep environments: part I — chemical kinetics. Journal of Geophysical Research: Oceans. 124(12):8852–8868.

Chapron L, Lartaud F, Le Bris N, Peru E, Galand PE. 2020. Local variability in microbiome composition and growth suggests habitat preferences for two reef-building cold-water coral species. Frontiers in Microbiology. 11:275.

Chatterjee S, Dickens GR, Bhatnagar G, Chapman WG, Dugan B, Snyder GT, Hirasaki GJ. 2011. Pore water sulfate, alkalinity, and carbon isotope profiles in shallow sediment above marine gas hydrate systems: a numerical modeling perspective. Journal of Geophysical Research: Solid Earth. 116(B9).

Chen C, Lin TH, Watanabe HK, Akamatsu T, Kawagucci S. 2021. Baseline soundscapes of deep-sea habitats reveal heterogeneity among ecosystems and sensitivity to anthropogenic impacts. Limnology and Oceanography. 66(10):3714–3727.

Cheng H, Lawrence Edwards R, Shen C-C, Polyak VJ, Asmerom Y, Woodhead J, Hellstrom J, Wang Y, Kong X, Spötl C. 2013. Improvements in ^{230}Th dating, ^{230}Th and ^{234}U half-life values, and U–Th

isotopic measurements by multi-collector inductively coupled plasma mass spectrometry. Earth and Planetary Science Letters. 371–372:82–91.

Chevalier N, Bouloubassi I, Birgel D, Crémière A, Taphanel M-H, Pierre C. 2011. Authigenic carbonates at cold seeps in the Marmara Sea (Turkey): a lipid biomarker and stable carbon and oxygen isotope investigation. Marine Geology. 288(1):112–121.

Chhatre VE, Emerson KJ. 2017. StrAuto: automation and parallelization of STRUCTURE analysis. BMC Bioinformatics. 18(1):1–5.

Childress JJ, Fisher CR. 1992. The biology of hydrothermal vent animals: physiology, biochemistry and autotrophic symbioses. Oceanography and Marine Biology Annual Review. 30:337–441.

Cho W, Shank TM. 2010. Incongruent patterns of genetic connectivity among four ophiuroid species with differing coral host specificity on North Atlantic seamounts. Marine Ecology. 31:121–143.

Church TM, Mooers CNK, Voorhis AD. 1984. Exchange processes over a Middle Atlantic bight shelf-break canyon. Estuarine, Coastal and Shelf Science. 19(4):393–411.

Clarke KR. 1993. Non-parametric multivariate analyses of changes in community structure. Australian Journal of Ecology. 18(1):117–143.

Clarke KR, Gorley RN. 2006. Primer. Plymouth (UK): PRIMER-e Ltd. p. 866.

Clarke KR, Gorley RN. 2015. PRIMER v7: user manual/tutorial. In: PRIMER-e Ltd., editor. Plymouth (UK). p. 18.

Clarke KR, Warwick RM. 2001. Change in marine communities. An approach to statistical analysis and interpretation. In: PRIMER-e Ltd., editor. Plymouth (UK). p. 1–168.

Cleland J, Kazanidis G, Roberts JM, Ross SW. 2021. Distribution of megabenthic communities under contrasting settings in deep-sea cold seeps near northwest Atlantic canyons. Frontiers in Marine Science. 885.

Cock PJ, Antao T, Chang JT, Chapman BA, Cox CJ, Dalke A, De Hoon MJ. 2009. Biopython: freely available Python tools for computational molecular biology and bioinformatics. Bioinformatics. 25(11):1422–1423.

Cohen A, Holcomb M. 2009. Why corals care about ocean acidification. Oceanography 22:118–127.

Colaco A, Martins I, Laranjo M, Pires L, Leal C, Prieto C, Costa V, Lopes H, Rosa D, Dondo PR, Serrao-Santos R 2006. Annual spawning of the hydrothermal vent mussel, *Bathymodiolus azoricus*, under controlled aquarium, conditions at atmospheric pressure. Journal of Experimental Marine Biology and Ecology. 333(2):166–171.

Collias EE, Rona MR, McMannus DA, Creager JS. 1963. Machine processing of geologic data. Seattle (WA): University of Washington. Report No.: Technical Report Number 87.

Coma R, Zabala M, Gili JM. 1995. Sexual reproductive effort in the Mediterranean gorgonian *Paramuricea clavata*. Marine Ecology Progress Series. 185–192.

Cordes EE, Bergquist DC, Fisher CR. 2009. Macro-ecology of Gulf of Mexico cold seeps. Annual Review of Marine Science. 1:143–168.

Cordes EE, Bergquist DC, Shea K, Fisher CR. 2003. Hydrogen sulphide demand of long-lived vestimentiferan tube worm aggregations modifies the chemical environment at deep-sea hydrocarbon seeps. Ecology Letters. 6(3):212–219.

Cordes EE, Carney SL, Hourdez S, Carney RS, Brooks JM, Fisher CR. 2007. Cold seeps of the deep Gulf of Mexico: community structure and biogeographic comparisons to Atlantic equatorial belt seep communities. Deep Sea Research I. 54:637–653.

Cordes EE, Cunha MR, Galeron J, Mora C, Olu-Le Roy K, Sibuet M, Van Gaever S, Vanreusel A, Levin LA. 2010. The influence of geological, geochemical, and biogenic habitat heterogeneity on seep biodiversity. Marine Ecology: an Evolutionary Perspective. 31(1):51–65.

Cordes EE, Hourdez S, Predmore BL, Redding ML, Fisher CR. 2005. Succession of hydrocarbon seep communities associated with the long-lived foundation species *Lamellibrachia luymesi*. Marine Ecology Progress Series. 305:17–29.

Cordes EE, Jones DOB, Schlacher TA, Amon DJ, Bernardino AF, Brooke S, Carney R, DeLeo DM, Dunlop KM, Escobar-Briones EG, et al. 2016. Environmental impacts of the deep-water oil and gas industry: a review to guide management strategies. Frontiers in Environmental Science. 4.

Cordes EE, McGinley MP, Podowski E., Becker EL, Lessard-Pilon S, Viada, ST, Fisher, CR 2008. Coral communities of the deep Gulf of Mexico. Deep Sea Research Part I: Oceanographic Research Papers. 55:777–787.

Cordes EE, Nybakken JW, VanDykhuizen G. 2001. Reproduction and growth of *Anthomastus ritteri* (Octocorallia: Alcyonacea) from Monterey Bay, California, USA. Marine Biology. 138:491–501.

Cosca MA, Essene EJ, Geissman JW, Simmons WB, Coates DA. 1989. Pyrometamorphic rocks associated with naturally burned coal beds, Powder River Basin, Wyoming. American Mineralogist. 74(1-2):85–100.

Costello MJ, Chaudhary C. 2017. Marine biodiversity, biogeography, deep-sea gradients, and conservation. Current Biology. 27(11):R511–R527.

Costello MJ, McCrea M, Freiwald A, Lundalv T, Jonsson LG, Bett BJ, Van Weering T, De Haas H, Roberts JM, Allen D. 2005. Role of cold-water coral *Lophelia pertusa* coral reefs as fish habitat in the NE Atlantic. In: Freiwald A, Roberts JM, editors. Cold-water corals and ecosystems. Berlin: Springer Verlag. p. 771–805.

Cowart DA, Matabos M, Brandt MI, Marticorena J, Sarrazin J. 2020. Exploring environmental DNA (eDNA) to assess biodiversity of hard substratum faunal communities on the Lucky Strike vent field (Mid-Atlantic Ridge) and investigate recolonization dynamics after an induced disturbance. Frontiers in Marine Science. 6:783. doi:10.3389/fmars.2019.00783.

Cowen RK, Gawarkiewicz G, Pineda J, Thorrold SR, Werner FE. 2007. Population connectivity in marine systems: an overview. Oceanography. 20(3):14–21.

Cowen RK, Sponaugle S. 2009. Larval dispersal and marine population connectivity. The Annual Review of Marine Science. 1:443–466.

Coykendall DK, Cornman RS, Prouty NG, Brooke S, Demopoulos AW, Morrison CL. 2019. Molecular characterization of *Bathymodiolus* mussels and gill symbionts associated with chemosynthetic habitats from the US Atlantic margin. PLoS ONE. 14(3):e0211616.

Craddock C, Hoeh WR, Lutz RA, Vrijenhoek RC. 1995. Extensive gene flow among mytilid (*Bathymodiolus thermophilus*) populations from hydrothermal vents of the eastern Pacific. Marine Biology. 124(1):137–146.

Crespo-Medina M, Meile C, Hunter K, Diercks A-R, Asper VL, Orphan VJ, Tavormina PL, Nigro LM, Battles JJ, Chanton JP, et al. 2014. The rise and fall of methanotrophy following a deepwater oil-well blowout. Nature Geoscience. 7:423–427.

Csanady GT, Hamilton P. 1988. Circulation of slopewater. Continental Shelf Research. 8(5-7):565–624.

Cutler EB. 1975. Zoogeographical barrier on the continental slope off cape lookout, North Carolina. Deep Sea Research and Oceanographic Abstracts. 22(12):893–901.

Cyr F, van Haren H, Mienis F, Duineveld G, Bourgault D. 2016. On the influence of cold-water coral mound size on flow hydrodynamics, and vice versa. Geophysical Research Letters. 43(2):775–783.

D'souza NA, Subramaniam A, Juhl AR, Hafez M, Chekalyuk A, Phan S, Yan B, MacDonald IR, Weber SC, Montoya JP. 2016. Elevated surface chlorophyll associated with natural oil seeps in the Gulf of Mexico. Nature Geoscience. 9(3):215–218.

Dahan M, Benayahu Y. 1997. Reproduction of *Dendronephthya hemprichi* (Cnidaria: Octocorallia): year-round spawning in an azooxanthellate soft coral. Marine Biology. 129:573–579.

Danecek P, Auton A, Abecasis G, Albers CA, Banks E, DePristo MA, 1000 Genomes Project Analysis Group. 2011. The variant call format and VCFtools. Bioinformatics. 27(15):2156–2158.

Danovaro R, Gambi C, Dell'Anno A, Corinaldesi C, Fraschetti S, Vanreusel A, Vincx M, Gooday AJ. 2008. Exponential decline of deep-sea ecosystem functioning linked to benthic biodiversity loss. Current Biology. 18:1–8.

Davey JW, Blaxter ML. 2010. RADSeq: next-generation population genetics. Briefings in Functional Genomics. 9(5-6):416–423.

Davies AJ, Duineveld GCA, Lavaleye MSS, Bergman MJN, van Haren H, Roberts JM. 2009. Downwelling and deep-water bottom currents as food supply mechanisms to the cold-water coral *Lophelia pertusa* (Scleractinia) at the Mingulay Reef Complex. Limnology and Oceanography. 54:620–629.

Davies AJ, Duineveld GCA, van Weering TCE, Mienis F, Quattrini AM, Seim HE, Bane JM, Ross SW. 2010. Short-term environmental variability in cold-water coral habitat at Viosca Knoll, Gulf of Mexico. Deep Sea Research Part I: Oceanographic Research Papers. 57:199–212.

Davies AJ, Guinotte JM. 2011. Global habitat suitability for framework-forming cold-water corals. PLoS ONE. 6:e18483.

Davies AJ, Wisshak M, Orr JC, Murray Roberts J. 2008. Predicting suitable habitat for the cold-water coral *Lophelia pertusa* (Scleractinia). Deep Sea Research Part I: Oceanographic Research Papers. 55:1048–1062. doi:10.1016/j.dsr.2008.04.010.

de Goeij JM, van Oevelen D, Vermeij MJA, Osinga R, Middelburg JJ, de Goeij AFPM, Admiraal W. 2013. Surviving in a marine desert: the sponge loop retains resources within coral reefs. Science. 342(6154):108–110.

De Leo FC, Ross SW. 2019. Large submarine canyons of the United States Outer Continental Shelf atlas. Sterling (VA): U.S. Department of the Interior, Bureau of Ocean Energy Management. 51 p. Report No.: OCS Study BOEM 2019-066.

De Leo FC, Smith CR, Rowden AA, Bowden DA, Clark MR. 2010. Submarine canyons: hotspots of benthic biomass and productivity in the deep sea. Proceedings of the Royal Society B: Biological Sciences. 277:2783−2792.

Dean WE. 1974. Determination of carbonate and organic matter in calcareous sediments and sedimentary rocks by loss on ignition; comparison with other methods. Journal of Sedimentary Research. 44:242–248.

Dell'Anno A, Pusceddu A, Corinaldesi C, Canals M, Heussner S, Thomsen L, Danovaro R. 2013. Trophic state of benthic deep-sea ecosystems from two different continental margins off Iberia. Biogeosciences. 10(5):2945–2957.

DeMaster DJ, Pope RH, Levin LA, Blair NE. 1994. Biological mixing intensity and rates of organic carbon accumulation in North Carolina slope sediments. Deep Sea Research Part II: Topical Studies in Oceanography. 41:735–753.

Demopoulos AWJ, Bourque JR, and Frometa J. 2014. Biodiversity and community composition of sediment macrofauna associated with deep-sea *Lophelia pertusa* habitats in the Gulf of Mexico. Deep Sea Research Part I: Oceanographic Research Papers. 93:91–103.

Demopoulos AWJ, Gualtieri D, Kovacs K. 2010. Food-web structure of seep sediment macrobenthos from the Gulf of Mexico. Deep Sea Research Part II: Topical Studies in Oceanography. 57:1972–1981.

Demopoulos AWJ, McClain-Counts J, Ross SW, Brooke S, Mienis F. 2017. Food-web dynamics and isotopic niches in deep-sea communities residing in a submarine canyon and on the adjacent open slopes. Marine Ecology Progress Series. 578:19–33.

Demopoulos AW, McClain-Counts JP, Bourque JR, Prouty NG, Smith BJ, Brooke S, Ross SW, Ruppel CD. 2019. Examination of *Bathymodiolus childressi* nutritional sources, isotopic niches, and food-web linkages at two seeps in the US Atlantic margin using stable isotope analysis and mixing models. Deep Sea Research Part I: Oceanographic Research Papers. 148:53–66.

Denes SL, Miksis-Olds JL, Mellinger DK, Nystuen JA 2014. Assessing the cross platform performance of marine mammal indicators between two collocated acoustic recorders. Ecological Informatics. 21:74–80.

Dennis KJ, Affek HP, Passey BH, Schrag DP, Eiler JM. 2011. Defining an absolute reference frame for 'clumped' isotope studies of CO_2. Geochimica et Cosmochimica Acta. 75(22):7117–7131.

Derkarabetian S, Castillo S, Koo PK, Ovchinnikov S, Hedin M. 2019. A demonstration of unsupervised machine learning in species delimitation. Molecular Phylogenetics and Evolution. 139:106562.

Desbruyères DG, Purkey SG, McDonagh EL, Johnson GC, King BA. 2016. Deep and abyssal ocean warming from 35 years of repeat hydrography. Geophysical Research Letters. 43:10356–10365. doi:10.1002/2016GL070413.

Deutsch C, Ferrel A, Seibel B, Pörtner HO, Huey RB. 2015. Ecophysiology. Climate change tightens a metabolic constraint on marine habitats. Science. 348(6239):1132–1135. doi:10.1126/science.aaa1605.

Dillon WP, Klitgord KD, Paull CK. 1983. Mesozoic development and structure of the continental margin off South Carolina. In: Gohn GS, editor. Studies related to the Charleston, South Carolina, earthquake of 1886. Tectonics and seismicity. Washington (DC): U.S. Geological Survey. p. 27.

Dillon WP, Popenoe P. 1988. The Blake Plateau Basin and Carolina Trough. In: Sheridan RE, Grow JA, editors. The Atlantic continental margin. Boulder (CO): Geological Society of America. p. 291–328.

Distel DL, Lane DJ, Olsen GJ, Giovannoni SJ, Pace B, Pace NR, Felbeck H. 1988. Sulfur-oxidizing bacterial endosymbionts: analysis of phylogeny and specificity by 16S rRNA sequences. Journal of Bacteriology. 170(6):2506–2510.

Djurhuus A, Closek CJ, Kelly RP, Pitz KJ, Michisaki RP, Starks HA, Walz KR, Andruszkiewicz EA, Olesin E, Hubbard K, et al. 2020. Environmental DNA reveals seasonal shifts and potential interactions in a marine community. Nature Communications. 11:254.

Djurhuus A, Pitz K, Sawaya NA, Rojas-Márquez J, Michaud B, Montes E. 2018. Evaluation of marine zooplankton community structure through environmental DNA metabarcoding. Limnology and Oceanography. Methods. 16:209–221.

Dodds LA, Roberts JM, Taylor AC, Marubini F. 2007. Metabolic tolerance of the cold-water coral *Lophelia pertusa* (Scleractinia) to temperature and dissolved oxygen change. Journal of Experimental Marine Biology and Ecology. 349:205–214.

Doney S, Ruckelshaus M, Duffy J, Barry J, Chan F, English C, Galindo H, Grebmeier J, Hollowed A, Knowlton N, et al. 2012. Climate change impacts on marine ecosystems. Annual Review of Marine Science. 4:11–37. doi:10.1146/annurev-marine-041911-111611.

Donner SD, Skirving WJ, Little CM, Oppenheimer M, Hoegh-Guldberg O. 2005. Global assessment of coral bleaching and required rates of adaptation under climate change. Global Change Biology. 11:2251–2265.

Dorey N, Gjelsvik Ø, Kutti T, Büscher JV. 2020. Broad thermal tolerance in the cold-water coral *Lophelia pertusa* from Arctic and Boreal Reefs. Frontiers in Physiology. 10:1636.

Doughty CL, Quattrini AM, Cordes EE. 2014. Insights into the population dynamics of the deep-sea coral genus Paramuricea in the Gulf of Mexico. Deep Sea Research Part II: Topical Studies in Oceanography. 99:71–82. doi:10.1016/j.dsr2.2013.05.023.

Dray S, Dufour AB. 2007. The ade4 package: implementing the duality diagram for ecologists. Journal of Statistical Software. 22:1–20.

Drazen JC, Sutton TT. 2017. Dining in the deep: the feeding ecology of deep-sea fishes. Annual Review of Marine Science. 9:337–366.

Duineveld G, Lavaleye M, Berghuis E, de Wilde P. 2001. Activity and composition of the benthic fauna in the Whittard Canyon and the adjacent continental slope (NE Atlantic). Oceanologica Acta. 24(1):69–83.

Duineveld GCA, Jeffreys RM, Lavaleye MSS, Davies AJ, Bergman MJN, Watmough T, Witbaard R. 2012. Spatial and tidal variation in food supply to shallow cold-water coral reefs of the Mingulay Reef complex (Outer Hebrides, Scotland). Marine Ecology Progress Series. 444:97–115.

Duineveld GCA, Lavaleye MSS, Bergman MJN, de Stigter H, Mienis F. 2007. Trophic structure of a cold-water coral mound community (Rockall Bank, NE Atlantic) in relation to the near-bottom particle supply and current regime. Bulletin of Marine Science. 81(3):449–467.

Dullo WC, Flögel S, Rüggeberg A. 2008. Cold-water coral growth in relation to the hydrography of the Celtic and Nordic European continental margin. Marine Ecology Progress Series. 371:165–176.

Duperron S, Lorion J, Samadi S, Gros O, Gaill F. 2009. Symbioses between deep-sea mussels (mytilidae: Bathymodiolinae) and chemosynthetic bacteria: diversity, function and evolution. Comptes Rendus Biologies. 332(2-3):298–310.

Duperron S, Sibuet M, MacGregor BJ, Kuypers MM, Fisher CR, Dubilier N. 2007. Diversity, relative abundance and metabolic potential of bacterial endosymbionts in three *Bathymodiolus* mussel species from cold seeps in the Gulf of Mexico. Environmental Microbiology. 9(6):1423–1438.

Eaton DA, Overcast I. 2020. ipyrad: interactive assembly and analysis of RADseq datasets. Bioinformatics. 36(8):2592–2594.

Eckelbarger KJ, Tyler PA, Langton RW. 1998. Gonadal morphology and gametogenesis in the sea pen *Pennatula aculeata* (Anthozoa: Pennatulacea) from the Gulf of Maine. Marine Biology. 132:677–690.

Edwards LR, Chen JH, Wasserburg GJ. 1987. ^{238}U–^{234}U–^{230}Th–^{232}Th systematics and the precise measurement of time over the past 500,000 years. Earth and Planetary Science Letters. 81(2-3):175–192.

EEZ-SCAN 87. 1991. Atlas of the U.S. Exclusive Economic Zone, Atlantic continental margin. Washington (DC): U.S. Geological Survey. 174 p.

Elith J, Ferrier S, Huettmann F, Leathwick J. 2005. The evaluation strip: a new and robust method for plotting predicted responses from species distribution models. Ecological Modelling. 186(3):280–289.

Elvert M, Boetius A, Knittel K, Jørgensen BB. 2003. Characterization of specific membrane fatty acids as chemotaxonomic markers for sulfate-reducing bacteria involved in anaerobic axidation of methane. Geomicrobiology Journal. 20(4):403–419.

Elvert M, Hopmans EC, Treude T, BoetiusA, Suess E. 2005. Spatial variations of methanotrophic consortia at cold methane seeps: implications from a high-resolution molecular and isotopic approach. Geobiology. 3(3):195–209.

Epstein S, Buchsbaum R, Lowenstam HA, Urey HC. 1953. Revised carbonate-water isotopic temperature scale. Bulletin of the Geological Society of America. 64(11):1315–1326.

Erickson KL, Pentico A, Quattrini AM, McFadden CS. 2021. New approaches to species delimitation and population structure of anthozoans: two case studies of octocorals using ultraconserved elements and exons. Molecular Ecology Resources. 21(1):78–92.

Estaki M, Jiang L, Bokulich NA, McDonald D, Gonzáles A, Kosciolek T, Martino C, Zhu Q, Birmingham A, Vázquez-Baeza Y, et al. 2020. QIIME2 enables comprehensive end-to-end analysis of diverse microbiome data and comparative studies with publicly available data. Current Protocols in Bioinformatics. 70:e100.

Etnoyer P, Warrenchuk J. 2007. A catshark nursery in a deep gorgonian field in the Mississippi Canyon, Gulf of Mexico. Bulletin of Marine Science. 81:553–559.

Ewing J, Ewing M, Leyden R. 1966. Seismic-profiler survey of Blake Plateau. AAPG Bulletin. 50(9):1948–1971.

Excoffon AC, Acuña FH, Zamponi MO, Genzano GN. 2004. Reproduction of the temperate octocoral *Tripalea clavaria* (Octocorallia: Anthothelidae) from sublittoral outcrops off Mar del Plata, Argentina. Journal of the Marine Biological Association of the United Kingdom. 84(4):695–699.

Eyring V, Bony S, Meehl GA, Senior CA, Stevens B, Stouffer RJ, Taylor KE.2016. Overview of the Coupled Model Intercomparison Project Phase 6 (CMIP6) experimental design and organization. Geoscientific Model Development. 9:1937–1958. doi:10.5194/gmd-9-1937-2016.

Faircloth BC. 2013. Illumiprocessor: a trimmomatic wrapper for parallel adapter and quality trimming.

Faircloth BC. 2016. PHYLUCE is a software package for the analysis of conserved genomic loci. Bioinformatics. 32(5):786–788.

Faircloth BC, Sorenson L, Santini F, Alfaro ME. 2013. A phylogenomic perspective on the radiation of ray-finned fishes based upon targeted sequencing of ultraconserved elements (UCEs). PLoS ONE. 8(6):e65923.

Faith DP. 1992. Conservation evaluation and phylogenetic diversity. Biological Conservation. 61:1–10.

Faith DP. 2002. Quantifying biodiversity: a phylogenetic perspective. Conservation Biology. 16:248–252.

Fanelli E, Cartes JE, Rumolo P, Sprovieri M. 2009. Food-web structure and trophodynamics of mesopelagic-suprabenthic bathyal macrofauna of the Algerian basin based on stable isotopes of carbon and nitrogen. Deep Sea Research Part I: Oceanographic Research Papers. 56(9):1504–1520.

Feehan KA, Waller RG, Häussermann V. 2019. Highly seasonal reproduction in deep-water emergent *Desmophyllum dianthus* (Scleractinia: Caryophyllidae) from the Northern Patagonian Fjords. Marine Biology. 166:52.

Fernandez-Arcaya U, Ramirez-Llodra E, Aguzzi J, Allcock AL, Davies JS, Dissanayake A, Harris P, Howell K, Huvenne VAI, Macmillan-Lawler M, et al. 2017. Ecological role of submarine canyons and need for canyon conservation: a review. Frontiers in Marine Science. 4(5).

Ferrier-Pagès C, Rottier C, Beraud E, Levy O. 2010. Experimental assessment of the feeding effort of three scleractinian coral species during a thermal stress: effect on the rates of photosynthesis. Journal of Experimental Marine Biology and Ecology. 390:118–124.

Findlay HS, Hennige SJ, Wicks LC, Navas JM, Woodward EMS, Roberts JM. 2014. Fine-scale nutrient and carbonate system dynamics around cold-water coral reefs in the northeast Atlantic. Scientific Reports. 4:3671.

Fisher CR. 1993. Oxidation of methane by deep-sea mytilids in the Gulf of Mexico. In: Oreland RS, editor. Biogeochemistry of global change: radiatively active trace gasses. New York (NY): Chapman and Hall. p. 606–618.

Fisher CR, MacDonald IR, Sassen R, Young CM, Macko SA, Hourdez S, Carney RS, Joye S, McMullin E. 2000. Methane ice worms: *Hesiocaeca methanicola* colonizing fossil fuel reserves. Naturwissenschaften. 87:184–187.

Flint H, Waller R, Tyler P. 2007. Reproductive ecology of *Fungiacyathus marenzelleri* from 4100 m depth in the Northeast Pacific Ocean. Marine Biology. 151:843–849.

Follett CL, Repeta DJ, Rothman DH, Xu L, Santinelli C. 2014. Hidden cycle of dissolved organic carbon in the deep ocean. Proceedings of the National Academy of Sciences. 111(47):16706–16711.

Folmer O, Black M, Hoeh W, Lutz R, Vrijenhoek R. 1994. DNA primers for amplification of mitochondrial cytochrome c oxidase subunit I from diverse metazoan invertebrates. Molecular Marine Biology and Biotechnology. 3(5):294–299.

Forget A, Fredette V. 1962. Sodium azide selective medium for the primary isolation of anaerobic bacteria. Journal of Bacteriology. 83:1217–1223.

Fossing H, Jorgensen BB. 1989. Measurement of bacterial sulfate reduction in sediments: evaluation of a single-step chromium reduction method. Biogeochemistry. 8:205–222.

France S, Hoover LL. 2001. Analysis of variation in mitochondrial DNA sequences (ND3, ND4L, MSH) among Octocorallia (=Alcyonaria) (Cnidaria: Anthozoa). Bulletin of the Biological Society of Washington. 10:110–118.

Fratantoni PS, Pickart RS. 2007. The western North Atlantic shelfbreak current system in summer. Journal of Physical Oceanography. 37(10):2509–2533.

Freiwald A, Fosså JH, Grehan A, Koslow T, Roberts JM. 2004. Cold-water coral reefs. Cambridge (UK): UNEP-WCMC. 84 p.

Freiwald A, Henrich R, Pätzold J. 1997. Anatomy of a deep-water coral reef mound from Stjernsund, West-Finnmark, Northern Norway. SEPM. 56:141–162.

Freiwald A, Wilson JB. 1998. Taphonomy of modern deep, cold-temperate water coral reefs. Historical Biology. 13(1):37–52.

Fry B. 2007. Coupled N, C and S stable isotope measurements using a dual-column gas chromatography system. Rapid Communications in Mass Spectrometry. 21:750–756.

Fumagalli M. 2013. Assessing the effect of sequencing depth and sample size in population genetics inferences. PLoS ONE. 8(11):e79667. doi:10.1371/ journal.pone.0079667.

Gage JD, Tyler PA. 1991. Deep-sea biology: a natural history of organisms at the deep-sea floor. Cambridge (UK): Cambridge University Press.

Gaines SD, Gaylord B, Gerber LR, Hastings A, Kinlan BP. 2007. Connecting places: the ecological consequences of dispersal in the sea. Oceanography. 20(3):90–99.

Galand PE, Chapron L, Meistertzheim A-L, Peru E, Lartaud F. 2018. The effect of captivity on the dynamics of active bacterial communities differs between two deep-sea coral species. Frontiers in Microbiology. 9:2565.

Galand PE, Remize M, Meistertzheim A-L, Pruski AM, Peru E, Suhrhoff TJ, Le Bris N, Vétion G, Lartaud F. 2020. Diet shapes cold-water corals bacterial communities. Environmental Microbiology. 22(1):354–368.

Galaska M, Liu G, Quattrini A, West D, Bracco A, Erickson K, Herrera S. 2021. Seascape genomics reveals metapopulation connectivity network of *Paramuricea biscaya* in the northern Gulf of Mexico. Frontiers in Marine Science. 8:790929.

Galkiewicz JP, Pratte ZA, Gray MA, Kellogg CA. 2011. Characterization of culturable bacteria isolated from the cold-water coral *Lophelia pertusa*. FEMS Microbiology Ecology. 77(2):333–346.

Galkiewicz JP, Stellick SH, Gray MA, Kellogg CA. 2012. Cultured fungal associates from the deep-sea coral *Lophelia pertusa*. Deep Sea Research Part I: Oceanographic Research Papers. 67:12–20.

García Molinos J, Schoeman DS, Brown CJ, Burrows MT. 2019. VoCC: An R package for calculating the velocity of climate change and related climatic metrics. Methods in Ecology and Evolution. 10(12):2195–2202.

Gates-Rector SD, Blanton TN. 2019. The Powder Diffraction File: a quality materials characterization database. Powder Diffraction. 34:352–360.

GEBCO Compilation Group. 2021. GEBCO 2021 grid. Liverpool (UK): NERC EDS British Oceanographic Data Centre NOC. doi:10.5285/c6612cbe-50b3-0cff-e053-6c86abc09f8f.

Geller J, Meyer C, Parker M, Hawk H. 2013. Redesign of PCR primers for mitochondrial cytochrome c oxidase subunit I for marine invertebrates and application in all-taxa biotic surveys. Molecular Ecology Resources. 13:851–861.

Georgian SE, DeLeo D, Durkin A, Gomez CE, Kurman M, Lunden JJ, Cordes EE. 2016. Oceanographic patterns and carbonate chemistry in the vicinity of cold-water coral reefs in the Gulf of Mexico: implications for resilience in a changing ocean. Limnology and Oceanography. 61:648–665. doi:10.1002/lno.10242.

Georgian SE, Dupont S, Kurman M, Butler A, Stromberg SM, Larsson AI, Cordes EE. 2016. Biogeographic variability in the physiological response of the cold-water coral *Lophelia pertusa* to ocean acidification. Marine Ecology-An Evolutionary Perspective. 37(6):1345–1359.

Georgian SE, Shedd W, Cordes EE. 2014. High-resolution ecological niche modelling of the cold-water coral *Lophelia pertusa* in the Gulf of Mexico. Marine Ecology Progress Series. 506:145–161.

Gibbs M, Leduc D, Nodder SD, Kingston A, Swales A, Rowden AA, Mountjoy J, Olsen G, Ovenden R, Brown J, Bury S, et al. 2020. Novel application of a compound-specific stable isotopes (CSSI) tracking technique demonstrates connectivity between terrestrial and deep-sea ecosystems via submarine canyons. Frontiers in Marine Science. 7:608. doi:10.3389/fmars.2020.00608.

Gignoux-Wolfsohn SA, Aronson FM, Vollmer SV. 2017. Complex interactions between potentially pathogenic, opportunistic, and resident bacteria emerge during infection on a reef-building coral. FEMS Microbiology Ecology. 93(7). doi:10.1093/femsec/fix080.

Gilhooly WPI, Carney RS, Macko SA. 2007. Relationships between sulfide-oxidizing bacterial mats and their carbon sources in northern Gulf of Mexico cold seeps. Organic Geochemistry. 38(3):380–393.

Gillooly JF. 2001. Effects of size and temperature on metabolic rate. Science. 293:2248–2251.

Girard F, Fu B, Fisher CR. 2016. Mutualistic symbiosis with ophiuroids limited the impact of the Deepwater Horizon oil spill on deep-sea octocorals. Marine Ecology Progress Series. 549:89–98.

Gold S. 2020. The isolation, identification, and characterization of bacteria associated with the deep-sea coral *Lophelia pertusa* [thesis]. Cullowhee (NC): Western Carolina University.

Gómez CE, Wickes L, Deegan D, Etnoyer PJ, Cordes EE. 2018. Growth and feeding of deep-sea coral *Lophelia pertusa* from the California margin under simulated ocean acidification conditions. PeerJ. 6:e5671.

Gori A, Ferrier-Pagès C, Hennige SJ, Murray F, Rottier C, Wicks LC, Roberts JM. 2016. Physiological response of the cold-water coral *Desmophyllum dianthus* to thermal stress and ocean acidification. PeerJ. 4:e1606.

Gori A, Reynaud S, Orejas C, Ferrier-Pagès C. 2015. The influence of flow velocity and temperature on zooplankton capture rates by the cold-water coral *Dendrophyllia cornigera*. Journal of Experimental Marine Biology and Ecology. 466:92–97.

Govindarajan AF, Francolini RD, Jech JM, Lavery AC, Llopiz JK, Wiebe PH, Zhang W. 2021. Exploring the use of environmental DNA (eDNA) to detect animal taxa in the mesopelagic zone. Frontiers in Ecology and Evolution. 9:574877.

Grasshoff K, Ehrhardt M, Kremling K. 1983. Methods of seawater analysis. 2nd edition. Weinheim(DE): Wiley. 419 p.

Gray JS, Elliott M. 2009. Ecology of marine sediments: from science to management. Oxford University Press.

Gražulis S, Daškevič A, Merkys A, Chateigner D, Lutterotti L, Quirós M, Serebryanaya NR, Moeck P, Downs RT, LeBail A. 2012. Crystallography Open Database (COD): an open-access collection of

crystal structures and platform for world-wide collaboration. Nucleic Acids Research. 40:D420–D427. doi:10.1093/nar/gkr900.

Griggs GB, Carey AG, Kulm LD. 1969. Deep-sea sedimentation and sediment-fauna interaction in Cascadia Channel and on Cascadia Abyssal Plain. Deep Sea Research. 16(2):157–166.

Grossman E, Ku TL. 1986. Oxygen and carbon isotope fractionation in biogenic aragonite: temperature effects. Isotope Geoscience. 59:59–74.

Grupe1 BM, Krach ML, Pasulka AL, Maloney JM, Levin LA, Frieder CA. 2015. Marine Ecology. 36:91–108.

Guinotte JM, Georgian S, Kinlan BP, Poti M, Davies AJ. 2017. predictive habitat modeling for deep-sea corals in U.S. waters. In: Hourigan TF, Etnoyer PJ, Cairns SD, editors. The state of deep-sea coral and sponge ecosystems of the United States. Silver Spring (MD). 24 p. Report No.: NOAA Technical Memorandum NMFS-OHC-4.

Guinotte JM, Orr J, Cairns S, Freiwald A, Morgan L, George R. 2006. Will human-induced changes in seawater chemistry alter the distribution of deep-sea scleractinian corals? Frontiers in Ecology and the Environment 4:141–146.

Guisan A, Thuiller W, Zimmermann NE. 2017. Habitat suitability and distribution models: with applications in R. Cambridge University Press.

Guppy R, Bythell JC. 2006. Environmental effects on bacterial diversity in the surface mucus layer of the reef coral *Montastraea faveolata*. Marine Ecology Progress Series. 328:133–142.

Haalboom S, de Stigter H, Duineveld G, van Haren H, Reichart G-J, Mienis F. 2021. Suspended particulate matter in a submarine canyon (Whittard Canyon, Bay of Biscay, NE Atlantic Ocean): assessment of commonly used instruments to record turbidity. Marine Geology. 434:106439.

Hansson L, Agis M, Maier C, Weinbauer MG. 2009. Community composition of bacteria associated with cold-water coral *Madrepora oculata*: within and between colony variability. Marine Ecology Progress Series. 397:89–102.

Hanz U, Wienberg C, Hebbeln D, Duineveld G, Lavaleye M, Juva K, Dullo WC, Freiwald A, Tamborrino L, Reichart GJ, et al. 2019. Environmental factors influencing benthic communities in the oxygen minimum zones on the Angolan and Namibian margins. Biogeosciences. 16(22):4337–4356.

Hare JA, Cowen RK. 1996. Transport mechanisms of larval and pelagic juvenile bluefish (*Pomatomus saltatrix*) from South Atlantic Bight spawning grounds to Middle Atlantic Bight nursery habitats. Limnology and Oceanography. 41(6):1264–1280.

Harris PT, Whiteway T. 2011. Global distribution of large submarine canyons: geomorphic differences between active and passive continental margins. Marine Geology. 285:69–86.

Harris RMB, Beaumont LJ, Vance TR, Tozer C, Remenyi TA, Perkins-Kirkpatrick SE, Mitchell PJ, Nicotra AB, McGregor S, Andrew NR, et al. 2018. Biological responses to the press and pulse of climate trends and extreme events. Nature Climate Change. 8:579–587. doi:10.1038/s41558-018-0187-9.

Harrison P. 2011. Sexual reproduction of scleractinian corals. In: Dubinsky Z, Stambler N, editors. Coral reefs: an ecosystem in transition. New York (NY): Springer. p. 59–85.

Harrold C, Light K, Lisin S. 1998. Organic enrichment of submarine-canyon and continental-shelf benthic communities by macroalgal drift imported from nearshore kelp forests. Limnology and Oceanography. 43(4):669–678.

Hashimoto J, Okutani T. 1994. Four new mytilid mussels associated with deepsea chemosynthetic communities around Japan. Venus. 53(2):61–83.

Hazel JE, Edwards LE, Bybell LM. 1984. Significant unconformities and the hiatuses represented by them in the Paleogene of the Atlantic and Gulf Coastal Province. In: Schlee JS, editor. Interregional unconformities and hydrocarbon accumulations. Tulsa (OK): American Association of Petroleum Geologists. p. 59-66.

Heaton TJ, Köhler P, Butzin M, Bard E, Reimer RW, Austin WEN, Bronk Ramsey C, Grootes PM, Hughen KA, Kromer B, Reimer PJ, Adkins J, Burke A, Cook MS, Olsen J, Skinner LC. 2020. Marine20—the marine radiocarbon age calibration curve (0-55,000 cal BP). Radiocarbon. 62(4):779–820. doi:10.1017/RDC.2020.68.

Hebbeln D, Wienberg C, Dullo W-C, Freiwald A, Mienis F, Orejas C, Titschack J. 2020. Cold-water coral reefs thriving under hypoxia. Coral Reefs. 39:853–859. doi:10.1007/s00338-020-01934-6.

Hecker B. 1985. Fauna from a cold sulfur-seep in the Gulf of Mexico: comparison with hydrothermal vent communities and evolutionary implications. Bulletin of the Biological Society of Washington. 6:465–473.

Hecker B. 1990.Variation in megafaunal assemblages on the continental margin south of New England. Deep Sea Research Part A: Oceanographic Research Papers. 37(1):37–57.

Hecker B, Logan DT, Gandarillas FE, Gibson PR. 1983. Megafaunal assemblages in Lydonia Canyon, Baltimore Canyon, and selected slope areas. In: Canyon and Slope Processes Study, final report prepared for the U.S. Department of the Interior. Washington (DC): Minerals Management Service.

Heiderich J, Todd RE. 2020. Along-stream evolution of gulf stream volume transport. Journal of Physical Oceanography. 50:2251–2270.

Heijs SK, Aloisi G, Bouloubassi I, Pancost RD, Pierre C, Damsté JSS, Gottschal JC, Van Elsas JD, Forney LJ. 2006. Microbial community structure in three deep-sea carbonate crusts. Microbial Ecology. 52(3):451–462.

Hein J, Koschinsky A, Mikesell M, Mizell K, Glenn C, Wood R. 2016. Marine phosphorites as potential resources for heavy rare earth elements and yttrium. Minerals. 6(3):88. doi:10.3390/min6030088.

Henderson G, Burton K. 1999. Using ($^{234}U/^{238}U$) to assess diffusion rates of isotope tracers in ferromanganese crusts. Earth and Planetary Science Letters. 170(3):169–179. doi:10.1016/S0012-821X(99)00104-1.

Henderson MJ, Huff DD, Yoklavich MM. 2020. Deep-sea coral and sponge taxa increase demersal fish diversity and the probability of fish presence. Frontiers in Marine Science. 7:593844.

Hennige SJ, Wicks LC, Kamenos NA, Bakker DCE, Findlay HS, Dumousseaud C, Roberts JM. 2014. Short-term metabolic and growth responses of the cold-water coral *Lophelia pertusa* to ocean acidification. Deep Sea Research Part 2: Topical Studies in Oceanography. 99:27–35.

Hennige SJ, Wolfram U, Wickes L, Murray F, Roberts JM, Kamenos NA, Schofield S, Groetsch A, Spiesz EM, Aubin-Tam ME, et al. 2020. Crumbling reefs and cold-water coral habitat loss in a future ocean: evidence of "coralporosis" as an indicator of habitat integrity. Frontiers in Marine Science. 7:668. doi:10.3389/fmars.2020.00668.

Henry LA, Roberts JM. 2007. Biodiversity and ecological composition of macrobenthos on cold-water coral mounds and adjacent off-mound habitat in the bathyal Porcupine Seabight, NE Atlantic. Deep Sea Research Part I: Oceanographic Research Papers. 54:654–672. doi:10.1016/j.dsr.2007.01.005.

Hernandez-Agreda A, Leggat W, Bongaerts P, Ainsworth TD. 2016. The microbial signature provides insight into the mechanistic basis of coral success across reef habitats. mBio. 7(4):e00560-16.

Hernandez-Avila I, Guerro-Castro E, Bracho C, Rada M, Ocana FA, Pech D. 2018. Variation in species diversity of deep-water megafauna assemblages in the Caribbean across depth and ecoregions. PLoS ONE. 13(8):e0201269.

Herrera S, Baco A, Sánchez JA. 2010. Molecular systematics of the bubblegum coral genera (Paragorgiidae, *Octocorallia*) and description of a new deep-sea species. Molecular Phylogenetics and Evolution. 55:123–135.

Herrera S, Shank TM. 2016. RAD sequencing enables unprecedented phylogenetic resolution and objective species delimitation in recalcitrant divergent taxa. Molecular Phylogenetics and Evolution. 100:70–79.

Hessler RR, Smithey WM, Boudrias MA, Keller CH, Lutz RA, Childress JJ. 1988. Temporal change in megafauna at the Rose Garden hydrothermal vent (Galapagos Rift; eastern tropical Pacific). Deep Sea Research Part A: Oceanographic Research Papers. 35(10-11):1681–1709.

Hessler RR, Wilson GDF. 1983. The origin and biogeography of malacostracan crustaceans in the deep sea. Evolution, Time and Space: the Emergence of the Biosphere. 23:227–254.

Heyl T, Gilhooly WP, Chambers RM, Gilchrist GW, Macko SA, Ruppel CD, Van Dover CL. 2007. Characteristics of vesicomyid clams and their environment at the Blake Ridge cold seep, South Carolina, USA. Marine Ecology Progress Series. 339:169–184.

Hidaka K, Kawaguchi K, Murakami M, Takahashi M. 2001. Downward transport of organic carbon by diel migratory micronekton in the western equatorial pacific: its quantitative and qualitative importance. Deep Sea Research Part 1: Oceanographic Research Papers. 48(8):1923–1939.

Hijmans RJ. 2021. raster: geographic data analysis and modeling. R package version 3.4-13.

Hilário A, Metaxas A, Gaudron SM, Howell KL, Mercier A, Mestre NC, Ross, RE, Thurnherr AM, Young C. 2015. Estimating dispersal distance in the deep sea: challenges and applications to marine reserves. Frontiers in Marine Science. 2:6.

Hilbig B. 1994. Faunistic and zoogeographical characterization of the benthic infauna on the Carolina continental slope. Deep Sea Research Part II: Topical Studies in Oceanography. 41(4-6):929–950.

Hill L, Hector A, Hemery G, Smart S, Tanadini M, Brown N. 2017. Abundance distributions for tree species in Great Britain: a two-stage approach to modeling abundance using species distribution modeling and random forest. Ecology and Evolution. 7:1043– 1056. doi:10.1002/ece3.2661.

Hinrichs K, Boetius A. 2002. The anaerobic oxidation of methane: new insights in microbial ecology and biogeochemistry. In: Wefer G, Billett D, Hebbeln D, Jørgensen BB, Schlüter M, Weering TCE, editors. Ocean margin systems. Berlin (DE): Springer. p. 457–477.

Hoehler TM, Alperin MJ, Albert DB, Martens CS. 1994. Field and laboratory studies of methane oxidation in an anoxic marine sediment: evidence for a methanogen-sulfate reducer consortium. Global Biogeochemical Cycles. 8(4):451–463.

Holcomb P, Hoffpauir B, Hoyson M, Jackson D, Deerinck T, Marrs G, Dehoff M, Wu J, Ellisman M, Spirou G. 2013. Synaptic inputs compete during rapid formation of the calyx of Held: a new model system for neural development. Journal of Neuroscience. 33(32):12954–12969. doi:10.1523/JNEUROSCI.1087-13.

Holden NE. 1990. Total half-lives for selected nuclides. Pure and Applied Chemistry. 62:941–958.

Hollister CD. 1973. Atlantic Continental Shelf and slope of the United States; texture of surface sediments from New Jersey to southern Florida. Washington (DC): U.S. Geological Survey. 29 p. Report No.: Professional Paper 529-M.

Horn BKP. 1981. Hill shading and the reflectance map. Proceedings of the IEEE. 69:14–47.

Hornbach MJ, Lavier LL, Ruppel CD. 2007. Triggering mechanism and tsunamogenic potential of the Cape Fear Slide complex, US Atlantic margin. Geochemistry, Geophysics, Geosystems. 8(12).

Hourdez S, Weber RE, Green BN, Kenney JM, Fisher CR. 2002. Respiratory adaptations in a deep-sea orbiniid polychaete from Gulf of Mexico brine pool NR-1: metabolic rates and hemoglobin structure/function relationships. Journal of Experimental Biology. 205:1669–1681.

Hourigan TF, Cairns SD, Reed JK, Ross SW. 2017. Deep-sea coral taxa in the U.S. southeast region: depth and geographical distribution. Washington (DC): U.S. Department of Commerce, National Oceanic and Atmospheric Administration.

Houston KA, Haedrich RL. 1984. Abundance and biomass of macrobenthos in the vicinity of Carson Submarine Canyon, northwest Atlantic Ocean. Marine Biology. 82(3):301–305.

Hubbard DK. 1997. Reefs as dynamic systems. In: Birkeland EC, editor. Life and death of coral reefs. New York (NY): Springer. p 43–67.

Huisman J. 2017. Pedigree reconstruction from SNP data: parentage assignment, sibship clustering and beyond. Molecular Ecology Resources. 17(5):1009–1024.

Hung C-W, Huang K-H, Shih Y-Y, Lin Y-S, Chen H-H, Wang C-C, Ho C-Y, Hung C-C, Burdige DJ. 2016. Benthic fluxes of dissolved organic carbon from gas hydrate sediments in the northern South China Sea. Scientific Reports. 6:29597.

Hunt GL, Drinkwater KF. 2005. Background on the climatology, physical oceanography and ecosystems of the sub-Arctic seas: appendix to the ESSAS Science Plan. Plymouth (UK): GLOBEC International Project Office. 111 p. Report No.: GLOBEC Report 20.

Huntington KW, Eiler JM, Affek HP, Guo W, Bonifacie M, Yeung LY, Thiagarajan N, Passey B, Tripati A, Daëron M. 2009. Methods and limitations of 'clumped' CO_2 isotope (Delta47) analysis by gas-source isotope ratio mass spectrometry. Journal of Mass Spectrometry. 44(9):1318–1329.

Hurrel J, Holland M, Gent P, Ghan S, Kay J, Kushner P, Lamarque J-F, Large WG, Lawrence D, Lindsay K, et al. 2020. NCAR CESM1-CAM5-SE-HR model output prepared for CMIP6 HighResMIP hist-1950. Version 20210701. Earth System Grid Federation.

Huson D, Beier S, Flade I, Górska A, El-Hadidi M, Mitra S, Ruscheweyh H, Tappu R. 2016. Community edition - interactive exploration and analysis of large-scale microbiome sequencing data. PLoS Computational Biology. 12(6):e1004957. doi:10.1371/journal.pcbi.1004957.

Huvenne VAI, Tyler PA, Masson DG, Fisher EH, Hauton C, Hühnerbach V, Le Bas TP, Wolff GA. 2011. A picture on the wall: innovative mapping reveals cold-water coral refuge in submarine canyon. PLoS ONE, 6(12):e28755.

Iken K, Brey T, Wand U, Voigt J, Junghans P. 2001. Food web structure of the benthic community at the porcupine abyssal plain (NE Atlantic): a stable isotope analysis. Progress in Oceanography. 50(1-4):383–405.

Illumina. 2016. 16S metagenomic sequencing library preparation. Part# 15044223. Rev. B. support.illumina.com/documents/documentation/chemistry_documentation/16s/.

Jablonski D, Sepkoski Jr JJ, Bottjer DJ, Sheehan PM. 1983. Onshore-offshore patterns in the evolution of Phanerozoic shelf communities. Science. 222(4628):1123–1125.

Jaffey AH, Flynn KF, Glendenin LE, Bentley WC, Essling AM. 1971. Precision measurement of half-lives and specific activities of ^{235}U and ^{238}U. Physical Review C. 4:1889–1906.

Jahnke M, Casagrandi R, Melià P, Schiavina M, Schultz ST, Zane L, Procaccini G. 2017. Potential and realized connectivity of the seagrass *Posidonia oceanica* and their implication for conservation. Diversity and Distributions. 23:1423–1434. doi:10.1111/ddi.12633.

Jansen J, Hill NA, Dunstan PK, McKinlay J, Sumner MD, Post AL, Eléaume MP, Armand LK, Warnock JP, Galton-Fenzi BK, et al. 2018. Abundance and richness of key Antarctic seafloor fauna correlates with modelled food availability. Nature Ecology & Evolution. 2:71–80.

Jeffreys RM, Lavaleye MSS, Bergman MJN, Duineveld GCA, Witbaard R. 2011. Do abyssal scavengers use phytodetritus as a food resource? Video and biochemical evidence from the Atlantic and Mediterranean. Deep Sea Research Part I: Oceanographic Research Papers. 58(4):415–428.

Jeffreys RM, Wolff GA, Murty SJ. 2009. The trophic ecology of key megafaunal species at the Pakistan margin: evidence from stable isotopes and lipid biomarkers. Deep Sea Research Part I: Oceanographic Research Papers. 56(10):1816 –1833.

Jenness J. 2013. DEM Surface Tools. Jenness Enterprises. http://www.jennessent.com/arcgis/surface_area.htm

Jensen A, Frederiksen R. 1992. The fauna associated with the bank-forming deep-water coral *Lophelia pertusa* (Scleractinaria) on the Faroe shelf. Sarsia. 77(1):53–69.

Johannes R, Tepley L. 1974. Examination of feeding of the reef coral *Porites lobata* in situ using time lapse photography. Proceedings of the 2nd International Coral Reef Symposium. 1:127–131.

Johnson MP, White M, Wilson A, Würzberg L, Schwabe E, Folch H, Allcock AL. 2013. A vertical wall dominated by *Acesta excavata* and *Neopycnodonte zibrowii*, part of an under-sampled group of deep-sea habitats. PLoS ONE. 8(11):e79917.

Jombart T. 2008.. adegenet: a R package for the multivariate analysis of genetic markers. Bioinformatics. 24(11):1403–1405.

Jorgensen BB. 1978. A comparison of methods for the quantification of sulfate reduction in coastal marine sediments. Geomicrobiology Journal. 1(1):11–27.

Jorgensen BB. 1989. Sulfate reduction in marine sediments from the Baltic Sea-North Sea transition. Ophelia. 31(1):1–15.

Joseph C, Campbell KA, Torres ME, Martin RA, Pohlman JW, Riedel M, Rose K. 2013. Methane-derived authigenic carbonates from modern and paleoseeps on the Cascadia margin: mechanisms of formation and diagenetic signals. Palaeogeography, Palaeoclimatology, Palaeoecology. 390:52–67.

Joye SB. 2020. The geology and biogeochemistry of hydrocarbon seeps. Annual Review of Earth and Planetary Sciences. 48:205–231.

Joye SB, Boetius A, Orcutt BN, Montoya JP, Schulz HN, Erickson MJ, Lugo SK. 2004. The anaerobic oxidation of methane and sulfate reduction in Gulf of Mexico cold seeps. Chemical Geology. 205(3-4):219–238.

Joye SB, Bowles MW, Samarkin VA, Hunter KS, Niemann H. 2010. Biogeochemical signatures and microbial activity of different cold-seep habitats along the Gulf of Mexico deep slope. Deep Sea Research Part II: Topical Studies in Oceanography. 57(21-23):1990–2001.

Joye SB, Connell TL, Miller LG, Oremland RS, Jellison RS. 1999. Oxidation of ammonia and methane in an alkaline, saline, lake. Limnology and Oceanography. 44(1):178–188.

Juniper SK, Sibuet M. 1987. Cold seep benthic communities in Japan subduction zones: spatial organization, trophic strategies and evidence for temporal evolution. Marine Ecology Progress Series. 40(1):115–126.

Kahn AS, Yahel G, Chu JWF, Tunnicliffe V, Leys SP. 2015. Benthic grazing and carbon sequestration by deep water glass sponge reefs. Limnology and Oceanography. 60(1):78–88.

Kanehisa M, Sato Y. 2020. KEGG mapper for inferring cellular functions from protein sequences. Protein Science. 29(1):28–35.

Kaplan MB, Mooney TA. 2016. Coral reef soundscapes may not be detectable far from the reef. Scientific Reports. 6.

Kaplan M, Mooney T, Partan J, Solow A. 2015. Coral reef species assemblages are associated with ambient soundscapes. Marine Ecology Progress Series. 533:93–107. doi:10.3354/meps11382.

Karl DM, Beversdorf L, Bjorkman KM, Church MJ, Martinez A, Delong EF. 2008. Aerobic production of methane in the sea. Nature Geoscience. 1:473-478.

Kastner M, Elderfield H, Martin JB, Tarney J, Pickering KT, Knipe RJ, Dewey JF. 1991. Fluids in convergent margins: what do we know about their composition, origin, role in diagenesis and importance for oceanic chemical fluxes? Philosophical Transactions of the Royal Society of London. Series A: Physical and Engineering Sciences. 335(1638):243–259.

Katoh K, Misawa K, Kuma K, Miyata T. 2002. MAFFT: a novel method for rapid multiple sequence alignment based on a fast Fourier transform. Nucleic Acids Research. 30(14):3059–3066.

Katoh K, Standley DM. 2013. MAFFT multiple sequence alignment software version 7: improvements in performance and usability. Molecular Biology and Evolution. 30:772–780.

Keller GH, Lambert D, Rowe G, Staresinic N. 1973. Bottom currents in the Hudson Canyon. Science. 180(4082):181–183.

Kelley D, Richards C. 2020. oce: analysis of oceanographic data. [accessed November 24, 2020]. https://CRAN.R-project.org/package=oce.

Kellogg CA. 2019. Microbiomes of stony and soft deep-sea corals share rare core bacteria. Microbiome. 7:90.

Kellogg CA, Goldsmith DB, Gray MA. 2017. Biogeographic comparison of *Lophelia*-associated bacterial communities in the western Atlantic reveals conserved core microbiome. Frontiers in Microbiology. 8:796.

Kellogg CA, Goldsmith DB, Voelschow JJ. 2021. Coral microbiome preservation and extraction method comparison—raw data. Washington (DC): U.S. Geological Survey. doi:10.5066/P96GBWDM.

Kellogg CA, Lisle JT, Galkiewicz JP. 2009. Culture-independent characterization of bacterial communities associated with the cold-water coral *Lophelia pertusa* in the northeastern Gulf of Mexico. Applied and Environmental Microbiology. 75(8):2294–2303.

Kellogg CA, Pratte ZA. 2021. Unexpected diversity of *Endozoicomonas* in deep-sea corals. Marine Ecology Progress Series. 673:1–15. doi:10.3354/meps13844.

Kellogg CA, Ross SW, Brooke SD. 2016. Bacterial community diversity of the deep-sea octocoral *Paramuricea placomus*. PeerJ. 4:e2529. doi:10.7717/peerj.2529.

Kellogg CA, Voelschow JJ. 2021. Cold-water coral microbiomes (*Acanthogorgia* spp., *Desmophyllum dianthus*, and *Lophelia pertusa*) from the Gulf of Mexico and Atlantic Ocean off the southeast coast of the United States—raw data. Washington (DC): U.S. Geological Survey. doi:10.5066/P9Z1HPKR.

Kellogg CA, Voelschow JJ. 2023. Functional gene microarray data from cold-water corals (*Acanthogorgia* spp. *Desmophyllum dianthus*, *Desmophyllum pertusum*, and *Enallopsammia profunda*) from the Atlantic Ocean off the southeast coast of the United States—raw data. Washington (DC): U.S. Geological Survey. doi:10.5066/P9RPE8YX.

Kembel SW, Cowan PD, Helmus MR, Cornwell WK, Morlon H, Ackerly DD, Blomberg SP, Webb CO. 2010. Picante: R tools for integrating phylogenies and ecology. Bioinformatics. 26:1463–1464.

Kenney JF, Keeping ES. 1954. Mathematics of statistics, part one. Princeton (NJ): D. Van Nostrand Company, Inc. 348 p.

Kimes NE, Van Nostrand JD, Weil E, Zhou J, Morris PJ. 2010. Microbial functional structure of *Montastraea faveolata*, an important Caribbean reef-building coral, differs between healthy and yellow-band diseased colonies. Environmental Microbiology. 12(2):541–556.

Kinlan BP, Gaines SD, Lester SE. 2005. Propagule dispersal and the scales of marine community process. Diversity and Distributions. 11:139–148.

Kiriakoulakis K, Fischer E, Wolff GA, Freiwald A, Grehan A, Roberts JM. 2005. Lipids and nitrogen isotopes of two deep-water corals from the North-East Atlantic: initial results and implications for their nutrition. In: Freiwald A, Roberts JM, editors. Cold-water corals and ecosystems. Berlin (DE): Springer-Verlag. p. 715–729.

Kishishita M, Ushijima T, Ozaki Y, Ito Y. 1980. New medium for isolating Propionibacteria and its application to assay of normal flora and human facial skin. Applied Environmental Microbiology. 40(6):1100–1105.

Klages M, Boetius A, Christensen JP, Deubel H, Piepenburg D, Schewe I, Soltwedel T. 2003. The benthos of Arctic seas and its role for the carbon cycle at the seafloor. In: Stein R, Macdonald RW, editors. The organic carbon cycle in the arctic ocean. Heidelberg (DE): Springer. p. 139–167.

Knittel K, Boetius A. 2009. Anaerobic oxidation of methane: progress with an unknown process. Annual Review of Microbiology. 63(1)311–334.

Kochevar RE, Childress JJ, Fisher CR, Minnich E. 1992. The methane mussel: roles of symbiont and host in the metabolic utilization of methane. Marine Biology. 112(3):389–401.

Krumbein WC. 1934. Size frequency distribution of sediments. Journal of Sedimentary Petrology. 4:65–77.

Kruse J, Rennenberg H, Adams MA. 2011. Steps towards a mechanistic understanding of respiratory temperature responses: Tansley review. New Phytologist. 189:659–677.

Kumar S, Stecher G, Li M, Knyaz C, Tamura K. 2018. MEGA X: molecular evolutionary genetics analysis across computing platforms. Molecular Biology and Evolution. 35(6):1547–1549.

Lacroix F, Ilyina T, Mathis M, Laruelle GG, Regnier P. 2021. Historical increases in land-derived nutrient inputs may alleviate effects of a changing physical climate on the oceanic carbon cycle. Global Change Biology. 27:5491– 5513. doi:10.1111/gcb.15822.

Laliberté E, Lambers H, Burgess TI, Wright SJ. 2015. Phosphorus limitation, soil-borne pathogens and the coexistence of plant species in hyperdiverse forests and shrublands. New Phytologist. 206(2):507–521.

Laliberté E, Legendre P. 2010. A distance-based framework for measuring functional diversity from multiple traits. Ecology. 91(1):299–305.

Lange V, Böhme I, Hofmann J, Lang K, Sauter J, Schöne B, Paul P, Albrecht V, Andreas JM, Baier DM, et al. 2014. Cost-efficient high-throughput HLA typing by MiSeq amplicon sequencing. BMC Genomics. 15:63–63.

Laroche O, Kersten O, Smith CR, Goetze E. 2020. Environmental DNA surveys detect distinct metazoan communities across abyssal plains and seamounts in the western Clarion Clipperton Zone. Molecular Ecology. 29:4588–4604. doi:10.1111/mec.15484.

Larsson A. 2014. AliView: a fast and lightweight alignment viewer and editor for large datasets. Bioinformatics. 30:3276–3278.

Larsson A, Lundälv T, van Oevelen D. 2013. Skeletal growth, respiration rate and fatty acid composition in the cold-water coral *Lophelia pertusa* under varying food conditions. Marine Ecology Progress Series. 483:169–184.

Larsson A, Purser A. 2011. Sedimentation on the cold-water coral *Lophelia pertusa*: cleaning efficiency from natural sediments and drill cuttings. Marine Pollution Bulletin. 62(6):1159–1168.

Lawler SN, Kellogg CA, France SC, Clostio RW, Brooke SD, Ross SW. 2016. Coral-associated bacterial diversity is conserved across two deep-sea Anthothela species. Frontiers in Microbiology. 7:458.

Lawson CR, Hodgson JA, Wilson RJ, Richards SA. 2014. Prevalence, thresholds and the performance of presence–absence models. Methods in Ecology and Evolution. 5(1):54–64. doi:10.1111/2041-210X.12123.

Lawson T. 1991. Principles of biological filtration. In: Proceedings from the Aquaculture Symposium; 1991 Apr 4–6; Ithaca (NY).

Le Tissier MDA, Clayton B, Brown BE, Spencer Davis P. 1994. Skeletal correlates of density banding and an evaluation of radiography as used in sclerochronology. Marine Ecology Progress Series. 110:29–44.

Lee STM, Davy SK, Tang S-L, Kench PS. 2017. Water flow buffers shifts in bacterial community structure in heat-stressed Acropora muricata. Scientific Reports. 7:43600.

Lee TN, Yoder JA, Atkinson LP. 1991. Gulf Stream frontal eddy influence on productivity of the southeast U.S. Continental Shelf. Journal of Geophysical Research. 96(C12):22191–22205. doi:10.1029/91JC02450.

Legeckis RV. 1979. Satellite observations of the influence of bottom topography on the seaward deflection of the Gulf Stream off Charleston, South Carolina. Journal of Physical Oceanography. 9:483–497.

Leonte M, Kessler JD, Kellermann MY, Arrington EC, Valentine DL, Sylva SP. 2017. Rapid rates of aerobic methane oxidation at the feather edge of hydrate stability in the waters of Hudson Canyon, US Atlantic Margin. Geochimica et Cosmochimica Acta. 204:375–387.

Leray M, Ho S, Lin I, Machida RJ. 2018. MIDORI server: a webserver for taxonomic assignment of unknown metazoan mitochondrial encoded sequences using a curated database. Bioinformatics. 34(21):3753–3754.

Leray M, Yang JY, Meyer CP, Mills SC, Agudelo N, Ranwez V, Boehm JT, Machida RJ. 2013. A new versatile primer set targeting a short fragment of the mitochondrial COI region for metabarcoding metazoan diversity: application for characterizing coral reef fish gut contents. Frontiers in Zoology. 10:34. doi:10.1186/1742-9994-10-34.

Leterme SC, Pingree RD. 2008. The Gulf Stream, rings and North Atlantic eddy structures from remote sensing (Altimeter and SeaWiFS). Journal of Marine Systems. 69:177–190.

Levin LA. 2005. Ecology of cold seep sediments: interactions of fauna with flow, chemistry and microbes. Oceanography and Marine Biology - An Annual Review. 43:1–46.

Levin LA, Baco AR, Bowden DA, Colaco A, Cordes EE, Cunha MR, Demopoulos AWJ, Gobin J, Grupe BM, Le J, et al. 2016. Hydrothermal vents and methane seeps: rethinking the sphere of influence. Frontiers in Marine Science. 3:72. doi:10.3389/fmars.2016.00072.

Levin LA, Etter RJ, Rex MA, Gooday AJ, Smith CR, Pineda J, Stuart CT, Hessler RR, Pawson D. 2001. Environmental influences on regional deep-sea species diversity. Annual Review of Ecology and Systematics. 32:51–93.

Levin LA, Le Bris N. 2015. The deep ocean under climate change. Science. 350:766–768.

Levin LA, Mendoza GF. 2007. Community structure and nutrition of deep methane-seep macrobenthos from the North Pacific (Aleutian) Margin and the Gulf of Mexico (Florida Escarpment). Marine Ecology. 28:131–151.

Levin LA, Sibuet M. 2012. Understanding continental margin biodiversity: a new imperative. Annual Review of Marine Science. 4(2012):79.

Levin LA, Ziebis W, Mendoza GF, Bertics VJ, Washington T, Gonzalez J, Thurber AR, Ebbe B, Lee RW. 2013. Ecological release and niche partitioning under stress: lessons from dorvilleid polychaetes in sulfidic sediments at methane seeps. Deep Sea Research Part II. 92:214–233.

Levin LA, Ziebis W, Mendoza GF, Growney VA, Tryon MD, Brown KM, Mahn C, Gieskes JM, Rathburn AE. 2003. Marine Ecology Progress Series. 265:123–139.

Levin LA, Ziebis W, Mendoza GF, Growney-Cannon V, Walther S. 2006. Recruitment response of methane-seep macrofauna to sulfide-rich sediments: an in situ experiment. Journal of Experimental Marine Biology and Ecology. 330:132–150.

Li H. 2013. Aligning sequence reads, clone sequences and assembly contigs with BWA-MEM. arXiv preprint. arXiv:1303.3997.

Li H, Durbin R. 2009. Fast and accurate short read alignment with Burrows–Wheeler transform. Bioinformatics. 25(14):1754–1760.

Liaw A, Wiener M. 2002. Classification and regression by randomForest. R News. 2/3:18–22.

Lin TH, Chen C, Watanabe HK, Kawagucci S, Yamamoto H, Akamatsu T. 2019. Using soundscapes to assess deep-sea benthic ecosystems. Trends in Ecology & Evolution. 34(12):1066–1069.

Little CT, Vrijenhoek RC. 2003. Are hydrothermal vent animals living fossils?. Trends in Ecology & Evolution. 18(11):582–588.

Littman RA, Willis BL, Pfeffer C, Bourne DG. 2009. Diversities of coral-associated bacteria differ with location, but not species, for three acroporid corals on the Great Barrier Reef. FEMS Microbiology Ecology. 68:152–163.

Lohrmann A. 2001. Monitoring sediment concentration with acoustic backscattering instruments. 5 p. Report No.: Nortek Tehcnical Note 003.

Loyd SJ, Sample J, Tripati RE, Defliese WF, Brooks K, Hovland M, Torres M, Marlow J, Hancock LG, Martin R, et al. 2016. Methane seep carbonates yield clumped isotope signatures out of equilibrium with formation temperatures. Nature Communications. 7(1):12274.

Lunden JJ, Georgian SE, Cordes EE. 2013. Aragonite saturation states at cold-water coral reefs structured by *Lophelia pertusa* in the Northern Gulf of Mexico. Limnology and Oceanography. 58:1147–1147. doi:10.4319/lo.2013.58.1.0354.

Lunden JJ, McNicholl CG, Sears CR, Morrison CL, Cordes EE. 2014. Acute survivorship of the deep sea coral *Lophelia pertusa* from the Gulf of Mexico under acidification, warming, and deoxygenation. Frontiers in Marine Science. 1(78):1–12.

Luu K, Bazin E, Blum MGB. 2017. pcadapt: an R package to perform genome scans for selection based on principal component analysis. Molecular Ecology Resources. 17(1):67–77.

MacAvoy SE, Carney RS, Fisher CR, Macko SA. 2002. Use of chemosynthetic biomass by large, mobile, benthic predators in the Gulf of Mexico. Marine Ecology Progress Series. 225:65–78.

MacAvoy SE, Morgan E, Carney RS, Macko SA. 2008. Chemoautotrophic production incorporated by heterotrophs in Gulf of Mexico hydrocarbon seeps: an examination of mobile benthic predators and seep residents. Journal of Shellfish Research. 27(1):153–161.

MacDonald IR, Reilly JF, Guinasso Jr NL, Brooks JM, Carney RS, Bryant WA, Bright TJ. 1990. Chemosynthetic mussels at a brine-filled pockmark in the northern Gulf of Mexico. Science. 248(4959):1096–1100.

MacGregor BJ, Biddle JF, Harbort C, Matthysse AG, Teske A. 2013. Sulfide oxidation, nitrate respiration, carbon acquisition and electron transport pathways suggested by a draft genome of a single orange Guaymas Basin Beggiatoa (Cand. Maribeggiatoa) sp. filament. Marine Genomics. 11:53–65.

Maciolek N, Grassle JF, Boehm PD, Dade B, Brown B. 1986. Study of biological processes on the US mid-Atlantic slope and rise. Second interim report. Report for May 1984–September 1985. Duxbury (MA): Battelle New England Marine Research Lab.

Maciolek N, Grassle JF, Hecker B, Boehm PD, Brown B. 1987. Study of biological processes on the US mid-Atlantic slope and rise. Volume 1. Executive summary. Report for March 1984–March 1986. Duxbury (MA): Battelle Ocean Sciences.

Maddison WP, Maddison DR. 2019. Mesquite: a modular system for evolutionary analysis. Version 2.6.

Mah CL. 2015. A new Atlantic species of *Evoplosoma* with taxonomic summary and in situ observations of Atlantic deep-sea corallivorous Goniasteridae (Valvatida; Asteroidea). Marine Biodiversity Records. 8:e5.

Maher RL, Rice MM, McMinds R, Burkepile DE, Vega Thurber R. 2019. Multiple stressors interact primarily through antagonism to drive changes in the coral microbiome. Scientific Reports. 9:6834.

Maier C, de Kluijver A, Agis M, Brussaard CPD, van Duyl FC, Weinbauer MG. 2011. Dynamics of nutrients, total organic carbon, prokaryotes and viruses in onboard incubations of cold-water corals. Biogeosciences. 8(9):2609–2620.

Maier C, Weinbauer MG, Gattuso JP. 2019. Fate of Mediterranean scleractinian cold-water corals as a result of global climate change. a synthesis. In: Orejas C, Jiménez C, editors. Mediterranean cold-water corals: past, present and future. Coral reefs of the world. Cham (CH): Springer International Publishing. p. 517–529.

Maier SR, Bannister RJ, van Oevelen D, Kutti T. 2020. Seasonal controls on the diet, metabolic activity, tissue reserves and growth of the cold-water coral *Lophelia pertusa*. Coral Reefs. 39:173–187.

Maier SR, Kutti T, Bannister RJ, van Breugel P, van Rijswijk P, van Oevelen D. 2019. Survival under conditions of variable food availability: resource utilization and storage in the cold-water coral *Lophelia pertusa*. Limnology and Oceanography. 64:1651–1671.

Mandal S, Treuren W, White RA, Eggesbo M, Knight R, Peddada S. 2015. Analysis of composition of microbiomes: a novel method for studying microbial composition. Microbial Ecology in Health and Disease. doi:10.3402/mehd.v26.27663.

Mangum CP, Rhodes WR. 1970. The taxonomic status of quill worms: genus *Hyalinoecia* (Polychaeta: Onuphidae), from the North American Atlantic Continental Slope. Postilla. 144:1–13.

Manheim F, Pratt R, McFarlin P. 1980. Composition and origin of phosphorite deposits of the Blake Plateau. In: Symposium at the 10th International Congress on Sedimentology; 1978 Jul 9–14; Jerusalem (IL).

Marchese C. 2015. Biodiversity hotspots: a shortcut for a more complicated concept. Global Ecology and Conservation. 3:297–309.

Markle RG, Bryan GM. 1983. Stratigraphic evolution of Blake Outer Ridge. American Association of Petroleum Geologists Bulletin. 67:666–683.

Marlow JJ, Hoer D, Jungbluth SP, Reynard LM, Gartman A, Chavez MS, El-Naggar MY, Tuross N, Orphan VJ, Girguis PR. 2021. Carbonate-hosted microbial communities are prolific and pervasive methane oxidizers at geologically diverse marine methane seep sites. Proceedings of the National Academy of Sciences. 118:e2006857118.

Marlow JJ, Steele JA, Case DH, Connon SA, Levin LA, Orphan VJ. 2014a. Microbial abundance and diversity patterns associated with sediments and carbonates from the methane seep environments of Hydrate Ridge, OR. Frontiers in Marine Science. 1:44.

Marlow JJ, Steele JA, Ziebis W, Thurber AR, Levin LA, Orphan VJ. 2014b. Carbonate-hosted methanotrophy represents an unrecognized methane sink in the deep sea. Nature Communications. 5:5094.

Martin S, Thouzeau G, Chauvaud L, Jean F, Guérin L, Clavier J. 2006. Respiration, calcification, and excretion of the invasive slipper limpet, *Crepidula fornicata* L.: implications for carbon, carbonate, and nitrogen fluxes in affected areas. Limnology and Oceanography. 51:1996–2007.

Matos F, Company J, Cunha M. 2021. Mediterranean seascape suitability for *Lophelia pertusa*: living on the edge. Deep Sea Research Part I: Oceanographic Research Papers. 170:103496.

Matos L, Mienis F, Wienberg C, Frank N, Kwiatkowski C, Groeneveld J, Thil F, Abrantes F, Cunha MR, Hebbeln D. 2015. Interglacial occurrence of cold-water corals off Cape Lookout (NW Atlantic): first evidence of the Gulf Stream influence. Deep Sea Research Part I: Oceanographic Research Papers. 105:158–170.

Matsumoto R. 1990. Vuggy carbonate crust formed by hydrocarbon seepage on the continental shelf of Baffin Island, northeast Canada. Geochemical Journal. 24(3):143–158.

Mayer L, Jakobsson M, Allen G, Dorschel B, Falconer R, Ferrini V, Lamarche G, Snaith H, Weatherall P. 2018. The Nippon Foundation—GEBCO Seabed 2030 Project: the quest to see the world's oceans completely mapped by 2030. Geosciences. 8(2). doi:10.3390/geosciences8020063.

Mayzaud P, Conover RJ. 1988. O:N atomic ratio as a tool to describe zooplankton metabolism. Marine Ecology Progress Series. 45:289–302.

McArthur J, Walsh J. 1984. Rare-earth geochemistry of phosphorites, Chemical Geology. 47(3–4):191–220. doi:10.1016/0009-2541(84)90126-8.

McCartney MA, Burton ML, Lima TG. 2013. Mitochondrial DNA differentiation between populations of black sea bass (*Centropristis striata*) across Cape Hatteras, North Carolina (USA). Journal of Biogeography. 40(7):1386–1398.

McCauley M, Jackson CR, Goulet TL. 2020. Microbiomes of Caribbean octocorals vary over time but are resistant to environmental change. Frontiers in Microbiology. 11:1272.

McClain-Counts JP, Bourque JR, Demopoulos AWJ. 2022. Stable isotope, seep megafauna video analysis, and macrofauna of submarine canyons, deep-sea corals and seep habitats in the western Atlantic from 2018–2019. Washington (DC): U.S. Geological Survey. doi:10.5066/P97W00RM.

McClain-Counts JP, Demopoulos, AWJ, Ross SW. 2017. Trophic structure of mesopelagic fishes in the Gulf of Mexico revealed by gut content and stable isotope analyses. Marine Ecology. 38(4).

McClenaghan B, Fahner N, Cote D, Chawarski J, McCarthy A, Rajabi H, Singer G, Hajibabei M. 2020. Harnessing the power of eDNA metabarcoding for the detection of deep-sea fishes. PLoS ONE. 15(11):e0236540. doi: 10.1371/journal.pone.0236540.

McCook LJ, Ayling T, Cappo M, Choat JH, Evans RD, De Freitas DM, Heupel M, Hughes TP, Jones GP, Mapstone B, et al. 2010. Adaptive management of the Great Barrier Reef: a globally significant demonstration of the benefits of networks of marine reserves. Proceedings of the National Academy of Sciences. 107(43):18278–18285. doi:10.1073/pnas.0909335107.

McFadden CS, Benayahu Y, Pante E, Thoma JN, Nevarez PA, France SC. 2011. Limitations of mitochondrial gene barcoding in Octocorallia. Molecular Ecology Resources. 11:19–31.

McFadden CS, Brown AS, Brayton C, Hunt CB, van Ofwegen LP. 2014. Application of DNA barcoding in biodiversity studies of shallow-water octocorals: molecular proxies agree with morphological estimates of species richness in Palau. Coral Reefs. 33:275–286.

McFadden CS, Donahue R, Hadland BK, Weston R. 2001. A molecular phylogenetic analysis of reproductive trait evolution in the soft coral genus *Alcyonium*. Evolution. 55(1):54–67. doi:10.1111/j.0014-3820.2001.tb01272.x.

McFadden CS, Gonzalez A, Imada R, Shi SS, Hong P, Ekins M, Benayahu Y. 2019. Molecular operational taxonomic units reveal restricted geographic ranges and regional endemism in the Indo-Pacific octocoral family Xeniidae. Journal of Biogeography. 46:992–1006.

McFadden CS, van Ofwegen LP. 2012. Stoloniferous octocorals (Anthozoa, Octocorallia) from South Africa, with descriptions of a new family of Alcyonacea, a new genus of Clavulariidae, and a new species of *Cornularia* (Cornulariidae). Invert Systematics 26:331.

McKenna A, Hanna M, Banks E, Sivachenko A, Cibulskis K, Kernytsky A, DePristo MA. 2010. The genome analysis toolkit: a MapReduce framework for analyzing next-generation DNA sequencing data. Genome Research. 20(9):1297–1303.

McMurdie PJ, Holmes S. 2013. phyloseq: an R package for reproducible interactive analysis and graphics of microbiome census data. PLoS ONE. 8:e61217. doi:10.1371/journal.pone.0061217.

McVeigh D, Skarke A, Dekas AE, Borrelli C, Hong W-L, Marlow JJ, Pasulka A, Jungbluth SP, Barcoi RA, Djurhuus A. 2018. Characterization of benthic biogeochemistry and ecology at three methane seep sites on the northern US Atlantic margin. Deep Sea Research Part II: Topical Studies in Oceanography. 150:41–56.

McWilliam JN, Hawkins AD. 2013. A comparison of inshore marine soundscapes. Journal of Experimental Marine Biology and Ecology. 446:166–176. doi:10.1016/j.jembe.2013.5.012.

Meinen CS, Johns WE, Moat B, Smith RH, Johns EM, Rayner D, Frajka-Williams E, Garcia RF, Garzoli SL. 2019. Structure and variability of the Antilles Current at 26.5°N. Journal of Geophysical Research: Oceans. 124(6):3700–3723.

Meinen CS, Perez RC, Dong S, Piola AR, Campos E. 2020. Observed ocean bottom temperature variability at four sites in the Northwestern Argentine Basin: evidence of decadal deep/abyssal warming amidst hourly to interannual variability during 2009–2019. Geophysical Research Letters. 47:e2020GL089093. doi:10.1029/2020GL089093.

Meistertzheim A-L, Lartaud F, Arnaud-Haond S, Kalenitchenko D, Bessalam M, Le Bris N, Galand PE. 2016. Patterns of bacteria-host associations suggest different ecological strategies between two reef building cold-water coral species. Deep Sea Research Part I: Oceanographic Research Papers. 114:12–22.

Menot L, Galeron J, Olu K, Caprais C, Crassous P, Khripounoff A, Sibuet M. 2010. Spatial heterogeneity of macrofaunal communities in and near a giant pockmark area in the deep Gulf of Guinea. Marine Ecology. 31(1):78–93.

Mercier A, Hamel JF. 2011. Contrasting reproductive strategies in three deep-sea octocorals from eastern Canada: *Primnoa resedaeformis*, *Keratoisis ornata*, and *Anthomastus grandifloras*. Coral Reefs. 30:337–350.

Mercier A, Sun Z, Baillon S, Hamel JF. 2011. Lunar rhythms in the deep sea: evidence from the reproductive periodicity of several marine invertebrates. Journal of Biological Rhythms. 26(1):82–86.

Metaxas A, Lacharité M, de Mendonça SN. 2019. Hydrodynamic connectivity of habitats of deep-water corals in Corsair Canyon, Northwest Atlantic: a case for cross-boundary conservation. Frontiers in Marine Science. 6:159. doi:10.3389/fmars.2019.00159.

Meyers KS, Wagner JKS, Ball B, Turner PJ, Young CM, Van Dover CL. 2016. Hyalinoecia artifex: field notes on a charismatic and abundant epifaunal polychaete on the US Atlantic Continental Margin. Invertebrate Biology. 135:211–224.

Middelburg JJ, Mueller CE, Veuger B, Larsson AI, Form A, van Oevelen D. 2015. Discovery of symbiotic nitrogen fixation and chemoautotrophy in cold-water corals. Scientific Reports. 5:17962.

Mienis F, de Stigter HC, White M, Duineveld G, de Haas H, van Weering TCE. 2007. Hydrodynamic controls on cold-water coral growth and carbonate-mound development at the SW and SE Rockall Trough Margin, NE Atlantic Ocean. Deep Sea Research Part I: Oceanographic Research Papers. 54:1655–1674.

Mienis F, Duineveld GCA, Davies AJ, Lavaleye MMS, Ross SW, Seim H, Bane J, van Haren H, Bergman MJN, de Haas H, et al. 2014. Cold-water coral growth under extreme environmental conditions, the Cape Lookout area, NW Atlantic. Biogeosciences. 11:2543–2560.

Mienis F, Duineveld GCA, Davies AJ, Ross SW, Seim H, Bane J, van Weering TCE. 2012. The influence of near-bed hydrodynamic conditions on cold-water corals in the Viosca Knoll area, Gulf of Mexico. Deep Sea Research Part I: Oceanographic Research Papers. 60:32–45.

Mikkelsen N, Erlenkauser H, Killingley JS, Berger WH. 1982. Norwegian corals: radiocarbon and stable isotopes in *Lophelia pertusa*. Boreas. 5:163–171.

Miksis-Olds JL, Stabeno PJ, Napp JM, Pinchuk AI, Nystuen JA, Warren JD, Denes SL. 2013. Ecosystem response to a temporary sea ice retreat in the Bering Sea. Progress in Oceanography. 111:38–51. doi:10.1016/j.pocean.2012.10.010.

Miller AK, Kerr AM, Paulay G, Reich M, Wilson NG, Carvajal JI, Rouse GW. 2017. Molecular phylogeny of extant Holothuroidea (Echinodermata). Molecular Phylogenetics and Evolution. 111:110–131.

Miller GM, Kroon FJ, Metcalfe S, Munday PL. 2015. Temperature is the evil twin: effects of increased temperature and ocean acidification on reproduction in a reef fish. Ecological Applications. 25:603–620. doi:10.1890/14-0559.1.

Miller RM, Dunham JP, Amores A, Cresko WA, Johnson EA. 2007. Rapid and cost-effective polymorphism identification and genotyping using restriction site associated DNA (RAD) markers. Genome Research. 17:240–248.

Milliman JD, Emery KO. 1968. Sea levels during the past 35,000 years. Science. 162:1121–1123.

Minh BQ, Schmidt HA, Chernomor O, Schrempf D, Woodhams MD, von Haeseler A, Lanfear R. 2020. IQ-TREE 2: new models and efficient methods for phylogenetic inference in the genomic era. Molecular Biology and Evolution. 37:1530–1534.

Mintenbeck K, Jacob U, Knust R, Arntz WE, Brey T. 2007. Depth-dependence in stable isotope ratio $\delta^{15}N$ of benthic POM consumers: the role of particle dynamics and organism trophic guild. Deep-Sea Research Part I: Oceanographic Research Papers. 54(6):1015–1023.

Mioduchowska M, Czyz M, Goldyn B, Kur J, Sell J. 2018. Instances of erroneous DNA barcoding of metazoan invertebrates: are universal *cox1* gene primers too "universal"? PLoS ONE. doi:10.1371/journal.pone.0199609.

Miyamoto Y, Zhang H, Cheng X, Rubio A. 2017. Modeling of laser-pulse induced water decomposition on two-dimensional materials by simulations based on time-dependent density functional theory. Physical Review B. 96:115451.

Montgomery JC, Jeffs A, Simpson SD, Meekan M, Tindle C. 2006. Sound as an orientation cue for the pelagic larvae of reef fishes and decapod crustaceans. Advances in Marine Biology. 51:143–196.

Montgomery M, Kwon H, Dreyer J, Xuan Y, McEnally C, Pfefferle L. 2021. Effect of ammonia addition on suppressing soot formation in methane co-flow diffusion flames. Proceedings of the Combustion Institute. 38(2):2497–2505. doi:10.1016/j.proci.2020.06.094.

Morato T, González-Irusta JM, Dominguez-Carrió C, Wei CL, Davies A, Sweetman AK, Taranto GH, Beazley L, Garcia-Alegre A, Grehan A, et al. 2020. Climate-induced changes in the suitable habitat of cold-water corals and commercially important deep-sea fishes in the North Atlantic. Global Change Biology. 26(4):2181–2202. doi:10.1111/gcb.14996.

Morrison CL. 2019. An update on cold seeps in the northwestern Atlantic Ocean. Silver Spring (MD): U.S. Department of Commerce, National Oceanic and Atmospheric Administration; [accessed 2024 Jan 29]. https://oceanexplorer.noaa.gov/okeanos/explorations/ex1903/background/seeps/.

Morrison CL, Ross SW, Nizinski MS, Brooke S, Jarnegren J, Waller R, Johnson RL, King TL. 2011. Genetic discontinuity between regional populations of *Lophelia pertusa* in the North Atlantic Ocean. Conservation Genetics. 12:713–729.

Morrison CL, Springmann MJ. 2017. Chapter 3: Genetic connectivity among natural *Lophelia pertusa* reefs and shipwrecks in the Gulf of Mexico. In: Demopoulos AWJ, Ross SW, Kellogg CA, Morrison CL, Nizinski M, Prouty NG, Bourque JR, Galkiewicz JP, Gray MA, Springmann MJ, et al., editors. Deepwater Program: *Lophelia II*, continuing ecological research on deep-sea corals and deep-reef habitats in the Gulf of Mexico. Washington (DC): U.S. Geological Survey. 269 p. Report No.: Open-File Report 2017–1139.

Morrison CL, Weinnig AM, Aunins AW, Salamone R. 2023. Single nucleotide polymorphisms (SNPs) for population genomics of the cold-water coral *Desmophyllum pertusum* (=*Lophelia pertusa*). Washington (DC): U.S. Geological Survey. doi:10.5066/P9AC566M.

Morrow KM, Bourne DG, Humphrey C, Botté ES, Laffy P, Zaneveld J, Uthicke S, Fabricius KE, Webster NS. 2015. Natural volcanic CO_2 seeps reveal future trajectories for host-microbial associations in corals and sponges. ISME Journal. 9:894–908.

Morrow KM, Moss AG, Chadwick NE, Liles MR. 2012. Bacterial associates of two Caribbean coral species reveal species-specific distribution and geographic variability. Applied and Environmental Microbiology. 78(18):6438–6449.

Mortensen P, Buhl-Mortensen L. 2005. Morphology and growth of the deep-water gorgonians *Primnoa resedaeformis* and *Paragorgia arborea*. Marine Biology. 147:775–788.

Mortensen PB. 2001. Aquarium observations on the deep-water coral *Lophelia pertusa* (L., 1758) (scleractinia) and selected associated invertebrates. Ophelia. 54:83–104.

Mortensen PB, Fosså JH. 2006. Species diversity and spatial distribution of invertebrates on deep-water Lophelia reefs in Norway. In: Proceedings of 10th International Coral Reef Symposium; 2004 Jun 28 – Jul 2; Okinawa (JP). p 1849–1868.

Mortensen PB, Rapp HT. 1998. Oxygen- and carbon isotope ratios related to growth line patterns in skeletons of *Lophelia pertusa* (*L*) (Anthozoa: Scleractinia): implications for determination of linear extension rates. Sarsia. 83:433–446.

Mortensen PB, Roberts JM, Sundt RC. 2000. Video-assisted grabbing: a minimally destructive method of sampling azooxanthellate coral banks. Journal of the Marine Biological Association of the UK. 80(2):365–366 doi:10.1017/S0025315400001983.

Mosher CV, Watling L. 2009. Partners for life: a brittle star and its octocoral host. Marine Ecology Progress Series. 397:81–88.

Mouchet MA, Villéger S, Mason NW, Mouillot D. 2010. Functional diversity measures: an overview of their redundancy and their ability to discriminate community assembly rules. Functional Ecology. 24(4):867–876.

Mountain GS, Tucholke BE. 1985. Mesozoic and Cenozoic geology of the US Atlantic Continental Slope and rise. In: Poag CW, editor. Geologic evolution of the United States Atlantic Margin. New York (NY): Van Nostrand Reinhold Co. p. 293–341.

Mueller CE, Larsson AI, Veuger B, Middelburg JJ, van Oevelen D. 2014. Opportunistic feeding on various organic food sources by the cold-water coral *Lophelia pertusa*. Biogeosciences. 11(1):123–133.

Müller WA, Jungclaus JH, Mauritsen T, Baehr J, Bittner M, Budich R, Bunzel F, Esch M, Ghosh R, Haak H, et al. 2018. A higher-resolution version of the Max Planck Institute Earth System Model (MPI-ESM1.2-HR). Journal of Advances in Modeling Earth Systems. 10(7):1383–1413.

Murray F, De Clippele LH, Hiley A, Wicks L, Roberts JM, Hennige S. 2019. Multiple feeding strategies observed in the cold-water coral *Lophelia pertusa*. Journal of the Marine Biological Association UK. 99:1281–1283.

Nagelkerken I, Van der Velde G, Van Avessaath PH. 1997. A description of the skeletal development pattern of the temperate coral *Carophyllia smithii* based on internal growth lines. Journal of the Marine Biological Association UK. 77:375–387.

Nakajima R, Yamakita T, Watanabe H, Fujikura K, Tanaka K, Yamamoto H, Shirayama Y. 2014. Species richness and community structure of benthic macrofauna and megafauna in the deep-sea

chemosynthetic ecosystems around the Japanese archipelago: an attempt to identify priority areas for conservation. Diversity and Distributions. 20:1160–1172.

National Ocean Survey. 1976. Jacksonville: bathymetric map NH 17-5, scale 1:250,000.

National Ocean Survey. 1978a. Hoyt Hills: bathymetric map NH 17-3, scale 1:250,000.

National Ocean Survey. 1978b. Harrington Hill: bathymetric map NH 18-1, scale 1:250,000.

National Ocean Survey. 1978c. Richardson Hills: bathymetric map NI 18-10, scale 1:250,000.

National Ocean Survey. 1978d. Stetson Mesa: bathymetric map NH 17-6, scale 1:250,000.

National Ocean Survey. 1978e. Cape Fear: bathymetric map NI 18-7, scale 1:250,000.

National Research Council. 2003. Ocean noise and marine mammals. Washington (DC): The National Academies Press. doi:10.17226/10564.

Naumann MS, Orejas C, Ferrier-Pagès C. 2014. Species-specific physiological response by the cold-water corals *Lophelia pertusa* and *Madrepora oculata* to variations within their natural temperature range. Deep Sea Research Part II: Topical Studies in Oceanography. 99:36–41.

Neave MJ, Apprill A, Ferrier-Pagès C, Voolstra CR. 2016. Diversity and function of prevalent symbiotic marine bacteria in the genus *Endozoicomonas*. Applied Microbiology and Biotechnology. 100(19):8315–8324.

Nei M. 1987. Molecular evolutionary genetics. New York (NY): Columbia University Press. 514 p.

Neulinger SC, Järnegren J, Ludvigsen M, Lochte K, Dullo WC. 2008. Phenotype-specific bacterial communities in the cold-water coral *Lophelia pertusa* (Scleractinia) and their implications for the coral's nutrition, health, and distribution. Applied and Environmental Microbiology. 74(23):7272–7285.

Neumann AC, Kofoed JW, Keller GH. 1977. Lithoherms in the Strait of Florida. Geology. 5:4–10.

New AL, Smeed DA, Czaja A, Blaker AT, Mecking JV, Mathews JP, Sanchez-Franks A. 2021. Labrador Slope Water connects the subarctic with the Gulf Stream. Environmental Research Letters. 16(8):084019.

Nizinski M. 2016. Cruise report: 2016 NOAA Ship *Pisces* expedition to Carolina Canyons. Washington (DC): U.S. Department of Commerce, National Oceanic and Atmospheric Administration, National Marine Fisheries Service. 10 p. Report No.: PC-1605 Cruise Report.

NOAA. 2018. Summary report for the Atlantic Seafloor Partnership for Integrated Research and Exploration Science Planning Workshop. Silver Spring (MD): U.S. Department of Commerce, National Oceanic and Atmospheric Administration, Office of Oceanic and Atmospheric Research, Office of Ocean Exploration and Research; [accessed 2024 Jan 29]. https://oceanexplorer.noaa.gov/explorations/aspire/aspire-workshop-report.pdf.

Obelcz J, Brothers D, Chaytor J, Brink UT, Ross SW, Brooke S. 2014. Geomorphic characterization of four shelf-sourced submarine canyons along the U.S. Mid-Atlantic continental margin. Deep Sea Research Part II: Topical Studies in Oceanography. 104:106–119.

O'Donnell JL, Kelly RP, Shelton AO, Samhouri JF, Lowell NC, Williams GD. 2017. Spatial distribution of environmental DNA in a nearshore marine habitat. PeerJ. 5:e3044.

Oksanen J, Blanchet FG, Kindt, Legendre P, Minchin PR, O'Hara RB, Simpson GL, Solymos P, Stevens MHH, Wagner H. 2020. Vegan: community ecology package. R package version 2.2-0. http://CRAN.Rproject.org/package=vegan.

Oliveira A, Santos AI, Rodrigues A, Vitorino J. 2007. Sedimentary particle distribution and dynamics on the Nazaré canyon system and adjacent shelf (Portugal). Marine Geology. 246(2):105–122.

Olson ND, Ainsworth TD, Gates RD, Takabayashi M. 2009. Diazotrophic bacteria associated with Hawaiian *Montipora* corals: diversity and abundance in correlation with symbiotic dinoflagellates. Journal of Experimental Marine Biology and Ecology. 371:140–146.

Olu K, Cordes EE, Fisher CR, Brooks JM, Sibuet M, Desbruyères D. 2010. Biogeography and potential exchanges among the Atlantic equatorial belt cold-seep faunas. PLoS ONE. 5(8):e11967.

Olu K, Lance S, Sibuet M, Henry P, Fiala-Médioni A, Dinet A. 1997. Cold seep communities as indicators of fluid expulsion patterns through mud volcanoes seaward of the Barbados accretionary prism. Deep Sea Research Part I: Oceanographic Research Papers. 44(5):811–841.

Olu-Le Roy K, Caprais JC, Fifis A, Fabri MC, Galeron J, Budzinsky H, Le Ménach K, Khripounoff A, Ondréas H, Sibuet M. 2007. Cold-seep assemblages on a giant pockmark off West Africa: spatial patterns and environmental control. Marine Ecology. 28:115–130.

Orejas C, Gori A, Iacono CL, Puig P, Gili JM, Dale MRT. 2009. Cold-water corals in the Cap de Creus canyon, northwestern Mediterranean: spatial distribution, density and anthropogenic impact. Marine Ecology Progress Series. 397:37–51.

Orejas C, Gori A, Rad-Menéndez C, Last KS, Davies AJ, Beveridge CM, Sadd D, Kiriakoulakis K, Witte U, Roberts JM. 2016. The effect of flow speed and food size on the capture efficiency and feeding behaviour of the cold-water coral *Lophelia pertusa*. Journal of Experimental Marine Biology and Ecology. 481:34–40.

Orejas C, Lopez-Gonzalez PJ, Gili JM, Teixido N, Gutt J, Arntz WE. 2002. Distribution and reproductive ecology of the Antarctic octocoral *Ainigmaptilon antarcticum* in the Weddell Sea. Marine Ecology Progress Series. 231:101–114. doi:10.3354/meps231101.

Orphan VJ, Hinrichs KU, Ussler III W, Paull CK, Taylor LT, Sylva SP, Hayes JM, Delong EF. 2001. Comparative analysis of methane-oxidizing archaea and sulfate-reducing bacteria in anoxic marine sediments. Applied and Environmental Microbiology. 67(4):1922–1934.

Page HM, Fisher CR, Childress JJ. 1990. Role of filter-feeding in the nutritional biology of a deep-sea mussel with methanotrophic symbionts. Marine Biology. 104:251–257.

Palardy J, Grottoli A, Matthews K. 2005. Effects of upwelling, depth, morphology and polyp size on feeding in three species of Panamanian corals. Marine Ecology Progress Series. 300:79–89.

Palter JB, Lozier MS. 2008. On the source of Gulf Stream nutrients. Journal of Geophysical Research: Oceans. 113(C6).

Pantos O, Bongaerts P, Dennis PG, Tyson GW, Hoegh-Guldberg O. 2015. Habitat-specific environmental conditions primarily control the microbiomes of the coral *Seriatopora hystrix*. ISME Journal. 9(9):1916–1927.

Pappalardo P, Fernández M. 2014. Mode of larval development as a key factor to explain contrasting effects of temperature on species richness across oceans. Global Ecology and Biogeography. 23(1):12–23.

Parada AE, Needham DM, Fuhrman JA. 2016. Every base matters: assessing small subunit rRNA primers for marine microbiomes with mock communities, time series and global field samples. Environmental Microbiology. 18(5):1403–1414.

Parks SE, Miksis-Olds JL, Denes SL. 2014. Assessing marine ecosystem acoustic diversity across ocean basins. Ecological Informatics. 21:81–88. doi:10.1016/j.ecoinf.2013.11.003.

Parmentier E, Berten L, Rigo P, Aubrun F, Nedelec SL, Simpson SD, Lecchini D. 2015. The influence of various reef sounds on coral-fish larvae behaviour. Journal of Fish Biology. 86(5):1507–1518.

Partyka ML, Ross SW, Quattrini AM, Sedberry GR, Birdsong TW, Potter J, Gottfried S. 2007. Southeastern United States deep-sea corals (SEADESC) initiative: a collaboration to characterize areas of habitat forming deep-sea corals. Silver Spring (MD): U.S. Department of Commerce, National Oceanic and Atmospheric Administration. 176 p. Report No.: NOAA Technical Memorandum OAR OER 1.

Paul EA, Newton JD. 1961. Studies of aerobic non-symbiotic nitrogen-fixing bacteria. Canadian Journal of Microbiology. 7:7–13.

Paull CK, Dillon WP. 1980. Structure, stratigraphy, and geologic history of Florida-Hatteras Shelf and inner Blake Plateau. AAPG Bulletin. 64(3):339–358.

Paull CK, Dillon WP. 1981. Appearance and distribution of the gas hydrate reflection in the Blake Ridge region, offshore southeastern United States, miscellaneous field studies map 1252. Washington (DC): U.S. Geological Survey.

Paull CK, Hecker B, Commeau R, Freeman-Lynde RP, Neumann C, Corso WP, Curray J. 1984. Biological communities at the Florida Escarpment resemble hydrothermal vent taxa. Science. 226(4677):965–967.

Paull CK, Lorenson TD, Borowski WS, Ussler III W, Olsen K, Rodriguez NM. 2000. Isotopic ratios of methane, ethane, carbon dioxide, inorganic carbon and organic matter from ODP Leg 164 sites. PANGAEA. doi:10.1594/PANGAEA.803647.

Paull CK, Ussler III, W, Borowski WS, Spiess FN. 1995. Methane-rich plumes on the Carolina continental rise: associations with gas hydrates. Geology. 23(1):89–92.

Petchey OL, Gaston KJ. 2002. Functional diversity (FD), species richness and community composition. Ecology letters. 5(3):402–411.

Peterson BJ, Fry B. 1987. Stable isotopes in ecosystem studies. Annual Review of Ecology, Evolution, and Systematics. 18:293–320.

Phrampus BJ, Lee TR, Wood WT. 2020. A global probabilistic prediction of cold seeps and associated SEAfloor FLuid Expulsion Anomalies (SEAFLEAs). Geochemistry, Geophysics, Geosystems. 21(1):e2019GC008747. doi:10.1029/2019GC008747.

Pielou EC. 1966. The measurement of diversity in different types of biological collections. Journal of Theoretical Biology. 13:131–144.

Pierdomenico M, Gori A, Guida VG, Gili JM. 2017. Megabenthic assemblages at the Hudson Canyon Head (NW Atlantic margin): habitat-faunal relationships. Progress in Oceanography. 157(Suppl. C):12–26.

Pijanowski BC, Villanueva-Rivera LJ, Dumyahn SL, Farina A, Krause BL, Napoletano BM, Gage SH, Pieretti N. 2011. Soundscape ecology: the science of sound in the landscape. BioScience. 61(3):203–216. doi:10.1525/bio.2011.61.3.6.

Pile AJ, Young CM. 1999. Plankton availability and retention efficiencies of cold-seep symbiotic mussels. Limnology and Oceanography. 44(7):1833–1839.

Pillai BR, Diwan AD. 2002. Effects of acute salinity stress on oxygen consumption and ammonia excretion rates of the marine shrimp. Journal of Crustacean Biology. 22:8.

Pilliod DS, Goldberg CS, Arkle RS, Waits LP. 2013. Estimating occupancy and abundance of stream amphibians using environmental DNA from filtered water samples. Canadian Journal of Fisheries and Aquatic Sciences. 70:1123−1130.

Pinet PR, Popenoe P. 1985. A scenario of Mesozoic-Cenozoic ocean circulation over the Blake Plateau and its environs. Geological Society of America Bulletin. 96(5):618–626.

Pinnegar JK, Polunin NVC. 1999. Differential fractionation of δ13C and δ15N among fish tissues: implications for the study of trophic interactions. Functional Ecology. 13(2):225–231.

Pires DE, Ascher DB, Blundell TL. 2014. DUET: a server for predicting effects of mutations on protein stability using an integrated computational approach. Nucleic Acids Research. 42(W1):W314–W319.

Plowman CQ 2017. Reproductive patterns of cold-seep mussels in the Gulf of Mexico and northwestern Atlantic [thesis]. Eugene (OR): University of Oregon June 2017. 67 p.

Poag CW. 1991. Rise and demise of the Bahama-Grand Banks gigaplatform, northern margin of the Jurassic proto-Atlantic seaway. Marine Geology. 102:63–130.

Poag CW, Sevon WD. 1989. A record of Appalachian denudation in postrift Mesozoic and Cenozoic sedimentary deposits of the U.S. Middle Atlantic continental margin. Geomorphology. 2(1-3):119–157.

Pogoreutz C, Rädecker N, Cárdenas A, Gärdes A, Wild C, Voolstra CR. 2018. Dominance of *Endozoicomonas* bacteria throughout coral bleaching and mortality suggests structural inflexibility of the *Pocillopora verrucosa* microbiome. Ecology and Evolution. 8(4):2240–2252.

Pohlman JW, Bauer JE, Waite WF, Osburn CL, Chapman NR. 2010. Methane hydrate-bearing seeps as a source of aged dissolved organic carbon to the oceans. Nature Geoscience. 4:37–41.

Pollock FJ, McMinds R, Smith S, Bourne DG, Willis BL, Medina M, Thurber RV, Zaneveld JR. 2018a. Coral-associated bacteria demonstrate phylosymbiosis and cophylogeny. Nature Communications. 9(1):4921.

Pollock J, Glendinning L, Wisedchanwet T, Watson M. 2018b. The madness of microbiome: attempting to find consensus "best practice" for 16S microbiome studies. Applied and Environmental Microbiology. 84(7):e02627–02617.

Popenoe P. 1980. Single-channel seismic-reflection profiles collected on the northern Blake Plateau. Washington (DC): U.S. Geological Survey. Report No.: Open-file Report 80-1265.

Popenoe P. 1994. Bottom character map of the northern Blake Plateau. Washington (DC): U.S. Geological Survey. 35 p. Report No.: Open-file Report 93-724.

Popenoe P, Dillon WP. 1996. Characteristics of the continental slope and rise off North Carolina from GLORIA and seismic-reflection data: the interaction of downslope and contour current processes. In: Gardner JV, Field ME, Twichell DC, editors. Geology of the United States seafloor: the view from GLORIA. Cambridge (UK): Cambridge University Press. p. 59–79.

Popenoe P, Henry VJ, Idris FM. 1987. Gulf trough—the Atlantic connection. Geology. 15(4):327–332.

Popenoe P, Manheim FT. 2001. Origin and history of the Charleston Bump-geological formations, currents, bottom conditions, and their relationship to wreckfish habitats on the Blake Plateau. American Fisheries Society Symposium. 25:43–94.

Popenoe P, Schmuck EA, Dillon WP. 1993. The Cape Fear landslide: slope failure associated with salt diapirism and gas hydrate decomposition. In: Schwab WC, Lee HJ, Twichell DC, editors. Submarine landslides: selective studies in the U.S. Exclusive Economic Zone. Washington (DC): U.S. Geological Survey Bulletin. p. 40–53.

Poppe LJ, Williams SJ, Paskevich VF. 2005. U.S. Geological Survey East-coast sediment analysis: procedures, database, and GIS data. Reston (VA): U.S. Geological Survey. Report No.: Open-File Report 2005-1001. https://pubs.usgs.gov/publication/ofr20051001.

Pörtner HO, Bock C, Mark FC. 2017. Oxygen-and capacity-limited thermal tolerance: bridging ecology and physiology. Journal of Experimental Biology. 220(15):2685–2696.

Pratt RM. 1963. Bottom currents on the Blake Plateau. Deep Sea Research and Oceanographic Abstracts. 10(3):245–249.

Pratt RM. 1968. Atlantic Continental Shelf and slope of the United States - physiography and sediments of the deep-sea basin. Washington (DC): U.S. Geological Survey. 44 p. Report No.: Professional Paper 529-B.

Pratt RM, Heezen BC. 1964. Topography of the Blake Plateau. Deep Sea Research and Oceanographic Abstracts. 11(5):721–728.

Pratte ZA, Kellogg CA. 2021. Comparison of preservation and extraction methods on five taxonomically disparate coral microbiomes. Frontiers in Marine Science. 8:684161. doi:10.3389/fmars.2021.684161.

Pratte ZA, Stewart FJ, Kellogg CA. 2023. Functional gene composition and metabolic potential of deep-sea coral-associated microbial communities. Coral Reefs. 42:1011–1023. doi:10.1007/s00338-023-02409-0.

Price MN, Dehal PS, Arkin AP. 2010. FastTree 2 – approximately maximum-likelihood trees for large alignments. PLoS ONE. 5(3):e9490. doi:10.1371/journal.pone.0009490.

Pritchard JK, Stephens M, Donnelly P. 2000. Inference of population structure using multilocus genotype data. Genetics. 155(2):945–959.

Prouty NG, Baker MC. 2021. Water-column environmental variables and accompanying discrete CTD measurements collected offshore the U.S. Mid- and South Atlantic. Washington (DC): U.S. Geological Survey.

Prouty NG, Roark EB, Andrews AH, Robinson LF, Hill T, Sherwood O, Williams B, Guilderson T, Fallon S. 2017. Age, growth rates, and paleoclimate studies in deep-sea corals of the United States. In: Hourigan TF, Etnoyer PJ, Cairns SD, editors. The state of deep-sea coral and sponge ecosystems of the United States. Silver Spring (MD): U.S. Department of Commerce, National Oceanic and Atmospheric Administration. p. 22. Report No.: NOAA Technical Memorandum NMFS-OHC-4.

Prouty NG, Sahy D, Ruppel CD, Roark EB, Condon D, Brooke S, Ross SW, Demopoulos AWJ. 2016. Insights into methane dynamics from analysis of authigenic carbonates and chemosynthetic mussels at newly-discovered Atlantic margin seeps. Earth and Planet Science Letters. 449:332–344.

Prouty NG, Schiff J, Roark EB. 2020. Radiocarbon dating of deep-sea black corals collected along the southeastern United States. Washington (DC): U.S. Geological Survey.

Puig P, Ogston AS, Mullenbach BL, Nittrouer CA, Sternberg RW. 2003. Shelf-to-canyon sediment-transport processes on the Eel continental margin (northern California). Marine Geology. 193(1):129–149.

Puig P, Palanques A, Martín J. 2014. Contemporary sediment-transport processes in submarine canyons. Annual Review of Marine Science. 6(1):53–77.

Purser A, Larsson AI, Thomsen L, van Oevelen D. 2010. The influence of flow velocity and food concentration on *Lophelia pertusa* (Scleractinia) zooplankton capture rates. Journal of Experimental Marine Biology and Ecology. 395:55–62.

Quast C, Pruesse E, Yilmaz P, Gerken J, Schweer T, Yarza P, Peplies J, Glöckner FO. 2013. The SILVA ribosomal RNA gene database project: improved data processing and web-based tools. Nucleic Acids Research. 41:D590–D596.

Quattrini AM, Etnoyer PJ, Doughty C, English L, Falco R, Remon N, Rittinghouse M, Cordes EE. 2014. A phylogenetic approach to octocoral community structure in the deep Gulf of Mexico. Deep Sea Research Part II: Topical Studies in Oceanography. 99:92–102.

Quattrini AM, Faircloth BC, Dueñas LF, Bridge TC, Brugler MR, Calixto-Botía IF, DeLeo D, Forêt S, Herrera S, Lee SMY, et al. 2018. Universal target-enrichment baits for anthozoan (Cnidaria)

phylogenomics: new approaches to long-standing problems. Molecular Ecology Resources. 18(2):281–295.

Quattrini AM, Gómez CE, Cordes EE. 2017. Environmental filtering and neutral processes shape octocoral community assembly in the deep sea. Oecologia. 183:221–236.

Quattrini AM, Herrera S, Adams JM, Grinyó J, Allcock AL, Shuler A, Wirshing HH, Cordes EE, McFadden CS. 2022. Phylogeography of *Paramuricea*: the role of depth and water mass in the evolution and distribution of deep-sea corals. Frontiers in Marine Science. 9:849402. doi:10.3389/fmars.2022.849402.

Quattrini AM, Nizinski MS, Chaytor JD, Demopoulos AWJ, Roark EB, France SC, Moore JA, Heyl T, Auster PJ, Kinlan B, Ruppel C, Elliott KP, Kennedy BRC, Lobecker E, Skarke A, Shank TM. 2015. Exploration of the canyon-incised continental margin of the northeastern United States reveals dynamic habitats and diverse communities. PLoS ONE. 10(10):e0139904.

Quattrini AM, Partyka ML, Ross SW. 2009. Aspects of the reproductive biology of the skate *Fenestraja plutonia* (Garman) off North Carolina. Southeastern Naturalist. 8(1):55–70.

Quattrini AM, Rodríguez E, Faircloth BC, Cowman PF, Brugler MR, Farfan G, Hellberg ME, Kitahara MV, Morrison CL, Paz-Garcia DA, et al. 2020. Paleoclimate ocean conditions shaped diversification of coral skeletal composition through deep time. Nature Ecology & Evolution. 20:12–34.

Quattrini AM, Ross SW, Carlson MCT, Nizinski MS. 2012. Megafaunal-habitat associations at a deep-sea coral mound off North Carolina, USA. Marine Biology. 159:1079–1094.

Quinlan AR, Hall IM. 2010. BEDTools: a flexible suite of utilities for comparing genomic features. Bioinformatics. 26(6):841–842.

R Core Team. 2018. R: a language and environment for statistical computing. Vienna (AT): R Foundation for Statistical Computing. https://www.R-project.org/.

R Core Team. 2019. R: a language and environment for statistical computing. Vienna (AT): R Foundation for Statistical Computing. https://www.R-project.org/.

R Core Team. 2021. R: a language and environment for statistical computing. Vienna (AT): R Foundation for Statistical Computing. https://www.R-project.org/.

Radford CA, Stanley JA, Jeffs AG. 2014. Adjacent coral reef habitats produce different underwater sound signatures. Marine Ecology Progress Series. 505:19–28.

Radice VZ, Quattrini AM, Wareham VE, Edinger EN, Cordes EE. 2016. Vertical water mass structure in the North Atlantic influences the bathymetric distribution of species in the deep-sea coral genus *Paramuricea*. Deep Sea Research Part I: Oceanographic Research Papers. 116:253–263.

Raick X, Di Iorio L, Gervaise C, Lossent J, Lecchini D, Parmentier E. 2021. From the reef to the ocean: revealing the acoustic range of the biophony of a coral reef (Moorea Island, French Polynesia). Journal of Marine Science and Engineering. 9(4).

Raina J-B, Tapiolas D, Willis BL, Bourne DG. 2009. Coral-associated bacteria and their role in the biogeochemical cycling of sulfur. Applied and Environmental Microbiology. 75(11):3492–3501.

Rambaut A, Drummond AJ. 2009. Tracer: MCMC trace analysis tool, version 1.5. Oxford (UK): University of Oxford.

Rao S. 1977. Soil microorganisms and plant growth. New Delhi (IN): IBH Publishing Co. p. 254–255.

Rau GH, Teyssie JL, Rassoulzadegan F, Fowler SW. 1990. $^{13}C/^{12}C$ and $^{15}N/^{14}N$ variations among size-fractionated marine particles: implications for their origin and trophic relationships. Marine Ecology Progress Series. 59(1/2):33–38.

Redfield AC. 1934. On the proportions of organic derivations in sea water and their relation to the composition of plankton. In: Johnstone J, editor. James Johnstone memorial volume. Liverpool (UK): University Press of Liverpool. p. 176–192.

Redfield AC. 1958. The biological control of chemical factors in the environment. American Scientist. 46:205–222.

Reeburgh WS. 1976. Methane consumption in Cariaco trench waters and sediments. Earth and Planetary Science Letters. 28(3):337–344.

Reed JK, Weaver DC, Pomponi SA. 2006. Habitat and fauna of deep-water *Lophelia pertusa* coral reefs off the southeastern US: Blake Plateau, Straits of Florida, and Gulf of Mexico. Bulletin of Marine Science. 78(2):343–375.

Reigel AM, Owens SM, Hellberg ME. 2020. Reducing host DNA contamination in 16S rRNA gene surveys of anthozoan microbiomes using PNA clamps. Coral Reefs. 39:1817–1827.

Reis MAM, Almeida JS, Lemos PC, Carrondo MJT. 1992. Effect of hydrogen sulfide on growth of sulfate reducing bacteria. Biotechnology and Bioengineering. 40(5):593–600.

Rengstorf AM, Yesson C, Brown C, Grehan AJ. 2013. High-resolution habitat suitability modelling can improve conservation of vulnerable marine ecosystems in the deep sea. Journal of Biogeography. 40(9):1702–1714.

Repeta DJ, Ferron S, Sosa OA, Johnson CG, Repeta LD, Acker M, DeLong EF, Karl DM. 2016. Marine methane paradox explained by bacterial degradation of dissolved organic matter. Nature Geoscience. 9:884–887.

Rex MA, Etter JJ. 2010. Deep-sea biodiversity: pattern and scale. Cambridge (MA): Harvard University Press.

Rex MA, McClain CR, Johnson NA, Etter RJ, Allen JA, Bouchet P, Waren A. 2005. A source sink hypothesis for abyssal biodiversity. The American Naturalist. 165(2):163–178.

Rhoads DC, Hecker B. 1994. Processes on the continental slope off North Carolina with special reference to the Cape Hatteras region. Deep Sea Research Part II: Topical Studies in Oceanography. 41(4-6):965–980.

Riahi K, Van Vuuren DP, Kriegler E, Edmonds J, O'neill BC, Fujimori S, Bauer N, Calvin K, Dellink R, Fricko O, et al. 2017. The shared socioeconomic pathways and their energy, land use, and greenhouse gas emissions implications: an overview. Global Environmental Change. 42:153–168.

Ritchie KB. 2006. Regulation of microbial populations by coral surface mucus and mucus-associated bacteria. Marine Ecology Progress Series. 322:1–14.

Rix L, de Goeij JM, van Oevelen D, Struck U, Al-Horani FA, Wild C, Naumann MS. 2018. Reef sponges facilitate the transfer of coral-derived organic matter to their associated fauna via the sponge loop. Marine Ecology Progress Series. 589:85–96.

Roberts JM, Anderson RM. 2002. A new laboratory method of monitoring deep-sea coral polyp behaviour. Hydrobiologia. 471:143–148.

Roberts JM, Wheeler AJ, Freiwald A. 2006. Reefs of the deep: the biology and geology of cold-water coral ecosystems. Science. 312(5773):543–547.

Roberts JM, Wheeler AJ, Freiwald A, Cairns S. 2009. Cold-water corals: the biology and geology of deep-sea coral habitats. Cambridge (UK): Cambridge University Press.

Robertson CM, Demopoulos AWJ, Bourque JR, Mienis F, Duineveld GCA, Lavaleye MSS, Koivisto RKK, Brooke SD, Ross SW, Rhode M, et al. 2020. Submarine canyons influence macrofaunal diversity and density patterns in the deep-sea benthos. Deep Sea Research Part I: Oceanographic Research Papers. 159:103249.

Robinson CA, Bernhard JM, Levin LA, Mendoza GF, Blanks JK. 2004. Surficial hydrocarbon seep infauna from the Blake Ridge (Atlantic Ocean, 2150 m) and the Gulf of Mexico (690–2240 m). Marine Ecology. 25(4):313–336.

Robinson LF, Adkins JF, Frank N, Gagnon AC, Prouty NG, Brendan Roark E, van de Flierdt T. 2014. The geochemistry of deep-sea coral skeletons: a review of vital effects and applications for paleoceanography. Deep Sea Research Part II: Topical Studies in Oceanography. 99:184–198.

Roder C, Bayer T, Aranda M, Kruse M, Voolstra CR. 2015. Microbiome structure of the fungid coral *Ctenactis echinata* aligns with environmental differences. Molecular Ecology. 24(13):3501–3511.

Rogener MK, Bracco A, Hunter KS, Saxton MA, Joye SB. 2018. Long-term impact of the Deepwater Horizon oil well blowout on methane oxidation dynamics in the northern Gulf of Mexico. Elementa: Science of the Anthropocene. 6:73.

Rogener M-K, Hunter KS, Rabalais NN, Roberts BJ, Bracco A, Stewart FJ, Joye SB. 2021. Pelagic denitrification and methane oxidation in oxygen-depleted waters of the Louisiana shelf. Biogeochemistry. 154:231–254.

Rogers AD. 1999. The biology of *Lophelia pertusa* (*Linnaeus* 1758) and other deep-water reef-forming corals and impacts from human activities. International Review of Hydrobiology. 84:315–406. doi:10.1002/iroh.199900032

Romera-Castillo C, Letscher RT, Hansell DA. 2016. New nutrients exert fundamental control on dissolved organic carbon accumulation in the surface Atlantic Ocean. Proceedings of the National Academy of Sciences. 113(38):10497–10502.

Romero-Romero S, Molina-Ramírez A, Höfer J, Duineveld G, Rumín-Caparrós A, Sanchez-Vidal A, Canals M, Acuña JL. 2016. Seasonal pathways of organic matter within the Avilés submarine canyon: food web implications. Deep Sea Research Part I: Oceanography Research Papers. 117:1–10.

Rona PA. 1970. Submarine canyon origin on upper continental slope off Cape Hatteras. The Journal of Geology. 78(2):141–152.

Rosenberg E, Kellogg CA, Rohwer F. 2007. Coral microbiology. Oceanography. 20(2):114–122.

Ross S, Brooke S, Baird E, Coykendall E, Davies A, Demopoulos A, France S, Kellogg C, Mather R, Mienis F, et al. 2017. Exploration and research of mid-Atlantic deepwater hard bottom habitats and shipwrecks with emphasis on canyons and coral communities: Atlantic Deepwater Canyons Study. Draft report. Sterling (VA): U.S. Department of the Interior, Bureau of Ocean Energy Management, Atlantic OCS Region. 1000 p. Report No.: OCS Study BOEM 2017-060.

Ross SW. 2006. Review of distribution, habitats, and associated fauna of deep water coral reefs on the southeastern United States continental slope (North Carolina to Cape Canaveral, FL). In: Unpublished report to South Atlantic Fishery Management Council. Charleston (SC). 2nd edition. 37 p.

Ross SW, Nizinski MS. 2007. State of deep coral ecosystems in the us southeast region: Cape Hatteras to southeastern Florida. In: The state of deep coral ecosystems of the United States. Silver Spring (MD): U.S. Department of the Commerce, National Oceanic and Atmospheric Administration. Report No.: NOAA Technical Memorandum CRCP-3. p. 233–270.

Ross SW, Rhode M, Quattrini AM. 2015. Demersal fish distribution and habitat use within and near Baltimore and Norfolk Canyons, US middle Atlantic slope. Deep Sea Research Part I: Oceanographic Research Papers. 103:137–154.

Ross SW, Quattrini AM. 2007. The fish fauna associated with deep coral banks off the southeastern United States. Deep Sea Research Part I: Oceanographic Research Papers. 54:975–1007.

Ross SW, Quattrini AM. 2009. Deep-sea reef fish assemblage patterns on the Blake Plateau (Western North Atlantic Ocean). Marine Ecology. 30(1):74–92.

Ross SW, Quattrini AM, Roa-Varón AY, McClain JP. 2010. Species composition and distributions of mesopelagic fishes over the slope of the north-central Gulf of Mexico. Deep Sea Research Part II: Topical Studies in Oceanography. 57:1926–1956.

Rowden AA, Pearman TR, Bowden DA, Anderson OF, Clark MR. 2020. Determining coral density thresholds for identifying structurally complex vulnerable marine ecosystems in the deep sea. Frontiers in Marine Science. 7:95.

Rowe GT, Menzies RJ. 1969. Zonation of large benthic invertebrates in the deep-sea off the Carolinas. Deep Sea Research and Oceanography Abstracts. 16(5):531–537.

Rowe GT, Polloni PT, Haedrich RL. 1982. The deep-sea macrobenthos on the continental margin of the northwest Atlantic Ocean. Deep Sea Research Part I: Oceanographic Research Papers. 29(2):257–278.

Rowe GT, Polloni PT, Horner SG. 1974. Benthic biomass estimates from the northwestern Atlantic Ocean and the northern Gulf of Mexico. Deep Sea Research and Oceanographic Abstracts. 21(8):641–650.

Rowe GT. 1971. Observations on bottom currents and epibenthic populations in Hatteras Submarine Canyon. Deep Sea Research and Oceanographic Abstracts. 18(6):569–581.

Ruiz-Ramos DV, Saunders M, Fisher CR, Baums IB. 2015. Home bodies and wanderers: sympatric lineages of the deep-sea black coral *Leiopathes glaberrima*. PLoS ONE. 10(10):e0138989.

Ruppel C. 2003. In search of ice shrimp and gas hydrate at the Blake Ridge Diapir. Silver Spring (MD): U.S. Department of Commerce, National Oceanic and Atmospheric Administration; [accessed 2024 Jan 29]. https://oceanexplorer.noaa.gov/explorations/03windows/logs/jul30/jul30.html.

Rypina II, Llopiz JK, Pratt LJ, Lozier MS. 2014. Dispersal pathways of American eel larvae from the Sargasso Sea. Limnology and Oceanography. 59(5):1704–1714.

Saba VS, Griffies SM, Anderson WG, Winton M, Alexander MA, Delworth TL, Hare JA, Harrison MJ, Rosati A, Vecchi GA, et al. 2016. Enhanced warming of the Northwest Atlantic Ocean under climate change. Journal of Geophysical Research: Oceans. 121(1):118–132.

Sabourin TD, Stickle WB. 1981. Effects of salinity on respiration and nitrogen excretion in two species of echinoderms. Marine Biology. 65:91–99.

Sahling H, Galkin SV, Salyuk A, Greinert J, Foerstel H, Piepenburg D, Suess E. 2003. Depth-related structure and ecological significance of cold-seep communities—a case study from the Sea of Okhotsk. Deep Sea Research Part I: Oceanographic Research Papers. 50(12):1391–1409.

Sahling H, Rickert D, Lee RW, Linke P, Suess E. 2002. Macrofaunal community structure and sulfide flux at gas hydrate deposits from the Cascadia convergent margin, NE Pacific. Marine Ecology Progress Series. 231:121–138.

Sanders HL, Hessler RR, Hampson GR. 1965. An introduction to the study of deep-sea benthic faunal assemblages along the Gay Head-Bermuda transect. Deep Sea Research and Oceanographic Abstracts. 12(6):845–867.

Santini L, Benítez-López A, Maiorano L, Čengić M, Huijbregts MA. 2021. Assessing the reliability of species distribution projections in climate change research. Diversity and Distributions. 27(6):1035–1050.

Savidge DK, Bane Jr JM. 2001. Wind and gulf stream influences on along-shelf transport and off-shelf export at Cape Hatteras, North Carolina. Journal of Geophysical Research: Oceans. 106(C6):11505–11527.

Schaff T, Levin L, Blair N, DeMaster D, Pope R, Boehme S. 1992. Spatial heterogeneity of benthos on the Carolina continental slope: large (100 km)-scale variation. Marine Ecology Progress Series. 88:143–160.

Schlacher TA, Schlacher-Hoenlinger MA, Williams A, Althaus F, Hooper JNA, Kloser R. 2007. Richness and distribution of sponge megabenthos in continental margin canyons off southeastern Australia. Marine Ecology Progress Series. 340:73–88.

Schlager W. 1981. The paradox of drowned reefs and carbonate platforms. Geological Society of America Bulletin. 92(4):197–211.

Schlee J. 1973. Atlantic Continental Shelf and slope of the United States — sediment texture of the northeastern part. Reston (VA): U.S. Geological Survey. Report No.: Professional Paper 529-L.

Schloss PD, Westcott SL, Ryabin T, Hall JR, Hartmann M, Hollister EB, Lesniewski RA, Oakley BB, Parks DH, Robinson CJ, et al. 2009. Introducing mothur: open-source, platform-independent, community-supported software for describing and comparing microbial communities. Applied and Environmental Microbiology. 75:7537–7541.

Schöttner S, Hoffmann F, Wild C, Rapp HT, Boetius A, Ramette A. 2009. Inter- and intra-habitat bacterial diversity associated with cold-water corals. ISME Journal. 3(6):756–759.

Schulte PM. 2015. The effects of temperature on aerobic metabolism: towards a mechanistic understanding of the responses of ectotherms to a changing environment. Journal of Experimental Biology. 218:1856–1866.

Schulzweida, U. 2019. CDO user guide (Version 1.9.8). doi:10.5281/zenodo.3539275.

Sedberry GR, McGovern JC, Pashuk O. 2001. The Charleston Bump: an island of essential fish habitat in the Gulf Stream. American Fisheries Society Symposium. 25:3–24.

Seim H, Edwards C. 2019. Upper-slope jets and Gulf Stream filaments inshore of the Charleston Bump during winter 2012. Journal of Physical Oceanography. 49(6):1423–1438.

Shannon CE, Weaver W. 1949. The mathematical theory of communication. Urbana (IL): University of Illinois Press.

Shearer TL, van Oppen MJH, Romano SL, Wörheide G. 2002. Slow mitochondrial DNA sequence evolution in the Anthozoa (Cnidaria). Molecular Ecology. 11:2475–2487.

Shen CC, Lawrence Edwards R, Cheng H, Dorale JA, Thomas RB, Moran SB, Weinstein SE, Edmonds HN. 2002. Uranium and thorium isotopic and concentration measurements by magnetic sector inductively coupled plasma mass spectrometry. Chemical Geology. 185(3–4):165–178.

Shepard FP, Dill RF. 1966. Submarine canyons and other sea valleys. Chicago (IL): Rand McNally and Co. 381 p.

Shepard FP, Marshall NF, McLoughlin PA, Sullivan GG. 1979. Currents in submarine canyons and other seavalleys. Tulsa (OK): American Association of Petroleum Geologists.

Sheridan RE, Crosby JT, Bryan GM, Stoffa PL. 1981. Stratigraphy and structure of southern Blake Plateau, northern Florida Straits, and northern Bahama Platform from multichannel seismic reflection data. AAPG Bulletin. 65(12):2571 –2593.

Sheridan RE, Crosby JT, Kent KM, Dillon WP, Paull CK. 1981. The geology of the Blake Plateau and Bahamas region. In: Kerr JW, Fergusson AJ, Machan LC, editors. Geology of the North Atlantic Borderlands. Calgary (CA): Canadian Society of Petroleum Geologists. p. 487–502.

Sherwood OA, Edinger EN. 2009. Ages and growth rates of some deep-sea gorgonian and antipatharian corals of Newfoundland and Labrador. Canadian Journal of Fisheries and Aquatic Sciences. 66:142–152.

Shiu JH, Yu SP, Fong CL, Ding JY, Tan CJ, Fan TY, Lu CY, Tang SL. 2020. Shifting in the dominant bacterial group *Endozoicomonas* is independent of the dissociation with coral symbiont algae. Frontiers in Microbiology. 11:1791.

Sidall ME, Fontanella FM, Watson SC, Kvist S, Erseus C. 2009. Barcoding bamboozled by bacteria: convergence to metazoan mitochondrial primer targets by marine microbes. Systematic Biology. 58(4):445–451.

Simpson SD, Meekan MG, Jeffs A, Montgomery JC, McCauley RD. 2008. Settlement-stage coral reef fish prefer the higher-frequency invertebrate-generated audible component of reef noise. Animal Behaviour. 75(6):1861–1868. doi:10.1016/j.anbehav.2007.11.004

Simpson SD, Meekan MG, Montgomery JC, McCauley RD, Jeffs A. 2005. Homeward sound. Science. 308(5719):221.

Skarke A, Ruppel C, Kodis M, Brothers D, Lobecker E. 2014. Widespread methane leakage from the sea floor on the northern US Atlantic margin. Nature Geoscience. 7(9):657–661.

Slabbekoorn H, Bouton N. 2008. Soundscape orientation: a new field in need of sound investigation. Animal Behaviour. 4(76):e5–e8.

Smith CR, De Leo FC, Bernardino AF, Sweetman AK, Arbizu PM. 2008. Abyssal food limitation, ecosystem structure and climate change. Trends in Ecology & Evolution. 23(9):518–528.

Smith KF, Brown JH. 2002. Patterns of diversity, depth range and body size among pelagic fishes along a gradient of depth. Global Ecology and Biogeography, 11(4):313–322.

Snelgrove PVR, Smith CR. 2002. A riot of species in an environmental calm: the paradox of the species-rich deep-sea floor. Oceanography and Marine Biology: an Annual Review. 40:311–342.

Sokolova IM, Frederich M, Bagwe R, Lannig G, Sukhotin AA. 2012. Energy homeostasis as an integrative tool for assessing limits of environmental stress tolerance in aquatic invertebrates. Marine Environmental Research. 79:1–15.

Solorzano L. 1969. Determination of ammonia in natural waters by the phenolhypochlorite method. Limnology and Oceanography. 14(5):799–801.

Solorzano L, Sharp JH. 1980. Determination of total dissolved phosphorus and particulate phosphorus in natural waters. Limnology and Oceanography. 25(4):754–758.

Somero GN. 2010. The physiology of climate change: how potentials for acclimatization and genetic adaptation will determine “winners” and “losers.” Journal of Experimental Biology. 213:912–920.

Sowers DC. 2020. Utilizing extended continental shelf (ECS) and ocean exploration mapping data for standardized marine ecological classification of the US Atlantic margin (2020.28260193) [dissertation]. Durham (N): University of New Hampshire.

Speck MD, Donachie SP. 2012. Widespread oceanospirillaceae bacteria in *Porites* spp. Journal of Marine Biology. 2012:746720.

Staaterman E, Paris CB, DeFerrari HA, Mann DA, Rice AN, D’Alessandro EK. 2014. Celestial patterns in marine soundscapes. Marine Ecology Progress Series. 508:17–32.

Stadnitskaia A, Muyzer G, Abbas B, Coolen MJL, Hopmans EC, Baas M, van Weering TCE, Ivanov MK, Poludetkina E, Sinninghe Damsté JS. 2005. Biomarker and 16S rDNA evidence for anaerobic

oxidation of methane and related carbonate precipitation in deep-sea mud volcanoes of the Sorokin Trough, Black Sea. Marine Geology. 217(1):67–96.

Stanley DJ, Sheng H, Lambert DN, Rona PA, McGrail DW, Jenkyns JS. 1981. Current-influenced depositional provinces, continental margin off Cape Hatteras, identified by petrologic method. Marine Geology. 40(3-4):215–235.

Stanley JA, Radford CA, Jeffs AG. 2012. Location, location, location: finding a suitable home among the noise. Proceedings of the Royal Society B: Biological Sciences. 279(1742):3622–3631.

Stefanescu C, Moralesnin B, Massuti E. 1994. Fish assemblages on the slope in the Catalan Sea (western Mediterranean) - influence of a submarine-canyon. Journal of the Marine Biological Association of the UK. 74(3):499–512.

Stetson TR. 1961. Report on Atlantis cruise #266, June–July 1961. Woods Hole (MA): Woods Hole Oceanographic Institute. Report No.: 61-35.

Stetson TR, Squires DF, Pratt RM. 1962. Coral banks occurring in deep water on the Blake Plateau. American Museum Novitates. 2114:1–39.

Stetson TR, Uchupi E, Milliman JD. 1969. Surface and subsurface morphology of two small areas of the Blake Plateau. Gulf Coast Association of Geological Societies Transactions. 19:131–142.

Stoeckl N, Hicks C, Mills M, Fabricius K, Esparon M, Kroon F, Sangha K, Costanza R. 2011. The economic value of ecosystem services in the Great Barrier Reef: our state of knowledge. Annals of the New York Academy of Sciences. 1219:113–133. doi:10.1111/j.1749-6632.2010.05892.x.

Stöhr S, Segonzac M. 2005. Deep-sea ophiuroids (*Echinodermata*) from reducing and non-reducing environments in the North Atlantic Ocean. Journal of the Marine Biological Association of the United Kingdom. 85(2):383–402.

Stuiver M. 1980. Workshop on 14C data reporting. Radiocarbon. 22(3):964–966.

Stuiver M, Polach HA. 1977. Discussion reporting of 14C data. Radiocarbon. 19(3):355–363.

Stuiver M, Reimer PJ, Reimer RW. 2021. CALIB 8.2. http://calib.org.

Sueur J, Pavoine S, Hamerlynck O, Duvail S. 2008. Rapid acoustic survey for biodiversity appraisal. PLoS ONE. 3(12):e4065. doi:10.1371/journal.pone.0004065.

Sulak KJ, Ross SW. 1996. Lilliputian bottom fish fauna of the Hatteras upper middle continental slope. Journal of Fish Biology. 49:91–113.

Summers N, Watling L. 2021. Upper Bathyal Pacific Ocean biogeographic provinces from octocoral distributions. Progress in Oceanography. 191:102509.

Sun J, Zhang Y, Xu T, Zhang Y, Mu H, Zhang Y, Qian PY. 2017. Adaptation to deep-sea chemosynthetic environments as revealed by mussel genomes. Nature Ecology & Evolution. 1(5):0121.

Sunagawa S, Woodley CM, Medina M. 2010. Threatened corals provide underexplored microbial habitats. PLoS ONE. 5(3):e9554.

Supek F, Bošnjak M, Škunca N, Šmuc T. 2011. REVIGO summarizes and visualizes long lists of gene ontology terms. PLoS ONE. 6(7):e21800.

Swart PK, Murray ST, Staudigel PT, Hodell DA. 2019. Oxygen isotopic exchange between CO_2 and phosphoric acid: implications for the measurement of clumped isotopes in carbonates. Geochemistry, Geophysics, Geosystems. 20(7):3730–3750.

Sweetman AK, Thurber AR, Smith CR, Levin LA, Mora C, Wei CL, Gooday AJ, Jones DOB, Rex M, Yasuhara M, et al. 2017. Major impacts of climate change on deep-sea benthic ecosystems. Elementa: Science of the Anthropocene. 5:4.

Taylor MW, Radax R, Steger D, Wagner M. 2007. Sponge-associated microorganisms: evolution, ecology, and biotechnological potential. Microbiology and Molecular Biology Reviews. 71(2):295–347.

Taylor RB, Barnes DJ, Lough JM. 1993. Simple models of density band formation in massive corals. Journal of Experimental Marine Biology and Ecology. 167:109–125.

Teichert BMA, Eisenhauer A, Bohrmann G, Haase-Schramm A, Bock B, Linke P. 2003. U/Th systematics and ages of authigenic carbonates from Hydrate Ridge, Cascadia Margin: recorders of fluid flow variations. Geochimica et Cosmochimica Acta. 67(20):3845–3857.

Tendal OS. 1992. The North Atlantic distribution of the octocoral *Paragorgia arborea* (L., 1758) (Cnidaria, Anthozoa). Sarsia. 77:213–217.

Teske A, Nelson DC. 2006. The genera *Beggiatoa* and *Thioploca*. Prokaryotes. 6:784–810.

Thaler AD, Saleu W, Carlsson J, Schultz TF, Van Dover CL. 2017. Population structure of *Bathymodiolus manusensis*, a deep-sea hydrothermal vent-dependent mussel from Manus Basin, Papua New Guinea. PeerJ. 5:e3655.

Thiem Ø, Ravagnan E, Fosså JH, Berntsen J. 2006. Food supply mechanisms for cold-water corals along a continental shelf edge. Journal of Marine Systems. 60(3-4):207–219.

Thomas EA, Liu R, Amon D, Copley JT, Glover AG, Helyar SJ, Sigwart JD. 2020. *Chiridota heheva*—the cosmopolitan holothurian. Marine Biodiversity. 50(6):1–13.

Thomsen L, Van Weering TCE. 1998. Spatial and temporal variability of particulate matter in the benthic boundary layer at the N.W. European Continental Margin (Goban Spur). Progress in Oceanography. 42(1-4):61–76.

Thomsen L, Gust G. 2000. Sediment erosion thresholds and characteristics of resuspended aggregates on the western European continental margin. Deep Sea Research Part I: Oceanographic Research Papers. 47(10):1881–1897.

Thuiller W, Georges D, Engler R, Breiner F. 2016. biomod2: ensemble platform for species distribution modeling.

Thuiller W, Lafourcade B, Engler R, Araújo MB. 2009. BIOMOD–a platform for ensemble forecasting of species distributions. Ecography. 32(3):369–373.

Thurber AR, Sweetman AK, Narayanaswamy BE, Jones DOB, Ingels J, Hansman RL. 2014. Ecosystem function and services provided by the deep sea. Biogeosciences. 11(14):3941–3963.

Timmers PHA, Welte CU, Koehorst JJ, Plugge CM, Jetten MSM, Stams AJM. 2017. Reverse methanogenesis and respiration in methanotrophic archaea. Archaea. 2017:1654237.

Titschack J, Thierens M, Dorschel B, Schulbert C, Freiwald A, Kano A, Takashima C, Kawagoe N, Li X. 2009. Carbonate budget of a cold-water coral mound (Challenger Mound, IODP Exp. 307). Marine Geology. 259(1-4):36–46.

Tittensor DP, Baco AR, Brewin PE, Clark MR, Consalvey M, Hall-Spencer J, Rowden AA, Schlacher T, Stocks KI, Rogers AD. 2009. Predicting global habitat suitability for stony corals on seamounts. Journal of Biogeography. 36:1111–1128.

Todd PA, Heery EC, Loke LH, Thurstan RH, Kotze DJ, Swan C. 2019. Towards an urban marine ecology: characterizing the drivers, patterns and processes of marine ecosystems in coastal cities. Oikos. 128(9):1215–1242.

Todd RE. 2017. High-frequency internal waves and thick bottom mixed layers observed by gliders in the Gulf Stream. Geophysical Research Letters. 44(12):6316–6325.

Todd RE. 2020. Export of Middle Atlantic Bight shelf waters near Cape Hatteras from two years of underwater glider observations. Journal of Geophysical Research: Oceans. 125(4).

Tonolla D, Lorang MS, Heutschi K, Gotschalk CC, Tockner K. 2011. Characterization of spatial heterogeneity in underwater soundscapes at the river segment scale. Limnology and Oceanography. 56(6):2319–2333.

Torres-Beltrán M, Mueller A, Scofield M, Pachiadaki MG, Taylor C, Tyshchenko K, Michiels C, Lam P, Ulloa O, Jürgens K, et al. 2019. Sampling and processing methods impact microbial community structure and potential activity in a seasonally anoxic fjord: Saanich Inlet, British Columbia. Frontiers in Marine Science. 6:132. doi:10.3389/fmars.2019.00132.

Triezenberg PJ, Hart PE, Childs JR. 2016. National Archive of Marine Seismic Surveys (NAMSS): a USGS data website of marine seismic reflection data within the U.S. Exclusive Economic Zone (EEZ). Washington (DC): U.S. Geological Survey. doi:10.5066/F7930R7P.

Tsounis G, Orejas C, Reynaud S, Gili J, Allemand D, Ferrier-Pagès C. 2010. Prey-capture rates in four Mediterranean cold-water corals. Marine Ecology Progress Series. 398:149–155.

Tsuchiya M. 1989. Circulation of the Antarctic intermediate water in the North-Atlantic Ocean. Journal of Marine Research. 47(4):747–755.

Tucholke BE, Bryan GM, Ewing JI. 1977. Gas-hydrate horizons detected in seismic profiler data from the western North Atlantic. AAPG Bulletin. 61:698–707.

Tunnicliffe V, McArthur AG, McHugh D. 1998. A biogeographical perspective of the deep-sea hydrothermal vent fauna. Advances in Marine Biology. 34:353–442.

Turner CR, Miller DJ, Coyne KJ, Corush J, Orb L. 2014. Improved methods for capture, extraction, and quantitative assay of environmental DNA from Asian bigheaded carp (*Hypophthalmichthys* spp.. PLoS ONE. 9:e114329. doi:10.1371/journal.pone.0114329.

Turner PJ, Ball B, Diana Z, Fariñas-Bermejo A, Grace I, McVeigh D, Powers MM, Van Audenhaege L, Maslakova S, Young CM, et al. 2020. Methane seeps on the US Atlantic margin and their potential importance to populations of the commercially valuable deep-sea red crab, *Chaceon quinquedens*. Frontiers in Marine Science. 7:75.

Tyack PL, Frisk G, Boyd I, Urban E, Seeyave S. 2015. International Quiet Ocean Experiment Science Plan. Woods Hole (MA): Scientific Committee on Oceanic Research, Partnership for Observation of the Global Oceans. 111 p.

Tyler PA, Bronsdon SK, Young CM, Rice AL. 1995. Ecology and gametogenic biology of the genus *Umbellula* (Pennatulacea) in the North-Atlantic Ocean. Internationale Revue der Gasamten Hydrobiolgie. 80(2):187–199.

Tyler PA, Campos-Creasy LS, Giles LS. 1993. Environmental control of quasi-continuous and seasonal reproduction in deep-sea benthic invertebrates; preliminary observations. In: Young CM, Eckelbarger KJ, editors. Reproduction, larval biology and recruitment of the deep-sea benthos. Chapter 8; p. 158–178.

Tyler PA, Grant A, Pain SL, Gage JD. 1982. Is annual reproduction in deep-sea echinoderms a response to variability in their environment? Nature. 300(5894):747–750.

Tyler PA, Young CM. 1999. Reproduction and dispersal at vents and cold seeps. Journal of the Marine Biological Association of the UK. 79(2):193–208.

Tyler P, Young CM, Dolan E, Arellano SM, Brooke SD, Baker M. 2007. Gametogenic periodicity in the chemosynthetic cold-seep mussel *"Bathymodiolus" childressi*. Marine Biology. 150:829–840.

Uchupi E. 1988. The Atlantic continental margin: U.S. Robert E. Sheridan and John A. Grow, eds. Geological Society of America, Boulder, CO, 1988. x, 610 pp., illus., + charts in slipcase. $49.50. The Geology of North America, vol. 1-2. Science. 241(4873):1693. doi:10.1126/science.241.4873.1693.

Uchupi E, Emergy KO, Bowin C, Phillips JD. 1976. Continental margin off western Africa: Senegal to Portugal. AAPG Bulletin. 60:809–878.

UK Biodiversity Group. 2000. Tranche 2 action plans. Volume V: maritime species and habitats. Peterborough (UK): English Nature. 242 p.

Valentine DL, Reeburgh WS. 2008. New perspectives on anaerobic methane oxidation. Environmental Microbiology. 2(5):477–484.

Valentine DL, Reeburgh WS, Blanton DC. 2000. A culture apparatus for maintaining H_2 at sub-nanomolar concentrations. Journal of Microbiological Methods. 39(3):243–251.

Valentine PC. 1987. The shelf-slope transition; canyon and upper slope sedimentary processes on the southern margin of Georges Bank. Washington (DC): U.S. Geological Survey.

Van Bleijswijk JDL, Whalen C, Duineveld GCA, Lavaleye MSS, Witte HJ, Mienis F. 2015. Microbial assemblages on a cold-water coral mound at the SE Rockall Bank (NE Atlantic): interactions with hydrography and topography. Biogeosciences. 12(14):4483–4496.

Van de Water JAJM, Melkonian R, Voolstra CR, Junca H, Beraud E, Allemand D, Ferrier-Pagès C. 2016. Comparative assessment of Mediterranean gorgonian-associated microbial communities reveals conserved core and locally variant bacteria. Microbial Ecology. 73(2):446–478.

Van Dover CL, Aharon P, Bernhard JM, Caylor E, Doerries M, Flickinger W, Vrijenhoek R. 2003. Blake Ridge methane seeps: characterization of a soft-sediment, chemosynthetically based ecosystem. Deep Sea Research Part I: Oceanographic Research Papers. 50(2):281–300.

Van Haren H, Mienis F, Duineveld GCA, Lavaleye MSS. 2014. High-resolution temperature observations of a trapped nonlinear diurnal tide influencing cold-water corals on the Logachev mounds. Progress in Oceanography. 125:16–25.

Vega Thurber RL, Correa AMS. 2011. Viruses of reef-building scleractinian corals. Journal of Experimental Marine Biology and Ecology. 408:102–113.

Vermeij MJA, Marhaver KL, Huijbers CM, Nagelkerken I, Simpson SD. 2010. Coral larvae move toward reef sounds. PLoS ONE. 5(5).

Vetter EW, Dayton PK. 1998. Macrofaunal communities within and adjacent to a detritus-rich submarine canyon system. Deep Sea Research Part II: Topical Studies in Oceanography. 45:25–54.

Vetter EW, Smith CR, De Leo FC. 2010. Hawaiian hotspots: enhanced megafaunal abundance and diversity in submarine canyons on the oceanic islands of Hawaii. Marine Ecology. 31:183–199.

Vezzulli L, Pezzati E, Huete-Stauffer C, Pruzzo C, Cerrano C. 2013. 16SrDNA pyrosequencing of the Mediterranean gorgonian *Paramuricea clavata* reveals a link among alterations in bacterial holobiont members, anthropogenic influence and disease outbreaks. PLoS ONE. 8(6):e67745.

Vokhshoori NL, Mccarthy MD, Close HG, Demopoulos AW, Prouty NG. 2021. New geochemical tools for investigating resource and energy functions at deep-sea cold seeps using amino acid δ15N in chemosymbiotic mussels (*Bathymodiolus childressi*). Geobiology. 19:601–617.

Voolstra CR, Ziegler M. 2020. Adapting with microbial help: microbiome flexibility facilitates rapid responses to environmental change. BioEssays. 42(7):2000004.

Wagner JK, McEntee MH, Brothers LL, German CR, Kaiser CL, Yoerger DR, Van Dover CL. 2013. Cold-seep habitat mapping: high-resolution spatial characterization of the Blake Ridge Diapir seep field. Deep Sea Research Part II: Topical Studies in Oceanography. 92:183–188.

Walbridge S, Slocum N, Pobuda M, Wright DJ. 2018. Unified geomorphological analysis workflows with benthic terrain modeler. Geosciences. 8:94. doi:10.3390/geosciences8030094.

Waller RG, Tyler PA, Gage JD. 2002. Reproductive ecology of the deep-sea scleractinian coral *Fungiacyathus marenzelleri* (Vaughn 1906) in the northeast Atlantic Ocean. Coral Reefs. 21:325–331.

Waller RG, Tyler PA. 2005. The reproductive biology of two deep-water, reef building scleractinians from the North East Atlantic Ocean. Coral Reefs. 24:514–522.

Waller RG, Tyler PA. 2011. Reproductive patterns in two deep-water solitary corals from the north-east Atlantic — *Flabellum alabastrum* and *F. angulare* (Cnidaria: Anthozoa: Scleractinia. Journal of the Marine Biological Association of the UK. 91:669–675. doi:10.1017/S0025315410000822.

Waller RG, Tyler PA, Gage JD. 2005. Sexual reproduction in three hermaphroditic deep-sea *Caryophyllia* species (Anthozoa: Scleractinia) from the NE Atlantic Ocean. Coral Reefs. 24:594–602.

Wang C, Wang X, Liu D, Wu H, Lü X, Fang Y, Cheng W, Luo W, Jiang P, Shi J. 2014. Aridity threshold in controlling ecosystem nitrogen cycling in arid and semi-arid grasslands. Nature Communications. 5:4799.

Wang Q, Alowaifeer A, Kerner P, Balasubramanian N, Patterson A, Christian W, Tarver A, Dore JE, Hatzenpichler R, Bothner B, et al. 2021. Aerobic bacterial methane synthesis. Proceedings of the National Academy of Sciences. 118(27):e2019229118.

Wang X-C, Chen RF, Whelan J, Eglinton L. 2001. Contribution of "old" carbon from natural marine hydrocarbon seeps to sedimentary and dissolved organic carbon pools in the Gulf of Mexico. Geophysical Research Letters. 28(17):3313–3316.

Watling L, France SC, Pante E, Simpson A. 2011. Biology of deep-water octocorals. In: Lesser M, editor. Advances in Marine Biology. Volume 60. London (UK): Elsevier. p. 41–122.

Weems RE, Bachman J, Rayburn WT, McCloud Jr JR. 2021. A vertebrate ichnofauna from the late Pleistocene (Sangamon Interglacial) TABB formation at Stratford Hall Plantation, Westmoreland County, Virginia USA. In: Hunt AP, Lichtig AJ, Lucas SG, editors. Fossil record 7. Albuquerque (NM): New Mexico Museum of Natural History & Science. p. 505–512.

Weinnig AM, Gómez CE, Hallaj A, Cordes EE. 2020. Cold-water coral (*Lophelia pertusa*) response to multiple stressors: high temperature affects recovery from short-term pollution exposure. Scientific Reports. 10:1768.

Weir BS, Cockerham CC. 1984. Estimating F-statistics for the analysis of population structure. Evolution. 38(6):1358–1370. doi:10.1111/j.1558-5646.1984.tb05657.x.

Wentworth CK. 1929. Method of computing mechanical composition types in sediments. GSA Bulletin. 40:771–790.

Wenz GM. 1962. Acoustic ambient noise in ocean: spectra and sources. Journal of the Acoustical Society of America. 34(12):1936–1956.

Wild C, Mayr C, Wehrmann L, Schottner S, Naumann M, Hoffmann F, Rapp HT. 2008. Organic matter release by cold water corals and its implication for fauna-microbe interaction. Marine Ecology Progress Series. 372:67–75.

Wilford DC, Miksis-Olds JL, Martin SB, Howard DR, Lowell K, Lyons AP, Smith MJ. 2021. Quantitative soundscape analysis to understand multidimensional features. Frontiers in Marine Science. 8:672336. doi:10.3389/fmars.2021.672336.

Williams RG, McDonagh E, Roussenov VM, Torres-Valdes S, King B, Sanders R, Hansell DA. 2011. Nutrient streams in the North Atlantic: advective pathways of inorganic and dissolved organic nutrients. Global Biogeochemical Cycles. 25(4).

Wilson GA, Rannala B. 2003. Bayesian inference of recent migration rates using multilocus genotypes. Genetics. 163(3):1177–1191.

Wilson JB. 1979. Patch development of the deep-water coral *Lophelia pertusa* (L.) on Rockall Bank. Journal of the Marine Biological Association of the U.K. 59:165–177.

Wilson MFJ, O'Connell B, Brown C, Guinan JC, Grehan AJ. 2007. Multiscale terrain analysis of multibeam bathymetry data for habitat mapping on the continental slope. Marine Geodesy. 30:3–35.

Witte U. 1996. Seasonal reproduction in deep-sea sponges triggered by vertical flux. Marine Biology. 124:571–581.

Yakimov MM, Cappello S, Crisafi E, Trusi A, Savini A, Corselli C, Scarfi S, Giuliano L. 2006. Phylogenetic survey of metabolically active microbial communities associated with the deep-sea coral *Lophelia pertusa* from the Apulian plateau, Central Mediterranean Sea. Deep Sea Research Part I: Oceanographic Research Papers. 53:62–75.

Yasuhara M, Danovaro R. 2016. Temperature impacts on deep-sea biodiversity. Biological Reviews. 91(2):275–287.

Yesson C, Taylor ML, Tittensor DP, Davies AJ, Guinotte J, Baco A, Black J, Hall-Spencer JM, Rogers AD. 2012. Global habitat suitability of cold-water octocorals. Journal of Biogeography. 39:1278–1292.

Young CM, He R, Emlet RB, Li Y, Qian H, Arellano SM, Van Gaest A, Bennett KC, Wolf M, Smart TI, Rice ME. 2012. Dispersal of deep-sea larvae from the Intra-American seas: simulations of trajectories using ocean models. Integrative and Comparative Biology. 52(4):483–496.

Yu Z, Qi Z, Hu C, Liu W, Huang H. 2013. Effects of salinity on ingestion, oxygen consumption and ammonium excretion rates of the sea cucumber *Holothuria leucospilota*. Aquaculture Research. 44:1760–1767.

Zalasiewicz J, Williams M, Waters CN. 2014. Can an Anthropocene Series be defined and recognized? Geological Society, London, Special Publications. 395(1):39–53.

Zaneveld JR, Burkepile DE, Shantz AA, Pritchard C, McMinds R, Payet JP, Welch R, Correa AMS, Lemoine NP, Rosales S, et al. 2016. Overfishing and nutrient pollution interact with temperature to disrupt coral reefs down to microbial scales. Nature Communications. 7:11833.

Zarza E, Connors EM, Maley JM, Tsai WL, Heimes P, Kaplan M, McCormack JE. 2018. Combining ultraconserved elements and mtDNA data to uncover lineage diversity in a Mexican highland frog (Sarcohyla; Hylidae). PeerJ. 6:e6045.

Zarza E, Faircloth BC, Tsai WL, Bryson Jr RW, Klicka J, McCormack JE. 2016. Hidden histories of gene flow in highland birds revealed with genomic markers. Molecular Ecology. 2520:5144–5157.

Zeevi Ben-Yosef D, Benayahu Y. 1999. The gorgonian coral *Acabaria biserialis*: life history of a successful colonizer of artificial substrata. Marine Biology. 135:473–481.

Zhang N, Lin M, Snyder GT, Kakizaki Y, Yamada K, Yoshida N, Matsumoto R. 2019. Clumped isotope signatures of methane-derived authigenic carbonate presenting equilibrium values of their formation temperatures. Earth and Planetary Science Letters. 512:207–213.

Zhang WG, Gawarkiewicz GG. 2015. Dynamics of the direct intrusion of Gulf Stream ring water onto the Mid-Atlantic Bight shelf. Geophysical Research Letters. 42(18):7687–7695.

Zhang X-Y, Zhang Y, Xu X-Y, Qi S-H. 2013. Diverse deep-sea fungi from the South China Sea and their antimicrobial activity. Current Microbiology. 67(5):525–530.

Ziegler M, Grupstra CGB, Barreto MM, Eaton M, BaOmar J, Zubier K, Al-Sofyani A, Turki AJ, Ormond R, Voolstra CR. 2019. Coral bacterial community structure responds to environmental change in a host-specific manner. Nature Communications. 10:3092.

10 Bibliography

Adinolfi F. 1990. Oil and gas developments in Atlantic Coastal Plain and Outer Continental Shelf in 1989. AAPG Bulletin. 74(10B):42–45.

Altieri AH, Harrison SB, Seemann J, Collin R, Diaz RJ, Knowlton N. 2017. Tropical dead zones and mass mortalities on coral reefs. PNAS. 114:3660–3665.

Baker EJ, Kellogg CA. 2014. Comparison of three DNA extraction kits to establish maximum yield and quality of coral-associated microbial DNA. Washington (DC): U.S. Geological Survey. 18 p. Report No.: Open-File Report 2014-1066.

Barnett TP, Pierce DW, AchutaRao KM, Gleckler PJ, Santer BD, Gregory JM, Washington WM. 2005. Penetration of human-induced warming into the world's oceans. Science. 309:284–287.

Billett DS, Lampitt RS, Rice AL, Mantoura RF. 1983. Seasonal sedimentation of phytoplankton to the deep-sea benthos. Nature. 302(5908):520–522.

Buhl-Mortensen L, Mortensen PB. 2004. Symbiosis in deep-water corals. Symbiosis. 37:33–61.

Carreiro-Silva M, Andrews AH, Braga-Henriques A, de Matos V, Porteiro FM, Santos RS. 2013. Variability in growth rates of long-lived black coral *Leiopathes* sp. from the Azores (Northeast Atlantic). Marine Ecology Progress Series. 473:189–199.

Chen X, Tung KK. 2014. Varying planetary heat sink led to global-warming slowdown and acceleration. Science. 345:897–903.

Donner SD, Skirving WJ, Little CM, Oppenheimer M, Hoegh-Guldberg O. 2005. Global assessment of coral bleaching and required rates of adaptation under climate change. Global Change Biology. 11:2251–2265.

Everett MV, Park LK. 2018. Exploring deep-water coral communities using environmental DNA. Deep Sea Research Part II: Topical Studies in Oceanography. 150:229–241.

FAO. 2008. Report of the Technical Consultation on International Guidelines for the Management of Deep-Sea Fisheries in the High Seas. Rome (IT): Food and Agriculture Organization of the United Nations.

Findlay HS, Artioli Y, Moreno-Navas J, Hennige SJ, Wicks LC, Huvenne VAI, Woodward EMS, Roberts JM. 2013. Tidal downwelling and implications for the carbon biogeochemistry of cold-water corals in relation to future ocean acidification and warming. Global Change Biology. 19:2708–2719.

Glazier A, Herrera S, Weinnig A, Kurman M, Gómez CE, Cordes EE. 2020. Regulation of ion transport and energy metabolism enables certain coral genotypes to maintain calcification under experimental ocean acidification. Molecular Ecology. 29:1657–1673.

Heiderich J, Todd RE. 2020. Along-stream evolution of gulf stream volume transport. Journal of Physical Oceanography. 50(8):2251–2270.

Hoegh-Guldberg O, Bruno JF. 2010. The impact of climate change on the world's marine ecosystems. Science. 328:1523–1528.

Holden NE. 1990. Total half-lives for selected nuclides. Pure and Applied Chemistry. 62(5):941–958.

Huson DH, Beier S, Flade I, Gorska A, El-Hadidi M, Mitra S, Ruscheweyh H, Tappu R. 2016. MEGAN community edition – interactive exploration and analysis of large-scale microbiome sequencing data. PLoS Computation Biology. doi:10.1371/journal/pcbi.1004957.

Jaffrey A, Flynn K, Glendenin L, Bentley W, Essling A. 1971. Precision measurement of half-lives and specific activities of ^{235}U and ^{238}U. Physical Review C. 4(5):1889–1906. doi:10.1103/PhysRevC.4.1889.

Juva K, Flögel S, Karstensen J, Linke P, Dullo WC. 2020. Tidal dynamics control on cold-water coral growth: a high-resolution multivariable study on eastern Atlantic cold-water coral sites. Frontiers in Marine Science. 7:132.

Krieger K, Wing B. 2002 Megafauna associations with deepwater corals (*Primnoa* spp.) in the Gulf of Alaska. Hydrobiologia. 471(1-3):83–90.

Kurman MD, Gómez CE, Georgian SE, Lunden JJ, Cordes EE. 2017. Intra-specific variation reveals potential for adaptation to ocean acidification in a cold-water coral from the Gulf of Mexico. Frontiers in Marine Science. 4:111.

Lessard-Pilon SA, Podowski EL, Cordes EE, Fisher CR. 2010. Megafauna community composition associated with *Lophelia pertusa* colonies in the Gulf of Mexico. Deep Sea Research Part II: Topical Studies in Oceanography. 57:1882–1890.

Leterme SC, Pingree RD. 2008. The Gulf Stream, rings and North Atlantic eddy structures from remote sensing (Altimeter and SeaWiFS). Journal of Marine Systems. 69:177–190.

Matsumoto AK, Lynch-Stieglitz J. 2003. Persistence of Gulf Stream separation during the Last Glacial period: implications for current separation theories. Journal of Geophysical Research. 108. doi:10.1029/2001JC000861.

Miller KJ. 1997. Genetic structure of black coral populations in New Zealand's fiord. Marine Ecology Progress Series. 161:123–132.

Miller KJ. 1998. Short-distance dispersal of black coral larvae: inference from spatial analysis of colony genotypes. Marine Ecology Progress Series. 163:225–233.

Miller K, Williams A, Rowden AA, Knowles C, Dunshea G. 2010. Conflicting estimates of connectivity among deep-sea coral populations. Marine Ecology. 31:144–157.

Olsson IU. 1970. The use of oxalic acid as a standard. In: Olsson IU, editor. Radiocarbon variations and absolute chronology. New York (NY): John Wiley & Sons. p. 17.

Parmesan C, Yohe G. 2003. A globally coherent fingerprint of climate change impacts across natural systems. Nature. 421:37–42.

Parrish FA, Baco AR, Kelley C, Reiswig H. 2017. State of deep-sea coral and sponge ecosystems of the U.S. Pacific Islands region. In: Hourigan TF, Etnoyer PJ, Cairns SD, editors. The state of deep-sea coral and sponge ecosystems of the United States. Silver Spring (MD): U.S. Department of Commerce, National Oceanic Atmospheric Administration. p. 40.

Pinet PR, Popenoe P. 1982. Blake Plateau: control of miocene sedimentation patterns by large-scale shifts of the Gulf Stream axis. Geology. 10(5):257–259.

Pinet PR, Popenoe P, Nelligan DF. 1981. Gulf Stream: reconstruction of Cenozoic flow patterns over the Blake Plateau. Geology. 9(6):266–270.

Pohlman JW, Kaneko M, Heuer VB, Coffin RB, Whiticar M. 2009. Methane sources and production in the northern Cascadia margin gas hydrate system. Earth and Planetary Science Letters. 287(3–4):504–512.

Popenoe P. 1990. Paleogeography and paleo-oceanography of the Miocene of the Southeastern United States. In: Burnett WC, Riggs SR, editors. Phosphate deposits of the world: Neogene to modern phosphorites. New York (NY): Cambridge University Press. p. 352–380.

Popenoe P. 1994. Bottom character map of the northern Blake Plateau. Washington (DC): U.S. Geological Survey. 35 p. Report No.: Open-file Report 93-724.

Popenoe P, Schmuck EA, Dillon WP. 1993. The Cape Fear landslide: slope failure associated with salt diapirism and gas hydrate decomposition. In: Schwab WC, Lee HJ, Twichell DC, editors. Submarine landslides: selective studies in the U.S. Exclusive Economic Zone. Washington (DC): U.S. Geological Survey Bulletin. p. 40–53.

Price N, Muko S, Legendre L, Steneck R, van Oppen M, Albright R, Ang Jr P, Carpenter R, Chui A, Fan T, et al. 2019. Global biogeography of coral recruitment: tropical decline and subtropical increase. Marine Ecology Progress Series. 621:1–17.

Prouty NG, Roark EB, Buster NA, Ross SW. 2011. Growth-rate and age distribution of deep-sea black corals in the Gulf of Mexico. Marine Ecology Progress Series. 423:101–115.

Prouty NG, Storlazzi CD, McCutcheon AL, Jenson JW. 2014. Historic impact of watershed change and sedimentation to reefs along west-central Guam. Coral Reefs. 33(3):733–749.

Reed JK, Messing CG, Walker BK, Brooke S, Correa TBS, Brouwer M, Udouj T, Farrington S. 2013. Habitat characterization, distribution, and areal extent of deep-sea coral ecosystems off Florida, Southeastern U.S.A. Caribbean Journal of Science. 47(1):13–30.

Reimer P. 2013. IntCal13 and Marine13 radiocarbon age calibration curves 0–50,000 years cal BP. Radiocarbon. 55(4):1869–1887.

Roark EB, Guilderson TP, Dunbar RB, Fallon SJ, Mucciarone DA. 2009. Extreme longevity in proteinaceous deep-sea corals. Proceedings of the National Academy of Sciences. 106(13):5204–5208.

Roark EB, Guilderon TP, Dunbar RB, Ingram BL. 2006. Radiocarbon-based ages and growth rates of Hawaiian deep-sea corals. Marine Ecology Progress Series. 327:1–14.

Roark EB, Guilderson TP, Flood-Page S, Dunbar RB, Ingram BL, Fallon SJ, McCulloch M. 2005. Radiocarbon-based ages and growth rates of bamboo corals from the Gulf of Alaska. Geophysical Research Letters. 32(4):L04606.

Rowden AA, Anderson OF, Georgian SE, Bowden DA, Clark MR, Pallentin A, Miller A. 207. High-resolution habitat suitability models for the conservation and management of vulnerable marine ecosystems on the Louisville Seamount Chain, South Pacific Ocean. Frontiers in Marine Science. 4.

Schaff T, Levin L. 1994. Spatial heterogeneity of benthos associated with biogenic structures on the North Carolina continental slope. Deep-Sea Research II: Topical Studies in Oceanography. 41(4-6):901–918.

Schmidtko S, Stramma L, Visbeck M. 2017. Decline in global oceanic oxygen content during the past five decades. Nature. 542:335–339.

Sibuet M, Olu K. 1998. Biogeography, biodiversity and fluid dependence of deep-sea cold-seep communities at active and passive margins. Deep Sea Research Part II: Topical Studies in Oceanography. 45(1-3):517–567.

Somero GN. 2012. The physiology of global change: linking patterns to mechanisms. Annual Review of Marine Science. 4:39–61.

Suess E. 2014. Marine cold seeps and their manifestations: geological control, biogeochemical criteria and environmental conditions. International Journal Of Earth Sciences. 103(7):1889–1916.

Uchupi E. 1967. The continental margin south of Cape Hatteras, North Carolina: shallow structure. Southeastern Geology. 8(4):155–177.

Wijffels S, Roemmich D, Monselesan D, Church J, Gilson J. 2016. Ocean temperatures chronicle the ongoing warming of Earth. Nature Climate Change. 6:116–118.

Williams B, Risk MJ, Ross SW, Sulak KJ. 2006. Deep-water antipatharians: proxies of environmental change. Geology. 34:773–776.

Williams B, Risk MJ, Ross SW, Sulak KJ. 2007. Stable isotope data from deep-water antipatharians: 400-year records from the southeastern coast of the United States of America. Bulletin of Marine Science. 81:437–447.

Zar JH. 1999. Biostatistical analysis. Upper Saddle River (NJ): Prentice Hall.

Appendix A. Data Management with Links to All Data Repositories

Open Science Framework (OSF)

OSF is maintained and developed by the Center for Open Science (COS), a 501(c)3 non-profit organization. COS is supported through grants from a variety of supporters, including Federal agencies, private foundations, and commercial entities.

COS established a $250,000 preservation fund for hosted data in the event that COS had to curtail or close its offices. If activated, the preservation fund will preserve and maintain read access to hosted data. This fund is sufficient for 50+ years of read access hosting at present costs. COS will incorporate growth of the preservation fund as part of its funding model as data storage scales.

The following link will direct to the OSF homepage and the following tables show links to available data in various categories.

OSF | Deep SEARCH - https://osf.io/4c9pt/

Table A-1. Data available through OSF

In the following tables, the column header is linked to the OSF page containing the content listed below each header (ND=No Data).

Predictive Habitat Models	Reports	Richardson discovery paper	Processed water chemistry data
Outputs from predictive habitat models developed as part of Deep SEARCH	Quarterly reports Cruise reports	ADEON_Cruise1_SAV_CTD.xlsx	AT41 carbonate chemistry_CTDonly.xlsx
Quarterly Report/Mission Planning May 2018	2017-Demopoulos-*Pisces*-cruise-report.pdf	available data sets.xlsx	2018 AT41 Cruise
ArcGIS_Enseble_ESRIIGrid_Files.zip	Atlantic Canyons-1st quarterlyNov2017.pdf	Canyons_LopheliaReefData_04052020.xlsx	AT41 carbonate chemistry_CTDonly.xlsx
Deep SEARCH_Targets_Pred_Mod_Alcy.jpg	Atlantic Canyons-3rd quarterlyApr2018.pdf	cover letter-final.docx	Basket Maps
Deep SEARCH_Targets_Pred_Mod_Alcy.mpk	Atlantic Canyons-4th quarterlyAug1 2018.pdf	dive locations.xlsx	CTD Data
Deep SEARCH_Targets_Pred_Mod_Scler.jpg	Atlantic Canyons-5th quarterlyNov1 2018.pdf	Fig 3.png	Dive Logs
Deep SEARCH_Targets_Pred_Mod_Scler.mpk	Atlantic Canyons-6th quarterlyFeb1 2019_31Jan19.pdf	Fig1_16Apr.pdf	Dive Plans
ND	BMCC18_Cruise_Report_final.pdf	Isotope table.xlsx	Dive Summaries
ND	Cruise Report NF1909.pdf	OceanographyFigure_Final_2March2020.jpg	Nav
ND	Cruise Report RB1903-210619.pdf	reef table.xlsx	OSF Storage (United States)
ND	Cruise Report-AT41-19Aug-2Sept2018 a.pdf	RH_SpeciesTable.xlsx	Plan of the Day
ND	Deep SEARCH-2nd quarterly-Jan2018.pdf	Richardson discovery ms EC CM 18Dec18.docx	ND
ND	Deep SEARCH-10th quarterly1December-29 Feb2020-27Feb2020.pdf	Richardson discovery ms.docx	ND
ND	Deep SEARCH-7th quarterlyMar02-Jun 01 2019_29May19.pdf	Richardson ms 0417_clean.docx	ND
ND	Deep SEARCH-11th quarterly letter-1March-31 May2020	Richardson_VariableContrib.xlsx	ND

Predictive Habitat Models	Reports	Richardson discovery paper	Processed water chemistry data
ND	Deep SEARCH-10th quarterly1December-29 Feb2020-27Feb2020	RichardsonHillsReefMap.pdf	ND
ND	Deep SEARCH-12th quarterly - 31 Aug 2020	Science_manuscript_Cordes et al_combined.pdf	ND
ND	Deep SEARCH-13th quarterly - 2-28-2021	ND	ND
ND	Deep SEARCH-14th quarterly - 31 Aug 2021	ND	ND
ND	Deep SEARCH-14th quarterly Appendices - 31 Aug 2021	ND	ND

Cruises

2017 *Sentry* Cruise	2018 AT41 Cruise	2018 BMCC Cruise	2019 RB1903 Cruise	2019 NF1909 Cruise
Proposed mapping areas	Basket Maps	BCMM18_Cruise_Report_TS_eec_amw.docx	CTD data	2019 NF1909 Cruise
mapping coordinates.xlsx	CTD Data	BCMM18_Cruise_Summary.doc	OSF Storage (United States)	CTD logsheets scans
2017 *Sentry* cruise	Dive Logs	BCMM18_Event_Log.xlsx	RB1903_MasterSampleSheet_RENAV.xlsx	Sample Logs & Data
ND	Dive Plans	BMCC 2018 itinerary AMW.xlsx	RB1903_renav_ALL.csv	EK60 Screengrabs
ND	Dive Summaries	BMCC_sites_map2.jpg	ND	Photos & Videos
ND	Nav	BMCC18_Deep SEARCH_Master_Sample_Sheet.xlsx	ND	PODs
ND	Plan of the Day	ND	ND	CTD data
ND	Processed water chemistry data	ND	ND	ND

Principal Investigators/Collaborators

Cordes	**Demopoulos**	**Joye**	**Lunden**
Cordes Lab data and deliverables	Demopoulos-Deep SEARCH-Isotopes.xlsx - 5/22/2020	AT41_sediment_geochemistry.csv	14 May 2020 All data from my work with the Deep SEARCH project can be found in one of the following folders on OSF:
Richardson Reef Complex Terrain	Demopoulos-Deep SEARCH-Samples.xlsx - 5/22/2020	AT41_watercolumn_geochemistry.csv	Cruise data from CTD casts are located in each cruise component OSFHOME —> Deep SEARCH —> cruise ID —> CTD Data • Furu and I are going through and QA/QCing these data and will update the group if substantial changes are made.
Contains raster (.tif or .asc) files containing data for terrain variables (e.g., depth, slope, etc.) at Richardson Reef Complex.	FrameGrabs_ForID - 6/23/2020	RB19-03_sediment_geochemistry.csv	Processed seawater chemistry data (including total alkalinity, pH, omega aragonite) are located in a separate component OSFHOME —> Deep SEARCH —> Processed water chemistry data • I am updating these files to include calculations for omega calcite and pCO2. If you have any questions about any of the above data, please e-mail me at jlunden@temple.edu
Video Annotation Video_Morphospecies_IDs	Annelida, Arthropoda, Cnidaria, Echinodermata, Mollusca, Others, Porifera	RB19-03_watercolumn_geochemistry.csv	ND
Video annotation data generated by dive for Deep SEARCH and select *Okeanos Explorer* dives. Each file contains one dive of data coded by vehicle and dive number. Habitat (dominant and subdominant substrates, profile, etc.) and submersible (lasers, on bottom) data were annotated in the Cordes Laboratory. Submersible navigation and sensor data are appended by timestamp where available.	Demopoulos-Deep SEARCH-Isotopes.xlsx - 5/22/2020	ND	ND
Porifera, Cnidaria, Echinodermata, Arthropoda, Hagfish	ND	ND	ND

Principal Investigators/Collaborators

Sutton	**Kellogg**	**Brooke**	**Miksis-Olds**
Nancy Foster 1909 Trawl	AT41 5/12/2020	Respiration experimentsRespiration data from Lp, Mo and P. sp. at 7,12,16,20 deg	Passive Acoustic Data
NF1909 Trawling Sample Data_021220.xlsx , 5/11/2020 12:40:00 PM	2018-AT41-Cruise Kellogg sample list.xlsx	Lophelia pertusa, Madrepora oculata, Paramuricid sp TBD	There are four data files in this Passive Acoustic Data folder. The Albex01 files contain passive acoustic data from the short ALBEX lander deployment. The Albex02 data files contain data from the long Albex lander deployment.
ND	RB1903 5/12/2020	Transplant modelsThese are object files that show the model outputs from the transplanted fragments, The final file shows transplant metrics.	Albex01_richhills_pkSPL.xlsx, Albex01_richhills_rmsSPL.xlsx, Albex02_richhills_pkSPL2.xlsx, Albex02_richhills_rmsSPL2.xlsx
ND	2019-RB1903-Cruise Kellogg sample list.xlsx	Video files - corals only *Alvin* dives 2018, *Jason* dives 2019	ADEON CTD data
ND	ND	Reproduction files	The ADEON CTD data contains a year of data from the ADEON SAV and WIL sites that overlap with Deep SEARCH. The data were retrieved on two cruises identified as EN615 and EN626. There are 6 months of dat in each deployment. The data contains salinity, temperature, and dissolved oxygen time series. the ReadMe files for each cruise provide additional processing details.
ND	ND	Respiration experiments - Lophelia pertusa, Madrepora oculata, Paramuricid sp TBD	ADEON_CruiseEN615_SAV_CTD.xlsx, ADEON_CruiseEN615_WIL_CTD.xlsx, ADEON_CruiseEN626_SAV_CTD.xlsx, ADEON_CruiseEN626_WIL_CTD.xlsx, MicroCAT readme - data recoveredby EN615 June2018.txt, MicroCAT readme - data recoveredby EN626 Nov2018.txt

Principal Investigators/Collaborators

Prouty	**Mienis**	**2021 Annual Meeting Presentations**
Chaytor_Prouty Carbonate Samples List 051320.xlsx 5/13/2020	Lander data Richardson	Annual_Meeting_2021_Brooke community
Prouty Deep-sea Coral Samples List 051220.xlsx 5/13/2020	Lander data Richardson 2019 short deployment	Annual_Meeting_2021_Coral_Symbiosis_Kellogg_Updates
Prouty Water Samples List 051220.xlsx 5/13/2020	Lander data Richardson 2019 long deployment	Annual_Meeting_2021_Cordes_Physiology
ND	Lander data Richardson 2018 long	Annual_Meeting_2021_Demopoulos_field_eco
ND	ND	Annual_Meeting_2021_ecology
ND	ND	Annual_Meeting_2021_eDNA_Morrison_Aunins
ND	ND	Annual_Meeting_2021_Miksis-Olds_Acoustics
ND	ND	Annual_Meeting_2021_Outreach_Davenport
ND	ND	Annual_Meeting_2021_PI_Updates_Joye
ND	ND	Annual_Meeting_2021_PI_Updates_Template_Oceanography
ND	ND	Annual_Meeting_2021_PopGen_Updates_Final
ND	ND	Annual_Meeting_2021_PredictiveModeling_Gasbarro

NOAA National Centers for Environmental Information

https://data.noaa.gov/onestop/

https://www.ncei.noaa.gov/access/search/index

Submission 1 - 10 April 2018

1. *Pisces* 2017 (PC1705):

- Oceanographic data: Accession number 0232264): https://www.ncei.noaa.gov/access/metadata/landing-page/bin/iso?id=gov.noaa.nodc:0232264
- Operations Report: https://doi.org/10.25923/8myk-p193
- Quarterly Report: https://doi.org/10.25923/6fbb-xe21
- Data Summary: https://doi.org/10.25923/cq9c-qp98

Over 15,000 images (over 550GB) have NOT yet been archived, as our archive managers are determining the best way forward for that volume of data.
*Geophysical data is in their backlog and will be added.

Deep SEARCH Cruise 1-1

• planning-bathy- This is the bathy provided by science for planning purposes • docs- Documents pertaining to the cruise such as launch positions and dive statistic summaries • plots- Auto-generated data plots from the post processing pipeline. These plots are included in the cruise report. • products- The best at-sea derived data products from the cruise organized by dive number • dives- All raw and processed data from individual dives • planning- Files pertaining to mission planning. These are not generally needed by science • combined_grids- Grids spanning more than one dive or local survey area site. • raw-usbl- Log and conguration les from the Sonardyne USBL system • svp- Sound velocity proles used during the cruise • surface_photos- Misc photos on deck	Within each dive directory the following directories are included: • blueview- This contains any data products created from the blueview sonar. The blueview sonar is a forward looking sonar, operating at 900KHz with a 90 degree eld of view. • sss-sbp/hf-sss- This directory contains data products generated from the 410kHz sidescan sonar system. hf-sss stands for high-frequency sidescan sonar. • sss-sbp/lf-sss- This directory contains data products generated from the 120kHz sidescan sonar system. lf-sss stands for low-frequency side scan. • sbp -This directory contains SEGY, seismic-unix, and image les derived from the Edgetech sub-bottom proler. • multibeam- This directory contains the data products from *Sentry*'s Reson multibeam sonar including grd and pdf les. The Reson multibeam sonar normally operates at 400KHz • photos- This directory contains thumbnails and movies of the photos collected by *Sentry*. Full resolution photos can be found in the dives directory. • scc- SCCs are 1Hz ASCII les containing post processed navigation and selected other science data. The timestamps on the SCCs can be matched to other data products.

Deep SEARCH Cruise 1-2

2017-demopoulos • dives ○ *Sentry* 456 ▪ products ○ *Sentry* 456 ▪ Multibeam at a Glance	PC1705_PostCruise ▪ data ▪ layers ▪ PC1705.gdb	*Pisces_Sentry_* Maps Analyzed Photo Data ▪ Chem and Photo CSVs ▪ Maps ▪ Science Files ▪ Selected_Snapshots

Submission 2 - 5 November 2019

Ron Brown-Jason-6-2019

Submission 3 - 3 August 2021

Nancy Foster (NF1909)

Sentry data (PC 17-05)-additional

2. *Atlantis* 2018 (AT41)

- Oceanographic data: Accession number 0229612) https://www.ncei.noaa.gov/archive/accession/0229612
- Multibeam: https://www.ngdc.noaa.gov/ships/atlantis/AT41_mb.html
- Water Column Sonar: https://noaa-wcsd-pds.s3.amazonaws.com/index.html#data/raw/*Atlantis*/AT41/
- Cruise Summary: https://doi.org/10.25923/tepz-1243
- Cruise Report: https://doi.org/10.25923/3rg3-d269
- Dive Summaries: https://repository.library.noaa.gov/gsearch?ref=docDetails&related_series=AT-41&type_of_resource=Dive%20Summary

Working to get processed gravity from R2R into archive
Video are still being discussed with the archive managers for best way forward

3. RV *Brooks McCall* (BMCC 2018)

- Oceanographic data: Accession number 0226957) https://www.ncei.noaa.gov/archive/accession/0226957
- Cruise Summary: https://doi.org/10.25923/zt4v-c035
- Cruise Report: https://doi.org/10.25923/zwxg-9z28

4. Ron Brown 2019 (RB1903)

- Oceanographic data: Accession number 0229074) https://www.ncei.noaa.gov/archive/accession/0229074
- Multibeam data: https://www.ngdc.noaa.gov/ships/noaa_ship_ronald_h_brown_r104_/RB-19-03_mb.html
- Cruise Summary: https://doi.org/10.25923/ea89-0k83
- Cruise Report: https://doi.org/10.25923/9q9b-d783
- Dive Summaries: https://repository.library.noaa.gov/gsearch?ref=docDetails&related_series=RB-1903&type_of_resource=Dive%20Summary

Subbottom data & Scene images are in backlog of new trackline archive
Video are still being discussed with the archive managers for best way forward

5. *Nancy Foster* 2019 (NF1909)

- Oceanographic data: Accession number 0250440) https://www.ncei.noaa.gov/access/metadata/landing-page/bin/iso?id=gov.noaa.nodc:0250440
- Multibeam data: https://www.ngdc.noaa.gov/ships/nancy_foster/NF1909_mb.html

EK60 Screen Grabs are in archive backlog but will be added soon
Cruise Report has not been submitted to the NOAA IR yet

NCBI Sequence Read Archive

246 samples Population Connectivity

Kellogg, C.A., Goldsmith, D.B., and Voelschow, J.J. (2021). Coral microbiome preservation and extraction method comparison—raw data. U.S. Geological Survey data release. http://doi.org/10.5066/P96GBWDM

The raw data files associated with this data release have also been submitted to the NCBI Sequence Read Archive under BioProject number PRJNA544686.

Kellogg, C.A. and J.J. Voelschow (2021) Cold-water coral microbiomes (Acanthogorgia spp. Desmophyllum dianthus, and Lophelia pertusa) from the GOM and Atlantic Ocean off the southeast coast of the United States–raw data. U.S. Geological Survey Data Release, https://doi.org/10.5066/P9Z1HPKR

The raw data files associated with this data release have also been submitted to the NCBI Sequence Read Archive under BioProject number PRJNA699458.

NCEI Ocean Archive

https://www.ncei.noaa.gov/access/world-ocean-database-select/dbsearch.html
CTD data from RB-19-03
NCEI Accession Number 0207828. This number is a tracking identifier for the NCEI Ocean Archive.
CTD data from NF-19-09

Spatial Data - USGS

Spatial data collected during Deep SEARCH Surveys AT41, PC-17-05, and RB1903 in shapefile and GeoTIFF formats. The data were submitted to NCEI. The data files general attributes and spatial information follow.

1) ShipTracksDeep SEARCH.shp- polyline (Z) shapefile of survey vessel navigation:
2) VehicleTracksDeep SEARCH- polyline (z) shapefile of AUV/navigation for *Sentry*, *Alvin*, *Jason*
3) Deep SEARCHPlanDiveLoc—point shp showing PLANNED dive locations with common names. WGS 84 Coordinate system
4) Multibeam Depth Grids:
    a. **RB1903EM122__25mCube.tif**- 25m res GeoTIFF of 12 kHz multibeam from the NOAA Ship *Ronald H. Brown*. UTM 18N NAD83, depth in meters MSL
    b. PC1705_JD257_10m.tiff, PC1705_JD263_10m.tiff- 10-m res GeoTIFF of 70kHz multibeam from the NOAA Ship *Pisces.* UTM18N, WGS84, depth in meters MSL
    c. PC-17-05 *Sentry* Multibeam. 1-m resolution GeoTIFFs from the 3 AUV *Sentry* dives using Reson 7125
        i. Dive454_1mUTM18.tif
        ii. Dive455-1mUTM18.tif
        iii. Dive456_1mUTM18
    d. BlakePlateau 25m 1120.tif- Compilation of all multibeam data available at the time of *Jason*'s Feb 2020 Deep SEARCH Update. Data Source NOAA/NCEI. Has since been superseded by new *Okeanos Explorer* data collection.

Deep SEARCH Atlantic Corals, Seeps and Canyons Dive Metadata

Cruise	Dive #	Site	Ecosystem Type	Latitude	Longitude	Depth Range
EX1806	1	Blake Escarpment N	Soft Sediment & Hardgrounds	32.052	-76.844	1,675–1,736
EX1806	4[1]	Blake Escarpment S	Sot Sediment & Hardgrounds	30.940	-77.328	1,246–1,310
EX1806	5	Stetson Mesa S	Lophelia	29.374	-79.826	705–734
EX1806	6	Stetson Mesa N	Lophelia	30.497	-79.763	709–789
EX1806	7	Richardson Reef (S)	Lophelia	31.771	-77.362	778–873
EX1806	8	Richardson Scarp	Sediment & Hardgrounds	32.095	-77.546	868–1,006
EX1806	10[2]	Cape Fear	Lophelia (all dead)	33.697	-76.342	370–452
EX1806	14	Hatteras Canyon	Canyon (sediment & hardgrounds)	35.297	-74.947	302–510
EX1806	15	Keller Canyon	Canyon (sediment & hardgrounds)	35.539	-74.801	506–728
EX1806	16	Pea Island Seeps	Cold Seep/Canyon	35.708	-74.813	328–521
EX1806	17	Currituck Landslide	Scarp/Wall	36.229	-74.463	1,747–1,881
AT41	AL4961	Pea Island Seeps	Cold Seep	35.705	-74.813	408–511
AT41	AL4962	Richardson Reef	Lophelia	32.014	-77.396	750–820
AT41	AL4963	Richardson Reef	Lophelia	31.985	-77.416	750–820
AT41	AL4964	Blake Deep	Hardgrounds & Sediment	31.323	-77.245	1,200–1,273
AT41	AL4965	Stetson Banks	Hardgrounds & Sediment	32.012	-78.314	434–545
AT41	AL4966	Stetson Banks	Hardgrounds & Sediment	32.070	-78.374	395–403
AT41	AL4967	Blake Ridge	Cold Seep	32.495	-76.190	2,166
AT41	AL4968	Cape Fear Coral Mound	Lophelia	33.576	-76.468	378–458
AT41	AL4969	Pamlico Canyon	Canyon (sediment & wall)	34.937	-75.169	1100
AT41	AL4970	Norfolk Canyon	Canyon (sediment & hardgrounds)	37.043	-74.315	1,665–1,943
RB1903	J2-1128	Richardson Reef	Lophelia	31.880	-77.374	731–762
RB1903	J2-1129	Richardson Reef	Lophelia	31.985	-77.413	690–708
RB1903	J2-1130	Savannah Banks	Lophelia	31.754	-79.195	511–553
RB1903	J2-1131	Blake Deep	Soft Sediment & Hardgrounds	31.285	-77.237	1,306–1,359
RB1903	J2-1132[3]	Pamlico Canyon	Canyon (sediment & hardgrounds)	34.914	-75.184	1,136–1,839
RB1903	J2-1133	Pea Island Seeps	Cold Seep	35.675	-74.792	300–353
RB1903	J2-1134	Kitty Hawk Seep	Cold Seep	35.926	-74.805	214–476
RB1903	J2-1135[4]	Cape Lookout Deep	Hardgrounds & Sediment	33.916	-75.832	940–1,029
RB1903	J2-1136	Blake Ridge	Cold Seep	32.493	-76.190	2,140–2,164
RB1903	J2-1137	Cape Fear Seep	Cold Seep	32.979	-75.929	2,592–2,608
RB1903	J2-1138	Richardson Reef (West)	Lophelia	31.893	-77.699	658–758
EX1903L2	1	Canaveral Deep	Lophelia	28.250	-79.598	714–805
EX1903L2	2	Stetson Mesa South Mounds	Lophelia	29.102	-79.598	770–805
EX1903L2	4	Blake Plateau Knolls	Lophelia	29.650	-78.469	754–826
EX1903L2	5	Central Plateau Mounds	Lophelia	30.495	-78.112	786–826
EX1903L2	8	Central Blake Plateau Scarp	Sediment & Hardgrounds	30.921	-78.083	870–1,012
EX1903L2	10[5]	Richardson Reef	Lophelia & Sediment	32.095	-77.665	754–890

Cruise	Dive #	Site	Ecosystem Type	Latitude	Longitude	Depth Range
EX1903L2	12	Deep Pamlico Canyon	Canyon (sediment)	34.581	-74.688	3,265- 3,490
EX1903L2	14	Bodie Island Seep	Cold Seep	35.735	-74.812	298–445
EX1903L2	19	Norfolk Deep Seep	Norfolk Deep Seep	36.86505°	-74.486	1,522–1,615

Notes:
NOAA dive description says there are scleracs on this dive, probably just cup corals but worth investigating
Might be interesting to compare communities on relict mound vs. thriving one
Long dive (16h); No Lp so can be used for absence data
No Lp, so can be used for absence data
Dive is on the off-reef 'jellyfish'

Richardson Reef

Dive #	Latitude	Longitude	Depth Range	Bottom time (h)
EX1806-7	31.771	-77.362	778–873	5.89
AL4962	32.014	-77.396	750–820	6.53
AL4963	31.985	-77.416	750–820	4.58
J2-1128	31.880	-77.374	731–762	9.5
J2-1129	31.985	-77.413	690–708	11.25
J2-1138	31.893	-77.699	658–758	6.02
EX1903L2-4	29.650	-78.469	754–826	6.89
EX1903L2-5	30.495	-78.112	786–826	4.52
EX1903L2-10	32.095	-77.665	754–890	7.03

US National Museum Specimen Data

The US National Museum has been closed to receiving specimens due to COVID. When they reopen, the remainder of specimens that are in researcher's labs will be accepted. The table below is a list of the specimens processed through the NMNH as of Dec 2022.

Catalog Number	Primary Coll Number	Taxon	Original Count	Kind of Voucher	Event/Site	Preparation
1606518	AT41-18-052	Swiftia casta (Verrill, 1883) : Plexauridae : Gorgonacea : Anthozoa : Cnidaria	1	Voucher	CES IRN 13135378 :Sample no. BOEM/Deep-SEARCH/2018-AT41-AL4965 : North Atlantic Ocean : : : North America : United States : : : : Stetson Banks : Centroid Latitude 32 0 44.189 N : Centroid Longitude 78 18 48.083 W : : Date coll. 26 Aug 2018 : Sta. Q4-2 : A - DATA TRUNCATED	Alcohol (Ethanol)
1606519	AT41-18-014	: : Alcyonacea : Anthozoa : Cnidaria	1	Voucher	CES IRN 13135409 :Sample no. BOEM/Deep-SEARCH/2018-AT41-AL4962 : North Atlantic Ocean : : : North America : United States : : : : Stetson Deep : Centroid Latitude 32 0 33.7 N : Centroid Longitude 77 23 45 W : : Date coll. 23 Aug 2018 : Sta. B6-1 : *Atlantis* - DATA TRUNCATED	Alcohol (Ethanol)

Catalog Number	Primary Coll Number	Taxon	Original Count	Kind of Voucher	Event/Site	Preparation
1606520	AT41-18-109	Lateothela grandiflora (Tixier-Durivault & D'Hondt, 1974) : Anthothelidae : Gorgonacea : Anthozoa : Cnidaria	1	Voucher	CES IRN 13135924 :Sample no. BOEM/Deep-SEARCH/2018-AT41-AL4968 : North Atlantic Ocean : : : North America : United States : : : : Cape Fear Mounds : Centroid Latitude 33 34 29.701 N : Centroid Longitude 76 27 56.563 W : : Date coll. 29 Aug 2018 : Sta. Q10- - DATA TRUNCATED	Alcohol (Ethanol)
1606521	AT41-18-113	: : : Anthozoa : Cnidaria	1	Voucher	CES IRN 13135926 :Sample no. BOEM/Deep-SEARCH/2018-AT41-AL4968 : North Atlantic Ocean : : : North America : United States : : : : Cape Fear Mounds : Centroid Latitude 33 34 31.880 N : Centroid Longitude 76 28 4.4621 W : : Date coll. 29 Aug 2018 : Sta. Q1-3 - DATA TRUNCATED	Alcohol (Ethanol)
1606522	AT41-18-091	: : : Ophiuroidea : Echinodermata	1	Voucher	CES IRN 13135927 :Sample no. BOEM/Deep-SEARCH/2018-AT41-AL4967 : North Atlantic Ocean : : : North America : United States : : : : Blake Ridge : Centroid Latitude 32 29 41.289 N : Centroid Longitude 76 11 23.082 W : : Date coll. 28 Aug 2018 : Sta. Slurp4-1 - DATA TRUNCATED	Alcohol (Ethanol)
1606523	AT41-18-111	Paramuricea sp. : Plexauridae : Gorgonacea : Anthozoa : Cnidaria	1	Voucher	CES IRN 13135930 :Sample no. BOEM/Deep-SEARCH/2018-AT41-AL4968 : North Atlantic Ocean : : : North America : United States : : : : Cape Fear Mounds : Centroid Latitude 33 34 22.123 N : Centroid Longitude 76 27 55.477 W : : Date coll. 29 Aug 2018 : Sta. B3-2 - DATA TRUNCATED	Alcohol (Ethanol)
1606524	AT41-18-122	Trachythela sp. : Clavulariidae : Alcyonacea : Anthozoa : Cnidaria	1	Voucher	CES IRN 13135929 :Sample no. BOEM/Deep-SEARCH/2018-AT41-AL4969 : North Atlantic Ocean : : : North America : United States : : : : Pamlico Canyon : Centroid Latitude 34 56 25.367 N : Centroid Longitude 75 10 3.3597 W : : Date coll. 30 Aug 2018 : Sta. Q5-2 : - DATA TRUNCATED	Alcohol (Ethanol)
1606525	AT41-18-118	Acanthogorgia sp. : Acanthogorgiidae : Gorgonacea : Anthozoa : Cnidaria	1	Voucher	CES IRN 13135933 :Sample no. BOEM/Deep-SEARCH/2018-AT41-AL4969 : North Atlantic Ocean : : : North America : United States : : : : Pamlico Canyon : Centroid Latitude 34 56 15.19 N : Centroid Longitude 75 10 10.917 W : : Date coll. 30 Aug 2018 : Sta. Q3-1 : - DATA TRUNCATED	Alcohol (Ethanol)
1606526	AT41-18-040	Stauropathes punctata (Roule, 1905) : Schizopathidae : Antipatharia : Anthozoa : Cnidaria	1	Voucher	CES IRN 13135935 :Sample no. BOEM/Deep-SEARCH/2018-AT41-AL4964 : North Atlantic Ocean : : : North America : United States : : : : Blake Escarpment : Centroid Latitude 31 19 25.792 N : Centroid Longitude 77 14 28.769 W : : Date coll. 25 Aug 2018 : Sta. Q8-2 - DATA TRUNCATED	Alcohol (Ethanol)
1606527	AT41-18-042	Stauropathes sp. : Schizopathidae : Antipatharia : Anthozoa : Cnidaria	1	Voucher	CES IRN 13135937 :Sample no. BOEM/Deep-SEARCH/2018-AT41-AL4964 : North Atlantic Ocean : : : North America : United States : : : : Blake Escarpment : Centroid Latitude 31 19 20.940 N : Centroid Longitude 77 14 42.17 W : : Date coll. 25 Aug 2018 : Sta. B5-1 - DATA TRUNCATED	Alcohol (Ethanol)

Catalog Number	Primary Coll Number	Taxon	Original Count	Kind of Voucher	Event/Site	Preparation
1606528	AT41-18-007	: Primnoidae : Gorgonacea : Anthozoa : Cnidaria	1	Voucher	CES IRN 13135938 :Sample no. BOEM/Deep-SEARCH/2018-AT41-AL4962 : North Atlantic Ocean : : : North America : United States : : : : Stetson Deep : Centroid Latitude 32 0 49.2 N : Centroid Longitude 77 23 45.0 W : : Date coll. 23 Aug 2018 : Sta. Q4-3 : Atlant - DATA TRUNCATED	Alcohol (Ethanol)
1606529	AT41-18-012	Eunicella modesta Verrill, 1883 : Gorgoniidae : Gorgonacea : Anthozoa : Cnidaria	1	Voucher	CES IRN 13135943 :Sample no. BOEM/Deep-SEARCH/2018-AT41-AL4962 : North Atlantic Ocean : : : North America : United States : : : : Stetson Deep : Centroid Latitude 32 0 30.5 N : Centroid Longitude 77 23 40.4 W : : Date coll. 23 Aug 2018 : Sta. Q5-2 : Atlant - DATA TRUNCATED	Alcohol (Ethanol)
1606530	AT41-18-047	: Plexauridae : Gorgonacea : Anthozoa : Cnidaria	1	Voucher	CES IRN 13135944 :Sample no. BOEM/Deep-SEARCH/2018-AT41-AL4965 : North Atlantic Ocean : : : North America : United States : : : : Stetson Banks : Centroid Latitude 32 0 54.362 N : Centroid Longitude 78 19 26.621 W : : Date coll. 26 Aug 2018 : Sta. R1-1A : - DATA TRUNCATED	Alcohol (Ethanol)
1606531	AT41-18-065	: Zoanthidae : Zoanthidea : Anthozoa : Cnidaria	1	Voucher	CES IRN 13135946 :Sample no. BOEM/Deep-SEARCH/2018-AT41-AL4966 : North Atlantic Ocean : : : North America : United States : : : : Stetson Banks : Centroid Latitude 32 4 11.105 N : Centroid Longitude 78 22 16.105 W : : Date coll. 27 Aug 2018 : Sta. B1-1 : A - DATA TRUNCATED	Alcohol (Ethanol)
1606532	AT41-18-059	: : Alcyonacea : Anthozoa : Cnidaria	1	Voucher	CES IRN 13135950 :Sample no. BOEM/Deep-SEARCH/2018-AT41-AL4965 : North Atlantic Ocean : : : North America : United States : : : : Stetson Banks : Centroid Latitude 32 0 45.005 N : Centroid Longitude 78 18 48.491 W : : Date coll. 26 Aug 2018 : Sta. B1-1 : A - DATA TRUNCATED	Alcohol (Ethanol)
1606533	AT41-18-119	Asteroschema sp. : Asteroschematidae : Phrynophiurida : Ophiuroidea : Echinodermata	1	Voucher	CES IRN 13135952 :Sample no. BOEM/Deep-SEARCH/2018-AT41-AL4969 : North Atlantic Ocean : : : North America : United States : : : : Pamlico Canyon : Centroid Latitude 34 56 15.19 N : Centroid Longitude 78 10 10.917 W : : Date coll. 30 Aug 2018 : Sta. Q3-2 : - DATA TRUNCATED	Alcohol (Ethanol)
1606534	AT41-18-048	: Plexauridae : Gorgonacea : Anthozoa : Cnidaria	1	Voucher	CES IRN 13135961 :Sample no. BOEM/Deep-SEARCH/2018-AT41-AL4965 : North Atlantic Ocean : : : North America : United States : : : : Stetson Banks : Centroid Latitude 32 0 54.362 N : Centroid Longitude 78 19 26.621 W : : Date coll. 26 Aug 2018 : Sta. R1-1B : - DATA TRUNCATED	Alcohol (Ethanol)
1606535	AT41-18-127	Paramuricea sp. : Plexauridae : Gorgonacea : Anthozoa : Cnidaria	1	Voucher	CES IRN 13135964 :Sample no. BOEM/Deep-SEARCH/2018-AT41-AL4969 : North Atlantic Ocean : : : North America : United States : : : : Pamlico Canyon : Centroid Latitude 34 56 20.240 N : Centroid Longitude 75 10 12.934 W : : Date coll. 30 Aug 2018 : Sta. B4-1 : - DATA TRUNCATED	Alcohol (Ethanol)

Catalog Number	Primary Coll Number	Taxon	Original Count	Kind of Voucher	Event/Site	Preparation
1606536	AT41-18-068	: Primnoidae : Gorgonacea : Anthozoa : Cnidaria	1	Voucher	CES IRN 13135965 :Sample no. BOEM/Deep-SEARCH/2018-AT41-AL4966 : North Atlantic Ocean : : : North America : United States : : : : Stetson Banks : Centroid Latitude 32 4 11.105 N : Centroid Longitude 78 22 16.105 W : : Date coll. 27 Aug 2018 : Sta. B1-2 : A - DATA TRUNCATED	Alcohol (Ethanol)
1606537	AT41-18-015	Chrysogorgia sp. : Chrysogorgiidae : Gorgonacea : Anthozoa : Cnidaria	1	Voucher	CES IRN 13135968 :Sample no. BOEM/Deep-SEARCH/2018-AT41-AL4962 : North Atlantic Ocean : : : North America : United States : : : : Stetson Deep : Centroid Latitude 32 0 33.7 N : Centroid Longitude 77 23 45 W : : Date coll. 23 Aug 2018 : Sta. B6-3A : Atlanti - DATA TRUNCATED	Alcohol (Ethanol)
1606538	AT41-18-035	Paragorgia sp. : Paragorgiidae : Gorgonacea : Anthozoa : Cnidaria	1	Voucher	CES IRN 13135971 :Sample no. BOEM/Deep-SEARCH/2018-AT41-AL4964 : North Atlantic Ocean : : : North America : United States : : : : Blake Escarpment : Centroid Latitude 31 19 21.1 N : Centroid Longitude 77 14 42.497 W : : Date coll. 25 Aug 2018 : Sta. Q5-1 : - DATA TRUNCATED	Alcohol (Ethanol)
1606539	AT41-18-033	Stichopathes sp. : Antipathidae : Antipatharia : Anthozoa : Cnidaria	1	Voucher	CES IRN 13135972 :Sample no. BOEM/Deep-SEARCH/2018-AT41-AL4964 : North Atlantic Ocean : : : North America : United States : : : : Blake Escarpment : Centroid Latitude 31 19 20.938 N : Centroid Longitude 77 14 42.178 W : : Date coll. 25 Aug 2018 : Sta. Q3-1 - DATA TRUNCATED	Alcohol (Ethanol)
1606540	AT41-18-062	: Plexauridae : Gorgonacea : Anthozoa : Cnidaria	1	Voucher	CES IRN 13135978 :Sample no. BOEM/Deep-SEARCH/2018-AT41-AL4965 : North Atlantic Ocean : : : North America : United States : : : : Stetson Banks : Centroid Latitude 32 0 52.010 N : Centroid Longitude 78 19 29.555 W : : Date coll. 26 Aug 2018 : Sta. B4-1 : A - DATA TRUNCATED	Alcohol (Ethanol)
1606541	AT41-18-016	Chrysogorgia sp. : Chrysogorgiidae : Gorgonacea : Anthozoa : Cnidaria	1	Voucher	CES IRN 13135982 :Sample no. BOEM/Deep-SEARCH/2018-AT41-AL4962 : North Atlantic Ocean : : : North America : United States : : : : Stetson Deep : Centroid Latitude 32 0 33.7 N : Centroid Longitude 77 23 45 W : : Date coll. 23 Aug 2018 : Sta. B6-3B : Atlanti - DATA TRUNCATED	Alcohol (Ethanol)
1606542	AT41-18-129	Acanthogorgia sp. : Acanthogorgiidae : Gorgonacea : Anthozoa : Cnidaria	1	Voucher	CES IRN 13135989 :Sample no. BOEM/Deep-SEARCH/2018-AT41-AL4969 : North Atlantic Ocean : : : North America : United States : : : : Pamlico Canyon : Centroid Latitude 34 56 14.838 N : Centroid Longitude 75 10 11.685 W : : Date coll. 30 Aug 2018 : Sta. B5-1 : - DATA TRUNCATED	Alcohol (Ethanol)
1606543	AT41-18-032	: Isididae : Gorgonacea : Anthozoa : Cnidaria	1	Voucher	CES IRN 13135990 :Sample no. BOEM/Deep-SEARCH/2018-AT41-AL4964 : North Atlantic Ocean : : : North America : United States : : : : Blake Escarpment : Centroid Latitude 31 19 20.942 N : Centroid Longitude 77 14 42.173 W : : Date coll. 25 Aug 2018 : Sta. Q4-1 - DATA TRUNCATED	Alcohol (Ethanol)

Catalog Number	Primary Coll Number	Taxon	Original Count	Kind of Voucher	Event/Site	Preparation
1606544	AT41-18-126	Swiftia sp. : Plexauridae : Gorgonacea : Anthozoa : Cnidaria	1	Voucher	CES IRN 13135996 :Sample no. BOEM/Deep-SEARCH/2018-AT41-AL4969 : North Atlantic Ocean : : : North America : United States : : : : Pamlico Canyon : Centroid Latitude 34 56 15.118 N : Centroid Longitude 75 10 10.949 W : : Date coll. 30 Aug 2018 : Sta. Q9-1 : - DATA TRUNCATED	Alcohol (Ethanol)
1606545	AT41-18-053	: : : Anthozoa : Cnidaria	1	Voucher	CES IRN 13135998 :Sample no. BOEM/Deep-SEARCH/2018-AT41-AL4965 : North Atlantic Ocean : : : North America : United States : : : : Stetson Banks : Centroid Latitude 32 0 52.583 N : Centroid Longitude 78 19 25.883 W : : Date coll. 26 Aug 2018 : Sta. Q6-2 : A - DATA TRUNCATED	Alcohol (Ethanol)
1606546	AT41-18-107	: Plexauridae : Gorgonacea : Anthozoa : Cnidaria	1	Voucher	CES IRN 13136003 :Sample no. BOEM/Deep-SEARCH/2018-AT41-AL4968 : North Atlantic Ocean : : : North America : United States : : : : Cape Fear Mounds : Centroid Latitude 33 34 29.033 N : Centroid Longitude 76 27 55.718 W : : Date coll. 29 Aug 2018 : Sta. Q3-1 - DATA TRUNCATED	Alcohol (Ethanol)
1606547	AT41-18-061	: : : Anthozoa : Cnidaria	1	Voucher	CES IRN 13136005 :Sample no. BOEM/Deep-SEARCH/2018-AT41-AL4965 : North Atlantic Ocean : : : North America : United States : : : : Stetson Banks : Centroid Latitude 32 0 51.409 N : Centroid Longitude 78 19 10.785 W : : Date coll. 26 Aug 2018 : Sta. B2-4 : A - DATA TRUNCATED	Alcohol (Ethanol)
1606548	AT41-18-137	Distichoptilum sp. : Protoptilidae : Pennatulacea : Anthozoa : Cnidaria	1	Voucher	CES IRN 13136006 :Sample no. BOEM/Deep-SEARCH/2018-AT41-AL4970 : North Atlantic Ocean : : : North America : United States : : : : Norfolk Canyon : Centroid Latitude 37 2 52.547 N : Centroid Longitude 74 18 46.622 W : : Date coll. 31 Aug 2018 : Sta. B4-1 : - DATA TRUNCATED	Alcohol (Ethanol)
1606549	AT41-18-005	: Plexauridae : Gorgonacea : Anthozoa : Cnidaria	1	Voucher	CES IRN 13136008 :Sample no. BOEM/Deep-SEARCH/2018-AT41-AL4962 : North Atlantic Ocean : : : North America : United States : : : : Stetson Deep : Centroid Latitude 32 0 49.2 N : Centroid Longitude 77 23 45.0 W : : Date coll. 23 Aug 2018 : Sta. Q4-1 : Atlant - DATA TRUNCATED	Alcohol (Ethanol)
1606550	AT41-18-054	: Plexauridae : Gorgonacea : Anthozoa : Cnidaria	1	Voucher	CES IRN 13136012 :Sample no. BOEM/Deep-SEARCH/2018-AT41-AL4965 : North Atlantic Ocean : : : North America : United States : : : : Stetson Banks : Centroid Latitude 32 0 52.583 N : Centroid Longitude 78 19 25.883 W : : Date coll. 26 Aug 2018 : Sta. Q6-3 : A - DATA TRUNCATED	Alcohol (Ethanol)
1606551	AT41-18-039	: : Antipatharia : Anthozoa : Cnidaria	1	Voucher	CES IRN 13136014 :Sample no. BOEM/Deep-SEARCH/2018-AT41-AL4964 : North Atlantic Ocean : : : North America : United States : : : : Blake Escarpment : Centroid Latitude 31 19 25.792 N : Centroid Longitude 77 14 28.769 W : : Date coll. 25 Aug 2018 : Sta. Q8-1 - DATA TRUNCATED	Alcohol (Ethanol)

Catalog Number	Primary Coll Number	Taxon	Original Count	Kind of Voucher	Event/Site	Preparation
1606552	AT41-18-029	Swiftia casta (Verrill, 1883) : Plexauridae : Gorgonacea : Anthozoa : Cnidaria	1	Voucher	CES IRN 13136021 :Sample no. BOEM/Deep-SEARCH/2018-AT41-AL4963 : North Atlantic Ocean : : : North America : United States : : : : Richardson Ridge : Centroid Latitude 31 59 3.835 N : Centroid Longitude 77 24 38.40 W : : Date coll. 24 Aug 2018 : Sta. B1-2 : - DATA TRUNCATED	Alcohol (Ethanol)
1606553	AT41-18-055	: Primnoidae : Gorgonacea : Anthozoa : Cnidaria	1	Voucher	CES IRN 13136023 :Sample no. BOEM/Deep-SEARCH/2018-AT41-AL4965 : North Atlantic Ocean : : : North America : United States : : : : Stetson Banks : Centroid Latitude 32 0 52.647 N : Centroid Longitude 78 19 29.085 W : : Date coll. 26 Aug 2018 : Sta. Q7-2 : A - DATA TRUNCATED	Alcohol (Ethanol)
1606554	AT41-18-116	Paragorgia sp. : Paragorgiidae : Gorgonacea : Anthozoa : Cnidaria	1	Voucher	CES IRN 13136025 :Sample no. BOEM/Deep-SEARCH/2018-AT41-AL4969 : North Atlantic Ocean : : : North America : United States : : : : Pamlico Canyon : Centroid Latitude 34 56 28.788 N : Centroid Longitude 75 9 58.217 W : : Date coll. 30 Aug 2018 : Sta. Q1-1 : - DATA TRUNCATED	Alcohol (Ethanol)
1606555	AT41-18-049	: Isididae : Gorgonacea : Anthozoa : Cnidaria	1	Voucher	CES IRN 13136029 :Sample no. BOEM/Deep-SEARCH/2018-AT41-AL4965 : North Atlantic Ocean : : : North America : United States : : : : Stetson Banks : Centroid Latitude 32 0 44.189 N : Centroid Longitude 78 18 48.083 W : : Date coll. 26 Aug 2018 : Sta. Q4-1 : A - DATA TRUNCATED	Alcohol (Ethanol)
1606556	AT41-18-063	Leiopathes sp. : Leiopathidae : Antipatharia : Anthozoa : Cnidaria	1	Voucher	CES IRN 13136032 :Sample no. BOEM/Deep-SEARCH/2018-AT41-AL4965 : North Atlantic Ocean : : : North America : United States : : : : Stetson Banks : Centroid Latitude 32 0 52.010 N : Centroid Longitude 78 19 29.555 W : : Date coll. 26 Aug 2018 : Sta. B5-1 : A - DATA TRUNCATED	Alcohol (Ethanol)
1606557	AT41-18-138	Anthoptilum sp. : Anthoptilidae : Pennatulacea : Anthozoa : Cnidaria	1	Voucher	CES IRN 13136034 :Sample no. BOEM/Deep-SEARCH/2018-AT41-AL4970 : North Atlantic Ocean : : : North America : United States : : : : Norfolk Canyon : Centroid Latitude 37 2 58.974 N : Centroid Longitude 74 18 54.432 W : : Date coll. 31 Aug 2018 : Sta. B5-1 : - DATA TRUNCATED	Alcohol (Ethanol)
1606558	AT41-18-135	Acanella sp. : Isididae : Gorgonacea : Anthozoa : Cnidaria	1	Voucher	CES IRN 13136040 :Sample no. BOEM/Deep-SEARCH/2018-AT41-AL4970 : North Atlantic Ocean : : : North America : United States : : : : Norfolk Canyon : Centroid Latitude 37 2 46.039 N : Centroid Longitude 74 18 46.745 W : : Date coll. 31 Aug 2018 : Sta. Q9-1 : - DATA TRUNCATED	Alcohol (Ethanol)
1606559	AT41-18-006	: Plexauridae : Gorgonacea : Anthozoa : Cnidaria	1	Voucher	CES IRN 13136041 :Sample no. BOEM/Deep-SEARCH/2018-AT41-AL4962 : North Atlantic Ocean : : : North America : United States : : : : Stetson Deep : Centroid Latitude 32 0 49.2 N : Centroid Longitude 77 23 45.0 W : : Date coll. 23 Aug 2018 : Sta. Q4-2 : Atlant - DATA TRUNCATED	Alcohol (Ethanol)

Catalog Number	Primary Coll Number	Taxon	Original Count	Kind of Voucher	Event/Site	Preparation
1606560	AT41-18-124	: Isididae : Gorgonacea : Anthozoa : Cnidaria	1	Voucher	CES IRN 13136042 :Sample no. BOEM/Deep-SEARCH/2018-AT41-AL4969 : North Atlantic Ocean : : : North America : United States : : : : Pamlico Canyon : Centroid Latitude 34 56 11.961 N : Centroid Longitude 75 10 6.5797 W : : Date coll. 30 Aug 2018 : Sta. Q8-2 : - DATA TRUNCATED	Alcohol (Ethanol)
1606561	AT41-18-136	Protoptilum sp. : Protoptilidae : Pennatulacea : Anthozoa : Cnidaria	1	Voucher	CES IRN 13136046 :Sample no. BOEM/Deep-SEARCH/2018-AT41-AL4970 : North Atlantic Ocean : : : North America : United States : : : : Norfolk Canyon : Centroid Latitude 37 2 50.686 N : Centroid Longitude 74 18 45.607 W : : Date coll. 31 Aug 2018 : Sta. Q12-1 : - DATA TRUNCATED	Alcohol (Ethanol)
1606562	AT41-18-043	: Isididae : Gorgonacea : Anthozoa : Cnidaria	1	Voucher	CES IRN 13136047 :Sample no. BOEM/Deep-SEARCH/2018-AT41-AL4964 : North Atlantic Ocean : : : North America : United States : : : : Blake Escarpment : Centroid Latitude 31 19 21.08 N : Centroid Longitude 77 14 42.4 W : : Date coll. 25 Aug 2018 : Sta. B2-2 : - DATA TRUNCATED	Alcohol (Ethanol)
1606563	AT41-18-038	Chrysogorgia sp. : Chrysogorgiidae : Gorgonacea : Anthozoa : Cnidaria	1	Voucher	CES IRN 13136050 :Sample no. BOEM/Deep-SEARCH/2018-AT41-AL4964 : North Atlantic Ocean : : : North America : United States : : : : Blake Escarpment : Centroid Latitude 31 19 25.654 N : Centroid Longitude 77 14 38.234 W : : Date coll. 25 Aug 2018 : Sta. Q9-1 - DATA TRUNCATED	Alcohol (Ethanol)
1606564	AT41-18-024	Paragorgia sp. : Paragorgiidae : Gorgonacea : Anthozoa : Cnidaria	1	Voucher	CES IRN 13136052 :Sample no. BOEM/Deep-SEARCH/2018-AT41-AL4963 : North Atlantic Ocean : : : North America : United States : : : : Richardson Ridge : Centroid Latitude 31 59 4.048 N : Centroid Longitude 77 24 40.95 W : : Date coll. 24 Aug 2018 : Sta. Q6-1 : - DATA TRUNCATED	Alcohol (Ethanol)
1606565	AT41-18-041	: Plexauridae : Gorgonacea : Anthozoa : Cnidaria	1	Voucher	CES IRN 13136056 :Sample no. BOEM/Deep-SEARCH/2018-AT41-AL4964 : North Atlantic Ocean : : : North America : United States : : : : Black Escarpment : Centroid Latitude 31 19 25.643 N : Centroid Longitude 77 14 38.230 W : : Date coll. 25 Aug 2018 : Sta. Q10- - DATA TRUNCATED	Alcohol (Ethanol)
1606566	AT41-18-141	: Isididae : Gorgonacea : Anthozoa : Cnidaria	1	Voucher	CES IRN 13136106 :Sample no. BOEM/Deep-SEARCH/2018-AT41-AL4970 : North Atlantic Ocean : : : North America : United States : : : : Norfolk Canyon : Centroid Latitude 37 2 52.547 N : Centroid Longitude 74 18 46.622 W : : Date coll. 31 Aug 2018 : Sta. Q10-1 : - DATA TRUNCATED	Alcohol (Ethanol)
1606567	AT41-18-037	: Plexauridae : Gorgonacea : Anthozoa : Cnidaria	1	Voucher	CES IRN 13136110 :Sample no. BOEM/Deep-SEARCH/2018-AT41-AL4964 : North Atlantic Ocean : : : North America : United States : : : : Blake Escarpment : Centroid Latitude 31 19 20.373 N : Centroid Longitude 77 14 30.30 W : : Date coll. 25 Aug 2018 : Sta. Q7-1 - DATA TRUNCATED	Alcohol (Ethanol)

Catalog Number	Primary Coll Number	Taxon	Original Count	Kind of Voucher	Event/Site	Preparation
1606568	AT41-18-051	Leiopathes sp. : Leiopathidae : Antipatharia : Anthozoa : Cnidaria	1	Voucher	CES IRN 13136126 :Sample no. BOEM/Deep-SEARCH/2018-AT41-AL4965 : North Atlantic Ocean : : : North America : United States : : : : Stetson Banks : Centroid Latitude 32 0 44.854 N : Centroid Longitude 78 18 48.234 W : : Date coll. 26 Aug 2018 : Sta. Q5-1 : A - DATA TRUNCATED	Alcohol (Ethanol)
1606569	RB-19-026	: Plexauridae : Gorgonacea : Anthozoa : Cnidaria	1	Voucher	CES IRN 13136132 :Sample no. BOEM/Deep-SEARCH/2019-J2-1129 : North Atlantic Ocean : : : North America : United States : : : : : : : : Date coll. 2019 : Sta. Q5-04 : *Atlantis* RV : : : : Gear ROV	Alcohol (Ethanol)
1606570	RB-19-030	Swiftia casta (Verrill, 1883) : Plexauridae : Gorgonacea : Anthozoa : Cnidaria	1	Voucher	CES IRN 13136133 :Sample no. BOEM/Deep-SEARCH/2019-J2-1129 : North Atlantic Ocean : : : North America : United States : : : : : : : : Date coll. 2019 : Sta. Q5-12 : *Atlantis* RV : : : : Gear ROV	Alcohol (Ethanol)
1606571	RB-19-028	Swiftia casta (Verrill, 1883) : Plexauridae : Gorgonacea : Anthozoa : Cnidaria	1	Voucher	CES IRN 13136134 :Sample no. BOEM/Deep-SEARCH/2019-J2-1129 : North Atlantic Ocean : : : North America : United States : : : : : : : : Date coll. 2019 : Sta. Q5-10 : *Atlantis* RV : : : : Gear ROV	Alcohol (Ethanol)
1606572	RB-19-004	: : : Hydrozoa : Cnidaria	1	Voucher	CES IRN 13136138 :Sample no. BOEM/Deep-SEARCH/2019-J2-1128 : North Atlantic Ocean : : : North America : United States : : : : : : : : Date coll. 2019 : Sta. B2-002 : *Atlantis* RV : : : : Gear ROV	Alcohol (Ethanol)
1606573	RB-19-031	Anthomastus sp. : Alcyoniidae : Alcyonacea : Anthozoa : Cnidaria	1	Voucher	CES IRN 13136141 :Sample no. BOEM/Deep-SEARCH/2019-J2-1129 : North Atlantic Ocean : : : North America : United States : : : : : : : : Date coll. 2019 : Sta. Q5-06 : *Atlantis* RV : : : : Gear ROV	Alcohol (Ethanol)
1606574	RB-19-032	Swiftia casta (Verrill, 1883) : Plexauridae : Gorgonacea : Anthozoa : Cnidaria	1	Voucher	CES IRN 13136143 :Sample no. BOEM/Deep-SEARCH/2019-J2-1129 : North Atlantic Ocean : : : North America : United States : : : : : : : : Date coll. 2019 : Sta. Q5-02 : *Atlantis* RV : : : : Gear ROV	Alcohol (Ethanol)
1606575	RB-19-003	Swiftia casta (Verrill, 1883) : Plexauridae : Gorgonacea : Anthozoa : Cnidaria	1	Voucher	CES IRN 13136145 :Sample no. BOEM/Deep-SEARCH/2019-J2-1128 : North Atlantic Ocean : : : North America : United States : : : : : : : : Date coll. 2019 : Sta. B2-001 : *Atlantis* RV : : : : Gear ROV	Alcohol (Ethanol)
1606576	RB-19-033	Aphrocallistes sp. : Aphrocallistidae : Hexactinosida : Hexactinellida : Porifera	1	Voucher	CES IRN 13136147 :Sample no. BOEM/Deep-SEARCH/2019-J2-1129 : North Atlantic Ocean : : : North America : United States : : : : : : : : Date coll. 2019 : Sta. Q7-03 : *Atlantis* RV : : : : Gear ROV	Alcohol (Ethanol)
1606577	RB-19-043	Lateothela grandiflora (Tixier-Durivault & D'Hondt, 1974) : Anthothelidae : Gorgonacea : Anthozoa : Cnidaria	1	Voucher	CES IRN 13136149 :Sample no. BOEM/Deep-SEARCH/2019-J2-1129 : North Atlantic Ocean : : : North America : United States : : : : : : : : Date coll. 2019 : Sta. Q8-02 : *Atlantis* RV : : : : Gear ROV	Alcohol (Ethanol)

NCBI’s Sequence Read Archive

The Sequence Read Archive is a bioinformatics database that provides a public repository for DNA sequencing data, especially the "short reads" generated by HTS, which are typically less than 1,000 base pairs in length.

Accession	Study	Object Status	Bioproject Accession	Biosample Accession	Sample Name	Library ID	Species	Title	Library Strategy	Library Source	Library Selection	Library Layout	Platform	Instrument Model	Design Description	Filetype	Filename	Filename2
SRR17008493	SRP340375	new	PRJNA769076	SAMN23390761	AT-41-18-093	AT-41-18-093	Ophioctenella acies	RAD-seq of deep-sea invertebrates	RAD-seq	GENOMIC	Restriction Digest	single	Illumina	Illumina HiSeq 4000	Restriction site enzyme pstI used on gDNA	fastq	AT-41-18-093.fq.gz	-
SRR17008492	SRP340375	new	PRJNA769076	SAMN23390762	AT41-18-094	AT41-18-094	Ophioctenella acies	RAD-seq of deep-sea invertebrates	RAD-seq	GENOMIC	Restriction Digest	single	Illumina	Illumina HiSeq 4000	Restriction site enzyme pstI used on gDNA	fastq	AT41-18-094.fq.gz	-
SRR17008481	SRP340375	new	PRJNA769076	SAMN23390763	AT-41-18-095	AT-41-18-095	Ophioctenella acies	RAD-seq of deep-sea invertebrates	RAD-seq	GENOMIC	Restriction Digest	single	Illumina	Illumina HiSeq 4000	Restriction site enzyme pstI used on gDNA	fastq	AT-41-18-095.fq.gz	-
SRR17008470	SRP340375	new	PRJNA769076	SAMN23390764	AT-41-18-096	AT-41-18-096	Ophioctenella acies	RAD-seq of deep-sea invertebrates	RAD-seq	GENOMIC	Restriction Digest	single	Illumina	Illumina HiSeq 4000	Restriction site enzyme pstI used on gDNA	fastq	AT-41-18-096.fq.gz	-
SRR17008459	SRP340375	new	PRJNA769076	SAMN23390765	AT-41-18-097	AT-41-18-097	Ophioctenella acies	RAD-seq of deep-sea invertebrates	RAD-seq	GENOMIC	Restriction Digest	single	Illumina	Illumina HiSeq 4000	Restriction site enzyme pstI used on gDNA	fastq	AT-41-18-097.fq.gz	-
SRR17008447	SRP340375	new	PRJNA769076	SAMN23390766	AT-41-18-098	AT-41-18-098	Ophioctenella acies	RAD-seq of deep-sea invertebrates	RAD-seq	GENOMIC	Restriction Digest	single	Illumina	Illumina HiSeq 4000	Restriction site enzyme pstI used on gDNA	fastq	AT-41-18-098.fq.gz	-

Accession	Study	Object Status	Bioproject Accession	Biosample Accession	Sample Name	Library ID	Species	Title	Library Strategy	Library Source	Library Selection	Library Layout	Platform	Instrument Model	Design Description	Filetype	Filename	Filename2
SRR17008436	SRP340375	new	PRJNA769076	SAMN23390767	AT-41-18-099	AT-41-18-099	Ophioctenella acies	RAD-seq of deep-sea invertebrates	RAD-seq	GENOMIC	Restriction Digest	single	Illumina	Illumina HiSeq 4000	Restriction site enzyme pstI used on gDNA	fastq	AT-41-18-099.fq.gz	-
SRR17008426	SRP340375	new	PRJNA769076	SAMN23390768	AT-41-18-100	AT-41-18-100	Ophioctenella acies	RAD-seq of deep-sea invertebrates	RAD-seq	GENOMIC	Restriction Digest	single	Illumina	Illumina HiSeq 4000	Restriction site enzyme pstI used on gDNA	fastq	AT-41-18-100.fq.gz	-
SRR17008425	SRP340375	new	PRJNA769076	SAMN23390769	AT41-18-119	AT41-18-119	Asteroschema clavigerum	RAD-seq of deep-sea invertebrates	RAD-seq	GENOMIC	Restriction Digest	single	Illumina	Illumina HiSeq 4000	Restriction site enzyme pstI used on gDNA	fastq	AT41-18-119.fq.gz	-
SRR17008457	SRP340375	new	PRJNA769076	SAMN23390770	AT41-18-120	AT41-18-120	Asteroschema clavigerum	RAD-seq of deep-sea invertebrates	RAD-seq	GENOMIC	Restriction Digest	single	Illumina	Illumina HiSeq 4000	Restriction site enzyme pstI used on gDNA	fastq	AT41-18-120.fq.gz	-
SRR17008491	SRP340375	new	PRJNA769076	SAMN23390771	CM-00549	CM-00549	Asteroschema clavigerum	RAD-seq of deep-sea invertebrates	RAD-seq	GENOMIC	Restriction Digest	single	Illumina	Illumina HiSeq 4000	Restriction site enzyme pstI used on gDNA	fastq	CM-00549.fq.gz	-
SRR17008490	SRP340375	new	PRJNA769076	SAMN23390772	CM-00572	CM-00572	Asteroschema clavigerum	RAD-seq of deep-sea invertebrates	RAD-seq	GENOMIC	Restriction Digest	single	Illumina	Illumina HiSeq 4000	Restriction site enzyme pstI used on gDNA	fastq	CM-00572.fq.gz	-
SRR17008489	SRP340375	new	PRJNA769076	SAMN23390773	RB-10-094	RB-10-094	Asteroschema clavigerum	RAD-seq of deep-sea invertebrates	RAD-seq	GENOMIC	Restriction Digest	single	Illumina	Illumina HiSeq 4000	Restriction site enzyme pstI used on gDNA	fastq	RB-10-094.fq.gz	-

Accession	Study	Object Status	Bioproject Accession	Biosample Accession	Sample Name	Library ID	Species	Title	Library Strategy	Library Source	Library Selection	Library Layout	Platform	Instrument Model	Design Description	Filetype	Filename	Filename2
SRR17008488	SRP340375	new	PRJNA769076	SAMN23390774	RB-19-064	RB-19-064	Asteroschema clavigerum	RAD-seq of deep-sea invertebrates	RAD-seq	GENOMIC	Restriction Digest	single	Illumina	Illumina HiSeq 4000	Restriction site enzyme pstI used on gDNA	fastq	RB-19-064.fq.gz	-
SRR17008487	SRP340375	new	PRJNA769076	SAMN23390775	RB-19-068	RB-19-068	Ophiocreas oedipus	RAD-seq of deep-sea invertebrates	RAD-seq	GENOMIC	Restriction Digest	single	Illumina	Illumina HiSeq 4000	Restriction site enzyme pstI used on gDNA	fastq	RB-19-068.fq.gz	-
SRR17008486	SRP340375	new	PRJNA769076	SAMN23390776	AT41-18-090	AT41-18-090	Chiridota heheva	RAD-seq of deep-sea invertebrates	RAD-seq	GENOMIC	Restriction Digest	single	Illumina	Illumina HiSeq 4000	Restriction site enzyme sbfI used on gDNA	fastq	AT41-18-090.fq.gz	-
SRR17008485	SRP340375	new	PRJNA769076	SAMN23390777	AT41-18-103	AT41-18-103	Chiridota heheva	RAD-seq of deep-sea invertebrates	RAD-seq	GENOMIC	Restriction Digest	single	Illumina	Illumina HiSeq 4000	Restriction site enzyme sbfI used on gDNA	fastq	AT41-18-103.fq.gz	-
SRR17008484	SRP340375	new	PRJNA769076	SAMN23390778	CM-00496	CM-00496	Chiridota heheva	RAD-seq of deep-sea invertebrates	RAD-seq	GENOMIC	Restriction Digest	single	Illumina	Illumina HiSeq 4000	Restriction site enzyme sbfI used on gDNA	fastq	CM-00496.fq.gz	-
SRR17008483	SRP340375	new	PRJNA769076	SAMN23390779	RB-19-147	RB-19-147	Chiridota heheva	RAD-seq of deep-sea invertebrates	RAD-seq	GENOMIC	Restriction Digest	single	Illumina	Illumina HiSeq 4000	Restriction site enzyme sbfI used on gDNA	fastq	RB-19-147.fq.gz	-
SRR17008482	SRP340375	new	PRJNA769076	SAMN23390780	RB-19-179	RB-19-179	Chiridota heheva	RAD-seq of deep-sea invertebrates	RAD-seq	GENOMIC	Restriction Digest	single	Illumina	Illumina HiSeq 4000	Restriction site enzyme sbfI used on gDNA	fastq	RB-19-179.fq.gz	-

Accession	Study	Object Status	Bioproject Accession	Biosample Accession	Sample Name	Library ID	Species	Title	Library Strategy	Library Source	Library Selection	Library Layout	Platform	Instrument Model	Design Description	Filetype	Filename	Filename2
SRR17008480	SRP340375	new	PRJNA769076	SAMN23390781	RB-19-180	RB-19-180	Chiridota heheva	RAD-seq of deep-sea invertebrates	RAD-seq	GENOMIC	Restriction Digest	single	Illumina	Illumina HiSeq 4000	Restriction site enzyme sbfI used on gDNA	fastq	RB-19-180.fq.gz	-
SRR17008479	SRP340375	new	PRJNA769076	SAMN23390782	RB-19-181	RB-19-181	Chiridota heheva	RAD-seq of deep-sea invertebrates	RAD-seq	GENOMIC	Restriction Digest	single	Illumina	Illumina HiSeq 4000	Restriction site enzyme sbfI used on gDNA	fastq	RB-19-181.fq.gz	-
SRR17008478	SRP340375	new	PRJNA769076	SAMN23390783	RB-19-182	RB-19-182	Chiridota heheva	RAD-seq of deep-sea invertebrates	RAD-seq	GENOMIC	Restriction Digest	single	Illumina	Illumina HiSeq 4000	Restriction site enzyme sbfI used on gDNA	fastq	RB-19-182.fq.gz	-
SRR17008477	SRP340375	new	PRJNA769076	SAMN23390784	RB-19-183	RB-19-183	Chiridota heheva	RAD-seq of deep-sea invertebrates	RAD-seq	GENOMIC	Restriction Digest	single	Illumina	Illumina HiSeq 4000	Restriction site enzyme sbfI used on gDNA	fastq	RB-19-183.fq.gz	-
SRR17008476	SRP340375	new	PRJNA769076	SAMN23390785	RB-19-184	RB-19-184	Chiridota heheva	RAD-seq of deep-sea invertebrates	RAD-seq	GENOMIC	Restriction Digest	single	Illumina	Illumina HiSeq 4000	Restriction site enzyme sbfI used on gDNA	fastq	RB-19-184.fq.gz	-
SRR17008475	SRP340375	new	PRJNA769076	SAMN23390786	RB-19-185	RB-19-185	Chiridota heheva	RAD-seq of deep-sea invertebrates	RAD-seq	GENOMIC	Restriction Digest	single	Illumina	Illumina HiSeq 4000	Restriction site enzyme sbfI used on gDNA	fastq	RB-19-185.fq.gz	-
SRR17008474	SRP340375	new	PRJNA769076	SAMN23390787	RB-19-186	RB-19-186	Chiridota heheva	RAD-seq of deep-sea invertebrates	RAD-seq	GENOMIC	Restriction Digest	single	Illumina	Illumina HiSeq 4000	Restriction site enzyme sbfI used on gDNA	fastq	RB-19-186.fq.gz	-

Accession	Study	Object Status	Bioproject Accession	Biosample Accession	Sample Name	Library ID	Species	Title	Library Strategy	Library Source	Library Selection	Library Layout	Platform	Instrument Model	Design Description	Filetype	Filename	Filename2
SRR17008473	SRP340375	new	PRJNA769076	SAMN23390788	RB-19-187	RB-19-187	Chiridota heheva	RAD-seq of deep-sea invertebrates	RAD-seq	GENOMIC	Restriction Digest	single	Illumina	Illumina HiSeq 4000	Restriction site enzyme sbfI used on gDNA	fastq	RB-19-187.fq.gz	-
SRR17008472	SRP340375	new	PRJNA769076	SAMN23390789	RB-19-188	RB-19-188	Chiridota heheva	RAD-seq of deep-sea invertebrates	RAD-seq	GENOMIC	Restriction Digest	single	Illumina	Illumina HiSeq 4000	Restriction site enzyme sbfI used on gDNA	fastq	RB-19-188.fq.gz	-
SRR17008471	SRP340375	new	PRJNA769076	SAMN23390790	RB-19-189	RB-19-189	Chiridota heheva	RAD-seq of deep-sea invertebrates	RAD-seq	GENOMIC	Restriction Digest	single	Illumina	Illumina HiSeq 4000	Restriction site enzyme sbfI used on gDNA	fastq	RB-19-189.fq.gz	-
SRR17008469	SRP340375	new	PRJNA769076	SAMN23390791	RB-19-191	RB-19-191	Chiridota heheva	RAD-seq of deep-sea invertebrates	RAD-seq	GENOMIC	Restriction Digest	single	Illumina	Illumina HiSeq 4000	Restriction site enzyme sbfI used on gDNA	fastq	RB-19-191.fq.gz	-
SRR17008468	SRP340375	new	PRJNA769076	SAMN23390792	RB-19-063	RB-19-063	Paramuricea	RAD-seq of deep-sea invertebrates	RAD-seq	GENOMIC	Restriction Digest	single	Illumina	Illumina HiSeq 4000	Restriction site enzyme pstI used on gDNA	fastq	RB-19-063.fq.gz	-
SRR17008467	SRP340375	new	PRJNA769076	SAMN23390793	RB-19-073	RB-19-073	Paramuricea	RAD-seq of deep-sea invertebrates	RAD-seq	GENOMIC	Restriction Digest	single	Illumina	Illumina HiSeq 4000	Restriction site enzyme pstI used on gDNA	fastq	RB-19-073.fq.gz	-
SRR17008466	SRP340375	new	PRJNA769076	SAMN23390794	RB-19-075	RB-19-075	Paramuricea	RAD-seq of deep-sea invertebrates	RAD-seq	GENOMIC	Restriction Digest	single	Illumina	Illumina HiSeq 4000	Restriction site enzyme pstI used on gDNA	fastq	RB-19-075.fq.gz	-

Accession	Study	Object Status	Bioproject Accession	Biosample Accession	Sample Name	Library ID	Species	Title	Library Strategy	Library Source	Library Selection	Library Layout	Platform	Instrument Model	Design Description	Filetype	Filename	Filename2
SRR17008465	SRP340375	new	PRJNA769076	SAMN23390795	RB-19-078	RB-19-078	Paramuricea	RAD-seq of deep-sea invertebrates	RAD-seq	GENOMIC	Restriction Digest	single	Illumina	Illumina HiSeq 4000	Restriction site enzyme pstI used on gDNA	fastq	RB-19-078.fq.gz	-
SRR17008464	SRP340375	new	PRJNA769076	SAMN23390796	RB-19-087	RB-19-087	Paramuricea	RAD-seq of deep-sea invertebrates	RAD-seq	GENOMIC	Restriction Digest	single	Illumina	Illumina HiSeq 4000	Restriction site enzyme pstI used on gDNA	fastq	RB-19-087.fq.gz	-
SRR17008463	SRP340375	new	PRJNA769076	SAMN23390797	RB-19-112	RB-19-112	Paramuricea	RAD-seq of deep-sea invertebrates	RAD-seq	GENOMIC	Restriction Digest	single	Illumina	Illumina HiSeq 4000	Restriction site enzyme pstI used on gDNA	fastq	RB-19-112.fq.gz	-
SRR17008462	SRP340375	new	PRJNA769076	SAMN23390798	AT41-18-041	AT41-18-041	Paramuricea	RAD-seq of deep-sea invertebrates	RAD-seq	GENOMIC	Restriction Digest	single	Illumina	Illumina HiSeq 4000	Restriction site enzyme pstI used on gDNA	fastq	AT41-18-041.fq.gz	-
SRR17008461	SRP340375	new	PRJNA769076	SAMN23390799	AT41-18-111	AT41-18-111	Paramuricea	RAD-seq of deep-sea invertebrates	RAD-seq	GENOMIC	Restriction Digest	single	Illumina	Illumina HiSeq 4000	Restriction site enzyme pstI used on gDNA	fastq	AT41-18-111.fq.gz	-
SRR17008460	SRP340375	new	PRJNA769076	SAMN23390800	AT41-18-118	AT41-18-118	Paramuricea	RAD-seq of deep-sea invertebrates	RAD-seq	GENOMIC	Restriction Digest	single	Illumina	Illumina HiSeq 4000	Restriction site enzyme pstI used on gDNA	fastq	AT41-18-118.fq.gz	-
SRR17008458	SRP340375	new	PRJNA769076	SAMN23390801	AT41-18-127	AT41-18-127	Paramuricea	RAD-seq of deep-sea invertebrates	RAD-seq	GENOMIC	Restriction Digest	single	Illumina	Illumina HiSeq 4000	Restriction site enzyme pstI used on gDNA	fastq	AT41-18-127.fq.gz	-

Accession	Study	Object Status	Bioproject Accession	Biosample Accession	Sample Name	Library ID	Species	Title	Library Strategy	Library Source	Library Selection	Library Layout	Platform	Instrument Model	Design Description	Filetype	Filename	Filename2
SRR17008456	SRP340375	new	PRJNA769076	SAMN23390802	AT41-18-016	OCT002	Plumarella	RAD-seq of deep-sea invertebrates	RAD-seq	GENOMIC	Restriction Digest	paired	Illumina	Illumina NovaSeq 6000	Target Capture of UCEs and exons	fastq	OCT002_ATCATTCC_L001_R1_001.fastq.gz	OCT002_ATCATTCC_L001_R2_001.fastq.gz
SRR17008455	SRP340375	new	PRJNA769076	SAMN23390803	AT41-18-022	OCT003	Plumarella	RAD-seq of deep-sea invertebrates	RAD-seq	GENOMIC	Restriction Digest	paired	Illumina	Illumina NovaSeq 6000	Target Capture of UCEs and exons	fastq	OCT003_CAGCGTTA_L001_R1_001.fastq.gz	OCT003_CAGCGTTA_L001_R2_001.fastq.gz
SRR17008454	SRP340375	new	PRJNA769076	SAMN23390804	AT41-18-055	OCT008	Plumarella	RAD-seq of deep-sea invertebrates	RAD-seq	GENOMIC	Restriction Digest	paired	Illumina	Illumina NovaSeq 6000	Target Capture of UCEs and exons	fastq	OCT008_TAATGCGC_L001_R1_001.fastq.gz	OCT008_TAATGCGC_L001_R2_001.fastq.gz
SRR17008453	SRP340375	new	PRJNA769076	SAMN23390805	AT41-18-068	OCT009	Plumarella	RAD-seq of deep-sea invertebrates	RAD-seq	GENOMIC	Restriction Digest	paired	Illumina	Illumina NovaSeq 6000	Target Capture of UCEs and exons	fastq	OCT009_GACTAGTA_L001_R1_001.fastq.gz	OCT009_GACTAGTA_L001_R2_001.fastq.gz
SRR17008452	SRP340375	new	PRJNA769076	SAMN23390806	RB-19-001	OCT091	Plumarella	RAD-seq of deep-sea invertebrates	RAD-seq	GENOMIC	Restriction Digest	paired	Illumina	Illumina NovaSeq 6000	Target Capture of UCEs and exons	fastq	OCT091_TGTGTTAA_L001_R1_001.fastq.gz	OCT091_TGTGTTAA_L001_R2_001.fastq.gz
SRR17008451	SRP340375	new	PRJNA769076	SAMN23390807	RB-19-002	OCT092	Plumarella	RAD-seq of deep-sea invertebrates	RAD-seq	GENOMIC	Restriction Digest	paired	Illumina	Illumina NovaSeq 6000	Target Capture of UCEs and exons	fastq	OCT092_CCGCTGTT_L001_R1_001.fastq.gz	OCT092_CCGCTGTT_L001_R2_001.fastq.gz
SRR17008450	SRP340375	new	PRJNA769076	SAMN23390808	RB-19-007	OCT093	Plumarella	RAD-seq of deep-sea invertebrates	RAD-seq	GENOMIC	Restriction Digest	paired	Illumina	Illumina NovaSeq 6000	Target Capture of UCEs and exons	fastq	OCT093_TACTGTTA_L001_R1_001.fastq.gz	OCT093_TACTGTTA_L001_R2_001.fastq.gz

Accession	Study	Object Status	Bioproject Accession	Biosample Accession	Sample Name	Library ID	Species	Title	Library Strategy	Library Source	Library Selection	Library Layout	Platform	Instrument Model	Design Description	Filetype	Filename	Filename2
SRR17008449	SRP340375	new	PRJNA769076	SAMN23390809	RB-19-009	OCT094	Plumarella	RAD-seq of deep-sea invertebrates	RAD-seq	GENOMIC	Restriction Digest	paired	Illumina	Illumina NovaSeq 6000	Target Capture of UCEs and exons	fastq	OCT094_TAAGTACC_L001_R1_001.fastq.gz	OCT094_TAAGTACC_L001_R2_001.fastq.gz
SRR17008448	SRP340375	new	PRJNA769076	SAMN23390810	RB-19-011	OCT095	Plumarella	RAD-seq of deep-sea invertebrates	RAD-seq	GENOMIC	Restriction Digest	paired	Illumina	Illumina NovaSeq 6000	Target Capture of UCEs and exons	fastq	OCT095_ACCTTAGA_L001_R1_001.fastq.gz	OCT095_ACCTTAGA_L001_R2_001.fastq.gz
SRR17008446	SRP340375	new	PRJNA769076	SAMN23390811	RB-19-013	OCT096	Plumarella	RAD-seq of deep-sea invertebrates	RAD-seq	GENOMIC	Restriction Digest	paired	Illumina	Illumina NovaSeq 6000	Target Capture of UCEs and exons	fastq	OCT096_AAGGCAAT_L001_R1_001.fastq.gz	OCT096_AAGGCAAT_L001_R2_001.fastq.gz
SRR17008445	SRP340375	new	PRJNA769076	SAMN23390812	RB-19-018	OCT097	Plumarella	RAD-seq of deep-sea invertebrates	RAD-seq	GENOMIC	Restriction Digest	paired	Illumina	Illumina NovaSeq 6000	Target Capture of UCEs and exons	fastq	OCT097_AAGCAATA_L001_R1_001.fastq.gz	OCT097_AAGCAATA_L001_R2_001.fastq.gz
SRR17008444	SRP340375	new	PRJNA769076	SAMN23390813	RB-19-019	OCT098	Plumarella	RAD-seq of deep-sea invertebrates	RAD-seq	GENOMIC	Restriction Digest	paired	Illumina	Illumina NovaSeq 6000	Target Capture of UCEs and exons	fastq	OCT098_AACAAGGC_L001_R1_001.fastq.gz	OCT098_AACAAGGC_L001_R2_001.fastq.gz
SRR17008443	SRP340375	new	PRJNA769076	SAMN23390814	RB-19-024	OCT099	Plumarella	RAD-seq of deep-sea invertebrates	RAD-seq	GENOMIC	Restriction Digest	paired	Illumina	Illumina NovaSeq 6000	Target Capture of UCEs and exons	fastq	OCT099_AAGTTATC_L001_R1_001.fastq.gz	OCT099_AAGTTATC_L001_R2_001.fastq.gz
SRR17008442	SRP340375	new	PRJNA769076	SAMN23390815	RB-19-025	OCT100	Plumarella	RAD-seq of deep-sea invertebrates	RAD-seq	GENOMIC	Restriction Digest	paired	Illumina	Illumina NovaSeq 6000	Target Capture of UCEs and exons	fastq	OCT100_AAGTTGGA_L001_R1_001.fastq.gz	OCT100_AAGTTGGA_L001_R2_001.fastq.gz

Accession	Study	Object Status	Bioproject Accession	Biosample Accession	Sample Name	Library ID	Species	Title	Library Strategy	Library Source	Library Selection	Library Layout	Platform	Instrument Model	Design Description	Filetype	Filename	Filename2
SRR17008441	SRP340375	new	PRJNA769076	SAMN23390816	RB-19-035	OCT102	Plumarella	RAD-seq of deep-sea invertebrates	RAD-seq	GENOMIC	Restriction Digest	paired	Illumina	Illumina NovaSeq 6000	Target Capture of UCEs and exons	fastq	OCT102_AAGTCGTG_L001_R1_001.fastq.gz	OCT102_AAGTCGTG_L001_R2_001.fastq.gz
SRR17008440	SRP340375	new	PRJNA769076	SAMN23390817	RB-19-038	OCT103	Plumarella	RAD-seq of deep-sea invertebrates	RAD-seq	GENOMIC	Restriction Digest	paired	Illumina	Illumina NovaSeq 6000	Target Capture of UCEs and exons	fastq	OCT103_AAGGAGTT_L001_R1_001.fastq.gz	OCT103_AAGGAGTT_L001_R2_001.fastq.gz
SRR17008439	SRP340375	new	PRJNA769076	SAMN23390818	RB-19-039	OCT104	Plumarella	RAD-seq of deep-sea invertebrates	RAD-seq	GENOMIC	Restriction Digest	paired	Illumina	Illumina NovaSeq 6000	Target Capture of UCEs and exons	fastq	OCT104_TGCATTGC_L001_R1_001.fastq.gz	OCT104_TGCATTGC_L001_R2_001.fastq.gz
SRR17008438	SRP340375	new	PRJNA769076	SAMN23390819	RB-19-040	OCT105	Plumarella	RAD-seq of deep-sea invertebrates	RAD-seq	GENOMIC	Restriction Digest	paired	Illumina	Illumina NovaSeq 6000	Target Capture of UCEs and exons	fastq	OCT105_TTATGTAT_L001_R1_001.fastq.gz	OCT105_TTATGTAT_L001_R2_001.fastq.gz
SRR17008437	SRP340375	new	PRJNA769076	SAMN23390820	RB-19-041	OCT106	Plumarella	RAD-seq of deep-sea invertebrates	RAD-seq	GENOMIC	Restriction Digest	paired	Illumina	Illumina NovaSeq 6000	Target Capture of UCEs and exons	fastq	OCT106_TTGGTCCG_L001_R1_001.fastq.gz	OCT106_TTGGTCCG_L001_R2_001.fastq.gz
SRR17008435	SRP340375	new	PRJNA769076	SAMN23390821	RB-19-042	OCT107	Plumarella	RAD-seq of deep-sea invertebrates	RAD-seq	GENOMIC	Restriction Digest	paired	Illumina	Illumina NovaSeq 6000	Target Capture of UCEs and exons	fastq	OCT107_GTACAGCT_L001_R1_001.fastq.gz	OCT107_GTACAGCT_L001_R2_001.fastq.gz
SRR17008434	SRP340375	new	PRJNA769076	SAMN23390822	RB-19-044	OCT108	Plumarella	RAD-seq of deep-sea invertebrates	RAD-seq	GENOMIC	Restriction Digest	paired	Illumina	Illumina NovaSeq 6000	Target Capture of UCEs and exons	fastq	OCT108_GGACAACG_L001_R1_001.fastq.gz	OCT108_GGACAACG_L001_R2_001.fastq.gz

Accession	Study	Object Status	Bioproject Accession	Biosample Accession	Sample Name	Library ID	Species	Title	Library Strategy	Library Source	Library Selection	Library Layout	Platform	Instrument Model	Design Description	Filetype	Filename	Filename2
SRR17008433	SRP340375	new	PRJNA769076	SAMN23390823	RB-19-048	OCT109	Plumarella	RAD-seq of deep-sea invertebrates	RAD-seq	GENOMIC	Restriction Digest	paired	Illumina	Illumina NovaSeq 6000	Target Capture of UCEs and exons	fastq	OCT109_GTCCACTC_L001_R1_001.fastq.gz	OCT109_GTCCACTC_L001_R2_001.fastq.gz
SRR17008432	SRP340375	new	PRJNA769076	SAMN23390824	RB-19-049	OCT110	Plumarella	RAD-seq of deep-sea invertebrates	RAD-seq	GENOMIC	Restriction Digest	paired	Illumina	Illumina NovaSeq 6000	Target Capture of UCEs and exons	fastq	OCT110_TTCAGAAC_L001_R1_001.fastq.gz	OCT110_TTCAGAAC_L001_R2_001.fastq.gz
SRR17008431	SRP340375	new	PRJNA769076	SAMN23390825	RB-19-051	OCT111	Plumarella	RAD-seq of deep-sea invertebrates	RAD-seq	GENOMIC	Restriction Digest	paired	Illumina	Illumina NovaSeq 6000	Target Capture of UCEs and exons	fastq	OCT111_GTGTTGTA_L001_R1_001.fastq.gz	OCT111_GTGTTGTA_L001_R2_001.fastq.gz
SRR17008430	SRP340375	new	PRJNA769076	SAMN23390826	RB-19-056	OCT112	Plumarella	RAD-seq of deep-sea invertebrates	RAD-seq	GENOMIC	Restriction Digest	paired	Illumina	Illumina NovaSeq 6000	Target Capture of UCEs and exons	fastq	OCT112_ACGCCACT_L001_R1_001.fastq.gz	OCT112_ACGCCACT_L001_R2_001.fastq.gz
SRR17008429	SRP340375	new	PRJNA769076	SAMN23390827	RB-19-057	OCT113	Plumarella	RAD-seq of deep-sea invertebrates	RAD-seq	GENOMIC	Restriction Digest	paired	Illumina	Illumina NovaSeq 6000	Target Capture of UCEs and exons	fastq	OCT113_ACGGCAGA_L001_R1_001.fastq.gz	OCT113_ACGGCAGA_L001_R2_001.fastq.gz
SRR17008428	SRP340375	new	PRJNA769076	SAMN23390828	RB-19-201	OCT124	Plumarella	RAD-seq of deep-sea invertebrates	RAD-seq	GENOMIC	Restriction Digest	paired	Illumina	Illumina NovaSeq 6000	Target Capture of UCEs and exons	fastq	OCT124_CAGACCAC_L001_R1_001.fastq.gz	OCT124_CAGACCAC_L001_R2_001.fastq.gz
SRR17008427	SRP340375	new	PRJNA769076	SAMN23390829	RB-19-203	OCT125	Plumarella	RAD-seq of deep-sea invertebrates	RAD-seq	GENOMIC	Restriction Digest	paired	Illumina	Illumina NovaSeq 6000	Target Capture of UCEs and exons	fastq	OCT125_TACATAGA_L001_R1_001.fastq.gz	OCT125_TACATAGA_L001_R2_001.fastq.gz

Accession	Study	Object Status	Bioproject Accession	Biosample Accession	Sample Name	Library ID	Species	Title	Library Strategy	Library Source	Library Selection	Library Layout	Platform	Instrument Model	Design Description	Filetype	Filename	Filename2
SRR16232392	SRP340375	new	PRJNA769076	SAMN22089731	CM-00128	CM-00128	Bathymodiolus heckerae	RAD-seq of Bathymodiolus	RAD-seq	GENOMIC	Restriction Digest	single	Illumina	Illumina HiSeq 4000	Restriction site enzyme pstI used on gDNA	fastq	CM-00128.fq.gz	-
SRR16232391	SRP340375	new	PRJNA769076	SAMN22089732	CM-00129	CM-00129	Bathymodiolus heckerae	RAD-seq of Bathymodiolus	RAD-seq	GENOMIC	Restriction Digest	single	Illumina	Illumina HiSeq 4000	Restriction site enzyme pstI used on gDNA	fastq	CM-00129.fq.gz	-
SRR16232480	SRP340375	new	PRJNA769076	SAMN22089733	CM-00130	CM-00130	Bathymodiolus heckerae	RAD-seq of Bathymodiolus	RAD-seq	GENOMIC	Restriction Digest	single	Illumina	Illumina HiSeq 4000	Restriction site enzyme pstI used on gDNA	fastq	CM-00130.fq.gz	-
SRR16232469	SRP340375	new	PRJNA769076	SAMN22089734	CM-00131	CM-00131	Bathymodiolus heckerae	RAD-seq of Bathymodiolus	RAD-seq	GENOMIC	Restriction Digest	single	Illumina	Illumina HiSeq 4000	Restriction site enzyme pstI used on gDNA	fastq	CM-00131.fq.gz	-
SRR16232458	SRP340375	new	PRJNA769076	SAMN22089735	CM-00132	CM-00132	Bathymodiolus heckerae	RAD-seq of Bathymodiolus	RAD-seq	GENOMIC	Restriction Digest	single	Illumina	Illumina HiSeq 4000	Restriction site enzyme pstI used on gDNA	fastq	CM-00132.fq.gz	-
SRR16232447	SRP340375	new	PRJNA769076	SAMN22089736	CM-00133	CM-00133	Bathymodiolus heckerae	RAD-seq of Bathymodiolus	RAD-seq	GENOMIC	Restriction Digest	single	Illumina	Illumina HiSeq 4000	Restriction site enzyme pstI used on gDNA	fastq	CM-00133.fq.gz	-
SRR16232436	SRP340375	new	PRJNA769076	SAMN22089737	CM-00134	CM-00134	Bathymodiolus heckerae	RAD-seq of Bathymodiolus	RAD-seq	GENOMIC	Restriction Digest	single	Illumina	Illumina HiSeq 4000	Restriction site enzyme pstI used on gDNA	fastq	CM-00134.fq.gz	-

Accession	Study	Object Status	Bioproject Accession	Biosample Accession	Sample Name	Library ID	Species	Title	Library Strategy	Library Source	Library Selection	Library Layout	Platform	Instrument Model	Design Description	Filetype	Filename	Filename2
SRR16232425	SRP340375	new	PRJNA769076	SAMN22089738	CM-00135	CM-00135	Bathymodiolus heckerae	RAD-seq of Bathymodiolus	RAD-seq	GENOMIC	Restriction Digest	single	Illumina	Illumina HiSeq 4000	Restriction site enzyme pstI used on gDNA	fastq	CM-00135.fq.gz	-
SRR16232414	SRP340375	new	PRJNA769076	SAMN22089739	CM-00136	CM-00136	Bathymodiolus heckerae	RAD-seq of Bathymodiolus	RAD-seq	GENOMIC	Restriction Digest	single	Illumina	Illumina HiSeq 4000	Restriction site enzyme pstI used on gDNA	fastq	CM-00136.fq.gz	-
SRR16232403	SRP340375	new	PRJNA769076	SAMN22089740	CM-00137	CM-00137	Bathymodiolus heckerae	RAD-seq of Bathymodiolus	RAD-seq	GENOMIC	Restriction Digest	single	Illumina	Illumina HiSeq 4000	Restriction site enzyme pstI used on gDNA	fastq	CM-00137.fq.gz	-
SRR16232390	SRP340375	new	PRJNA769076	SAMN22089741	CM-00138	CM-00138	Bathymodiolus heckerae	RAD-seq of Bathymodiolus	RAD-seq	GENOMIC	Restriction Digest	single	Illumina	Illumina HiSeq 4000	Restriction site enzyme pstI used on gDNA	fastq	CM-00138.fq.gz	-
SRR16232379	SRP340375	new	PRJNA769076	SAMN22089742	CM-00139	CM-00139	Bathymodiolus heckerae	RAD-seq of Bathymodiolus	RAD-seq	GENOMIC	Restriction Digest	single	Illumina	Illumina HiSeq 4000	Restriction site enzyme pstI used on gDNA	fastq	CM-00139.fq.gz	-
SRR16232368	SRP340375	new	PRJNA769076	SAMN22089743	CM-00140	CM-00140	Bathymodiolus heckerae	RAD-seq of Bathymodiolus	RAD-seq	GENOMIC	Restriction Digest	single	Illumina	Illumina HiSeq 4000	Restriction site enzyme pstI used on gDNA	fastq	CM-00140.fq.gz	-
SRR16232357	SRP340375	new	PRJNA769076	SAMN22089744	CM-00141	CM-00141	Bathymodiolus heckerae	RAD-seq of Bathymodiolus	RAD-seq	GENOMIC	Restriction Digest	single	Illumina	Illumina HiSeq 4000	Restriction site enzyme pstI used on gDNA	fastq	CM-00141.fq.gz	-

Accession	Study	Object Status	Bioproject Accession	Biosample Accession	Sample Name	Library ID	Species	Title	Library Strategy	Library Source	Library Selection	Library Layout	Platform	Instrument Model	Design Description	Filetype	Filename	Filename2
SRR16232523	SRP340375	new	PRJNA769076	SAMN22089745	CM-00142	CM-00142	Bathymodiolus heckerae	RAD-seq of Bathymodiolus	RAD-seq	GENOMIC	Restriction Digest	single	Illumina	Illumina HiSeq 4000	Restriction site enzyme pstI used on gDNA	fastq	CM-00142.fq.gz	-
SRR16232512	SRP340375	new	PRJNA769076	SAMN22089746	CM-00143	CM-00143	Bathymodiolus heckerae	RAD-seq of Bathymodiolus	RAD-seq	GENOMIC	Restriction Digest	single	Illumina	Illumina HiSeq 4000	Restriction site enzyme pstI used on gDNA	fastq	CM-00143.fq.gz	-
SRR16232501	SRP340375	new	PRJNA769076	SAMN22089747	CM-00144	CM-00144	Bathymodiolus heckerae	RAD-seq of Bathymodiolus	RAD-seq	GENOMIC	Restriction Digest	single	Illumina	Illumina HiSeq 4000	Restriction site enzyme pstI used on gDNA	fastq	CM-00144.fq.gz	-
SRR16232490	SRP340375	new	PRJNA769076	SAMN22089748	CM-00146	CM-00146	Bathymodiolus heckerae	RAD-seq of Bathymodiolus	RAD-seq	GENOMIC	Restriction Digest	single	Illumina	Illumina HiSeq 4000	Restriction site enzyme pstI used on gDNA	fastq	CM-00146.fq.gz	-
SRR16232482	SRP340375	new	PRJNA769076	SAMN22089749	CM-00148	CM-00148	Bathymodiolus heckerae	RAD-seq of Bathymodiolus	RAD-seq	GENOMIC	Restriction Digest	single	Illumina	Illumina HiSeq 4000	Restriction site enzyme pstI used on gDNA	fastq	CM-00148.fq.gz	-
SRR16232481	SRP340375	new	PRJNA769076	SAMN22089750	CM-00149	CM-00149	Bathymodiolus heckerae	RAD-seq of Bathymodiolus	RAD-seq	GENOMIC	Restriction Digest	single	Illumina	Illumina HiSeq 4000	Restriction site enzyme pstI used on gDNA	fastq	CM-00149.fq.gz	-
SRR16232479	SRP340375	new	PRJNA769076	SAMN22089751	CM-00150	CM-00150	Bathymodiolus heckerae	RAD-seq of Bathymodiolus	RAD-seq	GENOMIC	Restriction Digest	single	Illumina	Illumina HiSeq 4000	Restriction site enzyme pstI used on gDNA	fastq	CM-00150.fq.gz	-

Accession	Study	Object Status	Bioproject Accession	Biosample Accession	Sample Name	Library ID	Species	Title	Library Strategy	Library Source	Library Selection	Library Layout	Platform	Instrument Model	Design Description	Filetype	Filename	Filename2
SRR16232478	SRP340375	new	PRJNA769076	SAMN22089752	CM-00151	CM-00151	Bathymodiolus heckerae	RAD-seq of Bathymodiolus	RAD-seq	GENOMIC	Restriction Digest	single	Illumina	Illumina HiSeq 4000	Restriction site enzyme pstI used on gDNA	fastq	CM-00151.fq.gz	-
SRR16232477	SRP340375	new	PRJNA769076	SAMN22089753	CM-00153	CM-00153	Bathymodiolus heckerae	RAD-seq of Bathymodiolus	RAD-seq	GENOMIC	Restriction Digest	single	Illumina	Illumina HiSeq 4000	Restriction site enzyme pstI used on gDNA	fastq	CM-00153.fq.gz	-
SRR16232476	SRP340375	new	PRJNA769076	SAMN22089754	CM-00154	CM-00154	Bathymodiolus heckerae	RAD-seq of Bathymodiolus	RAD-seq	GENOMIC	Restriction Digest	single	Illumina	Illumina HiSeq 4000	Restriction site enzyme pstI used on gDNA	fastq	CM-00154.fq.gz	-
SRR16232475	SRP340375	new	PRJNA769076	SAMN22089755	CM-00155	CM-00155	Bathymodiolus heckerae	RAD-seq of Bathymodiolus	RAD-seq	GENOMIC	Restriction Digest	single	Illumina	Illumina HiSeq 4000	Restriction site enzyme pstI used on gDNA	fastq	CM-00155.fq.gz	-
SRR16232474	SRP340375	new	PRJNA769076	SAMN22089756	CM-00157	CM-00157	Bathymodiolus heckerae	RAD-seq of Bathymodiolus	RAD-seq	GENOMIC	Restriction Digest	single	Illumina	Illumina HiSeq 4000	Restriction site enzyme pstI used on gDNA	fastq	CM-00157.fq.gz	-
SRR16232473	SRP340375	new	PRJNA769076	SAMN22089757	CM-00158	CM-00158	Bathymodiolus heckerae	RAD-seq of Bathymodiolus	RAD-seq	GENOMIC	Restriction Digest	single	Illumina	Illumina HiSeq 4000	Restriction site enzyme pstI used on gDNA	fastq	CM-00158.fq.gz	-
SRR16232472	SRP340375	new	PRJNA769076	SAMN22089758	CM-00160	CM-00160	Bathymodiolus heckerae	RAD-seq of Bathymodiolus	RAD-seq	GENOMIC	Restriction Digest	single	Illumina	Illumina HiSeq 4000	Restriction site enzyme pstI used on gDNA	fastq	CM-00160.fq.gz	-

Accession	Study	Object Status	Bioproject Accession	Biosample Accession	Sample Name	Library ID	Species	Title	Library Strategy	Library Source	Library Selection	Library Layout	Platform	Instrument Model	Design Description	Filetype	Filename	Filename2
SRR16232471	SRP340375	new	PRJNA769076	SAMN22089759	CM-00161	CM-00161	Bathymodiolus heckerae	RAD-seq of Bathymodiolus	RAD-seq	GENOMIC	Restriction Digest	single	Illumina	Illumina HiSeq 4000	Restriction site enzyme pstI used on gDNA	fastq	CM-00161.fq.gz	-
SRR16232470	SRP340375	new	PRJNA769076	SAMN22089760	CM-00163	CM-00163	Bathymodiolus heckerae	RAD-seq of Bathymodiolus	RAD-seq	GENOMIC	Restriction Digest	single	Illumina	Illumina HiSeq 4000	Restriction site enzyme pstI used on gDNA	fastq	CM-00163.fq.gz	-
SRR16232468	SRP340375	new	PRJNA769076	SAMN22089761	CM-00165	CM-00165	Bathymodiolus heckerae	RAD-seq of Bathymodiolus	RAD-seq	GENOMIC	Restriction Digest	single	Illumina	Illumina HiSeq 4000	Restriction site enzyme pstI used on gDNA	fastq	CM-00165.fq.gz	-
SRR16232467	SRP340375	new	PRJNA769076	SAMN22089762	CM-00166	CM-00166	Bathymodiolus heckerae	RAD-seq of Bathymodiolus	RAD-seq	GENOMIC	Restriction Digest	single	Illumina	Illumina HiSeq 4000	Restriction site enzyme pstI used on gDNA	fastq	CM-00166.fq.gz	-
SRR16232466	SRP340375	new	PRJNA769076	SAMN22089763	CM-00167	CM-00167	Bathymodiolus heckerae	RAD-seq of Bathymodiolus	RAD-seq	GENOMIC	Restriction Digest	single	Illumina	Illumina HiSeq 4000	Restriction site enzyme pstI used on gDNA	fastq	CM-00167.fq.gz	-
SRR16232465	SRP340375	new	PRJNA769076	SAMN22089764	CM-00168	CM-00168	Bathymodiolus heckerae	RAD-seq of Bathymodiolus	RAD-seq	GENOMIC	Restriction Digest	single	Illumina	Illumina HiSeq 4000	Restriction site enzyme pstI used on gDNA	fastq	CM-00168.fq.gz	-
SRR16232464	SRP340375	new	PRJNA769076	SAMN22089765	CM-00169	CM-00169	Bathymodiolus heckerae	RAD-seq of Bathymodiolus	RAD-seq	GENOMIC	Restriction Digest	single	Illumina	Illumina HiSeq 4000	Restriction site enzyme pstI used on gDNA	fastq	CM-00169.fq.gz	-

Accession	Study	Object Status	Bioproject Accession	Biosample Accession	Sample Name	Library ID	Species	Title	Library Strategy	Library Source	Library Selection	Library Layout	Platform	Instrument Model	Design Description	Filetype	Filename	Filename2
SRR16232463	SRP340375	new	PRJNA769076	SAMN22089766	HRS-1704-CM-35	CM-0035	Bathymodiolus heckerae	RAD-seq of Bathymodiolus	RAD-seq	GENOMIC	Restriction Digest	single	Illumina	Illumina HiSeq 4000	Restriction site enzyme pstI used on gDNA	fastq	HRS-1704-CM-35.fq.gz	-
SRR16232462	SRP340375	new	PRJNA769076	SAMN22089767	RB-19-114	RB-19-114	Bathymodiolus heckerae	RAD-seq of Bathymodiolus	RAD-seq	GENOMIC	Restriction Digest	single	Illumina	Illumina HiSeq 4000	Restriction site enzyme pstI used on gDNA	fastq	RB-19-114.fq.gz	-
SRR16232461	SRP340375	new	PRJNA769076	SAMN22089768	RB-19-115	RB-19-115	Bathymodiolus heckerae	RAD-seq of Bathymodiolus	RAD-seq	GENOMIC	Restriction Digest	single	Illumina	Illumina HiSeq 4000	Restriction site enzyme pstI used on gDNA	fastq	RB-19-115.fq.gz	-
SRR16232460	SRP340375	new	PRJNA769076	SAMN22089769	RB-19-116	RB-19-116	Bathymodiolus heckerae	RAD-seq of Bathymodiolus	RAD-seq	GENOMIC	Restriction Digest	single	Illumina	Illumina HiSeq 4000	Restriction site enzyme pstI used on gDNA	fastq	RB-19-116.fq.gz	-
SRR16232459	SRP340375	new	PRJNA769076	SAMN22089770	RB-19-117	RB-19-117	Bathymodiolus heckerae	RAD-seq of Bathymodiolus	RAD-seq	GENOMIC	Restriction Digest	single	Illumina	Illumina HiSeq 4000	Restriction site enzyme pstI used on gDNA	fastq	RB-19-117.fq.gz	-
SRR16232457	SRP340375	new	PRJNA769076	SAMN22089771	RB-19-118	RB-19-118	Bathymodiolus heckerae	RAD-seq of Bathymodiolus	RAD-seq	GENOMIC	Restriction Digest	single	Illumina	Illumina HiSeq 4000	Restriction site enzyme pstI used on gDNA	fastq	RB-19-118.fq.gz	-
SRR16232456	SRP340375	new	PRJNA769076	SAMN22089772	RB-19-119	RB-19-119	Bathymodiolus heckerae	RAD-seq of Bathymodiolus	RAD-seq	GENOMIC	Restriction Digest	single	Illumina	Illumina HiSeq 4000	Restriction site enzyme pstI used on gDNA	fastq	RB-19-119.fq.gz	-

Accession	Study	Object Status	Bioproject Accession	Biosample Accession	Sample Name	Library ID	Species	Title	Library Strategy	Library Source	Library Selection	Library Layout	Platform	Instrument Model	Design Description	Filetype	Filename	Filename2
SRR16232455	SRP340375	new	PRJNA769076	SAMN22089773	RB-19-120	RB-19-120	Bathymodiolus heckerae	RAD-seq of Bathymodiolus	RAD-seq	GENOMIC	Restriction Digest	single	Illumina	Illumina HiSeq 4000	Restriction site enzyme pstI used on gDNA	fastq	RB-19-120.fq.gz	-
SRR16232454	SRP340375	new	PRJNA769076	SAMN22089774	RB-19-121	RB-19-121	Bathymodiolus heckerae	RAD-seq of Bathymodiolus	RAD-seq	GENOMIC	Restriction Digest	single	Illumina	Illumina HiSeq 4000	Restriction site enzyme pstI used on gDNA	fastq	RB-19-121.fq.gz	-
SRR16232453	SRP340375	new	PRJNA769076	SAMN22089775	RB-19-122	RB-19-122	Bathymodiolus heckerae	RAD-seq of Bathymodiolus	RAD-seq	GENOMIC	Restriction Digest	single	Illumina	Illumina HiSeq 4000	Restriction site enzyme pstI used on gDNA	fastq	RB-19-122.fq.gz	-
SRR16232452	SRP340375	new	PRJNA769076	SAMN22089776	RB-19-123	RB-19-123	Bathymodiolus heckerae	RAD-seq of Bathymodiolus	RAD-seq	GENOMIC	Restriction Digest	single	Illumina	Illumina HiSeq 4000	Restriction site enzyme pstI used on gDNA	fastq	RB-19-123.fq.gz	-
SRR16232451	SRP340375	new	PRJNA769076	SAMN22089777	RB-19-124	RB-19-124	Bathymodiolus heckerae	RAD-seq of Bathymodiolus	RAD-seq	GENOMIC	Restriction Digest	single	Illumina	Illumina HiSeq 4000	Restriction site enzyme pstI used on gDNA	fastq	RB-19-124.fq.gz	-
SRR16232450	SRP340375	new	PRJNA769076	SAMN22089778	RB-19-125	RB-19-125	Bathymodiolus heckerae	RAD-seq of Bathymodiolus	RAD-seq	GENOMIC	Restriction Digest	single	Illumina	Illumina HiSeq 4000	Restriction site enzyme pstI used on gDNA	fastq	RB-19-125.fq.gz	-
SRR16232449	SRP340375	new	PRJNA769076	SAMN22089779	RB-19-126	RB-19-126	Bathymodiolus heckerae	RAD-seq of Bathymodiolus	RAD-seq	GENOMIC	Restriction Digest	single	Illumina	Illumina HiSeq 4000	Restriction site enzyme pstI used on gDNA	fastq	RB-19-126.fq.gz	-

Accession	Study	Object Status	Bioproject Accession	Biosample Accession	Sample Name	Library ID	Species	Title	Library Strategy	Library Source	Library Selection	Library Layout	Platform	Instrument Model	Design Description	Filetype	Filename	Filename2
SRR16232448	SRP340375	new	PRJNA769076	SAMN22089780	RB-19-127	RB-19-127	Bathymodiolus heckerae	RAD-seq of Bathymodiolus	RAD-seq	GENOMIC	Restriction Digest	single	Illumina	Illumina HiSeq 4000	Restriction site enzyme pstI used on gDNA	fastq	RB-19-127.fq.gz	-
SRR16232446	SRP340375	new	PRJNA769076	SAMN22089781	RB-19-128	RB-19-128	Bathymodiolus heckerae	RAD-seq of Bathymodiolus	RAD-seq	GENOMIC	Restriction Digest	single	Illumina	Illumina HiSeq 4000	Restriction site enzyme pstI used on gDNA	fastq	RB-19-128.fq.gz	-
SRR16232445	SRP340375	new	PRJNA769076	SAMN22089782	RB-19-129	RB-19-129	Bathymodiolus heckerae	RAD-seq of Bathymodiolus	RAD-seq	GENOMIC	Restriction Digest	single	Illumina	Illumina HiSeq 4000	Restriction site enzyme pstI used on gDNA	fastq	RB-19-129.fq.gz	-
SRR16232444	SRP340375	new	PRJNA769076	SAMN22089783	RB-19-130	RB-19-130	Bathymodiolus heckerae	RAD-seq of Bathymodiolus	RAD-seq	GENOMIC	Restriction Digest	single	Illumina	Illumina HiSeq 4000	Restriction site enzyme pstI used on gDNA	fastq	RB-19-130.fq.gz	-
SRR16232443	SRP340375	new	PRJNA769076	SAMN22089784	RB-19-131	RB-19-131	Bathymodiolus heckerae	RAD-seq of Bathymodiolus	RAD-seq	GENOMIC	Restriction Digest	single	Illumina	Illumina HiSeq 4000	Restriction site enzyme pstI used on gDNA	fastq	RB-19-131.fq.gz	-
SRR16232442	SRP340375	new	PRJNA769076	SAMN22089785	RB-19-132	RB-19-132	Bathymodiolus heckerae	RAD-seq of Bathymodiolus	RAD-seq	GENOMIC	Restriction Digest	single	Illumina	Illumina HiSeq 4000	Restriction site enzyme pstI used on gDNA	fastq	RB-19-132.fq.gz	-
SRR16232441	SRP340375	new	PRJNA769076	SAMN22089786	RB-19-133	RB-19-133	Bathymodiolus heckerae	RAD-seq of Bathymodiolus	RAD-seq	GENOMIC	Restriction Digest	single	Illumina	Illumina HiSeq 4000	Restriction site enzyme pstI used on gDNA	fastq	RB-19-133.fq.gz	-

Accession	Study	Object Status	Bioproject Accession	Biosample Accession	Sample Name	Library ID	Species	Title	Library Strategy	Library Source	Library Selection	Library Layout	Platform	Instrument Model	Design Description	Filetype	Filename	Filename2
SRR16232440	SRP340375	new	PRJNA769076	SAMN22089787	RB-19-134	RB-19-134	Bathymodiolus heckerae	RAD-seq of Bathymodiolus	RAD-seq	GENOMIC	Restriction Digest	single	Illumina	Illumina HiSeq 4000	Restriction site enzyme pstI used on gDNA	fastq	RB-19-134.fq.gz	-
SRR16232439	SRP340375	new	PRJNA769076	SAMN22089788	RB-19-135	RB-19-135	Bathymodiolus heckerae	RAD-seq of Bathymodiolus	RAD-seq	GENOMIC	Restriction Digest	single	Illumina	Illumina HiSeq 4000	Restriction site enzyme pstI used on gDNA	fastq	RB-19-135.fq.gz	-
SRR16232438	SRP340375	new	PRJNA769076	SAMN22089789	RB-19-136	RB-19-136	Bathymodiolus heckerae	RAD-seq of Bathymodiolus	RAD-seq	GENOMIC	Restriction Digest	single	Illumina	Illumina HiSeq 4000	Restriction site enzyme pstI used on gDNA	fastq	RB-19-136.fq.gz	-
SRR16232437	SRP340375	new	PRJNA769076	SAMN22089790	RB-19-137	RB-19-137	Bathymodiolus heckerae	RAD-seq of Bathymodiolus	RAD-seq	GENOMIC	Restriction Digest	single	Illumina	Illumina HiSeq 4000	Restriction site enzyme pstI used on gDNA	fastq	RB-19-137.fq.gz	-
SRR16232435	SRP340375	new	PRJNA769076	SAMN22089791	RB-19-138	RB-19-138	Bathymodiolus heckerae	RAD-seq of Bathymodiolus	RAD-seq	GENOMIC	Restriction Digest	single	Illumina	Illumina HiSeq 4000	Restriction site enzyme pstI used on gDNA	fastq	RB-19-138.fq.gz	-
SRR16232434	SRP340375	new	PRJNA769076	SAMN22089792	RB-19-139	RB-19-139	Bathymodiolus heckerae	RAD-seq of Bathymodiolus	RAD-seq	GENOMIC	Restriction Digest	single	Illumina	Illumina HiSeq 4000	Restriction site enzyme pstI used on gDNA	fastq	RB-19-139.fq.gz	-
SRR16232433	SRP340375	new	PRJNA769076	SAMN22089793	RB-19-140	RB-19-140	Bathymodiolus heckerae	RAD-seq of Bathymodiolus	RAD-seq	GENOMIC	Restriction Digest	single	Illumina	Illumina HiSeq 4000	Restriction site enzyme pstI used on gDNA	fastq	RB-19-140.fq.gz	-

Accession	Study	Object Status	Bioproject Accession	Biosample Accession	Sample Name	Library ID	Species	Title	Library Strategy	Library Source	Library Selection	Library Layout	Platform	Instrument Model	Design Description	Filetype	Filename	Filename2
SRR16232432	SRP340375	new	PRJNA769076	SAMN22089794	RB-19-141	RB-19-141	Bathymodiolus heckerae	RAD-seq of Bathymodiolus	RAD-seq	GENOMIC	Restriction Digest	single	Illumina	Illumina HiSeq 4000	Restriction site enzyme pstI used on gDNA	fastq	RB-19-141.fq.gz	-
SRR16232431	SRP340375	new	PRJNA769076	SAMN22089795	RB-19-142	RB-19-142	Bathymodiolus heckerae	RAD-seq of Bathymodiolus	RAD-seq	GENOMIC	Restriction Digest	single	Illumina	Illumina HiSeq 4000	Restriction site enzyme pstI used on gDNA	fastq	RB-19-142.fq.gz	-
SRR16232430	SRP340375	new	PRJNA769076	SAMN22089796	RB-19-143	RB-19-143	Bathymodiolus heckerae	RAD-seq of Bathymodiolus	RAD-seq	GENOMIC	Restriction Digest	single	Illumina	Illumina HiSeq 4000	Restriction site enzyme pstI used on gDNA	fastq	RB-19-143.fq.gz	-
SRR16232429	SRP340375	new	PRJNA769076	SAMN22089797	RB-19-144	RB-19-144	Bathymodiolus heckerae	RAD-seq of Bathymodiolus	RAD-seq	GENOMIC	Restriction Digest	single	Illumina	Illumina HiSeq 4000	Restriction site enzyme pstI used on gDNA	fastq	RB-19-144.fq.gz	-
SRR16232428	SRP340375	new	PRJNA769076	SAMN22089798	RB-19-145	RB-19-145	Bathymodiolus heckerae	RAD-seq of Bathymodiolus	RAD-seq	GENOMIC	Restriction Digest	single	Illumina	Illumina HiSeq 4000	Restriction site enzyme pstI used on gDNA	fastq	RB-19-145.fq.gz	-
SRR16232427	SRP340375	new	PRJNA769076	SAMN22089799	RB-19-150	RB-19-150	Bathymodiolus heckerae	RAD-seq of Bathymodiolus	RAD-seq	GENOMIC	Restriction Digest	single	Illumina	Illumina HiSeq 4000	Restriction site enzyme pstI used on gDNA	fastq	RB-19-150.fq.gz	-
SRR16232426	SRP340375	new	PRJNA769076	SAMN22089800	RB-19-151	RB-19-151	Bathymodiolus heckerae	RAD-seq of Bathymodiolus	RAD-seq	GENOMIC	Restriction Digest	single	Illumina	Illumina HiSeq 4000	Restriction site enzyme pstI used on gDNA	fastq	RB-19-151.fq.gz	-

Accession	Study	Object Status	Bioproject Accession	Biosample Accession	Sample Name	Library ID	Species	Title	Library Strategy	Library Source	Library Selection	Library Layout	Platform	Instrument Model	Design Description	Filetype	Filename	Filename2
SRR16232424	SRP340375	new	PRJNA769076	SAMN22089801	RB-19-152	RB-19-152	Bathymodiolus heckerae	RAD-seq of Bathymodiolus	RAD-seq	GENOMIC	Restriction Digest	single	Illumina	Illumina HiSeq 4000	Restriction site enzyme pstI used on gDNA	fastq	RB-19-152.fq.gz	-
SRR16232423	SRP340375	new	PRJNA769076	SAMN22089802	RB-19-153	RB-19-153	Bathymodiolus heckerae	RAD-seq of Bathymodiolus	RAD-seq	GENOMIC	Restriction Digest	single	Illumina	Illumina HiSeq 4000	Restriction site enzyme pstI used on gDNA	fastq	RB-19-153.fq.gz	-
SRR16232422	SRP340375	new	PRJNA769076	SAMN22089803	RB-19-154	RB-19-154	Bathymodiolus heckerae	RAD-seq of Bathymodiolus	RAD-seq	GENOMIC	Restriction Digest	single	Illumina	Illumina HiSeq 4000	Restriction site enzyme pstI used on gDNA	fastq	RB-19-154.fq.gz	-
SRR16232421	SRP340375	new	PRJNA769076	SAMN22089804	RB-19-155	RB-19-155	Bathymodiolus heckerae	RAD-seq of Bathymodiolus	RAD-seq	GENOMIC	Restriction Digest	single	Illumina	Illumina HiSeq 4000	Restriction site enzyme pstI used on gDNA	fastq	RB-19-155.fq.gz	-
SRR16232420	SRP340375	new	PRJNA769076	SAMN22089805	RB-19-156	RB-19-156	Bathymodiolus heckerae	RAD-seq of Bathymodiolus	RAD-seq	GENOMIC	Restriction Digest	single	Illumina	Illumina HiSeq 4000	Restriction site enzyme pstI used on gDNA	fastq	RB-19-156.fq.gz	-
SRR16232419	SRP340375	new	PRJNA769076	SAMN22089806	RB-19-157	RB-19-157	Bathymodiolus heckerae	RAD-seq of Bathymodiolus	RAD-seq	GENOMIC	Restriction Digest	single	Illumina	Illumina HiSeq 4000	Restriction site enzyme pstI used on gDNA	fastq	RB-19-157.fq.gz	-
SRR16232418	SRP340375	new	PRJNA769076	SAMN22089807	RB-19-158	RB-19-158	Bathymodiolus heckerae	RAD-seq of Bathymodiolus	RAD-seq	GENOMIC	Restriction Digest	single	Illumina	Illumina HiSeq 4000	Restriction site enzyme pstI used on gDNA	fastq	RB-19-158.fq.gz	-

Accession	Study	Object Status	Bioproject Accession	Biosample Accession	Sample Name	Library ID	Species	Title	Library Strategy	Library Source	Library Selection	Library Layout	Platform	Instrument Model	Design Description	Filetype	Filename	Filename2
SRR16232417	SRP340375	new	PRJNA769076	SAMN22089808	RB-19-159	RB-19-159	Bathymodiolus heckerae	RAD-seq of Bathymodiolus	RAD-seq	GENOMIC	Restriction Digest	single	Illumina	Illumina HiSeq 4000	Restriction site enzyme pstI used on gDNA	fastq	RB-19-159.fq.gz	-
SRR16232416	SRP340375	new	PRJNA769076	SAMN22089809	RB-19-160	RB-19-160	Bathymodiolus heckerae	RAD-seq of Bathymodiolus	RAD-seq	GENOMIC	Restriction Digest	single	Illumina	Illumina HiSeq 4000	Restriction site enzyme pstI used on gDNA	fastq	RB-19-160.fq.gz	-
SRR16232415	SRP340375	new	PRJNA769076	SAMN22089810	RB-19-161	RB-19-161	Bathymodiolus heckerae	RAD-seq of Bathymodiolus	RAD-seq	GENOMIC	Restriction Digest	single	Illumina	Illumina HiSeq 4000	Restriction site enzyme pstI used on gDNA	fastq	RB-19-161.fq.gz	-
SRR16232413	SRP340375	new	PRJNA769076	SAMN22089811	RB-19-162	RB-19-162	Bathymodiolus heckerae	RAD-seq of Bathymodiolus	RAD-seq	GENOMIC	Restriction Digest	single	Illumina	Illumina HiSeq 4000	Restriction site enzyme pstI used on gDNA	fastq	RB-19-162.fq.gz	-
SRR16232412	SRP340375	new	PRJNA769076	SAMN22089812	RB-19-164	RB-19-164	Bathymodiolus heckerae	RAD-seq of Bathymodiolus	RAD-seq	GENOMIC	Restriction Digest	single	Illumina	Illumina HiSeq 4000	Restriction site enzyme pstI used on gDNA	fastq	RB-19-164.fq.gz	-
SRR16232411	SRP340375	new	PRJNA769076	SAMN22089813	RB-19-165	RB-19-165	Bathymodiolus heckerae	RAD-seq of Bathymodiolus	RAD-seq	GENOMIC	Restriction Digest	single	Illumina	Illumina HiSeq 4000	Restriction site enzyme pstI used on gDNA	fastq	RB-19-165.fq.gz	-
SRR16232410	SRP340375	new	PRJNA769076	SAMN22089814	RB-19-166	RB-19-166	Bathymodiolus heckerae	RAD-seq of Bathymodiolus	RAD-seq	GENOMIC	Restriction Digest	single	Illumina	Illumina HiSeq 4000	Restriction site enzyme pstI used on gDNA	fastq	RB-19-166.fq.gz	-

Accession	Study	Object Status	Bioproject Accession	Biosample Accession	Sample Name	Library ID	Species	Title	Library Strategy	Library Source	Library Selection	Library Layout	Platform	Instrument Model	Design Description	Filetype	Filename	Filename2
SRR16232409	SRP340375	new	PRJNA769076	SAMN22089815	RB-19-167	RB-19-167	Bathymodiolus heckerae	RAD-seq of Bathymodiolus	RAD-seq	GENOMIC	Restriction Digest	single	Illumina	Illumina HiSeq 4000	Restriction site enzyme pstI used on gDNA	fastq	RB-19-167.fq.gz	-
SRR16232408	SRP340375	new	PRJNA769076	SAMN22089816	RB-19-168	RB-19-168	Bathymodiolus heckerae	RAD-seq of Bathymodiolus	RAD-seq	GENOMIC	Restriction Digest	single	Illumina	Illumina HiSeq 4000	Restriction site enzyme pstI used on gDNA	fastq	RB-19-168.fq.gz	-
SRR16232407	SRP340375	new	PRJNA769076	SAMN22089817	RB-19-169	RB-19-169	Bathymodiolus heckerae	RAD-seq of Bathymodiolus	RAD-seq	GENOMIC	Restriction Digest	single	Illumina	Illumina HiSeq 4000	Restriction site enzyme pstI used on gDNA	fastq	RB-19-169.fq.gz	-
SRR16232406	SRP340375	new	PRJNA769076	SAMN22089818	RB-19-170	RB-19-170	Bathymodiolus heckerae	RAD-seq of Bathymodiolus	RAD-seq	GENOMIC	Restriction Digest	single	Illumina	Illumina HiSeq 4000	Restriction site enzyme pstI used on gDNA	fastq	RB-19-170.fq.gz	-
SRR16232405	SRP340375	new	PRJNA769076	SAMN22089819	RB-19-171	RB-19-171	Bathymodiolus heckerae	RAD-seq of Bathymodiolus	RAD-seq	GENOMIC	Restriction Digest	single	Illumina	Illumina HiSeq 4000	Restriction site enzyme pstI used on gDNA	fastq	RB-19-171.fq.gz	-
SRR16232404	SRP340375	new	PRJNA769076	SAMN22089820	RB-19-172	RB-19-172	Bathymodiolus heckerae	RAD-seq of Bathymodiolus	RAD-seq	GENOMIC	Restriction Digest	single	Illumina	Illumina HiSeq 4000	Restriction site enzyme pstI used on gDNA	fastq	RB-19-172.fq.gz	-
SRR16232402	SRP340375	new	PRJNA769076	SAMN22089821	RB-19-173	RB-19-173	Bathymodiolus heckerae	RAD-seq of Bathymodiolus	RAD-seq	GENOMIC	Restriction Digest	single	Illumina	Illumina HiSeq 4000	Restriction site enzyme pstI used on gDNA	fastq	RB-19-173.fq.gz	-

Accession	Study	Object Status	Bioproject Accession	Biosample Accession	Sample Name	Library ID	Species	Title	Library Strategy	Library Source	Library Selection	Library Layout	Platform	Instrument Model	Design Description	Filetype	Filename	Filename2
SRR16232401	SRP340375	new	PRJNA769076	SAMN22089822	RB-19-174	RB-19-174	Bathymodiolus heckerae	RAD-seq of Bathymodiolus	RAD-seq	GENOMIC	Restriction Digest	single	Illumina	Illumina HiSeq 4000	Restriction site enzyme pstI used on gDNA	fastq	RB-19-174.fq.gz	-
SRR16232400	SRP340375	new	PRJNA769076	SAMN22089823	RB-19-175	RB-19-175	Bathymodiolus heckerae	RAD-seq of Bathymodiolus	RAD-seq	GENOMIC	Restriction Digest	single	Illumina	Illumina HiSeq 4000	Restriction site enzyme pstI used on gDNA	fastq	RB-19-175.fq.gz	-
SRR16232399	SRP340375	new	PRJNA769076	SAMN22089824	RB-19-176	RB-19-176	Bathymodiolus heckerae	RAD-seq of Bathymodiolus	RAD-seq	GENOMIC	Restriction Digest	single	Illumina	Illumina HiSeq 4000	Restriction site enzyme pstI used on gDNA	fastq	RB-19-176.fq.gz	-
SRR16232398	SRP340375	new	PRJNA769076	SAMN22089825	RB-19-177	RB-19-177	Bathymodiolus heckerae	RAD-seq of Bathymodiolus	RAD-seq	GENOMIC	Restriction Digest	single	Illumina	Illumina HiSeq 4000	Restriction site enzyme pstI used on gDNA	fastq	RB-19-177.fq.gz	-
SRR16232397	SRP340375	new	PRJNA769076	SAMN22089907	RB-19-178	RB-19-178	Bathymodiolus childressi	RAD-seq of Bathymodiolus	RAD-seq	GENOMIC	Restriction Digest	single	Illumina	Illumina HiSeq 4000	Restriction site enzyme pstI used on gDNA	fastq	RB-19-178.fq.gz	-
SRR16232396	SRP340375	new	PRJNA769076	SAMN22089826	HRS-1704-CM-004	CM-004	Bathymodiolus childressi	RAD-seq of Bathymodiolus	RAD-seq	GENOMIC	Restriction Digest	single	Illumina	Illumina HiSeq 4000	Restriction site enzyme pstI used on gDNA	fastq	HRS-1704-CM-004.fq.gz	-
SRR16232395	SRP340375	new	PRJNA769076	SAMN22089827	HRS-1704-CM-005	CM-005	Bathymodiolus childressi	RAD-seq of Bathymodiolus	RAD-seq	GENOMIC	Restriction Digest	single	Illumina	Illumina HiSeq 4000	Restriction site enzyme pstI used on gDNA	fastq	HRS-1704-CM-005.fq.gz	-

Accession	Study	Object Status	Bioproject Accession	Biosample Accession	Sample Name	Library ID	Species	Title	Library Strategy	Library Source	Library Selection	Library Layout	Platform	Instrument Model	Design Description	Filetype	Filename	Filename2
SRR16232394	SRP340375	new	PRJNA769076	SAMN22089828	HRS-1704-CM-007	CM-007	Bathymodiolus childressi	RAD-seq of Bathymodiolus	RAD-seq	GENOMIC	Restriction Digest	single	Illumina	Illumina HiSeq 4000	Restriction site enzyme pstI used on gDNA	fastq	HRS-1704-CM-007.fq.gz	-
SRR16232393	SRP340375	new	PRJNA769076	SAMN22089829	HRS-1704-CM-009	CM-009	Bathymodiolus childressi	RAD-seq of Bathymodiolus	RAD-seq	GENOMIC	Restriction Digest	single	Illumina	Illumina HiSeq 4000	Restriction site enzyme pstI used on gDNA	fastq	HRS-1704-CM-009.fq.gz	-
SRR16232389	SRP340375	new	PRJNA769076	SAMN22089830	HRS-1704-CM-011	CM-011	Bathymodiolus childressi	RAD-seq of Bathymodiolus	RAD-seq	GENOMIC	Restriction Digest	single	Illumina	Illumina HiSeq 4000	Restriction site enzyme pstI used on gDNA	fastq	HRS-1704-CM-011.fq.gz	-
SRR16232388	SRP340375	new	PRJNA769076	SAMN22089831	HRS-1704-CM-015	CM-015	Bathymodiolus childressi	RAD-seq of Bathymodiolus	RAD-seq	GENOMIC	Restriction Digest	single	Illumina	Illumina HiSeq 4000	Restriction site enzyme pstI used on gDNA	fastq	HRS-1704-CM-015.fq.gz	-
SRR16232387	SRP340375	new	PRJNA769076	SAMN22089832	HRS-1704-CM-017	CM-017	Bathymodiolus childressi	RAD-seq of Bathymodiolus	RAD-seq	GENOMIC	Restriction Digest	single	Illumina	Illumina HiSeq 4000	Restriction site enzyme pstI used on gDNA	fastq	HRS-1704-CM-017.fq.gz	-
SRR16232386	SRP340375	new	PRJNA769076	SAMN22089833	HRS-1704-CM-019	CM-019	Bathymodiolus childressi	RAD-seq of Bathymodiolus	RAD-seq	GENOMIC	Restriction Digest	single	Illumina	Illumina HiSeq 4000	Restriction site enzyme pstI used on gDNA	fastq	HRS-1704-CM-019.fq.gz	-
SRR16232385	SRP340375	new	PRJNA769076	SAMN22089834	HRS-1704-CM-021	CM-021	Bathymodiolus childressi	RAD-seq of Bathymodiolus	RAD-seq	GENOMIC	Restriction Digest	single	Illumina	Illumina HiSeq 4000	Restriction site enzyme pstI used on gDNA	fastq	HRS-1704-CM-021.fq.gz	-

Accession	Study	Object Status	Bioproject Accession	Biosample Accession	Sample Name	Library ID	Species	Title	Library Strategy	Library Source	Library Selection	Library Layout	Platform	Instrument Model	Design Description	Filetype	Filename	Filename2
SRR16232384	SRP340375	new	PRJNA769076	SAMN22089835	HRS-1704-CM-023	CM-023	Bathymodiolus childressi	RAD-seq of Bathymodiolus	RAD-seq	GENOMIC	Restriction Digest	single	Illumina	Illumina HiSeq 4000	Restriction site enzyme pstI used on gDNA	fastq	HRS-1704-CM-023.fq.gz	-
SRR16232383	SRP340375	new	PRJNA769076	SAMN22089836	HRS-1704-CM-025	CM-025	Bathymodiolus childressi	RAD-seq of Bathymodiolus	RAD-seq	GENOMIC	Restriction Digest	single	Illumina	Illumina HiSeq 4000	Restriction site enzyme pstI used on gDNA	fastq	HRS-1704-CM-025.fq.gz	-
SRR16232382	SRP340375	new	PRJNA769076	SAMN22089837	HRS-1704-CM-028	CM-28	Bathymodiolus childressi	RAD-seq of Bathymodiolus	RAD-seq	GENOMIC	Restriction Digest	single	Illumina	Illumina HiSeq 4000	Restriction site enzyme pstI used on gDNA	fastq	HRS-1704-CM-028.fq.gz	-
SRR16232381	SRP340375	new	PRJNA769076	SAMN22089838	HRS-1704-CM-029	CM-029	Bathymodiolus childressi	RAD-seq of Bathymodiolus	RAD-seq	GENOMIC	Restriction Digest	single	Illumina	Illumina HiSeq 4000	Restriction site enzyme pstI used on gDNA	fastq	HRS-1704-CM-029.fq.gz	-
SRR16232380	SRP340375	new	PRJNA769076	SAMN22089839	HRS-1704-CM-031	CM-031	Bathymodiolus childressi	RAD-seq of Bathymodiolus	RAD-seq	GENOMIC	Restriction Digest	single	Illumina	Illumina HiSeq 4000	Restriction site enzyme pstI used on gDNA	fastq	HRS-1704-CM-031.fq.gz	-
SRR16232378	SRP340375	new	PRJNA769076	SAMN22089840	HRS-1704-CM-033	CM-033	Bathymodiolus childressi	RAD-seq of Bathymodiolus	RAD-seq	GENOMIC	Restriction Digest	single	Illumina	Illumina HiSeq 4000	Restriction site enzyme pstI used on gDNA	fastq	HRS-1704-CM-033.fq.gz	-
SRR16232377	SRP340375	new	PRJNA769076	SAMN22089841	HRS-1704-CM-037	CM-037	Bathymodiolus childressi	RAD-seq of Bathymodiolus	RAD-seq	GENOMIC	Restriction Digest	single	Illumina	Illumina HiSeq 4000	Restriction site enzyme pstI used on gDNA	fastq	HRS-1704-CM-037.fq.gz	-

Accession	Study	Object Status	Bioproject Accession	Biosample Accession	Sample Name	Library ID	Species	Title	Library Strategy	Library Source	Library Selection	Library Layout	Platform	Instrument Model	Design Description	Filetype	Filename	Filename2
SRR16232376	SRP340375	new	PRJNA769076	SAMN22089842	HRS-1704-CM-039	CM-039	Bathymodiolus childressi	RAD-seq of Bathymodiolus	RAD-seq	GENOMIC	Restriction Digest	single	Illumina	Illumina HiSeq 4000	Restriction site enzyme pstI used on gDNA	fastq	HRS-1704-CM-039.fq.gz	-
SRR16232375	SRP340375	new	PRJNA769076	SAMN22089843	HRS-1704-CM-041	CM-041	Bathymodiolus childressi	RAD-seq of Bathymodiolus	RAD-seq	GENOMIC	Restriction Digest	single	Illumina	Illumina HiSeq 4000	Restriction site enzyme pstI used on gDNA	fastq	HRS-1704-CM-041.fq.gz	-
SRR16232374	SRP340375	new	PRJNA769076	SAMN22089844	HRS-1704-CM-043	CM-043	Bathymodiolus childressi	RAD-seq of Bathymodiolus	RAD-seq	GENOMIC	Restriction Digest	single	Illumina	Illumina HiSeq 4000	Restriction site enzyme pstI used on gDNA	fastq	HRS-1704-CM-043.fq.gz	-
SRR16232373	SRP340375	new	PRJNA769076	SAMN22089845	HRS-1704-CM-045	CM-045	Bathymodiolus childressi	RAD-seq of Bathymodiolus	RAD-seq	GENOMIC	Restriction Digest	single	Illumina	Illumina HiSeq 4000	Restriction site enzyme pstI used on gDNA	fastq	HRS-1704-CM-045.fq.gz	-
SRR16232372	SRP340375	new	PRJNA769076	SAMN22089846	HRS-1704-CM-047	CM-047	Bathymodiolus childressi	RAD-seq of Bathymodiolus	RAD-seq	GENOMIC	Restriction Digest	single	Illumina	Illumina HiSeq 4000	Restriction site enzyme pstI used on gDNA	fastq	HRS-1704-CM-047.fq.gz	-
SRR16232371	SRP340375	new	PRJNA769076	SAMN22089847	HRS-1704-CM-049	CM-049	Bathymodiolus childressi	RAD-seq of Bathymodiolus	RAD-seq	GENOMIC	Restriction Digest	single	Illumina	Illumina HiSeq 4000	Restriction site enzyme pstI used on gDNA	fastq	HRS-1704-CM-049.fq.gz	-
SRR16232370	SRP340375	new	PRJNA769076	SAMN22089848	HRS-1704-CM-051	CM-051	Bathymodiolus childressi	RAD-seq of Bathymodiolus	RAD-seq	GENOMIC	Restriction Digest	single	Illumina	Illumina HiSeq 4000	Restriction site enzyme pstI used on gDNA	fastq	HRS-1704-CM-051.fq.gz	-

Accession	Study	Object Status	Bioproject Accession	Biosample Accession	Sample Name	Library ID	Species	Title	Library Strategy	Library Source	Library Selection	Library Layout	Platform	Instrument Model	Design Description	Filetype	Filename	Filename2
SRR16232369	SRP340375	new	PRJNA769076	SAMN22089849	HRS-1704-CM-055	CM-055	Bathymodiolus childressi	RAD-seq of Bathymodiolus	RAD-seq	GENOMIC	Restriction Digest	single	Illumina	Illumina HiSeq 4000	Restriction site enzyme pstI used on gDNA	fastq	HRS-1704-CM-055.fq.gz	-
SRR16232367	SRP340375	new	PRJNA769076	SAMN22089850	HRS-1704-CM-058	CM-058	Bathymodiolus childressi	RAD-seq of Bathymodiolus	RAD-seq	GENOMIC	Restriction Digest	single	Illumina	Illumina HiSeq 4000	Restriction site enzyme pstI used on gDNA	fastq	HRS-1704-CM-058.fq.gz	-
SRR16232366	SRP340375	new	PRJNA769076	SAMN22089851	HRS-1704-CM-061	CM-061	Bathymodiolus childressi	RAD-seq of Bathymodiolus	RAD-seq	GENOMIC	Restriction Digest	single	Illumina	Illumina HiSeq 4000	Restriction site enzyme pstI used on gDNA	fastq	HRS-1704-CM-061.fq.gz	-
SRR16232365	SRP340375	new	PRJNA769076	SAMN22089852	HRS-1704-CM-063	CM-063	Bathymodiolus childressi	RAD-seq of Bathymodiolus	RAD-seq	GENOMIC	Restriction Digest	single	Illumina	Illumina HiSeq 4000	Restriction site enzyme pstI used on gDNA	fastq	HRS-1704-CM-063.fq.gz	-
SRR16232364	SRP340375	new	PRJNA769076	SAMN22089853	HRS-1704-CM-067	CM-067	Bathymodiolus childressi	RAD-seq of Bathymodiolus	RAD-seq	GENOMIC	Restriction Digest	single	Illumina	Illumina HiSeq 4000	Restriction site enzyme pstI used on gDNA	fastq	HRS-1704-CM-067.fq.gz	-
SRR16232363	SRP340375	new	PRJNA769076	SAMN22089854	HRS-1704-CM-069	CM-069	Bathymodiolus childressi	RAD-seq of Bathymodiolus	RAD-seq	GENOMIC	Restriction Digest	single	Illumina	Illumina HiSeq 4000	Restriction site enzyme pstI used on gDNA	fastq	HRS-1704-CM-069.fq.gz	-
SRR16232362	SRP340375	new	PRJNA769076	SAMN22089855	MAS283	MAS283	Bathymodiolus childressi	RAD-seq of Bathymodiolus	RAD-seq	GENOMIC	Restriction Digest	single	Illumina	Illumina HiSeq 4000	Restriction site enzyme pstI used on gDNA	fastq	MAS283.fq.gz	-

Accession	Study	Object Status	Bioproject Accession	Biosample Accession	Sample Name	Library ID	Species	Title	Library Strategy	Library Source	Library Selection	Library Layout	Platform	Instrument Model	Design Description	Filetype	Filename	Filename2
SRR16232361	SRP340375	new	PRJNA769076	SAMN22089856	MAS284	MAS284	Bathymodiolus childressi	RAD-seq of Bathymodiolus	RAD-seq	GENOMIC	Restriction Digest	single	Illumina	Illumina HiSeq 4000	Restriction site enzyme pstI used on gDNA	fastq	MAS284.fq.gz	-
SRR16232360	SRP340375	new	PRJNA769076	SAMN22089857	MAS285	MAS285	Bathymodiolus childressi	RAD-seq of Bathymodiolus	RAD-seq	GENOMIC	Restriction Digest	single	Illumina	Illumina HiSeq 4000	Restriction site enzyme pstI used on gDNA	fastq	MAS285.fq.gz	-
SRR16232359	SRP340375	new	PRJNA769076	SAMN22089858	MAS286	MAS286	Bathymodiolus childressi	RAD-seq of Bathymodiolus	RAD-seq	GENOMIC	Restriction Digest	single	Illumina	Illumina HiSeq 4000	Restriction site enzyme pstI used on gDNA	fastq	MAS286.fq.gz	-
SRR16232358	SRP340375	new	PRJNA769076	SAMN22089859	MAS288	MAS288	Bathymodiolus childressi	RAD-seq of Bathymodiolus	RAD-seq	GENOMIC	Restriction Digest	single	Illumina	Illumina HiSeq 4000	Restriction site enzyme pstI used on gDNA	fastq	MAS288.fq.gz	-
SRR16232356	SRP340375	new	PRJNA769076	SAMN22089860	MAS289	MAS289	Bathymodiolus childressi	RAD-seq of Bathymodiolus	RAD-seq	GENOMIC	Restriction Digest	single	Illumina	Illumina HiSeq 4000	Restriction site enzyme pstI used on gDNA	fastq	MAS289.fq.gz	-
SRR16232355	SRP340375	new	PRJNA769076	SAMN22089861	MAS290	MAS290	Bathymodiolus childressi	RAD-seq of Bathymodiolus	RAD-seq	GENOMIC	Restriction Digest	single	Illumina	Illumina HiSeq 4000	Restriction site enzyme pstI used on gDNA	fastq	MAS290.fq.gz	-
SRR16232354	SRP340375	new	PRJNA769076	SAMN22089862	MAS291	MAS291	Bathymodiolus childressi	RAD-seq of Bathymodiolus	RAD-seq	GENOMIC	Restriction Digest	single	Illumina	Illumina HiSeq 4000	Restriction site enzyme pstI used on gDNA	fastq	MAS291.fq.gz	-

Accession	Study	Object Status	Bioproject Accession	Biosample Accession	Sample Name	Library ID	Species	Title	Library Strategy	Library Source	Library Selection	Library Layout	Platform	Instrument Model	Design Description	Filetype	Filename	Filename2
SRR16232353	SRP340375	new	PRJNA769076	SAMN22089863	MAS292	MAS292	Bathymodiolus childressi	RAD-seq of Bathymodiolus	RAD-seq	GENOMIC	Restriction Digest	single	Illumina	Illumina HiSeq 4000	Restriction site enzyme pstI used on gDNA	fastq	MAS292.fq.gz	-
SRR16232352	SRP340375	new	PRJNA769076	SAMN22089864	MAS293	MAS293	Bathymodiolus childressi	RAD-seq of Bathymodiolus	RAD-seq	GENOMIC	Restriction Digest	single	Illumina	Illumina HiSeq 4000	Restriction site enzyme pstI used on gDNA	fastq	MAS293.fq.gz	-
SRR16232528	SRP340375	new	PRJNA769076	SAMN22089865	MAS295	MAS295	Bathymodiolus childressi	RAD-seq of Bathymodiolus	RAD-seq	GENOMIC	Restriction Digest	single	Illumina	Illumina HiSeq 4000	Restriction site enzyme pstI used on gDNA	fastq	MAS295.fq.gz	-
SRR16232527	SRP340375	new	PRJNA769076	SAMN22089866	MAS297	MAS297	Bathymodiolus childressi	RAD-seq of Bathymodiolus	RAD-seq	GENOMIC	Restriction Digest	single	Illumina	Illumina HiSeq 4000	Restriction site enzyme pstI used on gDNA	fastq	MAS297.fq.gz	-
SRR16232526	SRP340375	new	PRJNA769076	SAMN22089867	MAS298	MAS298	Bathymodiolus childressi	RAD-seq of Bathymodiolus	RAD-seq	GENOMIC	Restriction Digest	single	Illumina	Illumina HiSeq 4000	Restriction site enzyme pstI used on gDNA	fastq	MAS298.fq.gz	-
SRR16232525	SRP340375	new	PRJNA769076	SAMN22089868	MAS299	MAS299	Bathymodiolus childressi	RAD-seq of Bathymodiolus	RAD-seq	GENOMIC	Restriction Digest	single	Illumina	Illumina HiSeq 4000	Restriction site enzyme pstI used on gDNA	fastq	MAS299.fq.gz	-
SRR16232524	SRP340375	new	PRJNA769076	SAMN22089869	MAS306	MAS306	Bathymodiolus childressi	RAD-seq of Bathymodiolus	RAD-seq	GENOMIC	Restriction Digest	single	Illumina	Illumina HiSeq 4000	Restriction site enzyme pstI used on gDNA	fastq	MAS306.fq.gz	-

Accession	Study	Object Status	Bioproject Accession	Biosample Accession	Sample Name	Library ID	Species	Title	Library Strategy	Library Source	Library Selection	Library Layout	Platform	Instrument Model	Design Description	Filetype	Filename	Filename2
SRR16232522	SRP340375	new	PRJNA769076	SAMN22089870	MAS310	MAS310	Bathymodiolus childressi	RAD-seq of Bathymodiolus	RAD-seq	GENOMIC	Restriction Digest	single	Illumina	Illumina HiSeq 4000	Restriction site enzyme pstI used on gDNA	fastq	MAS310.fq.gz	-
SRR16232521	SRP340375	new	PRJNA769076	SAMN22089871	MAS311	MAS311	Bathymodiolus childressi	RAD-seq of Bathymodiolus	RAD-seq	GENOMIC	Restriction Digest	single	Illumina	Illumina HiSeq 4000	Restriction site enzyme pstI used on gDNA	fastq	MAS311.fq.gz	-
SRR16232520	SRP340375	new	PRJNA769076	SAMN22089872	MAS313	MAS313	Bathymodiolus childressi	RAD-seq of Bathymodiolus	RAD-seq	GENOMIC	Restriction Digest	single	Illumina	Illumina HiSeq 4000	Restriction site enzyme pstI used on gDNA	fastq	MAS313.fq.gz	-
SRR16232519	SRP340375	new	PRJNA769076	SAMN22089873	MAS314	MAS314	Bathymodiolus childressi	RAD-seq of Bathymodiolus	RAD-seq	GENOMIC	Restriction Digest	single	Illumina	Illumina HiSeq 4000	Restriction site enzyme pstI used on gDNA	fastq	MAS314.fq.gz	-
SRR16232518	SRP340375	new	PRJNA769076	SAMN22089874	MAS320	MAS320	Bathymodiolus childressi	RAD-seq of Bathymodiolus	RAD-seq	GENOMIC	Restriction Digest	single	Illumina	Illumina HiSeq 4000	Restriction site enzyme pstI used on gDNA	fastq	MAS320.fq.gz	-
SRR16232517	SRP340375	new	PRJNA769076	SAMN22089875	MAS321	MAS321	Bathymodiolus childressi	RAD-seq of Bathymodiolus	RAD-seq	GENOMIC	Restriction Digest	single	Illumina	Illumina HiSeq 4000	Restriction site enzyme pstI used on gDNA	fastq	MAS321.fq.gz	-
SRR16232516	SRP340375	new	PRJNA769076	SAMN22089876	MAS322	MAS322	Bathymodiolus childressi	RAD-seq of Bathymodiolus	RAD-seq	GENOMIC	Restriction Digest	single	Illumina	Illumina HiSeq 4000	Restriction site enzyme pstI used on gDNA	fastq	MAS322.fq.gz	-

Accession	Study	Object Status	Bioproject Accession	Biosample Accession	Sample Name	Library ID	Species	Title	Library Strategy	Library Source	Library Selection	Library Layout	Platform	Instrument Model	Design Description	Filetype	Filename	Filename2
SRR16232515	SRP340375	new	PRJNA769076	SAMN22089877	MAS323	MAS323	Bathymodiolus childressi	RAD-seq of Bathymodiolus	RAD-seq	GENOMIC	Restriction Digest	single	Illumina	Illumina HiSeq 4000	Restriction site enzyme pstI used on gDNA	fastq	MAS323.fq.gz	-
SRR16232514	SRP340375	new	PRJNA769076	SAMN22089878	MAS326	MAS326	Bathymodiolus childressi	RAD-seq of Bathymodiolus	RAD-seq	GENOMIC	Restriction Digest	single	Illumina	Illumina HiSeq 4000	Restriction site enzyme pstI used on gDNA	fastq	MAS326.fq.gz	-
SRR16232513	SRP340375	new	PRJNA769076	SAMN22089879	MAS327	MAS327	Bathymodiolus childressi	RAD-seq of Bathymodiolus	RAD-seq	GENOMIC	Restriction Digest	single	Illumina	Illumina HiSeq 4000	Restriction site enzyme pstI used on gDNA	fastq	MAS327.fq.gz	-
SRR16232511	SRP340375	new	PRJNA769076	SAMN22089880	MAS338	MAS338	Bathymodiolus childressi	RAD-seq of Bathymodiolus	RAD-seq	GENOMIC	Restriction Digest	single	Illumina	Illumina HiSeq 4000	Restriction site enzyme pstI used on gDNA	fastq	MAS338.fq.gz	-
SRR16232510	SRP340375	new	PRJNA769076	SAMN22089881	MAS339	MAS339	Bathymodiolus childressi	RAD-seq of Bathymodiolus	RAD-seq	GENOMIC	Restriction Digest	single	Illumina	Illumina HiSeq 4000	Restriction site enzyme pstI used on gDNA	fastq	MAS339.fq.gz	-
SRR16232509	SRP340375	new	PRJNA769076	SAMN22089882	MAS340	MAS340	Bathymodiolus childressi	RAD-seq of Bathymodiolus	RAD-seq	GENOMIC	Restriction Digest	single	Illumina	Illumina HiSeq 4000	Restriction site enzyme pstI used on gDNA	fastq	MAS340.fq.gz	-
SRR16232508	SRP340375	new	PRJNA769076	SAMN22089883	MAS341	MAS341	Bathymodiolus childressi	RAD-seq of Bathymodiolus	RAD-seq	GENOMIC	Restriction Digest	single	Illumina	Illumina HiSeq 4000	Restriction site enzyme pstI used on gDNA	fastq	MAS341.fq.gz	-

Accession	Study	Object Status	Bioproject Accession	Biosample Accession	Sample Name	Library ID	Species	Title	Library Strategy	Library Source	Library Selection	Library Layout	Platform	Instrument Model	Design Description	Filetype	Filename	Filename2
SRR16232507	SRP340375	new	PRJNA769076	SAMN22089884	MAS343	MAS343	Bathymodiolus childressi	RAD-seq of Bathymodiolus	RAD-seq	GENOMIC	Restriction Digest	single	Illumina	Illumina HiSeq 4000	Restriction site enzyme pstI used on gDNA	fastq	MAS343.fq.gz	-
SRR16232506	SRP340375	new	PRJNA769076	SAMN22089885	MAS537	MAS537	Bathymodiolus childressi	RAD-seq of Bathymodiolus	RAD-seq	GENOMIC	Restriction Digest	single	Illumina	Illumina HiSeq 4000	Restriction site enzyme pstI used on gDNA	fastq	MAS537.fq.gz	-
SRR16232505	SRP340375	new	PRJNA769076	SAMN22089886	MAS539	MAS539	Bathymodiolus childressi	RAD-seq of Bathymodiolus	RAD-seq	GENOMIC	Restriction Digest	single	Illumina	Illumina HiSeq 4000	Restriction site enzyme pstI used on gDNA	fastq	MAS539.fq.gz	-
SRR16232504	SRP340375	new	PRJNA769076	SAMN22089887	MAS540	MAS540	Bathymodiolus childressi	RAD-seq of Bathymodiolus	RAD-seq	GENOMIC	Restriction Digest	single	Illumina	Illumina HiSeq 4000	Restriction site enzyme pstI used on gDNA	fastq	MAS540.fq.gz	-
SRR16232503	SRP340375	new	PRJNA769076	SAMN22089888	MAS541	MAS541	Bathymodiolus childressi	RAD-seq of Bathymodiolus	RAD-seq	GENOMIC	Restriction Digest	single	Illumina	Illumina HiSeq 4000	Restriction site enzyme pstI used on gDNA	fastq	MAS541.fq.gz	-
SRR16232502	SRP340375	new	PRJNA769076	SAMN22089889	MAS542	MAS542	Bathymodiolus childressi	RAD-seq of Bathymodiolus	RAD-seq	GENOMIC	Restriction Digest	single	Illumina	Illumina HiSeq 4000	Restriction site enzyme pstI used on gDNA	fastq	MAS542.fq.gz	-
SRR16232500	SRP340375	new	PRJNA769076	SAMN22089890	MAS543	MAS543	Bathymodiolus childressi	RAD-seq of Bathymodiolus	RAD-seq	GENOMIC	Restriction Digest	single	Illumina	Illumina HiSeq 4000	Restriction site enzyme pstI used on gDNA	fastq	MAS543.fq.gz	-

Accession	Study	Object Status	Bioproject Accession	Biosample Accession	Sample Name	Library ID	Species	Title	Library Strategy	Library Source	Library Selection	Library Layout	Platform	Instrument Model	Design Description	Filetype	Filename	Filename2
SRR16232499	SRP340375	new	PRJNA769076	SAMN22089891	MAS544	MAS544	Bathymodiolus childressi	RAD-seq of Bathymodiolus	RAD-seq	GENOMIC	Restriction Digest	single	Illumina	Illumina HiSeq 4000	Restriction site enzyme pstI used on gDNA	fastq	MAS544.fq.gz	-
SRR16232498	SRP340375	new	PRJNA769076	SAMN22089892	MAS545	MAS545	Bathymodiolus childressi	RAD-seq of Bathymodiolus	RAD-seq	GENOMIC	Restriction Digest	single	Illumina	Illumina HiSeq 4000	Restriction site enzyme pstI used on gDNA	fastq	MAS545.fq.gz	-
SRR16232497	SRP340375	new	PRJNA769076	SAMN22089893	MAS547	MAS547	Bathymodiolus childressi	RAD-seq of Bathymodiolus	RAD-seq	GENOMIC	Restriction Digest	single	Illumina	Illumina HiSeq 4000	Restriction site enzyme pstI used on gDNA	fastq	MAS547.fq.gz	-
SRR16232496	SRP340375	new	PRJNA769076	SAMN22089894	MAS548	MAS548	Bathymodiolus childressi	RAD-seq of Bathymodiolus	RAD-seq	GENOMIC	Restriction Digest	single	Illumina	Illumina HiSeq 4000	Restriction site enzyme pstI used on gDNA	fastq	MAS548.fq.gz	-
SRR16232495	SRP340375	new	PRJNA769076	SAMN22089895	MAS549	MAS549	Bathymodiolus childressi	RAD-seq of Bathymodiolus	RAD-seq	GENOMIC	Restriction Digest	single	Illumina	Illumina HiSeq 4000	Restriction site enzyme pstI used on gDNA	fastq	MAS549.fq.gz	-
SRR16232494	SRP340375	new	PRJNA769076	SAMN22089896	MAS550	MAS550	Bathymodiolus childressi	RAD-seq of Bathymodiolus	RAD-seq	GENOMIC	Restriction Digest	single	Illumina	Illumina HiSeq 4000	Restriction site enzyme pstI used on gDNA	fastq	MAS550.fq.gz	-
SRR16232493	SRP340375	new	PRJNA769076	SAMN22089897	MAS551	MAS551	Bathymodiolus childressi	RAD-seq of Bathymodiolus	RAD-seq	GENOMIC	Restriction Digest	single	Illumina	Illumina HiSeq 4000	Restriction site enzyme pstI used on gDNA	fastq	MAS551.fq.gz	-

Accession	Study	Object Status	Bioproject Accession	Biosample Accession	Sample Name	Library ID	Species	Title	Library Strategy	Library Source	Library Selection	Library Layout	Platform	Instrument Model	Design Description	Filetype	Filename	Filename2
SRR16232492	SRP340375	new	PRJNA769076	SAMN22089898	MAS552	MAS552	Bathymodiolus childressi	RAD-seq of Bathymodiolus	RAD-seq	GENOMIC	Restriction Digest	single	Illumina	Illumina HiSeq 4000	Restriction site enzyme pstI used on gDNA	fastq	MAS552.fq.gz	-
SRR16232491	SRP340375	new	PRJNA769076	SAMN22089899	MAS553	MAS553	Bathymodiolus childressi	RAD-seq of Bathymodiolus	RAD-seq	GENOMIC	Restriction Digest	single	Illumina	Illumina HiSeq 4000	Restriction site enzyme pstI used on gDNA	fastq	MAS553.fq.gz	-
SRR16232489	SRP340375	new	PRJNA769076	SAMN22089900	MAS554	MAS554	Bathymodiolus childressi	RAD-seq of Bathymodiolus	RAD-seq	GENOMIC	Restriction Digest	single	Illumina	Illumina HiSeq 4000	Restriction site enzyme pstI used on gDNA	fastq	MAS554.fq.gz	-
SRR16232488	SRP340375	new	PRJNA769076	SAMN22089901	MAS555	MAS555	Bathymodiolus childressi	RAD-seq of Bathymodiolus	RAD-seq	GENOMIC	Restriction Digest	single	Illumina	Illumina HiSeq 4000	Restriction site enzyme pstI used on gDNA	fastq	MAS555.fq.gz	-
SRR16232487	SRP340375	new	PRJNA769076	SAMN22089902	MAS556	MAS556	Bathymodiolus childressi	RAD-seq of Bathymodiolus	RAD-seq	GENOMIC	Restriction Digest	single	Illumina	Illumina HiSeq 4000	Restriction site enzyme pstI used on gDNA	fastq	MAS556.fq.gz	-
SRR16232486	SRP340375	new	PRJNA769076	SAMN22089903	MAS557	MAS557	Bathymodiolus childressi	RAD-seq of Bathymodiolus	RAD-seq	GENOMIC	Restriction Digest	single	Illumina	Illumina HiSeq 4000	Restriction site enzyme pstI used on gDNA	fastq	MAS557.fq.gz	-
SRR16232485	SRP340375	new	PRJNA769076	SAMN22089904	MAS561	MAS561	Bathymodiolus childressi	RAD-seq of Bathymodiolus	RAD-seq	GENOMIC	Restriction Digest	single	Illumina	Illumina HiSeq 4000	Restriction site enzyme pstI used on gDNA	fastq	MAS561.fq.gz	-

Accession	Study	Object Status	Bioproject Accession	Biosample Accession	Sample Name	Library ID	Species	Title	Library Strategy	Library Source	Library Selection	Library Layout	Platform	Instrument Model	Design Description	Filetype	Filename	Filename2
SRR16232484	SRP340375	new	PRJNA769076	SAMN22089905	MASm32	MASm32	Bathymodiolus childressi	RAD-seq of Bathymodiolus	RAD-seq	GENOMIC	Restriction Digest	single	Illumina	Illumina HiSeq 4000	Restriction site enzyme pstI used on gDNA	fastq	MASm32.fq.gz	-
SRR16232483	SRP340375	new	PRJNA769076	SAMN22089906	MASm36	MASm36	Bathymodiolus heckerae	RAD-seq of Bathymodiolus	RAD-seq	GENOMIC	Restriction Digest	single	Illumina	Illumina HiSeq 4000	Restriction site enzyme pstI used on gDNA	fastq	MASm36.fq.gz	-

Data Submission to NOAA—Confirmation Letter

UNITED STATES DEPARTMENT OF COMMERCE
National Oceanic and Atmospheric Administration
OCEANIC AND ATMOSPHERIC RESEARCH
Office of Ocean Exploration and Research
Silver Spring, MD 20910

August 25, 2021

Dr. Gary Wolff
14391 South Dowling Road
College Station, TX 77845

Dear Dr. Wolff,

I have confirmed with NOAA's National Centers for Environmental Information (NCEI) that all project data for DEEP SEARCH have been received. The following data have been received and either have been or will be archived:

PC1705:
- Multibeam, Side Scan Sonar, Configurations
- Docs, Nav, Photos, Plots, Subsea accom, Subsea iridium, Topside comms

AT41:
- Gravimeter, Multibeam, water column, subbottom
- ADCP, Alvin data, CTD, Underway data
- Video

BMCC18:
- CTD, event and sample logs, landers, piston core data

RB1903:
- Multibeam, subbottom, scene image products
- ADCP, CTD, XBT, Jason data, lander data, PODs, PPI data, SCS data, system volume info, Tif grabs, vehicle data,
- Documents, Images, Highlights 1080, video

NF1909:
- EK60 screen grabs, multibeam
- ADCP, CTD, lander data, PODs, SCS data, TGS data
- Documents, Bio lab photos, photos, video

As the NOAA project manager for this effort, I will continue to work with NCEI to ensure that the above data are appropriately archived, and no further action is required from TDI Brooks International, Inc. at this time.

Sincerely,

Caitlin Adams
Deputy Chief (Acting), Science and Technology Division
NOAA Ocean Exploration

Appendix B. Publications and Conference Presentations

Abstracts

Deep SEARCH_Abstracts - Quattrini

Quattrini, A.M., McIver, T.C. 2019 Functional and Phylogenetic Diversity of Fishes in Deep-Sea Coral Habitats along the southeastern U.S. coast. International Symposium of Deep-Sea Corals, poster.

Reef fish communities characteristic of deep-sea coral habitats at depths of ~400–800 m have been well documented off the southeastern U.S. coast in the western North Atlantic. This study, a component of Deep SEARCH, builds on a decade of previous work in the region to investigate both functional and phylogenetic diversity of fish assemblages occupying *Lophelia pertusa* habitats. These biodiversity measures can be useful in guiding conservation priorities, while providing a more in-depth understanding of ecosystem function. To estimate functional diversity, we compiled traits for all fish species documented from recently collected ROV video data (2017–2018) and previously published ROV and otter trawl data (2000–2014). Traits chosen for analyses included diverse attributes of fish ecology, such as trophic breadth, trophic group, water-column position, and maximum size, which are known to influence fish functional roles. To examine whether unique or endemic lineages were present at deep-coral habitats, we calculated Faith's Phylogenetic Diversity metric using the ray-finned fish tree of life in the R package fishtree. Diversity estimates were calculated for fish assemblages occupying both *L. pertusa* habitats and off-reef habitats to determine whether deep-sea coral bioherms exhibit higher functional and/or phylogenetic diversity compared to off-reef habitats. Abundant fish species representing 84% of all fishes observed at deep-sea coral habitats were *Laemonema melanurum*, *Nezumia* spp. *Hoplostethus mediterraneus*, *Hoplostethus occidentalis*, *Synaphobranchus* sp. and *Eptatretus lopheliae*. This study is ongoing and future work will include comparing results from deep-sea coral habitats to other rugged, deep-sea habitats (cold seeps, coral gardens, submarine canyons) in the region.

Saso E, Quattrini AM, Auscavitch SR, Allcock AL, Cordes EE, McFadden, CS. 2021. Biogeography of deep-sea octocoral communities in the North Atlantic. 16th.

Deep-Sea Biology Symposium, poster.

The deep ocean is magnificent in scale, yet our understanding of deep-sea faunal biogeography is constrained by scarce observations skewed towards megafaunal communities. Deep-sea octocorals (Anthozoa) are globally distributed across an expansive bathymetric range, where they inhabit seamounts, submarine canyons and hardbottom reefs. These long-lived and phenotypically diverse ecosystem engineers build complex heterogenous structures hosting diverse faunal assemblages and engage in symbioses with fish and invertebrate species. Despite their importance to ecosystem functioning, octocorals have been the focus of relatively few biogeographical studies. While technological advances have facilitated sampling of deep benthos, questions of octocoral biogeography and species endemicity are complicated still by cryptic species and unresolved taxonomy. Recent studies have found species distributions to be more strongly influenced by depth and water mass than geographic distance, yet this pattern has not been corroborated for octocorals throughout the deep North Atlantic nor across ocean basins to date. Here, we determine biogeographic patterns of phylogenetic species diversity and composition across spatial scales using environmental and species presence data from several expeditions in the western Atlantic off the U.S. eastern seaboard, the eastern Atlantic off Ireland, the GOM and the Caribbean Sea. Octocoral specimens were collected during ROV and *Alvin* dives from 312 to 2,800 m water depth. *28S* and mt*MutS* genes were sequenced to delimit molecular operational taxonomic units and determine species relatedness in phylogenetic diversity analyses. We investigated the roles of specific

depth-related abiotic variables (i.e., water mass, temperature) and habitat features on distribution and community composition within a phylogenetic framework. The slow-growing and highly adapted nature of octocorals makes them extremely susceptible to disturbances and changing ocean conditions. Awareness of the environmental gradients impacting connectivity is key to informing successful management strategies to conserve these foundation species across the North Atlantic Ocean basin.

Saso E, Quattrini AM, Auscavitch SR, Allcock AL, Cordes EE, McFadden, CS. 2021. Biogeography of deep-sea octocoral communities in the North Atlantic. ASLO Aquatic Sciences, poster.

The deep ocean is magnificent in scale, yet our understanding of deep-sea faunal biogeography is constrained by scarce observations skewed towards megafaunal communities. Deep-sea octocorals (Anthozoa) are globally distributed across an expansive bathymetric range, where they inhabit seamounts, submarine canyons and hardbottom reefs. These long-lived and phenotypically diverse ecosystem engineers build complex heterogenous structures hosting diverse faunal assemblages and engage in symbioses with fish and invertebrate species. Despite their importance to ecosystem functioning, octocorals have been the focus of relatively few biogeographical studies. While technological advances have facilitated sampling of deep benthos, questions of octocoral biogeography and species endemicity are complicated still by cryptic species and unresolved taxonomy. Recent studies have found species distributions to be more strongly influenced by depth and water mass than geographic distance, yet this pattern has not been corroborated for octocorals throughout the deep North Atlantic nor across ocean basins to date. Here, we determine biogeographic patterns of phylogenetic species diversity and composition across spatial scales using environmental and species presence data from several expeditions in the western Atlantic off the U.S. eastern seaboard, the eastern Atlantic off Ireland, the GOM and the Caribbean Sea. Octocoral specimens were collected during ROV and *Alvin* dives from 312 to 2,800 m water depth. *28S* and mt*MutS* genes were sequenced to delimit molecular operational taxonomic units and determine species relatedness in phylogenetic diversity analyses. We investigated the roles of specific depth-related abiotic variables (i.e., water mass, temperature) and habitat features on distribution and community composition within a phylogenetic framework. The slow-growing and highly adapted nature of octocorals makes them extremely susceptible to disturbances and changing ocean conditions. Awareness of the environmental gradients impacting connectivity is key to informing successful management strategies to conserve these foundation species across the North Atlantic Ocean basin.

DM. DeLeo, C. Morrison, M. Sei, V. Salamone, A.Demopoulos and A.M. Quattrini

Genetic diversity and connectivity of chemosynthetic seep mussels (*Bathymodiolus* spp.) from the U.S. Mid-Atlantic margin. 16th Deep-Sea Biology Symposium, Oral.

Deep-sea mussels in the genus *Bathymodiolus* have unique adaptations to colonize hydrothermal vent and cold-seep environments throughout the world's oceans. These invertebrates function as important ecosystem engineers, creating heterogenous habitat and promoting biodiversity in the deep sea. Despite their ecological significance, efforts to assess the diversity and connectivity of this group are extremely limited. Here, we present the first genomic-scale diversity assessments of the recently discovered bathymodiolin cold-seep communities along the U.S. Mid-Atlantic margin, dominated by *Bathymodiolus childressi* as well as known communities of *B. heckerae*. *Bathymodiolus childressi* mussels were collected at various depths from three seep sites- Norfolk Canyon Seep, Baltimore Canyon Seep, and Chincoteague Seep. The vast majority of *B. heckerae* samples were collected from a deeper site at Blake Ridge. DNA was extracted and sequenced using a RAD-seq approach from a total of 177 bathymodiolins with confirmed species identities as either *B. childressi* (n=81) or *B. heckerae* (n=96). RAD-seq data were assembled discretely for each species with iPYRAD using a reference genome and analyzed to examine genetic diversity and population structure within and between seep sites. Assessments of genetic differentiation using SNP data revealed high gene flow and minimal diversification among individuals, as well as high inbreeding for both species. No evidence was found for diversification with depth in *B.*

childressi likely due to their life histories, including high dispersal capabilities. Kinship analyses indicated a high degree of relatedness among individuals indicative of local recruitment, though our data suggest shallower communities serve as source populations for deeper seep sites. We also discovered loci under selection in *B. childressi* (400–2,200 m) and *B. heckerae* (2200–3,300 m) that elucidate depth-related adaptations, potentially lending to the diversification of *Bathymodiolus* mussels despite the high gene flow and widespread dispersal capabilities of this group.

Abstract OS2020 - Brooke

Title: How will future climate changes influence deep sea coral life histories?

Author: Sandra Brooke, Florida State University

2020 Ocean Sciences Session: https://agu.confex.com/agu/osm20/prelim.cgi/Session/85804

In the western Atlantic, several species of broadcast-spawning, deep-sea coral show synchrony in their reproductive cycles, with more advanced maturity in the fall than the spring. Off New Zealand, gametogenesis of three species of stony corals (*S. variabilis, Enallopsammia rostrata, Goniocorella dumosa*) was also synchronized among species, with spawning occurring in April–May; however, *S. variabilis* from the western Atlantic were immature in May. Synchrony in the timing of reproductive cycles within a location is evidence that common factors are influencing multiple species and location-specific differences in spawning of con-specifics allows identification of those drivers. Understanding reproductive strategy and timing of spawning in deep-sea corals can inform studies of connectivity and community resilience, and also has management implications in areas where human activities may damage deep-sea coral habitats or negatively affect coral early life-history stages. One of the projected future changes in climate conditions will influence patterns of primary productivity and therefore food delivery to the deep seafloor. These changes may create mis-match between timing of food delivery to the seafloor and energetic needs for reproduction. This presentation will show evidence for spawning synchronicity across different deep-sea coral taxa in the western North Atlantic and discuss implications of projected future conditions in this region.

ISDSC Brooke Abstract 2

In situ growth rates of three scleractinians at an anamolous deep coral mound in the southeastern US.

Sandra Brooke (other authors TBD)

Deep-coral reefs in the southeastern USA are constructed primarily by *Lophelia pertusa*, with structural contributions by *Madrepora oculata*. *Enallopsammia profunda* is a less common reef-building species in this region, and is endemic to the western Atlantic. The average temperatures of the deep-coral reefs in this region ranges from ~6–8ºC. In August 2018, the Deep SEARCH project (funded by BOEM, NOAA and USGS) explored a series of mound features that were mapped earlier that year by the NOAA Ship *Okeanos Explorer*. These features were *Lophelia bioherms* in depths of ~850–690 m, with an unusually high percentage cover of live coral. The temperature and oxygen profiles at these sites were very different from most of the coral mounds in the region, with temperatures of ~5ºC at 800 m, with a rapid increase to 9-10ºC at ~ 750 m. The tops of the mounds were colonized by yellow, heavily calcified morphotypes of *Enallopsammia cf profunda* apparently thriving at 11ºC.

During the 2018 cruise, fragments of *Lophelia pertusa, Enallopsammia profund*a and *Madrepora oculata* were collected from the using the *Alvin* submersible, stained with calcein and redeployed the following

day at 695 m, close to the original collection site. These fragments were collected in April 2019 (9 months after deployment) and were assessed for survival and growth. Growth rates were measured using the calcein stain bands, and a novel 3D modeling technique was also applied to assess volumetric change in the fragments over time. Survival of all species was high but growth was lower than documented for these species elsewhere in the region and in the literature.

This presentation will discuss the observed growth rates in the context of the unusual environmental conditions at this newly explored deep-coral area.

Deep SEARCH Publications_Presentations - CMorrison

Publications:

Coykendall, D.K., Cornman, R.S., Prouty, N.G., Brooke, S., Demopoulos, A.W.J., and Morrison, C.L., 2019, Molecular characterization of *Bathymodiolus* mussels and gill symbionts associated with chemosynthetic habitats from the U.S. Atlantic margin: PLoS ONE, v. 14, no. 3, art. e0211616, https://doi.org/10.1371/journal.pone.0211616.

Goldsmith, D.B., Kellogg, C.A., Morrison, C.L., Gray, M.A., Stone, R.P., Waller, R.G., Brooke, S.D., Ross, S.W., 2018, Comparison of microbiomes of cold-water corals *Primnoa pacifica* and *Primnoa resedaeformis*, with possible link between microbiome and host genotype: Scientific Reports, 8:12383. doi:10.1038/s41598-018-30901-z

Quattrini, A.M., E. Rodríguez, B.C. Faircloth, P.F. Cowman, M.R. Brugler, G.A. Farfan, M.E. Hellberg, M.V. Kitahara, C.L. Morrison, D.A. Paz-Garcia, J.D. Reimer, and C.S. McFadden. 2020. Paleoclimate ocean conditions shaped the diversification of coral skeletal composition through deep time. Nature Ecology and Evolution, 4: 1531-1538. https://doi.org/10.1038/s41559-020-01291-1

Sautter, L.R.; C.L. Morrison; K. Cantwell; D. Sowers; E. Lobecker. 2019. Windows to the Deep 2018: Exploration of the Southeast US Continental Margin. In Raineault, N.A., and J. Flanders, eds. 2019. New Frontiers in ocean exploration: The E/V *Nautilus*, NOAA Ship *Okeanos Explorer*, and RV *Falkor* 2018 field season. Oceanography 32(1), supplement, 150 pp., https://doi.org/10.5670/oceanog.2019.supplement.01.

Cantwell, K., Sautter, L., Morrison, C., Sowers, D., Bowman, A. 2020. Cruise Report: EX-18-06, Windows to the Deep 2018 (ROV & Mapping). United States. National Oceanic and Atmospheric Administration. Office of Oceanic and Atmospheric Research; Office of Ocean Exploration and Research; https://doi.org/10.25923/50hx-3p68

Quattrini, A.M., Nizinski, M.S., Lunden, J.J., Mienis, F., Morrison, C.L., Sautter, L., Seim, H., Todd, R.E., Reed, J. Cold-water coral reefs of the Southeastern United States. Book chapter, in review

Presentations:

Coleman, H., Duncan, L., Morrison, C.L. Prioritizing deep-sea corals in the exploration and characterization of U.S. waters, abstract submitted to Ocean Sciences meeting 2022

The deep ocean contains some of the least understood ecosystems on earth. In an effort to improve our knowledge of the deep seafloor, sub-bottom, and water column, the U.S. government convened the National Ocean Mapping, Exploration, and Characterization (NOMEC) Council in June 2020. The NOMEC Council coordinates Federal agency policy and actions and supports collaboration with partners and stakeholders. Under the Council, the Interagency Working Group on Ocean Exploration and Characterization (IWG-OEC) facilitates cooperative deep-sea (>40 m) data collection with the potential

to satisfy many overlapping data needs. Activities prioritized by the IWG-OEC span exploratory initial assessments to comprehensive characterization in support of research, resource management, policy-making, and applied mission objectives. Deep-sea corals and sponges, often important hotspots of biodiversity and habitat for many fisheries species, will benefit greatly from these activities. Since they are easily damaged by certain fishing gears, describing deep-sea coral and sponge habitats is an important aspect of site characterization from a fishery management perspective. As such, the NOAA Fisheries' Deep Sea Coral Program played a significant role in drafting the benthic ecology component of an implementation plan for the NOMEC Strategy. The IWG-OEC Implementation Plan identifies thematic and geographic priorities for ocean exploration and characterization, as well as relevant data needs and challenges. Data collected to satisfy these priorities will inform ocean-based solutions to biodiversity loss and management of healthy and productive ecosystems, including deep-sea coral and sponge habitats. This presentation will describe the prioritization process and results, with emphasis on their relevance for corals and sponges, that sets the stage for unprecedented multi-sectoral collaborative exploration and characterization.

DeLeo, D.M., Morrison, C.L., Sei, M., Salamone, V., Demopoulos, A., Quattrini, A.M. Genetic diversity and connectivity of chemosynthetic cold seep mussels from the U.S. Mid-Atlantic margin. abstract submitted to Ocean Sciences meeting 2022

Several recently discovered cold-seep communities along the U.S. Atlantic margin are dominated by deep-sea mussels *Gigantidas childressi* and *B. heckerae* (subfamily Bathymodiolinae). These invertebrates function as important ecosystem engineers, creating heterogeneous habitat and promoting biodiversity in the deep sea. Despite their ecological significance, efforts to assess the diversity and connectivity of this group are extremely limited. Here, we present the first genomic-scale diversity assessments for U.S. Atlantic margin *Gigantidas childressi* and *B. heckerae* populations. DNA was extracted and sequenced using a RAD-seq approach from a total of 177 bathymodiolins. RAD-seq data were assembled discretely for each species with iPYRAD using a reference genome and analyzed to examine genetic diversity and population structure within and between seep sites. Assessments of genetic differentiation using SNP data revealed high gene flow among sites in *G. childressi* and no evidence was found for diversification with depth, likely due to their high dispersal capabilities. Kinship analyses indicated a high degree of relatedness among individuals indicative of local recruitment among and within sites, though our data suggest shallower and more northern sites serve as source populations for *G. childressi* occurring deeper. We also discovered loci under selection in *G. childressi* and *B. heckerae* that elucidate differences in developmental genes and depth-related and metabolic adaptations to chemosynthetic environments. To expand the geographic scope of connectivity assessments in bathymodiolins across the North Atlantic Ocean and improve predictions and decision making leading to wise resource management, samples are being analyzed in collaboration with researchers in the European Union's Horizon 2020 (ATLAS) campaign.

DeLeo, D.M., Morrison, C.L., Sei, M., Salamone, V., Demopoulos, A., Quattrini, A.M. Genetic diversity and connectivity of chemosynthetic cold seep mussels from the U.S. Mid-Atlantic margin. DSBS 2021.

Deep-sea mussels in the genus Bathymodiolus have unique adaptations to colonize hydrothermal vent and cold-seep environments throughout the world's oceans. These invertebrates function as important ecosystem engineers, creating heterogenous habitat and promoting biodiversity in the deep sea. Despite their ecological significance, efforts to assess the diversity and connectivity of this group are extremely limited. Here, we present the first genomic-scale diversity assessments of the recently discovered bathymodiolin cold-seep communities along the U.S. Mid-Atlantic margin, dominated by Bathymodiolus childressi as well as known communities of B. heckerae. Bathymodiolus. childressi mussels were collected at various depths from three seep sites- Norfolk Canyon Seep, Baltimore Canyon Seep and

Chincoteague Seep. The vast majority of B. heckerae samples were collected from a deeper site at Blake Ridge. DNA was extracted and sequenced using a RAD-seq approach from a total of 177 bathymodiolins with confirmed species identities as either B. childressi (n=81) or B. heckerae (n=96). RAD-seq data were assembled discretely for each species with iPYRAD using a reference genome and analyzed to examine genetic diversity and population structure within and between seep sites. Assessments of genetic differentiation using SNP data revealed high gene flow and minimal diversification among individuals, as well as high inbreeding for both species. No evidence was found for diversification with depth in B. childressi likely due to their life histories, including widespread dispersal capabilities. Kinship analyses indicated a high degree of relatedness among the samples indicative of local recruitment, though our data suggest shallower communities serve as source populations for deeper canyon sites. We also discovered loci under selection in B. childressi (400–2,200 m) and B. heckerae (2,200–3,300 m) that elucidate depth-related adaptations, potentially lending to the diversification of Bathymodiolus mussels despite the high gene flow and widespread dispersal capabilities of this group.

Weinnig, A.M., Morrison, C.L., Salamone, V., Aunins, A.W., Quattrini, A.M. Population genomic structure of cold-water corals found along the Southeastern U.S. continental margin. Abstract submitted to OSM 2022 meeting.

Cold-water corals are foundational to ecosystems found along various geologic formations, including banks, mounds, and canyons in the deep sea. Through continued deep-sea exploration along the southeastern coast of the U.S. in recent years, a broader range of cold-water coral habitats have been revealed. The connectivity and genetic structuring of populations throughout a region influence a species resilience and probability of recovery from anthropogenic impacts. By gaining a comprehensive understanding of population connectivity, more effective management may be prioritized. In an effort to assess the connectivity and population genetic structure of common cold-water corals species found along the southeastern coast of the U.S., we performed a target-capture genomic approach on members of the genus Plumarella (n=28) and RAD-seq on collections of Lophelia pertusa (n = 120) and Desmophyllum dianthus (n=68). These samples, collected over at 10-year period and a wide geographic area (waters off of Florida through the mid-Atlantic), will provide insight into the population structure of corals that generate mounds (L. pertusa), those that colonize L. pertusa skeleton and rocky reefs (Plumarella) and those found primarily along canyon walls (D. dianthus). The generation of SNP data from the RAD-seq approach will provide the opportunity to compare and contrast previously collected microsatellite data for L. pertusa to investigate whether both data sets generate similar patterns of limited connectivity among the southeastern U.S. populations. To broaden the geographic scope of connectivity analysis and gain a more comprehensive understanding of population structure across the North Atlantic Ocean, we are working with collaborators to expand this data set across the Atlantic through the NOAA Atlantic Seafloor Partnership for Integrated Research and Exploration (ASPIRE) and European Union's Horizon 2020 (ATLAS) campaigns.

Aunins, A., Morrison, C. 2021. Assessment of eDNA as a biomonitoring tool for vulnerable North Atlantic deep-sea habitats. MBARI seminar series, 21 April.

HTS of targeted "barcode" loci in DNA extracted from marine environmental samples such as water and sediments (metabarcoding of environmental DNA, or eDNA) has recently exploded in popularity due to the ability to generate a taxonomic community profile that usually surpasses what is obtainable from using traditional monitoring methods in terms of biodiversity and detection of rare taxa. Indeed, given the existing poor biodiversity inventory of many marine habitats coupled with their high cost and difficulty of access, eDNA biomonitoring of these remote ecosystems is attractive if reliable taxonomic inventories are obtained for a modest cost and with little required sample material. As part of the Deep SEARCH (Deep Sea Exploration to Advance Research on Coral/Canyon/Cold Seep Habitats) project, we collected water samples from eight ROV *Jason II* dives using two identical 12L Niskin bottles at sites within canyon, cold-seep, and cold-water coral reef habitats along the U.S. Atlantic coast in April 2019. Use of an ROV

allowed controlled water sample collection near features of interest. Duplicate 1-L seawater samples filtered through a 0.2 µm Sterivex and 10 L of seawater filtered through a 0.8 µm cellulose nitrate filter were collected from each Niskin. Metabarcoding of microbial 16S rRNA, metazoan 18S rRNA, and mitochondrial 12S and cox1 sequences from eDNA extracted from water samples were performed on an Illumina MiSeq. The 1L and 10L samples recovered largely the same communities, suggesting the smaller volume is adequate for assessing community composition. Differentiation among habitats in both microbial and metazoan community structure evidenced through multiple ordination and comparative analyses was clear, with the strongest differentiation between the shallow (~200 m) and deep (~2,000 m) cold-seep habitats. The implications of our findings for biomonitoring in the deep sea, as well as plans for expanding our analyses to include other barcode loci, water-column eDNA samples collected via CTD, and reference database augmentation through genome skimming will be discussed.

Morrison, C.L., Aunins, A.W. 2020. Applications of Genomic Tools for Enhanced Management of Deep-sea Biological Resources. USGS-BOEM Information Exchange seminar, November, 2020.

Effective biodiversity assessment and management requires an understanding of fundamental features of geographical distributions of organisms along with roles they play in ecosystem processes and services. For organisms that inhabit deep-sea environments, biodiversity inventories often lag those in other environments due to cost and difficulty accessing and sampling these habitats. With the growing need for information regarding deep-sea benthic biological resources to guide potential management decisions associated with conventional and renewable energy and marine minerals, a variety of genomic tools are being applied to various marine samples (from tissues to water) to inform species identifications, biodiversity assessments, ecology, and food-web dynamics. This webinar exchange will provide examples of recent and on-going applications of genomics tools including phylogenomics, population genomics and environmental DNA (eDNA) metabarcoding that allow for maximum utility of deep-sea samples and rapid advancements in knowledge of various deep-sea habitats in U.S. waters. Opportunities to apply genomic tools to additional regions and habitats where resource management needs exist will be discussed.

Aunins, A., Morrison CL, Kellogg, C. 2020. Assessment of eDNA as a biomonitoring tool for vulnerable deep-sea habitats. GEOBON online conference, June.

HTS of targeted “barcode” loci in DNA extracted from marine environmental samples such as water and sediments (metabarcoding of environmental DNA, or eDNA) has exploded in popularity over the last few years due to the ability to generate a taxonomic community profile that usually surpasses what is obtainable from using traditional monitoring methods in terms of biodiversity and detection of rare taxa. Indeed, given the existing poor biodiversity inventory of many marine habitats coupled with their high cost and difficulty of access, eDNA biomonitoring of these remote ecosystems is attractive if reliable taxonomic inventories are obtained for a modest cost and with little required sample material. As part of the Deep SEARCH (Deep Sea Exploration to Advance Research on Coral/Canyon/Cold Seep Habitats) project, we collected water samples from eight ROV *Jason II* dives using two identical mounted 12L Niskin bottles at sites within canyon, cold-seep, and cold-water coral reef habitats along the U.S. Atlantic coast in April 2019. Use of an ROV allowed controlled water sample collection near features of interest. Duplicate samples of 1 L of seawater filtered through a 0.2 µm Sterivex and 10 L of seawater filtered through a 0.8 µm cellulose nitrate filters were collected from each Niskin. Metabarcoding of microbial 16S rRNA and metazoan 18S rRNA sequences from eDNA extracted from water samples were performed on an Illumina MiSeq. The 1L and 10L samples recovered largely the same communities on each dive and did not differ significantly in patterns of alpha richness. Differentiation among habitats in both microbial and metazoan community structure evidenced through multiple ordination and comparative analyses was clear, with the strongest differentiation between the shallow (~200 m) and deep (~2,000 m) cold-seep habitats. The implications of our findings for biomonitoring in the deep sea, as well as plans for

expanding our analyses to include other barcode loci and water-column samples collected via CTD, will be discussed.

Aunins, A.W., Morrison, C.L., Kellogg, C.A. 2020. Assessing deep-sea marine metazoan and bacterial community structure in cold-seep, canyon, and cold-water coral reef habitats using high-throughput sequencing of DNA extracted from water samples. Poster presentation, 2020 Ocean Sciences Meeting, San Diego, CA

HTS of targeted "barcode" loci in DNA extracted from marine environmental samples such as water and sediments (metabarcoding of environmental DNA, or eDNA) has exploded in popularity over the last few years due to the ability to generate a taxonomic community profile that usually surpasses what is obtainable from using traditional monitoring methods in terms of biodiversity and detection of rare taxa. Indeed, given the poor biodiversity inventory of many marine habitats coupled with their high cost and difficulty of access, eDNA biomonitoring of these remote ecosystems is attractive if it can reliably inventory the taxa present for a modest cost and with little required sample material. Most applications of metabarcoding to deep-sea environments such as canyons to date have utilized sediments, though the use of water sampling is increasing. As part of the Deep SEARCH (Deep Sea Exploration to Advance Research on Coral/Canyon/Cold Seep Habitats) project, we collected water samples from among 10 ROV *Jason II* dives using two identical mounted Niskin bottles at sites within canyon, cold-seep, and coral reef habitats along the U.S. Atlantic coast in April 2019. Use of an ROV allowed controlled water sample collection near features of interest. One- and 10-L samples of seawater were filtered through separate 0.2 µm Sterivex filters from each Niskin, as well as 10 L of water filtered through 0.8 µm glass fiber prefilters from each 10L Sterivex. Here, we discuss preliminary results of metazoan and bacterial metabarcoding efforts, providing insight into the impact of filter pore size and volume of water filtered on the community recovered, as well as baseline levels of biodiversity of the habitats sampled. In addition, we describe progress on building a mitogenomic reference database to assist with both taxonomic assignment and new metabarcoding primer design.

Cantwell, K., Morrison, C., Weinnig, A., White, M., Wagner A., Sautter, L. 2020. Windows to the Deep: new discoveries from two years of exploration on the Southeastern US continental margin. 2020 Ocean Sciences Meeting, San Diego, CA, 18 February.

The waters offshore the SEUS are some of the least explored areas on the US East Coast. This region has a unique continental margin- including the extensive Blake Plateau, yet has major gaps in bathymetry data and contains numerous benthic features that are poorly understood. During 2018–2019, NOAA's Office of Ocean Exploration and Research (OER) and partners sponsored six mapping and ROV cruises onboard NOAA Ship *Okeanos Explorer* as part of the Atlantic Seafloor Partnership for Integrated Research and Exploration (ASPIRE). These expeditions (EX1805, EX1806, EX1903 L1 & L2, EX1906, EX1907) have changed what we know about the biota and offshore resources of this region. Multibeam bathymetry revealed previously unknown intraslope terraces, karstic features, unusually flat seafloor terrain when compared to predictions made by satellite altimetry, and the geographic distribution of numerous biogenic mounds on the Blake Plateau. ROV dives (250–3,500 m) surveyed minimally explored features, including giant bedforms, coral mounds, submarine canyons and landslides, and cold seeps, which provide a variety of habitat types for benthic and mobile fauna. Many exciting observations were made- diverse and high diversity coral and sponge communities including one of the largest deep-sea coral reef habitats found to date in US waters, life-history and dramatic predation events, species range extensions and sightings of rare species, and unusual fluid seepage at a seep site. Data from these expeditions are now publicly available to the science community and resource managers for additional analysis. Through 2021, NOAA and partners will continue to support ocean exploration efforts to address outstanding bathymetry gaps and science priorities in the region. This presentation will review new findings, provide context for future analysis, and demonstrate the value of collaborative community-driven exploration to address a range of science and resource management priorities.

Morrison, C.L., Aunins, A., Lunden J.J., Brooke, S., Ross, S.W. 2020. Depth-related barriers to genetic connectivity among northwestern Atlantic Lophelia pertusa populations. 2020 Ocean Sciences Meeting, San Diego, CA.

The cold-water coral *Lophelia pertusa* is a cosmopolitan species and a major constituent of deepwater coral banks in the northwestern Atlantic Ocean. Extrapolation from recent multibeam mapping data and visual observations revealed a greater extent of deep-coral habitat off the southeastern U.S. coast than previously known. Knowledge regarding the degree of connectivity between *L. pertusa* populations off the SEUS coast and the GOM is imperative to effective management and mitigation efforts given that the degree of connectivity will influence the stability of populations over time (resilience) as well as their probability of recovery from potential anthropogenic impacts. Recent *L. pertusa* collections expanded the geographic coverage (waters off Florida through the mid-Atlantic) and depth range (215–800 m), allowing for a more thorough investigation into the forces that structure populations. Thirteen highly variable microsatellite markers were used to genotype over 400 samples *of L. pertusa* representing 14 deep reefs and canyon locations. Like previous analyses, discontinuity was detected between the GOM and Northwestern Atlantic populations offshore of the southeastern coast. However, weak yet significant genetic structuring was detected among *L. pertusa* locations off the southeastern coast, suggesting limited connectivity. An isolation-by-depth pattern of gene flow was supported, with genetic distinction apparent among populations shallower and deeper than 500 m, which may be explained by different water masses these populations experience. To expand the geographic scope of connectivity analyses and improve predictions and decision making leading to wise resource management across the North Atlantic Ocean, RAD-seq will be coordinated through the NOAA Atlantic Seafloor Partnership for Integrated Research and Exploration (ASPIRE) and European Union's Horizon 2020 (ATLAS) campaigns.

Zilberberg, C., Leocorney, P., Kitahara, M.V., Morrison, C., Capel, K.C.C. 2019. Genetic diversity and connectivity of the corals Lophelia pertusa, Solenosmilia variabilis and Madrepora oculata in the Southwestern Atlantic. Oral presentation at the 7th International Deep-Sea Coral Symposium, Cartegena, Colombia, 31 July, 2019.

Deepwater coral reefs are highly diverse ecosystems, which have been suffering from anthropogenic impacts. High levels of genetic diversity and connectivity are often related to the ability of a population to persist large impacts, increasing the resilience of the population. The scleractinian corals Lophelia pertusa, Solenosmilia variabilis and Madrepora oculata are cosmopolitan species and also the most important Brazilian deepwater reef builders. The present study aims to evaluate levels of genetic diversity and connectivity of these three species at three basins in the southeastern coast of Brazil (Santos, Campos and Espírito Santo), ranging over 600 km and including samples from approximately 200 to 1120 m depth, collected by SENSIMAR project -PETROBRAS. Levels of genetic diversity, estimated by five microsatellite loci for each species, differed among species, with *L. pertusa* having the highest level, followed by M. oculata and S. variabilis. The lowest diversity of S. variabilis could be a consequence of the use of heterologous primers. Even with high levels of genetic diversity, heterozygous deficiencies were found for all species at most basins. Bayesian analyses of genetic structure suggest that there are two structured populations of L. pertusa, with no clear geographic pattern. For M. oculata, however, analyses suggest three genetic clusters, with one possibly being depth related. Contrasting to the other two species, no evidence of genetic structure was found for S. variabilis, suggesting one single panmictic population for this species. The present study is the first to evaluate levels of genetic diversity and connectivity of deepwater coral populations in the southwestern Atlantic and shows that within the same region, divergent levels of genetic diversity and connectivity can be found among different species.

Morrison, C.L. The exploration of coral banks off the SE US Coast. Invited seminar, College of Charleston, 8 April 2019

The 2018 field season was exciting for scientists involved in a multi-agency (USGS, BOEM, NOAA) study of the little-known natural resources that exist off the United States' Southeast Coast. The study, called Deep SEARCH (Deep Sea Exploration and Research of Coral/Canyon/Seep Habitats), aims to improve our understanding of the distribution, ecology and geologic foundation of sensitive deep-sea habitats between 30 and 160 miles offshore of North and South Carolina and Georgia. Two research expeditions mapped close to 30,000 square kilometers of sea floor and explored several diverse and dynamic ecosystems using remotely operated and human-occupied vehicles. This seminar will focus on biogenic coral mounds, including a previously unknown and substantial linear array of mounds approximately 160 miles off the coast of South Carolina. A brief introduction to the Deep SEARCH project will be given, along with video and image highlights from these habitats in our own backyard.

Morrison, C.L. Windows to the Deep: Characterizing Vulnerable Ecosystems off the SE US Coast. LSC evening seminar, 27 March 2019

Members of the Leetown Science Center are involved in a study of the little-known deep-sea natural resources that exist off the United States' Southeast Coast. The study, called Deep SEARCH (Deep Sea Exploration and Research of Coral/Canyon/Seep Habitats), aims to improve our understanding of the distribution, ecology and geologic foundation of sensitive deep-sea habitats offshore of Virginia through Georgia. In 2018, two research expeditions explored several diverse and dynamic ecosystems using remotely operated and the *Alvin* human-occupied submersible. Interslope terraces, sedimented plains, slopes of submarine canyons, and biogenic coral mounds were characterized, including a substantial linear array of coral mounds approximately 160 miles off the coast of South Carolina. This seminar will highlight videos and images from these habitats, introducing the exciting biodiversity in our own backyard.

Morrison, C.L. Windows to the Deep: Characterizing Vulnerable Ecosystems off the SE US Coast. Invited webinar for NOAA Deep Sea Coral Research & Technology Program' coordination meeting, 28 March 2019

The 2018 field season was exciting for scientists involved in a multi-agency (USGS, BOEM, NOAA) study of the little-known natural resources that exist off the United States' Southeast Coast. The study, called Deep SEARCH (Deep Sea Exploration and Research of Coral/Canyon/Seep Habitats), aims to improve our understanding of the distribution, ecology, and geologic foundation of sensitive deep-sea habitats between 30 and 160 miles offshore of North and South Carolina and Georgia. Two research expeditions mapped close to 30,000 square kilometers of sea floor and explored several diverse and dynamic ecosystems using remotely operated and human-occupied vehicles. This seminar will focus on recent submersible and ROV dives at biogenic coral mounds, including a previously unknown and substantial linear array of mounds approximately 160 miles off the coast of South Carolina. A brief introduction to the Deep SEARCH project will be given, along with video and image highlights from these dives that highlight the biology observed.

Morrison, C.L., 2019, Putting an extensive and previously undetected Lophelia reef into context: Genetic connectivity among Northwestern Atlantic Lophelia populations. ASLO Aquatic Sciences Meeting, Special Symposium "Turning the Lights on for Deep-sea Ecosystems in the Caribbean, Gulf of Mexico, and U.S. S.E. Atlantic", San Juan, Puerto Rico, Feb. 2019.

Multibeam mapping data collected during May and June of 2018 by the NOAA Ship *Okeanos Explorer* revealed extensive mound and ridge features on the seafloor in the northwestern Atlantic Ocean near Richardson Hills, approximately 160 miles East of Charleston, SC. Recent visual inspection of these

features by ROV (Deep Discoverer; NOAA) and Human Occupied Vehicle (*Alvin*; Woods Hole Oceanographic Institution) suggests that mound formation has been driven by the dominant reef-building deep-sea coral *Lophelia pertusa*. However, the Richardson Hills mounds lie outside a protected area designated as Coral Habitat Areas of Particular Concern. Knowledge regarding the extent of larval exchange between the Richardson Hills *L. pertusa* population and others off the southeastern U.S. coast and the GOM is imperative to effective management and mitigation efforts given that the degree of connectivity will influence the stability of populations over time (resilience) as well as their probability of recovery from potential anthropogenic impacts. Population structuring was assessed using 14 highly variable microsatellite markers and over 400 samples *of L. pertusa* representing 14 deep reefs and canyon populations. Population genetic analyses indicate weak yet significant structuring and moderate gene flow. Among Atlantic populations, an isolation-by-distance pattern of gene flow was not supported. Instead, the Richardson Hills population shared the most genetic similarity with the Cape Lookout to the North and Miami Terrace to the South. Results will be discussed in terms of oceanographic conditions that may influence connectivity and resilience of these unique and fragile ecosystems.

Flood, R.D., Sautter, L.R., Morrison, C.L., 2019, ROV studies of abyssal furrows on the Blake Bahama Outer Ridge, ASLO Aquatic Sciences Meeting, Special Symposium "Turning the Lights on for Deep-sea Ecosystems in the Caribbean, Gulf of Mexico, and U.S. S.E. Atlantic", San Juan, Puerto Rico, Feb. 2019.

The Blake-Bahama Outer Ridge in the western North Atlantic is swept by the WBUC, a steady, southward-flowing deep current that is part of the Great Ocean Conveyor Belt. Furrow bed forms occur in several zones south and west of the Blake-Bahama Outer Ridge crest where there are regular, overlapping hyperbolic echoes. Features associated with furrows can occasionally be observed on surface-ship mulitbeam echosounders, but individual furrow troughs can be difficult to detect. One zone of irregular topography on multibeam maps is about 150 km wide, extends from 3 300 to 3 520 m water depth, and has irregular but linear features that appear to be aligned with bottom currents. The objective of EX1806 ROV Dive 03 was to determine if these bottom features were indeed furrows. The ROV measured seafloor elevation on an 840 m track and photographed the sea floor. The ROV crossed two distinct furrow troughs with rippled walls that were about 20-m wide, 3- to 5-m deep and spaced about 300 m apart. The furrow troughs are aligned parallel to the westward-flowing bottom current observed during the dive. Unusual aspects of these furrows are the irregular spacing and that elevations of adjacent trough floors and of adjacent inter-trough areas differ by 15 to 20 m. The larger-scale topography observed by the ROV was consistent with the multibeam data, although the smaller depressions related to the furrow troughs were not observed. Conclusions are that the furrow is a common bed form in parts of the continental margin, its form may be more complex in some areas and it may create local habitats.

Morrison, C.L., Sautter, L. 2019. Windows to the Deep: Characterizing Vulnerable Ecosystems off the Southeastern U.S. Coast. LSC Lunch & Learn Seminar, 13 February 2019.

The 2018 field season was exciting for scientists involved in a multi-agency (USGS, BOEM, NOAA) study of the little-known natural resources that exist off the United States' Southeast Coast. The study, called Deep SEARCH (Deep Sea Exploration and Research of Coral/Canyon/Seep Habitats), aims to improve our understanding of the distribution, ecology and geologic foundation of sensitive deep-sea habitats between 30 and 160 miles offshore of North and South Carolina and Georgia. Two research expeditions mapped close to 30,000 square kilometers of sea floor and explored several diverse and dynamic ecosystems using remotely operated and human-occupied vehicles. Interslope terraces, sedimented plains, slopes of submarine canyons, and biogenic coral mounds were characterized, including a previously unknown and substantial linear array of mounds approximately 160 miles off the coast of South Carolina. A brief introduction to the Deep SEARCH project will be given, along with video and image highlights from these habitats in our own backyard.

Data Releases:

Morrison CL, Coykendall DK, Cornman RS. Molecular characterization of deep-sea bathymodiolin mussels and gill symbionts from the U.S. mid-Atlantic margin. US Geological Survey data release; 2019. https://doi.org/10.5066/F7HX1BZN

Other:

Dissertation:

2020, **A. Weinnig**: (Temple University)

Thesis title: INDEPENDENT AND INTERACTING EFFECTS OF MULTIPLE ANTHROPOGENIC STRESSORS ON COLD-WATER CORALS, Morrison was committee member.

Cordes Presentation

Cordes. Invited Seminar. 2021. *Spatial management of offshore drilling to avoid impacts to vulnerable deep-sea ecosystems*. Online Webinar hosted by The Society for the Protection of Nature, Tel Aviv, Israel

Professor Erik Cordes from Temple University will present (in English) the risks to deep-sea habitats as a result of oil and gas explorations, and the required measures to mitigate those risks (emphasizing large safety-buffer zones). Erik will also present some case studies where risks' mitigation measures were successfully applied (20 minutes+ 5 minutes for Q&As).

Cordes. Invited Seminar. 2020. *Exploration of hydrocarbon seep ecosystems and their ties to the deep ocean and the blue economy*. NOAA/NOS Science Seminar Series. (virtual)

In recent years, new exploration technologies and techniques have revealed an abundance of hydrocarbon seeps along continental margins worldwide. With the increasing industrialization of the deep sea resulting from the development of the blue economy, the study and management of these ecosystems has become of paramount importance. In this seminar, we will review the methods used to discover locations of active oil and gas release from the seafloor and sample the communities associated with them in order to understand the relationships between the seeps and the surrounding deep ocean. We will then discuss how to apply this knowledge to the effective and sustainable management of these systems, with a focus on offshore energy development.

Cordes. Invited Seminar. 2020. Exploration to inform management of the blue economy and to protect hydrocarbon seep ecosystems. iAtlantic Webinar Series, EU iAtlantic Project

In recent years, new exploration technologies and techniques have revealed an abundance of hydrocarbon seeps along continental margins worldwide. With the increasing industrialization of the deep sea resulting from the development of the blue economy, the study and management of these ecosystems has become of paramount importance. In this seminar, we will review the methods used to discover locations of active oil and gas release from the seafloor and sample the communities associated with them in order to understand the relationships between the seeps and the surrounding deep ocean. We will then discuss how to apply this knowledge to the effective and sustainable management of these systems, with a focus on offshore energy development.

Cordes. Invited Seminar. 2020. Deep-Sea Exploration for Research, Assessment, and Management. Graduate School of Oceanography, University of Rhode Island, Narragansett, RI

[no abstract]

Cordes. Invited Participant. 2020. Habitat Protection and Ecosystem-Based Management Panel, South Atlantic Fisheries Management Council Meeting (virtual)

[no abstract]

Cordes. Invited Panelist. 2019. Community Impacts of Oil and Gas Development. SciLine workshop for journalists, State College, PA

[no abstract]

Cordes. Invited Plenary Speaker. 2019. What are the limits of deep-sea coral distribution? International Symposium on Deep-Sea Corals, Cartagena, Colombia

Through increased exploration and ocean floor mapping, we are discovering that deep-sea corals are everywhere. Octocoral and antipatharian colonies can appear on the smallest rocks (or nodules) down to abyssal depths. Scleractinian corals were thought to be limited by aragonite saturation state, but recent findings of solitary corals and even colonial forms in waters undersaturated with respect to aragonite challenge that notion. There are correlations between coral distribution and other oceanographic conditions (including temperature, dissolved oxygen, food availability, water mass boundaries, etc.) but what is the relative significance of these factors and how are they affected by the geomorphology of the habitat? Are the more haphazard biological processes of reproduction, dispersal, and recruitment more significant than these oceanographic conditions? Are there other important interspecific biological interactions that we are still not taking into account? Even once a coral arrives and begins to grow, under what conditions can the transition occur from isolated individuals to assemblages and interacting communities of coral gardens and cold-water coral mounds? We will discuss recent studies that address some of these questions and explore the information required to answer others.

Cordes. 2019. Oral Presentation. Discovery of an extensive coral reef ecosystem off of the US Southeast Atlantic coast. ASLO Aquatic Sciences Meeting, San Juan, Puerto Rico.

Coral reefs are iconic ecosystems that support high biomass and diversity in generally nutrient-poor regions of the world's oceans. In the deep ocean, corals reefs exist but their distributions are poorly understood. Recent mapping efforts by the NOAA Ship *Okeanos Explorer* followed by additional mapping by the RV *Atlantis* revealed linear features composed of a series of low-lying mounds that had gone unnoticed in previous, coarser-resolution surveys. Additional mapping was accomplished by the RV *Atlantis*. Three dives were made to the area, one with the ROV Deep Discoverer and two with the *Alvin*. On all of these dives, the substrate was entirely composed of coral skeleton—a mix of coral rubble, standing dead coral, and live coral cover primarily near the crests of the mounds. From these observations, it was determined that the linear features were composed of a series of coral reefs totaling approximately 200 km in length within the 1,200 km^2 area where the reefs reside. Predictive habitat models based on existing data placed a low probability of live scleractinian corals in the area. Models including the new observations indicate that areas of the seafloor that were previously overlooked are highly likely to support additional coral habitats. Numerous human interests intersect with this newly discovered reef habitat, including fisheries and potentially oil and gas development. Potential exploitation of these resources necessitates further exploration of these features and other unmapped areas of the seafloor.

Cordes. 2018. Invited Seminar. Bringing light to the depths of the ocean. University of New Hampshire, Durham, NH

[no abstract]

Deep SEARCH_Gasbarro Abstracts

Gasbarro R, Margolin A, Sowers D, Quattrini A, McIver T, Saso E, Bourque J, Brooke S, Cordes EE (2022). Distribution, functional diversity and projections of climate impacts on the cold-water coral reef fauna of the Southeast USA. Ocean Sciences Meeting, Submitted for Oral Presentation.

Coral reefs support an array of ecosystem functions and a diverse associated fauna. On the deep seafloor (> 200 m depth), azooxanthellate CWCs exist in every ocean basin and form reefs and mound provinces spanning hundreds of kilometers with diversity that rivals shallow-water reefs. Despite this, the ecological niches of CWC-associated fauna and their distribution remain poorly resolved, limiting first-order estimations of biodiversity and potential impacts of climate change. Since 2018, numerous expeditions have built upon baseline efforts in the SEUS, expanding the area of bathymetry and visual surveys and confirming the presence of reef tracts and tens of thousands of apparent CWC mounds. Here, we synthesize biological, oceanographic, and terrain data collected during these surveys with regional climate model data to build joint species distribution models for CWC-associated fauna in a Hierarchical Modeling of Species Communities framework. We provide the first margin-wide, high-resolution predictions of (i) presence, abundance, and diversity of CWC-associated taxa (ii) functional diversity and the relative abundance of traits affecting ecosystem functioning (e.g., filter feeding) (iii) the importance of species associations in shaping CWC communities (iv) unique biotopes via classification and (v) comparisons of the above across taxonomic groups and size classes. By calculating the local contribution to beta diversity at each mapped grid cell, our results support coral mounds and other geomorphological features as regionally important biodiversity reservoirs. Projections of our models to 2100 reveal the potential for negative impacts of climate change on the SEUS CWC reef fauna, including habitat compression, range shifts, and diversity declines. Our results have important implications for offshore resource management, and for estimations of the nutrient storage and fluxes within and across CWC ecosystems now and in the future.

Gasbarro R, Margolin A, Sowers D, Cordes EE (2021). Suitable habitat and depth-driven climate refugia for *Lophelia pertusa* on the southeastern US margin. Deep-Sea Biology Symposium. Poster Presentation. Brest, France.

Reef-forming corals on the deep seafloor support numerous ecosystem functions and harbor a diverse and abundant associate fauna, yet their ecological niche boundaries and spatial distribution remain poorly resolved. In 2018-19, mapping expeditions and submersible dives on the US Atlantic margin confirmed the presence of numerous sites hosting rich coral reef ecosystems where previous, coarser predictive models placed a low probability for suitable coral habitat. Here, we use these newly acquired bathymetry and coral distribution data to create ensemble habitat suitability models for both the presence and abundance (% cover) of *Lophelia pertusa*, the primary reef-forming species in the region. In addition, we use the latest global climate data from the IPCC's Climate Model Intercomparison Project to project the distribution and abundance of the species from present-day to 2050 and 2100 in four emissions scenarios ranging from a 'sustainable future' to 'business-as-usual.' Our results suggest that the deeper, more eastward sites in the region may act as spatial climate-change refugia for *L. pertusa*, and that this deep refugia effect will be more pronounced in higher emissions scenarios. While the present-day model extends the known distribution of *L. pertusa*, the climate projections predict some degree of range contraction regardless of scenario. Using megafaunal data generated from video annotation of 14 submersible dives in the region, we also create joint species distribution models to predict functional diversity shifts with climate change and the concomitant decline in live coral cover. These novel first-order estimates presented of climate-driven declines in *L. pertusa* and the downstream effects on associate biodiversity will be key in prioritizing areas for management, exploration, and in creating energy budgets for this highly productive region.

Gasbarro R (2021). Climate Change & Corals in the Deep Western North Atlantic. Mid-Atlantic Regional Council on the Ocean. Webinar.

No abstract available—discussion of cold-water coral habitats on the Atlantic margin and the potential effects of climate change on their extent and persistence.

Gasbarro R, Margolin A, Sowers D, Cordes EE (2020). Lophelia pertusa on the southeast US margin: distribution, abundance, and potential climate refugia. Deep-Sea Biology Symposium. Oral Presentation. Virtual.

Coral reefs support key ecosystem processes and harbor an abundant and diverse fauna, yet their ecological niche and distribution on the deep (> 200 m) seafloor remain poorly understood. Recent mapping expeditions and submersible dives on the US Atlantic margin have confirmed the presence of numerous coral mounds and linear reef structures that were not detected in coarser-resolution surveys. Previous predictive habitat models for scleractinians placed a low probability of corals in much of this area. Here, we use these newly acquired bathymetry and coral distribution data to create predictive habitat models both for the presence and abundance (% cover) of *Lophelia pertusa*, the primary reef-forming species. In addition, the distribution of coral mounds in two different regions was estimated using a pixel-based, semi-automated classification method. Our results suggest that large swaths of seafloor surrounding the new observations that are likely to support scleractinians. We also test the validity of the model by projecting it onto two sites surveyed on subsequent ROV dives and assessing model performance in predicting *L. pertusa* presence and abundance. Notably, these areas are outside of the Mid-Atlantic Fisheries Management Council Deep-Sea Coral Habitat Areas of Particular Concern (HAPC) and may represent climate refugia for reef-building corals due to their location eastward of the main axis of the Gulf Stream. We test this climate refugia hypothesis using data from multiple climate-change scenarios. These models represent an extension of the realized niche of this species, and may aid in conservation and exploration efforts through prediction of other of *L. pertusa* presence, abundance, and climate refugia.

Gasbarro R, Lunden J, Cordes EE (2020). Drivers of Lophelia pertusa distribution on the mid-US Atlantic margin revealed by habitat suitability modeling at multiple scales. Oral Presentation. Ocean Sciences Meeting. San Diego, CA, USA.

Coral reefs support key ecosystem processes and harbor an abundant and diverse fauna, yet their ecological niche and distribution on the deep (> 200 m) seafloor remain poorly understood. Recent mapping expeditions and submersible dives on the the U.S. Atlantic margin have confirmed the presence of numerous coral mounds and linear reef structures that were not detected in coarser-resolution surveys. Previous predictive habitat models for scleractinians placed a low probability of corals in much of this area. Here, we use these newly acquired bathymetry and coral distribution data, in conjunction with regional mapping products and NOAA deep-sea coral records, to create predictive habitat models for *Lophelia pertusa*, the primary reef-forming species. In addition, the density of carbonate mounds in two different regions was estimated using a pixel-based, semi-automated classification method. The models indicate large swaths of seafloor surrounding the new observations that are likely to support scleractinians. We also test the validity of the model by projecting it onto two sites surveyed on subsequent ROV dives. The model performed well at both of these sites, predicting the distribution of observed *L. pertusa*. Notably, these areas are outside of the Mid-Atlantic Fisheries Management Council Deep-Sea Coral Habitat Areas of Particular Concern (HAPC) and may represent climate refugia for reef-building corals. These models represent an extension of the realized niche for this species, and may aid in conservation and exploration efforts through prediction of other areas of *L. pertusa* presence.

Jay Lunden

2020 Lunden, J.J., F. Mienis, R. Gasbarro, A. Hallaj, A. Keller, A.W.J. Demopoulos, M. Joye, & E.E. Cordes. "Spatio-Temporal Oceanographic Variability at Deep-Sea Coral Sites along the U.S. Atlantic Margin. 2020 Ocean Sciences Meeting, San Diego, CA. 18 Feb. Oral.

2019 Lunden, J.J., A. Keller, A.W.J. Demopoulos, M. Joye, & E.E. Cordes. "Regional Oceanographic Influences on Specialized Deep-Sea Ecosystems along the U.S. Atlantic Margin." 2019 Aquatic Sciences Meeting; San Juan, PR. 20 Feb. Oral

Lunden et al ASLO 2020_final

SPATIO-TEMPORAL OCEANOGRAPHIC VARIABILITY AT Deep-SEA CORAL SITES ALONG THE U.S. ATLANTIC MARGIN

Jay Lunden[1], Ryan Gasbarro[1], Adam Hallaj[1], Abigail Keller[1], Furu Mienis[2], Erik Cordes[1]

[1]Department of Biology, Temple University, Philadelphia PA USA

[2]Royal Netherlands Institute for Sea Research and Utrecht University, Netherlands

In recent years, several collaborative projects under the ASPIRE campaign have sought to enhance our understanding of the occurrence and distribution of deep-sea corals within US waters. Notably, fieldwork conducted by both the Deep SEARCH program and the *Okeanos Explorer* has resulted in the repeated collection of oceanographic data at multiple locations across a deep-sea coral province along the SEUS margin at depths to ~1,000 m. Since 2018, six cruises have visited sites in the region between April and October, with each making CTD deployments and sampling water to characterize the water column overlying the deep-sea coral province. Coupled with long-term deployments (>6 months) of benthic landers, our understanding of the oceanographic influences on the benthos has significantly increased. Generally, deep-sea coral sites within the region are heavily influenced by western North Atlantic Central Water (100–500-m depth) and Western Atlantic Subarctic Intermediate Water (500–1,500 m depth). However, variability in several oceanographic properties, including temperature, salinity, and dissolved oxygen was observed over daily to seasonal scales. Notably, deep-sea coral sites in the region experience considerable variation in oxygen saturation, ranging from a high of > 300 $\mu mol \cdot kg^{-1}$ in the spring months (April–May) to a low of 160 $\mu mol \cdot kg^{-1}$ in the summer (August); furthermore, the coral sites are influenced by strong currents and large fluctuations in temperature (± 6°C) were observed down to 800 m depth during events (days–weeks). This variability is likely due to several factors, including meandering of the Gulf Stream, potential intrusion of fresh groundwater, and the influence of Arctic Intermediate Water on the Blake Plateau. Ultimately, the results of this study contribute to our understanding of the niche in which deep-sea corals thrive and emphasizes the significance of interdisciplinary collaboration to collect repeated datasets in deepwater habitats.

Jennifer Miksis-Olds – Publications

Publications

Wilford, DC, Miksis-Olds, JL, Martin, SB, Howard, DR, Lowell, K, Lyons, AP, Smith, MJ. (2021). Quantitative Soundscape Analysis to Understand Multidimensional Features. Frontiers in Marine Science, 8: 672336. doi:10.3389/fmars.2021.672336

Wilford, DC (2021). Quantification of marine acoustic environments. MS Thesis. University of New Hampshire.

Presentations

Miksis-Olds, J, Wilford, D, Martin, J (2019). Atlantic Deepwater Ecosystem Observatory Network soundscapes of deep-sea habitats. 5th Underwater Acoustics Conference & Exhibition. Crete, Greece. 30 June - July 5.

Rhoads, AC, Mienis, F, Lunden, J, Miksis-Olds, J, Wilford, D, Davies, A (2020). Variability in soundscape and environmental conditions at a Southeastern Atlantic cold-water coral reef. eDeep-Sea Biology Society Conference. Virtual Meeting. August 20-21.

Kellogg-Deep SEARCH Products

Presentations

Kellogg, C.A. and Z.A. Pratte, 2021, Surprising diversity of Endozoicomonas in deep-sea corals. Joint Florida-Southeastern Branches of the American Society for Microbiology virtual meeting, online, March 25-26, 2021.

The deep ocean hosts a large diversity of azooxanthellate cold-water corals whose associated microbiomes remain to be described. While the bacterial genus *Endozoicomonas* has been widely identified as a dominant associate of tropical and temperate corals, it has rarely been detected in deep-sea corals. Determining microbial baselines for these cold-water corals is a critical first step to understanding the ecosystem services their microbiomes contribute, while providing a benchmark against which to measure responses to environmental change or anthropogenic impacts. Samples of *Acanthogorgia aspera*, *A. spissa*, *Desmophyllum dianthus* and *Lophelia pertusa* (*Desmophyllum pertusum*) were collected from western Atlantic sites off the US East Coast and the northeastern GOM. Microbiomes were characterized by 16S rRNA gene amplicon surveys. Although *D. dianthus* and *L. pertusa* have been combined into a single genus due to their genetic similarity, their microbiomes were significantly different. Interestingly, the *L. pertusa* from two Atlantic sites were unlike *L. pertusa* from around the world because their microbiome was dominated by distinct *Endozoicomonas*. The *Acanthogorgia* species were collected from submarine canyons in different geographic regions, but their microbiomes were extremely similar and also dominated by *Endozoicomonas*. This is the first report of coral microbiomes dominated by *Endozoicomonas* occurring below 1,000 meters, at temperatures near 4°C.

Kellogg, C.A., 2021, Comparison of the microbiomes of three deep-sea scleractinian corals. 14th International Coral Reef Symposium, Virtual, July 18-23, 2021.

While previous microbiome research has focused on *Lophelia pertusa*, a widely distributed cold-water scleractinian that can create large three-dimensional bioherms in the deep ocean, attention to other stony corals in the deep sea lags behind. Our objectives were to capture baseline microbiome information for two additional cold-water scleractinian species, *Desmophyllum dianthus* and *Enallopsammia profunda*, and then conduct direct comparisons across the three corals' microbiomes to tease apart questions about drivers of similarity and dissimilarity in microbiome composition. We collected samples of *L. pertusa*, *D. dianthus*, and *E. profunda* from the western Atlantic during 2017–2019 as part of the Deep SEARCH research effort. We were able to obtain *L. pertusa* from sites at 5°C, 7°C, and 11°C to investigate temperature effects on its microbiome. Further, we were able to collect an orange morph as well as the dominant (in this area) white morph of *L. pertusa*, and both white and yellow morphs of *E. profunda*. Finally, we specifically chose *D. dianthus* in order to address the taxonomic topic of combining *L. pertusa* and *D. dianthus* into a single genus based on genetic information in spite of the two corals being extremely morphologically different (branching colonial vs. single polyp cup). Microbial community DNA was extracted using the Qiagen DNeasy PowerBiofilm kit and amplicon libraries of 16S rRNA genes were generated using V4 primers and version 2 chemistry on an Illumina MiSeq. Additionally, DNA samples were applied to functional gene microarrays to provide information about carbon-,

nitrogen-, and sulfur-cycling abilities within these corals' microbiomes. The host coral is typically the strongest driver of microbiome composition, but having directly comparable data from these three abundant and often co-occurring cold-water corals allows us to address questions both between and within the corals about the effects of temperature, depth (as a proxy for differences in food quality/quantity), and color morphs on microbiome composition both within and between the coral species. This information is foundational to our efforts to understand the role microbiome composition plays in coral susceptibility or resilience to environmental change or disease.

Lectures [no associated abstracts]

2021, Coral Microbial Ecology: From Snorkeling to Submersibles, University of Miami, Department of Biology Seminar Series (via Internet), November 15, 2021 (Invited speaker)

2021, The Importance of Benchmark Microbiomes for Deep-Sea Coral Management (and the Bonus of Unexpected Discoveries!), USGS-BOEM Science Exchange, (via Internet), Sept 16, 2021

2020, Microbial Diversity of Deep-Sea Corals, Manchester University, Marine Biology class, Manchester, IN (via Internet), Sept 25, 2020

2020, Microbial Diversity of Deep-Sea Corals, Ivybridge University of the Third Age (U3A), Devon, England (via Internet), July 22, 2020

2020, Deep-sea coral microbiomes as a source for novel natural products, Marine Natural Products Gordon Research Conference, Ventura, CA, February 27, 2020 (Invited speaker)

Journal articles

Pratte, Z.A. and C.A. Kellogg (2021) Comparison of Preservation and Extraction Methods on Five Taxonomically Disparate Coral Microbiomes Frontiers in Marine Science 8:684161 DOI: 10.3389/fmars.2021.684161

All animals are host to a multitude of microorganisms that are essential to the animal's health. Host-associated microbes have been shown to defend against potential pathogens, provide essential nutrients, interact with the host's immune system, and even regulate mood. However, it can be difficult to preserve and obtain nucleic acids from some host-associated microbiomes, making studying their microbial communities challenging. Corals are an example of this, in part due to their potentially remote, underwater locations, their thick surface mucopolysaccharide layer, and various inherent molecular inhibitors. This study examined three different preservatives (RNAlater, DNA/RNA Shield, and liquid nitrogen) and two extraction methods (the Qiagen PowerBiofilm kit and the Promega Maxwell RBC kit with modifications) to determine if there was an optimum combination for examining the coral microbiome. These methods were employed across taxonomically diverse coral species, including deep-sea/shallow, stony/soft, and zooxanthellate/azooxanthellate: *Lophelia pertusa*, *Paragorgia johnsoni*, *Montastraea cavernosa*, *Porites astreoides*, and *Stephanocoenia intersepta*. Although significant differences were found between preservative types and extraction methods, these differences were subtle, and varied in nature from coral species to coral species. Differences between coral species were far more profound than those detected between preservative or extraction method. We suggest that the preservative types presented here and extraction methods using a bead-beating step provide enough consistency to compare coral microbiomes across various studies, as long as subtle differences in microbial communities are attributed to dissimilar methodologies. Additionally, the inclusion of internal controls such as a mock community and extraction blanks can help provide context regarding data quality, improving downstream analyses.

Kellogg, C.A. and Z.A. Pratte (2021) Unexpected diversity of Endozoicomonas in deep-sea corals. MEPS 673:1-15. DOI 10.3354/meps13844

The deep ocean hosts a large diversity of azooxanthellate cold-water corals whose associated microbiomes remain to be described. While the bacterial genus Endozoicomonas has been widely identified as a dominant associate of tropical and temperate corals, it has rarely been detected in deep- sea corals. Determining microbial baselines for these cold-water corals is a critical first step to understanding the ecosystem services their microbiomes contribute, while providing a benchmark against which to measure responses to environmental change or anthropogenic effects. Samples of *Acanthogorgia aspera*, *A. spissa*, *Desmophyllum dianthus*, and *D. pertusum (Lophelia pertusa*) were collected from western Atlantic sites off the US East Coast and from the northeastern GOM. Microbiomes were characterized by 16S rRNA gene amplicon surveys. Although *D. dianthus* and *D. pertusum* have recently been combined into a single genus due to their genetic similarity, their microbiomes were distinctly different. The *Acanthogorgia* spp. were collected from submarine canyons in different regions, but their microbiomes were extremely similar and dominated by Endozoicomonas. This is the first report of coral microbiomes dominated by Endozoicomonas occurring below 1,000 m, at temperatures near 4°C. *D. pertusum* from two Atlantic sites were also dominated by distinct Endozoicomonas, unlike D. pertusum from other sites described in previous studies, including the GOM, the Mediterranean Sea, and a Norwegian fjord.

Data releases

Kellogg, C.A., D.B. Goldsmith, and J.J. Voelschow (2021). Coral microbiome preservation and extraction method comparison—raw data. US Geological Survey data release. http://dx.doi.org/10.5066/P96GBWDM

The files in this data release are the raw 16S rRNA gene amplicon DNA sequence files from 90 samples of tropical and cold-water corals, as well as sequence files from a mock community and extraction blanks for the kits used for DNA extraction. The tropical coral samples (three species) were collected under permit FKNMS-2017-064 (Kellogg) in March 2018 from a nursery in the Florida Keys National Marine Sanctuary and temporarily housed at the facility of Mote Marine Laboratory & Aquarium's Elizabeth Moore International Center for Coral Reef Research & Restoration in Summerland Key, Florida (FL). The cold-water coral samples (two species) were collected in August 2018 from two locations in the Atlantic Ocean (Pamlico Canyon and Richardson Hills). The purpose of this experiment was to compare preservation and DNA extraction methods across tropical and cold-water corals. Three preservation methods were employed: RNAlater, DNA/RNA Shield, and flash-freezing in liquid nitrogen.

Extraction of DNA from the samples occurred at the Coral Microbial Ecology Laboratory in St. Petersburg, FL using the Qiagen DNeasy PowerBiofilm DNA Isolation Kit and the Promega Maxwell RSC Blood DNA kit . Library preparation and DNA sequencing were conducted by Glomics, Inc. (Norman, Oklahoma) using primers 515F/806RB to target the V4 variable region of the 16S rRNA gene on a MiSeq sequencing system with v2 chemistry to obtain paired-end 250-bp reads. The raw data files associated with this data release have also been submitted to the NCBI Sequence Read Archive under BioProject number PRJNA544686. For more information, please see the README file and metadata files.

Pratte, Z.A., and Kellogg, C.A, 2021, Comparison of preservation and extraction methods on five taxonomically disparate coral microbiomes: Frontiers in Marine Science, https://doi.org/10.3389/fmars.2021.684161.

Kellogg, C.A. and J.J. Voelschow (2021) Cold-water coral microbiomes (Acanthogorgia spp. Desmophyllum dianthus, and Lophelia pertusa) from the Gulf of Mexico and Atlantic Ocean off the

southeast coast of the United States–raw data. US Geological Survey Data Release, https://doi.org/10.5066/P9Z1HPKR

The files in this data release are the raw 16S rRNA gene amplicon DNA sequence files from 28 samples of deep-sea corals *Acanthogorgia aspera, Acanthogorgia spissa, Desmophyllum dianthus,* and *Lophelia pertusa*, as well as an extraction blank for the Qiagen PowerBiofilm kit used for DNA extraction. The samples were collected during four research cruises from various locations in the GOM and the Atlantic Ocean off the US East Coast in deep-sea coral ecosystems from 2013 to 2019 for microbial analysis.

Extraction of DNA from the samples occurred at the USGS Coral Microbial Ecology Laboratory in St. Petersburg, FL, using Qiagen's DNeasy PowerBiofilm kit. PCR amplification and sequencing were performed by RTSF Genomics Core at Michigan State University using primers 341F/806R to target the V3-V4 region of the 16S rRNA gene on a MiSeq sequencing system with v2 chemistry to obtain paired-end 250-bp reads. The raw data files associated with this data release have also been submitted to the NCBI Sequence Read Archive under BioProject number PRJNA699458. For more information, please see the README file and metadata files.

Kellogg, C.A. and Pratte, Z.A., 2021, Unexpected diversity of *Endozoicomonas* in deep-sea corals: Marine Ecology Progress Series, v.673, article 13844, 15 p., https://doi.org/10.3354/meps13844.

U.S. Department of the Interior (DOI)
DOI protects and manages the Nation's natural resources and cultural heritage; provides scientific and other information about those resources; and honors the Nation's trust responsibilities or special commitments to American Indians, Alaska Natives, and affiliated island communities.

Bureau of Ocean Energy Management (BOEM)
BOEM's mission is to manage development of U.S. Outer Continental Shelf energy and mineral resources in an environmentally and economically responsible way.

BOEM Environmental Studies Program
The mission of the Environmental Studies Program is to provide the information needed to predict, assess, and manage impacts from offshore energy and marine mineral exploration, development, and production activities on human, marine, and coastal environments. The proposal, selection, research, review, collaboration, production, and dissemination of each of BOEM's Environmental Studies follows the DOI Code of Scientific and Scholarly Conduct, in support of a culture of scientific and professional integrity, as set out in the DOI Departmental Manual (305 DM 3).